Akihiro Sasoh · Toshiyuki Aoki
Masahide Katayama *Editors*

31st International Symposium on Shock Waves 2

Applications

Springer

31st International Symposium on Shock Waves 2

Akihiro Sasoh • Toshiyuki Aoki
Masahide Katayama
Editors

31st International Symposium on Shock Waves 2

Applications

Springer

Editors
Akihiro Sasoh
Department of Aerospace Engineering
Nagoya University
Nagoya, Japan

Masahide Katayama
Institute of Innovative Research
Tokyo Institute of Technology
Tokyo, Japan

Toshiyuki Aoki
Department of Energy
and Environmental Engineering
Kyushu University
Kasuga, Fukuoka, Japan

ISBN 978-3-319-91016-1 ISBN 978-3-319-91017-8 (eBook)
https://doi.org/10.1007/978-3-319-91017-8

Library of Congress Control Number: 2018965422

This Springer imprint is published by the registered company Springer Nature Switzerland AG.
The registered company address is: Gewerbestrasse 11, 6330 Cham, Switzerland

Preface

Shock wave is fascinating physical nature accompanied by various applications. The 31st International Symposium on Shock Waves (ISSW31) was a continuation in the series of sixty-year-lasting, biannual symposia on shock waves that have been held all over the world since 1957 at MIT, Boston, MA, USA. This is the third one held in Japan after ISSW18, which was held in Sendai in 1991 when the name of symposia was changed to the present one. Before that the tenth symposium was held in Kyoto in 1975. ISSW31 was held at Toyoda Auditorium, Nagoya University, Nagoya, Japan, during July 9–14, 2017.

ISSW31 was attended by 352 registered participants from 32 countries. Out of the participants 116 were graduate students. This large part of students, as large as one-third, should lead to promising future of our shock wave community. Student competition was conducted among 43 students who made an entry with submission of full paper by the deadline, which was about a month earlier than that for the other presentations. With respect to each candidate, his/her paper was evaluated by two referees, and presentation by another two. The top 12 students obtained an award that was offered by the International Shock Wave Institute (ISWI). Including 5 guests, 43 accompanying persons, 15 participants from sponsors, and 18 organizing staff, the ground total number of the participants was 433.

The International Advisory Committee (IAC) that consisted of 54 members from 21 countries chose 9 world-renowned scientists to deliver 9 invited plenary lectures in different shock wave–related disciplines. Unfortunately, one plenary lecture was cancelled due to the lecturer's problem. The invited plenary lectures included the traditional Paul Vieille Lecture in the opening session, which was given by Professor Zongling Jiang, Institute of Mechanics, Chinese Academy of Sciences, and the Irvine Israel Glass Lecture by Professor Kazuyoshi Takayama, Tohoku University. The inaugural Ray Stalker Lecture was planned to be presented by Professor Joanna Austin, California Institute of Technology, who unfortunately could not make it herself due to an urgent matter arising en-route. It was presented on her behalf by

Vince Wheatley from the University of Queensland. The other plenary lecturers were Prof. Oren Sadot, Prof. Dana D. Dlott, Dr. Nabiha Chaumeix, Prof. Noel T. Clemens, and Prof. Kazuhisa Fujita.

After reviewing 417 submitted abstracts by two independent reviewers to each, 287 and 103 were accepted for oral and poster presentations, respectively. Unfortunately, by the time the meeting started 96 accepted presentations were withdrawn due to failure of full paper submission, lack of travel funds, etc. Finally, 294 peer-reviewed contributed papers, 241 oral and 53 poster, were presented in addition to the plenary lectures. The oral sessions were held in parallel by either four or five. The sessions included five of "Supersonic and Hypersonic Flows" sessions, three of "Detonation and Combustion," "Richtmyer-Meshkov Instability" and "Diagnostics/Flow Visualization" sessions each, and two of "Shock Wave Reflection/Interaction," "Blast Waves," "Plasmas/Magnetohyrdrodynamics," "Shock/Boundary Layer Interaction," "Multiphase Flow" "Shock Waves in Internal Flows," "Shock Wave Interaction with Various Media," "Numerical Methods" sessions each.

Following the tradition of ISSW, several social programs offered opportunities for the participants to further develop scientific/personal communications and exchanges in more relaxed ways, which could induce serendipity, innovations, and international collaboration projects. The excursion participants visited Takayama, an old town, and Shirakawa-go, a World Heritage, historic village characterized by Gassho-zukuri, that is a steep-pitched, thatched roof designed to shed against heavy snow. Watching Ground Sumo Tournament and Shocking Sound Waves, concert by participants, were specially organized menus in this symposium. The accompanying persons' program on Monday was Inuyama Tour featured by Ukai watching. Thursday tour was to visit Toyota Commemorative Museum of Industry and Technology and Tokugawa Art Museum.

The arrangements for ISSW31 were well initiated with valuable advices from Professor Gabi Ben-Dor, Chair of ISSW30 in Tel Aviv. The ISSW31 was officially hosted by the Japan Society of Fluid Mechanics with financial support from Japan Society for the Promotion of Science as Grant-in-Aid for Publication of Scientific Research Results, KAKENHI, co-hosted by International Shock Wave Institute (ISWI), Shock Wave Research Society of Japan, and School of Engineering, Nagoya University. Also ISSW31 was co-sponsored by Society for Promotion of Space Science, Nagoya Convention & Visitors Bureau, Tokai Institute of Fluid and Heat Engineering, Nagoya University, Nobby Tech Ltd., nac Image Technology Inc., Photron Ltd., Shimadzu co., Beams Inc., USAC Inc., and Tokyo Instruments Inc. On behalf of my two co-chairs, Prof. Toshiyuki Aoki and Dr. Masahide Katayama, both of whom are vice presidents of Shock Wave Research Society of Japan, and the organizing committee, we thank all the participants, sponsors, and supporting societies/organizations, owing to whom this symposium was concluded to be a great success.

ISSW32 will be held in Singapore in July 2019 led by a team chaired by Professor Boo Cheong Khoo, National University of Singapore. The ISSW33 in 2021 will be held in Brisbane, co-hosted by the University of Queensland, the University of Southern Queensland, and the University of New South Wales in Canberra. The respective co-chairs are Richard Morgan, David Buttsworth, and Harald Kliene.

Co-Chairs, ISSW31

Nagoya, Japan — Akihiro Sasoh
Kasuga, Japan — Toshiyuki Aoki
Tokyo, Japan — Masahide Katayama

Contents

Volume II

Strength and Frequency of Underwater Shock Waves Related to Sterilization Effects on a Marine Bacterium

J. Wang, A. Abe, N. Ito, and K. Nishibayashi

Abstract The paper reported on a study of sterilization effects on marine *Vibrio* sp. under different strength and frequencies of underwater shock waves generated by electric discharges. Bio-experiments were carried out with the induced bubbles behind the underwater shock waves in a cylindrical water chamber. Propagation behaviors of the shock wave in the water chamber are analyzed using an axisymmetric numerical simulation, and pressure measurement is also carried out. The generation of the bubbles is investigated using an optical method. As a result, the marine bacteria are completely inactivated in a short time, and it is clarified that sterilization effect is closely related with the number density of bubbles, pressure, and frequencies of underwater shock waves.

1 Introduction

Underwater shock wave has been extensively applied in the fields of medical engineering, food sciences, material processing, and other industries. Abe et al. [1] proposed the application of underwater shock wave to the sterilization of ships' ballast water by using microbubble motion. To investigate the potential of this shock sterilization method, Wang and Abe [2] carried out a bio-experiment of marine *Vibrio* sp. using the underwater shock waves with a frequency of 1 Hz and the microbubbles produced by a bubble generator in a circular-flow water tank. They clarified a high sterilization effect in the presence of both the shock waves and microbubbles and also pointed out that cavitation bubbles generated behind the focus of the underwater shock wave showed a potential for the inactivation of

J. Wang (✉)
Key Laboratory for Mechanics in Fluid Solid Coupling Systems, Institute of Mechanics, Chinese Academy of Sciences, Beijing, China

School of Engineering Science, University of Chinese Academy of Sciences, Beijing, China

A. Abe · N. Ito · K. Nishibayashi
Graduate School of Maritime Sciences, Kobe University, Kobe, Japan

A. Sasoh et al. (eds.), *31st International Symposium on Shock Waves 2*,
https://doi.org/10.1007/978-3-319-91017-8_1

marine bacteria. Hence, they produced a cylindrical water chamber to understand the contribution of the cavitation bubbles to the sterilization [3]. Cavitation bubbles could be produced by the concentration of the reflected underwater shock waves at the wall of the cylindrical water chamber, and an effective sterilization was obtained in a short time. The sterilization mechanism of these cavitation bubbles is as follows: bubbles produced by the concentration of the underwater shock waves begin collapsing motion just after they interact with the reflected shock waves at the inner wall of the water chamber or the next coming shock waves. Eventually, rebound shock waves and free radicals are generated by the collapse of cavitation bubbles, and marine bacteria near the bubbles are killed biochemically and mechanically.

In the paper, to clarify sterilization effect of underwater shock waves with the induced bubbles, bio-experiments with marine *Vibrio* sp. are carried out under different conditions of electric discharges in a cylindrical water chamber. Propagation behaviors of the underwater shock wave are numerically analyzed using an axisymmetric TVD scheme. On the other hand, pressure measurement is also carried out at the central axis of the water chamber. In addition, an optical observation with a video camera is used to investigate the generation of bubbles in the water chamber. The sterilization effects are discussed using different strength and frequencies of the underwater shock waves.

2 Bio-Experimental Setup

Figure 1 shows a bio-experimental arrangement. Experimental devices consisted of a cylindrical water chamber [4], a high-voltage power supply generating the shock waves (HPS 18 K-A, Tamaoki Electronics Co., Ltd.), a pulse generator, and a system of pressure measurement including a fiber optical probe hydrophone (FOPH 2000) and an oscilloscope. This cylindrical water chamber consisted of two equivalent parts, namely, the upper part was a test chamber and the lower part was an electric discharge chamber. A silicone film of 0.1 mm thick was used to separate the two chambers. Cell experiments with marine *Vibrio* sp. were carried out in the test chamber. In the experiments, samples extracted from the water chamber was diluted

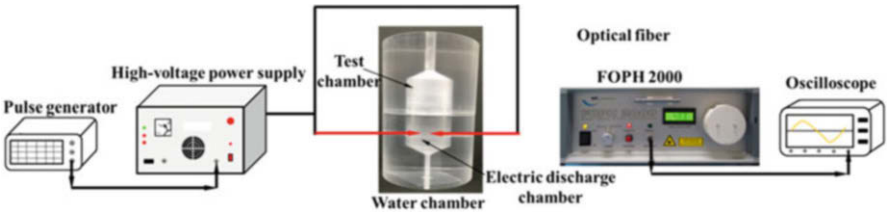

Fig. 1 Schematic of experimental setup with cylindrical water chamber

serially and then spread on agar plates. The plates were incubated for 24 h at 30 °C. Finally, the cell viability in 1 ml was evaluated by the numbers of colony-forming cells in agar plates on the basis of the dilution ratio.

3 Results and Discussion

Based on the study by Wang and Abe [3], an axisymmetric numerical simulation was used to analyze the propagation of an underwater shock wave in the cylindrical water chamber. This simulation code was executed by a second-order accurate implicit TVD finite differential scheme, and Tait equation was used as the equation of the state for water in this code. The underwater shock wave was generated by the instant release of high pressure in a small dense water sphere shown in Fig. 2 (1). The initial density ratio to the ambient, the initial pressure ratio, and the diameter of the water sphere were decided to 1.030, 728, and 3.5 mm in this simulation by comparison with the experimental pressure attenuation of a spherical expanding underwater shock wave in their study [3]. In Fig. 2 (2), the spherical underwater shock wave was propagating in the water chamber, reflected at the inner wall, and concentrated at the central axis. Next, it was found the concentrated shock waves propagated following negative pressure region, so that the tensile stress regions were clearly found behind that. Cavitation bubbles were thought to be generated in the tensile stress region.

Figure 3 shows time variations of the pressure obtained from experimental measurement and numerical analysis at 30 mm from the discharge point. The black line indicates the results of experimental data and the green line for the numerical analysis. In the figure, the first and second waves were found at the same timing between the experimental and numerical results, but they did not agree quantitatively. Furthermore, after 35 μs there was no coincidence between them. In particular, all the negative pressures were estimated to be larger in the numerical result. These quantitative differences were caused by the use of Tait equation, and cavitation generation was not assumed in this simulation. In the experimental profile, pressure of the second shock wave was lower than that of the first wave. The result was probably caused with the little movement of the discharge position

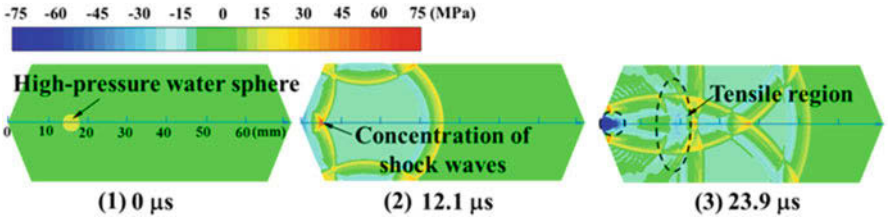

Fig. 2 Numerical pressure distribution in water chamber

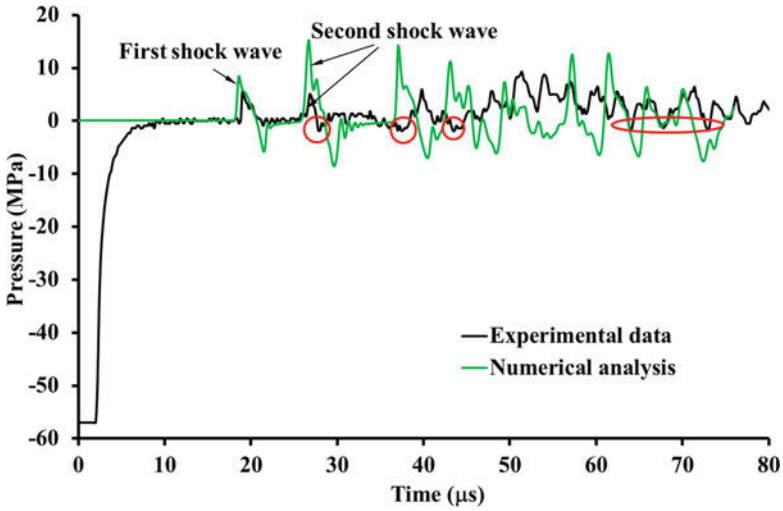

Fig. 3 Comparison of pressure records between experimental measurement and numerical analysis at distance of 30 mm from discharge point

and the inner-wall condition of the water chamber, and so on. The tensile regions marked by the circles were clearly observed in the experimental result. These strong tensile stresses could cause the generation of cavitation bubbles, so that the pressure variations were affected by the motions of the bubbles after 30 μs in the experimental profile. However, the effect of the cavitation bubble was not considered in the numerical simulation; therefore the pressure variations were different after the second shock wave.

Figure 4 shows estimation of the number of viable cells after an electric discharge of 31.6 kV in the test chamber. The initial density of marine *Vibrio* sp. was about 4.62×10^4 cfu/ml. The solid squares on the red curve represent the reference data obtained from the solution of the marine bacteria without the action of any shock waves. The number of viable cells hardly changed throughout the course of the experiment. The solid diamonds on the blue curve present the results of the bio-experiment predicted by the colony number of viable cells grown on the agar plates, as shown in the photos. Here, the electric discharge was triggered once every second, i.e., the applied frequency of the shock waves was 1 Hz. Samples were taken from the test chamber at 30, 60, 90, 100, and 110 s, diluted serially, and then spread on the agar plates. The agar plates in the photos had the same dilution. It was found that the gradient of the curve increased gradually after every sample extraction. Finally, the marine bacteria were found to have been killed completely after about 100 s. This result indicates that the sterilization efficiency increased gradually after every sample extraction. The pressure of the shock wave at each electric discharge is thought to be constant. Hence, this suggests that the number density of the bubbles can increase with the sample extraction.

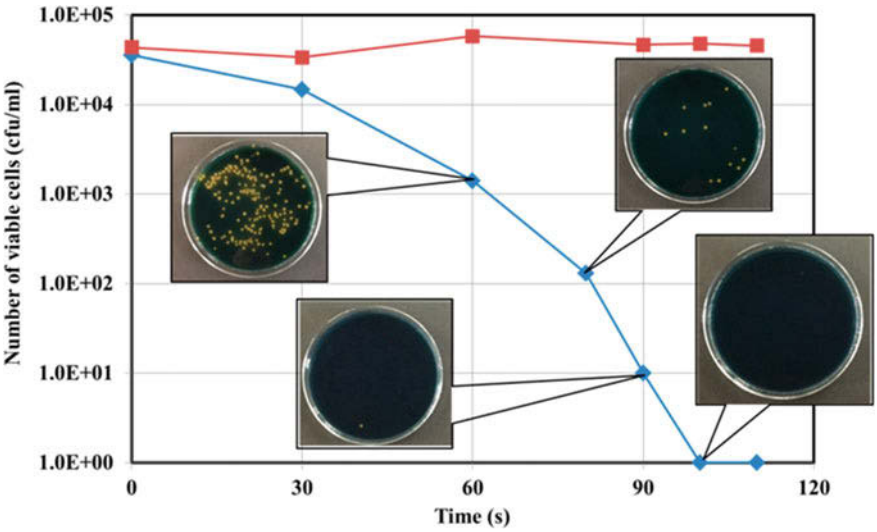

Fig. 4 Estimation of number of viable cells at electric discharge of 31.6 kV: ■ without action of shock waves, ◆ with the action of shock waves

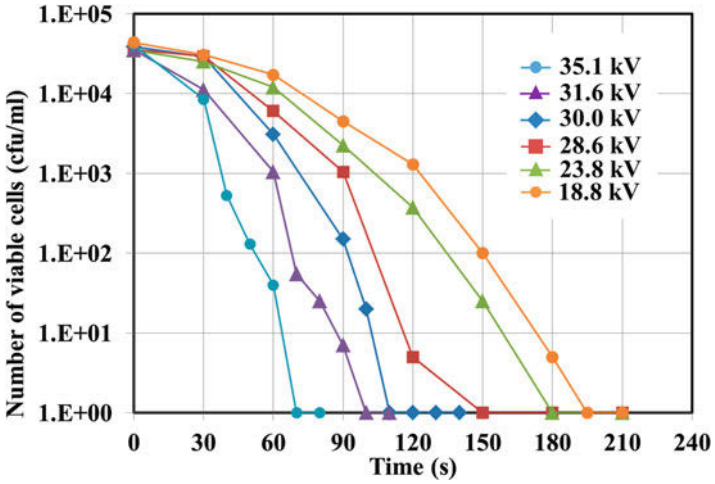

Fig. 5 Bio-experimental results obtained with electric discharge of 35.1 kV–18.8 kV

Figure 5 shows estimates of the number of viable cells obtained with an electric discharge of 35.1 kV–18.8 kV. The applied frequency of shock waves was 1 Hz. The plots shown in this figure are of the averages for six sets of bio-experimental data. The initial concentration of the marine bacteria was about 4.85×10^4 cfu/ml. From this figure, the marine bacteria were completely killed after about 70 s with an electric discharge of 35.1 kV. In the case of an 18.8-kV discharge, the time

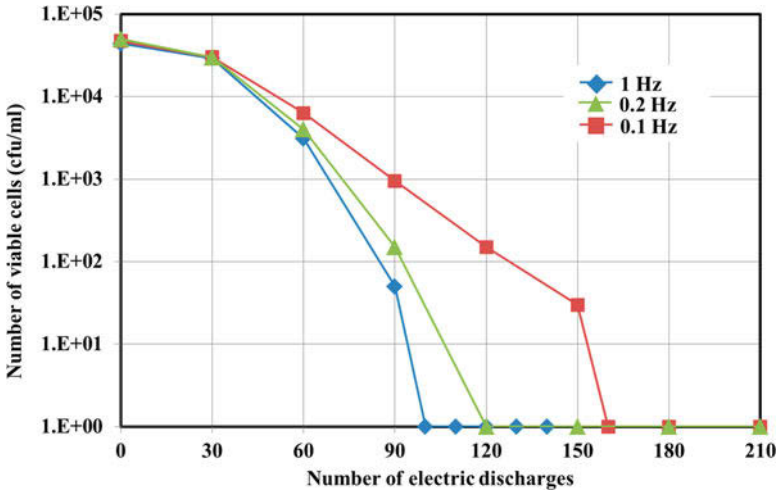

Fig. 6 Estimation of number of viable cells at electric discharge of 31.6 kV. ◆ 1 Hz, ▲ 0.2 Hz, and ■ 0.1 Hz

required to attain a complete sterilization was about 190 s. Thus, we can say that the sterilization effect increased with the output power of the electric discharge. The resulting shock pressures are mainly responsible for these results because the pressures behind the shock wave fronts increase with the output power. On the other hand, from the results obtained with an electric discharge of 30.0 kV to 18.8 kV, the gradients of the curves were found to be almost the same during the first 30 s, after which the differences in the sterilization effect arose. This suggests that the effective sterilization was not induced during the first 30 s. The reason for this could be that a significant number of bubbles had not been generated in the test chamber before the first extraction.

Figure 6 shows estimates of the number of viable cells at an electric discharge of 31.6 kV under different applied frequencies of the shock waves. The solid diamonds, triangles, and squares represent the results of the bio-experimental obtained with 1 Hz, 0.2 Hz, and 0.1 Hz, respectively. The other experimental conditions were the same as that in Fig. 5. This figure shows that the number of the electric discharges at which perfect sterilization is obtained increased as the applied frequency of the shock waves decreased. As shown in Fig. 6, the gradients of the three curves were almost the same during the first 30 shoots. This suggests that the strength of the collapsing motion were the same during this period, i.e., the generated bubbles in the test chamber could almost disappear before the arrival of the next shock wave. Given the results shown in Figs. 2 and 3, these bubbles were thought to be generated by the concentration of the reflected shock waves. Subsequently, the differences in the sterilization effect were apparent. These differences indicate that many bubbles remained upon the arrival of the next shock wave with frequencies of 1 Hz and 0.2 Hz. These remaining bubbles were thought to be other than

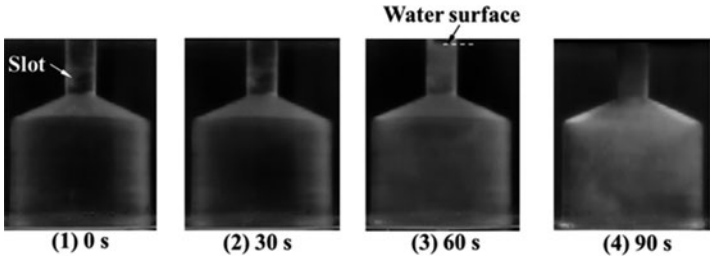

Fig. 7 Photos of test chamber at 31.6-kV electric discharge with sample extraction

the cavitation bubbles generated behind the reflected shock waves, given that the lifetimes of cavitation bubbles are in the order of millisecond. From those experimental situations, it was assumed that these bubbles were produced by other causes.

Figure 7 shows photos of the test chamber with an electric discharge of 31.6 kV before the sample extractions. Due to the light refraction and low transparency of the cylindrical water chamber, the states in the chamber were a little unclear. However, we could recognize the generation of the bubbles by the change of the white area in the photos. By comparing with the photo at 0 s, we can see that the state in the test chamber has barely changed from that in Fig. 7 (2). At 60 s, the number of remaining bubbles increased, and then, at 90 s, the test chamber became full of generated bubbles. During the experiments, the water surface in the slot went slightly down with every sample extraction of 0.1 ml taken from the cell suspension. However, the volume of the extracted samples was small in contrast to the total volume of the cell suspension in the test chamber, so that it can be negligible. From the observation of the test chamber, the rapid rise-and-fall motion of the water surface in the slot was found with the triggers of the electric discharges. At this time, air in the slot was brought into the cell suspension, and simultaneously tremendous bubbles were observed in the test chamber. The remaining bubbles at 60 s and 90 s in Fig. 7 were thought to be generated in this way. The movement of the water surface could be caused by the oscillation of the silicone film between the two chambers. The underwater electric discharge produces a vapor bubble between the electrodes after the generation of the shock waves. The vapor bubble contracts following expansions so that the collapsing motion of the vapor bubble resulted in the oscillation of the silicone film and then the generation of the bubbles in the test chamber.

4 Conclusions

The sterilization effects on marine *Vibrio* sp. were investigated with the underwater shock waves and induced bubbles in a cylindrical water chamber. Bio-experiments were carried out under different strength and frequencies of the shock waves

generated by the electric discharges. The numerical analysis showed that the shock wave propagating in the water chamber was reflected at the inner wall of the water chamber and then concentrated at the central axis of the cylinder and also predicted the generation possibility of cavitation bubble generation behind the reflected shock waves. Moreover, the shock wave-cavitation interaction was also confirmed in experimental pressure profile. Given the optical observation, the generated bubbles in the test chamber contained the cavitation bubbles behind the concentration of the reflected shock waves and bubbles produced by the oscillation of the silicone film between the two chambers due to rapid expansion and contraction of a vapor bubble at the electrodes. It was found that the bubbles resulting in the effective sterilization were from the latter. The results of the bio-experiments showed the marine bacteria were completely killed in a short time, and a large number density of bubbles, a high pressure, and a high frequency of incident shock wave give rise to an excellent sterilization effect. There is a possibility of a high sterilization effect in the presence of underwater shock wave alone.

Acknowledgments A part of this work was supported by JSPS KAKENHI Grant Number 16H04600 and 16 K14512.

References

1. A. Abe, H. Mimura, H. Ishida, K. Yoshida, Shock Waves **17**, 1–2 (2007)
2. J. Wang, A. Abe, J. Mar. Sci. Technol. **21**, 4 (2016)
3. J. Wang, A. Abe, in *proceedings of 7th PAMMES and AMEC in Hong Kong*, China (2017)
4. J. Wang et al., in *proceedings of the symposium on shock wave in Japan*, Yokosuka (2017)

Effects of Liquid Impurity on Laser-Induced Gas Breakdown in Quiescent Gas: Experimental and Numerical Investigations

T. Ukai, H. Zare-Behtash, C. White, and K. Kontis

Abstract This paper reports that the presence of liquid impurity significantly affects the shock wave structure induced by laser-induced gas breakdown in a quiescent gas. A spherical blast wave is formed when there are no suspended liquid particles, whereas an elliptic shaped blast wave appears in gas breakdown with the presence of suspended liquid particles. The elliptic shaped blast wave has a higher overpressure magnitude on the perpendicular axis of the laser path.

1 Introduction

Laser-induced gas breakdown has the ability to change the flow characteristics due to rapid local heating. The local high temperature induces the generation of plasma and a spherical blast wave, and then a vortex ring is formed due to the asymmetric shape of the plasma region in the laser focal position [1]. According to both numerical and experimental investigations of laser energy addition ahead of a bow shock wave [2, 3], the high-temperature region and the vortex ring both contribute to a drag reduction. Therefore, the laser-induced gas breakdown can be used in engineering applications such as flow control [4] as well as laser plasma igniters [5].

Laser-induced gas breakdown for engineering applications is not necessarily used in an ideal gas without any impurities. The laser beam may interact with atmospheric aerosols including liquid and solid particles when laser-induced gas breakdown is applied to energy addition around an aircraft. The thermal structure from laser-induced breakdown will be altered by the interaction with atmospheric

The original version of this chapter has been revised and is now available open access. A correction to this chapter is available at https://doi.org/10.1007/978-3-319-91017-8_149

T. Ukai (✉)
Department of Mechanical Engineering, Osaka Institute of Technology, Osaka, Japan
e-mail: takahiro.ukai@oit.ac.jp

H. Zare-Behtash · C. White · K. Kontis
School of Engineering, University of Glasgow, Glasgow, UK

A. Sasoh et al. (eds.), *31st International Symposium on Shock Waves 2*,
https://doi.org/10.1007/978-3-319-91017-8_2

aerosols. There is a possibility that several plasma regions can be formed due to vaporization of the suspended aerosols. When considering interaction of a laser beam with a material, a vapor plume is formed due to vaporization from material melting, and the interaction between the vapor and the laser beam results in ionization of the gas [6]. The ionized gas can absorb laser energy; thereafter a shock wave induced by an absorption wave is generated [7]. The vapor-laser interaction is related to plasma formation as well as shock wave generation. It is expected that laser-particle interactions can lead to the generation of several plasma regions; thus a different shock wave structure would appear compared with gas breakdown in pure air.

In this study, the liquid impurity effect on laser-induced gas breakdown was experimentally investigated using flow visualization and numerically using three-dimensional Navier–Stokes equations. This research focuses on the behavior of shock wave propagation and shock-shock interaction in laser-induced gas breakdown, rather than the plasma kernel dynamics.

2 Experimental Setup

A laser beam was focused in a quadrilateral stainless steel vacuum chamber with a volume of 0.138 m^3. The chamber has a top quartz window of 98 mm in diameter and a pair of side quartz windows of 137 mm in diameter. The chamber was connected to a vacuum pump, and nitrogen gas was supplied until the pressure within the chamber recorded 100 kPa after evacuating the air. The nitrogen gas was passed through a particle generator (TSI, model: 9307–6, 1000 L/min of aerosol flow rate) to provide olive oil particles 1 μm in diameter. The mixture of nitrogen gas with suspended olive oil was supplied to the chamber. When considering laser-induced gas breakdown without the liquid impurity effects, nitrogen gas is directly supplied to the chamber. A pressure sensor and k-type thermocouple were installed on the chamber. These signals were monitored using a data acquisition system (National Instruments Corp., model: NI-9205 for pressure monitoring and NI-9213 for temperature monitoring) driven by LabVIEW. In the present experiments, the pressure and the temperature in the chamber were $P_0 = 99.6 \pm 0.3$ kPa and $T_0 = 293.3 \pm 1.8$ K, respectively.

To induce the laser energy focusing in the chamber, a Q-switched pulsed Nd:YAG laser beam with a wavelength of 532 nm was employed. A concave lens with a focal length of −50 mm expands the laser beam, and a second convex lens with a focal length of 150 mm collimates the laser beam. The laser beam then passes through the top window of the chamber. The collimated laser beam is focused in the chamber by a convex lens with a focal length of 100 mm. The laser energy in the vicinity of the laser focal position was 188.0 ± 1.9 mJ/pulse.

The laser-induced blast wave was visualized using high-speed schlieren photography with a standard Z-type optical arrangement. The schlieren system consists of a 450–1000 W continuous light source with an Xe–Hg arc lamp (Newport, model:

66921), a condenser lens with a focal length of 70 mm, an iris diaphragm, a pair of 203.3-mm-diameter concave mirrors with a focal length of 1829 mm, a knife-edge, an imaging lens, and a high-speed camera HPV-1 (Shimadzu, special resolution, 312 × 260 pixels). The images were acquired at a frame rate of 500 kfps with an exposure time of 1 μs.

3 Computational Method

The numerical work uses the finite-volume OpenFOAM software package. The compressible flow solver rhoCentralFoam was chosen. This is a three-dimensional, transient, density-based compressible Navier–Stokes solver based on the central-upwind schemes of Kurganov and Tadmor [8]; hence it is second-order accurate in space. In this work, a backward difference time scheme is utilized, and so the results are also second-order accurate in time. The gas properties are set to be those of nitrogen initially at a temperature of 293.3 K and a pressure of 99.6 kPa to remain consistent with the experiments. Despite the large temperature increment introduced by the laser energy deposition, a constant viscosity of 1.76×10^5 Pa s and a constant specific heat at constant pressure C_p of 1040 J/kg/K are used throughout the current work. Such simplifications have previously been shown to be acceptable for capturing the shock wave behavior in these kinds of problems [1].

The energy deposited by the laser beam increases the temperature and pressure of the gas on a small timescale. As such, the heat addition is assumed to take place at constant density. The temperature increase ΔT in the gas after the laser is fired is calculated as

$$\Delta T = \frac{\Delta E}{\rho \cdot C_V \cdot V} \tag{1}$$

where ΔE is the energy added by the laser pulse, ρ is the ambient gas density, C_v is the specific heat of the gas at constant volume, and V is the laser perturbation focal volume, which, in the current work, is estimated from a size of plasma region in the experimental results at early times.

Any numerical cells that fall within the spherical radius of the laser perturbation focal volume have their temperature increased by ΔT, and the pressure is increased by the same factor. Real gas effects, such as chemical reactions, due to this large increment in temperature are not considered in the current numerical work.

Once the simulation begins, the large gradients of temperature and pressure act as sources of acceleration on the right-hand side of the Navier–Stokes equations, converting the internal energy to kinetic energy and resulting in the formation of a shock wave that propagates outward. The numerical domain is axisymmetric, and all simulations in the current work use a variable time step with a maximum Courant number of 0.8.

4 Results and Discussion

Different shock wave formation/propagation are apparent in laser-induced gas breakdown with and without particles. Figure 1 shows experimental schlieren images of gas breakdown without particles. Rapid local heating due to the laser focusing results in plasma generation, which can be seen as the bright region in the schlieren images. A laser-induced blast wave also propagates spherically into the surrounding gas. A spherical laser-induced blast wave is observed at an elapsed time of 4 μs in gas breakdown without particles. On the other hand, an elliptic shaped blast wave appears in gas breakdown with particles at the same time (Fig. 2).

Two bright regions related to plasma generation appear at an elapsed time of 8 μs (Fig. 2c), which results in two laser-induced blast waves being produced in close proximity to one another. Thereafter, a longitudinal elliptic shaped blast wave is formed due to the interaction of the two laser-induced blast waves. It is expected that the laser beam with a narrow beam waist impinges on the particles at both the ideal laser focal position as well as the upper part of the ideal laser focal position. This results in the generation of two gas breakdown regions along the beam path. The location of the multiple laser focal points may depend on the particle density and laser energy level. The shock wave fronts that propagate toward the opposite laser focal point impinge one another; hence a transmitted shock wave (TSW) appears.

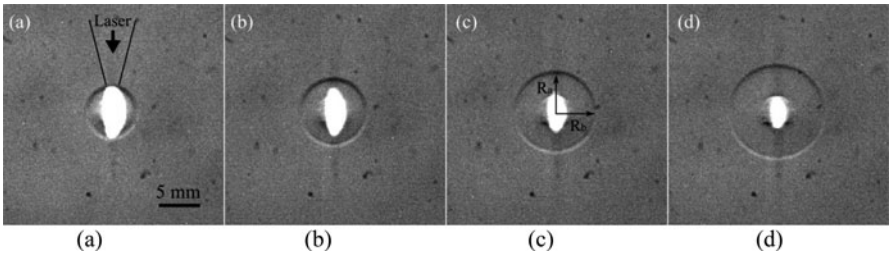

Fig. 1 Experimental schlieren images of gas breakdown without particles. (**a**) $\Delta t = 4$ μs, (**b**) $\Delta t = 6$ μs, (**c**) $\Delta t = 8$ μs, and (**d**) $\Delta t = 10$ μs

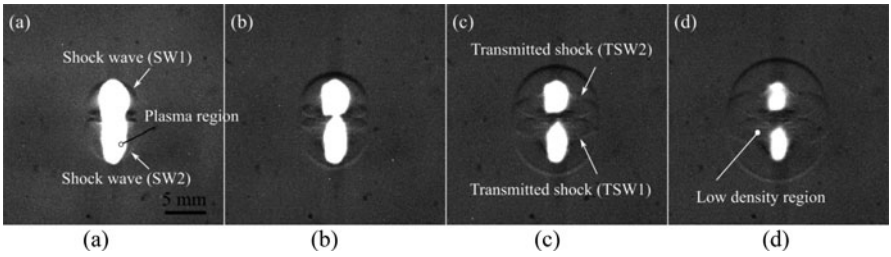

Fig. 2 Experimental schlieren images of gas breakdown with particles. (**a**) $\Delta t = 4$ μs, (**b**) $\Delta t = 6$ μs, (**c**) $\Delta t = 8$ μs, and (**d**) $\Delta t = 10$ μs

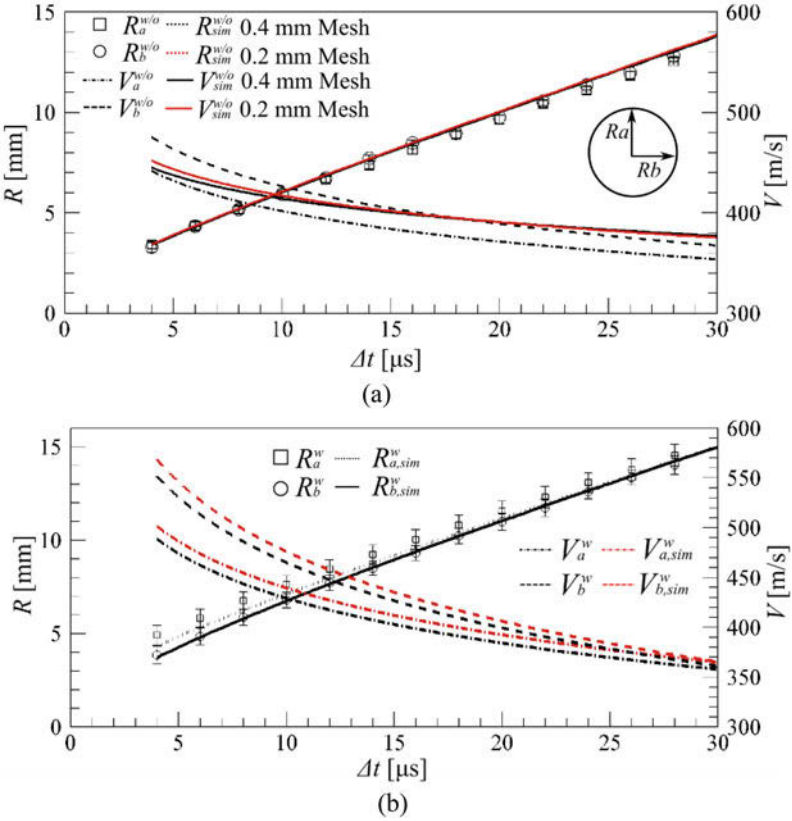

Fig. 3 Comparison of experimental and numerical shock velocities and radii. (**a**) Without particles. (**b**) With particles

The TSW interacts with the thermal heated region at the laser focal point, which results in distorting the spherical shape of the TSW. This is because the local shock Mach number decreases in the heated region.

The numerical results show good agreement with the experimental results for both gas breakdown with and without particles. In the gas breakdown without particles from experimental results (Fig. 3a), the longitudinal shock wave radius $R_a{}^{w/o}$ is the same as the lateral shock radius $R_b{}^{w/o}$. The error bars show the standard deviation from six repetitions. Additionally, the longitudinal shock wave velocity of $V_a{}^{w/o}$ is similar to the lateral one $V_b{}^{w/o}$. The velocities are obtained by logarithmic approximation. From the numerical results, both shock radius and shock velocity are in good agreement with the experimental results. There is little difference between the results with a cell size of 0.4 mm and 0.2 mm, so the 0.4 mm size is used for the remainder of the numerical.

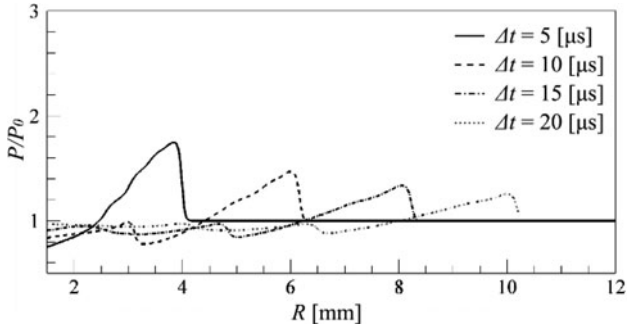

Fig. 4 Pressure history in gas breakdown without particles

From the experimental results of gas breakdown with particles, $R_a{}^w$ is slightly larger than $R_b{}^w$ because of the elliptic shaped blast wave; however, the longitudinal and lateral shock radii become the same with time. The error bars show the standard deviation due to 12 repetitions. In the numerical simulation, two heated spots at the same focal location as the experiments were used as the initial conditions. Since the numerical results show good agreement with the experimental results, it can be deduced that the hypothesis that the laser beam is focused at two different locations appears to be correct.

The shock wave generated in gas breakdown with particles is stronger than without particles. Figures 4 and 5 show the pressure history from the simulations, with and without particles, respectively. The pressure rise at the shock wave front is followed by an immediate decay to a negative value formed in the laser-induced blast wave. Then, the negative value induces a pressure rise so that pressure recovers to the atmospheric pressure. The time between the primary pressure rise and the pressure recover is almost the same, independent of the interaction with particles, but the pressure magnitude differs. The overpressure along the x-axis is highest because the shock waves generated from the two focal points interact at this location, which results in shock focusing. This tendency is similar to the velocity history (Fig. 3) where the velocity $V_b{}^w$ is the highest at an elapsed time of 5 μs.

In the pressure history along the y-axis (Fig. 5b), a second pressure rise at the shock front of the TSW appears. The simplification of the initially uniform high-temperature and high-pressure region in the simulations does not result in an accurate capture of the low-density bubble behavior; thus, the location of the second pressure rise, corresponding to the location of the TSW in Fig. 2, is not expected to correspond with the experimental result due to different shock-bubble interaction behavior. Future numerical work will focus on improving the low-density region behavior. For example, it is known that the heated region takes the form of a teardrop shape rather than a sphere [9].

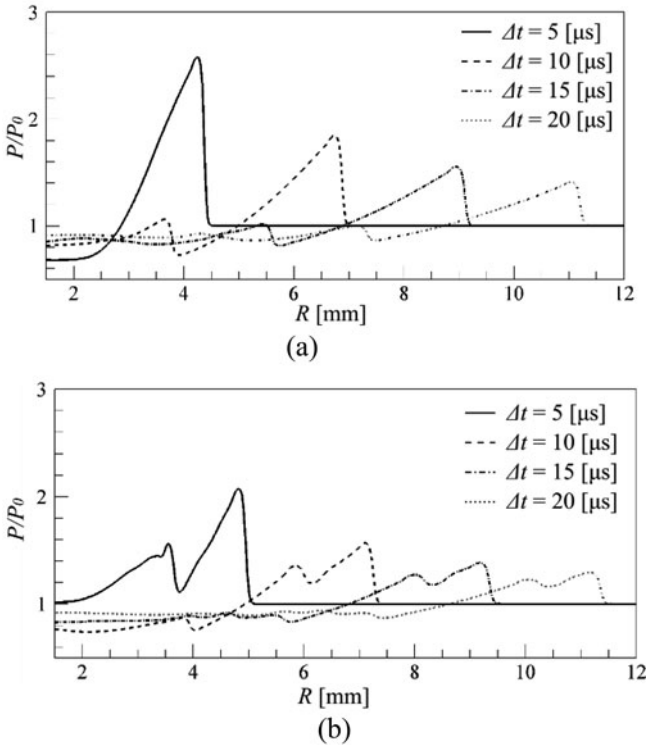

Fig. 5 Pressure history in gas breakdown with particles. (**a**) Along the x-axis. (**b**) Along the y-axis

5 Conclusion

This study experimentally and numerically investigated the liquid impurity effect on laser-induced gas breakdown in quiescent gas. When gas breakdown was induced with particles present, an elliptic shaped blast wave was generated, whereas a spherical blast wave was formed without particles at the same elapsed time. It is concluded that the presence of olive oil particles causes the laser beam to focus on more than one point, which results in the generation of multiple laser energy deposition zones along the beam path. In gas breakdown with particles, a larger overpressure magnitude appeared on the perpendicular axis of the laser path.

Acknowledgement We would like to dedicate this paper to Prof. Margaret Lucas at the University of Glasgow for her kind arrangement of the usage of the high-speed camera and to Dr. Richard Green at the University of Glasgow for setting up the laser facility. This research work was supported by European Commission, H2020-MSCA-IF (Project reference: 654318). The laser facility was supplied by National Wind Tunnel Facility project (EPSRC grant number: EP/L024888/1).

References

1. H. Yan et al., AIAA J. **41**, 10 (2003)
2. Y. Ogino et al., Phys. Fluids **066102**, 21 (2009)
3. J.-H. Kim et al., AIAA J. **49**, 9 (2011)
4. R. Kandala, G.V. Candler, AIAA J. **42**, 11 (2004)
5. J.A. Syage et al., J. Appl. Phys. **64**, 1499 (1998)
6. D. Bauerle, *Laer Processing and Chemistry* (Springer, New York, 2011), pp. 4–5
7. C. Boulmer-Leborgne, J. Hermann, B. Dubreuil, Plasma Sources Sci. Technol. **2**, pp. 219–226 (1993)
8. C.J. Greenshields et al., Int. J. Numer. Methods Fluids **63**, 1 (2010)
9. S. Ghosh, K. Mahesh, J. Fluid Mech. **605**, pp. 329–354 (2008)

Air Blast from a Structural Reactive Material Solid

F. Zhang, M. Gauthier, and C. V. Cojocaru

Abstract A reactive hot spot concept was investigated for fine fragmentation of a structural reactive material (SRM) solid under explosive loading to augment air blast through rapid reaction of fine SRM fragments. Micro-sized MoO_3 particles were distributed in a particulate aluminum base in $10Al + MoO_3$, which was consolidated into a full-density solid. The SRM solid was made of a thick-walled cylindrical casing containing a high explosive. Intermetallic reactions of micro-sized MoO_3 and nearby Al under explosive loading created heat and gas products to form microscale hot spots that initiated local fractures leading to fine fragments of the rest of Al. Experiments in a cylindrical chamber demonstrated the presence of a large amount of fine Al fragments, whose prompt reaction after detonation significantly enhanced the primary and near-field blast wave, thus verifying the concept.

1 Introduction

A structural reactive material (SRM) is defined to comprise a micrometric mixture of energetic metals and metal compounds, consolidated to its theoretical maximum density (TMD). A SRM thus bears both macroscale continuum solid properties (energy, density, strength, etc.), and grain-scale properties of reactivity and dissimilarity (discontinuities in impedance, hardness, etc.). As an open area of new materials, SRM has a great application potential, including energy sources for air blast through reaction of fine fragments of a SRM solid under explosive loading [1].

High porosity in a reactive material solid does promote fine fragmentation but results in a deficit in TMD, thus leading to a low mechanical strength, which conflicts with the definition of a SRM solid. From the intrinsic grain-scale properties

F. Zhang (✉)
Defence Research and Development Canada, Medicine Hat, AB, Canada
e-mail: fan.zhang@drdc-rddc.gc.ca

M. Gauthier · C. V. Cojocaru
National Research Council Canada, Boucherville, QC, Canada

A. Sasoh et al. (eds.), *31st International Symposium on Shock Waves 2*,
https://doi.org/10.1007/978-3-319-91017-8_3

of dissimilarity and reactivity, a reactive hot spot concept has been introduced through distributing micro-sized reactive materials in a fuel-rich SRM solid, such as copper oxide (CuO) particles consolidated in a particulate aluminum base [2]. Intermetallic or thermite reactions of these micro-sized materials under explosive loading created heat and gas products to form microscale hot spots that initiated local fractures leading to fine fragments of the rest of the SRM. In the present study, the reactive hot spot concept is further studied in a SRM solid of micro-sized molybdenum oxide (MoO_3) distributed in a particulate aluminum base under explosive loading with a detonation pressure range of 25–34 GPa.

2 Experimental Procedures

The SRM solid comprises a micro-sized composite 10Al + MoO_3, with a fuel richness ratio of 5 under a global stoichiometric assumption. Local diffusion-dominant reactions of Al with distributed MoO_3 particles are near stoichiometric in an atomic ratio of $N_{Al}/N_{MoO3} = 2$ and serve as hot spots. This results in a heat of reaction of 4.703 kJ/g within the hot spot volume and gas products O, O_2, AlO, Al_2O, MoO, MoO_2 etc. at 4600 K from an equilibrium constant volume explosion calculation with all phase changes. Under the explosive detonation condition, the shocked temperature of the macro-sized SRM solid may not reach the thermite ignition temperature. However, shock dynamics on dissimilar Al and MoO_3, local structural discontinuities and any micro voids, shear instability, and plastic deformation can generate intense heat and high temperatures beyond the ignition threshold of the hot spot material.

Powders selected were atomized $d_{50} = 35$ μm Al and ≤ 44 μm MoO_3. The mixture was mechanically premixed and consolidated into a SRM solid, using hot isostatic pressing (HIP), at a density of 3.19 g/cm^3, practically reaching 100% TMD. The porosity was evaluated to be 1.46 vol%, from a Clemex image analysis of the polished cross sections depicted in Fig. 1, using a scanning electron microscope (SEM). It can be seen that the MoO_3 is well distributed within the volume in favor of diffusive reaction. The SRM solid was made into a hollow cylinder, 3.35 cm in inner diameter (ID), 4.36 cm in outer diameter (OD), and 9.4 cm in length (140 g in weight), covered with two planar lids connected with four screws for each. It contained either a 100 g RDX-based composition C4 explosive (HE1, detonation velocity $D_{CJ} = 8.0$ km/s and pressure $P_{CJ} = 25$ GPa) or a HMX-based explosive (HE2, $D_{CJ} = 8.5$ km/s and $P_{CJ} = 34$ GPa), with a total casing-to-explosive mass ratio of $M/C = 1.78$. In order for comparison, a baseline 6061-T6 continuum Al casing was also tested.

Fragmentation and blast experiments of the SRM solid under explosive loading were conducted subsequently in a 1.18 m diameter and 2.1 m^3 closed steel chamber using a cylindrically axisymmetric configuration. In the case of fragmentation tests, the experiments were designed to collect the primary fragments from the casing cylinder for its fragment size distribution analysis. Thus, the top and bottom planar

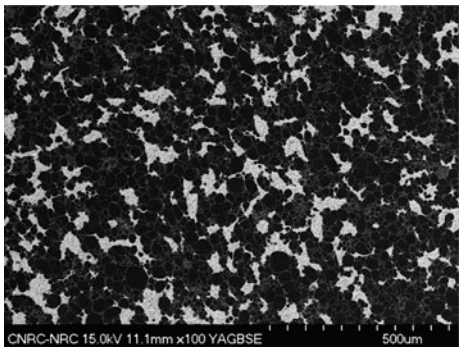

Fig. 1 SEM for HIPed $10Al + MoO_3$:Al in dark gray and MoO_3 in light gray

lids were made of mild steel, whose fragments were easily removed by a magnet after a test. The chamber was in its vertical configuration filled with purified snow with an argon-filled charge cavity in the center. The snow, packed in the chamber with a density of 0.38–0.4 g/cm^3, acted both to quench early reaction of SRM fragments and to soft-catch the fragments before impacting the chamber walls [3]. The 20 cm diameter and 40-cm-long charge cavity had a charge suspending in its center aligned accurately at the chamber center through a template set. The charge cavity dimension resulted in about 5 times charge diameter and length; this acted both to ensure a full casing expansion and fragmentation at the local atmosphere pressure and to quench any early reaction of SRM fragments in packed snow. The chamber was then closed and flushed with argon for 10 minutes to ensure the charge cavity is filled with argon to the local atmosphere pressure (92.1–93.3 kPa). The explosive was detonated at its top using an RP83 detonator. After each experiment, it was observed that fragments were stopped within the packed snow, outermost at 8–10 cm from the chamber circumferential wall for the large fragments. The snow containing all fragments was removed from the chamber and stored in containers to melt. The melt water containing the fragments was filtered through a mesh 400 sieve and a less than 1 μm paper filter. The wet fragments were vacuum-dried in an oven at 80 °C. The sizes of dried fragments were determined using sieves with a distribution of <37, 37–74, 74–125, 125–420, 420–1000, 1000–2000, 2000–4000, 4000–6300, 6300–9500, and >9500 μm. The iron-content fragments were removed using a permanent magnet.

For blast experiments, the SRM casing cylinder was covered with two 6061-T6 Al lids as opposed to steel to prevent impact-induced chamber damage. The cylindrical charge was suspended horizontally in the same axis and at the center of the horizontally configured cylindrical chamber (Fig. 2). Detonation, initiated from an RP83 detonator, propagated along the charge axis toward the camera window, while the expansion of SRM fragments took place in the radial direction toward the chamber cylindrical wall. A Phantom high-speed camera was set in face to the chamber window. An Endevco piezoresistive pressure transducer B was mounted on the chamber cylindrical wall, facing the charge center for a normal reflection measurement. Another Endevco transducer E was set on an in-house

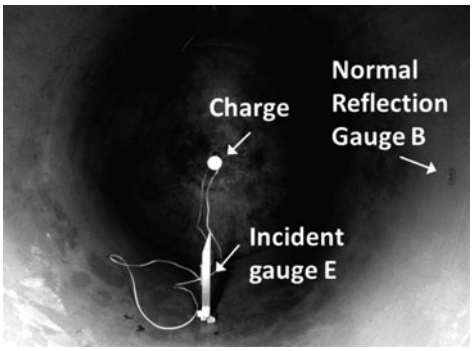

Fig. 2 The axisymmetric test configuration of a 2.1 m^3 cylindrical chamber

designed mount at a radius of $R = 39$ cm from the charge center to measure a near-field incident blast pressure. The chamber was sealed at a local atmospheric air pressure of 92.3–93.7 kPa and temperature of 11–20 °C. After each test, the residue fragments and explosion solid products were recovered.

3 Results and Discussion

The primary fragments of the full casing cylinder mass were recovered after each fragmentation experiment, and the obtained fragment size distributions are summarized in Fig. 3. It indicates that the primary fragments in a size range below 125 μm constitute more than 40% mass fraction of the SRM solid, 3 times that from the pure Al solid. Structural discontinuities in impedance, hardness, etc. between Al (2.7 g/cm^3 density) and MoO_3 (4.7 g/cm^3 density) helped for the fine fragmentation. Exceptionally, XRD analysis of the fine fragments identified the composition of Al (dominant), MoO_2, Al_2O_3, Mo, $AlMo_3$, Al_3Mo, Al_8Mo_3, etc. These intermetallic compounds provided a clear evidence for the Al-MoO_3 hot spot thermite reaction within the SRM solid during the detonation shock loading followed by fine fragmentation.

The effect of fine primary fragments on blast performance was studied from experiments in the same chamber in its horizontal axisymmetrical configuration filled with air. Figure 4 illustrates the reaction process of fragments from the baseline pure Al casing, obtained from the 13.15 μs frame-rate high-speed photography. Limited fine fragments react after detonation (the four jets at a 90° interval originate from the four screw connections of lids to the casing). Significant and rapid reaction is observed only as the fragments impact on the chamber cylindrical wall showed in the fifth frame at 302 μs, where the fragments undergo their secondary fragmentation. Such fragment reactions can be described as target impact-induced fragment reaction.

For the 10Al + MoO_3 casing, in contrast, a significant incipient reaction of a large number of fine fragments appears promptly after detonation (Fig. 5), before

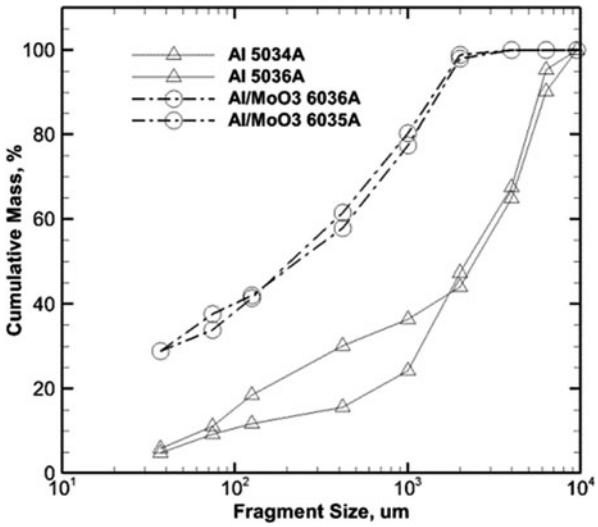

Fig. 3 Fragment size distributions from the $10Al + MoO_3$ and 6061-T6 Al casings

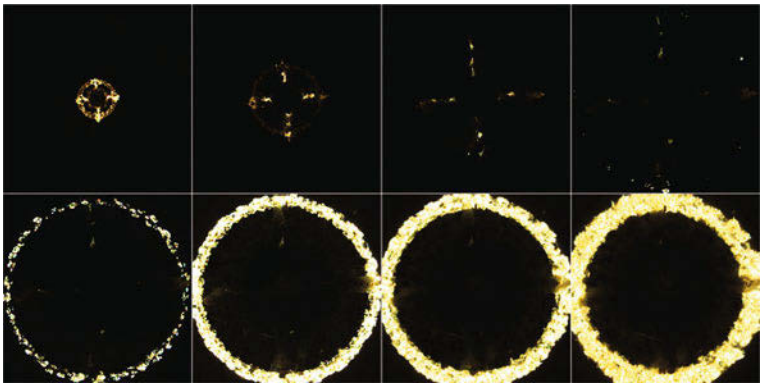

Fig. 4 Al fragment reactions after HE1 detonation and upon wall impact, frames at 52, 105, 184, 289, 302, 315, 328, and 354 μs (#5085)

fragments impacting the chamber circumferential wall (i.e., at 276 μs on the fifth frame). Such primary fragment reaction can be called detonation shock-induced fragment reaction. When compared to Fig. 4, the fragment travel and fireball expansion are faster than that from the baseline Al solid. The reaction radiation pattern after wall impact (the 6th–8th frames) also appears to be dominated by much finer secondary fragments than that from the Al solid.

Pressure results given in Fig. 6 show that the Al-MoO_3 cased charges, with respect to the Al cased charges using the same explosive HE1, provide a >18% increase in primary shock peak at incident gauge E ($R = 39$ cm) and a 50% increase in normal-reflected shock peak at wall gauge B ($R = 59$ cm). The stronger blast wave from the Al-MoO_3 is also dictated at gauge E through the faster second peak (after

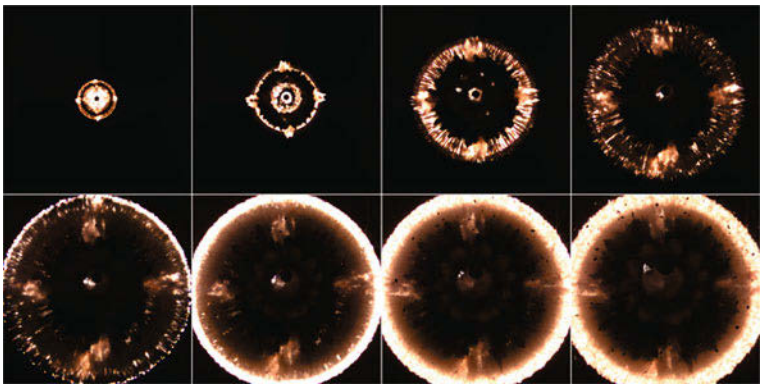

Fig. 5 SRM fragment reactions after HE2 detonation and upon wall impact, frames at 52, 105, 184, 236, 276, 289, 315, and 342 μs (#6055)

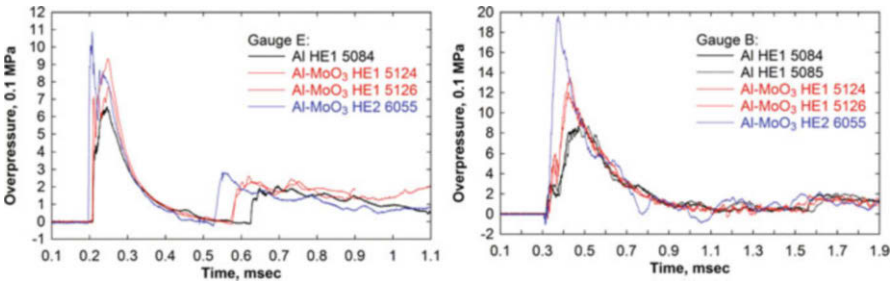

Fig. 6 Blast pressure fronts at incident gauge E, $R = 39$ cm (left), and on the chamber wall gauge B, $R = 59$ cm (right)

0.5 ms in Fig. 6) which results from the wall reflection. The increase in primary shock peak at gauge E indicates combustion of more primary fine fragments, while the increase in reflected shock peak at gauge B is a combined effect from both higher incident peak and reaction of the impact-induced fine fragments.

For both SRM and Al solid under the HE1 loading, a precursor and primary two-shock front structure can be clearly observed on gauge B at $R = 59$ cm, while on gauge E at $R = 39$ cm, the precursor shock starts to emerge from the primary shock. The precursor shock is a typical near-field phenomenon of an SRM-cased charge explosion, associated with ballistic air shocks attached to fragment clusters that traverse the primary blast front [1]. A substantial increase in both reflected precursor and reflected primary shock at $R = 59$ cm also suggests that more energy has been released through fine fragment combustion from the Al-MoO_3 than that from the Al solid before and at the time of impact.

A further increase in blast peaks is evident in Fig. 6 through more efficient reactive hot spot fine fragmentation of the SRM solid using the higher detonation pressure explosive HE2. The prompt reaction of more primary fine fragments, upon

explosive detonation and as the fragment cloud expands, leads to a continuous enhancement of the primary blast wave as it propagates. Figure 6 shows $a > 50\%$ increase in primary shock peak at incident gauge E and a 125% increase in normal-reflected shock peak at gauge B, with respect to the results from the pure Al casings. No precursor shock is observed within the test range for the SRM solid in this case due to the faster running primary blast front.

In late times, the explosion pressure reached the same equilibrium value measured from all gauges, that is, the so-called quasi-static overpressure (QSP) for the closed chamber explosion. The value of QSP is proportional to the total energy amount released as a long-time solution in a closed volume. Measured at 50–100 ms, the QSP reached 420–432 kPa for both Al and Al-MoO_3 casings using HE1. This result, together with the blast front results in Fig. 6, indicates that under the same amount of the total energy released, the part of the energy promptly released to augment the early blast front is significantly more from the Al-MoO_3 casing than that from the Al casing. The QSP is increased to 490 kPa for the Al-MoO_3 casing using HE2.

A full recovery of fragments and solid products was achieved after each experiment in the closed chamber. The mass of <1 mm powder amounts 92–94 wt.% of the total recovered fragments for the Al-MoO_3 solid. This provides a more than 20 wt.% increase when compared with the same-sized powder masses from the pure Al solid, thus indicating a greater casing mass burnt out in fragment reaction of the SRM solid. XRD analysis has been conducted for the post-explosion residues of <1 mm powder from the $10Al + MoO_3$ casings. As expected, the α-Al_2O_3 was present dominantly, largely from the reaction of Al with the explosive detonation products and air. There are clear evidences of new compounds formed as the Al-MoO_3 reaction products, such as $Al_2(MoO_4)_3$ and Al_5Mo, indicating the extent of the thermite reaction. Some traces of non-reacted MoO_3 are also identified but much less significant.

4 Conclusions

Structural reactive material is an open area of material science, consolidated from a micro- or nanoscale granular mixture of reactive materials toward the mixture theoretical maximum density (TMD) with little porosity, to ensure both high energy density and mechanical strength. In order to promptly release energy from a SRM solid to augment air blast, mechanisms for generating fine primary fragments will be needed particularly from a thick SRM casing cylinder under explosive loading. Under high detonation pressure, SRM fine fragmentation mechanisms can be established based on its intrinsic grain-scale properties of dissimilarity and reactivity. The present paper proposes a mechanism of reactive hot spots interposed in a SRM solid. This is achieved through distributing micro-sized metal oxide particles in a granular metal, which is consolidated toward the mixture TMD in a fuel-rich ratio. Thermite reaction between metal fuel and metal oxide under

explosive loading creates heat and gas products to form microscale hot spots, which initiates local fractures leading to fine fragments of the rest of fuel metal.

On the basis of the previous study on a cold-sprayed 6Al + CuO SRM solid, the reactive hot spot concept for fine fragmentation has been further investigated in a HIPed 10Al + MoO_3 SRM solid through both primary fragmentation experiments and explosion experiments in a closed chamber. The results of a significant increase in fine primary fragments are consistent with substantially faster fragment fireball expansion, stronger primary and near-field air blast, and a significant increase in the reaction solid products. These results, together with the intermetallic reaction products evidenced during the SRM solid fragmentation, clearly show the feasibility of the fine fragmentation mechanism for a SRM solid under explosive loading, namely, through the micro length-scale thermite reactions (i.e., the reactive hot spots) distributed within the SRM solid. The amounts of heat release and gas products are important criteria in the choice of hot spot reactive materials for a SRM solid to produce fine fragmentation. Furthermore, the high detonation pressure is important in order to exceed the shock initiation threshold for the hot spot reactive material reactions within the SRM solid.

Acknowledgments The significant effort and support of Brain Eichelbaum, Kiril Mudri, Ryen Stallmann, Robin Laing, Louis Gagne, Karl Baker, and the technical staff from the Suffield Field Operations Section in conducting the experiments are gratefully acknowledged.

References

1. F. Zhang, L. Donahue, W.H. Wilson, in *The Effect of Charge Structural-Reactive-Metal Cases on Air Blast*. Proc. 14th Detonation Symposium (ONR-351-10-185, 2010), pp. 2–12
2. F. Zhang, A. Bacciochini, B. Jodoin, M. Radulescu, R. Ripley, in *A Hot Spot Concept to Enhance Fragmentation of Structural-Reactive-Material Casings*. Proc. 15th Detonation Symposium, (ONR-43-280-15, 2014), pp. 1356–1366
3. W.H. Wilson, F. Zhang, K. Kim, in *Fine Fragmentation Distribution from Structural Reactive Material Casings under Explosive Loading*. Shock Compression of Condensed Matter-2015, (AIP Conf. Proc. 1793, 2015), https://doi.org/10.1063/1.4971531

Experimental Study on Configuration Effects of Supersonic Projectiles in Transitional Ballistic Regimes

C. M. Athira and G. Rajesh

Abstract The flow field associated with a moving projectile in the transitional ballistic regime is highly complicated and unsteady. The projectile interactions with the surrounding flow field affect the aerodynamic force acting on the projectile and have great impact on its stability, control, and dispersion characteristics. There are interesting fluid dynamic phenomena in this regime where the projectile interacts with the unsteady jet. One of the profound interactions is a situation in which the projectile overtakes the primary blast wave in the vicinity of the gun muzzle itself where the blast wave is very strong. In the present study, experiments are conducted with projectiles of cylindrical, conical, and hemispherical shapes, in order to understand the characteristics of projectile-flow field interactions and the projectile overtaking phenomenon, in particular. Flow field is captured using time-resolved schlieren flow visualization technique. The behavior of different shaped projectiles in the transitional ballistic regime is analyzed to understand the configuration effects. The various overtaking regimes are also identified by constructing the *x-t* diagram from the trajectory information obtained by image processing.

1 Introduction

Transitional ballistics refers to the immediate vicinity of the launch tube where the flow field is highly complicated and time-dependent. As the projectile starts moving in the launch tube, it compresses the air ahead of it, and a strong shock wave will be generated depending on the projectile velocity and the launch tube length. This shock gets diffracted at the exit of the launch tube resulting in the formation of primary blast wave (PBW) moving at a velocity u_s. The primary blast wave is followed by a contact discontinuity that separates the air exiting from the launch tube and the atmospheric air compressed by the primary blast wave. The discharge of air, which was previously present in the launch tube, results in an unsteady jet

C. M. Athira · G. Rajesh (✉)
Department of Aerospace Engineering, Indian Institute of Technology Madras, Chennai, India
e-mail: rajesh@ae.iitm.ac.in

A. Sasoh et al. (eds.), *31st International Symposium on Shock Waves 2*,
https://doi.org/10.1007/978-3-319-91017-8_4

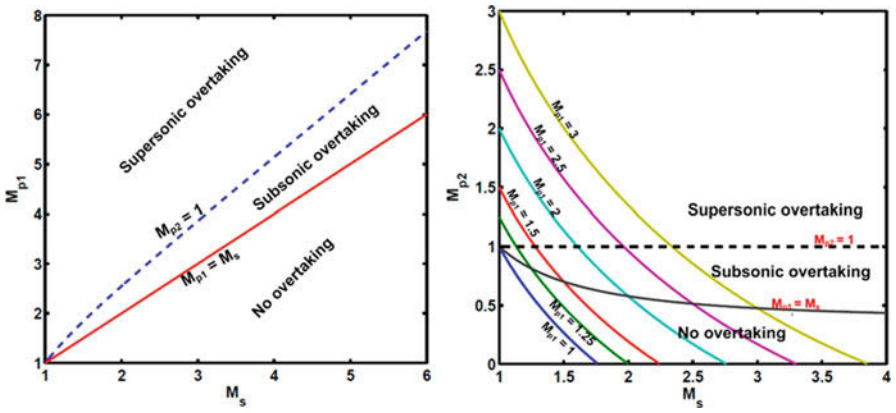

Fig. 1 Regimes of possible subsonic and supersonic overtaking

structure into which the projectile gets discharged [1]. Depending on the unsteady jet relative Mach number, it may be underexpanded or even subsonic. A shock may or may not form in front of the projectile depending on the projectile relative Mach number with respect to the bulk motion (with u_2 velocity) created by the primary blast wave. The discharge of high-pressure gas behind the projectile, which was previously present in the pump tube of the two-stage air gun, results in the formation of a secondary blast wave (SBW) followed by a highly underexpanded supersonic jet with wake structures behind the projectile. As the projectile moves through the transitional ballistic regime, it interacts with the surrounding flow field. The important interactions that affect the aerodynamics of a moving projectile are the interaction of the projectile with the unsteady jet within primary and secondary blast waves and the interaction of projectile with the primary blast wave, usually referred to as the projectile overtaking phenomenon. The overtaking phenomenon was analytically [2, 3] approximated, and different flow regimes were analytically identified as shown in Fig. 1, where M_s is the primary blast wave Mach number (u_s/a_1), M_{p1} is the projectile Mach number (u_p/a_1), and M_{p2} is the relative Mach number of the projectile ($(u_p - u_2)/a_2$) [3]. In the present work, an attempt is made to capture the flow features in the transitional ballistic regimes of supersonic and subsonic projectiles of various configurations. Identification of various regimes of overtaking has also been attempted by constructing the x-t diagram of the projectiles using images obtained from time-resolved schlieren techniques.

2 Methodology

Projectiles are accelerated to desired Mach numbers using a two-stage air gun in the Department of Aerospace Engineering, IIT Madras (Fig. 2). Various shaped projectiles such as cylindrical, conical, and hemispherical have been employed in the experiments.

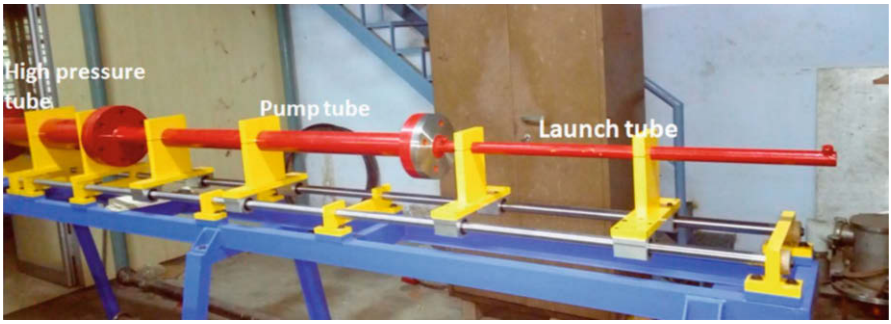

Fig. 2 Two-stage air gun showing high-pressure tube, pump tube, and launch tubes

The flow field characteristics and the projectile motion were visualized using time-resolved schlieren technique. The images were captured using Phantom v2512 high-speed camera which is capable of recording images at 25000 frames per second at full resolution of 1 mega pixel and a maximum of 1 million frames per second at reduced resolutions. These images are processed to understand various flow phenomena that are happening in the transitional ballistic regime. The trajectory information (*x*-*t* diagram) for both blast wave and the projectile also traced from image processing.

3 Results and Discussion

Experiments were conducted to understand the flow field characteristics of different shaped projectiles. With the available experimental setup, the region of visibility is very small, and there is no noticeable attenuation for the blast wave.

3.1 Subsonic Projectile

Figure 3 shows the series of events happening in the case of a conical projectile discharged with a subsonic speed. At t = 0 μs, the primary blast wave just get discharged from the launch tube. It emerges as a spherical blast wave followed by a contact discontinuity. This contact discontinuity is diffused to the surrounding flow as seen in Fig. 3 at t = 2288.16 μs. The air which was previously present in the launch tube, discharged as a subsonic jet (t = 3377.76 μs) followed by the projectile. As soon as the projectile gets ejected from the launch tube, the high-pressure gas behind it will be discharged as a secondary blast wave. Since the projectile is moving with a subsonic Mach number, the secondary blast overtakes the projectile as soon as it is diffracted from the launch tube as observed in Fig. 3 at

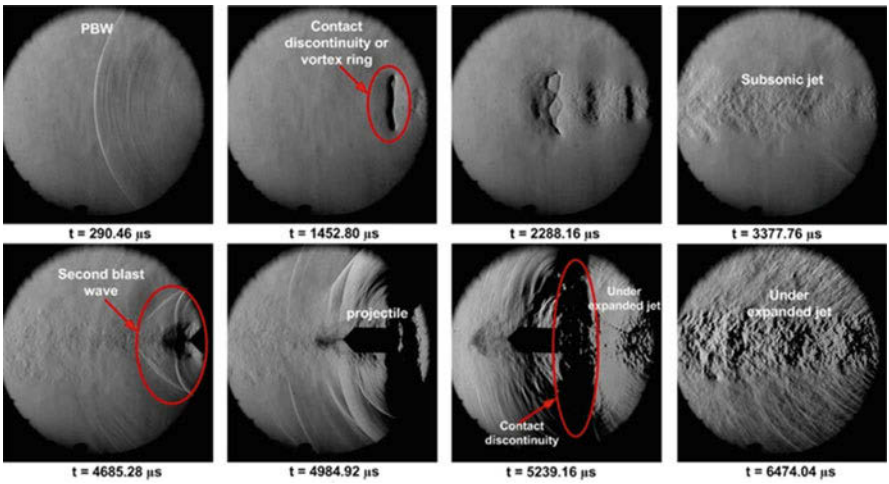

Fig. 3 Conical projectile moving at a subsonic Mach number of 0.6404 (images are captured with a resolution of 384 × 400 and 110,000 fps, calibrated to 0.511 mm/pixel)

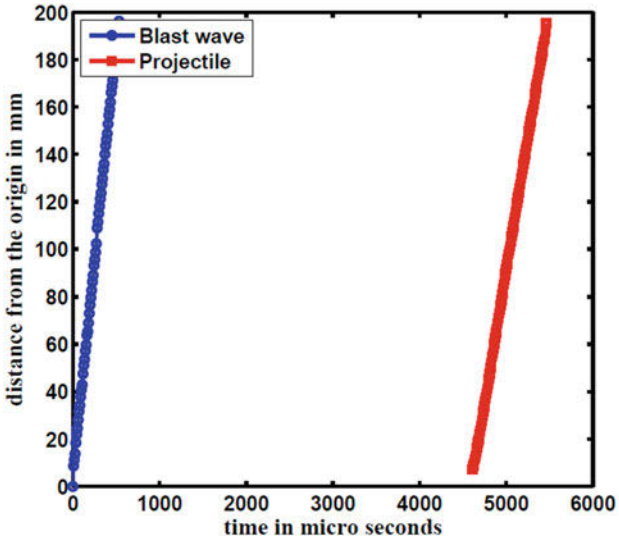

Fig. 4 Trajectory of the blast wave and the projectile corresponding to Fig. 3

t = 4685.28 μs. At t = 5239.16 μs, the secondary blast wave completely overtakes the projectile, and a dark shaded contact discontinuity is visible followed by the underexpanded jet. Projectiles of cylindrical and hemispherical shapes also exhibit similar flow structures.

The trajectories of the blast wave and the projectile are traced from the schlieren images and are shown in Fig. 4. The *x-t* diagram is almost linear, which implies

that the blast wave is not attenuating within the small visible region. The average velocity of the blast wave is 361.9 m/s and that of the projectile is 222.35 m/s.

3.2 Supersonic Projectiles

The series of events associated with the launch of a supersonic conical projectile is shown in Fig. 5. Behind the PBW, there are multiple shock structures visible in the flow field which are visualized in Fig. 5 at t = 463.08 μs and t = 735.48 μs. This may be due to nonuniform acceleration of the projectile inside the launch tube caused by multiple shock reflections between the projectile base and the piston front end in the pump tube. Following these multiple shock structures, a comparatively thicker contact discontinuity appears with a supersonic underexpanded jet behind it. The projectile with a low supersonic velocity is discharged to this underexpanded jet. The secondary blast stays behind the projectile and is not overtaking it (t = 1716.12 μs). A contact discontinuity and a highly underexpanded jet are generated due to the discharge of high-pressure gas which was previously present in the pump tube. The flow characteristics associated with cylindrical and conical projectile are almost the same with slight differences probably due to subsonic and supersonic Mach numbers of the projectiles, which will be quantitatively explained in Sect. 3.3.

Figure 6 shows the trajectories of the primary blast wave and the projectile corresponding to Fig. 5. The average velocity of the blast wave is 354.06 m/s and that of the projectile is 435.26 m/s. The position-time (x-t) diagrams can

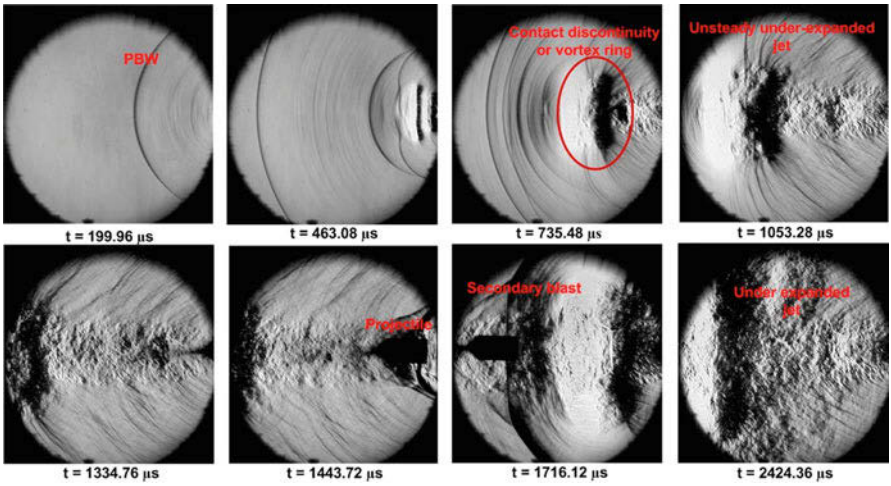

Fig. 5 Conical projectile moving at a supersonic Mach number of 1.2537 (images are captured with a resolution of 384 × 400 and 110,000 fps, calibrated to 0.511 mm/pixel)

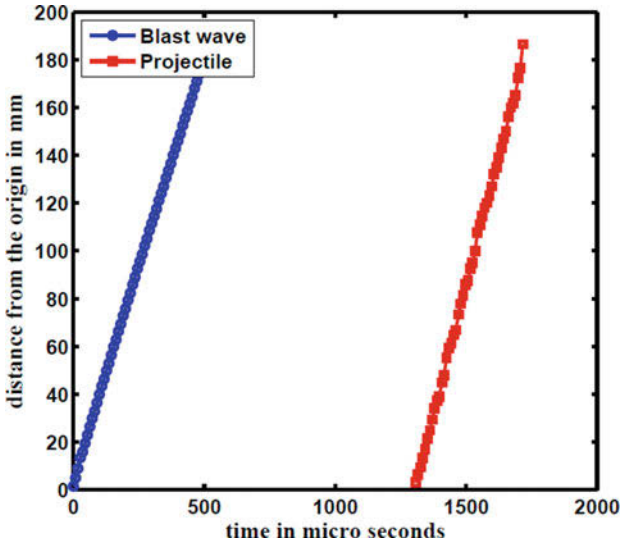

Fig. 6 Trajectory of the blast wave and the projectile corresponding to Fig. 5

be further manipulated to get the instantaneous fluctuating velocities. From the instantaneous velocities, it is possible to obtain the instantaneous accelerations. This instantaneous acceleration history of a projectile can roughly predict the aerodynamic characteristics of the projectile provided the temporal resolutions are quite good.

3.3 Projectile Overtaking Phenomenon

The details of all the experiments conducted are given in Table 1. It is seen from the flow field images that no shock structure was observed ahead of the projectile moving inside the PBW, even when the relative Mach number (Mp_2) is supersonic. The relative Mach number, M_{p2}, is calculated based on the presence of a single blast wave ahead of the projectile, whereas multiple shock structures were visible from the schlieren images due to the nonuniform acceleration of the projectile inside the lunch tube. This might induce errors in the calculation of the relative velocity, particularly, the velocity of the induced flow (u_2) behind the PBW. Moreover, M_{p2} is only slightly supersonic, which results in the formation of a weak detached shock ahead of the projectile. These weak shock structures may not be distinguishable from the Mach radiation structures, which were formed on the vortical structures in the supersonic jet shear layers upstream of the projectile.

The possible overtaking criteria in the experiments are tabulated in Table 1. These results imply that, as the shock Mach number (M_s) increases, there is a corresponding increase in the projectile Mach number (M_{p1}) for a given config-

Table 1 Summary of experiments with projectile Mach number greater than that of primary blast wave

Expt No.	Configuration	M_s	M_{p1}	M_{p2}
1	Conical	1.0027	1.1684	1.1629
2	Conical	1.0056	1.2143	1.2027
3	Conical	1.0198	1.2537	1.2131
4	Conical	1.0915	1.4657	1.2819
5	Conical	1.1605	1.6208	1.3061
6	Cylindrical	1.0617	1.3553	1.2309
7	Cylindrical	1.1877	1.4860	1.1317
8	Hemispherical	1.1147	1.4419	1.2161

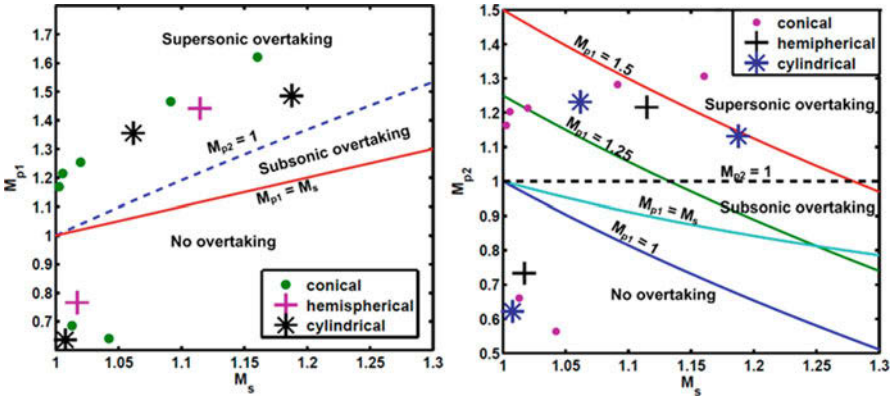

Fig. 7 Experimental results in different overtaking regimes

uration. However, this is not true when M_s and M_{p1} are compared for different configurations, For example, comparing experiments 5 and 7, it can be noted that the projectile is moving with a higher velocity in case of conical shape even though the blast wave Mach number is slightly lesser than that of the cylindrical shaped projectile. Similar trends can be observed for hemispherical and conical cases as seen from experiments 4 and 8. These indicate the trivial trend that conical projectiles experience slightly lesser drag in the transitional ballistic regimes compared to cylindrical and hemispherical ones when traveling with low supersonic Mach numbers. In Fig. 7, supersonic and subsonic experimental results are plotted in M_{p1}-M_s plane as well as in M_{p2}-M_s plane to indicate different overtaking regimes and possibility of overtaking.

4 Conclusions

The flow fields around moving projectiles of various configurations in transitional ballistic regimes have been experimentally captured using time-resolved schlieren imaging techniques. The *x*-*t* diagram of the projectiles and the primary blast waves

have been constructed using image processing. It has been found that the primary blast wave is not a single blast but consists of multiple waves owing to the nonuniform acceleration of the projectile due to multiple shock reflections between projectile and piston in the pump tube. Depending upon the initial condition, there can be subsonic or supersonic jet, onto which the projectile gets discharged. The projectile overtaking phenomenon is analyzed using one-dimensional approximation and is categorized as no overtaking, subsonic overtaking, and supersonic overtaking regimes. The various one-dimensional overtaking scenarios have been experimentally identified from the *x*-*t* diagram of the projectiles and the blast wave. Projectiles with conical shape experience comparatively less drag due to its aerodynamic shape. The aerodynamic characteristics of the projectile can be approximately predicted by processing the images obtained from schlieren.

References

1. Z. Jiang et al., Numerical study on blast flow fields induced by supersonic projectiles discharged from shock tubes. Phys. Fluids **10**, 277 (1997)
2. H. Ahmadikia, E. Shirani, *Transonic and Supersonic Overtaking of a Projectile Preceding a Shock Wave, International Center for Theoretical Physics*, Rept. IC/2001/**48** (2001)
3. G. Rajesh et al., Projectile aerodynamics overtaking a shock wave. J. Spacecr. Rockets **45**, 1251 (2008)

Non-ideal Blast Waves from Particle-Laden Explosives

Q. T. Pontalier, M. G. Lhoumeau, and D. L. Frost

Abstract When an explosive charge is surrounded by an inert granular material, the resulting blast overpressure is attenuated due to the transfer of the chemical energy released to the kinetic energy of the material and energy dissipation during compaction of the porous particle bed. In the present paper, the effect of various parameters on the blast wave attenuation and profile during explosive particle dispersal is explored with a multiphase hydrocode. The results indicate that as the particles are accelerated, the blast overpressure falls below the blast pressure for a homogeneous charge of the same mass in the near field but then recovers at a scaled distance of about 5 as the particles decelerate. Although the peak overpressure is reduced in the near field, the overall loading on a nearby structure may actually be increased when the interaction of the flow and particles with the structure are taken into account.

1 Introduction

The free-field air blast wave that is generated from detonating a high explosive charge is a potential hazard for personnel as well as nearby structures. Hence, the mitigation of blast effects is an important practical consideration for a variety of military and civilian applications. A common technique for mitigating the peak overpressure from an explosive blast wave is to embed particles within the explosive or surround the explosive charge with a layer of inert liquid of granular material. In the latter case in which the explosive charge is surrounded by a layer of inert particles, the mitigation of the blast wave has been attributed primarily to two effects: (i) *inertial* effects due to the transfer of momentum to the particles from the shock wave and expanding products of the explosive and (ii) *compaction* effects due to shock compression of the porous particle bed and possibly fracturing of the

Q. T. Pontalier · M. G. Lhoumeau · D. L. Frost (✉)
Mechanical Engineering Department, McGill University, Montreal, QC, Canada
e-mail: david.frost@mcgill.ca

A. Sasoh et al. (eds.), *31st International Symposium on Shock Waves 2*,
https://doi.org/10.1007/978-3-319-91017-8_5

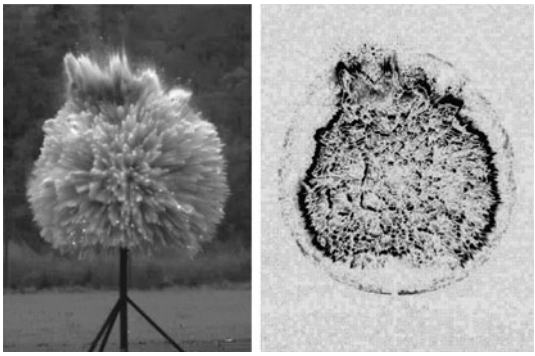

Fig. 1 Left: Single video frame taken 1.8 ms after detonation of a spherical charge containing 75 g of the explosive C4 surrounded by a layer of glass beads. Right: Image generated by subtracting consecutive video images to better visualize the location of the blast wave

particles [1]. In the case of a liquid mitigant, thermal effects due to the vaporization of the liquid may also potentially play a role, although it has been found in past work that the heat transfer and phase change processes are too slow for these effects to be significant on the time scale of the blast propagation [1].

A number of studies have been carried out to examine the blast mitigation performance of various aqueous foams, bubbly or homogeneous liquids, and solid particles of various materials (including sand, steel, ceramic, glass, porcelain, plastic, claydite, polyethylene, perlite, and pumice) [1–6]. Typically, the mitigation performance is reported in terms of the degree of attenuation of the peak shock overpressure (and positive-phase impulse) at a given distance as a function of the ratio of the mass of mitigant to the mass of explosive, or M/C, as compared to that of a homogeneous explosive. A recent systematic experimental study considered the relative blast mitigation performance of a wide variety of solid particles, liquids, and liquid/particle slurries [7]. In this study, the blast pressure in the mid-field range was recorded by fast-response pressure instrumentation. In the near field, the blast pressure was determined from high-speed photography by tracking the blast wave trajectory, differentiating it to obtain the shock Mach number, and then using the Rankine-Hugoniot relation to infer the shock pressure. An example of a frame from the video record used for this procedure is shown in Fig. 1, which illustrates the image processing technique that enhances the visibility of the blast wave. The results of this study indicated that a layer of particles surrounding the explosive charge resulted in a greater blast attenuation performance than a liquid layer, suggesting that the energy dissipation during compaction of the particle bed plays an important role. Furthermore, the rate of decay of the blast overpressure for both liquid and solid mitigated charges is slower than for a bare explosive charge in the near field, suggesting that a radially expanding particle/droplet cloud collectively perturbs the gas behind the shock wave, effectively acting as a porous piston, augmenting the local pressure, and influencing the propagation of the blast wave itself.

From past experiments [7], it is apparent that the inertial effect plays a dominant role, given the strong dependence of the pressure attenuation on the mass ratio M/C. However, the relative importance of other parameters, such as the initial solid fraction ϕ_{solid} and particle size, on blast mitigation is poorly understood. The present

paper consists of a computational study using a multiphase hydrocode to determine the influence of key parameters on the blast wave attenuation and structure.

2 Model

The calculations were carried out using the EDEN multiphase hydrocode developed by scientists at Fluid Gravity Engineering Ltd. (St. Andrews, UK) and extensively validated with experiments on the explosive dispersal of particles [8]. Using the same numerical models described in [8], 1D spherical calculations were carried out for two-phase gas-particle flows. The same compaction model was used as in [9], where Milne et al. compared the calculation results for particle compaction and dispersal directly with experimental radiographs and found that the assumption that the compaction energy is *not* recovered upon expansion gave the best agreement with experiments.

The baseline calculation considered a 100 g spherical C4 explosive charge surrounded by a layer of 50 μm glass particles with a material to explosive mass ratio of $M/C = 10$ and initial solid fraction of the particle bed of 0.60. The parameter space that will be reported includes the following range: two types of particle that were used (glass and steel), three particle sizes that were considered (50 μm, 0.5 mm, and 5 mm), three values of the M/C ratio (1, 10, 100), and three values of the bed solid fraction (0.50, 0.60, and 0.85).

3 Results and Discussion

In this section, the results of the hydrocode calculations are presented, with the peak overpressures plotted as a function of the scaled distance Z defined by:

$$Z = \frac{R}{(m_{C4} \times \varepsilon)^{1/3}}, \tag{1}$$

where R is the distance from the explosion center in m, m_{C4} is the mass of C4 in kg, and ε is the effectiveness factor relative to a TNT equivalent and set to a value of 1.39. The results for the blast waves from mitigated charges are compared with reference values for a homogenous explosive as tabulated by Kinney and Graham [10].

3.1 *Effect of Dispersed Particles on Decay of Pressure Traces*

To give an overview of the influence of the surrounding particle layer on the blast wave dynamics, it is instructive to compute the blast pressure history at several locations together with the particle volume fraction history and compare it to the blast decay for a homogeneous charge of the same explosive mass at the same locations. This comparison is made in Fig. 2 for the baseline case of a layer of 50 μm glass particles, with $M/C = 10$ and a solid fraction of 0.60, and compared with the blast wave history for a homogeneous bare charge. At a scaled distance of 0.33, the particles arrive shortly after the blast wave and strongly perturb the pressure decay, locally raising the pressure to a value comparable to the peak overpressure. At a

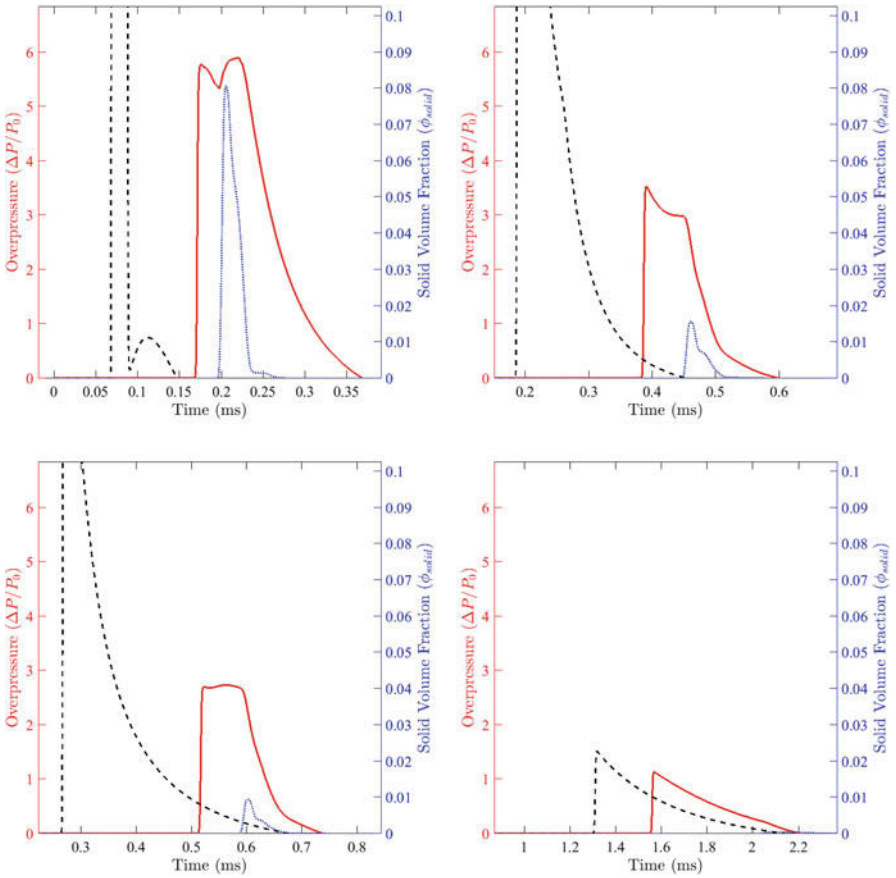

Fig. 2 Comparison of the blast pressure history for a homogeneous charge (dashed black lines) with that of the same charge surrounded with a layer of 50 μm glass particles ($M/C = 10$; $\phi_{\text{solid}} = 0.60$) at scaled distances of $Z = 0.33$, 0.65, 0.82, and 3.27 (red curves). The particle volume fraction is also shown (dotted blue curves)

distance of 0.65, the peak particle volume fraction is below 0.02 and the perturbation to the pressure decay is still present, but less pronounced. As the particle cloud expands still further, the particle/flow interaction weakens, and the blast pressure profile eventually relaxes to the same shape as for an ideal blast wave (as shown in the plot at $Z = 3.3$).

3.2 *Effect of M/C Ratio and Solid Fraction ϕ_{solid}*

The effect of the mass ratio *M/C* on the decay of the peak blast wave overpressure with scaled distance is shown in Fig. 3 for the baseline case of 100 g C4 with 50 μm glass beads with a solid fraction of 0.60. As expected, increasing the mass ratio *M/C* leads to a greater attenuation of the blast overpressure with distance. It is interesting to note that in the very near field, just after the shock emerges from the particle bed, the blast overpressure can be on the order of that of an unconfined charge, presumably due to the piston effect of the early motion of the densified particle layer. As the particle layer is accelerated outward, the energy transfer to the particles causes a sharp reduction in the blast overpressure. Still in the near field, the blast pressure decay rate is reduced as the particle interaction with the local flow perturbs the local pressure field and reduces the decay rate of the blast wave pressure. This transition in the decay rate of the pressure occurs at a scaled distance of about 0.3 for $M/C = 10$. At this scaled distance, the blast pressure attenuation, relative to a bare charge, is near the maximum value. At farther distances from the

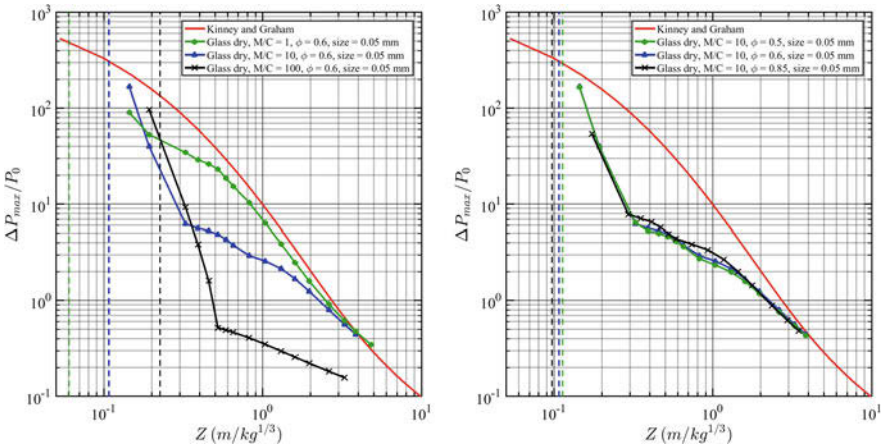

Fig. 3 Blast overpressure decay as a function of scaled distance Z for 50 μm glass particles. Left: Effect of mass ratio *M/C* for a solid fraction of 0.6. Right: Effect of solid fraction for $M/C = 10$. The vertical dashed lines correspond to the location of the initial outer surface of the particle layer, with the layer thickness increasing with *M/C*, but decreasing with ϕ_{solid}. The solid red line gives the blast decay for a homogeneous explosive charge

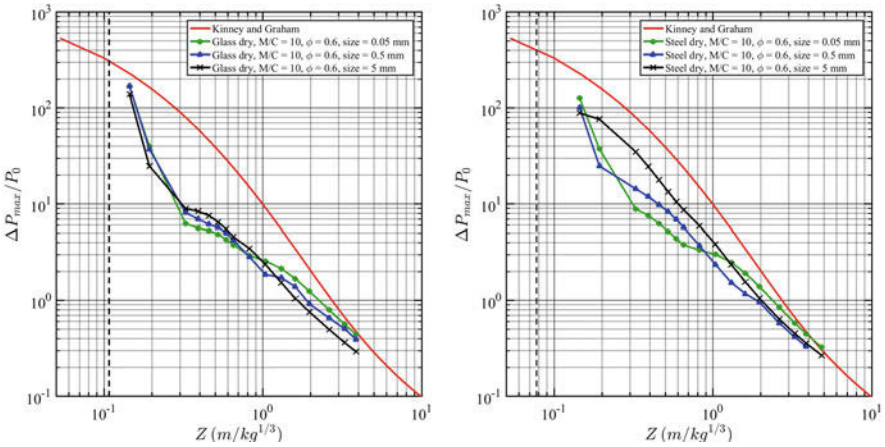

Fig. 4 Effect of particle size on the blast decay for glass (left) and steel (right) particles, for a mass ratio of $M/C = 10$ and solid fraction of 0.60

charge, the overpressure decays more slowly and approaches the same value as for an unmitigated charge. Hence, in effect, for $M/C = 10$, the addition of the particle layer only serves to mitigate the blast overpressure in the range of about $0.15 < Z < 5$. The calculations were repeated for steel particles, and it was found that the effect of M/C on the blast decay was essentially the same for both glass and steel particles.

The effect of the initial solid fraction on the blast overpressure decay for glass and steel particles is also shown in Fig. 3. Increasing the initial solid fraction of the particle bed has a small influence on the blast peak overpressure, with the highest solid fraction considered resulting in slightly less blast attenuation. This is consistent with the argument that some energy dissipation occurs during the dynamic compaction of the particle bed. With a higher initial solid fraction, the work done during bed compaction is smaller, which leads to a reduced mitigation effect.

3.3 Effect of Particle Size

Figure 4 shows the effect of particle size on the blast overpressure mitigation. For glass particles, the particle size has little effect on the blast decay rate, whereas for steel particles, the effect of particle size is more pronounced. In this case, in the range of $0.3 < Z < 1$, the blast attenuation increases with a reduction in particle size, presumably since the smaller the particle size, the greater the overall drag on the particles, so that more energy is extracted from the flow during particle acceleration, reducing the blast pressure, and conversely more energy is given back to the flow during particle deceleration.

4 Conclusions

The mitigation of the blast peak pressure from an explosive charge by surrounding it by a layer of either glass or steel particles has been investigated numerically in 1D with a multiphase hydrocode and compared with the pressure decay for a homogeneous explosive charge. The results illustrate that the explosive particle dispersal reduces the peak blast wave overpressure, but only in the near-mid field (i.e., for scaled distances less than about 5). The explosive energy release is partially transferred to the kinetic energy of the particles, which is then transferred back to internal energy of the flow as the particles decelerate due to drag. The collective interaction of the particles with the flow perturbs the blast wave and results in a non-ideal pressure profile in the near field. The loading on nearby structures will depend on not just the blast pressure but also on the pressure impulse as well as the impulse due to particle collisions with the structure which depends on the particle momentum flux. In some cases the total structural impulse may actually be increased by accelerating inert material as has been observed in previous experiments with particle-loaded explosives [11]. Hence the mitigation of the impulse applied to a structure by surrounding an explosive with particles is dependent on the distance from the charge and, more generally, on the complex interaction of the multiphase flow generated with the structure.

Acknowledgments The authors acknowledge the helpful discussions and the assistance with the use of the EDEN hydrocode from A. Milne and A. Longbottom of Fluid Gravity Engineering Ltd.

References

1. R.M. Allen et al., Experimental and numerical study of free-field blast mitigation. AIP Conf. Proc. **706**, 823 (2004)
2. M. Cheng et al., Numerical study of water mitigation effects on blast wave. Shock Waves **14**, 217 (2005)
3. B.E. Gel'fand, Blast waves attenuation in two-phase media, in *Symposium on Interdisciplinary Shock Wave Research*, Sendai, Japan, 2004, pp. 150–166
4. A. Britan, H. Shapiro, G. Ben-Dor, *Foams for Blast Mitigation* (Foam Engineering: Fundamentals, John Wiley & Sons, 2012), Ch. 19, pp. 477–512
5. V.F. Nesterenko, Shock (blast) mitigation by soft condensed matter. MRS Symp. Proc. **759**, MM4.3.1–MM4.3.12 (2003)
6. B. Langhorst et al., Material systems for blast-energy dissipation, in *Proceedings of the IMPLAST 2010 Conference*, Providence, Rhode Island, USA, 2010, pp. 1–8
7. Q. Pontalier et al., Blast mitigation by granular materials and liquids in spherical geometry, in *24th International Symposium on Military Aspects of Blast and Shock*, MABS, Halifax, Canada, 2016, pp. 1–19
8. A.M. Milne et al., Dynamic fragmentation of blast mitigants. Shock Waves **20**, 41 (2010)
9. A.M. Milne et al., Dynamic fragmentation of powders in spherical geometry. Shock Waves **24**, 501 (2014)
10. G.F. Kinney, K.J. Graham, *Explosive Shocks in Air* (2nd edition), (Springer, Berlin1985)
11. D.L. Frost et al., Particle momentum effects from the detonation of heterogeneous explosives. J. Appl. Phys. **101**, 113529 (2007)

Attenuation of Blast Wave in a Duct with Expansion Region (Effects of Configuration, Porous Panel, and Acoustic Material)

M. Ishiguro and Y. Takakura

Abstract With recent increase of cars, the noise problem has been caused by exhaust sounds generated from exhaust pipes, which consist of weak pressure waves called blast waves. To diminish the noise, a silencer is installed in front of the exhaust pipe. In the present study, reflectors were installed in the high-pressure portion of the shock tube to generate blast waves, and as silencer models, three basic types of expansion regions were combined with four types of porous panels and acoustic material of glass wool. The pressure decay was investigated by transmission and reflection factors to the incident blast wave, together with pressure histories and high-speed movies by the shadowgraph method. As results, it was confirmed that the porous panel contributed to weaken the blast wave to some extent, while the acoustic material does greatly: the one-stage expansion model with a porous panel and glass wool recorded the highest decay of the peak over pressure for transmission and the two-stage expansion model with those showed the second highest. The acoustic material also contributed to decay of reflected shock waves propagating toward an upstream duct.

1 Introduction

Recently, it has become important to attenuate the shock wave on environmental problems. The present research focuses on reducing the exhaust noise released from exhaust pipes of cars, which is related to weak and pulsed shock waves of about Mach 1.1 [1], and a silencer is set up in front of the exhaust duct to decrease the pressure rise.

M. Ishiguro · Y. Takakura (✉)
Graduate School of Tokai University, Hiratsuka, Japan
e-mail: takakura@tokai-u.jp

A. Sasoh et al. (eds.), *31st International Symposium on Shock Waves 2*,
https://doi.org/10.1007/978-3-319-91017-8_6

The pulsed shock waves appearing in the exhaust pipe are considered to be blast waves. The blast wave is an unsteady pressure wave where the shock wave is accompanied by expansion waves. In this research the blast waves are generated in a shock tube [2, 3].

Here, silencer models with an expansion region in a pipe are presented with the sound-absorbing material. About the silencer model, Sekine et al. investigated the configurations of one-stage expansion, two-stage expansion, and insert types from the viewpoint of shock wave attenuation [4], and Sakamoto et al. did from the viewpoint of blast wave attenuation quantitatively [2]. Recently in the industrial silencers, it is of the mainstream to combine the basic configurations above stated and acoustic materials, but the effects are not open to the public. Further in public reports, the blast wave seldom appears as the incident wave.

From this viewpoint, the authors previously reported that the silencer models with a porous panel and the acoustic material showed better attenuation effects for both transmission and reflection factors than the models without those [5, 6, 7]. Further in the present research, the effects of porous panels covering the expansion region were investigated about the arrangement of holes and the porosity.

The aim of the present research is to investigate, in a shock tube, the decay of blast waves about the three types of expansion region, one-stage type, two-stage type, and front-slope type without and with acoustic material of glass wool, including effects of porous panels, by qualitative interpretation for high-speed shadowgraph photography and by quantitative measurements on pressure.

2 Experimental Setup

2.1 Shock Tube

Figure 1 shows a schematic diagram of the shock tube used in the present study. The high-pressure chamber and the low-pressure chamber are formed by a circular duct with an inner diameter 144.6 mm and a rectangular duct with height 120 mm and width 40 mm, respectively. Using a direct-current rupture device [3], the diaphragm with Nichrome wire adhered is broken by burning off with electricity.

In the high-pressure chamber, a blast wave generator is installed. The generation mechanism of blast waves is that the backward expansion waves, generated in the high-pressure side immediately after rupture, are reflected by the end of the high-pressure section and follow the preceding shock wave (see Ref. [6] about the generation principle). The blast wave generator consists of four plates with a very small gap between the plates and the chamber wall, the first plate nearest to the diaphragm acts mainly as the end of the high-pressure section, and the other plates slightly adjust smoothness of the blast wave.

In the low-pressure chamber, an expansion region (200 mm) of silencer models with an inflow duct (750 mm) and an outflow duct (500 mm) is installed.

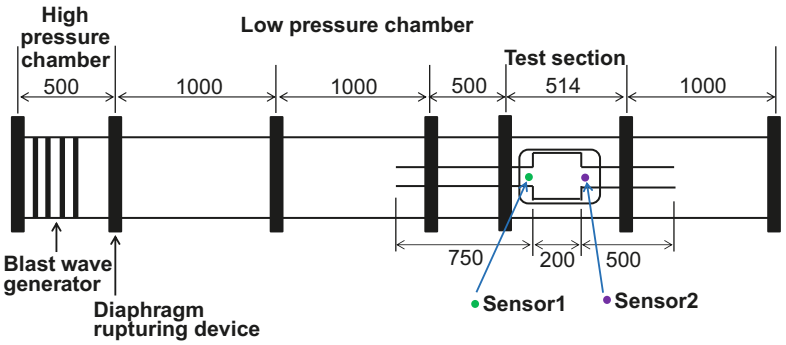

Fig. 1 Schematic diagram of shock tube

2.2 Experimental Condition

Throughout the present research, the pressure ratio is about 2 (the gauge pressure in the high-pressure section is set as 0.1 MPa, and the low-pressure section is open to the atmosphere), and the length of high-pressure section, i.e., distance from the diaphragm to the nearest plate, is 100 mm. The measured Mach number of the blast wave is 1.16. In addition, the theoretical shock Mach number at pressure ratio 2 is also 1.16.

2.3 Silencer Models

In the present study, three basic types of expansion configurations covered with a porous panel were adopted without and with acoustic material, and totally five types of silencer models are shown in Fig. 2. Model (a) shows the detail of one-stage expansion model, where the height of inflow and outflow ducts is $d = 35$ mm, the length and height of expansion region are $L = 200$ or 250 mm and $D = 75$ mm, and the ratio of heights is $D/d = 2.14$, which are common in all models. According to JIS (Japanese Industrial Standards) for silencers [8], D/d should be less than 3.5, whose condition applies to the present case. In all the models, pressure sensors 1 and 2 are set up just in upstream and downstream sides of the expansion region, respectively. Model (b) is a two-stage expansion model, where the expansion region is partitioned into two chambers with a central connecting duct, whose height X is set as $X = 35$ mm. Model (c) is a front-slope model, where the upstream wall has inclination, whose angle α is changed for $\alpha = 15°, 30°, 45°$. Models (d) and (e) correspond to models (a) and (b) with incombustible glass wool as the sound-absorbing material, respectively.

The porous panels with thickness of 1 mm were generated with the arrangement of holes shown in Fig. 3a, b. By combinations of the interspace between holes, l,

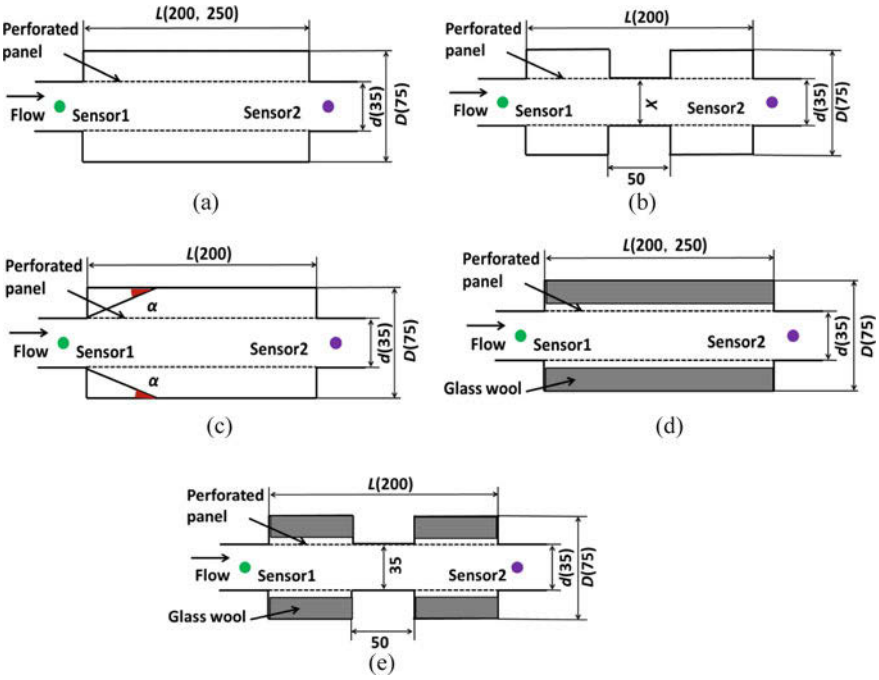

Fig. 2 Model geometries without and with acoustic material. (**a**) One-stage expansion model. (**b**) Two-stage expansion model. (**c**) Front-slope model. (**d**) One-stage expansion with glass wool. (**e**)Two-stage expansion with glass wool

and the diameter of holes, φ, four types of plates were generated with the porosity, ψ. The porosity can be calculated from Fig. 3a as $= \frac{\pi \varnothing^2}{2\sqrt{3}l^2}$. As shown in Table 1, in the case of expansion length $L = 200$ mm, for plates A-1, A-2, and A-3 (with different porosity), the diameter of holes is changed under the common interspace of holes; for plates A-3 and B-1 (with different porosity), the hole diameter is unchanged while the hole interspace is changed; and for plates A-1 and B-1 (with same porosity), both the diameter and the interspace are changed. In the case of expansion length $L = 250$ mm, plates C-1, C-2, C-3, and D-1 have the same relation corresponding to plates A-1, A-2, A-3, and B-1.

3 Results and Discussion

Experimental results are evaluated as follows. Let $(\Delta P_{in})_{max}$ and $(\Delta P_{out})_{max}$ be the maximum pressure rise of the incident wave just in upstream side of the expansion region (at sensor 1) and the maximum pressure rise of the transmitted wave propagating just into downstream side of that (at sensor 2) and $(\Delta P_{ref})_{max}$ be

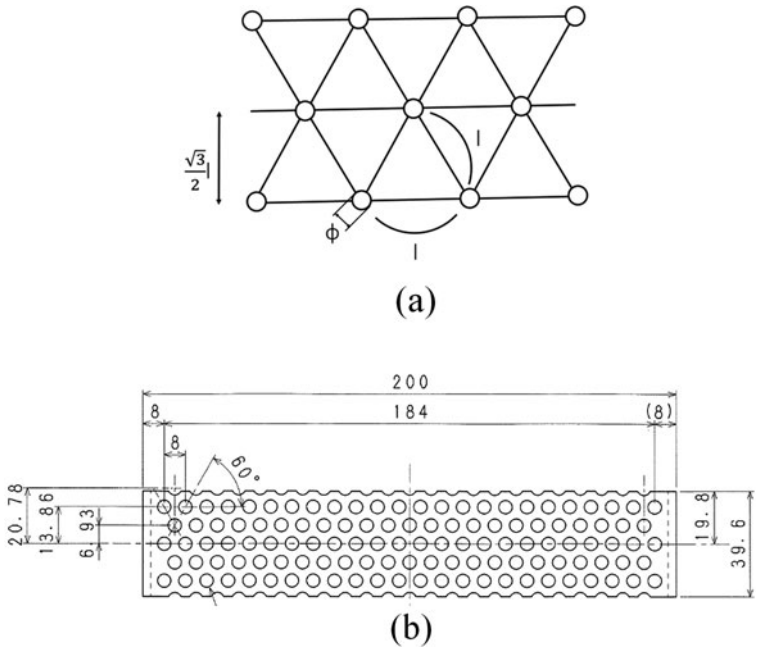

Fig. 3 Porous panel. (**a**) Arrangement of holes. (**b**) Whole view of porous panel ($L = 200$ mm)

Table 1 Design of porous panel

	Length of expansion region L (mm)	Interspace between holes l (mm)	Diameter of holes Φ (mm)	Porosity ψ (%)
A-1	200	8	5	35.4%
A-2			3.5	17.4%
A-3			2.5	8.9%
B-1		4	2.5	35.4%
C-1	250	8	5	35.4%
C-2			3.5	17.4%
C-3			2.5	8.9%
D-1		4	2.5	35.4%

the maximum pressure rise of the reflected wave (at sensor 1), and then the pressure decay factors are defined by two ways:

Comparison 1) Decay Factor for Transmission

$$\eta_{P1} = (\Delta \mathrm{P}_{out})_{max}/(\Delta \mathrm{P}_{in})_{max}$$

Comparison 2) Decay Factor for Reflection

$$\eta_{P2} = \left(\Delta \mathrm{P}_{ref}\right)_{max}/(\Delta \mathrm{P}_{in})_{max}$$

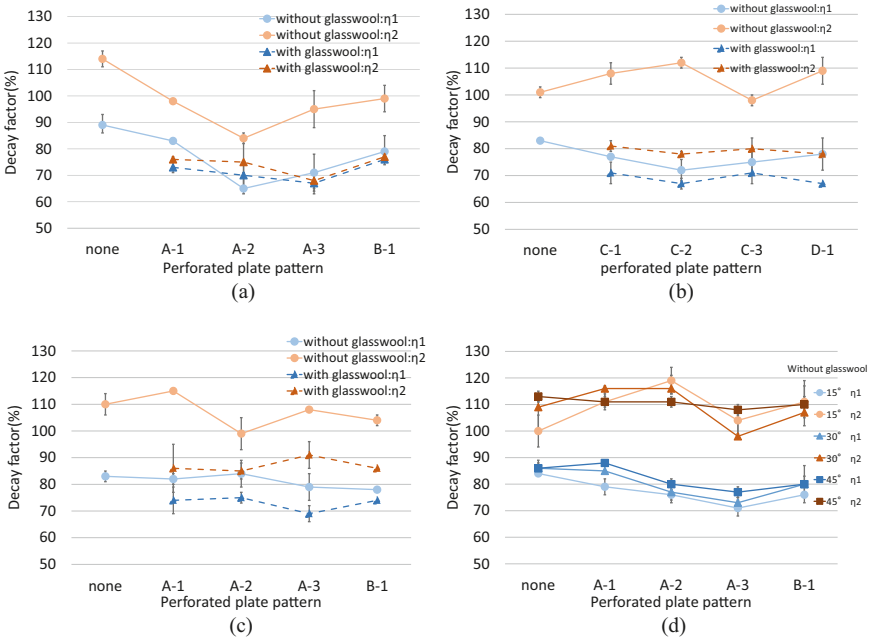

Fig. 4 Comparison of decay factors for transmission and reflection. (**a**) One-stage expansion models ($L = 200$ mm). (**b**) One-stage expansion models ($L = 250$ mm). (**c**) Two-stage expansion models ($L = 200$ mm). (**d**) Front-slope models ($L = 200$ mm)

The results of decay factors for transmission and reflection are summarized in Fig. 4a–d.

3.1 One-Stage Expansion Model with Porous Panel

Figure 5a illustrates phenomena in time history of shadowgraph visualization images in the case with porous panel A-1. At (a-1) the incident blast wave passes the sensor 1; at (a-2) the shock wave emitted from the duct is diffracted by the expansion waves generated at the corner of the duct, ejecting vortices from the main conduit to the expansion region through the porous panel; the resultant cylindrical shock appears to reflect regularly at the upper and lower walls; at (a-3) transition seems to occur from the regular to the Mach reflection at the wall; and at (a-4) the shock wave transmits into the outflow duct, passing sensor 2, and at the same time, the Mach stem reflects upstream at the end wall of the expansion region; the high pressure behind the reflected shock causes ejection of vortices from the expansion region to the central conduit, forming the shock wave in the main conduit.

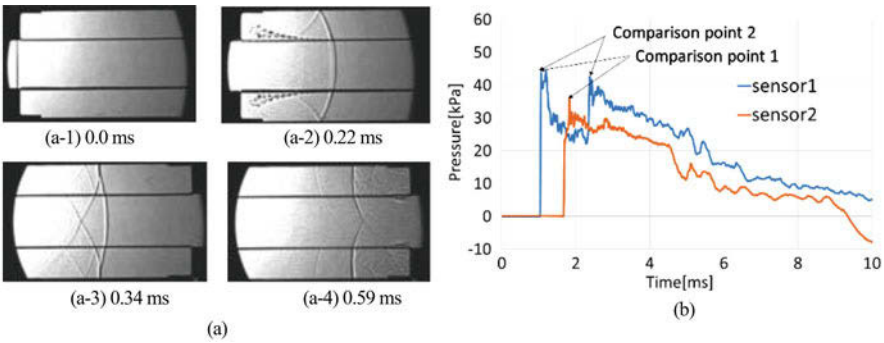

Fig. 5 One-stage expansion model (with porous panel A-1) without grass wool. (**a**) Shadowgraph photography. (**b**) Pressure histories

In the pressure histories of Fig. 5b, sensor 1 shows rapid pressure rise and then the second rise about 1.3 ms after the first rise, which is considered from the visualization images that the first rise is generated by the incident shock and the second one is by the reflected shock propagating upstream to the entrance. By comparisons 1 and 2, the decay factors for transmission and reflection are evaluated as $\eta_{P1} = 83\%$ and $\eta_{P2} = 98\%$, respectively, as indicated as panel A-1 in Fig. 4a.

In the case of $L = 200$ mm with a porous panel A or B (Fig. 4a), both the decay factors showed values less than 100%, while in the case of $L = 250$ mm with a porous panel C or D (Fig. 4b), the decay factor for transmission showed comparable values to those of $L = 200$ mm but the decay factor for reflection showed values greater than 100%. The reason can be considered that the airflow behind the incident shock at the wave head has a gradual pressure decay in the blast wave and therefore the effect to weaken the reflected shock is attenuated as the time for the shock to go and return becomes longer.

3.2 One-Stage Expansion Model with Porous Panel and Glass Wool

Figure 6a, b shows phenomena in shadowgraph visualization images and pressure histories, respectively, in the case with porous panel A-1 and glass wool. In the enlarged view of the shadowgraph, we can see the phenomena that numerous waves are generated from the porous panel and interacted with the shock front, which lead to remarkable decay effects for the shock wave. By comparisons 1 and 2, the decay factors for transmission and reflection are evaluated as $\eta_{P1} = 73\%$ and $\eta_{P2} = 76\%$, respectively, as indicated in Fig. 4a.

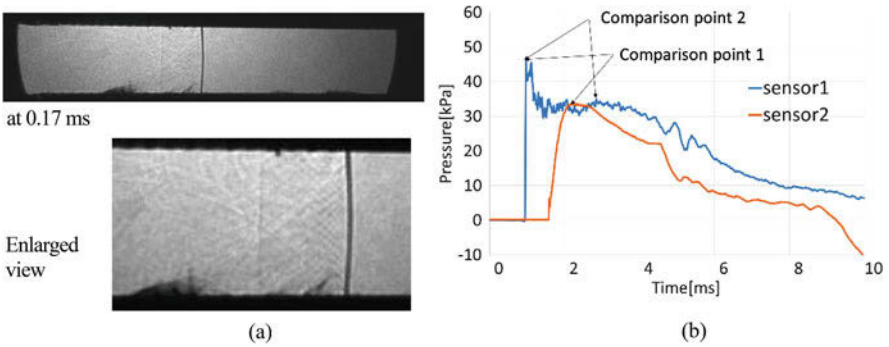

Fig. 6 One-stage expansion model (with porous panel A-1) with glass wool. (**a**) Shadowgraph photography. (**b**) Pressure histories

4 Conclusion

1. In the cases of basic configurations only without a porous panel, for transmission decay, two-stage expansion and front-slope types had enhanced effects, compared with a one-stage type, while for reflective decay, any type did not show attenuation effects.
2. In the cases with a porous panel covering the expansion region, the one-stage expansion type was most effective in both the transmission and reflective decay factors.
3. About the effects of porous panels:
   (i) In the case of same porosity, no difference was detected in decay factors.
   (ii) In the transmission decay, panel A-2 was most effective for the one-stage expansion type and panel A-3 was for the front-slope type.
   (iii) Porous panels have the decay effects for both the transmission and reflection, which is related to the net length of the porous panel.
4. About the effects of an acoustic material:
   as for the model with glass wool, excellent decay effects were detected for both the transmission and reflection.

On the basis of the foregoing, the one-stage expansion model with a porous panel and acoustic material was most effective for both the decay factors.

References

1. N. Sekine, S. Matsumura, K. Takayama, O. Ono, K. Itoh, Initiation and propagation of shock waves in the exhaust pipe of an internal combustion engines. Trans. Jpn. Soc. Mech. Eng., Ser. B **54**(498), 527–531 (1988). https://doi.org/10.1299/kikaib.54.527

2. I. Sakamoto, F. Higashino, K. Higuchi, Decay of pressure waves passing through expansion region in a two dimensional duct. Trans. Jpn. Soc. Mech. Eng., Ser. B **67**(657), 1170–1176 (2001). https://doi.org/10.1299/kikaib.67.1170
3. T. Namiki, R. Shimamura, K. Ohki, Y. Takakura, Rupturing device and generation characteristics of shock and blast waves, in *Proceedings of the Symposium on Shock Waves in Japan*, 2014, p-04
4. N. Sekine, O. Onodera, K. Takayama, Study of silencer characteristics in a gas flow with shock wave (1st report, propagation of shock wave in the silencer). Trans. Jpn. Soc. Mech. Eng., Ser. B **60**(575), 2315–2320 (1994). https://doi.org/10.1299/kikaib.60.2315
5. M. Ishiguro, K. Shinkai, R. Shimamura, H. Gunzi, Y. Takakura, *Attenuation of Blast Wave by Expansion Region in a Duct (Effect of Expansion Configuration and Acoustic Material)*, FLUCOME2015, paper No.32 (2015)
6. M. Ishiguro, K. Shinkai, R. Shimamura, H. Gunji, Y. Takakura, Attenuation effect of expansion configuration and acoustic material on propagation of blast waves in a duct. J. Flow Control Measur. Vis. **4**(3), 79–92 (2016). https://doi.org/10.4236/jfcmv.2016.43008
7. M. Ishiguro, Y. Takakura, Attenuation of Blast Waves in a Duct (Effect of expansion region configuration and acoustic materials), Trans. Jpn. Soc. Mech. Eng., G0500202 (2016)
8. JIS (Japanese Industrial Standards) B 8379 Silencer for air pressure (2009)

Enhancement of the DDT Process with Energetic Solid Particle

Van Bo Nguyen, Quoc Thien Phan, Jiun-Ming Li, Boo Cheong Khoo, and Chiang Juay Teo

Abstract In the pulse detonation engine development, it is believed that the presence of solid particles can rapidly accelerate the flame speed and facilitate a rapid transition to the detonation. In this study, numerical simulations are performed to investigate the dynamics of the deflagration-to-detonation transition (DDT) in the pulse detonation engines using aluminium particles. The DDT process and detonation wave propagation towards the unburnt hydrogen/air mixture containing aluminium particles are numerically studied using the Eulerian-Lagrangian approaches. The numerical results show that the aluminium particles not only shorten the DDT length but also reduced the DDT time. The improvement of the DDT process is primarily attributed to the heat released from the aluminium particle surface chemical reactions. The temperature associated with the DDT process is higher than the case of no energetic particle added, with an accompanying rise in the pressure. The more aluminium particles are added, the more heat is released in the combustion process, thereby, resulting in a faster DDT process. In essence, energetic particles contribute to the DDT process of successfully transiting to detonation waves for the (failure) cases, in which the fuel mixture can be either too lean or too rich.

1 Introduction

Both experimental and numerical studies have shown that the presence of a dense cloud of particles in front of an accelerating flame can lead to a formation of the reflected shock waves, which can facilitate a rapid transition to detonation. In particular, experimental works in [1, 2] have shown that the metallic particle reacts

V. B. Nguyen (✉) · Q. T. Phan · J.-M. Li · B. C. Khoo
Temasek Laboratories, National University of Singapore, Singapore, Singapore
e-mail: tslngvb@nus.edu.sg

C. J. Teo
Department of Mechanical Engineering, National University of Singapore, Singapore, Singapore

A. Sasoh et al. (eds.), *31st International Symposium on Shock Waves 2*,
https://doi.org/10.1007/978-3-319-91017-8_7

with gas phase species and enhance the performance of the propellant gas mixture. In a subsequent study [3], the magnesium particles are used to examine their effects on the detonation characteristics of the methane/air mixture. They indicated that the detonation velocity could increase with the proper choice of particle size and concentration. The study [4] showed that increasing the solid particle volume fraction can reduce the DDT length. In other words, adding the energetic solid particles into the reacting gas phase can significantly improve performance characteristics of the pulse detonation engines. However, a clear explanation or mechanism of the added energetic particles on the DDT process is not quite fully understood. Thus, it is necessary to revisit this problem to understand better how the energetic particles can contribute to the improvement of the DDT process in pulse detonation engine.

In this study, the Eulerian-Lagrangian approaches are employed to describe mathematical models of the problem. In particular, the continuous gas phase is expressed in the Eulerian frame of references, while solid particles are described in the Lagrangian frame of references. The interaction between gas phase flows and the solid particle is modelled through the source terms at corresponding equations. For the reacting solid particle, the one-step surface reaction model is employed to model for the reaction between a solid particle with surrounding gas phase, while combustion model of the gas phase employs detailed chemical kinetics of hydrogen/air mixture. This paper is organized as the following: Sect. 2 shows the mathematical models and the numerical models for the continuous gas phase, solid particle phase, and sub-models. Section 3 comprises the numerical validations. Section 4 presents the numerical setup, results, and discussions. Section 5 is the conclusions of this study.

2 Governing Equations and Numerical Methods

2.1 Governing Equations

Assume that the problem involves reacting solid particles and the premixed gas mixture of hydrogen and air. The gas mixture is compressible and reacting flows. The reacting particle is the aluminium particles. The chemical kinetics of the gas phase is modelled using details of chemical kinetics of 9 species and 19 reversible chemical reactions [5], while the chemical kinetics of the solid surface reaction is modelled using the one-step chemical reaction model. The interaction between gas phase and the solid particle is modelled using two-way interaction models. Moreover, there is no interaction between particle and particle. The conservative equations of density, momentum, energy, and species for the gaseous continuum phase are given as the following:

$$\frac{\partial \rho}{\partial t} + \nabla . (\rho \overline{u}) = S_{P,m} \tag{1}$$

$$\frac{\partial \rho \overline{u}}{\partial t} + \nabla .\left(\rho \overline{u}\,\overline{u}\right) - \left\{\nabla .\left(\mu \nabla \overline{u}\right) + \nabla .\left(\mu \left(\left(\nabla \overline{u}\right)^T - \frac{2}{3} tr\left(\nabla u\right)\right)\right)\right\} = -\nabla p + S_{P,\overline{u}} \tag{2}$$

$$\frac{\partial \rho E}{\partial t} + \nabla .\left(\rho \overline{u} E\right) = \frac{Dp}{Dt} + S_{rad} + S_{ch} + S_{p,E} \tag{3}$$

$$\frac{\partial \rho Y_i}{\partial t} + \nabla .\left(\rho \overline{u} Y_i\right) - \nabla .D\nabla Y_i = S_{ch,i} + S_{p,Y_i} \tag{4}$$

In Eqs. (1, 2, 3, 4), ρ is density of the gas mixture, $\overline{u}$ is vector velocity field, μ is dynamic viscosity, p is pressure field, E is total energy, and Y_i is mass fraction of species i. Here, $S_{p,\,m}$ is mass source term, $S_{p,\overline{u}}$ is momentum source term, S_{rad} is thermal radiation source term, S_{ch} is chemical reaction source term, $S_{p,\,E}$ is source term of heat energy, $S_{ch,\,i}$ is source term for species i due to chemical reactions, and S_{p,Y_i} is source term for mass transfer. For turbulence, the k-omega SST turbulence model is employed in this study.

In the Lagrangian expression, every individual particle is computed along its trajectory inside the computational domain. During the movement, the particle interacts with the surrounding gas phase via exchange of momentum, heat, and mass. Following are the governing equations for the solid particle phase:

$$\frac{\partial x}{\partial t} = u_p \tag{5}$$

$$m_p \frac{\partial u_p}{\partial t} = \sum\nolimits_i F_i \tag{6}$$

$$m_p c_{p,s} \frac{\partial T}{\partial t} = h_k A_p \left(T_g - T_d\right) + \varepsilon \sigma_{SB} \left(T_{rad}^4 - T_p^4\right) + \sum\nolimits_i S_{h,i} \tag{7}$$

In Eqs. (5, 6, 7), (x) is the location of the particle, (u_p) is the velocity of the particle, F_i is the force acting on particle, $(S_{h,\,i})$ is heat exchange between particle and the surrounding gas mixture, T_p is the particle temperature, T_g is the temperature of surrounding gas, and $\varepsilon \sigma_{SB} \left(T_{rad}^4 - T_p^4\right)$ is radiation source term.

The chemical kinetics comprises a detailed chemical kinetic model for the premixed gas mixture of H_2/air and a one-step chemical reaction for the surface reaction of the aluminium particle and surrounding air. For the gas mixture, the chemical reactions of 9 species (O_2, H, OH, O, H_2, H_2O, N_2, HO_2, and H_2O_2), proposed by O'Conaire [5], are described in 19 reversible chemical reactions. All species are assumed to be thermally perfect, and their thermal properties are obtained from Chemkin database [6]. The transport coefficients are determined using the Sutherland correlation [7]. For the aluminium particle, the surface

chemical reaction of the aluminium particles with surrounding air is modelled using one-step chemical reaction, which is controlled by both the diffusion rate and kinetic rate [8, 9]. This model accounts for both effects of diffusion of the surrounding gas phase and kinetic rate of the chemical reaction of aluminium and air, which is expressed as $4AL_{(s)} + 3O_2 \rightarrow 2AL_2O_3$. Details of the diffusion-kinetic chemical reaction can be referred to Refs. [10–12].

2.2 Numerical Methods

The equations governing for the gas mixture in Sect. 2.1 are discretized using the finite volume method as integrals over control volumes. The computational domain is spatially discretized into a series of small control volumes, named "cells". The density-based solver, developed in OpenFOAM [13], is used to solve for the discretization form of these compressible, viscous, and reacting governing equations. In particular, the convective flux terms are computed using HLLC scheme [14] with the slope limiter [15] to capture for the strong shock waves the detonation problem. For the boundary conditions, the non-slip and reflected boundary conditions are applied on the velocity field at the solid walls, while the outflow boundary condition is applied at the outlet of the detonation chamber. The adiabatic boundary condition is applied on the temperature field at the solid walls, and the Neumann boundary condition is applied at the outlet of the detonation chamber. The zero gradient boundary condition is applied on the pressure at a solid wall, and outflow boundary condition is applied at the outlet of detonation chamber.

The governing equations for the particle are solved in the discretized form. The standard semi-implicit Euler method is employed to advance the solution of the discretization equations in time. At every time step (Δt) of solving for the fluid flow, the solver is applied for the Lagrangian particle system first. To save on computational time, the particles are calculated as small groups of certain particles with identical parameters. Regarding the boundary conditions, the rebound boundary condition is applied on the velocity of the solid particle when it makes impact on the solid wall, while the "escape" boundary condition is applied at the outlet of the detonation chamber. In addition, the combustion process of the premixed mixture is described via the reaction progress variable ($c(x, t)$). See the reference [16] for the details. Here $c = 0$ represents the unburnt mixture, whereas $c = 1$ represents the completely burned mixture.

3 Numerical Validation

In this section, the numerical DDT process is validated through a comparison between the current numerical results and experimental data in the GraVent DDT Database [17]. The mixture of 25.1% of hydrogen and air is filled into the detonation chamber homogenously at the ambient temperature of 293 K and pressure of 101,325 Pa. The length of detonation chamber is 5400 mm, while the width is

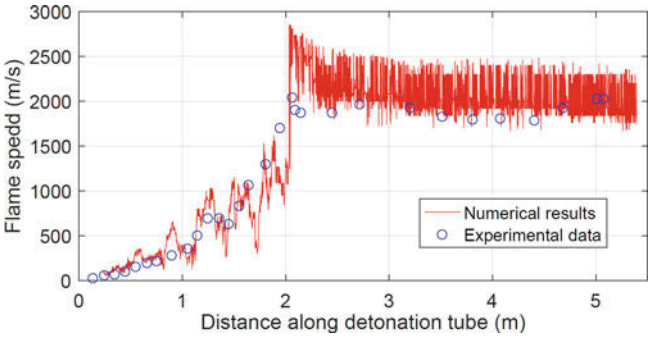

Fig. 1 Comparison of numerical results and experimental data [17]

60 mm. The seven obstacles are regularly placed in the chamber from the location of $x = 250$ mm to the downstream with the distance between the two obstacles of 300 mm. The blockage ratio of the obstacles is 30%. The whole computational domain is discretized using structure mesh with $\Delta x = \Delta y = 1$mm. In the simulation, a small hotspot with high temperature of 2300 K located at the left end is used to ignite the flame. Figure 1 shows the comparison between the numerical results and experimental data [17] for the flame speed versus flame front position. It can be seen that the numerical results are in reasonably good agreement with experimental data in both the trend and magnitude at the same location. Both numerical results and experimental data show that the deflagration successfully transits to detonation at location of about $x = 2000$ mm. Moreover, the average simulated velocity is about 2010 m/s which is closely to the measured 1965 m/s.

4 Numerical Results and Discussions

4.1 Numerical Setup

In this study, two scenarios are employed to explore the influence of aluminium particles on the DDT process, which are (1) comparison of the aluminium particle added to the no-particle-added case and (2) effects of the different particle volume fraction on the DDT process. A 2D computational domain of the chamber is set up for the simulations. The computational domain is discretized using a uniform rectangular grid of $\Delta x = \Delta y = 1\ mm$. The chosen mesh grid size of 1 mm is selected from the careful mesh grid convergence study. Initially, the premixed mixture of the hydrogen and air at equivalence ratio of 1.0 is introduced homogeneously in the computational domain under the pressure of 1.0 bar and temperature of 300 K. The initial diameter of particles is generated using the Rosin-Rammer distribution. The combustion process is started by using a small region with a high temperature of 2000 K (see Fig. 2).

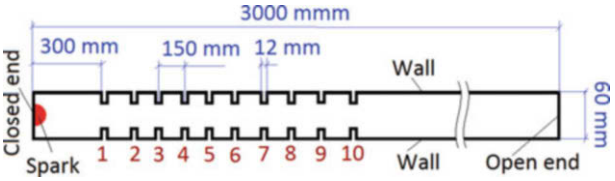

Fig. 2 Geometry model of the detonation chamber

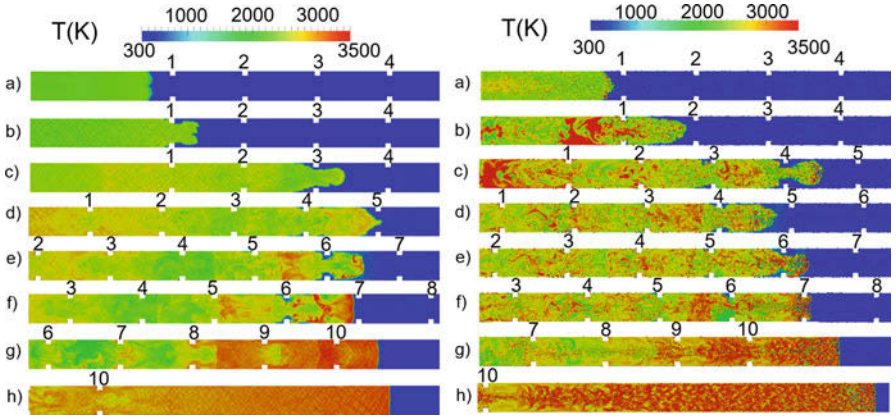

Fig. 3 Comparison of the temperature contour (in Kelvin) for the two cases

4.2 Comparison of the Aluminium Particle Added and No Particle Added

The two cases are Case 1 aluminium particles added and Case 2 no particle added to the chamber. In these cases, the premixed mixture of hydrogen/air at the equivalent ratio of 1.0 is initialized at the ambient temperature of 300 K and pressure of 1.0 bar. In Case 1, the particles are uniformly distributed inside the chamber with the volume fraction of 1/10000. Figure 3 shows the comparison of the temperature contour of the mixture at different times during the DDT process and detonation wave propagation. The temperature is expressed in Kelvin unit and plotted for the same range from 300 K to 3500 K. The blue colour shows the low value, while the red colour shows the high value of temperature. Case 1 is plotted with the presence of the particles. In general, contours (a–d) show the temperature in the deflagration (flame acceleration) stage during the acceleration process. Contours (e–f) demonstrate the temperature at the time when strong shock waves are formed and the deflagration is successfully transiting to detonation waves. Contours (g–h) show the temperature at stable CJ detonation wave propagation process. It is observed that the temperature is higher in Case 1 at all the three stages. In Case 1, the particles initially take some heat energy and manifested as temperature rise on the particles for the subsequent surface chemical reactions. As the energy is released from the

surface chemical reaction locally, eventually the temperature of the gas mixture becomes higher than Case 2. It is clear that surface chemical reaction has strongly influenced and led to the temperature rise at the deflagration stage. Locally rising temperature can cause instability in the combustion process. The local instability and high temperature have enabled DDT to be achieved at the shortest length. Thus, the higher temperature and stability of the flame can accelerate the flame and results in a shorter DDT length and time.

4.3 Effect of the Aluminium Particle Volume Fraction

In this section, numerical simulations are performed for different particle volume fractions added into the detonation chamber to study the effect of aluminium particle volume fraction on the DDT process. Four different amounts of energetic aluminium particles are mixed with hydrogen/air premixed mixture at the equivalence ratio (fuel/air) of about 0.85 leading to four corresponding particle volume fractions of 1/1000, 1/10000, 1/100000, and 1/1000000 (henceforth called Cases 1, 2, 3, and 4, respectively). Figure 4 presents the comparison of the temperature contours for the

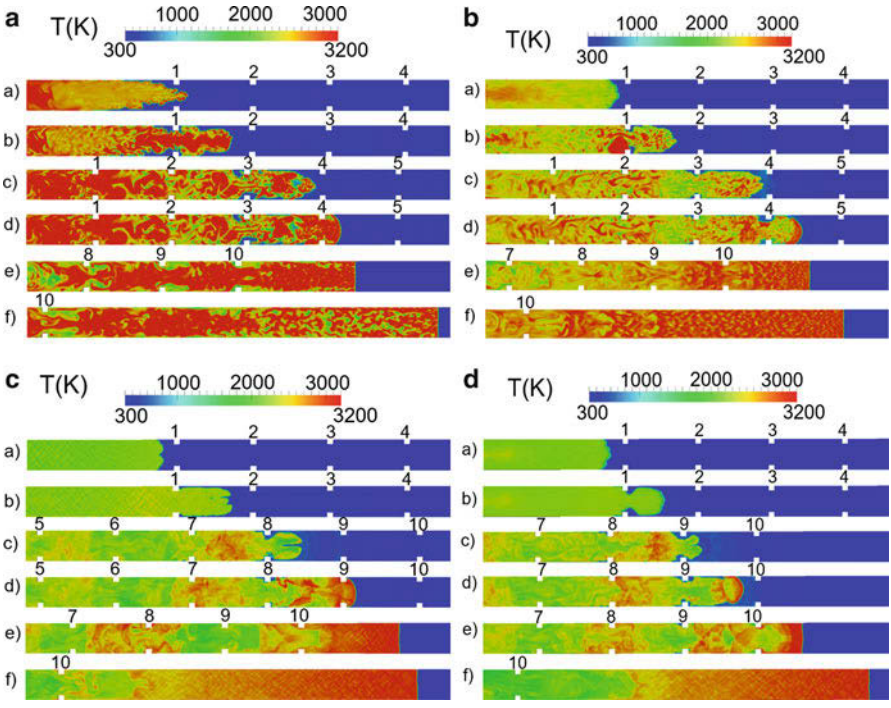

Fig. 4 Comparison of temperature contour for the four cases (1–4). (**a**) Case 1: volume fraction of 1/1000. (**b**) Case 2: volume fraction of 1/10000. (**c**) Case 3: volume fraction of 1/100000. (**d**) Case 4: volume fraction of 1/1000000

four Cases 1–4 at deflagration process (a–b), transition stage (c–d), and detonation stage (e–f). In general, it is observed that the higher volume fraction of aluminium particles added into the detonation chamber results in a higher temperature in the combustion process since more quantity of aluminium particles contribute to the chemical reactions of the burning process. The temperature is locally very high for the region of dense particles. In fact, the temperature fluctuates more intensely for Cases I and II as compared to Cases III and IV. The instability and high local temperature create hotspots and shock waves occurring earlier for the higher particle volume fraction, thus leading the deflagration successfully transiting to detonation waves earlier. Temperature contours (d) indicate that the successful detonation waves are formed at about the fourth obstacle for Case 1, at about the sixth obstacle for Case 2, at about the ninth obstacle for Case 3, and at about the tenth obstacle for Case 4.

5 Conclusions

In this study, numerical simulations are performed for both the "no particle" and "aluminium particle" cases. The energetic aluminium particles have a significant influence on the dynamics of the DDT process via primarily the heat energy released from surface chemical reactions. The effect of the difference volume fractions is also studied. Simulations are performed for the particle volume fractions at 1/1000, 1/10000, 1/10000, and 1/1000000, which are mixed with the same mixture of fuel/air flow at the equivalent ratio of 0.85. Both the temperature and pressure are higher for the case of higher particle volume fraction. As more particle volume fraction is added, there is more heat released from the particle surface chemical reactions. Thus, both the DDT length and DDT time are shortened with the higher particle volume fraction added. However, more combustion instabilities are rising as the higher particle volume fraction added.

References

1. B. Veyssiere et al., in *IVth International Workshop on Ram Accelerators*, Poitiers (France), 1999a
2. B. Veyssiere et al., *Control of Detonation Processes* (Elex-KM, Moscow, 2000), pp. 61–63
3. B. Veyssiere et al., Shock Waves **12**(2), 227 (2002)
4. F. Zhang, J. Propuls. Power **22**(6), 1289 (2006)
5. M.Ó. Conaire et al., Int. J. Chem. Kinet. **603**, 36 (2004)
6. R. Kee et al., *Chemkin Collection*, Release 3.6 (2000)
7. R. Bird et al., *Transport Phenomena* (Wiley, New York, 2001)
8. M.A. Trunov et al., Propell. Explos. Pyrotech **30**(1), 36–43 (2005a)
9. M.A. Trunov et al., Combust. Flame **140**, 310 (2005b)
10. M.W. Beckstead, Int. Aerodynamic. Solid Rocket Propulsion. RTO-EN-023 (2002)
11. M.W. Beckstead, Shock Waves **41**(5), 533 (2005)

12. Y. Huang et al., Combust. Flame **156**, 5 (2009)
13. J.G. Christopher, *OpenFOAM User Guide*, version 2.1.x. (2012)
14. E.F. Toro et al., Shock Waves **4**(1), 25 (1994)
15. J.G. Christopher, OpenFOAM Wiki Limiters (2010)
16. K.N. Bray et al., Acta Astronaut. **4**(3–4), 291 (1977)
17. L.R. Boeck, P. Katzy, J. Hasslberger et al., *The GraVent DDT database.* Shock Waves **26**(5), 683 (2016)

Large-Scale Computation of Direct Initiation of Cylindrical Detonations

H. Shen and M. Parsani

Abstract We investigate the direct initiation of cylindrical detonations in free space by performing large-scale computations on a supercomputer. The two-dimensional (2D) compressible reactive Euler equations with a one-step chemical reaction model are solved by a well-validated upwind CE/SE scheme using up to 1.6 billion mesh points. Numerical results imply that one-dimensional (1D) approaches can only interpret the direct initiation mechanism of stable detonations. Inherent multi-dimensional instabilities have a significant influence on the direct initiation of unstable detonations. On one hand, multi-dimensional instabilities make the detonation more unstable and increase the risk of failure of the detonation. On the other hand, the collision of transverse waves generated from multi-dimensional instabilities leads to the initiation of local overdriven detonations that can enhance the overall self-sustainability of the global process. The competition between these two effects is an important mechanism to interpret the direct initiation of multi-dimensional detonations.

1 Introduction

Many combustible gases can form self-sustainable detonations via deflagration-to-detonation transition (DDT) process or direct initiation using a powerful source energy [1]. In the problem of direct initiation, it is important to estimate the critical energy that can be used to direct ignite detonations. Due to the complexity and multi-scale property of this problem, many previous theories and computations on the direct initiation of detonation were based on 1D assumptions [2–4]. These 1D approaches suffer, by nature, from severe limitations when they are used to describe detonations with inherent multi-dimensional structures observed in experiments.

H. Shen (✉) · M. Parsani
Extreme Computing Research Center (ECRC) Computer, Electrical and Mathematical Sciences & Engineering (CEMSE), King Abdullah University of Science and Technology (KAUST), Thuwal, Saudi Arabia
e-mail: hua.shen@kaust.edu.sa

A. Sasoh et al. (eds.), *31st International Symposium on Shock Waves 2*,
https://doi.org/10.1007/978-3-319-91017-8_8

The complex multi-dimensional instabilities are not yet clearly understood. It is therefore extremely difficult, if not impossible, to build a theoretical model that accounts for multi-dimensional effects. Using highly resolved large-scale computations to gain some insights into the physical process is an efficient approach.

In this study, we aim to explore the role of multi-dimensional instabilities in direct initiation of detonations via large-scale computations. To this end, we extend a well-validated upwind conservation element solution element (CE/SE) code [5–7] to simulate the direct initiation of cylindrical detonations in one and two dimensions. We performed all the 2D simulations using Shaheen XC40 which is a supercomputer installed at King Abdullah University of Science and Technology (KAUST).

2 Mathematical Model and Numerical Method

Neglecting viscosity, heat transfer, diffusion, and body forces, 1D cylindrical detonations are modeled by the inviscid, unsteady 1D reactive compressible Euler equations with a cylindrical geometrical source term [4], and 2D cylindrical detonations are modeled by the 2D reactive compressible Euler equations. The specific total energy with the perfect gas assumption is calculated as

$$e = \frac{p}{(\gamma - 1)\,\rho} + \frac{1}{2}\mathbf{v} \cdot \mathbf{v} + YQ, \tag{1}$$

where ρ, $\mathbf{v}$, p, Y, γ, and Q denote the density, velocity vector, pressure, reactant mass fraction, specific heat ratio, and heat released by the chemical reaction, respectively. The chemical reaction rate is modeled by the one-step model, and the reaction rate is derived by the classic Arrhenius equation:

$$\omega = -kYe^{-E_a/T}, \tag{2}$$

where T, k, and E_a are the temperature, constant pre-exponential factor, and the activation energy. The value of k is chosen to derive a unit half-reaction length ($L_{1/2}$) using the Zeldovich-von Neumann-Döring (ZND) model [8]. The other variables are non-dimensionalized with respect to the state of the unburned reactants.

A second-order upwind space-time CE/SE method [5, 6] coupled with a local Lax-Friedrichs flux is used to solve the 1D and 2D Euler equations. The chemical reaction source term is discretized using the implicit trapezoidal method.

3 Numerical Results and Discussions

We focus on the direct initiation of cylindrical detonations with $\gamma = 1.2$ and $Q = 50$. The stability of the detonation depends on the value of E_a. Based on the threshold of instability [9], we chose the following three representative cases: (a) stable case

with $E_a = 15$, (b) mildly unstable case with $E_a = 27$, and (c) highly unstable case with $E_a = 50$.

In 1D simulations, the computational size of domain is no less than 1000 $L_{1/2}$ with symmetric boundary condition on the left side and outflow boundary condition on the right side. In 2D simulations, the computational domain is [2000, 2000] $\times$ $L_{1/2}$ with non-reflective boundary conditions implemented on all the boundaries. A hot spot with $p_s = (\gamma-1)E_s$ and $T_s = 20$ for $x \leq 1$ in 1D and for $\sqrt{(x-1000)^2 + (y-1000)^2} \leq 1$ in 2D is adopted. All the simulations are run using 20 points/$L_{1/2}$, which means the total number of mesh points is 1.6 billion in 2D simulations. With our CE/SE scheme for solving the 2D reactive Euler equations, such a mesh density yields 24 billion unknowns. The 2D code is parallelized using a domain-decomposition approach and is run using 40,000 CPU cores.

3.1 Stable Case with $E_a = 15$

We first perform 1D simulations, increasing E_s from 1.8×10^4 to 10^5. As seen from the shock pressure distribution shown in Fig. 1, three typical regimes are observed. When $E_s = 10^5$, a supercritical regime is observed. In this case, P_{sh} first decays to a value slightly below ZND value (P_{ZND}) due to the geometric curvature and then quickly approaches to P_{ZND}. A critical regime occurs when $E_s = 1.9 \times 10^4$, 2×10^4 and 3×10^4, in which case P_{sh} first decays to a sub-ZND value and then quickly runs up after certain distances. The run-up distance increases exponentially as E_s decreases. When E_s decreases to 1.8×10^4, the detonation does not occur within the current computational domain. This case refers to the subcritical regime. We note that, if the computational domain is long enough, the detonation may be eventually initiated using one-step chemistry [10].

Next we perform corresponding 2D simulations with the same source energies. The same initiation regimes are observed when we use the same source energies as the 1D simulations. Taking $E_s = 2 \times 10^4$ as an example (see Fig. 2), the 2D

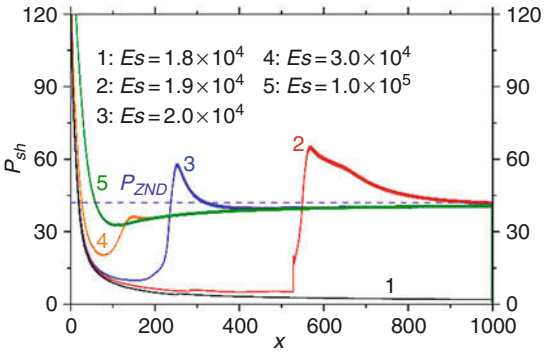

Fig. 1 1D shock pressure as a function of position and source energy for the stable case with $E_a = 15$

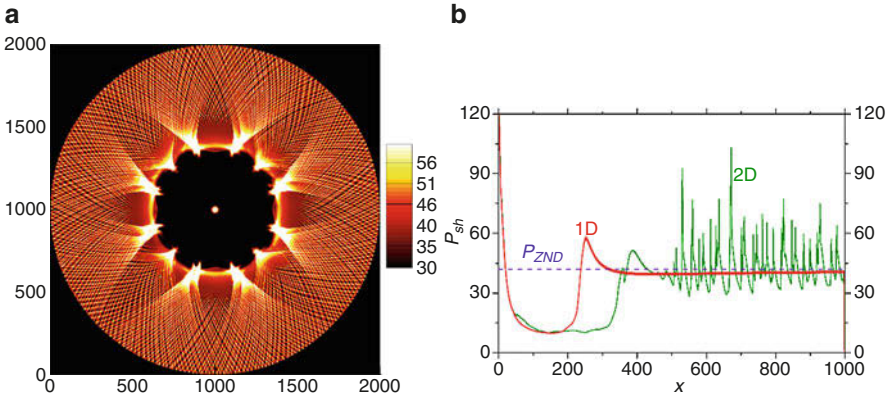

Fig. 2 (**a**) 2D contours of the shock pressure and (**b**) comparison of the shock pressure profile along $y = 1000$ of the 2D simulation with the 1D simulation for the stable case with $E_a = 15$ and $E_s = 2 \times 10^4$

solution matches very well with the 1D solution at the initial stage, but after some distance, the 2D solution starts to deviate the 1D solution due to multi-dimensional instabilities. Although the run-up distances of the shock pressure are different in different directions, the overall 2D initiation regime is consistent with the 1D detonation at the same source energy.

3.2 Mildly Unstable Case with $E_a = 27$

In 1D simulations, E_s increases from 2.2×10^5 to 5.1×10^5 in 10^4 increments. Second critical source energies for successful direct initiation of mildly unstable detonations were found by 1D numerical studies of Eckett et al. [4] and Mazaheri [10]. In our 1D simulations, as seen in Fig. 3, detonations are successfully initiated for $E_s = 2.4 \times 10^5$, 3.8×10^5 to 4.1×10^5, and 5.1×10^5. In contrast, detonations fail in the other cases. This behavior suggests that the current 1D solutions admit at least three critical energies, i.e., 2.4×10^5, 3.8×10^5, and 5.1×10^5.

Based on the 1D simulations, we initiate 2D detonations with $E_s = 2.4 \times 10^5$ (the first 1D critical energy), 3.5×10^5 (between the first and the second 1D critical energies), 4×10^5 (slightly above the second 1D critical energy), and 4.5×10^5 (between the second and the third 1D critical energies). As seen in Fig. 4, the detonations fail in the first two cases with relatively lower source energies, although the 1D detonation with $E_s = 2.4 \times 10^5$ is successful. Numerical experiments show that the detonation succeeds when $E_s \geq 4 \times 10^5$. This implies that there may exist a unique critical energy (approximately 4×10^5) for this mildly unstable 2D case.

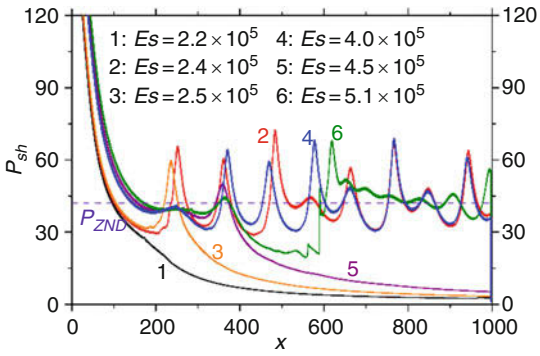

Fig. 3 1D shock pressure as a function of position and source energy for the mildly unstable case with $E_a = 27$

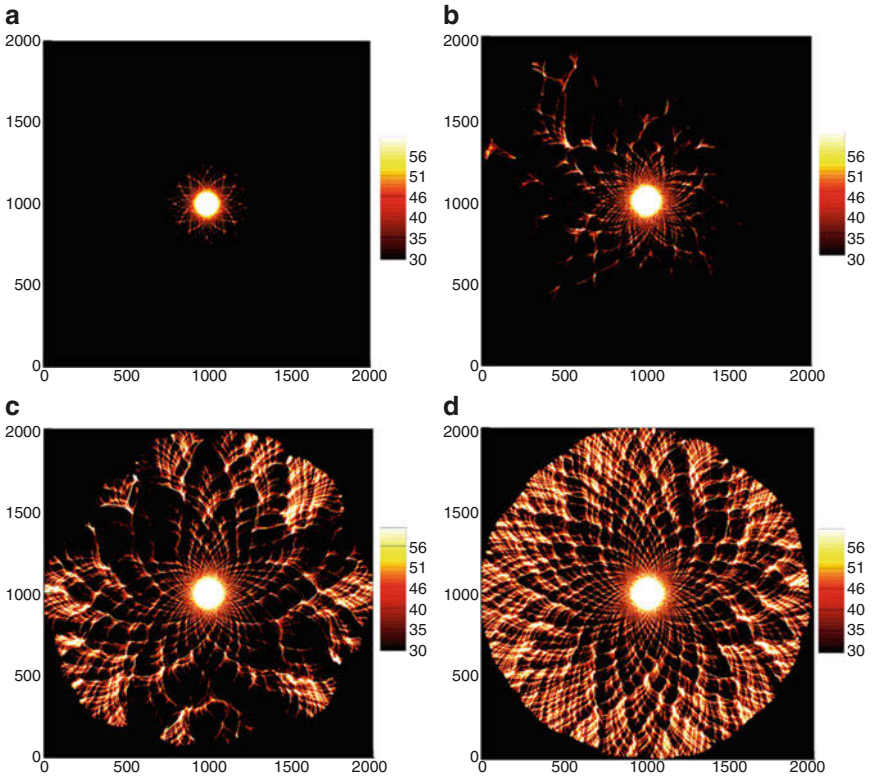

Fig. 4 2D shock pressure contours for the mildly unstable detonations with $E_a = 27$ at different source energies (**a**) $E_s = 2.4 \times 10^5$. (**b**) $E_s = 3.5 \times 10^5$. (**c**) $E_s = 4 \times 10^5$. (**d**) $E_s = 4.5 \times 10^5$

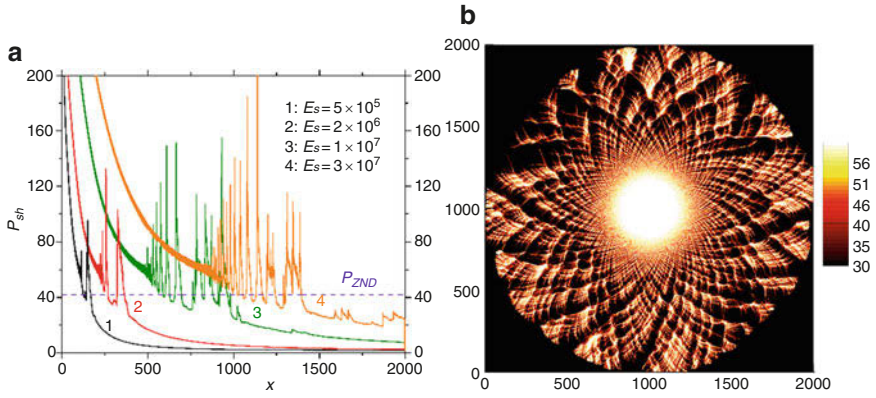

Fig. 5 (**a**) 1D shock pressure as a function of position and source energy and (**b**) 2D shock pressure contours at $E_s = 1.5 \times 10^6$ for the highly unstable case with $E_a = 50$

3.3 *Highly Unstable Case with $E_a = 50$*

We increase the source energies from 4×10^5 to 3×10^7 in 5×10^5 increments. As observed in Fig. 5a, although the propagating distance increases as the source energy increases, the detonation will eventually fail after a highly oscillatory stage. The 2D detonation, however, can be successfully initiated when the source energy reaches to 1.5×10^6 (see Fig. 5b).

3.4 *Discussions*

The direct initiation mechanism of detonations is dominated by a competition between heat release of chemistry and unsteadiness. The numerical results show that instabilities of multi-dimensional detonations are inevitable. In the stable case, heat release overwhelms unsteadiness, and hence the initiation regimes in 1D and 2D are consistent despite multi-dimensional instabilities emerge in 2D detonations. In the mildly unstable case, the competition between heat release and unsteadiness is very piercing, which results in multiple 1D critical energies. While in the highly unstable case, excessive unsteadiness arising from the strong 1D instabilities dominates the initiation process, and detonations always fail in 1D. But in the direct initiation of 2D unstable cases, multi-dimensional instabilities play a double-sword role, and totally different results from 1D cases are observed. On one hand, multi-dimensional instabilities make the detonation more unstable and increase the risk of failure of the detonation. On the other hand, multi-dimensional instabilities can generate transverse waves, and the collision of transverse waves leads to the initiation of local overdriven detonations that can enhance the overall self-sustainability of the global

process. The competition between these two effects is an important mechanism of the direct initiation of multi-dimensional detonations. When *Es* is small, the first effect is more important. This explains why the initiation of the detonation succeeds in 1D but fails in 2D in the mildly unstable case with $E_a = 27$ and $E_s = 2.4 \times 10^5$. However, the second effect becomes dominant when E_s increases. Therefore, unstable detonations can be directly initiated in 2D when E_s exceeds a critical value. More detailed results and discussions can be found in Ref. [11].

4 Conclusion

The 1D assumption only provides a valid approach to understanding the direct initiation of stable detonations, and multi-dimensional effects must be included in a predictive model of direct initiation of unstable detonations.

Acknowledgment The authors are thankful for the computing resources of the Supercomputing Laboratory and the Extreme Computing Research Center at King Abdullah University of Science and Technology.

References

1. J.H.S. Lee, Annu. Rev. Fluid Mech. **16**, 311 (1984)
2. Y.B. Zeldovich, S.M. Kogarko, N.N. Simonov, Sov. Phys. Tech. Phys. **1**, 1689 (1956)
3. L.T. He, P. Clavin, J. Fluid Mech. **277**, 227 (1994)
4. C.A. Eckett, J.J. Quirk, J.E. Shepherd, J. Fluid Mech. **421**, 147 (2000)
5. H. Shen, C.-Y. Wen, D.L. Zhang, J. Comput. Phys. **288**, 101 (2015)
6. H. Shen, C.-Y. Wen, J. Comput. Phys. **305**, 775 (2016)
7. H. Shen, C.-Y. Wen, M. Parsani, C.-W. Shu, J. Comput. Phys. **330**, 668 (2017)
8. W. Fickett, W.C. Davis, *Detonation* (University of California Press, Berkeley, 1979)
9. H.I. Lee, D.S. Stewart, J. Fluid Mech. **216**, 103 (1990)
10. K. Mazaheri, PhD thesis, McGill University, Montreal, Canada, 1997
11. H. Shen, M. Parsani, J. Fluid Mech. **813**, R4 (2017)

Numerical Study on a Cycle of Liquid Pulse Detonation Engines

Van Bo Nguyen, Quoc Thien Phan, Jiun-Ming Li, Boo Cheong Khoo, and Chiang Juay Teo

Abstract A typical cycle of a liquid pulse detonation engine (PDE) often involves three main processes, which are injection and evaporation process, deflagration-to-detonation transition process (DDT), and detonation propagation process. These three processes often include a number of complex subprocesses, which strongly influence the performance characteristics of the engine. Thus, it is important to understand the physical and chemical insights of these processes in an operating cycle of the liquid PDE to improve the engine performance characteristics. In this study, numerical simulations are performed to simulate for the complete operating cycle of the liquid PDE. The numerical method is developed based on the Eulerian–Lagrangian approaches. Particularly, the continuous vapour phase is described using Navier–Stokes equations in the Eulerian frame of reference, while the liquid fuel droplets are modelled using discrete phase model in the Lagrangian frame of reference. The liquid fuel is injected into the detonation chamber through a cone nozzle injector model. The evaporation process of the liquid droplet is modelled using the D-square law. The density-based solver with a shock-capturing scheme is employed to simulate for both the DDT and detonation propagation processes. The combustion process is modelled through the reduced chemical kinetic model of Jet-A fuel. The obtained numerical results are in good agreement with both the experimental and numerical data. Both physical and chemical insights of the operating cycle are investigated. The obtained results show that the evaporation process and mixing process play a key role in the homogeneity of the fuel/air vapour mixture. The deflagration wave can successfully transit to detonation wave for a certain range of injected fuel mass flow rate. The DDT length strongly depends on the temperature of incoming airflow as well as liquid fuel mass flow rate.

V. B. Nguyen · Q. T. Phan · J.-M. Li · B. C. Khoo (✉)
Temasek Laboratories, National University of Singapore, Singapore, Singapore
e-mail: tslhead@nus.edu.sg

C. J. Teo
Department of Mechanical Engineering, National University of Singapore, Singapore, Singapore

A. Sasoh et al. (eds.), *31st International Symposium on Shock Waves 2*,
https://doi.org/10.1007/978-3-319-91017-8_9

1 Introduction

In pulse detonation engine (PDE) development, the use of the liquid fuel is always of interest due to their advantages, such as higher energy density, smaller storage tanks, and safer compared to gas fuel [1]. In the past few years, several investigations of liquid-fueled detonation engine have been reported for both experimental and numerical studies [2–8]. Liquid fuels, often used in the propulsion system, are jet fuels (e.g. Jet-A, Jet-A1, JP, etc.). In fact, the use of the liquid fuel often involves many other subprocesses and much more complex compared to pure gas fuel (e.g. liquid injection, multiphase flows, evaporation, atomization, breakup, chemical mixing, deflagration-to-detonation transition (DDT), detonation process, etc.). However, to gain understanding of the dynamics of all processes in the whole operating cycle of the detonation engine, as well as to improve the performance characteristics of the pulse detonation engine, it is necessary to study all processes in detail.

A complete operating cycle of the detonation engine often involves three main processes, which are injection process, deflagration-to-detonation transition process, and detonation propagation process. Although significant studies have been conducted in the liquid detonation applications, which are ranging in many different aspects of the problem [9–13] (such as the atomization and droplet size effects [9], heat transfer [10], incomplete reaction and reaction beyond the Chapman–Jouguet plane [11], turbulence–chemistry mixing [12], evaporation process [13], excessive fuel-rich conditions for cold starting [8], etc.), a detailed study on both physical and chemical insights of a complete operating cycle of the liquid-fueled detonation engine needs some rooms for the investigation. Thus, in this study, numerical simulations are performed to study the dynamics of three main processes of the operating cycle of the PDE. In particular, the Eulerian–Lagrangian approaches are employed in the numerical simulations. The vapour phase is treated as a continuous phase and described in the Eulerian frame of references, while liquid fuel droplets are treated as discrete phase and expressed in the Lagrangian frame of reference. The two-way interaction models and sub-models are introduced and implemented. The paper is organised as the following: Sect. 1 is an introduction; Sect. 2 introduces mathematical models and the numerical models; Sect. 3 presents the numerical setup and validation, numerical results, and discussions; and Sect. 4 concludes the content of this paper.

2 Mathematical and Numerical Models

As mentioned in the previous section, the complete operating cycle of a liquid-fueled pulse detonation engine includes both liquid and vapour phase. The vapour phase is described using the compressible, reacting Navier–Stokes equations, while

liquid droplets are expressed through the location, momentum, and energy equations in the Lagrangian forms. The two-way interaction between the liquid phase and vapour phase is expressed through source terms.

2.1 Eulerian–Lagrangian Approaches

The compressible, reacting Navier–Stokes equations are employed to mathematically model for the continuity, momentum, energy, and species equations of the vapour phase as follows:

$$\frac{\partial \rho}{\partial t} + \nabla.(\rho u) = S_{d,m,} \tag{1}$$

$$\frac{\partial \rho u}{\partial t} + \nabla.(\rho u u) - \left\{ \nabla.(\mu \nabla u) + \nabla.\left(\mu \left((\nabla u)^T - \frac{2}{3} tr\,(\nabla u) \right) \right) \right\} = -\nabla p + S_{d,u}, \tag{2}$$

$$\frac{\partial \rho E}{\partial t} + \nabla.(\rho u E) = \frac{Dd}{Dt} + S_{rad} + S_{ch} + S_{d,E}, \tag{3}$$

$$\frac{\partial \rho Y_i}{\partial t} + \nabla.(\rho u Y_i) - \nabla.D\nabla Y_i = S_{ch,i} + S_{d,Y_i}. \tag{4}$$

In these expressions, ρ is density, u is velocity field, μ is dynamic viscosity, p is pressure field, E is total energy, and Y_i is mass fraction of species ith. The mass source term, $S_{d,\,m}$, is arising from the liquid fuel evaporation. $S_{d,\,u}$ is momentum exchanged with liquid droplets. S_{rad} is thermal energy arising from radiation. S_{ch} is the chemical reaction energy. $S_{d,\,E}$ is the heat transfer from vapour phase to liquid droplets. $S_{ch,\,i}$is the change of the species *i*th due to chemical reactions. S_{d,Y_i} is the change of species *i*th due to evaporation process. In addition, the turbulence is modelled using the shear-stress transition (SST) model. This blending model is developed from k-epsilon and k-omega model that can simulate well for the flow at the near-wall as well as at the far-field region. In fact, the improvement of the near-wall capability of the SST model certainly benefits for the combustion simulations.

For the droplet modelling, the trajectory and velocity of an individual liquid droplet are tracked in the Lagrangian frame of references. During the droplet lifetime, the liquid droplet exchanges its mass, momentum, and energy with vapour phase. This two-way interaction is modelled by a set of sub-models. The following are the governing equations:

$$\frac{\partial x}{\partial t} = u_d \tag{5}$$

$$m_d \frac{\partial u_d}{\partial t} = \sum\nolimits_i F_i \tag{6}$$

$$m_d c_{d,s} \frac{\partial T}{\partial t} = h_k A_d \left(T_v - T_d\right) + \varepsilon \sigma_{SB} \left(T_v^4 - T_d^4\right) + \sum\nolimits_i S_{h,i} \tag{7}$$

$$\frac{\partial m_d}{\partial t} = \sum\nolimits_i S_{m,i} \tag{8}$$

In Eqs. (5, 6, 7, 8), x is droplet position, and u_d is droplet velocity. F_i is external forces acting on droplet (e.g. drag force, gravity force, pressure gradient force). $S_{h,\,i}$ is the heat transfer between droplet and surrounding vapour phase. T_d is droplet temperature. T_v is surrounding vapour phase temperature. $\sum_i S_{m,\,i}$ is the mass transfer in the evaporation process.

2.2 Injection and Sub-models

The injection and evaporation process includes the following sub-models: injection model, breakup model, dispersion model, drag model, heat transfer model, and evaporation model. For the injection model, the cone injection model developed in OpenFOAM is employed in this study [14]. The initial size distribution of the liquid droplet follows the probability density function using Rosin–Rammer. The direction of the droplet is modelled by directing them within the spray angle. The initial velocity of the droplet is calculated based on the difference between the injection pressure and the pressure inside the detonation chamber. For breakup model, the Rayleigh–Taylor and Kelvin–Helmholtz breakup model (RT–KH breakup model) is employed to model for the droplet breakup [15]. The Kelvin–Helmholtz breakup model is often used to model for the separation of small droplets from the initial drop. The disintegration of the droplets in the catastrophic breakup regimes is modelled by the Rayleigh–Taylor breakup model. The radius of the new droplets is determined using conservation of mass. For the drag mode, the liquid droplet is assumed to be a perfect sphere. Thus, the spherical drag coefficient model can be applied [16]. For dispersion model, the stochastic dispersion model [17] is employed to model for the fluctuating velocity caused by the turbulence of vapour phase influenced by the transient motion of the droplet. For heat transfer, the Ranz–Marshall heat transfer model [18] is used to account for the heat transfer from liquid fuel droplet to the surrounding gas and vice versa. This model is based on the convective heat transfer of the droplet with uniform temperature. For the evaporation process, the D-square law evaporation model is employed to model for the amount of liquid fuel evaporating to the vapour phase [19].

2.3 Combustion Modelling

In this study, the combustion model makes use of the reduced chemical kinetic model of Jet-A fuel which was proposed by [20]. In this model, the surrogate fuel is represented by species $C_{11}H_{21}$. The model involves 18 chemical reactions of 15 species. The thermal properties (e.g. specific heat constant (C_p), enthalpy (h), Gibusi energy) of each species and mixture are computed using NASA polynomial functions with seven coefficients that are obtained from Chemkin II database [21]. The transport coefficients (dynamic viscosity, kinematic viscosity, and thermal conductivity) are determined using the Sutherland correlation [16].This chemical kinetic model has validated again the experimental data for ignition time, laminar flame speed, and adiabatic temperature (see [20] for details).

2.4 Numerical Method

For the vapour phase modelling, the Eulerian approach is employed to solve for the continuous vapour phase. The governing equations of the mixture vapour are discretized using finite volume method as integrals over control volumes. The computational domain is spatially discretized into small control volumes, named "cells". By applying the finite volume method, discretized formulations can be formulated for the terms of the transport equations. These include divergence, gradient and Laplace operators, time discretization, and source terms. The density-based solver, developed in OpenFOAM [14], is employed to solve for the discretization form of the compressible reacting Navier–Stokes equations (Eqs. 1, 2, 3, 4). The convective flux terms are computed using HLLC scheme with the slope limiter [22]. For the turbulent model, the RANS-based turbulence model employed in this work is the shear-stress transition (SST) model [23].

For the liquid droplet modelling, the governing equations (Eqs. 5, 6, 7, 8) of the liquid droplet are solved in the discretized form [14]. These discretized equations are solved using numerical integration in time. In particular, the standard semi-implicit Euler method was employed to advance the solution of the discretization equations in time. At every time step (Δt) of solving fluid flow iteration, the solver is applied for Lagrangian droplet system first. If Δt is large and the numerical cell size is small, a droplet can travel through several cells within a time step. Thus, the time step (Δt_p) of droplet is split into smaller size using adaptive time-step size method to accurately evaluate for all source terms at each computational cell that droplet passes through. Note that the two-way interaction between vapour phase and liquid droplet phase is updated through the calculated sub-models at every time step.

3 Numerical Results and Discussions

3.1 Numerical Validation

In this subsection, numerical results of the hollow cone are compared with Sandia's experimental data [24] to validate for the injection and evaporation processes. In particular, the liquid penetration and fuel mass fraction at some stand-off distance are used for the validation. For experimental setup, the n-dodecane liquid fuel at a temperature of 353 K is injected into the hot chamber with an ambient temperature of 900 K through the cone nozzle with an inner diameter of 90 μm at the exit. The injection pressure is 150 MPa, while ambient pressure is 6 MPa. The total mass of 3.5 mg of liquid fuel is injected into the chamber within 1.5 ms with discharge coefficient of 0.86. The experiment is set up to ensure that there is no oxygen in the test chamber. For numerical setup, the cylinder with radius of 200 mm and length of 400 mm is used in the simulations to ensure that the wall boundary conditions do not affect the spray pattern. The hollow cone nozzle model placed at top-centred is used to inject the liquid fuel into the chamber. The chosen mesh grid size is 0.5 mm, and time-step size is 5.0e-7 s.

Figure 1 shows the comparison of the liquid penetration between the current numerical result and Sandia's experimental data. In this figure, the liquid penetration length is plotted versus the injection time. It is clear that the numerical is slightly lower than experimental data at the beginning. However, it is comparable to the experimental data after 0.2 ms. Figure 2 shows the comparison of the mass fraction of the fuel vapour phase at two stand-off distances of 25 mm and 45 mm from nozzle exit between current numerical results and Sandia's experimental data. It can be seen that our numerical results are in good agreement with experimental data at both planes of the two stand-off distances. In other words, our numerical simulation platform can accurately simulate the injection process and evaporation process. For the validation of the DDT and detonation propagation process, the liquid fuel spray pattern and the flame speed along the centreline of detonation chamber are used to compare with our experimental data. (Note that these validations are not shown here due to the page limitation.)

3.2 Numerical Setup

In this section, numerical simulations are performed for the complete operating cycle of the detonation engines, which are injection, deflagration-to-detonation, and detonation propagation processes. The geometry model of the detonation tube is 2D which is used to simulate for the original 3D chamber geometry used in our experimental works (see Fig. 3). The Jet-A1 liquid fuel at a temperature of 300 K is injected into the detonation tube at an ambient pressure of about 1 bar to mix

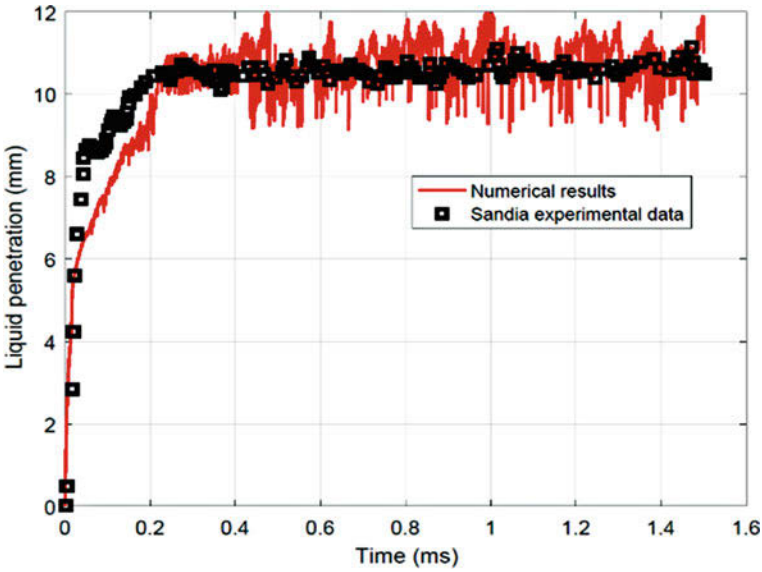

Fig. 1 Comparison of the liquid penetration

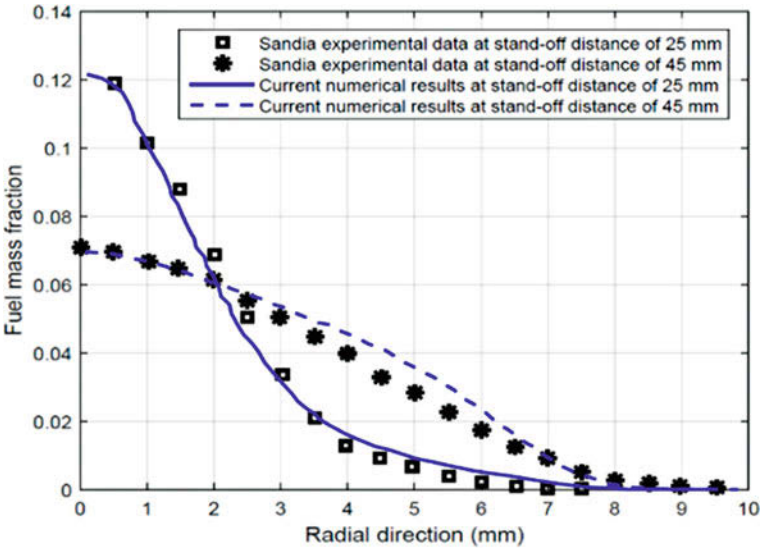

Fig. 2 Comparison of the fuel mass fraction at different stand-off distance

with incoming air flows at an incoming velocity of 35 m/s. The injection pressure is about 70 bars. The temperature of incoming airflow is about 500 K (70 °C), which is preheated before entering to the detonation tube. Mass flow rate of liquid fuel is about 7.3 g/s, while the mass flow rate of hot air flow is about 90 g/s (or the

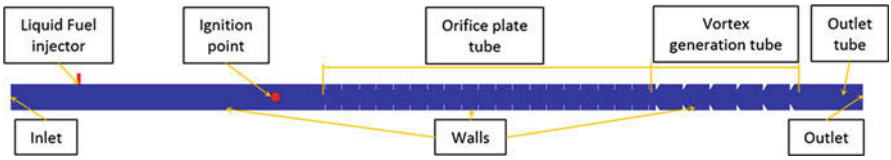

Fig. 3 Geometry model for TL's detonation tube

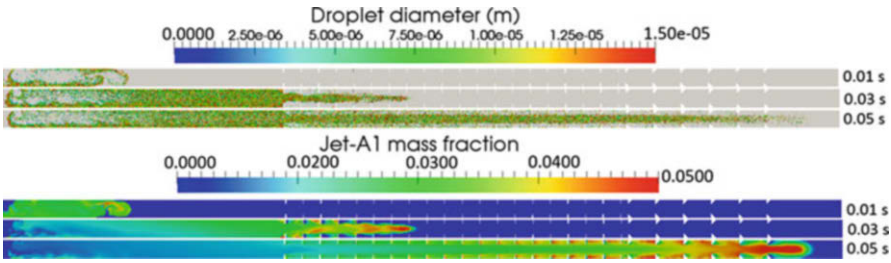

Fig. 4 Droplet distribution and fuel mass fraction contour at different times

equivalent ratio of about 1.1). Mass flow rate boundary conditions are applied on the inlet, nonslip boundary conditions are applied on walls, and outflow conditions are applied to the outlet. The injection time is about 0.05 s.

3.3 Numerical Results and Discussion

Figure 4 shows the droplet distribution coloured by its diameter and the mass fraction of Jet-A1 fuel vapour at different times, respectively. In the figure, the blue colour represents for small size, while red colour represents for big size. The droplet distribution strongly depends on the vapour flow structure, obstacles, vortex generation, and flow turbulence, while the size of the existence droplet depends on the ambient temperature, evaporation rate, and breakup and time of its life. The biggest size of the droplet is about 15 μm, which is just injected from nozzle exit. The droplet at the centreline of the tube moves faster than the one located nearby the walls and obstacles. The mass fraction of the fuel vapour is great vapour front due to both longer evaporation time and higher evaporation rate as the ambient temperature remains high. The evaporation rate reduces in time as the ambient temperature is cooling down by a cold liquid fuel injected into the chamber.

Figure 5 shows the temperature contours at a different time during the DDT and detonation wave propagation process, while Fig. 6 shows the pressure contours. Figure 5a, b express the temperature contour at the low flame speed. Figure 5c–f describe the temperature contour at high flame speed, and Fig. 5g–i show the temperature contour at detonation propagation process. Figure 6a expresses the pressure contour at the low flame speed, while Fig. 6b–f describe

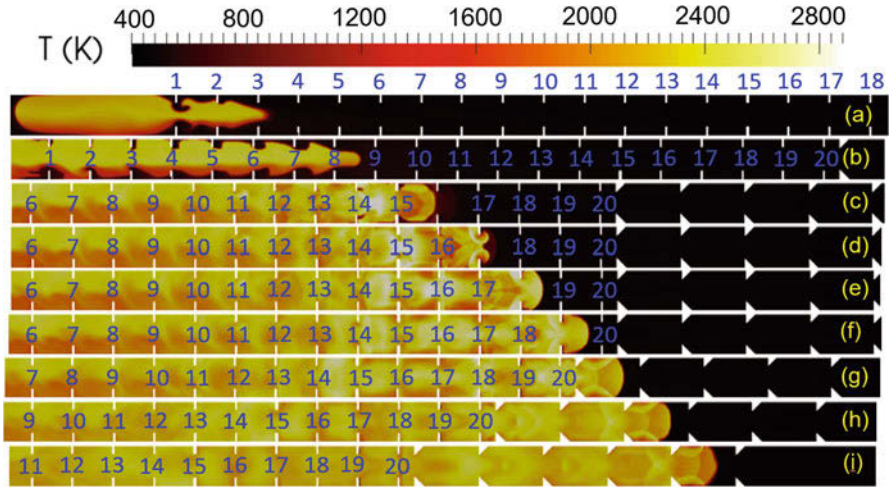

Fig. 5 Temperature contour

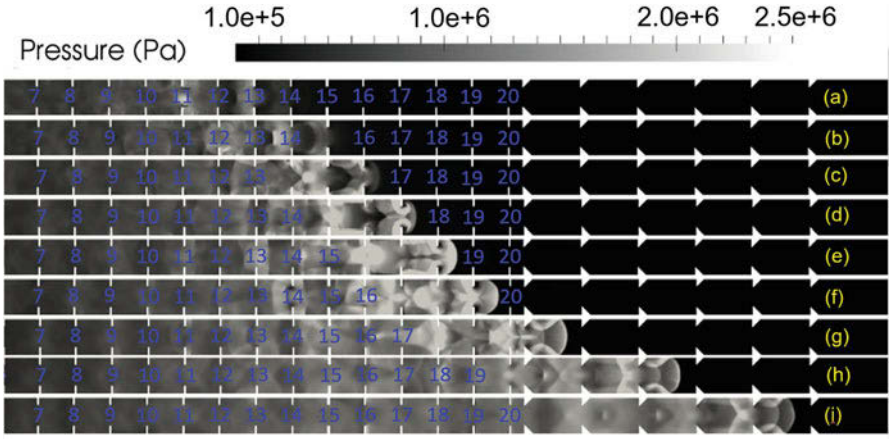

Fig. 6 Pressure contour

the pressure contour at high flame speed and Fig. 6g–i show the pressure contour at detonation propagation process. In the low flame speed stage, the flame propagates at low velocity, which is ranging from 0 to 300 m/s. The effects of compressibility are not significant. Some weak hotspots are created but not strong enough to form strong shock waves. In the high-speed flame stage, the flame propagates at high velocity (300–1800 m/s). The effects of compressibility are significant. The strong hotspots are created and form strong shock waves. The deflagration wave successfully transits to detonation wave. In the detonation wave propagation process, the detonation wave is sustained and propagates at about the constant velocity of about 1800 m/s, which is close to our experimental data.

4 Conclusions

In this study, the numerical simulation platform based on Eulerian–Lagrangian approaches for the liquid-fueled PDE has been implemented and validated. The obtained numerical results are in good agreement with experimental data. The simulations are performed for a complete operating cycle of the PDE, which includes three processes: injection, DDT, and detonation wave propagation processes. The DDT process includes low and high turbulent flame speed stages. The detonation wave propagates at 1800 m/s, which is close to the experimental data.

References

1. S. Cheatham, K. Kailasanath, J. Combust. Theor. Model. **9**, 23 (2005)
2. S.M. Frolov, J. Propuls. Power **22**(6), 1162 (2006)
3. W. Fan et al., J. Combust. Flame **133**, 441 (2003)
4. C.M. Brophy et al., *High-Speed Deflagration and Detonation* (ELEX-KM Publishers, Moscow, 2001), p. 207
5. Schauer, F.R, et al., AIAA paper, 2005-1343 (2005)
6. K. Kailasanath, J. Propuls. Power **22**(6), 788 (2006)
7. Carter, J.D., Lu, F.K., AIAA paper, 2011-6089 (2011)
8. J.M. Li et al., J. Propuls. Power **33**, 71 (2017)
9. E.K. Dabora et al., Proc. Combust. Inst. **12**, 19 (1969)
10. K.W. Ragland et al., J. Phys. Fluids **11**, 2377 (1968)
11. S.A. Gubin, M. Sichel, J. Combust. Sci. Technol. **17**, 109 (1977)
12. R.S. Miller, J. Bellan, J. Fluid Mech. **384**, 293 (1999)
13. S.K. Aggarwal, F. Peng, J. Eng. Gas Turbines Power **117**, 453 (1995)
14. OpenFOAM, *User Guide, Version 2.1.1*, 2012., http://www.openfoam.org
15. A. Wierzba, J. Exp. Fluids **9**, 59–64 (1993)
16. A.B. Liu, D. Mather, R.D. Reitz, SAE Technical Paper 930072, SAE, 1993
17. P. J. O'Rourke, PhD thesis, Princeton University, Princeton, 1981
18. W.E. Ranz, W.R. Marshall Jr., Part I, II. Chem. Eng. Prog. **48**(3), 141–146 (1952)
19. C.K. Law, H.K. Law, AIAA J. **20**(4), 522 (1982)
20. A. Kumud, J. AIAA, 2010 (1515)
21. R. J. Kee et al., Chemkin Collection, Release 3.6, 2000., http://www.sandia.gov/chemkin
22. E.F. Toro, M. Spruce, W. Speares, Shock Waves **4**(1), 25–34 (1994)
23. F.R. Menter, AIAA J. **32**(8), 1598–1605 (1994)
24. http://public.ca.sandia.gov/ecn/cvdata /target condition/sprayA.php (2011)

Experimental Investigation on the Flame-Shock Wave Interactions in a Confined Combustion Chamber

Jianfu Zhao, Lei Zhou, Haiqiao Wei, Dongzhi Gao, and Zailong Xu

Abstract An experiment was carried out to investigate the development and interactions of the flame and shock wave in a newly designed constant volume combustion bomb (CVCB). In this work, a stoichiometric hydrogen-air mixture was used as test fuel. An orifice plate was mounted in the middle of the CVCB to obtain flame acceleration and promote turbulent flame formation. The evolutions of flame and shock wave were captured by the high-speed schlieren photography. The flame propagation was divided into four stages: (1) laminar flame, (2) jet flame, (3) turbulent flame and (4) flame-shock wave interactions. And the development of the shock wave was observed detailedly. In addition, the effects of the initial pressure on the flame and shock wave were studied. The results show that the flame propagation velocity increased with the increase of initial pressure. The propagation velocity of the forward shock wave showed no obvious differences at different initial pressures, but the reflected shock wave from the end wall decayed faster at a higher initial pressure.

1 Introduction

In order to deal with the transportation problems of air pollution, energy insecurity and climate change, engine downsizing has been followed with interests due to its significant advantages in light-weight and compactness [1]. However, knock is likely to occur with high boost, which becomes a severe barrier for achieving high thermal efficiency. It is generally accepted that engine knock is the result of auto-ignition in the end-gas before it is reached by the flame front emanating from the spark plug [2]. Essentially, this abnormal combustion phenomenon is extremely relevant to flame-shock interactions [3]. Understanding the flame-shock

J. Zhao · L. Zhou · H. Wei (✉) · D. Gao · Z. Xu
State Key Laboratory of Engines, Tianjin University, Tianjin, China
e-mail: whq@tju.edu.cn

A. Sasoh et al. (eds.), *31st International Symposium on Shock Waves 2*,
https://doi.org/10.1007/978-3-319-91017-8_10

interactions in a confined space not only is of fundamental significance but also commands practical interest, such as understanding the mechanism, prediction and suppression of knock.

Flame-acoustic/shock wave interactions have been widely studied through experiments or simulations [4–6]. Xiao et al. [7] experimentally demonstrated the periodical interaction of the flame with the pressure wave because of the contact of flame front with the lateral walls. However, the pressure wave or acoustic wave was not directly observed experimentally. The initial pressure is a key parameter in the combustion process. And it is believed that high pressure increases the probability of knock through the onset of auto-ignition [8].

The objective of the present work is to reveal the flame evolution and shock wave development as well as their interactions in a confined space. And the effects of the initial pressure on the flame and shock wave were investigated quantitatively. The experimental study was conducted in a newly designed CVCB with an orifice plate. The orifice plate was used to achieve flame acceleration and produce turbulent flame and shock waves at different levels. High-speed schlieren photography was employed to capture the flame configuration and the shock wave. A stoichiometric hydrogen-air mixture was chosen as the test fuel because of its fast flame propagation velocity and the ease to form a shock wave ahead of the flame front. This study might provide a new insight into the turbulent flame-shock wave interactions and the mechanism of knock.

2 Experimental Apparatus and Procedure

The experiment was conducted in a newly designed CVCB experimental apparatus shown in Fig. 1 including a constant volume combustion chamber, a high-speed schlieren photography system, a pressure recording system, a temperature control system, an intake and exhaust system, a high-voltage ignition system and a synchronization program. The combustion chamber is a closed cylindrical cavity with an inner diameter of 100 mm and volume of 2.32 L. An orifice plate is mounted in the middle of the combustion chamber to accelerate the flame. The high-speed schlieren photography is employed to capture the flame and shock wave at the frame rate of 70,000 fps and exposure time of 1 μs.

Initially, the combustion chamber is heated up to the target temperature (373 K) by the temperature control system. The stoichimetric H_2-air mixture is obtained by the partial pressure method. And the air is heated up first to 333 K. Before igniting, the H_2-air mixture is initially premixed for 2 minutes to achieve the homogeneous mixture. At last, the spark igniter and high-speed camera are triggered simultaneously by the synchronization program. In this study, the uncertainty measures for initial pressure and temperature are no more than 0.05 bar and 2 K, respectively.

In this study, the flame propagation velocity is calculated based on the time derivation of the flame tip position, distance from the ignition point. And this was

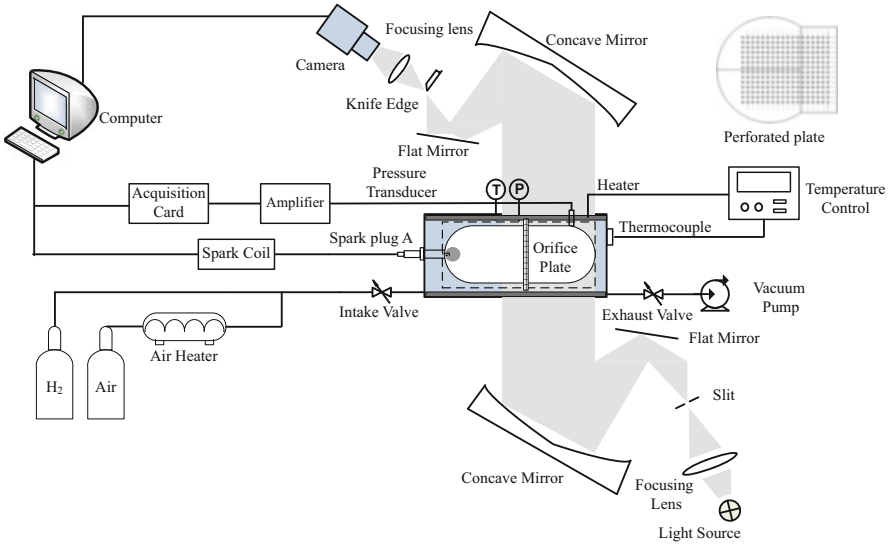

Fig. 1 Experimental apparatus

called flame tip velocity in the text. And a velocity point was calculated from the difference in the centerline flame position between consecutive frames. Based on a framing rate of 70,000 frames per second and a resolution of 0.18 mm/pixel, the uncertainty is 12.6 m/s.

3 Results and Discussions

3.1 Flame Evolution in the CVCB

A series of chronological schlieren images are divided into four groups based on the flame morphology and velocity in Fig. 2a to show the flame evolution in the right part of the combustion vessel. And a fitted curve is obtained to show the variation of the flame tip velocity with position quantitatively in Fig. 2b. And the experimental data was obtained at initial pressure = 4 bar and $\Phi = 1$.

The flame evolution was divided into four main stages, including laminar flame, jet flame, turbulent flame and flame-shock wave interactions. Constrained by the size of the optical visual region, only the final phase of the laminar flame could be observed. (1) In the laminar flame stage: As shown in the schlieren images, cellular flame surface appeared due to the Darrieus-Landau (DL) instability and thermal-diffusion instability. And because of the confinement of the orifice plate, the flame tip velocity decreased as approaching the orifice plate. (2) In the jet flame stage: The flame was separated into several jet flames after passing through the orifice

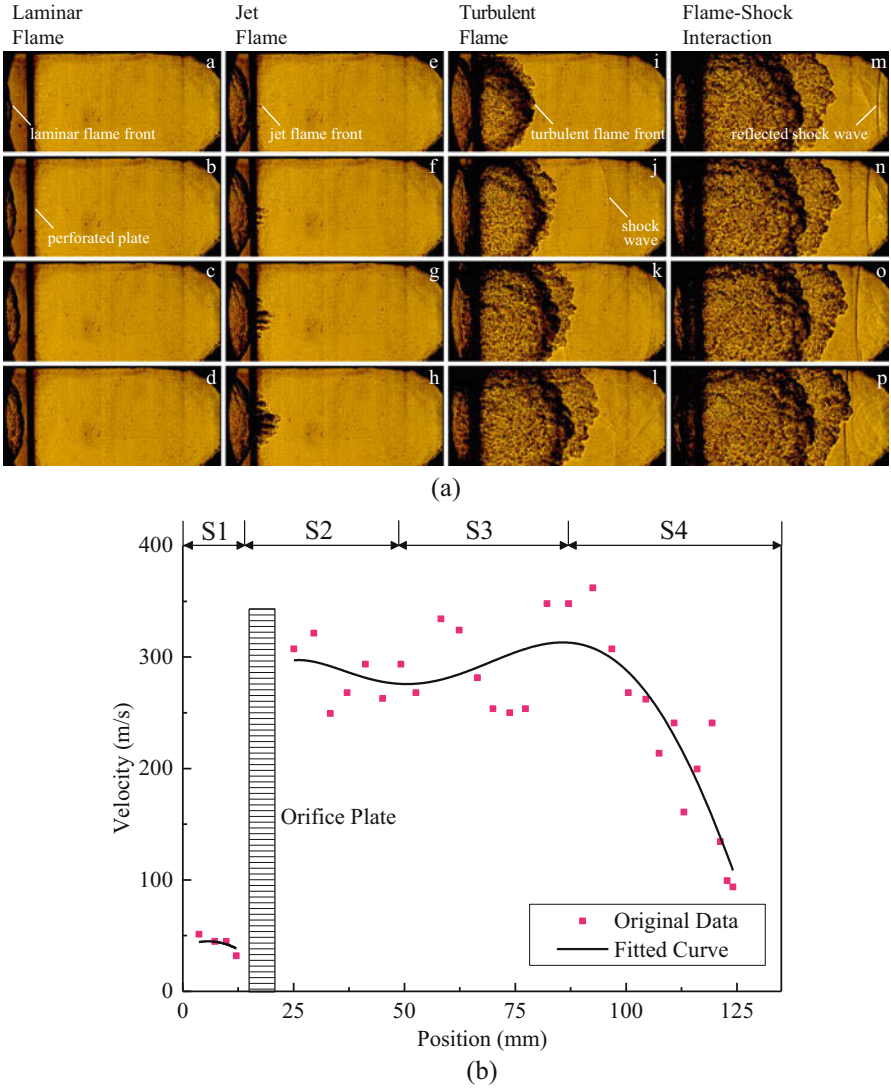

Fig. 2 Flame evolution in the right part of the CVCB (**a**) Schlieren images of the flame evolution (**b**) Variation of the flame tip velocity

plate with velocity increasing steeply. As the flame approached the orifice plate, the unburned gas mixture was accelerated steeply due to the throttling action across the orifice plate. When the flame passed through the orifice plate, it was entrained by the fast flow. And a spherical flame was divided into a series of jet flames by the orifice plate, consequently the area of the flame surface increased. This caused increase of the flame tip velocity. Subsequently, as the jet flame departed from

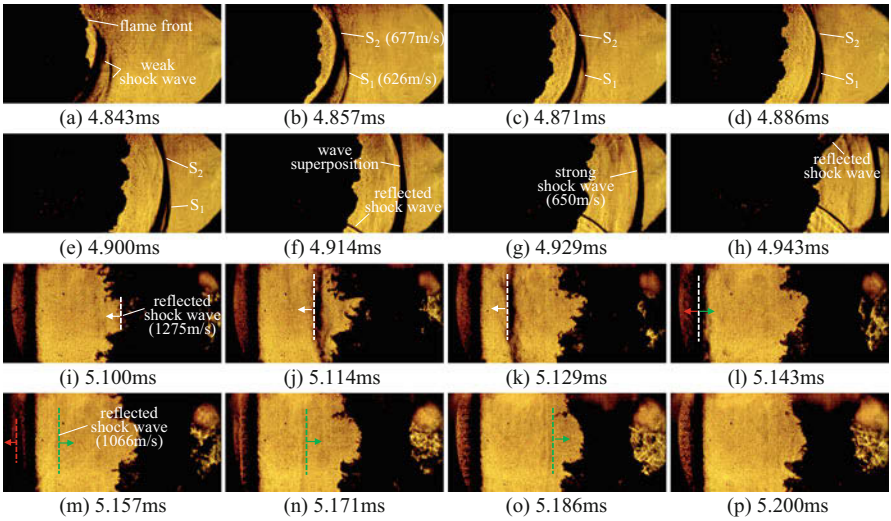

Fig. 3 Schlieren images of shock wave development

the orifice plate, the flame tip velocity decreased. This is because that the area of the flame surface decreased as the small jet flames coalesced together. (3) In the turbulent flame stage: The flame tip velocity increased gradually due to the turbulent flame self-acceleration, which was validated in the previous work [9]. And due to compression of the flame front, an obvious forward shock wave appeared in the unburned gas mixture. (4) In the flame-shock wave interactions stage: After the shock wave reached the end wall, a reflected shock wave was bounced back from the end wall and spread against the forward flame. Impacted by the reflected shock wave and the confinement of the end wall, the flame tip velocity decreased in the end region.

3.2 Development of the Shock Wave

Figure 3 shows the time-stamped images of shock wave development. Since some shock waves are weak and difficult to recognize, they are marked by dotted line in the images. These images were obtained at the conditions of an initial pressure of 8 bar and an equivalence ratio of 1.

Due to the compression of the flame front, obvious disturbance region in front of flame was formed. At 4.843 ms, two pressure discontinuity surfaces (shock waves) could be observed obviously. The first shock wave spread at a velocity of 626 m/s, while the second shock wave spread at 677 m/s. The velocity of the second shock was faster than the first one, which was easy to be understood. After the shock wave passed, the pressure and temperature of the local gas increased. And according to

the gas dynamic, the pressure wave propagated faster under higher temperature. As time went on, the interval between the two shock waves decreased gradually shown from Fig. 3a–f. When the second shock wave overtook the first shock wave, they coalesced together and produced a stronger shock wave. And the strong shock wave spread at a velocity of 650 m/s.

At 4.914 ms, a reflected shock wave bounced from the lower wall could be observed in the images. After that another reflected shock wave was bounced back from the upper wall at 4.943 ms. Impacted by the continuous forward shock waves and reflected shock waves bounced back from the lower and upper wall, the end of the optical visual region became messed, making it difficult to be observed. Thus, the reflected shock wave from the end wall was not recognized in the unburned gas. However, this reflected shock wave (marked by white dotted line. Note that the color version can be obtained online) passed through the reaction region and can be observed in the burned gas at 5.100 ms. The reflected shock wave spread in the burned gas at a velocity of 1275 m/s. After reaching the orifice plate, this shock wave was divided into two parts. A part went across the orifice plate (marked by the red dotted line), and another part was bounced back (marked by the green dotted line). Constrained by the size of the optical visual region, the shock wave, which went across the orifice plate, was only captured once by the camera. The reflected shock wave from the orifice plate spread in the burned gas at a velocity of 1066 m/s. Compared with other shock waves, this reflected shock wave was relatively light in greyscale. And this reflected shock wave vanished in the reaction region gradually.

3.3 Effect of Initial Pressure on the Flame and Shock Wave

The variation of the flame velocity with position at initial pressures of 2, 4, 6 and 8 bar is shown in Fig. 4a. As shown the flame tip velocity decreased after 90 mm due the flame-shock wave interactions at all initial pressures. Therefore, the interval from 20 to 90 mm is selected to calculate the mean flame tip velocity. And a comparison of the mean flame tip velocity at different initial pressures is also shown in Fig. 4a. Figure 4b shows the variation of the shock wave velocity with position at initial pressures of 4, 6 and 8 bar. Note that the positive value means the forward propagation and the negative value means the backward propagation.

As discussed in Sect. 3.1, the flame evolution experienced jet flame stage, turbulent flame stage, and flame-shock wave interactions stage after the orifice plate. In Fig. 4a, the variation of the flame tip velocity followed the tendency at every initial pressure. And the mean flame tip velocity increased as the initial pressure increased. Noted that the flame tip velocity at an initial pressure of 8 bar reduced to negative value after 90 mm, meaning that the flame propagation reversed. This is because that the fast flame tip velocity induced strong shock waves and intense flame-shock wave interactions.

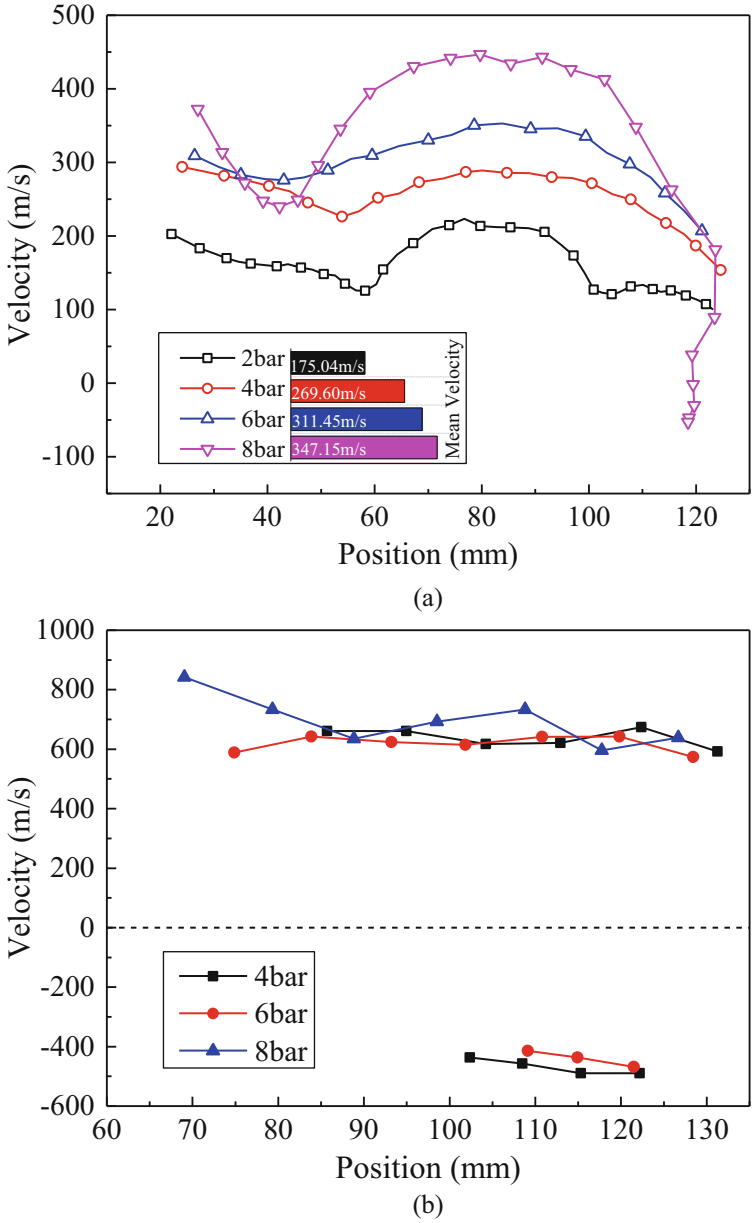

Fig. 4 Effect of the initial pressure on the flame and shock wave (**a**) Variation of the flame velocity at different initial pressures (**b**) Variation of the shock wave velocity at different initial pressures

As shown in Fig. 4b, a visible shock wave appeared at approximately 69 mm at initial pressure = 8 bar, earlier than 74 mm at initial pressure = 6 bar and 85 mm at initial pressure = 4 bar. This is related to the flame tip velocity. However, the value of the forward shock wave showed little differences at all initial pressures. As discussed before, the reflected shock wave at an initial pressure of 8 bar could not be recognized due to the mess in the end region. Thus, reflected shock wave velocity was measured only at an initial pressure of 4 and 6 bar. And the reflected shock wave decayed faster at initial pressure = 6 bar than 4 bar. This is because the flame spread faster and stronger pressure waves were induced, causing more obvious inhibition on the reflected shock wave.

4 Conclusion

A combustion process associated with flame-shock wave interactions was observed in a newly designed constant volume combustion bomb with an orifice plate. The flame evolution and shock wave development were captured by high-speed schlieren photography, demonstrating that the flame evolution with an orifice plate consists of four stages: (1) laminar flame, (2) jet flame, (3) turbulent flame and (4) flame-shock wave interactions. And the development of the shock wave was observed detailedly. When the flame propagated from one end to the other end in a confined space for premixed combustion, it would generate a disturbance flow with a weak shock or compression wave at the front of the flame. Consequently, the flame acceleration rendered the compression wave to be stronger, until an adequate stronger flame tip velocity generated a shock of considerable amplitude. And the shock wave would be reflected at the wall.

The effects of the initial pressure on the propagation of the flame and shock wave were investigated quantitatively. Turbulent flame tip velocity increased with the increasing initial pressure. The forward shock wave propagation velocity showed no obvious differences at different initial pressures, but the reflected shock wave from the end wall decayed faster at higher initial pressure.

Acknowledgments The work is supported by National Natural Science Foundation of China (Grant No. 91641203, 51476114, 51606133).

References

1. C.D. Rakopoulos, E.G. Giakoumis, Second-law analyses applied to internal combustion engines operation. Prog. Energ. Combust. **32**, 1 (2006)
2. Y. Qi, Z. Wang, J. Wang, X. He, Effects of thermodynamic conditions on the end gas combustion mode associated with engine knock. Combust. Flame **162**, 11 (2015)
3. J. Pan, G. Shu, P. Zhao, H. Wei, Z. Chen, Interactions of flame propagation, auto-ignition and pressure wave during knocking combustion. Combust. Flame **164**, 3 (2015)

4. A. Petchenko, V. Bychkov, V. Akkerman, L. Eriksson, Flame–sound interaction in tubes with nonslip walls. Combust. Flame **149**, 4 (2007)
5. A. Robert, S. Richard, O. Colin, T. Poinsot, LES study of deflagration to detonation mechanisms in a downsized spark ignition engine. Combust. Flame **162**, 7 (2015)
6. G. Ciccarelli, C.T. Johansen, M. Parravani, The role of shock–flame interactions on flame acceleration in an obstacle laden channel. Combust. Flame **157**, 11 (2010)
7. H. Xiao, Q. Wang, X. Shen, S. Guo, J. Sun, An experimental study of distorted tulip flame formation in a closed duct. Combust. Flame **160**, 9 (2013)
8. D. Bradley, G.T. Kalghatgi, Influence of autoignition delay time characteristics of different fuels on pressure waves and knock in reciprocating engines. Combust. Flame **156**, 12 (2009)
9. F. Wu, G. Jomaas, C.K. Law, An experimental investigation on self-acceleration of cellular spherical flames. Proc. Combust. Inst. **34**, 1 (2013)

The Influence of Spatial Heterogeneity in Energetic Material on Non-ideal Detonation Propagation

Hongbin Li, Jiangling Li, Lei Zhao, Cha Xiong, Xiaocheng Mi, and Andrew J. Higgins

Abstract A series of different explosive media, homogeneous or heterogeneous, was selected to examine the influences on detonation propagation in two-dimensional explosive slab bounded by a layer of inert gas with the same thermodynamic properties as reactive media. The explosive system studied is an ideal gas with a single exothermic reaction governed by a pressure-dependent reaction rate (p^k) with a pressure exponent of $k = 3$. The heterogeneity of explosive media is imposed via a series of sinusoidal ripples in density with different wavelengths while maintaining constant pressure. The numerical simulations are initialized with a ZND solution for the ideal CJ detonation, and the detonation is allowed to propagate into the explosive layer. The results showed that the detonation in the heterogeneous medium exhibits a three-wave structure of complex shock interactions. The detonation is able to propagate into a significantly thinner layer of explosive and can exhibit a greater velocity than the corresponding homogeneous case. Also, the detonation velocity is higher during propagating in the more heterogeneous explosive medium, and the critical thickness of explosive layer that detonation can successfully propagate is also thinner in the more heterogeneous explosive medium.

1 Introduction

The propagation of detonation wave in the homogeneous explosive media has been widely studied for a long time. However, the real explosive media is always nonuniform. In polycrystalline solid explosives, the initiation and growth of reaction are controlled by localization of the shock energy at heterogeneous centers such as

H. Li · J. Li (✉) · L. Zhao · C. Xiong
School of Power and Energy, Northwestern Polytechnical University, Xi'an, China
e-mail: lihongbin@mail.nwpu.edu.cn; lijianling@mail.nwpu.edu.cn

X. Mi · A. J. Higgins
Department of Mechanical Engineering, McGill University, Montreal, QC, Canada

A. Sasoh et al. (eds.), *31st International Symposium on Shock Waves 2*,
https://doi.org/10.1007/978-3-319-91017-8_11

pores and explosive grain boundaries, commonly referred to as "hot spots" in the explosives literature. While the media itself is uniform, the temperature sensitivity of Arrhenius governed kinetics results in the wave structure being dominated by spatial and temporal instabilities that are usually manifested as a cellular structure of the wave.

The propagation of detonation waves in explosive media is dominated by the spatial heterogeneity of the media or the heterogeneous structure of the detonation wave itself [1]. The previous studies [2, 3] have showed that shock interactions resulting from heterogeneities enable the detonation to propagate in charges thinner than the critical thickness of the equivalent homogeneous explosive. This paper is an extension to further investigate the influence of spatial heterogeneity on non-ideal detonation propagation near the limit. A series of explosives with two types of heterogeneous variations, $\sin(x)$ and $\sin^3(x)$ liked, were tested to examine the influences of spatial heterogeneity on detonation propagation.

2 Problem Description and Numerical Technique

2.1 Problem Description

The problem examined is detonation propagation in a charge of explosive bounded by inert, yielding confinement, as shown schematically in Fig. 1.

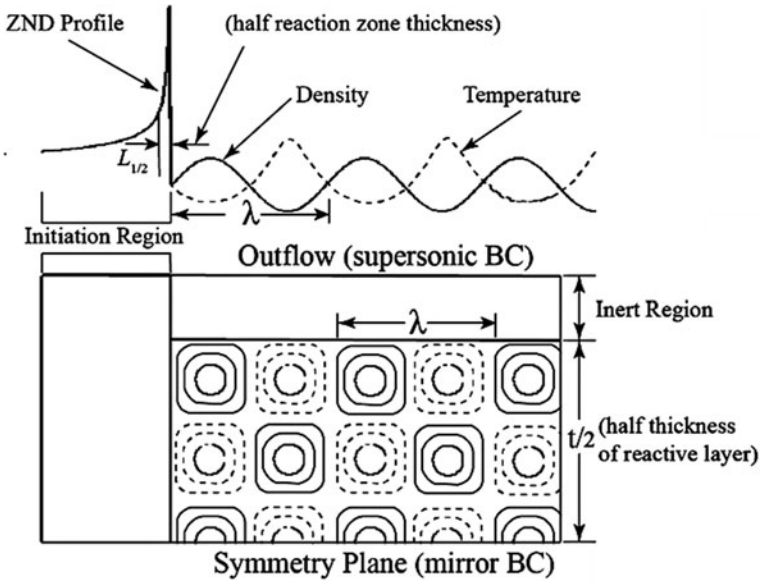

Fig. 1 Schematic representation of problem

The detonation wave is governed by a pressure-dependent reaction model (p^k) with a pressure exponent of $k = 3$, as shown in Eq. (1).

$$\dot{Z} = \frac{dZ}{dt} = A\,(1 - Z)\left(\frac{p}{p_{\mathrm{CJ}}}\right)^k \tag{1}$$

where Z is the reaction progress variable ($Z = 0$ for unreacted, $Z = 1$ for fully reacted). The value of A is arbitrary, and the results here will be reported in terms of half reaction zone length of the ideal CJ detonation. A pressure-dependent reaction model, as opposed to the more familiar Arrhenius reaction model, is used so that the resulting detonation wave is less susceptible to instability [4]. It should be emphasized that this study does not attempt to model any real explosive system. In many ways, this study is more relevant to condensed-phase explosives, with the ideal gas law being used for convenience and simplicity.

The detonation is initialized with a one-dimensional ZND-type wave propagating at the ideal CJ detonation velocity and is then allowed to propagate into a layer of finite thickness in a two-dimensional slab bounded by an inert confinement layer. The initial temperature, density, and pressure of the inert confinement layer are the same as the explosive layer, but the reaction progress variable $Z = 1$ in the inert confinement layer.

The spatial heterogeneity of the explosive layer is introduced via a sinusoidal ripple in density, as shown as Eq. (2),

$$\rho = \rho_1 \left\{1 + \sigma\left[\sin\left(\frac{2\pi}{\lambda}\,(x - x_1)\right)\cos\left(\frac{2\pi}{\lambda}\,y\right)\right]^n\right\} \tag{2}$$

where x is the direction of detonation propagation, x_1 denotes the location of the transition from the initiation region to the region bounded by inert gas, and y is the direction perpendicular to propagation. The amplitude of the variation σ is fixed at 0.5 for this study, and the wavelength of the sinusoid, λ, is varied over two orders of magnitude in different simulations. The spatial heterogeneity is also able to be changed by varying the value of integer n. Two types of spatial heterogeneity with $n = 1$ and $n = 3$ are numerically investigated. While maintaining the pressure constant in the explosive media, the temperature is varied with the reciprocal of the density, which ensures the total mixture chemical energy content of heterogeneous system remained the same with homogeneous system. This system can be thought as a gaseous explosive wherein pockets of cold, dense gas mixture alternate in a chessboard pattern with pockets of warm, low-density gas, while the total pressure and energetic content of the gas remain constant in comparison to the equivalent homogeneous gas mixture.

2.2 Numerical Technique

The governing unsteady, two-dimensional inviscid Euler equations with the pressure-dependent reaction rate source term described above in Cartesian coordinates are solved on a uniform computational grid. The computations are performed in the lab-fixed reference frame, and a generalized coordinate transformance method is employed. The finite-volume algorithm and a third-order TVD Runge-Kutta method [5] are used for spatial discretization and temporal discretization. The AUSM+ scheme [6] is used to deal with the inviscid flux as a sum of the convective and pressure terms, due to recognizing the convection and acoustic waves as two physically distinct processes. The source term is dealt with by using a second-order accurate Strang operator splitting method [7] and fully Newton-Raphson implicit method. The boundary condition along the x-axis is a mirror boundary condition (axis of symmetry), so that only the upper half of the layer is simulated in the case of a two-dimensional slab. The upper boundary of the computational domain (above the inert layer) is a supersonic outflow condition to ensure that no reflected waves return into the computational domain. For accelerating numerical simulation process, a parallel method-based MPI is used. The resolution of computational grid was 9.5 computational cells per half reaction zone length, i.e., $\Delta x \approx 9.5\, L_{1/2}$.

3 Results and Discussions

3.1 Structures of Detonation Front

When the thickness of reactive layer $t = 195.7\, L_{1/2}$ ($L_{1/2}$ is the half reaction zone thickness of the ideal CJ detonation, which was estimated by ZND model, respectively), the structures of detonation wave for homogeneous case and heterogeneous cases for $n = 1$ and $n = 3$ with $\lambda = 5\, L_{1/2}$ are shown in Fig. 2. This study further confirmed that spatial heterogeneity has a strong influence on detonation structures. For homogeneous case, the detonation front exhibits a very smooth, laminar-like structure. However, the results of heterogeneous cases demonstrated that detonation wave structure in the heterogeneous medium is unstable and exhibits a complex three-wave structure of complex shock interactions. Heterogeneous media has heterogeneous acoustic impedance that will result in local shock diffraction and focusing, leading to shock interactions. These nonlinear interaction feedback to the energy release required to support the detonation via the pressure-dependent reaction rate. The pressure results in the occurrence of transverse waves, and the difference of detonation wave velocity results in the wrinkle on detonation wave front.

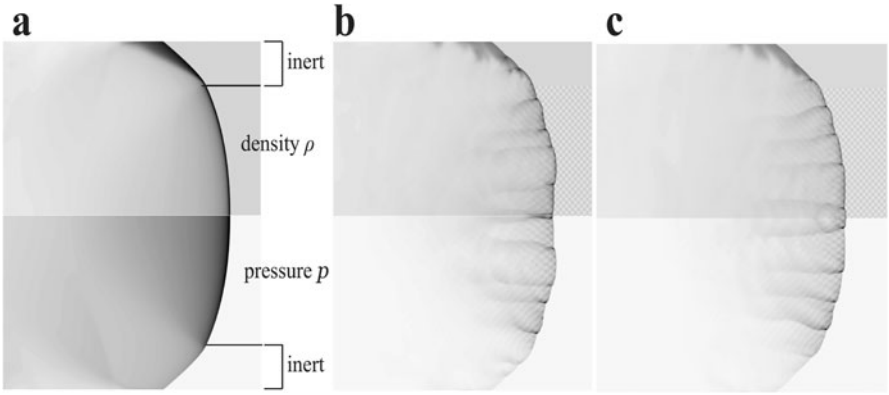

Fig. 2 Structure of detonation wave for homogeneous case and heterogeneous cases. (**a**) Homogeneity, (**b**) $n = 1$, (**c**) $n = 3$

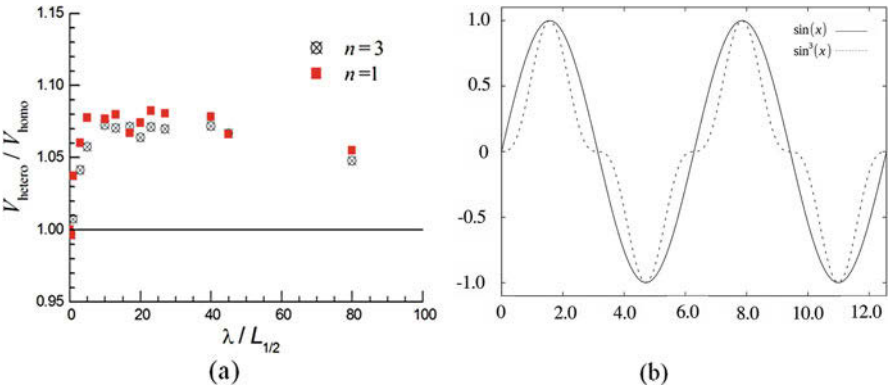

Fig. 3 The comparison of two heterogeneous media. (**a**) detonation velocities in two ($\sin(x)$ ($n = 1$) and $\sin^3(x)$ ($n = 3$) typed) heterogeneous media, (**b**) the comparison of two ($\sin(x)$ ($n = 1$) and $\sin^3(x)$ ($n = 3$) typed) sinusoidal ripples

3.2 Detonation Velocity in Different Heterogeneous Media

According to the location of detonation wave obtained in different times, the averaged detonation velocity could be calculated. Due to the large pulsations of the shock front, particularly in the case of large λ, it was necessary to track the wave for a considerable distance (a distance of 2000 $L_{1/2}$, corresponding to approximately 10 thicknesses of the charge) in order to obtain an effective average velocity. Figure 3a showed the variations of detonation velocity with sinusoid wavelength λ both for heterogeneous cases $n = 1$ and $n = 3$. In these simulations, the thickness of reactive layer $t = 195.7\ L_{1/2}$.

The detonation velocity in heterogeneous media (V_{hetero}) was normalized with the detonation velocity in the equivalent homogeneous media (V_{homo}). For hetero-

geneous cases, both $n = 1$ and $n = 3$, the detonation velocity in the heterogeneous explosive is higher than that in the homogeneous explosive. The detonation velocity varies as the wavelength of spatial heterogeneity, and the maximum velocity occurred in the range of 10–40 times the half reaction zone length approximately.

Additionally, the detonation velocity for the heterogeneous case $n = 1$ is higher than that for $n = 3$. The difference of the two types of spatial heterogeneity introduced by a sinusoidal ripple in density was shown in Fig. 3b. The sine function of $\sin(x)$ is more bulged than $\sin^3(x)$, which means that the deviation of the initial density and acoustic impedance of explosive from the balanced homogeneous state for heterogeneous case $n = 1$ ($\sin(x)$) is larger than that for heterogeneous case $n = 3(\sin^3(x))$. More spatial heterogeneity resulted in a more strong nonlinear interaction feedback to the energy release and a higher detonation velocity was obtained.

3.3 The Critical Thickness of Detonation Propagation

In order to investigate the effect of heterogeneity upon the ability of a detonation to propagate in a thinner layer, a wavelength of $\lambda = 40\ L_{1/2}$ was selected for the imposed heterogeneity, and simulations were conducted with different thicknesses of the detonable layer. Figure 4 plotted the variations of detonation velocity as a function of the inverse of the thickness of a two-dimensional explosive layer bounded by the inert confinement for homogeneous case and heterogeneous cases for $n = 1$ and $n = 3$. The detonation velocity was normalized with the

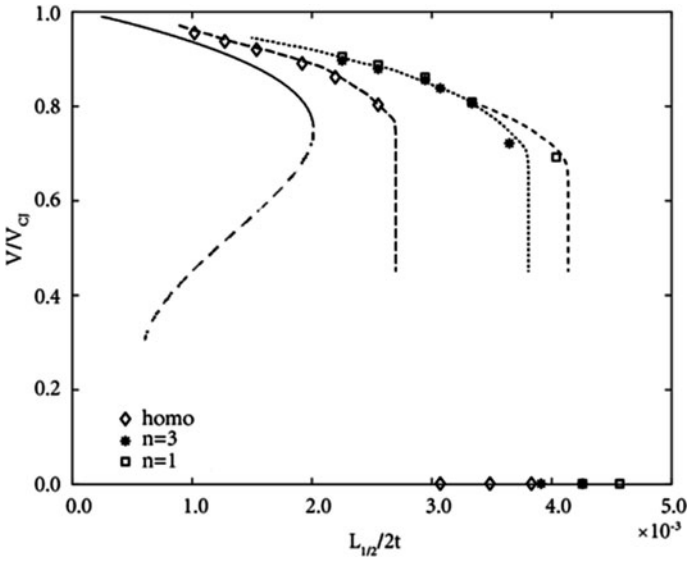

Fig. 4 Detonation velocity as a function of the thickness of a two-dimensional layer bounded by inert gas in homogeneous and two heterogeneous media

ideal Chapman-Jouguet detonation velocity in homogeneous media with rigid confinement (V_{CJ}). The wave velocity is plotted in this fashion, following the convention of the condensed-phase detonation literature, so that extrapolation to the y-axis should yield the ideal CJ velocity. As shown in Fig. 4, there exists a critical thickness for two-dimensional slab, due to significantly lateral losses in the yielding confinement. The heterogeneous case for $n = 1$ has the smallest critical thickness, while the critical thickness in homogeneous case is the biggest. The results indicated that spatial heterogeneity can extend the detonation limit. The detonation in heterogeneous system is able to propagate into a significantly thinner layer than the equivalent homogeneous system and can exhibit a greater velocity than the corresponding homogeneous case. With a larger spatial heterogeneity, a smaller critical thickness will be obtained.

4 Conclusions

The presence of a heterogeneous variation in the density of an explosive medium has been seen to have a significant influence on non-ideal detonation propagation. The spatial heterogeneity results in the occurrence of transverse waves, and the detonation wave exhibits complex three-wave structure of shock interactions. The introduction of spatial heterogeneity could promote detonation propagation and result in the increase of detonation velocity compared to the equivalent homogeneous system. Spatial heterogeneity can extend the detonation limit and enable detonation wave to propagate at near limit conditions at greater velocities and in thinner layers than in comparison to the corresponding homogeneous case. With a larger spatial heterogeneity, a smaller critical thickness will be obtained.

An extension of the present work is to introduce random heterogeneity into the explosive media and to further investigate the influence of heterogeneity on non-ideal detonation propagation.

Acknowledgments This work was supported by the National Natural Science Foundation of China (No. 11572258, No. 91441201), NASF(No.U1730134), the Science Challenge Project (No. TZ2016001), the opening project of State Key Laboratory of Explosion Science and Technology (Beijing Institute of Technology)(No. KFJJ17-04M), and the Fundamental Research Funds for the Central Universities (No. 3102017Ax006).

References

1. A.J. Higgins, J. Phys. Conf. Ser. **500**(5), 052016 (2014)
2. J. Li, X. Mi, A.J. Higgins, Phys. Fluids **27**, 027102 (2015)
3. J. Li, X. Mi, A.J. Higgins, Proc. Combust. Inst. **35**(2), 2025–2032 (2015)
4. M. Short, D.S. Stewart, J. Fluid Mech. **368**, 229–262 (1998)
5. C. Shu, S. Osher, J. Comput. Phys. **77**(2), 439–471 (1988)
6. M. Liou, C. Steffen, J. Comput. Phys. **107**(1), 23–39 (1993)
7. G. Strang, SIAM J. Numer. Anal. **5**(3), 506–517 (1968)

Experimental Research on the Detonation in Gaseous Mixtures with Suspended Aluminum Particles

X. Zhang, H. Chen, J. Li, S. Zhang, and H. Yu

Abstract The experiments have been performed in a horizontal detonation tube having a 13-m-long test section with 224 mm internal diameter. The suspended aluminum particles are spherical with a diameter range of 1–50 μm, using a particle concentration of 300 g/m^3 approximately. It is found that the single-front and double-front detonation waves can propagate in a mixture of $\varphi = 1.0$ H_2–air and aluminum particles which react with water vapor produced by gaseous detonation. The pressure records show that the detonation structure is double front when using 50 or 30 μm aluminum particles and that single front when using 20, 10, or 1 μm ones. However, these single-front detonation waves don't have the same properties. The detonation velocity using 1 μm particles is increased by 3.3% from the value of the baseline gas detonation as the heat release between particles and gases starts before the sonic surface and supports the shock, while the 10 and 20 μm ones start behind the sonic surface, so the detonation velocities cannot be increased. The single-front structure displayed in pressure records using 10 and 20 μm particles is because of the delay of the second front which is too short to distinguish in the pressure records.

X. Zhang · J. Li
State Key Laboratory of High-Temperature Gas Dynamics, Institute of Mechanics, Chinese Academy of Sciences, Beijing, China

H. Chen · S. Zhang · H. Yu
State Key Laboratory of High-Temperature Gas Dynamics, Institute of Mechanics, Chinese Academy of Sciences, Beijing, China

School of Engineering Science, University of Chinese Academy of Sciences, Beijing, China
e-mail: hongchen@imech.ac.cn

A. Sasoh et al. (eds.), *31st International Symposium on Shock Waves 2*,
https://doi.org/10.1007/978-3-319-91017-8_12

1 Introduction

As a fuel additive or a powder fuel in some power engines, metal particles take advantages of high density and high enthalpy of combustion [1]. To have a deeper understanding of the combustion process of metal particles and provide a theoretical basis for taking advantage of metal particles in the high-velocity and high-temperature gas with complex chemistry, the hybrid detonation experiments of gaseous mixtures with suspended aluminum particles have been proposed.

Detonation in gas-particle mixtures can be classified into three main categories, depending upon the different chemical properties of the components [2]:

1. "Heterogeneous detonations": all the combustible is contained in the solid particles, and the oxidizer is in the gaseous phase.
2. "Hybrid detonation": the combustible is contained in both solid and gaseous components.
3. "Dusty detonation": the solid particles are inert and do not participate in chemical reactions, chemical reactions just between the gaseous phase.

Hybrid detonation experiments have been carried out in gaseous mixtures with suspended aluminum powder by Veyssiere [3, 4] and Zhang [2]. Veyssiere performed experiments in a vertical tube with 6 m length and 69 mm internal diameter, while Zhang did in a horizontal one with 10 m length and 80 mm internal diameter. In the experiments, micron-sized aluminum powder was chosen, and the hydrogen-air or acetylene-air gaseous mixtures were oxygen-rich mostly. From their experimental results, it is uncovered that hybrid detonation structures are various according to the sequence of heat release, which comes from both gaseous reactions and reactions between particles and gases, behind the leading shock front. The hybrid detonation structure exists in three states. In the first case, only one discontinuity front exists, and the detonation is supported by the energy released both by gaseous reactions and particle-gas reactions, so it is called "single-front detonation." In the second case, the particles remain inert upstream of the CJ plane, and the reactions with gases occur downstream of the CJ plane, so the detonation front is supported only by the energy released from gaseous explosives. That is called "pseudo gas detonation." In the third case, two detonation fronts exist: the first one is supported by gaseous reactions and the second one by reactions between particles and gaseous products, so it is "double-front detonation."

In order to have a deeper understanding of the combustion process of metal particles and provide a theoretical basis for taking advantage of metal particles in the high-velocity and high-temperature gas with complex chemistry, the hybrid detonation experiments of gaseous mixtures with suspended aluminum particles have been proposed. The experiments have been performed in a horizontal detonation tube having a 13-m-long test section with 224 mm internal diameter.

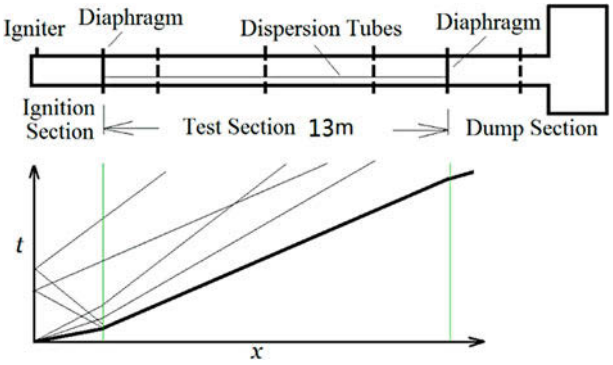

Fig. 1 Schematic diagram of the detonation tube and x-t wave diagram

2 Experiment Conditions

The detonation tube as schematically shown in Fig. 1 consists of three main parts: an ignition section, a detonation test section, and a dump tank. The ignition section is 3 m long, and the detonation test section is 13 m long. Both of them are 224 mm in diameter. The dust was dispersed by turbulent jets before ignition referring to the method of Zhang [5]. The dust dispersion system contains dispersion tubing with a row of 1.0 mm holes 50 mm apart pointing downward to the bottom. Before an experiment beginning, the aluminum powder was placed evenly along the slot on the bottom of the detonation tube. The dust will be dispersed as soon as the gas jets out of the holes, and the blowing gas is inert high-pressure nitrogen.

At the beginning of an experiment, the test section is fulfilled by stoichiometric H_2-air gaseous mixture, and the ignition section is fulfilled by stoichiometric H_2-O_2 for a strong initiation. The suspended aluminum particles are spherical with a diameter range of 1–50 μm, using a particle concentration of 300 g/m^3 approximately. The ignition and dispersion timing sequence is defined by the test to ensure a fairly uniform dispersion.

3 Different Hybrid Detonation Structures

3.1 Single-Front Detonation

When the aluminum particle diameter is 1, 10, or 20 μm, the experimental detonation wave has one single front. Figure 2 displays pressure records using 1 μm particles. The detonation velocity is measured to be 1926 m/s, increased by 3.3% from the value of the baseline gas detonation, and the pressure behind the

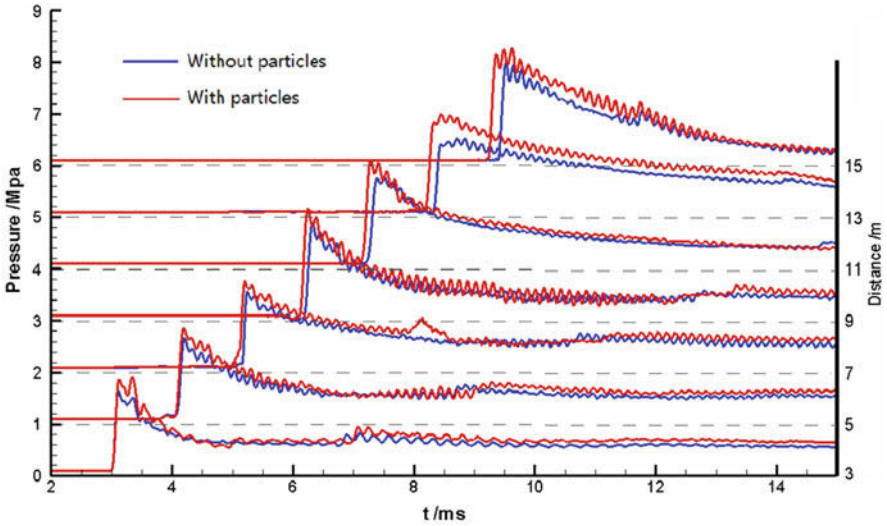

Fig. 2 Pressure records of a detonation in a hybrid H_2-air-aluminum particle mixture (1 μm, 280 g/m^3 aluminum particles, 1.0 Bar, $\varphi = 1.0$ H_2-air)

shock is increased by 10%. In this case, the particles heat release starts before the sonic surface and supports the shock.

The curves using 10 μm and 20 μm are shown in Figs. 3 and 4. They both have only one front but they are not entirely similar with one using 1 μm. The pressures behind the shock are both increased by 40% nearly, but the velocity is decreased a little.

3.2 Double-Front Detonation

As shown in Figs. 5 and 6, a double-front structure appears with the aluminum particle size increased to a value. When using 30 μm particles, the first leading shock has a velocity of 1866 m/s close to the value of the baseline, but the pressure after the first shock is a little lower. And the second front has an approximate velocity of 1889 m/s, so the distance between the two fronts is almost constant. The remarkable difference using 50 μm particles is that the second front has a much lower velocity of 1671 m/s.

With the increase of the aluminum particle size, the aluminum particle needs more time for heat transfer, so the reactions between particles and gases begin behind the gaseous sonic plane and cannot influence the first leading shock. Then the particles start chemical reactions in gaseous detonation products. So the first leading shock is only supported by gaseous detonation in the double-front structure, while the second one is supported by particles' combustion.

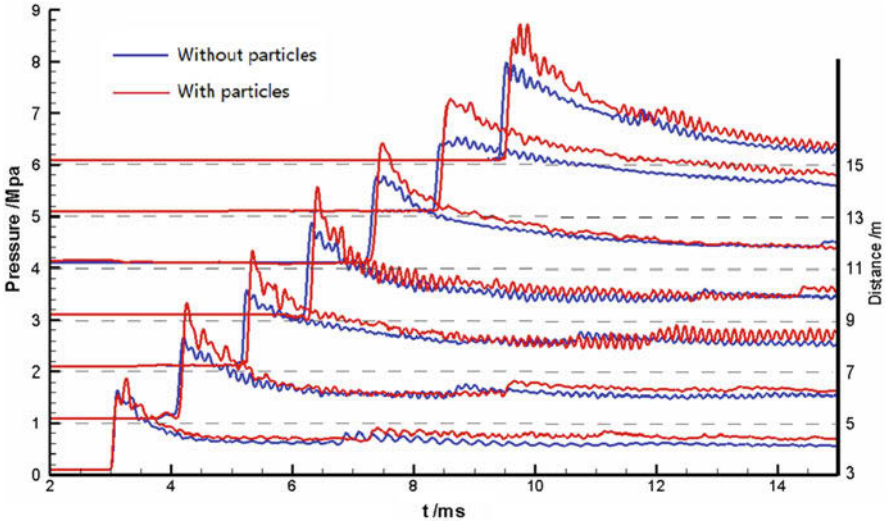

Fig. 3 Pressure records of a detonation in a hybrid H_2-air-aluminum particle mixture (10 μm, 350 g/m^3 aluminum particles, 1.0 Bar, $\varphi = 1.0$ H_2-air)

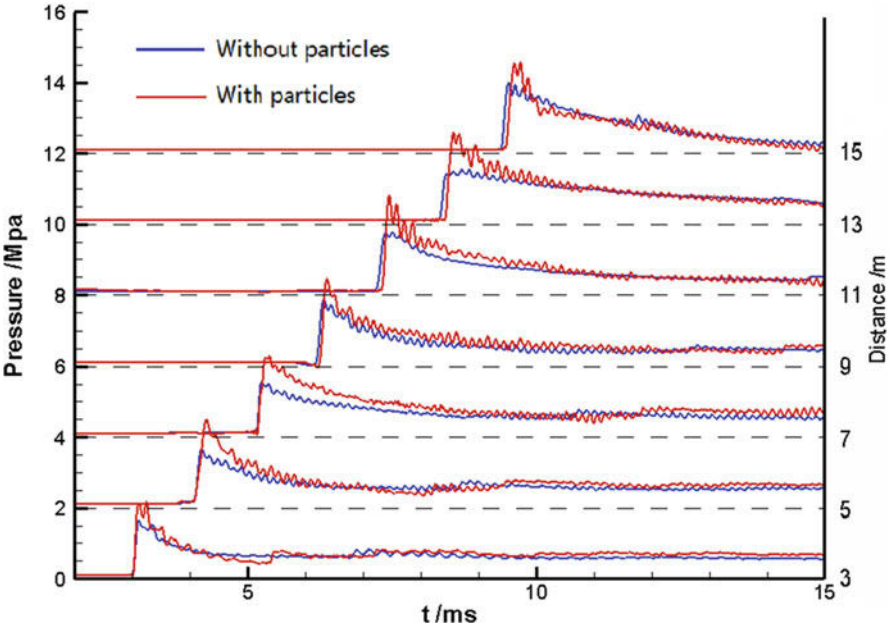

Fig. 4 Pressure records of a detonation in a hybrid H_2-air-aluminum particle mixture (20 μm, 300 g/m^3 aluminum particles, 1.0 Bar, $\varphi = 1.0$ H_2-air)

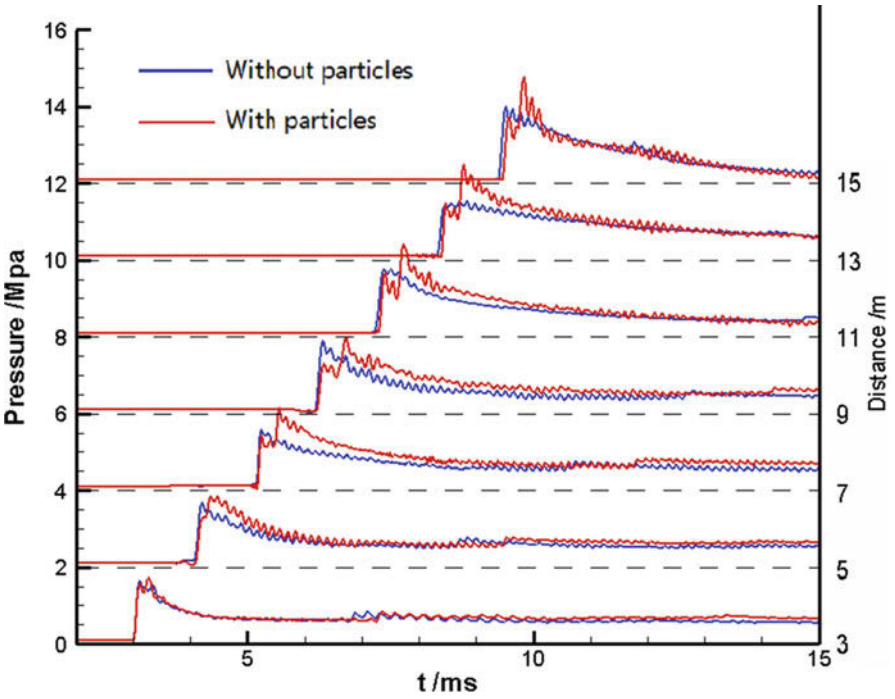

Fig. 5 Pressure records of a detonation in a hybrid H_2-air-aluminum particle mixture (30 μm, 300 g/m^3 aluminum particles, 1.0 Bar, $\varphi = 1.0$ H_2-air)

4 Ignition Delay of the Aluminum Particles

The particles heat release does not take place closely after the shock as gas, so the structure of hybrid detonation is multiplex. It is important that the sequence of heat release comes from both gaseous reactions and reactions between particles and gases.

A quantitative numerical model for steady hybrid detonations in gaseous mixtures with particles in suspension was used to predict the detonation structure numerically [6, 7]. The main assumptions and the method of solution are described in detail in the references. By solving a system of ordinary differential equations and fulfilling the equivalent CJ condition for non-ideal detonations, Fig. 7 gives the numerical results of the ignition delay of aluminum particles with different diameters assuming that the ignition temperature is 933 K or 1350 K. With the increase in particle size, the heat transfer slows down. The 2 μm aluminum particles only need a few millimeters to reach the ignition temperature behind the gaseous shock, while 50 μm aluminum particles need 0.34 m to 933 K or 0.78 m to 1350 K. The sonic plane is only about 1 mm behind the gaseous shock by the calculation

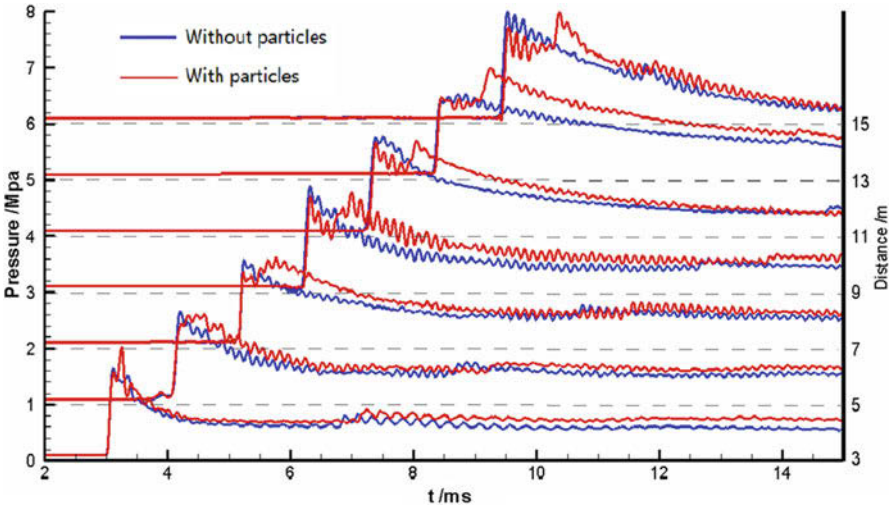

Fig. 6 Pressure records of a detonation in a hybrid H_2-air-aluminum particle mixture (50 μm, 275 g/m^3 aluminum particles, 1.0 Bar, $\varphi = 1.0$ H_2-air)

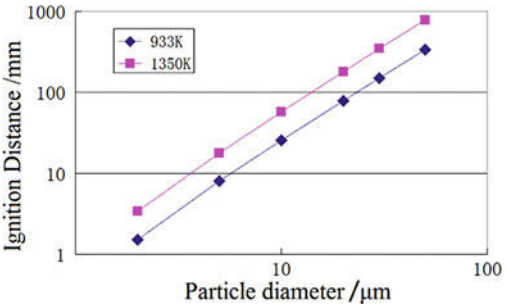

Fig. 7 Ignition delay of aluminum particles with different diameters

result in these cases. As a result, only when the aluminum particle size is small enough, the ignition can occur before the gaseous sonic plane.

When the diameter is 1 μm, the particles heat release starts before the sonic surface and supports the shock, so the detonation velocity and the pressure behind the shock are both increased. While the 10–50 μm ones start behind the sonic surface, the detonation velocities cannot be increased. The larger the particles, the longer they reach the ignition temperature; thus a second shock wave supported by a late energy release can propagate with 30 μm or 50 μm aluminum particles. Based on the experimental results and calculation analysis, the single-front structure but not a double-front one displayed in pressure records using 10 and 20 μm particles is because of the delay of the second front which is too short to distinguish in the pressure records. A variety of cases are summarized in Table 1.

Table 1 Different hybrid detonation structures

Particle diameter/μm	Detonation structure in pressure records	Ignition position
1	Single front	Before the sonic surface
10		Behind the sonic surface
20		
30	Double front	
50		

5 Conclusion

It is found that the single-front and double-front detonation structures can propagate in a mixture of $\varphi = 1.0$ H_2-air and aluminum particles which react with water vapor produced by gaseous detonation. The pressure records show that the detonation structure is double front when using 50 or 30 μm aluminum particles and single front when using 20, 10, or 1 μm ones. However, these single-front detonation waves don't have the same properties. When the diameter is 1 μm, the particles heat release starts before the sonic surface and supports the shock, so the detonation velocity and the pressure behind the shock are both increased from the value of the baseline gas detonation, while the 10 and 20 μm ones start behind the sonic surface, so the detonation velocities cannot be increased. The single-front structure displayed in pressure records using 10 and 20 μm particles is because of the delay of the second front which is too short to distinguish in the pressure records.

References

1. M.W. Beckstead, *A summary of aluminum combustion*, Internal Aerodynamics in Solid Rocket Propulsion, Belgium, 2002
2. F. Zhang, *Detonation of gas-particle flow*, Shock Wave Science and Technology Reference Library: Heterogeneous Detonation, 2009
3. B. Veyssiere, Detonation in gas-particle mixtures. J. Propuls. Power **1269**, 22 (2006)
4. B. Veyssiere, W. Ingignoli, Existence of the detonation cellular structure in two-phase hybrid mixtures. Shock Waves **291**, 12 (2003)
5. F. Zhang, H. Gronig, DDT and detonation waves in dust-air mixtures. Shock Waves **53**, 11 (2003)
6. B. Veyssiere, B.A. Khasainov, Structure and multiplicity of detonation regimes in heterogeneous hybrid mixtures. Shock Waves **171**, 4 (1994)
7. B.A. Khasainov, B. Veyssiere, Initiation of detonation regimes in hybrid two-phase mixtures. Shock Waves **9**, 6 (1996)

Large Eddy Simulation of Mixing Characteristic in the Cold Rotating Detonation Chamber

R. Zhou, B. L. Tian, X. P. Li, and J. P. Wang

Abstract Two-dimensional large eddy simulation (LES) for supersonic compressible multicomponent flow is carried out to investigate the mixing characteristic of the cold non-premixed RDE with different injection strategies. According to the instantaneous and quasi-stead time-averaged flow field, the nonuniform mixing characteristic is presented. The turbulence eddy structure generated by the K-H instability is the main mechanism for promoting the mixing of fuel and oxidizer. Combining the rich and lean combustion limits, the area of the detonation is identified. It is found that the area of the detonation is only a narrow layer near the head end. To improve the mixing efficiency near the head end in the non-premixed RDE, the oxygen injection position and hydrogen injection angle are adjusted preliminary. The mixing characteristics and the area of the detonation are analyzed in detail. The present research can provide the important reference and guidance for the experimental injection design of the RDE.

1 Introduction

Rotating detonation engines (RDE) have been extensively studied in recent years, because of their low complexity and very high power density. Successful experimental research and comprehensive numerical simulation analysis on RDE have been performed in Russia, Poland, China, the USA, France, Japan, and so on [1].

R. Zhou (✉) · B. L. Tian
Institute of Applied Physics and Computational Mathematics, Beijing, China

X. P. Li
Research Center of Heat and Mass Transfer Institute of Engineering Thermophysics, Chinese Academy of Sciences, Beijing, China

J. P. Wang
College of Engineering, Peking University, Beijing, China

A. Sasoh et al. (eds.), *31st International Symposium on Shock Waves 2*,
https://doi.org/10.1007/978-3-319-91017-8_13

However, in the stage of the feasibility study of RDE, most of the numerical simulation studies were based on the ideal premixed injection, which are different from the non-premixed injection design in the real experimental device.

In a real RDE's chamber, the fuel and the oxidizer injected continuously into the combustion chamber and mixing rapidly are essential for maintaining long-duration stable operation of RDE. It is the inevitable trend to carry out the more realistic (non-premixed injection) numerical simulation based on the consistent design with experimental injection geometry. At present, most of the numerical researches on the non-premixed RDE are based on the RANS method. For example, Frolov [2] carried out 3D simulations of RDE with separated supply of hydrogen and air using the finite volume discretization. Stoddard [3] studied the effect of the injection conditions on the non-premixed flow field using ANSYS Fluent-based RANS method considering S-A turbulence model. The above research, based on RANS method, can obtain time-averaged characteristics of the flow field, but that cannot reveal the transient process. Cocks [4] studied firstly the mixing and detonation processes in the non-premixed RDE using RANS-LES method, and the transient characteristics of the flow field are described initially.

This study just focuses on the below work: The injection and mixing processes of hydrogen and oxygen are investigated and analyzed in the non-premixed cold RDE, using the two-dimensional large eddy simulation (LES). The physical mechanism of hydrogen/oxygen mixing is understood further in RDE. The mixing equivalence ratio distribution of hydrogen/oxygen in the combustion chamber is presented, and the area of the detonation is resolved accordingly. The above studies can provide quantitatively information for the injection configuration design and the suitable injection conditions.

2 Computational Description

The Favre-filtered Navier-Stokes equations for the unsteady compressible Newtonian fluids with heat and species transfer are solved using a density-based compressible solver, astroFoam, which is developed based on the standard rhoCentralFoam solver distributed with OpenFOAM v2.3.0. The numerical approach used in this research can be seen in Ref. [5].

The combustion chamber of RDE is a coaxial cylindrical channel. The rectangular slice of RDE along radial direction is chosen as the two-dimensional computational schematic, as shown in Fig. 1. The width of combustion chamber is $H = 10$ mm. The length of the combustion chamber is $L = 100$ mm. The high-pressure oxygen jet is injected into the chamber from the slit at the middle of the head end, while the high-pressure hydrogen jet is injected into the chamber from the slit on the outer wall. The width of the two injection slits are $D = 2$ mm. The high-pressure hydrogen jet mixes with the high-pressure oxygen jet in the combustion chamber.

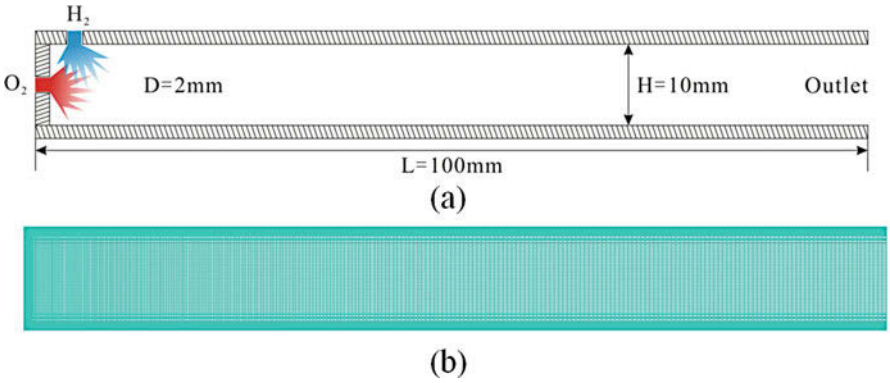

Fig. 1 Computational schematic. (**a**) Top, physical model, and (**b**) Bottom, computational grids

Figure 1b shows the computational grids. The 2D structure grid is carried out, and the total number of grid reaches 0.278 million. The grid size of the first layer at the inner wall, the outer wall, and the head end is 0.01 mm. There are 50 grids in the injection slit; therefore the grid size is 0.04 mm. The grid size is 0.2 mm near the central region of the flow field. In order to increase the numerical dissipation, the grid size along the flow direction increases to 0.5 mm near the chamber exit.

The static temperature of oxygen jet and hydrogen jet is 300 K. Oxygen jet and hydrogen jet are both injected into the chamber at Mach number Ma = 1.0. The static pressure of oxygen jet is 20 atm, while the static pressure of hydrogen jet is 10 atm. Therefore when their injection areas are the same, the total equivalence ratio of hydrogen jet and oxygen jet, injected into the chamber, is just $\Phi = 1.0$. In the simulations, the adiabatic and nonslip boundary conditions are used on the outer wall, the inner wall, and the head end. Because the Mach numbers of hydrogen jet and oxygen jet are 1.0, the pressure, temperature, and velocity at the injection boundary are fixed. In the chamber outlet, the extrapolation boundary condition is used. The initial pressure and temperature are 1 atm and 300 K.

3 Results and Discussion

3.1 Instantaneous Flow and Instabilities

In the baseline case, oxygen is injected into the chamber from the slit, which is D = 2 mm width, along the axial direction at y/D = 2.5. Hydrogen is injected into the chamber from the D = 2 mm slit on the outer wall along the radial direction, whose position is x/D = 1.5. It is about 0.3 ms from the hydrogen and oxygen injected into the chamber to flow out from the chamber. Figure 2 shows the instantaneous distributions of hydrogen mass fraction, temperature, and streamwise

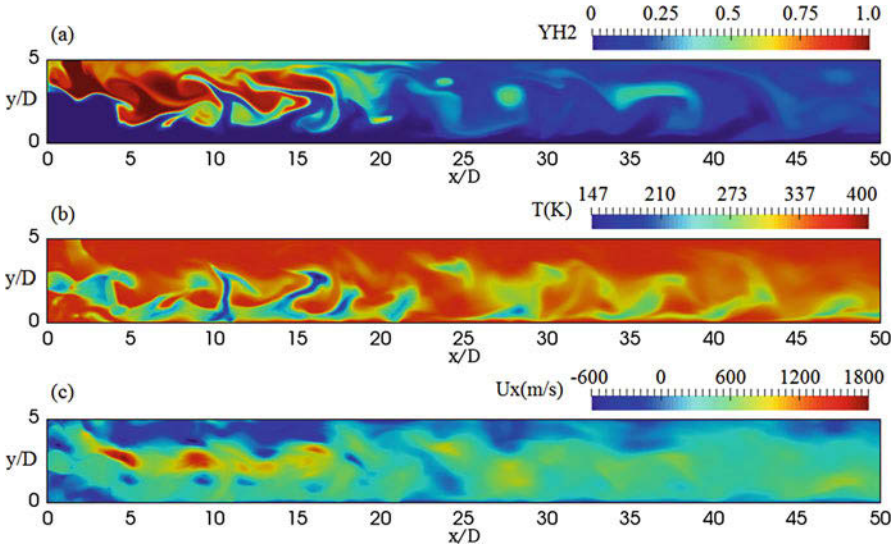

Fig. 2 Instantaneous contours of various flow properties at t = 2 ms. (**a**) Hydrogen mass fraction, (**b**) Temperature, (**c**) Streamwise velocity

velocity at t = 2 ms. At that time, the flow field has already been quasi-steady state. The high-pressure hydrogen and oxygen jets are expanded rapidly near the exit of injection. The classical underexpanded feature is observed including Mach barrel, low-temperature, and high-speed region in flow field. In the process of underexpanded jet, the minimum temperature is reduced to 150 K, which is only half of the initial temperature of the jet. The maximum velocity of the flow field is increased to 1800 m/s, which is obviously higher than the velocity of hydrogen and oxygen jets.

The large-scale vortex structures are formed and fall off alternately on the shear layer of hydrogen and oxygen jets, because of the Kelvin-Helmholtz (K-H) instability. Therefore there is a very strong unsteady characteristic in the flow field. The mixing of hydrogen and oxygen is enhanced considerably under the influence of the vortex structures, which is the main mechanism for the mixing of hydrogen and oxygen. These vortex structures are transported downstream and become larger gradually with the development of the flow. At the same time, the low-temperature fluid generated by the underexpanded jets is also transported downstream. In addition, the backflow zone exists near both sides of hydrogen and oxygen jets, as shown in Fig. 2c, which can promote the local mixing.

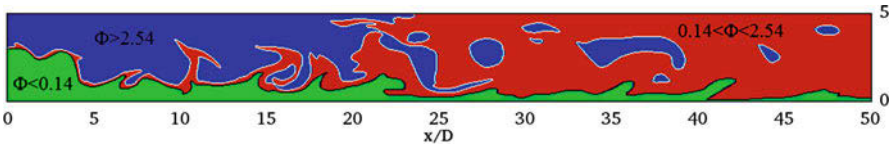

Fig. 3 Instantaneous distribution for local equivalence ratio

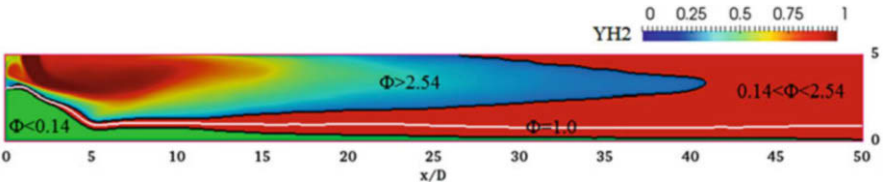

Fig. 4 Time-averaged equivalence ratio distribution

3.2 Mixing Characteristic

When the initial pressure is 1.0 atm, the rich combustion limit and the lean combustion limit of hydrogen and oxygen are 2.54 and 0.14 [6], respectively. Figure 3 shows the instantaneous distribution for local equivalence ratio, and the three different color areas are the equivalence ratio larger than 2.54 (blue area), less than 0.14 (green area), and between 0.14 and 2.54 (red area). The detonation wave may be initiated successfully and propagate stably only in the area of equivalence ratio between 0.14 and 2.54 (red area). At x/D < 25, the area of the detonation is very narrow, only near the shear layer. With the influence of the jet shear and the vortex structure entrainment, the area of the detonation is becoming larger and larger along streamwise direction. In the experimental design of RDE, the initiation and propagation of the detonation are arranged near the head end of the chamber; therefore, increasing the area of the detonation near the head end is significant for the stable operation of RDE.

The above instantaneous flow has a strong time heterogeneity, and the turbulent fluctuation is intense. Figure 4 shows the hydrogen mass fraction of time averaged and the contour lines of the mixing equivalence ratio. The area of the detonation is maintained stably within a wide area at x/D > 40. The area between the equivalence ratios from 1.0 to 2.54 is rich fuel, and the area between the equivalence ratios from 0.14 to 1.0 is lean fuel. The area of rich fuel is obviously wider than the lean fuel region. It is consistent with the instantaneous distribution that the area of the equivalence ratio $0.14 < \Phi < 2.54$ is small near the head end, especially at x/D < 10, only a narrow layer. Therefore the question, how to increase the area of the detonation near the head end of the RDE chamber, is will be a signification study work.

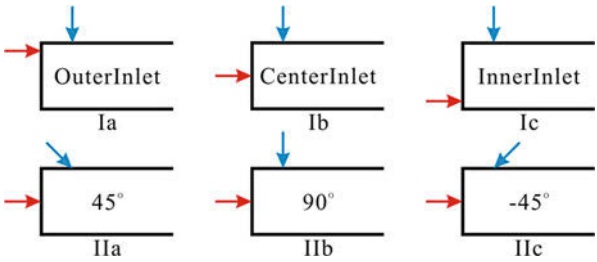

Fig. 5 Different non-premixed injection strategies

3.3 Effect of Non-premixed Injection Strategies

According to the investigation of the above baseline case, it is known that the area of the detonation is only a narrow layer near the head end, which is a disadvantage to the initiation of successful and stable propagation of the detonation in RDE. Therefore we investigate the effects of the injection position of oxygen jet and the injection direction of hydrogen jet on the mixing process of hydrogen/oxygen and the area of the detonation, trying to improve the mixing efficiency by adjusting the injection design preliminary.

Besides the above baseline case, as shown in Ib and IIb in Fig. 5, we also simulate four more cases, as shown in Ia, Ic, IIa, and IIc in Fig. 5. Cases Ia, Ib, and Ic represent that the oxygen jets are injected near the outer wall, at the middle of the head end, and near the inner wall successively, while cases IIa, IIb, and IIc represent that the hydrogen jets are injected along the positive 45° direction, 90° direction, and negative 45° direction successively.

The vortex scale and the position of the jet shear layer will be affected by the different injection designs. Compared to oxygen injected near the outer wall and at the middle of the head end, when it is injected near the inner wall, the vortex scale is larger, the turbulent fluctuation is more intense, and the downstream flow field is more uniform, as shown in Fig. 6. Therefore the mixing level in case of the oxygen injection near the inner wall (Ic) is better than that in case of oxygen injection at the middle (Ib) and outer slits (Ia), while the mixing level in case of the hydrogen injected along the negative 45° direction (IIc) is better than that in case of along the positive 45° direction (IIa) and along the 90° direction (IIb).

Figure 7 shows the area percentage where the local equivalence ratio is smaller than the lean limit $\Phi < 0.14$, between rich and lean limit $0.14 < \Phi < 2.54$, and larger than rich limit $\Phi > 2.54$ successively. We think that the more the area percentage of the local equivalence ratio between lean and rich limits $0.14 < \Phi < 2.54$ is, the better the mixing level of the hydrogen jet and the oxygen jet is. In case of the oxygen injection at the inner slit, the area percentage of the detonation is 55.97%, which is larger than 44.55% in case of at the middle slit and 43.26% at the outer slit. In case of the hydrogen injection along negative 45° direction, the area percentage of the detonation is 59.78%, which is larger than 44.55% along the 90° direction and 51.73% along the positive 45° direction. In summary, compared with the other

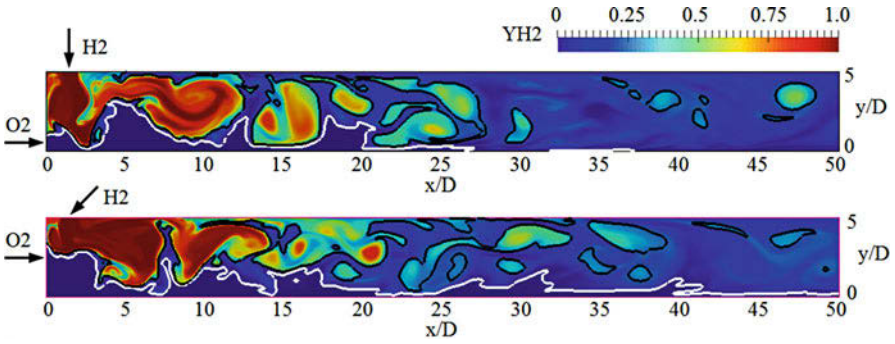

Fig. 6 Instantaneous distribution of mass fraction for hydrogen and isoline of mixing equivalence ratio; top,, Case Ic, and bottom,, Case IIc

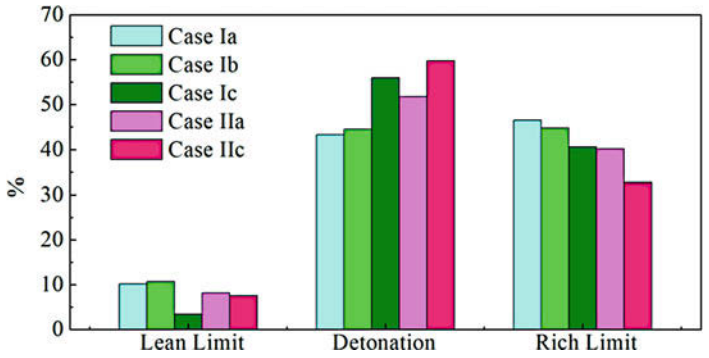

Fig. 7 The area calculations of local equivalence ratio larger than rich limit $\Phi > 2.54$, between rich and lean limit $0.14 < \Phi < 2.54$, and smaller than lean limit $\Phi < 0.14$

four cases Ia, Ib (IIb), Ic, and IIa, the hydrogen jet injected along the negative 45° direction (IIc) is an advantage to efficient mixing of hydrogen jet and oxygen jet in RDE.

4 Conclusions

Two-dimensional large eddy simulation (LES) for supersonic compressible multi-component flow is carried out to investigate the mixing characteristic of the cold non-premixed RDE with different injection strategies. The evolution processes of hydrogen/oxygen injected, jet shear, and mixing are revealed. According to the instantaneous and quasi-stead time-averaged flow field, the nonuniform mixing characteristic is presented. In the non-premixed RDE flow field, there are underexpanded feature, large-scale eddy structure, and recirculation zone, and the turbulence eddy structure generated by the K-H instability is the main mechanism for promoting the mixing of fuel and oxidizer.

Combining the rich and lean combustion limits, the area of the detonation is identified. It is found that the area of the detonation is only a narrow layer near the head end. To improve the mixing efficiency near the head end in the non-premixed RDE, the oxygen injection position and hydrogen injection angle are adjusted preliminary. The mixing characteristics and the area of the detonation are analyzed in detail. In case of the oxygen injection at the inner slit, the vortex scale is larger, the turbulent fluctuation is more intense, and the downstream flow field is more uniform. The mixing distance to maintain a wide area of the detonation is also shorter. Therefore the mixing level in case of the oxygen injection at the inner slit is better than that in case of oxygen injection at the middle and outer slits, while the mixing level in case of the hydrogen injection along the negative 45° direction is better than that in case of hydrogen injection along the 90° and positive 45° directions.

Acknowledgments The work was supported by the National Natural Science Foundation of China (Grant No.11602028; No. 11502029).

References

1. P. Wolanski, Detonation propulsion. Proc. Combust. Inst. **34**, 125–158 (2013)
2. S.M. Frolov et al., Three-dimensional numerical simulation of the operation of a rotating-detonation chamber with separate supply of fuel and oxidizer. Combust. Explos. Shock Waves **32**(2), 56–65 (2013)
3. W.A. Stoddard et al., Computational analysis of existing and altered rotating detonation engine inlet designs, AIAA paper. 2014-3668
4. P.A.T. Cocks et al., High fidelity simulations of a non-premixed rotating detonation engine, AIAA paper. 2016-0125
5. X.P. Li et al., Large-Eddy simulation of time evolution and instability of highly under-expanded sonic jets. AIAA J. **54**(10), 3191–3211 (2016)
6. S.R. Turns, *An Introduction to Combustion: Concepts and Applications* (The McGraw-Hill Companies, New York, 1996)

Research on the Continuous Rotating Detonation Wave in a Hollow Chamber with Laval Nozzle

Shijie Liu, Hailong Zhang, and Weidong Liu

Abstract In the present study, H_2/air CRD is achieved in a hollow chamber with Laval nozzle both experimentally and numerically. Three rotating patterns are obtained, which are one-wave, two dominant peak one-wave (TDPO), and two-wave modes, and the flow-field structure and effect of the nozzle contraction ratio are detailed. Both the propagation frequency and detonation wave number increase with the increase of equivalence ratio (ER) or nozzle contraction ratio. Shock wave reflection occurs at the nozzle converging section, and its upstream reflected shock wave will interact with the fresh mixture zone and inlet, leading to different rotating patterns and propagation characteristics.

1 Introduction

Due to the bad mixing efficiency near the face plate, a high-temperature combustible layer may exist in front of the combustion flame in the liquid rocket combustor. This provides the condition for the formation of continuous rotating detonation (CRD). So CRD may be one of the causations inducing the tangential combustion instability of the liquid rocket engine. However, the configurations of the traditional CRD and liquid rocket engines are different. The liquid rocket engine usually has a cylindrical combustor and a Laval nozzle, while an annular combustor is usually adopted by the CRD engine.

Due to the high propagation frequency and roughly steady thrust, CRD engine has a huge potential in the propulsion applications, and lots of research has been carried out about it. Annular combustion chambers have been used by most of the CRD research [1–3], and detonation waves have been realized under both room-temperature [1, 2] and high-temperature (840 K) [3] inflows. CRD in the cylindrical combustor without nozzle has also been obtained experimentally [4, 5]

S. Liu (✉) · H. Zhang · W. Liu
Science and Technology on Scramjet Laboratory, National University of Defense Technology, Changsha, China
e-mail: liushjijie@nudt.edu.cn

A. Sasoh et al. (eds.), *31st International Symposium on Shock Waves 2*,
https://doi.org/10.1007/978-3-319-91017-8_14

and numerically [6], and its rotating modes are similar to that in the annular combustor. To improve the propulsive performance of CRD engine, the effects of nozzle configurations have been studied numerically by using an annular combustor [7–9]. Compared with constant-area nozzle, the thrust performance of divergent and Laval nozzles are better [7, 8]. The convergent-divergent configuration of the Laval nozzle can also reduce the pressure oscillations [9].

There are many resemblances between CRD and tangential combustion instability in liquid rocket engine, but the configurations of these engines are different. To further clarify the relationship between them, CRD research has been carried out experimentally by using a hollow chamber with Laval nozzle [10], the configuration of which is nearly the same as liquid rocket engine. Three rotating patterns have been obtained, and the pressure oscillation characteristics are detailed [10]. In this paper, the corresponding numerical investigations will be carried out, and the flowfield structure and effect of the nozzle contraction ratio will be analyzed.

2 Physical Model and Numerical Scheme

Figure 1 shows the schematic diagram of the CRD combustor and nozzle. The diameter and length of the combustor are 100 and 80 mm, respectively. The axial length between the nozzle inlet and throat is 100 mm. The nozzle contraction ratio ε is defined as the area ratio between the chamber and throat. Gaseous air and hydrogen are used in the test. For the test, air is injected through a slot with the width of 0.7 mm, and hydrogen is injected through 90 orifices with a diameter of 0.7 mm. For the CFD, the injection and mixing processes are neglected, and premixed hydrogen/air mixture is used, which is injected from a 5 mm wide annular slot. The total pressure and temperature of the premixed mixture are 1.08 atm and 300 K, respectively. The axial length between the nozzle outlet and throat is 100 mm for the test, while it is just 10 mm for the CFD.

Using the one-step chemistry kinetic model and Euler equations, three-dimensional numerical simulations are performed. The governing equations are solved with a high-resolution shock-capturing WENO scheme, and time integration is performed by using the second-order Runge-Kutta method. This numerical method has been used successfully in our previous numerical studies [11, 12]. The slip wall boundary conditions are imposed at the outer wall and left side wall. The right side of the domain is set as the outlet boundary, with the back pressure of 5 kPa. Depending on the local Mach number at the exit, either subsonic or supersonic outlet boundary condition is adopted.

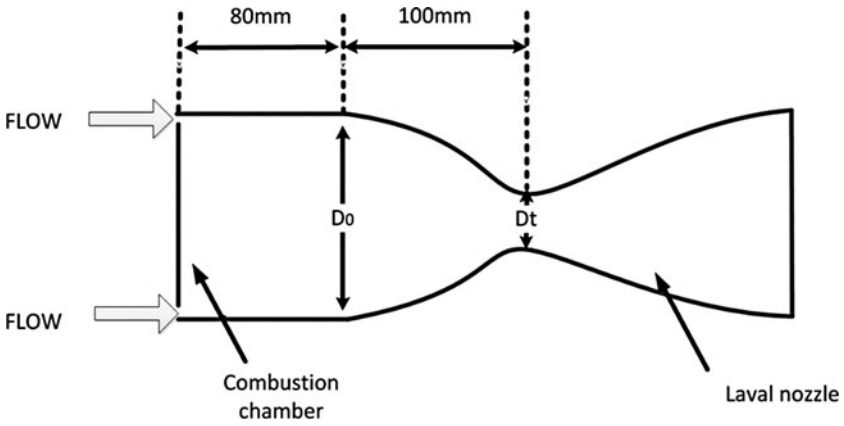

Fig. 1 Schematic diagram of the CRD combustor and nozzle

3 Results and Discussion

Series of tests have been carried out by changing the propellant mass flow rate and nozzle, and the air mass flow rate, equivalence ratio (ER), and nozzle contraction ratio range 353–372 g/s, 0.35–1.1, and 2–12, respectively. H2/air CRD has been realized successfully in this model engine. Among all the tests, three CRD rotating patterns are obtained, which are defined as one-wave, two dominant peak one-wave (TDPO), and two-wave modes [10].

Figure 2 shows the frequency distributions under different test conditions, and it is seen that the rotating frequency increases with the increase of ER and nozzle contraction ratio. For $2 \leq \varepsilon \leq 6$, CRD propagates as the one-wave mode under all the ER conditions. When$8 \leq \varepsilon \leq 12$, the detonation wave number increases by increasing the ER. The critical ER value is about 0.8–09 for $\varepsilon = 8$, while it is about 0.7–0.8 for $10 \leq \varepsilon \leq 12$. It means that the nozzle contraction ratio has a significant effect on the rotating pattern. It is easier to get more detonation waves with larger nozzle contraction ratio.

3.1 One-Wave Mode

One-wave mode has two different types. One is that the pressure oscillations possess only one dominant peak during every interval while the other possesses two. Figure 3 shows the simulation results of the typical one-wave mode ($\varepsilon = 2$, ER $= 1$), which is labeled as SC#1. Fresh mixtures are injected from the left side continuously, and a rotating detonation wave ① is formed near the inlet, ahead of which there is a fresh mixture zone ⑥. With the detonation products expanding to the exit, an oblique shock wave ② is set up at the bottom of the detonation

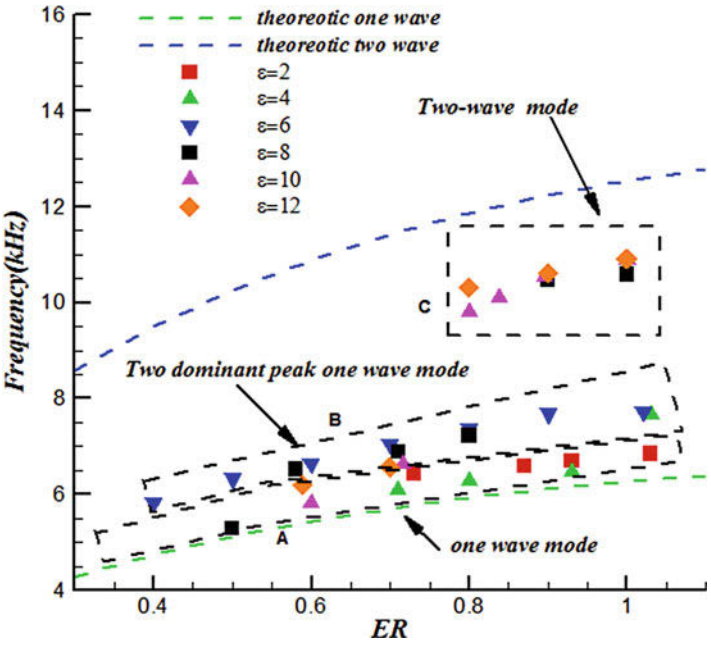

Fig. 2 Propagation frequency distribution of all the tests

wave, which reflects with the nozzle converging section, leading to the formation of upstream reflected shock wave ③ and downstream reflected shock wave ④. There is a contact surface ⑤ between the combustion products of different cycles. The dominant frequency of SC#1 is 6.66 kHz, and the rotating velocity at the outer wall is 2091 m/s.

In order to analyze the flow field clearly, the chamber is splitted and extended to a two-dimensional plane along the circumferential direction. Figure 4 shows the pressure and temperature contours on the outer wall of typical one-wave mode. Since the contraction ratio is small, the reflected shock wave is weak, which just attaches the rotating detonation wave front at the downstream location. So there is only one dominant pressure peak during every interval for the pressure evolution at the inlet, just as shown in Fig. 3c.

3.2 Two Dominant Peak One-Wave Mode

By increasing the nozzle contraction ratio, the reflected shock wave can lead to different pressure oscillation characteristics. Figure 5 shows the three-dimensional (3D) simulation results of two dominant peak one-wave mode, which is labeled as SC#2, and its nozzle contraction ratio is 4, larger than that of SC#1. The dominant

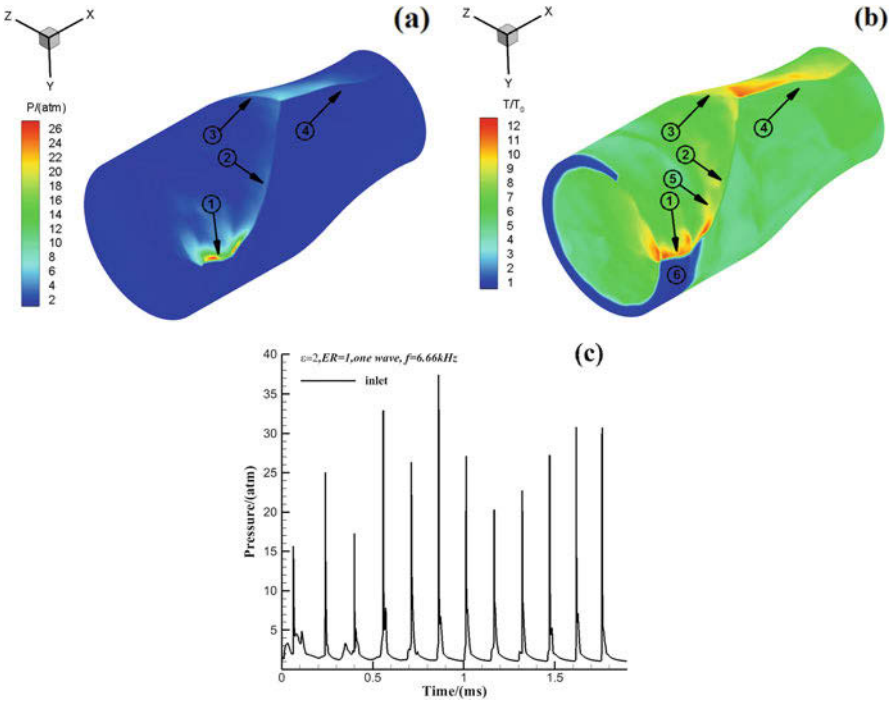

Fig. 3 3D simulation results of typical one-wave mode (SC#1, $\varepsilon = 2$, ER $= 1$): (**a**) pressure contours, (**b**) temperature contours, (**c**) pressure evolution at the inlet

frequency is 6.78 kHz, which is larger than that of SC#1. It indicates that the rotating frequency increases with the increase of the nozzle contraction ratio, which coincides with the test results. The rotating velocity at the outer wall is 2130 m/s. Due to the curvature effect, shock reflection occurs at the outer wall. It is shown in Fig. 5b that the detonation front is curved and the inner front is ahead of the outer one, so the rotating velocity at the outer wall can be larger than the CJ value.

Figure 6 shows the pressure and temperature contours on the outer wall of two dominant peak one-wave mode. Although the shock wave reflection exists in all tests, the reflection strength varies with the change of the nozzle contraction ratio. Due to the larger ε, the Mach reflection location of SC#2 is more upstream than that of SC#1. The upstream reflected shock wave attaches the contact surface ahead of the detonation wave, and it reflects again at the inlet plane. Figure 5c shows the pressure evolution at the location 60 mm from the inlet. Due to the reflected shock wave, there is another pressure peak during every rotating period, and the pressure oscillation characteristics coincide well with the test results shown in Ref. [10].

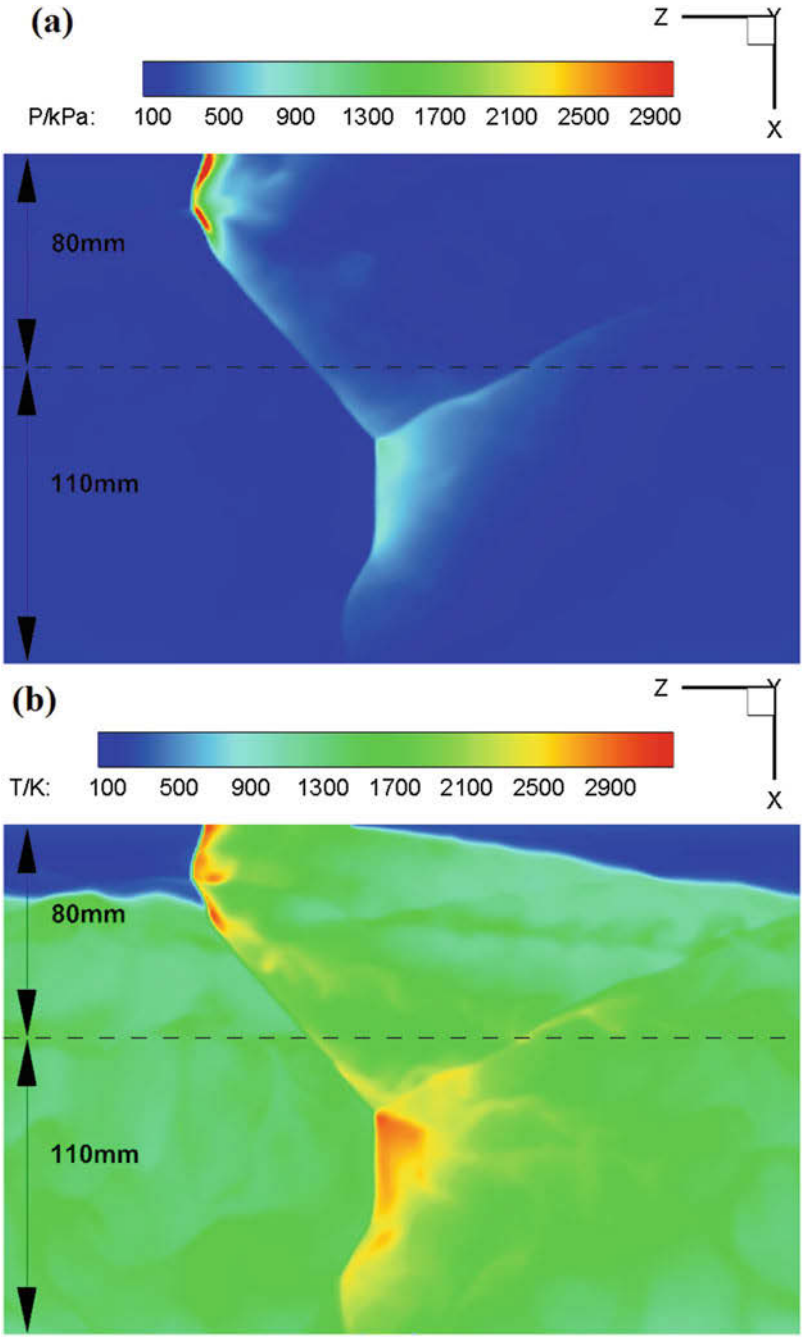

Fig. 4 Contours of pressure and temperature on outer lateral of typical one-wave mode (SC#1, $\varepsilon = 2$, ER $= 1$): (**a**) pressure contour, (**b**) temperature contour

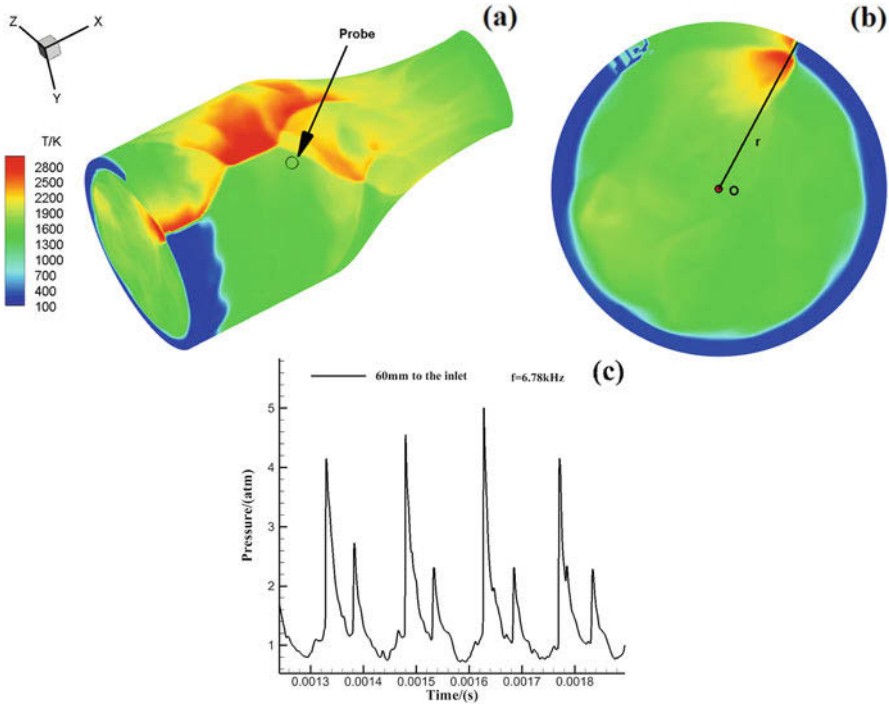

Fig. 5 3D simulation results of two-dominant peak one-wave mode (SC#2, $\varepsilon = 4$, ER $= 1$). (**a**) Overview. (**b**) The inlet plane. (**c**) The pressure oscillation at the location 60 mm to inlet

3.3 Two-Wave Mode

Figure 7 shows the 3D simulation results of two-wave mode ($\varepsilon = 6$, ER $= 1$), which is labeled as SC#3. The three simulation cases adopt the same ignition method. An ignition zone with high pressure, high temperature and large circumferential velocity is located at the left end of the combustor. Then a rotating detonation wave is induced, propagating within the chamber and adjusting itself with the boundary conditions. Finally, the mass flow rate and CRD propagation process will approach to a steady state. There is just one detonation wave for SC#1 and SC#2, while two detonation waves are obtained in SC#3. The detonation wave height of two-wave mode is much less than that of one-wave mode. The dominant frequency of SC#3 is 11.2 kHz, much larger than that of the one-wave mode. Its rotating velocity is 1758 m/s, less than that of the one-wave mode, which coincides with the test results.

Figure 8 shows the pressure and temperature contours on the outer wall of two-wave mode. Although the nozzle contraction ratio of SC#3 is the largest, the strength of the shock wave reflection is less than that of SC#2 because of its weak oblique shock wave strength. The upstream reflection shock wave penetrates the oblique

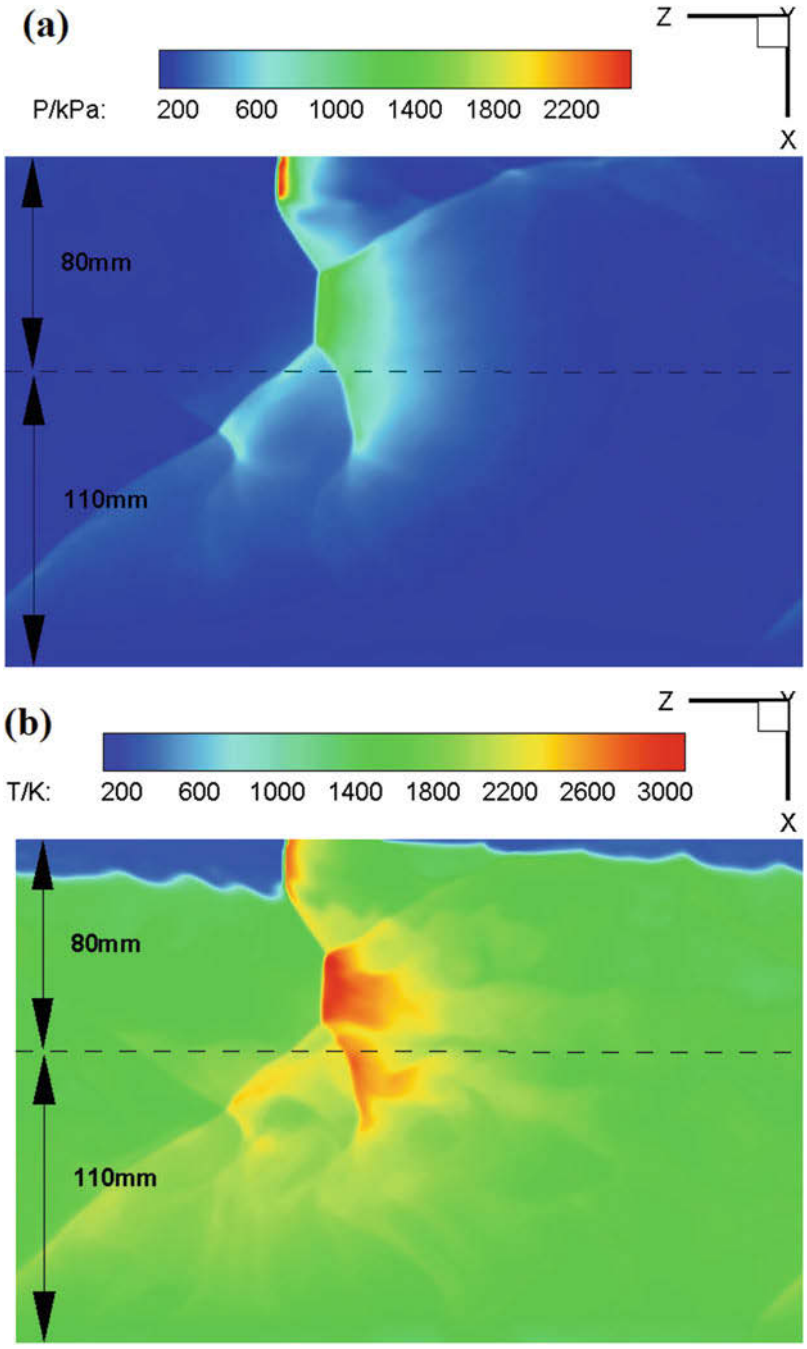

Fig. 6 Contours of pressure and temperature on outer lateral of two dominant peak one-wave mode (SC#2, $\varepsilon = 4$, ER $= 1$): (**a**) pressure contour, (**b**) temperature contour

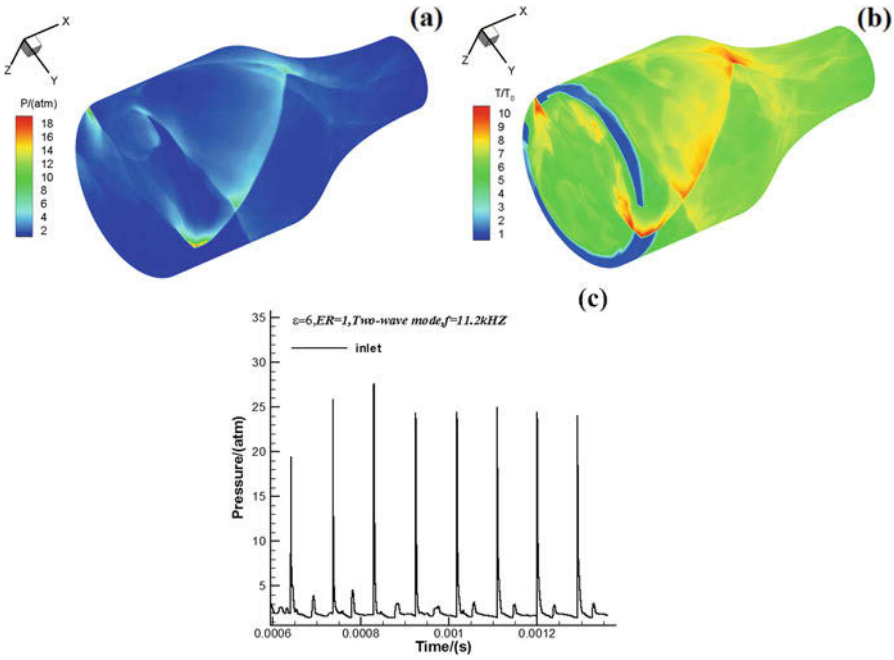

Fig. 7 3D simulation results of two-wave mode (SC#3, $\varepsilon = 6$, ER $= 1$). (**a**) Pressure contours. (**b**) Temperature contours. (**c**) Pressure oscillation at the inlet

shock wave and attaches on the inlet plane, leading to the little pressure peaks during every rotating circle as shown in Fig. 7c.

4 Conclusions

Through this research, the feasibility of CRD in a hollow chamber with Laval nozzle is demonstrated, the configurations of which is nearly the same as the liquid rocket engine. Three rotating patterns are obtained, which are one-wave, two dominant peak one-wave (TDPO), and two-wave modes, and the flow-field structure and effect of the nozzle contraction ratio are detailed. Both the propagation frequency and detonation wave number increase with the increase of equivalence ratio (ER) or nozzle contraction ratio. Shock wave reflection occurs at the nozzle converging section, and its upstream reflected shock wave will interact with the fresh mixture zone and inlet, leading to different rotating patterns and propagation characteristics.

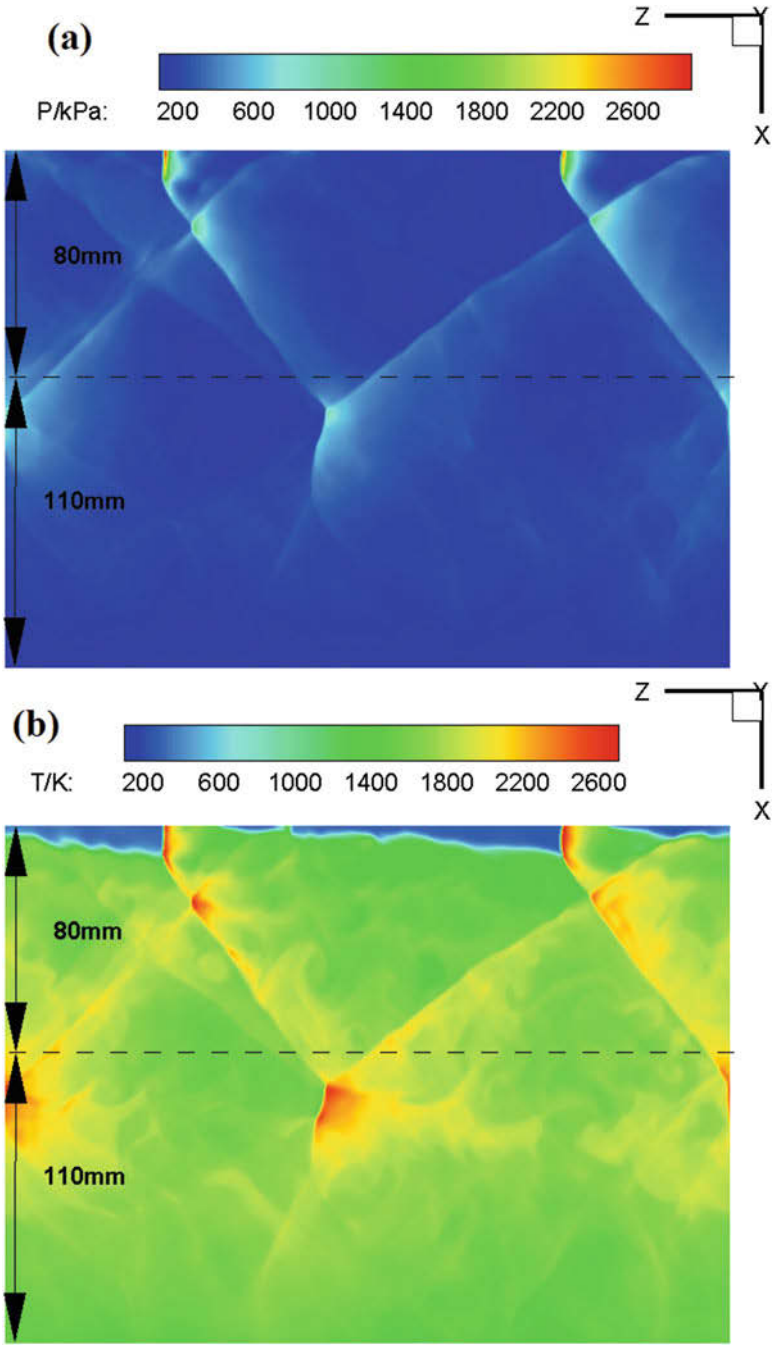

Fig. 8 Contours of pressure and temperature on outer lateral of two-wave mode (SC#3, $\varepsilon = 6$, ER $= 1$): (**a**) pressure contour, (**b**) temperature contour

Acknowledgments The authors gratefully acknowledge the support of the National Natural Science Foundation of China (No. 91541103 and No. 51476186) for this work.

References

1. S.J. Liu, Z.Y. Lin, W.D. Liu, W. Lin, F.C. Zhuang, Experimental realization of H2/air continuous rotating detonation in a cylindrical combustor. Combust. Sci. Technol. **184**, 1302–1317 (2012)
2. W. Lin, J. Zhou, S.J. Liu, Z.Y. Lin, F.C. Zhuang, Experimental study on propagation mode of H2/air continuously rotating detonation wave. Int. J. Hydrog. Energy **40**, 1980–1993 (2015)
3. C. Wang, W.D. Liu, S.J. Liu, L.X. Jiang, Z.Y. Lin, Experimental investigation on detonation combustion patterns of hydrogen /vitiated air within annular combustor. Exp. Thermal Fluid Sci. **66**, 269–278 (2015)
4. W. Lin, J. Zhou, Z.Y. Lin, S.J. Liu, An experimental study on CH4/O2 continuously rotating detonation wave in a hollow combustion chamber. Exp. Thermal Fluid Sci. **62**, 122–130 (2015)
5. H.L. Zhang, W.D. Liu, S.J. Liu, Effects of inner cylinder length on H2/air rotating detonation. Int. J. Hydrog. Energy **41**, 13281–13293 (2016)
6. X.M. Tang, J.P. Wang, Y.T. Shao, Three-dimensional numerical investigations of the rotating detonation engine with a hollow combustor. Combust. Flame **162**, 997–1008 (2015)
7. T.H. Yi, J. Lou, C. Turangan, Effect of nozzle shapes on the performance of continuously rotating detonation engine. AIAA 2010-152
8. Y.T. Shao, M. Liu, J.P. Wang, Continuous detonation engine and effects of different types of nozzles on its propulsion performance. Chin. J. Aeronaut. **23**, 645–650 (2010)
9. S. Etoa, N. Tsuboib, K. Takayukic, A.K. Hayashid, Three-dimensional numerical simulation of a rotating detonation engine: Effects of the throat of a converging-diverging nozzle on engine performance. Combust. Sci. Technol. **188**, 2105–2116 (2016)
10. H.L. Zhang, W.D. Liu, S.J. Liu, Experimental investigations on H2/air rotating detonation wave in the hollow chamber with Laval nozzle. Int. J. Hydrog. Energy **42**, 3363–3370 (2017)
11. S.J. Liu, Z.Y. Lin, W.D. Liu, W. Lin, M.B. Sun, Experimental and three-dimensional numerical investigations on H2/air continuous rotating detonation wave. J. Aerosp. Eng. **227**, 326–341 (2013)
12. S.J. Liu, Z.Y. Lin, M.B. Sun, W.D. Liu, Thrust vectoring of a continuous rotating detonation engine by changing the local injection pressure. Chin. Phys. Lett. **28** (2011)

Experimental Research on a Long-Duration Operation of a Rotating Detonation Engine

J. Nishimura, K. Ishihara, K. Goto, K. Matsuoka, J. Kasahara, A. Matsuo, I. Funaki, H. Mukae, K. Yasuda, D. Nakata, K. Higashino, and H. Moriai

Abstract Detonation engines have higher thermal efficiency than conventional engines. It is capable of shortening the combustor since the combustion process of detonation completes in quite a short time. Therefore, many researches on detonation engines have been conducted around the world. An RDE can be used as a kick rocket motor for deep-space exploration. However, there are some problems to be solved prior to the practical use of an RDE. One of the most critical problems is heat-transfer problem. High heat load in the combustor is expected. Thus, it is necessary to evaluate the heat-transfer characteristics of an RDE. To realize the space use of an RDE, we conducted long-duration combustion tests and vacuum tests. We succeed in 6-second and 10-second operations of an RDE using C/C composites. And from the vacuum tests, thrust performance is evaluated. We achieved 272 s of specific impulse under the low back pressure of 22.0 kPa.

1 Introduction

An engine using detonation waves is called a detonation engine. It became clear that detonation cycle has higher thermal efficiency than Humphry cycle and Brayton cycle by analysis of detonation cycle. From this, many researches on detonation

J. Nishimura (✉) · K. Ishihara · K. Goto · K. Matsuoka · J. Kasahara
Nagoya University, Nagoya, Japan
e-mail: nishimura@prop2.nuae.nagoya-u.ac.jp

A. Matsuo
Keio University, Yokohama, Japan

I. Funaki
JAXA Institute of Space and Astronautical Science, Sagamihara, Japan

H. Mukae · K. Yasuda · D. Nakata · K. Higashino
Muroran Institute of Technology, Muroran, Japan

H. Moriai
Mitsubishi Heavy Industries, Ltd., Komaki, Japan

A. Sasoh et al. (eds.), *31st International Symposium on Shock Waves 2*,
https://doi.org/10.1007/978-3-319-91017-8_15

engines have been conducted around the world. There are two kinds of detonation engines; one is a pulse detonation engine (PDE) [1, 2], the other is a rotating detonation engine (RDE). A PDE has a straight tube combustor and generates pulsed thrust. Researches on a PDE combined with a turbine and a rocket system using PDE have been conducted. An RDE has an annular combustor and continuously generates thrust. Researches on a propulsion system using an RDE [3–5] and the structure of detonation waves in the combustor [6] have been conducted. There are several problems to be solved prior to the practical use of an RDE though application of an RDE as a kick rocket motor is expected. One of the most critical problems is heat-transfer problem. It is reported that the combustor is subjected by strong heat load. It is estimated that heat flux at the combustor wall surface is approximately 1 10 MW/m^2 [7–9]. There are some researches to decrease the heat load at the combustor wall [10, 11]. The objective is a practical use of an RDE as a kick rocket motor for deep-space exploration. Long-duration ground combustion tests in the atmosphere and vacuum tests in the low back pressure are presented.

2 Experimental Apparatus

The RDE used in experiments is shown in Fig. 1. The combustor is annular type. The RDE is mainly composed of copper. In the long-duration tests, the wall around combustion chamber is consisted of C/C composites which have a high heat resistance. In the vacuum tests, the wall around the combustion chamber is composed of copper instead of C/C composites.

The fuel is gaseous ethylene, and the oxidizer is gaseous oxygen. The fuel is injected into combustion chamber through the 120 pairs of injector holes. The injector holes of the oxidizer are also 120 sets. The fuel and the oxidizer collide at the right angle to each other.

The temperature of the combustor is measured by k-type thermocouples. The placement of the thermocouples is shown in Fig. 2. The temperature is measured at distances of 1 and 2 mm from the outer cylindrical wall. The thermocouples were installed in the cross sections at $z = 2$, 9, 18, 35, and 65 mm and nozzle throat ($z = 0$ mm is the bottom of combustion chamber).

The pre-detonator is used to initiate detonation. The detonation wave initiated on the pre-detonator propagates into the combustion chamber and ignites main propellant. Finally, the rotating detonation waves are generated and starts the RDE.

The vacuum tests are conducted in the vacuum chamber with a volume of 36.6 m^3. The long-duration tests are performed in the Aerospace Plane Research Center of Muroran Institute of Technology.

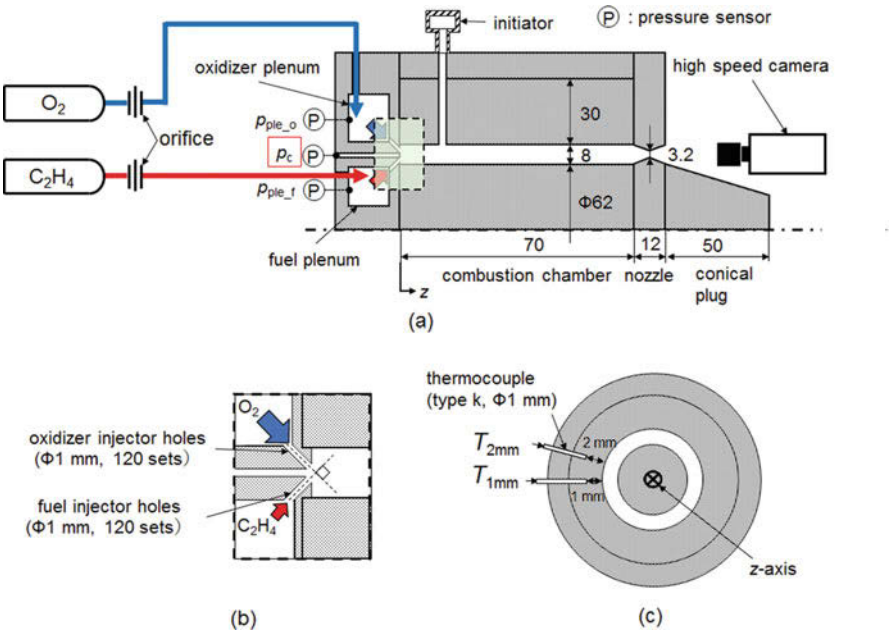

Fig. 1 Schematic of the RDE: (**a**) the combustor, (**b**) the injector, (**c**) cross-sectional view of the combustor and positions of the thermocouples

Fig. 2 Pictures of the vacuum chamber

3 Experimental Results

3.1 Vacuum Tests

The vacuum tests are conducted in the vacuum chamber. The picture of the vacuum chamber is shown in Fig. 2. Experimental conditions of vacuum test are shown in Table 1. Experimental results of thrust and combustion pressure of one experiment are shown in Fig. 3. The operating duration is 0.4 s. Average thrust and average

Table 1 Experimental conditions of vacuum tests

Shot number	Propellant mass flow rate $\dot{m}$[g/s]	Equivalence ratio Φ[-]	Average back pressure p_b [kPa]
sh#V1	335	1.03	22.0

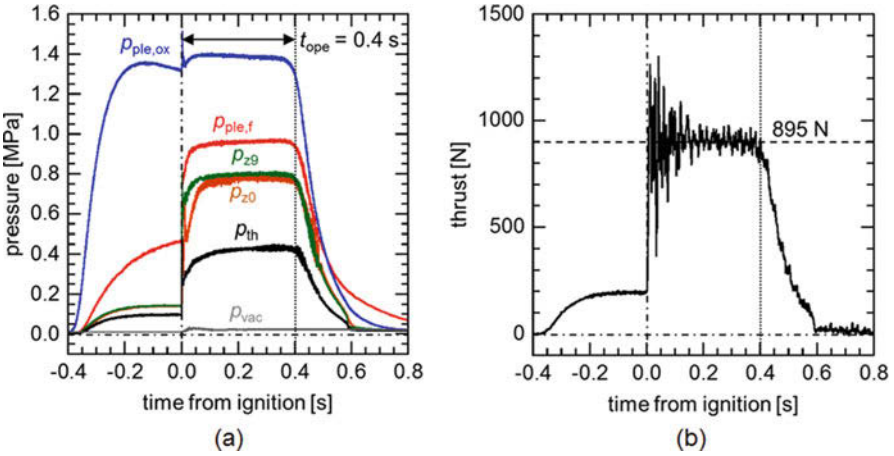

Fig. 3 Experimental results of a vacuum test sh#V1: (**a**) pressure, (**b**) thrust

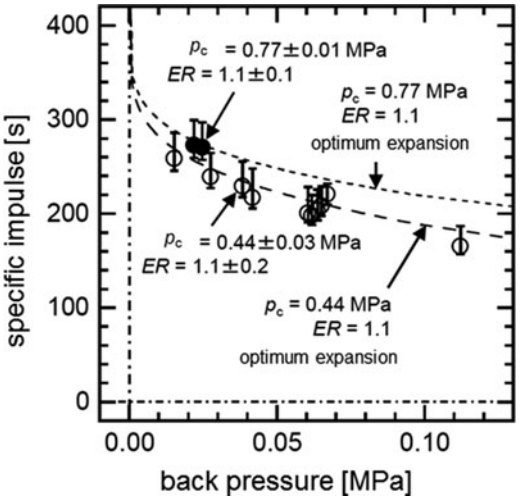

Fig. 4 Relationship the specific impulse and the back pressure

combustion pressure are 895 N and 0.77 MPa, respectively. The specific impulse is calculated as 272 s by average thrust and propellant mas flow rate.

Some experimental results of vacuum tests are shown in Fig. 4. The horizontal axis shows the average back pressure, and vertical axis shows the specific impulse. The two kinds of solid dash line in Fig. 4 indicate theoretical-specific impulse calculated by NASA-CEA.

Table 2 Experimental conditions of long-duration tests

Shot number	Propellant mass flow rate $\dot{m}$[g/s]	Equivalence ratio Φ[-]	Operation duration t_{ope}[s]
sh#1_long	96	1.63	10.2
sh#2_long	214	0.90	6.3

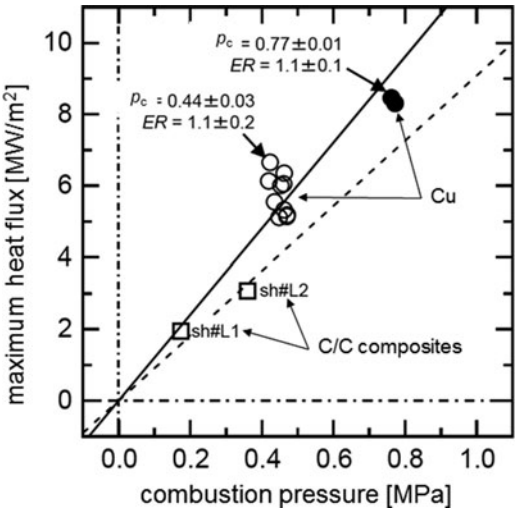

Fig. 5 The history of heat flux of the long-duration test

3.2 Long-Duration Tests

Experimental conditions of long-duration tests are shown in Table 2. In the long-duration tests, C/C composites are used for the wall of combustion chamber instead of copper to resist high heat load. Experimental results of thrust, combustion pressure at $z = 0$ mm of sh#L2, are shown in Fig. 5. The average value of combustion pressure was 0.359 MPa. According to $T_{1\text{mm}}$ and $T_{2\text{mm}}$ obtained by combustion tests, the heat flux in the outer wall in the combustor is estimated by the following equation:

$$\dot{q} = \lambda \frac{\Delta_T}{\Delta_r} = \lambda \frac{\mathrm{T_{1mm}\text{-}T_{2mm}}}{0.001} \ [\mathrm{W/m2}] \tag{1}$$

Here, λ is thermal conductivity. The values of λ of copper and C/C composites are 386 W/mK and 35 W/mK, respectively. It is assumed that the value of λ is constant. The relationship of the maximum heat flux and the combustion pressure is shown in Fig. 5. The vertical axis indicates the maximum value of the heat flux during operation. The heat flux depends on combustion pressure and is reduced in the case of using C/C composites.

4 Conclusion

We succeeded in 6-second and 10-second ground tests and vacuum tests of an RDE using C_2H_4-O_2 under the back pressure of 22.0 kPa and achieved the specific impulse of 272 s. From long-duration tests, it is elucidated that heat flux depends on the combustion pressure.

References

1. J. Kasahara, A. Hasegawa, T. Nemoto, H. Yamaguchi, T. Yajima, T. Kojima, J. Propuls. Power **25**, 173 (2009)
2. Matsuoka, K., Morozumi, T., Takagi, S., Kasahara, J., Matsuo, A., Funaki, I. J Propuls. Power **32**(2), pp. 383–391 (2016)
3. S. Maeda, S. Sumiya, J. Kasahara, Y. Sasamoto, A. Matsuo, Proc. Combust. Inst. **33**(2), 1973 (2013)
4. H. Nakayama, J. Kasahara, A. Matsuo, I. Funaki, Proc. Combust. Inst. **33**(2), 1939 (2016)
5. K. Ishihara, J. Nishimura, K. Goto, K. Matsuoka, J. Kasahara, A. Matsuo, I. Funaki, in *54th Symposium (Japanese) on Combustion*. E322, 2016
6. S. Nakagami, K. Matsuoka, J. Kasahara, A. Matsuo, I. Funaki, AIAA Paper 2015-4102, 2015
7. F.A. Bykovskii, E.F. Vedernikov, Heat flux to combustor walls during continuous spin detonation of fuel-air mixtures. Combus Explos Shock Waves **45**, 70 (2009)
8. S.W. Theuerkauf, F. Schauer, R. Anthony, J. Hoke, AIAA Paper. 2015-1603, 2015
9. Y. Kato, K. Ishihara, K. Matusoka, J. Kahasara, A. Matsuo, I. Funaki, AIAA Paper. 2016-1406, 2016
10. S. Claflin, International Workshop on Detonation for Propulsion 2015, 2012
11. A. Naples, M. Fotia, S. Theuerkauf, J. Hoke, F. Schauer, in *25th International Colloquium on the Dynamics of Explosions and Reactive Systems*. ICDERS 0019, 2015

Decaying Modes of Propagation of Detonation and Flame Front in Narrow Channel

S. V. Golovastov and G. Yu. Bivol

Abstract Decaying modes of propagation of flame front in narrow channel for acetylene-air mixtures were investigated experimentally using optical methods of diagnostics. Experiments were carried out using an open detonation channel of square cross section with transverse dimension of 3 mm and length of 1000 mm. It was connected to the detonation tube of large diameter 20 mm and length of 3000 mm. Trajectories of propagation of glowing combustion products (streak images) and frames of the reaction zone were obtained. Oscillating form of the propagation of the combustion inside the narrow channel after the decay of the stationary Chapman-Jouguet detonation into the shock wave and the flame front was registered. Parameters of velocity oscillation were obtained. The time interval of oscillations and spatial interval were measured. After the decay of the detonation wave, the average velocity of the flame front decreases first to 1000 m/s and then to 200 m/s. Minimum recorded value of the flame velocity was presented. It was shown that in spite of the substantial thermal losses to the channel walls, the propagation of detonation-like galloping combustion is possible in channels of subcritical size.

1 Introduction

Typically, a propagation of detonation in subcritical narrow channels is accompanied by spinning or galloping modes of propagation. These phenomena are due to the intense heat transfer from a reaction zone to the walls, as well as an interaction of the shock front and the reaction zone with a boundary layer.

Detailed analysis of propagation in spinning mode can be found in [1]. The average speed of propagation of the spinning detonation wave is comparable with the velocity D of Chapman-Jouguet detonation, while the instantaneous values can

S. V. Golovastov (✉) · G. Y. Bivol
Joint Institute for High Temperatures of the Russian Academy of Sciences (JIHT RAS), Moscow, Russia

A. Sasoh et al. (eds.), *31st International Symposium on Shock Waves 2*,
https://doi.org/10.1007/978-3-319-91017-8_16

vary in the range of 0.6–1.1 *D* [2]. Transition from the diagonal forms of propagation to the spinning ones in rectangular channels is of particular interest [3–5].

Unlike the spinning detonation, the average velocity of galloping detonation, as a rule, is about 0.7–0.85 *D* [6, 7]. Parameters of galloping detonation, such as period and pitch along the axis, can be found in [8]. The nonstationary modes of propagation of the combustion, including galloping detonation, are described in detail in [9] for ethylene/oxygen mixtures. It was shown that, under certain conditions, the flame velocity can assume an oscillating regime. However, the average velocity of such flame front did not exceed 7 m/s. It was shown in [10] that reinitiation of detonation is possible in a narrow channel after the decay of the detonation wave. In these investigations the initial decay of the detonation wave was carried out as a result of the detonation transition into a narrow flat channel.

When working with acetylene, oxygen is most often used as an oxidizer [2, 8, 11, 12]. Mixtures of acetylene with oxygen have the smallest width of the detonation cell, the value of which, depending on the ratio of components, does not exceed 1 mm. The greatest practical interest may be a mixture of acetylene with air. For such mixtures, the width of the detonation cell will be higher than 4–5 mm [13]. Thus, the propagation of detonation in channels with transverse dimensions close to 3 mm can be essentially nonstationary in character and differ from the galloping pattern of detonation propagation.

The present work is devoted to a series of experimental investigations of the decaying mode of the flame front in oscillating mode for acetylene-air mixture, when the average velocity is significantly lower than the velocity for the stationary Chapman-Jouguet detonation. The aim of the work was to determine the dynamic parameters of the flame propagation and concentration limits for the decaying flame propagation in acetylene-air mixture.

2 Scheme of the Experimental Setup

Experiments were carried out using a detonation channel of square cross section. Transverse dimension of the channel was 3 mm; the length of the channel was 1000 mm. It was connected to the detonation tube of large diameter 20 mm and length of 3000 mm (Fig. 1). The second end of the narrow channel was opened

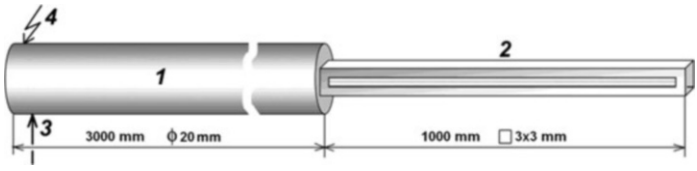

Fig. 1 Scheme of the experimental setup. 1 cylindrical detonation tube, 2 channel of square cross section, 3 gas supply system, 4 spark gap

to the atmosphere, so that the pressure inside the channel and the detonation tube was equaled to atmospheric pressure. The absence of the closed end in the narrow channel allows to avoid the spread of the reflected shock-wave perturbations inside the channel.

Acetylene-air mixture was supplied to the closed end of the detonation tube. After a time of 3–10 s after the filling, the mixture was ignited. Ignition was carried out by a spark discharge at the closed end of the tube. A deflagration-to-detonation transition was observed through 1.5–2.5 m along the detonation tube by piezoelectric pressure transducers. So, the stationary detonation of Chapman-Jouguet was registered at the entry of the rectangular channel.

Acetylene-air mixture allows to carry out the experiments in a rather narrow channel with sufficient luminosity in the visible range. Using the high-speed camera "Videosprint" (Videoscan Ltd.), trajectories of propagation of glowing combustion products (streak images) and frames of the reaction zone were obtained. Streak-mode settings were as follows: frequency 170,000 fps, exposure 1 μs, and resolution 1280*3 pixels; frame settings were as follows: 12,000–13,200 fps, 1 μs, and 1280*100 pixels. For detailed investigation of a structure of the flame front, the Schlieren system on a base of IAB-451 was used. The frame settings were as follows: 27,800–28,100 fps, 1 μs, and 1280*100 pixels.

3 Experimental Results and Discussion

Figure 2 shows a series of frames of the flame front and combustion products in the optical range after the detonation wave enters into the narrow rectangular channel. Data are given for a mixture with ER = 1.4 (ER – equivalence ratio, molar excess of fuel). Acetylene with air in this ratio gives a bright glow with a sharp registration of the flame front.

As seen from the first frame, the flame front corresponds to the front of the detonation wave. Intensive glow at the top and bottom edges is due to optical highlights on the metal surfaces. The velocity of the flame front between two frames

Fig. 2 Serial frames of the flame front and combustion products for acetylene-air mixture (ER = 1.4) in inverted colors after entry into the narrow channel. Time interval between frames is 80 μs

sharply dropped; it was about 1000 m/s, which is sufficiently lower than the speed of the stationary detonation 1866 m/s [14].

As can be seen from the subsequent frames, the flame front stretches along the axis. The average velocity of propagation of the flame front decreases. The exact numerical values of the flame front velocities taking into account the oscillations are presented below. At the same time, oscillation of the width of the zone of hot reaction products is recorded. The least value of the width of the luminescence area is 20 mm, and the maximum is 70 mm.

Such dynamics is characteristic for the galloping detonation. However, in this case, the propagation is not quasi-stationary in the region of a certain value of the velocity. The gradual decrease in the average value of the flame front speed indicates the significant role of heat losses on the channel walls. This leads to the complete decay of the detonation wave. However, the form of wave attenuation does not have a monotonic form.

Registration with the Schlieren system made it possible to establish that the oscillating nature of the propagation of the flame front is accompanied not only by a change in the geometric shape of the flame front. Figure 3 shows shadow images of the dynamics of the flame front and shock-wave perturbations in the narrow channel.

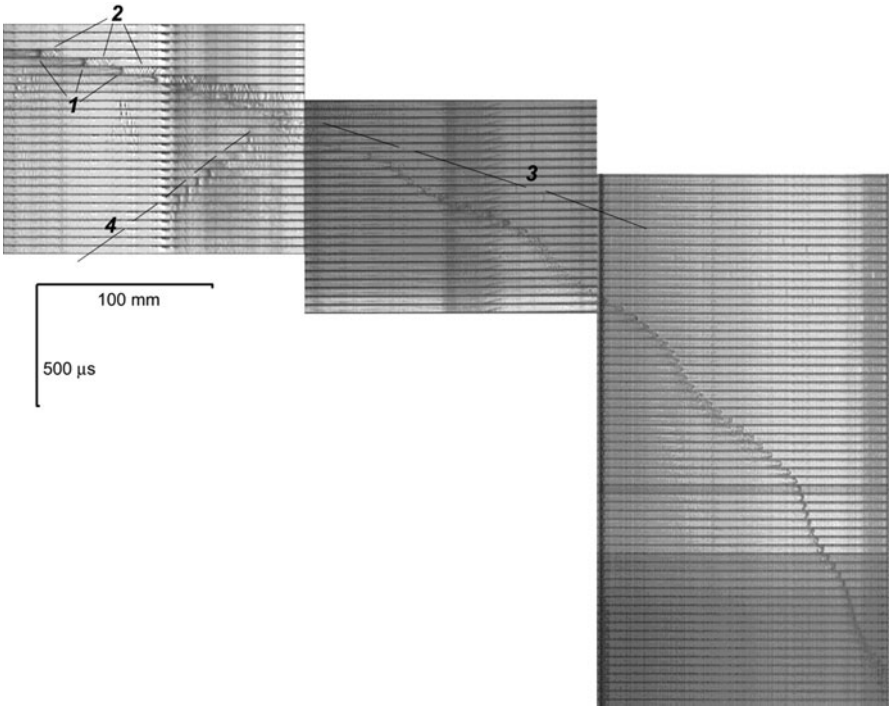

Fig. 3 Schlieren diagram of the flame front propagation in acetylene-air mixture (ER = 1.4). Time interval between frames is 34 μs. 1 flame front, 2 oblique shock waves, 3 shock wave, 4 opposite shock wave

At the initial stage, ahead of the flame front (*1*), a system of oblique shock waves (*2*) is formed, which arises from the transition from the wide detonation tube to the narrow one. At the same time, the flame front has a flat structure. After 100 μs after the entrance of the detonation wave into the channel, the flame front undergoes changes. Due to the fact that the transverse channel size does not exceed the size of the detonation cell of the acetylene-air mixture (4–5 mm) [13], further propagation of the detonation combustion is not possible. The presence of thermal losses leads to the fact that the flame front stretches along the axis, as was observed with direct optical observation.

After 300 μs, the camera records the acceleration of the flame front, which may be caused by an increase of the reaction zone after the combustion front slows down. At the moment of acceleration of the flame front, in accordance with a gas-dynamic discontinuity, two shock waves are formed. One of these waves is directed along the motion of the flame front (*3*), and the other is directed in the opposite direction (*4*). As was to be expected, the shock wave directed to the opposite direction is more clearly recorded by the Schlieren system. However, this does not mean that the intensity of this wave is greater than the intensity of the direct wave, since the motion of the backward wave occurs over hot combustion products.

The further dynamics of the flame front is repeated. After acceleration, the flame front becomes flat. However, unlike the detonation front, there is noticeable distortion in the boundary layer region. The acceleration of the front is followed by slowing and stretching along the channel axis.

Figure 4 shows the streak images of the flame front dynamics and combustion products in the visible optical range for three mixtures of acetylene with air: ER = 0.9, ER = 1.0, and ER = 1.4. For all three mixtures, the non-stationary propagation of the flame front with a monotonically decreasing mean velocity is registered.

On the base of the streak images of the flame front, it is possible to plot evolutions of the velocity upon the distance along the channel axis or time starting from

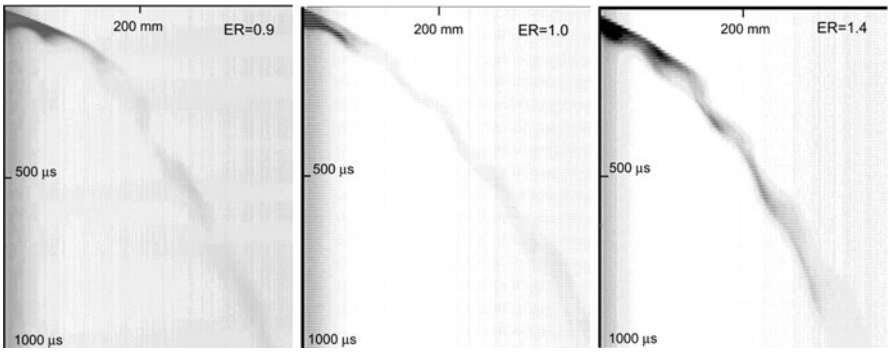

Fig. 4 Streak images of the flame front and combustion products for acetylene-air mixtures in the narrow channel in inverted colors for ER = 0.9, ER = 1.0, and ER = 1.4

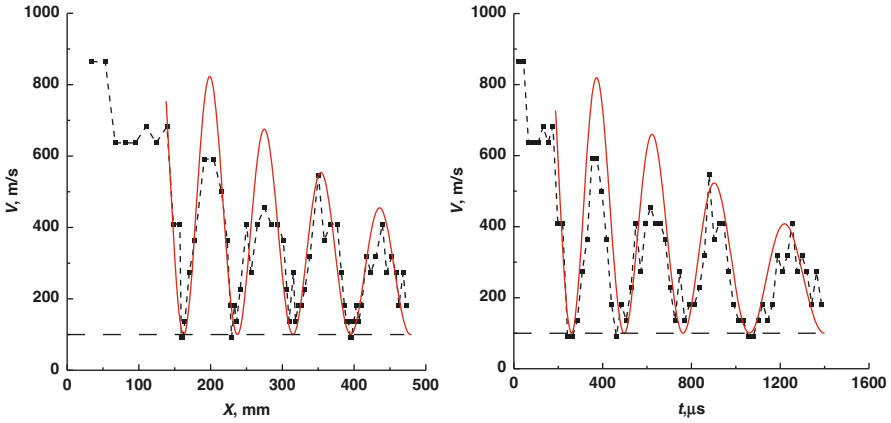

Fig. 5 Evolution of the flame front velocity along the axis of the channel (*left*) and time (*right*). ER = 1.4

the moment of entry of the detonation wave into the channel. Figure 5 shows the evolution of the flame front velocity for the mixture with ER = 1.4. The dependence of the velocity on both parameters has an oscillatory character with damping. In this case, the minimum value of the flame front velocity is the same and equal to 100 m/s for each cycle, which is several times lower for quasi-stationary galloping detonation. Both the time interval and the spatial interval between the local accelerations of the flame front gradually increase. The average value of the oscillation period for the mixture with the ratio ER = 1.4 is 214 μs, while the spatial interval is 72 mm. This distance corresponds to a dimensionless distance of 24 channel transverse dimension 3 mm. It should be noted that the obtained oscillation period and spatial values of periodic changes in absolute value turn out to be close to the parameters for the acetylene-oxygen mixture presented in [8]. A significant difference of the present data, as noted above, is that the data are obtained for acetylene-air mixtures, which is characterized by higher width of the detonation cell. It reduces the probability of the reinitiation of detonation. Thus, in spite of the substantial thermal losses to the channel walls, the propagation of detonation-like galloping combustion is possible in channels of subcritical dimensions. The oscillating form of propagation of the flame front registered in this study was observed in the range of ER from 0.6 to 1.8. With the change in the value of ER from 0.5 and lower or 2.0 or higher, a monotonic slowing down of the flame front was observed without the flame front oscillations.

4 Conclusions

Using the optical methods of diagnostics, the process of propagation of the flame front in the subcritical transverse dimension channel has been studied for acetylene-air mixture. The obtained data made it possible to detect the oscillating form of

the propagation of the combustion in the narrow channel after the decay of the stationary Chapman-Jouguet detonation into the shock wave and the flame front. The time interval of oscillations was about 214 μs, while the spatial interval was about 72 mm. Immediately after the decay of the detonation wave, the average velocity of the flame front decreases first to 1000 m/s and then to 200 m/s. At that, the minimum recorded value of the flame velocity was about 100 m/s for each cycle. Thus, in spite of the substantial thermal losses to the channel walls, the propagation of detonation-like galloping combustion is possible in channels of subcritical size. With the change in the value of ER from 0.5 and lower or 2.0 or higher, a monotonic slowing down of the flame front was observed without the flame front oscillations.

Acknowledgments This work was supported by the Russian Foundation for Basic Research under grant no. 15-38-70017, 16-38-00682-mol-a and grant of President of the Russian Federation no. SP-1501.2016.1.

References

1. Z.W. Huang, M.H. Lefebvre, P.J. Van Tiggelen, Experiments on spinning detonations with detailed analysis of the shock structure. Shock Waves **10**, 119 (2000)
2. Y. Wu, J.H.S. Lee, Stability of spinning detonation waves. Combust Flame. **162**, 2660 (2015)
3. H.S. Dou, B.C. Khoo, Effect of initial disturbance on the detonation front structure of a narrow duct. Shock Waves **20**, 163 (2010)
4. Y. Huang, H. Ji, F. Lien, H. Tang, Numerical study of three-dimensional detonation structure transformations in a narrow square tube: From rectangular and diagonal modes into spinning modes. Shock Waves **24**, 375 (2014)
5. C. Wang, Z. Yongyao, Z. Bo, Numerical simulation of flame acceleration and deflagration-to-detonation transition of ethylene in channels. J Loss Prev Process Ind. **43**, 120 (2016)
6. A.A. Vasil'ev, Quasi-steady regimes of wave propagation in active mixtures. Shock Waves **18**, 245 (2008)
7. N. Tsuboi, Y. Morii, A.K. Hayashi, Two-dimensional numerical simulation on galloping detonation in a narrow channel. Proc Combust Inst. **34**, 199 (2013)
8. V.I. Manzhalei, Low-velocity detonation limits of gaseous mixtures. Combus Explos Shock Waves. **35**, 294 (1999)
9. M.-H. Wu, C.-Y. Wang, Reaction propagation modes in millimeter-scale tubes for ethylene/oxygen mixtures. Proc. Combust. Inst. **33**, 2287 (2011)
10. M.-H. Wu, W.-C. Kuo, Transmission of near-limit detonation wave through a planar sudden expansion in a narrow channel. Combust. Flame **159**, 3414 (2012)
11. A. Camargo, H.D. Ng, J. Chao, J.H.S. Lee, Propagation of near-limit gaseous detonations in small diameter tubes. Shock Waves **20**, 499 (2010)
12. Y. Gao, H.D. Ng, J.H.S. Lee, Experimental characterization of galloping detonations in unstable mixtures. Combust. Flame **162**, 2405 (2015)
13. A.A. Vasil'ev, Cell size as the main geometric parameter of a multifront detonation wave. J Propul Power. **22**, 1245 (2006)
14. F. Zhang, *Shock Waves Science and Technology Library, 6: Detonation Dynamics* (Springer Science & Business Media, Berlin-Heidelberg, 2012), pp. 266–267

Design and Measurement of Injection Gas Concertation in Rotating Detonation Engines via Diode Laser Sensors

Po-Hsiung Chang, Jiun-Ming Li, Boo Cheong Khoo, Lei Li, Jie Ming Teh, and Chiang Juay Teo

Abstract For an air-breathing rotating detonation engine (RDE), in practice a relatively low drop of stagnation pressure of combustor and lower losses from air injection/inlet are desirable. A 6 inch diameter RDE running with pressure ratio cross air injection around and less than chocked condition was developed and examined to investigate its operating characteristics. Further, design and measurement of fuel concertation ahead of and downstream the injection surface are being undertaken via tunable diode laser absorption spectroscopy (TDLAS) technique. Experimental results show that the ethylene/air RDE can be operational even though the injection pressure ratio is lower than chocked condition. The TDLAS system was designed to apply Md-IR (3.411 μm) and Near-IR (1.625 μm) diode lasers to scan absorption features of ethylene and CO_2 of the product gas, respectively. From these results, one could have a better understanding on local equivalent ratios and their distribution immediately before the arrival of the rotating detonation and study whether the product gas would flow back to the air plenum and their effects on RDE performance, in particular for the engines operating at the relatively low injection pressure ratio. This part of work is being tested and will be reported in the presentation.

1 Introduction

Rotating detonation engine (RDE) has been investigated as an alternative solution to further increase thermal efficiency for propulsion applications, and many works have been done in measuring and numerically simulating the combustion processes in RDEs [1, 2]. As the detonation phenomenon inside RDEs depends on the local

P.-H. Chang (✉) · J.-M. Li · B. C. Khoo
Temasek Laboratories, National University of Singapore, Singapore, Singapore
e-mail: tslljm@nus.edu.sg

L. Li · J. M. Teh · C. J. Teo
Department of Mechanical Engineering, National University of Singapore, Singapore, Singapore

A. Sasoh et al. (eds.), *31st International Symposium on Shock Waves 2*,
https://doi.org/10.1007/978-3-319-91017-8_17

conditions instantaneously before the detonation front passes by, the local pressures, temperatures, and equivalence ratios would be radical factors that can dominate the stability and performance of RDEs. From most previous numerical or experimental studies, the pressure ratios cross air/fuel injection were set to a value as high as 10:1 or above 4 to present potential flame flashback and the product gas back to the air/fuel plenum [1–3]. However, it is not practical as developing the RDE for the air-breathing application. When applying low injection pressure ratio, the local equivalence ratios of the reactants could be largely affected by the mixing effectiveness and the product gas. The measurement of fuel concentration is always difficult for researchers to understand and precisely control the performance of RDEs. In order to solve this problem, the present paper proposes to measure the local fuel and product gas concentration adjacent the injection in RDEs using tunable diode laser absorption spectroscopy. This technique can determine the most vital solution for fuel/air injection design in RDEs.

2 Experiments

2.1 Rotating Detonation Engines

The design of the RDE at the National University of Singapore was based on a design used at the Air Force Research Laboratory, USA. This design was chosen as its successful test cases have been widely documented [2]. Figure 1a shows the cross section of the RDE and the fuel and oxidizer passages for non-premixed injection strategy. Fuel entered the annular channel through 120 $\times$ 0.89 mm holes, while the oxidizer enters the annular channel through a slot with height of 0.89 mm. This design causes the oxidizer to impinge onto the fuel, wishing to achieve good mixing within limited period ahead of incoming detonation front radically. The channel width of this test was 7.62 mm. Note that the hole diameter and slot height for the fuel and air injection part were set to get planned injection pressure ratio based on the air supply system. The airflow rate was controlled by a Tescom ER3000 Electronic Pressure Controller that provided flow between 0.1 kg/s and 0.186 kg/s for the current RDE test. The flow rate of ethylene was measured using an Alicat Flowmeter.

Three static pressure transduces (Kulite and Omega) were used to monitor the pressures at fuel plenum, air plenum, and annular channel. Another three dynamic transducers (PCB 113B24) were placed along the walls of the cylinder spaced 120° apart to measure the propagation speed of the detonation wave. Additionally, a high-speed camera (Photron SA-Z) set at 60 kHz frequency and 3 μs exposure time was used for capturing the sequence of rotating detonation/combustion wave from ignition by an ethylene-oxygen predetonator. LabVIEW was used in conjunction with a National Instruments PXI system to control the test procedures, e.g., delivering transistor-transistor logic signals at desired durations, frequencies, and delays to control the sequence of fuel injection and ignition. Figure 1b shows a typical photography of the firing RDE in our laboratory.

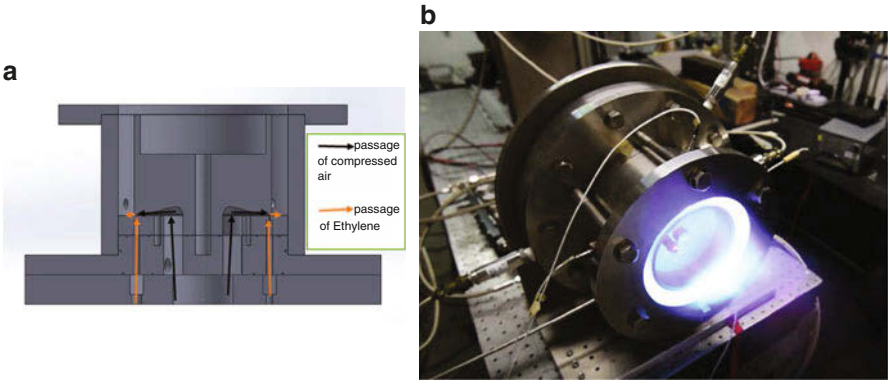

Fig. 1 (**a**) RDE cross section, (**b**) RDE firing test

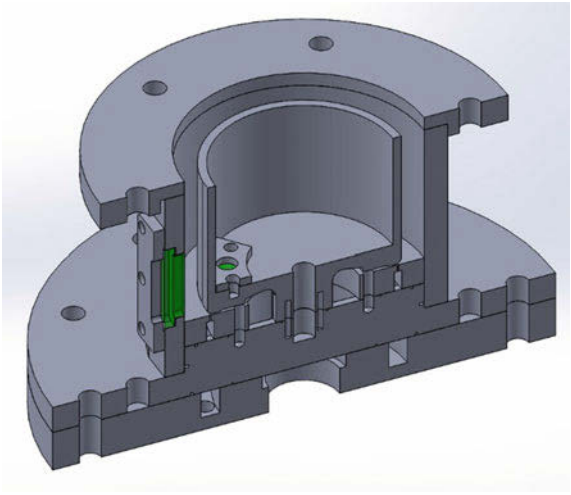

Fig. 2 Detailed drawing for two optical accesses near injection region

2.2 Gas Diagnostics Near Injection

Because the onset and sustainability of detonation waves strongly rely on the local equivalence ratios ahead of waves' front, a proper mixing and fuel-air concertation from injection is a vital parameter for a successful RDE [3]. Tunable diode laser can be used to measure fuel concentration based on Beer-Lambert law, and it has been proved a powerful tool for fuel concentration measurement in many applications [4]. Since it measures the absorption of a laser beam, only small optical accessible window would be needed. Figures 2 and 3 show the design of optically accessible ready for TDLAS measurement focusing on injection part in RDE. Main components of tunable diode laser system consist of one Md-IR (centered at 3.411 μm, DFB ICL from Nanoplus GmbH) and one Near-IR (centered

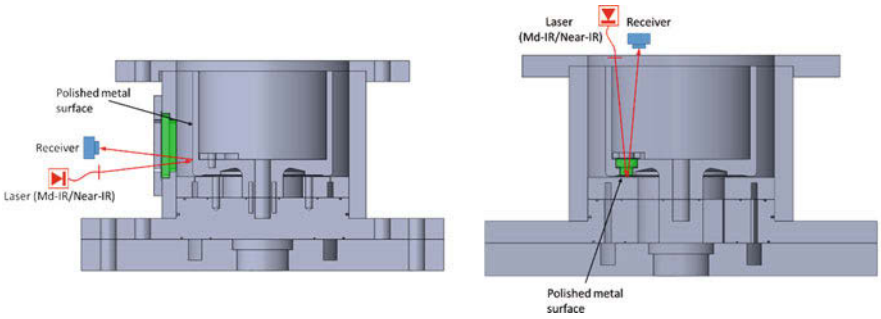

Fig. 3 The arrangement of two laser paths

at 1.625 μm, DFB from NTT Electronics) tunable diode laser sources and two detectors at corresponding wavelengths (photovoltaic detector from VIGO System S.A. and gain InGaAs detector from Thorlabs). The selection of Md-IR is due to the obviously higher absorbance of hydrocarbon fuel at this range of wavelength, while the Near-IR wavelength is to capture absorption features of CO_2 in the product gas. Two optical accesses were arranged for aiming to two positions; those are at the annular channel near the injection region and at air plenum just ahead of the injection (see Fig. 3). There were two polished surface dedicated to reflect the laser beam back to the detectors. Based on Beer-Lambert law as shown below:

$$\mathrm{A}b_{\overline{\upsilon}} \equiv -\ln\left(\frac{I}{I_o}\right)_{\overline{\upsilon}} = \sigma\left(\overline{\upsilon}, T\right) n_a L \tag{1}$$

where I/I_o is the fractional transmission, n_a is the number density of absorbing species, and σ is the absorption cross section. In such system layout arrangement, the distance of the laser beam path is a constant. Thus, the local fuel concentration could be estimated calculable. The technique has been tested to be valid in our previous PDE experimental setup. The concentration of the mixture of ethylene/air and JetA1/air in the PDE tube can be successfully quantified prior to the occurrence of detonation/combustion. The measurements of fuel concentration in various testing conditions are still in progress. Some results are under post-processing which need to combine with the remaining work using another injection configuration to draw conclusions. More results will be presented in the symposium.

3 RDE Experimental Results

Figure 4 shows the operational space of present RDE testing. As described above, this study focuses on the relatively low injection pressure ratios for the purpose of decreasing total pressure losses. The injection pressure ratios were manipulated at the ranges from 1.3 to 2.2. The total mass flow rate appeared a little low compared to the previous studies by other groups (generally 0.2–2 kg/s). The equivalence ratios,

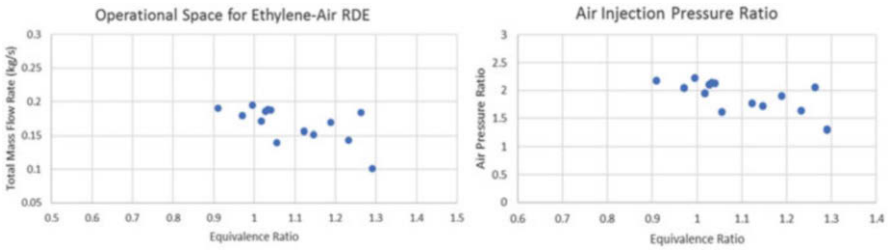

Fig. 4 Operational space of RDE testing (total mass flow rate, air injection pressure ratio, equivalence ratio)

Fig. 5 High-speed image of rotating detonation/ combustion wave from ignition

determined from ethylene and airflow rates, were from 0.9 to 1.3. Each testing was controlled to supply fuel for 0.9 s.

Figure 5 shows one typical result of the high-speed images of our RDE sequence. As observed from previous studies, after ignition by the predetonator, it is mostly possible to have multiple combustion waves propagating in the same or reverse direction. With time going by, finally, there would be single or multiple waves sustained in a RDE, which mainly depends on the total mas flow rate. This indicates

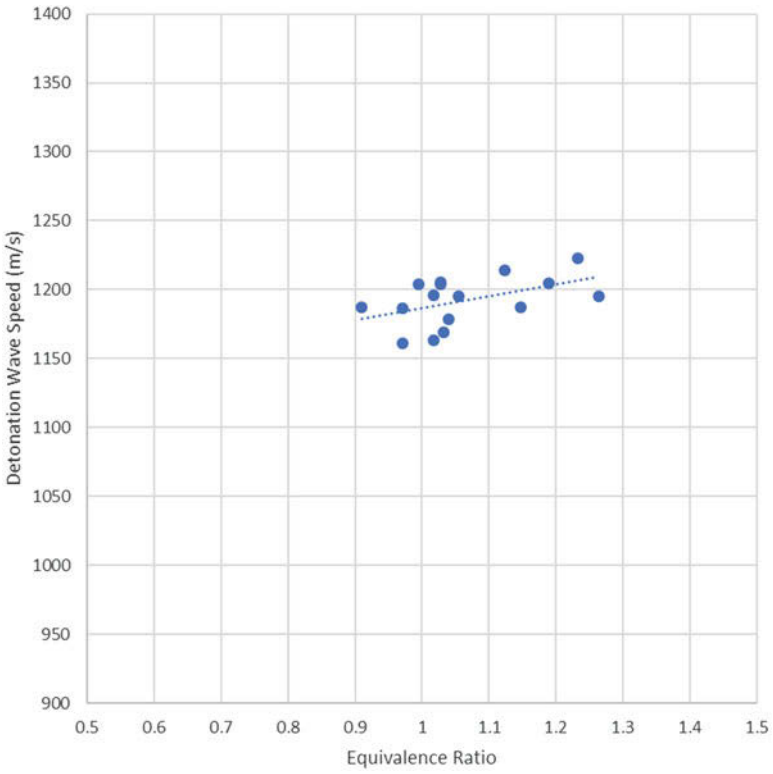

Fig. 6 Measured detonation wave speeds for ethylene-air RDE

that it is difficult to estimate wave speed accurately only from the pressure data. Therefore, as analyzing the wave speed, we monitored numbers of rotating wave from high-speed images to assist the analysis. Figure 6 shows the detonation wave speeds obtained by all the test cases. Although none of the test cases managed to achieve the Chapman-Jouguet detonation wave velocity of 1800 m/s, an average of 67% of the CJ velocity was achieved for all the test cases combined. This is in comparison to 51% of the CJ velocity achieved by the ethylene/air RDE developed and tested by the University of Cincinnati [5] and 75% of the CJ velocity achieved by the hydrogen/air RDE developed by the AFRL [2]. Failure to reach CJ velocity could be due to unexpected equivalence ratios and/or mixing with the product gas of which cause the reactants mixture to be contaminated. This is the reason why we proposed to apply tunable diode laser to gauge the reactants and product gas concertation near the injection region, to find a way to examine the performance of the injection in RDEs.

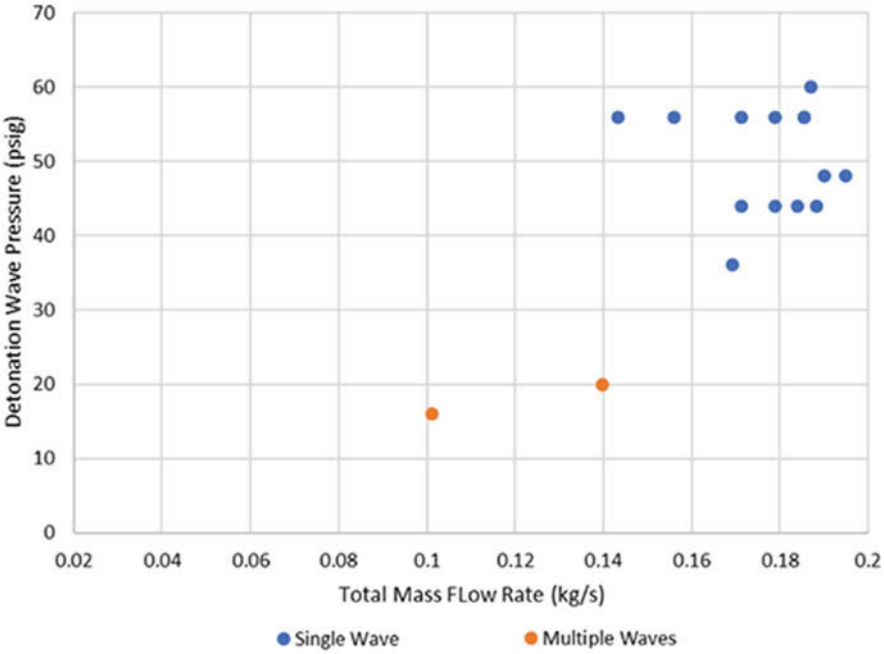

Fig. 7 Pressure rise of rotating detonation

Furthermore, from Fig. 4's injection pressure ratio, it can be found that although all the firing test cases can achieve 67% CJ detonation wave, not all of them were within the choked limit of 1.89. It is also found that for ethylene, all the test cases were beyond the choked limit. These results show that it is not a necessary criterion of high injection pressure ratio for achieving rotating detonation. However, at lower total mass flow rate and also lower air injection pressure ratio, the pressure rise gained is much lower (red color), see Fig. 7, which needs further investigations.

4 Summary

A 6 inch diameter RDE applying low air injection pressure ratio 1.3–2.2 was experimentally investigated for the purpose of decreasing total pressure losses. The obtained speeds of rotating detonation waves were around 67% the CJ velocity even if the choked condition was not attained at the injection. This velocity discrepancy from theoretical CJ value can be attributed to dynamic variation of local equivalence ratio ahead of detonation front due to poor mixing and/or influence from the product gas as it back to the air plenum. To have more understating on this problem, design and measurement of concertation of the reactants and the product gas adjacent the

injection are being carried out by utilizing Md-IR and Near-IR tunable diode lasers absorption spectroscopy. More results will be presented in the symposium.

Acknowledgments This work was supported by NUS Temasek Laboratories. The authors would like to acknowledge the assistance from Lim Kim Seng and Lee Beng Teck.

References

1. D. Schwer, K. Kailasanath, Proc. Combust. Inst. **33**, 2195–2202 (2011)
2. B.A. Rankin, M.L. Fotia, D.E. Paxson, J.L. Hoke, F.R. Schauer, AIAA 2015-0877 (2015)
3. D.F. Dausen, C.M. Brophy, R.G. Wright, J.D. Marde, AIAA 2012-3944 (2012)
4. C.S. Goldenstein, R.M. Spearrin, R.K. Hanson, Appl. Opt. **55**(3), 479–484 (2016)
5. J. Wilhite, R. Driscoll, A.St. George, V. Anand, E. Gutmark, AIAA 2016-1650 (2016)

Investigation of High-Frequency Pulse Detonation Cycle with Fuel Phase Transition

H. Taki, K. Takao, N. Hirota, K. Matsuoka, J. Kasahara, H. Watanabe, A. Matsuo, and T. Endo

Abstract To achieve the pulse detonation (PD) operation at high frequency, it is essential to shorten deflagration-to-detonation transition (DDT). Increasing the initial pressure of detonable mixture is a valid way to solve this problem. Then, we carried out the PD operation at 1010 Hz with the total pressure of supplied oxidizer changed. A combustor having the length of 100 mm and the inner diameter of 10 mm was used, and pure oxygen and supercritical ethylene were used as propellant. The PD operations at 1010 Hz were successful, and the decrease of DDT distance by approximately 50% was confirmed by increasing the initial pressure of detonable mixture by 242%. In addition, PD operation at higher frequency was demonstrated. With a combustor which has the length of 60 mm and the inner diameter of 10 mm, seven-cycle PD operation at 1916 Hz was carried out, and the average of measured flame propagation speed was in good agreement with the estimated detonation speed.

1 Introduction

A pulse detonation engine (PDE) is an internal combustion engine (ICE) in which fuel is intermittently burned by self-sustained detonations [1]. Burning temperature in a detonation is higher than that in an isobaric combustion, and thermal efficiency of a PDE is higher than that of a conventional ICE. In addition, because detonation wave propagates at supersonic speed, it is possible to burn in a short time and limited space and to miniaturize a combustor.

H. Taki (✉) · K. Takao · N. Hirota · K. Matsuoka · J. Kasahara
Nagoya University, Nagoya, Japan
e-mail: taki@prop2.nuae.nagoya-u.ac.jp

H. Watanabe · A. Matsuo
Keio University, Yokohama, Japan

T. Endo
Hiroshima University, Higashihiroshima, Japan

A. Sasoh et al. (eds.), *31st International Symposium on Shock Waves 2*,
https://doi.org/10.1007/978-3-319-91017-8_18

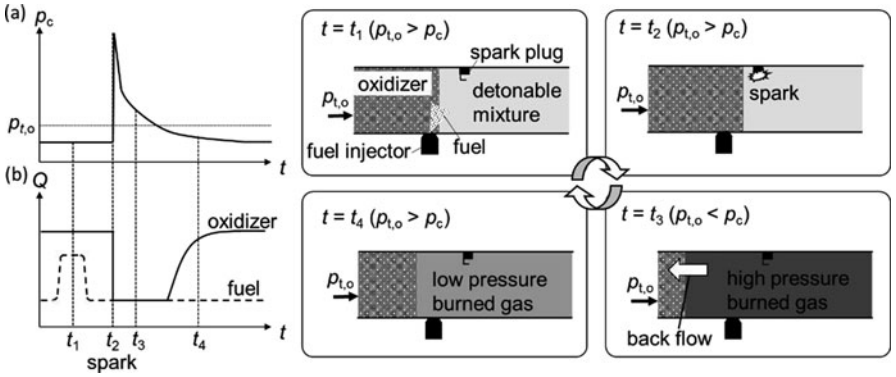

Fig. 1 Pulse detonation cycle

In a pulse detonation combustor (PDC), the following processes are repeated: (1) filling oxidizer and fuel (detonable mixture), (2) ignition and deflagration-to-detonation transition (DDT), (3) propagation of detonation wave, (4) blowdown of high-pressure burned gas ,and (5) purging residual low-pressure burned gas. Of these processes, durations of (3) and (4) are governed by gas dynamics [2] and depend on only length of a combustor if the composition of detonable mixture is fixed. For a high thrust destiny with a compact combustor, it is essential to realize a pulse detonation (PD) cycle at high frequency and to shorten processes (1), (2), and (5). Many PD operation methods were proposed to shorten processes (1) and (5) [3–7]. Figure 1 shows the conceptual scheme of valveless PDC, oxidizer feed line of which has the same inner diameter as a combustor. Figure 1a shows an ideal pressure history in a combustor at the same position as a spark plug [8], and the horizontal dash line shows total pressure of oxidizer $p_{t,o}$. Figure 1b shows history of fuel and oxidizer flow rate corresponding to pressure history. The right figures show schematic illustrations of material distribution in a PDC at each specified time shown in (a) and (b). A PDC has a valveless oxidizer feed line, spark plug for ignition, and fuel injector.

At $t = t_1$, detonable mixture is filled up ($p_{t,o} > p_c$). At $t = t_2$, mixture is ignited by a spark plug and DDT occurs. At this time, fuel injection is stopped, and only oxidizer is supplied to a combustor ($p_{t,o} > p_c$). At $t = t_3$, detonation wave propagates, and high-pressure burned gas is generated. Burned gas interrupts oxidizer supply because pressure in a combustor becomes higher than that of oxidizer ($p_{t,o} < p_c$) and a portion of burned gas flows backward upstream of a combustor. At $t = t_4$, pressure of burned gas is decreased by rarefied expansion waves from an open end of a combustor, and oxidizer is supplied again ($p_{t,o} > p_c$). Using this operation method, Matsuoka et al. demonstrated the PD operation at 800 Hz with ethylene-oxygen mixture [9].

On the other hand, many studies on shortening DDT process with Shchelkin spiral and/or obstacle have been carried out [10]. However, it has some problems,

such as the pressure loss and cooling of obstacles themselves. DDT can also be shortened because of condition of detonable mixture at time for spark, and increasing initial pressure of detonable mixture is one of the valid ways. Kuznetsov et al. demonstrated DDT distance was shorten by the increase of initial pressure of mixture [11]. In this paper, the initial pressure of detonable mixture was increased, and shortening DDT distance was confirmed in multi-cycle PD operation at 1010 Hz. Furthermore, a PD operation at 1916 Hz was also demonstrated.

2 Experimental Arrangement

Figure 2 shows the combustors used in this experiment, which are called Types A and B. The x coordinate is the central axis of a combustor along the flow, with the origin corresponding to the position of spark plug (NGK Spark Plug Co., Ltd., CR8HSA).

The section of $x \geq 0$ mm was combustor and the section of $x < 0$ mm was feed line. The open ends of Types A and B were at $x = 100$ and 60 mm, respectively, and inner diameter of a combustor was $id_{c2} = 10$ mm. At $x = -30$ mm, the piezoelectric fuel injector (BOSCH, HDEV4) was installed. Ion probes (NGK Spark Plug Co., Ltd., CR8HSA) [12] were installed at the sidewall of the combustor at intervals of 20 mm and used to measure flame propagation speed. A pressure transducer (PT2, PCB Piezotronics, Inc, 113B24) was installed at $x = 40$ mm and used to measure pressure in a combustor p_c. Furthermore, a pressure transducer (PT1, KELLER, 23 series) was installed at $x = -220$ mm for Type A and $x = -260$ mm for Type B to measure total pressure of supplied oxidizer $p_{t,o}$. The pressure of oxidizer could be changed because the flow of oxidizer was choking, and PD operations with ethylene-oxygen mixture were demonstrated.

Figure 3 shows the operating sequence, in which signal for fuel injection and ignition (solid line), real operation of them (broken lone), and corresponding pressure history at $x = 40$ mm in S2 were showed. The horizontal axis shows time from ignition signal.

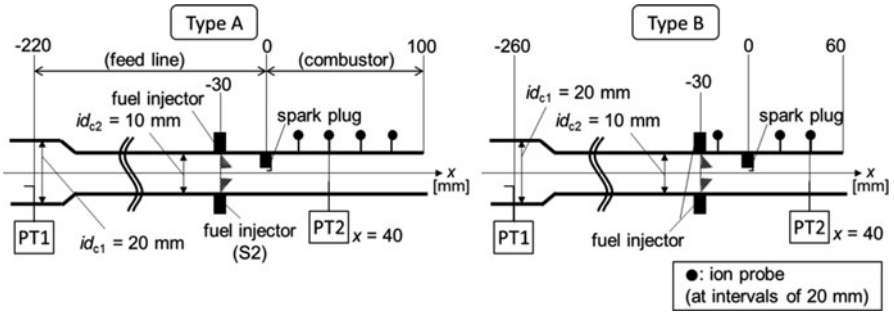

Fig. 2 Pulse detonation combustor used in experiment (unit: mm)

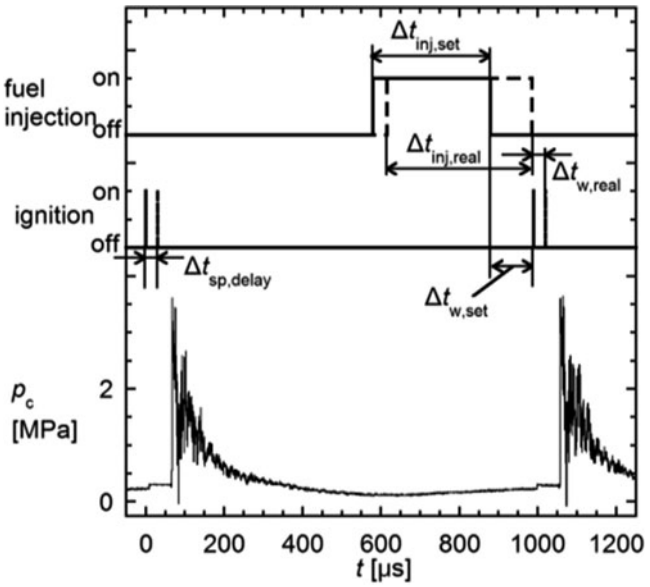

Fig. 3 Operating sequence

We carried out PD operations under three conditions: low-pressure condition (S1), high-pressure condition (S2), and high-frequency condition (S3). In S1 and S2, a combustor of Type A with the length of 100 mm was used, and that of Type B with the length of 60 mm was used in S3. In S1, single injector was used, and two injectors were used in S2 and S3 to uniform equivalence ratio. The summary of the experimental condition was shown in Table 1.

The total pressure of supplied oxidizer and the pressure of detonable mixture p_d were measured just before combustion with PT1 and PT2, respectively, and p_d was increased by a factor of 1.8 between S1 and S2. The mass flow rate of oxidizer and fuel was measured in advance experiment. In S1 and S2, injection duration was set at $\Delta t_{inj,set} = 300$ μs, and real injection duration was estimated at $\Delta t_{inj,real} = 370 \pm 10$ μs by visualization of injection with high-speed camera. Therefore, duty ratio (injection duration/duration for one PD cycle) was estimated $DR = 37 \pm 1\%$. Assuming the delay time was not changed depending on operation frequency, real injection duration and duty ratio under the high-frequency condition S3 were estimated at $\Delta t_{inj,real} = 250 \pm 10$ μs ($\Delta t_{inj,set} = 180$ μs) and $DR = 48 \pm 2\%$, respectively. As shown in Fig. 3, waiting duration for ignition was empirically set at $\Delta t_{w,set} = 110$ μs. Considering response delay, real waiting duration was $\Delta t_{w,real} = 34 \pm 13$ μs. In S1 and S2, the experiments were repeated three times.

Table 1 Experimental condition

	Operation frequency	Oxidizer supply pressure	Pressure of detonable mixture	Mass flow rate of oxidizer	Mass flow rate of fuel	Fuel injection pressure	Equivalence ratio
	f_{ope} [Hz]	$p_{t,o}$ [MPa]	p_d [kPa]	$\dot{m}_o$ [g/s]	$\dot{m}_f$ [g/s]	p_{inj} [MPa]	ER [−]
S1	1010	0.23 ± 0.01	135 ± 1	45.2 ± 0.5	4.9 ± 0.3	5.84 ± 0.03	0.38 ± 0.03
S2	0.55 ± 0.01	244 ± 3	97.8 ± 3.9	9.9 ± 0.6	0.35 ± 0.04		
S3	1916	0.57	216				

3 Result and Discussion

3.1 Flame Propagation Speed and Pressure History

Figure 4 shows flame propagation speed measured with ion probes. The vertical and horizontal error bars are standard deviation in all cycles and distance between two ion probes, respectively. The detonable mixture flows at high speed, so detonation speed was estimated to be the sum of Chapman-Jouguet detonation speed D_{CJ} and speed of detonable mixture u_d (gray-colored areas in Fig. 4). The CJ detonation speed was estimated by NASA-CEA [13] with equivalence ratio *ER*, pressure p_d (see Table 1), and temperature T_d of detonable mixture. T_d was roughly estimated to be 400–500 K. Assuming detonable mixture flowed at sound speed, u_d was estimated by NASA-CEA [13]. In S1, flame propagation speed came up to 102% of $D_{CJ} + u_d$ at $T_d = 400$ K in the section of $60 < x < 80$ mm, and DDT distance was roughly estimated to be $40 < x_{DDT} < 60$ mm. In regard to S2, DDT distance was estimated to be $0 < x_{DDT} < 20$ mm. The increase of initial pressure of detonable mixture by 240% decreased DDT distance approximately by half.

Figure 5 shows the pressure history measured at $x = 40$ mm. The gray-colored areas show CJ detonation pressure p_{CJ} estimated by NASA-CEA [13]. In S1, the average of peak pressures in all cycles was $p_{peak} = 2.0 \pm 0.5$ MPa, and peak pressure in most cycles were lower than estimated CJ detonation pressure $p_{CJ} = 1.9$–2.3 MPa because DDT occurs downstream of $x = 40$ mm. The average of peak pressures measured in S2 (except cycles in which peak pressure was lower than 1.0 MPa) was $p_{peak} = 3.9 \pm 0.7$ MPa and in good agreement with $p_{CJ} = 3.3$–4.2 MPa, and it is considered the DDT distance was shortened by increasing initial pressure of detonable mixture.

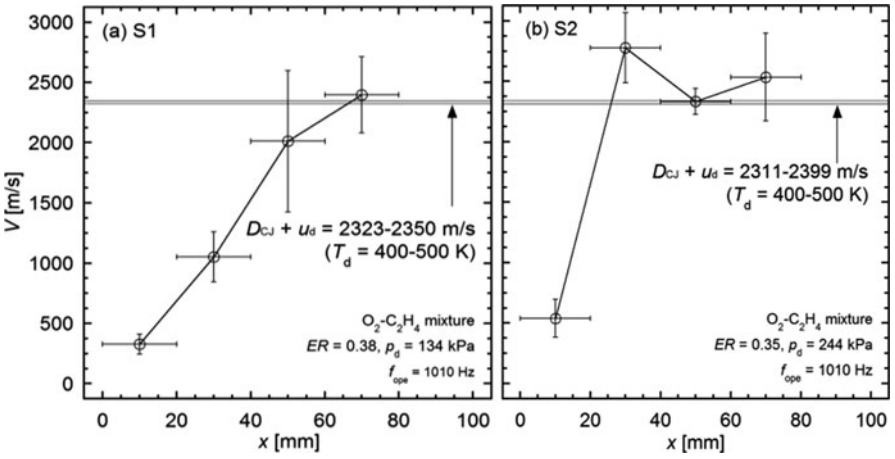

Fig. 4 Flame propagation speed (**a**) Low-pressure condition, (**b**) High-pressure condition

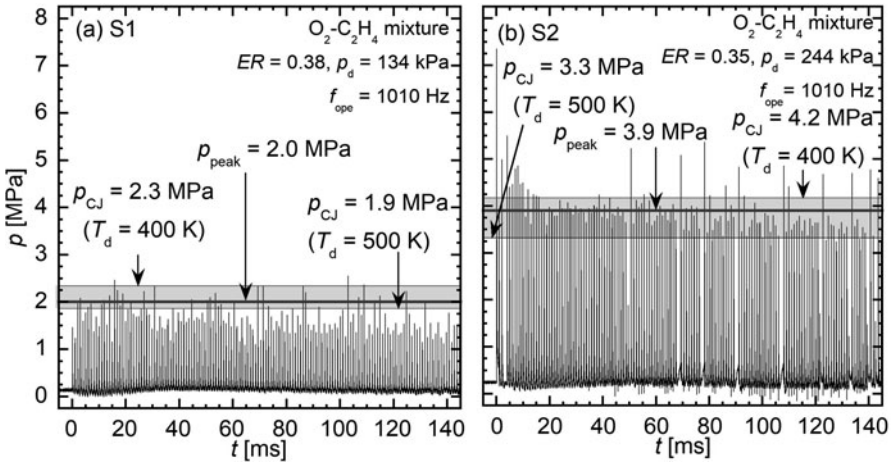

Fig. 5 Pressure history (**a**) Low-pressure condition, (**b**) High-pressure condition

3.2 Comparison with Numerical Calculation

The pressure history at $x = 40$ mm in experiment was compared with that of numerical calculation [14] because it was difficult to estimate temperature of detonable mixture T_d. The results were shown in Fig. 6. The horizontal axis shows time τ at which pressure rapidly increased and the pressure histories in the 100th cycle were shown as gray lines. The black lines show numerical calculation with T_d as parameter. As the initial condition, total pressure $p_{t,o}$ and total temperature $T_{t,o}$ of oxidizer and equivalence ratio ER were used (shown in Fig. 6). In experiments, the waiting duration for ignition $\Delta t_{w,real}$ exists, when only oxidizer was filled. The speed of oxygen u_o was calculated, and the length of refilled oxygen was estimated to be $u_o \times \Delta t_{w,real} = 10$ mm. Therefore, the detonable mixture was set in the region of $-20 < x < 100$ mm.

From the comparison result in Fig. 6a, the peak pressure in experiment was lower than that in calculation because the DDT has occurred downstream of $x = 40$ mm where a pressure transducer was installed. In regard to pressure after decline, the values of experiment in (a) and (b) were in good agreement with that of calculation with $T_d = 400$–500 K.

3.3 Result of Combustion Test at 1916 Hz

Figure 7a shows flame propagation speed, and the average speed of seven cycles was 2278 m/s, which was in good agreement with estimated speed $D_{CJ} + u_d = 2273$–2307 m/s (gray-colored area in (a)) by NASA-CEA [13] with ER, p_d (see Table 1)

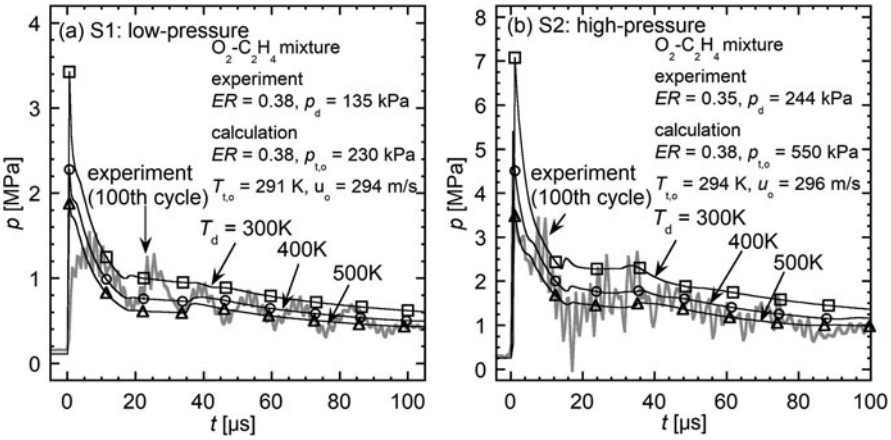

Fig. 6 Comparison between result of experiment and calculation (**a**) S1, (**b**) S2

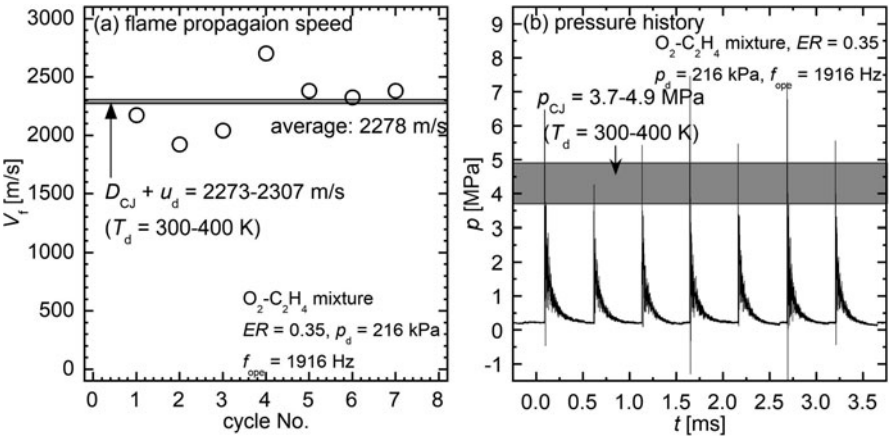

Fig. 7 (**a**) Flame propagation speed, (**b**) Pressure history (S3)

and $T_{\mathrm{d}} = 300$–400 K. Figure 7b shows pressure history at $x = 40$ mm. In some cycles, peak pressures were over CJ detonation pressure (gray-colored area in (b)). It was suggested that temperature of detonable mixture was lower than 300 K because the number of operation cycles was small and detonable mixture was cooled by latent heat of phase transition from supercritical to gas ethylene immediately after injection.

4 Conclusion

It is essential to realize a PD cycle at high frequency for high thrust destiny with a compact combustor. Therefore, shortening deflagration-to-detonation transition (DDT) process is necessary. Then, the initial pressure of the detonable mixture was changed, and we carried out PD operation at 1010 Hz with a combustor which has a length of 100 mm and an inner diameter of 10 mm. As a result, the DDT distance was decreased by approximately 50% by an increase of the initial pressure of detonable mixture by 242%. In addition, seven-cycle PD operation at 1916 Hz was demonstrated with a combustor which has a length of 60 mm.

Acknowledgment This work was subsidized by the Grant-in-Aid for Scientific Research (B) (No.26820371), the Toukai Foundation for Technology, the Paloma Environmental Technology Development Foundation, and the Tatematsu Foundation.

References

1. K. Kailasanath, Recent developments in the research on pulse detonation engines. AIAA J. **41**(2), 145–159 (2003)
2. T. Endo et al., Pressure history at the thrust wall of a simplified pulse detonation engine. AIAA J. **42**(9), 921–1930 (2004)
3. T. Takahashi et al., Experiments on energy balance and thermal efficiency of pulse detonation turbine engine. Sci. Technol. Energ. Ma. **73**, 5–6 (2012)
4. T. Endo, Thermal spray by pulsed detonations, in *2013 International Workshop on Detonation for Propulsion*, 2013
5. K. Wang et al., Study on a liquid-fueled and valveless pulse detonation rocket engine without the purge process. Energy **71**, 605 (2014)
6. M.H. Wu, T.H. Lu, Development of a chemical microthruster based on pulsed detonation. J. Micromech. Microeng. **22**(10), 105040 (2012)
7. K. Matsuoka et al., Development of a liquid-purge method for high-frequency operation of pulse detonation combustor. Combust. Sci. Technol. **187**(5), 747–764 (2015)
8. H. Watanabe et al., Numerical investigation on burned gas backflow in liquid fuel purge method, in *55th AIAA Aerospace Sciences Meeting*, 2017
9. K. Matsuoka, Experimental study on control technique of pulsed detonation, in *2016 International Workshop on Detonation for Propulsion*, 2016
10. O. Peraldi et al., Criteria for transition to detonation in tubes. Symp. Combust. **21**(1), 1629–1637 (1988)
11. M. Kuznetsov et al., DDT in a smooth tube filled with a hydrogen–oxygen mixture. Shock Waves **14**(3), 205–215 (2005)
12. Y. Hamamoto et al., Combustion diagnostics using a spark plug as ion probe. Jpn. Soc. Mech. Eng. **60**, 572 (1944)
13. S. Gordon, B.J. McBride, *Computer Program for Calculation of Complex Chemical Equilibrium Compositions and Applications*, NASA Reference Publication. 1311 (1994)
14. K. Matsuoka et al., Investigation of fluid motion in valveless pulse detonation combustor with high-frequency operation. Proc. Combust. Inst. **36**(2), 2641–2647 (2017)

Numerical Study of Hydrogen–Air Detonation in Vibrational Non-equilibrium

L. S. Shi, P. Zhang, C. Y. Wen, H. Shen, M. Parsani, and D. L. Zhang

Abstract The effects of vibrational non-equilibrium and vibration–chemistry coupling on hydrogen–air detonation are numerically investigated by solving reactive Euler equations coupled with a multiple vibrational temperature-based model. Detailed hydrogen–air reaction kinetic is utilized, Landau–Teller model is adopted to solve the vibrational relaxation process, and the coupled vibration–chemistry vibration model is used to evaluate the vibration–chemistry coupling. It is shown that the relaxation process and vibration–chemistry coupling considerably influence the hydrogen–air detonation structure, highlighting the importance of correct treatment of vibrational non-equilibrium in detonation simulations.

1 Introduction

The complex multiscale physical phenomena in hydrogen detonation have been studied by numerical simulations for some years. These studies have focused on various aspects of detonation: projectile-induced detonation [1], rectangular/diagonal modes in three-dimensional hydrogen–air detonation [2], and the deflagration-to-detonation transition [3]. Due to the intrinsically unsteady and highly nonlinear characteristics of detonation and the unclear mechanism of reactions under extreme conditions, the detailed fundamental characteristics of detonation remain poorly

L. S. Shi · P. Zhang · C. Y. Wen (✉)
Department of Mechanical Engineering, The Hong Kong Polytechnic University, Hung Hom, Hong Kong
e-mail: cywen@polyu.edu.hk

H. Shen · M. Parsani
King Abdullah University of Science and Technology (KAUST), Computer Electrical and Mathematical Science and Engineering Division (CEMSE), Extreme Computing Research Center (ECRC), Thuwal, Saudi Arabia

D. L. Zhang
State Key Laboratory of High Temperature Gas Dynamics, Institute of Mechanics, Chinese Academy of Sciences, Beijing, China

A. Sasoh et al. (eds.), *31st International Symposium on Shock Waves 2*,
https://doi.org/10.1007/978-3-319-91017-8_19

understood. The vibrational degree of freedom in air is relatively slowly equilibrated in high-enthalpy flows [4, 5], and the resulting vibration–chemistry coupling has been widely researched [6, 7]. The time scales of vibrational relaxation are comparable to those of ignition behind the detonation wave [8]. This overlap has necessitated careful investigation with a combination of computational and practical approaches to the physical processes and vibrational relaxation involved.

In this paper, several two-dimensional simulations are performed for a stoichiometric hydrogen–air mixture at 1 atm and 300 K, under the various assumptions of vibrational equilibrium, non-equilibrium, or vibration–chemistry coupling, to understand the underlying physics. The computations are performed using the supercomputer Shaheen XC-40 installed at King Abdullah University of Science and Technology.

2 Methodology

The space–time conservation element and solution element (CE/SE) method [9] is a compact numerical scheme in which only the information of the neighboring mesh points is required for each time step, making it ideal for large-scale computing. This method has been developed [10–12], implemented, and validated in several studies of variable complex flows, including compressible multicomponent flows [13] and gaseous detonations [14, 15]. In this study, the CE/SE method was extended to solve the two-dimensional unsteady reactive Euler equation:

$$\frac{\partial \mathbf{U}}{\partial t} + \frac{\partial \mathbf{F}}{\partial x} + \frac{\partial \mathbf{G}}{\partial y} = \mathbf{S} \tag{1}$$

where $\mathbf{U}$ is the conserved vector, consisting of the individual species densities, ρ_i; the momentums, ρu and ρv; the total energy, E; and the vibrational energies of the different molecular species, $\rho_i e_{\mathrm{v,i}}$:

$$\mathbf{U} = \left[\rho_1, \cdots, \rho_{\mathrm{Ns}}, \rho u, \rho v, E, \rho_i e_{\mathrm{v},1}, \cdots, \rho_{\mathrm{Nm}} e_{\mathrm{v,Nm}}\right] \tag{2}$$

with $\mathrm{N_S}$ the number of species and $\mathrm{N_m}$ the number of molecular species. $\mathbf{F}$ and $\mathbf{G}$ are the corresponding fluxes in the x and y directions, respectively.

It was assumed that the vibrational energy was decoupled from the translational–rotational energy. The total energy E comprises the energy in the translational–rotational mode, enthalpy of formation, vibrational energy, and flow kinetic energy:

$$E = \sum_{i=1}^{\mathrm{Ns}} \rho_i C_{v,\mathrm{tr},i} T_{\mathrm{tr}} + \sum_{i=1}^{\mathrm{Ns}} \rho_i h_i^0 + \sum_{\text{molecule}} \rho_i e_{\mathrm{v},i}\left(T_{\mathrm{v},i}\right) + \frac{1}{2}\rho\left(u^2 + v^2\right) \tag{3}$$

The vibrational energy of molecule i is expressed as a function of the species gas constant, vibrational temperature $T_{\mathrm{v},i}$, and characteristic vibrational temperature θ_i:

$$e_{\mathrm{v},i}\left(T_{\mathrm{v},i}\right) = R_i \frac{\theta_i}{e^{\theta_i / T_{\mathrm{v},i}} - 1} \tag{4}$$

S is the source term that represents the chemical reactions and energy exchange between translational–rotational energy and individual vibrational energies. The chemical reactions were modeled by the mechanisms for high-pressure high-temperature hydrogen combustion [16], which include nine species (H_2, O_2, H, O, OH, HO_2, H_2O, H_2O_2, and N_2) and 23 reactions. Nitrogen was modeled as an inert diluent. The calculation of chemical reaction rates according to the CHEMKIN manual [17] was embedded in the codes. The ignition delay times calculated in this work agreed well with the data from Burke et al. [16].

The interspecies vibrational relaxation times were calculated using Millikan and White's formulation [18], and the vibrational energy relaxation rates were calculated using the Landau–Teller model [19]:

$$S_{\mathrm{tr-v},i} = \rho_i \frac{e_{\mathrm{v},i}\left(T_{\mathrm{tr}}\right) - e_{\mathrm{v},i}\left(T_{\mathrm{v},i}\right)}{\tau_i} \tag{5}$$

The physically consistent coupled vibration–chemistry vibration (CVCV) model [6] was applied to evaluate the effect of vibrational non-equilibrium on the reaction rates. In this model, the chemical reaction rate is modified by an efficiency function, $\varphi(T_{\mathrm{tr}}, T_{\mathrm{v}}) = k(T_{\mathrm{tr}}, T_{\mathrm{v}}) / k^E(T_{\mathrm{tr}})$:

$$\varphi\left(T_{\mathrm{tr}}, T_{\mathrm{v}}\right) = \frac{Q\left(T_{\mathrm{tr}}, E_{\mathrm{d}}\right)}{Q\left(T_{\mathrm{tr}}, E_{\mathrm{d}}\right)} \cdot \frac{e^{-\frac{\alpha E_{\mathrm{a}}}{RT}} Q\left(\Gamma, \alpha E_{\mathrm{a}}\right) + Q\left(T^0, E_{\mathrm{d}}\right) - Q\left(T^0, \alpha E_{\mathrm{a}}\right)}{e^{-\frac{\alpha E_{\mathrm{a}}}{RT}} Q\left(-U, \alpha E_{\mathrm{a}}\right) + Q\left(T^*, E_{\mathrm{d}}\right) - Q\left(T^*, \alpha E_{\mathrm{a}}\right)} \tag{6}$$

where $1/\Gamma = 1/T_{\mathrm{v}} - 1/T_{\mathrm{tr}} - 1/U$, $1/T^0 = 1/T_{\mathrm{v}} - 1/U$, and $1/T^* = 1/T_{\mathrm{tr}} - 1/U$ with coefficient $\alpha = 0.8$, $U = E_{\mathrm{d}}/5R$, and $Q(T, E) = [1 - \exp(-E/RT)]/[1 - \exp(-\theta_{\mathrm{v}}/T)]$.

3 Results

The computational domain was filled with a stoichiometric hydrogen−air mixture with initial conditions of $P_0 = 1$ atm and $T_0 = 300$ K. The left, upper, and lower sides of the computational domain were treated with slip-wall boundary conditions. A narrow area with $T_s = 4000$ K and $P_s = 90$ atm was used to ignite the mixture, and small energy perturbations were added in this hot region to trigger the instabilities. In the simulations, variations in the form or size of the perturbations were found to exert a negligible influence on the final cellular sizes and regularities provided

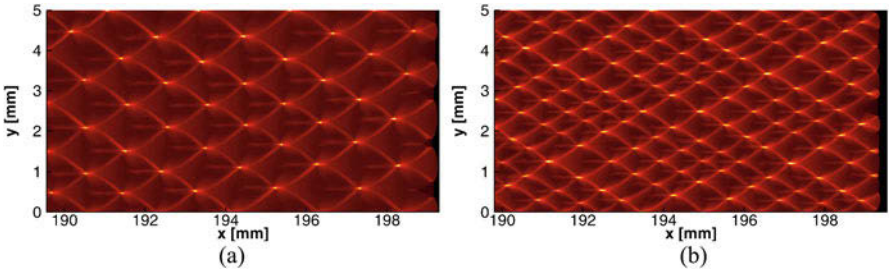

Fig. 1 (**a**) Detonation cellular pattern under assumption of thermodynamic equilibrium. (**b**) Detonation cellular pattern with finite transfer rate of molecular translational–rotational energy to vibrational energy

that the detonation waves were long enough. Three cases were considered: (1) the vibrational modes were assumed to be equilibrated with the translational–rotational modes; (2) the vibrational modes were assumed to be frozen across the shock wave and then relax to equilibrium via the Millikan–White relation; and (3) based on the second case, the chemical mechanisms were manipulated by the CVCV model [6].

3.1 Influence of Vibrational Relaxation

For the thermal equilibrium case, after the shock wave propagated a relatively long distance (more than 100 cell lengths), it was observed that the cellular structures tended to become stable (Fig. 1a). The average cell width was around 1.11 mm.

However, in the simulation featuring (uncoupled) vibrational relaxation, the distribution of the cell widths was slightly irregular. Most of the cells shrank to between 0.5 and 0.8 mm, with an average value of 0.63 mm (Fig. 1b). The effect of temperature on the rate of the reaction $H + O_2 = OH + O$ was significant [20]. In this simulation, the initial conditions included a dense mixture of H_2, O_2, and N_2 molecules, and their vibrational temperatures were frozen across the shock wave. This elevated the post-shock translational–rotational temperature, because the vibrationally frozen condition allowed additional energy to be stored in the form of translational–rotational modes [21]. The elevated translational–rotational temperature further accelerated the reactions and resulted in smaller cells. The difference between the first two assumptions was more significant than that reported in H_2-O_2-Ar detonation [15], despite the different initial conditions and reaction kinetics used. This difference may have arisen from the diluent species: the vibrational relaxation process in our system, with the molecular diluent nitrogen (of which the molar fraction in the current simulation was 55.6%), is more complex than that with the atomic diluent argon (of which the molar fraction in Shi et al. [15] was 70%).

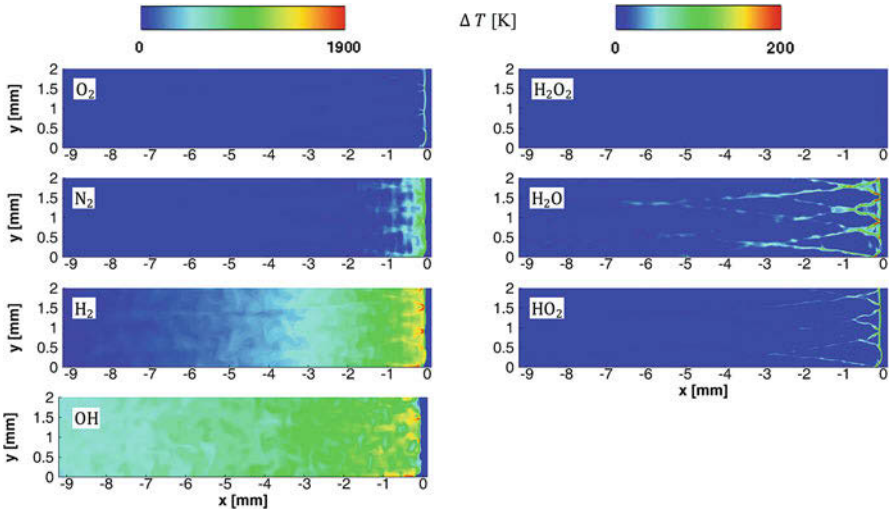

Fig. 2 Differences between translational–rotational temperature and species vibrational temperature ($T_{\mathrm{tr}} - T_{\mathrm{v},i}$) near the bottom region of the computational domain in Fig. 1b

3.2 Influence of Vibration–Chemical Coupling

After the shock passed through the mixture, O_2 approached thermal equilibrium most quickly, whereas the vibrational temperature of N_2 increased more gradually, and it took much longer distance before H_2 reached thermal equilibrium (see Fig. 2).

The effect of the ignition delay time on the reaction-zone structure was considerable. In typical post-shock conditions of hydrogen–air detonation, the sensitivity analysis for individual reaction rates revealed that the ignition delay time was most sensitive to the chain branching reaction $H + O_2 = O + OH$. When evaluating the effect of vibration–chemistry coupling using the CVCV model, the reaction rates were multiplied by an efficiency factor, which was a function of translational–rotational temperature and species vibrational temperature. From Fig. 3, it can be observed that even a very small difference between the vibrational temperature and the translational–rotational temperature suppressed the reaction rate significantly.

Because there was a region in which individual vibrational temperatures deviated from the translational temperature, the cellular structure in the third case was significantly affected by the vibration–chemistry coupling (Fig. 4); the cellular structure was found to be irregular, with average cell widths of roughly 3.33 mm across the simulation domain.

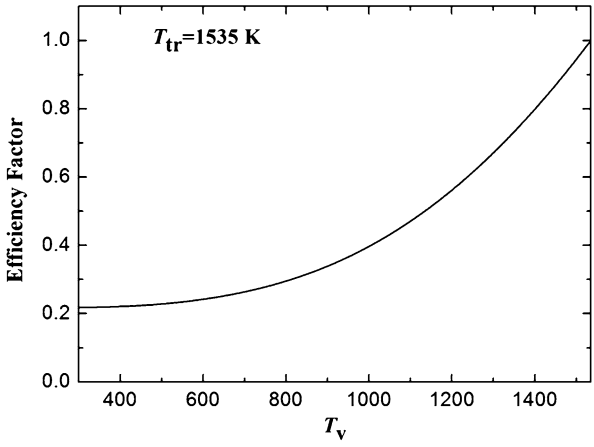

Fig. 3 Efficiency factor for reaction $H + O_2 \rightarrow O + OH$, with the translational–rotational temperature fixed at 1535 K

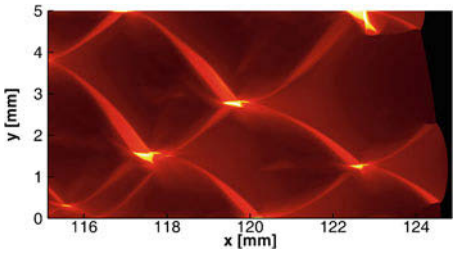

Fig. 4 Detonation cellular pattern using CVCV model

4 Conclusion

Time-dependent numerical simulations were performed using a detailed reaction model to evaluate the effect of vibrational non-equilibrium on the unstable hydrogen–air detonation, in which the vibrational equilibrium was evaluated for each individual species. The analyses indicated that under post-shock conditions, the reaction most sensitive to the ignition delay time was the chain branching reaction $H + O_2 = O + OH$. When the vibration–chemistry coupling was considered, the reaction rates were greatly suppressed in the non-equilibrium region. Compared with the vibration–chemistry coupling case, our results imply that a numerical simulation that failed to account for the vibrational relaxation process and its coupling with the chemistry would be likely to underestimate the detonation cell size.

Acknowledgment We are grateful for the computing resources of the Supercomputing Laboratory and the Extreme Computing Research Center at King Abdullah University of Science and Technology. This research was supported by Hong Kong Innovation and Technology Commission (no. ITS/334/15FP) and Natural Science Foundation of China project, numbered 11372265.

References

1. M.J. Kaneshige, *Gaseous Detonation Initiation and Stabilization by Hypervelocity Projectiles* (California Institute of Technology, Pasadena, 1999)
2. N. Tsuboi et al., Three-dimensional numerical simulation for hydrogen/air detonation: Rectangular and diagonal structures. Proc. Combust. Inst. **29**, 2 (2002)
3. V.N. Gamezo et al., Numerical simulations of flame propagation and DDT in obstructed channels filled with hydrogen–air mixture. Proc. Combust. Inst. **31**, 2 (2007)
4. R. Millikan, D. White, Vibrational relaxation in air. AIAA J. **2**, 10 (1964)
5. V. Komarov, Role of vibrational relaxation in the nonequilibrium flow of air in nozzles. J. Appl. Mech. Tech. Phys. **19**, 2 (1978)
6. O. Knab et al., Theory and validation of the physically consistent coupled vibration-chemistry-vibration model. J. Thermophys. Heat Transf. **9**, 2 (1995)
7. C. Park, Assessment of a two-temperature kinetic model for dissociating and weakly ionizing nitrogen. J. Thermophys. Heat Transf. **2**, 1 (1988)
8. B. Taylor et al., Estimates of vibrational nonequilibrium time scales in hydrogen-air detonation waves, in *24th International Colloquium on the Dynamics of Explosive and Reactive Systems*, Taipei, Taiwan, July 2013
9. S.-C. Chang, The method of space-time conservation element and solution element—A new approach for solving the Navier-Stokes and Euler equations. J. Comput. Phys. **119**, 2 (1995)
10. H. Shen, C.-Y. Wen, A characteristic space–time conservation element and solution element method for conservation laws II. Multidimensional extension. J. Comput. Phys. **305**, 775–792 (2016)
11. H. Shen et al., Robust high-order space–time conservative schemes for solving conservation laws on hybrid meshes. J. Comput. Phys. **281**, 375–402 (2015)
12. H. Shen et al., A characteristic space–time conservation element and solution element method for conservation laws. J. Comput. Phys. **288**, 101–118 (2015)
13. H. Shen et al., Maximum-principle-satisfying space-time conservation element and solution element scheme applied to compressible multifluids. J. Comput. Phys. **330**, 668–692 (2017)
14. H. Shen, M. Parsani, The role of multidimensional instabilities in direct initiation of gaseous detonations in free space. J. Fluid Mech. **813**, R4 (2017)
15. L. Shi et al., Assessment of vibrational non-equilibrium effect on detonation cell size. Combust. Sci. Technol. **189**, 5 (2016)
16. M.P. Burke et al., Comprehensive H2/O2 kinetic model for high-pressure combustion. Int. J. Chem. Kinet. **44**, 7 (2012)
17. R.J. Kee et al., *CHEMKIN-III: A FORTRAN chemical kinetics package for the analysis of gas-phase chemical and plasma kinetics*, Sandia national laboratories report SAND96-8216 (1996)
18. R.C. Millikan, D.R. White, Systematics of vibrational relaxation. J. Chem. Phys. **39**, 12 (1963)
19. W.G. Vincenti, C.H. Kruger, *Introduction to Physical Gas Dynamics* (Krieger, Malabar, 1965), pp. 198–206
20. Z. Hong et al., A new shock tube study of the H + O 2 → OH + O reaction rate using tunable diode laser absorption of H 2 O near 2.5 μm. Proc. Combust. Inst. **33**, 1 (2011)
21. M.F. Campbell et al., Dependence of calculated postshock thermodynamic variables on vibrational equilibrium and input uncertainty. J. Thermophys. Heat Transf. **31**, 586–608 (2017)

Aerodynamic Force Measurement in a Large-Scale Shock Tunnel

Yunpeng Wang, Yunfeng Liu, Changtong Luo, and Zonglin Jiang

Abstract Force tests were conducted at the long-duration-test shock tunnel JF12, which has been designed and built in the Institute of Mechanics, Chinese Academy of Sciences. The performance tests demonstrated that this facility is capable of reproducing a flow of dry air at Mach numbers from 5 to 9 at more than 100 ms test duration. Therefore, the traditional internal strain-gauge balance was considered for the force tests used in this large impulse facility. However, when the force tests are conducted in a shock tunnel, the inertial forces lead to low-frequency vibrations of the test model, and its motion cannot be addressed through digital filtering because a sufficient number of cycles cannot be found during a shock tunnel run. The post-processing of the balance signal thus becomes extremely difficult when an averaging method is employed. Therefore, the force measurement encounters many problems in an impulse facility, particularly for large and heavy models. The objective of the present study is to develop pulse-type sting balance by using a strain-gauge sensor, which can be applied in the force measurement that 100 ms test time, especially for the force test of the large-scale model. Different structures of the S-series (i.e., sting shaped balances) strain-gauge balance are proposed and designed, and the measuring elements are further optimized to overcome the difficulties encountered during the measurement of aerodynamic force in a shock tunnel. In addition, the force tests were conducted using two large-scale test models in JF12, and the S-series strain-gauge balances show good performance in the force measurements during the 100 ms test time.

1 Introduction

For a conventional hypersonic shock tunnel, owing to instantaneous flow field and short test time (generally 500 μs-20 ms) [1–4], the mechanical vibration of the

Y. Wang (✉) · Y. Liu · C. Luo · Z. Jiang
State Key Laboratory of High Temperature Gas Dynamics, Institute of Mechanics, Chinese Academy of Sciences, Beijing, China
e-mail: wangyunpeng@imech.ac.cn

A. Sasoh et al. (eds.), *31st International Symposium on Shock Waves 2*,
https://doi.org/10.1007/978-3-319-91017-8_20

model-balance-support (MBS) system occurs and cannot be damped during a shock tunnel run. For the MBS system, the lowest natural frequency of 1 kHz is sometimes required for the test time of typically 5 ms to obtain improved measurement results [2]. The higher the natural frequencies, the better the justification for the neglected acceleration compensation. For such test conditions, many researchers proposed several special balances to measure the aerodynamic forces in the impulse facilities, that is, accelerometer balance [5–7], stress-wave force balance [8–10], free-flight measurement technique [11–16], and compensated balance [17]. Owing to the very short test time, however, the mature technology was undeveloped for the force measurements in a shock tunnel.

The hypersonic detonation-driven shock tunnel, JF12, was developed based on the backward-running detonation driver technique. Its performance tests demonstrated that the facility is capable of reproducing the pure airflow with Mach numbers from 5 to 9 at altitude of 25–50 km. Based on test duration of more than 100 ms, the stiff construction balance, that is, the traditional internal strain-gauge balance (SGB), was considered for use in the force test in the JF12 long-test-duration impulse facility because of its mature technology and low cost of the strain gauge. However, when the force test is conducted in a shock tunnel, the inertial forces lead to low-frequency vibrations of the model, and its motion cannot be addressed through digital filtering because a sufficient number of cycles cannot be found during a shock tunnel run. This condition implies restriction on the model size and mass as its natural frequencies are inversely proportional the length scale of the model. Based on these technical difficulties, S-series (sting-series) pulse-type SGBs were proposed, and the measuring element structure of SGB was optimized by finite element method (FEM). The maximum loads (i.e., normal force) are from 500 to 12,000 N for the test models with different scales. The finite element computations were performed to analyze the vibrational characteristics of the MBS system to ensure enough cycles of the balance signal and high measuring sensitivity, especially axial element structure, during the 100 ms test. In addition, the force tests were conducted by using two large-scale cones. The S-series SGBs show good performance, and the frequencies of the MBS system increase as a result of the stiff construction of SGB.

2 Strain-Gauge Balances Built at JF12 Shock Tunnel

We used the strain-gauge sensor to measure the aerodynamic loads in the JF12 shock tunnel. The strain-gauge sensor has enough high-frequency response for the force test during a test period of more than 100 ms. The experimental and computational results show that the SGB, with the optimized structures, can be used in this long-test-duration shock tunnel. Therefore, S-series pulse-type SGBs were designed and fabricated for the force tests of JF12.

In this paper, two SGBs, JF12-ISG3-D053-S01 (hereafter referred to as S01) and JF12- ISG6-D106-S03-II (S03-II), are described in detail as the examples of S-series

Table 1 Simultaneous component load ranges (N, Nm)

Serial no.	X	Y	Z	M_x	M_y	M_z
S01	1000	2000	–	–	–	100
S03-II	4000	12,000	12,000	100	400	400

pulse-type SGB. The difference between S01 and S03-II is the element structure of axial load. The balance S01 was further optimized in the aspect of the measuring element of the axial load based on the axial element of S03-II. The performances of S01 and S03-II were examined to determine which type is better for the force measurement in the JF12 shock tunnel.

All the SGBs use only one rectangular beam to measure the components of normal force, side force, yawing moment, and pitching moment. The moment center is located at the center of the rectangular beam. The S01 is a three-component (i.e., axial force X, normal force Y, and pitching moment Mz) sting balance, and the S03-II is the six-component one. Based on the structures of S-series SGB, therefore, four strain gauges are used for the axial load element in the case of S01 and eight strain gauges for the S03-II. These strain-gauge sensors are arranged in a Wheatstone bridge to measure the strain produced by the loads. The output voltage of a balance bridge changes as a function of the strain at the bridge location produced by the applied loads. Table 1 provides details of the load range for two balances used in the present study. The S-series balances with different limited loads are used for the test models with different scales.

3 Design and Optimization of S-Series SGBs

To design and construct a high-stiffness SGB that can meet certain demands, all aspects of the balance technology must be investigated. In this study, only the structure of SGB is considered. From the point of view of structure, these high demands on the balance can be expressed as (1) low interference between each element, (2) high stiffness, (3) low stress level at the strain-gauge positions and related parts, and (4) capability to tolerate errors from the temperature gradients. Among these demands, the important properties for this transport type balance, such as the stiffness, the sensitivity, and the interference, were investigated in the present study.

Owing to the same rectangular beam for measuring Y, Z, M_y, and M_z, the present study focuses on the design and optimization in the axial element structure. To examine the sensitivity performance of the measuring element, the strain computations were conducted in the cases of S01 and S03-II. The findings are shown in Figs. 1 and 2. The first case is the axial force of 1000 N (limited load) acting on the moment center of S01. In this case, the strain output of the axial force element is 336 $\mu\varepsilon$, while the output of the normal force element is only 15 $\mu\varepsilon$. Minimal strain is generated on the rectangular beam when an axial force of 1000 N is applied at the moment center of S01, and vice versa. The effect of the axial force on the

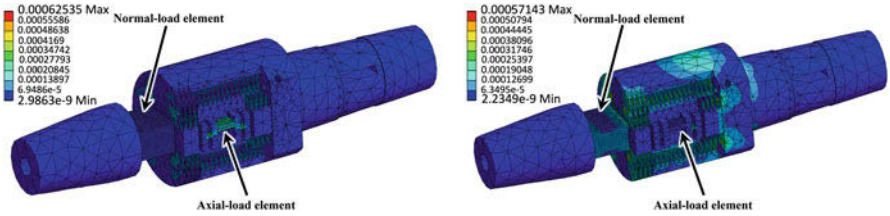

Fig. 1 Strain contours of S01 (left, axial force of 1000 N; right, normal force of 2000 N)

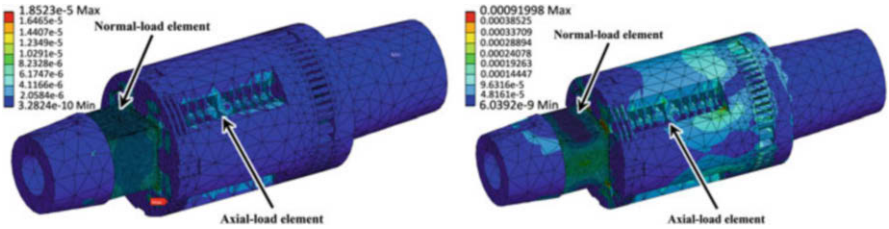

Fig. 2 Strain contours of S03-II (left, axial force of 4000 N; right, normal force of 12,000 N)

Table 2 Combining loading error and repeatability (%)

	Serial no.	X	Y	Z	M_x	M_y	M_z
Error	S01	0.03	0.26	–	–	–	0.12
	S03-II	0.222	0.248	0.38	0.43	0.034	0.054
Repeatability	S01	0.03	0.03	–	–	–	0.05
	S03-II	0.137	0.229	0.256	0.186	0.082	0.071

rectangular beam is very small because of the optimized axial force element. In the S03-II case, however, when the axial force of 4000 N (limited load) is applied at the moment center, the strain of the rectangular element becomes 17 $\mu\varepsilon$ and that of the axial load element is only 40 $\mu\varepsilon$. This result means that the interference of the axial force is larger in the case of S03-II than that of S01. Additionally, the measuring sensitivity of the axial force element of S03-II is also significantly lower than that of S01.

In the same manner, we calculated the cases of the limited normal load acting on S01 and S03-II (see Fig. 2). The case of S01 shows a smaller interference from the normal force where it is less than 5%, while the case of S03-II is more than 70%.

Table 2 shows the calibration performances (i.e., the error and the repeatability) of the S01 and S03-II by the static calibration. The structures of the present balance show good accuracy and precision in the static calibration. The table shows that the axial force of S01 has highest accuracy and precision because of the optimized measuring element. Almost the close errors of the normal force were obtained for the two balances because of the same structure of measuring element, i.e., the rectangular beam.

4 Force Tests

The force tests were conducted in the JF12 shock tunnel to check the performance of the pulse-type sting balances. In the tests, the average stagnation pressure was 2.5 MPa, and the average stagnation temperature was 2200 K. These conditions resulted in an average freestream Mach 7 and an average unit Reynolds number of approximately 0.8×10^6 per meter. In addition, the model was supported by a tail sting mounted on the support mechanism in the test section. The force tests were conducted at nominal angles of attack 5° with zero sideslip angle.

In the experiments, two cones with 10° semivertex angle were used; these were made of aluminum alloy and are 0.75 m and 1.5 m long, respectively (see Fig. 3). The balances S01 and S03-II were used for the smaller and larger cones, respectively, in the force tests. The cone is the standard model and has data available in the literature.

Figure 4 shows the balance voltage signals of the normal force. The case of S03-II shows minimal response (strain output) because of the rectangular beam with large size and high stiffness. Moreover, the frequency of S03-II is also higher than that of S01. The signals were processed at the time range of 96 ms. The two frequencies, i.e., 30.52 Hz and 61.04 Hz, were found using fast Fourier transformation (FFT) analysis in the case of S01. Obviously, at least three cycles can be found during the 100 ms test time. Therefore, the averaging method can be used in the data post-processing.

Additionally, prior to the shock tunnel run, the three-dimensional designs of the MBS system are modeled. A series of computations, including the static structure, dynamics, and modal analysis, is conducted by using FEA. The numerical results can be used to estimate the experimental results, such as the vibrational frequency and cycle number of the MBS system, during the limited test time. Based on FEA of the MBS system, the modal frequencies in the normal direction, 34 and 46 Hz,

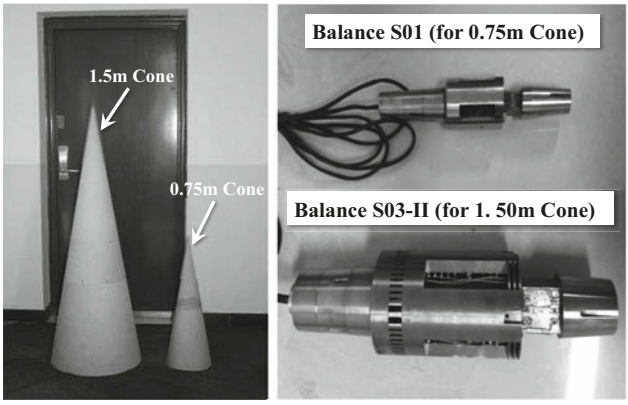

Fig. 3 Two large-scale cones and S-series balances used in the present force tests

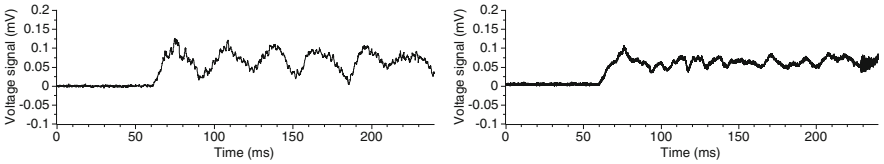

Fig. 4 Voltage signals of normal force by the S01 (left) and S03-II (right)

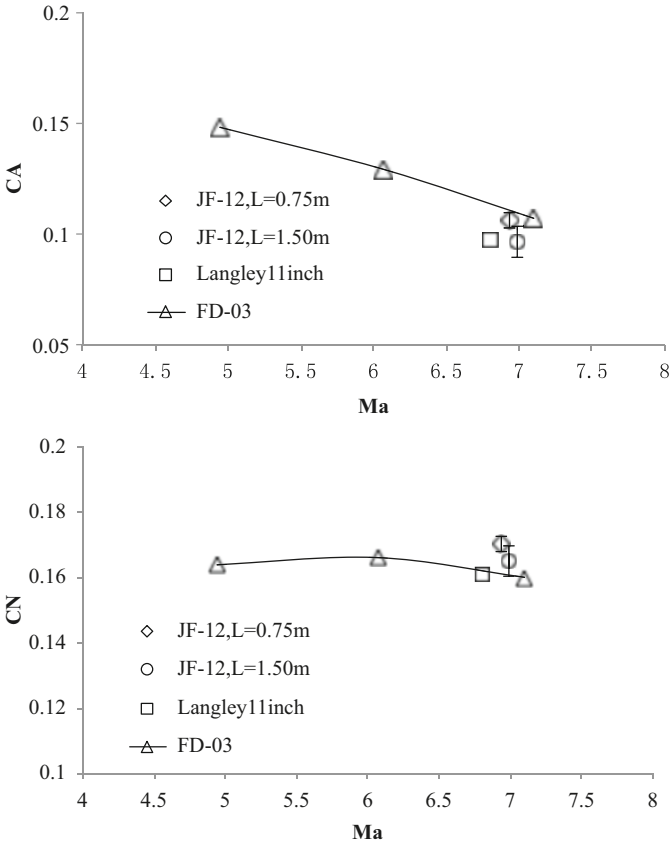

Fig. 5 Aerodynamic coefficient comparison for S01 (0.75 m cone) and S03-II (1.5 m cone)

can be obtained for the cases of S01 and S03-II, respectively. FEM results have a good agreement with the force tests and FEA successfully predicted the vibration performance of the MBSS. In this study, the modal frequency of MBS system, $f \geq 2/t$ Hz (here, t is the test time, e.g., t is approximately 100 ms, then f should be equal and greater than 20 Hz), is used as a design criterion, where at least the two cycles can be found in the balance signal.

Figure 5 presents a comparison of the test results for S01 and S03-II. Some data were obtained by other conventional hypersonic wind tunnels. The results have good

agreement with the data on Langley 11 inch ($T_0 = 630$ K) wind tunnel. In the case of NASA, Mach number is 6.8 and Reynolds number (L) is 0.81×10^6. A comparison with the NASA data shows that the normal and axial force coefficients decreased by 2.61% and 4.69%, respectively, in the case of S01.

5 Conclusion

S-series pulse-type SGBs were designed and optimized for the force tests in the JF12 shock tunnel with long test duration. The range of the maximum load (the normal force of the sting type SGBs) is from 500 to 12,000 N for the test models with different scales. Two sting pulse-type SGBs were compared and analyzed in the aspects of FEM calculation, static calibration, and output signal. The S01, with the optimized axial load element, shows good performance, where its accuracy and precision increase as a result of the higher measuring sensitivity. In addition, the large oscillations of the normal loads have minimal effects on the axial load signal because of the structural optimization. S-series balances were used in the force tests of two large-scale cones in the JF12 shock tunnel. The test results show good agreement with the other wind tunnel data. The structural performance of S-series SGBs fully complies with the requirements of force measurements during 100 ms, especially the measuring capability of the axial load.

Acknowledgments This work was supported by the National Natural Science Foundation of China (Grant No.11672357).

References

1. P.J. Arrington, R.J. Joiner, A.J. Henderson. *Longitudinal Characteristics of Several Configurations at Hypersonic Mach Numbers in Conical and Contoured Nnozzles*, NASA TN D-2489 (1954)
2. L. Bernstein. *Force Measurement in Short-Duration Hypersonic Facilities*. AGARDograph No. 214 (1975)
3. K. Naumann, H. Ende, G. Mathieu, A. George, Millisecond aerodynamic force measurement with side-jet model in the isl shock tunnel. AIAA J. **31**, 1068–1074 (1993)
4. K. Naumann, H. Ende, A novel technique for aerodynamic force measurements in shock tubes. AIP Conf. Proc. **208**, 653–658 (1990)
5. R. Joarder, G. Jagadeesh, A new free floating accelerometer balance system for force measurements in shock tunnels. Shock Waves **13**, 409–412 (2003)
6. S. Saravanan, G. Jagadeesh, K.P.J. Reddy, Aerodynamic force measurement using 3-component accelerometer force balance system in a hypersonic shock tunnel. Shock Waves **18**, 425–435 (2009)
7. N. Sahoo, D.R. Mahapatra, G. Jagadeesh, S. Gopalakrishnan, K.P.J. Reddy, An accelerometer balance system for measurement of aerodynamic force coefficients over blunt bodies in a hypersonic shock tunnel. Meas. Sci. Technol. **14**, 260–272 (2003)

8. M.J. Robinson, J.M. Schramm, K. Hannemann, Design and implementation of an internal stress wave force balance in a shock tunnel. CEAS Space J. **1**, 45–57 (2011)
9. S.R. Sanderson, J.M. Simmons, S.L. Tuttle, A drag measurement technique for free-piston shock tunnels, AIAA Paper 91-0540 (1991)
10. D.J. Mee, W.J.T. Daniel, J.M. Simmons, Three-component force balance for flows of millisecond duration. AIAA J. **34**(3), 590–595 (1996)
11. F. Seiler, G. Mathieu, A. George, J. Srulijes, M. Havermann, Development of a free flight force measuring technique (ffm) at the isl shock tube laboratory, in *25th International Symposium on Shock Wave*, Bangalore, India, 2005
12. P. Wey, M. Bastide, B. Martinez, J. Srulijes, P. Gnemmi, Determination of aerodynamic coeffcients from shock tunnel free- flight trajectories, in *Proceedings of the 28th Aerodynamic Measurement Technology, Ground Testing and Flight Testing Conference*, New Orleans, USA, 2012
13. B. Martinez, M. Bastide, P. Wey, Free-flight measurement technique in shock tunnel, in *Proceedings of the 30th Aerodynamic Measurement Technology and Ground Testing Conference*, Atlanta, USA, 2014
14. H. Tanno, T. Komuro, K. Sato, K. Fujita, S.J. Laurence, Free-flight measurement technique in the free-piston shock tunnel hiest. Rev. Sci. Instrum. **85**, 045112 (2014)
15. H. Tanno, T. Komuro, K. Sato, K. Itoh, T. Yamada, Free-flight tests of reentry capsule models in free-piston shock tunnel, AIAA Paper 2013-2979 (2013)
16. S.J. Laurence, S. Karl, An improved visualization-based force-measurement technique for short-duration hypersonic facilities. Exp. Fluids **48**, 949–965 (2010)
17. E. Marineau, M. MacLean, E. Mundy, M. Holden, Force measurements in hypervelocity flows with an acceleration compensated strain gage balance. J. Spacecr. Rockets **49**(3), 474–482 (2012)

Trial Implementation of TiN Surface Coating for a Main Piston Towards Reducing the Opening Time for a Diaphragmless Driver Section

S. Udagawa, W. Garen, T. Inage, M. Ota, and K. Maeno

Abstract In this study, we have performed TiN coating for a free piston to decrease the abrasion resistance between the free piston and a housing, consisted of a main piston. The thickness of the TiN layer on the surface is 2 μm. The opening time of the main piston is measured by using the surface-coated free piston. As a consequence, the opening time of the main piston is achieved 500 μs for 2 mm stroke. Additionally, the shock wave has been generated in the glass tubes with 2, 3, and 4 mm diameter to confirm the shock wave propagation. The shock wave measurements are performed at the several points along the axial direction of the tube by using laser differential interferometer. Consequently, the shock wave propagation is confirmed by using the surface-coated free piston. Moreover, the experimental efficiency is drastically improved especially at the initial experimental process. However, TiN coating partly disappeared by repeated use.

1 Introduction

Recently, the micro-shock waves are highly noticed from researchers in several fields of science. It is well known that the shear stress and the heat transfer between

S. Udagawa (✉)
Aerospace Engineering Course, Tokyo Metropolitan College of Industrial Technology, Tokyo, Japan
e-mail: udagawa@metro-cit.ac.jp

W. Garen
Department of Photonics, University of Applied Science Emden/Leer, Emden, Germany

T. Inage
Faculty of Engineering, Shonan Institute of Technology, Fujisawa, Japan

M. Ota
Graduate School and Faculty of Engineering, Chiba University, Chiba, Japan

K. Maeno
National Institute of Technology, Kisarazu College, Kisarazu, Japan

A. Sasoh et al. (eds.), *31st International Symposium on Shock Waves 2*,
https://doi.org/10.1007/978-3-319-91017-8_21

a test gas and a wall lead to significant deviations from the normal theory of a shock wave, especially in small diameter shock tubes [1, 2].

In our previous study, we developed the diaphragmless driver section with two pistons for a small diameter shock tube [3, 4], based on the technique which was invented and applied by Oguchi et al. and Maeno et al. [5–7]. According to our experimental results, the longer shock wave forming distance occurred by the slower actuation of the main piston, which is one of the components that constitute the diaphragmless driver section, at the initial opening process [8]. Therefore, we improved the main piston, named a UMO (Udagawa-Maeno-Oguchi) valve, consisted of the diaphragmless driver section to achieve the faster actuation of the main piston especially at the initial opening process. Consequently, the opening time of the main piston was achieved about 85% reduction by the improvement of the structure for the main piston. According to our results, the shock wave forming distance becomes shorter with decreasing the opening time of the main piston. Additionally, the wear track is observed on the free piston surface. The wear track leads to infection for the motion of the free piston. As a Consequence, a few problems for UMO valve still exist especially for the reproducibility of the shock wave measurements [9, 10].

In this study, we have performed TiN coating for a free piston to decrease the abrasion resistance between the free piston and a housing, consisted of a main piston. The opening time of the main piston is measured by using the surface-coated free piston. Additionally, the shock wave propagation in small diameter tubes is confirmed.

2 Diaphragmless Driver Section with Two Pistons

The diaphragmless driver section with quick actuation is developed and invented by the several researchers. A rapid opening valve with unique structure and operating mechanism was developed. The piston orthogonally actuates rapidly from the shock wave traveling direction by using the magnet [11]. According to their experimental results, the magnet installed inside the driver section leads to the rapid actuation of the piston. The diaphragmless driver section with two pistons that we developed is also installed the magnet inside the free piston to obtain the effect of the rapid actuation [10].

Figure 1 shows the schematic drawing of the diaphragmless driver section with two pistons. The unique modification point from MO valve [6, 7] is the replacement of the main piston. The modified main piston (UMO valve) consists of a free piston with a magnet and a housing made of Ti-based alloy. The housing, which is perforated for the gas vent holes, and the magnet, settled inside the free piston, are to prevent the unintended actuation of the free piston which is induced by the resistance between the free piston and the housing. The aim of this improvement is to achieve the faster opening time by the impulse transfers from the housing to the free piston, especially at the initial opening process. Firstly, the housing actuates

at the initial opening process. The free piston is actuated by the collision, which is occurred after that the housing moves the backlash δx between the housing and the free piston. The opening time of the main piston is reduced drastically by UMO valve. According to our results, the shock wave forming distance becomes shorter with decreasing the opening time of the main piston [10].

3 TiN Coating for the Free Piston Surface

Figure 1a shows the free piston without the surface coating used in our previous study. The wear track occurred by the abrasion is observed on the surface as shown in Fig. 1a. It is predicted that the wear track leads to infection for the motion of the free piston. Actually, the reproducibility of experiment becomes wrong by repeated use. As a consequence, a few problems for UMO valve still exist especially for the reproducibility of the shock wave measurements. It is generally known that the Ti-based alloy has high strength ratio, the weak point for the abrasion resistance. Thus, we have performed the TiN coating to increase the abrasion resistance for the free piston as shown in Fig. 2b. The thickness of the TiN layer on the surface is 2 μm.

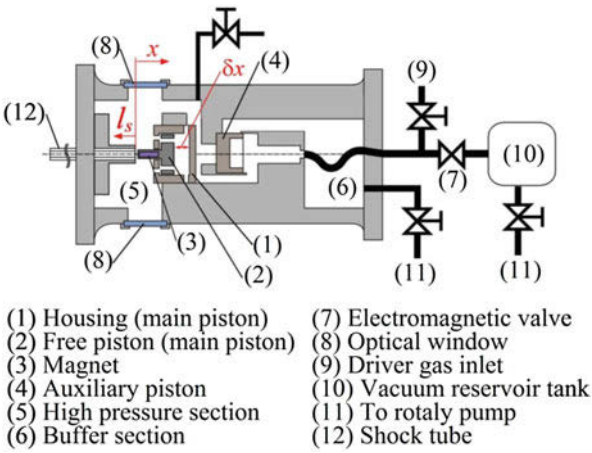

Fig. 1 Schematic drawing of the diaphragmless driver section with UMO valve

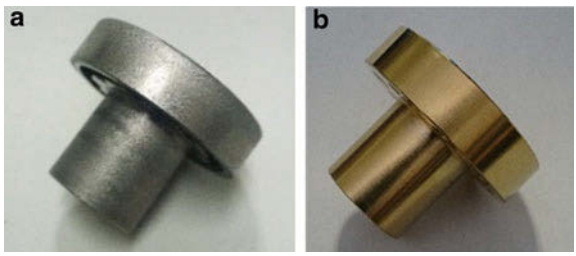

Fig. 2 (**a**) Non-coated free piston used in the previous study, (**b**) TiN-coated free piston

4 Measurement System

4.1 Measurement System for the Valve Opening Characteristics

Figure 3 shows the schematic drawing of the measurement system for the valve opening characteristics. The laser beam emitted from the He-Ne laser head is shaped to a sheet-shaped beam by passing through the Powell lens and the cylindrical lens. The sheet-shaped beam is focused by the cylindrical lens after passing through the observation windows. The focused beam enters a PIN photo detector at the focal point of the cylindrical lens. The signal from the photo detector is recorded to an oscilloscope. UMO valve is operated under the initial pressure ratio $p_4/p_1 = 9$ in this experiment.

4.2 Measurement System for the Shock Waves

Figure 4 shows the schematic drawing of the measurement system used in this study. The glass tube, which is connected to the high-pressure section, has the length $l = 1000$ mm. The position of the laser differential interferometer l_s can be changed. The inner diameter of the tubes is used as 2, 3, and 4 mm in this experiment. The pressure transducer is settled at the end of the tube to detect the reflected shock wave. The signals obtained from the interferometer and the pressure transducer are recorded to an oscilloscope. The initial pressure ratio p_4/p_1 is maintained constant as 9 at the driven pressure p_1 fixed 0.1 MPa. Helium and air are used as the driver and the test gas, respectively.

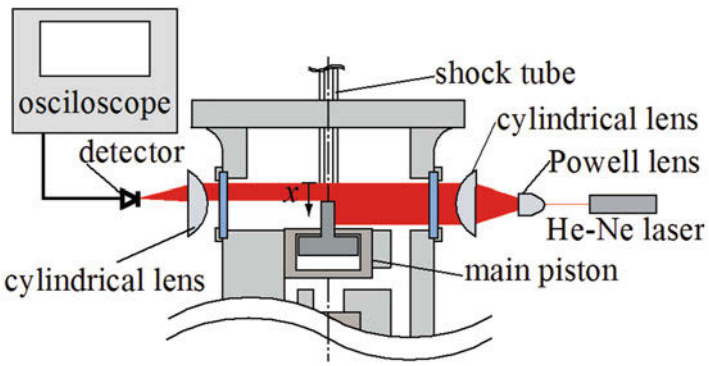

Fig. 3 Schematic drawing of the measurement system for the valve opening characteristics

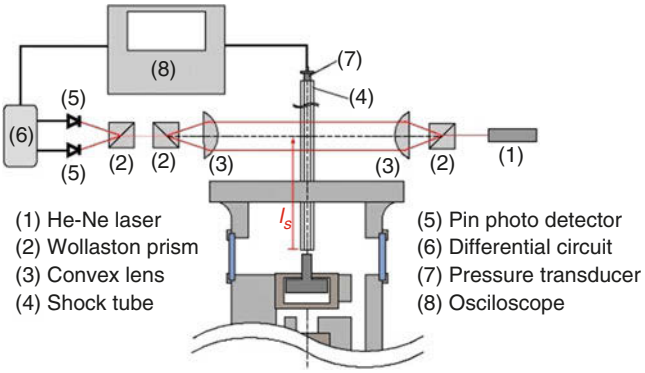

Fig. 4 Schematic drawing of the measurement system for the shock wave

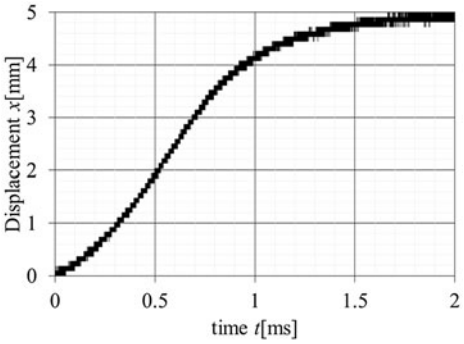

Fig. 5 The valve opening characteristics by using TiN-coated free piston

5 Experimental Results

5.1 Valve Opening Characteristics

Figure 5 shows the TiN-coated free piston trajectories obtained from the measurement system as shown in Fig. 3. The vertical and the horizontal axes are the displacement of the piston x and the time t, respectively. The experimental results show that UMO valve has quick opening characteristics. As a consequence, 500 μs for 2 mm stroke is achieved in case of TiN-coated free piston. However, the reduction of the opening velocity is not appeared clearly in this experiment.

5.2 Shock Wave Propagation

Figure 6 shows the Mach number distribution along the shock tubes. The horizontal and the vertical axes indicate the measurement position l_s and the Mach number Ms. The dashed line shows the theoretical results obtained from Rankine-Hugoniot

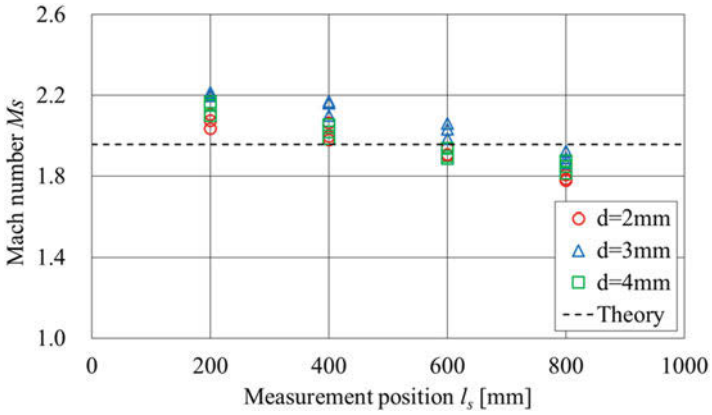

Fig. 6 Mach number distribution along the shock tube

relation. It is confirmed that the shock wave forming distance in this experiment exists at least 200 mm or less. It is also confirmed that the Mach number is decelerating with increasing the measurement position. It is attributed to the fact that the shock wave deceleration occurs by increasing of the friction effect. According to general consideration, the friction effect becomes increasing with decreasing the inner diameter of the shock tube d, which leads to increasing of the surface area per unit volume of the hot gas region behind the shock wave. However, there is no difference between the experimental results by changing d. It is attributed to the fact that the shock wave is accelerated by the effect of cross-sectional area reduction between the high-pressure section and the shock tube, which is produced by decrease of inner diameter d.

6 Conclusion

In this study, we performed TiN surface coating for the free piston, installed in UMO valve, made by Ti-based alloy to decrease the infection especially from the wear track occurred by the abrasion. The opening characteristics of UMO valve with TiN-coated free piston are measured. Additionally, the shock wave, which is generated by using TiN-coated free piston installed in UMO valve, propagating in the small diameter tubes is measured by using laser differential interferometer. As a consequence, the Mach number distribution along the shock tubes is obtained by changing the inner diameter of the tube d. From our experimental results, the following points can be concluded:

1. The opening characteristics of UMO valve with TiN-coated free piston is obtained as the trajectory of the free piston. The experimental results show that UMO valve with TiN-coated free piston has quick opening characteristics. As a

consequence, 500 μs for 2 mm stroke is achieved. However, the reduction of the opening velocity is not appeared clearly in this experiment. It is attributed to the fact that the TiN layer contributes to the reduction of the friction resistance, TiN layer, however, partly disappears by repeated use.

2. The shock wave forming distance in this experiment exists at least 200 mm of less. It is confirmed that the Mach number of the shock wave is monotonically decelerated along the shock tubes. It is attributed to the fact that the shock wave deceleration occurs by increasing of the friction effect. According to general consideration, the friction effect becomes increasing with decreasing the inner diameter of the shock tube d, which leads to increasing of the surface area per unit volume of the hot gas region behind the shock wave. However, there is no difference between the experimental results by changing d. It is attributed to the fact that the shock wave is accelerated by the effect of cross-sectional area reduction between the high-pressure section and the shock tube, which is produced by decrease of inner diameter d.
3. More modifications should be performed especially for TiN coating to maintain the opening characteristics of the UMO valve at repeated use. Additionally, more detailed experiments are required to estimate the influence of the shock wave attenuation by using smaller diameter shock tube.

Acknowledgments The first author would like to express his best gratitude to NDK Inc., Japan, especially for the cooperation in TiN surface coating.

References

1. M. Brouillette, Shock waves at micro scales. Shock Waves **13**, 3 (2003)
2. W. Garen et al., A novel mini-shock tube for generating shock waves at micro scales in turbulent and laminar gas flows, in *Proceedings of 25th ISSW*, 2005, pp. 746–750
3. S. Udagawa et al., Propagation characteristics of the shock wave in small diameter tubes at atmospheric initial driven pressure. Proc. 28th ISSW **1**, 529–534 (2011)
4. S. Udagawa et al., Development of a small diameter shock tube and measurement of basic characteristics. Trans. Jpn. Soc. Mech. Eng. B. **78**(785), 36–48 (2005) (in Japanese)
5. H. Oguchi et al., An experiment on interaction of shock wave with multiple-orifice plate by means of snap-action shock tube, in *Proceedings of 10th International Shock Tube Symposium*, 1975, pp. 386–391
6. K. Maeno et al., Study on shock waves in low temperature gas by means of a nondiaphragm shock tube, in *Proceedings of 15th ISSW*, 1986, pp. 563–569
7. K. Maeno et al, Experiment of vapor bubble collapse in low temperature R-12 under shock compression, in *Proceedings of 16th ISSW*, 1988, pp. 273–279
8. S. Udagawa et al., Interferometric measurement of the shock wave propagating in a small diameter circular tube. Kouku Uchu Gijutsu **11**, 99–105 (2012) (in Japanese)
9. S. Udagawa et al., Improvement of a diaphragmless driver section for a small diameter shock tube, in *Proceedings of 29th ISSW*, No.0246-000117, 2013
10. S. Udagawa et al., Behavior of the shock wave propagating in the small diameter tubes, in *Proceedings of 30th ISSW*, 2015, pp. 423–425
11. A. Abe et al., Performance evaluation of a diaphragmless shock tube with rapid opening valve assisted by magnetic force. Trans. Jpn. Soc. Mech. Eng. B. **79**(806), 99–110 (2013) (in Japanese)

Aerodynamic Force Measurement Techniques in JF12 Shock Tunnel

YF. Liu, YP. Wang, CK. Yuan, CT. Luo, and ZL. Jiang

Abstract An aerodynamic force test was conducted in JF12 long-test-time shock tunnel. The test time of JF12 is 100–130 ms. The nominal Mach number is Ma7.0 and the exit diameter of the contoured nozzle is Φ2.5 m. The total enthalpy is 2.5 MJ/kg which duplicates the hypersonic flight conditions of Ma 7.0 at 35 km altitude. The test model is the standard aerodynamic force model of 10° half-angle sharp cone. The length of the test model is 1.5 m and the weight is 57 kg. The aerodynamic forces were measured with a six-component strain balance. The experimental results show that in the 100–130 ms test duration, the signals of strain balance have 3–4 complete vibration cycles. The aerodynamic force coefficients of JF12 are in good agreement with that of conventional hypersonic wind tunnels. This research demonstrates that aerodynamic force test can be conducted in shock tunnel with test time longer than 100 ms.

1 Introduction

Conventional hypersonic wind tunnels usually produce test flows with low total temperature and low sound speed; therefore, the thermochemical reaction, one of the key mechanisms in hypersonic flows, is ignored in its experiments. As a result, the real-gas effects on the aerodynamic force and moment measurement become a very difficult problem in the hypersonic ground tests and were identified as an unknown "unknown" [1]. At an enthalpy of about 3 MJ/kg or higher, air molecules become vibrationally excited, dissociated, and ionized behind a shock wave. These real-gas phenomena absorb heat. As a result, the effective specific heat ratio decreases and compressibility increases.

Y. Liu (✉) · Y. Wang · C. Yuan · C. Luo · Z. Jiang
Institute of Mechanics, Chinese Academy of Sciences, Beijing, China

School of Engineering Sciences, University of Chinese Academy of Sciences, Beijing, China
e-mail: liuyunfeng@imech.ac.cn

A. Sasoh et al. (eds.), *31st International Symposium on Shock Waves 2*,
https://doi.org/10.1007/978-3-319-91017-8_22

These phenomena cause changes in pressure distribution and thereby aerodynamic characteristics of the hypersonic vehicle. To design an efficient hypersonic vehicle, the influence of real-gas effects on force and moment must be known accurately. To experimentally verify the accuracy of those design parameters, wind tunnel tests are needed. To produce flows with desired temperature, Mach number, and Reynolds number in the test section, such tunnels must be operated at very high enthalpies and reservoir pressures [2, 3].

Considering the thermochemistry in hypersonic flows, high-enthalpy shock tunnels are capable of generating high-temperature flows, but its effective test duration is too short to do force and moment measurement. Under the support of National Major Project of Scientific Instrumentation Research and Development, a super-large detonation-driven shock tunnel was developed based on backward-running detonation driver in Institute of Mechanics, Chinese Academy of Sciences in 2012 [4, 5]. It has the capability of reproducing pure airflows with Mach numbers from 5 to 9 at an altitude of 25–50 km. More important, it has a test duration of more than 100 ms which makes it the first shock tunnel in the world to conduct aerodynamic force and moment measurement by using conventional strain balances.

The force and moment measurement of hypersonic vehicles is one of the main long-term research projects of JF12 shock tunnel in order to study the aerodynamic characteristics under real-gas conditions. In this paper, as the first step of this project, we conducted the force and moment measurement of 10° half-angle sharp cone at Mach 7.0 under the duplicated hypersonic flight conditions of about 35 km altitude with the total enthalpy of 2.5 MJ/kg. The aim of this paper is to examine whether JF12 can be used to conduct force measurement and obtain high accuracy data in 100 ms test time. The primary experimental results are given and compared with conventional hypersonic wind tunnel results. This research will be continued further in JF12 shock tunnel under high-enthalpy conditions.

2 Experimental Setup and Test Model

The picture of JF12 long-test-time shock tunnel is shown in Fig. 1. The total length of the facility is 265 m. It consists of five main parts. From right to left, they are E-shaped vacuum tank and test section, nozzle, driven section, detonation driver section, and damping section. The contoured nozzle is 15 m long with an exit diameter of Φ2.5 m. The nominal Mach numbers are Ma5–7 with exchangeable throats. The driven section is 89 m in length and Φ720 mm in inner diameter. The detonation driver is 99 m in length and Φ400 mm in inner diameter. The driver is operated in the backward-running detonation mode. The detonation driver and the driven section are connected with a transition section by which the tube diameter is gradually reduced from Φ720 mm to Φ400 mm. There is a diaphragm rig between the detonation driver and the transition section, which is used to produce the proper incident shock wave in the shock tunnel after the direct detonation initiation.

Fig. 1 Photo of JF12 long-test-time shock tunnel

Fig. 2 The 10° half-angle cone model installed in JF12 shock tunnel

The test model is a 10° half-angle sharp cone, and it is a standard aerodynamic force model. There are many experimental results obtained in conventional hypersonic wind tunnels to compare with. The length of the model is 1.5 m with a base diameter of Φ528 mm. It is made of aluminum alloy and weighs 57 kg. Figure 2 is the photo of test model installed in JF12 shock tunnel. Pressure transducers were also installed on the bottom surface to measure the base pressure of the model during the experiments. Up to now, it is the biggest and most heavy aerodynamic force model in shock tunnel in the world.

Fig. 3 The six-component strain balance designed for JF12 shock tunnel

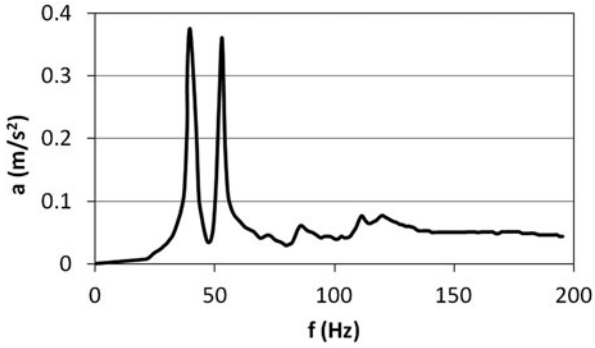

Fig. 4 The normal vibration frequency of JF12 model supporting system

A six-component strain balance specially designed for JF12 shock tunnel was used to measure the aerodynamic force and moment. Figure 3 shows the photo of this strain balance. The maximum diameter of this balance is Φ106 mm. In the JF12 shock tunnel experiments, the mechanical vibration of the test model, the balance, and the sting will not be damped within the test time of 100 ms. Therefore, the balance output signals contain inertial force. In order to reconstruct the force and moment from the balance output signals and obtain high quality data, we must make sure that we can get at least 3–4 complete vibration periods in the 100 ms test time. Therefore, the balance was designed with high stiffness. In addition, the strength of the sting and model supporting system was also strengthened.

Before the wind tunnel experiments, the vibration frequency of model supporting system of JF12 shock tunnel was measured by dynamic calibration with fracture-stick technique. The model supporting system includes the model, the balance, the sting, and the supporting equipment. The sting was made of alloy steel with a diameter of Φ100 mm. The vibration frequency in the normal direction was recorded by accelerometers, and the results are shown in Fig. 4. From Fig. 4 we can see that the first order modal frequency is about 40 Hz, which means that we can get at least four complete vibration periods in the normal force direction within 100 ms test time. In the axial force direction, the first order modal frequency is more

than 100 Hz. So, at least ten complete vibration periods can be obtained in 100 ms test time.

In this study, the nominal Mach number of the nozzle is Ma 7.0. The total enthalpy is 2.5 MJ/kg, and the total pressure is 3.0 MPa, which duplicates the flight conditions at about 35 km altitude. The test conditions were monitored by Pitot probes in each run. The free stream is assumed to be in equilibrium, and the parameters were calculated by considering real-gas effects in the stagnation chamber. The angles of attack were set to be −5°, 0°, 5°, 10°, and 14°, respectively. The angle of sideslip was zero. The runs at 5° angle of attack were repeated six times and the runs at other angles of attack were repeated three times in order to study the repeatability precision of force and moment measurement.

3 Results and Discussion

The typical output signals of the balance are shown in Fig. 5, including the axial force, normal force, and pitching moment. It can be seen clearly that the balance signals can be divided into two parts. In the first 30 ms, the signals are irregular, which means that the model undertakes irregular mechanical vibration. This is caused by the unsteady establishment process of the flow field. This unsteady starting process can also be confirmed by the base pressure signals of the model, which are shown in Fig. 6 here. Therefore, the results in this starting process cannot be used to calculate the aerodynamic force and moment.

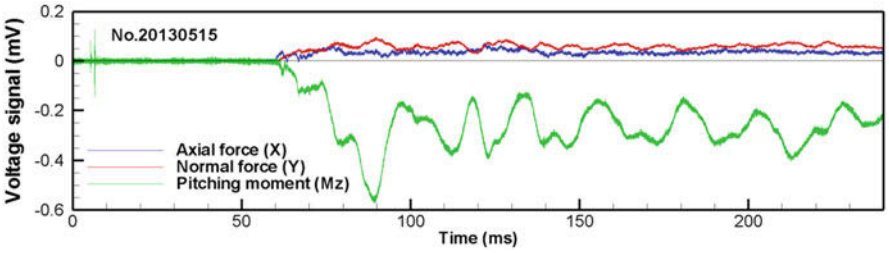

Fig. 5 Balance output signals of JF12 shock tunnel

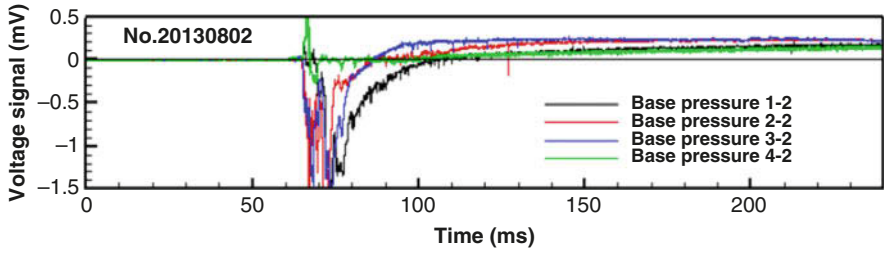

Fig. 6 Base pressure signals of JF12 shock tunnel

After the unsteady starting process, the output signals of the balance become regular, and there are at least three complete periodical cycles within the 100 ms test duration. The forces measured by the balance contain aerodynamic force and inertia force. The inertia force can be easily removed by averaging the balance signals. Therefore, we do not need to use acceleration compensation method to reconstruct the aerodynamic forces and moments. It means that the high accurate data could be obtained with this conventional strain balance by applying simple data processing techniques. As to the axial force, its high frequency oscillations make sure that there are more than ten periodical cycles to achieve high accurate data. The periodicity of the balance signal data from the JF12 shock tunnel indicates that its accuracy could be as high as that of conventional hypersonic wind tunnels.

The normal force coefficients and axial force coefficients at different attack angles are plotted in Figs. 7 and 8. The average results of FD-07, FD-03, and Langley 11-inch conventional low-enthalpy hypersonic wind tunnels are also shown in these figures for comparison [6]. All the JF12 experimental results are plotted in these figures, while only the average results of other wind tunnels are given. First of all, we can find that the force measurement data of JF12 shock tunnel has high repeatability precision. The repeatability error of normal force coefficient is less than $\pm 1.0\%$. The repeatability error of axial force coefficient is less than $\pm 2.0\%$.

From Figs. 7 and 8 we can see that normal force coefficients Cn of JF12 at different angles of attack agree very well with the results of other conventional hypersonic wind tunnels with a discrepancy of less than 1%. The coefficient of

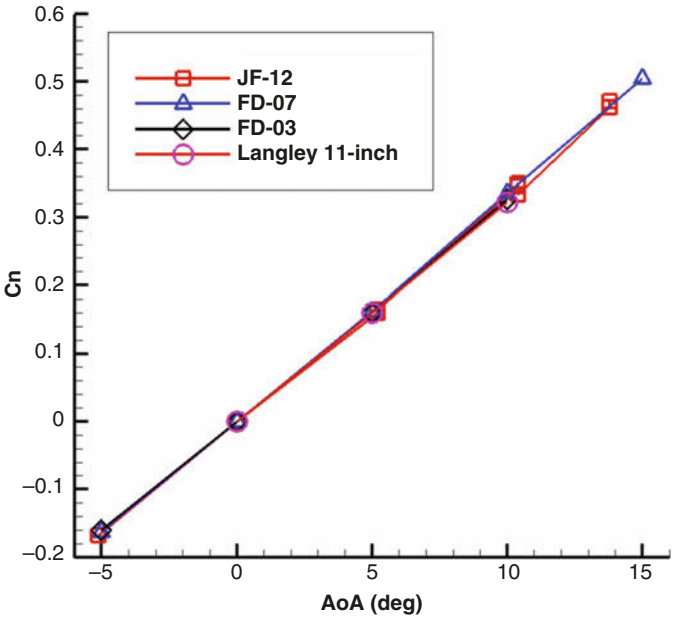

Fig. 7 The normal force coefficients at different attack angles

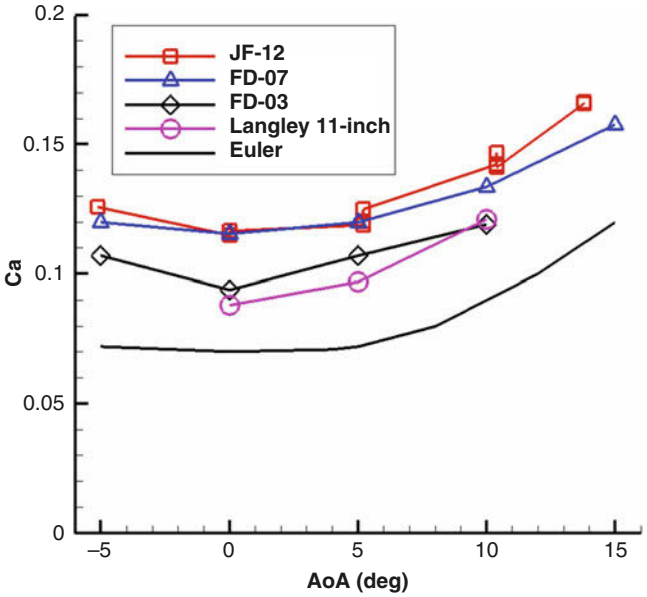

Fig. 8 The axial force coefficients at different attack angles

pressure center Xcp is also in accordance with the theory result of Xcp = 0.6874. The axial force can be divided into two parts: one is the pressure force and the other is the friction force. In Fig. 8, the axial force coefficients calculated by Euler equations are also shown. The difference between the experimental results and Euler results is the friction force coefficients. For the laminar boundary layer, the friction force coefficient is inversely proportional to the square root of the Reynolds number ReL based on the length of the model.

4 Conclusions

Aerodynamic force and moment measurements of a 10° half-angle sharp cone were carried out in JF12 shock tunnel at Mach 7.0 under the duplicated hypersonic flight conditions of about 35 km altitude. The results show that high accuracy force measurement data can be obtained in JF12 shock tunnel. The maximum repeatability error is less than 2%. The experimental results are in good agreement with that of conventional hypersonic wind tunnels. The discrepancy of normal force coefficients between JF12 and conventional hypersonic wind tunnels are less than 1%. These results demonstrate that aerodynamic force measurement by conventional strain balances can be conducted in shock tunnel which has a test time longer than 100 ms.

Acknowledgments The authors would like to thank all members of JF12 research group for their invaluable support. This research was supported by the National Natural Science Foundation of China (No. 11672312, No. 11532014).

References

1. J.J. Bertin, R.M. Cummings, Annu. Rev. Fluid Mech. **38**, 129 (2006)
2. J.R. Maus, B.J. Griffith, K.Y. Szema, J.T. Best, J. Spacecr. Rockets **21**, 136 (1984)
3. C. Park, J. Thermophys. Heat Tr. **11**, 10 (1997)
4. Z. Jiang, H. Yu, AIAA paper 2014-1012, 2014
5. Z. Jiang et al., Chin. J. Theor. Appl. Mech. **44**, 824 (2012)
6. H. Chen, ACTA Aerodynamica Sinica **18**, 345 (2002)

Optimising the X3R Reflected Shock Tunnel Free-Piston Driver for Long Duration Test Times

S. Stennett, D. E. Gildfind, and P. A. Jacobs

Abstract The X3R free-piston reflected shock tunnel is an alternate operating mode of the existing X3 expansion tube facility at The University of Queensland, which has been funded by Australia's Defence Science and Technology Group to provide ground testing capability for the full-scale HIFiRE 8 scramjet engine. Given X3R's origin as an expansion tube, its relatively short driver compared to its shock tube introduces unique design constraints during its condition development process, requiring careful tuning of the free piston to maximise the available test time. This paper details the ideal and equilibrium gas shock interactions required to provide the candidate Mach 7, 50 kPa dynamic pressure nozzle exit flow, the trends that arise as part of the driver composition selection and optimisation process, the free-piston tuning analysis used to maximise X3R's driver supply time given its short driver, and the modelling and analysis of facility operation using one-dimensional computational techniques.

1 Introduction

The supersonic combustion ramjet, or scramjet, is a modern flight engine concept theoretically capable of producing net thrust in the hypersonic regime and is envisioned for future applications in atmospheric hypersonic flight. The expense and risk associated with experimental testing of hypersonic vehicles require the use of ground testing facilities as a repeatable and comparatively inexpensive means to refine vehicle designs and validate expected hypersonic flow phenomena prior to a conclusive experimental flight test. These test flows are typically produced by impulse facilities, which process a test gas to a hypersonic state for a period on the order of micro- or milliseconds, depending on the facility size and type,

S. Stennett (✉) · D. E. Gildfind · P. A. Jacobs
The Centre for Hypersonics, The University of Queensland, St. Lucia, QLD, Australia
e-mail: s.stennett@uq.edu.au

A. Sasoh et al. (eds.), *31st International Symposium on Shock Waves 2*,
https://doi.org/10.1007/978-3-319-91017-8_23

through a sudden, explosive release of energy. While short duration, these test times are sufficient to gather important data about the hypersonic flow interactions of the vehicle.

Following the successful testing of a 1:2.75 subscale HIFiRE 8 scramjet engine in the 'T4' reflected shock tunnel [1], Australia's Defence Science and Technology Group (DST Group) approached The University of Queensland (UQ) to fund the commissioning of an impulse facility capable of testing a full-scale HIFiRE 8 scramjet engine. The facility would provide a nominal Mach 7, 50 kPa dynamic pressure flight condition for a period on the order of 10 ms: a sufficient duration to generate stable flow through the engine length and facilitate investigation of hydrocarbon combustion within the full-scale engine during experimental testing.

2 The X3R Reflected Shock Tunnel Facility

The 'X3R' free-piston reflected shock tunnel is a proposed facility modification [2] to the pre-existing 'X3' free-piston expansion tube [3], which utilises X3's free-piston driver and shock tubes, and adds a new Mach 7 nozzle and test section extension, illustrated in Fig. 1. X3R will be the largest free-piston reflected shock tunnel in Australia and will be capable of housing and testing larger-scale scramjet models than can currently be accommodated by other Australian impulse facilities [2].

Due to its origin as an expansion tube and hardware availability at the time of X3's commissioning, X3R's unique hardware dimensions (Table 1) introduce atypical design difficulties in the pursuit of a long duration HIFiRE 8 operating condition. The combination of relatively short driver tube and long shock tube makes suppling the driver conditions for sufficient duration to drive the downstream shock processes, while delaying the generation of strong expansion waves from the piston face [2], difficult. Careful tuning of the selected free-piston mass is pivotal in producing this long duration, stable test flow.

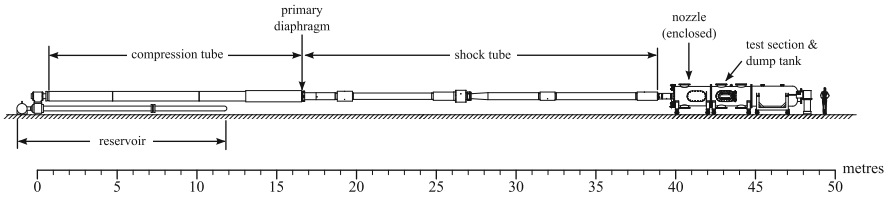

Fig. 1 X3R reflected shock tunnel configuration. (Adapted from Morgan and Gildfind [2])

Table 1 T4 and X3R facility comparison for Mach 7 operation

	Driver tube		Shock tube		Piston mass	Nozzle exit	
	L (m)	D (m)	l (m)	d (m)	m_p (kg)	M	d_e (m)
X3R	14	0.5	22	0.2–0.18	100, 200, 280	7	0.7572
T4	26	0.229	10	0.076	87.5	7	0.2732

3 Gas Composition Effects on the X3R Free-Piston Driver

A tailored perfect-gas operating condition was initially developed using point-process ideal gas reflected shock tunnel theory to investigate the driver composition trends and determine the associated free-piston dynamics and compression requirements, as the first step towards a tuned free-piston driver. Using the desired Mach 7, 50 kPa dynamic pressure nozzle exit condition as a starting point, ideal normal shock relations [4] were applied upstream through the facility's gas states to reverse-engineer the required initial test gas pressure (51.82 kPa) and incident shock velocity (1411 m/s). This analysis was validated using the ideal gas ESTCj [5] and PITOT [6] solvers.

Driver rupture and fill states were derived with respect to helium-argon percentage using isentropic relations [4], indicating the amount of free-piston compression required for the respective driver composition to drive the target incident shock. Higher argon percentages required greater compression to achieve the sound speed and pressure ratios needed to induce the correct shock velocity, and as rupture pressure was fixed for tailored operation (3.1 MPa), the initial driver pressure must be lowered to produce the target compression ratio λ (Fig. 2, left). These trends initially suggested higher helium concentrations were desirable given X3R's limited driver volume, as a longer driver gas slug remains at diaphragm rupture to drive the downstream processes and tailor the contact surface. The higher initial driver pressures and minimal piston compression required by these compositions, however, proved very difficult to tune. Additional factors including the facility's size, the cost of helium and the effect of the addition of orifice plates for piston tuning required the driver composition effects be investigated further before a driver condition was selected.

An ideal gas piston tuning analysis using Hornung theory [7] enabled optimisation of the piston dynamics through selection of an appropriate piston mass, orifice plate and reservoir pressure in order to catch the piston at its 'inflection' point, where it momentarily has zero velocity and acceleration [8]. Inflection requires the piston to do sufficient work to the driver gas that it is decelerated and halted at some point prior to the end of the driver tube, resulting in a transient driver pressure and temperature response following diaphragm rupture. Stalker [9] originally described this transient response with an 'overdrive' parameter, whereby the piston continues to compress the driver gas after rupture to a peak pressure state, which assists in its deceleration, before mass flow to the shock tube dominates the response and pressure is lost. A pressure deviation of 10% was recommended by Stalker as the

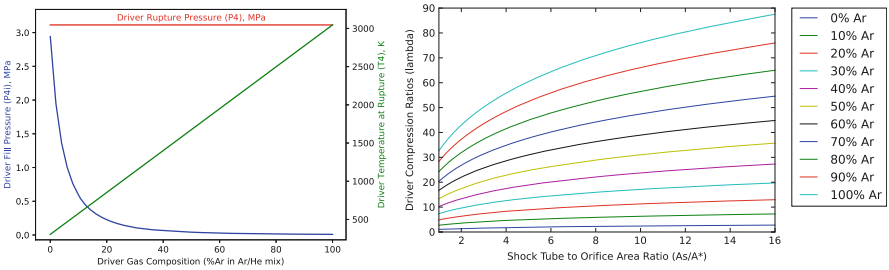

Fig. 2 Driver fill and rupture properties vs helium-argon composition (left) and tailored driver compression ratio vs orifice-plate to shock-tube area ratio (right)

basis of the 'driver supply time': a period where driver gas properties remain within the deviation of the rupture condition.

The implementation of an orifice plate at the primary diaphragm station allowed the piston dynamics to be tuned through control of the rate of driver gas loss to the shock tube. However, the steadily expands the choked driver gas akin to a diverging nozzle [10], requiring the driver rupture conditions be increased sufficiently to compensate for the performance loss through the expansion (Fig. 2, right). For the ideal gas driver conditions, these losses become significant as argon composition increased, requiring the driver to undergo additional compression to compensate for the expansion and further reducing the driver gas slug volume.

Iterative tuning of varying piston masses to achieve 10% overdrive and piston inflection revealed that increasing piston mass produced longer driver supply times. The greater piston mass enabled slower deceleration during the stroke and allowed driver pressures to be maintained for an extended period compared to lighter options.

4 One-Dimensional X3R Facility Modelling

A refined analysis was completed using an equilibrium thermochemical gas model and the target stagnation condition of 8.32 MPa and 2122 K for the T4 HIFiRE 8 experiments [11]. This nozzle supply condition was the basis of the X3R Mach 7 nozzle design, which was based on the original T4 nozzle used to produce an identical outflow condition. Equilibrium thermochemistry modes of ESTCj [5] and PITOT [6] were used to calculate and independently validate the updated shock speed (1427 m/s), initial test gas pressure (66.2 kPa) and driver rupture pressure (4.32 MPa) to generate tailored operation at the target stagnation condition.

The piston tuning analysis was repeated for the equilibrium gas modelled target conditions using X3R's 280 kg piston, by iterating orifice plate diameter and driver rupture conditions to match the target shock speed using PITOT while simultaneously achieving 10% overdrive and piston inflection using Hornung theory. Because

Table 2 Selection of tailored, tuned equilibrium gas helium-argon X3R driver conditions

He:Ar (%)	P_{4i} (kPa)	P_4 (MPa)	T_4 (K)	λ	P_R (MPa)	d^* (m)	t_D (ms)	x_{buf} (m)
10:90	15.3	9.42	3892	47.2	457.7	0.1100	4.52	0.107
30:70	26.5	8.68	3024	32.3	630.0	0.1175	5.79	0.167
50:50	53.8	7.87	2190	19.9	943.0	0.1270	8.00	0.294
70:30	145.0	7.07	1411	10.3	1631	0.1380	12.66	0.648
90:10	765.0	7.00	722.8	3.77	3875	0.1390	27.77	2.332

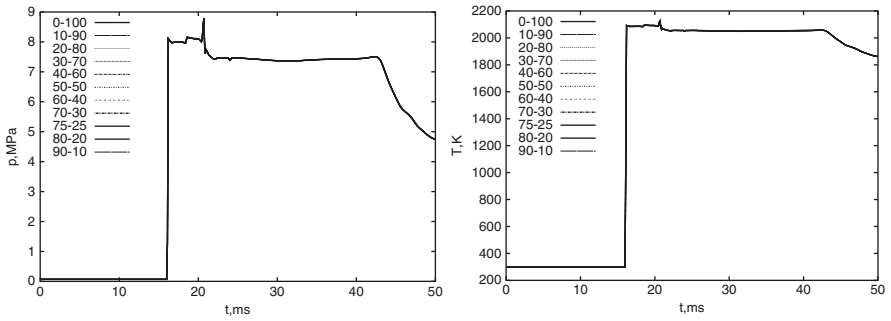

Fig. 3 Stagnation pressure (left) and temperature (right) for fixed driver

the pure helium driver required very little compression, it was not pursued as a free-piston driver option. Table 2 summarises a selection of driver conditions. At higher helium compositions, reduced compression ratios (λ) are required to achieve rupture, producing larger driver gas slugs that can be drained over a longer period using a larger orifice plate (d^*), but the piston must be accelerated quicker, requiring higher reservoir pressures (P_R). The longer stroke extends driver supply time (t_D) and achieves piston inflection earlier, requiring longer buffers (x_{buf}) to catch the piston at inflection. The dominating helium mass fraction at 90% helium partial pressure and above is hypothesised to be the cause of outliers in rupture pressure and orifice plate, but do not arise in Table 2.

Fixed driver and free-piston versions of X3R were simulated using the one-dimensional L1d3 code [12] to investigate the effects of the facility geometry and associated volume limitations on the predicted piston dynamics and operating conditions. The fixed driver model eliminated the free-piston dynamics by setting the full driver volume at the desired rupture conditions and allowed the facility response to be validated independent of the piston response, as if the driver were of an infinite length. From the simulations, it appeared that the conditions had become undertailored, as indicated by the pressure and temperature losses at 21 ms in Fig. 3, requiring respective increases to the driver fill and rupture conditions to correct the tailoring.

The free-piston simulations required large increases in reservoir pressure to match the theoretically predicted driver supply time and peak pressure due to Hornung's simplifying assumptions [7]. Figure 4 indicates that the tailoring-corrected

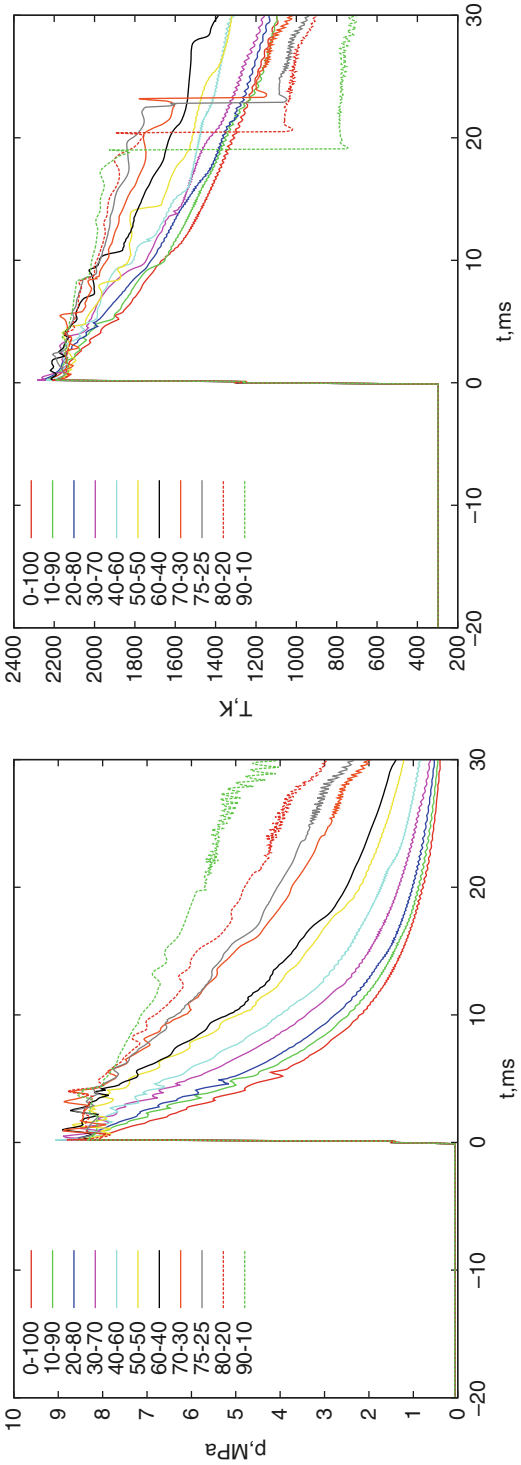

Fig. 4 Stagnation pressure (left) and temperature (right) for tailored, tuned free-piston driver

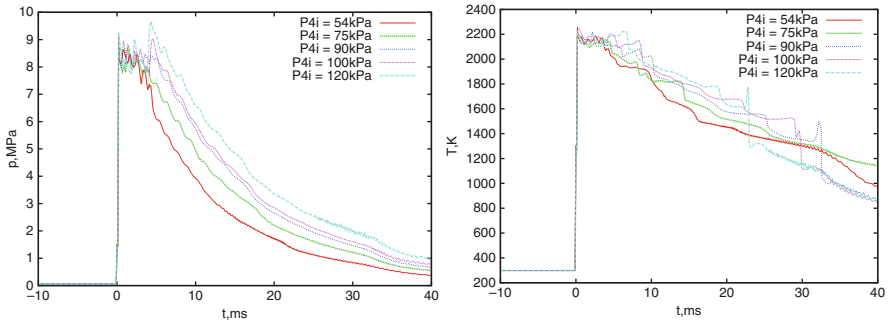

Fig. 5 Overtailoring effects on stagnation pressure (left) and temperature (right) for X3R 50:50 helium-argon driver condition

Table 3 Candidate X3R operating condition for 50:50 helium-argon driver and 280 kg piston

Test gas		Driver gas					Other properties	
P_1 (kPa)	T_1 (K)	P_{4i} (kPa)	T_{4i} (K)	P_4 (MPa)	T_4 (K)	λ	P_R (kPa)	d^* (m)
66.2	298.15	90.0	298.15	8.13	1806.3	14.9	4200	0.141

driver conditions maintained the target stagnation conditions for a maximum of approximately 5 ms, depending on driver composition, before rapid decay of pressure and temperature occurred. Interrogation of the associated x-t pressure contour plots revealed the strong driver expansion waves to be the cause of the step reductions in the condition, which are especially prevalent in the majority argon drivers, due to the large compression ratio and resulting small driver volume.

A candidate 50:50 helium-argon driver condition was selected to simultaneously reduce helium use while achieving the long stagnation hold time. To further increase test time, atypical driver tailoring techniques were applied. Driver properties were iteratively raised to produce increasingly overtailored conditions, in pursuit of an ideal strength compression wave that momentarily cancels the strong expansion waves, delaying condition decay and increasing stagnation hold time (Fig. 5). A driver condition providing 6 ms of hold time was found (Table 3) and selected as the candidate condition for future experimental validation.

A secondary concern of the proposed condition was the long-term piston dynamics. The arrival of the reflected shock at the piston induces a large force upon it, overcoming the residual reservoir pressure and sending it back up the driver tube, preventing its capture. Typically, reflected shock tunnels at UQ implement brakes to prevent upstream motion of the piston, but are currently not included on the X3 280 kg piston due to its expansion tube applications. The simulated candidate operating condition is expected to result in the piston striking the primary diaphragm station at 15 m/s following rebound, but further calibration between the L1d model and facility is required before action can be recommended regarding the piston response.

5 Conclusion

The X3R reflected shock tunnel will be a unique impulse facility which requires a precisely tuned piston at a carefully selected driver condition to maximise available test time. An ideal and thermochemical equilibrium gas analysis of the target Mach 7, 50 kPa dynamic pressure condition was initially completed, before consideration of the free-piston driver options. The relatively low-velocity incident shock (1427 m/s) required to produce the target 8.32 MPa, 2122 K stagnation condition enabled the feasibility of a range of helium-argon driver compositions to be investigated. X3R's relatively short driver requires the use of a slow, heavy piston to maximise driver supply time; however, stagnation condition hold time was limited by the arrival of strong expansion waves from the driver. An overtailored 50:50 helium-argon driver momentarily compensates for the expansions, increasing hold time to 6 ms, while maximising driver volume at rupture and minimising helium use. This condition will be pursued experimentally; to allow computational model calibration.

Acknowledgements This research is supported by the Australian Government's Research Training Program (RTP) and the Cooperative Research Centre for Space Environment Management (SERC Limited) through the Australian Government's Cooperative Research Centre Programme.

References

1. H. Alesi et al., A concept for the HIFiRE 8 flight test, in *22nd ESA Symposium on European Rocket and Balloon Programmes and Related Research*, 2015
2. R. Morgan, D. Gildfind, X3 reflected shock tunnel for extended flow duration, in *The 2014 Asia-Pacific International Symposium on Aerospace Technology*, 2014
3. A. Dann et al., Upgrade of the X3 super-orbital expansion tube, in *18th Australasian Fluid Mechanics Conference*, 2012
4. J. Anderson, *Modern Compressible Flow with Historical Perspective* (McGraw-Hill Education, Boston, 2003)
5. P. Jacobs et al., *Estimation of High-Enthalpy Flow Conditions for Simple Shock and Expansion Processes Using the ESTCj Program and Library*, UQ Mechanical Engineering Report 2011/02, 2011
6. C. James et al., Designing and simulating high enthalpy expansion tube conditions, in *The 2013 Asia-Pacific International Symposium on Aerospace Technology*, 2013
7. H. Hornung, *The Piston Motion in a Free-Piston Driver for Shock Tubes and Tunnels*, GALCIT Report FM 88-1, 1988
8. K. Itoh et al., Improvement of a free piston driver for a high-enthalpy shock tunnel. Shock Waves **8**(4), 215–233 (1998)
9. R. Stalker, A study of the free-piston shock tunnel. AIAA J. **5**(12), 2160–2165 (1967)
10. D. Gildfind et al., Free-piston driver performance characterisation using experimental shock speeds through helium. Shock Waves **25**(2), 169–176 (2015)
11. W. Chan et al., *Flowpath Design of an Axisymmetric Mach 7.0 Nozzle for T4*, UQ Mechanical Engineering Report 2013/02, 2013
12. P. Jacobs, *Using l_script to Define L1d Simulations*, UQ Mechanical Engineering Report 2005/09, 2005

Development of a Total Enthalpy and Reynolds Number Matched Apollo Re-entry Condition in the X2 Expansion Tunnel

T. G. Cullen, C. M. James, R. J. Gollan, and R. G. Morgan

Abstract This paper reports on the development of an expansion tunnel condition based on the peak heating point of the Apollo 4 trajectory. Particular emphasis is placed on replicating the total enthalpy and post-shock Reynolds number of the flow such that representative re-entry heating rates are generated. An analytical state-to-state facility model, PITOT, is used to perform the initial condition design using a secondary driver to increase performance. Deviations from ideal theory are seen when performing initial experiments, and no performance gain was evident using the secondary driver, possibly due to the thick Mylar secondary diaphragm. Nonideal facility performance is assessed and incorporated into the modelling whereupon a condition is chosen that closely matches the desired flow properties.

1 Introduction

Uncertainties in transition location and heating rate through transitional and turbulent boundary layers lead to large safety factors being used in the design of heat shields for atmospheric entry vehicles. Improving the understanding of these phenomena and the numerical modelling used to simulate atmospheric entry flow fields can help to reduce heat shield mass and thus increase payload mass fractions [1]. Particular attention is given to these issues in the design of the Crew Exploration Vehicle [2].

Behaviour within turbulent boundary layers on blunt bodies can be investigated in experimental facilities by observing natural transition or tripping the boundary layer and measuring the heating rates to the surface of the test model. Recent work in HIEST [3] demonstrated a capability to perform experiments within the low enthalpy portion of re-entry trajectories (<6 km/s). Expansion tunnels are uniquely suited to simulating the high enthalpy portion of a vehicles re-entry trajectory

T. G. Cullen (✉) · C. M. James · R. J. Gollan · R. G. Morgan
The University of Queensland, St Lucia, QLD, Australia
e-mail: t.cullen@uq.edu.au

A. Sasoh et al. (eds.), *31st International Symposium on Shock Waves 2*,
https://doi.org/10.1007/978-3-319-91017-8_24

(>6 km/s) since they avoid limitations inherent in reflected and non-reflected shock tunnels. The X series of expansion tunnels, specifically, utilise the free-piston driver technique to generate higher speed flows at reduced test times compared to other facilities. Therefore, data that is unobtainable elsewhere and is complementary to facilities such as HIEST can be generated.

To facilitate such studies, it has been proposed that the use of high-speed infrared imaging could provide additional information on the surface heating rates and would supplement the usual measurement techniques for these investigations. During the development and validation of this type of method for a short duration impulse facility such as X2, a better characterised re-entry flow field involving a laminar boundary layer is suitable. Once the method has been developed and validated, a tunnel condition that produces natural or tripped transition is to be investigated.

This paper discusses the development and initial analysis of an expansion tunnel condition that will produce a re-entry flow field with this laminar boundary layer in the X2 expansion tube facility at the University of Queensland, Australia. The condition to be designed is based on a point on the Apollo 4 trajectory and is considered to provide a representative earth re-entry condition with a laminar boundary layer suitable for this type of preliminary study. In addition, decades of research have led to plentiful data and analyses being available for the Apollo 4 mission. The specific trajectory point is detailed in Ref. [4] and is the point of peak total heating occurring at a mission time of 30,032 s, at an altitude of 60 km and a velocity of 10.3 km/s.

2 Facility Description

A schematic of the X2 expansion tunnel is shown in Fig. 1. The facility is powered by a free-piston driver and for the current work uses a 10.5 kg piston, a primary diaphragm of 2.5 mm thick cold rolled steel, and pure helium driver gas. The shock tube contains dry 79% N_2 and 21% O_2 by volume and is separated from the acceleration tube containing laboratory air by a thin aluminium diaphragm. The

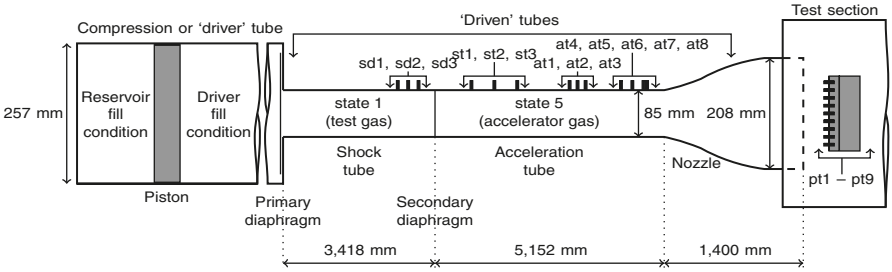

Fig. 1 Schematic of the X2 expansion tunnel facility (not to scale)

shock and acceleration tubes are instrumented with 14 PCB pressure transducers along their length as indicated. A Pitot rake is placed at the outlet of the hypersonic nozzle containing an additional nine transducers housed 17.5 mm apart in 15° cone head caps for the measurement of free-stream pressure. When using a secondary driver, the secondary diaphragm is 25 μm thick Mylar with a burst pressure of 136 kPa, and the tertiary diaphragm is 14 μm aluminium with a burst pressure of 14 kPa. In single-stage driver mode, only the aluminium diaphragm is present.

The facility currently has three driver conditions that each utilise primary diaphragms of differing thickness and driver gas mixtures of argon and helium [5]. These driver conditions, along with the ability to widely vary the initial fill pressures in the remainder of the facility sections, allow for the generation of a vast range of free-stream properties. A more complete and detailed description of the facility is presented in Ref. [5].

3 Test Flow Characterisation

The goal of designing a new facility condition is to obtain a specific set of flow properties near the surface of the model. When simulating planetary entry, these near-surface properties are ideally achieved by replicating the free-stream properties of the trajectory point. However, ground testing generally requires the use of models smaller than their real counterparts, and therefore, the flow field must be appropriately scaled from flight to the laboratory.

The goal of designing this condition around the chosen trajectory point is to produce a laminar boundary layer with a heating rate characteristic of re-entry; therefore, scaling of the total enthalpy and density-length scale is acceptable [6]. It is generally not possible to replicate the flight Mach number in an expansion tunnel due to the significantly higher free-stream temperature of the expansion tunnel test flow. Fortunately, due to the Mach number independence principle, the flow field parameters of interest can be replicated providing the Mach number is sufficiently high and the post-shock Reynolds number is matched [7]. The Apollo 4 free-stream properties are shown along with the post-shock Reynolds number in Table 1. The typical core flow size of the facility is 100 mm; therefore, a scaling factor from flight of 1:39.1 is utilised for density-length scaling.

Table 1 Apollo 4 free-stream and post-shock conditions based on data obtained from Ref. [4]

Parameter	Value	Parameter	Value
Altitude	59,792 m	Total enthalpy	52.2 MJ/kg
Velocity	10,252 m/s	Free-stream Reynolds number	7.44×10^5
Mach number	32.6	Post-shock Reynolds number	4.86×10^4

Direct measurement of the free-stream properties inside an expansion tunnel is difficult, and currently only 15° half-angle cone head pressure measurements are made at the nozzle exit. Static pressure measurements are made at 14 locations along the tube and are able to provide time of flight shock speed estimates. Therefore, the complex flow processes occurring in the expansion tube must be characterised by these limited measurements and an estimate of the test flow properties made.

For this study, the state-to-state analysis tool, PITOT, described in Ref. [8] is used to compute the properties of the various gas states within the facility. This tool is commonly used for condition design at UQ and gives estimates of gas states based on analytical and empirical expressions with typical computation times in the order of minutes. This fast turnaround time is ideal for condition design when one- and two-dimensional modelling can take tens and thousands of CPU hours, respectively.

PITOT uses normal shock relations, steady and unsteady expansion relations, and equilibrium gas chemistry to model the expansion tube processes and is able to account for facility-specific performance in order to provide gas state estimates.

4 Condition Development

4.1 Secondary Driver

For a given driver condition, the total enthalpy that can be imparted to the test gas prior to the unsteady expansion is a function of the shock tube shock speed which itself is a function of the test gas fill pressure. Higher fill pressures result in higher post-shock pressures and a lower test gas enthalpy. Since this condition has both a high enthalpy and pressure requirement, the driver condition capable of producing the strongest shock tube shock of those available is chosen. In addition, performance boosting using a secondary driver is explored.

A secondary driver is an additional tube and diaphragm arrangement placed between the primary driver and shock tubes and typically filled with a monatomic gas such as helium. The purpose of this is to generate post-shock conditions within the secondary driver that can drive a stronger shock through the shock tube than the primary driver could itself [9]. There exists a secondary driver fill pressure, for each shock tube fill pressure, at which the secondary driver delivers a maximum shock tube shock speed. Since the purpose of the secondary driver is to increase the shock tube shock speed, this is the ideal point of operation.

PITOT is used to model the facility across its operational envelope and computes the model post-shock properties at varying fill pressure combinations. The operational envelope of the facility consists of the combination of shock tube and acceleration tube fill pressures between 1 kPa and 14 kPa and 1 Pa and 600 Pa, respectively. For each combination of fill pressures, the secondary driver pressure is chosen so that it operates at its maximum performance. Figure 2 compares the test model post-shock properties, as computed by PITOT and normalised by their

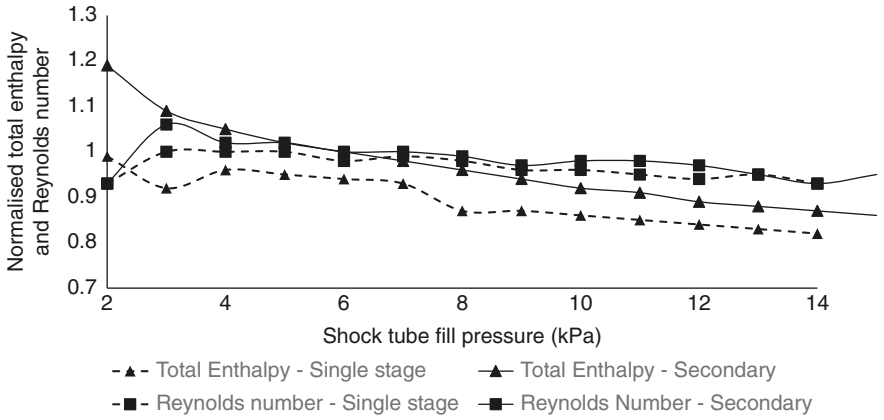

Fig. 2 Comparison of single-stage and secondary drivers

Table 2 Example of deviation of tunnel performance from theoretical predictions

Parameter	Theory	Experiment	Units
Secondary driver fill pressure	103	103 ± 1	kPa
Shock tube fill pressure	4.0	4.0 ± 0.02	kPa
Acceleration tube fill pressure	580	580 ± 1	Pa
Secondary driver shock speed	5763	5710 ± 50	m/s
Shock tube shock speed	6326	6020 ± 20	m/s
Acceleration tube shock speed	8427	7480 ± 70	m/s
15° Cone head pressure (kPa)	215	147 ± 22	kPa

target values, produced with both a single-stage driver and a secondary driver. The secondary driver outperforms the single-stage driver with respect to enthalpy by a consistent 10% while maintaining a similar Reynolds number; therefore, this configuration will be utilised going forward.

After the operational envelope has been computed for the secondary driver configuration, several experiments are run that span this envelope. An example result from one of these experiments is shown in Table 2, where the shock speeds are compared to values predicted by PITOT. The secondary driver shock speed matches well, while the shock tube and acceleration tube shock speeds differ significantly from the predictions. It should be noted that the difference in the cone pressure is a culmination of all upstream differences and is expected to be large. These deviations are due to well-known issues with expansion tunnels including diaphragm effects [10], Mirels effects [11], and non-geometric nozzle area ratios due to boundary layer growth.

To account for these deviations PITOT can perform a reflected shock at a diaphragm of specified strength to capture diaphragm effects, over-expand the test gas to a specified pressure to account for Mirels effects, and steadily expand the test gas through a specified effective nozzle area ratio to account for deviations

Table 3 Fill pressures and estimated model post-shock conditions for single-stage driver

Parameter	Value	Parameter	Value
Shock tube fill pressure	3000 pa	Free-stream temperature	5100 K
Acceleration tube fill pressure	250 pa	Free-stream pressure	28 kPa
Total enthalpy	48 MJ/kg	Free-stream velocity	8500 m/s
Post-shock Reynolds number	4.8×10^4	Free-stream Mach number	5.8
Test time	$\sim$200 μs	Free-stream Reynolds number	8.5×10^5

due to boundary layer growth. It is important to note that the accuracy of these model changes is limited and is simply a means to quantify the macroscopic effect on the flow of each of these phenomena such that an estimate of the flow properties can be computed. The modelling changes required to account for these deviations differ slightly across the operational envelope of the facility; therefore, they are computed and applied only in the region of the envelope surrounding the experiments performed. Once these deviations have been accounted for, the operational envelope can be computed once again. The set of fill pressures that produce the post-shock conditions closest to those desired can then be chosen.

4.2 Single-Stage Driver

Due to the performance of the secondary driver being less than predicted, the chosen condition was run experimentally without the secondary driver to assess performance of the single-stage arrangement compared to the two-stage arrangement. It was found that the shock tube shock speed between the two configurations was identical, demonstrating that for this set of pressures, the secondary driver had no performance gain or loss. Since the incorporation of a secondary driver reduces test time [9] and here provides no performance increase, it is of interest to instead develop a single-stage driver condition. This single-stage driver condition is developed in the same way as the previous condition, and the chosen fill pressures and resulting test flow properties are shown in Table 3.

Figure 3 presents the centre-line free-stream pressure trace measured at the nozzle exit for the chosen condition. Shock arrival is signified by a sharp increase in the initially low test-section pressure. A further rise followed by a reduction to a steady pressure level is evident and is characteristic of the nozzle start-up process. A region of approximately steady pressure of 120 kPa ($\pm$10%) indicative of test time exists for approximately 200 μs after which the pressure then starts to increase as the unsteady expansion flow moves through.

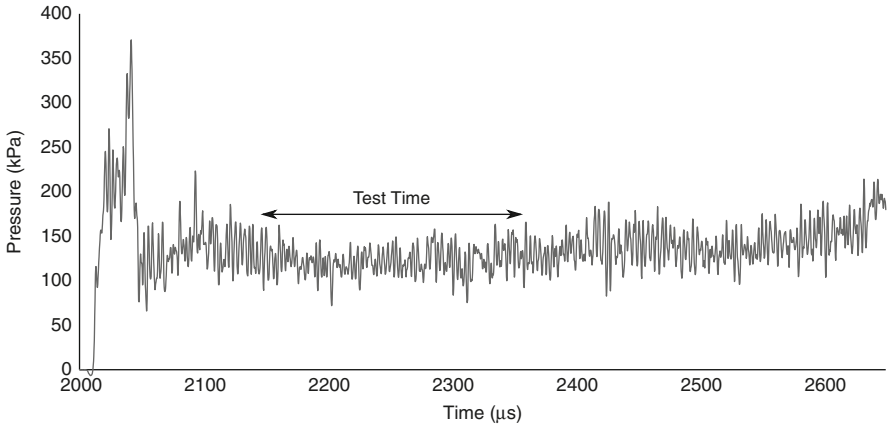

Fig. 3 Centre-line 15° half-angle cone head pressure trace at nozzle exit

5 Conclusions

This paper has detailed the development of a representative re-entry condition in the X2 expansion tunnel which replicates the Apollo 4 peak heating trajectory point at a scale of 1:39.1. Conditions such as these with a total enthalpy on the order of 50 MJ/kg and matched post-shock Reynolds number represent the unique contribution made to ground testing by expansion tunnel facilities. It has been shown that a performance increase was unable to be achieved here with the addition of a secondary driver. Consequently, the condition that can be achieved has slightly lower enthalpy than the desired flow condition; however, the post-shock Reynolds number is matched correctly. Ongoing work will include the detailed analysis of this condition using one- and two-dimensional computational fluid dynamics simulations to characterise the test flow in time and space. The developed condition, coupled with this analysis, will be used to develop and validate the use of high-speed infrared imaging in the X2 expansion tunnel.

Acknowledgements The first author would like to acknowledge the support of the Cooperative Research Centre for Space Environment Management (SERC Limited) through the Australian Government's Cooperative Research Centre Programme. This research is also supported by an Australian Government Research Training Program (RTP) Scholarship.

References

1. J.J. Bertin, R.M. Cummings, Fifty years of hypersonics: Where we've been, where we're going. Prog. Aerosp. Sci. **39**(6), 511–536 (2003)
2. B.R. Hollis, Blunt-body entry vehicle aerotherodynamics: Transition and turbulent heating. J. Spacecr. Rockets **49**(3), 435–449 (2012)

3. H. Tanno, T. Komuro, K. Sato, K. Itoh, Aeroheating measurements on capsule model with roughness in high enthalpy shock tunnel HIEST, in *2014 Asia-Pacific International Symposium on Aerospace Technology*, Shanghai, 24–26, September 2014
4. R.C. Ried Jr, W.C. Rochelle, J.D. Milhoan, *Radiative heating to the Apollo command module: Engineering prediction and flight measurement*, NASA TM X-58091, 1972
5. D.E. Gildfind, *Development of High Total Pressure Scramjet Flow Conditions Using the X2 Expansion Tube*, Ph.D. Dissertation, Centre for Hypersonics, University of Queensland, St Lucia, Queensland, Australia, 2012
6. H.G. Hornung, 28th Lanchester memorial lecture – *Experimental real-gas hypersonics*. Aeronaut. J. **92**(920), 379–389 (1988)
7. D. Kliche, C. Mundt, E.H. Hirschel, The hypersonic Mach number independence principle in the case of viscous flow. Shock Waves **21**(4), 307–314 (2011)
8. C. James, D. Gildfind, S. Lewis, R. Morgan, Implementation of a state-to-state analytical framework for the calculation of expansion tube flow properties, 2017, submitted to Shock Waves (2016)
9. D.E. Gildfind, C.M. James, P. Toniato, R.G. Morgan, Performance considerations for expansion tube operation with a shock-heated secondary driver. J. Fluid Mech. **777**, 364–407 (2015)
10. M. Wegener, M. Sutcliffe, R. Morgan, Optical study of a light diaphragm rupture process in an expansion tube. Shock Waves **10**(3), 167–178 (2000)
11. H. Mirels, Test time in low-pressure shock tubes. Phys. Fluids **6**(9), 1201–1214 (1963)

Liquid-Coupled Dual Piston Driver for Small-Scale Impulse Facilities

S. O'Byrne, R. McCormack, and H. Kleine

Abstract This paper describes initial visualisation experiments performed using a novel small-scale impulse facility, driven by two liquid-coupled pistons to provide rapid compression of gas in the driver tube and a sufficiently small shock tube diameter to not require a diaphragm. The facility is designed to be able to investigate the heat transfer behaviour of rapidly compressed gases at small physical scales. We present the design of the facility, comparison between predicted and measured piston motion and high-speed schlieren imaging of the resultant subsonic jet, using carbon dioxide as the test gas. The piston speed and displacement were much smaller than expected, due to the fit of the o-rings on the lower piston to the inner bore of the compression tube being too tight to allow free movement of the lower piston.

1 Introduction

1.1 Motivation and Previous Studies

Most impulsive shock tube or shock tunnel facilities are designed to be used at a relatively large scale, with diaphragms used to separate the driver and test gases [1]. For such facilities, it can typically be assumed that the flow is inviscid, as the diameter of the tubes is much greater than the thickness of the boundary layer. This is certainly not the case, however, when the tubes are very narrow, say on a millimetre scale. Flow through such capillary tubes driven by elevated temperatures and pressures is important in the study of micro-scale combustion and other chemical reaction systems [2], and it is therefore of interest to develop a device capable of driving such flows. For such a device to be useful in diagnostic development, it is also highly desirable for it to have a relatively short cycle time.

S. O'Byrne (✉) · R. McCormack · H. Kleine
University of New South Wales, Canberra, ACT, Australia
e-mail: s.obyrne@adfa.edu.au

A. Sasoh et al. (eds.), *31st International Symposium on Shock Waves 2*,
https://doi.org/10.1007/978-3-319-91017-8_25

Studies on shock propagation through capillaries have been performed using an externally generated shock wave passing through a capillary tube [3], but not by using compression to generate a pressure increase in the capillary itself. Small-scale hand-driven shock tunnel facilities like the Reddy tube have been designed [4] and tested [5] to be capable of producing hypersonic flows, but like conventional shock tubes, they require diaphragms to be burst for their operation. Also, for the hypersonic version of this facility, the shock tube diameter was some 30 times larger than the device presented here.

2 Design of the Device

The analytical and computational modelling of this small impulse facility was described first in [6], so these details will not be presented again here. A cross-section schematic of the facility is shown in Fig. 1. The main differences between this design and previous designs for small facilities are the use of a pair of pistons of different diameters, coupled using hydraulic fluid, and the use of disc spring washers to store the energy used to displace the coupled piston system.

By using a pair of fluid-coupled pistons, a relatively large force and small displacement on the larger piston can be transmitted to a smaller piston, accelerating it rapidly over a larger distance. If, as is the case here, the ratio of the diameters of the driver tube to the test gas 'shock' tube is large, then the compression process can be made rapid in comparison to the choked mass flux through the small-diameter 'shock' tube. This removes the need for a diaphragm and allows the device to potentially be used as a reciprocating facility, with a very short reload time.

The disc washers provide an easily controllable way to vary the displacement of the large piston: additional springs can be added to increase the stroke length of the upper piston. In this case, each of the 12 DS-100504 spring washers should deflect under the 28 kg load by 0.30 mm according to [7], upon which the calculations in the DIN 2092 standard for disc spring washer design [8] are based. In the current design, the load produces a more than 75% deflection of each disc spring. The disc springs are placed back-to-back, with the large radius contacting the lower inner surface of the piston and a spacer connected to the base plate of the device. This orientation of the springs increases the total displacement while keeping the stress-strain behaviour constant. Therefore the expected deflection of the piston upon firing should be approximately 3.6 mm. This, in turn, should increase the displacement of the upper piston by a factor determined by the square of the ratio of diameters of the two tubes containing the pistons. In this case, the upper piston should be displaced by 9 times the displacement of the lower piston, or 32.4 mm, neglecting the back pressure from the compression of the gas in the compression tube. If the piston were to travel this distance, starting 45 mm below the inlet to the shock tube and including the effect of the 45 mm long, 2 mm diameter cross tube used for the gas inlet, the volume would decrease by a factor of 3.25. Assuming adiabatic compression and negligible mass loss through the shock tube, the maximum CO_2 plenum pressure

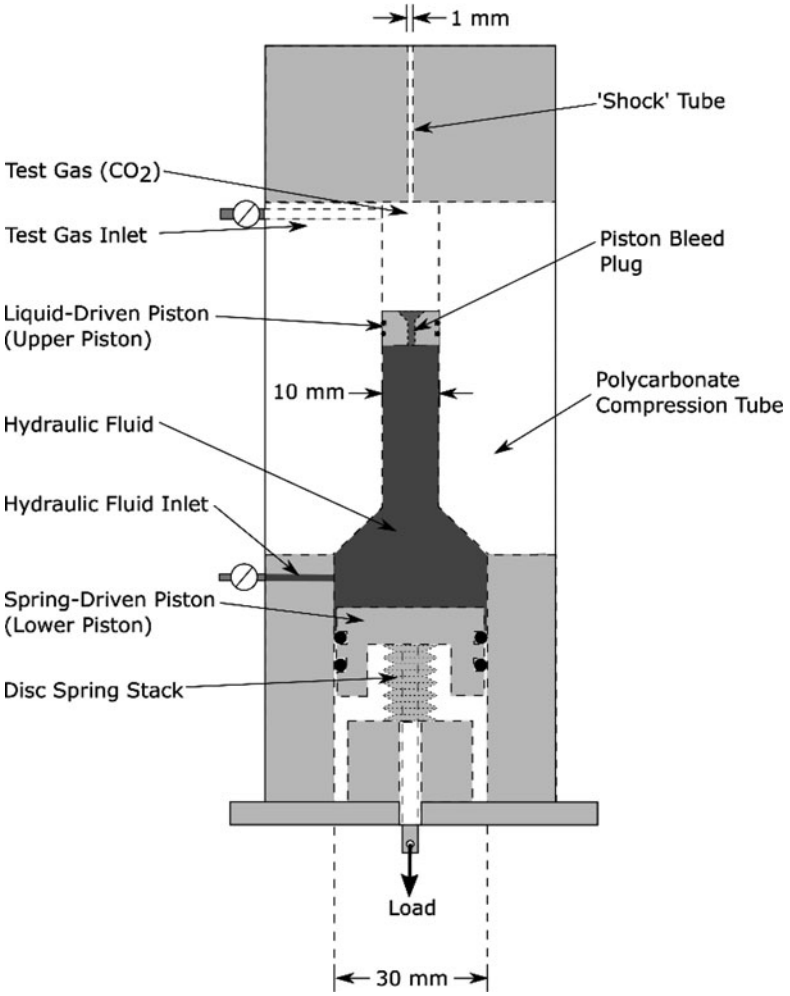

Fig. 1 Schematic of the facility (not to scale)

theoretically achievable would be approximately 4.5 times the initial pressure. The actual compression would be lower than this because of the back pressure on the piston balancing the spring force before the end of the stroke.

To determine the motion of the upper piston, the non-shaded portion of the compression tube in Fig. 1 was made from clear polycarbonate. We denote the smaller tube the 'shock tube', as it is analogous to the shock tube in a larger free-piston shock tube facility, although the viscous flow attenuation is too great at these conditions for a shock to be produced in this tube. This tube had a 1 mm diameter and 50 mm length, to ensure that the flow in the tube was fully developed laminar flow.

The experiments presented here were all performed using CO_2 initially at ambient pressure, exhausting from the top of the 'shock' tube, although the system has been designed to have a dump tank at the exit of the tube, allowing an arbitrary pressure gradient to be established in the 'shock tube'. Such a pressure gradient can be used to either accelerate or decelerate the flow in the tube.

2.1 Flow and Piston Motion Imaging System

The flow was visualised with an omnidirectional schlieren technique (circular cutoff) and recorded at speeds of up to 100,000 frames per second (fps) with a frame exposure time between 200 ns and 500 ns. The two spherical mirrors in the Z-type schlieren system have a focal length of 2.628 m. A Shimadzu HPV-X2 high-speed camera that provides 128 frames with 400 $\times$ 250 pixels resolution was used to generate the time-resolved image sequence. With the given recording speeds, the process was visualised for 1.28 ms. The light source was a commercial powerful photo flash (Metz CT4) that could provide sufficient illumination for about 1.5 ms. The chosen recording settings ensure that the initial phase of the jet generation, including the possible establishment of an expanding shock wave in the vicinity of the jet, could be captured.

The compression tube was filled with CO_2 gas for these experiments, to provide a stronger refractive index gradient than would occur for air flow. The use of CO_2 as the test gas provided a clearer visualisation over the very short radial extent of the jet.

2.2 Device Tests

For these preliminary device tests, the springs were compressed by means of a set of masses weighing 28.0 kg, tied using twine to the rod holding the disc springs in place under the piston. The test was initiated by cutting the twine. The imaging system was triggered using a light gate interrupted by the twine. The voltage rise on the light gate that occurs when the string is cut and falls through the gate generates the trigger signal that initiates the video capture. A total of five tests were run on the system, and the velocities of the piston and jet were reasonably consistent between all tests.

3 Results

3.1 Piston Motion

A second Shimadzu HPV-1 high-speed camera was used to investigate the motion of the upper piston, and selected images are presented in Fig. 2. The camera was operated at 16,000 frames per second, with an exposure time of 8 μs. As can be seen in the final image in the sequence, although some displacement of the piston was measured, the maximum displacement was only 0.36 times the 13.3 mm piston height, which is significantly less than the design displacement. This behaviour was reasonably consistent between runs of the facility. Upon further investigation, it was found that while the upper piston was free to move, the o-rings sealing the lower piston to the larger of the two cylindrical spaces in the two-piston compression system were very tight. The friction limited the motion of the lower piston to around 0.54 mm, possibly due to stretching of the o-rings used to make the seal rather than translation of the o-rings along the tube. No significant leakage of oil was apparent around either piston, and while there are certain to be losses associated with the constriction, these should not be great enough to cause the measured reduction in piston displacement.

3.2 Imaging of the Gas Jet

Figure 3 shows the development of the plume as a function of time at delay times of 0, 0.64 and 1.28 ms after the mass was released. The dark rectangle in the lower right of the image is the shadow of a cap screw used to affix the shock tube to the Perspex compression tube section. Initially, there is no disturbance in the flow, and then a fairly laminar jet begins to form as shown in the frame with the 0.64 ms delay.

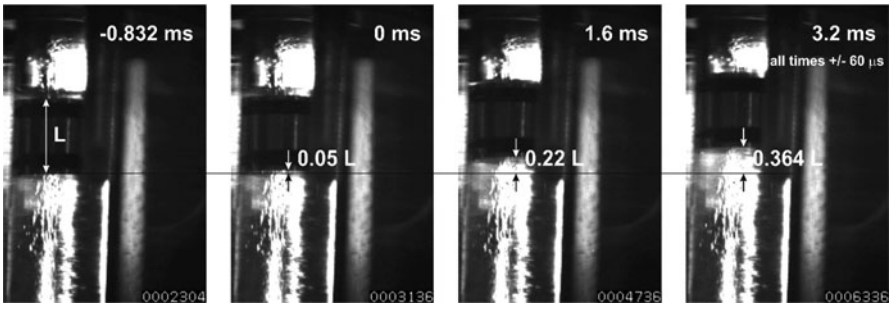

Fig. 2 Video stills showing piston displacement

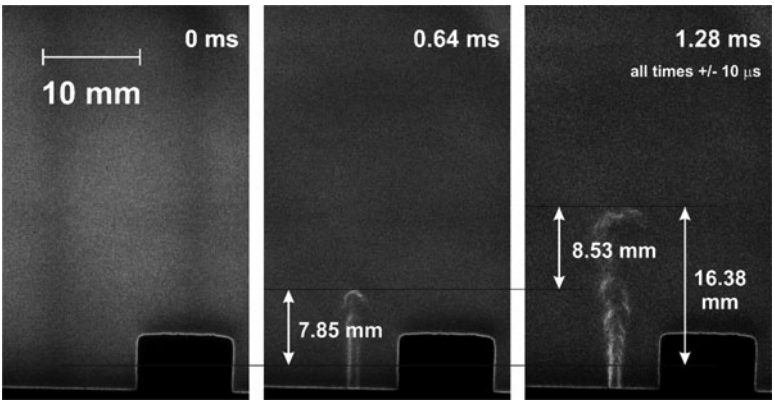

Fig. 3 Video stills showing jet development

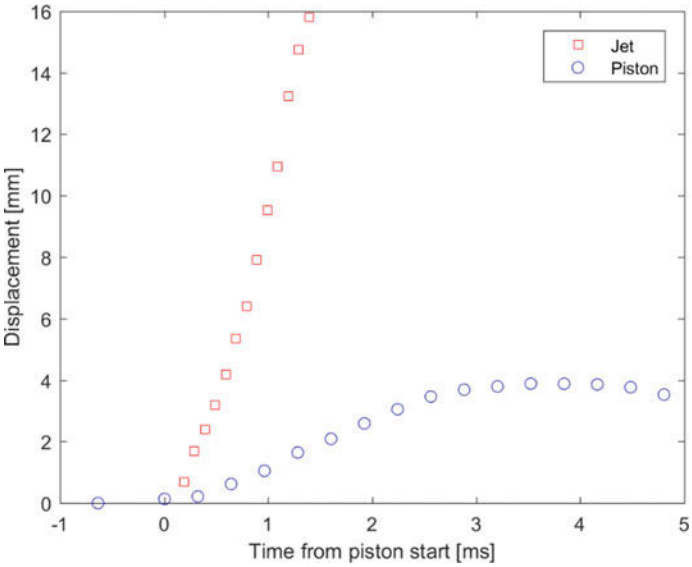

Fig. 4 Displacement plots for jet and piston

This jet begins to become less stable and forms a plume, which propagates upwards towards the top of the image. The motion of the piston shown in Fig. 3 was seen to be consistent over several runs of the facility.

Figure 4 shows the displacement of the top of the jet and the piston as a function of time for a characteristic run of the facility. The jet has a roughly uniform velocity of 13 m/s, while the piston moves much more slowly, having a peak speed of around 1.5 m/s. For a frictionless system, a force balance analysis like that described in [6] would indicate the expected piston velocity should be around 40 m/s.

The curves show that the jet has propagated to the top of the field of view of the image well before the piston reaches the point of maximum displacement, so the piston continues to drive the CO_2 gas jet from the bottom to the top of the image. It is also clear from Fig. 4 that the piston achieves maximum compression in the plenum region around 3–4 ms after the large piston is released and, after achieving a stable position for 1.5 ms, begins to be pushed backwards by the elevated pressure in the compression tube. The maximum displacement in this image is slightly smaller than that shown in Fig. 2, because the plot was obtained for a different run of the facility.

4 Conclusions and Future Work

A small-scale spring-driven diaphragmless impulse facility intended for the study of small-scale high-velocity flows has been designed and constructed. The use of two pistons of different diameters coupled with hydraulic fluid allows a small displacement of the larger piston to drive a much larger and faster displacement of the upper piston. At the small scales investigated with this facility, the flow in the 'shock tube' portion of the facility is typically subsonic. By imposing a pressure differential across the shock tube, using a dump tank placed at the end of the 'shock tube', we can potentially use the device to investigate the effect of slip for flows at high Knudsen numbers. This facility has potential for applications in microscale combustion and heat transfer.

For the measurements presented here, it was apparent that the motion of the lower piston was restricted by friction on the o-ring, producing a smaller displacement of the upper piston than would be predicted by a force balance analysis. A looser fit on the o-ring seal will help to improve the speed of the flow. In spite of this, the facility was able to produce a pulse of CO_2 gas at a speed of around 12 m/s after exhausting from the 50 mm long tube. This jet was clearly visible and consistent for all the tests of the system, and the high-speed video indicated that the head of the jet propagated with relatively constant speed over 2 ms, only slowing down a little as the plume reached the top of the visible part of the flow field.

References

1. A.G. Gaydon, I.R. Hurle, *The Shock Tube in High-Temperature Chemical Physics* (Chapman and Hall, London, 1963)
2. R. Arun, K. Heuy, S. Toshiaki, Open J. Fluid Dyn. **2**, 235–241
3. J. Giordano, J. Parisse, L. Biamino, J. Devesvre, P. Perrier, Phys. Fluids **22**(061703), 1–4 (2010)
4. C. Kumar, J. Reddy, Experiments in hand-operated, hypersonic shock tunnel facility. Shock Waves **26**(6), 845–849 (2016)

5. K. Reddy, N. Sharath, Curr. Sci. **104**(2), 172–176 (2013)
6. R. McCormack, Development of a Diaphragmless, Miniature, Liquid-Piston Shock Tube. in *55th AIAA Aerospace Sciences Meeting*, 2017, p. 2010
7. J.O. Almen, A. Laszlo, Trans. ASME **58**(4), 305 (1936)
8. DIN 2092:2006-03, *Tellerfedern – Berechnung* (Beuth, Berlin, 2006)

Initial Testing of a 2 m Mach-10 Free-Piston Shock Tunnel

Junmou Shen, Handong Ma, Chen Li, Xing Chen, and Bi Zhixian

Abstract A large-scale free-piston shock tunnel has been built in China Academy of Aerospace Aerodynamics (CAAA). The diameter of the nozzle exit is 2 m and the length is 12.4 m. The large-scale free-piston shock tunnel is called FD-21, which employed three running modes, such as conventional shock tunnel running mode, high-enthalpy shock running mode, and long-time running time mode. Conventional shock tunnel had finished to debug in 2016, which could provide fine flow quality. Calibrated rake and sharp cone model had been measured. High enthalpy shock runing tube is driven by free piston, which is been operating and soon will be accomplished. Next, the main structure of the FD-21 should be changed, shock tube will be divided into two parts, and third diaphragm will be installed between the two parts.

1 Introduction

To achieve the Mach number simulation, the conventional hypersonic wind tunnel increase the Mach number by reducing the temperature of the free stream. In this case, the actual fight velocity is significantly larger than the free stream velocity which high Mach number can be achieve in the tunnel [1]. When the Mach number of the vehicle is more than 9 or its velocity is more than 3 km/s [2], the kinetic energy of the flow is so large enough that high-temperature real air effects such as vibrational excitation, dissociation, and even ionization of the fluid molecules when the flow past the hypersonic velocity. The high flow velocity and subsequently the high-temperature real air effects are not duplicated in "cold" hypersonic wind tunnel.

To simulate the high-temperature real air effects, it is necessary to employ the "hot" wind tunnel, namely, high-enthalpy wind tunnel. High enthalpy can be obtained by raising the total internal energy or the total temperature of the test gas, such as arc-heated or combustion-heated tunnel and shock tunnel [3]. If the strength

J. Shen (✉) · H. Ma · C. Li · X. Chen · B. Zhixian
China Academy of Aerospace Aerodynamics, Beijing, China

A. Sasoh et al. (eds.), *31st International Symposium on Shock Waves 2*,
https://doi.org/10.1007/978-3-319-91017-8_26

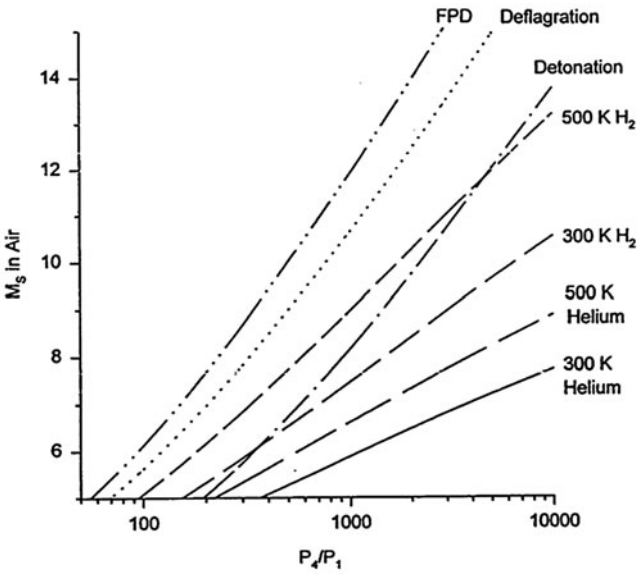

Fig. 1 Summary of primary shock speed performance for the different driven options [4]

of shock is enough strong, the shock tunnel can produce very high temperature and pressure.

The method for producing the shock wave is a major consideration, because it could determine the achievable total enthalpy and pressure level. There are some different techniques for increasing the incident shock strength, for instance, lighter gases driver, heated light gases driver, combustion-heated light gases driver, and free-piston driver. A comparison of the performance about the incident shock speed is reproduced from the reference in Fig. 1. The free-piston driver offers the greatest performance and operational flexibility among the different drivers [4]. The free-piston shock tunnels [5–8] such as T4, T5, HEG, and HIEST have already proven to be a superior technique for generating high-enthalpy flow. Here, to obtain high total enthalpy and total pressure, a large-scale free-piston shock tunnel (FD-21) is built.

Nowadays, the FD-21 is the largest-scale free-piston shock tunnel in the world. The free-piston shock tunnel was proposed by Stalker [9] in the 1960s, and the tunnels are referred to as Stalker tubes.

2 High-Enthalpy Free-Piston Shock Tunnel (FD-21)

FD-21 is a free-piston-driven shock tunnel in CAAA. The overall length of FD-21 is 170m, and it weights 600t. Figure 2 shows the schematic of FD-21. The compression tube is inserted between the secondary reservoir and the main diaphragm station,

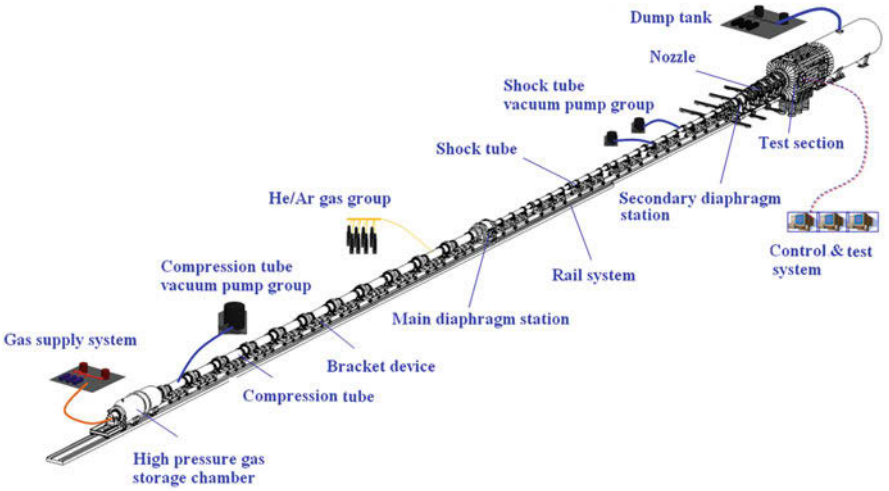

Fig. 2 Schematic of the high-enthalpy shock tunnel (FD-21)

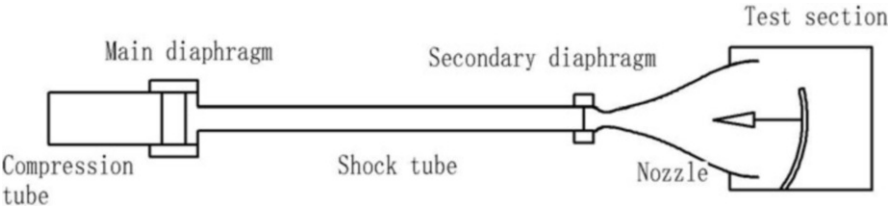

Fig. 3 Schematic of conventional shock tunnel's running mode

which has the length of 75 m and the diameter of 0.668 m. The shock tube is 32 m long with the diameter of 0.29 m. The diameter of nozzle exit is 2 m and the length is 12.4 m.

To monitor the shock speed, some pressure sensors are installed on the shock tube. From the data of pressure sensors, total enthalpy and total pressure could be obtained. In this test, the conventional shock running mode is chosen; Fig. 3 describes the schematic of conventional running mode. In this running mode, the length of compression tube is 13.5 m and the shock tube is 32 m.

When the FD-21 runs by conventional shock tunnel running mode, and there in no piston. The pressure of the compression tube is 10 Mpa, and the pressure of the shock tube. The evaluation of the free stream conditions in the test section of the FD-21 is performed by numerical analysis; at the same time, rake and sharp cone are used to calibrate free stream.

Table 1 The position of the pressure sensors

case	st1	st2	st3	st4	st5	st6
Distance(m)	4.00	8.00	16.00	28.00	29.50	30.70

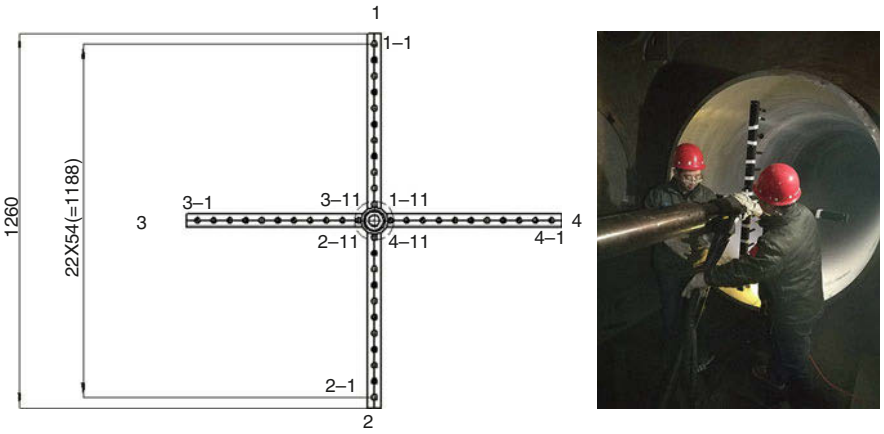

Fig. 4 FD-21 calibration rake-design drawing (*left*) and rake equipped with Pitot pressure transducers (*right*)

2.1 Nozzle Reservoir Condition

The nozzle reservoir temperature and pressure are obtained to compute with one-dimensional analysis of input parameters. The relevant input parameters are measured by shock speed and the nozzle reservoir pressure.

Several pressure sensors are put on in shock tube, and Table 1 shows the position of the sensors. Piezoresistive pressure transducers are manufactured by Kulite.

If the compress of compression tube is 10 Mpa and the shock tube is 50 KPa, the reservoir pressure is 1.89 MPa and the reservoir temperature is 1150 K.

2.2 Free Stream Condition

Based on the nozzle reservoir conditions, the free stream is subsequently determined by numerical simulation of the nozzle flow and calibration rake. A modular cross arm calibration rake is designed and manufactured. It could be employed to the detailed calibration of the test section. On this calibration rake, Pitot pressure, static pressure, and stagnation point heat transfer can be measured (Fig. 4).

An attempt is made to design a contour nozzle which uses the method of characteristics to obtain the uniform flow at the nozzle exit. The system of governing equations is discretized by a cell-centered finite volume method. We adopt Roe's flux difference splitting method [10] to evaluate inviscid numerical fluxes. The cell

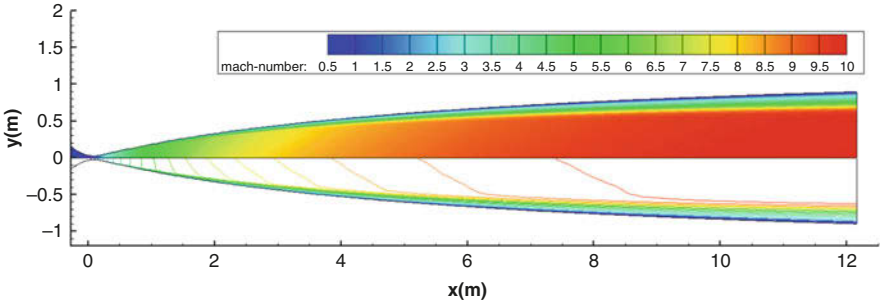

Fig. 5 Mach number contour

Fig. 6 Schlieren image

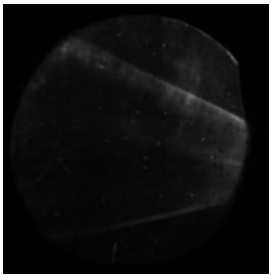

boundary values are used to evaluate the numerical fluxes which are obtained by the second-order MUSCL approach [11]. The discretized governing equations are integrated in time by the third-order Runge-Kutta method. Figure 5 shows the Mach number contour of the computational results.

For the pressure and temperature of free stream is very low, the air may be congealed. So a test is achieved in other shock tunnel which the stagnation condition and nozzle exit number are the same with the FD-21 condition. The free stream isn't congealed (See Fig. 6) in the low pressure and temperature, which the pressure is 46 Pa and the temperature is 54 K in the nozzle exit.

To examine the uniformity of nozzle flow, four measurement positions are distributed along the nozzle centerline at the test section. These distance from these pistions to the nozzle exit is x = 0 mm, x = 300 mm, x = 600 mm, x = 1000 mm, respectively. Figure 5 shows the Pitot pressure distribution when x is located in nozzle exit, namely, x = 0 mm. Numerical results and experimental data are compared in Fig. 7. By measuring the pitot pressure, the corresponding Mach number is deduced from the normal shock wave relation. Figure 7 shows the Mach number results obtained by flow field calibration are consistent with primary design. Numerical results agree with the experimental data.

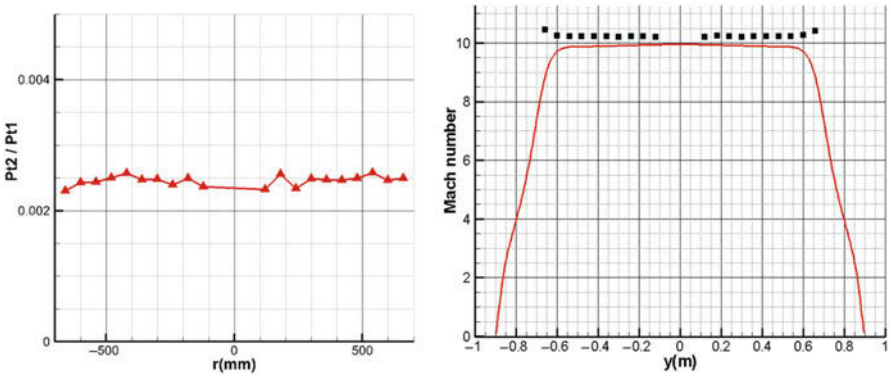

Fig. 7 Flow field calibration results P_{t2}/P_{t1} (left) and Pitot pressure corresponding to Mach number (right)

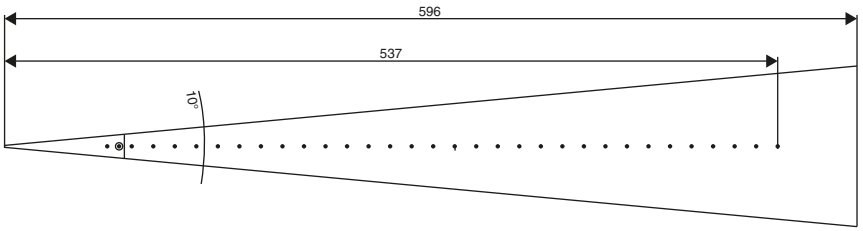

Fig. 8 Schematic of the sharp cone

2.3 Calibration of Flow Stream Quality

At the same stagnation condition, to verify the flow quality, a cone with a half angle of 5 degrees and a length of 590 mm is designed and manufactured and is shown in Fig. 8. Many sensors are installed on sharp cone which measured the heat flux. Figure 9 shows model in wind tunnel. Two test conditions are employed, namely, the angle of attack is 0° and 10°. For heating measurement, measurement results conform to the flow principle.

3 Conclusion

A large-scale free-piston shock tunnel has already built up in 2016 in CAAA. Three operation modes are designed to serve for the hypersonic tests. The conventional shock tunnel running mode which it has no piston has been validated at Ma = 10, and the calibration of the moderate- and high-enthalpy modes are performing.

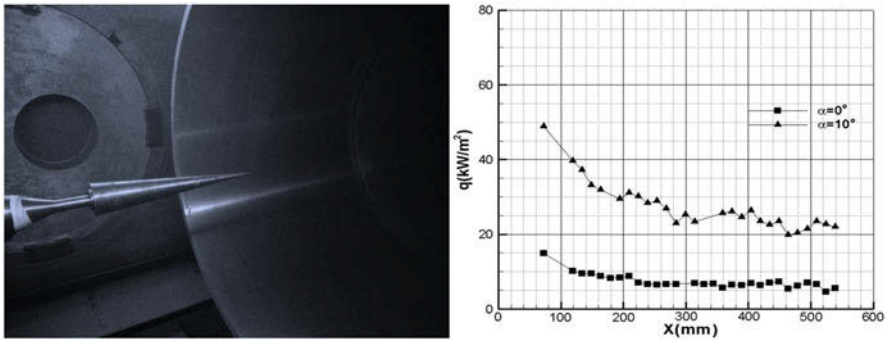

Fig. 9 The cone model installed in the test section (left) and heating measurement data (right)

The mechanism of the high-enthalpy flow should be analyzed for the debug of the FPST so that some problems, such as the numerical simulation of high-enthalpy flow in the shock tube, the parameters at the exit of the high-enthalpy nozzle, and the affection of the driver gases' contamination to the running time, could be solved in the future.

References

1. H.G. Hornung, Experimental hypervelocity flow simulation, needs, achievements and limitations, in *First Pacific International Conference on Aerospace Science and Technology*, Tainan, Taiwan, 1993
2. F.K. Lu, D.E Marren, *Advanced Hypersonic Test Facilities*. ISBN 978-7-5165-0955-5 (2002)
3. W.C. Moseley, J.C. Martino, *Apollo Wind Tunnel Testing Program Historical Development of General Configurations*, NASA TN D-3748 (1996)
4. R. J. Bakos, J.I. Erdos, Options for enhancement of the performance of shock-expanison tubes and tunnels, AIAA Paper 95-0799 (January 1995)
5. R.J. Stalker, Modern development in hypersonic wind tunnels. Aeronaut. J. **110**, 21–39 (2006)
6. H.G. Hornung, Performance data of the new free-piston shock tunnel at GALCIT, AIAA 92-3943 (1992)
7. G. Eitelberg, T.J. McIntyre, High enthalpy shock tunnel in Gottingen, AIAA 92-3955 (1992)
8. K. Itoh, S. Ueda, Design and construction of HIEST (High enthalpy shock tunnel), in *Proceedings of the International Conference on Fluid Engineering*, vol. 1 (JSME Press, Tokyo, 1997), pp. 353–358
9. R.J. Stalker, A study of the free-piston shock tunnel. AIAA J. **5**(12), 2160–2165 (1967)
10. P.L. Roe, Approximate Riernann solvers, parameter vectors, and difference schemes. J. Comput. Phys. **43**, 357–372 (1981)
11. B. Van Leer, Toward the ultimate conservative difference scheme. V. A second order sequel to Godunov's method. J. Comput. Phys. **32**, 101–136 (1979)

CFD Evaluation and Experiment Test of the Running Time of the Ludwieg Tube Quiet Wind Tunnel

Junmou Shen, Ying Zhang, Dan Wang, Ruiqu Li, and Jian Gong

Abstract The running time of the hypersonic Ludwieg tube quiet wind tunnel is very important to simulate the quiet flow field in the test section, which could contribute to rational utilization of the limited available time and affect the confidence coefficient of the data in the hypersonic transition experimental investigations. Thus, more knowledge on that processes could help to understand the running mode of the Ludwieg tube quiet tunnel and the propagation principle of the expansion wave series. To verify our computational method, the same parameter of the BAM6QT (the Boeing/AFOSR Mach-6 quiet tunnel at Purdue University) is used to compute, and it is agreed with our computational results. At the same time, the Mach4 of the nozzle is designed and built; the time of the flow stream is calibrated.

1 Introduction

Ludwieg tube is one type of the impulse tunnel, which is based on the expansion waves travelling upstream through the driver tube [1]. A fast-open valve is settled downstream of the test section and separates the high-pressure test gas. After the valve opens, the shock wave and the expansion wave come into being and run upstream and downstream, respectively. The expansion waves travel through the test section and nozzle and go into the drive tube finally. In the drive tube, the expansion wave series will reflect between the upstream end of the driver tube and the contraction of the nozzle.

A Ludwieg tube with a quiet nozzle has a bleeding slot. Ludwieg tube quiet wind will provide quiet flow field; the boundary layer of the nozzle maintains laminar. The quiet flow field for the investigations on the hypersonic transition is supplied by the highly polished nozzle with a bleeding slot, which is located in the subsonic section upstream of the throat of the nozzle.

J. Shen (✉) · Y. Zhang · D. Wang · R. Li · J. Gong
China Academy of Aerospace Aerodynamics, Beijing, China

A. Sasoh et al. (eds.), *31st International Symposium on Shock Waves 2*,
https://doi.org/10.1007/978-3-319-91017-8_27

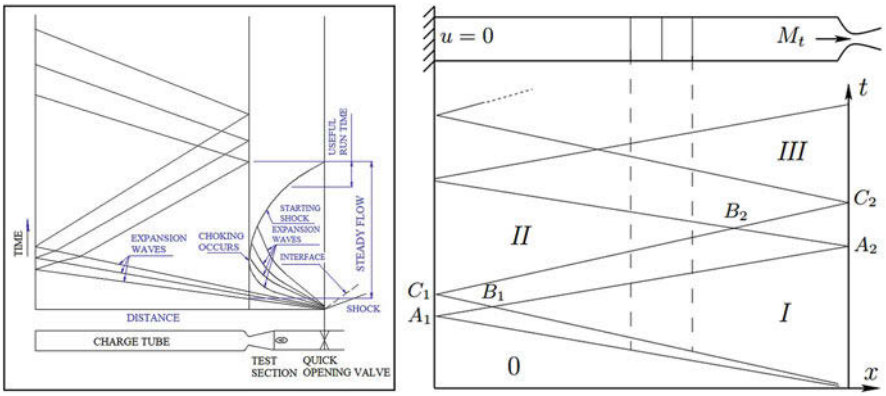

Fig. 1 Wind tunnel running process [3]

Because of the low operational cost and good flow quality, a Ludwieg tube quiet wind tunnel is a right alternative to ground-based experimental facility for hypersonic flow. During the running status of a Ludwieg tube quiet wind tunnel, no mechanism is necessary to control the temperature and pressure, so the tunnel can be described as an "intelligent" blowdown facility [2]. In the driver tube upstream of the nozzle, the expansion wave series will reflect between the upstream end of the drive tube and the throat, as highlighted in Fig. 1. The running time of the Ludwieg tube is generally defined as the time of the expansion wave periodic reflection in the drive tube, and if the wall boundary layer in the driver tube slowly thickens, the effective running time could be several period reflection processes of the expansion waves. The expansion wave travels up and down the driver tube, which creates a constant steady flow.

Computational fluid dynamics (CFD) will be used to simulate the flow from the valve through the test section of the Ludwieg tube with quiet tunnel. Of course, the numerical analysis on the running processes of the unsteady flow field in the Ludwieg tube with a quiet nozzle is a preliminary estimation, and the relative investigation in details would be performed.

2 Computational Methodology

2.1 Governing Equations and Numerical Methods

The governing equations are the axisymmetric compressible Navier-Stokes equation, the continuous equation, the energy conservation equation, and the state equation.

The system of governing equations is discretized by a cell-centered finite volume method. We adopt Roe's flux difference splitting method [4] to evaluate inviscid

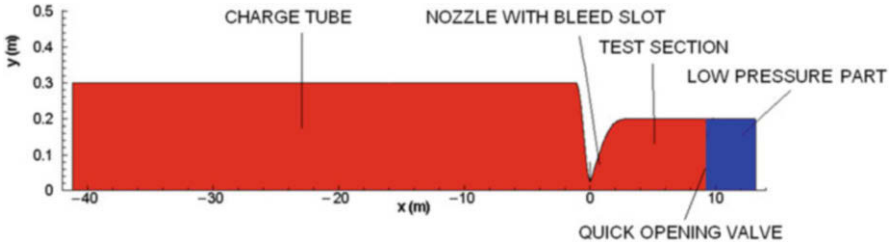

Fig. 2 Computational area system

numerical fluxes. The cell boundary values are used to evaluate the numerical fluxes which are obtained by the second-order MUSCL approach [5]. The discretized governing equations are integrated in time by the third-order Runge-Kutta method. The stepping time is 5×10^{-5}.

2.2 Computational Domain and Initial Conditions

The computational domain consists of high-pressure (a driven tube, a contoured nozzle with bleed slot, the test section) and low-pressure part. Namely, this domain is split into two parts: high-pressure part and low-pressure part (see Fig. 2). The quick opening valve is located between high-pressure part and low-pressure part.

Firstly, to verify our computational method, the same parameter of the Boeing/AFOSR Mach-6 quiet tunnel (BAM6QT) at Purdue University is used to compute. The BAM6QT at Purdue University is a blowdown facility which is designed as a Ludwieg tube. The charge tube is 37.4 long, and its diameter is 444.5 mm. The exit Mach number is 6, and the exit diameter is 240 mm.

Secondly, we design a new Ludwieg tube quiet tunnel. The regions include the drive tube with the length of 40 m and its diameter of 0.6 m, the nozzle with the length of 4.425 m, the exit Mach number of 6 and the exit diameter of 0.4 m, the bleeding slot with its gap width of 3.7 mm, the test section with the length of 6 m and the diameter of 0.4 m, and the diffusion section with the length of 4 m and the same diameter as the test section. The size of the Ludwieg tube is close to the BAM6QT in Purdue University. The initial pressure is 1 MPa, and the initial temperature is 450 K. The fast-open valve in the diffusion section is simplified as one diaphragm so that the opening of the valve could be assumed as an instant operation. See Fig. 2. The minimum grid size is 10^{-5} m in each grid direction, and the total grid points are 17,1200 points.

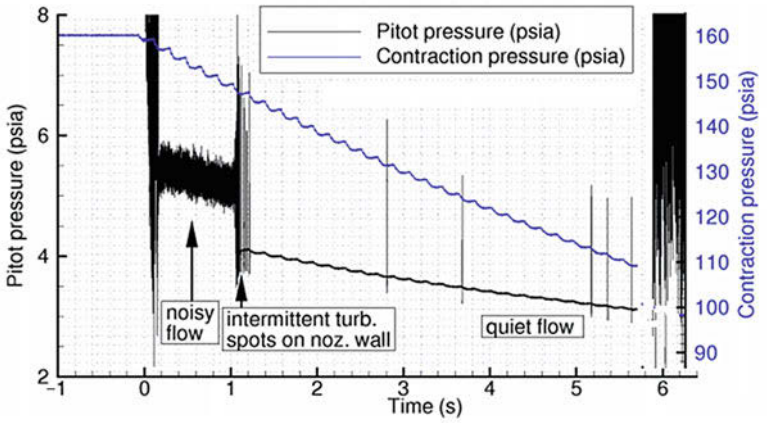

Fig. 3 Sample of contraction pressure [7]

2.3 Computational Results

To accurately acquire the computational modeling of the Ludwieg tube quiet tunnel [6], we had to compare experimental results to our results. The test results of BAM6QT at Purdue University could be inquired. Figure 3 shows the stepwise change of pressure as measured at the contraction wall [7, 8]. When the quick opening valve starts, an expansion wave travels upstream through the test section into the charge tube. There it reflects forth and back and changes the state of the air each time it passes. From the theory of expansion wave spread speed, the flow condition in the test section changes approximately 200 ms when the waves reaches the nozzle. Figure 4 shows a pressure trace computed and recorded during unsteady flow with an initial pressure of 145 psia. When the running time was $t = 0.8$ s, the nozzle exit Mach achieved the design demand. It agrees with the test results of BAM6QT.

When the computational method is verified, the calculation of the new design Ludwieg tube quiet tunnel was underway. Figure 2 shows the new design. Figure 5 shows the pressure versus time along the axis center line for different locations. The initial pressure P4 is 1 MPa; P is local static pressure. At the running time $t = 0$ s, when the quick opening valve just opens, the expansion waves will start to upstream and lower the pressure gradually. The flow condition in the test section changes to approximately 200 ms, which is equal to the time of the expansion wave periodic reflection. The nozzle exit Mach number versus time was shown in Fig. 6. The running time of the tunnel is about 6 s, expansion waves could pass through the nozzle into the charge tube. At this point, expansion waves will reflect at nozzle expansion part, and a shock wave system forms, which resulted in the exit Mach number magnified momentarily.

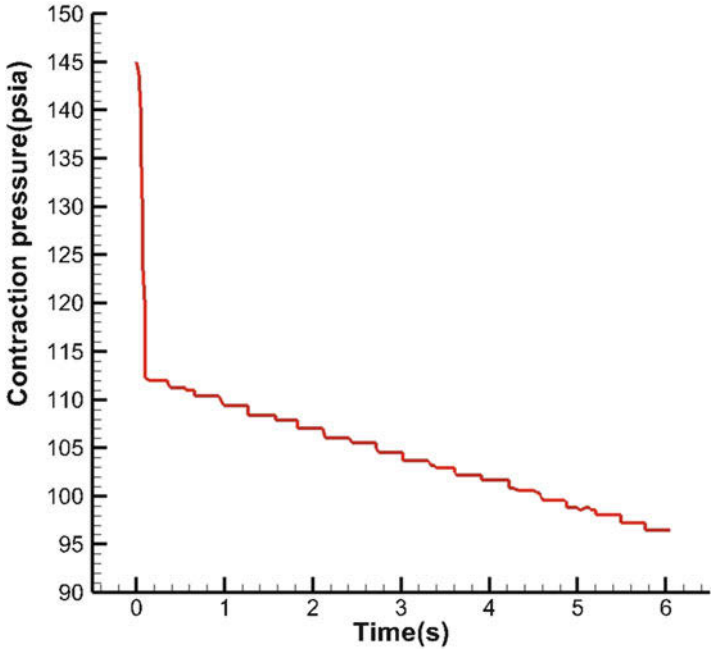

Fig. 4 Sample evaluation of contraction pressure

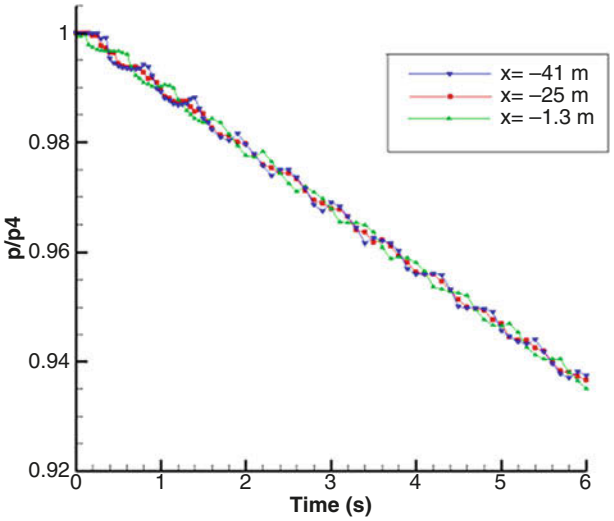

Fig. 5 The pressure of the charge tube

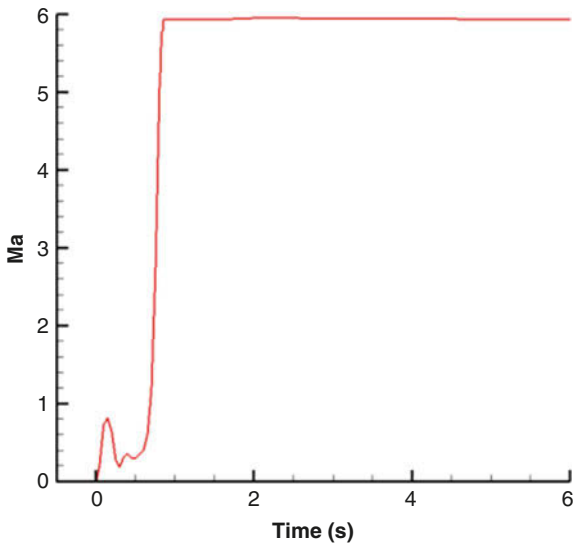

Fig. 6 The nozzle exit Mach number

When the quick opening valve switches on, the gas will flow in the wind. However, the new reflected shock will be formed in the nozzle expansion part, and the gas velocity is depressed within the short scope of time. From 0.3 s to 0.85 s, the Mach number gradually rises until the design index is achieved. When the running time t is 0.85 s, the nozzle exit Mach number achieved the design demand (see Fig. 7). At this same time, the streamlines superimposed with Mach number contours for flow are shown in Fig. 8. The bleed slot is located in upstream of the nozzle throat, and its field is quite complex.

The Mach number contour, resulting from a computation using the assumption that an ideal nozzle expansion is established, is shown in Fig. 9.

3 Experimental Test

3.1 Mach4 of the Nozzle Is Designed and Built

In order to prevent the air condensation, the Mach number is 6 in the test section whose driven section needs to heat. However, a large warm-proof device is time-consuming and high cost. For reducing the risk and studying the supersonic Ludwieg tube quiet wind, Mach4 of the quiet nozzle is designed and built. The diameter of the nozzle is 0.2 m. The Mach4 of the nozzle is inserted into a shock tube, which is made up of supersonic Ludwieg tube quiet wind. The shock tube has a length of 30 m, and the diameter is 0.13 m. The initial pressure of the driven tube is 1 MPa, and the initial temperature is 288 K. Before the nozzle is built, a lot of calculation

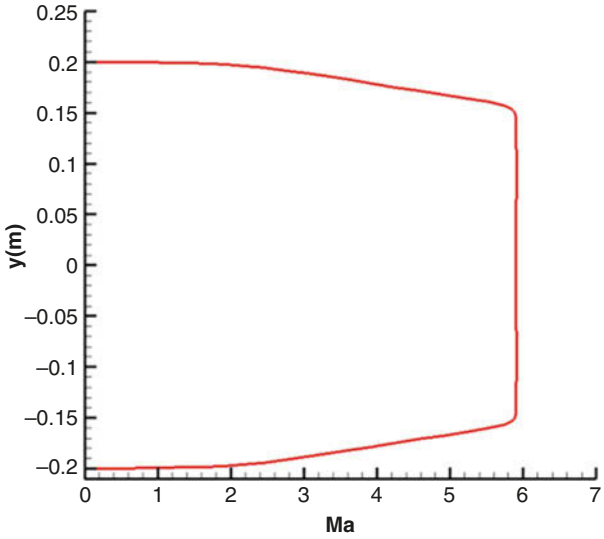

Fig. 7 Mach number contours of the nozzle exit

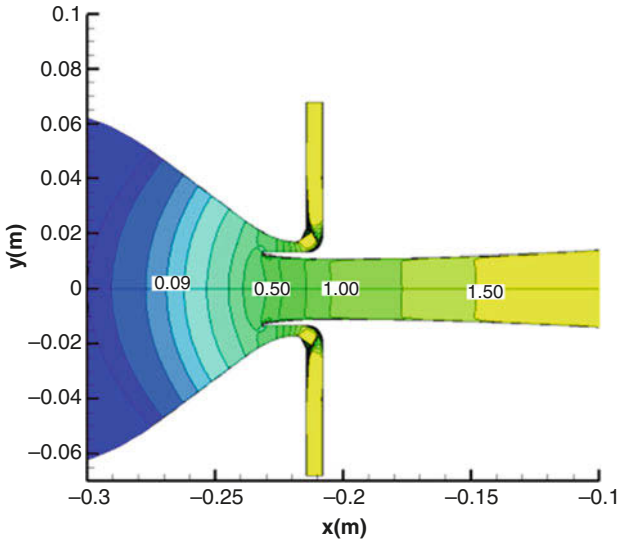

Fig. 8 Mach number contours of the bleed slot

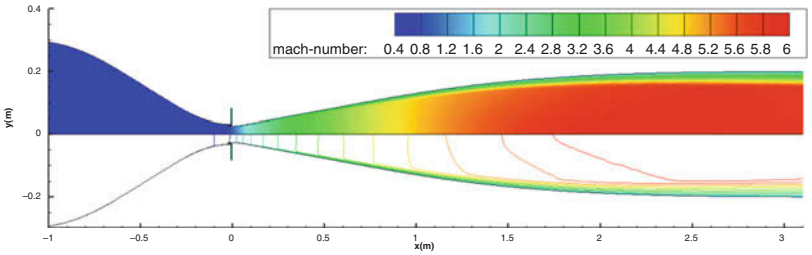

Fig. 9 Mach number contour for quiet nozzle flow

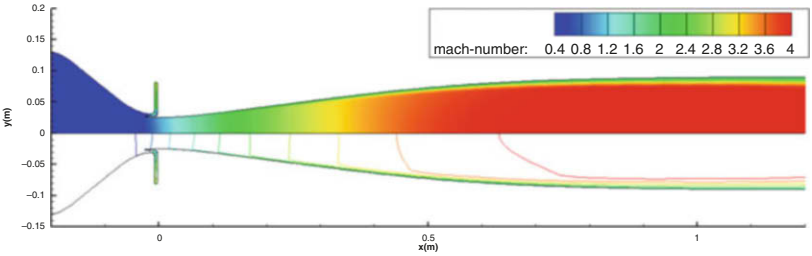

Fig. 10 Mach number contour for quiet nozzle flow

work has been finished. The minimum grid size is also 10^{-5} m in each grid direction, and the total grid points are 154,300 points. Figure 10 shows the numerical result of Mach number contours.

3.2 Quiet Flow Platform

It should be noted that March4 of quiet nozzle is chosen in the present operating condititon, for the the air of charge tube doesn't need to heat. To guarantee machining precision and the degree of finish, the nozzle is divided into five parts and is shown in Fig. 11. Its whole floating structure included shock tube, quiet nozzle, and test section. When quick opening valve or double diaphragm section which puts in downstream of the nozzle is running, the shock wave and the expansion wave come into being and run upstream and downstream, respectively. The expansion waves travel through the test section, throat, and into the driven tube finally. In the driven tube upstream of the nozzle, the expansion wave series will reflect between the upstream end of the driven tube and the throat.

The running time of the Ludwieg tube is generally defined as the time of the expansion wave periodic reflection in the driven tube, and if the wall boundary layer in the driven tube slowly thickens, the effective running time could be several period reflection processes of the expansion waves. The result shows that the running time

Fig. 11 Quiet flow calibrated platform

is more than 3 s. For the vacuum of the test section is less than 6 m3 and the driven tube is not enough large, the available running time is restrained when the pressure of the test section is more than the back pressure.

4 Conclusion

The study demonstrates the running process of unsteady flow in hypersonic Ludwieg tube quiet tunnel, which could describe the starting and sustaining process of a Ludwieg tube quiet tunnel. The present of the computational study indicated starting time to be approximately 0.85 s and the running time to continue about 6 s. The quiet flow field starting time of the BAM6QT at Purdue University is about 1 s, and the running time is about several seconds [9, 10]. The increase in starting process time and the running time is due to different sizes and the viscous effects (normal shock wave/boundary layer interaction near the nozzle exit). The flow condition in the test section changes to approximately 200 ms, which is equal to the time of the expansion wave periodic reflection.

In order to reduce the risk and studying the supersonic Ludwieg tube quiet wind, Mach4 of the quiet nozzle is built and tested. The result shows that the running time is more than 3 s and the Ludwieg quiet tunnel could be testified to continue several seconds.

References

1. H. Ludwieg, Der rohrwindkanal. Z. F. Flugwis. **3**(7), 206–216 (1955)
2. G. Koppenwaller, Hypersonic flow simulation in Ludwieg tube, in *International Symposium on Recent Advances in Experimental Fluid Dynamics*, IIT Kanpur India, 2000
3. H. Ludwieg, *Tube Wind Tunnel a Special Type Blowdown Tunnel*, AGARD Report 143 (1957)
4. P.L. Roe, Approximate Riernann solvers, parameter vectors, and difference schemes. J. Comput. Phys. **43**, 357–372 (1981)

5. B. Van Leer, Toward the ultimate conservative difference scheme. V. A second order sequel to Godunov's method. J. Comput. Phys. **32**, 101–136 (1979)
6. S.P. Schneider, *A Quiet Flow Ludwieg Tube for Study of Transition in Compressible Boundary Layers: Design and Feasibility*, Final report for NASA grant number NAG-1-1133. Period covered by report: 1 May 1990 to 1 May 1991 (1991)
7. S.P. Schneider et al., *High-Reynolds-Numbers Laminar Flow in the Mach-6 Quiet Flow Ludwieg Tube*, AIAA Paper 2006-3056 (June 2006)
8. S.P. Schneider, *Towards High-Reynolds-Number Quiet Flow in Hypersonic Wind Tunnels*, AD-FA9550-06-1-0182 (February 2009)
9. S.P. Schneider, *Initial Shakedown of Purdue Mach-6 Quiet-Flow Ludwieg Tube*, AIAA 2000-2592 (April 2000)
10. S.P. Schneider, The development of hypersonic quiet tunnels, in *37th AIAA Fluid Dynamics Conference and Exhibit*, 25–28, 2007

Development and Performance Study of Shock Tube with Extended Test Time for Materials Research

Jayaram Vishakantaiah, Gowtham Balasubramanian, and Subba Rao Keshava

Abstract This work focuses on the development of three unique types of high vacuum shock tubes for materials research. Shock tubes of various types such as simple material shock tube (MST), with extension (MST-E) and with reduction (MST-R) are studied. The major aim of this paper focuses on the augmentation of test time (t_{IE}), reflected shock pressure (P_5), and temperature (T_5) and to get an ideal shock strength for material interaction. The simple MST has a 2.1 m driver and 5.1 m driven sections of inner diameter 80 mm, MST-E has a driver extension of 2.3 m long, and MST-R is equipped with an area reduction at the end of the driven section having a convergent nozzle for shock focusing with an addition of 1.2 m long tube. All the experiments are performed with air as a test gas at 1.0 bar. The experimental results show a variation of t_{IE} of about 10% between the simple MST and MST-E. The MST-R shows an increase of P_5 and T_5 of about 60% and 15%, respectively, in the presence of air. Experimental results are compared with the 1-D normal shock relations (NSR) and KASIMIR software for validation. The results also show about 10–40% discrepancy between experiments and the various tools in all configurations. The experimental and theoretical results of all the three shock tube configurations are discussed in this paper.

1 Introduction

Simple shock tubes are employed as a research tool for producing shock waves since a century, followed by the invention of the first free piston driven shock tube (FPST) to generate high enthalpy shock waves [1]. From the past one decade, our Shock Induced Materials Chemistry Laboratory (SIMCL), Bengaluru, India,

J. Vishakantaiah (✉) · G. Balasubramanian
Shock Induced Materials Chemistry Laboratory, SSCU, Indian Institute of Science, Bengaluru, India
e-mail: jayaram@sscu.iisc.ernet.in

S. R. Keshava
Haldipur Hydraulieks, Bengaluru, India

A. Sasoh et al. (eds.), *31st International Symposium on Shock Waves 2*,
https://doi.org/10.1007/978-3-319-91017-8_28

is involved in developing unique shock tube facilities to study the interaction of strong shock wave with different forms of materials. Shock tubes are used as ground test facilities for various applications like aerospace, chemical kinetics, materials research, etc. In recent years shock tubes are used in materials research to study homogenous (gas-gas) and heterogeneous (gas-solid) interactions in millisecond timescales. The reaction time, pressure, and temperature of the shock-heated test gases play a major role to understand the aerothermodynamic reactions occurring on the surface of reentry space vehicles. To overcome the effects of non-ideal pressure and temperature in shock tubes, additional techniques such as driver inserts, driver extensions, etc. are also used [2, 3]. Some researchers also tried to increase the shock strength by focusing the shock waves using a convergent nozzle at the diaphragm station [4] and parabolic reflectors [5, 6] and also by focusing shock waves in water [7].

In this paper we present different configurations of shock tubes to increase the test time, reflected shock pressure, and temperature to study the material interaction with the shock-heated test gases. A novel idea of focusing shock wave using a convergent nozzle at the end of the driven section of shock tube is done for the first time to increase the reflected shock temperature and pressure.

2 Experimental Setup

The simple MST consisting of 2.1 m driver and 5.1 m long driven section with 80 mm inner diameter and 115 mm outer diameter available at SIMCL is used for materials research, which is capable of handling samples in the form of thin films, pellets, and fine powders [8]. Significant modifications of MST are done in the recent years, which include increasing the length of driver section of MST to twice its length (4.4 m) by connecting a U-shaped tube of radius 11.5 mm which is named as MST-E. The driver extension technique to increase the test time is reported in the literature [9]. The shock focusing technique is implemented in MST by connecting a 0.2 m long convergent nozzle with an area ratio of 8.8 and attaching a 1.2 m long extension tube having an inner diameter similar to the nozzle exit, named as MST-R. The MST-R is capable of increasing the shock strength thereby augmenting the T_5 and P_5.

In all the three configurations, it is essential to evacuate the driver section to low vacuum (10^{-3} mbar) using a rotary pump and the driven section to high vacuum (2×10^{-5} mbar) using a turbomolecular pumping system before filling the respective ultrahigh pure (UHP) gases for a high-quality materials research using shock tubes. In this paper all the experiments are performed by filling helium as a driver gas and 1 bar air as a test gas. The schematic diagrams of the different shock tube configurations are shown Fig. 1. The schematic of the simple MST with a driver and driven section, MST-E, and MST-R is shown in Fig. 1a–c. Typical pressure signals recorded using PCB pressure sensors for different configurations of shock tubes are shown in Fig. 2.

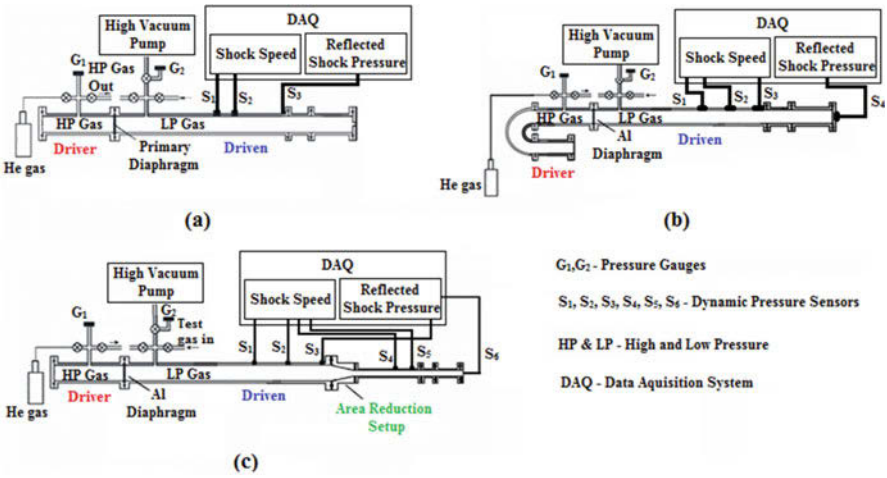

Fig. 1 Schematic diagram of the various configurations of shock tubes used for their performance evaluation: (**a**) Simple MST, (**b**) MST-E, (**c**) MST-R

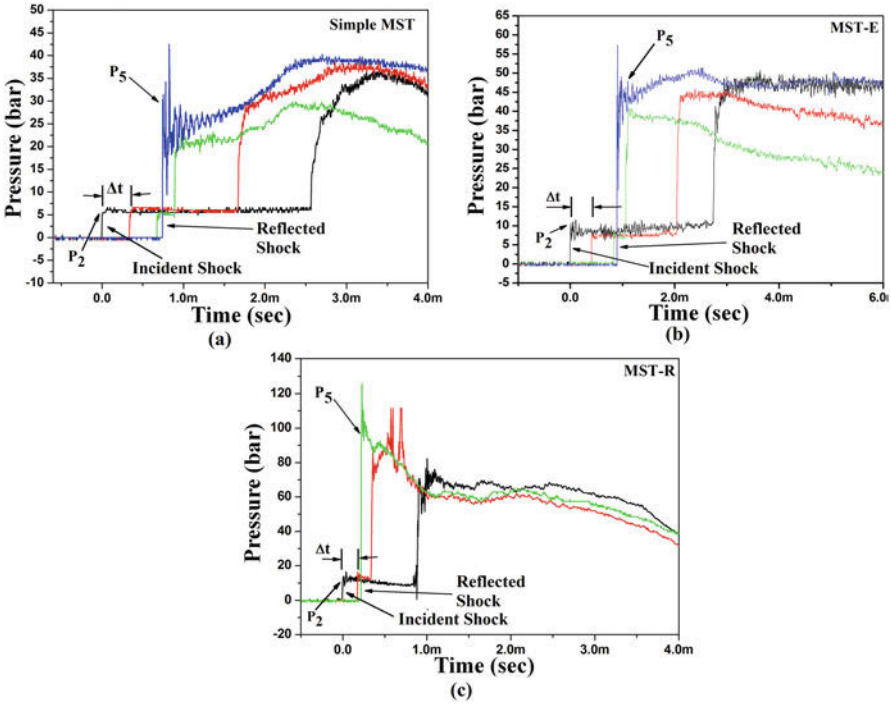

Fig. 2 Typical pressure profiles of various configurations of shock tubes used for their performance evaluation: (**a**) simple MST, (**b**) MST-E, (**c**) MST-R

2.1 Performance Evaluation Using Different Methods

Experiments are performed on all the three configurations of MST. The shock parameters such as shock Mach number (Ms), P_5, and test time are recorded using PCB pressure transducers. The pressure transducers mounted at the wall of shock tubes are used to acquire data by using high-frequency multichannel Tektronix digital oscilloscopes.

The KASIMIR program is used to simulate the various shock parameters and to compare it with the experimental values. The copyright of this shock tube simulation program was obtained from Stoßwellenlabor, RWTH Aachen/Shock Wave Laboratory, RWTH Aachen University, Germany. The program is based on a 1-D code which takes into account high temperature effects such as real gas effects and strong changes in the internal degrees of freedom due to chemical and thermal non-equilibrium conditions.

The time taken (Δt) for the shock to travel distance between the two pressure transducers ($\Delta L = 0.5$ and 0.25 m) was calculated from the acquired data. Another pressure sensor at the end of the shock tube records the reflected shock pressure (P_5). The time taken by the shock wave (Δt) to cross the two given sensor locations and the distance between sensors (ΔL) are used to find out the shock speed (V_S) and M_S. The M_S is then used to calculate the reflected shock temperature (T_5) at the end flange of the shock tube using 1-D normal shock relation (NSR) [10].

3 Results and Discussions

The augmentation of test time (t_{IE}), shock temperature, and pressure are the major goals of this work. It is evident that using MST-E and MST-R shock tubes, the t_{IE} has extended and P_5 and T_5 have augmented to a certain extent compared to the simple MST configuration.

The shock parameters for the present study using experiments are estimated from the plot of time versus pressure history as shown in Fig. 2. It is understood from the Fig. 2 that there is a significant difference in the constant pressure region between various configurations of shock tubes. The constant pressure region is more in the MST-E (Fig. 2b) shock tube compared to other configurations. In MST-R the immediate follow-up of contact surface and an expansion fan behind the P_5 and T_5 is considerably more as shown in Fig. 2c.

Due to the area change, the P_2 should be increased to a certain extent according to the 1-D normal shock relations for a given Ms, but in the experiments the P_2 remains the same before and after the reduction of MST-R. Additionally, due to the Mach number increase in the driven section after the reduction, P_2 rise before and after the area reduction has negligible difference.

In the experiments concerned with material interaction and combustion experiments in shock tubes, the reaction usually occurs at the stagnation region of the

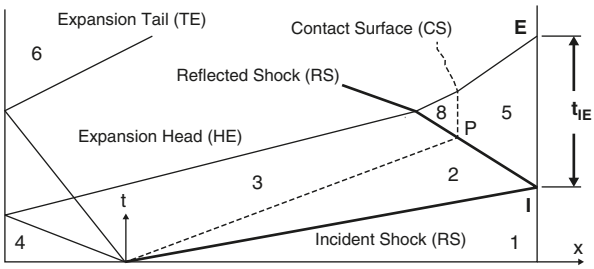

Fig. 3 Standard *x-t* plot of simple shock tubes for chemical kinetic studies [3]

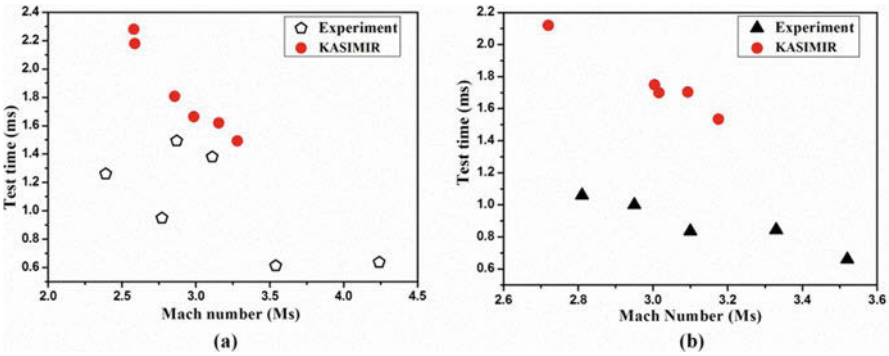

Fig. 4 Plot of test time (t_{IE}) versus shock Mach number (Ms) of (**a**) Simple MST, (**b**) MST-E shock tube

shock tube where the shock reflection causes T_5 and P_5 to increase. So behind reflected shock waves, the shock tube test time, t, is defined as the time between the reflected shock wave from the endwall (I) to the time the next wave (compression or expansion) arrives at the endwall (E) [3]. A standard plot of *x-t* diagram with the thermodynamic regions for a t_{IE} is shown in Fig. 3.

Comparing the experimental results, there is a slight increase in test time of 10% in MST-E than simple MST as shown in Fig. 4. The test time obtained using KASIMIR is overpredicted, and the solution has a discrepancy of about 15–60% for MST and MST-E as shown in Fig. 4. Test time calculation using experiments and prediction using KASIMIR was tedious for MST-R as there was lot of shock-shock interaction as the shock moves forward and also during the reflections. These reflections are most prominent for MST-R configuration. Due to the contact surface interference with the incident shock wave and the interactions later with the upcoming expansion waves, the test time vary with Ms. The Ms versus t_{IE} plot shown in Fig. 4a, b clearly indicates that the test time changes according to the Ms.

In order to validate the various shock parameters of different configurations of shock tubes, various tools are described in Sect. 2.1. Figure 5 shows the comparison of P_5/P_1 and T_5/T_1 of simple MST configuration. Figure 5a shows a good agreement of P_5/P_1 between 1-D NSR and KASIMIR, but there is a discrepancy of about 3–20% (avg.) in comparison with the experimental values. The

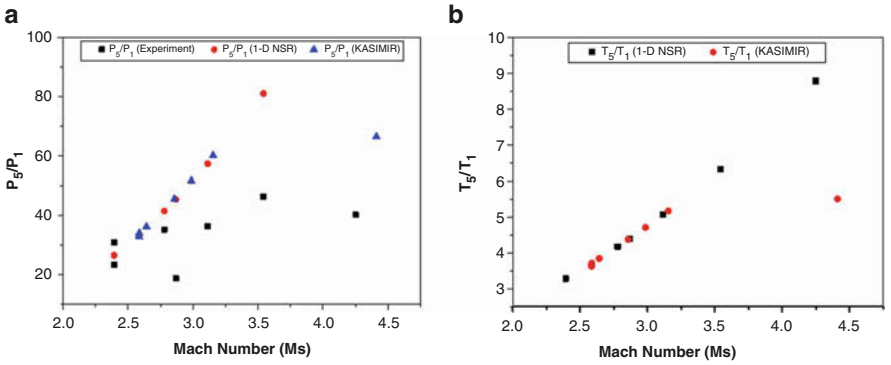

Fig. 5 Comparison of shock parameters between experiment and KASIMIR for simple MST: (**a**) Reflected shock pressure (P_5/P_1), (**b**) Reflected shock temperature (T_5/T_1)

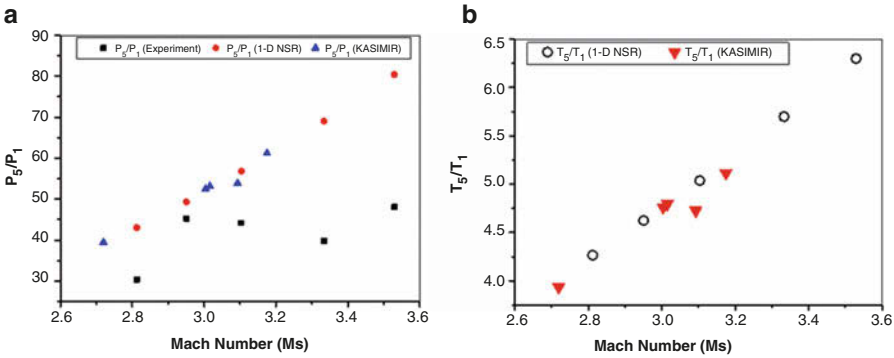

Fig. 6 Comparison of shock parameters between experiment and KASIMIR for MST-E: (**a**) Reflected shock pressure (P_5/P_1), (**b**) Reflected shock temperature (T_5/T_1)

absolute shock temperature measurement techniques are not available at present, so the temperatures (T_5/T_1) are estimated only by theoretical method. The plot of Ms versus T_5/T_1 for MST shows a similar trend in comparison with 1-D NSR and KASIMIR as shown in Fig. 5b. The discrepancy of Ms estimation between experiment and KASIMIR ranges about 5–15% in average for all configurations of shock tubes.

Similarly the MST-E and MST-R are also compared with various tools to validate the results. Figures 6 and 7 show the comparison of P_5/P_1 and T_5/T_1 of MST-E and MST-R, respectively. The discrepancy of P_5/P_1 and T_5/T_1 maintains its range of about 4–20% (avg.) as shown in Figs. 6a and 7a. On the other hand, T_5/T_1 has a good agreement for MST-E and MST-R as shown in Figs. 6b and 7b.

To achieve an extreme value of T_5 and P_5 of about 12000 K and 60 bar, experiments in MST-R were performed at different partial pressures of Ar test gas, and the results obtained are not presented here in this paper due to space constraints.

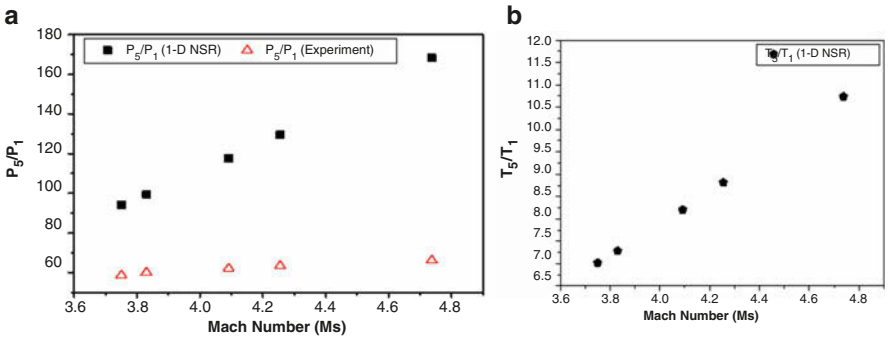

Fig. 7 Comparison of shock parameters between experiment and 1-D NSR for MST-R: (**a**) Reflected shock pressure (P_5/P_1), (**b**) Reflected shock temperature (T_5/T_1)

Such thermodynamic conditions are essential to study the interaction of UHTC materials with the shock-heated test gases.

4 Conclusion and Future Prospects

The experimental results show that the T_5 has been increased by approximately 15% in the MST-R setup and there is a 10% difference in t_{IE} between the simple MST and MST-E shock tubes. In all the different shock tube configurations, discrepancy in P_5/P_1 shows a variation of about 4–30%, but the variation of T_5/T_1 shows a similar trend. All the experiments are performed with air as a test gas. The plot of Mach number versus test time shows that the test time is inversely proportional to Mach number. In the MST-E configuration, the test time has a 10% increase compared to MST. The test time measured using KASIMIR is overpredicted, and the solution has a discrepancy of about 15–60% in all configurations.

So we conclude that our high vacuum shock tube facilities of different configurations are specially fabricated and calibrated to perform shock-induced materials research. The thermal and chemical non-equilibrium conditions prevailing in our shock tubes are suitable to disassociate the gas species and to interact with high temperature ceramic materials to study the catalytic and non-catalytic surface reactions.

Some issues like exploring the tailored mode condition of the shock tubes in various configurations are in progress, and this stands one of our interests to perform experiments for a longer test time at a constant and augmented P_5 and T_5.

Acknowledgments Financial supports from ISRO and STC-IISc, Government of India, are gratefully acknowledged. The authors thank Prof. K P J Reddy, Prof. G. Jagadeesh, and Mr. Abishek Khatta from the Department of Aerospace Engineering, Indian Institute of Science, Bengaluru, for their support and fruitful discussions on shock tube physics.

References

1. R.J. Stalker, AIAA J. **5**(12), 2160–2165 (1967)
2. Z. Hong et al., The use of driver inserts to reduce non-ideal pressure variations behind reflected shock waves. Shock Waves **19**, 113–123 (2009)
3. A.R. Amadio et al., Test-time extension behind reflected shock waves using CO_2-He and C_3H_8-He driver mixtures. Shock Waves **16**, 157–165 (2006)
4. R.A. Alpher, D.R. White, J. Fluid Mech. **3**(5), 457–470 (1958)
5. K. Izumi et al., Experimental and computational studies focusing processes of shock waves reflected from parabolic reflectors. Shock Waves **3**, 213–222 (1994)
6. B. Sturtevant, V.A. Kulkarny, J. Fluid Mech. **73**(4), 651–671 (1976)
7. M. Sommerfield, H.M. Muller, Exp. Fluids. **6**, 209–216 (1988)
8. V. Jayaram, Shock-induced reversible phase transformation from rutile to anatase in TiO_2 powders, in *SAMPE – 2016*, Long Beach, 2016
9. M.F. Campbell et al., Strategies for obtaining long constant-pressure test times in shock tubes. Shock Waves **25**, 651–665 (2015)
10. A.G. Gaydon, I.R. Hurle, *The Shock Tube in High-Temperature Chemical Physics* (Reihold Publishing Corporation, New York, 1963)

Measurement of Temperature Field Around Spiked Bodies at Hypersonic Mach Numbers

Sneh Deep, Yedhu Krishna, and Gopalan Jagadeesh

Abstract An investigation of a high enthalpy hypersonic flow has been made over an axisymmetric spiked body at a Mach number of 10.06. Temperature being one of the important physical quantities in hypersonic flows over such variable drag devices, this work aims at characterizing temperature in the shock layer for one such body. A flat-faced cylinder, with a diameter of 70 mm, and a conical nose spike of length 70 mm, screwed into it, were used for the experiments at zero angle of incidence. A well-established technique, the two-color ratio pyrometry (TCRP), has been used for temperature characterization using a DSLR camera. The results were in good agreement with the temperature predicted in the stagnation region by the STN (shock tube and nozzle calculations for equilibrium air) code.

1 Introduction

High enthalpy hypersonic flows ($h_0 \sim$ 5–25 MJ/kg or greater), upon interaction with a blunt body, result in a strong bow shock formation. This results in a higher drag coefficient, compared to that of a pointed body with an attached shock. For a reentry vehicle, to minimize the heating effect, it is advisable to have a body with high nose radius and drag coefficient. However, for efficient propulsion during takeoff, a body with low drag coefficient is necessary. This requirement led to the study of variable drag devices, one of them being a spiked body. The aerodynamics pertaining to flow over such devices, including flow separation and unsteadiness, have been extensively reported [1, 2]. A schematic of such a flow is shown in Fig. 1.

Experiments demonstrating reduction in drag force by coating blunt bodies with chromium involve heat addition studies in the shock layer [3]. Temperature being directly linked to heat transfer rates, a measurement of temperature in the shock layer over a spiked body, including any separated flow region, is important. In

S. Deep (✉) · Y. Krishna · G. Jagadeesh
Department of Aerospace Engineering, Indian Institute of Science, Bangalore, India

A. Sasoh et al. (eds.), *31st International Symposium on Shock Waves 2*,
https://doi.org/10.1007/978-3-319-91017-8_29

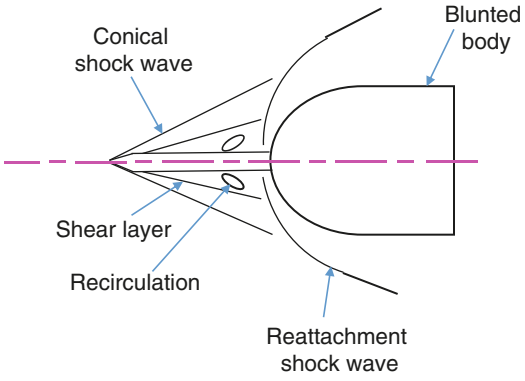

Fig. 1 Schematic of the flow field over a spiked blunt body

high enthalpy flows, temperature behind the shock may become so high that real gas effects set in. Rotational and vibrational modes are excited. At still higher temperatures, dissociation of diatomic gas molecules occurs.

Although researchers have looked at temperature distribution on a model surface in high speed flow [4], little attempt has been successfully made to characterize temperature in the shock layer. It is this lacuna that the current work intends to fill.

2 The Two-Color Ratio Pyrometry (TCRP)

Temperature determination using a conventional radiation pyrometer is dependent on the emissivity of the subject, which is seldom a constant and must be known explicitly. This is overcome by techniques such as two-color ratio pyrometry, which rely on the ratio of intensities at known wavelengths and assume that the emissivity of the subject remains constant in the visible region (400–700 nm), getting cancelled out in the ratio. A DSLR camera comes in handy, as it provides red, green, and blue (RGB) intensities at each sensor pixel, in the visible region of the spectrum. These intensity data may be used to ascertain two-color ratios, and each ratio can be connected to a temperature, via a calibration of the camera.

The theory behind the technique is elucidated in a different work [4]. Researchers have previously used DSLR and high-speed cameras for TCRP [4, 5]. The technique was also used at the Laboratory for Hypersonic and Shock Wave Research (LHSR), IISc.

2.1 Camera Calibration: Equipment Used and Steps Involved

A Canon EOS 750D camera, with an EF-S 18–55 mm lens, was used for procuring raw images. It has a high spatial resolution of 24.2 MP and can measure intensities with a vertical bit resolution of 16. A spectrally calibrated light source, Thorlabs SLS201/M stabilized tungsten-halogen calibration lamp, was used. The raw data of

its spectral radiance vs wavelength is available in the range of 300–2600 nm. Newport's 77250-MC, hand-operated monochromator was used for spectral calibration. It uses a model 77298 Grating Assembly, ruled with 1200 lines/mm, 360 nm blaze, and 200–1000 nm wavelength range. Before using the monochromator for camera calibration, the responsivity of the monochromator was characterized using the calibration lamp along with an 818-BB-27 silicon-biased photodetector of known spectral response. A schematic of the setup is shown in Fig. 2.

Step 1 involves determination of spectral RGB intensities, as counts per unit spectral radiance of the calibration lamp. Images were taken at steps of 10 nm, from 400 to 700 nm. This step yields the spectral sensitivity of the color filter array (CFA) for each of the RGB channels. Next, the spectral radiance $I(\lambda, T)$ in the visible region of the spectrum was simulated using Planck's equation. For every temperature, the simulated pixel response of the camera was determined by multiplying $I(\lambda, T)$ and the spectral sensitivity of the CFA. As a final step, the area under the red, green, and blue response curves is computed. A ratio between any two suitable color channels is considered. Each temperature yields a unique value for the intensity ratio, thus facilitating a temperature vs intensity ratio calibration curve. The responsivities of RGB pixel array after step 1 and the final calibration curve for the R/G and G/B ratio are shown in Fig. 3.

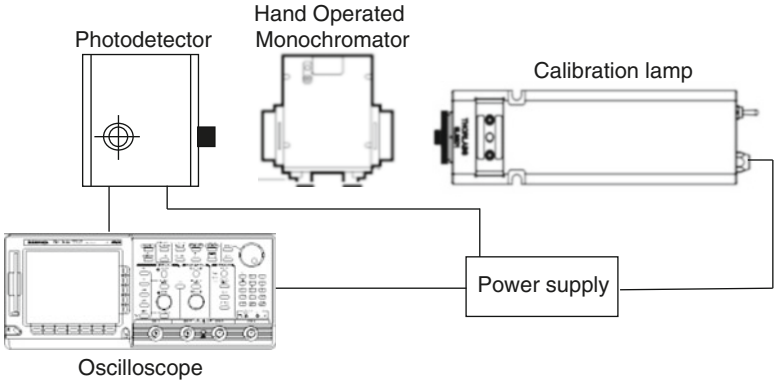

Fig. 2 Schematic of the setup for the determination of monochromator optical efficiency

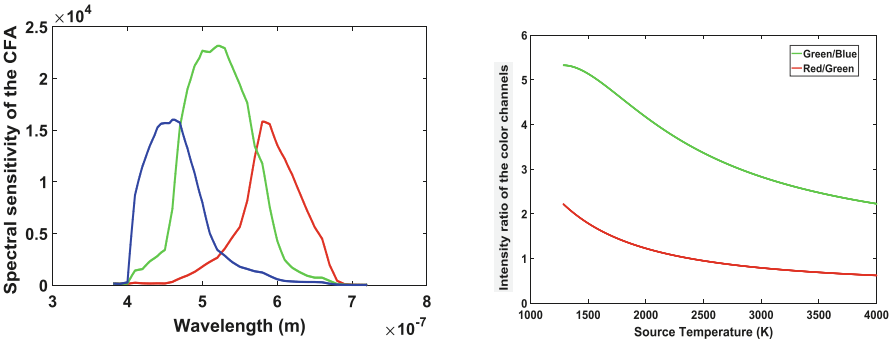

Fig. 3 Spectral sensitivity of the color filter array (CFA) and the final calibration curve

3 Experiment: Application to Hypersonic Flow

3.1 The Facility and Test Conditions

Experiments were carried out at the IISc HST3 shock tunnel, also known as the free piston driven shock tunnel (FPST), at a nozzle exit Mach number of 10.06. A schematic of the tunnel along with its major accessories is shown in Fig. 4.

The tunnel was operated in the reflected mode. A detailed description of the facility is mentioned elsewhere [6]. Helium was used as the driver gas, with an initial fill pressure of 700 mm of Hg (0.093 MPa). The driven gas (or the test gas) was air, at a pressure of 230 mm of Hg (0.0306 MPa). A primary aluminum diaphragm, 3 mm thick and with two 0.75 mm deep mutually perpendicular grooves, was used. It ruptures at approximately 10 MPa.

3.2 Test Model

A mild steel flat-faced cylindrical model with a forward facing spike has been used for the experiments. The cylinder has a diameter of 70 mm and a length of 120 mm. The spike has a diameter of 5 mm and is 70 mm long. It culminates in a cone with a semi-apex angle of 15°. The model has been provided with a sting to mount it in the test section. Figure 5 shows a photograph of the model along with the free stream direction.

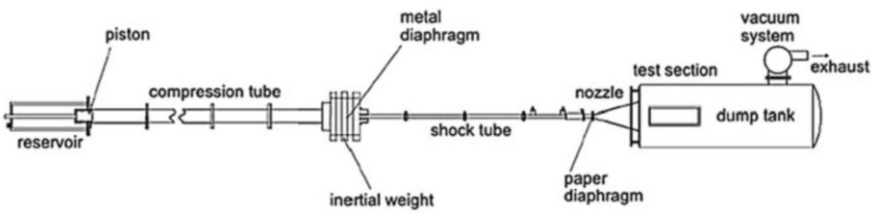

Fig. 4 Schematic of the FPST

Fig. 5 Photograph of the cylindrical model with a forward facing spike

4 Experimental Results and Discussions

The pressure signals obtained from the PCB pressure transducers mounted on the shock tube and the Pitot tube in the test section have been plotted in Fig. 6.

The first sharp pressure rise of the P2 and P5 transducers was used to calculate the incident shock speed in the shock tube, equal to 2364.35 m/s (Mach 6.8). The Pitot signal determined the steady test time, approximately 260 μs. The pressure in the stagnation region (P_5), i.e., behind the reflected shock, was measured as 8.882 MPa. Since we are dealing with extremely high enthalpy flows, ideal gas equations are no longer suitable for predicting the stagnation conditions. The conditions were estimated using the STN code [7], which takes into account real gas effects and is suitable up to 25,000 K. The stagnation temperature and enthalpy as obtained from STN are $T_5 = 3643$ K, $h_5 = 5.2$ MJ/kg.

The settings of the DSLR camera used for imaging the flow field are tabulated in Table 1.

Although a long exposure is used, most of the luminosity is only from the steady flow over the model. The rest of the period is idle (dark), which is anyways corrected by subtracting the dark image, acquired beforehand. The ISO is kept at a minimum, to prevent any undesired noise in the image. The raw image is used for image processing, done in MATLAB. The entire method is based on the assumption that gases emit as a gray body [8]. The flow field image is shown in Fig. 7, along with the "Canny" edge-detected image for clarity.

The above image shows the conical shock over the spike, which culminates into an aftershock in front of the cylinder. The R counts for this image were saturated; hence, the green/blue intensity ratio was used for temperature prediction in the aftershock region. Also, the G/B ratio is more sensitive to temperature changes at the temperature readings expected for this experiment. The final processed file obtained

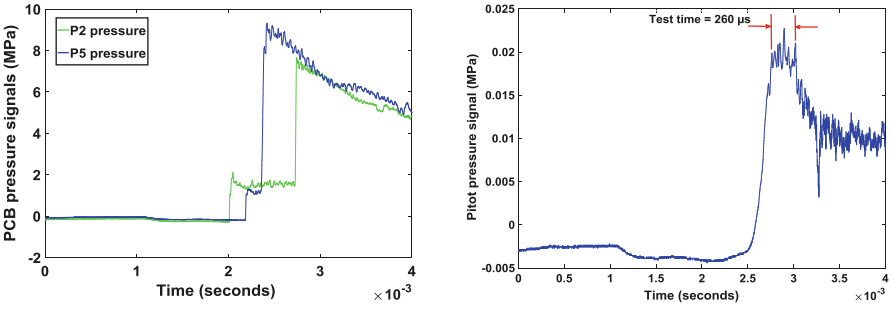

Fig. 6 Pressure variation as obtained from pressure transducers during the run

Table 1 Camera settings for imaging the hypersonic flow field

Mode	Manual: bulb (4 s exposure)
Image type	Raw (.CR2)
ISO speed	ISO-100

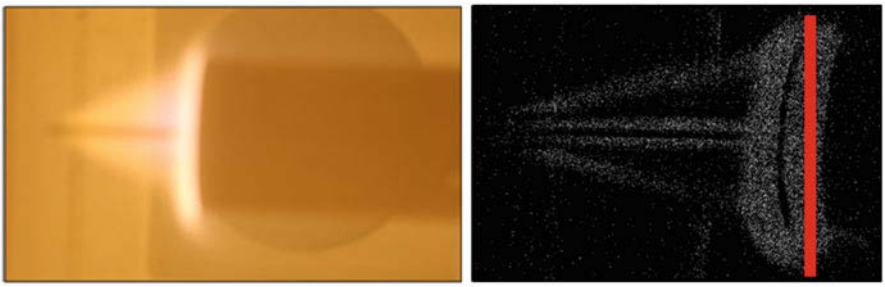

Fig. 7 Actual flow over the model and the corresponding edge detected image for clarity

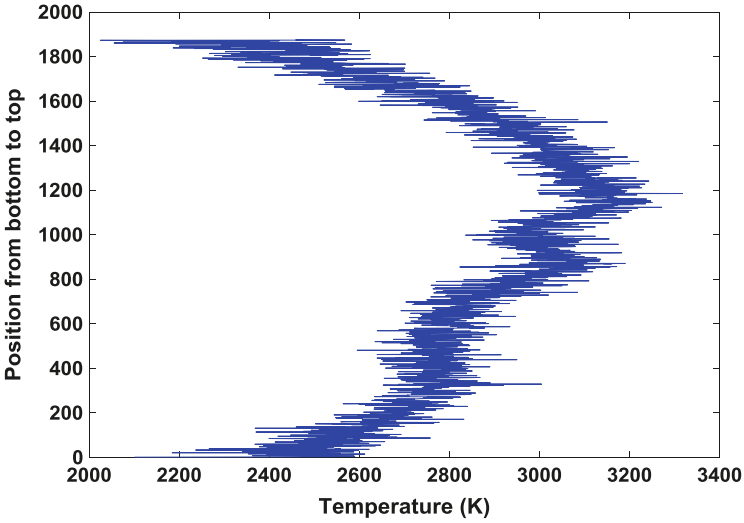

Fig. 8 Temperature variation along a vertical rectangle within the aftershock

was a 2D, spatially resolved temperature distribution in the aftershock region. Since the stagnation point lies in the aftershock region and facilitates comparison with the STN code, the authors were interested in that region only.

For comparison purpose, the temperature variation along the red vertical rectangle within the aftershock, close to the stagnation point has been graphed in Fig. 8. The temperature at any vertical location is obtained by averaging all the temperature readings along the width of the rectangle.

From the graph, the temperature at the stagnation point is close to 3200 K, which is within 12.2% of that predicted by the STN code. Since STN predicts the stagnation temperature at the nozzle entrance, after which the flow encounters losses, it is bound to decrease near the model. Also as one moves away from the stagnation point, the temperature reduces on either side, consistent with the theory. The conical shock layer will experience extremely low temperatures; however,

the region in Fig. 7 is illuminated, perhaps due to reflection from the aftershock layer. There the temperature is too low for TCRP to predict, both due to inherent limitations of the technique and due to noise being comparable to the signal.

5 Uncertainty

The total uncertainty in measuring the shock speed is within ±2.5%; pressure measurements are also within ±2.5%. The uncertainty involved in determining the G/B ratio for the illuminated image is within ±8%. This is because the measured temperatures are very sensitive to variations in color ratios in the temperature regimes involved in this study.

6 Conclusion and Future Work

TCRP technique has been used for the first time for characterizing temperature in the shock layer of a high enthalpy flow. The measurements obtained using the method agreed to within 12.2% of the value obtained using STN code. Though majority of the spectrum would be that of a gray body, some transition lines would appear at discrete wavelengths due to the dissociating species in the high-temperature region. As a future work, the authors aim to identify and measure these lines by emission spectroscopy and account for them in temperature prediction. Also, an electronic circuit is being built for automatic camera trigger, which will allow low-exposure-time measurements and, thus, better time resolution.

Acknowledgments The authors are grateful to Defence Research and Development Organization (DRDO), India, for their financial support in carrying out this work. Thanks also to Jeevan, Murthy, Kumar, Rajagopal, and Raghu Narayan for their contribution. Colleagues, namely, Tarandeep Singh, Dr. Mohammed Ibrahim. S and Abhishek Khatta are greatly acknowledged for their invaluable help in performing the experiments.

References

1. D.J. Maull, Hypersonic flow over axially symmetric spiked bodies. J. Fluid Mech. **8**(04), 584–592 (1960)
2. S.M. Bogdonoff, Preliminary investigations of spiked bodies at hypersonic speeds. J. Aerospace Sci. **26**(2), 65–74 (2012)
3. V. Kulkarni et al., Aerodynamic drag reduction by heat addition into the shock layer for a large angle blunt cone in hypersonic flow. Phys. Fluids **20**(8), 081703 (2008)
4. F. Zander, Surface temperature measurements in hypersonic testing using digital single-lens reflex cameras. J. Thermophys. Heat Transf. **30**(4), 919–925 (2016)

5. J.M. Densmore et al., High-speed digital color imaging pyrometry. Appl. Opt. **50**(17), 2659–2665 (2011)
6. S.K. Chintoo, *Experimental Investigation of Aerodynamic Interference Heating due to Protuberances on Flat Plates and Cones Facing Hypersonic Flows*. Ph.D. Dissertation, Department of Aerospace Engineering, Indian Institute of Science, Bangalore, 2013
7. R.M. Krek, P.A. Jacobs, *STN, Shock Tube and Nozzle Calculations for Equilibrium Air*, Research Report No: 2/93 (University of Queensland, Brisbane, 1993)
8. W. Finkelnburg, Conditions for blackbody radiation of gases. J. Opt. Sci. Am **39**(2), 185–186 (1949)

Three-Dimensional Laser Interferometric CT Density Measurement of Unsteady Flow Field Around a Cylinder Induced by Discharged Shock Wave from a Cylindrical Nozzle

D. Aoki, S. Nakazawa, K. Kurihara, and M. Ota

Abstract The study of shock wave is of significance in understanding supersonic flow. In this paper, we describe about the three-dimensional (3D) quantitative density measurement technique of unsteady and discharging shock waves. In the experimental research areas, the supersonic unsteady flow fields have been commonly observed by qualitative and two-dimensional (2D) visualization methods, such as shadowgraph, color schlieren, or 2D interferometric images. On the other hand, holography and computed tomography (CT) methods have been applied to the measurement of three-dimensional flow fields. The unsteady flow field around a cylinder by discharging shock wave from a cylindrical nozzle was successfully reconstructed by algebraic reconstruction technique (ART).

In this study LICT technique is applied to observe more complex flow field than our previous study induced by discharging unsteady shock wave around a cylinder from a cylindrical nozzle. Three-dimensional flow fields are reconstructed by ART. The obtained results and features of high-speed and unsteady flow field will be discussed.

1 Introduction

In recent years, in the experimental research areas, the supersonic unsteady flow fields have been commonly observed by qualitative and two-dimensional (2D) visualization methods, such as shadowgraph, schlieren, or 2D interferometric photograph images. On the other hand, holography and computed tomography (CT) methods have been applied to the measurement of three-dimensional (3D) flow fields. Subsonic and transonic free jets were studied by interferometric holography

D. Aoki (✉) · S. Nakazawa · K. Kurihara
Graduate School of Engineering, Chiba University, Chiba, Japan
e-mail: adta2138@chiba-u.jp

M. Ota
Graduate School and Faculty of Engineering, Chiba University, Chiba, Japan

A. Sasoh et al. (eds.), *31st International Symposium on Shock Waves 2*,
https://doi.org/10.1007/978-3-319-91017-8_30

[1], and also supersonic jets were studied by Soller et al. [2]. These flow fields were, however, steady and supersonic flows. In our previous study, the laser interferometric computed tomography (LICT) has been applied to the measurement of various 3D unsteady phenomena. The unsteady flow field included by shock waves discharging from three cylindrical nozzles and two inclined nozzles [3–5] was successfully reconstructed by filtered back projection (FBP) method or algebraic reconstruction technique (ART). The LICT measurement is the combination of Mach-Zehnder finite-fringe interferometry and computed tomography (CT) technique, where N2 pulsed laser is used as a light source.

Now, supersonic spacecraft is being investigated in the world. But it is difficult to analyze supersonic flow around the spacecraft experimentally. Therefore it is important to investigate unsteady flow field around the object by experimental method. In this study, The LICT technique is applied to observe the flow field around a cylinder induced by discharging unsteady shock waves from a cylindrical nozzle. In addition, high-resolution images can be obtained by using a digital camera. Three-dimensional flow fields are reconstructed by ART from finite-fringe interferograms with different projection angles with shot-by-shot operation of diaphragmless shock tube of similar delay times of laser pulse. We will report unsteady phenomena by supersonic around a cylinder from a cylindrical nozzle in this paper.

2 Experimental Apparatus

2.1 Diaphragmless Shock Tube

A diaphragmless shock tube is used to generate the shock waves with good reproducibility. Figure 1 shows a schematic diagram of the experimental apparatus. Optical system consists of a conventional digital camera (EOS Kiss X3, Canon

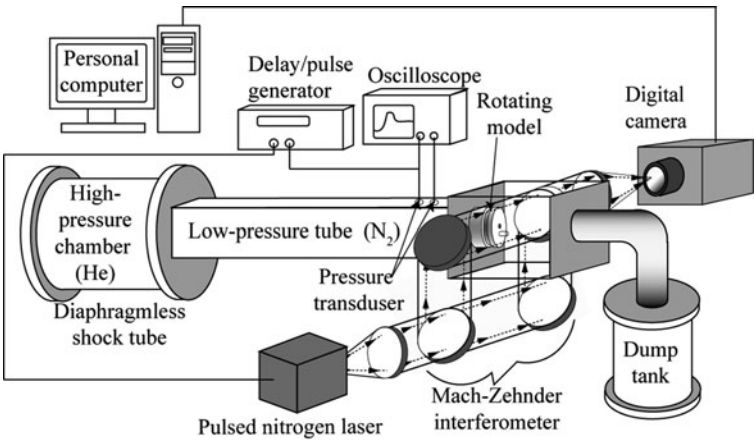

Fig. 1 Schematic diagram of experimental apparatus

Inc.), a Mach-Zehnder interferometer, and a pulsed nitrogen laser (UV14, Molectron Co. 4 mJ) as a light source. The cross section of the low-pressure tube is 40 mm × 40 mm square, and its length is 3.1 meters. The drive gas is high-pressure helium, and the test gas is low-pressure nitrogen. The incident Mach number M_i is calculated by the delay of pressure signals from two pressure transducers as shown in Fig. 1. In this experiment the distance between two pressure transducers is 47 mm, and the Mach number of the incident shock wave was fixed to 2.0.

2.2 Rotating Plug with Duct Model

The layout of the rotating plug is illustrated in Figs. 2 and 3. The shock wave generated by the diaphragmless shock tube passes through a rotating plug installed at the end of the low-pressure tube, and it is discharged into the test section from a cylindrical nozzle. Figure 3 shows the coordinate system of the rotating plug. The x and y coordinates rotate with rotating plug around the z-axis, while light axis s is fixed with the shock tube, where the rotation angle θ is defined as the angle between

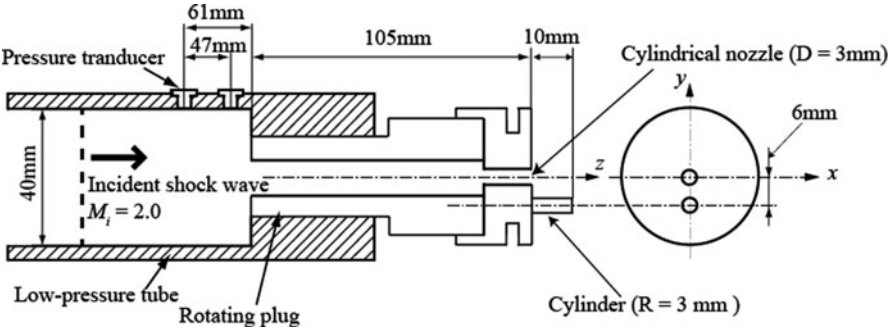

Fig. 2 Rotating plug with duct model

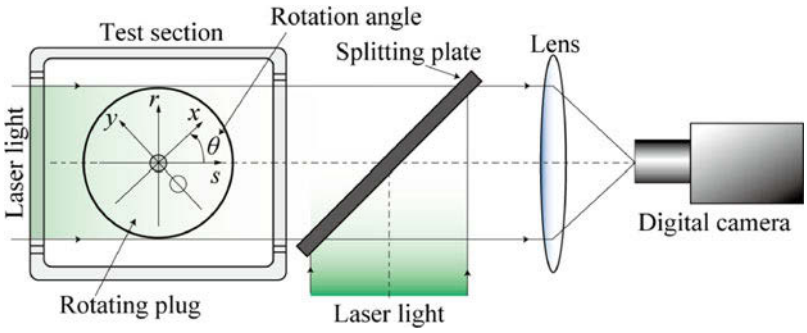

Fig. 3 Coordinate system of rotating plug

x- and s-axis. In order to obtain the multi-directional projection data, the rotation angle was set to the designated angle for each shot. The experiment was performed for 36 rotation angles between 0° and 180° at 5° intervals, taking benefit of the one-axis symmetrical characteristics of the flow field. The projection data of the flow field are obtained as the interferometric finite-fringe digital images, and each image is obtained at fixed plug rotation angle by each shot of shock tube experiment.

3 CT Reconstruction from Finite-Fringe Images

3.1 Projection Data

Each projection image is obtained by one shot of the shock tube in LICT measurement. Therefore, it is important to keep the accuracy of image data higher to obtain reconstructed image with high-quality CT reconstruction. To carry out the CT reconstruction with sufficiently high accuracy, the normalized frontal position z_s/D of the primary shock wave should be defined as shown in Fig. 4, where D (=3 mm) is the diameter of a circular nozzle and z_s is the frontal position of the primary shock wave measured along the z-axis in the digitized projection image. The accuracy of each experiment can be monitored with these parameters and incident Mach number M_i. In this study the selected parameter and their accuracies are $M_i = 2.0 \pm 1\%$ and $z_s/D = 2.22 \pm 1\%$.

To obtain 3D digitized reconstruction data of density distribution, each projection image has to be calculated by fringe tracking method, and its process is divided into three steps. First, fringes are tracked by tracking algorism. Second, the displacements ΔH of these fringes are calculated. Finally, the integrated quantity of density change is obtained according to the following expression:

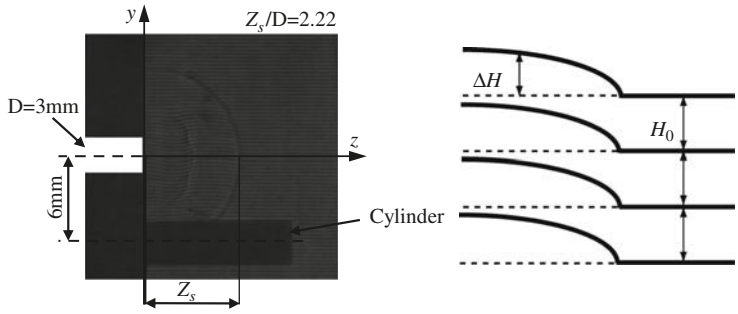

Fig. 4 An example of finite-fringe interferogram and displacement of fringes

$$\int (\rho - \rho_0)\, ds = \frac{\Delta H}{H_0} \times \frac{\lambda}{\mathrm{K}} \tag{1}$$

where ρ_0 is the initial density of test section, H_0 is the average initial spacing distance of fringes, λ is the wavelength of laser, and K is the Gladstone-Dale constant.

3.2 Reconstruction Technique

The algebraic reconstruction technique (ART) is selected for the algorithm of our CT reconstruction. The ART is one of the robust and basic reconstruction techniques. Filtered back projection (FBP) method is generally used as CT reconstruction technique; however, it requires a large number of projections for higher accuracy of reconstruction, and FBP sometimes produces strong artifacts from insufficient data parts, e.g., a cylinder which blocks the observation light. Therefore, ART can be a useful reconstruction technique for the reconstruction of the flow field around a cylinder.

4 Results and Discussion

In this section the experimental CT images reconstructed by ART are presented as the sliced 2D image and the 3D image with different locations. In addition, 3D density images are shown by isopycnic surface.

4.1 Results of Density Distribution on y-z Cross Section and Isopycnic Surface

Figure 5 shows a pseudo-color image of density distribution on *y-z* cross section and the isopycnic surface of the flow field. The blue part shows the domain of the lower density ($\rho/\rho 0 = 0.9$), and the yellow part shows the domain of the higher density ($\rho/\rho 0 = 1.08$). The black part shows a cylinder. This image shows several unsteady phenomena at fixed instance, for example, the primary shock wave (PSW) and an expansion wave (vortex). However, the calculated projection data contain the blank part which corresponds to the position of a cylinder, and it is suffering from many noise (artifacts).

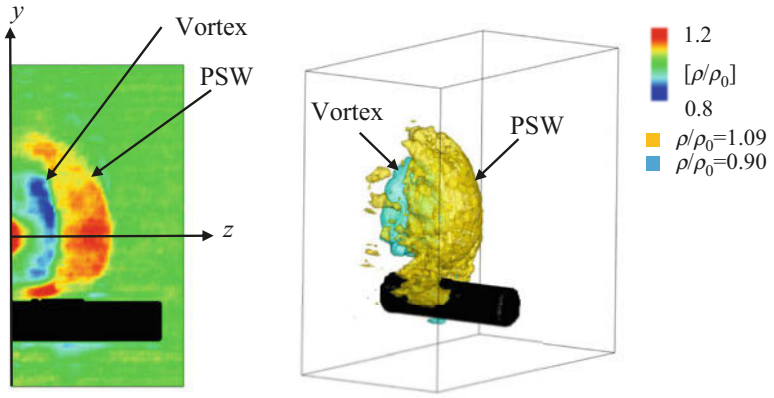

Fig. 5 Reconstructed density distribution on *y*-*z* cross section and isopycnic surface

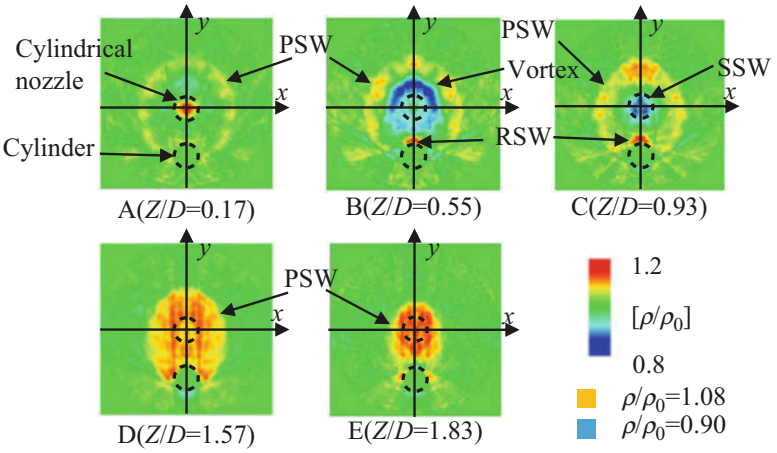

Fig. 6 Density distribution on *x*-*y* cross section

4.2 Results of the x-y Cross Section

Figure 6 shows the reconstructed 3D flow field of the *x*-*y* cross section in five different portions. The normalized position of each cross section *Z*/*D* is as follows: A, 0.17; B, 0.55; C, 0.93; D, 1.57; E, 1.83. In Fig. 6a, a primary shock wave (PSW) is clearly observed near the wall region. In Fig. 6b, a primary shock wave and the expansion wave (vortex) and reflected shock wave (RSW) from a cylinder are captured. In Fig. 6c, a primary shock wave and the secondary shock wave (SSW) are observed. In Fig. 6d, e, a primary shock wave can be observed clearly in comparison with Fig. 6a–c.

5 Conclusion

We have developed a laser interferometric CT (LICT) technique to observe 3D phenomena in shock tube experiments and applied to investigate the 3D features of shock-vortex flow around a cylinder discharging from a cylindrical nozzle. We confirmed that the 3D images of the shock-shock and shock-vortex interactions can be obtained by applying the present CT technique to the flow discharged from the rotating plug. The results show several unsteady phenomena interfered with a cylinder, for example, the primary shock wave, the secondary shock wave, and vortex. The behavior of the shock wave discharging from a cylindrical nozzle is captured three-dimensionally and quantitatively. The CT technique is expected to be a useful tool to study 3D shock dynamics. However, it is still necessary to improve the reconstruction algorithm to handle the blanked part in projection data, which will be developed in the future to catch the complicated phenomena of the flow field in detail.

References

1. L.T. Clark, D.C. Koepp, J.J. Thykkuttathil, Three-dimensional density field measurement of a transonic flow from a square nozzle using holographic interferometry. J. Fluids Eng. **99**, 737–744 (1977)
2. C. Soller, R. Wenskus, P. Middendorf, G.E.A. Meier, F. Obermeier, Interferometric tomography for flow visualization of density fields in supersonic jets and convective flow. Appl. Opt. **33**(14), 2921–2932 (1994)
3. M. Ota, T. Inage, K. Maeno, An extension of laser-interferometric CT measurement to unsteady shock waves and 3D flow around a columnar object. Flow Meas. Instrum. **18**, 295–300 (2007)
4. T. Aratani, T. Inage, M. Ota, K. Maeno, Application of high-speed camera to 4D-CT density measurement of unsteady shock-vortex flow discharged from two inclined and cylindrical holes, in *International Symposium on Experimental Mechanics, Taipei, Taiwan* (2012), pp. 1–5
5. Y. Miwa, T. Aratani, M. Ota, K. Maeno, Three dimensional laser interferometric CT density measurement of unsteady shock vortex interaction flow discharged from three cylindrical holes, in *International Symposium on Flow Visualization, Okinawa, Japan* (2014), pp. 1–8

Curved Shock Wave Propagation in Environment Stratosphere by Laser Ablation

D. T. Tran, C. Xie, and K. Mori

Abstract The technique of material removal from a solid target, called laser ablation, is used for a number of industrial applications, particularly in laser propulsion. When a solid surface is irradiated by an intense laser beam, the target surface is heated and ablated, which creates the impulse for the target in opposite direction. The ablated material interacts with ambient gas and then creates the curved shock wave around the target. By using Nd:YAG laser as an ablation source, the shock wave propagation in the stratosphere environment is studied experimentally. As a result, the shape and energy of shock wave show the difference due to the reduction of pressure. The impulse generated by laser ablation is found being insensitive in low ambient pressure.

1 Introduction

Laser ablation is a mass removal process by irradiating laser energy to a target material. Generally, due to the absorption of the incoming laser beam, the target surface is heated and then ejected in several states such as solid particles, liquid, or gas. In the vacuum condition, the ablated jet of material created an opposite force to the target. When increasing the ambient pressure, due to the presence of dense air particles, the ablated material is compressed. This phenomenon created a high-density area of ablated particles in front of the target, which continues to absorb the remaining laser energy and generate the plasma. The interaction between the ablated material and ambient gas generates a shock wave in the background region. Behind the shock wave, the local pressure increases rapidly and generates the impulse for the target.

The application of laser ablation in the laser propulsion is firstly proposed by Kantrowitz in 1972 [1]. A vehicle could be launched to low Earth orbit by a high-power laser station on the ground. The laser launch system was recognized

D. T. Tran (✉) · C. Xie · K. Mori
Department of Aerospace Engineering, Nagoya University, Nagoya, Japan

A. Sasoh et al. (eds.), *31st International Symposium on Shock Waves 2*,
https://doi.org/10.1007/978-3-319-91017-8_31

as a potentially low-cost, low-pollution propulsion system for the future. Previous studies on laser ablation were mainly focused on the impulse performance obtained in vacuum condition or at atmospheric pressure. A momentum coupling coefficient, C_m, is defined as the ratio of the impulse generated by laser ablation, and incident laser beam energy is a factor to evaluate the efficiency of laser propulsion. In 1988, Phipps et al. [2] formulated C_m characteristics of aluminum alloys experimentally in terms of laser parameters (intensity, pulse width, wavelength) in vacuum condition. By using the velocity interferometer system and schlieren visualization, the impulse generation and shock wave were investigated simultaneously in some cases of different ambient pressure, p_a [3]. The largest C_m was obtained with the combination of polyacetal target and TEA CO_2 laser at atmospheric pressure. However, the shock wave expansion was not clear at the low ambient condition. The influence of ambient pressure on C_m was also investigated by the other authors [4, 5]. C_m decreases monotonically with decreasing ambient pressure. The laser ablation was also studied numerically. The impulse generation on aluminum target with Nd:YAG laser pulse was simulated by Sakai [5]. The ablation vapor of material contributes to the impulse generation in a vacuum condition, while the gas dynamics of an ablation jet generates the impulse in higher pressure. At ambient atmosphere condition, Arnold et al. [6] presented an analytical model for the plume expansion. The expansion was described by two shock waves: internal and external. They found that this expansion is consistent with the point-blast theory by Sedov-Taylor [7].

In most past studies, the laser propulsion impulse was commonly measured in a vacuum state, atmospheric pressure, or some points of different pressure. However, the mechanism of the impulse generation has not been clear at low ambient pressure, particularly in stratosphere condition. Therefore, this study focuses on the relation between the shock wave expansion and value of C_m to better understand the impulse generation mechanism at low ambient pressure.

2 Experiment Setup

The experimental setup consists of a vacuum chamber equipped with two pumps for evacuation, as shown in Fig. 1. The chamber is filled with normal air. The pressure, p_a, is regulated from 10 Pa to 100 kPa by some pressure gauges. Laser ablation is performed using a Nd:YAG laser with the pulse duration of 5 ns, pulse energy of 0.7 J, and wavelength of 1064 nm. The laser beam is focused by a convex lens with a focal length $f = 200$ mm and irradiated onto a spherical aluminum metal placed in the chamber. The shot-to-shot pulse laser energy is examined by an energy meter (EM) (Model 1835-C, Newport Corporation). The variation of laser energy is controlled below 5%. For visualization, the shock wave expansion is captured with a framing schlieren system using a high-speed camera (HPV-X2 camera, Shimadzu Co, Ltd). As the light source, a laser light (Cavilux Ltd CAVILUX smart) with a 30 ns pulse duration is used. Two hundred fifty-six images for each test are recorded in the gray scale at a step of 200 ns.

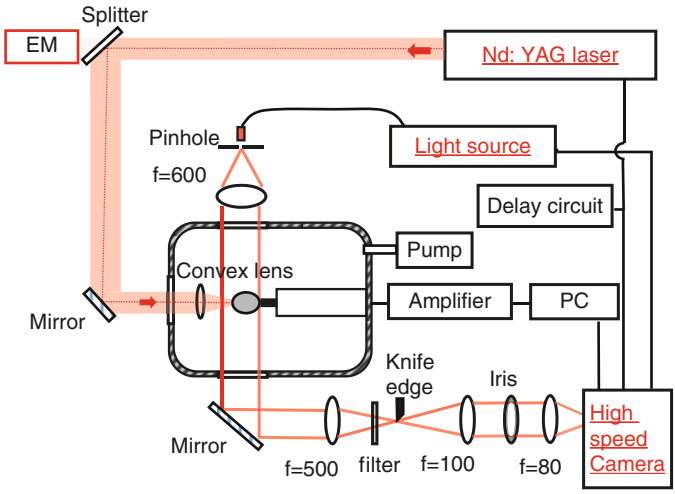

Fig. 1 Experimental setup

A spherical aluminum foil of 10 mm diameter is used as the target material. For impulse measurement, the target is mounted on a load cell (Kyowa Electronic Instruments) to measure the axial impulse.

3 Results

The plasma formation and shock wave position for ablation of the aluminum target in different ambient pressures are shown in Fig. 2. The delay time of framing schlieren images is 250 ns from beginning radiation. The laser energy is kept at 0.7 J, while the focal spot diameter is 1.3 mm. It should be noted that the experiment is conducted from $p_a = 10$ Pa. However, the shock wave is not visible until $p_a = 100$ Pa, as shown in Fig. 2a, which could be due to the low pressure of background gas as has been shown in the study of Gusarov et al. [8]. The background gas below 100 Pa cannot seriously influence both the gas dynamics and the ablation of the target surface. In the case of $p_a = 100$ Pa, at $t = 250$ ns, the plasma does not appear; the shock wave expands anisotropically. In the horizontal direction, the shock wave expands faster than the vertical direction, which is due to the absorption energy of vapor plume. When the target surface is heated by a laser beam, the number of vapor plume increases when time evolves. Sakai [5] shows that the laser energy is absorbed more strongly by high-temperature vapor by nearly 20%. Therefore, the vapor plume on the region of the incoming laser beam has more energy than the rest of the plume and then moves faster.

The effect of ambient pressure is observed from Fig. 2b–d. Due to the higher ambient pressure, the number of particles of air around the target increases. The

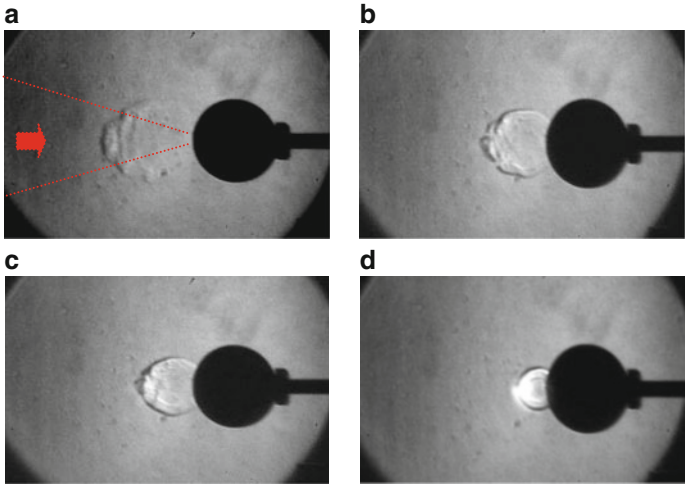

Fig. 2 Instantaneous shock wave at $t = 250$ ns from beginning laser beam at different ambient pressures (Laser energy $E_L = 0.7$ J, laser spot diameter 1.3 mm, laser fluence 52 J/cm^2). (**a**) $p_a = 100$ Pa. (**b**) $p_a = 400$ Pa. (**c**) $p_a = 1000$ Pa. (d) $p_a = 4000$ Pa

plasma formation and shock wave depend on the collision between vapor plume and the particles of gas. Generally, the high density of ambient species caused the increase of collision frequency and, hence, enhances the ionization [9]. As a result, the plasma energy increases, as shown by the luminous region in each schlieren image. The vapor plume compresses the ambient gas stronger, which creates the higher energy of shock wave. The expansion speed of shock wave reduces with the increase of ambient pressure. On the other hand, the shock wave also expands anisotropically in low ambient pressure. A tip of shock wave could be observed in Fig. 2c. Meanwhile, as shown in Fig. 2d, the shock wave expands spherically and slowly at high ambient pressure of 4000 Pa. The plasma lifetime is longest among all cases, as shown by the luminous area in front of the target. In high ambient pressure, the Sedov-Taylor solution [7] could be applied for the shock wave expansion. The shock wave position is determined based on the laser energy, density of air, and ablation time.

The impulse performance of laser ablation in a wide range of ambient pressure is shown in Fig. 3. By using a transversely excited atmosphere CO_2 laser, Andrew [10] showed that C_m was a function of pressure, which varied from 1 atm to 3.5 mtorr (0.46 Pa). The plasma shielding affects the impulse generation in high ambient pressure that discontinues the increase of the impulse. In this study, to avoid this phenomenon, Nd:YAG laser is used. The atmosphere air is charged to the chamber and p_a is varied from 10 Pa to 100 kPa. There are three cases of different spot diameters, $d_{sp1} = 1.3$ mm (fluence $\Phi_1 = 52$ J/cm^2), $d_{sp2} = 2.1$ mm (fluence $\Phi_2 = 19$ J/cm^2), and $d_{sp3} = 4.1$ mm (fluence $\Phi_3 = 5$ J/cm^2), that aim to examine the effect of the laser beam fluence to C_m. According to Phipps et al. [2], the relation

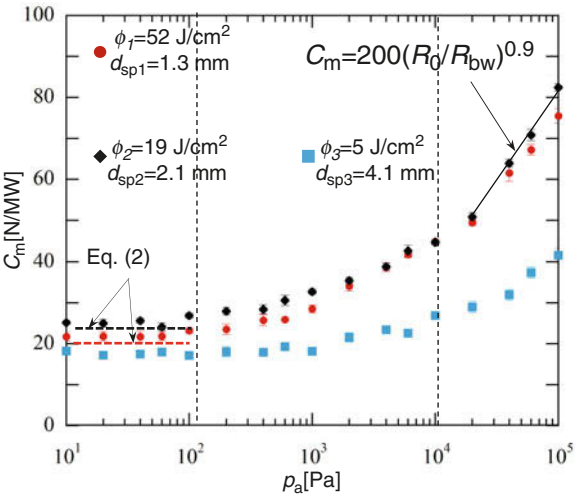

Fig. 3 The momentum coupling coefficient in a wide range of ambient pressure from 10 Pa to 100 kPa (Laser energy $E_L = 0.7$ J, three cases of spot laser diameter)

between laser intensity for the maximum of C_m and width laser pulse was shown as $I_{max}\sqrt{\tau}=8 \times 10^4$ [W/cm^2], where I_{max} is the threshold value. In cases 1 and 2, the intensity of incident laser beam is chosen above the threshold value, while the intensity is lower than the threshold value in case 3.

In the low ambient pressure, $p_a < 100$ Pa, C_m is found insensitive with ambient pressure. The impulse is generated due to the ejection of the solid material from the surface. The effect of the laser fluence to the impulse is consistent with the results conducted by CO_2 laser in a vacuum state [2]. In case 3, $I_3 < I_{max}$, the C_m shows the lowest value in three cases. When increasing the laser intensity, C_m reaches a maximum at I_2, thereafter declining with increasing intensity, as shown at I_1. This behavior is due to the ignition of the dense plasma in the vapor close to the target surface which mediates the coupling of laser energy to the material for $I > I_{max}$.

In high ambient pressure, C_m is found to be a function of the ambient pressure. The function is shown as a curve $220(R_0/R_{bw})^{0.9}$, which was defined for a circular disk in the previous study [11]. $R_0 = 5$ mm is the radius of the target, and R_{bw} is a function of the laser energy and ambient pressure, $(E_L/p_a)^{1/3}$.

The dependence of impulse generation on ambient pressure is consistent with the shock wave expansion in the schlieren images. The background gas greatly reduces the plume velocity, and thus the plume expansion is confined to a smaller region. The number of ablated plume increases in higher ambient pressure due to the confinement effect [9]. Therefore, the shock wave energy is stronger. The pressure behind the shock wave is higher and is maintained longer, which improves the impulse performance.

4 Conclusion

An experimental study for the plume expansion in laser ablation into the stratosphere condition is presented. The shock wave expansion due to the collision between ablated plume and ambient gas is captured by schlieren method. As the ambient pressure increases, the shock wave expansion velocity decreases monotonically, while the energy of shock increases. This phenomenon affects directly to the generation of the impulse. Cm, in the range of 15–85 N/MW, increases as a function of laser energy, density air, and radius of the target in high ambient pressure.

References

1. A. Kantrowitz, Propulsion to orbit by ground-based lasers. Astronaut. Aeronaut. **10**(5), 74–76 (1972)
2. C.R. Phipps Jr., T.P. Turner, R.F. Harrison, G.W. York, W.Z. Osborne, G.K. Anderson, X.F. Corlis, L.C. Haynes, H.S. Steele, K.C. Spicochi, T.R. King, Impulse coupling to targets in vacuum by KrF, HF, and CO_2 single-pulse laser. J. Appl. Phys. **64**, 1083 (1988)
3. K. Anju, K. Sawada, A. Sasoh, K. Mori, E. Zaretsky, Time-resolved measurements of impulse generation in pulsed laser-ablative propulsion. J. Propuls. Power **24**(2), 322–329 (2008)
4. D. Dufrene, P. Bournot, J.P. Caressa, G. Bosca, J. David, Pressure and impulse on an aluminum target from pulsed laser irradiation at reduced ambient pressure. Appl. Phys. Lett. **38**(4), 234–236 (1981)
5. T. Sakai, Impulse generation on aluminum target irradiated with Nd:YAG laser pulse in ambient gas. J. Propuls. Power **25**(2), 406–414 (2009)
6. N. Arnold, J. Gruver, J. Heitz, Spherical expansion of the vapor plume into ambient gas: An analytical model. Appl. Phys. A **69**, 87–93 (1999)
7. L.I. Sedov, *Similarity and Dimension Methods in Mechanics* (Academic Press, New York, 1969)
8. A.V. Gusarov, A.G. Gnedovets, I. Smurov, Gas dynamics of laser ablation: Influence of ambient atmosphere. J. Appl. Phys. **88**(7), 4352–4364 (2000)
9. H. Furusawa, T. Sakka, Y. Ogata, Characterization of ablated species in laser-induced plasma plume. J. Appl. Phys. **96**(2), 975–982 (2004)
10. A.V. Pakhomov, J. Lin, R. Tan, Air pressure effect on propulsion with transversely excited atmospheric CO_2 laser. AIAA J. **44**(1), 136–141 (2006)
11. K. Mori, R. Maruyama, K. Shimamura, Energy conversion and momentum coupling of the sub-kJ laser ablation of aluminum in air atmosphere. J. Appl. Phys. **118**, 073304 (2015)

Hypervelocity Test with a Detonation-Driven Expansion Tube

Z. Hu, K. Zhou, J. Peng, and Z. Jiang

Abstract A shock-expansion tube/tunnel is a ground-based test facility to generate hypervelocity test flows for the study of atmospheric reentry physics. Such a high enthalpy test flow features thermochemically non-equilibrium which may lead to critical difficulties in flow diagnostics and measurements. In addition, the test time of such an impulse facility is extremely short which implies a requirement of transducers with high-frequency response capability for model tests or flow diagnostics. In the present work, computations for non-equilibrium reacting flow are conducted to diagnose the key flow parameters and evaluate the test flow for facility upgrading. A conic nozzle is appended to the original facility and to obtain a larger test section and larger Mach numbers. Further experiments are conducted to visualize the overall flow structures over the test models by self-illumination of radicals at high-energy states post strong shock waves. The heat flux at the stagnation point is measured with specially designed thermal couples.

1 Introduction

When an orbital vehicle enters an atmosphere at a hypervelocity, the flow field around it features thermochemical non-equilibrium induced by extremely high-temperature post the strong shock wave. The thermal environment and aerodynamic force performance depend on the degree of the flow non-equilibrium. One of the challenges associated with the hypervelocity entry physics lies on the simulation of such a flow condition on a ground-based test facility. The primary difficulty is due to the extremely high total enthalpy or total temperature required to generate the hypervelocity test flow. Even such a high enthalpy flow can be realized in some

Z. Hu (✉) · K. Zhou · J. Peng · Z. Jiang
State Key Laboratory of High-temperature Gas Dynamics, Institute of Mechanics, Beijing, China

School of Engineering Science, University of Chinese Academy of Sciences, Beijing, China
e-mail: huzm@imech.ac.cn

A. Sasoh et al. (eds.), *31st International Symposium on Shock Waves 2*,
https://doi.org/10.1007/978-3-319-91017-8_32

specially designed shock tunnels, e.g., a shock-expansion tube/tunnel; the pulse operation mode with an extremely short test time leads to a lot of challenges in flow diagnostics and measurements.

The first shock-expansion tunnel named X-1 was set up at Queensland University [1] and is still in operation with a series of upgrading [2]. Several shock-expansion tunnels have been set up around the world, e.g., JX-1 in Japan [3], HYPULSE at GASL [4], LENS-X at CUBRC [5], and JF-16 at LHD IMECH [6–8], among others. X-1 and JX-1 are operated in a free-piston driven mode, while LENS-X is driven by heated light gases such as hydrogen or helium. JF-16 is a detonation-driven shock-expansion tunnel which was built based on a forward-detonation-driven shock tube [9, 10]. A detonation driver is capable of generating high enthalpy flows due to the high speed of sound and pressure of the driver gas.

The test time of the shock-expansion tunnel is extremely short as compared to a reflection shock tunnel of the similar scale which leads to difficulties in measurements and flow diagnostics. Generally, the test flow properties are predicted indirectly via other available measurements, e.g., static pressure measurements, shock speed measured by ionization probes, etc. A computer-aided flow diagnostic technique was applied for the prediction of JF-16 test conditions. A series of studies indicate that high level non-equilibrium and dissociation of oxygen occur in the test flow [11–13].

In the present work, CFD techniques coupled with available experimental data are used to determine the key parameters of the test flow, especially the composition variation due to the chemical non-equilibrium, in the shock-expansion tunnel. Based on the CFD outputs, the facility was upgraded by appending a conic nozzle to obtain larger test domain and cooled test flow after the steady expansion in the nozzle. With the upgraded test facility, visualization is conducted for several test models by self-illumination of radicals. In addition, the heat flux at the stagnation point is measured with specially designed thermal couples.

2 JF-16 Upgrading

The original JF-16 facility is operated in a shock-expansion tube mode [6, 7] which is shown in Fig. 1a, b. A series of simulations have been conducted according to the experimental runs to evaluate the performance and the test flow properties of the original facility. A test flow of 8.85 km/s, which is calculated using a chemical flow simulation with detailed chemistry kinetics, in the acceleration tube as shown in Fig. 2a is obtained in JF-16. Figure 2b shows the profile of mole fraction for each species at the transient when the second shock wave arrives at the test windows.

We can find that the test gas primarily consists of molecular nitrogen and atomic oxygen, i.e., N_2 and O. The dissociation of oxygen is due to the high temperature, $T_5 = 2665$ K, of the test flow as shown in Fig. 2a. Therefore, further expansion via a diverging tube is recommended to JF-16 to cool down the test flow. The upgrade has been completed by appending a conic nozzle to the original shock-expansion

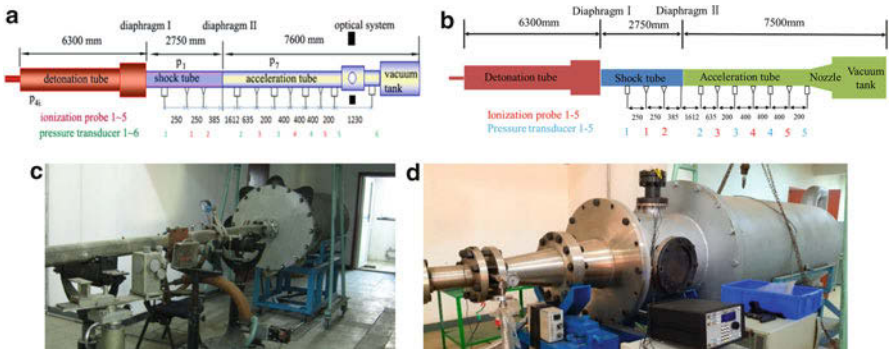

Fig. 1 Upgrading of JF-16, (**a**, **b**) Original shock-expansion tube [6, 7]; (**c**, **d**) Shock-expansion tunnel, with a conic nozzle [14, 15]

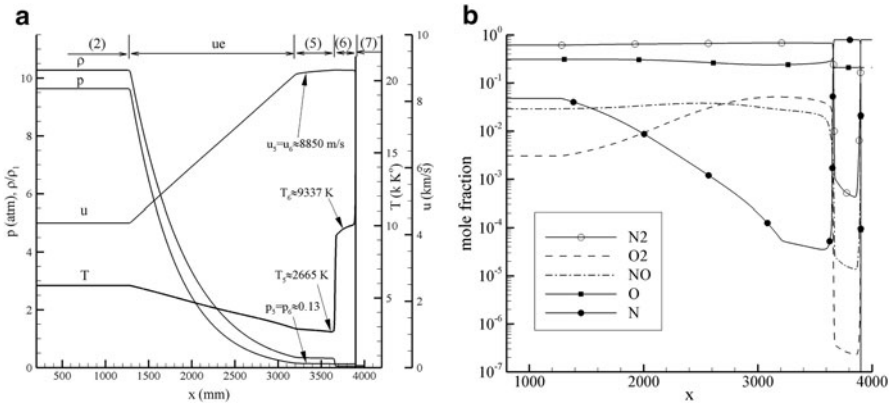

Fig. 2 The transient wave structure in the acceleration tube: (**a**) Key flow parameters; (**b**) Chemical composition of the test gas

tube [14, 15] as shown in Fig. 1c, d. Through the steady expansion in the nozzle, the test flow temperature is reduced to 950 K from 2665 K, while the Mach number is increased to 14 from 8. Simulations indicate that the oxygen atoms cannot be recombined since frozen flow maintains in the expansion nozzle. Nevertheless, the temperature of the test flow obtained in the upgraded facility is still higher than the requirement. As the total volume of the facility is insufficient, an expansion nozzle with a larger exit/entrance area ratio is not applicable. To further cool the test flow to appropriate temperature level, the facility need to be totally enlarged.

3 Flow Visualization and Model Test

The uniform test flow size reaches a diameter of 170 mm after the aforementioned upgrade of JF-16 shock-expansion tunnel. As such, test models of a larger size can be accommodated in the test section. Here, a half-sphere blunted model with a diameter of 50 mm and a half-cylinder blunted model with the same diameter are used for the flow visualization. Flow structures are captured directly from the self-illumination of radicals at high-energy states post the strong shock wave. The resolution of the camera (FASTCAM SA4) is 1024 $\times$ 1024 with a frame rate of 500 kfps.

Further experiments are conducted with the obtained hypervelocity flow over several test models of different geometries, such as wedge and double wedge, cone and double cone, cylinder, and sphere. Some transient images over the sphere and cylinder models are given in Fig. 3, where one can see the color variation which implies the variation of the degree of non-equilibrium in the high-temperature flow post the strong shock wave.

It was reported that the shock shape doesn't match in a computation-experiment integrated study from a CUBRC group [16, 17]. The uncertainty in thermochemical states of the freestream flow was supposed to be the primary, although not all, contributing factor to the mismatch. In a later study, however, a good agreement was achieved where the freestream flow condition of the test facility could be well determined [18]. Therefore, the test flow condition should be well predicted prior to the comparison study. A series of computations are conducted for comparison with the experiments. The freestream flow conditions for the simulation are determined with a computer-aided flow diagnostic technique [11–13]. The comparison is shown in Fig. 4 where the computed flow structures are superposed on the experimental photos. The agreement is acceptable which implies the well predicting of the test flow. For quantitative comparison, the standoff distances of the bow shock wave are listed in Table 1. Discrepancy can be seen obviously which may be caused by

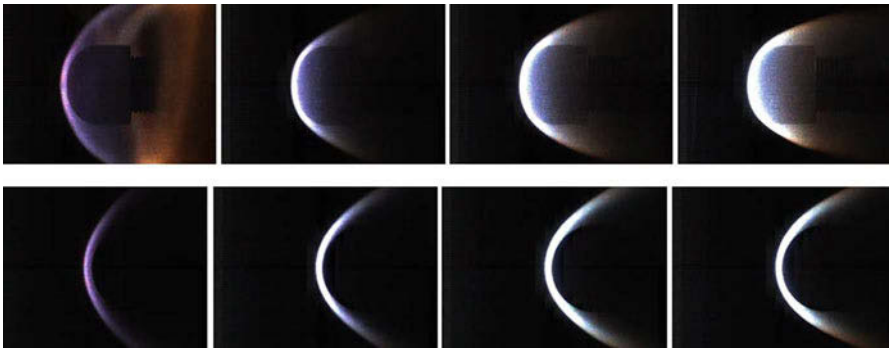

Fig. 3 Flow visualization by self-illumination of radicals post bow shock waves: upper, sphere; lower, cylinder ($V_\infty = 8$ km/s, time interval 33 μs)

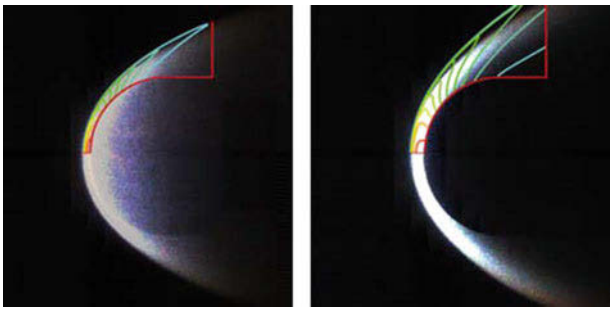

Fig. 4 Comparison between experiment and computation: (left) sphere-blunted model; (right) cylinder-blunted model

Table 1 Comparison of standoff distance

Model	Standoff (mm)		Discrepancy (%)
	Experiment	Computation	
Sphere	2.5	2.3	8
Cylinder	4.1	4.7	14.6

uncertainties in the flow diagnostics. One can also see the remarkable discrepancy in the bow shock shape within the outer region. The reason is still unclear currently, and a reasonable expectation is the uncertainty in the chemical model used for the computations especially for the flow domain where the expansion wave is predominant. Nevertheless, this problem is still open, and further studies on the uncertainties in the flow diagnostics and chemistry kinetics are required in the future.

As aforementioned, the test time of the shock-expansion tunnel is extremely short, around 100 μs. This leads to difficulties in flow measurement since the response time of a conventional transducer may exceed such a short duration. A specially designed sphere model has been applied for stagnation heat measurement [15]. As shown in Fig. 5, the sphere model of 50 mm in diameter, along with a coaxial thermal couple mounted at the stagnation point, is coated with a film of copper (averaged thickness 300 nm). Such a technique can significantly reduce the response time of the transducer. Several runs with different total enthalpies have been conducted for the measurement of stagnation heat flux, $\dot{Q}_{st}$. The comparison among experiments, De Filippis-Serpico formula [19], and computations are given in Table 2. For the test condition with a total enthalpy of 27 MJ/kg, the measured data agree with the predicted data using a non-catalytic wall condition. When the total enthalpy exceeds 35 MJ/kg, the experiment and prediction agree with each other under the full-catalytic wall condition. Such a finding implies the strong chemical non-equilibrium present in the stagnation region, and recombination of atoms occurs at the cool model surface.

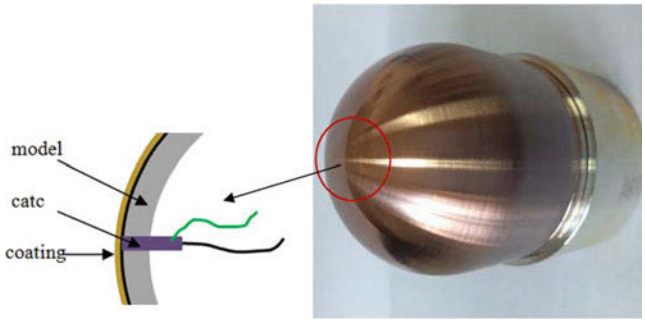

Fig. 5 Specially designed model for heat flux measurement (catc: coaxial thermal couple) [15]

Table 2 Stagnation heat $\dot{Q}_{st}$ measurement and comparison

Run no.	V_∞ (km/s)	H_0 (MJ/kg)	Experiment (MW/m^2)	De F-S (MW/m^2) [19]		CFD (MW/m^2)	
				FCW	NCW	FCW	NCW
1	7.1	27	7.9	14.5	7.2	15.1	7.1
2	7.9	35	21.5	22.2	10.7	23.2	10.1
3	8.8	45	32.5	31.3	15.9	29.6	13.3

4 Conclusions

A detonation-driven shock-expansion tunnel is set up to conduct hypervelocity flow test in the present work. With well-predicted test flow condition, acceptable agreement between experiments and computations can be achieved for the overall flow structure as well as the surface heat flux. Self-illumination images are captured in the flow visualization over several test models. Comparison with computations indicates a discrepancy within the outer region, while agreement is achieved in the stagnation region. The measurement of stagnation heat flux implies that recombination of atoms occurs along the cool model surface under the high total enthalpy condition which corresponds to a full-catalytic wall assumption.

Acknowledgments This work was supported by the National Natural Science Foundation of China under Grant No. 11672308 and 11532014.

References

1. R.G. Morgan, R.J. Stalker, Double diaphragm driven expansion tube, in *Proceedings of the 18th International Symposium on Shock Waves*, Sendai, Japan, 1991
2. M.P. Scott, *Development and Modeling of Expansion Tubes*. PhD Thesis, University of Queensland, St. Lucia, Australia, 2006

3. A. Sasoh, K. Ohnishi, K. Koremoto, K. Takayama, Operation design and performance of a free piston driven expansion tube, in *37th AIAA Aerospace Sciences Meting and Exhibition*, Reno, Nevada, AIAA paper 99-0825, 1999
4. R.S.M. Chue, C.Y. Tsai, R.J. Bakos, J.I. Erdos, R.C. Rogers, NASA's HYPULSE facility at GASL-A dual mode, dual driver reflected-shock/expansion tunnel, in *Advanced Hypersonic Test Facilities*, vol. 198, ed. by F. Lu, D. Marren (AIAA, 2002), pp. 29–71
5. M.S. Holden, T.P. Wadhams, M. MacLean, E. Mundy, Experimental studies in the LENS I and X to evaluate real gas effects on hypervelocity vehicle performance, in *45th AIAA Aerospace Sciences Meeting and Exhibit*, Reno, Nevada, AIAA paper 2007-204, 2007
6. Y.L. Gao, *Study on Hypervelocity Flow Generation Techniques and Essential Hypersonic Phenomena*. PhD Thesis, Institute of Mechanics, Beijing, China, 2008
7. B. Wu, *Study on the Interaction of Strong Shock Wave and the Hypervelocity Experimental Method*. PhD Thesis, Institute of Mechanics, Beijing, China, 2012
8. Z.L. Jiang, B. Wu, Y.L. Gao, W. Zhao, Z.M. Hu, Development of the detonation-driven expansion tube for orbital speed experiments. Sci. China Tech. Sci. **58**(4), 695–700 (2015)
9. H. Yu, B. Esser, M. Lenartz, H. Grönig, Gaseous detonation driver for a shock tunnel. Shock Waves **2**, 245–254 (1992)
10. Z. Jiang, W. Zhao, C. Wang, K. Takayama, Forward-running detonation drivers for high-enthalpy shock tunnels. AIAA J. **40**, 2009–2016 (2002)
11. Z.M. Hu, Z.L. Jiang, Numerical predictions for the hypervelocity test flow conditions of JF-16, in *29th International Symposium on Shock Waves*, Madison, America, 2013
12. Z.M. Hu, Z.L. Jiang, Computer-aid diagnostic of hypersonic test flow in a shock-expansion tube, in *The 9th Pacific Symposium on Flow Visualization and Image Processing*, Bisan, South Korea, 2013
13. Z.M. Hu, C. Wang, Z.L. Jiang, B.C. Khoo, On the numerical technique for the simulation of hypervelocity test flows. Comput. Fluids **2015**(106), 12–18 (2015)
14. K. Zhou, C.K. Yuan, Z. Hu, Z. Jiang, Test flow analysis and upgrade of JF-16 expansion tune. Acta. Aeronaut. et Astronaut. Sin. **37**, 3296–3303 (2016)
15. K. Zhou, *Experimental Study on Hypervelocity Flow with Expansion Tunnel*. PhD Thesis, Institute of Mechanics, Beijing, China, 2017
16. M. MacLean, M. Holden, Numerical assessment of data in catalytic and transitional flows for Martian entry, AIAA 2006-2946 (2006)
17. M. MacLean, T. Wadhams, M. Holden, Integration of CFD and experiments in the CUBRC LENS shock tunnel facilities to understand the physics of hypersonic and hypervelocity flows, in *4th Symposium on Integrating CFD and Experiments in Aerodynamics*, Rhode-Saint-Genese, Belgium, Set. 14–16, 2009
18. M. Sharma, A.B. Swantek, W. Flaherty, J.M. Austin, S. Doraiswamy, G.V. Candler, Evaluation of hypervelocity carbon dioxide blunt body experiments in an expansion tube facility, AIAA 2011-136 (2011)
19. F.D. Filippis, R. Savino, A. Martucci, Numerical-experimental correlation of stagnation point heat flux in high enthalpy hypersonic wind tunnel, AIAA Paper 2005-3277 (2005)

Shock Shape Transition on Spherically Blunted Cones in Hypersonic Flows

J. Martinez Schramm, K. Hannemann, and H. G. Hornung

Abstract Spherically blunted cones are commonly utilized as re-entry or entry capsules. Depending on the cone angle, the shock shape is either dominated by the spherical nose or the conical part. In flight a transition between these two situations might occur, and this can result in undesirable effects on the aerodynamic stability. To understand the shock shape transition behaviour in more detail, a systematic numerical and experimental study is ongoing. In the present article, the influence of vibrational non-equilibrium compared to frozen flow is discussed for sphere-cone configurations at zero-degree angle of attack.

1 Introduction

Wen and Hornung [12] showed that the shock stand-off distance Δ in front of a sphere for a calorically perfect gas is proportional to the density ratio ε across the shock wave:

$$\frac{\Delta}{R_N} = 0.78\,\frac{\rho_\infty}{\rho_S} = 0.78\,\varepsilon = 0.78\,\frac{\gamma - 1 + 2/M_\infty^2}{\gamma + 1} \tag{1}$$

with $\rho_\infty$the free stream density, ρ_S the density behind a normal shock, $\gamma$the specific heat ratio, M_∞ the free stream Mach number and R_N the sphere radius. If we consider the same flow over a sharp cone of a given half-angle Θ, the stand-off distance increases linearly with ε from a critical onset point ε_d. Further, if Θ is sufficiently small, the shock wave on the cone is conical and attached to the cone tip with supersonic flow downstream the shock. Details of this flow are described by

J. Martinez Schramm · K. Hannemann (✉)
German Aerospace Center, DLR, Institute for Aerodynamics and Flow Technology, Spacecraft Department, Göttingen, Germany
e-mail: Klaus.Hannemann@dlr.de

H. G. Hornung
GALCIT, Caltech, Pasadena, CA, USA

A. Sasoh et al. (eds.), *31st International Symposium on Shock Waves 2*,
https://doi.org/10.1007/978-3-319-91017-8_33

Taylor and Maccoll [11]. As Θ is increased beyond the detachment angle Θ_d, the Taylor-Maccoll solution does not exist, and the shock wave is detached. If the cone extends to a sharp shoulder with radius R measured from the axis, the flow behind the detached shock wave is subsonic up to a sonic line that extends between the shock wave and the shoulder. For a given half-cone angle and according to [5], the critical density ratio across a normal shock ε_d at the detachment point with $\Theta = \Theta_d$ is given by

$$\varepsilon_d = \frac{2}{\tan^2(\Theta/2 + \pi/4)} \tag{2}$$

From [6] it can be extracted that the linear growth of Δ/R is well approximated by

$$\frac{\Delta}{R} \simeq A\,(\varepsilon - \varepsilon_d) \tag{3}$$

where the factor A may be taken to be constant at 1.6 within the limited range of Θ of interest here. Combining Eqs. (2) and (3), we finally obtain, for flow over a sharp cone,

$$\frac{\Delta}{R_N} \simeq A\frac{R}{R_N}\left[\frac{\gamma - 1 + 2/M_\infty^2}{\gamma + 1} - \frac{2}{\tan^2(\Theta/2 + \pi/4)}\right] \tag{4}$$

Here we aim to test the theoretical/empirical considerations by performing experiments in the High Enthalpy Shock Tunnel Göttingen, HEG of the German Aerospace Center and by conducting a computational study utilizing the DLR TAU code [7, 10]. The investigations were conducted using a fixed free stream condition and capsule models of varying half-cone angles at zero-degree angle of attack. The condition was chosen such that the influence of vibrational excitation on the shock shape transition can be analysed.

2 High Enthalpy Shock Tunnel Göttingen

The High Enthalpy Shock Tunnel Göttingen (HEG) of the German Aerospace Center, DLR, is a free piston-driven shock tunnel which was commissioned for use in 1991 (see, e.g., [2]). Originally, HEG was designed for the investigation of the influence of high temperature effects such as chemical and thermal relaxation on the aerothermodynamics of entry or re-entry space vehicles. Subsequent extensions of the HEG operating range included the establishment of a number of low total specific enthalpy conditions and of complete scramjet engine ground-based testing capabilities [3, 4, 7]. The HEG operating condition used for the experiments described here is condition XIII. The mean reservoir conditions of the present test campaign are summarized in Table 1, and the resulting mean free stream conditions are given in Table 2. Detailed calibration of HEG condition XIII revealed that the free stream is in chemical and thermal equilibrium [3, 7].

Table 1 Mean reservoir conditions using air as test gas (HEG condition XIII)

p_0 [bar]	T_0 [K]	h_0 [MJ/kg]	ρ_0 [kg/m^3]
182.3	2742	3.251	23.34

Table 2 Mean free stream conditions using air as test gas (HEG condition XIII)

Ma	Re_m	p_{t2}	ρ	u	T	p
[−]	[1/m]	[kPa]	[g/m^3]	[m/s]	[K]	[Pa]
7.36	5.6×10^6	144.9	26.7	2416	267	2054

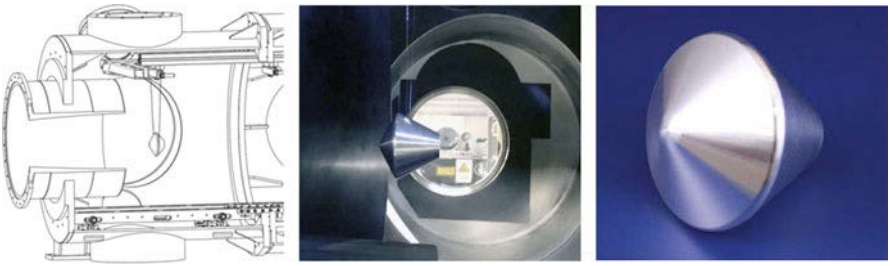

Fig. 1 Schematic (left) and photograph (middle) of the model setup in HEG; photograph of the model (right)

3 Experimental Setup

The models are made out of aluminium and have a typical mass of 0.5 kg. The present shock shape transition studies were combined with force measurements utilizing the free-flight force measurement technique [1, 4].

Therefore, two small holes of 0.6 mm diameter are drilled into the top at the axial position of the centre of mass. Plastic threads are glued into the drill holes, in order to mount the models at an angle of attack of $\alpha = 0°$. The threads are wrapped around a holder installed at the test section ceiling. Figure 1 (left, middle) shows a schematic and a photograph of the model setup in the test section. Figure 1 (right) shows a photograph of the model. The capsule geometry is defined in Fig. 2. While the shoulder radius of the capsules $R = 40$ mm, the expansion radius $R_S = 4$ mm on the shoulder, the nose radius $R_N = 16$ mm and the base angle $\Theta_B = 27°$ are kept constant, the cone angle Θ is varied between 50° and 75°.

Special care was taken to align the models without any yaw with respect to the nozzle exit plane. Upon flow arrival the threads break and the model flies freely during the test. A sequence of schlieren images showing the detachment process and the free flying phase is given in Fig. 3. The free-flight technique in conjunction with optical tracking requires recording high-contrast images of the model during the free flight. From these images the model location and orientation can be evaluated. Tracking algorithms used to conduct this procedure are described, e.g. in [9]. A detailed description of the technique applied to the experimental data presented here is given in [1].

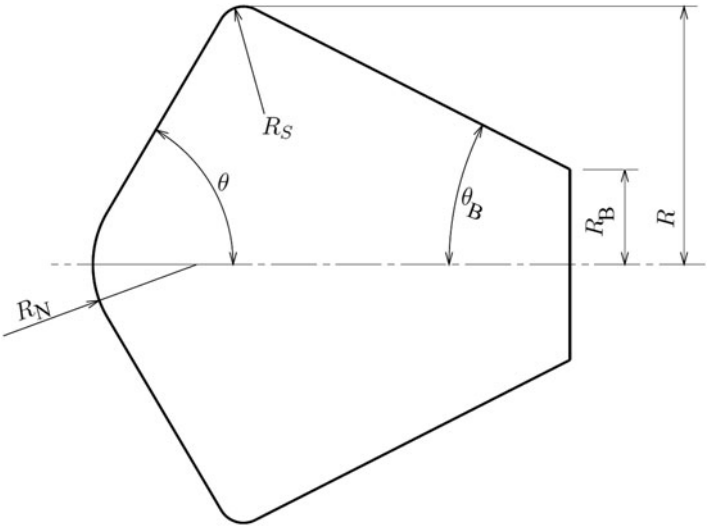

Fig. 2 Capsule model specifications

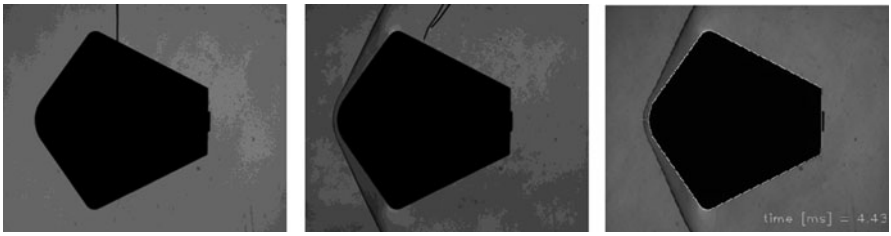

Fig. 3 Visualization of a capsule model prior to the run, at detachment from the threads and during the free-flight phase within the test time window (from left to right). The white line on the outer contour shows the detected geometry and the white line at the stagnation point the interrogation zone for the shock stand-off distance detection

The intensity distribution along the stagnation streamline is extracted from each image. This quantity is directly related to the density gradient due to the vertical orientation of the knife edge in the schlieren setup. The intensity distribution is subsequently interpolated, and the maximum is used as the position of the shock wave. The same procedure was applied to the density gradients obtained from the numerical simulation to locate the maximum gradient, i.e. the shock position.

4 Numerical Method

The computations for calorically perfect gas, chemical and thermal equilibrium and non-equilibrium were performed with the hybrid structured-unstructured DLR Navier-Stokes solver TAU [7, 10]. For the cases presented here, the AUSDMV flux

vector splitting scheme is used with HLLE gradient reconstruction. The equilibrium properties are calculated from partition functions or look-up tables. For the case of chemical non-equilibrium, the chemical source term is computed from the law of mass action by summation over all participating reactions. The forward reaction rate is computed using the modified Arrhenius law, and the backward rate is obtained from the equilibrium constant. For the consideration of thermal non-equilibrium, the relaxation rates of the vibrational energy for vib-vib and vib-trans coupling are computed according to Klomfaß [8].

5 Results

The measured shock shape transition is summarized in Fig. 4 (upper part) where schlieren images taken during the steady test time window are shown for varying half-cone angle Θ of the capsule configuration. In the lower part of Fig. 4, numerical schlieren images are shown highlighting particularly the shock shape and the modification of the sonic line during the shock shape transition process. It should be noted that for some cone angles, CFD data resulting from thermal equilibrium computations was utilized. Thereby the shock stand-off distance is not correctly reproduced; however, qualitatively the shock shape transition process proceeds in a similar way.

The measured and computed shock stand-off distance along the stagnation streamline is plotted in Fig. 5 (left). Different physico-chemical models describing the test gas air were applied in order to be able to quantify their influence on the observed shock shape transition. These models include the assumption chemical/thermal equilibrium (eq/teq), chemical non-equilibrium/thermal equilibrium

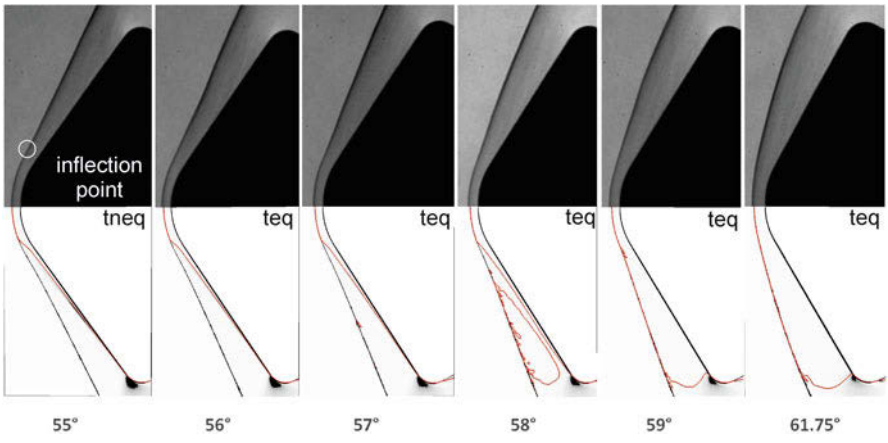

Fig. 4 Schlieren images showing the change in shock shape ahead of capsules with various half-cone angles Θ; experiment (upper part), CFD (lower part)

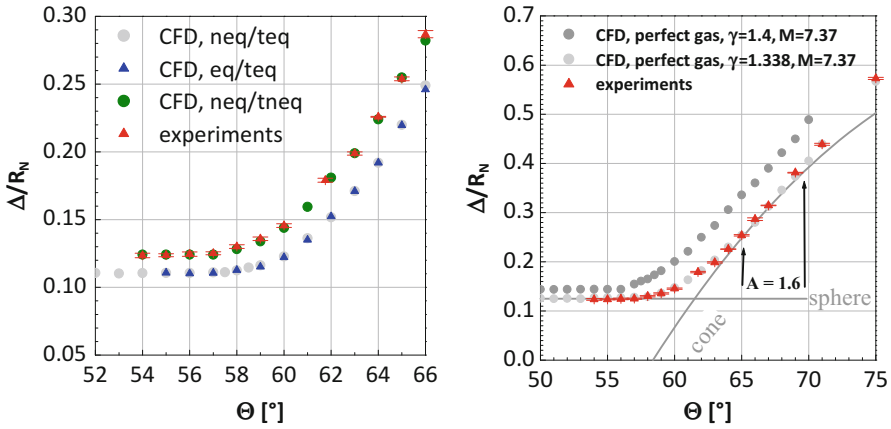

Fig. 5 Measured and computed normalized shock stand-off distance (left) and comparison with theoretical/empirical correlations (right)

(neq/teq) and chemical/thermal non-equilibrium (neq/tneq). The numerical results based on the model of a calorically perfect gas with $\gamma = 1.4$ (frozen flow) are given in addition to the theoretical/empirical correlations describing the shock stand-off distance in front of the sphere (Eq. (1)) and sharp cone (Eq. (4)) in Fig. 5 (right).

6 Discussion and Conclusions

Using HEG operating condition XIII and sphere-cone configurations with varying half-cone angle, the shock shape transition from the region where the shock stand-off distance is dominated by the spherical part to the region which is dominated by the conical part occurs in the range of approximately $58° < \Theta < 65°$. During this transition process, the structure of the sonic line changes. In addition to the subsonic region generated by the sphere shock in the vicinity of the symmetry axis, a second subsonic region occurs behind the oblique shock further away from the axis. Ultimately both subsonic regions merge, and a large subsonic region in front of the configuration exists, and the sonic line is anchored at the expansion shoulder. Further, the inflection point of the shock which is observed as long as the shock stand-off distance is dominated by the spherical part disappears for larger half-cone angles.

The comparison of the measured and computed shock stand-off distance clearly shows the influence of the different physico-chemical models. The measured values are best fitted by the assumption of a chemical and thermal non-equilibrium flow. However, the comparison between the chemical equilibrium and non-equilibrium assumption reveals that the chemistry can be considered to be in equilibrium. If high temperature effects are completely neglected, i.e. a frozen flow with $\gamma = 1.4$

(extracted from the HEG free stream) is computed, the shock stand-off distance is generally increased, and most importantly the shock shape transition region starts at lower half-cone angle (approximately $56° < \Theta < 62°$). It is assumed that this effect will be further increased at higher total specific enthalpy conditions where stronger dissociation of the oxygen and nitrogen molecules will occur and the flow is in chemical and thermal non-equilibrium.

A first attempt to derive a theoretical/empirical correlation to describe the asymptotic behaviour of the shock stand-off distance for the cone-dominated region was performed, and good agreement was obtained for the limited range of half-cone angles considered. The stand-off distance of the sphere-dominated region is well approximated by the Wen and Hornung correlation. However, since the correlation only describes the asymptotic behaviour, it cannot account for the smooth transition obtained by the present experimental and computational results.

References

1. D. Friedl, J. Martinez Schramm, K. Hannemann, Measurements by means of optical tracking in the High Enthalpy Shock Tunnel Göttingen, HEG, in *8th European Symposium on Aerothermodynamics for Space Vehicles*, Lisbon, Portugal, 02–06 March 2015
2. K. Hannemann, J. Martinez Schramm, S. Karl, Recent extensions to the High Enthalpy Shock Tunnel Göttingen (HEG), in *Proceedings of the 2nd International ARA Days "Ten Years after ARD"*, Arcachon, France, 21–23 October 2008
3. K. Hannemann, S. Karl, J. Martinez Schramm, J. Steelant, Methodology of a combined ground based testing and numerical modelling analysis of supersonic combustion flow paths. Shock Waves **20**(5), 353–366 (2010), Springer
4. K. Hannemann, J. Martinez Schramm, S. Karl, S.J. Laurence, Enhancement of free flight force measurement technique for scramjet engine shock tunnel testing, in *21st AIAA International Space Planes and Hypersonics Technologies Conference*, Xiamen, China, AIAA 2017-2235, 2017
5. W.D. Hayes, R.F. Probstein, *Hypersonic Flow Theory* (Academic Press, New York, 1959)
6. H.G. Hornung, J. Martinez Schramm, K. Hannemann, Sonic line and stand–off distance on re–entry capsule shapes, in *Proceedings of the 28th International Symposium on Shock Waves held in Manchester UK*, 17–22 July 2011, vol. 1, , ed. by K. Kontis (Springer, 2012)
7. S. Karl, *Numerical Investigation of a Generic Scramjet Configuration*. PhD thesis, Technical University Dresden, 2011
8. A. Klomfaß, *Hyperschallströmungen im thermischen Nichtgleichgewicht*. PhD thesis, RWTH Aachen, Berichte aus der Luft- und Raumfahrt, Shaker, 1995
9. S.J. Laurence, On tracking the motion of rigid bodies through edge detection and least-squares fitting. Exp. Fluids **52**(2), 387–401 (2012)
10. D. Schwamborn, T. Gerhold, R. Heinrich, The DLR Tau-Code: Recent applications in research and industry, in *Proceedings of the European Conference on Computational Fluid Dynamics ECCOMAS*, ed. by P. Wesseling, E. Onate, J. Periaux (TU Delft, The Netherlands, 2006)
11. G.I. Taylor, J.W. Maccoll, The air pressure on a cone moving at high speed. Proc. Roy. Soc. A **139**, 278–311 (1933)
12. C.-Y. Wen, H.G. Hornung, Non-equilibrium dissociating flow over spheres. J. Fluid Mech. **299** (1995)

Catalytic Recombination Characteristics of Atomic Oxygen on Material Surface by Optical Emission Spectroscopy

X. Lin, S. Wang, F. Li, S. Zhang, and X. Yu

Abstract Catalytic recombination of atomic oxygen, the main species of air ionization, on heat shield material surfaces was studied in a microwave plasma flow reactor. The atomic oxygen concentration profile above material samples was nonintrusive measured by optical emission spectroscopy. The catalytic recombination coefficients on material surfaces were deduced by the diffusion equation. The catalytic recombination coefficients for the heat shield materials at high temperature obtained in the present experiment are very important parameters for thermal shield design of space vehicles.

1 Introduction

The issue of hypersonic vehicle thermal protection remains a major challenge for the field of aerospace. During the reentry phase on earth or the continued flight in the earth's atmosphere, the air around the blunt head is heated to very high temperatures because of the compression effect of the strong shock. One of the most important physical phenomena occurring on the heat shield is the recombination of atomic oxygen on the spacecraft surface. The catalytic recombination coefficients for the heat shield materials at high temperature obtained in the present experiment are very important parameters for heat shield design for future space vehicles and the development of new high-temperature materials [1, 2].

Ground test simulations under atmospheric reentry conditions are therefore necessary to characterize and select base materials for heat shields [3–8]. The most essential conditions (high-temperature, low-pressure air plasma) for simulating the reentry phase of space vehicles are reproduced through carbon dioxide laser heating

X. Lin · S. Wang · F. Li · S. Zhang
State Key Laboratory of High Temperature Gas Dynamics, Institute of Mechanics, Chinese Academy of Sciences, Beijing, China

X. Yu (✉)
School of Engineering Science, University of Chinese Academy of Sciences, Beijing, China
e-mail: xlyu@imech.ac.cn

A. Sasoh et al. (eds.), *31st International Symposium on Shock Waves 2*,
https://doi.org/10.1007/978-3-319-91017-8_34

equipment and a microwave plasma generator in the Institute of Mechanics, CAS. Although such devices cannot completely simulate the characteristics of heating surface of the environment for aircraft, it can be simulated in a small sample surface catalytic process of local thermal environment, with good control (temperature, pressure range), lower operating costs [9].

In this paper, the catalytic recombination coefficients with different temperatures by optical emission spectroscopy are proposed. This provides useful information for the future thermal protection system of the spacecraft.

2 Facilities and Experiments

2.1 Experimental Setup

Experimental investigations have been carried out in the microwave plasma generator located in the Institute of Mechanics, CAS. Figure 1 presents the experimental setup for optical emission spectroscopy measurement. It contains a microwave plasma flow reactor, auxiliary heating of the CO_2 lasers, infrared thermometers, flow controllers, and the spectrum measurement system. In addition, the vacuum system consists of vacuum pumps, vacuum gauges, and other components. The output frequency of the microwave plasma flow reactor is 2450 MHz, associating with the maximum output power of 1 kW, and it consists of a silica tube with length of 50 cm and ZnSe viewport with diameter of 5 cm. The sample (20 mm diameter and 3 mm thickness) was placed in stagnation point position at the center of the discharge. In order to change the surface temperature of the sample, we use CO_2 lasers to heat the samples and the surface temperature measured by the infrared thermometer.

Spectral information was recorded using a Princeton Instruments Acton 2300. A 300 mm focal length spectrograph with three gratings was coupled to a gated intensified charge-coupled device (ICCD). A 1200 grooves/mm grating was used in the spectrometer giving a spectral resolution of 0.1 nm/pixel. An entrance slit width of 20 μm was used throughout the experiments. Furthermore, in order to obtain the concentration distribution of the axial surface, the lens collection system can shift up and down freely.

2.2 Evaluation of the Recombination Coefficients

An actinometry technique based on optical emission spectroscopy was used to determine the spatial variation of the relative atomic oxygen concentration profiles along the discharge region. The known quantity of argon (6%) is introduced in the flow, and the evolution of the relative intensities ratio I_O/I_{Ar} of the 844.6 nm (O line)

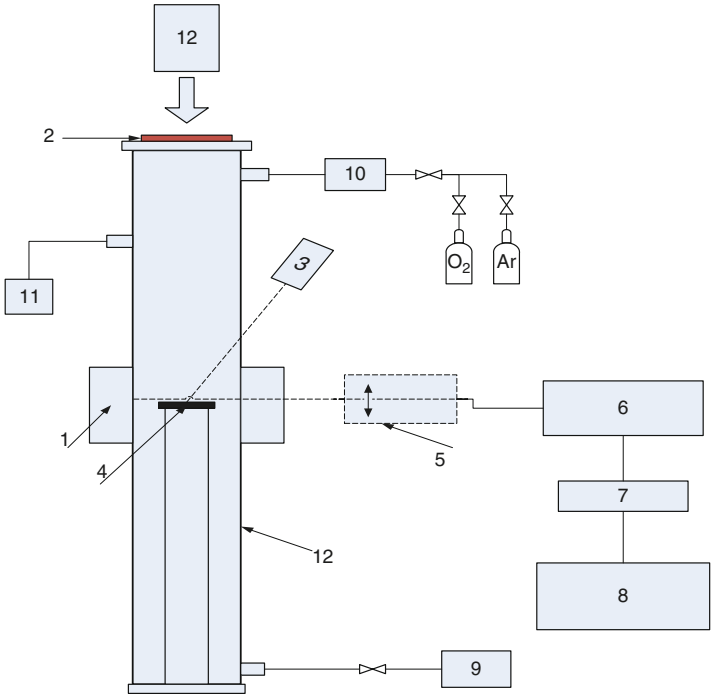

Fig. 1 Schematic of microwave plasma flow reactor and the emission spectroscopy measurement system (1. waveguide, 2. viewport, 3. infrared thermometer, 4. samples, 5. lens, 6. spectrometer, 7. ICCD, 8. computer, 9. vacuum pumps, 10. flow controllers, 11. vacuum gauges, 12. CO_2 lasers)

and 842.4 nm (Ar line) is surveyed along the discharge region through the window (diameter: 3 cm) in the waveguide. From the following equation [3]),

$$\gamma_O = \left(\frac{C_{O(x=L)}}{C_{O(x=0)}} - 1 \right) \frac{4 D_{O,O_2}}{V L} \tag{1}$$

the intensity ratio profile that leads to the determination of the recombination coefficient γ is obtained, where D_{O,O_2} the binary diffusion coefficient of O in oxygen, V the mean square atomic oxygen velocity and L the thickness of the boundary layer measured from the experiment and C_O the concentration of atomic oxygen, at the entrance of the reactor ($x = L$) and at the surface of sample ($x = 0$) respectively.

Taking into account flow temperature (T_L) and surface temperature (T_S) gradient, the oxygen concentration ratio is related to the measured intensities ratio I_O/I_{Ar} by

$$\frac{C_{O(x=L)}}{C_{O(x=0)}} = \frac{\left. \frac{I_O}{I_{Ar}} \right|_{X=L}}{\left. \frac{I_O}{I_{Ar}} \right|_{X=0}} \frac{T_s}{T_L} \tag{2}$$

In this experiment, we assume that thermal equilibrium is reached, so the sample surface and gas are at the same temperature. With the assumption, the recombination coefficient γ is deduced from Eq. (3)

$$\gamma_O = \left(\frac{\left.\frac{I_O}{I_{Ar}}\right|_{X=L}}{\left.\frac{I_O}{I_{Ar}}\right|_{X=0}} - 1 \right) \frac{4D_{O,\text{air}}}{VL} \tag{3}$$

3 Results and Discussions

The relative atomic oxygen concentrations are measured in the conditions which are mentioned in the above section. In the tests, we make use of different power lasers (30, 60 W) to change the surface temperatures, which are measured by an infrared thermometer ($\lambda = 2\mu m$).

Figures 2 and 3 present the relative atomic oxygen concentrations versus the distance from the sample surface for C/SiC and low-ablation C/C respectively. The data for both figures were measured during the same experimental conditions (T $\approx$ 653 K, P = 180 Pa). Figures 2 and 3 also show good reproducibility and obvious atomic oxygen concentration gradient.

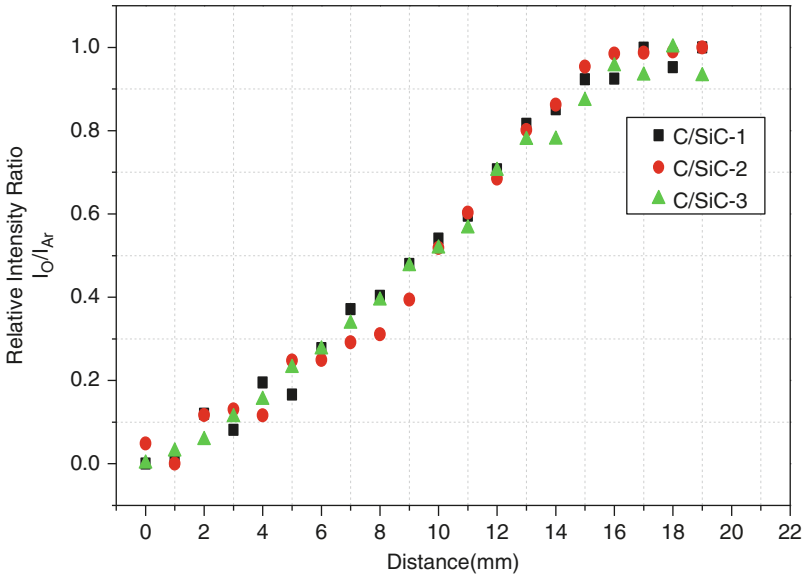

Fig. 2 The relative atomic oxygen concentration varies with the distance from the sample surface for C/SiC at 653 K and 180 Pa total air pressure

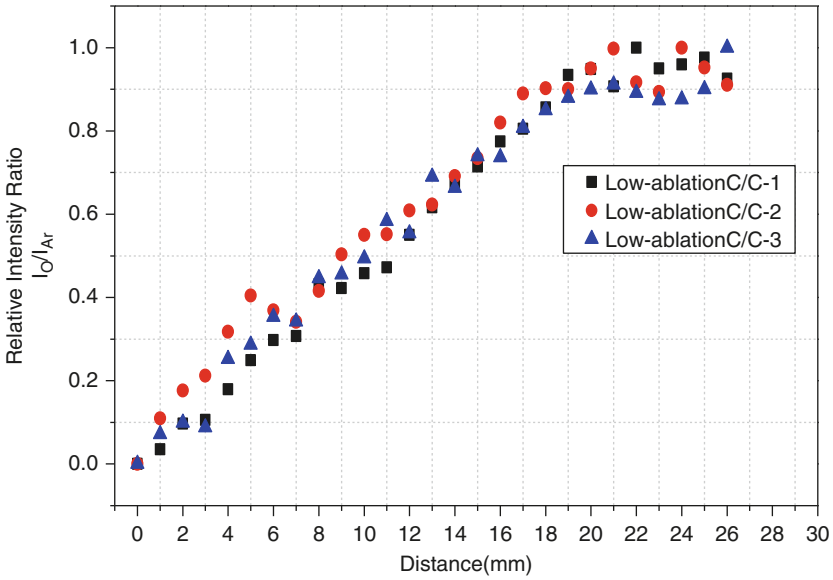

Fig. 3 The relative atomic oxygen concentration varies with the distance from the sample surface for low-ablation C/C at 623 K and 180 Pa total air pressure

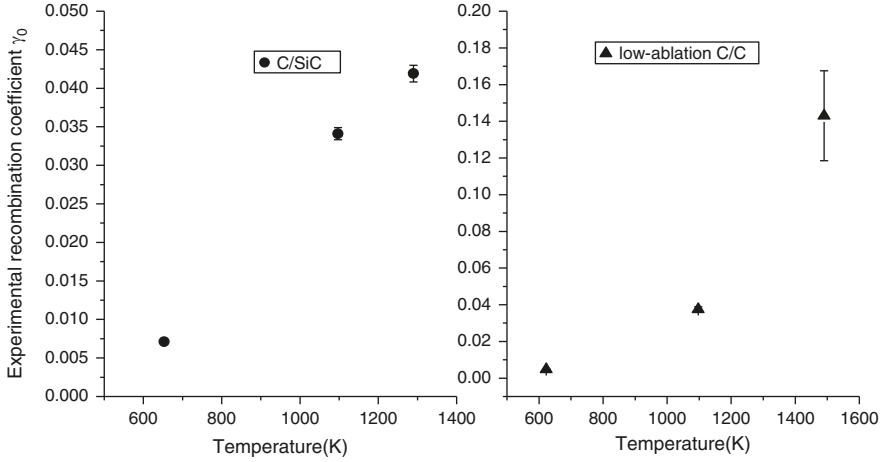

Fig. 4 Experimental recombination coefficient γ_O for atomic oxygen at 180 Pa total air pressure for C/SiC and low-ablation C/C at different temperatures

Through the catalytic reaction mechanism of the material, catalytic recombination coefficient of atomic oxygen will reach the maximum at a critical temperature [10]. Below the critical temperature, the coefficient meets the Arrhenius temperature law. The phenomena were also observed in this study. The values of the recombination coefficient γ_O have been calculated for each material as shown in Fig. 4.

4 Conclusion

By using atomic emission spectroscopy, the recombination coefficients of atomic oxygen γ_o for thermal protection materials, silicon carbide (SiC) and silica at different temperatures were obtained. The present experiments are very important for heat shield design of future space vehicles.

References

1. Y. Bian et al., *Aerothermodynamics* (USTC Press, Hefei, China, 1997)
2. J.D. Anderson, *Hypersonic and High Temperature Gas Dynamics* (McGraw-Hill Co, New York, 1989)
3. M. Balat-Pichelin et al., Chem. Phys. **291**, 181 (2003)
4. P. Kolodziej et al., AIAA **87**, 1637 (1987)
5. D.A. Stewart et al., NASA CP **2283**., Part 2, 827 (1983)
6. R.J. Willey, J. Thermophys. Heat Transf. **7**, 55 (1993)
7. C.D. Scott, *Aerothermodynamics and Planetary Entry*, Prog. Astronaut. Aeronaut. AIAA **77** (New York, 1981), pp. 192–212.
8. M. Balat et al., Appl. Surf. Sci. **120**, 225 (1997)
9. M. Balat-Pichelin, Chem. Phys. **340**, 217 (2007)
10. E.J. Jumper, J. Thermophys. Heat Transf. **8**, 460–465 (1994)

Influence of Dual Ignition on Test Conditions of a High-Enthalpy Shock Tunnel

Q. Wang, W. Zhao, J. W. Li, J. P. Li, P. Lu, and Z. L. Jiang

Abstract The forward mode is usually chosen to achieve high-enthalpy flows for a detonation-driven shock tunnel. In this paper, the dual-ignition system was developed to burst a metal diaphragm without its fragmentation under the forward operation mode. The influence of delay time on the test conditions of the high-enthalpy shock tunnel was investigated numerically. Results showed that the delay time should be set exactly, or it would affect the performance of the shock tunnel using the dual-ignition forward driving mode, i.e., the effective test or the stagnation temperature. The larger the delay time, the closer the CJ plane propagates to the primary diaphragm, the better consistent with the forward mode.

1 Introduction

Hypersonic technology is one of the most important research issues for aerospace program, and the development of modem reentry vehicles requires extensive testing in hypersonic facilities. Among the impulse facilities, cover hypersonic flows range from 2.5 to 45 MJ/kg, which corresponds to velocities from 2 to 10 km/s, respectively; shock tunnels show their advantages for the accommodation of relatively large-size models and low operational costs [1, 2]. The results achieved are used for the design process as well as for CFD code validation.

In view of enthalpy and pressure requirements for the shock tunnel, it must incorporate a high-performance driver. Among the existing driving techniques, the

Q. Wang · J. W. Li · J. P. Li
State Key Laboratory of High Temperature Gas Dynamics, Institute of Mechanics, Chinese Academy of Sciences, Beijing, China

W. Zhao (✉) · P. Lu · Z. L. Jiang
State Key Laboratory of High Temperature Gas Dynamics, Institute of Mechanics, Chinese Academy of Sciences, Beijing, China

School of Engineering Science, University of Chinese Academy of Sciences, Beijing, China
e-mail: zw@imech.ac.cn

A. Sasoh et al. (eds.), *31st International Symposium on Shock Waves 2*,
https://doi.org/10.1007/978-3-319-91017-8_35

detonation drivers are capable of producing high-enthalpy and high-pressure test flows simultaneously beside an easy operation and low capital investment [3]. The detonation driver, first proposed by Bird [4], has been studied by several investigators [5–7]. Nowadays, it is widely used for shock tubes and tunnels producing high-enthalpy flows for aerodynamic testing [8].

A detonation-driven shock tunnel can be operated in the backward mode with uniform driving quality to achieve longer driving time at a relatively low enthalpy level, such as JF-12, the biggest shock tunnel in the world so far, which is capable of reproducing the pure airflow with longer than 100 ms test duration [9]. On the contrary, to achieve high-enthalpy flows, the forward mode is proposed for its much higher driving capability. Unfortunately, fragments may be produced at the moment of rupturing the primary metal diaphragm under the forward mode, which would have the risk of breaking the test model or affecting the test flow quality, especially at high stagnation pressure conditions. Plastic diaphragms are employed in some laboratories to solve this problem. However, demerits such as test gas contamination would exist.

In this paper, the dual-ignition system developed to burst a metal diaphragm without its fragmentation under the forward operation mode was first stated. The influence of delay time on the test conditions was investigated numerically. The wave diagrams were also shown. We investigated the related rules accordingly in an effort to provide theoretical guidance for the design of the dual-ignition system and improve the stability of the test condition without fragments of the metal diaphragm, which provides powerful support for generating high-enthalpy flows.

2 Physical Problems

As for the forward mode, the detonation wave is ignited at ignition A as shown in Fig. 1. It subsequently propagates downstream toward the primary diaphragm and experts an impulsive force on it, which causes fragments off from the metal diaphragm. Thus, the test model may be broken or the test flow quality be affected by these fragments, which need to be minimized as possible in the shock tunnel experiments. Fortunately, the fragment problem can be basically ignored in the backward mode operation, where the detonation wave is ignited at ignition B near the primary diaphragm. The detonation wave propagates upstream and the diaphragm is burst by the stationary zone behind the Taylor wave, where the pressure, velocity, and temperature are much lower than the CJ plane. Figure 2 showed the diaphragms after the shock tube experiments, operated in the backward or forward driving mode, respectively. The experiments were conducted in the JF-X shock tunnel in the State Key Laboratory of High Temperature Gas Dynamics (LHD), Institute of Mechanics, Chinese Academy of Sciences (CAS), where the length of the driving section and the driven section were 6.5 m and 6.6 m, respectively, both with an inner diameter of 126 mm. Details of the shock tunnel can be found in literature [10]. It can be found in Fig. 2 that the diaphragm under the forward driving mode would shear off fragments, which needs to be solved for preferable experiments.

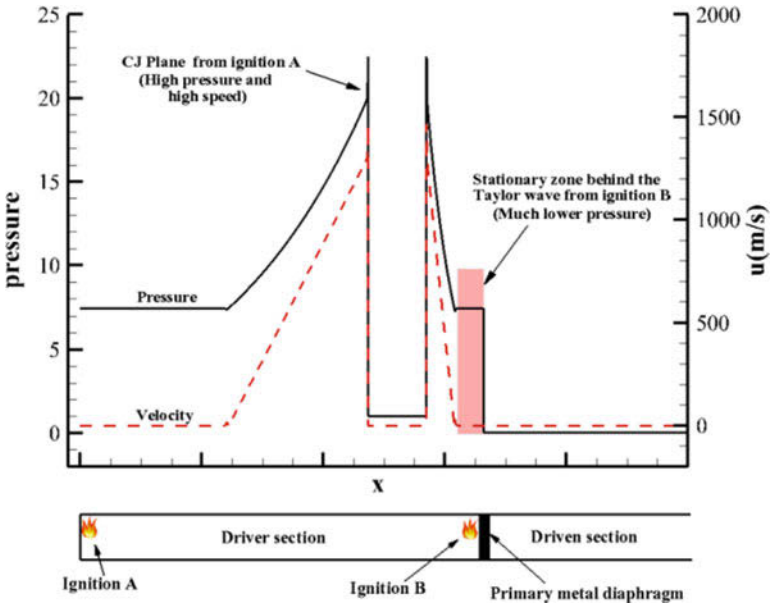

Fig. 1 Schematic diagram of working principle of the detonation system

Fig. 2 Diaphragms in experiments, with the left in backward driving and the right forward

To minimize the diaphragm fragments under the forward operation mode, the dual-ignition system was developed, with the schematic diagram of working principle shown in Fig. 2. The initiation tube A was first ignited at the left end of the driver section. Then the initiation tube B was ignited before the arrival of detonation wave generated from ignition A by a sequence control at the primary diaphragm position. The delay time was specified depending on the detonation chamber length and the detonation wave speed. Using this system, the advantages of bursting the metal diaphragm without its fragmentation by the relatively smaller

stationary zone pressure of backward driving model and generating high-enthalpy flows by the higher driving capability of forward driving model were combined. However, the influence of detonation by ignition B on the forward test condition needs to be investigated. Besides, the mixing quality of flammable mixtures and initiation model are difficult to control in actual experiments. It's thus hard to set the delay time of ignition B just right, where the diaphragm ruptures simultaneous with the arrival of the CJ plane from ignition A. Therefore, the influence of delay time on the test conditions of the high-enthalpy shock tunnel was also investigated in detail, which can provide theoretical guidance for the design of the dual-ignition system.

We plan to conduct a series of follow-up experiments to further explore the performance of the dual-ignition system in the future, but for the purposes of the present study, we went on to explore the phenomenon using a numerical method for its easier operation and better understanding provided. The initial pressure of the driving section was $P_{4i} = 1$ MPa, with the hydrogen-oxygen mixture ratio to be 2:1. And the pressure in the driven section was set to be 20 kPa at room temperature. Four cases were considered here, the backward mode, the forward mode, and the two types of the dual-ignition system with the delay time to be 1.28 ms and 1.76 ms, respectively, where the entire time for the detonation wave to propagate from ignition A to the primary diaphragm was 2.24 ms. The larger the delay time, the closer the CJ plane from ignition A propagates to the primary diaphragm.

3 Numerical Method

The shock tube involves detonation of the flammable mixtures in the detonation chamber and dissociation of the test gas (air in the paper) in the shock tube, which are rather complicated processes. Modeling all phenomena in detail is unrealistic. Also, the viscous term, heat conduction, and rupture process of the diaphragm are neglected.

The numerical method is based on a one-dimensional chemical nonequilibrium flow model, with the equations, written in conservation form,

$$A\frac{\partial U}{\partial t} + \frac{\partial AF(U)}{\partial x} - \frac{\partial A}{\partial x}H - S_c = 0 \tag{1}$$

where the state vector $U = (\rho_i, \rho, \rho u, e, \rho\alpha, \rho\beta)^T$, the flux vector $F = (\rho_i u, \rho u, \rho u^2 + p, (e + p)u, \rho\alpha u, \rho\beta u)^T$, the chemical reaction source term $S_c = \left(\dot{\omega}_i, 0, 0, 0, \dot{\omega}_\alpha, \dot{\omega}_\beta\right)$, and the wall pressure source term $H = (0, 0, p, 0, 0, 0)^T$, where ρ, u, e, p, and A are the density, velocity, total energy, and pressure of gas, and cross-sectional area, respectively. The subscript "i" denotes the species (O_2, N_2, O, N). α and β are the process parameters of the chemical induction and the chemical transformation, respectively; ω_α and ω_β are the rates of the chemical induction and the chemical transformation, respectively; and ω_i is the chemical source term for species i.

For the detonation process, a two-step chemical reaction model is used and ρ_i is set to 0 in the computation. For the details of this model, please refer to reference [11]. In addition, the finite-rate chemistry developed by Park [12] is used for air in the shock tube without ionization, considering five components, O_2, N_2, O, N, and NO. Based on these chemical reaction models and the dispersion-controlled dissipation scheme proposed by Jiang [13], a code has been developed and successfully applied to the simulations of a detonation-driven shock tube [14].

4 Results and Discussion

Stagnation conditions at the end of the driven section including pressure and temperature histories for the four calculating cases were shown in Fig. 3. First, simple comparison between the forward mode and backward mode was discussed. Although the stagnation pressure for the two tended to be the same value of almost 65 bar, the stagnation temperature for the forward mode was 50% higher than the backward mode due to its high driving capability, i.e., 6000 K and 4000 K in the present test condition. The forward driving mode is more easily to obtain a high-enthalpy test flow, and this is the reason we are continuously developing it. A detailed comparison between the two could be found in literature [3].

Here, we focused on the influence of the delay time of the dual-ignition system on the performance of the forward driving mode for a shock tunnel. It was found that the delay time had a significant influence on the effective test or the stagnation temperature of the forward mode, where the plateau pressure tended to be the same value of almost 65 bar for the three cases. However, it needed to be noted that the effective test time considered here took account only of the wave propagation structure, but not the gas reserves in the shock tube or driving gas contamination. Put aside the diaphragm issues, the forward mode had the longest effective test time,

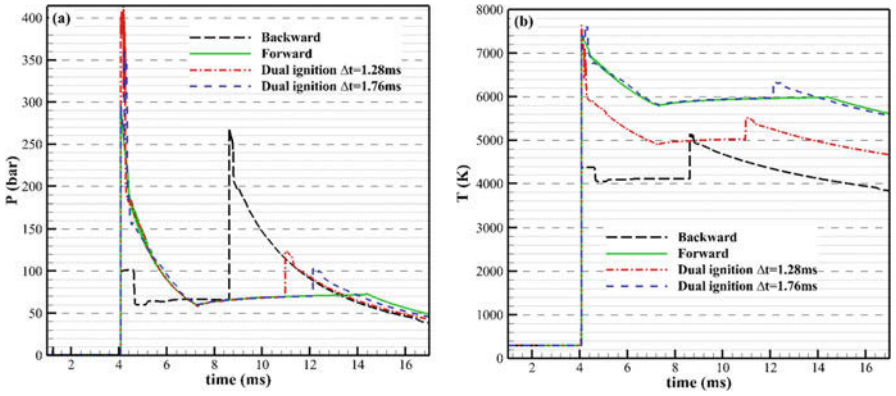

Fig. 3 Stagnation conditions at the end of the driven section: (**a**) Pressure and (**b**) Temperature

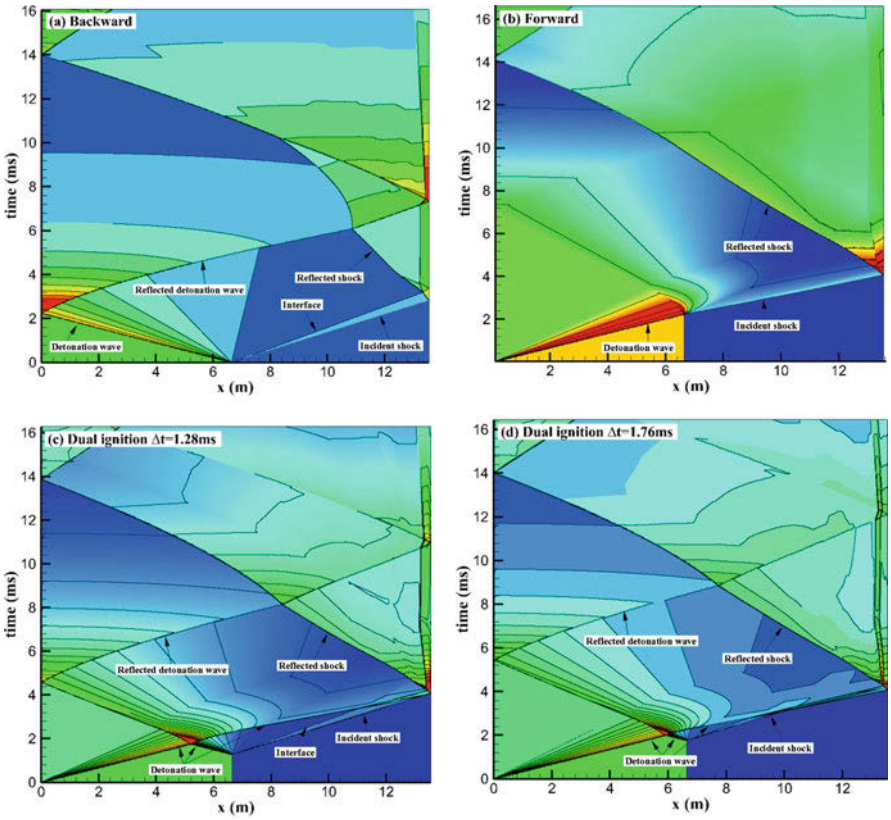

Fig. 4 *x-t* diagrams of density contours of the four cases

persisted from 8 to 14 ms in Fig. 3, namely, about 6 ms. The smaller the delay time, the shorter the effective test time, which persisted from 8 to 11 ms for the delay time of 1.28 ms and to 12 ms for the delay time of 1.76 ms. Unexpectedly, the stagnation temperature of the 1.28 ms condition was much lower than the forward condition, whereas the 1.76 ms case had almost the same temperature as the forward condition.

To better understand the causes of the above phenomena, the *x-t* wave diagram of the four cases were shown in Fig. 4, which can give a clear demonstration of the wave propagation. From these figures, it is found that the detonation-driven shock tube induces additional detonation waves as well as Taylor waves, as compared to a classical shock tube, where the essential differences for the four cases mainly lie in the relative locations at which the detonation waves reflect or intersect.

The characteristics of the backward detonation corresponds with that of a classical shock tube, whereas the effective test time is more easily to be affected by the reflected wave on the rear wall of the detonation section. No reflected detonation wave exists in the forward case, but the Taylor waves behind the detonation wave would have an effect on the stagnation conditions, that is, the sharp decline from

4 to 6 ms in Fig. 3. Thus, ideal tailored conditions can't be obtained in a forward driving mode. For the two dual-ignition conditions, two detonation waves would exist: one propagates upstream and the other downstream. The reflected wave from the upstream detonation would have an effect on the effective test times, that is, the earlier second rise in Fig. 3 compared to the forward case. The smaller the delay time, the earlier the upstream detonation wave reflected and the shorter the effective test time. Besides, the downstream detonation wave would directly go through the already opened diaphragm and run after the incident shock. For case with 1.76 ms delay time, the detonation wave overtakes the incident shock and has an enhancement on it. Nonetheless, the detonation wave does not overtake the incident shock before it reflects from the end wall of the driven section for the 1.28 ms case. Thus, the ignition B as the backward driving has an antecedent effect on the stagnation parameters. This leads to the temperature difference in Fig. 3b. In all, the ignition delay time has a great effect on the performance of the shock tube using the dual-ignition forward driving mode.

5 Conclusion

In this paper, the influence of delay time on the test conditions was investigated numerically. The wave diagrams were also shown. We reached a few interesting conclusions based on the numerical results obtained: the effective test or the stagnation temperature would be affected by the dual-ignition system. The larger the delay time, the closer the CJ plane propagates to the primary diaphragm, the later the reflected detonation wave affects the stagnation parameters, the better consistent with the forward mode. Thus, the delay time should be set exactly to retain the driving capability of the forward driving mode without diaphragm fragments.

Acknowledgments This work was supported by the National Natural Science Foundation of China (Grant Nos. 11402275 and 11472280).

References

1. Q. Wang et al., Comparative study on aerodynamic heating under perfect and nonequilibrium hypersonic flows. Sci. China Phys. Mech. Astron. **59**(2), 1–7 (2016)
2. S.L. Gai et al., Stagnation point heat flux in hypersonic high enthalpy flows. Shock Waves **2**(1), 43–47 (1992)
3. W. Zhao et al., Performance of a detonation driven shock tunnel. Shock Waves **14**(1–2), 53–59 (2005)
4. G. A. Bird, *A Note on Combustion Driven Tubes*, AGARD Report (May 1957)
5. B.H.K. Lee, Detonation driven in a shock tube. AIAA J. **5**(4), 791–792 (1967)
6. H.R. Yu et al., Gaseous detonation driver for a shock tunnel. Shock Waves **2**(4), 245–254 (1992)

7. J. I. Erdos, et al., *Dual Mode Shock Expansion/Reflected-Shock Tunnel*, AIAA Paper 97–0560 (1997)
8. F.K. Lu et al., Recent advances in detonation techniques for high-enthalpy facilities. AIAA J. **38**(9), 1676–1684 (2000)
9. Z. L. Jiang et al., *Experiments and Development of the Long-test-duration Hypervelocity Detonation-driven Shock Tunnel (LHDst)*, AIAA 2014-1012
10. J. W. Li et al., *Performance of a Detonation Driven Shock Tunnel*, AIAA 2017-2306
11. M. Sichel et al., A Two-step kinetics model for numerical simulation of explosion and detonation in H2-O2 mixtures. Proc. Math. Phys. Eng. Sci., 49–82 (2014)
12. C. Park, Review of chemical-kinetic problems of future NASA missions, I: Earth entries. J. Thermophys. Heat Transf. **7**(3), 385–398 (1993)
13. Z.L. Jiang et al., Dispersion conditions for non-oscillatory shock capturing schemes and its applications. Comput. Fluid Dyn. J. **4**(2), 137–150 (1995)
14. J.P. Li et al., Numerical study on backward-forward double detonation driver for high-enthalpy shock tubes. Chin. J. Theor. Appl. Mech. **39**(3), 343–349 (2007)

Ablation Measurements in a Low-Density Heat Shield Using Ablation Sensor Unit (ASU)

Y. Dantsuka, T. Sakai, K. Iwamoto, Y. Ishida, T. Suzuki, and K. Fujita

Abstract The detection performance of an ablation sensor, named Ablation Sensor Unit (ASU), which can measure surface recession, thermal decomposition of resin, and temperature of an ablative heat shield material, is demonstrated. A test specimen with embedded ASU is heated using a JAXA 750 kW arcjet wind tunnel facility under one operational condition. The amount of surface recession and char depth and temperature obtained by ASU are compared with the posttest measured values for the recovered test specimen and the surface temperature obtained by a two-color thermometry. The comparison shows that ASU is promising for a simultaneous and an in situ measurement of the ablation phenomena for the ablative heat shield.

1 Introduction

During an atmospheric entry of a spacecraft at a hypersonic speed, a shock wave is formed over the space vehicle, and the shock layer temperature is in the order of 10,000 K. In such a condition, an aerodynamic heating is so high that a thermal protection is needed when developing the spacecraft. A low-density ablative heat shield recently developed [1] has an advantage of lowering the mass of the spacecraft. To make the most out of this advantage, design tools such as ground testing and computational codes to determine sizing and margin of the heat shield should be reliable.

Flight ablation data are prerequisite to validate such design tools. We have recently developed a new ablation sensor which can be applicable to a flight

Y. Dantsuka
Nagoya University, Nagoya, Japan

T. Sakai (✉) · K. Iwamoto
Tottori University, Tottori, Japan
e-mail: tsakai@mech.tottori-u.ac.jp

Y. Ishida · T. Suzuki · K. Fujita
JAXA, Tokyo, Japan

A. Sasoh et al. (eds.), *31st International Symposium on Shock Waves 2*,
https://doi.org/10.1007/978-3-319-91017-8_36

environment [2, 3]. An ablative heat shield material exhibits its thermal protective performance by undergoing thermochemical decomposition such as surface recession and pyrolysis of resin under atmospheric heating conditions. Therefore, the ablation sensor was developed so as to measure the surface recession, char depth, and material temperature simultaneously. In addition, because the ablation sensor used was embedded into an ablative heat shield, it was miniaturized to minimize its intrusiveness into the heat shield. The ablation sensor is named as Ablation Sensor Unit (hereafter, ASU) [4].

The current development status of ASU is reported in this paper. The components and operational principles of ASU will be explained briefly, and an arcjet testing made to examine performance of ASU will be presented. Although some of the measured data were reported in [4], post-processing procedures are reevaluated in particular in determining the detection time for surface recession based on the study in [3].

2 Operational Principle of ASU [2, 3]

Cross-sectional view of the ablation sensor is shown in Fig. 1. It consists of a surface recession sensor and a char sensor. The char sensor is fabricated to work as a resistive circuit and is composed of two polyimide tubes onto which a resistive wire is spirally wound. The surface recession sensor consists of an ablative rod and optical fibers. ASU is a component assembled by inserting the recession sensor into the hollow part of the char sensor. Further details should be referred to in [2] and [3].

When an ablative heat shield is heated, the resin impregnated into the heat shield is thermally decomposed. In principle of the char sensor, the decomposition front is captured by utilizing the carbonization of polyimide tube used in the char sensor: the electrically connected region in the char sensor is moved in-depth with the decomposition front.

The surface recession sensor is designed to detect thermal emission transitions from the ablative material to the shock layer. Three optical fibers are used in this study, and each is embedded into the side surface of the ablative rod shifting its tip by about 2 mm. Thus, the thermal emission transition at 2, 4, and 6 mm away from the original front surface of a test specimen are measured.

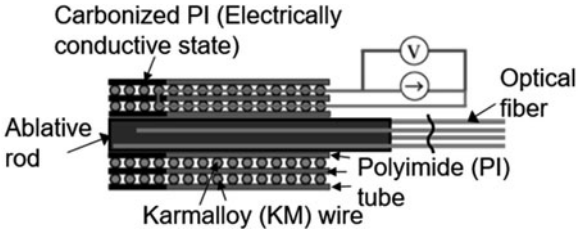

Fig. 1 A schematic diagram of ASU [2]

The thermal emission detected by the optical fibers is also used for a two-color temperature measurement. For this purpose, a Si-InGaAs tandem photodiode is incorporated in the surface recession sensor [3]. It should be noted that the head component of the surface recession sensor embedded into the ablative heat shield is unchanged. The optical temperature is deduced by the following formula:

$$\frac{I_{\mathrm{InGaAs}}(T)}{I_{\mathrm{Si}}(T)} = \frac{\int_0^\infty R_{\mathrm{InGaAs}}(\lambda)\, B_\lambda(T) d\lambda}{\int_0^\infty R_{\mathrm{Si}}(\lambda)\, B_\lambda(T) d\lambda} \tag{1}$$

where I and R denote the photodiode electrical current ratio obtained by the measurement and the wavelength responsivity for Si and InGaAs photodiode, respectively, and B_λ is the Planck function. The two-color temperature is calculated by solving Eq. (1) using an iterative method. For further details, refer to [3].

3 Test Specimen and Arcjet Wind Tunnel Operating Condition

Figure 2 shows a test specimen used in this study. The test specimen is a flat-faced cylinder with a diameter of 40 mm. ASU is embedded into the center of the test specimen as shown in Fig. 2b. When the ablative material is heated, the green portion shown in Fig. 2 is discolored to black. The black portion is visually inspected and is evaluated as char depth.

A 750 kW arcjet wind tunnel facility operated by JAXA is used for the heating test and its operating condition given in Table 1.

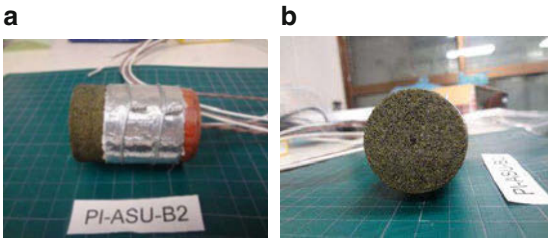

Fig. 2 A test specimen with ASU (**a**) Overall test specimen, (**b**) Front surface of test specimen

Table 1 Arcjet operating condition

Test gas	Air
Current, A	300
Mass flow rate, g/s	16
Pitot pressure, kPa	13.5
Cold wall heat flux, MW/m^2	1.7
Heating time, s	50

4 Results

The variation of the photodiode current obtained by the surface recession sensor is plotted against time in Fig. 3. The data are shown for both of Si and InGaAs photodiodes at each of the optical fiber positions. In the figure, each circle gives a detection time for surface recession at their respective optical fiber positions. As was established in [3], a detection time is determined by searching for the time when both of the photodiode currents decrease simultaneously. In Fig. 3b, the difference in the amounts of surface recession measured from the recovered test specimen and the recession sensor is compared. The sensor value is estimated from a linear approximation based on regression analysis of the detection time data shown in Fig. 3a. Satisfactory agreement of the amounts of surface recession is deduced from the figure.

Figure 4 shows the time evolution of char depth obtained by ASU. The char depth measured from the recovered test specimen is also shown in the figure. As shown, the char sensor underestimated the measured depth. A cause of the reason for this underestimation is attributed to the fact that the discolored region where ASU is inserted is relatively invasive compared to the one without ASU. Further discussions about this underestimation is beyond of the scope of the present study. Nevertheless, it can be said that a reasonable agreement is obtained between measurement and calculation.

In Fig. 5, the temperature obtained by the two-color principle using ASU (hereafter, referred to as ASU temperature) is plotted against time. The surface temperature data measured using pyrometer equipped in the arcjet wind tunnel is also plotted in the figure. The circles given in the figure represent the detection time explained earlier. It is expected that the in-depth temperature at the optical fiber position increases as the surface of the test specimen approaches it. Such

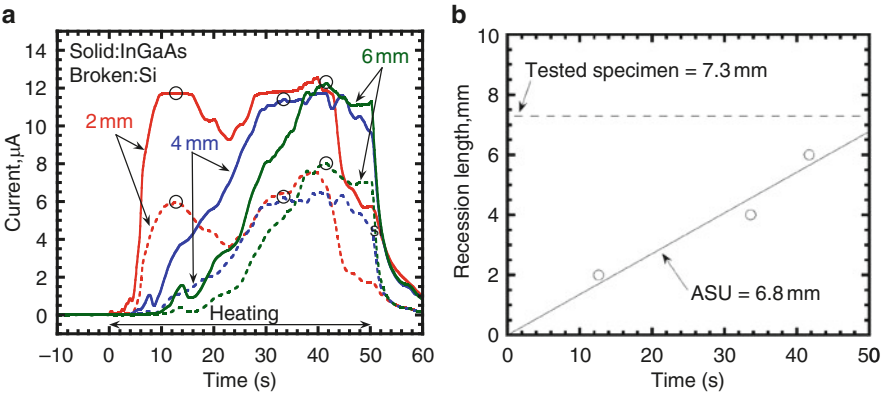

Fig. 3 Surface recession data obtained by ASU (**a**) Photodiode current, (**b**) Averaged speed of surface recession

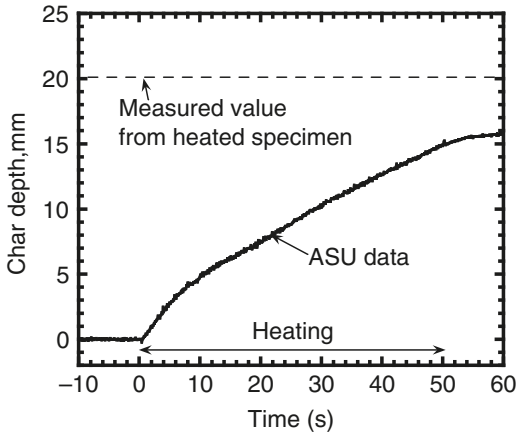

Fig. 4 Char depth data obtained by ASU

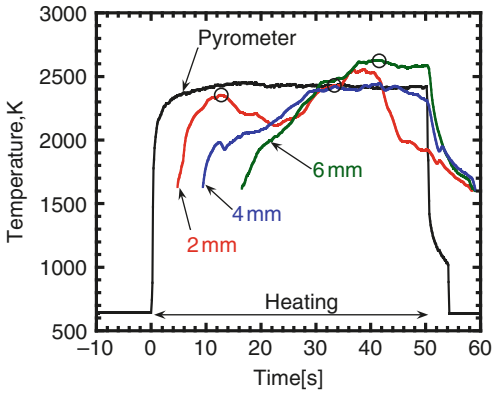

Fig. 5 Temperature data obtained by ASU

a trend can be observed qualitatively from Fig. 4, even though the temperature ramping behavior is different at the respective optical fiber positions. Surface temperature information is also expected from the ASU data at the detection time. A reasonable agreement is seen from the figure, although the ASU temperature may be relatively high compared to the pyrometer temperature data for the case of the 6 mm optical fiber.

5 Conclusion

A simultaneous measurement for surface recession, charring, and temperature of an ablative heat shield using ASU is demonstrated under one operating condition in an arcjet wind tunnel. Even though more data will be needed to evaluate an error range of ASU, the present data show a promising performance of ASU.

Acknowledgments This research was supported by Japan Society for Promotion of Science as Grant-in-Aid for Challenging Exploratory Research, No. 15K14251. The authors would like to thank Mr. Hirofumi Nakazawa and Mr. Yoichi Takagi for their support during the ablation sensor measurements, Dr. Keiichi Kawata of Aichi Center for Industry and Science Technology for laser processing of ablation rods, Mr. Bernard Otieno Owiti of Tottori University for proofreading of the present manuscript, and the staff of Wind Tunnel Technology Center of Japan Aerospace Exploration Agency (JAXA) for their support during arcjet testing.

References

1. H.Tran et al., NASA TM 110440, (1996)
2. T. Sakai et al., JTHT **31**(2), 307–317 (2017)
3. Y. Dantsuka et al., JTHT, posted on 16 November (2017)
4. K. Fujita, et al., AIAA Paper 2017-0899, (2017)

Driver Condition Development for High-Enthalpy Operation of the X3 Expansion Tube

A. Andrianatos, D. E. Gildfind, and R. G. Morgan

Abstract At the University of Queensland (UQ), there are two expansion tubes, X2 and the larger X3. In the past years, there have been many experimental campaigns investigating radiation in high-enthalpy flows in X2. X3 has not been used for similar experiments, although it is larger, it has been undergoing an extended period of upgrades and development, including a new lightweight piston and reservoir extension. This paper reports the progress made in developing high-enthalpy operation in X3 that will be used for future high-enthalpy experimental campaigns.

1 Introduction

During atmospheric entry, large amounts of energy are transferred from the gas flow around a vehicle to the vehicle's body by convection and radiation. At superorbital velocities the radiative heat transfer to a vehicle becomes a significant portion of the total heat transfer [1]. Unlike convection, radiative phenomena are still not well understood. When experimenting with scale models, if the total enthalpy and the density characteristic length product (ρL) are maintained, the flight condition and the experimental flow conditions are similar. This substitution, referred to as binary scaling [2], reproduces convective heating, Reynolds number, viscous effects, and binary reactions. If the flow is optically thin, the point-to-point radiative transmission is also scaled correctly as it depends on mass on the line of sight [2].

However, when the heat removed from streamtubes in the flow via radiation is considered, it is dependent on the volume of the streamtubes and scales with ρL^3, and the mass flux into the shock layer scales with ρL^2 [2]. This results in lower levels of heat being removed from the flow field via radiation during a scaled experiment when compared to the full-scale flight vehicle. If the radiative transfer is coupled

A. Andrianatos (✉) · D. E. Gildfind · R. G. Morgan
Centre for Hypersonics, School of Mechanical and Mining Engineering, University of Queensland, Brisbane, QLD, Australia
e-mail: uqaandri@uq.edu.au

A. Sasoh et al. (eds.), *31st International Symposium on Shock Waves 2*,
https://doi.org/10.1007/978-3-319-91017-8_37

with the flow field, the change in heat removal from the flow can result in different flow properties between the flight and experiment, and the similarity between the two will not be conserved with binary scaling.

Additionally, the nonequilibrium region in the shock layer is independent of density for a given velocity [3]. The radiation of the nonequilibrium region is determined from binary collisions; the intensity is proportional to density, and the spatial extent of the nonequilibrium is inversely proportional to density [4]. This leads to further effects that are not accounted for by binary scaling: truncation of the nonequilibrium region if it is larger than the shock detachment and collisional limiting when low densities are insufficient to maintain a population of excited states [3]. Nonequilibrium radiation is associated with a lack of collisions to reach equilibrium and is essentially a rarefied phenomenon, and it is still unknown how this scales with pressure [2].

These differences between the flow field around a full-scale flight vehicle and the scaled experimental flow make it difficult to produce a direct simulation to directly compare experiment and flight. The X3 expansion tube at UQ has the capability to experiment with larger models, for longer test times, compared to similar smaller scale facilities that produce the same conditions. This paper details the progress made to produce high-enthalpy (∼50–60 MJ/kg) superorbital flows in X3.

2 X3 Expansion Tube

X3 is the larger of two free driven expansion tubes at UQ which are primarily used for radiation experiments. A schematic of X3 is shown in Fig. 1. The high-pressure reservoir (leftmost side) supplies high-pressure air to push the piston along the compression tube, compressing and heating the driver gas (typically a mix of helium and argon) until it ruptures the primary diaphragm (typically 2 mm, 3 mm, or 4 mm mild steel). When the primary diaphragm ruptures, a shock is driven through the next sections of tube containing the test gas, and the shock processed test gas is first unsteadily expanded into the acceleration tube and then steadily expanded through the nozzle. The arrangement of X3 allows for multiple configurations of gas slug and diaphragms. If a secondary driver is used, the configuration is that outlined in Fig. 1; if no secondary driver is used, the shock tube will range from the primary diaphragm to either the secondary or tertiary diaphragm. Measurement locations

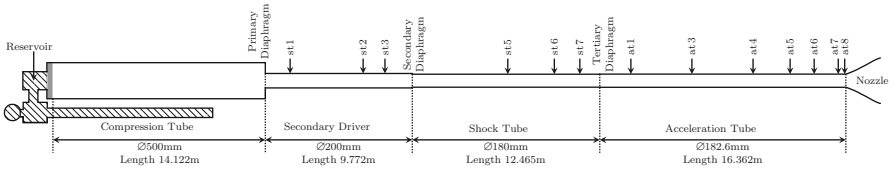

Fig. 1 X3 Schematic

are available along the length of the tube, st1–7 and at1–8, although some have been removed due to changes to X3's hardware, represented by missing numbers.

In 2014 a new lightweight piston weighing 100.8 kg was designed to replace the previous heavy piston (200 kg) [5], and since then an extension to the reservoir has also been installed and the effect on driver performance has been examined [6]. The objective for these upgrades was to increase the performance envelope of X3 in order to achieve high-enthalpy conditions.

To increase the performance of the compression tube, the sound speed of the compression tube gas when the primary diaphragm ruptures needs to be increased [6]. This can be achieved by either increasing the concentration of helium or increasing the overall compression ratio (i.e., higher temperature). Difficulties arise when contending with a free-piston-driven driver, as changing the gas composition or initial pressures can have detrimental effects on the piston behavior [6]. To avoid damage to the facility, the reservoir and compression tube fill pressures are chosen so the high-pressure gas in front of the piston can decelerate the piston before it strikes the end of the tube [7]. Increasing the sound speed of the driver gas increases the rate which it vents out of the compression tube at a given pressure, and for the piston dynamics to remain within acceptable limits [6], a lighter piston and larger reservoir are required.

3 Lightweight Piston Performance

This section will briefly cover the development of the piston trajectory and operating conditions that will be used during future operation of X3. Unlike a constant volume driver, the velocity of the piston at the time of diaphragm rupture continues to compress the compression tube gas after rupture maintaining a higher pressure for a longer duration. After diaphragm rupture this piston must also be decelerated to rest as it arrives at the end of the tube. If the precise location it stops is known, the piston can be caught with buffers sized the appropriate length, usually slightly ahead of the end of the tube.

Using the analysis outlined by Hornung [8], a range of potential piston trajectories were found for 2 mm thick steel diaphragms. The analysis returns an estimate of what the driver gas fill should be to achieve soft landing trajectory. Itoh [9] found that once the driver pressure variation exceeded beyond 10% of the rupture pressure (p_{rupt}), the gas was deemed to no longer represent the desired quasi steady condition. Using this limit, trajectories were found with a range of maximum pressures from $1.01p_{rupt}$ to $1.1p_{rupt}$, referred to as "overdrive" and a range of helium concentrations in Fig. 2.

Figure 2 displays some of the driver characteristics found for a range of overdrives over a range of helium concentrations for a 2 mm steel diaphragm. Plot (a) shows how the initial driver fill pressure changes for different concentrations of helium, with the remainder of the gas being argon. As helium has a high sound speed and vents from the compression tube faster, the amount of gas required to maintain

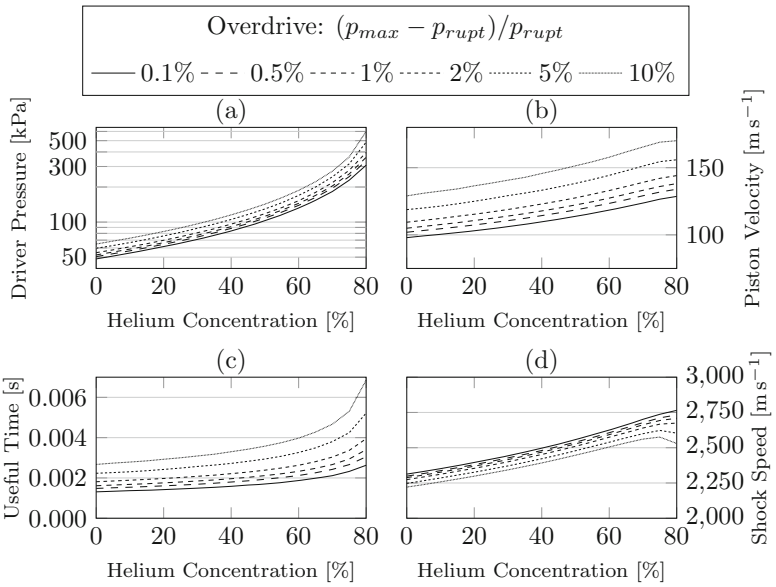

Fig. 2 Theoretical compression tube performance characteristics for lightweight piston: (**a**) compression tube fill pressures, (**b**) piston velocity at time of diaphragm rupture, (**c**) duration of useful compression tube pressure, (**d**) shock speed

a tuned trajectory increases exponentially with helium concentration, and the piston needs to be faster to match mass loss, shown in plot (b). As a consequence of the higher initial fill pressure, the steady pressure time increases (plot (c)), especially for concentrations higher than 60%. More importantly is how helium concentration affects shock speed in plot (d); increasing the helium concentration from 0% to 80% only increases the theoretical shock speed into 13.5 kPa air by ∼400 ms^{-1}. 13.5 kPa was chosen as it represents a condition of interest and the goal is to reach a shock speed of 4505 ms^{-1}. Attempts to increase helium concentration above 80% did not result in reasonable solutions.

Alternatively, if a condition is known for a 100% argon driver gas, helium can be substituted to the driver gas without changing the condition if the exit area of the compression tube is scaled [10] using an orifice plate. The contraction area between two driver gas constants can be scaled by the square root of the gas constant ratios as shown in Eq. 1:

$$\sqrt{\frac{A_2}{A_1}} = \frac{D_2}{D_1} = \left(\frac{R_1}{R_2}\right)^{0.25} \tag{1}$$

where A is compression tube exit area, D is diameter, R is driver mix gas constant, and subscripts 1 and 2 refer to different helium and argon mix ratios. The resulting shock speeds into 13.5 kPa air are shown in Fig. 3 for a 2 mm and 4 mm diaphragm.

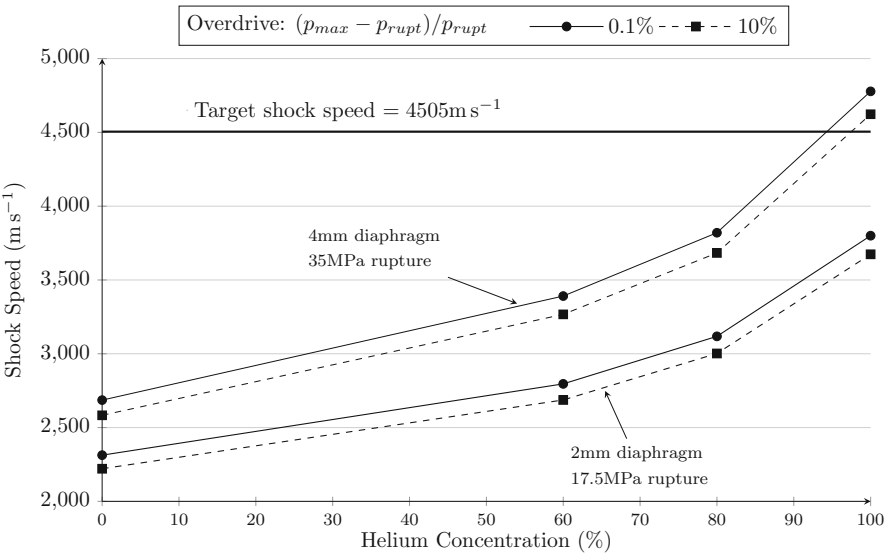

Fig. 3 Shock speeds into 13.5 kPa air for 2 mm diaphragm and 4 mm diaphragm compression tube conditions

Increasing helium concentration in this manner results in much larger increases in shock speed compared to without an orifice plate. From the theoretical results, the target condition can potentially be achieved by a 4 mm diaphragm and 100% helium. Work done on completing the piston trajectory is not presented here.

4 Experimental Shock Speeds

This section will cover the experimental results from the piston commissioning process. Conditions for 4 mm diaphragms were not conducted as it was found that the conditions in Figs. 2 and 3 require reservoir pressures that exceed the rated capacity. In place of the 4 mm diaphragm, a 3 mm diaphragm was used instead, and shots were completed for 0%, 60%, 75%, 85%, and 100% helium concentrations using the required orifice plates scaled from the 100% argon case.

Shock speeds in X3 are calculated by measuring the time it takes the shock pressure rise to travel between two adjacent transducer locations (see Fig. 1). Figure 4 shows the shock speeds measured for a variation of helium concentrations for a 2 mm diaphragm. For the 100% argon case, the pressure measurement at st1 appears to contain other features, possibly the startup of the shock, likely due to the vicinity of the diaphragm, so it is unknown how representative of the actual shock speed the first data point is. Another interesting observation is the shape of each curve; most give a consistent shock speed across the length of the tube except for

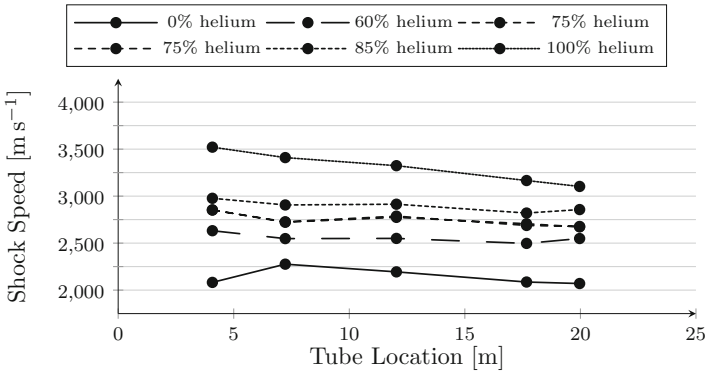

Fig. 4 Shock speeds produced using a 2 mm diaphragm into 13.5 kPa air

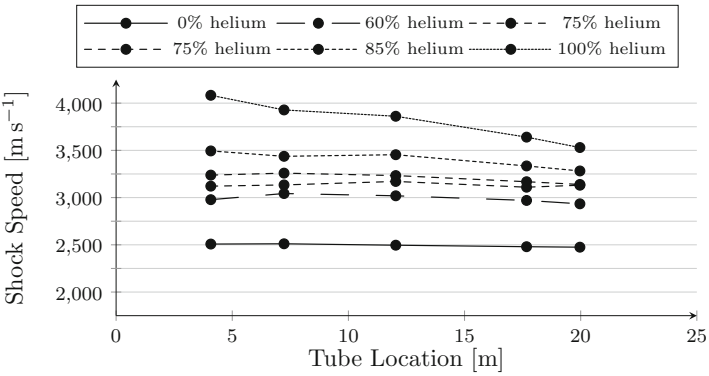

Fig. 5 Shock speeds produced using a 3 mm diaphragm into 13.5 kPa air

100% helium. This may be due to the size of the orifice plate, which reduces the area by 78% compared to the 0% helium case, and this may restrict the flow of the compression tube gas into the shock tube and results in a less consistent shock speed, or the possibility that expansion waves catch up to the shock quicker in a faster driver gas.

Similarly, Fig. 5 shows the shock speeds for the 3 mm diaphragm. The trend of the results is similar to Fig. 4. Most shock speeds are consistent with the exception 100% helium which shows a similar reduction in shock speed along the length of the tube, although the 0% helium case does not show the same variation in shock speed, even though the st1 pressure traces are similar.

Figure 6 shows the shock speeds in the acceleration tube continued on from the conditions in Fig. 5. As expected, the higher concentration of helium gives a faster shock speed in the shock tube and also the acceleration tube. All the shock speed traces show the same trend in attenuation, and the two 75% helium traces give very similar shock speeds, and considering that the two corresponding shock speeds in

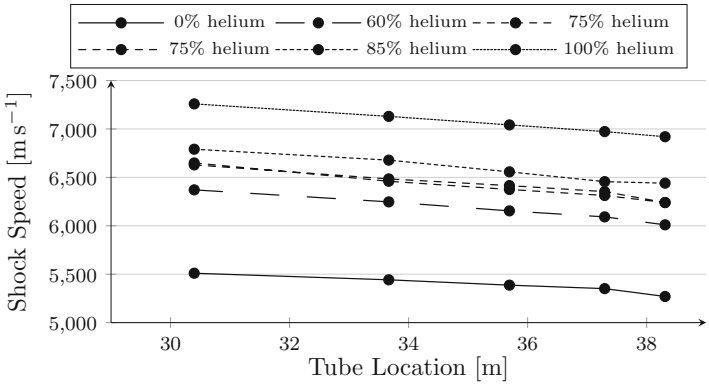

Fig. 6 Shock speeds in the acceleration tube produced by compression tube conditions with a 3 mm diaphragm

Fig. 5 were somewhat different from each other, except for the final data point, it may be inferred that the flow state that reaches the diaphragm has a large effect on the downstream flow process (i.e., in Fig. 5 the two 75% helium shock speeds converge at the final data point).

5 Conclusion

Preliminary investigations have been done to develop new driver operating conditions which will lead to new capabilities to perform large-scale superorbital experiments in X3. A range of conditions have been established using two thicknesses of primary diaphragm which provide a large performance envelope. A 13.5 kPa air shock tube fill was chosen as a crossover condition from X2, which is a relatively high fill pressure to other high-enthalpy experiments, which use fill pressure typically on the order of a few kilopascals. At the time of writing, a crossover condition for X2 has not yet been achieved. Future work will include experimenting at the X2 crossover condition or establishing similar superorbital capabilities in X3. Further driver development may also be done but will require further hardware development.

Acknowledgments The authors wish to thank Mr. F. De Beurs and Mr. N. Duncan for technical support; The Australian Research Council for support and funding; The Queensland Smart State Research Facilities Fund 2005 for support and funding; The Australian Space Research Program and the Australian Government Research Training Program Scholarship for support and funding.

References

1. J.R. Anderson, An engineering survey of radiating shock layers. AIAA J. **7**, 1665–1675 (1969)
2. R. Morgan et al., T., Impulse facilities for the simulation of hypersonic radiating flows, in *AIAA 38th Fluid Dynamics Conference and Exhibit*, Seattle, Washington, 2008
3. S. Sharma, E. Whiting, Modeling of nonequilibrium radiation phenomena – an assessment. J. Thermophys. Heat Transf., AIAA **10**, 385–396 (1996)
4. J. Camm et al., Absolute intensity of non-equilibrium radiation in air and stagnation heating at high altitudes. J. Quant. Spectrosc. Radiat. Transf. **1**, 53–75 (1961)
5. D. Gildfind, R. Morgan, J. Sancho, Design and commissioning of a new lightweight piston for the X3 Expansion Tube, in *29th International Symposium on Shock Waves*, 2014
6. A. Andrianatos, D. Gildfind, R. Morgan, Preliminary development of high enthalpy conditions for the X3 expansion tube, in *20th Australasian Fluid Mechanics Conference*, 20AFMC, 2016
7. D. Gildfind et al., Free-piston driver optimisation for simulation of high Mach number scramjet flow conditions. Shock Waves **21**, 559–572 (2011)
8. H. Hornung, *The Piston Motion in a Free-piston Driver for Shock Tubes and Tunnels*, GALCIT Report FM, 1988, pp. 88–1
9. K. Itoh et al., Improvement of a free piston driver for a high-enthalpy shock tunnel. Shock Waves **8**, 215–233 (1998)
10. D. Gildfind, C. James, R. Morgan, Free-piston driver performance characterisation using experimental shock speeds through helium. Shock Waves **25**, 169–176 (2015)

Calculation of Intensity Profiles Behind a Shock Wave Traveling in Air at Speeds Exceeding 12 km/s

A. Lemal, S. Matsuyama, S. Nomura, H. Takayanagi, and K. Fujita

Abstract This paper presents the recent efforts in computing the flow field and radiation behind a shock wave traveling in air at speeds exceeding 12 km/s to support the exploration mission currently considered at JAXA. The influence of the electron number density on the thermodynamic properties and ionization equilibrium constants was highlighted and quantified. The thermochemistry model in JAXA CFD code was upgraded and the flow field was computed. The populations of the excited states radiating in the vacuum ultraviolet (VUV) were computed with a collisional-radiative (CR) model. Subsequently, the radiative properties of the strongest radiators were computed with the models and database of JAXA spectral solver. The computed VUV post-shock intensity profiles were compared with shock-tube radiation measurements obtained in facilities operated at representative flight conditions. The influence of electron-impact excitation and radiative processes is discussed.

1 Introduction

Upcoming sample return missions considered at JAXA continue to generate strong motivation in designing advanced thermal protection systems (TPS) with low design margins, which are conducive to the reduction of the launching costs, the increase of the scientific value of the mission by embedding larger payloads and the enhancement of the reliability and safety of the reentry systems. The sizing of the TPS significantly relies upon the prediction of the radiative heat flux, which suffers from large uncertainty and can represent up to 50% of the total heating encountered by the spacecraft during reentry [1]. Thus, it requires an accurate and cost-effective modeling of the various physicochemical processes occurring in front of the spacecraft. The estimation of the radiative heat flux on a spacecraft during

A. Lemal (✉) · S. Matsuyama · S. Nomura · H. Takayanagi · K. Fujita
JAXA, Chofu Aerospace Centre, Tokyo, Japan
e-mail: adrien.lemal@star-ale.com

A. Sasoh et al. (eds.), *31st International Symposium on Shock Waves 2*,
https://doi.org/10.1007/978-3-319-91017-8_38

its entry into Earth's atmosphere requires the determination of the populations of the excited atomic and molecular states, which are highly dependent of the thermodynamic conditions. The latter can be determined by various approaches: multi-temperature or state-to-state models. In the former approach, it is assumed that the population of each internal energy mode follows a Boltzmann distribution at the characteristic temperature of the mode. To calculate these temperatures and the energy exchanged between energy modes, conservation equations for internal energy modes are added to the classical set of conservation equations for mass, momentum, and total energy [2, 3]. Within the frame of the missions currently considered at JAXA, peak heating is predicted to occur at high speeds and low density, which enhances the departure from Boltzmann equilibrium. The multi-temperature approach may not be sufficient anymore because the internal energy state populations may depart from Boltzmann distributions. State-to-state models, also called collisional-radiative (CR) models, are then required. In this approach, the internal states are considered individually and their populations are determined by considering collisional and radiative processes [4–10]. Previous works [11, 12] successfully predicted the intensity emitted by high-temperature air plasma behind a shock wave traveling at speeds ranging from 8 to 11 km/s. The missions currently considered at JAXA feature Earth's atmosphere entry speeds exceeding 12 km/s. In this extreme environment, the flow becomes significantly ionized and interacts strongly with the radiation field and therefore triggers the upgrade of the models previously developed. The manuscript is organized into four sections. Section 2 introduces the new ionization models. Section 3 briefly describes the computational tools. Section 4 compares the predictions with the experimental data. Section 5 concludes the manuscript and draws perspectives for future work.

2 Debye Screening Effect on Thermodynamics

As the shock speeds exceeds 12 km/s, the flow becomes significantly ionized and the electrons become the first drivers of atomic excitation and subsequent radiation. The production of electron depends on the ionization rate constants and the equilibrium constant. Fig. 1 compares the various sources [13–16] and illustrates a factor 5 agreement with the various authors as the temperature exceeds 10,000 K. Moreover, the electron concentration affects the thermodynamic properties of the flow [17]. The influence of this effect, so-called Debye screening, on the heat capacities and ionization equilibrium constant is illustrated in Fig. 2 [17–19]. The resulting values are shown to depart from the predictions from CEA code [18] when the temperature exceeds 10,000 K. It is therefore of paramount importance to provide a more accurate expression for the equilibrium constants. Following Tanaka et al. [20], the equilibrium constants were computed with the thermodynamic database of [17] and are displayed in Fig. 3 for various ionization potential lowering ΔI and compared in Fig. 4 with various sources [13–16, 20].

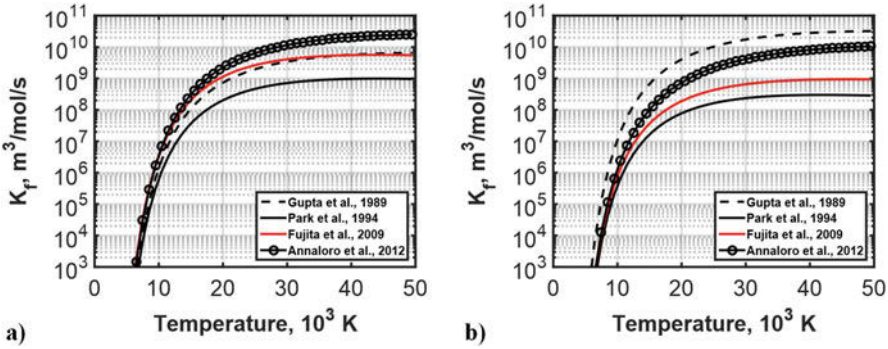

Fig. 1 Comparison of ionization rate constants for (**a**) N and (**b**) O atom [13–16]

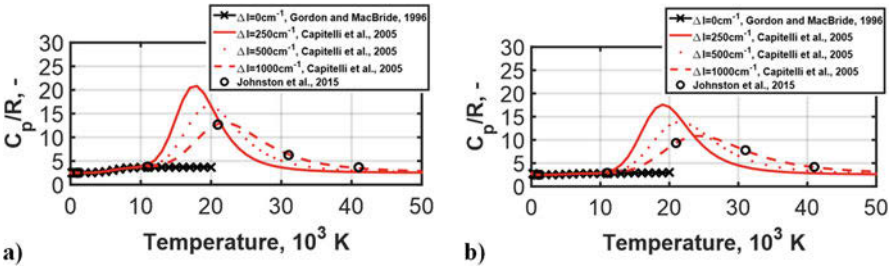

Fig. 2 Debye effect on the heat capacities for (**a**) N and (**b**) O atom [17–19]

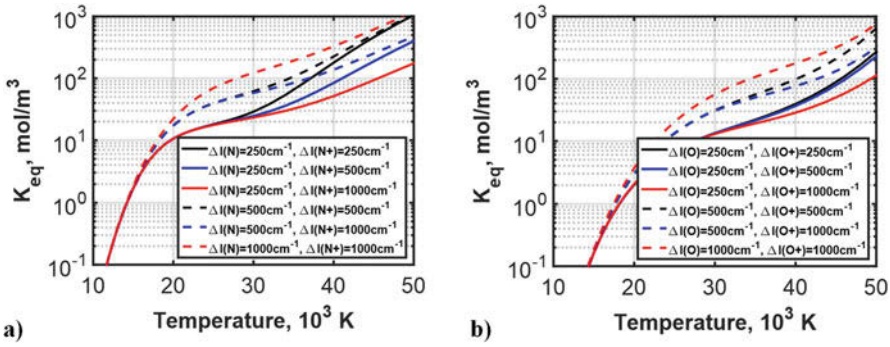

Fig. 3 Debye effect on ionization equilibrium constant for (**a**) N and (**b**) O atom [20]

3 Computational Framework

The simulation of shock-tube radiation measurements was thoroughly described in [11, 12] and encompasses the computation of the flow field, the populations of the excited states, and the spectral radiance. The spectral radiance was finally convoluted with the instrument spectral and spatial resolution functions. Thermal

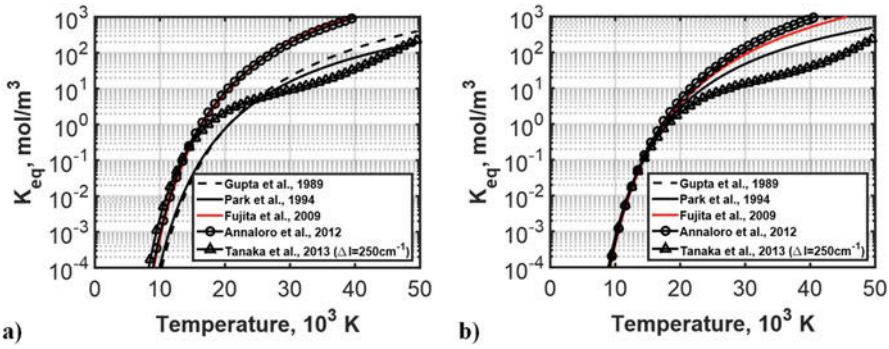

Fig. 4 Comparison of ionization equilibrium constant for (**a**) N and (**b**) O atom [13–16, 20]

Table 1 Selected conditions

Case	V_∞ [km/s]	p_∞ [Pa]	T_∞ [K]	λ [nm]	Facility	Smearing	Reference
a	12.45	13.3	300	175	NASA, EAST	Yes	[22, 23]
b	12.50	30.0	300	175	JAXA, HVST	No	[24]
c	13.64	26.6	300	175	NASA, EAST	Yes	[22, 23]
d	14.46	13.3	300	175	NASA, EAST	Yes	[22, 23]
e	14.50	5.40	300	175	JAXA, HVST	No	[24]
f	15.52	13.3	300	175	NASA, EAST	Yes	[22, 23]

nonequilibrium was modeled here with a two-temperature model [14, 15]. The populations of the atomic excited states were computed with the CR model described in [11, 12] under the quasi steady-state assumption. Specifically, the electron-impact excitation and ionization rate constants were taken from theoretical formulations that best match electron beam cross-section measurement data. Heavy-particle excitation processes with N and O as a colliding partner suffer from significant uncertainty [10], which drove the authors use the conservative rate constants from [4] as a baseline. The bound-bound radiative mechanisms that deplete the levels were modeled with the escape factor concept. The latter, hereafter labeled Λ, may be interpreted as the fraction of radiation that escapes from a point. If Λ_{ul} is set to 1, then all of the radiation escapes, meaning the gas is transparent, and there is no repopulation by absorption. Conversely, if Λ_{ul} is set to 0, then the repopulation and depletion of a level l due to absorption and emission cancel out, which may be interpreted as no net "escaping" radiation. Finally, the emission and absorption coefficients were calculated with the models of JAXA spectral solver SPRADIAN [21]. The radiation measurements, which were selected from [22–24] to validate the models, are listed in Table 1.

4 Results

Figure 5 displays the flow field temperatures and the species number densities which significantly contribute to the VUV heating, with the baseline model [15]. As shock speed increases, the thermal nonequilibrium portion decreases and ionization increases. The Debye screening effect and the new ionization equilibrium constants are shown to increase the electron number density. Fig. 6 compares the computed and measured intensity profiles. The measured radiance exhibits a peak due to nonequilibrium ionization and radiative cooling. Addressing the latter phenomenon requires coupled numerical strategies, which are beyond the scope of the present work. Here, cost-effective and straightforward approaches [11, 12] are tested, and their performances are quantified. Heavy particle impact processes generated an intensity spike a few millimeters behind the shock. The intensity of this spike was 5 times lower than the equilibrium values and was therefore smeared by the optics. For all cases investigated, the computed equilibrium intensity profile overpredicts the measurement. The intensity computed with the CR model ($\Lambda = 0$) and under the Boltzmann assumption at $T_{exc} = T_{Ve}$ agree well with each other, suggesting that the departure from equilibrium near the shock front is small enough to be smeared by the optics. The simulated intensity rise is overpredicted by the simulation because the latter assumes a strong coupling between the vibrational and electron temperature and because the data from [22, 23] were smeared. The intensity profile computed with the CR model ($\Lambda = 1$), which is lower than the equilibrium value because of the significant depletion of the quantum states, underpredicts the measured peak intensity. As speed increases, the radiance computed with the composition given by CEA [19] departs from the radiance computed by JONATHAN [15] as the former code computes less N ionization, thus greater intensity magnitude and narrower line profile.

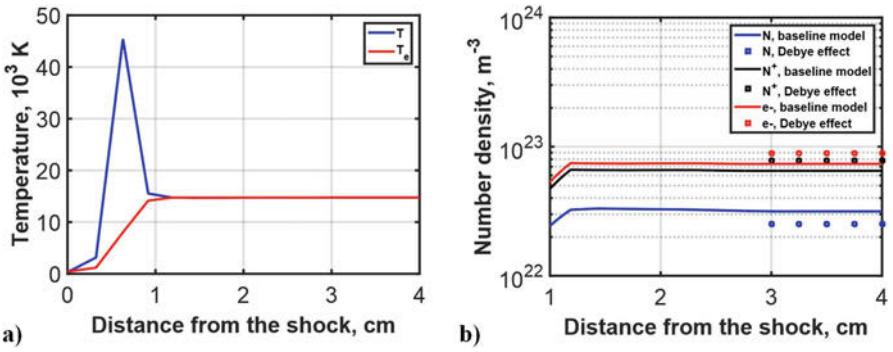

Fig. 5 Computed (**a**) temperatures and (**b**) number densities of N and electrons (case f)

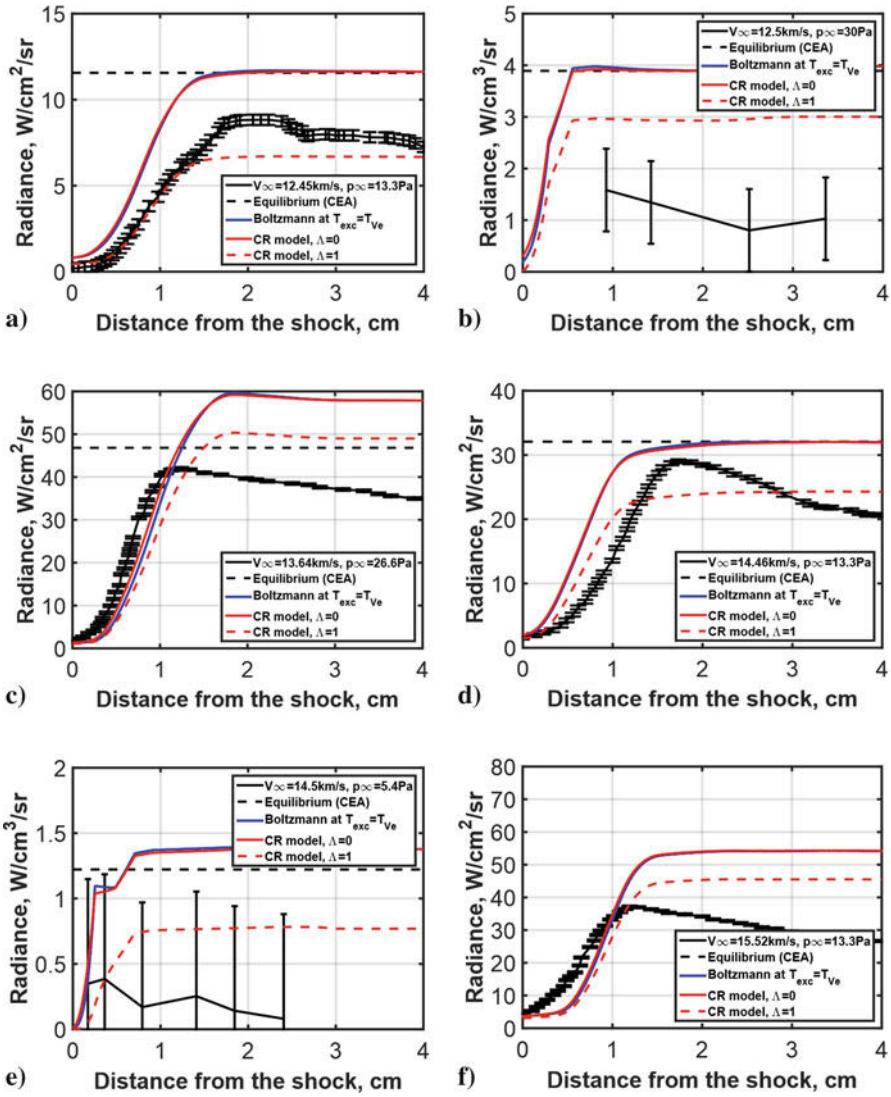

Fig. 6 Comparison between calculated and measured intensity profiles for the cases in Table 1

5 Conclusions

This paper presented the recent efforts in predicting the VUV radiation emitted in the shock layer of a spacecraft entering Earth's atmosphere at speeds exceeding 12 km/s. A nonequilibrium radiation model was developed, and its predictions were compared to shock-tube radiation measurements. The measured radiance was bounded by the simulations. To model the radiative cooling effect and optimize

the TPS design, ongoing work includes the implementation of consistent coupling between flow, collisional, and radiative processes. To further improve the performances of the simulations in the nonequilibrium zone, a three-temperature model T-T_V-T_e is under development and measurements near the shock front with less spatial smearing are currently being undertaken.

Acknowledgments The authors are indebted to Dr. A. M. Brandis and Dr. B. A. Cruden (NASA Ames Research Center) for providing their shock-tube radiation measurements and the resolution functions. Experimental devices were provided by the Japan Society for the Promotion of Science (JSPS) under the grant Kaken-Hi 26289326 and were gratefully acknowledged. Computer resources were provided by JAXA Supercomputer Server (JSS) and were gratefully acknowledged. Thanks are due Mrs. S. Nishimura (graduate student at Shizuoka University) for operating JAXA HVST facility under a tight schedule.

References

1. K. Fujita et al., *Assessment of Convective and Radiative Heating for Jupiter Trojan Sample Return Capsule*, AIAA paper 2014–2673, 2014
2. J. William, *Etude des processus physico-chimiques dans les écoulements détendus à haute enthalpie*. Ph. D thesis (in French), Université de Provence, France, 2000
3. T. Soubrie, *Prise en compte de l'ionisation et du rayonnement dans les rentrées terrestres et martiennes.* Ph. D thesis (in French), ISAE-ENSAE, France, 2006
4. C. Park, *Nonequilibrium Hypersonic Aerothermodynamics* (Wiley, New York, 1990), pp. 30–80
5. C.O. Johnston et al., J. Spacecr. Rocket. **45**(5), 879–890 (2008)
6. M. Panesi et al., J. Thermophys. Heat Transf. **25**(3), 361–373 (2011)
7. Y. Ogino et al., *Computational Code for Air Plasma Flow Field with Atomic and Molecular Processes*, AIAA paper 2012–3308, 2012
8. B. Lopez et al., J. Thermophys. Heat Transf. **27**(3), 404–413 (2013)
9. J. Annaloro, A. Bultel, Phys. Plasmas **21**(12), 15–31 (2014)
10. A. Lemal et al., J. Thermophys. Heat Transf. **30**(1), 226–239 (2016)
11. A. Lemal et al., J. Thermophys. Heat Transf. **30**(1), 197–210 (2016)
12. A. Lemal et al., J. Thermophys. Heat Transf. **32**(1), 256–261 (2018)
13. R. N. Gupta et al., *A Review of Reaction Rates, Thermodynamic and Transport Properties for the 11-species Air Model for Chemical and Thermal Nonequilibrium Calculations to 30000K*, NASA Technical Memorandum 101528, 1989
14. C. Park, J. Thermophys. Heat Transf. **7**(3), 385–398 (1993)
15. K. Fujita et al., *Development of JAXA Optimized Nonequilibrium Aerothermodynamics Analysis Code*, Technical report (in Japanese), JAXA, 2009
16. J. Annaloro et al., Phys. Plasma **19**, 1–15 (2012)
17. M. Capitelli et al., *Tables of Internal Partition Functions and Thermodynamic Properties of High-temperature Mars-atmosphere Species from 50K to 50000K*, Technical report STR-246, European Space Agency-ESTEC, 2005
18. C. O. Johnston et al., *Aerothermodynamic characteristics of 16–22 km/s Earth Entry*, AIAA paper 2015–3110, 2015
19. S. Gordon, B. Mac Bride, *Computer Program for Calculation of Complex Chemical Equilibrium Compositions and Applications. Part 1: Analysis*, Reference Publication 1311, NASA, 1994
20. K. Tanaka et al., J. IAPS **21**(1) (2013)

21. K. Fujita, T. Abe, *Spradian: Structured Package for Radiation Analysis. Theory and Application*, Technical report (in Japanese), JAXA, 1997
22. A. M. Brandis, C. O. Johnston, *Caracterization of Stagnation-point Heat Flux for Earth Entry*, AIAA paper 2014–2374, 2014
23. A. M. Brandis, B. A. Cruden, *Benchmark Shock Tube Experiments of Radiative Heating Relevant to Earth Re-entry*, AIAA paper 2017–1145, 2017
24. S. Nishimura et al., VUV Air Radiation Measurements at Shock Speed Exceeding 12 km/s, in *Proceedings of the 7th International RHTG Workshop, Stuttgart*, Germany, Nov. 2016

Revisiting Temperature Measurements at the Focus of Spherically Converging Shocks in Argon

M. Liverts and N. Apazidis

Abstract In this work, temperature measurements at the focus of spherically converging shock waves (CSWs) in argon are revisited. Spherical shock waves are produced inside a conventional circular shock tube, where initially plane shocks are transformed into spherically shaped shocks inside an axisymmetric smoothly converging section. As the CSW reflects from the window, the conditions become extreme so that the gas intensively glows. The light flash collected through the window by optical fibers is separately transferred into a diagnostic setup including a spectrometer. The gas temperature at the cone tip is then deduced from Planck's fit to the registered radiation spectrum. Maximum temperatures of order of 30,000 K are thus measured.

In this study 1D axisymmetric numerical simulation accounting for nonideal gas effects (excitation, Coulomb interaction, ionization, and radiation) assuming equilibrium is employed to study the details of the shock implosion. The prominent advantage of the numerical approach over approximate method used in (Liverts M, Apazidis N, Phys Rev Lett 116: 014501, 2016) is that the calculation can be extended to trace the behavior of the gas behind the reflected (diverging) shock that inevitably dictates the temperature dynamics at the implosion focus. As a result, a comparison between calculations and experimental data demonstrates an improved agreement.

1 Introduction

Converging shock waves (CSWs) can be found in a broad range of situations, from astronomical size events like supernova collapse, to microscopic events such as gas bubble sonoluminescence. A continuing interest in CSW studies is also motivated by applications demanding high-energy concentrations. The well-known self-similarity

M. Liverts (✉) · N. Apazidis
Mechanics, KTH Royal Institute of Technology, Stockholm, Sweden
e-mail: liverts@mech.kth.se

A. Sasoh et al. (eds.), *31st International Symposium on Shock Waves 2*,
https://doi.org/10.1007/978-3-319-91017-8_39

solution [2, 3] for cylindrical and spherical convergence describes a continuously accelerating CSW with ever increasing temperature and pressure as it approaches the focal singularity. Indeed, assuming the perfect gas law and the ideally shaped cylindrical and/or spherical shock wave steep front, an infinite energy concentration is expected at the implosion focus. In reality, however, once the shock acquires some critical intensity, the gas behind the shock front can no longer be described as perfect. Depending on the gas type and local thermodynamic conditions, the corresponding real gas mechanisms are initiated [4] and result in a substantially reduced shock wave intensity. The establishment of thermodynamic equilibrium requires a certain relaxation time increasing the shock front thickness (see, e.g., Refs. [5–7] considering planar shocks). This prevents the CSW from collapsing into a singular point and thus results in a less effective energy concentration.

Despite the extensive data obtained during a few decades on the nonideal gas effects in planar strong shocks [4–6], the application of this field toward CSWs seems lacking. In our recent study [1], we aimed to explore the range of maximum possible temperatures that can be expected during the spherical CSW implosion in gas. It was demonstrated, both theoretically and experimentally, that as the strength of the CSW increases, the nonideal gas effects become dominant and govern the evolution of gas properties. The discussion was limited by considering a monatomic gas, argon, therefore accounting for ionization, excitation, radiation, and Coulomb interaction effects. It was shown that the nonideal gas effects play a significant role in attenuation of the converging shock. Among others, the ionization presents a dominant energy sink, resulting in substantially reduced equilibrium temperatures at the focal point as compared to a perfect non-ionizing case. The calculations were based on approximate method, namely, geometrical shock dynamics (also known as CCW approximation [8]). While this approach provided fairly accurate agreement with the experimental data, it is expectedly limited to the converging stage only. Since the temperature at the focus is dictated by the dynamics behind the reflected shock, in this study, we aimed at applying a 1D axisymmetric nonideal gas numerical simulation to improve the prediction of the experimental data.

2 Experiment

Spherical CSWs were generated in a shock tube with a special test section designed along the same principles as those of Refs. [1, 9, 10]. The major advantages of this technique over the blast reflection methods are the abilities to (1) create symmetrical CSW front and (2) directly access for measurements the implosion core where the gas is initially undisturbed. The shock tube is equipped with a fast-opening valve (FOV in Fig. 1a), substituting the traditional way of diaphragm rupture and enabling automation of the experiment preparation. Helium was generally used as the driver gas to generate higher Mach number shocks, and the channel section was filled with argon. A circular shock tube channel is followed by a converging test section (see Fig. 1b, d) composed of the transformation segment (TS) and the conical segment

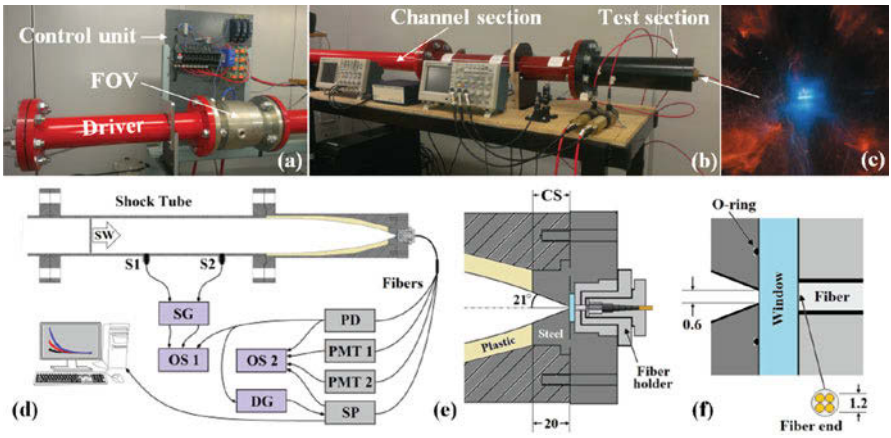

Fig. 1 (**a**–**b**) KTH shock tube facility, (**c**) light emitting hot gas core at the cone tip, (**d**) schematic diagram of shock tube and diagnostic setup, (**e**) zoomed area of conical segment, (**f**) zoomed cone tip with optical window and fiber details

(CS). The TS is designed to smoothly transform initially planar shock into a CSW of a spherical shape, avoiding Mach reflections and subsequent breakup of the front symmetry. The following CS with an inner axisymmetric conical profile (see Fig. 1e) ends in a tip cut with a 0.6 mm opening (Fig. 1f) which is sealed with a quartz window. As the shock converges toward the CS tip, the conditions become extreme so that the gas intensively glows (see Fig. 1c). The light flash collected through the window by optical fibers is separately transferred into a diagnostic setup as shown in Fig. 1d.

Pressure transducers S1 and S2 coupled into a signal conditioner SG recorded the incident shock time of arrival to estimate the initial shock intensity or Mach number. The light flash, produced at the shock focus, was collected by a four-furcated fiber-optic cable in which 4 fibers with 600 μm size cores are bundled at one end while split at the opposite. The fibers are solarization resistant with a transmission wavelength range 180–800 nm. Figure 1f demonstrates the fiber configuration inside the cable end directed toward the CS opening through the window. The collected light was then separately transferred into a photodiode (PD), two photomultiplier tubes (PMT 1 and 2), and a spectrometer (SP), as shown in Fig. 1d. The photodiode is a biased GaP detector with a response range 150–550 nm and response time ~10 ns and was used to register the light intensity integrated over the working range which is radiating during the focusing. The photomultiplier tubes having a response range 185–900 nm and a response time ~10 ns were equipped with band-pass interference filters with central wavelengths of 220 and 405 nm, respectively. A high-resolution echelle spectrometer with a wavelength range 250–850 nm was calibrated using mercury, deuterium, and wolfram lamps.

The gas temperature at the tip of the CS was deduced from the Planck fit to the radiation spectrum: $I_\lambda = A\lambda^{-5}[\exp(hc/kT) - 1]^{-1}$, where I_λ is the intensity

per unit wavelength λ, c is the speed of light, and A is the fitting parameter. To ensure that the spectra are measured during the instant of maximum temperature, both PMTs equipped with band-pass filters were employed. The ratio of intensities of two distinct wavelengths (220 nm and 405 nm) reduces the dependence on A, and the result is a function of the temperature. Varying the spectrometer delay time by DG, the maximum of the PMTs ratio and the instant of the spectrometer exposure gate (100 ns) are matched.

3 Calculation

Consider three-dimensional Euler equations:

$$\frac{\partial}{\partial t}\begin{bmatrix}\rho\\ \rho u\\ \rho v\\ \rho w\\ E\end{bmatrix}+\frac{\partial}{\partial x}\begin{bmatrix}\rho u\\ \rho u^2+p\\ \rho uv\\ \rho uw\\ uH\end{bmatrix}+\frac{\partial}{\partial y}\begin{bmatrix}\rho v\\ \rho uv\\ \rho v^2+p\\ \rho vw\\ vH\end{bmatrix}+\frac{\partial}{\partial z}\begin{bmatrix}\rho w\\ \rho uw\\ \rho vw\\ \rho w^2+p\\ wH\end{bmatrix}=0 \quad (1)$$

In situations with cylindrical and spherically symmetric flow Eq., (1) may be reduced to essentially one-dimensional equations with a geometric source term to account for the second and third spatial dimensions. The resulting governing equations read:

$$\frac{\partial}{\partial t}\begin{bmatrix}\rho\\ \rho u_r\\ E\end{bmatrix}+\frac{\partial}{\partial r}\begin{bmatrix}\rho u_r\\ \rho u_r^2+p\\ u_r H\end{bmatrix}=-\frac{j}{r}\begin{bmatrix}\rho u_r\\ \rho u_r^2\\ u_r H\end{bmatrix} \quad (2)$$

where t is time, r radial distance, ρ gas density, u_r gas radial velocity, p pressure, E total energy, and H total enthalpy and j = 0,1,2 refer to plane, cylindrical, and spherical symmetry, respectively.

Considering ideal gas equation of state, the system of Eq. (2) would be closed and easily solved; however the equation of state for the real monatomic ionizing gas is:

$$p=(1+\alpha_e)\,\rho RT-\frac{kT}{24\pi r_D^3}+\frac{\sigma}{3}T^4 \quad (3)$$

where R is specific gas constant, α_e ionization degree, and r_D Debye radius and the second and third terms are Coulomb correction and radiation pressure, respectively.

In a thermodynamic equilibrium (TE), the gas composed of electrons, ions, atoms, and photons can be described by statistical mechanics, where equilibrium distributions are characterized by the same temperature. When photons escape from an ionized gas, the balances involving electrons, ions, and atoms are inevitably affected. However, if the energy loss by radiation is small, the Saha-Boltzmann distribution is still a valid description of the system, and a local thermal equilibrium (LTE) is settled. Assuming LTE, the distribution of atoms and ionization products can be calculated using the Saha equations:

$$\frac{\alpha_{i+1}\alpha_e}{\alpha_i} = \left(\frac{2\pi m_e kT}{h^2}\right)^{3/2} \frac{m_A}{\rho} \frac{2Q_{i+1}}{Q_i} \exp\left(-\frac{I_{i+1}^{eff}}{kT}\right) \tag{4}$$

where m_e is the electron's mass, k is the Boltzmann's constant, h is Planck's constant, m_A is the mass of atom, α_i is the ion concentration in ionization stage i, Q_i is the electronic partition function in ionization stage i, and T is the absolute equilibrium temperature. The ith effective ionization potential is reduced due to Coulomb interactions $I_i^{eff} = I_i - (i+1)\, e^2/4\pi\varepsilon_0 r_D$, where e is the electron's charge and ε_0 is the vacuum permittivity [11].

The specific internal energy per unit mass of a monatomic ionizing gas can be written as:

$$\varepsilon = \frac{3}{2}(1+\alpha_e)\, RT + \frac{1}{m_A}\left[\sum_{i=1}^{l}\alpha_i \sum_{j=1}^{i} I_j^{eff} + \sum_{i=0}^{l}\alpha_i \frac{U_i}{Q_i}\right] + \frac{\sigma}{\rho}T^4 - \frac{kT}{8\pi\rho r_D^3} \tag{5}$$

where U_i is the total excitation energy of atom/ion in ionization stage i. The terms represent, respectively, translation, ionization, excitation, and radiation and the last term is due to Coulomb interactions.

Equation (2) can be solved numerically to a high degree of accuracy by a good one-dimensional numerical method. Roe's scheme [12] was applied in this case, owing to a prominent merit that the interactions between the wave propagation and the area changes can be accounted for simultaneously (the essence of the problem), i.e., the source term is already incorporated in the intermediate intercell flux. The application of Roe's scheme is almost straightforward in the case of ideal gas; however, considering an equation of state (3), some more complicated derivations of Roe's matrix, eigenvectors, eigenvalues, averages, and pressure derivatives are required. The scheme was extended to second-order algorithm using the idea of flux limiters and modified to disperse entropy-violating solutions. Complimented with charge conservation equations, the nonlinear system, namely, Eqs. (3, 4, 5), was solved using Newton-Raphson iterative methods, to update the corresponding variables (p, T, α_i) at every time step of the numerical algorithm.

4 Conclusion

Figure 2a demonstrates excellent agreement between exact (self-similarity), approximate (CCW), and present numerical calculations for cylindrical and spherical implosion in ideal gas. While exact and CCW solutions terminate at the implosion focus, the numeral simulation allows the computation of the following reflected shock trajectory and flow variables behind it. Figure 2b demonstrates spherical CSW trajectories in 5 noble gases accounting for nonideal effects assuming equilibrium. Having initially same Mach number the CSWs arrive the later the heavier is the test gas.

Focal temperatures of order of 30,000 K, in good agreement with nonideal gas calculations, were measured in argon using gas-dynamic shock tube facility. A prominent advantage of the numerical approach reported herein over the geometrical shock dynamics method used in [1] is that the present calculations can be extended to compute the flow variables behind the reflected shock (diverging shock after implosion). This reflected shock inevitably dictates the duration of the extreme conditions at the focal point, and therefore is meaningful for accurate interpretation of the experimental data. Figure 3 shows the comparison of the new numerical

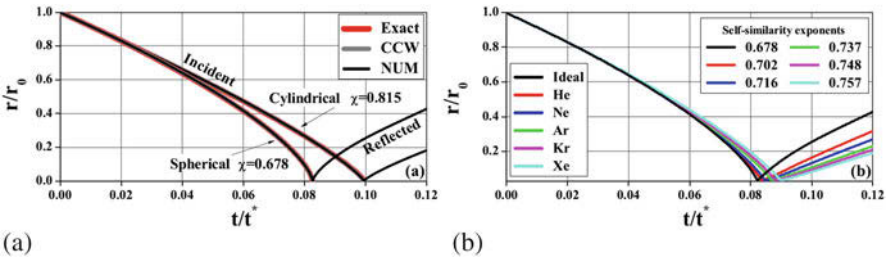

Fig. 2 CSW trajectories in (**a**) ideal gas, (**b**) noble gases with nonideal effects

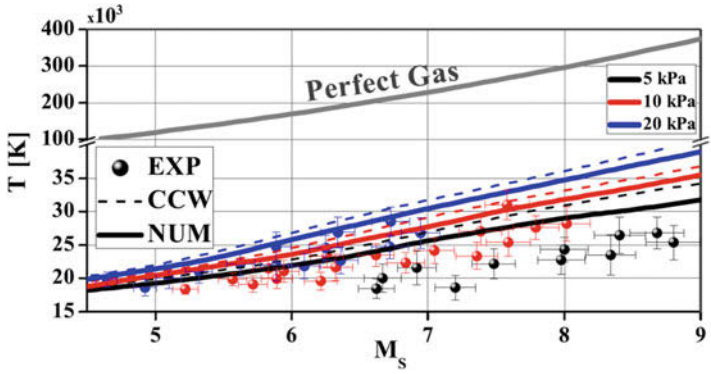

Fig. 3 Peak focal temperature vs incident shock Mach number

results with previous CCW calculations and experiments performed to estimate the focal temperatures of spherical CSWs in argon.

There are two features of the numerical simulation to emphasize at this stage: (1) the CSW front is numerically dispersed, and (2) the finite duration of the temperature maxima results in lower average temperature value. Importantly, both features reproduce the conditions met in reality. The actual shock front is broadened and the radiation (collected for temperature estimation) is integrated over the radiating gas volume and a finite time period during the measurements. As a result, the prediction of the numerical simulation approaches closer to the experimental points than that of a "more ideal" CCW calculation. This result indicates that the structure of the CSW front and the dynamics behind the reflected shock are important for the correct description of the experimental data collected at the implosion focus.

References

1. M. Liverts, N. Apazidis, Phys. Rev. Lett. **116**, 014501 (2016)
2. G. Guderley, Luftfahrtforschung **19**, 302 (1942)
3. L. D. Landau, E. M. Lifshitz, in *Fluid Mechanics, Course of Theoretical Physics*, ed. by J. B. Sykes, W. H. Reid, (Pergamon Press, Oxford/New York, 1987), p. 406
4. Ya. B. Zel'dovich, Yu. P. Raizer, in *Physics of Shock Waves and High-Temperature Hydrodynamic Phenomena*, ed. by W. D. Hayes, R. F. Probstein, (Dover, Mineola/New York, 2002), pp. 176–505
5. H. Petschek, S. Byron, Ann. Phys. (N.Y.) **1**, 270 (1957)
6. J.W. Bond, Phys. Rev. **105**, 1683 (1957)
7. L. Biberman, A. Mnatsakanyan, I. Yakubov, Sov. Phys. Usp. **13**, 728 (1971)
8. G.B. Whitham, *Linear and Nonlinear Waves* (Wiley, New York, 1974), p. 265
9. Z. Zhai, C. Liu, F. Qin, J. Yang, X. Luo, Phys. Fluids **22**, 041701 (2010)
10. M. Kjellander, N. Tillmark, N. Apazidis, Phys. Fluids **24**, 126103 (2012)
11. H.R. Griem, Phys. Rev. **128**, 997–1003 (1962)
12. P.L. Roe, Annu. Rev. Fluid Mech. **18**(1), 337–365 (1986)

Influence of Matrix Resin on Impact Resistance of CFRP by a Small Sphere

T. Kawai, T. Irisawa, Y. Tanabe, M. Nakayama, and A. Yoshimura

Abstract Since carbon fiber-reinforced plastic matrix composites (CFRPs) have the advantages of lightweight and high strength, they are promising candidates for structural materials of high-speed vehicles/aircrafts. With such use, foreign object impact is an inevitable risk for the materials; damage behavior or tolerance should be evaluated. Using several kinds of CFRPs with different matrix resins, epoxy and polyamide 6, a spherical projectile was impacted against the CFRPs to evaluate the effects of the matrix resins on the deformation behavior and debris amount. A high strain-to-break fiber and low-modulus matrix results in a higher dissipation energy with a larger deformation but lower amount of debris. The PA6 matrix composites, when having similar mechanical properties of the epoxy resin matrix composites, exhibit a similar behavior against spherical projectile impact regarding the deformation, debris amount, and dissipation energy.

1 Introduction

CFRP is expected to be one of the next-generation structural materials because of its lightweight and high strength and has been applied to the bodies of aircrafts, trains automobiles, etc. During their use, an inevitable risk is foreign object impact at a high velocity. In recent years, research studies aiming at the practical application of the CFRPs made of thermoplastic resins (CFRTPs) have been actively conducted for the purpose of high productivity and low production costs. Research, even though quite limited, has been conducted regarding the impact behavior and/or impact resistance using thermosetting resin-based CFRPs. However, very few research studies of the CFRTPs have been published. To obtain a high performance against

T. Kawai · T. Irisawa · Y. Tanabe (✉)
Department of Materials Design Innovation, Nagoya University, Nagoya, Japan
e-mail: tanabe.yasuhiro@material.nagoya-u.ac.jp

M. Nakayama · A. Yoshimura
Structures and Advanced Composite Research Unit, Aeronautical Technology Directorate, Japan Aerospace Exploration Agency, Tokyo, Japan

A. Sasoh et al. (eds.), *31st International Symposium on Shock Waves 2*,
https://doi.org/10.1007/978-3-319-91017-8_40

the impact of the CFRPs, especially the CFRTPs, it is necessary to investigate the difference between the CFRPs and CFRTPs of the behavior/resistance from the viewpoint of the matrix resins.

The aim of this study is to clarify the differences in the matrix resins against the impact by using polyamide 6 (PA6) and four different epoxy resin matrix composites, which leads to clarifying the differences in the CFRPs and CFRTPs.

2 Experimental Procedures

2.1 Materials

PA 6 and four epoxy resins, A to D, were used for the matrix. The reinforced carbon fiber was a fabric made using Toray T-700S (T). The epoxy resins were made of base epikote828 with different hardening agents having different molecular weights, i.e., the length of the linear molecular chains [1]. The PA6-based CFRTP was prepared by vacuum-assisted resin transfer molding (VaRTM) from ε-caprolactam polymerized at 140 °C. The epoxy resin-based CFRPs were cured at over 150 °C depending on the agents.

The dimensions and the volume fraction of the fiber were 70-mm × 70-mm and 2-mm thick with about a 60% volume. The strength, modulus, and strain-to-break of the composites are summarized in Table 1.

2.2 Impact Tests

A 4-mm diameter SUJ-2 sphere was vertically impacted against the specimens launched by a one-stage light-gas accelerator. The velocity was between 150 and 350 m/s. The dissipated energies per areal density were calculated from the difference in the kinetic energy of the projectiles before and after the penetration. Mass losses by the impact were measured using the difference in weight of the specimens before and after the impact.

Table 1 Mechanical properties of the T fiber specimens

Matrix Resin	Strength [MPa]	Modulus [GPa]	Strain-to-break [%]
PA6	705	65	1.46
A	987	60	1.61
B	1019	62	1.62
C	944	45	1.33
D	397	42	0.96

The three-dimensional (3D) deformations during the impact were measured using two high-speed video cameras. The details of the measurements are described in ref. [2]. The dissipated energies during the specimen's deformation were calculated using the obtained 3D data. Conical deformation (height w_{max}) of the specimens was assumed that a concentrated point load (P) acted on the center of a disc (radius a) whose circumference was fixed as expressed by Eq. (1), where D was the flexural rigidity. When the deformation of a specimen at the maximum impact velocity occurs and no visible damage is observed, all the kinetic energy ($E_{projectile}$) of the projectile was assumed to be dissipated as the deformation, which corresponds to Eq. (2). Details of the calculation are also described in ref. [2]. In Eq. (1), D is proportional to $P\ a^2\ /\ w_{max}$. When D is constant (assumed), D can be estimated by $a^2\ /\ w_{max.}$ The maximum deviation of the impact time, $t = 0$ μs, was less than 1 μs.

$$w_{max} = P\ a^2\ /\ (16\ \pi\ D) \quad \cdots \tag{1}$$

$$2\ E_{projectile} = m\ v^2 = P\ w_{max} = 8\ \pi\ D\ {w_{max}}^2 /\ a^2 \quad \cdots \tag{2}$$

3 Results and Discussion

3.1 Dissipation Energy and Mass Loss

The penetration limits of various CFRPs are shown in Fig. 1. The strength or strain-to-break of the CFRPs strongly affected the limits. The matrix resin and surface treatment of the carbon fiber also affect the limits, which also are shown in Fig. 1. In the figure, ARD and HTD indicate that the composites were prepared with a surface-treated and a non-surface-treated pitch-based high-modulus carbon fiber fabrics, respectively. The high-modulus or low strain-to-break fibers were significantly affected by the matrix resins regarding dissipation of the kinetic energies.

Fig. 1 also shows the mass loss of the surface-treated fiber composites. The order of the losses seems to be in a reverse order of the dissipation energies. The low-modulus matrix resulted in a higher dissipation energy and lower weight loss. Unfortunately, the adhesive strength between the carbon fiber and the matrix resins has not been measured for all the composites. Therefore, some ambiguity remains in the discussion, but the deformation, i.e., moving of carbon fiber in composites, should affect this behavior.

The left graph of Fig. 2 shows the dissipation energy per area density at the impact velocity of about 350 m/s. The energy increased in the order of B < PA6 < A < C < D. Based on this order, deformation of the specimens increased. This order of the dissipation energy was almost coincident with the order of the modulus and strain-to-break. It revealed that a high deformation dissipated a high

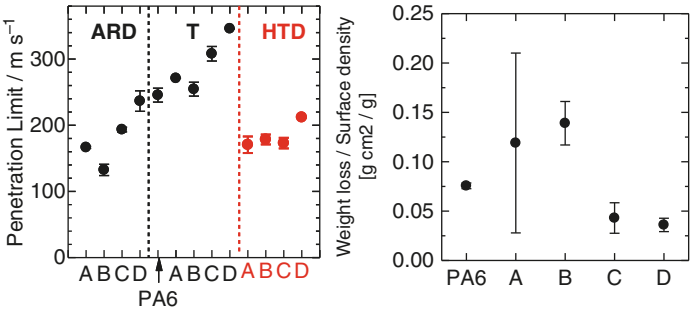

Fig. 1 Penetration limits (left) and weight loss per surface density for the T composites (right)

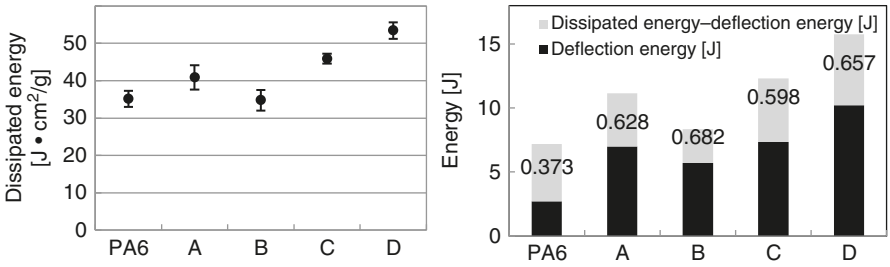

Fig. 2 Dissipation energies of the T composites and the ratio of deformation energy to the total ones

kinetic energy. The right figure of Fig. 2 shows the total dissipated energy during the impact, i.e., the deformation energy and consumed energy, the latter corresponding to the specimen damage such as crack initiation, propagation, delamination, kinetic energy of scattered debris, etc. The consumed energy was calculated from the difference between the dissipated and deflected energies. The ratio of deflection to the dissipated energies in the PA6 matrix composite was lower when compared to the others. As a result of the fragmentation test, the interfacial shear strength of the epoxy/CF was 97 MPa and that of PA6/CF was 44.6 MPa. A clear reason for this has not yet been obtained, but deboning at the interface may cause some amount of energy consumption.

3.2 Three-Dimensional Deformation Analysis

The deformation behaviors of the PA6 composite are shown in Fig. 3 as the profiles on the center plane of the cone. A higher impact velocity resulted in a taller/higher deformation. Figure 4 shows the behavior of the T-A and ARD-A composites. A high-modulus or low strain-to-break fiber showed a lower deformation. The deformation itself of the T-PA6 composite was lower than that of the T-A. The

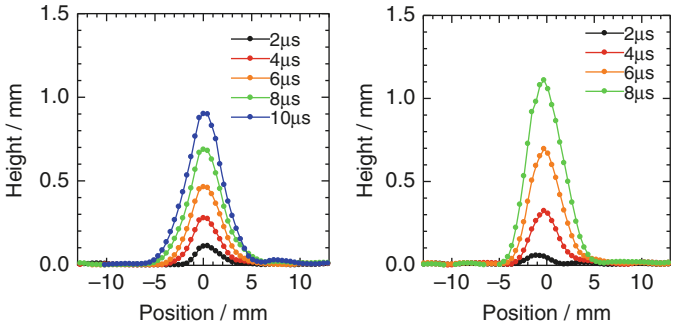

Fig. 3 The deformation profiles of PA6 composite in the center plane of the cones impacted at (left) 260 m/s, and (right) 345 m/s

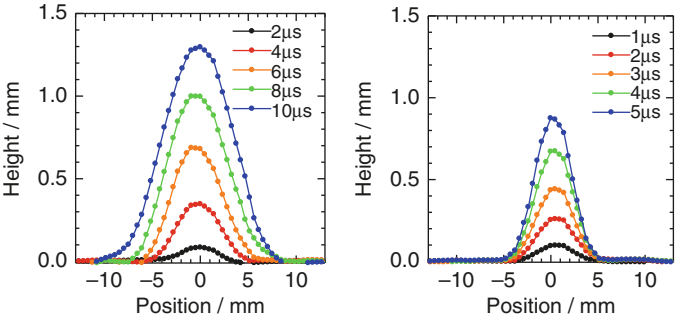

Fig. 4 The deformation profiles of (left) T-A at 343 at m/s and (right) ARD-A at 332 m/s in the center plane of the cones

deformation characteristics can be evaluated by the flexural rigidity of the specimens including strain rate effects. The flexural rigidities of the specimens are indicated as the parameter $a^2 / w_{\max}$. The parameters are summarized in Fig. 5 as a function of the elapsed time.

It was quite difficult to determine the exact impact time of 0 μs; thus the time of $t = 0$ μs in the figure was the original measured time of 1 μs for A-ARD or 2 μs for the others. In the same CFRTP of PA6-T, a higher velocity impact caused a lower $a^2 / w_{\max}$. Using the same fiber fabric but of a different fabric density (A-T and A-T2), the values seems to be same/similar. The fiber density did not affect the rigidity. The ARD fiber showed higher values as compared to the T fiber. The CFRTP of the PA6 matrix showed a similar behavior and properties to the CFRP of the A-type epoxy resin; both composites showed similar mechanical properties, even though the PA6-T was slightly weaker than that of A-T. The difference in the $a^2 / w_{\max}$ values may be caused by the strain rate effect, but the details have not yet been determined. In this velocity range and at room temperature, the CFRTPs showed a similar behavior to the CFRP versus the projectile impact, when the mechanical properties of both composites are similar.

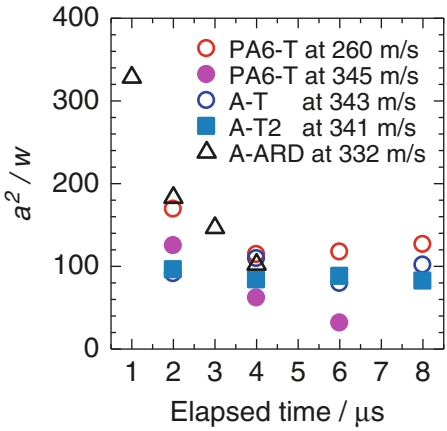

Fig. 5 A sort of flexural rigidity, a^2 / w_{max}, of various specimens as a function of elapsed time

4 Conclusions

Spherical projectile impact tests were carried out for different types of CFRPs and CFRTPs in the velocity range of 150 to 350 m/s in order to understand the effects of the matrix resins against their deformation behavior and debris amount and also to evaluate the energy dissipation ability. The following conclusions are summarized:

1. A high strain-to-break fiber and low-modulus matrix resin results in a higher dissipation energy with a higher deformation but a lower amount of debris.
2. A three-dimensional analysis using an image correlation technique is very useful to make a quantitative evaluation of the precise deformation behavior.
3. The PA6 matrix composite, having similar mechanical properties of the epoxy resin matrix composites, exhibited a similar behavior against the spherical projectile impact regarding the deformation, debris amount, dissipation energy.

Acknowledgments ε-Caprolactam for the PA6 matrix resin was supplied by Nagase ChemteX Corporation, Ltd. This research has been partly supported by MEXT KAKENHI, no.17 K06792 and no.2522091, and a fund for a collaboration research between JAXA and Nagoya University.

References

1. Y. Tanabe, M. Yamada, N. Kobayashi, N. Sato, M. Hashimoto, JCM Jpn. **39**, 16 (2013)
2. M. Yamada, Y. Tanabe, A. Yoshimura, T. Ogasawara, NIMA **646**, 219 (2011)

Improvement of Impact Resistance of Ceramics by Using Resin-Based Materials

S. Yamashita, T. Suzuki, S. Fujimori, T. Irisawa, and Y. Tanabe

Abstract Since ceramics are lightweight and have a sufficient strength, they have the potential to be used as a shield material. However, their low fracture toughness and low shape imparting inhibit their actual applications. To overcome the low fracture toughness and low shape imparting, layered structures joined with resin-based adhesives were conducted for use as protection against projectile impact. As the joining layer, a certain thickness above a certain level seemed to be required. No clear effects could be seen by changing the resin's composition and type. A backup plate, even thin, effectively reduced the debris scattering from the layered structures.

1 Introduction

Since ceramics are lightweight and have a sufficient strength, they have the potential to be used as a shield material. However, their low fracture toughness and low shape imparting inhibit their actual applications. New promising manufacturing and joining techniques have been developed, which will be capable of preparing complicated larger parts with ceramics [1]. The joining or joining layer significantly affects the fracture behavior [2, 3] as shown in Fig. 1. In our experiments to date, the joined (laminated or layered) ceramic plates showed a good resistance against projectile impact as compared to the bulk ones, even though a resin was used as the bonding agent. The resin layer suppresses crack propagation that was initiated in ceramics and reduced the scattered debris. The resin-joining technique can be applicable to parts used on the ground but also in space. However, limited experiments have prevented determining the required characteristics of the layer.

S. Yamashita · T. Suzuki · S. Fujimori · T. Irisawa · Y. Tanabe (✉)
Department of Materials Design Innovation, Nagoya University, Nagoya, Japan
e-mail: tanabe.yasuhiro@material.nagoya-u.ac.jp

A. Sasoh et al. (eds.), *31st International Symposium on Shock Waves 2*,
https://doi.org/10.1007/978-3-319-91017-8_41

Fig. 1 Rear-side views of bulk (left) and layered (right) ceramic plates impacted under a similar condition [2]

In this study, therefore, we investigated the characteristic relationships between the impact-resistance and the joining-layer characteristics, especially the thickness and configuration/composition. In addition to this investigation, the influence of the density and the porosity of the ceramic plates on the resistance against projectile impact are discussed from the view point of the characteristics of the layer.

2 Experimental Procedures

2.1 Materials

Two types of alumina ceramics were adapted; one was dense (the porosity was less than 2%) and the other was porous (the porosity was about 25%), and both consisted of 98%-Al_2O_3. The plates were 100-mm squares of 2 or 3 mm thickness for the dense and porous ones, respectively. A 4.3-mm thick dense alumina plate was also prepared for evaluating the layered or joining effect in alumina ceramics. Epoxy resin A (strength of 50 MPa, modulus of 3.1 GPa) was used as the joining material. Because the epoxy resin permeated into porous plates during the joining process, the plates were first immersed with the resin, and then two plates were joined with the resin. The densities of the original dense and porous plates were 3.75 g/cm^3 and 2.65 g/cm^3, respectively. The density of the porous plates after the resin impregnation became 2.90 g/cm^3. Joining of the two plates was made using a homemade adhesive (unique-blended epoxy resin) under some load. The adhesive resin layer was less than 0.1 mm in thickness. In the high-velocity impact tests using a two-stage light-gas accelerator (details are shown in Sect. 2.2.2), four- or three-layer joined plates were used that consisted of the same plates mentioned above and joined with the neat resin A.

In low-velocity impact tests using a one-stage light-gas accelerator (details are shown in Sect. 2.2.1), the resin was reinforced with a monolayer of carbon fiber

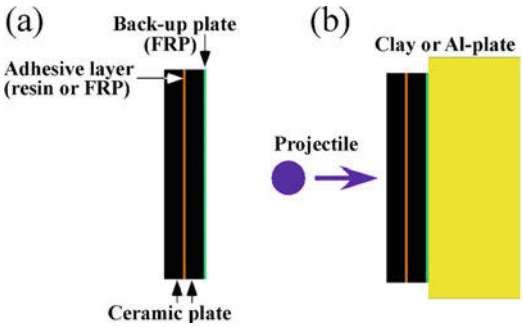

Fig. 2 Schematic illustration of (**a**) the specimen configuration consisting of the ceramic plates, the adhesive layer and the backup plate, and (**b**) specimen setup configuration

(Torayca: Toray) or a polyethylene fiber (Izanas: Toyobo) fabric, and the fiber reinforced plastics were used as the joining adhesives.

To reduce the amount of scattered debris, a thin fiber-reinforced plastic plate (backup plate) was adhered to the back face with the same resin of the matrix. Figure 2 shows the configuration of the layered structure and the backup plate.

2.2 Impact Tests

2.2.1 Low-Velocity Impact

A polycarbonate cylinder of 7-mm diameter × 10-mm height having a 4-mm diameter SUJ2 sphere on its top was accelerated using a one-stage light-gas accelerator at 250–350 m/s. The specimens were placed in a container having 5-cm thick oil clay at the bottom, which is schematically shown in Fig. 2b. The scattered volumes of the ceramic plates and concave volumes generated in the clay were measured as an indication of the damage or damage resistance.

A monolayer fiber-reinforced plastic was adhered on the back face of the specimens, which were also placed on the oil clay, for the purpose of decreasing the debris scattered toward the back.

2.2.2 High-Velocity Impact

A highly dense polyethylene cylinder of 7-mm diameter × 16-mm height with a 5-mm deep hole on the top was accelerated using a two-stage light-gas accelerator at 500–950 m/s. In the hole, a 1/4-inch SUJ2 sphere was fixed with an adhesive. The specimens were placed in a container and set on a 10-mm thick A1070-aluminum plate with a clay gap of less than 1-mm thick, as shown in Fig. 2b.

Table 1 Specimen characteristics, test conditions, dissipated weight, and protection ability upon impact

	Thickness [mm]	Weight[g]	Dissipated weight [%]	Concave volume [cm^3]	Concave volume per area density [cm^5/g]	Impact energy [J]
Dense	4.16	145	1.86	5.44	3.75	66.5
	4.27	150	2.13	6.14	4.09	68.0
Porous	6.25	179	1.45	2.58	1.44	65.5
	6.20	181	1.49	2.28	1.26	65.4
Dense with CF	4.99	161	1.55	3.82	2.37	59.2
	4.61	157	1.66	–	–	66.2
Porous with CF	7.30	182	0.93	2.31	1.27	65.2
	6.69	180	0.72	2.28	1.27	65.5

3 Results and Discussion

3.1 Low-Velocity Impact Tests

Table 1 shows the differences in the dissipated weight and concave volume. The layered porous plates showed smaller scattered volumes. It is considered that resin filled in the pores suppressed crack propagation in the ceramics, and that its high damping capacity dissipated the impact energy. This indicates that a layered porous plate structure has at least two advantages, i.e., lightweight and high impact resistance for a low-velocity impact. Moreover, a monolayer carbon fiber fabric definitely decreased the damage to both the specimen and the clay.

As the effects of the fiber or fabric on the results were not totally clear, additional experiments were then conducted. Other kinds of ceramic plates were joined with the A-resin but with different thickness, a nylon plate of 0.3-mm thickness, and a composite with a different resin B (strength of 0.7 MPa, modulus of 4.7 MPa). Bulk specimens, not a layered structure, of 4.3-mm thickness were also used as a reference. The results are summarized in Table 2. Because the adhesive strength between the resins or composites and the alumina plates have been uncertain, clear conclusions may be difficult. However, the thickness of the adhesive layer clearly affected the results, while no clear effect was observed regarding the resins themselves including the resin matrix carbon fiber-reinforced composites.

Table 3 shows the effects of a thin backup plate on the protection ability. Specimens with the backup plate (backed-up specimen) showed a good impact resistance as compared to the no backup ones that were the same as the 0.1-mm thick specimens in Table 2. The composition of the T-resin was adjusted to fit the plastic fiber fabric of Zairon® (PFRP-T), and then it appears not to be sufficient for the matrix resin for the CFRP. A backup plate with a sufficient resin composition and the appropriate reinforcement definitely worked against reducing damage to the parts.

Table 2 Dissipated weight and protection ability on impact

	Dissipated weight [%]	Concave volume per area density [cm^5/g]	Impact energy [J]
Bulk	7.06	2.36	54.3
	11.8	2.44	57.7
Less than 0.1-mm thick[a]	3.78	3.13	59.8
	3.82	2.55	64.3
1-mm thick[a]	5.05	2.17	46.3
	4.68	1.79	44.5
3-mm thick[a]	6.49	0.41	60.5
	4.86	0.76	58.1
Nylon	3.67	2.28	58.1
	3.88	4.34	59.7
CFRP-A[a] with monolayer CF	3.52	3.09	52.5
	3.61	1.98	54.5
CFRP-A[a] with eight-layer CF	2.26	0.62	58.6
CFRP-B with monolayer CF	3.83	2.13	61.9
	4.25	4.01	58.6

[a]the same resin was used

Table 3 Effects of fiber reinforced plastics on protection ability

	Concave volume per area density [cm^5/g]	Impact velocity [m/s]	Impact energy [J]
PFRP-T	1.36	328	62.6
CFRP-T	2.87	325	61.5
CFRP-A	1.60	328	62.5
CFRP-B	1.74	325	61.6

3.2 High-Velocity Impact Tests

Table 4 summarizes the results. Based on the mortem observations of the structure with dense plates, there was larger debris or a large number of visible debris, and also a larger cone-like crack (ejected from the structure) were generated as compared to those with the porous ones. This indicated that debris generation/scattering also occurred in places away from the impact point in the former structure. At the impact velocity of around 500 m/s, debris generated the crater on the Al-plate in the former, but the projectile seemed to create the crater in the latter as shown in Fig. 3. Specimens made of porous plates could not break a projectile at this velocity range; in contrast, specimens made of dense plates could do it.

At the higher velocity of 920 m/s, specimens of dense-1 and porous-1 with a similar thickness but different weight resulted in a similar concave depth in the

Table 4 Crater depth in backup Al-plates and volumes of initiated cone-like crack

	Thickness [cm]	Weight [g]	Volume of cone-like crack [cm^3]	Depth of crater in aluminum [mm]	Impact velocity [m/s]
Dense-1	1.03	101.4	11.1	2.2	926
Dense-2	1.04	99.7	7.9	1.0	503
Porous-1	0.89	61.4	3.4	2.5	920
Porous-2	1.21	84.0	3.6	1.9	589

Fig. 3 Pictures of craters initiated on Al-plate for (left) dense-2 and (right) porous-2

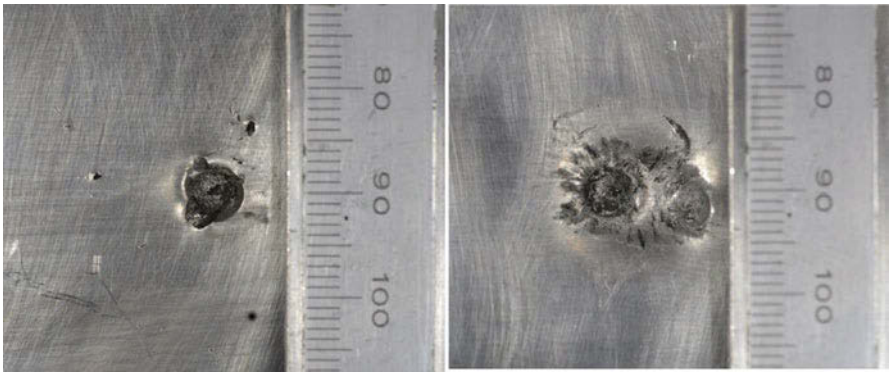

Fig. 4 Pictures of craters initiated on Al-plate for (left) dense-1 and (right) porous-1

aluminum plates as shown in Table 4 and Fig. 4. Moreover, the ejected volumes were smaller in specimens made of the porous plates than in those made of the dense plates. In this velocity range, specimens made of the porous plates were superior to those made of the dense ones with a smaller amount of debris and lightweight.

4 Conclusions

To overcome ceramic's low fracture toughness and low shape imparting, layered structures joined with resin-based adhesives were effective for use as protection parts against projectile impact. A projectile was impacted against layered ceramic plate structures at the velocity of 250–950 m/s. We investigated the effects of the density of the ceramic plates and the adhesives on the resistance or characteristics against impact. The following results were obtained:

(1) At least 3 mm thick resin-based adhesives significantly reduced the amount of debris and number of cracks at the impact velocity below 500 m/s.
(2) The influence of the resin's composition or type seemed to be low.
(3) Layered structures made of porous ceramic plates showed a better resistance or protection ability against impact at the velocity below 950 m/s, and decreased the amount of debris, but only a similar damage on back-side-placed plates.
(4) A composite plate, even thin, on the back face of the layered ceramics played a role in reducing the debris scattering.

Acknowledgments The authors appreciate Dr. K. Sekine and Mr. T. Kumazawa of Mino Ceramics Co. Ltd., for their useful comments and discussion. A part of this research was supported by JSPS KAKENHI, no.17 K06792 and no.2522091.

References

1. K. Sekine, T. Kumazawa, W.-B. Tian, H. Hyuga, H. Kita, J. Ceram. Soc. Jpn. **120**(1401), 207 (2012)
2. A. Tominaga, K. Sekine, Y. Tanabe, in *Influence of Joining and Plate Thickness on Impact Characteristics of Ceramics*, 3B2–3, SSWJ25, Sagamihara, Japan, 5–7 March 2014, in Japanese
3. K. Sekine, T. Kumazawa, Y. Tanabe, Int. J. Appl. Ceram. Technol. **12**(6), 1217 (2015)

Measurement of Plasma Formed by High-Speed Impact to Estimate Temperature at Impact Point

Y. Motoyama, K. Umeda, T. Sakai, S. Kinoshita, and K. Watanabe

Abstract Structures in space are at the risk of collision with space debris, motivating the study of high-speed impact phenomena. In high-speed impacts, the temperature increases rapidly at the impact point, possibly causing destruction at the impact point in addition to impact pressure. However, the influence of high temperature has not been elucidated because existing thermometers do not have sufficient time resolution to measure the increasing temperature at the impact point. In this study, plasma formed by high-speed impact was measured and observed to estimate the temperature at the impact point. High-speed impact experiments were performed using a gas gun to form plasma. A projectile impactor and target were made of aluminum alloy, and the projectile velocity was approximately 650 m/s. High-speed images and high-speed optical visualization images of the state of plasma diffusion were acquired using a high-speed camera. In the experiments, the electron temperature of the plasma was measured by employing the triple probe method, and it was confirmed that high-speed optical visualization images are useful for observing plasma diffusion behavior.

1 Introduction

Numerous debris objects exist in outer space traveling with velocities of the order of 7–8 km/s. When space debris collides with a satellite, it can reach a relative speed of approximately 10 km/s. Even if the debris is very small, its collision with a satellite causes a large amount of destruction. In order to develop shields to defend satellites from space debris, high-speed impact phenomena are studied.

Y. Motoyama (✉) · K. Umeda · T. Sakai
Department of Advanced Mechanical Engineering and Robotics, Ritsumeikan University, Kusatsu, Shiga, Japan

S. Kinoshita · K. Watanabe
Department of Mechanical Engineering, Ritsumeikan University, Kusatsu, Shiga, Japan
e-mail: keikow@fc.ritsumei.ac.jp

A. Sasoh et al. (eds.), *31st International Symposium on Shock Waves 2*,
https://doi.org/10.1007/978-3-319-91017-8_42

Destruction phenomena in high-speed impacts are caused by the transient temperature rise at the impact point in addition to the impact pressure. It is necessary to measure the temperature at the impact point to elucidate the destruction phenomena; however, a reliable temperature measurement method has not been established because current thermometers have insufficient time resolution to measure the transient temperature change.

In high-speed impacts, impact flashes are observed. Emissions from an impact flash have characteristics of blackbody radiation and line emission from excitation particles; the impact flash temperature can be estimated from them [1, 2]. Line emissions are characteristics of plasma, and it has been confirmed that plasma exists in impact flashes [3]. Therefore, it is conceivable that the plasma is associated with the high temperature.

In this study, plasma was measured to estimate the temperature at the impact point. High-speed impact experiments were performed, wherein a plasma-measuring instrument was set near the impact point. The plasma diffusion behavior from the impact point was observed in order to estimate the impact point temperature.

2 Experiments

2.1 Triple Probe Method

A probe method is employed to measure the plasma. By inserting the probe in the plasma, it is possible to measure the electron temperature of the plasma. In this study, a triple probe was employed to measure the electron temperature, because the plasma formed by high-speed impact is instantaneous and unstable [4]. Figure 1 shows the triple probe circuit. The triple probe is constructed from three probes, two power sources, and two resistors. I_1, I_2, and I_3 represent the current flowing into each probe.

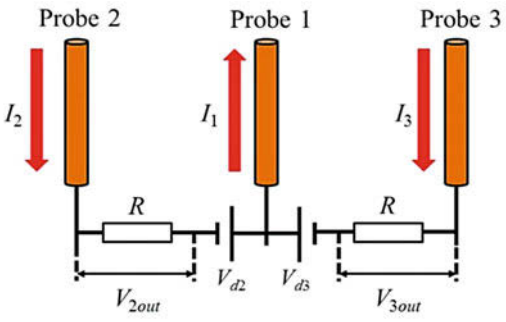

Fig. 1 Triple probe circuit

When the probes are inserted into the plasma, the currents satisfy Eq. (1).

$$I_1 = I_2 + I_3 \tag{1}$$

The electron temperature, T_e, was calculated by Eq. (2).

$$\frac{I_1 + I_2}{I_1 + I_3} = \frac{1 - \exp\left(-\frac{eV_{d2}}{kT_e}\right)}{1 - \exp\left(-\frac{eV_{d3}}{kT_e}\right)} \tag{2}$$

V_{d2} and V_{d3} represent the voltage of the power sources and k and e represent the Boltzmann's constant and electric charge, respectively, while S is the surface area of the probe.

In this study, the probes were made of copper wire having a length of 10 mm and diameter of 1 mm. Resistors R were 700 Ω each. The power source voltages, V_{d2} and V_{d3}, were 3 V and 13 V, respectively.

2.2 Experimental Setup

High-speed impact experiments were performed using a vertical light gas gun [5]. Figure 2 illustrates the experimental setup and Fig. 3 shows the projectile. The projectile was a hemispherical impactor with a radius of 7 mm and a weight of 7 g and was composed of aluminum alloy (A5052) with a polycarbonate sabot. A magnet in the sabot was used for velocity measurement. The velocity measurement device, which had three coils, was set at the exit of the launch tube, and the transit time between each coil was used to determine the projectile velocity. The target, too, was made of A5052 alloy and had a size (l × w × t) of 90 × 50 × 20 mm. The output signals of the triple probe, $V_{2\text{out}}$ and $V_{3\text{out}}$, were measured by a DL850 ScopeCorder (Yokogawa Meters & Instruments Corporation). The triple probe's position system was represented by XY coordinates as shown in Fig. 4. The impact point was set as the origin of the XY coordinate system. The coordinates of the tip of the probe were measured as (12, 2).

2.3 High-Speed Imaging Method

High-speed images and high-speed optical visualization images of the plasma were taken using a high-speed camera (ULTRA Cam; nac Image Technology Inc.) to observe the plasma diffusion behavior. The schlieren technique was employed as the optical visualization technique. It is possible for the schlieren technique to visualize density variation in air caused by the plasma diffusion. Figure 5 shows a schematic

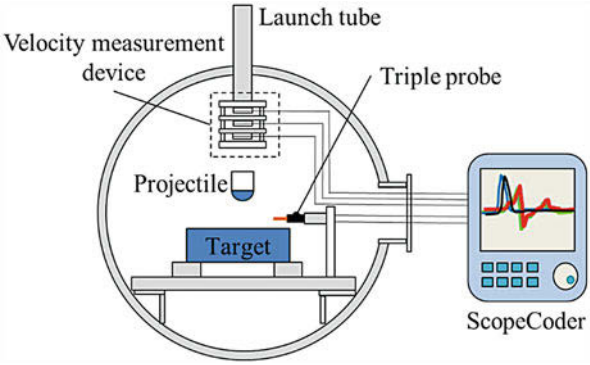

Fig. 2 Illustration of the experimental setup

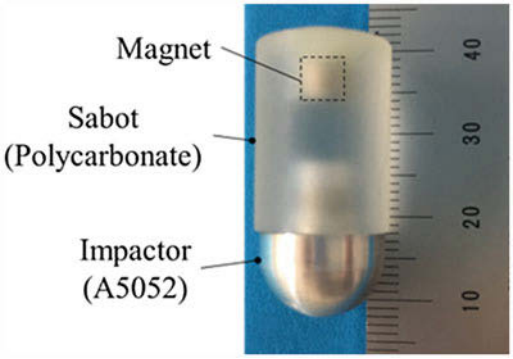

Fig. 3 The projectile

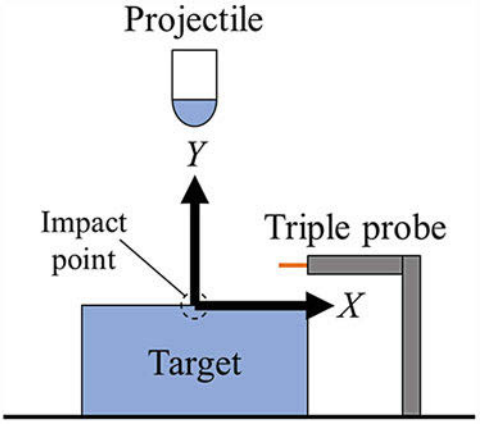

Fig. 4 Triple probe position coordinates

of the schlieren system, which was constructed from a metal-halide light source (NIPPON P·I CO., LTD.), a pinhole to produce a point light source, two plano-convex lenses, and a knife edge. Focal length of the plano-convex lenses A and B were 400 mm and 800 mm, respectively. The frame rate and exposure time for the high-speed camera were 1 Mfps and 0.2 μs, respectively.

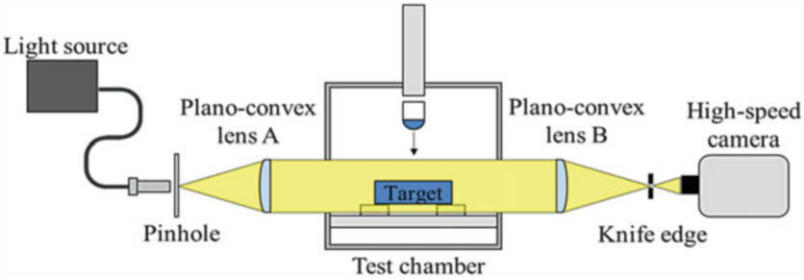

Fig. 5 Illustration of the schlieren system

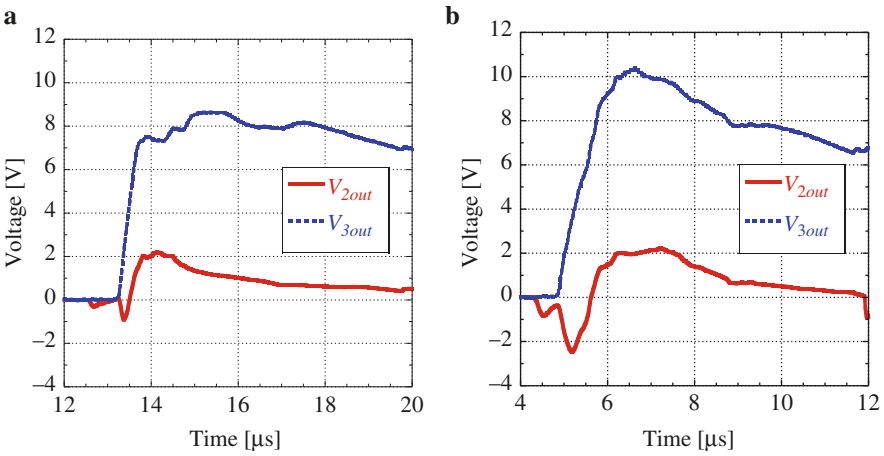

Fig. 6 Output signals of the triple probe at (**a**) taking high-speed images and (**b**) taking high-speed optical visualization images

3 Results and Discussion

The projectile velocity, measured by the velocity measurement device, was approximately 650 m/s. The time histories for V_{2out} and V_{3out} are shown in Fig. 6. The impact timing was 0 μs. Timing differences for the rising output signals were caused by the distance from the impact point. Figure 7 plots the transient electron temperature calculated from Eq. (2). In both experiments, the maximum electron temperature was approximately 20 eV. It was confirmed that the values recorded by the triple probe were reliable because the electron temperature had approximately the same value under identical experimental conditions for repeated trials of the experiment.

High-speed images are shown in Fig. 8. The impact timing was 0 μs. The impact flash reached the probe in about 5–6 μs from the time of impact. In Fig. 6a, the output signals of the triple probe rose from 12.5 to 13 μs. Not all of the impact flash was due to plasma, and it was observed that the plasma followed the impact flash.

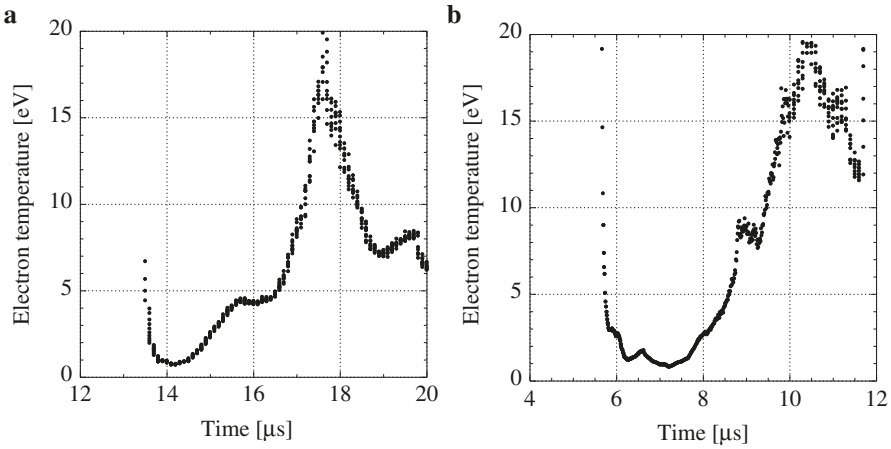

Fig. 7 Electron temperature (**a**) taking high-speed images and (**b**) taking high-speed optical visualization images

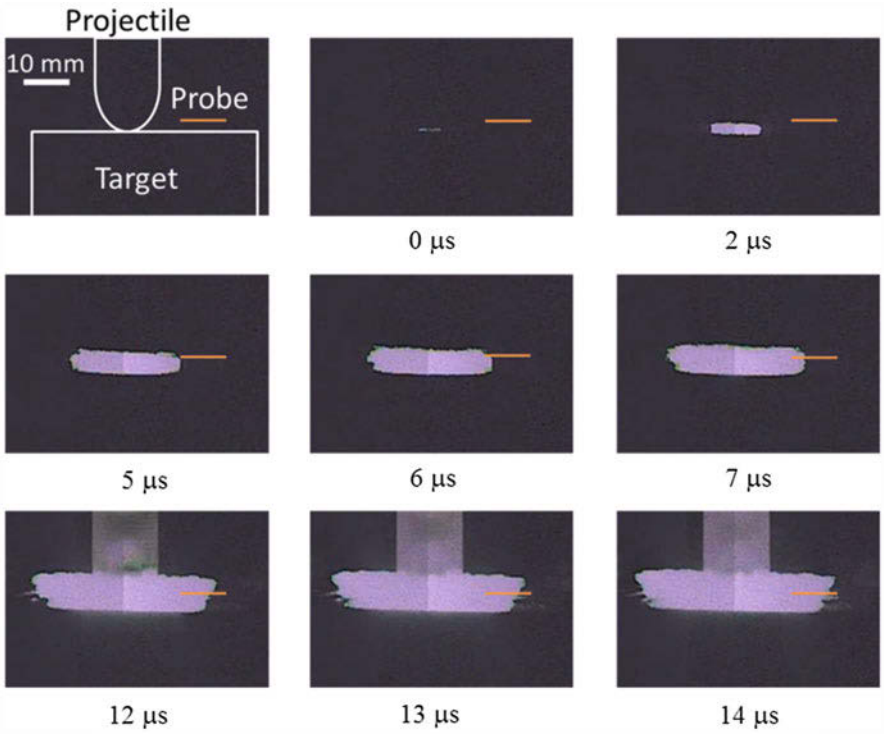

Fig. 8 High-speed images of diffusion of the plasma formed by the high-speed impact

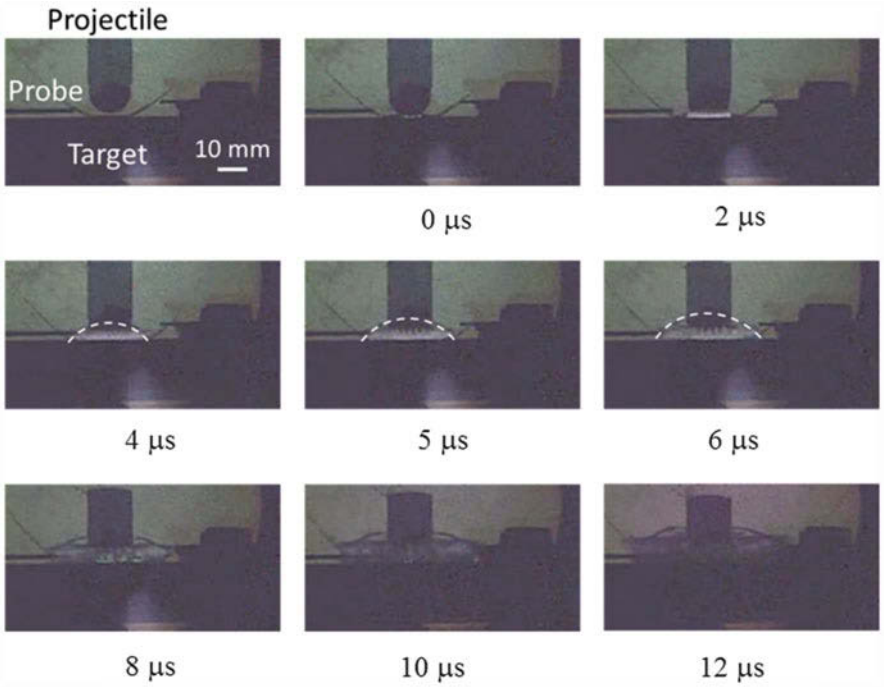

Fig. 9 High-speed optical visualization images by using schlieren technique. White dotted line shows density difference caused by the plasma diffusion

High-speed optical visualization images are shown in Fig. 9. The density difference curve (dotted in Fig. 9) reached the probe in 4–5 μs from the impact. This recording was in agreement with the time at which the output signals rose. It was, therefore, confirmed that the plasma diffusion behavior due to high-speed impact was accurately observed using the schlieren technique.

4 Conclusions

High-speed impact experiments were performed to measure the electron temperature of the plasma formed by such an impact by employing the triple probe method. High-speed images and high-speed optical visualization images of the plasma were acquired using a high-speed camera to observe the plasma diffusion behavior. The conclusions drawn from this study could be summarized as follows.

1. The maximum electron temperature was measured to be approximately 20 eV.
2. Behavior of the impact flash did not agree well with that predicted by the output signals of the triple probe. This suggests that not all of the impact flash formed by the high-speed impact was because of the plasma and that the plasma diffused following the impact flash.

3. The density variation curve agreed well with the output signals of the triple probe. It is, therefore, possible to observe the diffusion behavior of the plasma by employing high-speed optical visualization images supplemented by the schlieren technique.

References

1. G. Eichhorn, Measurements of the light flash produced by high velocity particle impact. Planet. Space Sci. **23**(11), 1519–1525 (1975)
2. B. Jean, T.L. Rollins, Radiation from hypervelocity impact generated plasma. AIAA J. **8**(10), 1742–1748 (1970)
3. J.D. Tandy et al., Examining the temporal evolution of hypervelocity impact phenomena via high-speed imaging and ultraviolet-visible emission spectroscopy. J. Appl. Phys. **116**(3), 1–13 (2014)
4. S.L. Chen, T. Sekiguchi, Instantaneous direct-display system of plasma parameters by means of triple probe. J. Appl. Phys. **36**(1), 35–50 (1965)
5. P.A. Gardiner, et al., Performance evaluation of single stage diaphragmless vertical gas gun for nitrogen and helium gas propellants. Mech. Eng. J. **3**(6), (2016). https://doi.org/10.1299/mej.16-00273

Application of Riemann Solver for Compressible and Non-Expanding Fluid to Impact on Regolith

K. Suzuki

Abstract The compressible and non-expanding (CNE) fluid model was applied to the numerical simulation of the high-speed impact of the regolith-like granular material. Assuming the different speeds of sound for the irreversible compression and reversible elastic unload/recompression processes, this model can describe the following features: (1) high-density fluid remains after all the motion stops, (2) the absence of the fluid, that is, the vacuum is allowed to exist, and (3) the crack can be formed in place of the expansion wave. The fundamental solutions of the Riemann problem, which are necessary for Godunov's method, are composed of the shock waves in the elastic process, the shock waves with the irreversible compression, the contact discontinuities, and the contact surfaces with the vacuum. The shock wave in the elastic process appears as the precursor to the irreversible compression. The numerical results of the one-dimensional regolith-on-regolith impact problems revealed that the phenomena are divided into the penetration stage and the bounce back stage. The ejection velocity decreases with the increase in the speed of sound for the unload process. In the two-dimensional oblique shock wave problems, the two-stage shock wave structure composed of the precursor wave and the irreversible compression wave was numerically simulated, and the relation between the wedge angle and the wave angles was obtained.

1 Introduction

Shock waves play an important role in various impact phenomena. For example, in a case of the crater formation on the regolith, the propagation of the shock wave from the impact point leaves high-density compressed material on and under the surface. The macroscopic behavior of the regolith-like material looks similar to a kind of compressible fluid. In fact, the pressure increases with the density, when it

K. Suzuki (✉)
Graduate School of Frontier Sciences, The University of Tokyo, Kashiwa, Japan
e-mail: kjsuzuki@k.u-tokyo.ac.jp

A. Sasoh et al. (eds.), *31st International Symposium on Shock Waves 2*,
https://doi.org/10.1007/978-3-319-91017-8_43

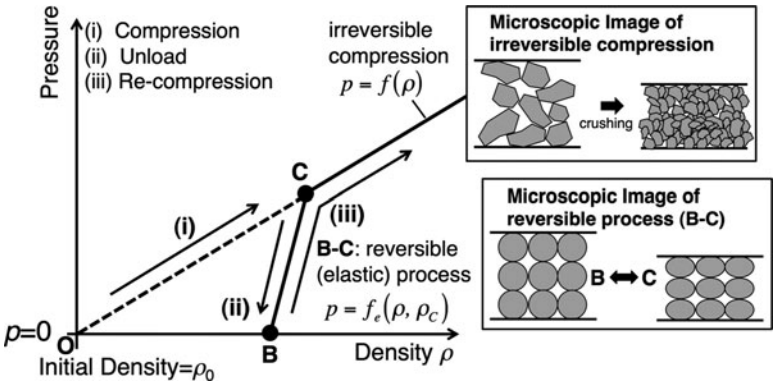

Fig. 1 Equation of state for CNE fluid

is compressed. However, once the compression stops, the pressure vanishes, and the compressed high-density regolith still remains. Such non-expanding nature allows the regolith (a) to form cracks in it, (b) to contact with vacuum, and (c) to leave compressed high-density zone after all the motions stop. To describe such properties that a conventional compressible gas model does not have, the compressible and non-expanding (CNE) fluid model was proposed, and the numerical scheme to solve the flow of the CNE fluid was developed based on the finite volume method and the exact Riemann solver [1].

For simplicity of analysis, the pressure p was assumed to be a linear function of the density ρ as shown in Fig. 1. When the fluid is compressed from the initial state O, the pressure increases with the density on the irreversible compression line given in Eq. (1):

$$p = c^2 \ (\rho - \rho_0) \tag{1}$$

After the compression stops at the state C, the pressure decreases on the line BC of Eq. (2):

$$p = c_s^2 \ (\rho - \rho_B)\,, \tag{2}$$

where the speed of sound for the elastic process c_s must larger than c in Eq. (1). The pressure vanishes at the state B with the density higher than the initial one. When the fluid is compressed again, the pressure increases on the line BC. After reaching the state C, the fluid is further compressed on the irreversible compression line. The fluid can be compressed or expanded on the line BC, while the compression along the line OC is irreversible. The microscopic images of those processes are shown in the inserts of the figure. The line BC is called as the "reversible (elastic) process" in this paper, because this process allows the density to decrease by $p/{c_s}^2$ at maximum. The density decrease is negligible for large c_s.

In the present study, the one-dimensional regolith-on-regolith impact problems and the two-dimensional oblique shock wave problems were numerically analyzed to discuss the applicability of the CNE fluid model to the analysis of the impact phenomena on the regolith-like granular material. The major objectives of the present study are (1) to clarify the role of the speed of sound in the reversible process in the simulation of the impact phenomena and (2) to clarify the fundamental features of the oblique shock wave formed in the CNE fluid.

2 Method of Analysis

In the CNE fluid model, the reversible process can start at any point on the irreversible compression line. The pressure cannot be uniquely determined only from the density. Though the temperature is not included in the state quantities, the energy, which is defined as a work done by the pressure, must be considered in addition to the density and the pressure [1]. The pressure is determined from the density and energy, which are calculated by solving the conservation equations of the mass and the energy, respectively.

We solved the Euler equations for the CNE fluid, neglecting the viscosity. In addition to the conservation equations of the mass, the momentum, and the energy, the volumetric fraction function ϕ was also numerically solved to capture the boundary between the fluid and the vacuum based on the VOF method [2]. The governing equations were solved with the finite volume method and Godunov's method [3]. For Godunov's method, a complete set of the fundamental solutions for the Riemann problem are necessary. The wave diagrams of the fundamental solutions for the CNE fluid are illustrated in Fig. 2. They are composed of the shock waves in the elastic process (S_e), the shock waves of the irreversible compression (S_i), the contact discontinuities (C^*), and the contact surfaces to the vacuum (C_{vac}). In the present study, the modified version [4] of the solution set [1] was used. A shock wave of the irreversible compression is replaced by the two-stage compression composed of S_e and S_i. S_e appears as the precursor to S_i as shown in the insert of Fig. 2. Such two-stage structure seems more realistic, considering that the formation of the precursor wave is inevitable unless any types of disturbances are eliminated in front of the irreversible compression.

To improve the spatial accuracy in the calculation, the second-order MUSCL method [1] was used. To sharply capture the boundary between the fluid and the vacuum, the step function-type distribution of the mass in a cell was assumed, and the area center of the fluid in each cell was calculated to determine the distribution pattern of the fluid in a cell [4]. The explicit Euler method was used for the time integration with the first-order accuracy for the one-dimensional problems. The extension to the two-dimensional problems was made by the fractional time-step method with the second-order accuracy in time [4].

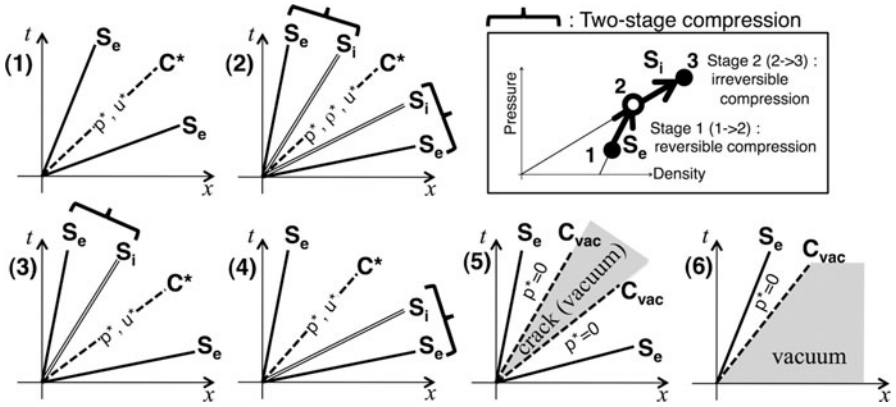

Fig. 2 Fundamental solutions of Riemann problem for CNE fluid

3 Results and Discussion

3.1 Validation by Solving One-Dimensional Riemann Problems

To validate the present computational method, the Riemann problems were numerically solved for the CNE fluid with $\rho_0 = 1800$ kg/m^3, $c = 300$ m/s, and $c_s = 3000$ m/s. The computational domain was -2 m $\leq x \leq 2$ m and the cell size was 0.01 m. The time step was determined from the Courant number 0.02 based on c_s. A small Courant number was required for stable calculation, because the pressure is quite sensitive to the error in the density.

The type (2) solution was successfully simulated as shown in Fig. 3. The conditions on the left and right sides of the Riemann problem are written in the figure. The precursor wave S_e propagates in front of the irreversible compression wave S_i on both sides of the contact discontinuity C^* in the wave diagram (Fig. 3a). The spatial distributions of the computed density and velocity agree well with those of the analytical solution (Fig. 3b).

3.2 One-Dimensional Impact Problem and Effect of the Presence of Elastic Process

The one-dimensional regolith-on-regolith impact problems were solved by using the CNE fluid model to clarify the role of the elastic process. The uncompressed density ρ_0 and the speed of sound for irreversible compression of the hypothetical regolith model were 1800 kg/m^3 and 300 m/s, respectively. The computation domain of -5 m $\leq x \leq 1.5$ m was uniformly discretized with the cell size 0.01 m. The target with the density ρ_0 was initially at rest in the region $x \leq 0$. The impactor with the

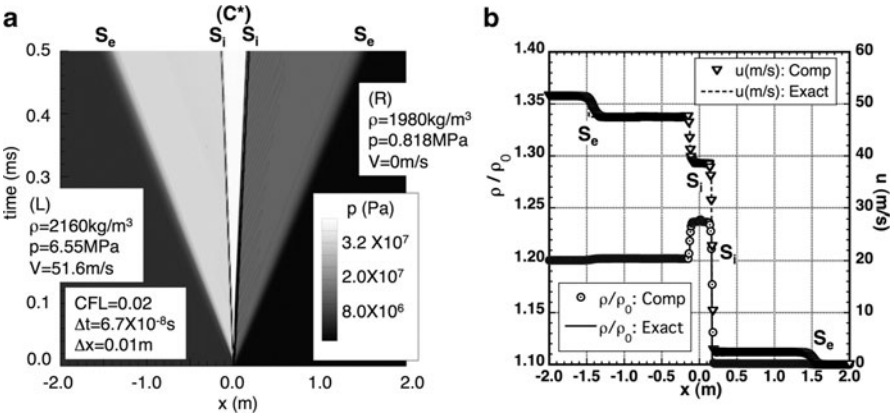

Fig. 3 Numerical simulation of type (2) solution of Riemann problem. (**a**) Wave diagram for pressure. (**b**) Distribution of density and velocity

length 0.4 m and the density ρ_0 was set with its center at $x = 1.0$ m. The pressure was zero all over the computational domain. At the bottom ($x = -5$ m), the rigid wall condition, where the velocity is zero and the specular reflection was applied for the other quantities, was assumed. The time-step size was the same as that in 3.1.

The effect of the elastic process on the result of the one-dimensional impact problem was investigated by varying c_s from 400 m/s to 3000 m/s. The impact velocity was 2000 m/s. The variation of the effective density ρ_e, which is defined as ρ / ϕ to consider the volumetric fraction of the fluid in each cell, on the time-depth map for the case with $c_s = 400$ m/s and 3000 m/s is shown in Figs. 4a, b, respectively. In both cases, the phenomena were roughly divided into two stages: the time zones before and after the maximum penetration depth. The former is characterized by the incident and reflected shock waves and the pressure rise behind them. In this zone, the pattern in Fig. 4a was almost the same as in Fig. 4b. However significant difference is observed between them in the latter time zone. In both cases, the upward motion of the fluid was driven by high pressure on the bottom behind the shock waves. In other words, the CNE fluid was bounced back after the compression by the impact. The upward velocity of the bounce back motion was much slower than the impact velocity. The bounce back became more significant with higher upward ejection velocity and lower fluid density for the case with lower c_s. Figure 5 shows the variation of the maximum depth of the surface, the maximum pressure, and the surface ejection velocity at $t = 40$ ms with c_s. The peak pressure increases, and the ejection velocity decreases with the increase in c_s, while the maximum penetration depth by the impact is hardly affected by c_s. In the present CNE fluid model, the bounce back motion of the fluid after the impact can be controlled by c_s, while the hardness of the material is apparently controlled by c.

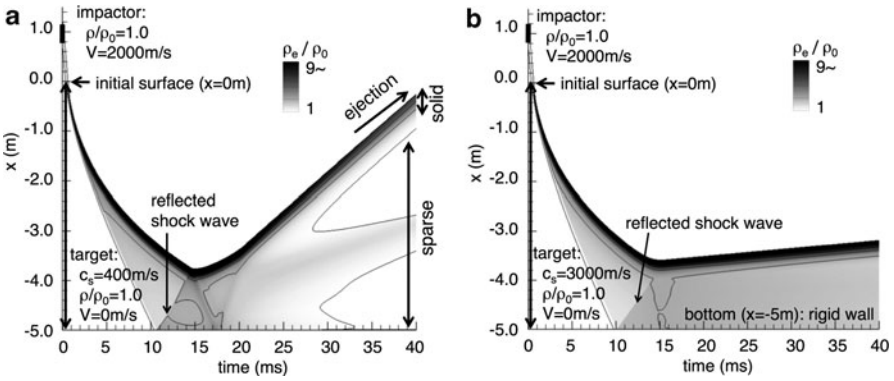

Fig. 4 Variation of effective density on time-depth map for 1D impact problem. (**a**) $c_s = 400$ m/s. (**b**) $c_s = 3000$ m/s

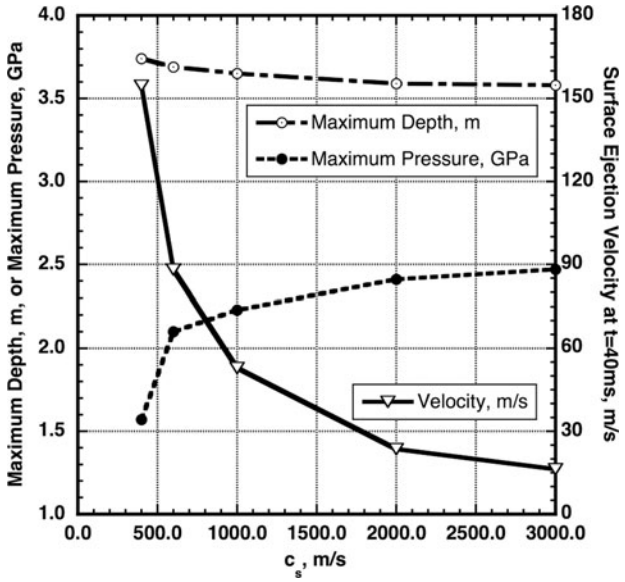

Fig. 5 Variation of maximum surface depth, maximum pressure, and surface ejection velocity at $t = 40$ ms with speed of sound in elastic process

3.3 Two-Dimensional Oblique Shock Wave

The two-dimensional oblique shock wave problem was solved for the CNE fluid. Figure 6a shows the typical result of the oblique shock wave in the CNE fluid. The freestream velocity V_∞ and the wedge angle θ are 2000 m/s and 6°, respectively. The other parameters are given in the figure. The freestream Mach number with respect to c_s is 2.0. Correspondingly to the two-stage compression seen in the one-

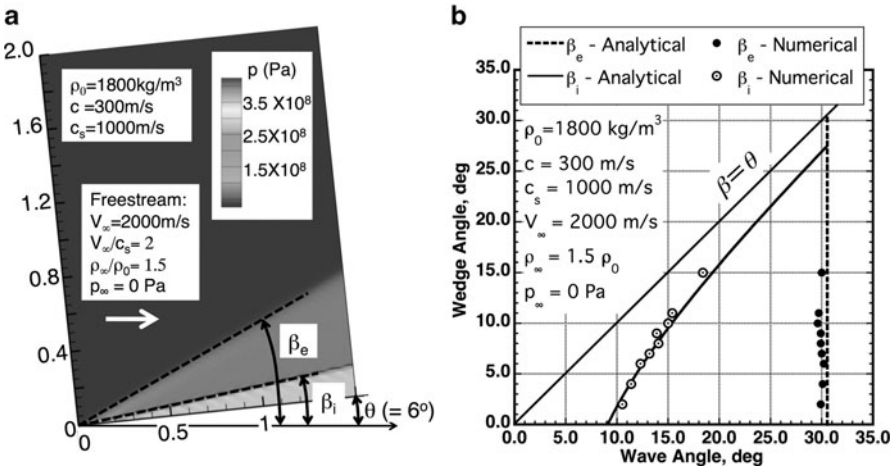

Fig. 6 Result of oblique shock wave problem for CNE fluid. (**a**) Pressure distribution. (**b**) Shock wave angles and wedge angle

dimensional Riemann problem (Fig. 2), the two-stage structure of the oblique shock waves appears. The upstream one is the shock wave in the elastic process. Behind this precursor shock wave, the density and pressure rise to those at the state C in Fig. 1. The density rise across this wave is negligible for large c_s. Considering the conservation laws, the precursor shock wave angle β_e is given by:

$$\beta_e = \sin^{-1}\left(\frac{c_s}{V_\infty}\sqrt{\frac{c_s^2\left(\rho_\infty - p_\infty/c_s^2\right) - c^2\rho_0}{\rho_\infty\left(c_s^2 - c^2\right)}}\right) \tag{3}$$

The shock wave angle of the irreversible compression β_i is analytically calculated in the same way. The relation between the shock wave angle and the wedge angle is shown in Fig. 6b. The computational results agree well with the analytical ones. The precursor shock wave angle does not depend on the wedge angle and is approximated by the Mach angle for c_s, when c_s is much larger than c. For the incident flow normal to the shock wave of the irreversible compression to be supersonic, the velocity component $V_\infty \sin\beta_i$ must be larger than c at least. In this case, β_i must be larger than about 8.6°, as shown in Fig. 6b.

4 Conclusion

For the numerical simulation of impact phenomena of the regolith-like granular material, the compressible and non-expanding (CNE) fluid model was tested by solving the one-dimensional regolith-on-regolith impact problems and the two-

dimensional oblique shock wave problems. The computational results show that the bounce back motion after the impact can be controlled by varying the speed of sound for the elastic process. The two-stage structure of the oblique shock waves was numerically simulated, and the relation between the wedge angle and the shock wave angles was obtained. Consequently, the CNE fluid model has a potential to describe the flow features of the regolith-like granular material that cannot be simulated by the conventional compressible gas model for its unique properties: (1) high-density fluid remains after all the motion stops, (2) the absence of the fluid, that is, the vacuum is allowed to exist, and (3) the crack can be formed in place of the expansion wave.

Acknowledgment This work is supported by Grant-in-Aid for Scientific Research (B) No. 16H04585 of Japan Society for the Promotion of Science.

References

1. K. Suzuki, *Compressible and Non-Expanding Fluid Model for Simulation of Impact Phenomena*, AIAA Paper 2016–4107 (2016)
2. C.W. Hirt, B.D. Nichols, Volume of Fluid (VOF) method for the dynamics of free boundaries. J. Comput. Phys. **39**, 201 (1981)
3. E.F. Toro, *Riemann Solvers and Numerical Methods for Fluid Dynamics* (Springer-Verlag, Berlin, 1997), pp. 201–220
4. K. Suzuki, *Numerical Simulation of High-Speed Impact on Regolith Using Compressible and Non-Expanding Fluid Model*, 31st International Symposium on Space Technology and Science, Matsuyama, ISTS 2017-k-47 (2017)

Mathematical Modeling of the Impact of High-Speed Metallic Plates

S. Fortova, P. Utkin, V. Shepelev, and T. Kazakova

Abstract The paper is devoted to the mathematical modeling of the problem of two metal plates impact using two approaches. In the first approach, the problem is solved using three-dimensional Euler equations and the stiffened gas equation of state for the media. The parameters of the equation of state are calibrated using wide-range equations of state computations of the parameters of shock waves which form after the impact. The second approach is based on one-dimensional two-fluid seven-equation model. In simulations of metal plates impact, we get two shocks after the initial impact that propagate to the free surfaces of the samples. The characteristics of shock waves are close (maximum relative error in characteristics of shocks is not greater than 7%) to the data from the wide-range equations of states computations.

1 Introduction

The study of the mechanisms and the laws of hydrodynamic instability development and turbulent flows in different fundamental and practical problems is among the most complicated modern issues of the continuum media mechanics. The best practices in natural and numerical experiments show that the modeling of the hydrodynamic instability development should be based on three-dimensional (3D) models the program realization of which demands huge computational costs.

The authors of the paper have developed for several years expandable software for the numerical solution of 3D Euler equations using different numerical

S. Fortova · V. Shepelev
Institute for Computer Aided Design of the Russian Academy of Sciences, Moscow, Russia

P. Utkin (✉)
Institute for Computer Aided Design of the Russian Academy of Sciences, Moscow, Russia
Moscow Institute of Physics and Technology, Dolgoprudny, Moscow Region, Russia

T. Kazakova
Moscow Institute of Physics and Technology, Dolgoprudny, Moscow Region, Russia

A. Sasoh et al. (eds.), *31st International Symposium on Shock Waves 2*,
https://doi.org/10.1007/978-3-319-91017-8_44

schemes including high-order methods [1, 2]. The software provides the solution of some problems of the hydrodynamic instability development theory. The obtained results however relate to the flows of ideal gas. At the same time, the effects of hydrodynamic instability development also take place in the media with much more complex equations of state (EOS). In natural experiments [3] on high-speed impact of metal plates, the 3D structures were found on the contact surface of the plates, and one of the possible reasons for the effect is the development of Rayleigh-Taylor instability. In our previous works [4, 5], we got the principal effect of 3D structures formation on the contact surface between colliding plates in the statement qualitatively corresponded to the experiment in [3]. The 3D Euler equations simulations for the media with the ideal gas equation of state were used. The quantitative correspondence however was not good. So the goal of the current work is the development of the mathematical model and the computational algorithm from [4] to obtain better agreement between the parameters of the process of high-speed metal plates impact.

The problem has a long history of investigations, and for the theoretical studies, different numerical approaches were used each with its own pros and cons. In the early studies of S.K. Godunov with coauthors, the problem was considered in two-dimensional Lagrangian statement [6, 7]. In [4, 8] as a result of two- and tree-dimensional gas-dynamics modeling, the multidimensional structures at the contact surface were obtained, and the assumptions about the mechanisms of the structures formation were done. In [9] the numerical simulations of waves formation under an oblique impact of metal plates during explosion welding on the basis of Maxwell relaxation model and molecular dynamics method were carried out. It was shown that the numerical simulation correctly reproduces the formation and evolution of waves on the contact boundary. The problem was also considered in [10] using powerful Euler-Lagrangian 3D computer code taking into account wide-range EOS of the metals.

The problem of high-speed impact of two plates is actually two-fluid problem at least at the initial stages of the process when the metals behave as non-mixing compressible fluids. At the same time, there is a lack of the works with consideration of the problem using the models of heterogeneous media mechanics. Another goal of the paper is the formulation of the one-dimensional (1D) two-fluid mathematical model, computational algorithm and fitting of the parameters of the numerical technology for both qualitative and quantitative description of the initial stage of two metal plates impact in the statement of [3].

2 Statement of the Problem

Consider the interaction of the lead plate with the thickness 2 mm (parallelepiped 5 mm $\times$ 5 mm $\times$ 2 mm in 3D, a segment [3 mm; 5 mm] in 1D statement) and the initial density 11,300 kg/m^3 with the steel plate with the thickness 3 mm (parallelepiped 5 mm $\times$ 5 mm $\times$ 3 mm in 3D, a segment [0 mm; 3 mm] in 1D statement) and the initial density 7900 kg/m^3 (see Fig. 1). The lead plate is thrown

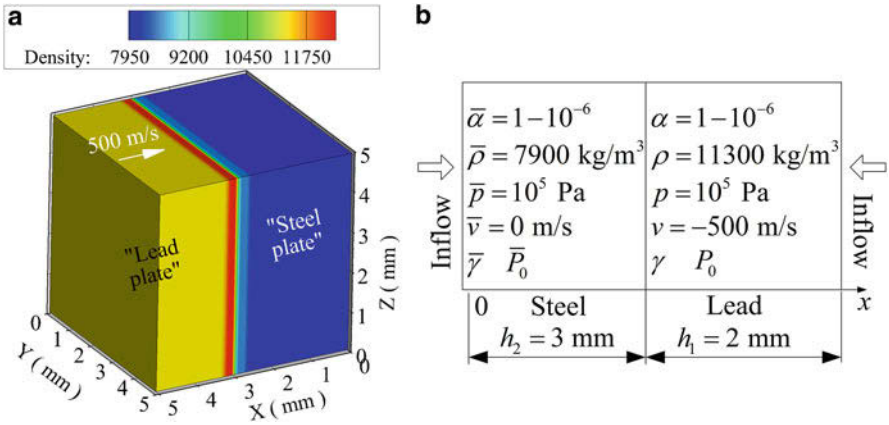

Fig. 1 To the statement of the problem: (**a**) 3D gas dynamics statement, predicted total density distribution in kg/m^3 after 0.1 μs after an impact; (**b**) 1D two-fluid statement

to the direction of steel one with the velocity 500 m/s. It is assumed that at the initial stage of the impact during first 10 μs, the metals behave as pseudo-fluids [3], so the gas dynamics approach is valid. The initial pressure is 10^5 Pa everywhere.

We set the inflow conditions at the boundaries $x = 0$ mm and $x = 5$ mm and periodic conditions at the others in 3D statement. The inflow values at $x = 0$ mm correspond to the initial conditions for the steel plate and at $x = 5$ mm to the lead one. As a result of metal plates interaction, two shock waves (SWs) are formed. The computation lasts up to the moment of SW arrival to the boundaries $x = 0$ mm or $x = 5$ mm. Computational grid is uniform with the cell size equal to 10^{-3} mm in 1D statement and contains 5000 cells. Computational grid is uniform and contains $100 \times 100 \times 100 = 10^6$ cells in 3D statement.

3 Mathematical Models and Numerical Algorithms

For the 3D statement, mathematical model is based on 3D nonstationary two-component Euler equations [1, 2] supplemented by stiffened gas EOS [7] with the parameters γ and P_0. Numerical algorithm is based on the spatial directions splitting technique and hybrid grid-characteristics method [1, 2]. For all matrix (Jacobian, the matrixes of left and right eigenvectors for the determinative system of equations) coefficient computations, the Roe averaging procedure is used taking into account the stiffened gas EOS [11]. The numerical approach in use is valid for the general EOS if the partial derivatives $(\partial p/\partial \varepsilon)_\rho$ and $(\partial p/\partial \rho)_\varepsilon$ are known (here and further the notations are standard).

The second approach is based on the system of equations from [12] which describes two-fluid compressible flows. Governing system of equation comprises

the mass, momentum, and energy conservation laws for both fluids. The specific features of the model are compressibility of fluids, non-equilibrium in velocities and pressures, non-equilibrium, the absence of conservative form of notation. Conservation laws are supplemented by transfer equation for the volume fraction for one of the fluids. The stiffened gas equations of state are used for each fluid with different values of γ and P_0 parameters. Computational algorithm for one time step integration consists of three stages. At first the hyperbolic step is carried out using HLL numerical scheme and then the velocityrelaxation procedure and the pressure relaxation procedure [13].

4 Results of the Numerical Experiments

4.1 3D Gas Dynamics Simulations

To reproduce quantitatively reasonable characteristics of metal plates impact, the parameters of stiffened gas EOS should be fitted using either experimental data or the results of simulations taking into account the wide-range EOS for metals. We use the results of simulations [14] obtained using wide-range EOS [15] and the numerical approach [10]. The results from [14] will be referred as reference values further; see Table 1.

Figure 2 illustrates the predicted fields of density and pressure at the time moment 0.5 μs after the impact. Density distribution in Fig. 1a at the earlier time moment shows both shock waves and contact surface which moves in the direction of the

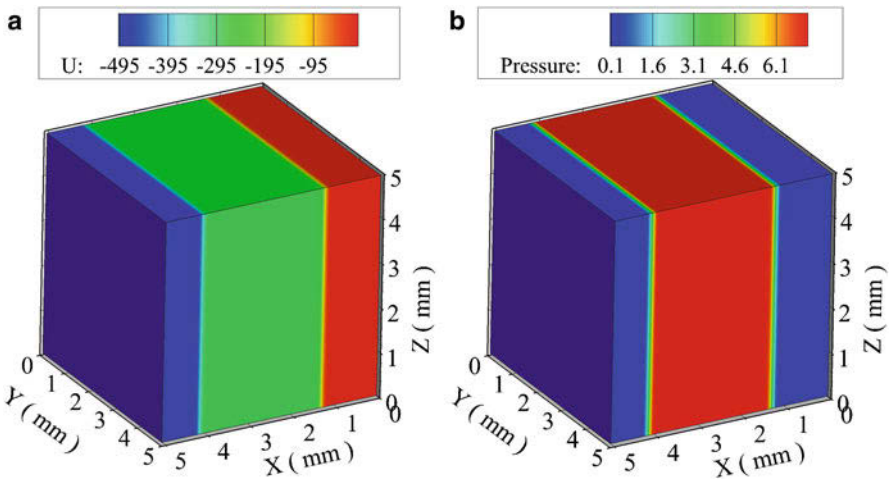

Fig. 2 Predicted distributions of (**a**) velocity in m/s and (**b**) pressure in GPa after 0.5 μs after an impact in 3D statement

steel plate. Figures 1a and 2 correspond to the parameters of stiffened gas EOS $\gamma = 3.0$ and $P_0 = 25$ GPa. The parameters were found as a result of parametric calculations in which we compared the calculated characteristics of both SWs with the reference values. Table 2 demonstrates the finally achieved agreement with the relative errors.

4.2 1D Two-Fluid Model Simulations

To satisfy the hyperbolicity conditions for the determinative system of equations, all computational cells should contain both fluids, so on the interval [0 mm; 3 mm], we set the volume fraction of lead equal to 10^{-6}, and on the interval [3 mm; 5 mm], we set the volume fraction of steel equal to 10^{-6}. A series of numerical experiments was carried out in order to fit the results of the calculations with stiffened gas EOS to the results of modeling using wide-range EOS. The parameters γ and P_0 for lead and steel plates were varied, and the shock speeds D_L and D_R, contact velocity v_{cont}, and pressure p_{cont}, post-shock densities (see Table 3), were compared with the reference values (see Table 1). For each parameter the relative error in comparison with the reference value was measured.

We started with the EOS parameters for the steel plate from [7] and some default parameters for the lead one. The largest error was obtained for the contact surface pressure and SW speeds. In calculation Nos. 2 and 3, the values of γ and P_0 for steel plate were increased. The errors for mentioned parameters became larger. The post-shock densities remained almost the same, and it is the general tendency for the following numerical experiments (the maximum relative error is 7% for all numerical experiments). The positive dynamics for the contact pressure and right SW speed was obtained with the decrease of P_0 for the steel plate in calculation No. 4. At the same time, the left SW speed was insensitive to the variation of the EOS parameters in calculations Nos. 1–4. In calculation Nos. 5–7, we successively decreased the value of γ for the lead plate and obtained the error 7% for the left SW speed. Figure 3 illustrates the predicted distributions of steel volume fraction and density, lead density, and contact pressure for the EOS parameter No. 7 in Table 3. Note that the numerical scheme is quite diffusive and should be improved (e.g., see [16]) but at the same time provides the robust calculation for the huge pressure gradients up to the five orders of magnitude.

Table 1 Reference parameters behind the shock waves in lead and steel

SW	Pressure, GPa	Density, kg/m^3	Gas velocity, m/s	SW speed, km/s
In steel	7.99	8246	211	4.72
In lead	7.99	12,830	211	1.97

Table 2 Predicted characteristics of SWs in calculation in 3D statement

SW	Pressure, GPa	Density, kg/m^3	Gas velocity, m/s	SW speed, km/s
In steel	7.24 (−7%)	8595 (+4%)	272 (+29%)	3.40 (−28%)
In lead	7.24 (−7%)	12,294 (−5%)	272 (+29%)	2.38 (+28%)

Table 3 Predicted characteristics of SWs in calculation in 1D two-fluid statement

	Lead		Steel					
No.	γ	P_0, GPa	γ	P_0, GPa	p_{cont}, GPa	v_{cont}, m/s	D_L, km/s	D_R, km/s
1	3.9	65.5	3.0	30.0	10.1 (+26%)	215 (+2%)	6.0 (+27%)	2.7 (+38%)
2	3.9	65.5	3.0	60.0	11.9 (+49%)	251 (+19%)	6.0 (+27%)	3.8 (+94%)
3	3.9	65.5	4.0	30.0	11.0 (+38%)	232 (+10%)	6.1 (+29%)	3.2 (+64%)
4	3.9	65.5	3.0	15.0	8.5 (+6%)	182 (−14%)	6.0 (+27%)	1.9 (−4%)
5	3.0	65.5	3.0	15.0	8.0 (+0%)	196 (−7%)	5.2 (+11%)	1.8 (−7%)
6	2.9	65.5	3.0	15.0	8.0 (+0%)	198 (−6%)	5.1 (+8%)	1.8 (−7%)
7	2.7	65.5	3.0	15.0	7.8 (−2%)	202 (−4%)	5.05 (+7%)	1.9 (−4%)

5 Conclusions

The 3D mathematical model based on the multicomponent Euler equations supplemented with the stiffened gas equation of state for the numerical investigation of the metal plates impact is described. The parameters of the stiffened gas equation of state are calibrated on the basis of the computations using wide-range equation of state for the metals. For the characteristics of the shock waves which are formed after the impact of two metal plates, the maximum error is in the range of 30%. The proposed numerical technique is suitable for the 3D numerical investigations of intensive directed energy flows on the substances taking into account the instability development on the contact surface.

The parametric numerical study of two metal plates impact using two-fluid approach in comparison with the simulations taking into account the wide-range EOS for the metals is carried out. In calculations the formation of two SW is obtained with the characteristics with maximum relative error of 7% in comparison with the reference values. The determinative system of equations [12] is used. Both metals are considered to be compressible media with stiffened gas equations of state. The computational algorithm is based on the operator splitting approach and HLL method for the approximation of the numerical flux and the nonconservative right-hand side terms.

The work of S.V. Fortova, P.S. Utkin, and V.V. Shepelev (Sects. 1, 2, 3, and 4.2) is supported by the Russian Science Foundation under grant 17-11-01293 and performed at the Institute for Computer Aided Design of RAS.

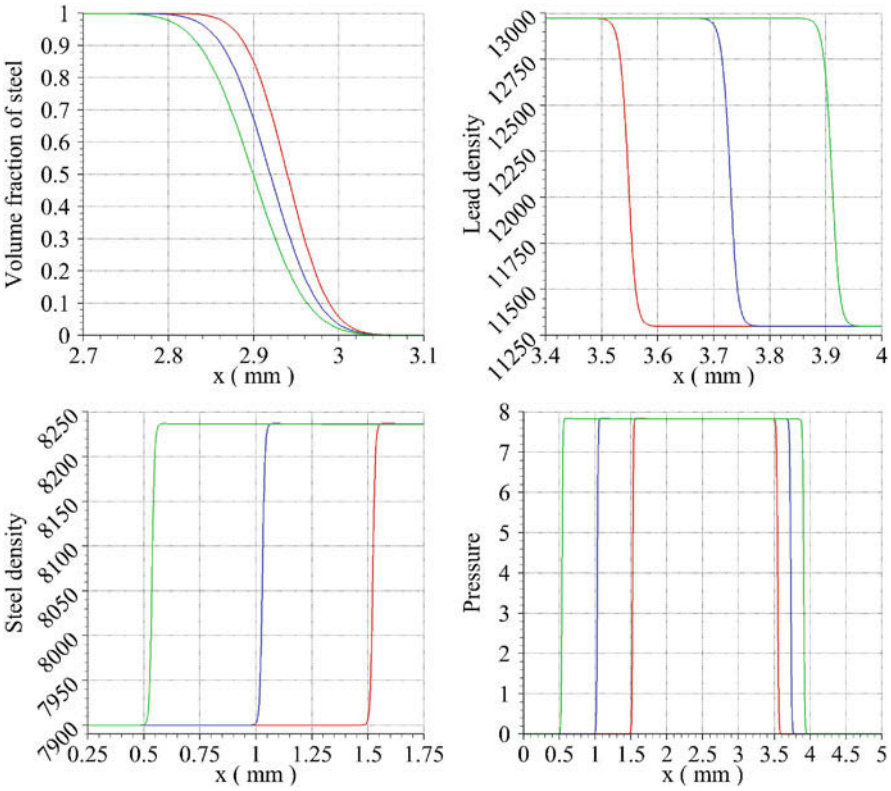

Fig. 3 Predicted distributions at the successive time moments in 1D two-fluid simulation, the red lines correspond to the time moment 0.3 mcs, the blue lines - 0.4 mcs, the green lines - 0.5 mcs

References

1. S. Fortova, L. Kraginskii, A. Chikitkin, E. Oparina, Math. Mod. Comput. Simul. **5**, 607 (2013)
2. M. Belotserkovskaya, A. Pronina, S. Fortova, V. Shepelev, Comput. Math. Math. Phys. **56**, 1162 (2016)
3. I.V. Yakovlev, Fizika goreniiy i vzryva. **9**, 447 (1973)
4. O. Belotserkovsky, S. Fortova, O. Troshkin, A. Pronina, I. Eriklintsev, S. Kozlov, Math. Mod. Comput. Simul. **8**, 497 (2016)
5. S. Fortova, V. Shepelev, A. Pronina, P. Utkin, J. Phys. Conf. Ser. **774**, paper No. 012028 (2016)
6. S. Godunov, A. Deribas, A. Zabrodin, N. Kozin, J. Comput. Phys. **5**, 517 (1970)
7. S. Godunov, A. Zabrodin, M. Ivanov, A. Krayko, G. Prokopov, *Numerical Solution of the Multidimensional Gas Dynamics Problems* (Nauka, Moscow, 1976)
8. V. Demchenko, M. Sergeev, Fluid Dyn. **38**, 923 (2003)
9. S. Godunov, S. Kiselev, I. Kulikov, V. Mali, Proc. Steklov Inst. Math. **281**, 12 (2013)
10. V. Fortov, V. Kim, I. Lomonosov, A. Matveichev, A. Ostrik, Int. J. Impact Eng. **33**, 244 (2006)
11. A. Kulikovskii, N. Pogorelov, A. Semenov, *Mathematical Aspects of Numerical Solution of Hyperbolic Systems* (Chapman and Hall/CRC, London, 2000)
12. R. Saurel, R. Abgrall, J. Comput. Phys. **150**, 425 (1999)

13. R. Saurel, O. Lemetayer, J. Fluid Mech. **431**, 239 (2001)
14. Shock Wave Database, http://www.ihed.ras.ru/rusbank/
15. V. E. Fortov, K. V. Khishchenko, P. R. Levashov, I. V. Lomonosov, Nucl. Instr. Meth. Phys. Res. **415**, 604 (1998)
16. S. Liang, W. Liu, L. Yuan, Comput. Fluids **99**, 156 (2014)

Study of Shock Impact Pressure Amplification and Attenuation of Acoustic Waves in E-Glass Material

Jayaram Vishakantaiah, Kannan K. R., Arvind Raj G., and K. P. J. Reddy

Abstract In this paper we present the amplification of shock pressure and attenuation of acoustic emission (AE) due to the impact of shock waves on multilayer E-glass armor materials having density of about 2000 kg/m^3 with thickness of 5 mm and 10 mm. Shock tubes are well known to produce desired shock strength for material interaction. In this work the E-glass material is made to interact with strong shock wave produced from material shock tube (MST). The peak pressure amplification at the back wall is caused by the transfer of gas momentum to the material mass. The 5-mm- and 10-mm-thick E-glass material shows the amplification of 10 and 3 times, respectively, with respect to the incident front-wall pressure at different Mach numbers. The AE is generated by sonic boom at the open end of the diaphragmless shock tube (DST). A constant shock Mach number of 1.3 is produced in the DST to study the attenuation characteristic of E-glass material. The E-glass materials were placed at different distance from the open end of the shock tube at an angle of 30° at either side of the shock tube axis to study the attenuation of AE. The result shows attenuation of about 42–4% for 5 mm and about 85–52% for 10 mm E-glass materials.

1 Introduction

From several years, devices like light gas gun, ballistic shock tube, explosive launchers, and conventional shock tubes are used to investigate hypervelocity impact on materials. Such devices are capable of producing strong shock waves and acoustic emission (AE). When shock wave enters, the open atmosphere produces large AE due to sonic boom. The E-glass materials with high density are used to

J. Vishakantaiah (✉) · K. K. R.
Shock Induced Materials Chemistry Laboratory, SSCU, Indian Institute of Science, Bengaluru, India
e-mail: jayaram@sscu.iisc.ernet.in

A. R. G. · K. P. J. Reddy
LHSR, Department of Aerospace Engineering, Indian Institute of Science, Bengaluru, India

A. Sasoh et al. (eds.), *31st International Symposium on Shock Waves 2*,
https://doi.org/10.1007/978-3-319-91017-8_45

study the effect of shock pressure amplification and attenuation of acoustic emission (AE). These materials are used to protect the civilian and military structure from blast waves. Complex samples of unstitched, intermediately stitched, and densely stitched TRANSONITE sandwich panels with 3-D woven E-glass composite are subjected to shock loadings to find the damage tolerance [1]. Whenever these E-glass composite materials are subjected to dynamic shock loading condition, the surface pressure spread over the entire structure. E-glass/epoxy composite laminates were evaluated for their mechanical properties and were subjected to shock loading of 7.2 MPa and estimated temperature of about 14,000 K for about 2 ms using free piston-driven shock tube [2]. Soft materials such as foams and fabrics are resulted in pressure amplification behind the reflecting surface caused by the non-permeability [3, 4]. The pressure amplification occurs at the back side of the material due to the transfer of gas momentum to the material mass by the impinging shock strength.

Peak pressure amplification and attenuation of acoustic emission were also studied on polyurethane foam materials [5]. The inertia of the material mass to the acoustic strain energy is the reason for the loss of acoustic energy. Nonlinear acoustic attenuation measurements are carried out on a borosilicate glass, where the absorption of high- and low-intensity acoustic waves fully depends on the temperature of the material [6]. Studies were also performed to attenuate AE, produced during detonation using porous foams and wire mesh as damping materials [7]. The dynamic behavior of sandwich composite made of E-glass vinyl-ester face sheets and graded core cell of various foam configurations resulted in the reduction of acoustic wave impedance mismatch between successive layers and due to the structural integrity [8]. In this paper an experimental setup to study shock impact pressure amplification and attenuation of acoustic emission for both 5 mm and 10 mm E-glass materials is presented.

2 Experimental Methods

Simple shock tube is used to study shock pressure amplification, and diaphragmless shock tube (DST) is used to study attenuation of acoustic emission. The experiments were performed on laminated E-glass armor materials having a density of 2000 kg/m^3 to understand peak pressure amplification due to shock dynamic pressure. Attenuation of acoustic emission experiment on the same material at different distances is recorded using acoustic sensors from the open end of the DST.

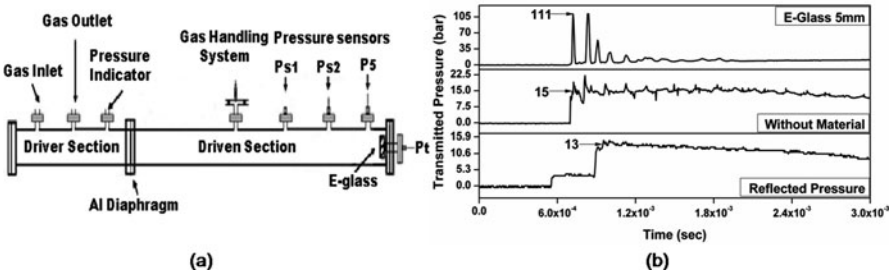

Fig. 1 (**a**) Schematic diagram of MST showing the position of transducers to measure the reflected shock pressure (P_5) and back-wall transmitted pressure (P_t). (**b**) Typical P_5 (front-wall pressure) and P_t pressure signals recorded without and with 5 mm E-glass material

2.1 Shock Wave Impact Experiments Using Material Shock Tube

The material shock tube (MST) consists of 2.1 m driver section and 5.1 m driven section with 80 mm inner and 115 mm outer diameter. The high-pressure driver section is separated from low-pressure driven section by an aluminum (Al) diaphragm. The thickness of the Al diaphragm dictates its bursting pressure which will influence the shock Mach number. The driven section is filled with air at one bar pressure. By pressurizing the driver section, the Al diaphragm ruptures at a critical pressure due to the pressure difference between the two sections. The rapid movement of the gas pressure inside the shock tube generates a strong shock wave, and it travels toward the end of the shock tube. The E-glass material is placed rigidly at the end flange of the shock tube. The provisions are made to fix the material to interact with the shock waves, and the pressure sensors were placed along the side wall and at the back wall. The schematic diagram of MST along with the position of the pressure sensors to acquire data is shown in Fig. 1a.

The E-glass material experiences the reflected shock pressure (P_5) at the front wall, and the transmitted shock pressure (P_t) at the back wall were acquired in a Tektronix digital storage oscilloscope (TDS2014B) as shown in Fig. 1b. Time taken (Δt) for the shock to travel the distance between the two pressure sensors ($\Delta L = 0.5$ m) is used to calculate the shock velocity ($V_S = \Delta L/\Delta t$) and the shock Mach number ($M_S = V_S/a_1$), where $a_1$is the speed of sound for the given test gas. The reflected shock temperature (T_5) for a given shock Mach number is estimated using the 1D normal shock equations [9].

Table 1 Experimental and estimated value of shock conditions for 5-mm- and 10-mm-thick E-glass materials

5-mm-thick E-glass			
Shock Mach number	Estimated reflected shock temperature T_5(K)	Reflected shock pressure P_5 (bar)	Transmitted first peak pressure P_t (bar)
2.1	805	13	111
2.8	1334	24	240
3.2	1580	30	303
3.4	1750	46	462
10-mm-thick E-glass			
2.1	810	10	32
2.6	1130	26	77
2.9	1390	37	115
3.2	1581	49	150

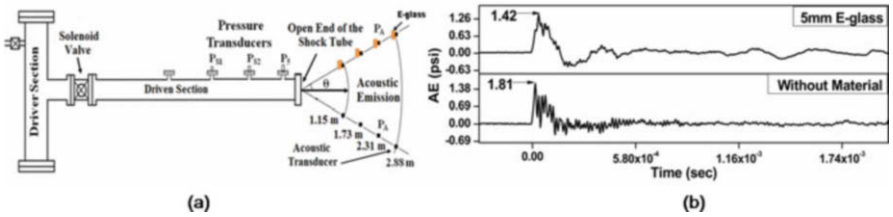

Fig. 2 (**a**) Schematic diagram of a diaphragmless shock tube (DST) showing the position of the acoustic pressure sensors from the open end of the shock tube, (**b**) typical AE signals recorded with and without E-glass material at 1.73 m distance

2.2 Acoustic Emission Experiments Using Diaphragmless Shock Tube

The acoustic emissions were produced by the DST, which consists of 1 m driver and 4 m driven section with 80 mm inner diameter. The driver section filled with compressed air of about 8 bar pressure and an electrically operated solenoid valve is opened to produce shock wave of about 1.3 Mach number. When the shock wave moved out from the open end of the DST and reaches the atmosphere, it produces a large AE due to the sonic boom, and these longitudinal sound waves travel further in the atmosphere. Experiments were performed by placing E-glass materials at a 30-degree angle from the end of the shock tube. The PCB acoustic pressure sensors (model: 103B02) mounted to measure AE with and without E-glass material at five different locations 0.583, 1.15, 1.73, 2.31, and 2.88 m from the open end of the DST are shown in Fig. 2a. The typical AE signals acquired at a distance of 1.73 m with and without E-glass materials using the Tektronix digital storage oscilloscope are shown in Fig. 2b.

Experiments were performed by placing two sensors at 30° from the open end of the DST starting with minimum distance of 0.583 m and maximum distance of 2.88 m to study attenuation of AE in the direction of propagation. Provisions are made to mount the acoustic pressure sensors with and without E-glass material to measure AE. The emitted AE propagates to the atmosphere from the source, and AE signals are recorded with and without materials using two different acoustic pressure sensors. Similarly experiments were repeated by changing the position of acoustic pressure sensors to 1.15, 1.73, 2.31, and 2.88 m distance. During each experiment, acoustic emission data acquired from both the sensors were stored in the Tektronix digital oscilloscope.

3 Results and Discussion

3.1 Shock Impact Pressure Amplification

The present experimental arrangement was made to study the shock pressure amplification. Shock tube experiments were performed with 5-mm- and 10-mm-thick E-glass material placed at the end flange of the shock tube at different Mach numbers. The experiments were carried out by rigidly fixing pressure sensor at the back side of E-glass material to record transmitted pressure. Significant pressure amplification is recorded at the back wall of the E-glass material. The first peak pressure recorded at the back wall of the 5-mm-thick E-glass material shows pressure amplification of about ten times, and for 10 mm thick, it shows three times amplification with respect to front-wall pressure.

The recorded pressure signals at the end flange of the shock tube with corresponding reflected shock front-wall pressure for 5-mm-thick E-glass materials is shown in Fig. 3a. The corresponding transmitted first peak pressure for 2.8 Mack number increases to 240 bar, and as the time progresses, its amplitude decays as shown in Fig. 3a. The plot of reflected shock and transmitted shock pressure versus different Mach numbers shows an amplification of 10 times as shown in Fig. 3b. Experiments were also performed for 10-mm-thick E-glass material which shows pressure amplification of about 3 times. The reflected (front wall) pressure is shown in Fig. 4a, and a plot of pressure versus shock Mach number is shown in Fig. 4b. The peak pressure amplification in the E-glass material due to the energy transformation from shock wave is a function of the material characteristics and thickness.

3.2 Attenuation of Acoustic Emission

Acoustic emission experiments were carried out on E-glass material at constant 1.3 Mach number using DST facility. We recorded the first arrival of the elastic

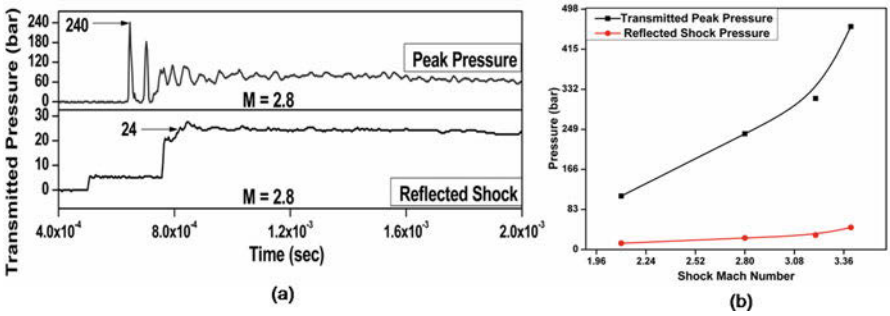

Fig. 3 Experimental data recorded for 5-mm-thick E-glass material (**a**) Typical reflected shock pressure and transmitted peak pressure signal recorded at 2.8 Mach number (**b**) Plot of reflected and transmitted shock pressure versus shock Mach number

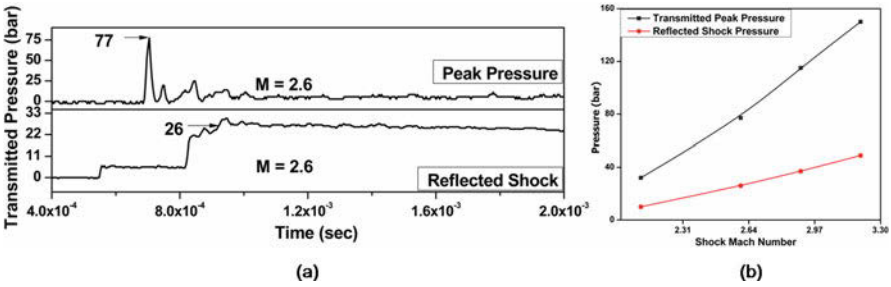

Fig. 4 Experimental data recorded for 10-mm-thick E-glass material (**a**) Typical reflected shock pressure and transmitted peak pressure signal recorded at 2.6 Mach number (**b**) Plot of reflected and transmitted shock pressure versus shock Mach number

waves from the exit of the DST using acoustic sensors located along 30° angle at a distance of 0.58, 1.15, 1.73, 2.31, and 2.88 m. The recorded AE data with and without E-glass materials are analyzed to understand the percentage of acoustic attenuation. The arrival of the original acoustic emission signals is detected using acoustic pressure sensor without mounting material and with mounting 5-mm- and 10-mm-thick E-glass material at 1.15 m distance from the open end of the shock tube as shown in Fig. 5a.

The acoustic pressure signal shows the attenuation of acoustic intensity from 2.8 psi to 2.4 psi of 5-mm-thick E-glass material and further reduction in acoustic energy from 2.8 psi to 0.8 psi for 10-mm-thick E-glass material. Plot of acoustic emission versus distance from the source of acoustic energy for 10 mm and 5 mm E-glass material and without material shows the nonlinear attenuation characteristic of the material as shown in Fig. 5b. Maximum percentage of attenuation recorded for E-glass material of thickness 5 mm is 42% and for 10 mm is 85% at near distance of 0.58 m, and for longer distance of 2.8 m, the attenuation ofAE drastically reduced

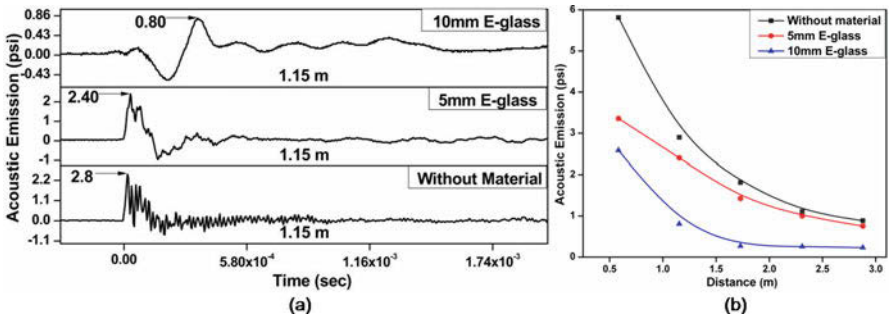

Fig. 5 (**a**) Experimental data recorded for 5 and 10 mm and without E-glass material at a distance of 1.15 m from the source of acoustic emission (**b**) Plot of first arrival peak of acoustic emission versus distance maintained for with 5 and 10 mm thick and without E-glass material

to 4% and 52% for 5-mm- and 10-mm-thick E-glass material, respectively. The attenuation of AE signal increases with the increase in the thickness of the E-glass material.

4 Conclusions

The interaction of shock wave with E-glass material was established to study the transmitted pressure amplification and attenuation of acoustic emission (AE). Amplification of shock pressure behind the E-glass material is a function of the impinging initial shock strength and material density. E-glass material of 5 mm and 10 mm thick shows constant pressure amplification of 10 and 3 times, respectively. An observation shows the thickness of the E- glass material and its physical property play an important role on the pressure amplification. The attenuation properties of the E-glass material are performed by shock-induced acoustic emission experiments. Due to the high density and less porosity of the material, the vibrational energy of the discrete particle in acoustic wave is unable to tunnel the material and get damped. The percentage attenuation in the intensity of acoustic emission ranges between 42–4% and 85–52% for 5 mm and 10 mm E-glass materials, respectively, with respect to the distances. Amplification of shock pressure and attenuation of AE are much less in the rigid E-glass material.

Acknowledgment Financial supports from the projects of DRDO, ISRO, and STC-IISc of the Government of India are gratefully acknowledged. The author thanks Dr. Madhu V. and Mr. Jayarami Reddy from DMRL for providing E-glass material and Professor G. Jagadeesh from the Department of Aerospace Engineering, Indian Institute of Science, Bangalore, for his support and encouragement.

References

1. S.A. Tekalur, A.E. Bogdanovich, A. Shukla, Comput. Sci. Tech. **69**, 736–753 (2009)
2. K.P.J. Reddy, et al., *Shock Interaction Studies on Glass Fibre Reinforced Epoxy Matrix Composites*, ISSW-29, (Springer, Cham, 2015), pp. 127–134
3. M.W. Seitz et al., Effect of compressible foam properties on pressure amplification during shock wave impact. Shock Waves **15**, 177–197 (2006)
4. C.G. Thom et al., Shock wave amplification by fabric materials. Shock Waves **19**, 736–753 (2009)
5. V. Jayaram, et al., in *Effect of Shock Induced Acoustic Emission and Shock Waves Impact on Polyurethane Foam*, 8th International Symposium on NDT in Aerospace, Bangalore (2016)
6. W. Arnold, S. Stein, K. Dransfeld, J. Non-Cryst. Solids **14**, 192–200 (1974)
7. A. Teodorczyk et al., Detonation attenuation by foams and wire meshes lining the walls. Shock Waves **4**, 225–236 (1995)
8. N. Gardner, E. Wang, A. Shukla, Comput. Struct. **94**, 1755–1770 (2012)
9. A.G. Gaydon, I.R. Hurle, *The Shock Tube in High Temperature Chemical Physics* (Reinhold Publishing Corporation, New York, 1963)

Computational Modeling of Recoilless Weapons Combat Training-Associated Blast Exposure

S. Wiri, A. Ritter, J. Bailie, C. Needham, and J. Duckworth

Abstract Military personnel are routinely exposed to blast as part of routine combat training with shoulder-fired weapons. Scientific, medical, and military leaders are beginning to recognize that use of shoulder-fired weapons may result in acute and potentially long-term physiological effects. However, the back blast generated from shoulder-fired weapons on the weapon operator has not been well characterized. By quantifying and modeling the full-body blast exposure from these weapons, better injury correlations can be constructed.

Blast exposure data from the Carl Gustav and Shoulder-Launched Multipurpose Assault Weapon (SMAW) were used to reverse engineer source terms for computational simulations of blast exposure on operators of these shoulder-mounted weapon systems. A propellant burn model provided the source term for each weapon to capture blast effects. Blast data from personnel-mounted gauges during routine

Disclaimer The view expressed herein are those of the authors and do not reflect the official policy or position of the Department of the Navy, Department of the Army, Department of Defense, or the US government.

S. Wiri (✉) · C. Needham
Applied Research Associates, Albuquerque, NM, USA
e-mail: swiri@ara.com

A. Ritter
Uniformed Services University of the Health Sciences, Bethesda, MD, USA

The Henry M. Jackson Foundation for the Advancement of Military Medicine, Bethesda, MD, USA

J. Bailie
Defense and Veterans Brain Injury Center, Silver Spring, MD, USA

Defense and Veterans Brain Injury Center, Camp Pendleton, CA, USA

Naval Hospital Camp Pendleton, Camp Pendleton, CA, USA

General Dynamics Health Solutions, Fairfax, VA, USA

J. Duckworth
Uniformed Services University of the Health Sciences, Bethesda, MD, USA

A. Sasoh et al. (eds.), *31st International Symposium on Shock Waves 2*,
https://doi.org/10.1007/978-3-319-91017-8_46

training was used to create initial, high-fidelity 3D computational fluid dynamic simulations using SHAMRC. These models were then improved upon using data collected from static gauges positioned around the individual weapons systems. The final simulation models for both the Carl Gustav and SMAW were in good agreement with the data collected from the personnel-mounted and static pressure gauges. Using the final simulation results, contour maps for peak overpressure and peak overpressure impulse on the gunner and assistant gunner for each weapon system were then created.

Reconstruction of the full-body blast loading enables a more accurate assessment of blast exposure which could be used to correlate with injury. By accurately understanding the blast exposure and its variations across an individual, more meaningful correlations with injuries including traumatic brain injury can be established. As blast injury thresholds become better defined, results from these reconstructions can provide important insights into approaches for reducing risk of injury to personnel operating shoulder-launched weapons.

1 Introduction

Many members of our military are routinely exposed to blast as part of combat training. This exposure can come from various activities such as demolitions, explosive ordnance, explosive breaching, and use of heavy weapons such as the Carl Gustav recoilless weapon. High levels of blast overpressure have a well-recognized deleterious impact to the auditory system, gastrointestinal system, lungs, and the brain. A spectrum of traumatic brain injury is shown in Fig. 1.

The mechanisms of injury and their relative contribution to clinical presentation and pathology are dynamic over the spectrum of traumatic brain injury (TBI) severity. Tissue-level pathology and apoptosis may be prominent in severe injury; diffuse axonal injury (DAI) and cytoskeletal disruption may be present in moderate injury, contusion demonstrating a relatively severe glutathione depletion, synaptic protein loss, oxidative damage, and mitochondrial dysfunction [1]. Concussion or mild traumatic brain injury (mTBI) demonstrates a spectrum of ultrastructural

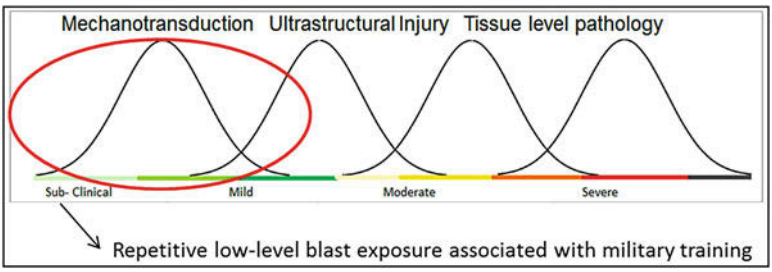

Fig. 1 Traumatic brain injury spectrum

injury, axonal dysfunction, altered neurotransmission, ion flux, glutamate release, protease activation, and energy dysregulation. Mechanisms such as inflammation are present across the spectrum of injury severity; however the inflammatory response varies in association with characteristics of the injury and the individual.

In sub-concussive blast exposure, we hypothesize that mechanotransduction, the process by which cells convert mechanical forces into electrochemical activity resulting in an array of intracellular biochemical responses and intercellular signaling, is the primary etiology associated with secondary neuronal injury, diffuse pathological changes, and chronic and/or progressive clinical symptoms reported in a subpopulation of individuals following repetitive sub-concussive blast exposures. Mechanotransductive mechanisms can affect physiological processes directly through the extracellular matrix (ECM) and cell adhesion molecules and transmembrane receptors attached to mechanosensitive intracellular structures that regulate mechanochemical signaling pathways [2]. Stretch-sensitive channels represent one of the best studied examples of mechanotransduction where a minute increase in lipid bilayer tension results in protein structural transformations and activation, which could account for the increased permeability of the blood-brain barrier (BBB) and the transformation of M1, pro-inflammatory, microglia seen in TBI spectrum neuroinflammation and other chronic neurodegenerative processes.

The primary objective of the current study was to develop a computational simulation of blasts from recoilless weapons. Computational simulations quantify blast load and, additionally, provide data on a wide variety of blast characteristics from these weapon systems including, but not limited to, peak pressure, positive phase duration, impulse, etc. To create simulation models, objective overpressure data was utilized to reverse engineer a source term for computational simulations of SMs firing shoulder-launched weapons. The models were developed using SHAMRC (Second-Order Hydrodynamic Automatic Mesh Refinement Code), a high-fidelity three-dimensional fluid dynamics tool [3], which has been used recently for blast exposure on human studies [4, 5].

2 Methods

Two weapon systems are considered in the present study: the Carl Gustav recoilless weapon with 84 mm high-explosive (HE) rounds and the Shoulder-Launched Multipurpose Assault Weapon (SMAW) with 83 mm high-explosive dual-purpose (HEDP) rounds. Pressure data was collected using BlackBox Biometrics (B3) Blast Gauge System (https://blastgauge.com/features/). Gauges were positioned on the head, chest, and shoulder of SMs operating shoulder-fired weapons in accordance with manufacturer recommendations. Additionally, Generation 5 blast gauges were mounted at static positions at multiple locations around the weapons (Fig. 2). Weapons were fired in open terrain, as part of a group training environment. Data collected from static gauges was used to improve models in SHAMRC for each weapon.

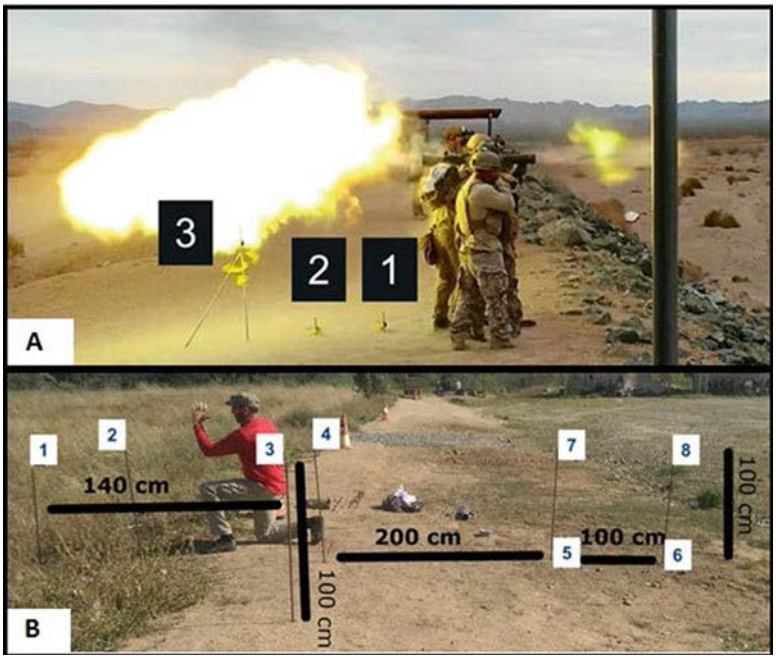

Fig. 2 Pressure sensors placed behind the Carl Gustav (**a**) and around the SMAW (**b**) shoulder-fired weapons

The blast gauge records 20 ms of pressure data and is triggered by a pressure threshold. The gauge saves 2 ms before and 18 ms after the designated pressure threshold is reached. For the current study, blast exposure threshold was set at 2.5 psi or approximately 17.2 kPa. In this study, the blast gauge data was processed using a 4-pole 50 kHz Butterworth filter. The mean pressure was then calculated for the first 0.5 ms, and the entire waveform was shifted (up or down) by the mean pressure value to correct for any positive or negative offset. The original data, as well as the baseline shift value, is stored with the processed data.

Open source information was used to create the geometry for both weapon systems. Unlike detonation of a high explosive, energy release from a burning propellant is dependent on the pressure in the weapon chamber. As a result, the mass and propellant types alone are not sufficient to create a source term for the blast. For the current analyses, the initial propellant burn model for each weapon system was created using data from personnel-mounted gauges. Pressure versus time history data was used to create a model for the energy release from the propellant and subsequent blast from each weapon in SHAMRC.

The SHAMRC simulation models were again adjusted to incorporate data obtained from the static gauges. The parameters used for the Carl Gustav and SMAW propellant burn models were selected to best match data. The equation for each weapon model describes a source term for energy added to the propellant as a function of time.

3 Results

Since the data showed good repeatability, a single representative waveform was selected when comparing the waveforms with the SHAMRC simulation for illustrative purposes. In Station 1 (Fig. 3a, b) and Station 2 (Fig. 3c), the SHAMRC simulation captures the initial peak followed shortly (approximately 0.4 ms and 0.27 ms for Station 1 and Station 2, respectively) afterward by the ground reflection. For Station 3 (Fig. 3d), the SHAMRC simulation captures the initial peak as well as the ground reflection that arrives about 3 ms later. The waveform shape and impulse in Station 1 agree well with the simulation (Fig. 3a,b). The pressure versus time history plots for Station 2 and 3 show the waveform shapes agree with the simulation (Fig. 3c, d), although the simulation pressure drops off faster than the data in Station 3. The slopes of the decay are similar between the data and the simulation, but the impulse is clearly lower in the simulation since the positive phase duration is lower in the simulation than the experiment.

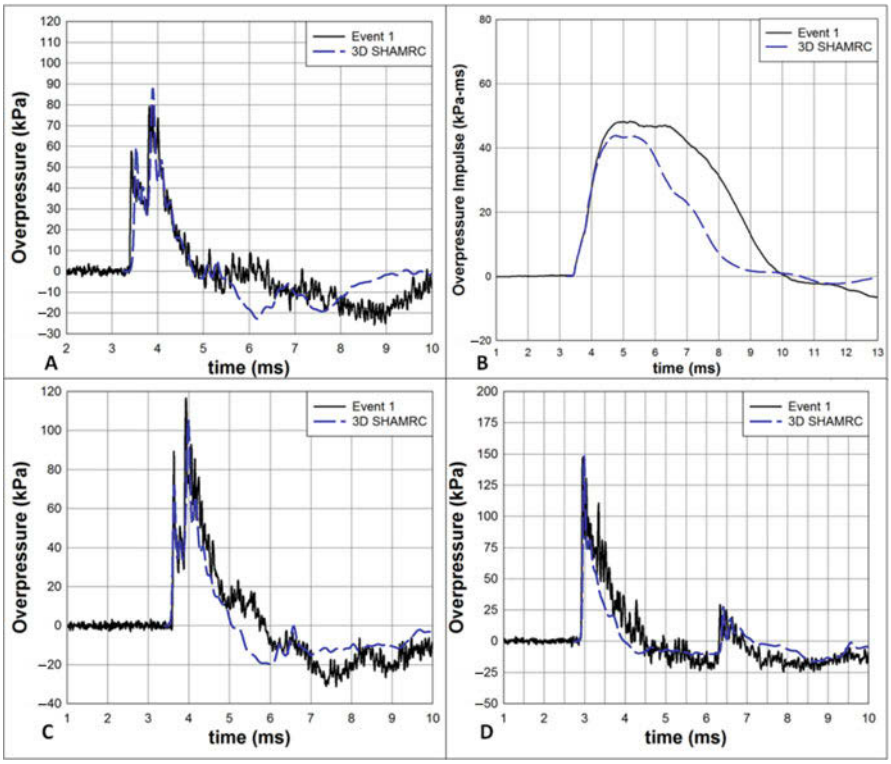

Fig. 3 Station 1 pressure (**a**) and impulse (**b**) data and pressure data for Stations 2 (**c**) and 3 (**d**) compared with SHAMRC simulation for Carl Gustav

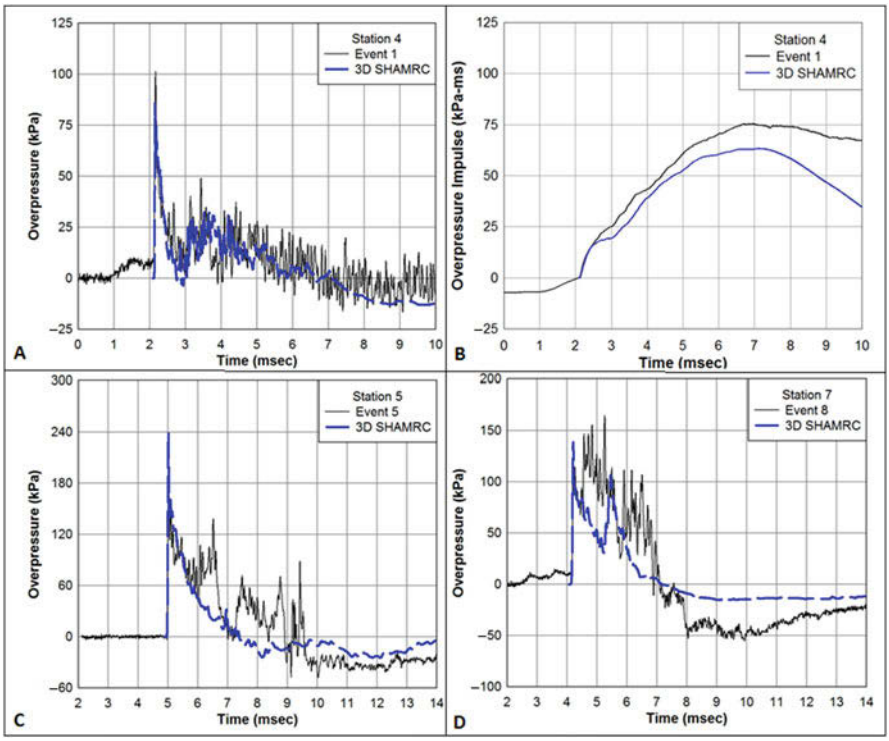

Fig. 4 Pressure versus time history (**a**) and impulse (**b**) comparison for Station 4 and pressure versus time history for Stations 5 (**c**) and 7 (**d**) around the SMAW

The SMAW waveform typically has multiple peaks in succession. Data from static pressure gauges mounted at eight locations around the SMAW was collected to compare with simulation results (Fig. 4). Averages across events (n = 12) for the overall peak pressure, initial peak pressures, and positive phase duration for the eight stations around the SMAW were calculated. As expected, the peak pressures are higher behind the weapon (Stations 5–8) than adjacent to the weapon (Stations 1–4). No data was recorded at Station 2 because the pressure was below the threshold setting (2.5 psi, ~17.24 kPa) used on the gauge. Since the gunner was kneeling, the gauge is closer to being in line with the weapon compared to the Carl Gustav.

When compared, the waveform shape from the SHAMRC simulation captures most of the features seen in the data from the static gauges (Fig. 4). The agreement was better for locations beside the weapon. The overpressure waveform shape and impulse from the simulation are in good agreement with the data for Station 4 (Fig. 4a, b). Stations 5 and 7 were behind the weapon, and the simulation misses some of the features on the waveform seen in the data. Large variation (147–373 kPa) in peak pressure for Station 7 (Fig. 4d) and to a lesser extent Station 8 could be due to variations in distance between the weapon, ground, and gauges,

attributed to gunner height. Similar to the Carl Gustav, when firing the weapon, variation in the height of the gunner and alignment of the weapon with the gauge could account for the variation seen in the data.

The mean positive phase duration at locations beside the weapon (Stations 1–4) was 3.6 ms to 4.6 ms, and the peak overpressure ranged from less than 2.5 psi to 5.5 psi. The weapon was placed 120 cm above the ground in the simulation.

4 Conclusion

We describe our approach to create a model to estimate blast exposure from shoulder-fired weapons on SMs. To our knowledge, the current work simulating blast exposure on operators of recoilless shoulder-fired weapons (Carl Gustav and SMAW) is novel in multiple aspects. Unlike much of the literature regarding recoilless weapons, we developed models to simulate the rearward expulsion of blast waves on the weapon operators. To do so, we employed a reverse engineering approach using personnel-mounted gauges to provide a base model and static overpressure gauge measurements to improve the simulation. The resultant simulation models are, therefore, not predictive in nature.

Detailed modeling provided by the type of simulation we describe can give medical scientists the ability to reliably identify relationships between repetitive exposure from these weapons systems and development of long-term health problems. The simulations accomplish this by providing more accurate details of the actual exposure levels across the body, as well as estimation of career exposure in the absence of objective blast overpressure recordings. This will have large consequences in the formation of policies to mitigate health consequences from occupational exposure, including amount of exposure over time and the development of personal protective equipment.

Acknowledgments Defense Advanced Research Projects Agency HU0001-14-1-0022, PI: J. Duckworth

References

1. G. Harish, A. Mahadevan, N. Pruthi, S.K. Sreenivasamurthy, V.N. Puttamallesh, T.S. Keshava Prasad, S.K. Shankar, M.M. Srinivas Bharath, Characterization of traumatic brain injury in human brains reveals distinct cellular and molecular changes in contusion and pericontusion. J. Neurochem **134**, 156–172 (2015). https://doi.org/10.1111/jnc.13082
2. M.A. Hemphill, S. Dauth, C.J. Yu, B.E. Dabiri, K.K. Parker, Traumatic brain injury and the neuronal microenvironment: A potential role for neuropathological mechanotransduction. Neuron **85**(6), 1177–1192 (2015). ISSN 0896-6273, https://doi.org/10.1016/j.neuron.2015.02.041., http://www.sciencedirect.com/science/article/pii/S0896627315001567

3. J.E. Crepeau, C.E. Needham, Verification and validation of SHAMRC for non-ideal Airblast (NIAB) phenomenology, in *Technical Report*, vol. 2. Defense Threat Reduction Agency (2010)
4. S. Wiri, C. Needham, Reconstruction of improvised explosive device blast loading to personnel in the open. Shock Waves **26**(3), 279–286 (2016). https://doi.org/10.1007/s00193-016-0644-1
5. X.G. Tan, A.J. Przekwas, G. Rule, K. Iyer, K. Ott, A. Merkle, Modeling articulated human body dynamics under a representative blast loading, in *ASME International Mechanical Engineering Congress and Exposition*, Denver, CO, 2011. Biomedical and Biotechnology Engineering: Nanoengineering for Medicine and Biology, pp. 71–78. ASME

Contribution of Cavitation Generation to Shock Wave Sterilization Effects in a Narrow Water Chamber

J. Wang, A. Abe, T. Koita, and M. Sun

Abstract The paper reports on the generation mechanism of cavitation bubbles in a narrow water chamber and the sterilization effects of these cavitation bubbles on marine bacteria. Underwater shock waves are generated by electric discharge. Propagation behaviors of the waves in the water chamber are investigated using an optical method. On the other hand, a bio-experiment with marine bacteria is also carried out to examine sterilization effects. It is found that the shear wave is produced in the wall material of the water chamber by the energy release of underwater electric discharge and results in the tensile stress arising in the water, and thereby cavitation bubbles are induced with the propagation of the shear wave. From the results of the bio-experiments, we confirm a high sterilization effect of the cavitation bubbles.

1 Introduction

Cavitation bubbles have been observed in many different fields, and their dynamic behaviors have been studied in detail experimentally, theoretically, and numerically. The phenomenon of the cavitation was first discovered in 1894 when the tests were made to determine why a ship could not reach its design speed during sea trials. The collapse of cavitation was found to reduce the performance of a propeller while also

J. Wang (✉)
Key Laboratory for Mechanics in Fluid Solid Coupling Systems, Institute of Mechanics, Chinese Academy of Sciences, Beijing, China

School of Engineering Science, University of Chinese Academy of Sciences, Beijing, China

A. Abe
Graduate School of Maritime Sciences, Kobe University, Kobe, Japan

T. Koita
Faculty of Engineering, Saitama Institute of Technology, Fusaiji, Fukaya, Saitama, Japan

M. Sun
Institute of Fluid Science, Tohoku University, Aoba-ku, Sendai, Miyagi, Japan

A. Sasoh et al. (eds.), *31st International Symposium on Shock Waves 2*,
https://doi.org/10.1007/978-3-319-91017-8_47

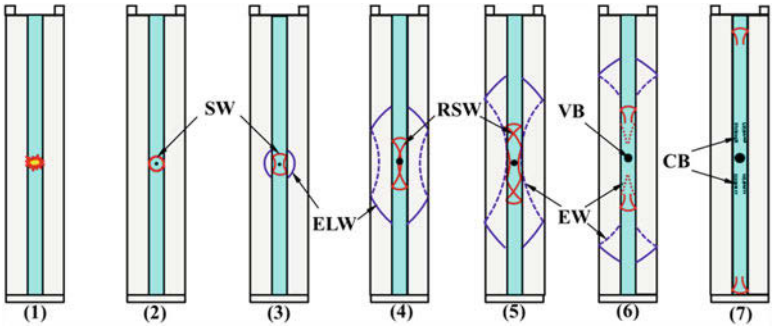

Fig. 1 Schematic of cavitation bubbles generated behind multiple waves induced by underwater electric discharge in narrow water chamber

giving rise to vibration and erosion. Song et al. [1] applied a high-power laser to the cleaning of the solid surface in liquid and pointed out that a liquid jet and collapse shock wave that were induced by the collapse of the laser-induced cavitation bubble resulted in a high-cleaning efficiency for the removal of particles. In the field of marine sciences, the collapse of microbubble was used to the sterilization of ships' ballast water [2]. When they carried out a bio-experiment to investigate the sterilization effect of the shock wave-microbubble interaction, Wang and Abe [3] found the cavitation bubbles generated behind the concentration of underwater shock waves have a potential to kill marine bacteria. On the other research, Koita et al. [4] observed the generation of cavitation bubbles behind the propagation of multiple waves produced by underwater electric discharge in a narrow water chamber. They thought that the interactions of the waves at the interface between the air and the acrylic wall induced the tensile stress in the water. As shown in Fig. 1, an underwater shock wave (SW) generated by an electrical discharge is reflected partly at the internal wall to form reflected shock waves (RSW) and that part of the SW entering the wall is propagated as an elastic wave (ELW). Expansion waves (EW) are produced by the reflection of the ELW at the interface between the air and the wall and then reenter the water. Cavitation bubbles (CB) are induced by tensile stress resulting from the EW. In addition, as a result of underwater electric discharge, large amounts of energy are released and then probably caused the deformation of the wall material due to the confined space, so that the shear wave propagating in the wall material would be produced and thereby the tensile stress arises in the water. The cavitation bubbles are also produced in this case.

From these backgrounds, considering the sterilizing potential of cavitation bubbles, it is interesting to understand the sterilization effect of the cavitation bubbles generated behind the multiple waves in a narrow water chamber. The paper aims to clarify the generation mechanism of the cavitation bubbles in a narrow water chamber and the sterilization effects of these cavitation bubbles on marine *Vibrio* sp. Propagation behaviors of the multiple waves generated by an underwater electric discharge are observed using an optical method. The sterilization effects are also discussed by the bio-experiments under different conditions.

2 Experiments

2.1 Bio-experiments

Figure 2 shows a schematic of the bio-experimental setup in a narrow water chamber. The dimensions of the narrow water chamber were 300 mm (H) × 240 mm (W) × 5 mm (D). As shown in Fig. 2, a bag made of a 0.1-mm silicone film was designed in the water chamber and filled with cell suspension of marine *Vibrio* sp. The dimensions of the silicone bag were 120 mm (H) × 100 mm (W) × 5 mm (D). Its acoustic impedance was almost the same as that of water. The discharge point was set up at a distance of about 20 mm from the bottom of the silicone bag in the water chamber. Underwater shock waves were continuously generated by a high-voltage pulse power supply and a pulse generator.

Figure 3 illustrates a considerable sterilization mechanism in the narrow water chamber. The cavitation bubbles generated behind the underwater shock waves interact with the reflected shock waves or the next coming shock wave. Finally, rebound shock waves and free radicals are generated by the collapse of the cavitation bubbles, and the marine bacteria around the bubbles are killed. A photo of the marine *Vibrio* sp. used in the bio-experiments is shown in Fig. 3c.

2.2 Optical Observation

To further investigate the mechanism whereby the cavitation bubbles were generated in the narrow water chamber, the optical observation was carried out in the box area by the dashed lines as shown in Fig. 4. In Fig. 4a, the water chamber was filled with

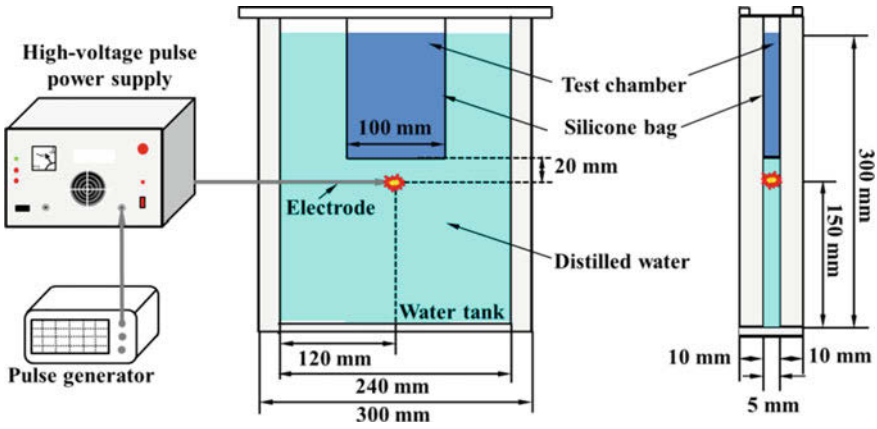

Fig. 2 Schematic of bio-experimental setup in narrow water chamber

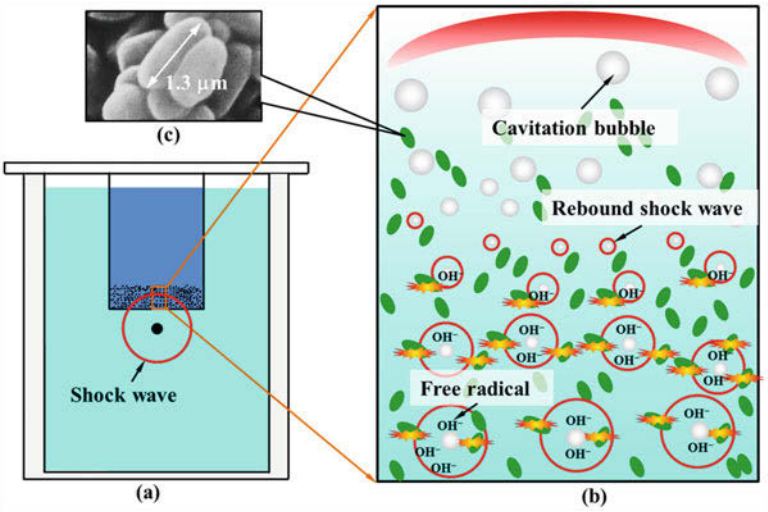

Fig. 3 Concept of sterilization mechanism using cavitation bubbles behind generated underwater shock waves: (**a**) Schematic of water chamber, (**b**) Collapse of cavitation bubbles and (**c**) A photo of marine *Vibrio* sp.

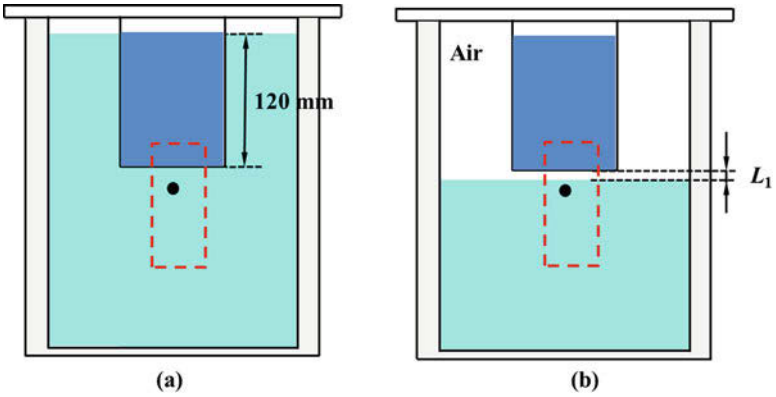

Fig. 4 Schematic of narrow water chamber used for optical observation: (**a**) Chamber full of distilled water, (**b**) Air layer of L_1 between water surface and silicone bag

distilled water, while the silicone bag contained artificial seawater. Figure 4b shows the other setup of the water chamber arranged with an air layer of L_1 between the water surface and the bottom of the silicone bag, to prevent underwater shock waves generated by electric discharge directly propagating into the silicone bag.

3 Results and Discussion

Figure 5 shows the multiple waves generated by an underwater electric discharge in the narrow water chamber, observed using the schlieren method. The output power of the electric discharge was 28.6 kV. The high-speed camera (i-SPEED 7, Nac Image Technology) captured images at a frame rate of 100 kfps and an exposure time of 300 ns. The resolution of the images was 840 × 216 pixels. In the figure, an ELW propagating in the acrylic wall and the SW generated by the electric discharge are observed in Fig. 5 (1). The SW is thought to be cylindrical due to the thickness of the water chamber. The images indicate that its propagating speed is about 1500 m/s. At 20 μs, the SW is reflected partly at the bottom of the silicone bag, as indicated by RSW 1, and then transmitted through the bag. At 30 μs, the secondary wave (second wave) has passed through the bag, and then its reflected wave (RSW 2) is observed behind the RSW 1. Moreover, the area of cavitation bubbles is found and grows with the passage of the second wave following the SW in the silicone bag. Therefore, we consider that the second wave is an expansion wave. The expansion wave can be caused by the reflection of the ELW at the interface between the air and the wall of the water chamber [4], the propagation of the shear stress propagating in

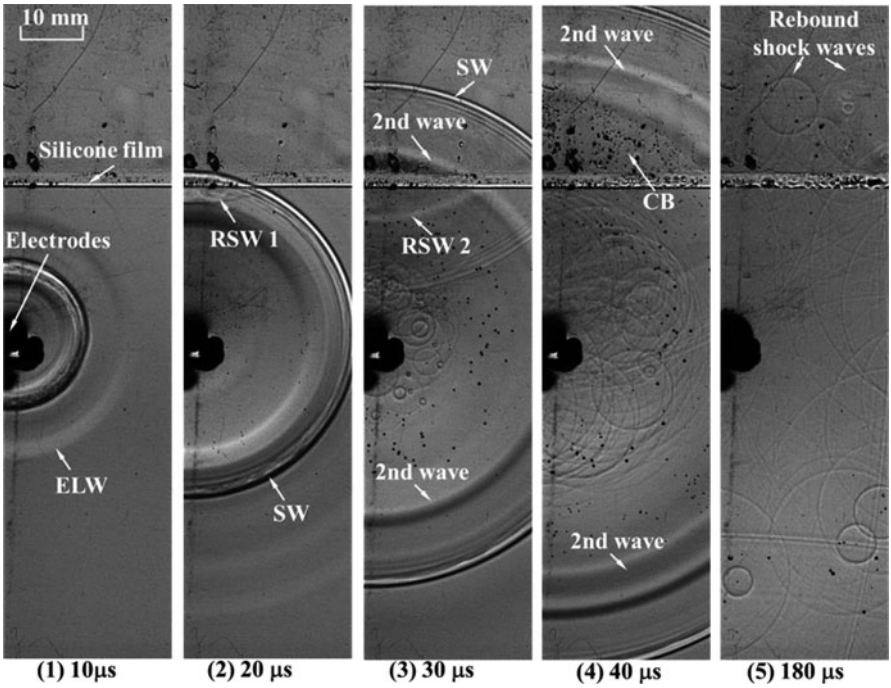

Fig. 5 Observation of multiple waves generated by underwater electric discharge in narrow water chamber using schlieren method

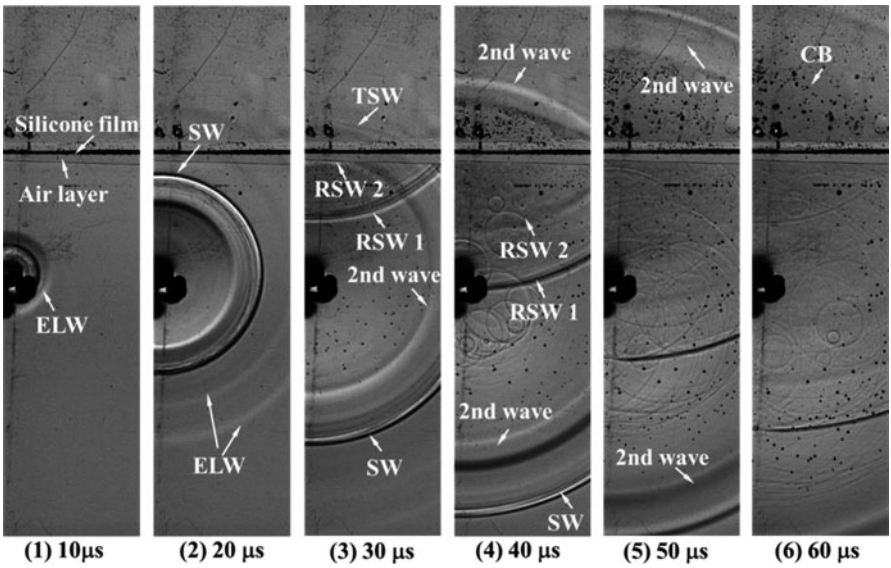

Fig. 6 Observation of multiple waves generated by underwater electric discharge with a 2-mm air layer

the wall material, or the concentration of underwater shock waves [3]. At 180 μs, the rebound shock waves generated by collapses of the cavitation bubbles are captured in the silicone bag. These results suggest that the cavitation bubble behind the expansion wave following SW is potentially capable of killing marine bacteria.

Figure 6 shows the observation of multiple waves generated by an underwater electric discharge with a 2-mm air layer. The experimental and high-speed-camera conditions were the same as those for Fig. 5. In this figure, we can see ELW in Fig. 6 (1) and (2). The RSW 1 is clearly captured when the SW is reflected by the air layer at 30 μs. Moreover, the second wave is being reflected from the air layer. The RSW 2 behind the RSW 1 is thought to be a compression wave. Although the propagation of an underwater shock wave is intercepted well by the air layer, we still find a transmitted shock wave (TSW) in the silicone bag. At 40 μs, the second wave is propagating in the silicone bag regardless of the air layer, and CB are generated behind the second wave. Therefore, the second wave could not be induced by the concentration of underwater shock waves. On the other hand, as shown in Fig. 1 (6), the EW propagating in wall material is in front of the SW so that the second wave is also not from the reflection of the ELW. From the images, it is found that the propagation speed of the wave is about 1469 m/s. Referring to the propagation velocity of shear wave in PMMA material, 1430 m/s, we argue that the second wave causing the generation of the CB is a shear wave travelling in the window material as a result of the release of large energy at the discharge point.

Figure 7 shows estimates of the number of viable cells for an electric discharges of 28.6 kV. The plots shown in this figure are of the averages for six sets of

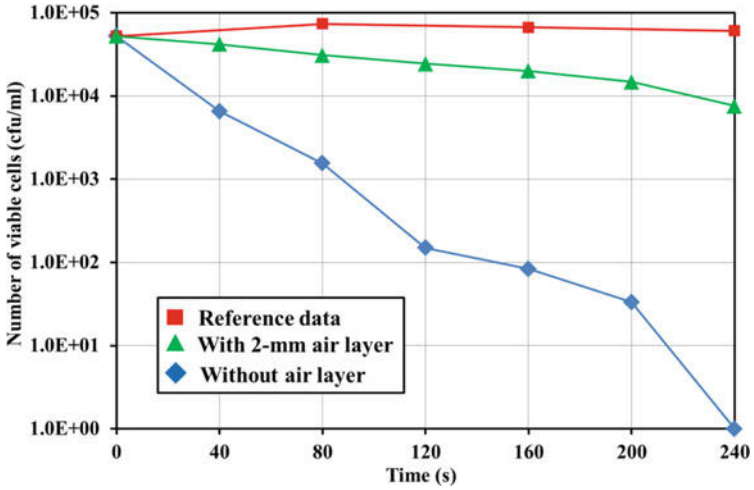

Fig. 7 Estimation of sterilization effect obtained with 28.6-kV electric discharges: ■ reference data, ▲ with 2-mm air layer, and ♦ without air layer

bio-experimental data. The solid squares are the reference data obtained from the solution of the marine bacteria without the action of any shock waves. The number of viable cells hardly changes throughout the course of the experiment. The solid triangles and diamonds represent the results of the bio-experiments obtained using an electric discharge of 28.6 kV with and without air layer between the water surface and the bottom of the silicone bag, respectively. The figure shows that after 4 min, all the marine bacteria are completely killed without air layer, while only one order of the number of marine bacteria are killed with a 2-mm air layer because of weak underwater shock waves in the silicone bag. Consequently, we can confirm that the cavitation bubbles generated in the water chamber contribute to inactivating marine bacteria. Furthermore, a shock wave inducing collapse of bubble plays an important role in the shock wave sterilization.

4 Conclusions

In the paper, we investigated the cause of cavitation bubbles in a narrow water chamber and also the contribution of these bubbles to the inactivation of marine bacteria. A bio-experiment with marine *Vibrio* sp. was carried out in a silicone bag that was set up in the narrow water chamber. Underwater shock waves were generated by electric discharges. To prevent the underwater shock waves propagating into the silicone bag, an air layer was introduced between the bag and the water surface of the chamber. The optical observation exhibited that the generation of the cavitation bubbles was induced by the tensile stress arising in

the water due to the propagation of the shear wave in the wall material of the water chamber. The shear waves were produced owing to the deformation of the wall material when large amounts of energy was instantly released by the electric discharge. From the results of the bio-experiments, it was confirmed that the collapse of cavitation bubbles contributes to the inactivation of marine bacteria.

Acknowledgments A part of this work was supported by JSPS KAKENHI Grant Number 16H04600 and 16 K14512. We also would like to sincerely thank Nac Image Technology Inc. for the supply of high-speed camera, i-SPEED 7.

References

1. W.D. Song et al., J. Appl. Phys. **95**(6) (2004)
2. A. Abe, H. Mimura, H. Ishida, K. Yoshida, Shock Waves **17**(1–2) (2007)
3. J. Wang, A. Abe, J. Mar. Sci. Technol. **21**(4) (2016)
4. T. Koita, K. Hayashi, M. Sun, in *Proceedings of the 29th International Symposium on Shock Waves*, vol. 2 (2015)

Shock Waves Confer Immunity Against Infections in Mice

Akshay Datey, Dipshikha Chakravortty, and Gopalan Jagadeesh

Abstract Shock waves are essentially nonlinear waves that propagate at supersonic speeds. Any sudden release of energy will result in the formation of shock waves. Personnel at the war fields are constantly exposed to shock waves generated by bombarding ammunition. The short-term and long-term effects of this exposure on various systems of the body are not clearly understood. In this study, we have shown for the first time that shock wave exposure confers protective immunity in a murine model. We have tested this with *Salmonella typhimurium* in Balb/c mice. War field conditions were mimicked in the laboratory using the diaphragmless shock tube. Infection challenges post shock wave exposure were evaluated by checking the organ load of *Salmonella* in the spleen, liver, and mesenteric lymph nodes. It was found that the bacterial load in these organs was significantly lower as compared to the control group of animals. The mechanism of this phenomenon was also addressed by measuring the cytokine levels in serum of the animals. It was observed that the proinflammatory cytokine expression is enhanced after exposure to shock waves. In a nutshell, we show that shock waves can induce protective immunity against infections by altering the levels of proinflammatory cytokines.

A. Datey
Centre for Biosystems Science & Engineering, Indian Institute of Science, Bangalore, India

Department of Microbiology & Cell Biology, Indian Institute of Science, Bangalore, India

Department of Aerospace Engineering, Indian Institute of Science, Bangalore, India

D. Chakravortty
Centre for Biosystems Science & Engineering, Indian Institute of Science, Bangalore, India

Department of Microbiology & Cell Biology, Indian Institute of Science, Bangalore, India

G. Jagadeesh (✉)
Centre for Biosystems Science & Engineering, Indian Institute of Science, Bangalore, India

Department of Aerospace Engineering, Indian Institute of Science, Bangalore, India
e-mail: jaggie@aero.iisc.ernet.in

A. Sasoh et al. (eds.), *31st International Symposium on Shock Waves 2*,
https://doi.org/10.1007/978-3-319-91017-8_48

1 Introduction

Shock waves or blast waves generated on the war fields are associated with damage to the human beings and the surroundings [1]. The generation of these shock waves is basically the mode of dissipation of the enormous amount of energy released during bomb explosions. It is a well-known fact that these waves cause severe damage and injury to the people it encounters during its propagation [2]. The damages include traumatic brain injury which involves brain hemorrhage and internal bleeding. This condition ultimately leads to the death of the person [6, 8]. Other effects of the shock waves include rupturing of the eardrum and injury to the organs which harbor a cavity in them, e.g., the lungs and the heart [2]. There are long-term effects of shock waves and treatments which involve the use of shock waves which are reported. These include hypertension, renal disorders, and disorders of the reproductive system [2]. The mechanism by which these effects are brought about by shock waves is not clearly understood [5]. The effect of shock waves on the immune system is also not studied. Immune system is one of the most important organ systems which dictates the overall health of an individual. Slight perturbation of the immune status of an individual may lead to a range of disorders from bacterial infections to severe autoimmune disorders [7]. Keeping these aspects in mind, we decided to study the effect of shock waves on the immune system. With all novel applications of shock waves at the laboratory levels which uses focused shock waves, we ventured to check the immune response to whole-body shock wave exposure. To mimic the war field conditions of shock wave generation, we have made use of a novel diaphragmless shock tube [3, 4]. This shock tube has the driver and the driven sections separated by a pneumatic valve which is triggered to open and release the driver gas into the driven section in a very short time (ms) [3]. This sudden release causes the generation of shock waves which travel with velocities greater than the local speed of sound. The animal to be exposed to shock waves is placed in a chamber at the far end of the driven section. The shock experienced by the animal in the chamber is accurately measured by pressure transducer mounted on the wall of the chamber. The pressure is maintained at 0.5 bar over pressure which is reported to be safe. For increased intensity of the shock wave, the number of shock wave exposures is varied. This part of the study describes the effects of the extracorporeal shock waves on the immune system of the murine model. It also highlights the potential of low-intensity shock waves in imparting protective immunity in the murine model of *Salmonella Typhimurium* infection.

2 Materials and Methods

2.1 Shock Wave Exposure in Mice

Four- to six-week-old Balb/c mice were exposed to shock waves in the diaphragmless shock tube at an overpressure of 0.5 bar. The pressure experienced by the mouse was measured using pressure transducers mounted on the wall of the animal-holding chamber.

2.2 S. typhimurium Infection and Bacterial Colonization

The mice were randomly segregated into two groups. Group 1 mice were exposed to shock waves (0.5 bar) one shot per day for 5 days. On day 6 the mice were challenged with 10^7 CFU virulent *S. typhimurium* via the oral route. At 5 days postinfection, the mice were sacrificed by cervical dislocation, and the liver, spleen, and mesenteric lymph nodes (MLN) were aseptically isolated, weighed, washed with sterile PBS, and homogenized. The homogenate was serially diluted and plated on SS agar to estimate the bacterial load in various organs. CFU was counted and represented as CFU/gm. wt. of the organ.

Group 2 mice were challenged with 10^7 CFU via the oral route and were exposed to shock waves 0.5 bar overpressure one shot per day for 5 days. On day 6 the animals were sacrificed; the organ burden was evaluated as described above.

2.3 Serum Cytokine Levels

BALB/c mice (4–6 weeks old) were exposed to shock waves as described above for 5 days. On day 6 the blood from the mice was collected via the retro-orbital route, and the serum was separated by centrifugation at 12000 rpm for 10 min and was stored at −80 °C until use. The serum was analyzed for the levels of proinflammatory cytokines (IL-6, IL-12, and TNF α) using the E-bioscience ELISA kit. The absorbance at 540 nm was measured and was plotted using the GraphPad Prism 5 software.

2.4 Survival Assay

Balb/c mice (n = 5), 4–6 weeks old, were exposed to shock waves at varying number of exposures ranging from one shot to three shots at 0.5 bar over pressure. At 24-h postexposure, the mice were challenged with a lethal dose of virulent *S. typhimurium* (10^8 CFU) via the oral route and were monitored for morbidity and mortality till day 7. The control mice received PBS instead of *S. typhimurium*. The survival and the death data was plotted using GraphPad Prism and was analyzed for statistical significance by the log-rank test.

3 Results and Discussion

To study the effect of shock waves on infection, the mice were exposed to the physiologically permissible pressure of shock waves (0.5 bar overpressure) (Fig. 1). There was no death that occurred upon exposure to these shock waves thus highlighting the fact that 0.5 bar overpressure is not lethal to the animal. Next, the mice were exposed to shock waves and subsequently infected with virulent *S. typhimurium*, and anothergroup of mice were infected and then exposed to shock waves as described. The bacterial colonization was evaluated in the liver, spleen, and mesenteric lymph nodes (Fig. 2). It was observed that the mice which were exposed to shock waves prior to infection had a significant reduction in the bacterial colonization in the organs as compared to the control group (Fig. 2). Interestingly the mice which were infected prior to the infection had a significant increase in the bacterial colonization in the organs. This observation hints at the involvement of the immune system to the response to shock waves. In the case of shock wave exposure prior to infection, a protective nature of shock wave can be seen, whereas the exposure after infection seems to show a deleterious effect for the mice where the pathogen is able to colonize better in the host. To further check for the immune response, the levels of proinflammatory cytokines (IL-6, IL-12, and TNF α) were quantified in the animals exposed to shock waves (Fig. 3a). It was observed that the levels of the cytokines were significantly high as compared to the unexposed animals. This indeed strengthens the belief of the protective nature of these waves. Next, to probe the effect of the number of shock wave exposures on the immunity status of the animal, the number of exposures was varied from 0 to 3 exposures per group. *S. typhimurium* infection was done 24 h postexposure, and the survival of the animals was monitored thereafter (Fig. 3b). Interestingly it was found that the animals which received higher number of shock wave exposures survived better as compared to the unexposed as well as the animals which received lower shock wave exposures. Eventually, all the animals died at the end of 7 days postinfection.

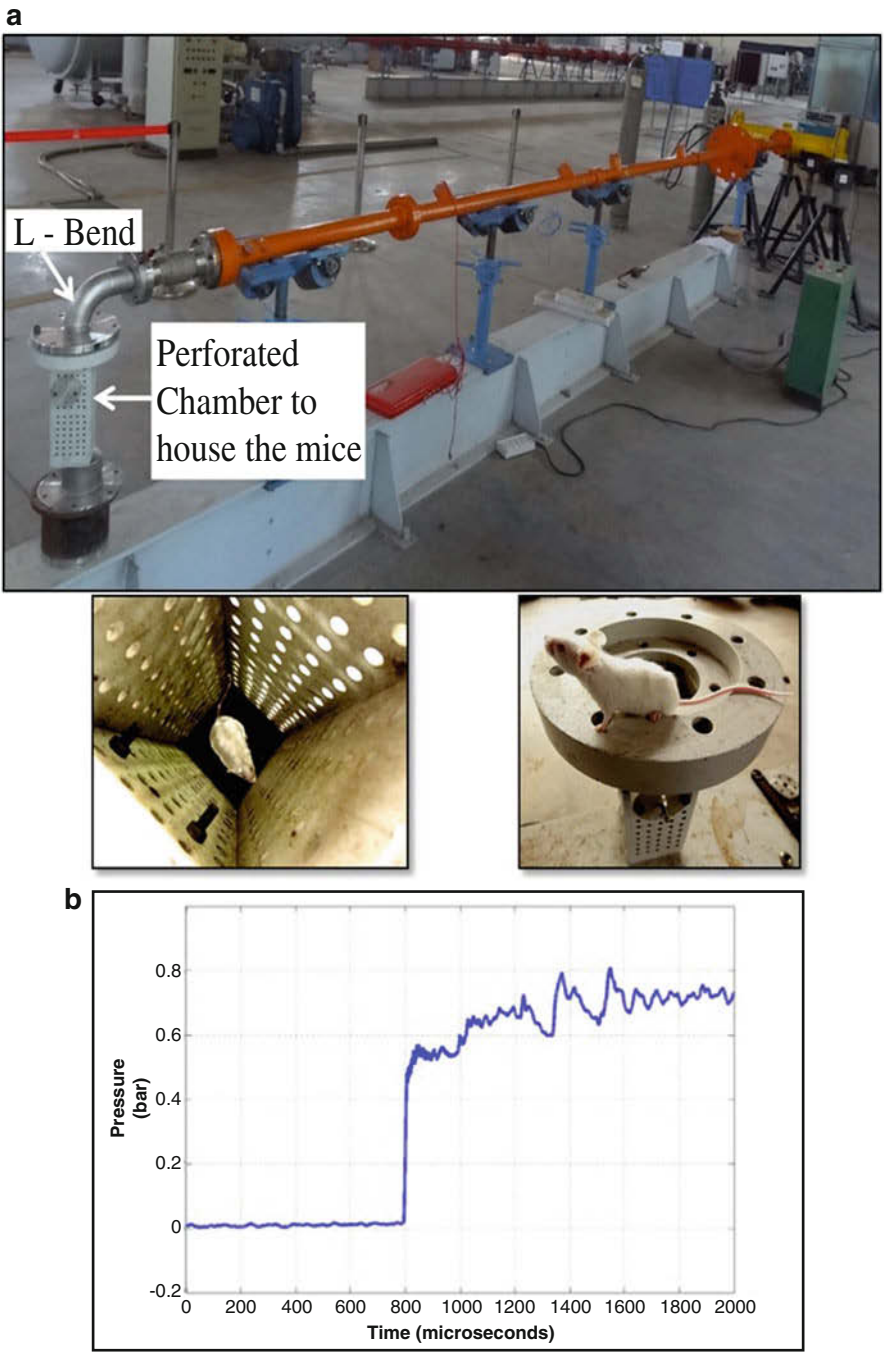

Fig. 1 (**a**) Diaphragmless shock tube. A laboratory method to generate shock waves with variable pressures. The end of the driven section is extended with an L bend and a perforated chamber to house the animal for shock wave exposure. (**b**) Pressure profile. The pressure transducer mounted on the wall of the chamber records the pressure experienced by the animal. For all experiments 0.5 bar overpressure is used

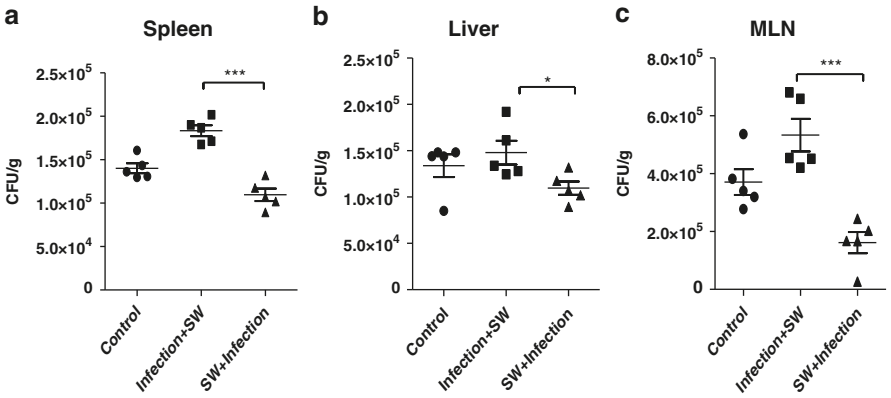

Fig. 2 Effect of shock waves on *Salmonella* infection. Balb/c mice (n = 5 per group) were segregated into two groups. **Group I** was orally infected with virulent *Salmonella* (10^7 CFU) and was exposed to shock waves (0.5 bar overpressure) one shot per day for 5 days. On day 6 the animals were sacrificed, and the liver, spleen, and MLN were aseptically removed and further processed. **Group 2** was exposed to shock waves (0.5 bar overpressure) one shot per day for 5 days and subsequently was challenged with *Salmonella* (10^7CFU). On day 6 postinfection, the animals were sacrificed, and the liver, spleen, and MLN were aseptically removed and further processed. The organ burden was calculated as CFU/g wt. of the organ and was compared across the two groups. Statistical analysis was done using Student's t test

All these observations taken together throw light on the beneficial effect of shock waves with respect to an individual. It appears that the shock waves, when used at a lower pressure, have beneficial effects and can be further tested for benefit in many other conditions of infection like sepsis leading to multi-organ failure and eventually death of the patient and antibiotic-resistant biofilm formation by a pathogen in the body.

4 Future Directions

- Understanding the mechanism of the immune protection upon shock wave exposure.
- Test the possible application of low-intensity shock waves as a combinatorial therapy for conditions, like sepsis, antibiotic-resistant microbial biofilms in vivo.

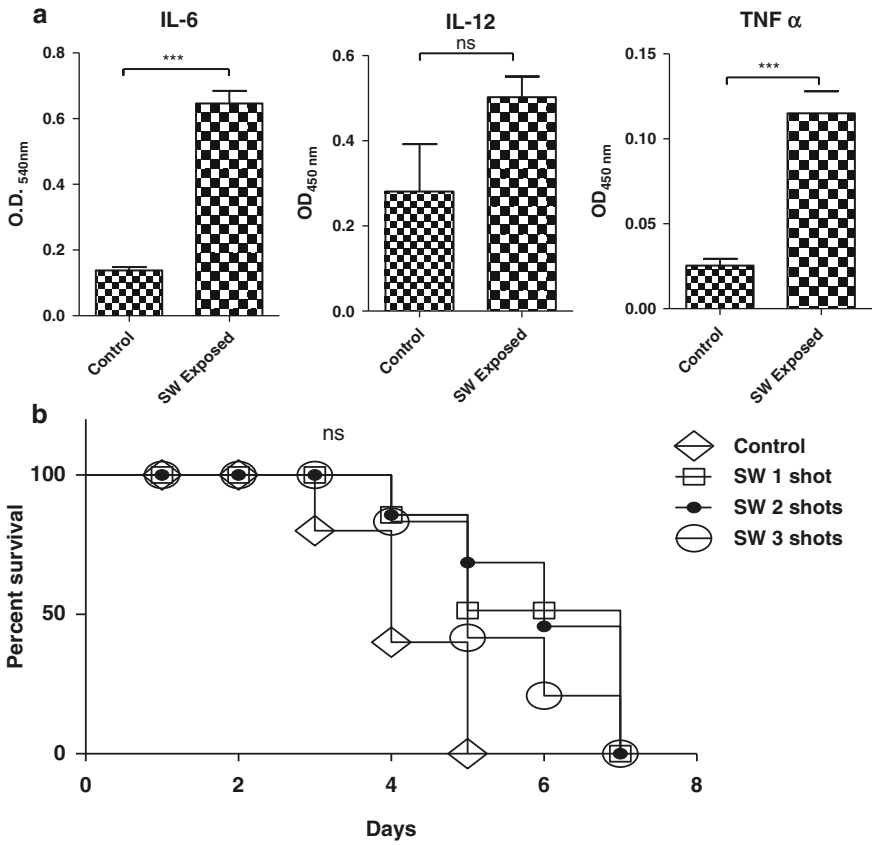

Fig. 3 (**a**) ELISAs to check the levels of proinflammatory cytokines IL-6, IL-12, and TNF α. Balb/c mice (n = 3) were exposed to shock waves at 0.5 bar overpressure. 24 h postexposure, the blood was collected, and the cytokine levels were checked in the serum. The statistical analysis was done by using the Student's t test. (**b**) **Survival assay**: Balb/c mice (n = 5) per group were subjected to varying number of shock wave exposures ranging from one shot to three shots. 24 h postexposure, the animals were challenged with virulent *Salmonella* (10^8 CFU) via the oral route and were monitored for morbidity and mortality. The data was analyzed by log-rank test

References

1. J.M. Wightman, S.L. Gladish, Ann Emerg Med **37**(6), 664–678 (2001)
2. M. Aboudara et al., Primary blast lung injury at a NATO role 3 hospital. J. R. Army Med. Corps **160**(2), 161–166 (2014)
3. G.A. Elder, A. Cristian, Blast-related mild traumatic brain injury: mechanisms of injury and impact on clinical care. Mt. Sinai J. Med. **76**(2), 111–118 (2009)

4. M.S. Hariharan et al., Diaphragmless shock wave generators for industrial applications of shock waves. Shock Waves **21**(3), 301–306 (2011)
5. M.J. Kane et al., Altered gene expression in cultured microglia in response to simulated blast overpressure: possible role of pulse duration. Neurosci. Lett. **522**(1), 47–51 (2012)
6. J.A. McAteer, A.P. Evan, The acute and long-term adverse effects of shock wave lithotripsy. Semin. Nephrol. **28**(2), 200–213 (2008)
7. J. Parkin, B. Cohen, An overview of the immune system. Lancet **357**(9270), 1777–1789 (2001)
8. J.M. Wightman, S.L. Gladish, Explosions and blast injuries. Ann. Emerg. Med. **37**(6), 664–678 (2001)

On the Relation Between the Shock Wave Thickness in Biomaterials and the Threshold for Blast-Induced Neurotrauma

M. I. P. Radulescu

Abstract It is found that the threshold for blast-induced neurotrauma documented from previous experiments in animals and cell cultures is approximately given by the criterion that the shock thickness be comparable to the characteristic dimension of a neuron cell (approximately 20 μm). The coincidence of the shock thickness with the characteristic dimension of the neuron cells supports the view that cell damage may be related to the localized mechanical deformation of cell components and shear for sufficiently strong and thin shocks. Our estimate of the shock wave thickness in biological material is based on the weak shock model of Thompson extended to materials whose compressibility can be modeled using the stiffened gas equation of state. Simulations of the transient relaxation of step function shocks into the steady shock profiles provided the time scale for the shock thickening when an impact-generated shock or much thinner air shock enters the biomaterial modeled. We find that air shocks will always be more damaging than those propagating through water at the same pressure level, consistent with experiment.

1 Introduction

The mechanism by which a blast wave induces neurotrauma is currently not known and subject to much speculation in the literature. The blast-induced neurotrauma to the brain is believed to be similar to that in civilian traumatic brain injuries from head impact [1, 2]. In both cases, the most difficult to monitor is the mild type of traumatic brain injury where shock wave pressure levels imposed by the external blast wave, or from sudden accelerations of the cranium, are only in the range of hundreds of kilopascals. In whole-body exposure, the symptoms are often cognitive [3]. This makes it difficult to assess the mechanism by which the first interaction of shock waves with the head and/or brain tissue triggers the complex

M. I. P. Radulescu (✉)
University of Ottawa, Ottawa, ON, Canada
e-mail: matei@uottawa.ca

A. Sasoh et al. (eds.), *31st International Symposium on Shock Waves 2*,
https://doi.org/10.1007/978-3-319-91017-8_49

biochemical path of blast-induced neurotrauma. Due to the unknown mechanisms, it is also more difficult to develop mitigation strategies. In the present study, we review the threshold data available in the literature for shock-induced neurotrauma in order to identify the likely mechanism of shock injury. We propose a novel criterion for shock-induced neurotrauma, which corresponds to the shock thickness being smaller than the cellular dimension, such that the deformation is associated with shear.

2 Review of Pressure Wave Amplitude for Blast-Induced Neurotrauma

The threshold for neurotrauma blast injury has been derived from both whole-body experiments and experiments of shock interaction with cellular cultures. Cernak and Noble provide a recent review of the available experimental studies on whole-body blast injuries [1]. Richmond et al. provide the tolerances and pathological observations for goats, dogs, cats, rabbits, guinea pigs, hamsters, rats, and mice after their exposure to the shock waves generated by high explosives in a blast tube [4]. Compressed air shock tubes were also used to generate shock waves and their interaction with goats, dogs, guinea pigs, and rats [5], where it was determined that the reflected shock wave pressure in air for injury was in the range of 100–200 kPa. Perhaps more relevant to human injury was the study of Bogo et al. on monkeys using compressed air shock tubes [6]. The monkeys were trained to perform auditory and visual discrimination avoidance tasks and exposed to a reflected shock-tube airblast of 200–350 kPa. Results indicated that immediate but transient mild performance decrement occurred. They also observed that the recovery time was brief (usually under 4 h) despite frank physical injuries. The blast waves from fuel-air explosive charges were studied on sheep and rats by Savic et al. [7]. The authors observed morphological, physiological, metabolic, and biochemical responses to whole-body exposure at similar pressure levels.

Simplified models of shock interaction with cellular cultures have been performed in recent years in order to determine the sequence of events leading to cellular modification or injury from exposure to blast. Such models studied the interaction of shocks in air or water with cellular cultures. Several laboratories have carried out such studies, either subjecting cultures to air blast [8–12] or submerging them for underwater shock [13–19]. While most experiments are difficult to interpret due to non-idealities associated primarily with the two-dimensional cellular cultures and confining surfaces, the experiments of Sawyer et al., which eliminated much of these non-idealities, determined that water shocks as weak as 300 kPa amplitude can give rise to subtle biochemical effects [19]. One interesting observation relates to the damage thresholds from shock waves propagating through a gaseous medium, or transmitted through water, in that the shocks through air were damaging at lower pressures than those in water.

A summary of the state of the art is that the shock pressure threshold for an effect on brain cells is approximately in the 100–300 kPa range, while the mechanism controlling this threshold is still unknown. Determining the mechanism is the subject of the present communication.

3 Working Hypothesis: Effect of Scale on the Deformation by Shock Waves

An interesting experimental clue relates to the significant differences observed when neurons are exposed to shock waves in air or in water, as reported in the previous studies outlined above [8–19]. Shock waves transmitted directly from a gaseous medium typically provided a larger cellular modification than those transmitted through an aqueous medium, although the shocks had similar pressure magnitudes. While the general belief is that such differences are due to the larger impulses generated in air shock tubes, and the importance of the Friedlander blast profile, this explanation is physically questionable. During time scales that are orders of magnitude longer than those associated with acoustic relaxation across the cell, there cannot be any pressure gradients across a cell. During these long events, the cell experiences a hydrostatic uniform pressure distribution. This observation suggests that the shock structure itself, with length and time scales sufficiently short to affect the dynamics of cell deformation, is likely to play a dominant role. This is particularly striking in the differences between experiments in air and water, since the shock thicknesses and characteristic time scales are fundamentally different in the two media.

Figure 1 shows the expected fundamental differences between the deformation at scales larger than the shock thickness (top) and smaller than the shock thickness (bottom). While the deformation at scales smaller than the shock thickness is primarily isotropic, the deformation at scales larger than the shock thickness takes on the familiar characteristic large shear deformation due to the passage of the shock. It thus is of interest to determine the thickness of shock waves in biomaterials for pressure amplitudes comparable with the documented thresholds in order to comment on the likely mechanism for the first cellular injury by shock waves.

4 The Thickness of Shocks Transmitted into Biomaterials

The nonlinearity of compressible flow gives rise to a unique shock thickness, controlled by viscous processes. The thickness of shock waves can be readily obtained from shock theory as a function of the shock amplitude. Since the shocks for the documented injuries propagating through biomaterial are in the weak, acoustic regime, a Navier-Stokes description is sufficient to describe the shock

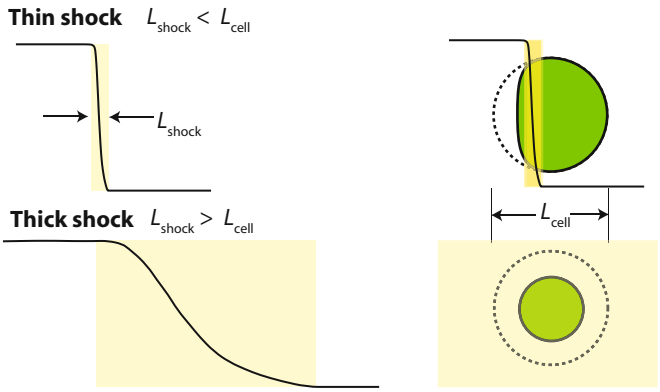

Fig. 1 Deformation of shock compression at scales larger than the shock thickness (top) and smaller than the shock thickness (bottom)

structure as a first estimate. For weak shock waves, the shock thickness is given approximately by Thompson [20] as:

$$\Delta \approx \frac{8}{3} \frac{\mu}{(M-1)\,\rho c} \tag{1}$$

where μ is the fluid viscosity, ρ is the density, c is the sound speed, and M is the shock wave Mach number relative to the quiescent mixture. The viscosity μ combines bulk and shear viscosity ($\mu = \mu_{\text{shear}} + 3/4\mu_{\text{bulk}}$). The Mach number appearing in Eq. (1) can be expressed in terms of the shock pressure, which is the control parameter of interest here. This requires an equation of state for the material, which characterizes its compressibility. For water and biological materials, the stiffened gas equation of state [21], which is identical to the Tait equation of state for nearly isentropic flows such as those of shock waves in the acoustic regime, relates the internal energy e to the medium's thermodynamic state:

$$e = (p + \gamma p_\infty) / ((\gamma - 1)\,\rho) \tag{2}$$

where the stiffening pressure p_∞ and the exponent γ are characteristics of a given material. The Rankine-Hugoniot jump conditions for a stiffened gas are obtained by manipulating the mass, momentum, and energy conservation laws across a shock wave in the usual way, yielding:

$$\begin{aligned} \frac{\rho_2}{\rho_1} &= \frac{(\gamma+1)M_s^2}{(\gamma-1)M_s^2+2} \\ \frac{p_2+p_\infty}{p_1+p_\infty} &= \frac{2\gamma M_s^2-(\gamma-1)}{\gamma+1} \end{aligned} \tag{3}$$

with the sound speed given by $c = \sqrt{\gamma (p + p_\infty)/\rho}$. The subscripts 1 and 2 denote the pre- and post-shock states, respectively. Since the Mach number can be expressed explicitly in terms of the shock pressure from Eq. (4), the shock thickness in Eq. (1) for a weak shock becomes:

$$\Delta \approx \frac{8}{3}\frac{\mu}{\rho c}\left(\sqrt{\frac{1}{2\gamma}\frac{p_2 + p_\infty}{p_1 + p_\infty}(\gamma + 1) + (\gamma - 1)} - 1\right)^{-1} \tag{4}$$

for a stiffened gas equation of state.

The following parameters are used to estimate the shock thickness in biomaterials: the viscosity of cytoplasm is taken as close to that of water $\mu = 2.8 \times 10^{-3}$ Pa. s [22]. According to Nakahara et al., the stiffened gas parameters for biomaterials are also close to those of water, yielding $\gamma \approx 7$ and $p_\infty \approx 296$ MPa [23]. We also take the density as that of water, yielding $p \approx 1000$ kg/m^3.

Figure 2 provides the variation of the shock thickness with shock overpressure predicted by Eq. (4). For reference, we have also calculated the shock thickness in air as a function of shock overpressure by integrating the corresponding ordinary differential equations for shocks that cannot be assumed as weak [20] with the properties of air following the outline of Chapdelaine and Radulescu [24]. The air shock wave is found to be approximately 100 times thinner than the water and biomaterial shock waves of the same overpressure.

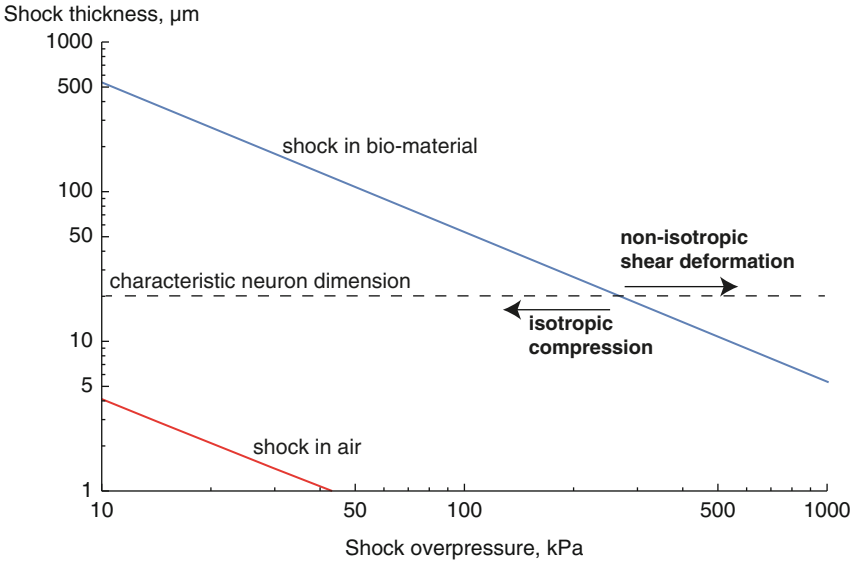

Fig. 2 The variation of the shock thickness with shock overpressure in biomaterials and in air and its comparison with the characteristic size of a neuron

The characteristic dimensions of neurons cell bodies are 4–100 μm, yielding a cellular body characteristic dimension (taken as the geometric mean) of 20 μm. According to the shock overpressure data shown in Fig. 2, shock waves in biomaterial thinner than this characteristic dimension of 20 μm will have overpressures larger than approximately 300 kPa. This is found in excellent agreement with the available experimental data for shock overpressures causing neural trauma, which ranged 100–300 kPa. This provides a strong indication that the mechanism for shock modification of cells is by shear deformation, as this is absent in shock waves thicker than the cell dimension.

It is also noteworthy that air shock waves are always thinner than shock waves in water or biomaterial by a factor of 100. We thus expect that all air shock waves transmitted directly into biomaterial to provide significant damage. This is in qualitative agreement with experiments, which showed that shock waves first generated in air are more conducive to damage than shocks transmitted in water.

In order to illustrate the relaxation of the shock structure in biomaterials to its steady-state thickness predicted above, we have solved numerically the evolution of the shock structure starting with an initial step function. This corresponds to asking the question of how long does it take for an air shock to disperse when entering a material with the properties of water.

The governing equations are the Navier-Stokes equations (e.g., see Ref. [24]), and the initial conditions correspond to a discontinuity where the pressure, density, and flow speed are given by the shock jump Eqs. (3). The Tait stiffened gas equation of state described the compressibility of the mixture. These have been solved numerically using the MG code developed by S. Falle at the University of Leeds [25]. The convective terms have been solved by a linear Riemann solver, while the viscous terms were solved by a central difference approximation. The method of fractional time steps was used to couple the convective and diffusive terms.

Figure 3 shows the evolution of the density profile at successive times for a shock Mach number of $M = 1.01$. The shock grows in a self-similar fashion, as expected for these shocks in the acoustic regime, and eventually saturates at its steady-state structure. The evolution of the shock thickness, defined here as the distance between the points of intersection of a tangent of the profile at its maximum slope with the constant lines of pre- and post-shock states, is shown in Fig. 4. As expected, the shock thickness grows initially as the square root of time, denoting a diffusive process, and saturates at a thickness in good agreement with the analytical result of Eq. (4).

The shock formation time can be taken, for example, as the intercept of the self-similar shock thickness growth with the line of constant steady-state shock thickness. The numerical results indicate that this time can be very well approximated by the diffusion time $t_{\text{formation}} \approx \Delta^2 / \left(\frac{\mu}{\rho}\right)$, while the distance travelled by a weak shock until it relaxes to its steady-state thickness, taking its speed as the sound speed, for simplicity, becomes $L_{\text{formation}} \approx c t_{\text{formation}}$. For reference, a 300 kPa shock driven into a biomaterial from an air shock, or sharp impact, will grow to its steady-state thickness predicted by (4) after travelling 20 cm. We thus see that for all practical purposes, shocks originating from air shocks or impact will always be

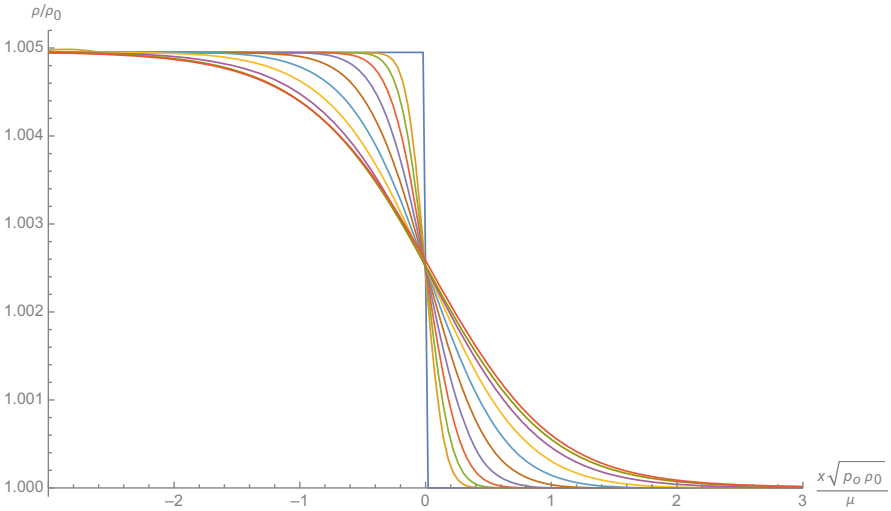

Fig. 3 The evolution of the shock structure of a weak shock ($M = 1.01$) in a biomaterial, when initiated by a sharp shock square wave discontinuity; successive curves are for $tp_0 \ / \ \mu$ of 0, 0.01, 0.02, 0.04, 0.08, 0.16, 0.32, 0.64, 1.28, 2.56, and 5.12

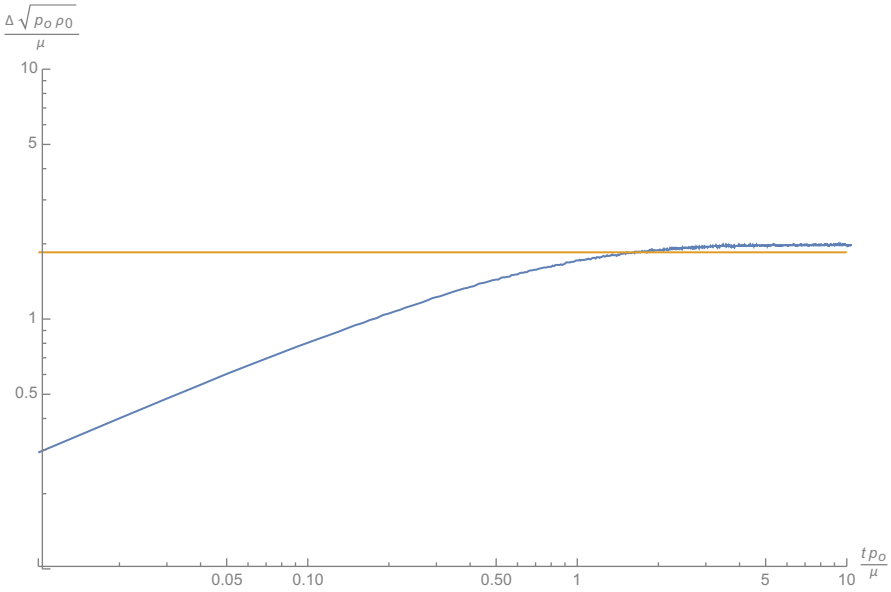

Fig. 4 The evolution of the shock thickness, orange line is the weak shock estimate

thinner than anticipated from steady-state considerations for travel distances less than this relaxation length. This explains why shock injury to cells from air shocks at the same pressure level is always more severe than those propagating through water.

5 Conclusion

Review of existing empirical data of blast-induced brain trauma indicates that the shock pressure threshold for injury is approximately 100–300 kPa overpressure. We find that this threshold coincides to the shock thickness being comparable with the neuron cell characteristic dimension of approximately 20 μm. Stronger shocks will gave thicknesses smaller than the cell dimensions, this giving rise to non-isotropic mechanical deformation and shear, while weaker ones yield thick shocks with vanishing shearing effects. The study also determined the relaxation laws for shock thicknesses to the steady-state estimates. The results offer a very likely reason why shocks in biomaterials originating from air shocks or explosives are more damaging than those generated through water. The very good correlation suggests that the threshold of damage by shock waves in cells is likely related to the localized mechanical deformation of the cells, which is controlled by the shock thickness. Further experimental work is clearly needed to substantiate this conjecture. If verified, however, it may open a new strategy for mitigating the effects of shock waves via shock structure dispersion.

References

1. I. Cernak, L.J. Noble-Haeusslein, J. Cereb. Blood Flow. Metab. **30**, 255 (2010)
2. S. Margulies, R. Hicks, J. Neurotrauma **26**, 925 (2009)
3. H.G. Belanger et al., J. Int. Neuropsychol. Soc. **15**, 1 (2009)
4. D.R. Richmond et al., *Air-Blast Studies with Eight Species of Mammals*, Lovelace Foundation for Medical Education and Research (Albuquerque, New Mexico, 1966)
5. E.G. Damon et al., Aerosp. Med. **39**, 1039 (1968)
6. V. Bogo et al., *The Effects of Airblast on Discriminated Avoidance Behavior in Rhesus Monkeys* (Defense Nuclear Agency, Washington, DC, 1971)
7. J. Savic et al., Vojnosanit. Pregl. **48**, 499 (1991)
8. P. Arun et al., Neuroreport **23**, 342 (2012)
9. P. Arun et al., Neuroreport **22**, 379 (2011)
10. G.B. Effgen et al., Front. Neurol. **3**(23), 1–12 (2012)
11. A.P. Miller et al., Front. Neurol. **6**(20), 1–16 (2015)
12. G.B. Effgen et al., J. Neurotrauma **31**, 1202 (2014)
13. Y.C. Chen et al., J. Neurotrauma **26**, 861 (2009)
14. M.J. Kane et al., Neurosci. Lett. **522**, 47 (2012)
15. S.R. Shepard et al., J. Surg. Res. **51**, 417 (1991)
16. L.Y. Leung et al., Mol. Cell. Biomech. **5**, 155 (2008)
17. N.E. Zander et al., J. Neurosci. Res. **93**, 1353 (2015)
18. P.J. VandeVord et al., Neurosci. Lett. **434**, 247 (2008)

19. T.W. Sawyer et al., J. Neurotrauma **34**, 517–528 (2017)
20. P.A. Thompson, *Compressible-Fluid Dynamics* (McGraw-Hill, New York, 1972)
21. R. Menikoff, Empirical equations of state for solids, in *Shock Wave Science and Technology Reference Library – Solids I*, ed. Y. Horie (Springer, Berlin, 2007)
22. A.M. Mastro et al., PNAS **81**, 3414 (1984)
23. M. Nakahara et al., Jpn. J. Appl. Phys. **47**, 3510 (2008)
24. S.S.M. Lau-Chapdelaine, M.I. Radulescu, Viscous solution of the triple-shock reflection problem. Shock Waves **26**, 551 (2016)
25. S.A.E.G. Falle, Mon. Not. R. Astr. Soc. **250**, 581 (1991)

Development of a Miniaturized Focused Shock Wave Generator for Medical Application

H. Yamamoto, K. Takayama, and H. Shimokawa

Abstract This paper reports the result of development of a miniaturized focused shock wave generator for a technological innovation in minimally invasive therapy. The focused shock waves generated from the tip of the shock wave ablation catheter reached 80 MPa of peak pressure and successfully damaged a slab of fresh potato. The depth of damaged area and the pulse laser energy were related to positive correlation. These results indicate the potential usefulness of our new shock wave ablation system.

1 Introduction

Although radiofrequency catheter ablation (RFCA) is quite effective for the treatment of tachyarrhythmias [1], it possesses two fundamental limitations. The first problem is the limitation of ablation depth, because joule heat generated by radiofrequency current attenuates inversely with the fourth root of distance. The second problem is the side effect by heating, such as the cerebral embolism caused by a blood clot and cardiac tamponade due to steam pop. Consequently, new method is required, which can eradicate arrhythmia source in deep part of cardiac muscle without heat generation. On the other hand, the noninvasive treatment using focused shock waves represented by shock wave lithotripsy (SWL) has progressed immensely in these last few decades [2]. However, the current systems

H. Yamamoto (✉)
Department of Cardiovascular Medicine, Graduate School of Medicine, Tohoku University, Sendai, Japan
e-mail: yamahiro@cardio.med.tohoku.ac.jp

K. Takayama · H. Shimokawa
Department of Cardiovascular Medicine, Tohoku University Hospital, Sendai, Japan

A. Sasoh et al. (eds.), *31st International Symposium on Shock Waves 2*,
https://doi.org/10.1007/978-3-319-91017-8_50

have relatively large focal width of around 5 mm for shock wave ablation method requiring precision. In order to overcome the problem, we are developing a shock wave ablation catheter system [3]. This paper reports the recent result of the development of a miniaturized shock wave generator produces acoustic pressures of the order of 80 MPa.

2 Experiments

2.1 Underwater Shock Wave Generation

SWCA system consists of a Q-switched Ho:YAG laser, a syringe pump, a main body of catheter, and a shock wave generator at the tip of catheter (Fig. 1). The shock wave generator, whose open end is sealed with silicone rubber film, is equipped with water supply and drainage system in order to remove air bubble and heat inside cavity.

Figure 2 shows schematic diagram of underwater micro shock wave focusing of SWCA. Underwater shock waves were generated by irradiations of Q-switched Ho:YAG laser (SLR, pulse energy, 15 $\sim$ 46 mJ; pulse width, 100 ns; wavelength, 2.1 μm, Sparkling Photon Inc., Japan) into water through optical fiber (0.4 mm core diameter low OH content quartz optical fiber).

The tip of optical fiber was set at the primary focus (F1) of truncated ellipsoidal cavity using precisely positioning device. Spherical shock waves generated at F1 converge on the secondary focus (F2) after reflection from the wall of the cavity.

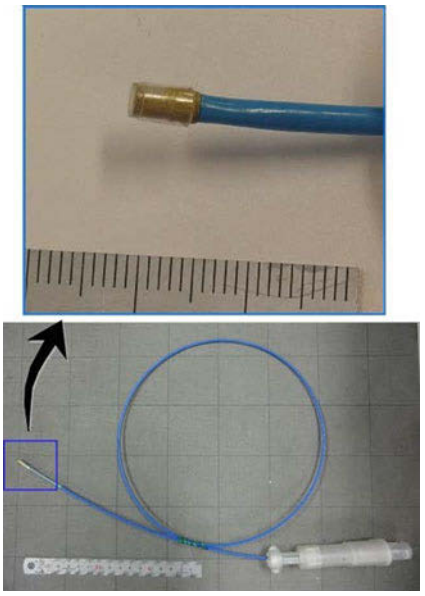

Fig. 1 A prototype of shock wave ablation catheter

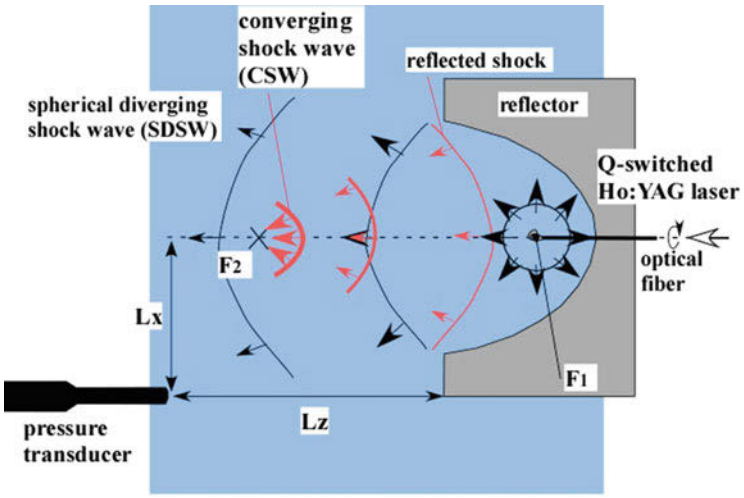

Fig. 2 Schematic diagram of underwater micro shock wave focusing of the shock wave catheter ablation (SWCA) system

2.2 Measurement Techniques

Figure 3 shows a schematic diagram of the experimental setup for pressure measurement. The test section is composed of a stainless steel chamber (100 mm in the inside diameter, 100 mm in depth) and an acryl window (140 mm × 140 mm × 25 mm), filled with pure water (Japanese Pharmacopoeia). Prior to experiment, the pure water was degassed in a vacuum chamber more than 1 h.

PVDF needle hydrophone with 0.5 mm sensitive diameter and 35 ns rise time (Dr. Müller Instruments Inc.) was used for pressure measurements. The signals are stored in a digital transient memory (DS-5534, Iwatsu electric co., ltd.) with sampling rate of 2GS/s.

Shadowgraph technique was used for visualization of shock wave motion. The image of phenomenon in the test section was taken with the high-speed camera (HPV-X2, Shimadzu corp., Japan). The inter-frame spacing, exposure time, and image resolution were 200 ns, 110 ns, and 400 × 250 pixel, respectively. The light source was pulsed diode laser (CAVILUX UHS, wavelength, 640 nm; pulse width, 10 ns, Cavitar Ltd., Finland) which emits light accurately in synchronization with the high-speed photography.

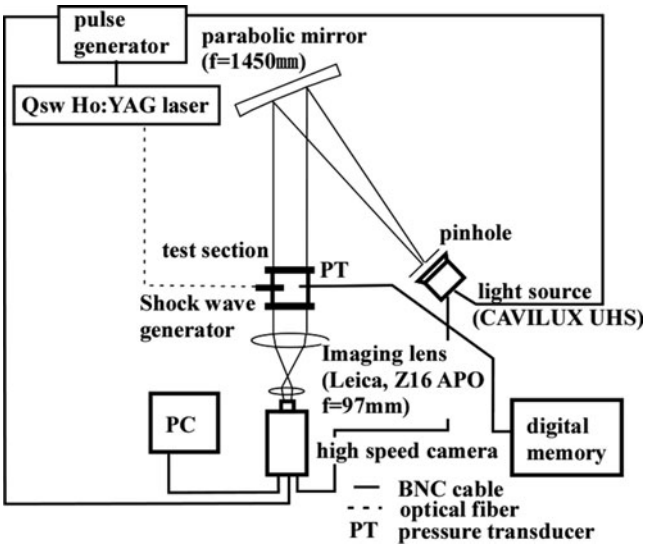

Fig. 3 Schematic diagram of optical setup

2.3 Ablation Performance Test

In order to evaluate the ablation ability of the miniaturized shock wave generator, in the previous study, we exposed focused shock waves to animal tissues in vivo. However, it was shown that a simple method of assessing the mechanical effects of the shock waves is to study the interaction with fresh potatoes that have high content of water [4]. In order to obtain preliminary results, we irradiated a slab of fresh potato with 180 shock waves. The maximum overpressure of shock waves at F2 were controlled between 30 MPa and 80 MPa.

3 Results

3.1 Shock Wave Focusing

Figure 4 shows time-resolved high-speed shadowgraph of shock focusing after laser irradiation. A spherical divergent shock wave (SDSW) emerges from the open end of reflector after 1.29 μs (b). The subsequent converging shock wave (CSW) converges on a spot 3.5 mm away from the open end (c). In particular, the size of focus region is smaller than 0.5 mm. Afterward the CSW diverges along the central axis of reflector.

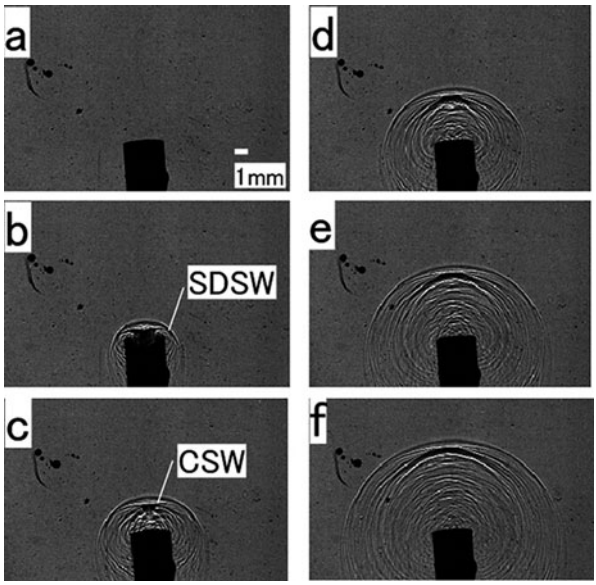

Fig. 4 Time-resolved high-speed shadowgraph of shock focusing, after laser irradiation: (**a**) 0.29 μs, (**b**) 1.29 μs, (**c**) 2.29 μs, (**d**) 3.29 μs, (**e**) 4.29 μs, and (**f**) 5.29 μs. SDSW, spherical diverging shock wave; CSW, converging shock wave

Figure 5 shows pressure distributions on the central axis (Lz) and on the line (Lx) normal to the central axis at F2. These distributions of positive and negative peak pressures show that focus region has an extension in axial direction.

Although the focal distance is recognized 3.5 mm by the result of visualization, the pressure peak is located at 1.5 mm before the focal distance of the reflector. The sensitive diameter of the pressure sensor is 0.5 mm, which is too large to accurately measure pressures of shock wave generated from this system, especially around the focus region. So, it is necessary to reexamine the procedure of pressure measurement.

3.2 Relationships Between Depth of Ablation and Laser Energy

Figure 6 shows a cross section of a slab of potato exposed by 180 shock waves at 80 MPa. The shock wave-induced damage regions were clearly dark colored. It is also clear that the damaged region extend beyond focus point.

Taking medical application of this system into consideration, it is important to control the degree of ablation. Figure 7 shows relationship between the depth of damaged area and the laser energy. No damage was observed less than 15 mJ/pulse; however between 17 mJ/pulse and 24 mJ/pulse, a positive correlation is observed between the depth of damaged area and the laser energy.

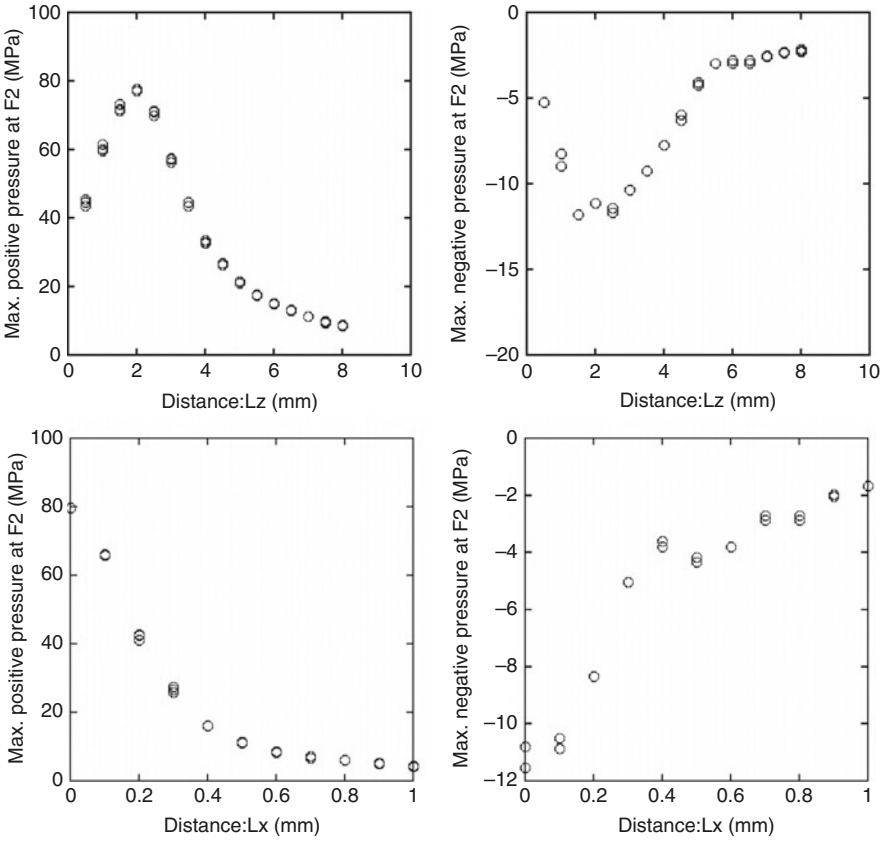

Fig. 5 Pressure distributions on the central axis (Lz) and on the line (Lx) normal to the central axis at F2

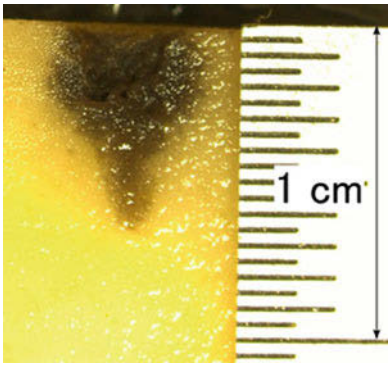

Fig. 6 A slab of potato exposed by 180 shock waves at 80 MPa

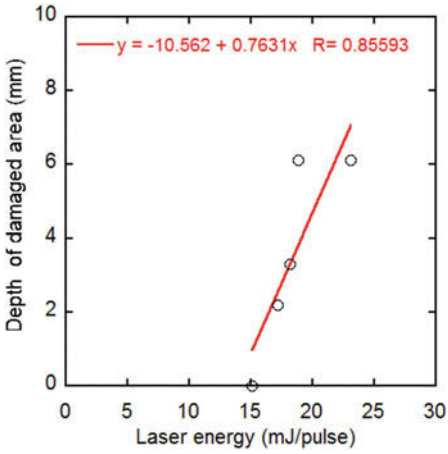

Fig. 7 Relationship between depth of damaged area and laser energy

4 Conclusion

We developed a miniaturized focused shock wave generator for medical application. It was demonstrated that the new shock wave ablation system is ablation depth controllable between 0 and 6 mm in a fresh potato. These results indicate the potential usefulness of our new system.

References

1. R.K. Thakur, G.J. Klein, R. Yee, Radiofrequency catheter ablation in patients with Wolf-Parkinson-White syndrome. Can. Med. Assoc. J. **151**(6), 771–776 (1994)
2. J.J. Rasswiler, T. Knoll, K. Köhrmann, J.A. MacAteer, J.E. Lingeman, R.O. Cleveland, M.R. Bailey, C. Chaussy, Shock wave technology and application: An update. Eur. Urol. **59**, 784–796 (2011)
3. Y. Hasebe, H. Yamamoto, K. Fukuda, K. Nishimiya, K. Hanawa, T. Shindo, M. Kondo, M. Nakano, Y. Wakayama, K. Takayama, H. Shimokawa, Development of a novel shock wave catheter ablation system – the first feasibility study in pigs. PLoS One **10**(1), e0116017 (2015)
4. P. Sunka, V. Babicky, M. Clupek, J. Benes, P. Pouckova, Localized damage of tissues induced by focused shock waves. IEEE Trans. Plasma Sci **32**(4), 1609–1613 (2004)

Intracellular Ca^{2+} Increase Evoked by Single Acoustic Pulses

A. Tsukamoto, T. Takahashi, S. Tada, and K. Nakagawa

Abstract Shock wave therapies require cellular responses. However, how shock waves interact with cells remains elusive. In this study, it was asked whether pressure discontinuities at wave fronts of shock waves are indispensable for evoking cellular responses. With shock wave irradiations, intracellular Ca^{2+} increase was evoked in endothelial cells. This cellular response was independent of pressure increment at front of shock waves. These results suggest that pressure discontinuity at wave front is not indispensable for evoking the cellular response.

1 Introduction

Shock waves enhance bone fracture healing and angiogenesis. In vitro, cultured cells respond to shock wave irradiations. Gene expressions those are related to bone fracture healing and angiogenesis have been observed [1]. Thus, it is supposed that those therapeutic effects rely on cellular responses induced by shock wave irradiations.

Pressure discontinuity is a typical character of shock waves. Across shock wave fronts, pressure drastically increases without continuity. One possible mechanism by which cells respond to shock wave irradiations could be that involving the pressure discontinuity. High peak pressure of propagating wave is an origin of the pressure discontinuity. Nonlinear effects allow waves with high peak pressure propagate faster, and they catch up with preceding waves. Thus, when peak pressure is relative low, the pressure discontinuity hardly develops.

In this study, shock waves with peak pressures of 1–10 MPa were generated with electrical discharge or laser irradiation. With those relatively low peak pressures,

A. Tsukamoto (✉) · T. Takahashi · S. Tada
National Defense Academy, Hashirimizu 1-10-20, Yokosuka, Japan
e-mail: tsuka@nda.ac.jp

K. Nakagawa
The University of Tokyo, Hongo 7-3-1, Bunkyo-ku, Tokyo, Japan

A. Sasoh et al. (eds.), *31st International Symposium on Shock Waves 2*,
https://doi.org/10.1007/978-3-319-91017-8_51

shock waves were irradiated on cells, and a cellular response were detected. As a cellular response, intracellular Ca^{2+} increase was detected. This cellular response is typically evoked by other mechanical stimulations [2, 3]. Pressure increments at wave front of shock waves were varied to understand whether pressure discontinuity at wave front is indispensable for evoking the cellular response.

2 Materials and Methods

2.1 Cell Culture

Bovine aortic endothelial cells (Lonza) were cultured in Dulbecco's Modified Eagle's Medium (DMEM, Sigma) supplemented with 10% fetal bovine serum, 1% penicillin-streptomycin (Gibco), and 2 mM L-glutamine (Sigma). After cells reached to confluence, cells were detached and seeded on cell chambers. Cell chambers were made of polystyrene sheets and silicone rubbers. At the bottom of cell chambers, polystyrene sheets were used. Acoustic impedances of polystyrene and water, 2.4×10^7 kg/m^2 s and 1.5×10^6 kg/m^2 s, are relatively similar. Thus, shock waves transmitted the bottom with high transmission efficiency. As walls of the cell chambers, silicone rubbers were used. Silicone rubbers were formed in a doughnut shape. After sterilizing with ethanol and UV, cells were seeded.

2.2 Fluorescence Imaging

Before experiments, cells were loaded with a fluorescent indicator fluo-4. In brief, cells were washed with HEPES solution and loaded with fluo-4 AM solution for 20 min in a room temperature. After the loading, cells were washed with HEPES solution. Loaded fluo-4 was excited with excitation lights with wavelength of 490 nm. Emission lights with wavelength of 510 nm was collected with an objective lens and imaged with a CCD camera (Fig. 1a). Fluorescence intensities were quantified to estimate intracellular Ca^{2+} intensity. When fluorescence intensities of fluo-4 increase, increase of intracellular Ca^{2+} intensity is indicated.

2.3 Shock Wave Irradiation

Shock waves were generated with electrical discharge or razer irradiation. Among two electrodes made of tungsten carbide, high voltages of 3–5 kV were applied and suddenly discharged. The generated shock waves were reflected with a spheroid stainless reflector. At first focus of spheroid, shock waves were generated. At second

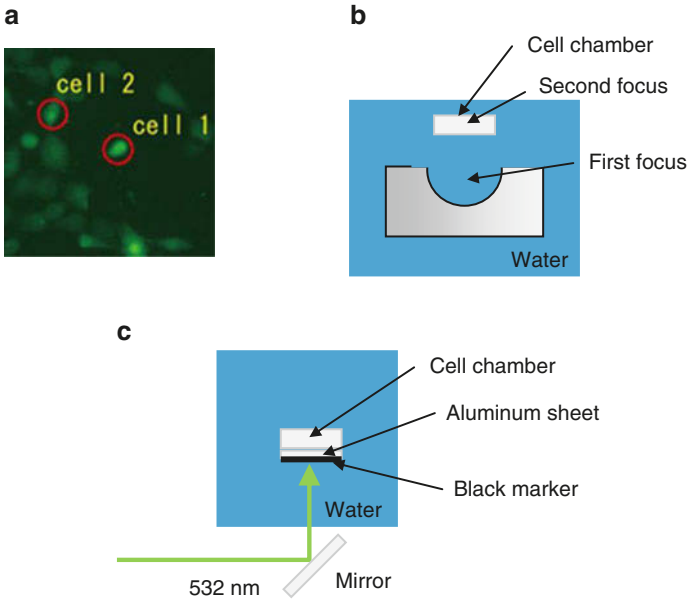

Fig. 1 Shock wave irradiation on cells (**a**) fluorescence image of cells seeded in a cell chamber, (**b**) shock wave irradiation with electrical discharge, (**c**) with laser irradiation

focus, shock waves were refocused (Fig. 1b). To generate shock waves with laser irradiations, laser with wavelength of 532 nm and pulse duration of 5 ns was used. Laser was irradiated on aluminum sheets with various thicknesses. Surfaces of aluminum sheets were painted with a black permanent marker. Irradiated razer was absorbed on the surface of aluminum sheets, and then shock waves were generated (Fig. 1c).

On cultured cells, single shots of shock waves were irradiated. When shock waves were irradiated, objective lens was removed to avoid interference between shock waves and the lens. When the lens was removed, fluorescence imaging was interrupted. The interruption was within 10 s.

3 Results

With electrical discharges, single-shot shock waves were generated. Those shock waves evoked intracellular Ca^{2+} increase in BAECs (Fig. 2). Within 20 s, fluorescence intensities returned to basal level before shock wave irradiation. Before and after the shock wave irradiation, fluorescence disappeared because objective lens which corrected the fluorescence was displaced to avoid interference with shock waves.

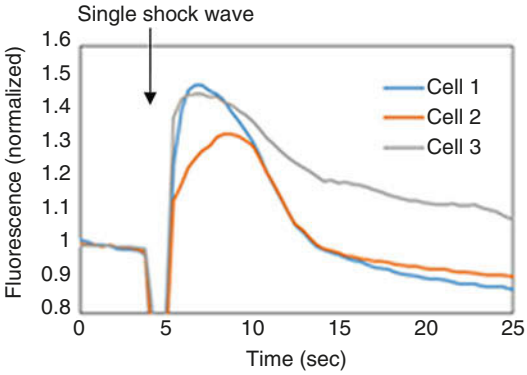

Fig. 2 Intracellular Ca^{2+} increase evoked by a single shock wave

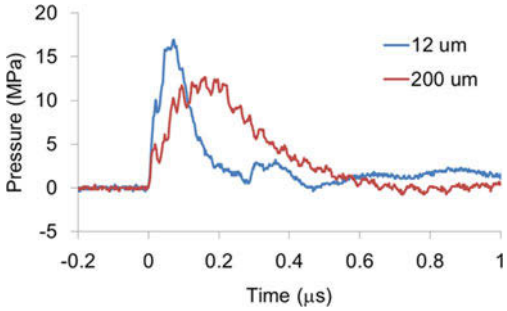

Fig. 3 Pressure profiles of shock waves with varied thickness of aluminum sheets

Biochemical inhibiting experiments indicated that both PLC cascade and mechanosensitive channel cascade involve in the intracellular Ca^{2+} increase. Those cascades are typically involved in intracellular Ca^{2+} increases evoked by other mechanical stimulations. Furthermore, the intracellular Ca^{2+} increase was independent of cellular detachment and cell membrane rupture. Thus, the intracellular Ca^{2+} increase was suggested to be a result of mechanosensing, in which intracellular proteins physically alter their morphologies and initiate biochemical cellular responses.

With laser irradiation on aluminum sheets, single shock waves were generated. By varying thickness of the aluminum sheets, pressure increments at wave front of shock waves were varied (Fig. 3). With those varied shock waves, fractions of responded cells were equivalent. These results indicate that pressure discontinuity at wave front is not indispensable for evoking the cellular response.

4 Discussions

Although pressure increments of shock waves were altered, fractions of responded cells were equivalent. This result indicates that pressure discontinuity at wave front is not indispensable for evoking the cellular response. Thus, it was supposed that

other physical parameter of shock wave is required for evoking the cellular response. Without the importance of discontinuous pressure increase, shock waves those evoking the cellular response might be called acoustic pulses.

It is possible that sensitivity of hydrophone was not enough to follow rapid pressure increment. If so, the decorrelation between pressure increment and cellular response is incredible.

5 Conclusion

Shock wave irradiations on endothelial cells evoked intracellular Ca^{2+} increase. However, this cellular response was independent of pressure increment at front of shock waves. These results suggest that pressure discontinuity at wave front is not indispensable for evoking the cellular response.

References

1. T. Nishida, H. Shimokawa, K. Oi, H. Tatewaki, T. Uwatoku, K. Abe, Y. Matsumoto, N. Kajihara, M. Eto, T. Matsuda, H. Yasui, A. Takeshita, K. Sunagawa, Extracorporeal cardiac shock wave therapy markedly ameliorates ischemia-induced myocardial dysfunction in pigs in vivo. Circulation **110**, 3055 (2004)
2. J.B. Lansman, T.J. Hallam, T.J. Rink, Single stretch-activated ion channels in vascular endothelial cells as mechanotransducers? Nature **325**, 811 (1987)
3. A. Tsukamoto, Y. Hayashida, K.S. Furukawa, T. Ushida, Spatio-temporal PLC activation in parallel with intracellular Ca^{2+} wave propagation in mechanically stimulated single MDCK cells. Cell Calcium **47**, 253 (2010)

A New Device for Crossing Chronic Total Occlusions

L.-P. Riel, S. Dion, M. Charlebois-Ménard, M. Brouillette, S. Bérubé, M.-A. Despatis, A. Benko, M.-É. Clavet, M.-J. Bertrand, P. Geoffroy, and J.-F. Tanguay

Abstract We report on the design and testing of a new minimally invasive device for crossing chronic total occlusions in the coronary and peripheral vasculature. The device is based on a novel shock wave generator that exploits inverse dispersion in solid waveguides to amplify the signal of broadband piezoelectric ultrasound transducers. Results of tests assessing the safety, efficacy, and mechanism of action of the device on a variety of surrogates, ex vivo arteries, and live animals are presented.

1 Introduction

Cardiovascular disease is the leading cause of death worldwide. This disease includes chronic total occlusions (CTOs), which are complete blockages of an artery. Unlike partial occlusions, CTOs are difficult to cross percutaneously using conventional guidewires (thin and flexible wires) because of the fibrotic and calcified nature of the blockage. CTO lesions are frequent in patients with peripheral and coronary artery disease, representing between 20% and 50% of treated lesions by transcatheter technique [1, 2]. Percutaneous intervention of CTO lesions has been associated with a lower procedural success rate; however, leaving these lesions untreated is associated with a higher risk of adverse events, including increased mortality, decreased quality of life, and increased health-care costs [3, 4]. Despite recent advancements in endovascular techniques and the development of dedicated

L.-P. Riel · S. Dion · M. Charlebois-Ménard · M. Brouillette (✉)
Shock Wave Laboratory, Université de Sherbrooke, Sherbrooke, QC, Canada

SoundBite Medical Solutions, Montréal, QC, Canada
e-mail: martin.brouillette@usherbrooke.ca

S. Bérubé · M.-A. Despatis · A. Benko
Sherbrooke University Hospital (CHUS), Sherbrooke, QC, Canada

M.-É. Clavet · M.-J. Bertrand · P. Geoffroy · J.-F. Tanguay
Montreal Heart Institute, Montréal, QC, Canada

A. Sasoh et al. (eds.), *31st International Symposium on Shock Waves 2*,
https://doi.org/10.1007/978-3-319-91017-8_52

devices to facilitate wire crossing of CTO lesions, procedural failure remains high [1, 5]. More importantly, most of these devices are challenging to use, and these techniques are associated with higher rates of procedural complications (e.g., perforation, tamponade), precluding their wide adoption by operators who are not CTO experts, pointing toward the need for more intuitive, safe, and user-friendly devices.

We report on the design and testing of a new minimally invasive device used to cross CTOs in the coronary and peripheral vasculature. The device is based on a novel shock wave generator which exploits inverse dispersion in solid waveguides [6] to amplify the signal of broadband piezoelectric ultrasound transducers to produce high-amplitude (∼500 Bars) and short-duration (∼1 microsecond) pressure pulses. These pulses are then propagated into small (∼0.35 mm) nondispersive waveguides, which have the same dimensions and properties as conventional guidewires, for percutaneous introduction into the vascular system. The distal tip of the nondispersive waveguide is then placed in contact with the occlusion where the arrival of the mechanical pulses locally erodes the hard calcified components of the CTO, enabling the waveguide to progress across the lesion.

2 System Description

The system comprises two main components: a disposable wire and a console that generates shock waves (Fig. 1) [7]. Shock waves have successfully been used in various medical therapies (kidney stone lithotripsy, treatment of chronic joint disorder, bone healing, and treatment of bone necrosis) and have shown the ability to selectively break calcium deposits without damaging the surrounding healthy elastic tissue.

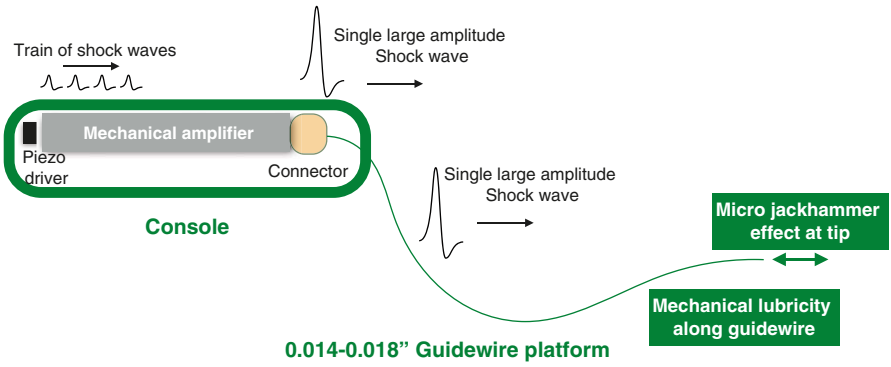

Fig. 1 Schematic of novel CTO crossing system

The system uses a novel generator to produce shock waves that are initially concentrated in the proximal end of a guidewire-like device. The shock waves are then propagated to the distal tip of the wire, resulting in a "micro jackhammer" effect (short distal tip displacement), which facilitates the passage of the device across the CTO.

The console converts electric power into pressure waves through the use of broadband piezoelectric transducers. Multiple amplification stages are used to increase the wave amplitude. The shock wave emission is pulsed at a low repetition rate (<50 Hz), which limits heat generation. The wire is similar in design to commercially available guidewires but has the ability to transmit shock waves across its length. The wire is currently available in 0.014 inch and 0.018 inch platforms to treat CTO lesions in both coronary and peripheral vessels.

3 Efficacy

This device was extensively tested on the bench using a variety of CTO surrogates such as egg shells, medical plasters, as well as calcified plaques obtained from leg amputations. Finally, full ex vivo CTO segments, also obtained from leg amputations, were successfully crossed in simulated procedures after unsuccessful attempts with commercial equipment. These segments could not be crossed by a stiff wire or the inactivated wire.

For example, the system was used to penetrate and successfully cross an occluded artery segment of an amputated leg. A segment of the posterior tibial artery was dissected from the leg by a vascular surgeon immediately after the amputation. The specimen was preserved in saline at −4 °C until the day of the procedure and then thawed at room temperature for at least 6 h. The artery segment was installed into a test tube for a simulated recanalization procedure (Fig. 2a). A guiding catheter was brought upstream of the artery segment, and an attempt to cross the occlusion was performed without success using a Confianza 12 guidewire (Abbott Vascular) over

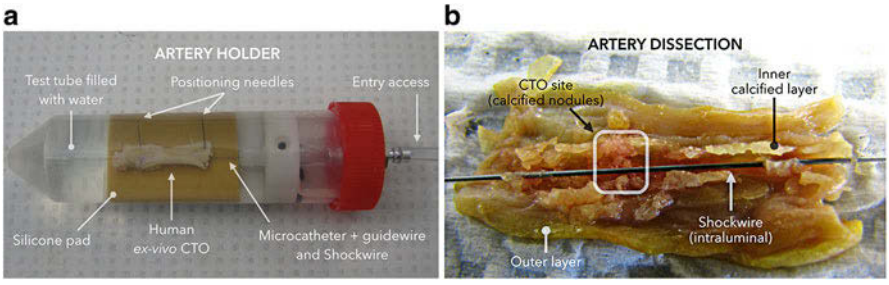

Fig. 2 Crossing of a human ex vivo CTO. (**a**) Experimental setup, (**b**) Artery dissection after successful crossing

an 0.014 inch FineCross support catheter (Terumo). A second unsuccessful attempt was made using the system without activation. Recanalization was then attempted using the activated wire, resulting in recanalization of occluded segment in seconds. After the crossing, the artery was dissected to reveal an array of calcified nodules within the artery which precluded crossing without energy (Fig. 2b).

4 Safety

Also, the safety of this method was assessed by subjecting live ex vivo pig arteries as well as live pigs to treatment in coronary arteries.

4.1 Ex Vivo Testing

The protocol consisted of sampling fresh coronary and carotid segments (about 10 mm in length) from healthy pigs within 20 min of the animal sacrificed (40 kg pigs were used). Four segments of each artery type were sampled per pig. The coronary segments were sampled from the left, the right, and the circumflex arteries. The carotid segments were samples from the common and subclavian arteries. The artery segments were kept alive and preserved in a Dulbecco's Modified Eagle's Medium (DMEM) with 10% fetal bovine serum and 1x penicillin streptomycin on ice.

Before exposure to the wire, three groups were randomly created with an equal number of coronary and carotid segments in each: Group I, control group exposed to a commercially available guidewire, MiracleBros 12 (Asahi) (N = 4); Group II, exposed to the Ultrasonic Wire device with its distal tip within the artery lumen (N = 8); and Group III, exposed to the wire device within the artery with its distal tip in direct contact with the artery wall (N = 4).

Within 2 h of the sampling, the artery segments were exposed to the control guidewire or to the wire with high-pressure pulses for a duration of 4.2 min. The bench test setup consists of a custom bath filled with the DMEM solution and having a silicon pad in the bottom. This pad is used to pin the artery segments in position using needles. The wire device or the control guidewire is introduced via an introducer and positioned at the middle of the artery segment. The position of the device is validated using a ruler and marks on the device. Once activated, the distal tip of the wire or the control guidewire is moved at slow speed back and forth +/−1 mm from its initial position to better cover the targeted zone inside the artery segment. The target zone represents the middle length of each artery segment.

After exposure to high-pressure pulses, the artery segments were incubated at 37 °C and with 5% of CO_2 for a period of 6 h. Finally, the artery segments were preserved in a 10% formaldehyde solution and transferred to the histology

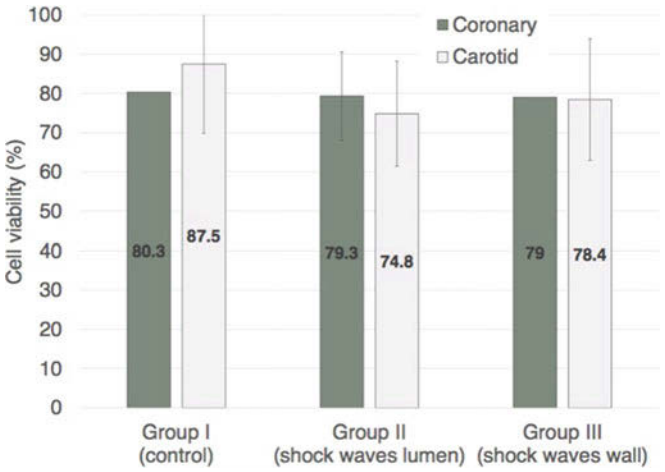

Fig. 3 Percentage cell viability results for the various groups and artery types (error bar = standard deviation)

laboratory for analysis. The artery segments were stained with hematoxylin and marked for PECAM-1. The percentage of endothelial cells expression (cell viability) was calculated as percentage of cells staining positively for PECAM-1 by the lumen circumference of the cross section. Arterial wall damage was also assessed visually by the examiner.

Figure 3 summarizes the cell viability levels for the different groups and artery types. The average results are presented with their respective standard deviation. From this, there is almost no difference in cell viability between the coronary and carotid artery types for the different groups. Similarly, there is almost no difference regarding the endothelial cell viability if the wire device is within the lumen (Group II) or if it is forced to be in contact with the wall (Group III). However the cell viability level is slightly lower when using the wire device when compared to the control Group I.

4.2 In Vivo Testing

The CTO guidewire was tested in three juvenile farm pigs at different output power levels (100%, 75%, 50%, and 0%) for 4 min and 10 s (i.e., 2500 shock wave pulses), with or without wire movement. This was performed in different segments of epicardial coronary arteries, while one coronary artery was used as a negative control. Acetylcholine (Ach) was infused at different concentrations (10–7, 10–6, 10–5, 10–4 mol/l), followed by 100 μg nitroglycerin (NTG). Coronary angiography was performed at baseline and after each dose of Ach and NTG,

along with QCA (quantitative coronary analysis) diameter measurements. After the procedure, animals were euthanized for histology and immunostaining analysis of vessel endothelium.

It is found that there is no clear correlation between lumen diameter by QCA and % power (energy) delivered by the wire, owing to the small sample size of this study which limits the statistical power to detect a difference between energy levels.

5 Conclusion

The described system is the first CTO device using a guidewire-like platform to deliver shock waves to the point of vascular occlusion. Although further human in vivo studies are needed to demonstrate the safety and efficacy of this new device, the results obtained so far provide a strong demonstration of the capability of the shock wave technology to successfully cross occlusions where prior attempts with conventional wires failed. While still speculative, it allows one to believe that shock wave wire technology may have a predominant role in the management of complex CTO lesions in the future. Ongoing feasibility and pilot studies will provide meaningful information regarding the capability of this technology to improve procedural success, decrease procedural complication, and simplify CTO procedures, both in coronary and peripheral fields.

This study was reviewed and approved by the institutional research board and ethics committee of the Centre Hospitalier Universitaire de Sherbrooke (CHUS) in Québec, Canada.

References

1. A.R. Galassi et al., Appropriateness of percutaneous revascularization of coronary chronic total occlusions: An overview. Eur. Heart J. **37**, 2692 (2016)
2. H. Al-Ameri et al., Devices to treat peripheral chronic total occlusions. J. Interv. Cardiol. **25**, 395 (2012)
3. G. Sianos et al., Recanalisation of chronic total coronary occlusions: 2012 consensus document from the EuroCTO club. EuroIntervention **8**, 139 (2012)
4. H.C. Wijeysundera et al., Relationship between initial treatment strategy and quality of life in patients with coronary chronic total occlusions. EuroIntervention **9**, 1165 (2014)
5. A.R. Galassi et al., Retrograde recanalization of chronic total occlusions in Europe: Procedural, in-hospital, and long-term outcomes from the multicenter ERCTO registry. J. Am. Coll. Cardiol. **65**, 2388 (2015)
6. M. Brouillette, S. Dion, L.-P. Riel, *Mechanical Wave Generator and Method Thereof*, U.S. Patent Application No. 61/377,519 (2010), International Patent Application No. PCT/US2011/049573 (2011)
7. M. Brouillette, S. Dion, L.-P. Riel, *Method and System for Generating Mechanical Pulses*, U.S. Patent Application No. 62/161,647 (2015), International Patent Application No. PCT/IB2016/052339 (2016)

Biological Effect of Shock Waves: Mechanism of Blast-Induced Traumatic Injury to Medical Application

A. Nakagawa, K. Ohtani, T. Kawaguchi, and T. Tominaga

Abstract Shock waves (SW) have been applied to a variety of medical treatments. Recent studies have focused on applications within microenvironments. On the other hand, blast-induced traumatic injury (bTBI) became a social problem after the Iraq and Afghanistan conflict, and SW is gaining attention to understand the mechanism of primary bTBI. This paper reports a preliminary experimental result of SW propagation in simulated biomedical materials for understanding mechanism of both potential complication of medical application of SW within the cranium and bTBI. SW, generated by detonating of a 10 mg silver azide (AgN_3) pellet, was interacted with a brain model using simulated biomedical materials. The process of SW interaction with a brain model was visualized by shadowgraph method and recorded by a high-speed video camera. The pressure history in a brain model was measured by a polyvinylidene fluoride needle hydrophone. The present experiment showed occurrence of complex wave front at specific location within the chamber and indicated the importance of understanding SW propagation effect when applying SW above certain overpressure. We will also summarize current research of complication of SW medical application and also bTBI.

1 Introduction

Shock waves (SW) have been applied to a variety of medical treatments. Recent studies have focused on applications within microenvironments, such as enhancing angiogenesis for the treatment of ischemic heart disease, chronic limb ischemia, cardiac/peripheral/cerebral emboli, and experimental application of SWs to enhance molecular transfer systems or target cells for cancer therapy. Although SWs are

A. Nakagawa (✉) · T. Kawaguchi · T. Tominaga
Department of Neurosurgery, Tohoku University Graduate School of Medicine, Sendai, Miyagi, Japan
e-mail: nakagawa@nsg.med.tohoku.ac.jp

K. Ohtani
Institute of Fluid Science, Tohoku University, Sendai, Miyagi, Japan

A. Sasoh et al. (eds.), *31st International Symposium on Shock Waves 2*,
https://doi.org/10.1007/978-3-319-91017-8_53

typically applied within the known limits of each organ or tissue injury threshold, several complications have been reported. The most common complications of SW treatment include hemorrhage secondary to vascular injury, pseudoaneurysm formation, arterial dissection, venous thrombosis, and pain. It is utmost important to understand the biological effect of SW for medical application [1].

Other urgent needs to understand the mechanism of biological effect of SW are issues related to blast-induced traumatic brain injury (bTBI). During past decades, TBI caused by blast is gaining much attention due to various problems observed among soldiers returning from Iraq and Afghanistan. TBI caused by explosive or blast events is traditionally divided into four phases: primary, secondary, tertiary, and quaternary blast injury. These phases of bTBI are biomechanically distinct and can be modeled in both in vivo and in vitro systems. The primary bTBI injury phase represents the response of brain tissue to the initial blast wave. Among the four phases of bTBI, there is a remarkable paucity of information about the mechanism of primary bTBI. On the other hand, 30 years of research on the medical application of SW has given us insight into the mechanisms of tissue in bTBI, including both air-mediated and underwater SW sources [2]. From a basic physics perspective, the typical blast wave consists of a lead SW followed by supersonic flow. The resultant tissue injury includes several features observed in primary bTBI, such as hemorrhage, edema, pseudoaneurysm formation, vasoconstriction, and induction of apoptosis, which are all well-described pathological findings within the SW literature.

In both situations, understanding of wave propagation of SW within cranium is critical though not understood sufficiently. Here, we will present preliminary results of investigation of propagation of SW in cranium model. We will also summarize the current medical application of SW and understandings of bTBI.

2 Methods

2.1 Shock Wave Induced Cranial Injury Model

For evaluating wave propagation and organs or tissue damage in cranium and brain model, we have applied microexplosive models which have been reported from our group [3]. SWs have been generated with the microexplosive AgN_3 weighing 10 mg attached to the tip of a 0.6-mm diameter quartz optical fiber and detonated by irradiation of Nd:YAG laser (neodymium:yttrium-aluminum-garnet laser; Laser Photonics Ltd. 1064 nm wavelength, 7 ns pulse width, and 20 mJ/pulse). The contribution of the laser energy to SW formation was negligible. The cranium was mimicked by acrylic cylinder (external diameter 24 mm, 1.5 mm thickness, 49 mm length), and the brain was mimicked by 20 wt% gelatin (Wako Junyaku, Co., Ltd.,).

2.2 Pressure Measurement

To monitor the focal pressure during the experiment, the transient pressure at the sidewall of the truncated ellipsoidal cavity was monitored using a polyvinylidene fluoride needle hydrophone (Muller Platte Gauge, Germany) with a 0.5-mm diameter sensing element, pressure range of −10 to 200 MPa, and rise time of 50 ns. These values are suited for temporally and spatially accurate pressure measurements. Measured data were stored and displayed on a digital oscilloscope (model DL 750; Yokogawa, Kyoto, Japan). The axial variation of pressures was measured in a series of preparatory experiments, and the dependence of the charge weight on the focus pressure was calibrated.

2.3 Visualization

The process of SW interaction with a brain model was visualized by shadowgraph method and recorded by a high-speed video camera. The experimental settings for visualization of SW propagation is developed using specially made acrylic chamber to contain the cell in the sterilized gelatin environment.

Schematic diagram of an experimental setup for SW interaction with the cranium and brain model is shown in Fig. 1.

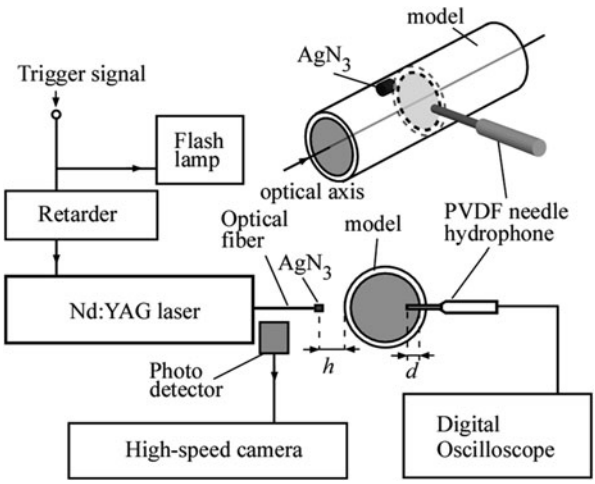

Fig. 1 Schematic diagram of an experimental setup for SW interaction with the cranium and brain model (left)

3 Results

Figure 2 shows that the spherical SWs generated within the gelatin layer repeat reflex and transmit, and the waves back to gelatin layer were organized as a whole as reflex wave accompanying multiple waves when SWs propagate in the vicinity of air in the gelatin-water-acrylic layer. The reflex wave is interfered by the pressure sensor placed immediately above the microexplosive. Figure 3 shows pressure history in the cranium and brain model.

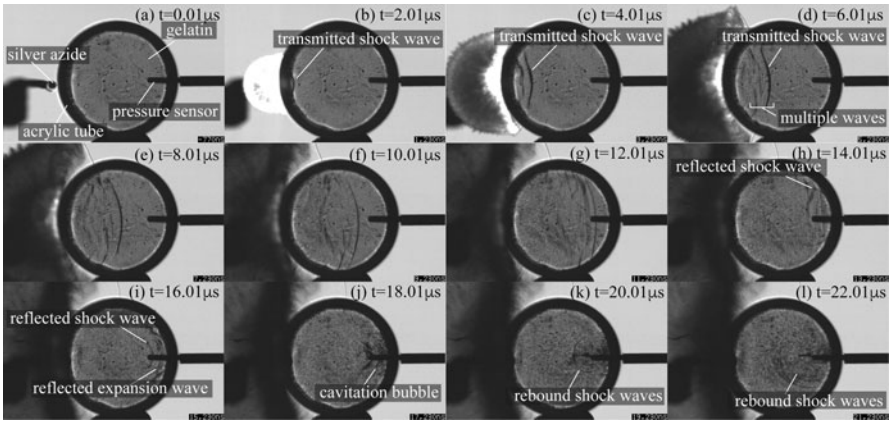

Fig. 2 Sequential shadowgraph images of microexplosive-induced SW interaction with the cranium and brain model ($h = 1$ mm, interframe time of 200 ns, exposure time 110 ns)

Fig. 3 Pressure history in the cranium and brain model

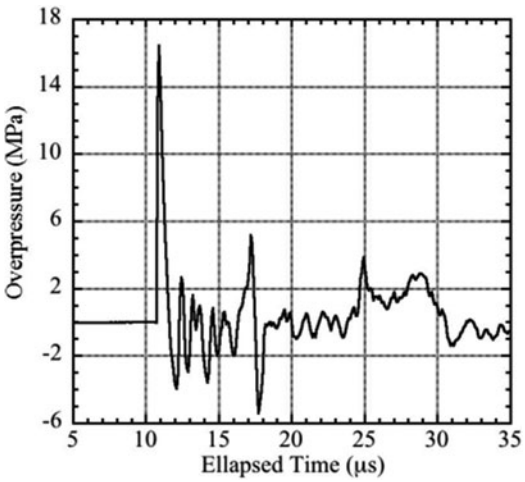

4 Discussion

The present experiment showed occurrence of complex wave front at specific location within the chamber mimicking the cranium. The effect of SWs on tissue can be divided roughly into direct effects (compression, shearing, and tensile stress) and indirect effects (shock/bubble interaction) [1, 4]. These effects are a function of the peak pressure (highest and lowest pressure found in an acoustic field for a particular extracorporeal SW lithotripsy unit and setting) [3, 4], rise time (a measure of how rapidly pressure changes from the ambient level to the maximum positive value and defined as the time required for pressure to increase from 10% to 90% of the maximum positive value) [4], pulse width (the amount of time pressure remains above a specified level, such as 50% of the peak positive pressure [full width at half maximum amplitude]) [4], impulse amplitude (the pressure integrated over time) [5], acoustic energy per pulse (equal to the product of pulse intensity integral taken at the position of peak positive pressure, cross-sectional area of the half-amplitude beam in the focal plane, and a constant that accounts for pressure nonuniformity across the area of the focal plane) [4], focal area (defined as cross-sectional area of the beam in the plane that contains the smallest of all beam cross-sectional areas of a lithotripsy acoustic field) [4], dose [6], and administration rate [7] of the wave profile. In addition, the "acoustic impedance" of each tissue along the SW propagation should be considered to understand the mechanisms of SW-induced tissue injury. Acoustic impedance represents an intrinsic property of matter in diagnostic ultrasonography. It is defined as the ratio of the acoustic pressure to the particle velocity, which reduces to the product of mass density, ρ, and the speed of sound, c, only for plane waves: $z = \rho c$, where z is the acoustic impedance. Acoustic impedance is important in ultrasonography and lithotripsy because of its role in the determination of the fraction of sound to be transmitted through an interface of dissimilar materials. However, it is important to note that SWs do not perfectly follow the theoretical behavior of linear acoustic waves.

SWs are generated using microexplosives [3]. In the absence of obstacles, the rapidly developing pressure waves of a free field SW expand uniformly outward in three dimensions from the center of the explosion [2]. The pressure profile shows a relatively simple rapid rise in pressure, followed by a fall in pressure. In contrast, the presence of obstacles results in a complicated propagation with multiple interferences and reflections. Both the pressure profile and the results of direct visualization illustrate how the complicated wave front cannot be characterized simply from the pressure profile. The complexity of wave propagation increases even more in a closed environment. Therefore, it is natural to assume that an analysis without the aid of such visualization and pressure measurements could be misleading, especially when analyzing the effect of a shock front on tissues. In the present experiment, complex wave front was observed at certain location which seemed to be derived from geometry of the container.

Due to the complex nature of SW effects on biological tissue, analyses require multidisciplinary approaches. At the same time, the collection of the biomechanical

and biological data underscores the limitations of the model. The impact of the shock front on the target, the transfer of the compression wave across the target, and the movement of this wave within the target are all affected by the size, geometry, and thickness of the target and also probably by the physical characteristics of the target including the container of the cells. In our previous study in rat model, we have applied mean underwater SW focus pressure of 1.0 ± 0.2 MPa and 12.5 ± 2.5 MPa. Former pressure range seems to represent mild injury (elongation of nucleus without apparent occurrence of hemorrhage and necrosis in the acute period), while the latter range seems to represent severe injury (formation of hemorrhage, necrosis surrounded by apoptosis in the acute period) histologically for underwater SW-induced brain injury [3]. Thorough histological investigation in animal model along with detailed measurement of pressure distribution would be necessary in the future study to understand this complex phenomenon.

5 Conclusion

We have developed experimental setup to evaluate SW propagation within cranium and interaction between the cranium and brain and found the complex interaction probably due to geometry of cranium.

References

1. M. Delius, Eur. Surg. Res. **34**, 30 (2002)
2. A. Nakagawa et al., J. Neurotrauma **28**, 1101 (2011)
3. K. Kato et al., J. Neurosurg. **106**, 667 (2007)
4. W.J. Davros et al., Radiology **178**, 397 (1991)
5. T. Kodama et al., Biophys. J. **79**, 1821 (2000)
6. M. Delius et al., Ultrasound Med. Biol. **14**, 117 (1988)
7. M. Delius et al., Ultrasound Med. Biol. **14**, 689 (1988)

Toward Noninvasive Drug Injection via Control of Laser-Induced Breakdown in Liquid

H. Ham, S. Yeo, H. Jang, and J. J. Yoh

Abstract A microjet with a maximum speed of 300 m/s and a diameter of 150 μm is ejected from a nozzle by the pulsed laser-induced bubble expansion. At every pulse of laser irradiation in the driving chamber, adverse air bubble growth has been a major issue in sustaining a uniform jet speed and overall performance of drug delivery. Here, a check valve is introduced to the drug chamber for controlling the flow dynamics inside and thus preventing ambient air from entering the nozzle. The newly designed valve in the laser-induced microjet injector proves that constant jet speed is possible regardless of the number of laser pulses, which allows the penetration of porcine skin to reach a depth well beyond 1.5–2.25 times the previously attained depths.

1 Introduction

Various types of drug injection devices have been applied as a method for parenterally administering a drug solution into the body in medical practices. A needle-type syringe is a method in which a needle is pierced into the skin for administering a piston-forced dose of drug from a syringe. Such a conventional needle-type syringe is simple in design and easy to use and has an advantage of quantitative administering of the targeted dose. However, such needle injection has been known to cause problems of painful procedure, infection and contamination due to wounds, and waste generation that arises from single use of needles [1].

In order to overcome such issues with the conventional approach, alternative methods such as needle-free injection capable of transdermal drug delivery have progressed in various notable ways. Of those methods, the laser-induced microjet relies on a high-speed injection of the drug dose into a target diameter of 150 μm [2].

H. Ham · S. Yeo · H. Jang · J. J. Yoh (✉)
Seoul National University, Seoul, South Korea
e-mail: jjyoh@snu.ac.kr

A. Sasoh et al. (eds.), *31st International Symposium on Shock Waves 2*,
https://doi.org/10.1007/978-3-319-91017-8_54

Unlike the bubbles generated by the laser irradiation in the driving chamber, the growing air bubbles in the lower drug chamber are unfavorable because the performance efficiency and penetration effect of the injector are greatly reduced with increasing air inflow into the nozzle. With increasing number of laser pulses and thus ejections from the nozzle, the adverse growth of air bubble inside the drug chamber is significant, which makes it practically impossible to use after multiple pulses of laser irradiation for medicine application, for instance.

Therefore, the present study is aimed at achieving a maximum efficiency of repeated microjet performance via removing the air bubbles in the drug chamber. Specifically, the present study is focused on maintaining the injection performance of the microjet and the penetration of the skin irrespective of repetition of injection. Specifically, the penetration depth should be kept constant with repeated injections. A ball check valve is designed and introduced for restrain of unfavorable condition encountered by the surrounding environment. In short, the present device provides a repetitive microjet injection that enables a drug solution equal to the amount of injected drug to be automatically replenished from the drug reservoir.

2 Materials and Methods

Shown in Fig. 1 is the microjet injector that is composed of an upper pressure chamber and the lower drug chamber with a side opening to a drug reservoir. An elastic membrane separates the drug from an upper driving liquid chamber. An

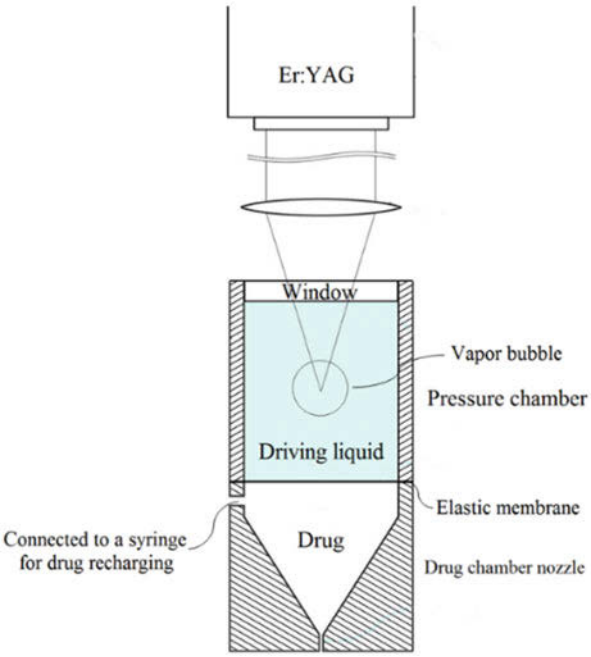

Fig. 1 Schematics of the microjet injector

Er:YAG laser is used to generate vapor bubbles inside the driving chamber, with a pulse duration of 150 μs and a wavelength of 2.940 μm.

2.1 Microjet Generation from a Micro Nozzle

Inside the microjet injector as described, the driving force of expanding the elastic membrane is due to the explosive vapor bubble growth upon laser irradiation in the driving chamber. Subsequently, per a laser pulse, the membrane expands toward lower drug chamber, causing a narrow microjet to exit through a nozzle of 150 μm in diameter.

2.2 A Ball Check Valved Nozzle

As shown in Fig. 2, the lower drug chamber is divided into two parts: upper drug chamber in contact with the elastic membrane and lower drug chamber designed with a ball check valve. The valve opens when the drug is ejected out of the nozzle. When the pressure inside the driving chamber is lowered, the check valve closes, and such the lower drug chamber is sealed without being affected by the atmospheric pressure outside the nozzle. The bearing ball has a diameter larger than the diameter of the connecting neck between the upper and lower drug chamber for automatic open-close actuation. The spring supports the valve motion.

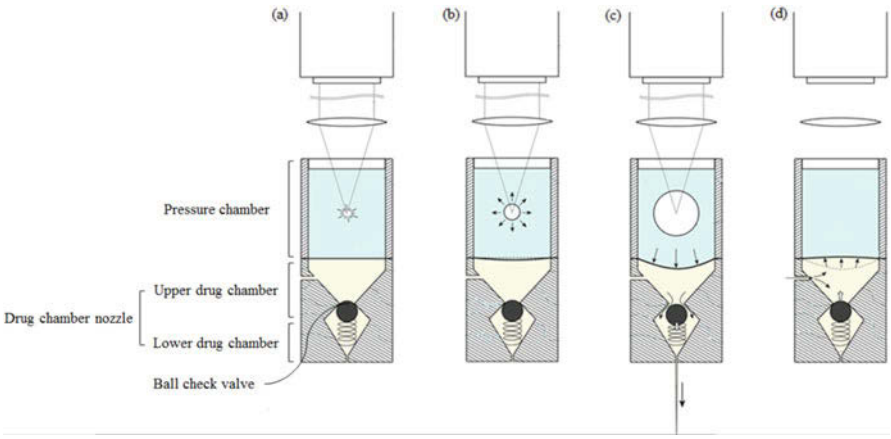

Fig. 2 Schematic of automatic injector utilizing a ball check valve. (**a**) A laser beam is irradiated in a driving chamber; (**b**) Laser-induced breakdown causes vapor bubble growth; (**c**) Valve opens and drug flows out of the nozzle; (**d**) Restoring membrane causes valve closure and prevents backflow of the air from outside ambient

2.3 Materials and Tissues

In order to illustrate the stable performance of the newly designed injector, a porcine skin is used which has the ultimate tensile strength of 10–30 MPa and 20–30 μm of stratum corneum thickness. Ultimate tensile strength of human skin is 2–15 MPa, which is less than that of pig skin treated in this study [3, 4]. The treated tissue samples are fixed in a 10% formaldehyde solution and then embedded in paraffin. The samples are sliced and stained with H&E (hematoxylin and eosin) dye. The cross-sectional view of the skin is taken by the photomicroscope (Axiophot).

3 Results and Discussion

Figure 3 shows jet velocity against the number of microjet ejection. Automatic corresponds to the injector with the ball check valve. Conventional injector showed the initial jet speed of 140 m/s, which then decreases to 20 m/s at about 400 microjet ejected. On the other hand, the automatic injector showed remarkable jet speed of 140 m/s and sustained throughout the repeated jet ejections up till 600 shots. This notable improvement is mainly due to the fact that air does not enter into the nozzle during the restoring motion of the elastic membrane after a single pulse of the laser.

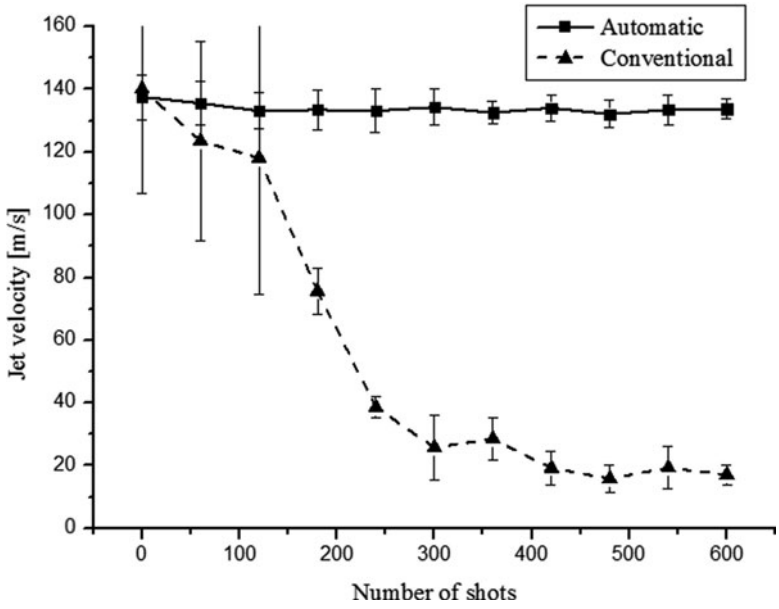

Fig. 3 Measured jet speed with respect to the number of microjet ejection

Table 1 Comparison drug penetration depth in the stratum corneum of porcine skin in cross-sectional images

Time [μs]	3	5	7	9	11	13	15	20
New								
Old						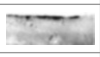		
Scale								

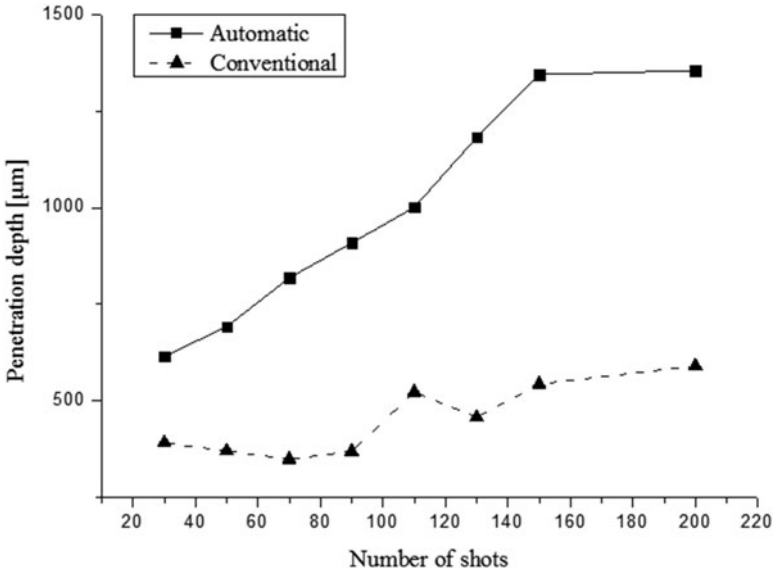

Fig. 4 Measured drug penetration depth in the stratum corneum of a porcine skin

Table 1 shows timed image showing the drug penetration in the stratum corneum of a porcine skin. The slope represents penetration efficiency, and each slope of both cases shows a different tendency in Fig. 4. This result proves that reliable injection performance can be achieved with the automatic injector.

Shown in Fig. 5a is a tree image as tattooed on to the porcine skin. To verify the penetration depth, the cross-sectional photomicroscope view of the porcine skin is captured by formalin-fixed paraffin-embedded (FFPE) method. Shown in the Fig. 5b is a porcine dermis, dyed in H&E (hematoxylin and eosin). The microjet penetration depth is approximately 672.98 ± 87.14 μm under the dermis layer.

In summary, the successful applications of the microjet in porcine skin are considered. The advancement in the microjet performance was attained via the newly designed injector that utilizes a ball check valve.

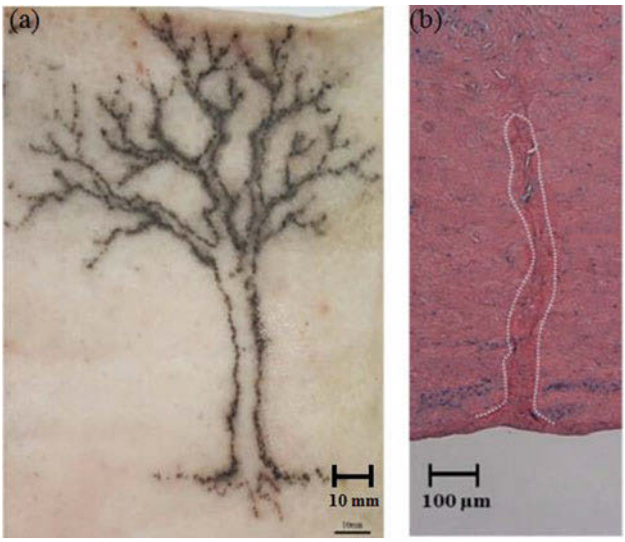

Fig. 5 Tattooed images of porcine skin, (**a**) Tree and (**b**) Penetrated depth

Acknowledgments Authors wish to acknowledge the financial supports from SNU Brain Fusion Program 2015 and National Research Foundation under NSL Program 2014 through IOER and IAAT at Seoul National University. Many valuable discussions with Prof. Cheol-Woong Sim of College of the Fine Arts and Prof. Woo-Cheol Lee of School of Dentistry are thankfully acknowledged.

References

1. C.A. Trépanier et al., Risk of cross-infection related to the multiple use of disposable syringes. Can. J. Anaesth. **37**, 156 (1990)
2. M. Park et al., Er:YAG laser pulse for small-dose splashback-free microjet transdermal drug delivery. Opt. Lett. **37**, 3894 (2012)
3. H. Khatam et al., Dynamic tensile characterization of pig skin. Acta Mech. Sinica **30**, 125 (2014)
4. J.A. Gallagher et al., Dynamic tensile properties of human skin. IRCOBI Conf. Proc. **12**, 59 (2012)

Current Trend in Cell Membrane Manipulation by Ultrasound and Underwater Shock Wave

S. F. Moosavi-Nejad and H. Hosseini

Abstract The paper presents our recent findings in reparable cell membrane manipulation by ultrasound and underwater shock wave. We introduced innovative in vitro methods including free suspension and capillary micro-gripping systems equipped with micro transducers to achieve the maximum level of experimental flexibility for capturing real-time highly magnified images of cell-microbubble interactions. Insonation of single cells and microbubbles parallel with high-speed microphotography and fluorescence microscopy allowed us to identify dynamic responses of cell membrane to microbubble streaming dynamics in correlation with sonoporation. Our results showed that bubble oscillation in close contact with the cell membrane can cause local deformation and transient porosity in the cell membrane with minimum cell toxicity.

1 Invited Presentation

Gene therapy has been one of the greatest challenges in biotechnology. Despite decades of worldwide research, it has seen only limited success rate [1]. Today, there is an urgent need to develop novel molecular delivery techniques with high transfection rates that are being less affected by the cell heterogeneity, have low cost, and avoid development of resistance mechanisms.

The crucial task for any method of gene transfection would be breaking through the cell membrane. In eukaryotic cells, the cell membrane is an essential feature of a cell, which regulates the movement of substances in and out of cells and separates them from surrounding medium. This selective permeable phospholipid

S. F. Moosavi-Nejad
Bioelectrics Department, Institute of Pulsed Power Science, Kumamoto University, Kumamoto, Japan

H. Hosseini (✉)
Bioelectrics Department, Institute of Pulsed Power Science & Graduate School of Science and Technology, Kumamoto University, Kumamoto, Japan
e-mail: hosseini@kumamoto-u.ac.jp

A. Sasoh et al. (eds.), *31st International Symposium on Shock Waves 2*,
https://doi.org/10.1007/978-3-319-91017-8_55

bilayer forms stable contacts with cytoskeletal proteins. Cytoskeleton-membrane interaction controls cellular functions such as cell motility, morphology, and intracellular transportation. It also provides the mechanical support and strengthens the plasma membrane. Understanding the role of cellular structures, specially cell cytoskeleton and their role in protecting the cell membrane, will prove vital for those techniques focused on the introduction of unauthorized molecules into the cell without damaging its viability [2].

Among different stimuli (biological, chemical, or physical), physical stresses are of particular interest, as they can transiently increase the permeability of the cell membrane. Recent progress in nanosecond duration ultrahigh voltage pulses provides exciting possibilities for the direct cell manipulation over conventional electroporation [3]. Meanwhile, we have been using ultrashort pulses to generate fine micro underwater shock waves, which can penetrate deep in soft tissue [4]. This unique characteristic makes them appropriate for delivering mechanical energy for DNA/drug and cancer ablation [5].

On the other hand, ultrasound and shock wave compare favorably with the other most popular physical methods for gene/drug transformation. Ultrasound and shock wave can be applied through totally noninvasive procedures taking advantage of focusing in soft tissue. This gives an enormous advantage to ultrasound and shock wave not only for in vitro and in vivo gene/drug delivery but also for clinical therapy [6]. The direct effects of low-intensity ultrasound differ from those produced by inertial/nonlinear cavitation caused by high-intensity ultrasound (HIFU) and shock wave focusing. While high-intensity ultrasound and focused shock wave cause irreversible damage by cavitation, low-intensity ultrasound when combined with microbubbles can temporally increase the cell membrane permeability without cell killing resulted from induced shear stress over the cell membrane [1, 2]. Our recent progress in micromanipulation of cell membrane by oscillating micro-/nanobubbles provides exciting possibilities for localized/adjustable DNA/drug delivery for variety of biological targets, which are presented during the lecture.

References

1. S. Moosavi-Nejad, S.H.R. Hosseini, H. Akiyama, K. Tachibana, Reparable cell sonoporation in suspension: Theranostic potential of microbubble. Theranostics **6**(4), 446–455 (2016)
2. S. Moosavi-Nejad, S.H.R. Hosseini, H. Akiyama, K. Tachibana, Optical observation of cell sonoporation with low intensity ultrasound. Biochem. Biophys. Res. Commun. **413**, 218–223 (2011)
3. S. Moosavi-Nejad, S.H.R. Hosseini, Current trends in bioelectrics for reversible cell membrane manipulation, comment on “physical methods for genetic transformation of fungi and yeast”. Phys. Life Rev. **11**, 212 (2014)
4. V. Menezes, H. Hosseini, S. Moosavi-Nejad, K.J. Irimpan, H. Akiyama, Motion of free-surface of shock-compressed water on emergence of rarefaction. Appl. Phys. Lett. **107**, 143701 (2015)

5. H. Hosseini, S. Moosavi-Nejad, H. Akiyama, V. Menezes, Shock wave interaction with interfaces between materials having different acoustic impedances. Appl. Phys. Lett. **104**, 103701 (2014)
6. S. Moosavi-Nejad, H. Takahashi, H. Hosseini, A. Watanabe, H. Endo, K. Narihira, T. Kikuta, K. Tachibana, Acute effects of sono-activated photocatalytic titanium dioxide nanoparticles on oral squamous cell carcinoma. Ultrason. Sonochem. **32**, 95–101 (2016)

Analysis of Deformation Process of a Bubble in an Elastic Capsule by Shock Waves and Their Medical and Biological Applications

M. Tamagawa, T. Imakado, and R. Ogasahara

Abstract This paper describes culture regeneration system combining cultivation promotion and capsule destruction using shock wave, especially the basic mechanism for its development such as deformation process of a bubble in a microcapsule composed of membrane, liquid, and gas bubble. Necessary tasks to optimize the improvement of cell culture rate and the microcapsule disintegration rate by pressure control are (1) investigation of the influence of amount of gas bubbles and pressure waveform on the threshold of capsule destruction due to bubble collapse and (2) estimation of threshold of pressure for the collapse. It is concluded that (1) maximum amplitude of bubble, which corresponds to the degree of damage, is decreasing as the gas ratio is increasing, and (2) maximum amplitude of bubble is also decreasing as the duration time becomes smaller order.

1 Introduction

Recently the shock wave phenomenon in biological tissue cells has been applied to extracorporeal shock wave lithotripsy (ESWL) treatment, osteoplasty surgery, or various medical techniques. As for development of advanced medical technology, micro-/nano-fluidics is an efficient tool for dealing them. It is necessary to know the fundamental mechanisms of the fluidics as the scale becomes smaller [1–3]. Especially controlling deformation and collapsing of a bubble is also one of the most expected topics in the medical fields.

We have proposed drug delivery systems (DDS) using shock waves and microcapsules including bubbles [4, 5]. In our previous investigations, the relations between the elasticity of capsule membrane and the probability of disintegration of membrane by shock wave are clarified, and deformation of a bubble inside capsule is large compared with the proper parameters such as gas ratio and thickness.

M. Tamagawa (✉) · T. Imakado · R. Ogasahara
Graduate School of Life Science and Systems Engineering, Kyushu Institute of Technology, Kitakyushu, Japan
e-mail: tama@life.kyutech.ac.jp

A. Sasoh et al. (eds.), *31st International Symposium on Shock Waves 2*,
https://doi.org/10.1007/978-3-319-91017-8_56

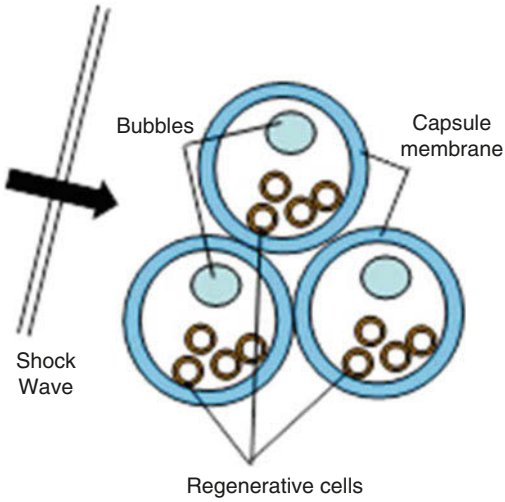

Fig. 1 Structure of microcapsules including gas bubbles and cells

On the other hand, in the field of regenerative medicine, regenerating cells and tissues efficiently and quickly is an important problem, but development of devices for efficient cell proliferation has not progressed sufficiently. In order to solve these problems, a method for efficiently progressing from an initial cell to a small-scale tissue formation is required. To solve this problem, a culture regeneration system combining acceleration of cultivation and capsule destruction using shock waves has been proposed (Fig. 1) [5]. In the system, shock waves are applied to bubble-encapsulated microcapsules, and they stimulate cells and destroy capsules at the same time (Fig. 2), and cells in the capsules are cultured for regenerative medicine.

Concerning about cell stimulation and capsule destruction, which are important parts of this system, there are complicated phenomena such as shock wave in the micro-region, bubble deformation behavior, and microjet. So the control method of the pressure wave is not sufficiently known except clinical data.

In this newly proposed system, necessary tasks to optimize the cell culture rate improvement and the microcapsule disintegration rate by pressure control are (1) investigation of the influence of amount of gas bubbles and pressure waveform on the threshold of capsule destruction due to bubble collapse and (2) estimation of threshold of pressure for the collapse. In particular, a mathematical model analysis of the relative size (gas/liquid ratio) of gas bubbles in microcapsules is done for evaluating above points.

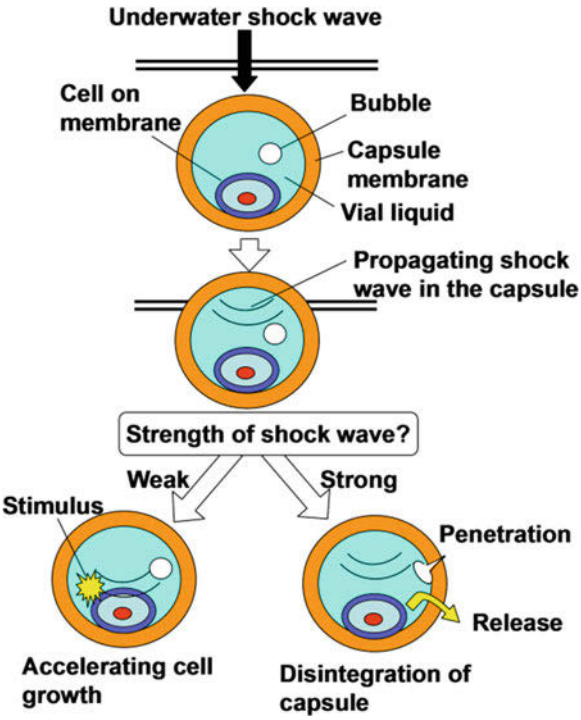

Fig. 2 Concept of new culture regeneration system

2 Analysis of a Bubble Deformation Process Using Gas Ratio and Duration

As for microcapsules of this system, important design factors for preparing capsules include the elasticity of the capsule membrane, the ratio of the capsule diameter to the bubble diameter, and the membrane thickness. The gas/liquid ratio obtained by dividing the gas diameter by the liquid diameter is picked up as a parameter.

In the previous investigations, to investigate the influence on the destruction of internal bubbles and capsule structure, observations of disintegration by using microscope were done [4]. In the experiments, pressure waves were applied to bubble-encapsulating microcapsules by a piezoelectric element, and the motion of the capsule and bubble deformation were taken by a high-speed CCD camera. By changing the frequency and pressure amplitude of the sinusoidal pressure wave and the sawtooth pressure wave using the gas/liquid ratio as the structural parameter, the deformation behavior of the average amplitude of the contained bubbles to find the threshold leading to the rupture is investigated. In this experiment, maximum pressure is about 0.8 MPa; MI (mechanical index) is 1.4 with sinusoidal wave of 414 kHz.

Figure 3 shows the typical deformation process in case of capsule damage. Figure 3a indicates initial status, and Fig. 3b indicates the status under the worked

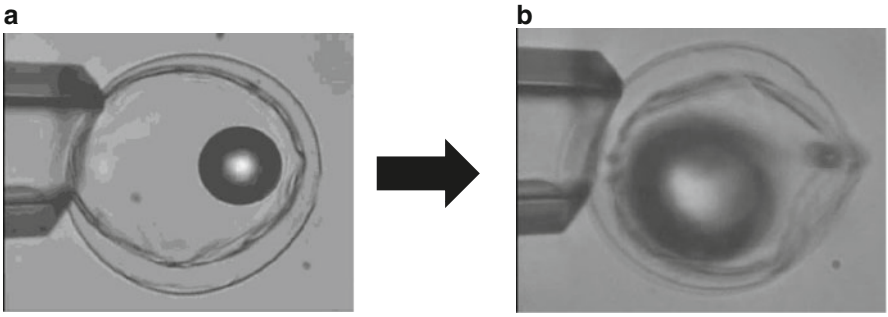

Fig. 3 Typical deformation process of a bubble in the capsule. (**a**) Initial bubble. (**b**) Microjet

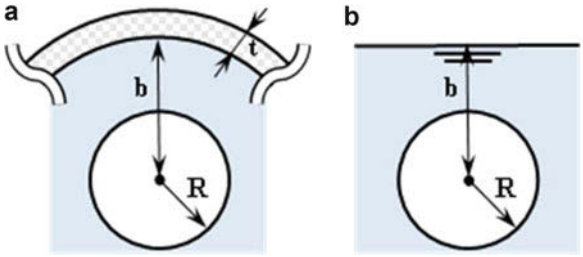

Fig. 4 Mathematical model of bubble oscillation in the capsule [5]. (**a**) A bubble in a microcapsule. (**b**) Simplified free surface model

pressure wave. The microjet can be found in Fig. 3b because the large deformation of the membrane can be found.

To investigate the effects of gas ratio on amplitude of bubble oscillation, the simplified mathematical model of bubble oscillation is constructed. In this model, elastic wall assumed to be free surface. Assuming that the curvature of capsule wall is small compared with bubble, oscillation of a bubble near free surface is modeled to be oscillation of a bubble in an elastic capsule as shown in Fig. 4.

As for the equations of bubble deformation process and motion, two variables are needed. One is radius of a bubble, and the other is distance from the free surface shown in Fig. 4. By using Lagrangian equations with the variable of radius and distance from the surface, the momentum equations for these variables are derived as follows [5]:

$$\ddot{R} = \frac{1}{R\left[1-\left(\frac{R}{2b}\right)\right]}\left\{ -\frac{1}{2}\left[3-4\left(\frac{R}{2b}\right)\right]\dot{R}^2 - \frac{7}{2}\left(\frac{R}{2b}\right)^2 \dot{R}\dot{b} + \frac{1}{4}\dot{b}^2 + \frac{1}{\rho}\left[P_0\left(\frac{R_0}{R}\right)^{3\kappa} - P_\infty - \frac{2\sigma}{R} - 4\mu\frac{\dot{R}}{R}\right]\right\} \tag{1}$$

$$\ddot{b} = \frac{1}{R\left[1-\left(\frac{R}{2b}\right)\right]}\left\{ \frac{33}{2}\left(\frac{R}{2b}\right)^2 \dot{R}^2 - 3\left[1-\left(\frac{R}{2b}\right)\right]\dot{R}\dot{b} + \frac{4}{3}\left(\frac{R}{2b}\right)^2 \dot{b}^2 + \frac{3}{\rho}\left[P_0\left(\frac{R_0}{R}\right)^{3\kappa} - P_\infty - \frac{2\sigma}{R} - 4\mu\frac{\dot{R}}{R}\right]\right\} \tag{2}$$

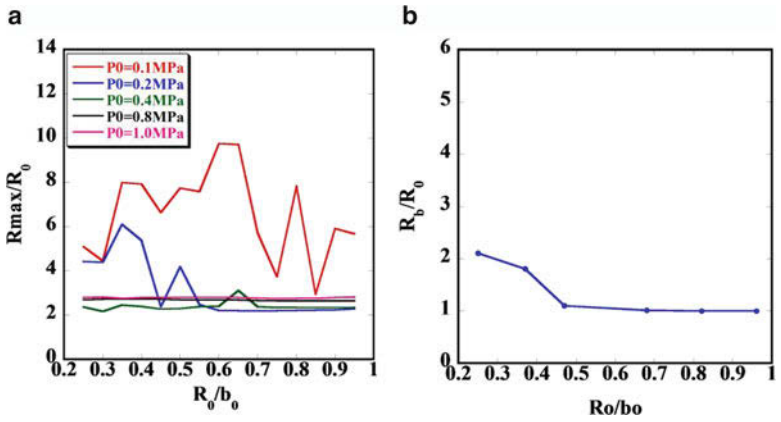

Fig. 5 Comparison of maximum amplitude of bubble deformation between mathematical model and experiment. (**a**) Mathematical model. (**b**) Experiment

where b is distance from the surface, R is bubble radius, R_0 is initial bubble radius, P_∞ is working pressure, P_0 is initial internal pressure, σ is surface tension, κ is heat capacity ratio, and b_0 is initial bubble distance from the surface. In this model, we deal the gas ratio of the present bubble as $d_g/d_l = R_0/b_0$. The amplitude of bubble oscillation $R_{\max}/R_0$ is obtained by calculating the above Eqs. (1)–(2). In this calculation, the working pressure is assumed to be the same sinusoidal wave as experimental one (414 kHz).

Figure 5a shows the relation between gas ratio and maximum amplitude of bubble oscillation with changing initial internal pressure. From this result, it is found that maximum amplitude of bubble is mostly decreasing as the gas ratio d_g/d_l is increasing. This trend is almost the same in case of higher internal pressure. Figure 5b shows the previous experimental results in case of initial internal pressure 0.2 MPa. So the calculation result corresponds to the result of experimental one. It is also found that the amplitude is decreasing as the initial internal pressure is increasing when the gas ratio is the same.

To investigate the effects of waveform, especially duration time of sawtooth wave, on the maximum amplitude, the duration time shown in Fig. 6a is used for these calculations. Assuming that the pressure wave for cell stimulation is preferred to have small duration time because of its low possibility of disintegration, duration time 1 ns and 1 ps are used in the calculation.

Figure 6b, c shows maximum amplitude of bubble oscillation near free surface by working sawtooth wave with duration $\tau_{L.}$ From these results, it is clearly found that maximum amplitude of bubble is also decreasing as the duration time such as ps becomes smaller for every gas ratio. In the next step, it is necessary to consider the effects of these constraint conditions such as surface curvature and elasticity of the membrane.

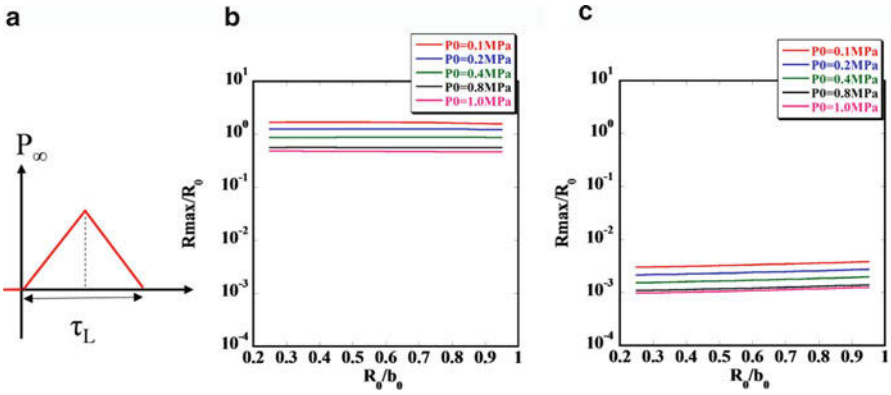

Fig. 6 Maximum amplitude of bubble oscillation near free surface by working sawtooth wave with duration $\tau_{L.}$ (**a**) Tooth wave with duration $\tau_{L.}$ (**b**) Maximum amplitude with gas ratio in case of $\tau_L = 1$ ns. (**c**) Maximum amplitude with gas ratio in case of $\tau_L = 1$ ps

3 Conclusions

In this paper, to optimize the improvement of cell culture rate and the microcapsule disintegration rate by pressure control, the influence of amount of gas bubbles and pressure waveform on the threshold of capsule destruction due to bubble collapse was investigated, and the following things are concluded:

1. Maximum amplitude of bubble is decreasing as the gas ratio is increasing; this amplitude corresponds to the degree of damage.
2. Maximum amplitude of bubble is also decreasing as the duration time such as ps becomes smaller.

For further investigations, the focused femtosecond pulse laser will be applied for this stimulation of cells.

References

1. A. Hashmi, G. Heiman, G. Yu, M. Lewis, H.J. Kwon, J. Xu, Microfluid. Nanofluid. **14**, 591–596, 10404-012-1077-5 (2012)
2. J.O. Kwon, J.S. Yang, S.J. Lee, K. Rhee, S.K. Chung, J. Micromech. Microeng. **21**, 11 (2011)
3. K. Matsumoto, I. Ueno, J. Phys. Conf. Ser. **147**, 012015 (2009)
4. M. Tamagawa, in *Proceedings of IMECE2011 ASME International Mechanical Engineering Congress*, Houston, Texas, IMECE2011-80697 (2011)
5. M. Tamagawa, in *Proceedings of IMECE2015 ASME International Mechanical Engineering Congress*, Houston, Texas, , USA, IMECE2015-52184 (2015)

Shock Waves Can Cure Biofilm Infections In Vivo in Combination with Antibiotics

Akshay Datey, Divyaprakash Gnanadhas, Dipshikha Chakravortty, and Gopalan Jagadeesh

Abstract Shock waves are essentially non-linear waves that propagate at supersonic speeds. Any sudden release of energy will result in the formation of shock waves. In this study, we have shown for the first time that catheter, skin and lung biofilm infections can be treated using shock waves combined with antibiotics. Many bacteria secrete a highly hydrated framework of extracellular polymer matrix on encountering suitable substrates and embed within the matrix to form a biofilm. Bacterial biofilms are observed on many medical devices and on epithelial and endothelial surfaces during infection. For endocarditis, periodontitis and lung infections in cystic fibrosis patients, biofilms are an important mode of growth. Bacteria within the polymeric hydrogel matrix are protected from antibiotics, and antibiotic concentration of more than 1000 times of the MIC may be required to treat these infections. Here, we have demonstrated that shock waves can be used to remove *Salmonella*, *Pseudomonas* and *Staphylococcus* biofilms in urinary catheters. The studies were extended to a *Pseudomonas* chronic pneumonia lung infection model and *Staphylococcus* skin suture infection model in mice. The biofilm infections in mice, treated with shock waves, became susceptible to antibiotics, unlike untreated

A. Datey
Centre for Biosystems Science & Engineering, Indian Institute of Science, Bangalore, India

Department of Microbiology & Cell Biology, Indian Institute of Science, Bangalore, India

Department of Aerospace Engineering, Indian Institute of Science, Bangalore, India

D. Gnanadhas
Department of Microbiology & Cell Biology, Indian Institute of Science, Bangalore, India

Department of Aerospace Engineering, Indian Institute of Science, Bangalore, India

D. Chakravortty
Centre for Biosystems Science & Engineering, Indian Institute of Science, Bangalore, India

Department of Microbiology & Cell Biology, Indian Institute of Science, Bangalore, India

G. Jagadeesh (✉)
Centre for Biosystems Science & Engineering, Indian Institute of Science, Bangalore, India

Department of Aerospace Engineering, Indian Institute of Science, Bangalore, India
e-mail: jaggie@aero.iisc.ernet.in

A. Sasoh et al. (eds.), *31st International Symposium on Shock Waves 2*,
https://doi.org/10.1007/978-3-319-91017-8_57

biofilms. Mice exposed to shock waves responded to ciprofloxacin treatment, while ciprofloxacin alone was ineffective in treating the infection. These results clearly demonstrate for the first time that shock waves, combined with antibiotic treatment, can be used to treat biofilm formation on medical devices as well as in situ infections.

1 Introduction

Shock waves are discontinuities travelling at supersonic speeds that are characterized by an abrupt change in pressure, temperature and density. They are generated in nature whenever the different elements in a fluid approach one another with a velocity higher than the local speed of sound at the present temperature. The unique character has widened the landscape of shock wave applications. Shock waves initially utilized in Aerospace research have found importance in bioengineering where extracorporeal shock waves are used as a noninvasive therapy in lithotripsy and wound healing and for treating avascular necrosis [1–3]. Previously we have used shock waves for vaccination and bacterial transformation [4–6]. A few reports suggest that laser-generated and extracorporeal shock waves can cause damage to the biofilm in vitro [7, 8]; however, the effects of shock waves on biofilms and the use of these shock waves as a therapy have not been reported. It is now recognized that many infections are initiated from biofilms [9, 10]. The US Centers for Disease Control and Prevention and National Institutes of Health have estimated that between 65% and 80% of infections are caused from biofilms [11]. A biofilm is an accumulation of microorganisms embedded in a polysaccharide matrix that is adherent to a solid biologic or non-biological surface [9, 10]. Bacteria contained within biofilms show resistance to antibiotics that is non-intrinsic. When the bacteria are released from the biofilm for planktonic growth, these same bacteria may be inherently sensitive to concentrations 1000–10,000-fold less than those required to kill bacteria contained with the biofilm [12]. This resistance is thought to be a consequence of the growth state of the bacteria and/or penetration of the antibiotic into the organisms most adjacent to the surface on which the film is growing [10].

Biofilms can be formed on most medical devices including urinary catheters, central venous catheters, peritoneal dialysis catheters, intrauterine devices, endotracheal tubes, prosthetic joints, voice prosthesis, mechanical heart valves and pacemakers [13–16] by a wide variety of bacteria including *Escherichia coli*, *Pseudomonas aeruginosa and Staphylococcus aureus*. Contamination of the indwelling device usually occurs after insertion [17]. Many pathogenic bacteria can biofilm in or on tissues; these in situ biofilms cause inflammation and tissue damage [18]. These biofilms may form on tonsils [19] and on respiratory tract surfaces, e.g. the paranasal sinuses [20]. Planktonic bacteria released from these biofilms can intermittently or continually disperse to cause chronic infections, or infections at sites distal to the biofilm. Here, we have successfully demonstrated the use of two different shock wave generators for the disruption of biofilms formed in vitro as well as in vivo conditions. The biofilms formed by *Salmonella*, *Pseudomonas* and *Staphylococcus* on urinary catheter surfaces have been exposed to shock waves produced by a hand-

held device. A diaphragmless shock tube has been used for in vivo treatment of *Pseudomonas* lung infection in mice. This is the first time an in vivo study of shock wave treatment of biofilms has been presented. The shock waves generated for the in vivo study have low amplitude and are repeatable. The studies show that, in combination with antibiotic therapy, shock waves have the potential to reduce the medical impact of lung and skin infections caused by bacteria.

2 Results

2.1 Biofilm Formation

Biofilms were grown on different substrates including plastic tubes and urinary catheters, using Gram-positive and Gram-negative bacteria including *Salmonella enterica serov*ar Typhimurium (*S.* Typhimurium), *Pseudomonas aeruginosa* and *Staphylococcus aureus*. Biofilm formation was validated using CV assay and scanning electron microscopy (Figs. 1 and 2).

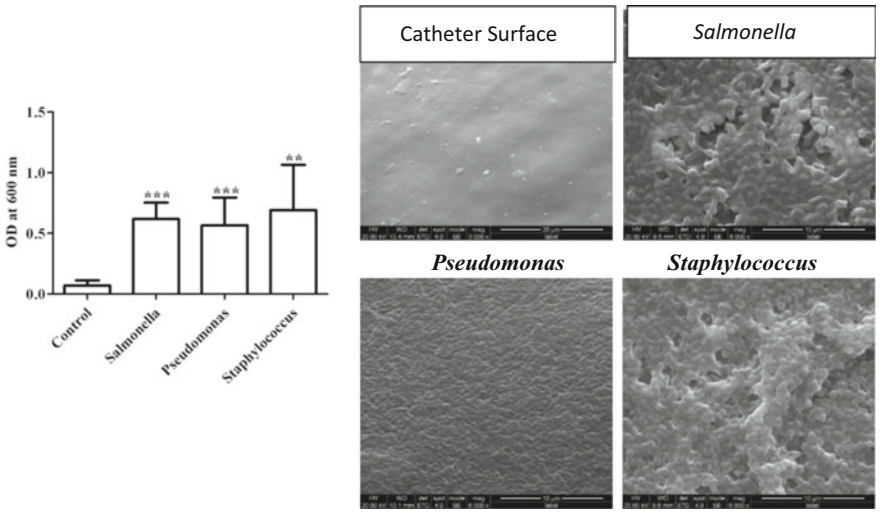

Fig. 1 Biofilm formation on urinary catheters

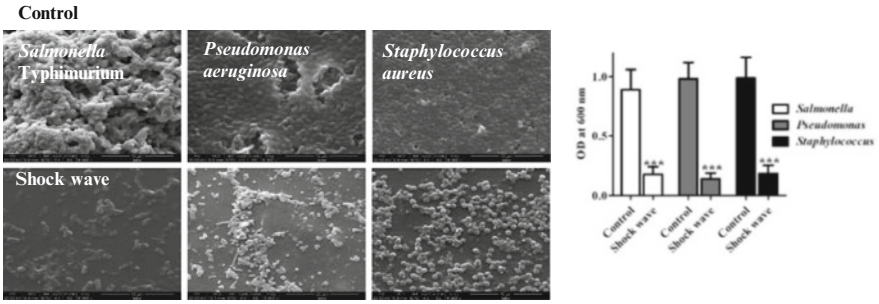

Fig. 2 Effect of shock waves on biofilm formation

2.2 Use of Shock Waves to Reduce Biofilm-Mediated Infection In Vivo

2.2.1 *P. aeruginosa* Pneumonia Model

The extracorporeal shock waves generated using the hand-held shock wave generator are of high energy and are localized to a small area. Performing in vivo studies using the same device that might cause tissue damage is possible. This holds good even for other devices that are used to generate shock waves for biological applications, like lithotripters. Therefore, for the in vivo studies, we have used diaphragmless shock tube (DST) which generates low-energy shock waves, and the area of impact is larger so as to expose the entire body of the mouse to shock waves [22]. A conventional shock tube is a simple device having two sections, a driver section and driven section, separated by a metal diaphragm. In the case of DST, the metal diaphragm is replaced by a pneumatic cylinder (Fig. 3). The use of a pneumatic cylinder in place of metal diaphragms reduces the time between successive runs as it does not require the replacement of a metal diaphragm for every run. Using the diaphragmless shock tube, shock waves of required strength (even as low as 0.8 bars over pressure which is required for our experiment) can be generated with high repeatability (Fig. 3). Mice were housed in a perforated chamber that is mounted with an L-shaped bend at the end of the shock tube (Fig. 4). The L-bend prevents the animals from entering into the shock tube. Also, the perforated chamber ensures that there are no reflections of the incident shock wave. The shock wave travelling through the L-shaped bend undergoes an attenuation of approximately 30% in strength [23, 24]. The various parameters of this shock tube are shown in the table. For the biological experiments, the diaphragmless shock tube was operated with a driver section pressure (P4) of 5 bars and driven section (P1) kept at atmospheric pressure (1 bar). The pressure jump obtained behind the shock wave (P2) was∼0.8 bar at the end of the shock tube with high repeatability. This pressure is measured at the end of the shock tube before the L-shaped bend. The energy contained in the incident shock wave is calculated using the method suggested

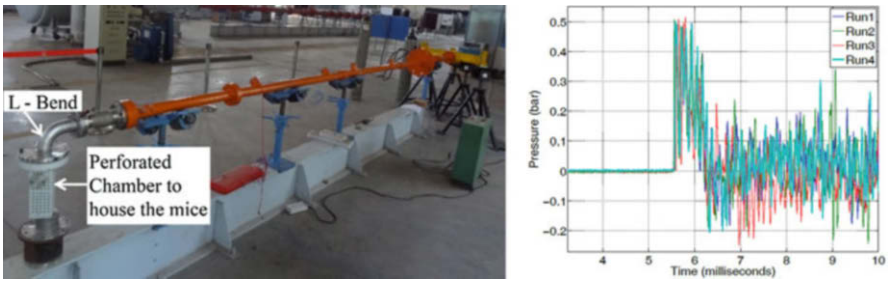

Fig. 3 The diaphragmless shock wave generator and the pressure profile

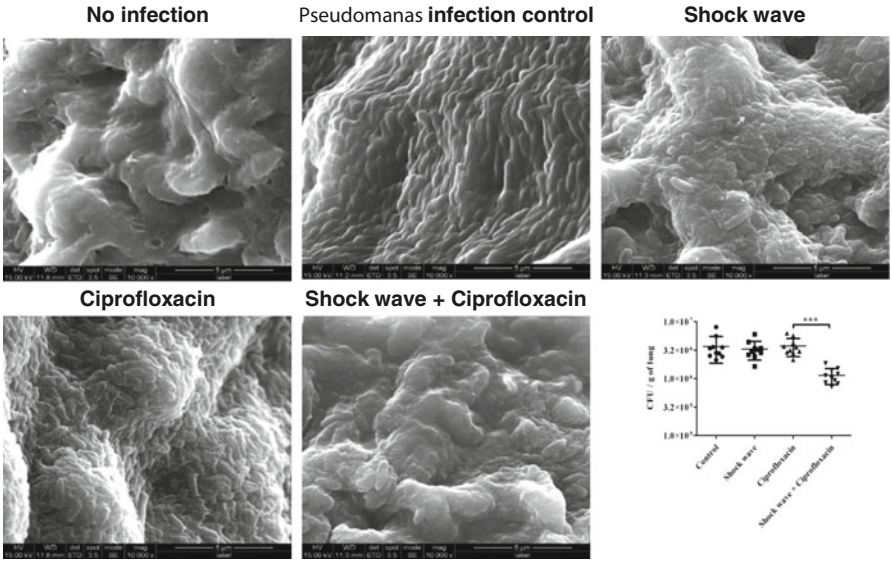

Fig. 4 Use of shock wave adjunct therapy in the treatment of murine *P. aeruginosa* lung infection

by Wang et al. [25]. The energy in the incident shock wave is calculated to be 205 mJ/mm^2. The mice in the perforated chamber experienced a peak overpressure of 0.48 bar. A specific impulse of 18.21 Pa.s/m^2 was felt by the mice in the chamber which is calculated by finding the area under the curve.

Mice that were infected intranasally with *P. aeruginosa* were treated with ciprofloxacin alone, with shock waves alone, or with a combination of shock wave and ciprofloxacin for 3 days. The mice were killed after 3 days of treatment, and the effect of treatment on the lung tissue was examined by SEM (Fig. 4), and the number of bacteria in lung homogenates determined by viable count (Fig. 4). Though the number of bacteria observed in SEM of tissues from mice treated with shock waves alone (Fig. 4) was greatly reduced compared with control mice, there was no reduction in the number of bacteria found in tissue homogenates by viable count (Fig. 4). The viable count results showed that *P. aeruginosa* infection in mice,

initiated by intranasally delivered agarose beads, was not sensitive to daily treatment with ciprofloxacin. In contrast, the combination of shock wave and ciprofloxacin treatments significantly reduced the number of bacteria in the lung, determined by viable count (Fig. 4). The impact of shock wave therapy on the survival of mice with *P. aeruginosa* pneumonia was also examined. At the end of the therapy, groups of eight mice were examined twice daily to determine when they became moribund. Infected mice given shock wave therapy alone or left untreated died within 10 days, whereas only two mice treated with ciprofloxacin alone survived. All mice provided with ciprofloxacin therapy and shock wave treatment survived.

3 Discussion

Biofilm formation occurs through different phases such as surface conditioning, attachment and colonization. Surface conditioning involves the adsorption of organic and inorganic nutrients which facilitate bacterial attachment. Initial attachment of the bacteria to the surface may be reversible involving Brownian movement and weak forces between the surfaces or may involve ligands (e.g. bacterial fimbriae) binding to cognate receptors [9, 10]. Regardless, the early interactions can soon become irreversible due to the production of extracellular polymeric substances (EPS) [33]. Much of the recent research aimed at preventing biofilm formation is focused on using novel materials or catheters coated with antibiotics. Antimicrobial peptide-coated implants have been developed to control the biofilm formation in these implants. We have used shock waves to disrupt biofilms in urinary catheters at physiological conditions, where the biofilms were grown in bovine or human urine. When the catheter-associated biofilms were treated with ciprofloxacin, there was no reduction in the number of bacteria, whereas ciprofloxacin treatment together with shock wave therapy significantly reduced the number of bacteria that could be observed or detected by viable count. The shock waves were not antibacterial. It is hypothesized that the very brief exposure to the wave ‘fractured’ the polysaccharide matrix surrounding the biofilm, liberating bacteria and possibly increasing access by the antibiotic. Further experiments were carried out to determine the effect of shock waves on in vivo biofilms. Mice that received both antibiotic and shock wave therapy after challenge with agarose beads coated with *P. aeruginosa* survived, whereas animals that received antibiotics alone usually succumbed to infection. Here we have shown for the first time that a single shock wave pulse of 205 mJ/mm^2 can be used to disrupt biofilm in vivo. Though the energy in the shock wave is much higher than that of the shock wave generated by the hand-held device, the area over which the shock wave is spread is larger. Therefore, the energy per unit cross-section area is lower than that of the hand-held device. Also, the peak overpressure of the shock wave is lower. The steady time duration of the shock wave is much longer in the case of the diaphragmless shock wave generator. Since ESWL is being routinely practised for treatment of unrelated medical conditions, shock wave-assisted biofilm disruption could be used to treat especially recalcitrant biofilm infections in hospital settings.

References

1. J. Ludwig et al., High-energy shock wave treatment of femoral head necrosis in adults. Clin. Orthop. Relat. Res. **387**, 119–126 (2001)
2. Y.-R. Kuo, C.-T. Wang, F.-S. Wang, Y.-C. Chiang, C.-J. Wang, Extracorporeal shock-wave therapy enhanced wound healing via increasing topical blood perfusion and tissue regeneration in a rat model of STZ-induced diabetes. Wound Repair Regen. **17**(4), 522–530 (2009)
3. C. Chaussy, E. Schmiedt, Extracorporeal shock wave lithotripsy (ESWL) for kidney stones. An alternative to surgery? Urol. Radiol. **6**(1), 80–87 (1984)
4. S.G. Rakesh et al., Development of micro-shock wave assisted dry particle and fluid jet delivery system. Appl. Microbiol. Biotechnol. **96**(3), 647–662 (2012)
5. G. Jagadeesh et al., Needleless vaccine delivery using micro-shock waves. Clin. Vaccine Immunol. **18**(4), 539–545 (2011)
6. G. Divya Prakash, R.V. Anish, G. Jagadeesh, D. Chakravortty, Bacterial transformation using micro-shock waves. Anal. Biochem. **419**(2), 292–301 (2011)
7. Z.D. Taylor, et al., Bacterial biofilm disruption using laser generated shockwaves. *Engineering in Medicine and Biology Society (EMBC), 2010 Annual International Conference of the IEEE*, pp. 1028–1032, 2010
8. S. Wanner et al., Low-energy shock waves enhance the susceptibility of staphylococcal biofilms to antimicrobial agents in vitro. J. Bone Joint Surg. Br. Vol. **93-B**(6), 824–827 (2011)
9. L. Hall-Stoodley, J.W. Costerton, P. Stoodley, Bacterial biofilms: From the natural environment to infectious diseases. Nat. Rev. Microbiol. **2**(2), 95–108 (2004)
10. D. Lebeaux, J.M. Ghigo, C. Beloin, Biofilm-related infections: Bridging the gap between clinical management and fundamental aspects of recalcitrance toward antibiotics. Microbiol. Mol. Biol. Rev. **78**(3), 510–543 (2014)
11. T. Coenye, H.J. Nelis, In vitro and in vivo model systems to study microbial biofilm formation. J. Microbiol. Methods **83**(2), 89–105 (2010)
12. K. Vasilev, J. Cook, H.J. Griesser, Antibacterial surfaces for biomedical devices. Expert Rev. Med. Devices **6**(5), 553–567 (2009)
13. I. Francolini, G. Donelli, Prevention and control of biofilm-based medical-device-related infections. FEMS Immunol. Med. Microbiol. **59**(3), 227–238 (2010)
14. M. Lleo et al., Adhesion to medical device materials and biofilm formation capability of some species of enterococci in different physiological states. FEMS Microbiol. Lett. **274**(2), 232–237 (2007)
15. D. Mack et al., Biofilm formation in medical device-related infection. Int. J. Artif. Organs **29**(4), 343–359 (2006)
16. E.E. Braxton Jr. et al., Role of biofilms in neurosurgical device-related infections. Neurosurg. Rev. **28**(4), 249–255 (2005)
17. I.I. Raad et al., Prevention of central venous catheter-related infections by using maximal sterile barrier precautions during insertion. Infect. Control Hosp. Epidemiol. **15**(4 Pt 1), 231–238 (1994)
18. M.E. Olson, H. Ceri, D.W. Morck, Interaction of biofilms with tissues, in *Medical Biofilms*, (Wiley, New York, 2005), pp. 125–148
19. J. Galli et al., Biofilm formation by Haemophilus influenzae isolated from adeno-tonsil tissue samples, and its role in recurrent adenotonsillitis. Acta Otorhinolaryngol. Ital. **27**(3), 134–138 (2007)
20. R. Mladina, N. Skitarelic, S. Music, M. Ristic, A biofilm exists on healthy mucosa of the paranasal sinuses: A prospectively performed, blinded, scanning electron microscope study. Clin. Otolaryngol. **35**(2), 104–110 (2010)
21. I.O. Samuelraj, G. Jagadeesh, K. Kontis, Micro-blast waves using detonation transmission tubing. Shock Waves **23**(4), 307–316 (2013)
22. M.S. Hariharan, S. Janardhanraj, S. Saravanan, G. Jagadeesh, Diaphragmless shock wave generators for industrial applications of shock waves. Shock Waves **21**(3), 301–306 (2011)

23. O. Igra, J. Falcovitz, L. Houas, G. Jourdan, Review of methods to attenuate shock/blast waves. Prog. Aerosp. Sci. **58**(0), 1–35 (2013)
24. K. Bhaskar, *Studies on Shock Wave Attenuation in Liquids*, MS Thesis, Indian Institute of Science, Bangalore, 2012
25. E. Wang, A. Shukla, Analytical and experimental evaluation of energies during shock wave loading. Int. J. Impact Eng. **37**(12), 1188–1196 (2010)
26. A. Heeckeren et al., Excessive inflammatory response of cystic fibrosis mice to bronchopulmonary infection with Pseudomonas aeruginosa. J. Clin. Invest. **100**(11), 2810–2815 (1997)
27. C.H. Chaussy, W. Brendel, E. Schmiedt, Extracorporeally induced destruction of kidney stones by shock waves. Lancet **316**(8207), 1265–1268 (1980)
28. J.E. Lingeman, J.A. McAteer, E. Gnessin, A.P. Evan, Shock wave lithotripsy: Advances in technology and technique. Nat. Rev. Urol. **6**(12), 660–670 (2009)
29. M. Delius, Medical applications and bioeffects of extracorporeal shock waves. Shock Waves **4**(2), 55–72 (1994)
30. A.J. Coleman, T. Kodama, M.J. Choi, T. Adams, J.E. Saunders, The cavitation threshold of human tissue exposed to 0.2-MHz pulsed ultrasound: Preliminary measurements based on a study of clinical lithotripsy. Ultrasound Med. Biol. **21**(3), 405–417 (1995)
31. M. Eroglu, E. Cimentepe, F. Demirag, E. Unsal, A. Unsal, The effects of shock waves on lung tissue in acute period: An in vivo study. Urol. Res. **35**(3), 155–160 (2007)
32. M. Delius et al., Biological effects of shock waves: Lung hemorrhage by shock waves in dogs—Pressure dependence. Ultrasound Med. Biol. **13**(2), 61–67 (1987)
33. R.M. Donlan, J.W. Costerton, Biofilms: Survival mechanisms of clinically relevant microorganisms. Clin. Microbiol. Rev. **15**(2), 167–193 (2002)
34. P. Stoodley, K. Sauer, D.G. Davies, J.W. Costerton, Biofilms as complex differentiated communities. Annu. Rev. Microbiol. **56**(1), 187–209 (2002)
35. H. Elgharably et al., First evidence of sternal wound biofilm following cardiac surgery. PLoS One **8**(8), e70360 (2013)
36. R.W. Crawford, D.L. Gibson, W.W. Kay, J.S. Gunn, Identification of a bile-induced exopolysaccharide required for Salmonella biofilm formation on gallstone surfaces. Infect. Immun. **76**(11), 5341–5349 (2008)
37. Y. Okajima, S. Kobayakawa, A. Tsuji, T. Tochikubo, Biofilm formation by Staphylococcus epidermidis on intraocular lens material. Invest. Ophthalmol. Vis. Sci. **47**(7), 2971–2975 (2006)
38. E. Ołdak, E.A. Trafny, Secretion of proteases by Pseudomonas aeruginosa biofilms exposed to ciprofloxacin. Antimicrob. Agents Chemother. **49**(8), 3281–3288 (2005)

Simulation of Shock-Bubble Interaction Using a Four-Equation Homogeneous Model

Eric Goncalves and Dia Zeidan

Abstract This paper presents a numerical study of air bubble collapse in water induced by the impact of a shock wave. Simulations are performed using an inviscid compressible one-fluid solver. Numerical results are displayed for single-bubble and twin-bubble cases in order to investigate the evolution of the maximum pressure during the collapse. The influence of the distance between bubble is also investigated.

1 Introduction

The investigation of the pressure peak developed by a collapsing cavitation bubble leading to erosion is of primary interest for hydraulic and marine applications. To clarify the physical mechanism, numerous experimental and numerical studies of the collapse of cavity in water under shock wave loading have been proposed [1–3]. Such shock-bubble interactions develop a high-speed liquid jet that penetrates through the bubble and emit a blast wave during the induced collapse. Both the jet and the shock waves are possible damaging mechanisms and worth further investigation.

In the present study, the flow field resulting from the interaction between a planar incident shock wave and one or two circular gas bubbles is investigated numerically. We describe the shock induced collapse, with particular consideration of the maximum pressure location and potential damage. Different cases are computed

The original version of this chapter was revised: Second Author's name has been updated. A correction to this chapter is available at https://doi.org/10.1007/978-3-319-91017-8_149

E. Goncalves (✉)
ENSMA, Institut Pprime, UPR 3346, CNRS, Chasseneuil-du-Poitou, France

D. Zeidan
ENSMA, Institut Pprime, UPR 3346, CNRS, Chasseneuil-du-Poitou, France

School of Basic Sciences and Humanities, German Jordanian University, Amman, Jordan
e-mail: eric.goncalves@ensma.fr

A. Sasoh et al. (eds.), *31st International Symposium on Shock Waves 2*,
https://doi.org/10.1007/978-3-319-91017-8_58

by varying both the distance between bubbles and the size of the second bubble. Simulations are performed using an inviscid compressible one-fluid code based on a four-equation system. It consists in solving three mixture conservation laws for the mass, momentum, and energy and a transport equation for the gas volume fraction [4, 5].

2 Models

The homogeneous mixture approach is used with the assumption of thermal and mechanical local equilibrium between pure phases. The model consists in three conservation laws for mixture quantities (mass, momentum, and total energy) with an additional equation for the void ratio. The expression for the void ratio equation α is:

$$\frac{\partial \alpha}{\partial t} + \vec{V}.\,\mathrm{grad}\,(\alpha) = \left(\frac{\rho_l c_l^2 - \rho_v c_v^2}{\frac{\rho_l c_l^2}{1-\alpha} + \frac{\rho_v c_v^2}{\alpha}} \right) \mathrm{div}\,\vec{V} \tag{1}$$

where c_k are the speed of sound of phase k and $\vec{V}$ the center-of-mass mixture velocity vector. The system has a hyperbolic nature with eigenvalues: $u - c_{\text{wallis}}, u, u, u + c_{\text{wallis}}$ where c_{wallis} is the propagation of acoustic waves without mass transfer [8].

To close the system, an equation of state (EOS) is necessary to link the pressure and the temperature to both the internal energy and density. For the pure phases, we used the convex stiffened gas EOS:

$$P(\rho, e) = (\gamma - 1)\rho(e - q) - \gamma P_\infty \qquad \text{and} \qquad T(\rho, h) = \frac{h - q}{C_p} \tag{2}$$

where $\gamma = C_p/C_v$ is the heat capacity ratio, C_p and C_v are thermal capacities, q is the energy of formation of the fluid, and P_∞ is a constant reference pressure. On the basis of the stiffened gas EOS for each pure phase, an expression for the pressure and the temperature can be deduced from the thermal and mechanical equilibrium assumption. It is worth noting that these expressions are available in all possible fluid states along with the function of the void ratio and mass fraction of gas $Y = \alpha\rho_v/\rho$:

$$P(\rho, e, \alpha, Y) = (\gamma(\alpha) - 1)\rho(e - q(Y)) - \gamma(\alpha)P_\infty(\alpha) \quad ; \quad T(\rho, h, Y) = \frac{h - q(Y)}{C_p(Y)} \tag{3}$$

$$\frac{1}{\gamma(\alpha) - 1} = \frac{\alpha}{\gamma_v - 1} + \frac{1 - \alpha}{\gamma_l - 1} \quad ; \quad C_p(Y) = YC_{p_v} + (1 - Y)C_{p_l}, \tag{4}$$

$$P_\infty(\alpha) = \frac{\gamma(\alpha) - 1}{\gamma(\alpha)} \left[\alpha \frac{\gamma_v P_\infty^v}{\gamma_v - 1} + (1 - \alpha) \frac{\gamma_l P_\infty^l}{\gamma_l - 1} \right] \quad ; \quad q(Y) = Yq_v + (1 - Y)q_l$$

3 Numerics

Numerical simulations are carried out using an in-house finite volume code solving the compressible inviscid system [4, 9]. Numerical fluxes are computed with a HLLC scheme. The second-order is obtained through the MUSCL extrapolation and the minmod slope limiter is used. Further, the numerical simulations of the initial-boundary value problems are accomplished using splitting approach. In such approach, one starts in solving the source-free homogeneous part of the whole system followed by solving the system of ordinary differential equations to obtain the complete solution. The numerical treatment of the boundary conditions is based on the inviscid characteristic relations.

4 Simulation Results

4.1 Single-Bubble Case

The considered test is similar to the one presented in [1, 7]. A cylindrical air bubble, 6 mm in diameter, is immersed in a water pool, under the following initial conditions: $\vec{V} = (0, 0)$ m/s, $P = 10^5$ Pa, $\rho_{\text{air}} = 1\,\text{kg/m}^3$, and $\rho_{\text{water}} = 1000\,\text{kg/m}^3$. Due to the symmetry of the problem, we only consider a half bubble. The center of the bubble is located at (8, 0) mm in the computational domain of size 24×12 mm. The bubble is collapsed by a normal shock wave moving at $M_{sh} = 1.72$, initially located at abscissa $x_{sh} = 4$ mm. The schematic diagram of the test case is given in Fig. 1. Simulations are performed using a uniform grid composed by 800×400 cells and a time step $\Delta t = 10^{-9}$ s.

Parameters of the EOSs and post-shock conditions are:

$$\begin{pmatrix}\gamma\\ P_\infty\\ \rho\end{pmatrix}_{\text{l}} = \begin{pmatrix}4.4\\ 6\times 10^8\text{Pa}\\ 1000\,\text{kg/m}^3\end{pmatrix};\ \begin{pmatrix}\gamma\\ P_\infty\\ \rho\end{pmatrix}_{\text{v}} = \begin{pmatrix}1.4\\ 0\,\text{Pa}\\ 1\,\text{kg/m}^3\end{pmatrix};\ \begin{pmatrix}\text{P}\\ \rho\\ \text{u}\end{pmatrix}_{\text{sh}} = \begin{pmatrix}1.9\,10^9\text{Pa}\\ 1323.65\,\text{kg/m}^3\\ 681.58\,\text{m/s}\end{pmatrix}$$

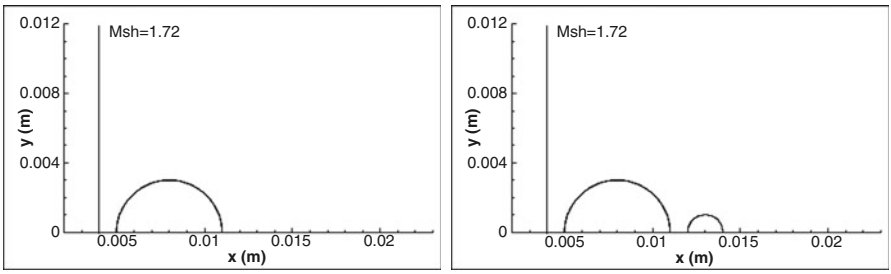

Fig. 1 Initial situation for the interaction, single-bubble (left) and twin-bubble (right)

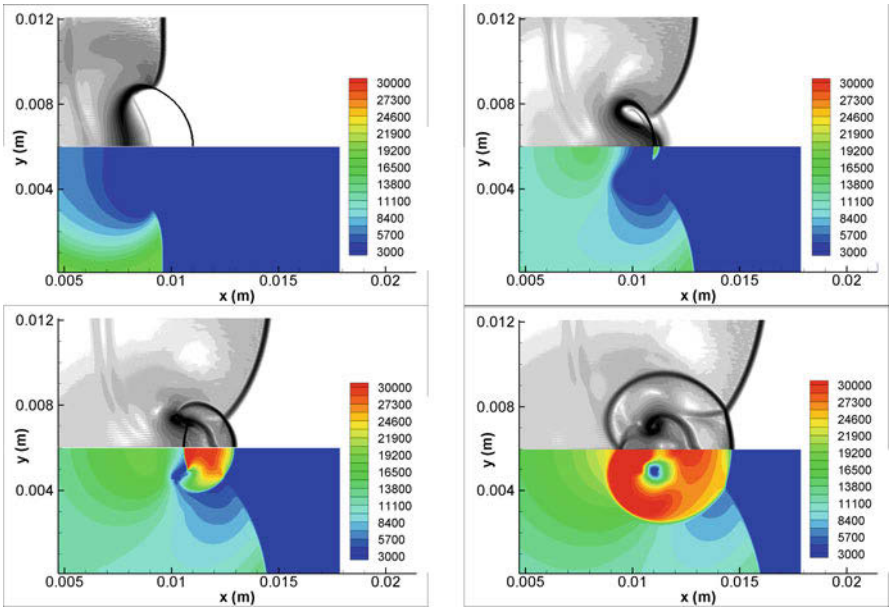

Fig. 2 Evolution of the density gradient modulus and the pressure (in bar) at times $t = 2$, 3.2, 3.8, and 4.4 μ s

The evolution of the density gradient modulus (Schlieren-type representation) and the pressure (in bar) are plotted in Fig. 2 at different instants. After the water shock wave has collided with the bubble, a strong rarefaction wave is reflected backwards from the interface, and a weak shock wave is transmitted inside of the bubble (time $t = 2\,\mu$ s). Due to the pressure difference between both sides, the bubble is asymmetrically contracted and spreads laterally in the process. This change in shape is driven by vorticity generated at the edge of the bubble due to the passage of the wave which induces a jet of water along the axis of flow symmetry. When this water jet impacts the stationary water at the front of the bubble (at time $t = 3.2\,\mu$ s), an intense blast wave also called water hammer shock is formed generating a high-pressure zone. The blast front, which expands continuously, is highly asymmetric due to the high-speed water jet (see Fig. 2 at time $t = 3.8\,\mu$ s). Caused by the leftward blast wave, secondary jets penetrate into the smaller bubbles and cut the initial bubble into four pieces. The interaction of the blast wave with the bubble fragments leads to high-pressure levels (at time $t = 4.4\,\mu$s). Moreover, the low-pressure area inside the vortices core is well illustrated.

The pressure evolution on the axis and the maximum pressure in the domain, plotted in Fig. 3, illustrate the high pressure reached during the cavity collapse. We can observe the first peak at time $t = 3.4\,\mu$ s when the water jet impacts the bubble front and the second peak (more intense, around 70,000 bar) at time $t = 4.4\,\mu$ s when the leftward blast wave collides the bubble fragments.

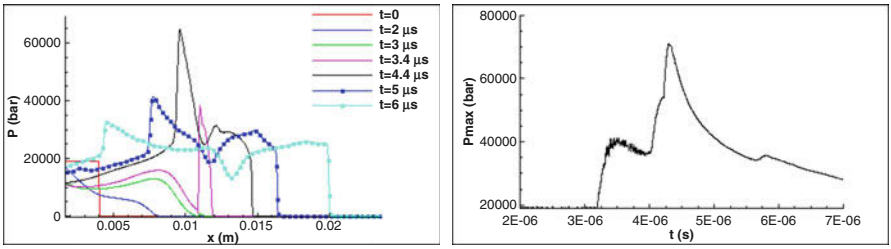

Fig. 3 Evolution of the axial (left) and maximum (right) pressure during the collapse

4.2 Double-Bubble Case

The second test is an extension of first one considering a second bubble placed behind the first bubble. The interdependence of bubbles and the possible intensification of the peak pressure is investigated. We introduce the distance S between the bubbles center. Different configurations are simulated by varying the inter-bubble distance and the second bubble diameter D_2. As suggested by Betney et al. [2] for two equally sized bubbles, the peak pressure intensity relatively to the first bubble value is the most intense when the ratio S/R is smaller than 2.5. We focus in the present study on strong cases where the potential damage is high. Numerical parameters are similar to the previous case.

First, we consider two equally sized bubbles (diameter $D_1 = D_2 = 6\,\text{mm}$) for which the distance $S = 7\,\text{mm}$ ($S/R = 2.33$). The evolution of the density gradient modulus and the pressure (in bar) are plotted in Fig. 4. For the first bubble, the collapse is similar to the single-bubble case. As shown by Lauer et al. [6], the second bubble collapse follows the same process for which the blast wave emitted by the first collapse plays the role of the incident shock. At time $t = 5\,\mu\text{s}$, the transmitted shock inside the second bubble is well illustrated. When the first blast wave impacts the second bubble, a high-speed jet is formed. On impact with the right front of the second bubble, a wider blast wave is generated leading to an intense pressure peak (time $t = 6.4\,\mu\text{s}$). At time $t = 7.6\,\mu\text{s}$, the second blast wave re-collapses the first bubble fragments, leading to a very high pressure.

The intensification of the second bubble collapse relative to the first one is illustrated in Fig. 5 where are plotted the pressure evolution on the axis and the maximum pressure during the collapse. For the first bubble, the pressure evolution is similar to the previous case. For the second bubble, the first peak corresponding to the impact of the high-speed jet forming the second blast wave is largely more intense than the first collapse (around 50% more). The intensity of the second peak due the impact of the second blast wave with bubble pieces is similar to the first collapse pressure level.

Secondly, we reduce the size of the second bubble for which the diameter $D_2 = D_1/3 = 2\,\text{mm}$ (see Fig. 1 on the right). Different cases are simulated by varying the inter-bubble distance S from 4.5 to 9 mm, so S/R_1 varies from 1.5 to 3.

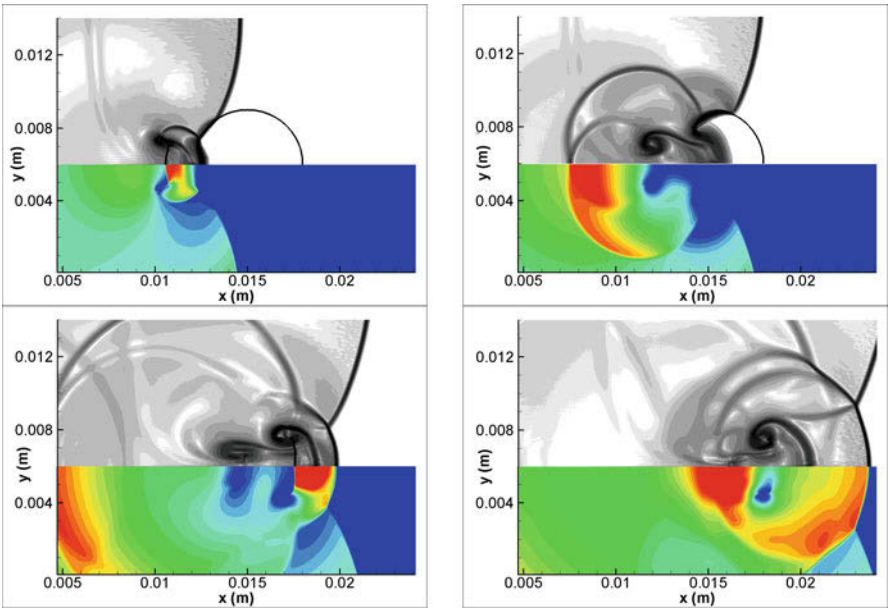

Fig. 4 Schlieren and pressure visualizations at times $t = 3.8$, 5, 6.4, and 7.6 μ s, $D_2 = D_1$

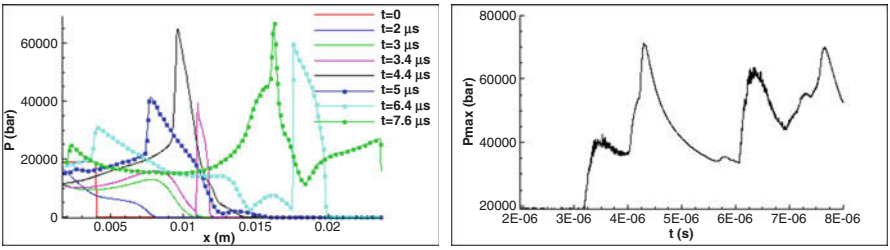

Fig. 5 Evolution of the axial pressure (left) and the maximum pressure (right), $D_2 = D_1$

Table 1 Maximum pressure peak (in bar) during the collapse

S/R_1	1.5	1.66	1.83	2	2.33	2.5	2.66	2.83	3
$D_2 = D_1$	–	–	–	–	70,380	–	–	–	–
$D_2 = D_1/3$	73,720	82,380	80,500	74,200	76,600	78,140	79,250	79,620	77,800

The obtained pressure peaks are given in Table 1. For all cases, the pressure peak is more intense in comparison with the equally sized bubble case. Moreover, we observe a non-monotonic evolution of the pressure peak with the distance S. The most intense pressure peak (around 82,400 bar, 15% higher that the single-bubble case) is simulated with $S = 5$ mm or $S/R_1 = 1.66$.

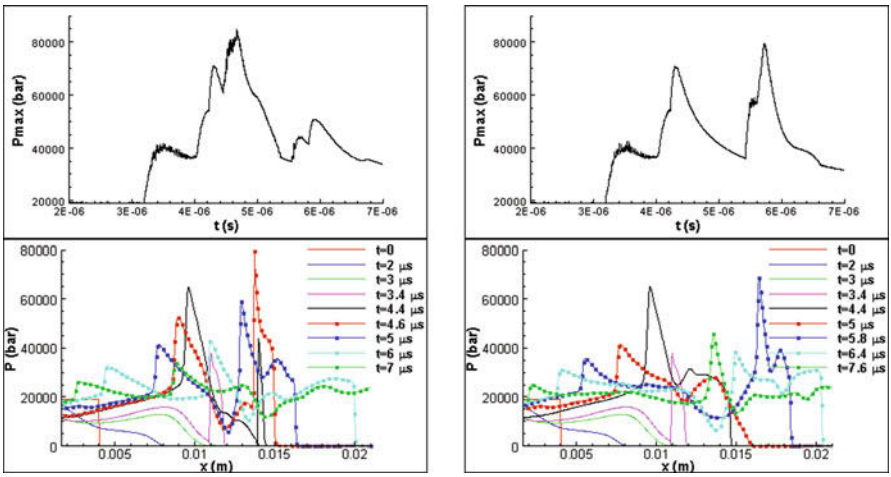

Fig. 6 Evolution of axial and maximum pressure during the collapse, $S/R_1 = 1.66$ (left) and $S/R_1 = 2.66$ (right), $D_2 = D_1/3$

The pressure evolutions (maximum and axial) during the collapse are plotted in Fig. 6 for cases $S/R_1 = 1.66$ and 2.66, respectively. For both cases, the second bubble is collapsed by the blast wave emitted by the first bubble. For the short inter-distance, the pressure peak due to the blast wave impacting bubble pieces (at time $t = 4.6\,\mu s$) is the most intense phenomenon. At time $t = 6\,\mu s$, the blast wave impacts the first bubble fragments generating a pressure peak around 50,000 Pa. For the second case, the pressure peak due to the water jet impact on the bubble interface is around 60,000 bar (50% more intense in comparison with the first bubble). At time $t = 5.8\,\mu s$, the most intense peak is generating by the impact of the blast wave with bubble pieces. Another peak (around 45,000 bar) appears at time $t = 7.6\,\mu s$ when the blast wave re-collapses the first bubble fragments.

5 Conclusion

This paper introduces a four-equation model for the simulation of shock-bubble interactions leading to the cavity collapse. For the single-bubble case, simulations captured the most phenomenon associated with this interaction such as the water jet formation, the bubble division, the formation of a high-pressure zone, and the generation of a strong blast wave shock which expands in the liquid. Inter-bubble effects are studied through a double-bubble collapse case. It is observed that the collapse of the second bubble is proceeded by the blast wave emitted by the first bubble collapse. Moreover, the second bubble collapse is even more intense than the first one leading to an amplification phenomenon. The variation of the inter-bubble distance shows that this parameter has a significant effect on the pressure peak generation.

References

1. G.J. Ball et al., Shock Waves **10**, 265 (2000)
2. M.R. Betney et al., Phys. Fluids. **27**, 036101 (2015)
3. N.K. Bourne, Shock Waves **11**, 447 (2002)
4. E. Goncalves, Comput. Fluids **72**, 1 (2013)
5. E. Goncalves, B. Charriere, Int. J. Multiphase Flow **59**, 54 (2014)
6. E. Lauer et al., Phys. Fluids **24**, 052104 (2012)
7. R.R. Nourgaliev et al., J. Comput. Phys. **213**, 500 (2006)
8. G. Wallis, *One-Dimensional Two-Phase Flow* (McGraw-Hill, New York, 1967)
9. D. Zeidan, Int. J. Comput. Fluid Dyn. **25**, 299 (2011)

A Study of Dispersion, Vaporization, and Combustion of Burnable Liquids Surrounding Charges

F. Togashi, J. D. Baum, O. A. Soto, R. Löhner, and J. Bell

Abstract A complex numerical simulation where blast waves interacted with a liquid, burnable simulant inside a chamber was conducted. The liquid simulant was dispersed by a small high explosive (HE) charge and then impacted by the blast wave produced by a significantly larger HE charge. The physics of the problem required numerical tools that allowed for (1) coupling of compressible and near-incompressible (+VOF) solvers, (2) a dropletization model by liquid bulk dispersion, (3) droplet breakup and vaporization, (4) a chemical package for combustion, and (5) a particle update technique. The resulting numerical code successfully simulated the scenario, and the predicted pressure agreed excellently with the measured data.

1 Introduction

The simulation of multiphase flows combining gaseous and liquid states has received considerable attention over the last 30 years [1–3]. There are a number of complications as compared to a single-phase flow simulation:

- The equation of state for the liquid phase tends to be complex and/or stiff (e.g., cavitation), leading to difficulties with exact or approximate Godunov solvers.
- The speed of sound in the liquid phase is much higher than that in the gas phase, requiring smaller time steps and lengthier runs.
- The liquid may break up into droplets that evaporate, mix, and react with the gas phase.

F. Togashi (✉) · J. D. Baum · O. A. Soto
Applied Simulations Inc., Potomac, MD, USA

R. Löhner
CFD Center, George Mason University, Fairfax, VA, USA

J. Bell
Defense Threat Reduction Agency, Fort Belvoir, VA, USA

A. Sasoh et al. (eds.), *31st International Symposium on Shock Waves 2*,
https://doi.org/10.1007/978-3-319-91017-8_59

With the maturity of single-phase flow codes, there has been increasing demand of combining gas and liquid flow models into a single run. Our approach has been to use different flow models and computational fluid dynamics (CFD) codes and to couple them via the immersed body method (see Sect. 2). In the gas region, the velocities of the liquid are imposed wherever liquid is present. For the liquid region, the pressures of the gas region are imposed wherever gas is present. If the liquid region can no longer be discretized via a continuum method such as the volume of fluid (VOF) or level set (LS) method, the fluid region is converted into particles (droplets), which are incorporated into the gas region.

The following study was conducted: a small HE charge was surrounded by a burnable liquid placed in a chamber. The explosive detonated, and the detonation products expanded the liquid whose interface then broke up into streaks and blobs. Due to shear, these blobs then broke into droplets that vaporized in the surrounding gas. Meanwhile, another high explosive, located further away in the chamber, detonated. The blast wave impacted the bulk liquid, droplets, and vapors. Over time, some droplets vaporized and reacted with the hot gas in the chamber. Still, most of the original liquid mass did not react and formed a liquid pool on the chamber's floor.

2 Numerical Methodology

2.1 Immersed Body Method

Consider the possibility of running solvers for gas and liquid concurrently on the same mesh. As the fluid moves through the domain, the elements and points of the mesh where each one of these models is valid change continuously. For the gas flow/solver region, the velocities of the liquid are imposed wherever liquid exists. For the liquid flow/solver region, the pressures of the gas are imposed wherever gas is present. In principle, both flow solvers could be running concurrently on different meshes. Conceptually (and when implemented) this is not different from traditional immersed body methodology [4–6]. Instead of having a rigidly moving body immersed in a compressible flow field, the "body" happens to be a near-incompressible liquid.

2.2 Dropletization

For the transition from liquid to blob, an approach similar to large eddy simulation is used. Once the near-incompressible VOF flow can no longer discretize the free surface accurately, the regions are transformed to blobs and transmitted to the compressible flow solver (see Fig. 1). In a first pass over the edges, the points that are

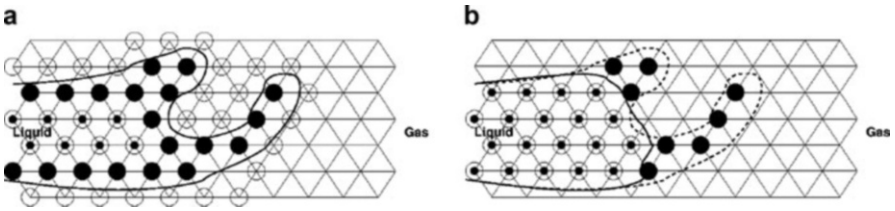

Fig. 1 Dropletization of "thin" regions (liquid to blob)

fully inside, on the border of the interface, or fully outside the liquid, are marked as shown in Fig. 1a. In a second (or subsequent) pass(es), a layer is added to the points marked as being in the liquid (Fig. 1b). This exposes points that are liquid but are in "thin" regions. The liquid mass at these points is subsequently transformed into blobs and passed to the compressible code handling the gas phase, where the droplets are treated as Lagrangian particles that can exchange mass, momentum, and energy with gas. To handle millions of particles, we agglomerate the N_P particles into so-called packets by integrating the equations for each individual particle under the assumption that the N_P particles behave equally [7].

2.3 Droplet Breakup and Vaporization

Once the blobs are transmitted to the compressible solver, they are allowed to break up further into smaller droplets. We implemented the breakup model based on three breakup modes, which are based on the widely used Reitz model [8] and the curve fits of Pilch and Erdman [9]. The breakup times of each mode are checked. If any of the possible breakup times is exceeded, the droplet was broken up. Droplet heat and mass transfer were also modeled based on the droplet's variables and the surrounding gas. Three vaporization modes are possible based on the vaporization temperature T_{vap} and the boiling temperature T_{boil}: (1) $T < T_{\text{vap}}$, (2) $T_{\text{vap}} \leq T < T_{\text{boil}}$, and (3) $T \geq T_{\text{boil}}$ [10].

2.4 Software Realization

Figure 2 shows the outline of the software realization of the procedure. A master code calls the compressible code for gas and near-incompressible code for liquid as subroutines. The only arguments passed in and out are the (volume) unknowns to be exchanged by the flow codes. The code computing the gas receives the liquid velocities and VOF mass fraction and outputs the pressures. The code computing the liquid in turn receives the pressures and outputs the velocities and VOF mass fraction. Please note that the solvers could in principle be different. In the present

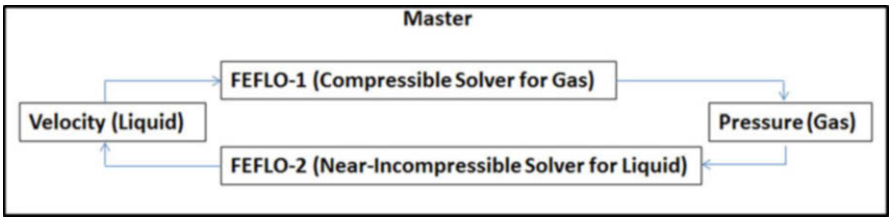

Fig. 2 Concurrent run of the same code via multiple instantiations

case, the original flow code (FEFLO) could be run as either compressible or near-incompressible (+VOF). Therefore, it is called twice with an "instantiation" indicator to differentiate the input and output files required and/or generated for each domain.

As stated above, FEFLO was used to solve both states. The code is based on unstructured grids and uses standard edge-based data structures for speed [11]. The code comprises the following modeling:

- For the gas part: an explicit TVD or FCT solver for chemically reacting, compressible flow [12]
- For the liquid part: a semi-explicit TVD solver for the advective-diffusive terms and a Poisson solver for the pressure terms of the near-incompressible flow [12]
- A volume of fluid approach for the free surface of the liquid [13]
- The CHEMKIN package [14] for chemistry (in this scenario, 26 species, 20 reduced reactions)
- A particle update technique that allows for droplet breakup and vaporization [7]

3 Numerical Result

Figure 3 shows the evolution of the velocity distribution of the gas and the iso-surface of the liquid/gas interface. A small spherical HE charge was detonated inside a cylinder of liquid. To capture the instability of the liquid interface which generates the fingers and droplets, we used a fine mesh with 1 mm resolution. To save CPU resources without compromising the result, a section of only 30° (1/8 cylinder) was computed. The evolution of the fingers on the interface was captured well, as shown in Fig. 3. Figure 4 shows the generation of blobs from the interface.

The computed data of the liquid dispersion step was then mirrored to form a single cylinder, copied and moved to form four more cylinders, and then placed in the correct location within the chamber. Figure 5 shows (a) the droplet diameter distribution and (b) the gas velocity and bulk liquid distribution at several time steps. As noted above, while the small HE charge within the liquid was detonated to disperse the liquid, another, larger charge, located about a meter away, was detonated. The resulting blast wave was just about to impact the droplet cloud

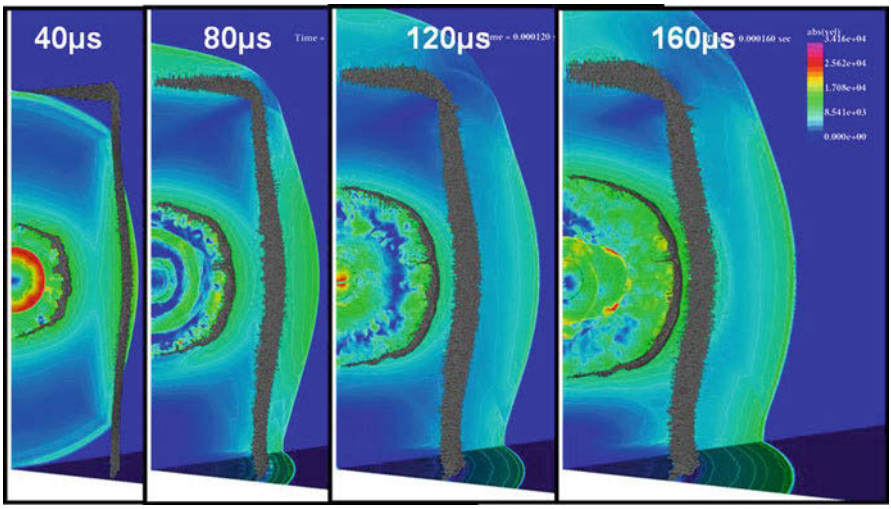

Fig. 3 Evolution of blast wave (colored distribution) and gas/liquid interface (gray iso-surface)

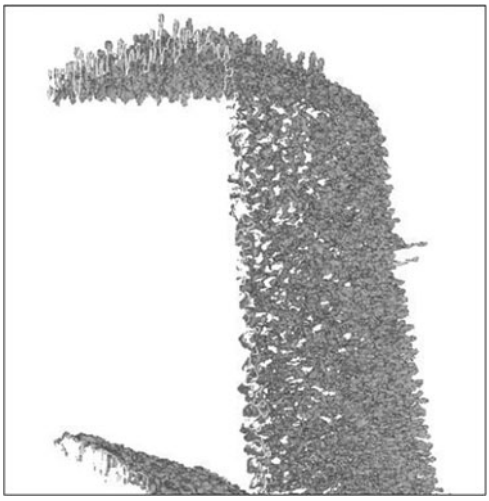

Fig. 4 Dropletization by the instability on gas/liquid interface

at 0.3 ms. The droplet cloud was responding, dispersing, and breaking up due to the reverberating blast wave within the chamber as shown in Fig. 5a. The smaller droplets were carried further than the large droplets due to less inertia. In contrast, the remaining bulk liquid stayed at the original location even after the blast wave passed through several times as shown in Fig. 5b.

Finally, Fig. 6 shows a comparison of the measured pressure history and the computational predictions. The pressure gauge was located on the inside wall of the chamber. The prediction matched excellently with the measured data.

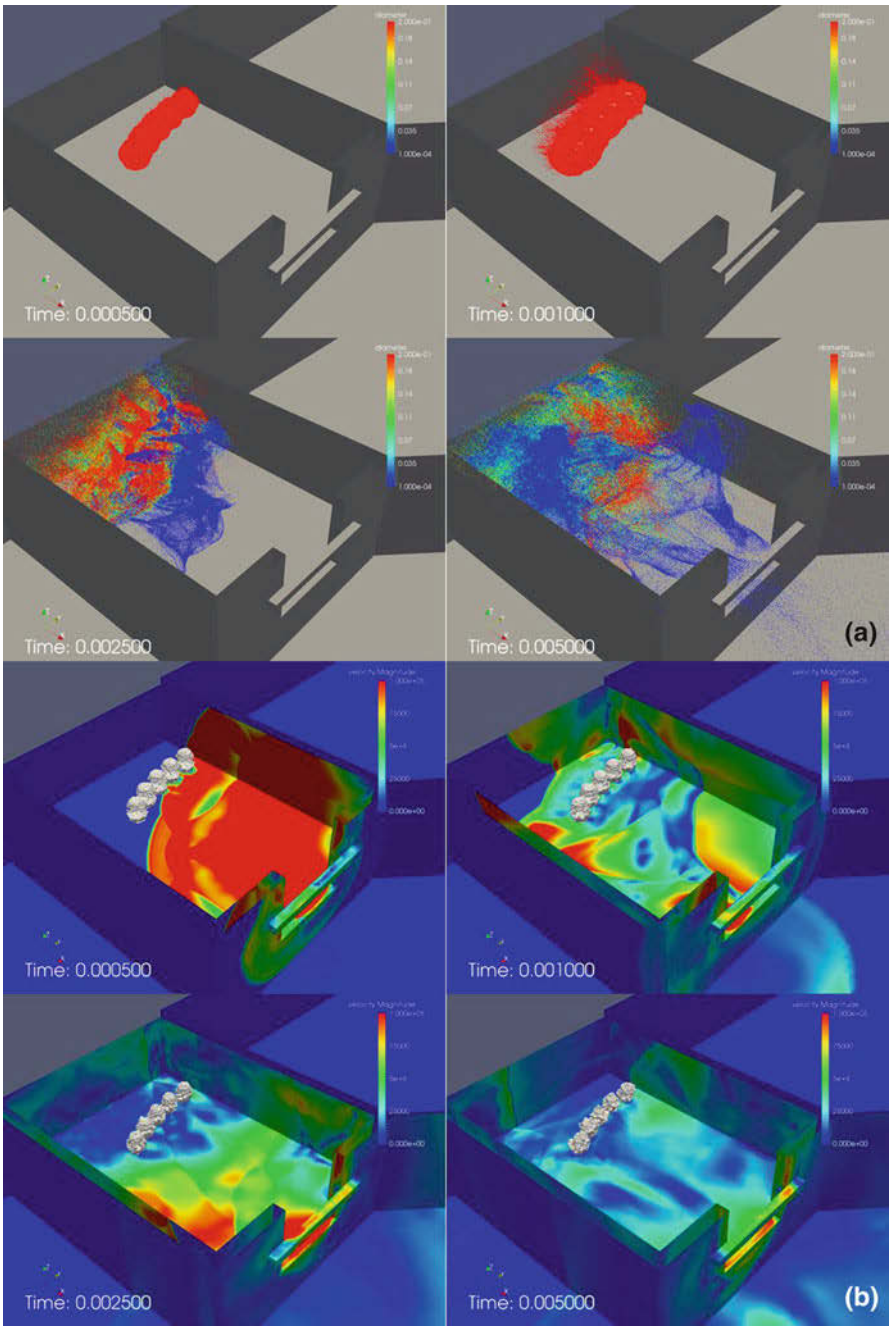

Fig. 5 (**a**) Droplet diameter distributions and (**b**) gas velocity and bulk liquid iso-surface at 0.5, 1.0, 2.5, and 5 ms

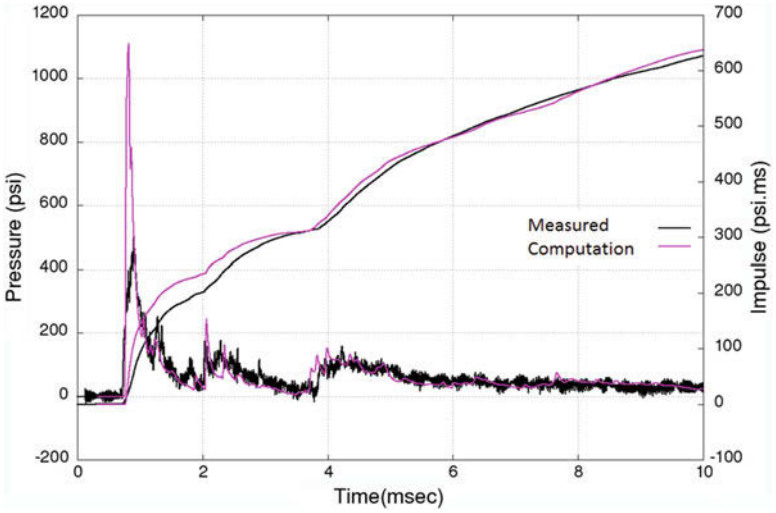

Fig. 6 Comparison of measured and computed pressure time histories

4 Concluding Remarks

A complex numerical simulation where blast waves interacted with a cloud of liquid burnable simulant inside a chamber was conducted. The overall numerical methodology comprises the following capabilities:

- Coupling of compressible and near-incompressible (+VOF) solvers to handle gas and liquid states
- A dropletization model to handle a transition from the bulk liquid to a droplet cloud
- A droplet breakup model and droplet evaporation model
- A chemical reaction package to handle the combustion of burnable vapor
- A particle update technique to treat the droplets as Lagrangian particles

The numerical code successfully simulated the scenario, and the predicted pressure agreed excellently with the measured data.

Future work includes extensive verification and validation as well as developing an implicit approach to extend the simulations to second or even minutes of real time.

References

1. R.J. LeVeque, K.M. Shyue, J. Comput. Phys. **123**(2), 354–368 (1996)
2. R. Saurel, R. Abgrall, J. Comput. Phys. **150**(2), 425–467 (1999)
3. B. Wang, H. Xu, Eng. Appl. Comput. Fluid Mech. **1**(4), 325–336 (2007)
4. E.A. Fadlun, R. Verzicco, P. Orlandi, J. Mohd-Yusof, J. Comput. Phs. **161**(1), 35–60 (2000)

5. R. Mittal, G. Iaccarino, Ann. Rev. Fluid Mech. **37**, 239–261 (2005)
6. C.S. Peskin, Acta Numer. **11**, 479–517 (2002)
7. R. Löhner, F. Camelli, J.D. Baum, F. Togashi, O. Soto, Comput. Part. Mech. **1**(2), 199–209 (2014)
8. J. Xin, L. Ricart, R.D. Reitz, Combust. Sci. Technol. **137**(1–6), 171–194 (1998)
9. M. Pilch, C.A. Erdman, Int. J. Multiph. Flow **13**(6), 741–757 (1987)
10. E. Gozali, S. Kamnis, S. Gu, Surf. Coat. Technol. **228**, 176–186 (2013)
11. R. Löhner, *Applied CFD Techniques* (Wiley, New York, 2008)
12. J.D. Baum, O. Soto, F. Togashi, R. Löhner, in *41st AIAA Fluid Dynamics Conference and Exhibit, Fluid Dynamics and Co-located Conferences*, AIAA 2011–3722
13. R. Löhner, C. Yang, E. Onate, Int. J. Numer. Methods Fluids **53**(8), 1315–1338 (2007)
14. R.J. Kee, F.M. Rupley, J.A. Miller, Sandia Report, No. SAND-89-8009 (1989)

Multi-scale Simulation of the Interaction of a Shock Wave and a Cloud of Particles

S. Taverniers, G. B. Jacobs, V. Fountoulakis, O. Sen, and H. S. Udaykumar

Abstract A multi-scale method is proposed in which resolved mesoscale simulations of the interaction of a normal moving shock with a rectangular cloud of particles yield a parametric representation of the drag due to these particles. This establishes a link between the meso- and macroscale through metamodels, which provide closure terms for a macroscale model. The latter is used to simulate a process-scale problem via an Eulerian-Lagrangian approach, assuming a point-particle representation of the particle phase. Results obtained using a traditional cloud-in-cell method with first-order particle-to-grid weighing are compared to those of the novel "SPARSE" algorithm which represents the entire particle cloud with a single macro-particle and approximates the actual cloud shape with a bivariate Gaussian distribution for the purpose of weighing the particle momentum and energy contribution to the carrier flow onto the Eulerian fluid grid. The resulting multi-scale approach has the potential to improve the accuracy and efficiency of shocked particle-laden flow simulations and enable simulation of realistic scales.

1 Introduction

Multi-scale problems with distinct meso- and macroscales appear in several important engineering applications. Examples include the dynamics of particle-laden gases, deformation of heterogeneous materials such as bones and concrete, heterogeneous explosives, sediment transport in river beds, and mesoscale models of blood flow. In such problems, computational approaches can typically resolve only a limited range of length and time scales. The unresolved or subgrid scales are coupled to the macroscale using a variety of multi-scale modeling frameworks

S. Taverniers · G. B. Jacobs (✉) · V. Fountoulakis
Department of Aerospace Engineering, San Diego State University, San Diego, CA, USA
e-mail: gjacobs@mail.sdsu.edu

O. Sen · H. S. Udaykumar
Department of Industrial and Mechanical Engineering, University of Iowa, Iowa City, IA, USA

A. Sasoh et al. (eds.), *31st International Symposium on Shock Waves 2*,
https://doi.org/10.1007/978-3-319-91017-8_60

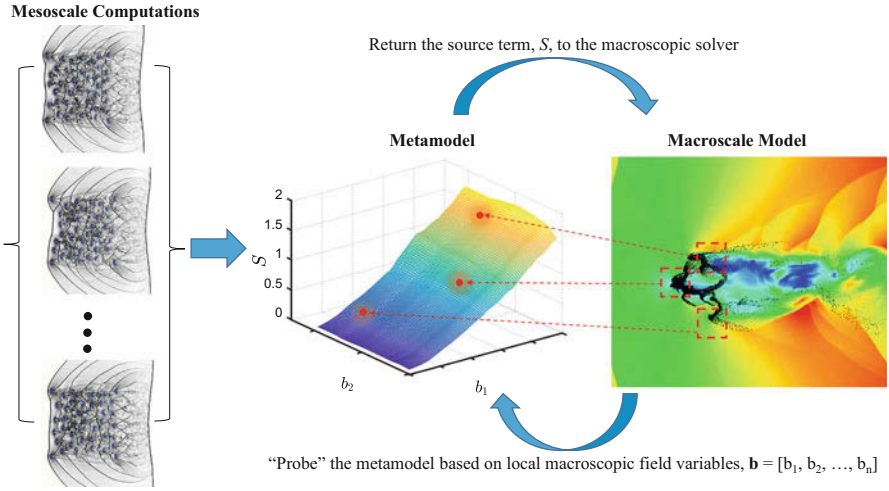

Fig. 1 A multi-scale approach to simulation of the interaction of a normal shock with a cloud of particles

such as patch dynamics, heterogeneous multi-scale modeling, multi-grid methods, wavelet-based methods, and others. In most multi-scale modeling frameworks, the subgrid scale physics is modeled using "closure laws" in homogenized (volume averaged/filtered/coarse-grained) macroscale systems of equations.

Traditionally, such closure laws are obtained from physical experiments, canonical theoretical constructs, or phenomenological arguments. With increasing computational power and improved physical models and algorithms, it is now possible to derive closure laws from highly resolved mesoscale simulations. In the current study, resolved mesoscale simulations of the interaction of a normal moving shock with a rectangular cloud of particles are used to find a parametric representation of closure terms in a macroscale model. Macroscale computations of the shock-fluid problem are performed for a typical process-scale problem, assuming a point-particle representation of the particle phase. The linkage between scales is established through metamodels that assimilate microscale physics into surrogate models and serve as closure models for the macroscale simulations (Fig. 1). Surrogate models [1, 2] for the drag of the particles in the cloud are generated as function of the shock Mach number (Ma) and volume fraction (ϕ) of the particle phase.

2 Mesoscale Computations of Shock-Particle Interactions

Typical mesoscale computations study the interaction of shocks with a cluster of physical particles. In this work, the particles are modeled as rigid cylinders inscribed within a representative volume element in the computational domain; the evolution

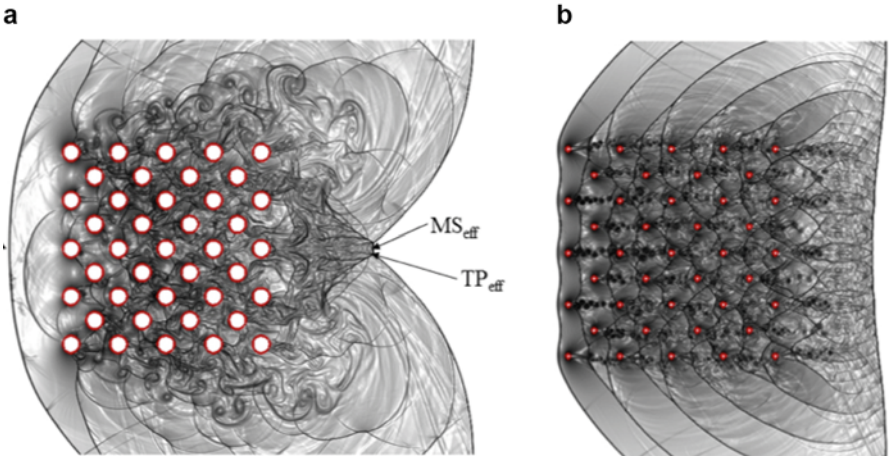

Fig. 2 Numerical Schlieren images of the interaction of a shock ($Ma = 3.5$) with a particle cluster of volume fraction (**a**) $\phi = 20\%$ and (**b**) $\phi = 1\%$ at $t^* = tu_s/l = 2.07$, where u_s is the velocity of the incoming shock, l is a characteristic length scale set to 1, and t^* is the nondimensional time in the compressible Euler equations

of drag around the cluster of particles is studied by solving the compressible Euler equations coupled with the ideal gas equation of state for air [3].

The mesoscale simulations show that both Ma and ϕ significantly influence the local flow dynamics around the particle cluster. For instance, numerical Schlieren images of shocks interacting with particles show that a higher particle volume fraction ϕ presents a greater obstruction to the incoming flow (Fig. 2a, b). Because of this, vortices are deflected transversely, and the transmitted shock has higher curvatures for higher ϕ (Fig. 2a, b). Similarly, for a given value of ϕ, altering the value of Ma is also observed to change the local flow features around the particle cluster (not shown here). Because both Ma and ϕ influence the dynamics of shock-particle interactions, the drag for particle clusters in mesoscale computations is expected to depend on Ma and ϕ; these are therefore selected as independent parameters of the surrogate model for drag.

3 Surrogate Models for Drag as a Function of Ma and ϕ

To obtain surrogate models for the drag as a function of Ma and ϕ, the drag forces around individual cylinders in the cluster are homogenized over space and time. Spatial homogenization is performed by computing the mean drag of the five central cylinders in the particle cluster. This spatially homogenized drag is further homogenized in time by averaging it over the time taken by the shock to traverse the particle cluster. The process of spatiotemporal homogenization yields a scalar value

for the representative drag for a given Ma and ϕ, which can be used for constructing surrogates for drag as a function of these parameters.

Surrogate models for drag on a cluster of particles interacting with shocks are developed using the modified Bayesian Kriging (MBKG) method. The MBKG method [4] assumes the inputs come from a stationary Gaussian random process, with a mean value of $\boldsymbol{P\lambda} + \boldsymbol{Z}$ and a covariance matrix $\sigma^2\beta\boldsymbol{I}$, i.e.,

$$f\left(\boldsymbol{x}_0\right) \sim \mathrm{MVN}\left(\boldsymbol{P\lambda} + \boldsymbol{Z}, \sigma^2\beta\boldsymbol{I}\right), \tag{1}$$

where $\boldsymbol{P\lambda}$ represents a polynomial mean structure, and $\boldsymbol{Z}$ is modeled as a Gaussian random process with zero mean and covariance $E[Z(\boldsymbol{x}_j)\, Z(\boldsymbol{x}_q)] = \sigma^2\boldsymbol{R}$. Here $\boldsymbol{R}$ is the spatial correlation of the input points, and the unknown parameters in the MBKG model are $\boldsymbol{\lambda}$, σ^2, $\boldsymbol{\theta}$, and β.

The MBKG method considers a probability distribution function over the weight space, representing the relative degrees of belief in different values for the model parameters. The function is initially set to a prior distribution. The observations, i.e., the inputs, are used to convert the prior distribution to a posterior distribution using Bayes' theorem. The posterior distribution is used to obtain desired (mean) values of the model parameters and the amount of uncertainty that remains in these values. In the present work, a Markov chain Monte Carlo method is used to estimate the parameters for the prior distribution for the MBKG method. Once the parameters of the prior distribution are estimated, the mean response and the credible sets are obtained as a function of the parameter space. More details on the MBKG method can be found in [3, 4].

Numerical experiments are conducted to compute the drag in a particle cluster for different values of Ma and ϕ [3]. These are used to obtain the mean drag using the MBKG method described above. A hypersurface of the drag is shown in Fig. 3.

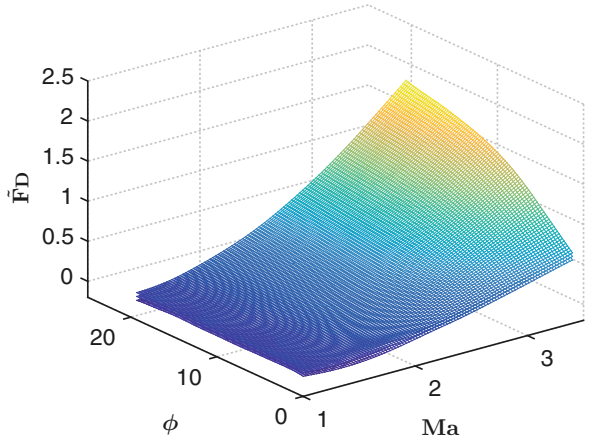

Fig. 3 Hypersurface of the drag in a particle cluster as a function of shock Mach number Ma and particle volume fraction ϕ

4 Bridging the Meso- and Macroscale Components

In the context of a multi-scale modeling framework, the drag in Fig. 3 serves as a numerical closure to the momentum equations in macroscale models such as particle-source-in-cell models [5, 6]. Over the course of macroscale computations, the latter need only "probe" the surrogate model for obtaining the drag at the local shock strength and number density. Therefore, the surrogate models discussed in the previous section demonstrate a way of transferring information from the mesoscale to the macroscale.

5 Macroscale Computations and the Subgrid Particle-Averaged Reynolds Stress Equivalent (SPARSE) Model

The Eulerian-Lagrangian (EL) approach introduced by Crowe et al. [5, 6] is one of the major models used for computing the interaction of a large number of particles with a turbulent flow on a macroscale level. The EL model traces each particle in its Lagrangian (i.e., co-moving) frame and treats it as a volumeless mathematical point; this makes tracing a large number of particles in a process-scale environment computationally feasible.

For a prohibitively large number of particles, groups of physical particles are amalgamated into a single computational "macro-particle" to reduce computational cost. This technique is known as cloud-in-cell (CIC) [6] and moves the macro-particles under the influence of the Stokes drag exerted on them by the fluid. In their conventional implementation, CIC approaches do not account for sub-particle cloud dynamics resulting from turbulent fluctuations or particle-particle interactions. A Lagrangian particle-cloud model is proposed that accounts for the effects of subgrid Reynolds stress-like interphase velocity and temperature fluctuations and the average carrier-phase velocity on the average position, velocity and temperature of the cloud, and couples with the carrier flow through a Gaussian source term in the fluid equations which are evaluated on an Eulerian grid.

When initially proposed in [7], this so-called subgrid particle-averaged Reynolds stress equivalent (SPARSE) model only addressed the particle momentum equation:

$$\frac{\mathrm{d}\boldsymbol{v}_p}{\mathrm{d}t} = f_1\left(\boldsymbol{u}-\boldsymbol{v_p}\right)\frac{\boldsymbol{u}-\boldsymbol{v_p}}{\tau_p} - \left(\frac{1}{\rho_p}\right)(\nabla P)_f \equiv f_1\left(\boldsymbol{a}\right)\frac{\boldsymbol{a}}{\tau_p} - \left(\frac{1}{\rho_p}\right)(\nabla P)_f, \quad (2)$$

where $\boldsymbol{a} \equiv \boldsymbol{u}-\boldsymbol{v_p}$, f_1 is a drag correction factor, τ_p is the particle time constant, ρ_p is the particle density, and P is the fluid pressure. Via a Taylor expansion of the particle

drag correction factor and a Reynolds decomposition of the particle positions and velocities, it is replaced (2) with

$$\frac{\mathrm{d}\overline{v}_{p,\ x}}{\mathrm{d}t} \approx \frac{1}{\tau_p}\left[f_1\left(\overline{\boldsymbol{a}}\right)\overline{a}_x + \frac{\mathrm{d}f_1\left(\overline{\boldsymbol{a}}\right)}{\mathrm{d}a_x}\overline{a'_x a'_x} + \frac{\mathrm{d}f_1\left(\overline{\boldsymbol{a}}\right)}{\mathrm{d}a_y}\overline{a'_x a'_y}\right] - \frac{1}{\rho_p}\left(\frac{\partial\overline{P}}{\partial x}\right)_f, \quad (3)$$

$$\frac{\mathrm{d}\overline{v}_{p,y}}{\mathrm{d}t} \approx \frac{1}{\tau_p}\left[f_1\left(\overline{\boldsymbol{a}}\right)\overline{a}_y + \frac{\mathrm{d}f_1\left(\overline{\boldsymbol{a}}\right)}{\mathrm{d}a_x}\overline{a'_x a'_y} + \frac{\mathrm{d}f_1\left(\overline{\boldsymbol{a}}\right)}{\mathrm{d}a_y}\overline{a'_y a'_y}\right] - \frac{1}{\rho_p}\left(\frac{\partial\overline{P}}{\partial y}\right)_f. \quad (4)$$

The original SPARSE model is improved by addressing the particle temperature equation:

$$\frac{\mathrm{d}T_p}{\mathrm{d}t} = \frac{Nu}{3\mathrm{Pr}}\frac{T_f - T_p}{\tau_p} \equiv f_2\left(\boldsymbol{a}\right)\frac{b}{\tau_p}, \quad (5)$$

where $b \equiv T_f - T_p$. Taylor expanding the conductivity f_2 and Reynolds averaging yields

$$\frac{\mathrm{d}\overline{T}_p}{\mathrm{d}t} = \frac{1}{\tau_p}\left[f_2\left(\overline{\boldsymbol{a}}\right)\overline{b} + \frac{\mathrm{d}f_2\left(\overline{\boldsymbol{a}}\right)}{\mathrm{d}a_x}\overline{a'_x b'} + \frac{\mathrm{d}f_2\left(\overline{\boldsymbol{a}}\right)}{\mathrm{d}a_y}\overline{a'_y b'}\right]. \quad (6)$$

Aside from replacing individual particle tracing with tracing of a single macro-particle, the SPARSE model also replaces first-order weighing with Gaussian weighing, in which the entire particle cloud is represented by a multivariate Gaussian distribution.

Figure 4a, b shows the fluid pressure profiles, with the particle positions superimposed, computed using the standard CIC approach with first-order weighing (a) and the SPARSE model with Gaussian weighing (b). The SPARSE calculation models the entire particle cloud using a single computational particle (center of

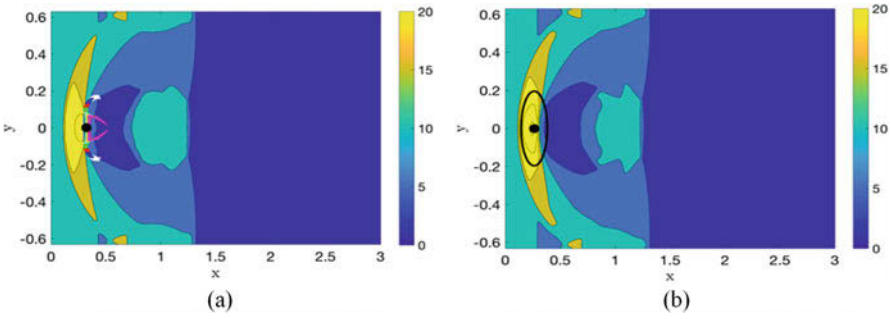

Fig. 4 Comparison of the fluid pressure profile for the standard CIC approach with first-order weighing (**a**) and the SPARSE model with Gaussian weighing (**b**)

ellipse) and represents its influence on the surrounding fluid as a bivariate Gaussian distribution (contour of ellipse). Comparison of (a) and (b) reveals that SPARSE captures the main features of the flow and approximates well the particle cloud's average position (indicated by the black dot). The parameters for these simulations were taken from [8].

6 Conclusions and Future Work

We find that the SPARSE approach successfully reproduces the main features of the shocked particle-laden flow as compared to a standard CIC simulation with first-order particle weighing. It also provides a good first-order approximation to the dynamics of the particle cloud. In ongoing work we are testing and validating the multi-scale framework against experimental data and further refining the SPARSE model by using more than one macro-particle to represent the full cloud.

References

1. O. Sen, S. Davis, G. Jacobs, H.S. Udaykumar, Evaluation of convergence behavior of metamodeling techniques for bridging scales in multi-scale multimaterial simulation. J. Comput. Phys. **294**, 585–604 (2015)
2. L. Zhao, K.K. Choi, I. Lee, A metamodeling method using dynamic kriging and sequential sampling, in *Proceedings of the 13th AIAA/ISSMO Multidisciplinary Analysis Optimization Conference*, Forth Worth, Texas, 13–15 September 2010
3. O. Sen, N.J. Gaul, K.K. Choi, G. Jacobs, H.S. Udaykumar, Evaluation of kriging based surrogate models constructed from mesoscale computations of shock interaction with particles. J. Comput. Phys. **336**, 235–260 (2017)
4. N.J. Gaul, M.K. Cowles, H. Cho, K.K. Choi, D. Lamb, Modified Bayesian Kriging for noisy response problems for reliability analysis, in *Proceedings of the ASME 2015 International Design Engineering Technical Conferences and Computers and Information in Engineering Conference*, *Volume 2B: 41st Design Automation Conference*, Boston, MA, 2–5 August 2015
5. C.T. Crowe, M.P. Sharma, D.E. Stock, The Particle-Source-In Cell (PSI-Cell) model for gas-droplet flows. J. Fluids Eng. **99**(2), 325–332 (1977)
6. C.T. Crowe, *Multiphase Flows with Droplets and Particles*, 2nd edn. (CRC Press, Boca Raton, 2012)
7. S. Davis, G.B. Jacobs, O. Sen, H.S. Udaykumar, SPARSE – A subgrid particle averaged Reynolds stress equivalent model: Testing with a priori closure. Proc. R. Soc. A **473**, 20160769 (2017)
8. G.B. Jacobs, W.S. Don, A high-order WENO-Z finite difference based particle-source-in-cell method for computation of particle-laden flows with shocks. J. Comput. Phys. **228**, 1365–1379 (2009)

Surface Jetting Induced by Explosion in Liquid Below an Immersed Bubble

Y. Zhu, G. Zhang, and J. Yang

Abstract The surface jets induced by an explosion below an immersed gas bubble in water are investigated experimentally. Typical phenomena including the bubble evolution and the jet formation are observed through high-speed photography. It is found that the inner jet resulting from the shock bubble interaction is the main cause of the surface jet. The velocity of the surface jet decreases with the initial depth of the bubble, and there exists a maximum bubble depth above which no surface jet occurs.

1 Introduction

An impact loading on a bulk of condensed matter may cause ejection of the matter in the case that defects exist on the surface of or inside the bulk. A typical example is the microjetting phenomenon which constantly occurs as a strong shock wave that reflects from a free surface [1]. The defects can be cavities or dopants. Many have been devoted to studying the jetting phenomenon due to surface defects [2] or surface curvature [3]. The jetting phenomenon due to inner defects is much less recognized, however. To extend the knowledge of the latter, we use a near-surface bubble immersed in water to mimic a single cavity defect in condensed matter and investigate the surface jetting phenomenon originating from it under the load of an underwater explosion.

As a significant part of the phenomenon, the interaction of the shock wave with the bubble, as well as the asymmetrical collapse of the bubble, has drawn plenty of attention for a long time. The collapse of the bubble is generally characterized by the formation of a small but strong inner jet in the direction of the shock wave [4]. The inner jet then penetrates the bubble, whereby the bubble turns into a toroidal shape in the later stage of development. Further impingement of the jet on

Y. Zhu (✉) · G. Zhang · J. Yang
Department of Modern Mechanics, University of Science and Technology of China, Hefei, China
e-mail: yujianrd@ustc.edu.cn

A. Sasoh et al. (eds.), *31st International Symposium on Shock Waves 2*,
https://doi.org/10.1007/978-3-319-91017-8_61

a nearby object surface was found to be a key mechanism of cavitation erosion [5] and extracorporeal shock wave lithotripsy [6]. With such engineering backgrounds, the interaction of the shock-induced collapse with a certain boundary or interface was also of great interest. Varied materials were tested, such as rigid walls [6, 7], thin aluminum films [6, 8], gelatin blocks [6, 9, 10], organic tissues [6], and so on. However, the response of the bubble near a free surface, which is the main concern of the present study, was barely reported. The features of the bubble evolution in this layout and the correspondence between the bubble evolution and the formation of surface jet are still unclear.

The current paper focuses on the interfacial phenomenon induced by an underwater explosion below a shallowly immersed bubble. Sequential images of the flows in development are captured, and the influences of the bubble depth are examined.

2 Experimental Method

The ideal of the experiments is to create a gas bubble in water in a straight vertical tube and then to generate an explosion at the bottom of the tube.

The experimental setup is illustrated in Fig. 1. The main test section is a round glass tube with an inner diameter of 32 mm mounted on a flat, acrylic base. Along the axis of the tube is a small capillary which connects to an empty piston syringe. Bubbles are generated by slowly injecting air into the water. The explosion is generated by an electrical discharge through a thin wire, where the current is sufficiently high to cause the wire to explode. The electrical supply is basically a series circuit which consists of a bank of capacitors, an electric relay controlled by outer signals, and two copper electrodes installed on the base plate for connecting to the exploding wire. In preparation of a test, we charge the capacitors to a certain voltage. Explosion takes place when the relay contacts. The current experiments use a total capacitance of 2000 μF and an initial charging voltage of 200 V.

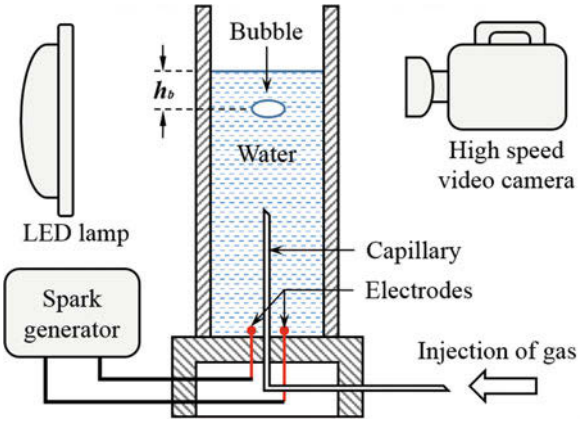

Fig. 1 Schematic of experimental setup

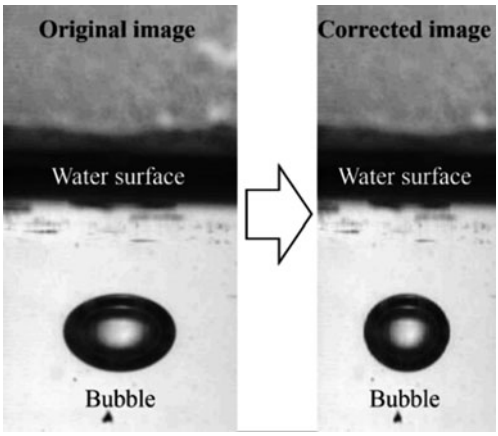

Fig. 2 An example of image correction

The tube is partially filled with water. The total height (or depth) of the water column is fixed as 70 mm for all tests. The head of capillary is about 20 mm below the water surface. In order to suppress the random drifting of the rising bubble, water solution of sodium dodecyl sulfate (SDS) instead of pure water is applied. The signal to trigger the relay is sent by a photodiode which detects the arrival of the bubble. The initial bubble depth, h_b, i.e., the distance between the water surface and the center of the bubble at the moment of explosion initiation, can be varied by adjusting the vertical position of the photodiode. An LED lamp is used to illuminate the test section, and a high-speed camera with a framing rate up to 20,000 fps is used to record the flow.

Because of the optical refraction of the round tube filled with water, the images of the bubbles in water are distorted. The distortion is calibrated using a flat plate with grids on it, based on which the images are corrected. An example of the images before and after the correction is shown in Fig. 2. One may find from the corrected image that the bubble is almost spherical. The diameters of the bubbles are about 2.0 mm.

3 Results and Discussion

The results with different bubble depth are presented. Figures 3, 4, and 5 show the high-speed sequential images of the three typical flows.

A representative case with a medium bubble depth, $h_b = 4.1$ mm, is shown in Fig. 3. When the explosion takes place, it emits light which illuminates the tube (0.1 ms). The whole water column rises at first due to the impulse of the explosion. In the first 0.2 ms, the bubble rises even faster because of the buoyancy caused by the acceleration of the water bulk, after which the main bubble migrates accordingly with the water column. At the same time, the disturbance of the explosion causes the bubble to oscillate periodically with alternative expansions and contractions. This phenomenon is evident in the horizontal direction, whereas, in the vertical direction,

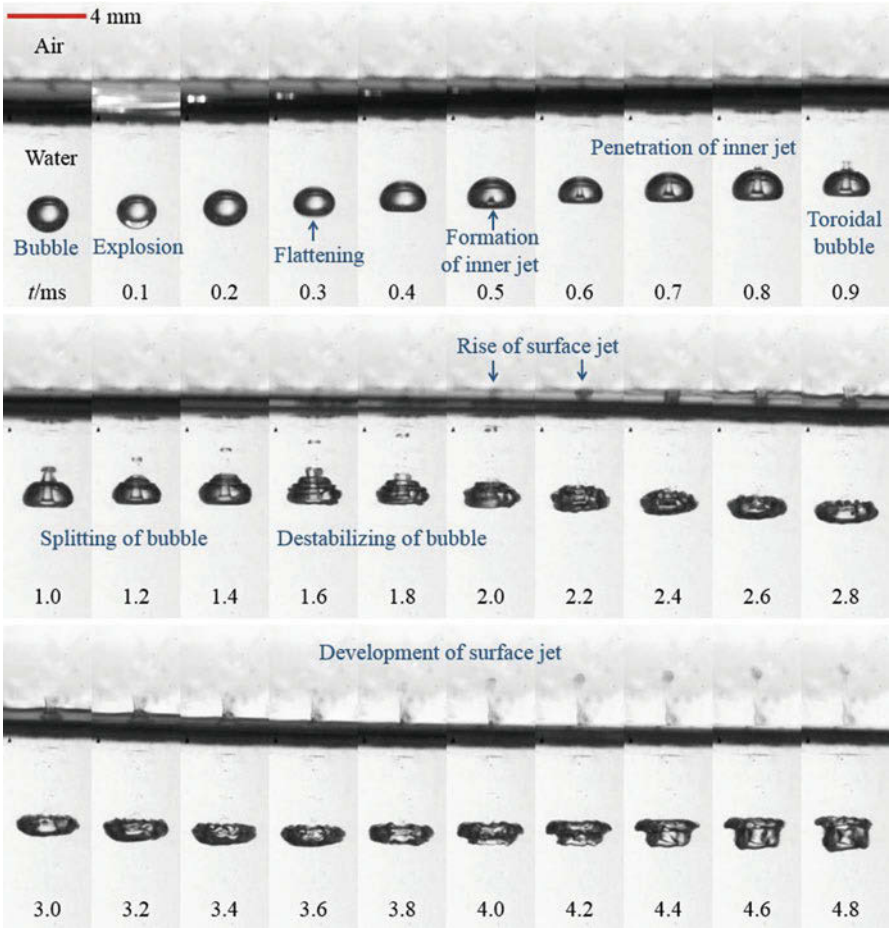

Fig. 3 High-speed sequential images showing the bubble evolution and the development of surface jet with an initial bubble depth of 4.1 mm

it is overwhelmed by the much severer bubble collapse process. The water surface rises to the maximum height at about 2.0 ms and then falls back. The main bubble follows a similar trend.

The vertical collapse of the bubble starts from the side facing the explosion, i.e., the bottom of the bubble in this study. As described in previous investigations [7, 8], the bottom of the bubble flattens at first and then develops an upward inner jet (0.5–0.7 ms). The inner jet is sharp and fast. Penetration of the inner jet further transforms the bubble into a toroidal shape (0.8–1.4 ms). The jet maintains a relatively high speed as it reenters the upper water. A part of the main bubble is entrained by the jet which then rolls up and splits from the main bubble to form a small ring bubble. The ring bubble can be roughly seen as a delayed marker of the jet frontier. When the jet flow reaches the free surface, a surface jet develops (2.0 ms). In this case, the velocity of the surface jet is about 1 m/s.

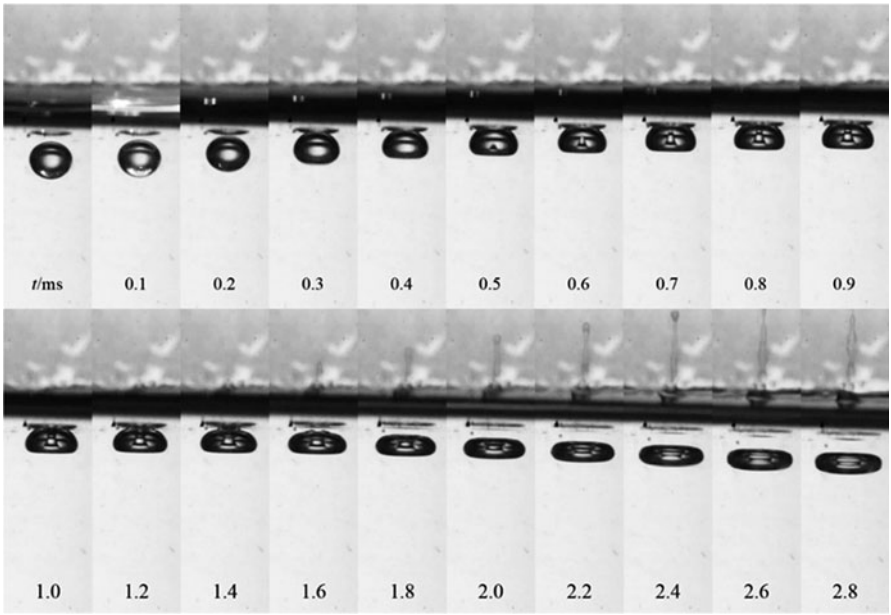

Fig. 4 High-speed sequential images showing the bubble evolution and the development of surface jet with an initial bubble depth of 1.3 mm

Reducing the bubble depth leads to a similar phenomenon. Figure 4 shows the result obtained with an extremely small depth, $h_b = 1.3$ mm. The initial bubble is almost attached to the free surface. After the explosion interacts with it, it actually floats to the surface, as shown in the frames after 0.3 ms. The formation of the inner jet takes place at about 0.5 ms, the same time as the former case. For the distance to the surface is smaller and there is less water in the way of the jet, the surface jet comes into forth earlier than the former case, and the jet velocity is much larger.

Increasing the bubble depth may lead to a different situation on the other hand. Because the strength of the jet flow attenuates when the jet pierces through the rest of the water, there must exist a maximum bubble depth higher than which the jet may not penetrate. Figure 5 shows the result with a bubble depth of 5.2 mm. Although the evolution of the overall water column and the bubble remains similar to the first case, the inner jet seems to fail to reach the free surface, and no surface jet is developed. The separated ring bubble which roughly marks the jet frontier stalls in the middle eventually, despite of the fast rising stage before 2.0 ms.

The experimentally obtained velocities of the surface jets with different bubble depths are summarized in Fig. 4. It shows that the velocity of surface jet decreases with the bubble depth. The critical bubble depth is about 4.5 mm. When the bubble depth is larger than the critical value, the inner jet may not penetrate the free surface, and hence no surface jet occurs (Fig. 6).

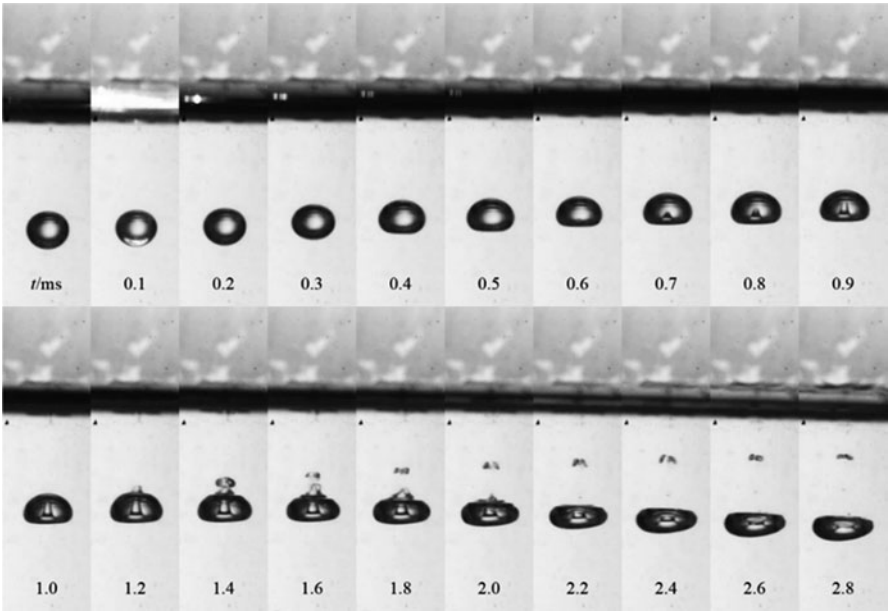

Fig. 5 High-speed sequential images showing the bubble evolution without surface jet with an initial bubble depth of 5.2 mm

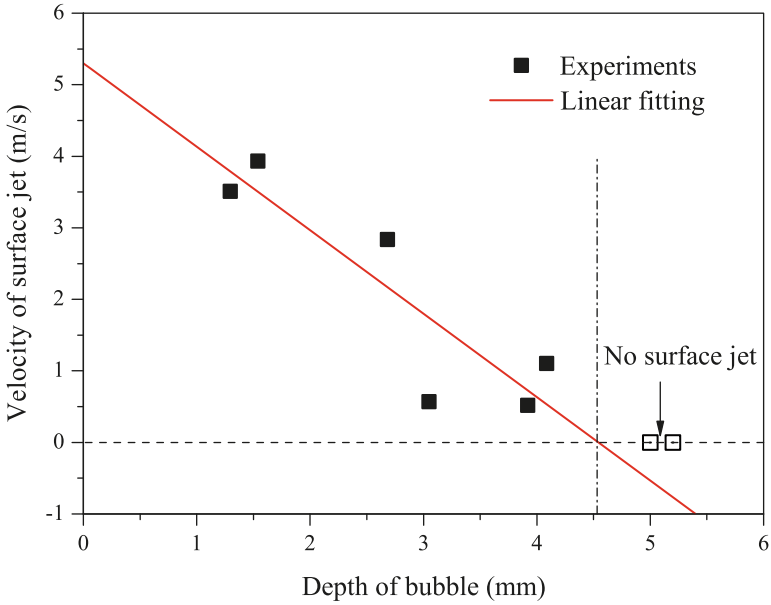

Fig. 6 Velocity of the surface jet varying with the bubble depth

4 Conclusion

The surface jets induced by the interaction of an explosion with a near-surface gas bubble in water were investigated experimentally. The interfacial flow including the bubble evolution and the jet formation was observed by the method of high-speed photography.

It is found that the bubble subsequent to the interaction of an underwater explosion may develop a small but strong jet inside the bubble. It is this inner jet that penetrates through the water column above the bubble and causes a jet on the surface. The velocity of the surface jet decreases with the depth of the immersed bubble, given the bubble size and the explosion energy are fixed. When the bubble is deeper than a certain depth, the inner jet cannot break up the free surface to cause a surface jet.

References

1. J.R. Asay, *Material Ejection from Shock-Loaded Free Surfaces of Aluminum and Lead*, SAND76-0542, (1976)
2. M.B. Zellner et al., Effects of shock-breakout pressure on ejection of micron-scale material from shocked tin surfaces. J. Appl. Phys. **102**, 013522 (2007)
3. A. Antkowiak, N. Bremond, S. LeDizes, E. Villermaux, Short-term dynamics of a density interface following an impact. J. Fluid Mech. **577**, 241 (2007)
4. C.D. Ohl, R. Ikink, Shock-wave-induced jetting of micron-size bubbles. Phys. Rev. Lett. **90**, 214502 (2003)
5. A. Philipp, W. Lauterborn, Cavitation erosion by single laser-produced bubbles. J. Fluid Mech. **361**, 77–116 (1998)
6. T. Kodama, K. Takayama, Dynamic behavior of bubbles during extracorporeal shock-wave lithotripsy. Ultrasound Med. Biol. **24**, 723–738 (1998)
7. Y. Tomita, A. Shima, T. Ohno, Collapse of multiple gas bubbles by a shock wave and induced impulsive pressure. J. Appl. Phys. **56**, 125 (2007)
8. A. Philipp, M. Delius, C. Scheffczyk, A. Vogel, W. Lauterborn, Interaction of lithotripter-generated shock waves with air bubbles. J. Acoust. Soc. Am. **93**, 2496 (1993)
9. T. Kodama, K. Takayama, N. Nagayasu, The dynamics of two air bubbles loaded by an underwater shock wave. J. Appl. Phys. **80**, 5587 (1996)
10. T. Kodama, Y. Tomita, Cavitation bubble behavior and bubble–shock wave interaction near a gelatin surface as a study of in vivo bubble dynamics. Appl. Phys. B Lasers Opt. **70**, 139–149 (2000)

Generation Frequency of Rebound Shock Waves from Bubble Collapses in Cavitation Jet

K. Nishibayashi, J. Wang, and A. Abe

Abstract In this paper, a method using cavitation jet is proposed to remove marine creatures adhered to the body of a ship. The flow with the cavitation jet is produced using a high-pressure pump and cavitation nozzle with an orifice plate. Rebound shock waves are expected to be continuously generated in the cavitation jet flow. In order to observe the behaviors of the rebound shock waves, experiments are carried out using the Schlieren method in a water tank. From the results of the visualization, it is found the generation frequency of the rebound shock wave reaches its peak at a close position to the nozzle exit. The behaviors of the rebound shock waves are also investigated under the influence of a wall boundary beside a cavitation jet. The results show that the position where the maximum generation frequency is obtained is at several ten times of an orifice diameter from the nozzle exit, and the generation frequency decreases due to the effect of the wall boundary.

1 Introduction

Recently, the importance of marine transportation has been rising in global economic activities, and there is no room for doubt that the Japanese economy is not maintained without ship transportation [1]. Considering the navigation cost of marine transportation, the fuel costs occupy half of the total running cost. Therefore, in the maritime economic field, reduction of fuel costs directly improve operating costs of ship [2]. In order to reduce fuel consumption, especially it is important to decrease drag on the hull in sea. One of the causes of drag generation

K. Nishibayashi · A. Abe (✉)
Graduate School of Maritime Sciences, Kobe University, Kobe, Japan
e-mail: a-abe@maritime.kobe-u.ac.jp

J. Wang
Key Laboratory for Mechanics in Fluid Solid Coupling Systems, Institute of Mechanics, Chinese Academy of Sciences, Beijing, China

School of Engineering Science, University of Chinese Academy of Sciences, Beijing, China

A. Sasoh et al. (eds.), *31st International Symposium on Shock Waves 2*,
https://doi.org/10.1007/978-3-319-91017-8_62

is marine creatures adhered to the hull. In addition, marine creatures carried by ships cause marine environmental hazard in the whole world. Therefore, ship's body should be always kept clean without adhesion of marine creatures. As one of the preventative measures, special paints are used, but perfect prevention is not expected, and chemical paints have potential risks to marine environment [3]. In fact, ships sometimes need to remove marine creatures from the hull. Generally, the cleaning is operated by sandblast in periodic maintenance on shore. Furthermore, note that dust of sandblast has a bad risk for human health [4].

It is well known that cavitating water jet is effective on cleaning and it has actually been used. It is thought that high cleaning effects are caused by micro-water jet and shock pressures generated from collapse of cavitation bubbles. Water jet is generated by a high-pressure pump and has extremely high energy per unit area [5]. Due to the use of water, there is no problem about dust generation. There is a lot of previous study of water jet behavior; however, the research on the characteristics of the cavitating water jet has not been sufficiently examined yet.

In this paper, in order to establish a method using cavitation jet to remove marine creatures from ship's body surface, the behavior of cavitation jet in water is considered experimentally. Bubbles discharged from a cavitation nozzle are collapsed by ambient pressure. Using cavitation jet, rebound shock waves and micro-jets are probably applied to cleaning of wall. Therefore, effective underwater cleaning may be expected by finding of appropriate conditions. In the experiments, a high-velocity water jet flow with cavitation is generated using a plunger pump and a cavitation nozzle with an orifice plate. Behaviors of cavitation flow discharged from a cavitation nozzle are observed by Schlieren method in a water tank. The generation frequencies of the rebound shock wave are investigated using optical images. Furthermore, we also discuss on the generation of rebound shock waves under the different conditions of the wall boundary beside the cavitation jet.

2 Experimental

Figure 1 shows a schematic of the experimental setup for observation of the cavitation jet flow. The system consisted of a stainless-made cavitation nozzle, a triplex plunger pumps (AJP-1700VGQ, Ryobi Limited), and a water tank with

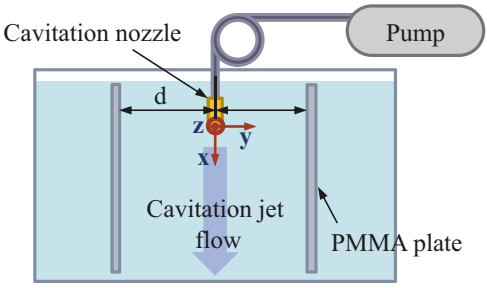

Fig. 1 Schematic of experimental setup for cavitation jet observation

450 mm (width) × 600 mm (length) × 450 mm (height). The dimensions of the cavitation nozzle were 30 mm in diameter and 130 mm in length that was vertically positioned toward the bottom in the water tank. Inside the cavitation nozzle, there was a stainless orifice plate of 15 mm in diameter and 2 mm in thickness with a 1-mm diameter orifice. To accelerate and pressurize water flow, the nozzle was connected to the pump. In the experiment, the applied pressure of the pump was 8.4 MPa. When the high-pressure water flow from the pump passed through the nozzle, the region of negative pressure was generated at the exit of the orifice plate, so that cavitation bubbles were discharged from the nozzle exit. As shown in Fig. 1, PMMA boards were set in the water tank as wall boundaries beside the cavitation jet. The cavitation jet flows were observed with a high-speed camera (HX-3, NAC Image Technology Inc.) using Schlieren method. The frame rate of the camera was 100 kfps and exposure time was 300 ns.

3 Results and Discussion

Figure 2 shows sequential images of the cavitation jet flow. The nozzle exit was on the right side of the images. The shadow of the cavitation jet flow stretches out long and thin from the nozzle exit to the left side. The maximum diameter of the shadow of cavitation cloud was measured about 15 mm from the image. In Figs. 2b and c, rebound shock waves, generated by the motion of cavitation cloud, were continuously observed at a position of about 40 mm from the nozzle exit. Following that, the rebound shock waves were generated at about 30 mm in Figs. 2d–f.

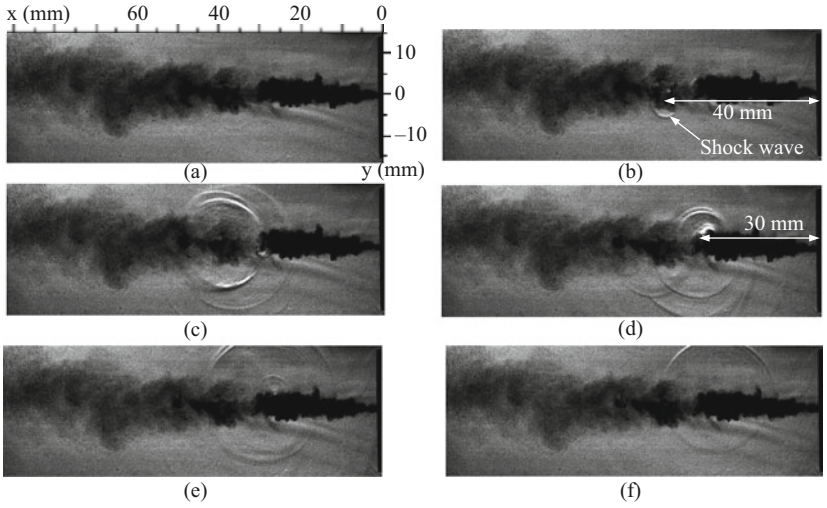

Fig. 2 Sequential observation of rebound underwater shock waves generated in cavitation jet. (**a**) 0 μs, (**b**) 10 μs, (**c**) 20 μs, (**d**) 30 μs, (**f**) 50 μs

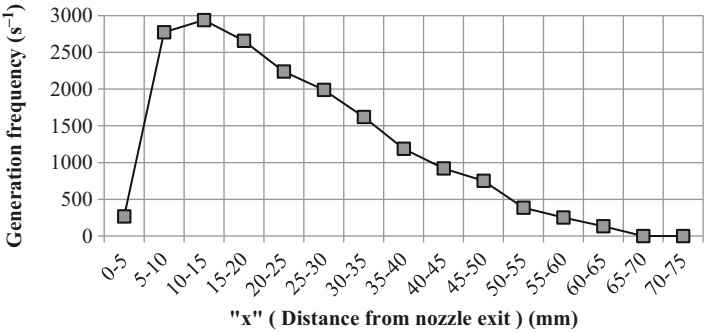

Fig. 3 Distributions of generation frequency along the x-axis

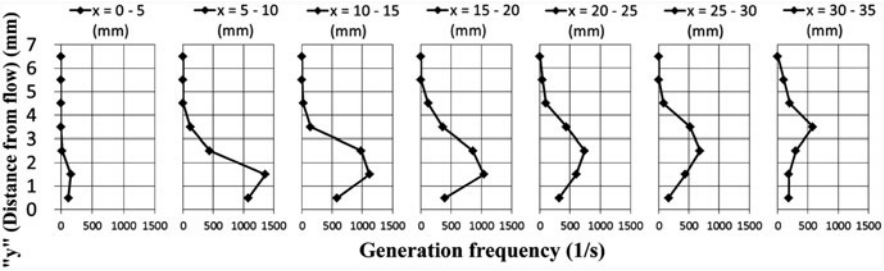

Fig. 4 Distributions of generation frequency along the y-axis

Fig. 3 shows the relationship between generation frequency and observation area along the x-axis defined in Fig. 1. The ordinate is the generation frequency of rebound shock waves, and the abscissa is the measured area of every 5 mm from the nozzle exit. The result shows that the peak value of the generation frequency appeared in the area of 10 mm to 15 mm distance from the nozzle exit. This phenomenon is closely related to the velocity of the cavitation jet flow. According to the principle of the nozzle flow, the flow velocity from the nozzle exit is assumed to be a constant value in the region within about 10-mm distance from the nozzle exit, and the flow velocity suddenly decreases beyond the boundary of around 10 mm from the exit [6]. The pressure increments with those velocity changes cause the beginning of motion of cavitation bubbles, so that a large number of rebound shock waves are generated in this area. From the position of 10 mm, the generation frequency decreases because the velocity of the flow gradually decreases with increase of x. As a result, the generation of the rebound shock wave is affected by the state of the water flow around the cavitation jet. Therefore, the experimental visualization of the rebound shock waves was carried out using a wall boundary beside the cavitation jet.

Figure 4 shows the change of the generation frequency of rebound shock wave along the y-axis defined in Fig. 1. The peak value of generation frequency reaches around 1400 s^{-1} at the $x = 5$–10-mm area. After that, the peak values decrease with

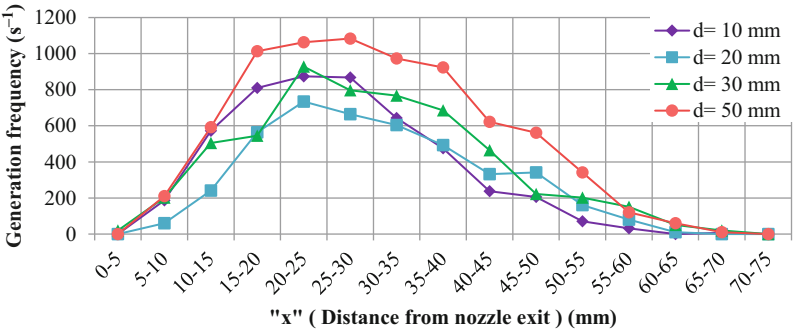

Fig. 5 Distributions of generation frequency along the x-axis setting up a wall boundary beside the cavitation jet

increase of x, and the position of the peak value moves to the y-direction, i.e., the position of peak value of generation frequency goes away from the x-axis along the downstream. In addition, the distributions of generation frequency gradually become gentle. The change in the flow velocity around the center axis of jet is considered to be small at the position more than 10 mm apart from the exit, so that it is hard to make the rebound of cavitation bubble. On the other hand, the peak value of the generation frequency tends to move outward with the distance from the nozzle exit because the cross section of jet increases with the flow dissipation.

Figure 5 shows distributions of generation frequency along the x-axis setting up a PMMA plate as a wall boundary beside the cavitation jet. The curves indicated by the symbols, diamonds, squares, triangles, and circles, are the results obtained when the distances between the wall and the central axis of the cavitation jet were 10 mm, 20 mm, 30 mm, and 50 mm, respectively. Comparing with Fig. 3, all peak values of the generation frequencies are obviously small, and the measurement areas corresponding to the peak frequencies are from 20 mm to 30 mm away from the nozzle exit. We consider that the spread of the cavitation flow is controlled not to be wide by a wall boundary near the jet, so that the pressure change with flow velocity becomes gradual; therefore, the generation number of the rebound shock wave decreases. In addition, in the measurement area of 20 mm to 50 mm, there is a tendency that the generation frequency changes with the position of the wall boundary. However, we can also see that the generation frequency distribution becomes relatively large and out of the tendency in the case of $d = 10$ mm. When the position of the wall boundary closes to the cavitation jet, the flow along wall boundary is formed by Coanda effect, and some conditions of cavitation collapse may be satisfied.

Figure 6 shows distributions of generation frequency along the y-axis setting up a wall boundary beside the cavitation jet. The values of generation frequency in this figure mean the sum of generation frequencies measured within $x = 70$. The solid circles and triangles represent the results obtained with 50-mm and 10-mm distances between the PMMA plate and the central axis of the jet. The total number

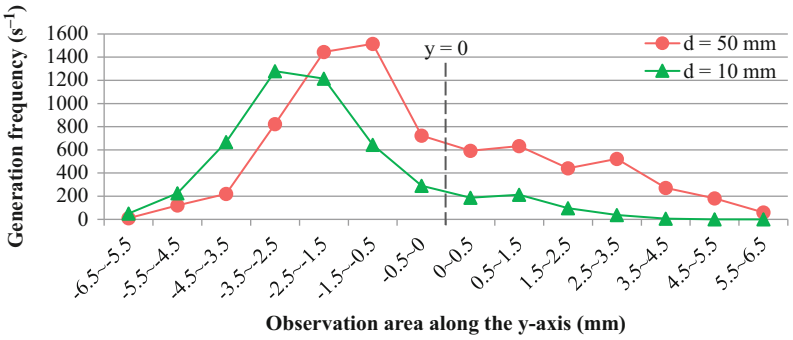

Fig. 6 Distributions of the sum of the generation frequencies measured within $x = 70$ along the y-axis setting up a wall boundary beside the cavitation jet: ● 50 mm, ▲ 10 mm

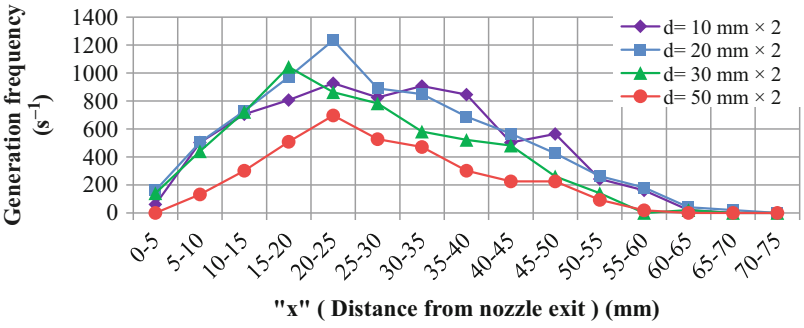

Fig. 7 Distributions of generation frequency along the x-axis setting up two wall boundaries

of generation frequencies of rebound shock waves in the left area is larger than that in the right area due to small changes of the flow velocity near the wall boundary. This tendency becomes remarkable with decrease of distance between a wall and cavitation flow.

Figure 7 shows distributions of generation frequency along the x-axis setting up wall boundaries at both sides of the cavitation jet. The solid diamond, squares, triangles, and circles indicate the results obtained with 10 × 2 mm, 20 × 2 mm, 30 × 2 mm, and 50 × 2 mm of distances between the two wall boundaries, respectively. From the figure, it is found that the generation frequency increases with decrease of the distance between two wall boundaries except the case of 10 × 2 mm. We consider that this phenomenon is concerned with the convection of the water between the wall and jet, and the convection in the wide space develops easier than that in the narrow space. The cavitation flow does not spread out due to the convection generated between two walls; as a result deceleration of the jet-flow velocity hardly generates so that motion of cavitation bubbles is also inactive. Therefore, it is assumed that the relationship between generation frequency and distance between walls of Fig. 7 shows the opposite relation to that of Fig. 5.

4 Conclusions

In this paper, behavior of a cavitation jet in water was investigated as an effective cleaning technique for marine creatures adhered to the hull. Rebound shock waves and micro-jets generated by the collapse of cavitation cloud were expected to remove these marine creatures. In the experiments, cavitation clouds were generated using a cavitation nozzle. The rebound shock waves generated in the jet flow were observed using the Schlieren method. In addition, a wall boundary was set up beside the cavitation jet. From optical images, the generation frequencies of the rebound shock wave were analyzed along the x- and y-axis of the flow. As a result, it was found that the generation frequency achieved its peak at a close position to the nozzle exit without a wall boundary. Furthermore, the position of the peak value in the y-direction moved toward the outer of flow with the distance of the x-direction. These results suggested that the collapse of cavitation is closely related to the change in the flow velocity. In the case of setting a wall boundary, the peak of generation frequency appeared far away from the nozzle exit. Using a wall boundary, the generation frequency increased with the distance between the wall and flow. For wall boundaries setting up at both sides of the jet, the generation frequency increased with decrease of the distance. It was thought that these phenomena were concerned with the convection of the flow between the wall and cavitation jet.

Acknowledgments A part of the study was supported by JSPS KAKENHI Grant Number 16H04600. In addition, we also would like to sincerely thank NAC Image Technology Inc. for the supply of camera.

References

1. Nippon Yusen Kabushiki Kaisha NYK Report Business Management Strategy, 2014
2. W. Simon, Tributyltin pollution on a global scale, An overview of relevant and recent research: Impacts and issues, WWF Living Planet Report, 2006
3. N. Alert, *Request for Assistance in Preventing Silicosis and Deaths From Sandblasting.* (DHHS (NIOSH) Publication, 1992), pp. 92–102
4. M. Szymczak, S. Tavoularis, A. Fahim, M. Vijay, Flow visualization of Cavitating, high-speed, submerged water jets. J. Eng. Ind. **113**(4), 485–489 (1991)
5. A. Guha, R.M. Barron, R. Balachandar, An experimental and numerical study of water jet cleaning process. J. Mater. Process. Technol. **211**(4), 610–618 (2011)
6. S. Sivakumar, R. Sangras, V. Raghavan, Characteristics of turbulent round jets in its potential-Core Region. J Mech Aeros Indus Mech Manuf Eng **6**(1) (2012)

Experimental Study on the Influence of Underwater Explosion Depth on the Disintegration of Thin Resin Plate Attached Microbubbles

T. Koita, M. Sun, Y. Fukushima, L. Guo, X. Zhao, and S. Kobayashi

Abstract This paper reports on the influence of underwater explosion depth on the disintegration of thin polystyrene plate attached microbubbles subjected to the underwater shock wave and the primary bubble induced by the explosion. The underwater explosion is created by the electrical discharge. The thin plate motion caused by the interaction of underwater shock wave and primary bubble with the plate is experimentally investigated and visualized by the shadowgraph method. The effect of explosion depth on the disintegration of plate is discussed by comparing visualized images. It was found that the disintegration of plate was depended on the explosion depth. It was also confirmed that the fragmentation of plate was caused not by the overpressure from microbubble collapse by the underwater shock wave loading but by the interaction of rebounding primary bubble with the plate in the experimental conditions of this study.

1 Introduction

Recently, A. Abe et al. [1, 2] studied experimentally and theoretically the generation of overpressure from microbubble collapse caused by the underwater shock wave loading. The microbubble is contracted immediately by the underwater shock wave loading, resulting in the rapid compression of gas inside the microbubble, so that the contracted microbubble emits the underwater shock wave with the overpressure. The microbubble expands after the bubble contraction. It is noticed above that these

T. Koita (✉)
Faculty of Engineering, Saitama Institute of Technology, Fusaiji, Fukaya, Saitama, Japan
e-mail: koita@sit.ac.jp

M. Sun
Institute of Fluid Science, Tohoku University, Aoba-ku, Sendai, Miyagi, Japan

Y. Fukushima · L. Guo · X. Zhao · S. Kobayashi
Graduate School of Engineering, Saitama Institute of Technology, Fusaiji, Fukaya, Saitama, Japan

A. Sasoh et al. (eds.), *31st International Symposium on Shock Waves 2*,
https://doi.org/10.1007/978-3-319-91017-8_63

studies clarified that the overpressure was about ten times higher than the peak pressure of incident underwater shock wave.

T. Koita and M. Sun et al. have studied experimentally the phenomena of disintegration of resin by the loading of underwater shock wave and primary bubble induced by the underwater explosion [3]. We focused recently on the study on disintegration of thin resin burrs generated in the resin injection molding by the underwater explosion [4, 5]. To develop the high-efficiency disintegration technique for thin burrs, we employed the thin resin plate simulating the burr and studied experimentally the disintegration method for thin resin plate using the overpressure from microbubble collapse by the interaction of underwater shock wave. We also investigated theoretically the dependence of microbubble diameter on the overpressure from microbubbles attached to the thin plate by the underwater shock wave loading [5]. In this study, we utilize not only the overpressure loading of underwater shock wave but also the interaction of primary bubble generated by the explosion with the thin plate to crash the plate efficiently. The interactions of overpressure from microbubble and primary bubble with the plate are depended on the explosion depth between the explosion point and the plate. So, the study on the effect of explosion depth on the fragmentation of plate is necessary to establish the disintegration technique for thin resin burrs.

The purpose of this study is to investigate experimentally the influence of explosion depth on the disintegration of thin resin plate. The interaction of underwater shock wave and primary bubble generated by the underwater explosion with the thin plate attached microbubbles by changing the explosion depth was visualized using an optical method. The effect of explosion depth on the serious behavior of the plate disintegration caused by these interactions was also discussed.

2 Experimental Setup

The underwater explosion was created by the electric discharge. Figure 1 shows a schematic diagram of the experimental model and the driver circuit of electrical discharge. The driver circuit consists of a high-voltage power source, a capacitor connected in parallel with the voltage source, a spark trigger, and two electrodes. The capacity of the capacitor, C, is 0.2 μF. The electrodes are connected with a 0.05 mm diameter copper wire. The voltage power, $V = 6.0$ kV, was tested. The total electrical discharge energy E_e can be estimated as $E_e = 0.5CV^2$. Therefore, the corresponding energy E_e is 3.6 J. The microbubbles were generated by the swirl flow-type microbubble generator (M2-LM/SUS, Nanoplanet Research Institute Co.). The purified water was used as the tested liquid and was supplied into the microbubble generator set in the test water tank from the other tank by the pump (W-P 125 W, HITACHI Ltd.). We set the optimum working condition of the microbubble generator, the discharging water flow rate of 15 L/min, and the suction atmosphere flow rate of 1 L/min by adjusting the valve located between the pump and the other tank and the needle valve of the gas flow meter. The microbubble size distribution

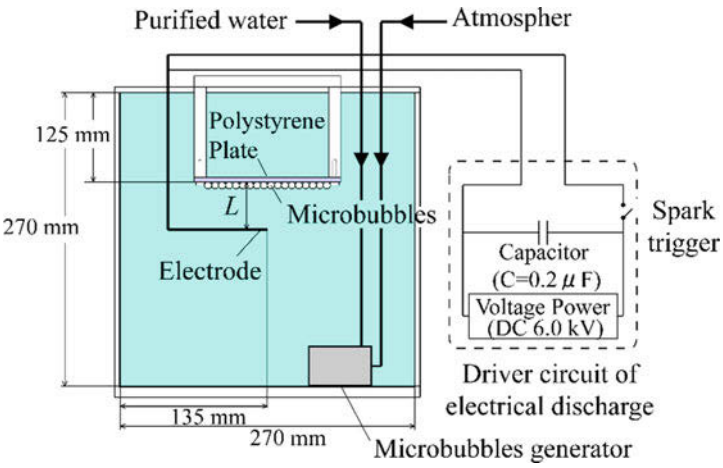

Fig. 1 Schematic diagram of the experimental setup and the driver circuit of electrical discharge

produced in the optimum working condition was investigated and clarified that the diameter of microbubble occupying the most production rate was 10 μm [1]. The thin polystyrene (PS) plate, resin plate, was employed. The thickness of PS plate is 0.1 mm. The plate was fixed to the acrylic rods with bolts as seen in Fig. 1. The area of plate subjected to the underwater shock wave loading is 100 × 100 mm. To coat only the bottom surface of PS plate with the microbubbles floating in the water, after the test tank was full up with the purified water including the microbubbles emitted by the generator, we installed immediately the plate in the test tank.

The effect of explosion depth L between the electrode and the bottom surface of plate on the disintegration of plate was investigated. In our previous experimental study, the maximum radial of primary bubble, R_{max}, was 9.0 mm at $E_e = 3.6$ J. In this study, $L/R_{max} = 1.00$ and 1.11 ($L = 9.0$, 10.0 mm) were tested to research the dependence of interference of the primary bubble with and without microbubbles attached to the PS plate.

The interaction of underwater shock wave with microbubble attached to the PS plate, the primary bubble motion near the plate, and the behavior of the plate were visualized by the shadowgraph method suppressing the light emission intensity generated by the electrical discharge [6]. Figure 2 shows the schematic diagram of the optical arrangement for visualization. These phenomena were recorded by a high-speed video camera, Phantom V2011. The frame rate and the exposure time of camera were, respectively, set to 10.0×10^5 frame/sec and 0.5 μs. A pulsed diode laser (Cavilux HF) was used as a light source. The laser wavelength is 810 nm and the power is 500 W. The zoom lens was installed in the camera to visualize in more detail. The focal length of lens is 200 mm and the F-number is 3.5. To record these phenomena with suppressing discharge, we mounted the bandpass filter (BPF) on the zoom lens and transmitted only the laser wavelength into the image sensor of

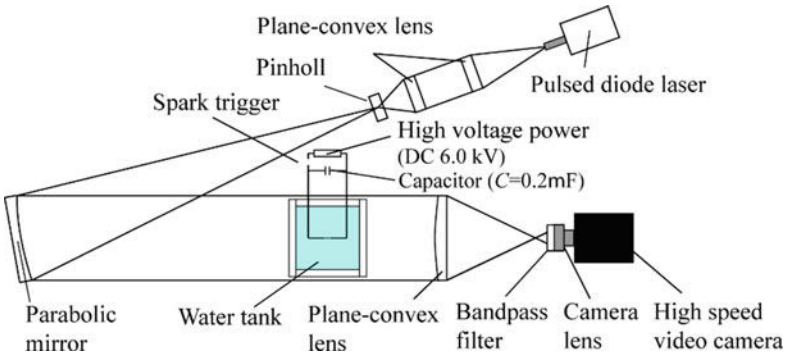

Fig. 2 Schematic diagram of the optical arrangement for visualization

camera. The center wavelength of BPF is 810 nm, which is the same as that of laser, and the half-value width is 10 nm.

3 Results and Discussion

3.1 $L/R_{max} = 1.00$ with Microbubbles

Figure 3 shows the recorded shadowgraph images for $L/R_{\max} = 1.00$. The underwater shock wave induced by the electrical discharge interacted with the microbubbles and the bottom surface of PS plate in Fig. 3b. As seen in Fig. 3b, the underwater shock waves were emitted by the collapsed microbubbles caused by the incident underwater shock wave loading. The incident underwater shock wave transmitted inside the PS plate, and the transmitted wave, shock wave, propagated into water above the plate. The shock waves from microbubbles interacted with each other, resulting in the generation of wave disturbance in Fig. 3c. After the propagation of shock waves, a primary bubble occurs due to the released energy of plasma by the electrical discharge. The plate deformed elastically into dome form as the primary bubble expanded as seen in Fig. 3d and e. Figure 3e shows that the bubble diameter had reached the maximum and hit the bottom surface of plate because of $L/R_{\max} = 1.00$. After that time, the bubble started contracting. By comparing qualitatively the location of upper surface of plate in Fig. 3d and f, the plate deformed downward when the primary bubble contracted. It was also observed that the fine bubbles were separated downward from the bottom surface of plate by the contraction of primary bubble in Fig. 3f. As seen in Fig. 3g–i, the primary bubble rebounded toward the plate because the value of L is the same as that of $R_{\max}$. When the primary bubble rebounded, the underwater shock wave emitted was observed in Fig. 3g. The rebounding bubble penetrated into the plate in Fig. 3h and i. After that, the bubble contracted near the plate in Fig. 3j. The second bubble

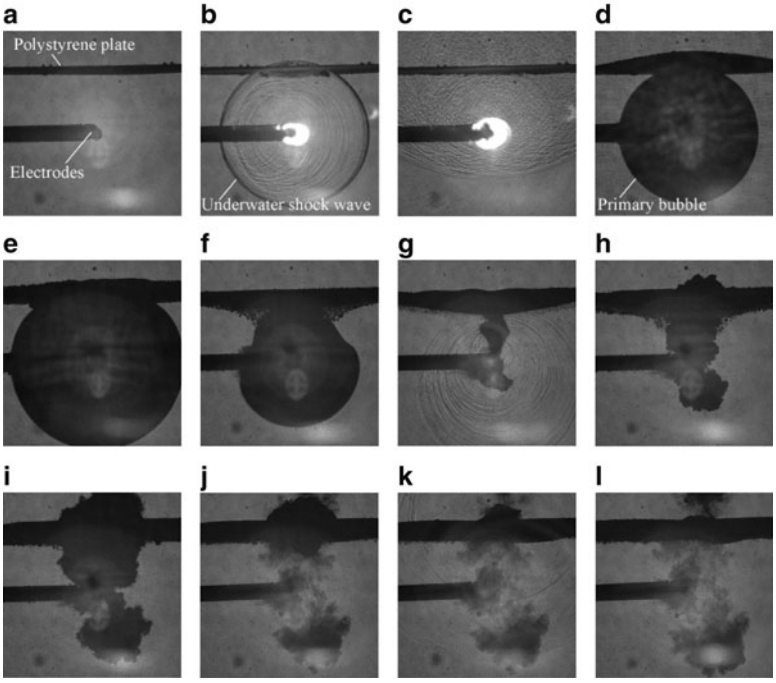

Fig. 3 Shadowgraph images of the behavior of thin PS plate attached microbubbles subjected to the underwater shock wave loading and the primary bubble motion for $L/R_{\max} = 1.00$ at $E_e = 3.6$ J. (**a**) $t = -2.77$ μs, (**b**) $t = 6.85$ μs, (**c**) $t = 16.9$ μs, (**d**) $t = 0.417$ ms, (**e**) $t = 0.957$ ms, (**f**) $t = 1.907$ ms, (**g**) $t = 2.167$ ms, (**h**) $t = 2.317$ ms, (**i**) $t = 2.707$ ms, (**j**) $t = 3.107$ ms, (**k**) $t = 3.237$ ms, (**l**) $t = 3.767$ ms,

rebounded occurred and moved upward the plate as seen in Fig. 3k and l. It is noticed that after the first and second bubble rebound were generated, the disintegration of plate is observed in Fig. 3l. In Fig. 3c, when the microbubble was collapsed by the underwater shock wave loading, the pit or crashing of thin PS plate did not appear. Although the overpressure from microbubbles is caused by the underwater shock wave loading, the decay time is nanosecond order [2, 5]. Therefore, it is possible to consider that the impulse loading the plate generated by the underwater shock wave caused by the microbubble collapse is less than the breaking strength of PS plate. It was found that the disintegration of plate was caused by interaction of rebound bubble with the plate in Fig. 3.

3.2 $L/R_{max} = 1.11$ with Microbubbles

Figure 4 shows the recorded shadowgraph images for $L/R_{\max} = 1.11$. The interaction of underwater shock wave and primary bubble with the thin PS plate attached

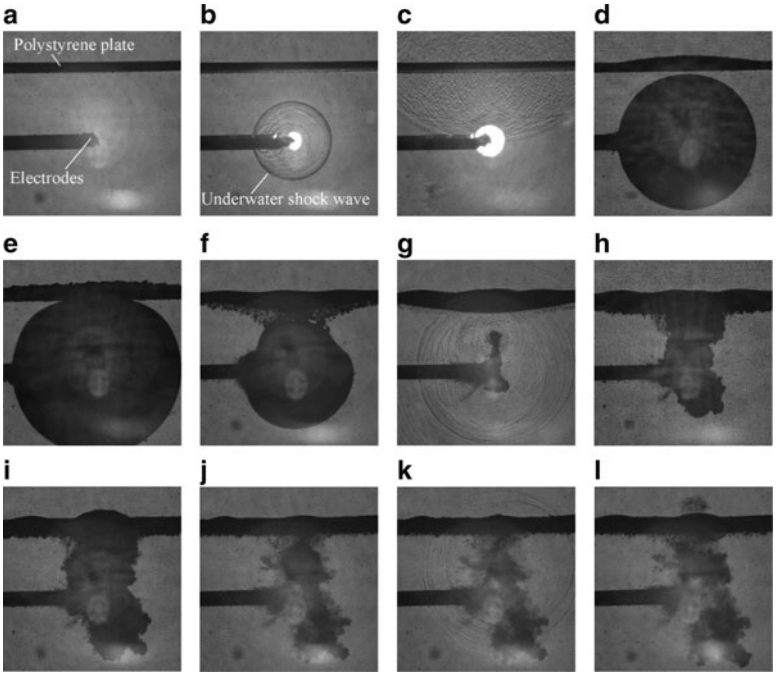

Fig. 4 Shadowgraph images of the behavior of thin PS plate attached microbubbles subjected to the underwater shock wave loading and the primary bubble motion for $L/R_{max} = 1.11$ at $E_e = 3.6$ J. (**a**) $t = -5.63$ μs, (**b**) $t = 4.73$ μs, (**c**) $t = 14.9$ μs, (**d**) $t = 0.473$ ms, (**e**) $t = 0.954$ ms, (**f**) $t = 1.904$ ms, (**g**) $t = 2.164$ ms, (**h**) $t = 2.314$ ms, (**i**) $t = 2.704$ ms, (**j**) $t = 3.084$ ms, (**k**) $t = 3.144$ ms, (**l**) $t = 3.604$ ms

microbubbles of $L/R_{max} = 1.11$ was almost similar with that of $L/R_{max} = 1.00$ as seen in Figs. 3 and 4. The underwater shock wave was emitted by the microbubble collapse caused by the incident underwater shock wave generated by the electrical discharge. The underwater shock wave from microbubbles interacted with each other, so that the wave disturbance occurred in Fig. 4c. As seen in Fig. 4d–f, the PS plate was deformed elastically upward and downward as the primary bubble expanded and contracted, respectively. The rebound shock wave generated by the primary bubble collapse was observed in Fig. 4g. The primary bubble rebounded toward the plate in Fig. 4h and i. After that, the bubble contracted between the plate and electrodes without the connection with the plate in Fig. 4j. The bubble collapsed and expanded again; the second rebound shock wave was emitted by the bubble collapse in Fig. 4k. It is noticed that the disintegration of PS plate did not appear in Fig. 4l. By comparing Fig. 3j–k with Fig. 4j–k, it was clearly found that the disintegration of thin PS plate was depended on the explosion depth, and the plate was broken by the primary bubble rebound by connecting with the plate. It is possible to consider that the plate is disintegrated by the water impact caused by the contraction of rebound primary bubble near the plate.

4 Conclusions

In the paper, we investigated experimentally the effect of the explosion depth on the disintegration of thin PS plate attached microbubbles subjected to the underwater shock wave and a primary bubble generated by the explosion. The underwater explosion was created by the electrical discharge. The experiment was carried out in the electrical discharge energy $E_e = 3.6$ J and the microbubble diameter of 10 μm. The explosion depth L between the electrode and the bottom surface of plate was changed, and $L/R_{\max} = 1.00$ and 1.11 were tested, where $R_{\max}$ was the maximum diameter of primary bubble at $E_e = 3.6$ J. We visualized the PS plate motion caused by the interaction of underwater shock wave and primary bubble with plate. By comparing visualized images of $L/R_{\max} = 1.00$ and 1.11, we also discussed the influence of L on the disintegration of plate. From the results, it was clearly found that the disintegration of thin PS plate was depended on the explosion depth and was generated in $L/R_{\max} = 1.00$. It was confirmed that the PS plate was destroyed not by the overpressure from microbubble collapse by the underwater shock wave loading but by the interaction of rebounding primary bubble with the plate in this experimental condition.

Acknowledgments Part of the work was carried out under JSPS KAKENHI Grant Number 15 K18300 and 17 K18066 and the Collaborative Research Project of the Institute of Fluid Science, Tohoku University.

References

1. A. Abe, K. Ohtani, K. Takayama, S. Nishio, H. Mimura, M. Takeda, J. Fluid Sci. Tech. **5**(2), 235–246 (2010)
2. B. Wan, N. Tsujii, S. Fukuda, A. Abe, Review of the faculty of maritime sciences. Kobe University **7**, 81–86 (2010)
3. T. Koita, T. Gonai, M. Sun et al., in *Proceedings of the 30th International Symposium on Shock Waves*, 35–36, 2015
4. T. Koita, M. Sun, Y. Fukushima, S. Kobayashi, in *Proceedings of the 13th International Conference on Flow Dynamics*, CRF-62, 2016
5. T. Koita, S. Kobayashi, M. Sun et al., in *Proceedings of the 35th Japanese Conference on Mathematical Sciences*, A304, 2016
6. T. Koita, M. Sun, in *Proceedings of the Symposium on Shock Waves in Japan*, 1B2-3, 2014

Numerical Study of the Flow Separation in a Rocket Nozzle

S. Zhu, Z. Chen, C. Zheng, H. Zhang, and Z. Huang

Abstract The flow separation phenomenon often occurs in large area ratio nozzles of rocket engines, in order to study the relationship between the combustion chamber pressure and the flow separation point and the effect of flow separation on the nozzle. The numerical simulation of nozzle under different chamber pressures is carried out by using computational fluid dynamics (CFD) method. The compressible Navier-Stokes equations are used to calculate the fluid region. One equation Spalart-Allmaras turbulence model is selected. A second-order implicit advection upstream splitting method (AUSM) scheme is employed for the convection term. The flow fields of nozzle under different nozzle pressure ratios are obtained, and the pressure distribution of nozzle and flow separation position are analyzed. The results show that the flow separation point departs from the inlet of the nozzle as the nozzle pressure ratio (NPR) increases. This research can provide a corresponding reference for the design and analysis of relevant nozzle.

1 Introduction

With the increasing demand of modern rocket carrying capacity, the rocket nozzle area ratio is increased. These rocket engines work from sea level up to high altitude with very low ambient pressure. Therefore, the flow separation often occurs in the rocket engine nozzle.

At ground, these types of engines operate in an overexpanded flow condition with an ambient pressure higher than the nozzle exit pressure. During the ascent as ambient pressure decreases, the initially overexpanded exhaust flow becomes adapted and finally transforms to the under-expanded [1]. In both conditions, the nozzle produces less than the maximum possible thrust. The flow separation phenomenon at nozzle occurs frequently during the start-up and shutdown of the

S. Zhu · Z. Chen (✉) · C. Zheng · H. Zhang · Z. Huang
Key Laboratory of Transient Physics, Nanjing University of Science and Technology, Nanjing, China
e-mail: chenzh@njust.edu.cn

A. Sasoh et al. (eds.), *31st International Symposium on Shock Waves 2*,
https://doi.org/10.1007/978-3-319-91017-8_64

rocket engine. Flow separation at nozzle walls is one of the potential origins of side loads. Side loads in the nozzle can cause undesirable results, such as nozzle vibration, shortened engine life, damage to the nozzle structure, etc. This problem appears in many rocket engines, such as the SSME of the American space shuttle [2], the Japanese LE-7A [3], and engines of European Ariane 5 [4, 5]. So, it is of great significance to study the flow separation of nozzle.

Massive investigations on the flow separation of nozzle were carried out, and many important research achievements have been acquired. Frey and Hagemann [6] conducted numerical computations of flows in a conical nozzle, and they have studied the separation position of the flow in nozzle and the parameters affecting the separation point. Onofri et al. [7] have numerically investigated the flow separation in the nozzle with overexpansion condition. Lü and Ye [8] have gotten the side loads and aeroelastic stability of a rocket nozzle by solving Navier-Stokes equations coupled with structural equation of motion.

Through the above analysis, we can see that it is very important to study the flow separation of rocket nozzle. So, in the present paper, the numerical simulation of a typical nozzle is carried out by using computational fluid dynamics method. The flow characteristics and the pressure variation in the nozzle are analyzed under different chamber pressures, which provide a solid foundation for further research in related fields.

2 Numerical Method

The Navier-Stokes equations are employed to compute the flow field. Spalart-Allmaras one equation model is employed for the turbulent model. The finite volume method based on AUSM (advection upstream splitting method) format is used to discrete the space. The second-order central difference scheme is applied to pursuing numerical approximation of the viscous term. The gas is ideal gas. The molecular viscosity is expressed in the following form of Sutherland law:

$$\mu = \mu_0 \left(\frac{T}{T_0} \right)^{3/2} \frac{\mathrm{T}_0 + \mathrm{S}}{\mathrm{T} + \mathrm{S}} \tag{1}$$

where the reference temperature $T_0 = 273.11$ K, the equivalent temperature $S = 110.56$ K, and the reference viscous coefficient $\mu_0 = 1.716 \times 10^{-5}$ kg/(m·s).

3 Problem Setup and Boundary Conditions

The fluid computational domain with the assigned boundary conditions is shown in Fig. 1, the diameter of the nozzle throat is 30.75 mm, the nozzle has a length of 228.51 mm, and the expansion ratio ε is 25. The length of the computational domain is 2100 mm, and the width is 1173 mm. The assigned boundary conditions as

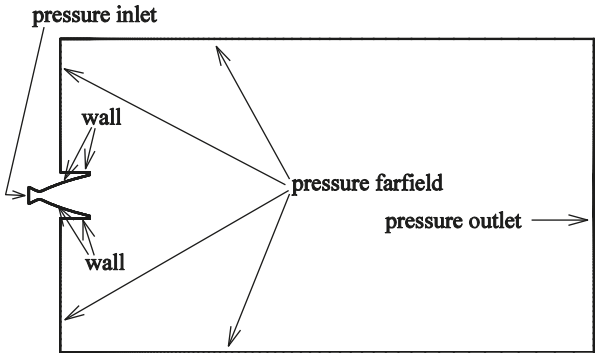

Fig. 1 Sketch of flow field computation region

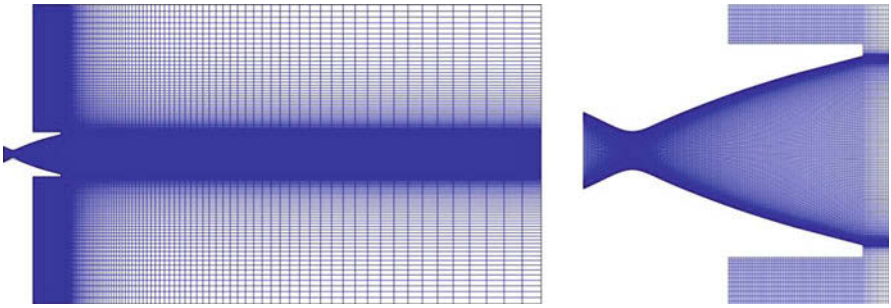

Fig. 2 Computational mesh for the nozzle

prescribed in Fig. 1 are declared as follows: the inlet of nozzle is set as the pressure inlet boundary condition, the high-pressure gas in the combustion chamber injects into the computational domain from the inlet of nozzle, and the nozzle pressure ratio (NPR) is defined as the pressure ratio between the inlet and exit of nozzle. Here, the NPRs vary from 3.948 to 14.804; the total temperature in the combustion chamber of nozzle is 3000 K. The pressure outlet boundary condition is specified on the right boundary. Nonslip boundary condition is assumed on the nozzle wall. Computational domain was set to a pressure of 1 atm, a temperature of 300 K, and a velocity of zero as initial condition.

The computational mesh used in the present study is shown in Fig. 2. There are approximately 40 cells in the boundary layer grid with first cell height of approximately y+=1.

4 Results and Discussion

The computed Mach number contours for different NPRs, 3.948, 4.935, 5.922, 6.908, 7.895, 8.882, 9.869, 10.856, 12.830, and 14.804, are plotted in Fig. 3. As we can see, the nozzle is in the state of overexpansion. The ratio of chamber pressure

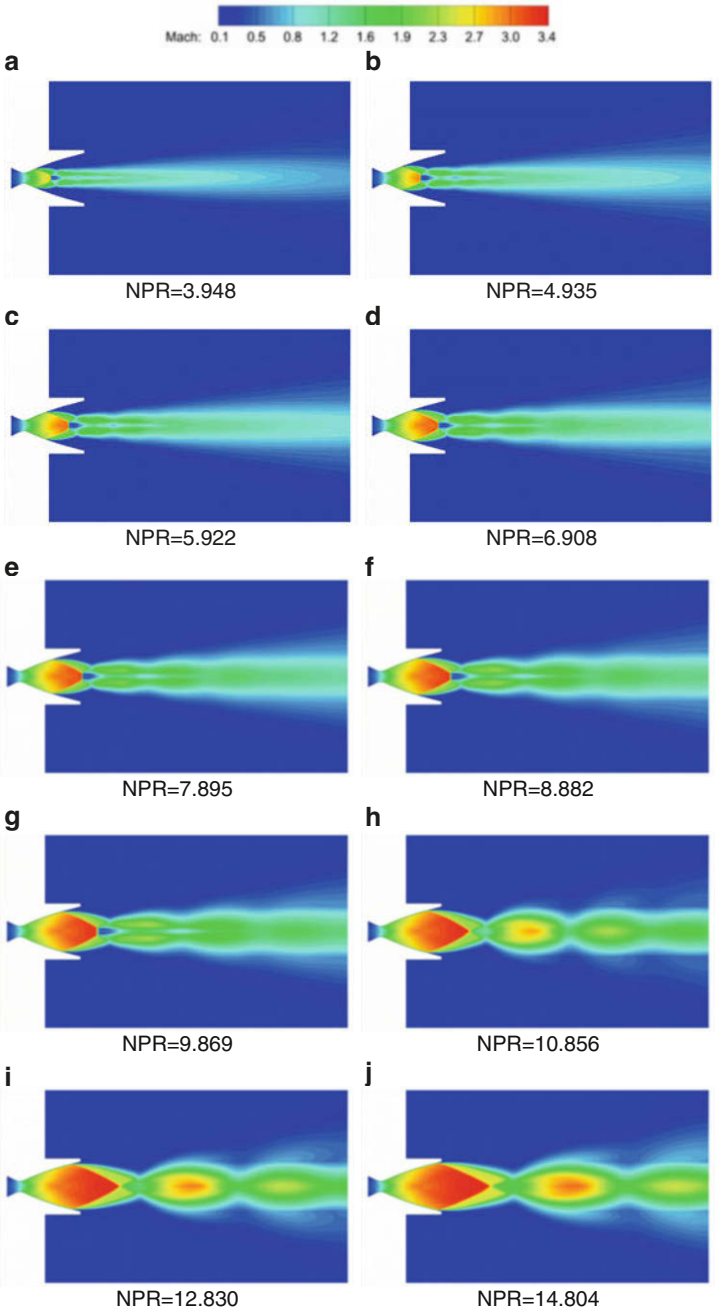

Fig. 3 The computed Mach number images for different NPRs. (**a**) NPR=3.948, (**b**) NPR=4.935, (**c**) NPR=5.922, (**d**) NPR=6.908, (**e**) NPR=7.895, (**f**) NPR=8.882, (**g**) NPR=9.869, (**h**) NPR=10.856, (**i**) NPR=12.830, (**j**) NPR=14.804

to ambient pressure is small, so there is a shock wave inside the nozzle. Flow separation phenomenon occurs in the nozzle; an oblique shock is generated at the separation point. When NPR is between 3.948 and 9.869, as shown in Fig. 3a–g, a normal shock wave is generated at the axis of the nozzle; the flow in the nozzle changes from supersonic to subsonic at the shock location. When NPR is less than or equal to 6.908, the normal shock is inside the nozzle, as shown in Fig. 3a–d. When NPR = 7.895, 8.882, and 9.869, the normal shock is outside the nozzle, as shown in Fig. 3e–g. With the increase of NPR, when NPR = 10.856, 12.830, and 14.804, as shown in Fig. 3h–j, there is no normal shock wave. The flow separation point departs from the inlet of the nozzle with the increase of NPR.

Figure 4 shows the pressure distribution of the nozzle under different NPRs; it can be seen from the figure, in the case of several NPRs in the present paper, that the flow separation phenomenon occurs in the nozzles. With the increase of NPR, the flow separation point is close to the nozzle exit. Figure 5 is the location of flow separation point in the nozzle under different NPRs; when the NPR is less than 10.856, the flow separation point increases linearly with the increase of NPR. When NPR is larger than 10.856, the flow separation point increases slowly with the increase of NPR. Figure 6 shows the relationship between the position of the normal shock wave and NPR; the position of the normal shock departs from the inlet of the nozzle as the NPR increases.

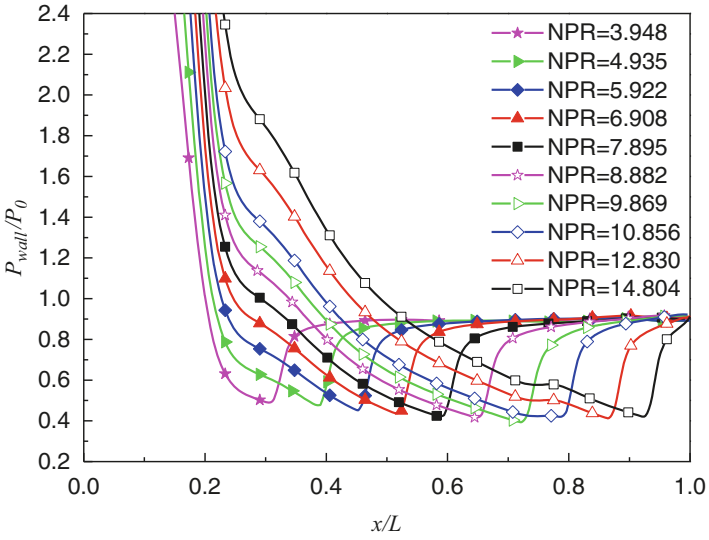

Fig. 4 Wall pressure distribution of internal flow field under different NPRs

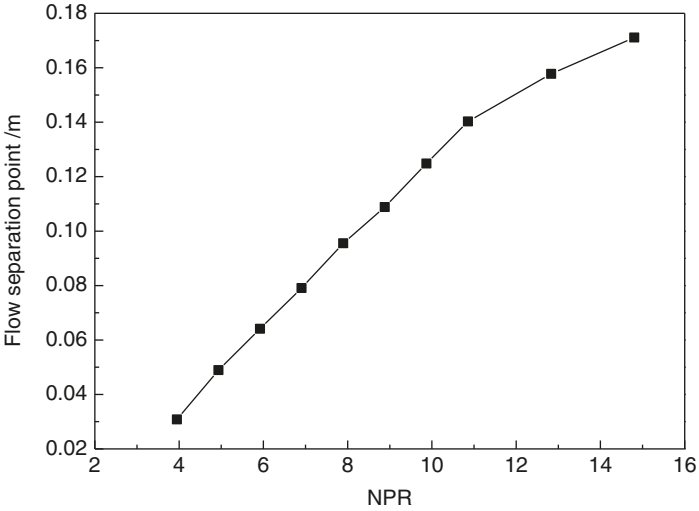

Fig. 5 Flow separation point in the nozzle under different NPRs

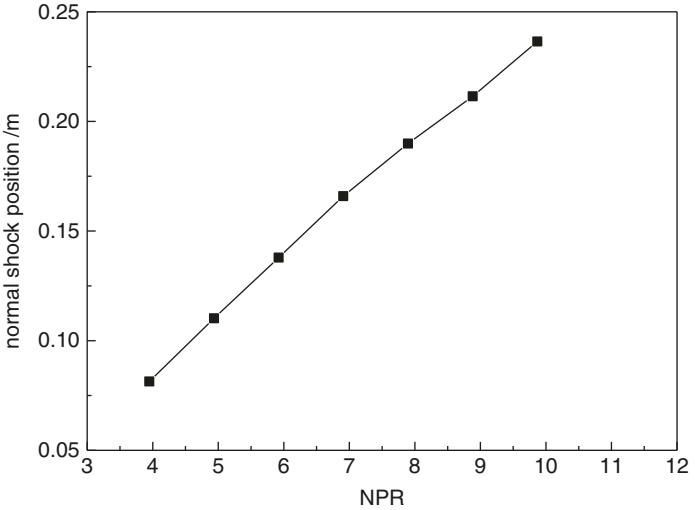

Fig. 6 Normal shock position under different NPRs

5 Conclusion

The numerical simulations of compressible flow passing through a 2D convergent-divergent nozzle with different nozzle pressure ratios are presented. The predicted results are obtained by solving the compressible Navier-Stokes equations; one equation Spalart-Allmaras turbulence model is used. The characteristics of nozzle flow fields under different NPRs are obtained; the variation of the flow separation point with NPR and the variation of the normal shock position are analyzed.

Acknowledgment This work was supported by the National Natural Science Foundation of China (Grant No. 11502117) and Jiangsu Province Graduate Student Training Innovation Project (KYLX16_0480).

References

1. M. Terhardt, G. Hagemann, M. Frey, Flow separation and side-load behavior of truncated ideal rocket nozzles. AIAA paper, 3686, 2001
2. T.S. Wang, M.J. Guidos, Transient three-dimensional side-load analysis of a film-cooled nozzle. J Propul Power. **25**(6) (2009)
3. Y. Watanabe, N. Sakazume, M. Tsuboi, LE-7A Engine Nozzle problems during transient operations, in *38th AIAA/ASME/SAE/ASEE Joint Propulsion Conference and Exhibit*. 3841, 2002
4. D. Perigo, R. Schwane, H. Wong, A numerical comparison of the flow in conventional and Dual Bell Nozzles in the presence of an unsteady external pressure environment, in *39th AIAA/ASME/SAE/ASEE Joint Propulsion Conference and Exhibit*. 4731, 2003
5. R. Schwane, Y. Xia, Investigation of nozzle stability by numerical fluid structure interaction calculation, in *43rd AIAA Aerospace Sciences Meeting and Exhibit*. 53, 2005
6. M. Frey, G. Hagemann, Restricted shock separation in rocket nozzles. J Propul Power **18**, 3 (2002)
7. M. Onofri, F. Nasuti, The physical origins of side loads in rocket nozzles, in *35th Joint Propulsion Conference and Exhibit*. 2587, 1999
8. G.L. Lü, Z.Y. Ye, Investigation on the mechanism of aeroelastic hazard during ground test of rocket nozzle. Sci. China Technol. Sci. **55**(9), 2462–2473 (2012)

Hybrid RANS/LES Simulation of Shock-Induced Separated Flow in Truncated Ideal Contour Nozzle

Eric Goncalves, B. Guillaume Lehnasch, and C. Julien Herpe

Abstract The present study is motivated by the flow analysis of supersonic nozzles used in the rocket launcher, more specifically about the generation of side loads. The work aims at identifying and at modeling the dominant elements of the organized structure of the flow in overexpanded rocket nozzles.

1 Introduction

When a convergent-divergent nozzle operates in overexpanded conditions, i.e., when the pressure at the nozzle exit is lower than the surrounding ambient pressure, it can lead to flow separation in the divergent part of the nozzle. This situation is observed during start-up and shut-down transients of rocket engine, and, despite the geometrical axisymmetry of the nozzle, asymmetrical separation appears leading to lateral pressure forces, or side loads, acting on the nozzle structures.

Supersonic nozzle flow separation is generally classified as restricted-shock separation (RSS) where the flow reattaches to the nozzle wall, or as free-shock separation (FSS), in which the flow does not reattach to the nozzle wall [1, 4, 7, 8, 10]. Figure 1 shows a schematic representation of the main characteristics of a free separation.

In the present study, a FSS configuration is investigated numerically in a truncated ideal contour (TIC) nozzle. The numerical strategy adopted aims at computing essentially the largest dynamical active scales of the flow in order to analyze the unsteady mechanisms leading to the low-frequency peak of side loads observed in rocket nozzles. It relies on a Delayed Detached Eddy Simulation (DDES), based on the Spalart-Allmaras turbulent model [9].

E. Goncalves (✉)
ENSMA, Institut Pprime, UPR 3346, CNRS, Chasseneuil-du-Poitou, France

B. G. Lehnasch · C. J. Herpe
ENSMA, Institut Pprime, UPR 3346, CNRS, Chasseneuil-du-Poitou, France

Centre National d'Études Spatiales (CNES) – Direction des Lanceurs, Paris, France
e-mail: eric.goncalves@ensma.fr

A. Sasoh et al. (eds.), *31st International Symposium on Shock Waves 2*,
https://doi.org/10.1007/978-3-319-91017-8_65

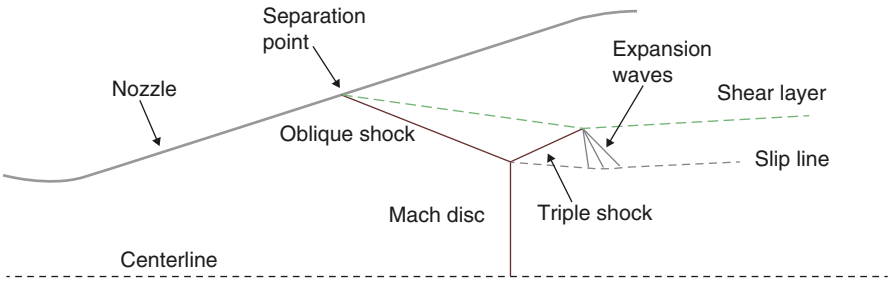

Fig. 1 Free-shock separation (FSS), extracted from [6]

2 Governing Equations and Turbulence Model

2.1 Unsteady Reynolds-Averaged Navier-Stokes Equations

The unsteady mass-weighted Reynolds-averaged Navier-Stokes (URANS) equations coupled with the one-equation Spalart-Allmaras turbulence model can be expressed as:

$$\frac{\partial w}{\partial t} + \operatorname{div}(F_c - F_v) = S \tag{1}$$

$$w = \begin{pmatrix} \rho \\ \rho\vec{V} \\ \rho E \\ \rho\tilde{\nu} \end{pmatrix} \quad ; \quad F_c = \begin{pmatrix} \rho\vec{V} \\ \rho\vec{V}\otimes\vec{V} + P\overline{\overline{I}} \\ (\rho E + p)\vec{V} \\ \rho\tilde{\nu}\vec{V} \end{pmatrix} \quad ; \quad F_v = \begin{pmatrix} 0 \\ \overline{\overline{\tau^v}} + \overline{\overline{\tau^t}} \\ (\overline{\overline{\tau^v}} + \overline{\overline{\tau^t}}).\vec{V} - \vec{q}^v - \vec{q}^t \\ (\mu + \rho\tilde{\nu}/\sigma_\nu)\,\mathrm{grad}\,\tilde{\nu} \end{pmatrix}$$

where w denotes the conservative variables, F_c and F_v the convective and viscous flux densities, and S the source terms which concern only the transport equation. The total stress tensor $\overline{\overline{\tau}}$ is evaluated following the Newton law and the Boussinesq assumption. The total heat flux vector $\vec{q}$ is obtained from the Fourier law with the constant Prandtl number hypothesis. The viscosity is determined by the Sutherland law.

2.2 DDES

The DDES model is obtained by allowing the length scale in the Spalart-Allmaras model to be proportional to the grid size far from the wall while remaining proportional to wall distance near the wall. This is achieved by redefining the wall distance d as follows:

$$\tilde{d} = d - f_d \max(0, d - C_{DES}\Delta) \quad \text{with} \quad \Delta = \max(\Delta_x, \Delta_y, \Delta_z) \tag{2}$$

$$f_d = 1 - \tanh\left([8r_d]^3\right) \quad \text{with} \quad r_d = \frac{\tilde{\nu}}{\sqrt{V_{i,j}V_{i,j}}\kappa^2 d^2} \tag{3}$$

where Δ represents a characteristic grid size and C_{DES} is a constant equal to 0.65 for homogeneous turbulence.

3 Numerics

Numerical simulations are carried out using an in-house finite-volume code solving the compressible RANS system on multi-block structured grids [3]. Time integration is performed through the dual time-stepping method with a second-order accuracy. Numerical fluxes are computed with a third-order Jameson scheme for which the dispersive error is canceled. The numerical treatment of the boundary conditions is based on the use of the characteristic relations of the Euler system.

4 Computational Setup

4.1 Geometry and Computational Domain

The considered geometry is a TIC nozzle designed and experimentally investigated in the Institut Pprime [5]. The fully adapted Mach number M_j is equal to 2.09. Figure 2 shows the computational domain in terms of throat radius R_t. The three-dimensional domain is axisymmetric around the symmetry axis shown in the figure and extends about 56 R_t from the exit nozzle in the axial direction. The outer boundary of the domain has a cylindrical shape with a radius of 22 R_t.

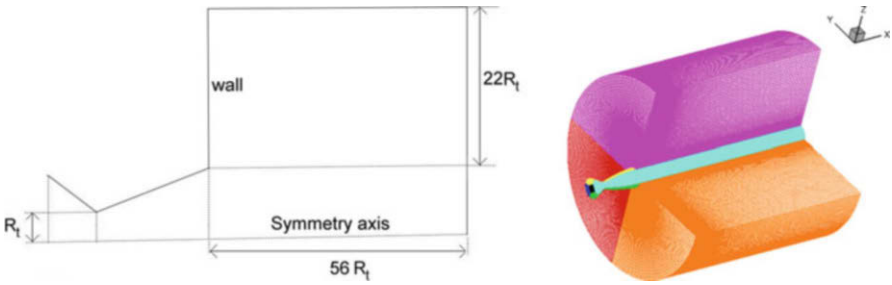

Fig. 2 Schematic representation of the computational domain and view of the grid

4.2 Computational Grid and Boundary Conditions

The butterfly-type mesh consists of 9 structured blocks and roughly 35 millions of nodes. A view of the grid is illustrated in Fig. 2. At the nozzle inlet boundary, stagnation conditions are imposed. At the domain outlet, a static pressure is fixed at the atmospheric value. The internal nozzle walls and the outside wall are treated as no-slip adiabatic walls. The working fluid is air, assumed to be a perfect gas.

5 Simulation Results

Simulations are performed using a time step $dt = 9.10^{-6}$ s for a total time of 0.15 s.

5.1 Flow Field

The predicted flow structure is illustrated in Fig. 3 by an instantaneous snapshot showing the distribution of the density gradient modulus (schlieren-like visualization) extracted on a streamwise plane. The waves' network involved in the flow is qualitatively well reproduced. We can observe the triple point where the Mach disk and the incident and reflected shocks interact and from where the slipstream emanates. Successive compression/expansion regions are also well highlighted. The average shock position provided by simulations is in very close agreement with the measurement.

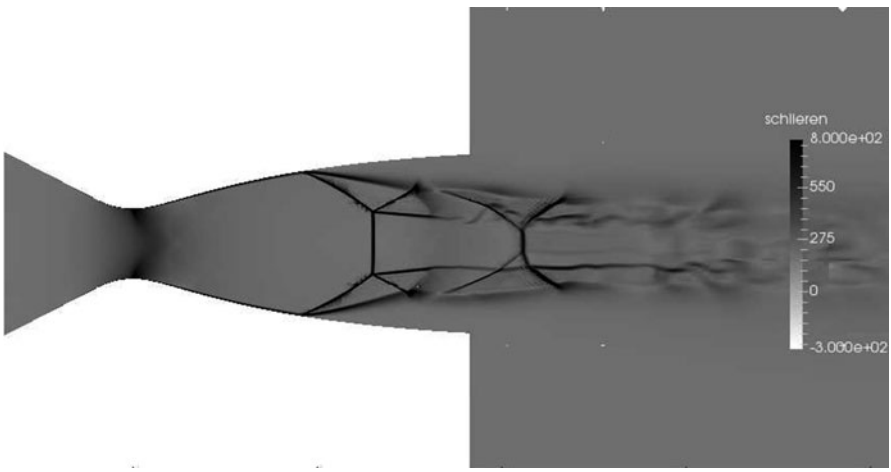

Fig. 3 Instantaneous density gradient magnitude on a streamwise cutting plane

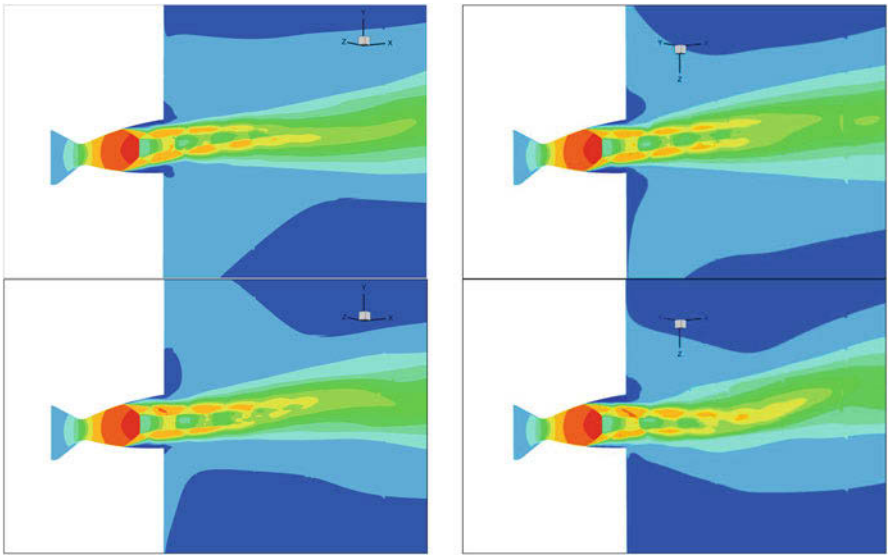

Fig. 4 Instantaneous longitudinal velocity component at different times in two orthogonal cutting planes; plane (x, y) (left) and plane (x, z) (right)

This visualization allows also to identify the unsteadiness sources captured by the present simulation. We note that the computation inhibits instabilities developing from the incident shock waves and the associated mixing layer. The amplification of convective instabilities is mainly observed in a downstream area corresponding to the interaction of expansion waves and the mixing layer emanating from the triple point. It would be therefore the advection and growth of these instabilities which would lead to the destabilization of the jet.

A qualitative visualization of the flow is proposed by plotting in Fig. 4 the longitudinal velocity component at different times in two orthogonal cutting planes (x, y) and (x, z). We observe the waves' network (oblique shocks, Mach disk) and the boundary layer separation reaching the exit section of the nozzle. Moreover, a flapping movement of the jet is highlighted in both orthogonal cutting planes, which shows the possible existence of an helicoidal mode of the jet.

5.2 Mean Wall Pressure and RMS Fluctuations

The mean wall pressure, evaluated as the time-averaged value obtained on the total simulation time, is plotted in Fig. 5 (left part) along a line inside the divergent. A very good agreement with the experimental data is observed and shows the ability of the considered methodology to well reproduce the pressure gradients in the separated area.

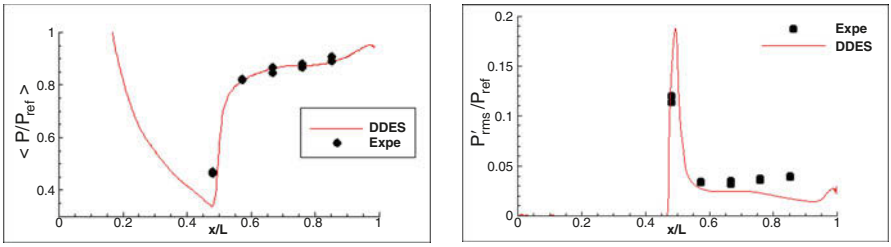

Fig. 5 Mean wall pressure (left) and RMS fluctuations (right)

The wall RMS pressure fluctuations are plotted in Fig. 5 (right part) along a line inside the divergent. Values of P'_{rms} are evaluated by subtracting the instantaneous pressure computed at each time step with the mean pressure. The intensity of pressure fluctuations is underestimated in the separated region in comparison with the experimental data. Discrepancies are moderate just behind the separation point (around 10–15%) and increase progressively as one moves toward the exit nozzle (up to 50%).

An estimation of the peak pressure just behind the shock wave is given by the following relation proposed by Dumnov [2]:

$$P'_{\text{rms}} = \frac{P_2 - P_1}{2\sqrt{2}} \tag{4}$$

where pressures P_1 and P_2 are evaluated upstream and downstream the shock, respectively. In the present case, we find $P'_{\text{rms}}/P_{\text{ref}} = 0.177$ that is in very good agreement with the obtained numerical value.

5.3 *Spectral Analysis*

The jet exiting from the nozzle undergoes a strong flapping motion at a high frequency around a Strouhal number $St = f D_t / U_{\text{ref}}$ close to 2. This result is in good agreement with the experimental value evaluated with the power spectral density (PSD) of the wall pressure monitored at five probes located at positions P_k along the divergent, as illustrated in Fig. 6. This peak was shown previously [5] to be mainly associated with the first azimuthal mode which could contribute to side loads. The energy at very low frequency is dominant (in particular with the first probe P1), which is consistent with the slow movement of the oblique shock wave along the wall. Due to the short simulation time (0.15 s), statistics are not enough converged, which lead to a high-frequency noise. Moreover, the amplitude of peaks at St$\simeq$ 2 is slightly underestimated by the simulation. Yet, these observations show the ability of the proposed numerical strategy to capture the dominant structure of the flow.

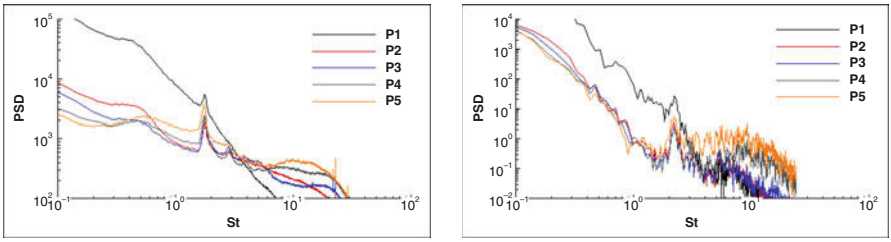

Fig. 6 Power spectral density of wall pressure fluctuations at five positions P_k along the divergent: experiment (left) and simulation (right)

6 Conclusion

The unsteady regime of an overexpanded jet flow in a TIC nozzle has been investigated in order to study the main characteristics of a FSS configuration. The numerical strategy adopted is mainly based on the DDES modeling approach. Results have been compared with experimental data and show the ability of the methodology to capture the flow topology (waves network, mean pressure, shock position) and the spectral behavior of fluctuating pressures inside the nozzle. A complex self-sustained flapping movement of the jet was predicted despite the moderate grid refinement. It was observed to be possibly issued from the destabilization of the internal shear layer interacting with the expansion and compression regions downstream of the first shock cell, suggesting that a kind of internal screech-like mechanism could play a significant role in the tonal jet behavior. The use of the present numerical strategy is therefore promising but needs further developments as the use of improved turbulence modeling and low-dissipative numerical schemes.

Acknowledgements The work presented is part of the nozzle research project ATAC led by the French Space Center (CNES). This work was performed using HPC resources from GENCI [TGCC] (Grant 2017 [A0012A10017]).

References

1. S. Deck, P. Guillen, J. Prop. Power **18**, 261 (2002)
2. G.E. Dumnov, AIAA 1996–3220 (1996)
3. E. Goncalves, R. Houdeville, Int. J. Comput. Fluid Dyn. **23**, 449 (2009)
4. A. Hadjadj, M. Onofri, Shock Waves **19**, 163 (2009)
5. V. Jaunet, S. Arbos-Torrent, G. Lehnasch, S. Girard, AIAA J., **55**(12), 4245 (2017)
6. R. Larusson, N. Andersson, L.E. Eriksson, J. Ostlund, AIAA 2014–4003 (2014)
7. E. Martelli, F. Nasuti, M. Onofri, Shock Waves **20**, 139 (2010)
8. A. Shams, G. Lehnasch, P. Comte, H. Deniau, T. Alziary de Roquefort, Comput. Fluids. **78**, 63 (2013)
9. P.R. Spalart, S. Deck, M.L. Shur, K.D Squires, M.K. Strelets, A. Travin, Theor. Comput. Fluids Dyn. **20**, 181 (2006)
10. R.H. Stark, B.H. Wagner, AIAA 2006–5208 (2006)

Experimental Study of TICTOP Nozzles

R. Stark and C. Génin

Abstract The new nozzle contour concept TICTOP is introduced and its experimental validation is presented. The TICTOP nozzle features a comparable performance like TOP nozzles, whereas reattached flow conditions during transient start-up and shutdown operation are avoided. A hypothesis on the formation of the cap-shock pattern in TOP nozzles is presented.

1 Introduction

European rocket engines typically feature TOP (thrust-optimized parabola) nozzles. The divergent supersonic contour part of this type of nozzles is composed from an introducing radius and a following skewed parabola. This approach results in a reduced overall length and a favorable nozzle exit wall pressure. The concept was first suggested by Rao [1, 2]. Unfortunately, TOP nozzles feature an internal recompression shock (Fig. 1, left). It originates shortly downstream of the nozzle throat and causes in combination with a Mach disk (MD), a reflected shock (RS), and a Mach ring (MR) the so-called cap-shock pattern. The cap-shock pattern is known to introduce, during the transient engine start-up and shutdown, a transition from free shock separation (FSS) to restricted shock separation (RSS) (Fig. 1, right). The deciding factor is the impulse balance downstream of the reflected shock (RS, red arrow) and the oblique separation shock (SS, blue arrow). The transition in flow pattern comes along with undesired huge side loads [3–8] that can damage the nozzle itself, the rocket engine, the actuator system, the rocket structure, and even the payload.

In contrast, a TIC (truncated ideal contour) nozzle features no internal shock. Its divergent supersonic ideal contour part is obtained using the method of characteris-

R. Stark (✉) · C. Génin
German Aerospace Center, DLR, Institute of Space Propulsion, Lampoldshausen, Germany
e-mail: ralf.stark@dlr.de

A. Sasoh et al. (eds.), *31st International Symposium on Shock Waves 2*,
https://doi.org/10.1007/978-3-319-91017-8_66

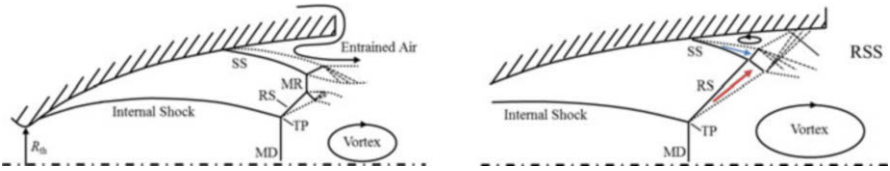

Fig. 1 Cap-shock pattern in TOP nozzles, free shock separation (left), and restricted shock separation (right)

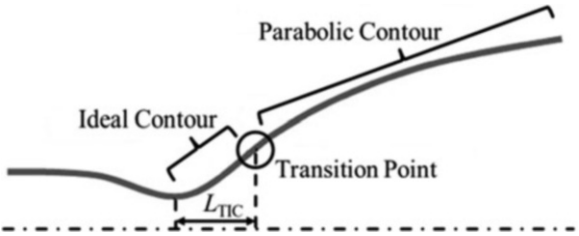

Fig. 2 TICTOP contour principle, taken from [9]

tics (MOC). The ideal contour nozzle possesses a uniform exit flow, but due to mass restrictions, the nozzle is truncated for rocket engine application [5–8].

The TICTOP nozzle is a new rocket nozzle contour concept suggested by Frey [9]. It combines the advantages of the two traditional contour concepts: the TIC with no internal recompression shock and, hence, a well-defined transient start-up behavior with acceptable side loads and the TOP with a reduced overall length and a favorable nozzle exit wall pressure. The TICTOP contour is initially designed as an ideal contour, followed by a skewed parabola downstream of a predefined transition point (Fig. 2). Without an internal shock and the resulting cap-shock pattern, a RSS flow state with accompanying huge transition side loads can be avoided, and the favorable wall pressure gradient of the nozzle end section is preserved.

The German Aerospace Center (DLR) and Airbus Safran Launchers (ASL) conducted a joint subscale test campaign to study the concept. For this reason 16 TICTOP contours, based on a DLR reference TOP nozzle, were designed by ASL and numerically investigated [9]. Finally, two TICTOP contours were selected, manufactured, and tested, including the DLR TOP.

2 Experimental Setup

The study was conducted at DLR's test facility P6.2 in Lampoldshausen. Figure 3 gives the facility flowchart with the high-pressure gaseous nitrogen supply storage and the feeding system, consisting of automatic valve, filter, pressure reducer, regulation valve, and mass flowmeter. The feeding system connects the fluid supply with the settling chamber that is mounted on a rig. The settling chamber is equipped with a set of grids and honeycombs to homogenize the flow. The mesh size is 4 mm^2,

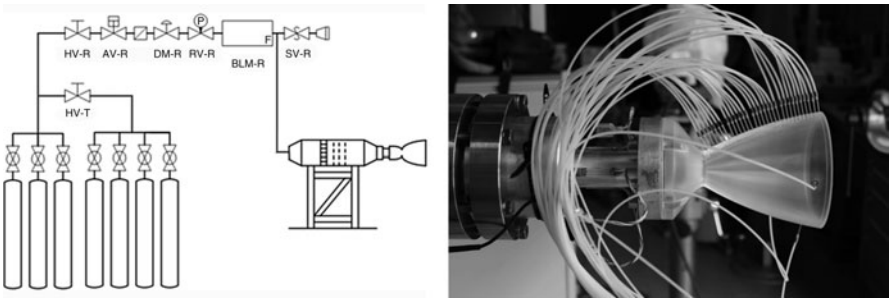

Fig. 3 Flowchart of test facility P6.2 (left) and TICTOP nozzle B1 mounted downstream of the bending tube on horizontal test rig (right)

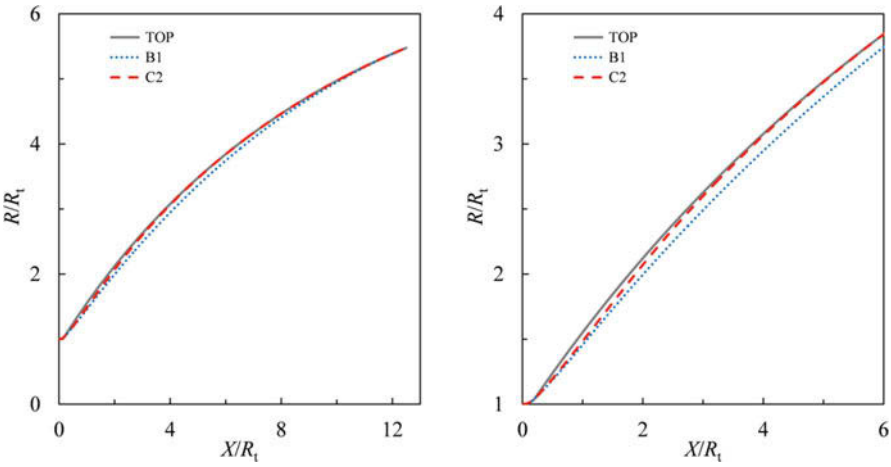

Fig. 4 Contour comparison (left) and related zoom (right)

reducing the effective cross section down to 64%. The tested nozzle specimen is mounted horizontally downstream of the settling chamber.

The facility features a total pressure up to 6 MPa with a mass flow up to 4.2 kg/s. Dry nitrogen is used as working fluid to avoid condensation effects (H_2O, CO_2, O_2, etc.). Its total temperature corresponds to the ambient temperature.

2.1 Test Specimens and Instrumentation

Three test specimens were made of acrylic glass, with a wall thickness of 8 mm and a throat radius of $R_{th} = 10$ mm. The contours of the reference TOP nozzle and the two TICTOP nozzles called B1 and C2 are given in Fig. 4. Whereas the TOP and C2 contours nearly match for the second half of the divergent section, the TOP and

Table 1 Design parameters of tested nozzles

	TOP	B1	C2
Ma_D	7.6	9.5	12
R_{th}, mm	10	10	10
L_{TIC}/R_{th}	–	1.08	1.8
Internal shock	Yes	No	Weak

B1 contours merge at the nozzle exit. The numerical survey [9] revealed no internal shock for B1 and a very weak internal shock for C2. The main design parameters of the nozzles are summarized in Table 1.

To identify whether a FSS or a RSS flow condition is present, three independent measurement methods were applied: (a) each nozzle was equipped with 33 wall pressure ports. The pressure was measured via 0.5 mm orifices, drilled perpendicularly into the nozzle wall. Small metal pipes and Teflon tubes connect the ports to XT-154-190 M-type Kulite pressure transducers (see Fig. 3, right). Due to sensor and mounting geometry, a filter of 160 Hz was used, while the signals were recorded with 1 kHz. (b) The nozzles were mounted downstream of a bending tube to determine the side loads. Using an 8 kHz filter, the signals were recorded with 25 kHz. (c) The nozzle exhaust jets were documented using a b/w 125 fps high-speed Schlieren imaging setup. Detailed descriptions of the measurement methods are given in ref. [10–12].

3 Results and Discussion

In total 21 test runs were performed. Each test run included a sequence with two fast and one slow total pressure rises to approx. 6 MPa. After 5 seconds of constant pressure, the total pressure was reduced rapidly. Figure 5, left, gives a comparison of TOP and B1 side loads during the first NPR (p_0/p_a) period. The TOP side load peaks for $t = 14.7$ s and $t = 17.2$ s indicate a RSS flow state during shutdown. The B1 nozzle showed only FSS flow state and no reattached flow condition in all tests. The distinct side load peaks at $t = 6.2$ s are due to a partially reattached flow caused by boundary layer transition, like described in reference [11]. Figure 5, right, gives the averaged overall side loads of the TOP and the B1 with its maximum and minimum values. For better comparison only condensation free flow states were considered. A detailed description of the test campaign and its complete results (including C2) are given in reference [13].

Figure 6 displays Schlieren images of all three nozzles at the common sequence time step $t = 10$ s. Due to differing supply pressures, the related NPRs vary slightly. The TOP (left) displays a classical cap-shock pattern. The internal shock is not visualized by the optical setup, but the triple point (TP), the reflected shock (RS), the Mach ring (MR), and the oblique separation shock (SS) appear clearly. The B1 is free of a recompressing internal shock, and the related Schlieren image (middle) features a Mach lens. Mach lenses are experimentally documented for nozzles with

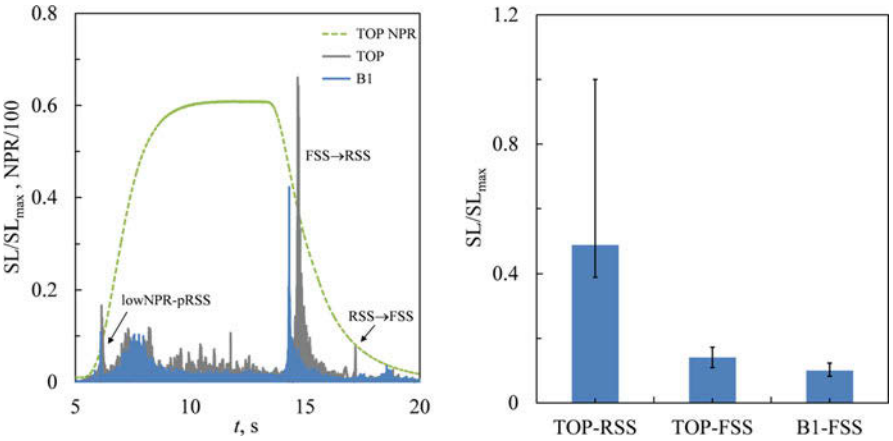

Fig. 5 Side loads of TOP and B1 during first NPR period (left) and averaging (right)

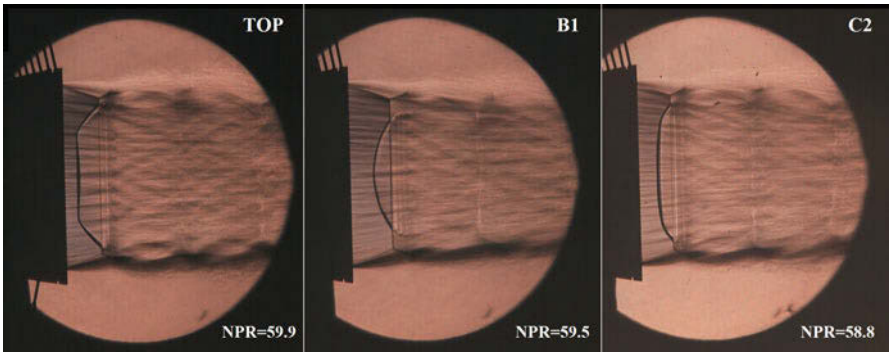

Fig. 6 Exhaust jet pattern of TOP (left), B1 (middle), and C2 (right) at $t = 10$ s

high design Mach numbers [14], and the source of it is the Mach number gradient in radial direction [14, 15]. The C2 Schlieren image reveals a mixed exhaust jet pattern. The Mach lens seems to be flattened by the impact of the weak C2 shock.

As the TOP and C2 contours nearly match, the separation characteristics for high NPRs are comparable. In both cases the introduced oblique separation shock is reflected by the Mach ring. The position of this shock/shock interaction was extracted from the Schlieren images, and the related separation position was determined using the wall pressure signals [11]. The resulting connecting line represents the separation shock. Averaged separation shock positions of the TOP and the C2 are compared for six NPR values in Fig. 7, left. For a better orientation, the TOP contour slope and the exit cross section are included. The separation shocks nearly match; only the C2 points of shock interaction are slightly radially shifted toward the nozzle symmetry axis. In Fig. 7, right, the TOP and the B1 characteristics are compared. As the contours merge not before the nozzle exit, the

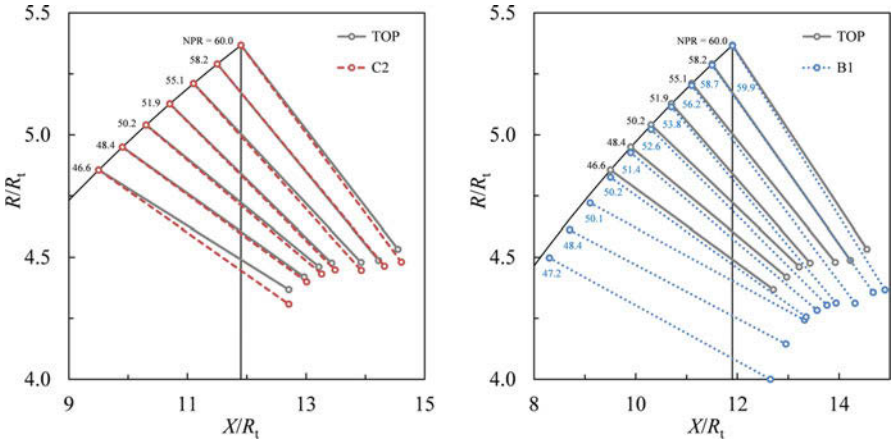

Fig. 7 Oblique separation shocks, TOP and C2 (left), TOP and B1 (right)

flow separation positions are different. The diameter of the B1 Mach lens is smaller than the diameter of the TOP cap shock. With increasing NPR the Mach lens passes the axial cap-shock position.

The Schlieren image evaluation in combination with the studies of Génin et al. [14] on shock deformation in high Mach number nozzles enables a new perspective on the formation of the cap-shock pattern in TOP nozzles. Following the accepted understanding, the internal recompression shock hits a Mach disk, where it is reflected. As a result the interaction point of oblique separation shock and Mach disk (or ring) is shifted downstream, and its diameter is reduced (red dots in Fig. 8, left). The comparison of the TOP, the B1, and the C2 exhaust flow pattern leads to the hypothesis that the internal recompression shock hits an already existing Mach lens (Fig. 8, right top) and deforms it to the "edged" cap-shock pattern (Fig. 8, right bottom). Hence, the interaction point of oblique separation shock and Mach lens is nearly not affected.

4 Conclusion

It was demonstrated that the introduced nozzle contour concept called TICTOP avoids the formation of an internal recompression shock and the resulting cap-shock pattern. Hence a RSS flow state with the accompanying is excluded.

The analysis of the exhaust jets illustrated that high Mach number rocket nozzles feature a Mach lens pattern. Comparing the studied nozzles leads to the hypothesis: If the nozzle features an internal recompression shock, the Mach lens is deformed into the cap-shock pattern. If the conclusion can be applied to hot flows has to be proofed.

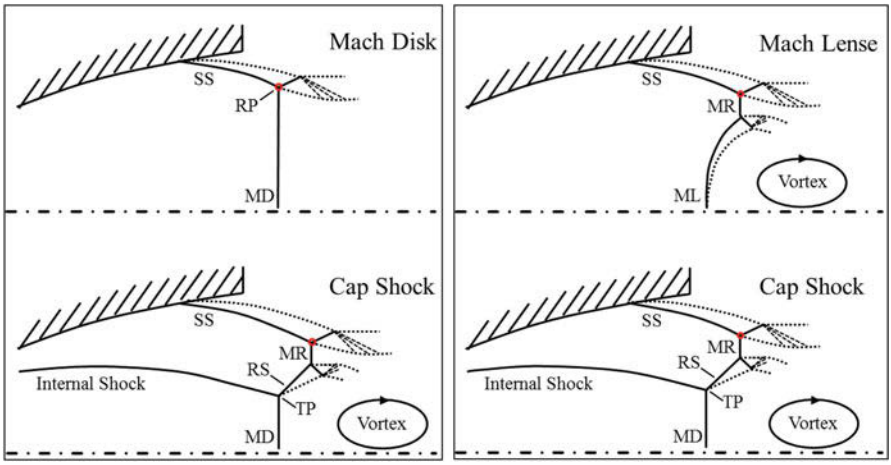

Fig. 8 Formation of cap-shock pattern, former understanding (left) and suggestion (right)

Acknowledgement The authors would like to thank Ying Luo, University of Sydney, for supporting the test data evaluation.

References

1. G. Rao, Exhaust nozzle contour for optimum thrust. Jet Propulsion **28**(6), 377–382 (1958)
2. G. Rao, Approximation of optimum thrust nozzle contour. ARS Journal **30**(6), 561 (1960)
3. R.A. Lawrence, *Symmetrical and unsymmetrical flow separation in supersonic nozzles*, Ph.D. Thesis, Inst. of Technology of Southern Methodist Univ., NASA CR 92587 (1967)
4. L.H. Nave and G. A. Coffey, *Sea level side loads in high-area-ratio rocket engines, 9th Propulsion Conference*, AIAA No. 73-1284, Las Vegas, 1973
5. M. Frey, *Behandlung von Strömungsproblemen in Raketendüsen bei Überexpansion*, Ph.D. Thesis, Univ. Stuttgart, Shaker Verlag, ISBN 3-8265-8806-1, 2001
6. J. Östlund, *Supersonic flow separation with application to rocket engine nozzles*, Technical Report 2004:07, ISNN 0348-467X, Royal Institute of Technology, Stockholm, 2004
7. P. Reijasse, *Aérodynamique des tuyères propulsives en sur-détente: decollement libre et charges laterals en regime stabilise*, Thèse Docteur, Université Paris VI, 2005
8. R. Stark, *Beitrag zum Verständnis der Strömungsablösung in Raketendüsen*, Ph.D. Thesis, RWTH Aachen, 2010
9. M. Frey, K. Makowka, T. Aichner, The TICTOP nozzle: A new nozzle contouring concept, CEAS Space Journal, published online first, doi: https://doi.org/10.1007/s12567-016-0139-z (2016)
10. R. Stark, C. Génin, Optimisation of a rocket nozzle side load reduction device. J. Propuls. Power **32**(6), 1395–1402 (2016)
11. R. Stark, B. Wagner, Experimental study of boundary layer separation in truncated ideal contour nozzles. Shock Waves **19**(3), 185–191 (2009)
12. C. Génin, R. Stark, Side loads in subscale dual bell nozzles. J. Propuls. Power **27**(4), 828–837 (2011)

13. M. Frey, K. Makowka, T. Aichner, R. Stark, C. Génin, The TICTOP nozzle – first experimental results, in *7th European Conference for Aeronautics and Space Sciences*, No. 359, Milan, Italy (2017)
14. C. Génin, R. Stark, S. Karl, Shock system deformation in high Mach number Rocket Nozzles, in *31st International Symposium on Shock Waves*, No. 425, Nagoya, Japan (2017)
15. A. Hadjadj, M. Onofri, Nozzle flow separation. Shock Waves **19**(3), 163–169 (2009)

Three-Dimensional Instability of Shock-Wave/Boundary-Layer Interaction for Rocket Engine Nozzle Applications

A. Sansica, J.-Ch. Robinet, Eric Goncalves, and J. Herpe

Abstract A fully three-dimensional analysis is carried out on an overexpanded rocket engine nozzle configuration to investigate the role of the internal shock-induced separation on the mechanism of generation of side loads during start-up and shutdown transients. A hybrid URANS/LES approach based on the delayed detached eddy simulation turbulence model is used. Reasonable good agreement is obtained between numerical and experimental results. The numerical wall-pressure spectrum shows a narrow peak that a dynamic mode decomposition reveals to be associated with a mode whose characteristics resemble the experimental azimuthal mode believed to be the cause of the generation of side loads.

1 Introduction

During sea-level start-up and shutdown transients, rocket engine nozzles operate in overexpanded conditions, and the appearance of unsteady low-frequency aerodynamic forces that develop around or within the nozzle can cause mechanical failure and therefore represent a major design constraint. Despite the axisymmetric

The original version of this chapter was revised: Sequence of the authors has been updated. A correction to this chapter is available at https://doi.org/10.1007/978-3-319-91017-8_148

A. Sansica (✉)
DynFluid Laboratory, Arts et Métiers ParisTech, 151 Boulevard de l'Hôpital, Paris, France

Centre National d'Études Spatiales (CNES) – Direction des Lanceurs, Paris, France
e-mail: andrea.sansica@ensam.eu

J.-Ch. Robinet
DynFluid Laboratory, Arts et Métiers ParisTech, 151 Boulevard de l'Hôpital, Paris, France

E. Goncalves
ENSMA, Institut Pprime, UPR 3346, CNRS, Chasseneuil-du-Poitou, France

J. Herpe
Centre National d'Études Spatiales (CNES) – Direction des Lanceurs, Paris, France

A. Sasoh et al. (eds.), *31st International Symposium on Shock Waves 2*,
https://doi.org/10.1007/978-3-319-91017-8_67

nature of the nozzle, the internal shock-wave/turbulent-boundary-layer interaction (SWTBLI) can cause large separation and non-axisymmetrical internal pressure distributions. During the development of the nozzle for the J-2S engine, Nave and Coffey [1] have clearly shown the existence of two separation configurations, namely, restricted shock separation (RSS) and free shock separation (FSS). In an RSS, the boundary layer separates and reattaches on the nozzle walls, confining a recirculation bubble within the nozzle. In an FSS, the flow does not reattach on the nozzle walls, and an unconfined recirculation region is created. Depending on the engine nozzle geometry and nozzle pressure ratio (NPR), either the RSS or the FSS configuration is selected. Although thrust-optimized contour (TOC) and thrust-optimized parabolic (TOP) nozzles are usually preferred due to their lower weight and shorter profile, Aghababaie [2] argued that truncated ideal contour (TIC) nozzles might be more advantageous due to the lower magnitude lateral forces, or side loads. As part of the aerodynamic nozzle and afterbody (ATAC) program driven by CNES, the interest is focused on a TIC configuration where the flow is in an FSS regime, for which the side loads are believed to be originated by a low-frequency unsteadiness associated with a self-sustained and azimuthal mode [3]. The exact mechanisms that cause these unsteady behaviors remain unclear. The advances in numerical modeling and computational resources allowed to carry out high space/time resolution studies [4, 5] and realize global linear stability analysis [6, 7] on this complex family of problems. In agreement with the experiments [8], these investigations suggested the origin of the unsteadiness to be located in the separation region, regardless of the nature of the upstream boundary layer. The objective of this study is to perform a fully three-dimensional (3D) analysis to better understand the role of the shock-induced separation on the mechanism of generation of the side loads. Some comparisons with the experiments carried out at Pprime Institute will also be shown.

2 Numerical Method and Code Features

The 3D Navier-Stokes (N-S) equations for a compressible perfect gas are considered. These equations govern the evolution of the state $q = [\rho, \rho u, \rho E, \rho \mu_t]^T$ in the conservative form, where ρ, u, E, and μ_t are the fluid density, velocity vector, total energy, and turbulent viscosity, respectively. The governing equations are written in the nondimensional form as

$$\frac{\partial q}{\partial t} = R(q), \tag{1}$$

where R is the differential nonlinear N-S operator in Cartesian coordinates. The explicit form of Eq. (1) is given in [7]. All numerical simulations in this report are run with an in-house CFD solver, named Phoenix. The code solves the compressible N-S equations on multi-block fully parallelized structured grids with a finite-volume approach. The spatial scheme used to calculate the convective fluxes is the Jameson-Schmidt-Turkel third-order scheme with artificial dissipation. All viscous terms

are differentiated by a second-order centered scheme. A hybrid RANS/Boussinesq approach based on delayed detached eddy simulation (DDES) [9] is used to model the turbulence. For unsteady computations, the dual time-stepping method is used [10]. The derivatives with respect to the physical time are discretized using a second-order extrapolation. The point Jacobi relaxation method is used to solve the implicit part of the dual time step.

2.1 Numerical Details

The numerical domain is composed of the nozzle and an exterior part. The numerical domain is divided into 13 blocks, 9 for the nozzle and core regions and 4 for the exterior part in a combination of classical O-grid and butterfly-grid configurations. The points are clustered at the wall and give $y^+ \approx 10$. In the nozzle and core regions, the grid resolution is $n_x = 770$ in the streamwise direction (570 in the nozzle and 200 in the exterior part) and $(n_r, n_\theta) = (120, 400)$ in the radial and azimuthal directions, respectively. For the exterior part, the grid resolution is $(n_x, n_r, n_\theta) = (200, 100, 400)$. For the selected NPR and inlet Mach number, the nozzle is in a FSS configuration. The air is considered a perfect gas ($\gamma = 1.4$ and $R = 287$ J/kg/K), and the viscosity is assumed to obey Sutherland's law (with TS = 110.4 K Sutherland's constant). No-slip velocity, adiabatic temperature, and pressure extrapolation boundary conditions are applied on the nozzle walls. Uniform velocity and pressure gradient are imposed at the inflow of the numerical domain. Characteristic boundary conditions are used at the domain lateral boundaries and outflow to minimize wave reflections. The distance between the throat and the nozzle exit (L) is used as reference length.

3 Results

3.1 Mean Flow

The mean flow is obtained by averaging over 32 samples during T/t0 = 18. Figure 1 shows the gradient of the mean density, in a Schlieren-like representation. An FSS configuration is correctly obtained, and the flow separates within the nozzle but does not reattach.

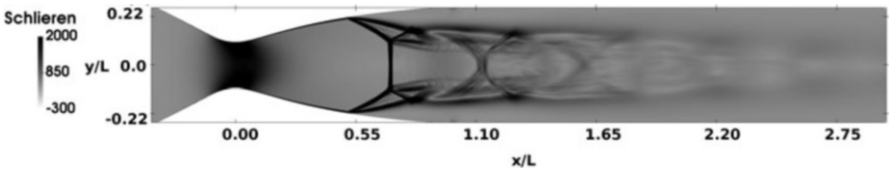

Fig. 1 Mean flow: longitudinal slice; contours of the mean density gradient

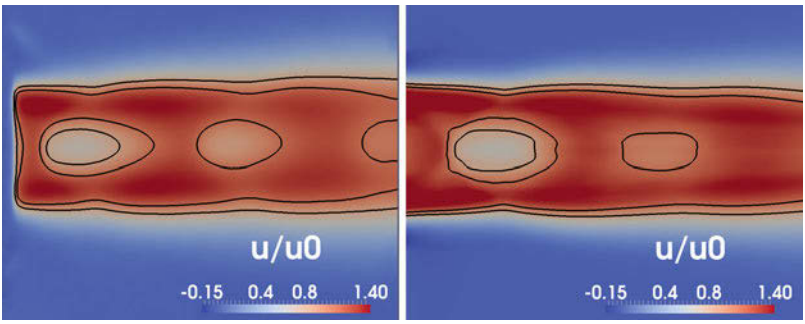

Fig. 2 Mean flow: experimental PIV (left) comparison against CFD (right). Contours of the streamwise velocity in the wake region (x/L = 1–2.2) and iso-lines for u/u0 = 0.85, 1.1

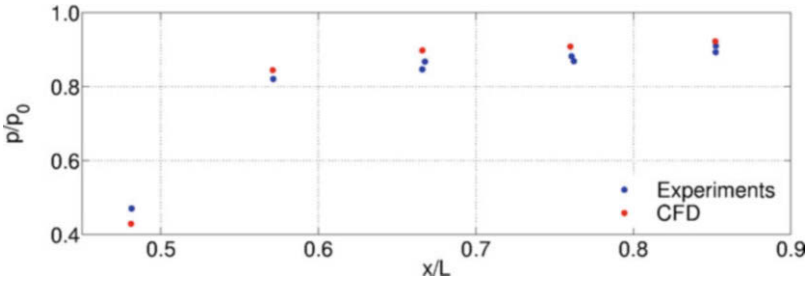

Fig. 3 Experimental (blue circles) comparison against CFD (red circles). Mean pressure in the longitudinal direction

In agreement with the experiments, it is possible to appreciate the correct streamwise positions of the Mach disk (x/L ≈ 0.72) and separation point (x/L ≈ 0.5). In addition, a reasonably good level of axial symmetry is obtained. It is interesting to see that the first shock seems to be much more intense with respect to the second one. As it will be clearer in the next section, the unsteadiness associated with the second shock is very strong and causes the shock to move over a larger streamwise range with respect to the first shock. Hence, the second shock appears to be smeared in a mean flow visualization. An experimental PIV representation of the wake region is compared against the mean flow.

Figure 2 shows the PIV and numerical contours of the streamwise velocity normalized by the inlet streamwise velocity u0. A good agreement can be observed in terms of transversal size and streamwise evolution of the wake. More importantly, the positions of the second and third shocks are satisfactorily determined. Several pressure probes have been located in specific streamwise locations on the nozzle walls as in the experiments. The experimental mean wall pressure normalized with the inlet pressure (p0) along the streamwise direction compares well against the numerical results, as shown in Fig. 3.

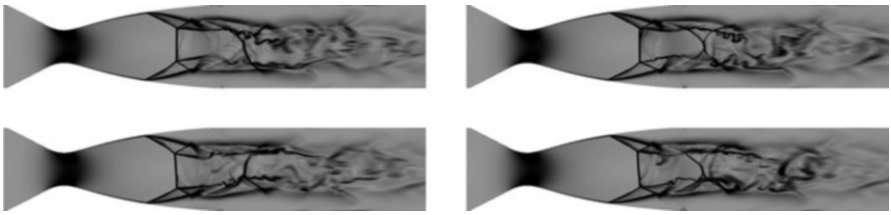

Fig. 4 Contours of the instantaneous density gradient at $t = 0$, T/4, T/2, 3 T/4 (clockwise)

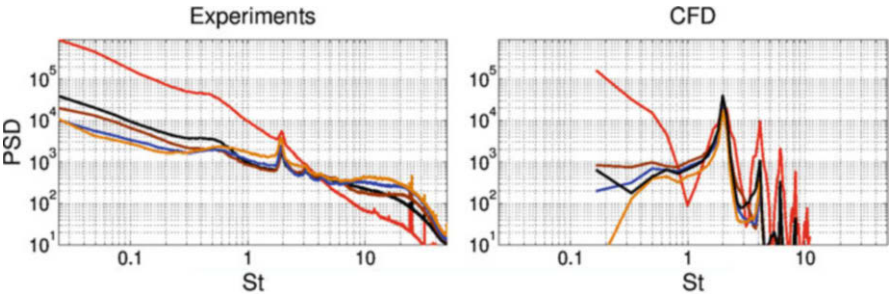

Fig. 5 Experimental (left) and numerical (right) PSDs in the longitudinal direction

3.2 *Unsteady Calculations*

A series of instantaneous Schlieren-like flow visualizations are reported in Fig. 4. While the first shock is tilting and causing the whole wake to oscillate in the transversal direction, the second shock moves in the streamwise direction at a higher frequency. The numerical power spectral density (PSD) distributions calculated from the wall-pressure time histories are compared with the experiments in Fig. 5. In agreement with the experimental results, a narrow peak at a Strouhal number (St = f D/u0, with f frequency and D throat diameter) of about 2 is present. Higher harmonics of the peak at St $\approx$ 2 appear in the numerical simulations.

3.3 *Dynamic Mode Decomposition*

A useful technique to investigate the relevant spatiotemporal dynamics of nonlinear systems is the dynamic mode decomposition (DMD) [11]. This modal decomposition allows the dynamics of each mode to be associated with a singular frequency by operating a linear combination of the snapshots obtained with the fully nonlinear N-S solver. The DMD method is applied to the 32 snapshots collected from the nonlinear calculations presented above, and the corresponding DMD spectrum is shown in Fig. 6. Since the snapshots are collected when the flow configuration reaches saturation, the growth rate associated with the DMD modes is meaningless

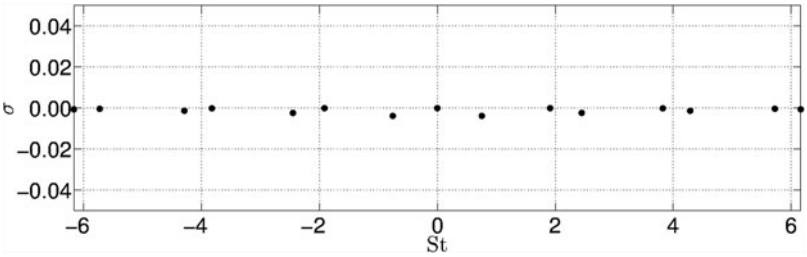

Fig. 6 Dynamic mode decomposition spectrum. Growth rate (σ) vs Strouhal (St)

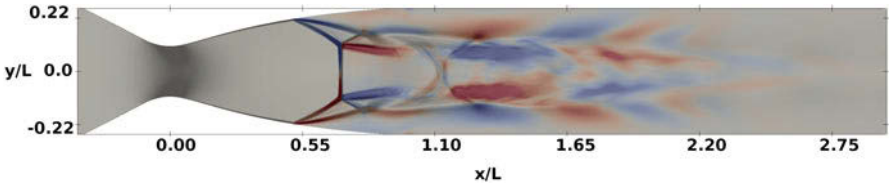

Fig. 7 Real part of the streamwise eigen-velocity for the mode at St $\approx$ 2 (red and blue levels for positive and negative streamwise perturbation velocity, respectively) plotted over the mean density gradient contours

in terms of stability and close to zero. However, it is interesting to check the modal shapes associated with each frequency. The mode associated with the frequency at St $\approx$ 2 (that the experiment and numerical wall-pressure spectra indicate as the most energetic peak) is shown in Fig. 7 by plotting the real part of the streamwise eigen-velocity and superimposed to the mean density gradient distribution. It is interesting to see that the DMD mode is strongly localized in the first shock, and in its proximity the shape is axial-symmetric.

Reconstructing the perturbation velocities associated with the DMD mode is possible to plot the iso-surface of the Q-criterion colored by the streamwise velocity, as shown in Fig. 8. Large annular structures in the near-wall region exit the nozzle slowly with respect to a faster core characterized by structures of smaller size, resembling the azimuthal mode found in the experiments carried out at Pprime Institute that is associated with the peak at St $\approx$ 2 and potentially responsible for the generation of side loads.

4 Conclusions

Fully nonlinear calculations have been performed for the TIC rocket engine nozzle. A DDES turbulence model has shown to yield to numerical solutions that agree satisfactorily with the mean flow experimental results within the nozzle and in the wake region. The PSD of the wall-pressure time histories at different longitudinal

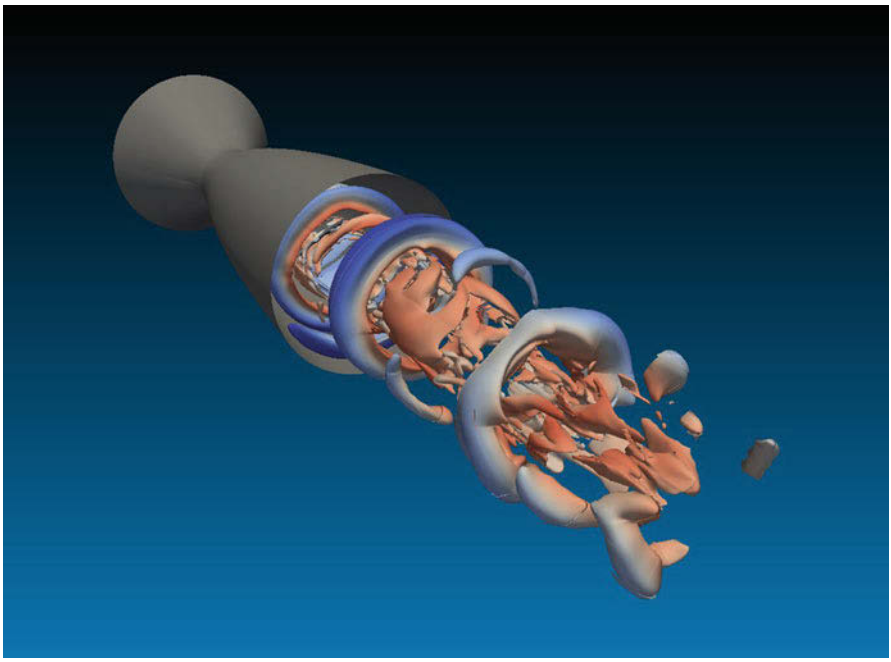

Fig. 8 Three-dimensional iso-surface of the reconstructed Q-criterion for the mode at St $\approx$ 2 and colored with the reconstructed streamwise velocity perturbation (increasing velocity from blue to red)

positions shows close agreement between the experiments and numerical simulations for a narrow peak at St $\approx$ 2. The DMD method is applied to 32 snapshots taken during the fully nonlinear simulations. The dynamics associated with the mode at St $\approx$ 2 shows strong activity in the first shock and in the shear layer. When the reconstructed Q-criterion is shown in a 3D view, it is possible to see large structures forming in the vicinity of the wall and are slowly shedding downstream in the jet, resembling the azimuthal mode found in the experiments. Future investigations will be carried out by performing global linear stability analysis in order to understand whether this peak is associated with a globally unstable mode and what is its precise role in the generation of side loads.

References

1. Nave, L. H. and Coffey, G. A., Sea level side loads in high-area-ratio rocket engines, AIAA Paper 1973-1284, 1973
2. Aghababaie, A., *Experimental Characterisation and Analytical Modelling of Rocket Nozzle Side-Loads,* PhD thesis, University of Bristol, 2013

3. Shams, A., *Contribution to the Numerical Simulation of Turbulent Shock-Induced Separated Flows,* PhD thesis, Universite de Poitiers, 2011
4. E. Touber, N.D. Sandham, Large-eddy simulation of low-frequency unsteadiness in a turbulent shock-induced separation bubble. Theor. Comput. Fluid Dyn. **23**, 79–107 (2009)
5. A. Sansica, N. Sandham, Z. Hu, Instability and low-frequency unsteadiness in a shock-induced laminar separation bubble. J. Fluid Mech. **798**, 5–26 (2016)
6. F. Sartor, C. Mettot, R. Bur, D. Sipp, Unsteadiness in transonic shock-wave/boundary-layer interactions: Experimental investigation and global stability analysis. J. Fluid Mech. **781**, 550–577 (2015)
7. F. Guiho, F. Alizard, J.-C. Robinet, Instabilities in oblique shock wave/laminar boundary-layer interactions. J. Fluid Mech. **789**, 1–35 (2016)
8. P. Dupont, C. Haddad, J. Ardissone, J.F. Débieve, Space and time organization of a shock wave/turbulent boundary layer interaction. Aerosp. Sci. Technol. **9**(7), 561–572 (2005)
9. P.R. Spalart, S. Deck, M.L. Shur, K.D. Squires, M.K. Strelets, A. Travin, A new version of detached-eddy simulation, resistant to ambiguous grid densities. Theor. Comput. Fluid Dyn. **20**, 181–195 (2006)
10. Jameson, A., Time-dependent calculations using multigrid with applications to unsteady flows past airfoils and wings*,* AIAA Paper 1991-1596, 1991
11. P.J. Schmid, Dynamic mode decomposition of numerical and experimental data. J. Fluid Mech. **656**, 5–28 (2010)

Shock Interactions in Thrust Optimised Parabolic (TOP) Nozzles during Start-Up and Shutdown

Ijaz Mohamed and G. Rajesh

Abstract The separation phenomenon in parabolic nozzles has long been studied in detail and is well documented. The parabolic nozzles are normally being operated in those regimes of pressure ratios where separation does not occur. However, during the start-up and shutdown transience, the operation of the nozzles inherently falls in the separation regimes due to the lower total pressures they experience. The present work is an attempt to study the shock structures in a thrust optimised parabolic (TOP) which occur during the separation process in nozzle and its interaction due to which either a free shock separation (FSS) or restricted shock separation is observed (RSS). The hysteresis of FSS↔RSS transition during the start-up and shutdown transiency is also studied. A complete transient analysis on shock structure interactions in 2D axisymmetric TOP nozzle of area ratio 36 was carried out, and the results were used to interpret the shock interactions, separation patterns and hysteresis effects.

1 Introduction

Flow separation inside the nozzle has been a major topic of discussion for the past few years. The unsteady nature of the separation along with its asymmetric nature generates severe lateral vibration loads on the nozzle which can be catastrophic. Nave and Coffey [1], while conducting cold tests of the subscale J-2S engine for the Apollo developmental program in 1970s, reported for the first time the reattachment of flow downstream of separation (RSS) accompanied with high levels of lateral vibrations. Later, numerical simulations by Chen et al. in 1994 [2] on subscale J-2S nozzle revealed the existence of flow reattachment (RSS). A trapped vortex was also revealed in the simulation. Nasuti and Onofri [3] through their simulations explained the role of this vortex in deviating the core flow to the walls. Frey and Hangemann

I. Mohamed · G. Rajesh (✉)
Department of Aerospace Engineering, Indian Institute of Technology Madras, Chennai, India
e-mail: rajesh@ae.iitm.ac.in

A. Sasoh et al. (eds.), *31st International Symposium on Shock Waves 2*,
https://doi.org/10.1007/978-3-319-91017-8_68

[4, 5] through their numerical investigation explained the reattachment phenomena of flow through the formation of a special shock pattern called cap shock. Cold flow experiments with subscale models of various nozzles were carried out by Jan Ostlund [6, 7], M. Frey, S.B. Verma [8], etc., and confirmed the presence of large lateral vibrations during FSS↔RSS transition. The side loads generated by unsteady and unsymmetrical flow separations act as a limiting factor in the performance optimisation of the rocket engine and hence have been a subject of research, both experimentally and numerically.

The present study is carried out on a thrust-optimised parabolic (TOP) nozzle of area ratio 36. TOP nozzles are skewed parabola approximation of thrust-optimised contour (TOC) nozzles which are generated through variational optimisation methods based on Lagrange multipliers. TOP nozzles are used in modern rocket engines like SSME and Vulcain. Nozzles like TOC and TOP features special kind of shock, generally called internal shock. Internal shocks are shock waves due to the coalescence of compression waves generated just downstream of the point of inflection (discontinuity in curvature) of nozzle divergent where the circular throat opens and meets the parabolic contour. The internal shock interacts with the separation shock and Mach reflection at various locations depending upon the nozzle pressure ratio (NPR). This interaction has a direct influence on the type of flow separation in the nozzle. A transient CFD analysis was carried with a commercially available software ANSYS FLUENT to understand the implication of shock interaction in determining the pattern of separation and in establishing a correlation for FSS↔ RSS transition criterion. Through the analysis a clear understanding on the physics of fluid flow and the hysteresis effect during the start-up and shutdown transiency is established.

2 CFD Simulation

A transient CFD analysis was carried out on a 2D axisymmetic TOP nozzle of area ratio 36. Compressible 2D axisymmetric Navier-Stokes equations were solved to numerically predict the flow fields. Two-equation SST-k-ω turbulence is used to close the equations.

Figure 1 shows the domain and boundary conditions used in the analysis. The nozzle inlet pressure was time varied at a prefixed ramp rate of (4.4 bar/s) using a user-defined function (UDF). The nozzle opens up to an extended domain to simulate the ambient conditions.

Analysis was done with coarser mesh of 2.43 Lakh cells and a finer mesh of 9.25 Lakh cells. The finer mesh size showed better separation accuracies (Fig. 2), and further mesh refinement showed no variation in separation pattern. Hence 9.25 Lakh mesh was used for further CFD analysis. Steady-state solution for a nozzle inlet pressure of 8 bar was used to initialise the domain, and inlet pressure was ramped up from 8 bar. Steady-state solution for a nozzle inlet pressure of 8 bar was used to initialise the domain, and inlet pressure was ramped up from 8 bar.

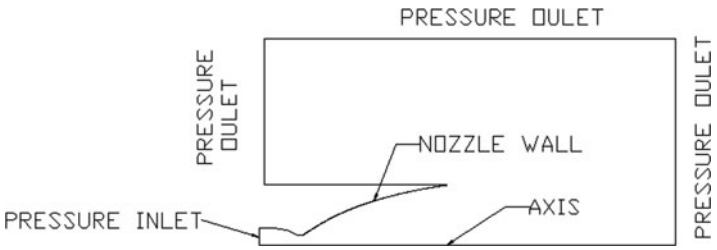

Fig. 1 Computational domain and boundary conditions

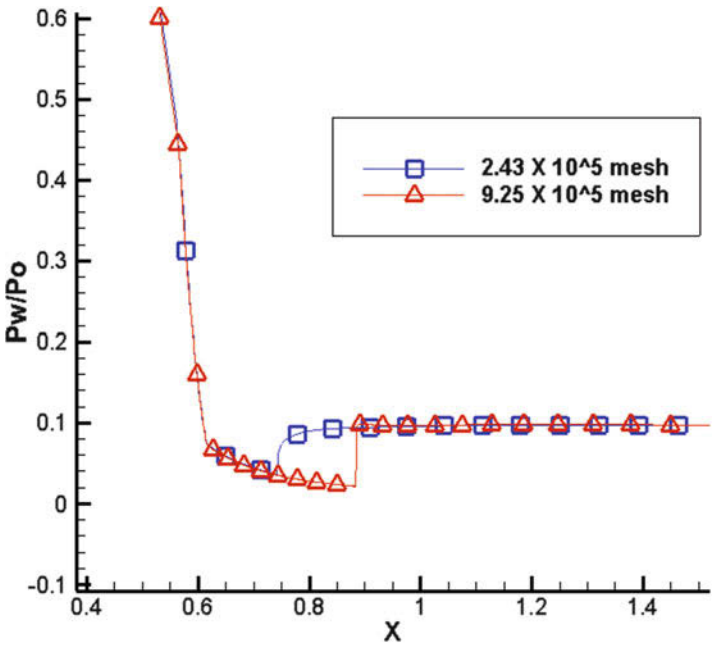

Fig. 2 Comparison of wall pressures for finer mesh and coarser mesh

3 Results and Discussions

3.1 Ramp-Up and Ramp-Down Sequence

The nozzle inlet pressure was ramped up from 8 bar to 24 bar at a ramping rate of 4.4 bar/s. During the ramp-up sequence before the nozzle inlet pressure reaches 18 bar, the flow was completely separating from the nozzle and no reattachment happens (FSS). Once the pressure reaches 18 bar, a sudden transition in flow separation pattern was noticed. The flow which was separated from the wall has reattached back to the wall, and flow expands to ambient pressure through a series of compression

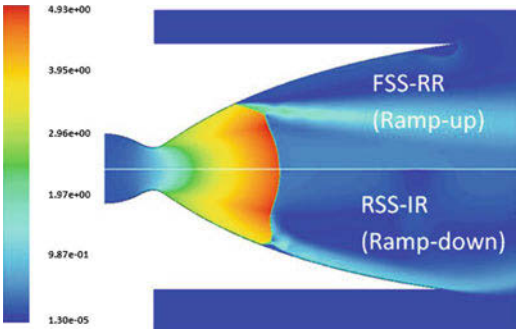

Fig. 3 Hysteresis effect in FSS↔RSS transition for NPR = 14

and expansion waves (RSS). During the up-ramping, FSS to RSS transition is always accompanied by an abrupt downstream shift of separation shock location. This sudden shift is due to the plateau pressure effect which is explained later. The RSS pattern of separation continued till 24 bar. With the increase in nozzle pressure ratio (NPR), the separation shock and separation bubble associated with RSS also move downstream. Ramp-down sequence was started from 24 bar and continued till the nozzle inlet pressure reaches 8 bar. It was observed that the RSS pattern was retained till the inlet pressure drops to 10 bar. Reverse transition from RSS to FSS happen below an NPR of 10 bar. Hence a clear sign of hysteresis in FSS↔RSS transition was seen (Fig. 3).

3.2 Shock-Flow Interactions in Parabolic Nozzles

Flow inside divergent section of the nozzle is generally divided into three zones, namely, kernel, radial gradient zone and uniform flow zone. In TOC nozzles, compression waves emanate from the point of inflection, coalesce and form a weak shock known as the internal shock. TOP nozzles are parabolic approximation of TOC nozzles and feature similar internal shock. The kernel of the nozzle is bounded by the internal shock. During the start-up and shutdown transiency, the nozzle operates in overexpanded state, and the flow separates from the wall. This separation is accompanied with a separation shock(s) which is oblique in nature. This separation shock gets reflected from the axis in the form of a Mach reflection. Hence the nozzle features a Mach disc at the centre. Flow inside the nozzle will always have a radial gradient $\frac{dP}{dr}$ which can be +ve or –ve. It can also be zero. From the analysis it is observed that the kernel of TOP nozzle is having a pressure gradient of $\frac{dP}{dr} < 0$. This –ve pressure gradient causes the Mach disc to bend backwards when moved radially outwards resulting in type 1 non-uniform flow Mach reflection as explained by Nasuti and Onofri [9]. Across the internal shock, there occurs a sudden jump in pressure, and afterwards the pressure gradually increases till the nozzle wall is reached. This +ve pressure gradient in radially outside direction causes the Mach disc to bend forwards when moved radially outwards resulting in type 2 non-

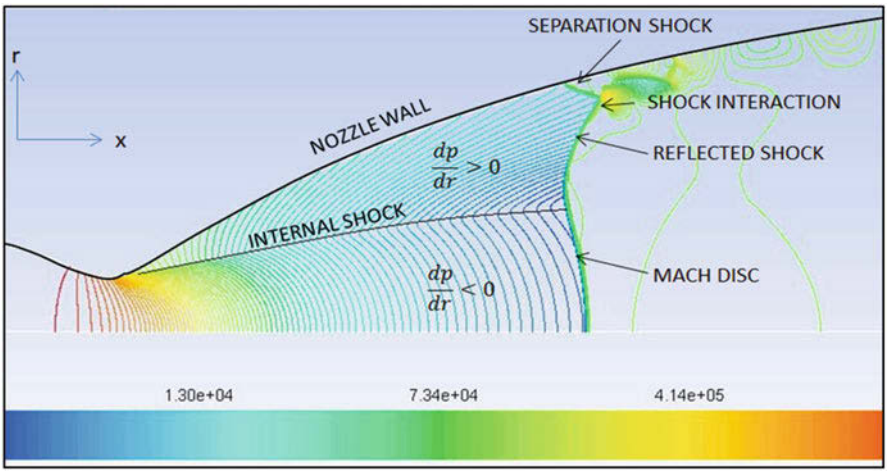

Fig. 4 Pressure contours at NPR = 24

uniform flow Mach reflection explained in [9]. Figure 4 shows the pressure gradients inside the nozzle and the shock structures resulting due to the upstream flow non-uniformities.

3.3 FSS to RSS Transition

To understand the reason for the transition of separation pattern from FSS to RSS transition, the analytical solutions for NPR = 8, 10, 12, 14, 16, 18, 20, 22 and 24 were compared.

Wall pressure plots (Fig. 5) of the nozzle for the pressure ramp-up shows that the FSS to RSS transition occurs at NPR steps from 16 to 18. In FSS the pressure rises to near ambient value through the separation shock; hence, the plateau pressure is near ambient. But in a RSS, the pressure inside the separation bubble is lower than the atmosphere, i.e. the plateau pressure associated with RSS is much lower compared to FSS. This means that the ΔP across the separation shock for RSS is much lower compared to FSS. Shocks of lower strength hence need to move forwards to adjust the pressure. This is the root reason for a rapid downstream shift of separation shock once the flow separation transits from FSS to RSS. The wall pressure plots for down-ramping (Fig. 6) show that the re-transition from RSS to FSS happens below a NPR < 10. Hence the transition from FSS to RSS at NPR > 16 during the ramp-up and re-transition from RSS to FSS at NPR < 10 are a clear sign of hysteresis with FSS↔RSS transition.

The Mach contours (Fig. 7) from the analysis show that the internal shock can interact either with the separation shock or the normal shock depending upon the

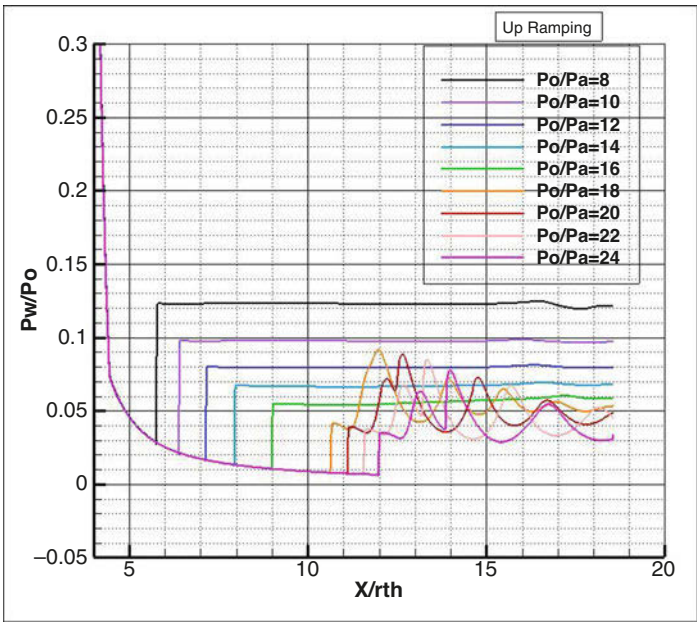

Fig. 5 Wall pressures during pressure ramp-up

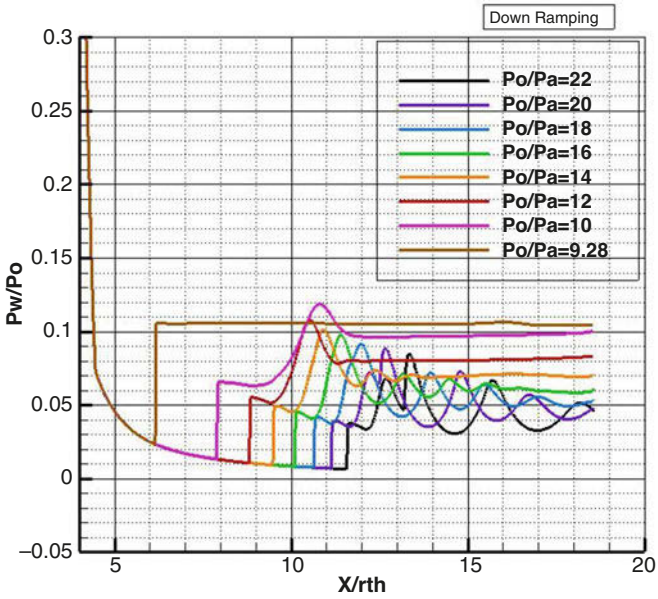

Fig. 6 Wall pressures during pressure ramp-down

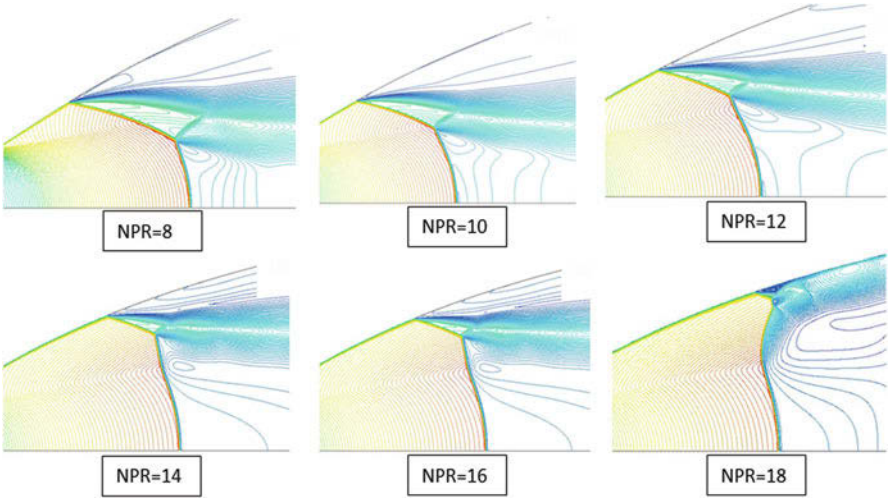

Fig. 7 Mach contours for different nozzle pressure ratios during pressure ramp-up

location of these shocks which in turn dependents on the nozzle pressure ratio. This interaction alters the flow pattern and influences the FSS↔RSS transition in the nozzle. When the nozzle pressure ratio is low, the internal shock will interact with the separation shock. Since the internal shock and separation shock both are of the same nature, they will coalesce, and no further interaction occurs. As the nozzle pressure ratio is increased further, the separation shock along with the normal shock moves downstream. As a result the interaction point of internal shock with oblique shock shifts downwards and finally reaches the triple point (t) of Mach reflection (MR). As the nozzle pressure ratio is increased further, the interaction point still shifts downwards to interact with the normal shock, and a new triple point is formed where the internal shock interacts with the Mach disc. The portion below the interaction (new triple point) will see a type 1 non-uniform MR, while the portion above the new triple point will see a type 2 non-uniform MR. The fluid flow above this triple point and approaching this reflected shock will see the shock as an oblique shock formed by a wedge. This reflected shock from the 'new triple point' will induce an outward radial momentum to the fluid resulting in the flow moving radially outwards. This can be correlated to the phenomenon of inviscid separation. But during the initial phases of this interaction (see NPR = 12,14 and 16 of Fig. 7), the length of reflected shock is smaller than the length of separation shock, and hence the outward radial momentum induced by reflected shock is not able to overcome the inward momentum induced by the separation shock. Hence the flow does not reattach to the wall and behaves like a FSS. As the nozzle pressure ratio is again increased, the Mach disc moves downstream and interaction point shifts further downwards (NPR = 18 in Fig. 7). During this phase the length of reflected shock increases, and also due to the downstream shift of separation shock, the length

of separation shock reduces gradually. At some point of time when the upward radial momentum induced by the reflected shock gains over the inward radial momentum induced by separation shock, the separated flow reattaches to the wall and becomes RSS. This results in further reduction of length and inward radial momentum of separation shock. Hence RSS become stable in the domain. An irregular reflection was observed at the interaction point of reflected shock and separation shock, and a secondary Mach stem is generated. When nozzle pressure ratio was again increased, the shock system move downstream, and the secondary Mach stem vanishes. The ultimate reason for FSS to RSS transition is the difference in shock lengths and hence the momentum as explained above. The shift in interaction point of internal shock below the triple point is adding only a favourable condition for FSS to RSS transition.

3.4 Hysteresis in FSS↔RSS Transitions

The hysteresis effect is so evident from the results of the CFD analysis. The transition from FSS to RSS during the pressure ramp-up happens at NPR > 16, and re-transition from RSS to FSS during pressure ramp-down happens during NPR < 10.

From Fig. 8, it is seen that during the ramp-down phase from NPR = 24, the flow separation point of RSS displaced upstream in the same rate as it was displaced downstream during the ramp-up phase. But it is seen that, even after the nozzle pressure ratio has reached back to the pressure ratio for FSS to RSS (i.e. at NPR = 16) during ramp-up, no re-transition from RSS to FSS was observed. It is also observed that the re-transition from RSS to FSS did not happen even after the separation shock at the same location where the flow transition happened from FSS to RSS during the up-ramping. Hence, it can be accounted that the hysteresis is with respect to pressure ratio as well as space. The RSS pattern continued with the separation point shifting upstream in the same rate till the nozzle pressure ratio reached Po/Pa = 10. Once the nozzle pressure ratio is reduced below 10, there is a change in flow separation pattern from RSS to FSS with a sudden shift is separation shock upstream.

The plateau pressure for FSS is very close to ambient pressures, while for RSS it is generally much below. To understand more on FSS↔RSS transition and its relationship with plateau, pressures (P_p) were plotted against point of separation in Fig. 9. However, it is observed that the plateau pressures of RSS and FSS are comparable at some location. This is marked as dual solution domain in the Po/P_p Vs X/r_{th} graph (Fig. 9). In the dual solution domain, FSS is observed during the pressure ramp-up, while RSS is observed during the ramp-down.

No such dual solution domain was reported earlier. In fact Ref. [10] reports a single transition point, where a dual solution is absent.

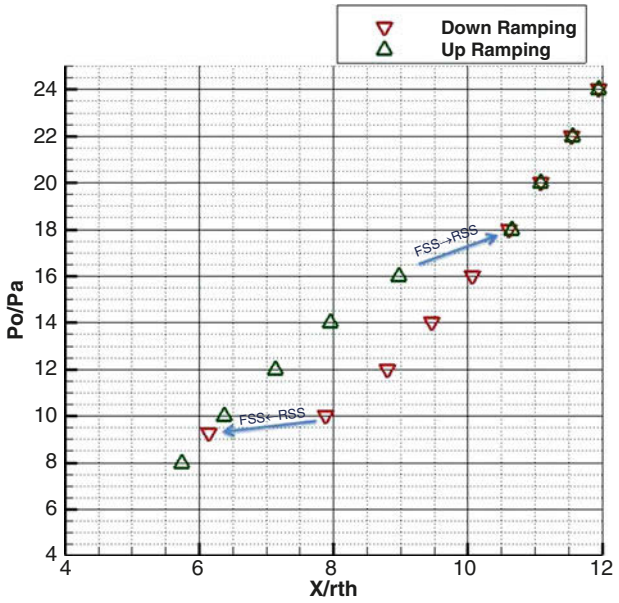

Fig. 8 Location of flow separation for various NPR of up- and down-ramping

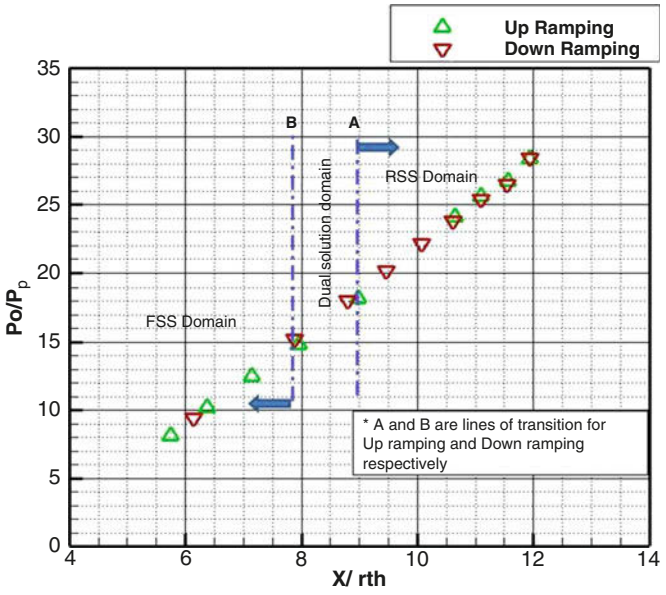

Fig. 9 Point of separation vs plateau pressures

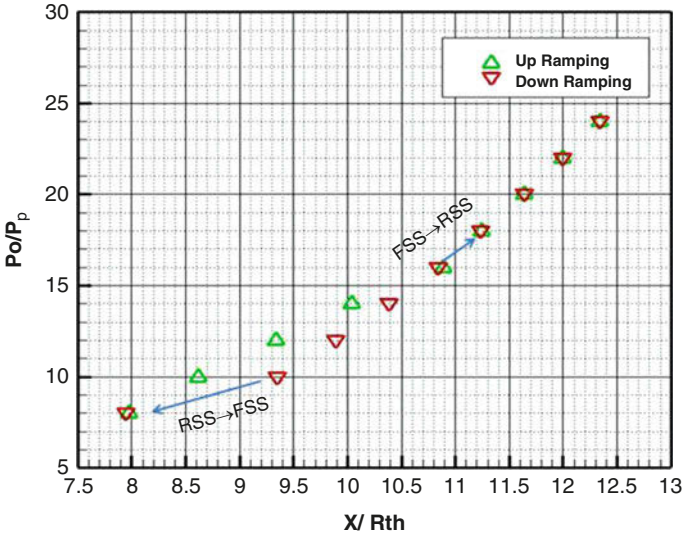

Fig. 10 Location of normal shock for various NPR up-ramping and down-ramping

Similar hysteresis in the location of central normal shock (Mach disc) for various pressure ratios for both pressure ramp-up and ramp-down shown in Fig. 10 also contributes to the hysteresis with FSS↔RSS transition.

4 Conclusions

The transient CFD analysis carried on AR 36 TOP nozzle was able to capture the hysteresis in RSS↔FSS transition. The internal shock, its point of interaction with the Mach disc and length of reflected shock and separation shock determine the transitions of flow separation in nozzle. Correlating the FSS↔RSS transition with the plateau pressure, a dual solution domain was established where the plateau pressures of FSS during ramp-up and plateau pressures of RSS during ramp-down coexists. The phenomenon of hysteresis is found out to be a summation of spatial hysteresis with movement of separation shock and normal shock (Mach disc).

References

1. L.H. Nave, G.A. Coffey, "Sea level side loads in high-area-ratio rocket engines, in *AIAA Paper 73-1284, AIAA/SAE 9th Propulsion Conference*, Las Vegas, Neveda, 1973
2. C.L. Chen, S.R. Chakravarthy, C.M. Hung, Numerical investigation of separated nozzle flows. AIAA J. **32**, 1836–1843 (1994)

3. F. Nasuti, M. Onofri, Viscous and Inviscid Vortex generation during Nozzle flow transients, AIAA 96-0076, June 1996
4. M. Frey, G. Hagemann, Status of flow separation prediction in Rocket Nozzles, AIAA 98-3619, 1998
5. M. Frey, G. Hagemann, Flow separation and side-loads in Rocket Nozzles, AIAA 99-2815, 1999
6. J. Östlund, Flow processes in Rocket Engine Nozzles with focus on flow separation and side-loads, Technical reports, Royal Institute of Technology Department of Mechanics, S-100 44 Stockholm, Sweden. (2002)
7. J. Östlund, T. Damgaard, M. Frey, Side-load phenomena in highly overexpanded Rocket Nozzles, AIAA-2001-3684
8. S.B Verma, Flow separation characteristics of a thrust optimized parabolic Nozzle in a high altitude simulation chamber, AIAA 2012-6658, 2012
9. F. Nasuti, M. Onofri, Shock structure in separated nozzle flows. Shock Waves **19**, 229–237 (2009)
10. E. Martelli, F. Nasuti, M. Onofri, Numerical calculation of FSS/RSS transition in highly overexpanded rocket nozzle flows. Shock Waves **20**, 139–146 (2010)

Shock System Deformation in High Mach Number Rocket Nozzles

C. Génin, R. Stark, and S. Karl

Abstract Flow overexpansion in supersonic nozzle, with or without flow separation, leads to the formation of a shock system composed of an oblique shock rooted at the nozzle wall and a Mach reflection. A study has been conducted on the shock system deformation for nozzles with high design Mach numbers, i.e., with high wall opening angle. An experimental test campaign was conducted on three cold flow sub-scale nozzles with Schlieren imaging. An important curvature of the Mach disk was demonstrated for the nozzle with the higher design Mach numbers and low nozzle pressure ratio conditions. The experimental observations were confirmed with numerical simulations realized with DLR in-house RANS solver TAU, which showed a sensitivity of the Mach disk shape to radial pressure gradients in the flow in its vicinity. In addition, the experiments indicated instability of the Mach lens at low NPR values, corresponding to a position of the Mach disk in the region of the highest pressure gradient.

1 Introduction

The overexpanded flow out of a supersonic nozzle features a shock system constituted of an oblique shock and a Mach reflection. The oblique shock is generated at the nozzle end or at the flow separation position in case of high overexpansion. In an ideal nozzle contour (TIC), the Mach reflection corresponds to a Mach disk orthogonal to the nozzle axis [1–3].

Previous experimental studies have shown the possibility of a Mach disk deformation under particular conditions. In order to better understand the reasons and conditions of apparition for this shock curvature, a series of tests, experimental

C. Génin (✉) · R. Stark
German Aerospace Center, DLR, Institute of Space Propulsion, Lampoldshausen, Germany
e-mail: chloe.genin@dlr.de

S. Karl
German Aerospace Center, DLR, Institute of Aerodynamics and Flow Technology, Göttingen, Germany

A. Sasoh et al. (eds.), *31st International Symposium on Shock Waves 2*,
https://doi.org/10.1007/978-3-319-91017-8_69

and numerical, has been conducted. Three TIC nozzle models were tested under similar conditions as part of a parametrical study. The design Mach number was chosen as parameter of interest. It determines the flow properties (pressure and Mach number) in the kernel of the flow, which interact with the shock system during overexpanded operations.

2 Experimental Analysis

2.1 Experimental Setup

Three TIC nozzle models were designed and tested at DLR's cold flow facility P6.2. The nozzle contours share a common subsonic geometry and present design Mach numbers between 4.8 and 5.8. The contours are designated as 20XX, where XX stands for the design Mach number (e.g., 2048 for a design Mach number of 4.8). The contours were truncated in order to reach full flowing conditions at a nozzle pressure ratio (NPR, ratio feeding over ambient pressure) of 50, which lies within the operation range of the facility. The test sequences consisted in slow pressure ramps from 0.1 up to 5.5 MPa. Figure 1 is a picture of nozzle 2053 mounted and instrumented on the test rig.

Wall pressure distribution was recorded through transducers placed regularly along the nozzle wall in 4 mm interval. The shock system out of each nozzle was

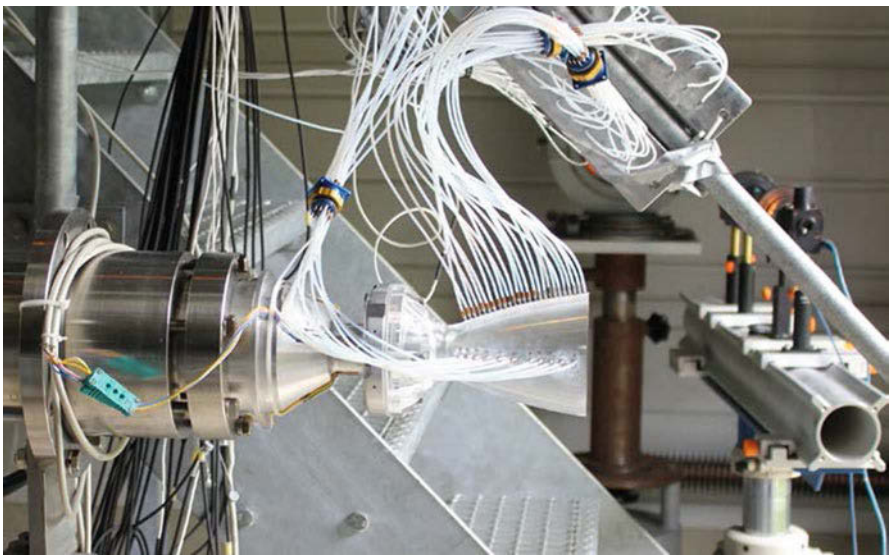

Fig. 1 Nozzle model 2053 mounted at test facility P6.2

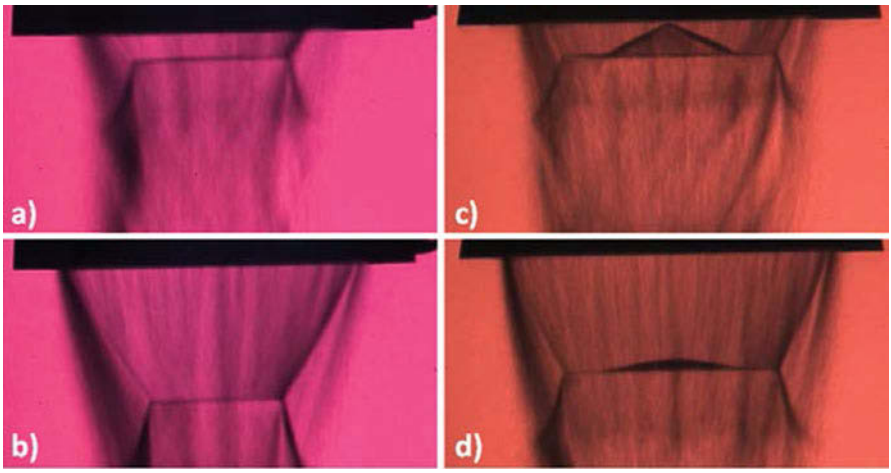

Fig. 2 Shock system, (**a**) 2048/NPR35, (**b**) 2048/NPR45, (**c**) 2058/NPR35, (**d**) 2058/NPR45

visualized with B/W Schlieren optics in Z-configuration and recorded with up to 2000 fps. More details on the experimental setup are given in references [4, 5].

2.2 Mach Disk Curvature

A comparison of the shock systems for the three nozzle models shows differences in the Mach reflection configuration. Nozzle 2048 presents a classical shock system with a Mach disk orthogonal to the nozzle axis for all NPRs, as illustrated Fig. 2 for NPR 35 (a) and 45 (b).

For the nozzles with higher design Mach number (2053 and 2058), a curvature of the Mach disk is visible. Figure 2c depicts the shock system out of nozzle 2058 at NPR 35. The Mach disk is bended in its center in the upstream direction. The deformation presents great amplitude in the axial direction. At NPR 45 (Fig. 2b), the deformation amplitude decreases in axial direction while the diameter of the curvature remains constant. Nozzle 2053 display the same behavior with slightly lower deformation amplitudes.

2.3 Shock System Instability

In addition to the deformation, the shock system of both nozzles with the higher design Mach number (2053 and 2058) presents instabilities at low NPRs. It can be seen that the shape and size of the Mach lens deforming the Mach disk are highly fluctuating, between curved and almost straight Mach disk configurations. Figure 3

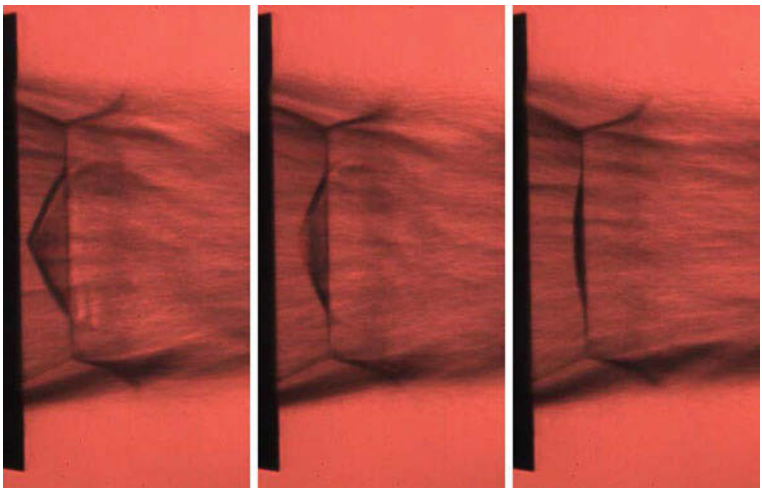

Fig. 3 Instability of the shock system, 2058/NPR36.5 configuration

is an example of three consecutive pictures taken in 0.5 ms interval of the shock system of nozzle 2058 at NPR 36.5. In the first picture, the Mach disk is bended in upstream direction in an almost triangular shape; in the second picture, the shock curvature has decreased and resembles a lens pressing against the Mach disk; and in the third picture, the lens depth has further decreased. The back and forth instability of the shock system takes place particularly at NPRs between 30 and 40. At these NPR values, the Mach reflection is still located near the nozzle end.

3 CFD Analysis of the Shock Curvature Phenomenon

Supplementary CFD analyses of the shock curvature phenomenon were carried out using the DLR Tau code [6]. Both, the 2048 and 2058, nozzle configurations were considered: The NPR was set to 45 (both nozzles) and 35 (2058 only). The flow was modeled as a calorically perfect gas with a gas constant of 297 J/kg/K and a ratio of specific heats of 1.4. Laminar viscosity was computed using Sutherland's law for gaseous nitrogen, and turbulence was treated by solving the Favre-averaged Navier-Stokes equations along with the Spalart-Allmaras one equation eddy-viscosity model [7]. The flow field was assumed to be two-dimensional and axisymmetric. The computational domain includes the complete nozzle with total reservoir conditions specified at its subsonic inlet and a far-field boundary with ambient conditions.

A comparison between experimental and numerical wall pressure distributions and Schlieren images for the 2048 and 2058 nozzle at NPR 45 is shown in Figs. 4 and 5, respectively. The numerical Schlieren images were generated by an overlay

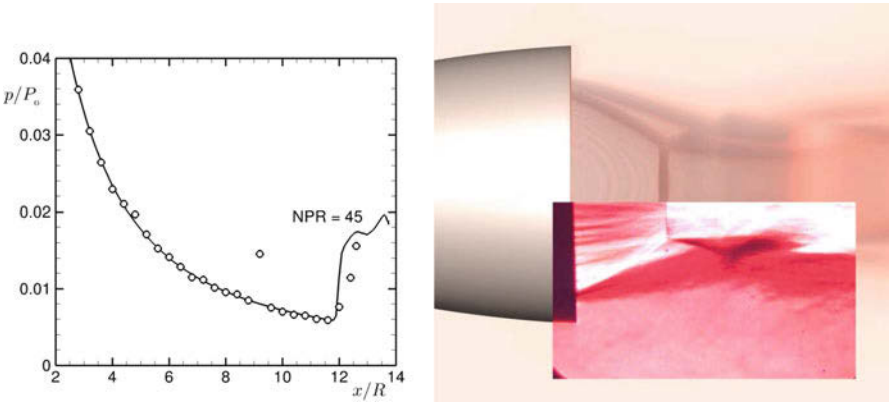

Fig. 4 Comparison of wall pressure distributions (left) and Schlieren (right) for 2048/NPR45 configuration

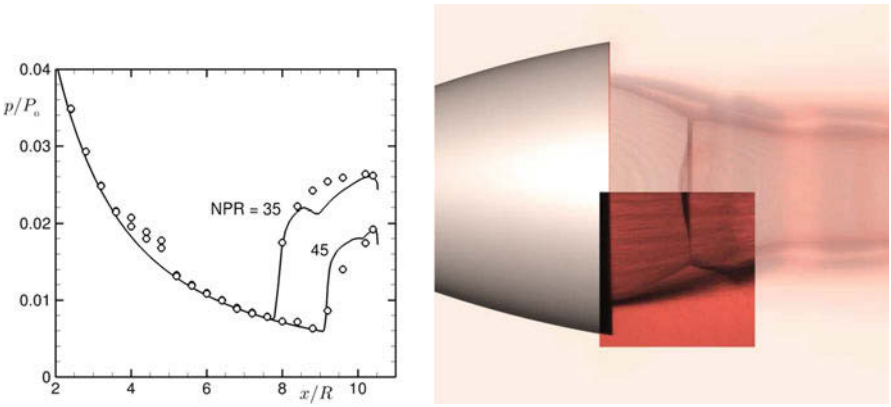

Fig. 5 Comparison of wall pressure distributions (left) and Schlieren (right) for 2058/NPR45 configuration

of a set of 25 transparent contour images of the density gradient magnitude which are staggered in the line of sight of the camera.

The results in Figs. 4 and 5 show good agreement of both the wall pressure distribution and the shock structure downstream of the nozzle exit. Both configurations feature flow separation in the vicinity of the nozzle exit. The occurrence of straight (2048) and curved (2058) Mach disks is reproduced by the numerical analyses. For NPR 35 the curvature of the Mach disk is underpredicted by the numerical results (Fig. 6 (left)), yet the qualitative agreement of the shock structure remains acceptable.

The numerical results indicate that radial pressure gradients in the nozzle exhaust jet are responsible for the observed curvature of the Mach disk. The right part of Fig. 6 shows visualizations of density gradient and static pressure in a 2D cut for the

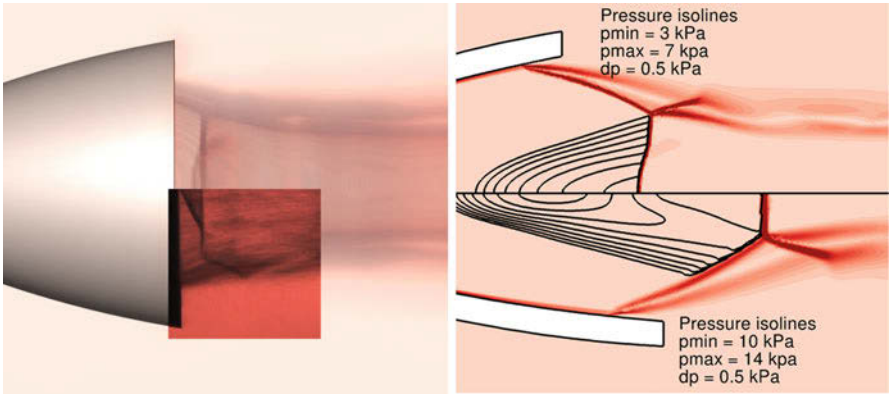

Fig. 6 Left: Schlieren comparison for 2058/NPR35 configuration; right: density gradient and static pressure isolines for 2058 (top) and 2048 (bottom) nozzles at NPR 45

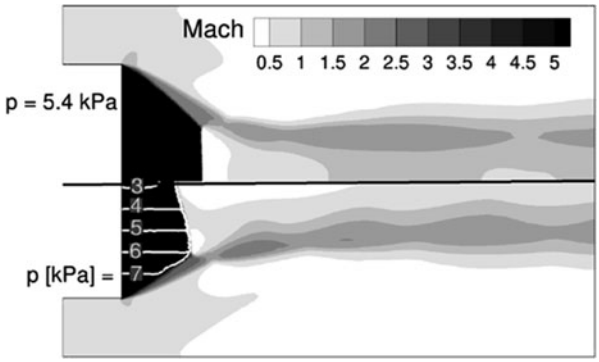

Fig. 7 Model problem of a two-dimensional planar shock reflection with constant pressure along the jet (top) and imposed pressure gradient (bottom)

2058 (top) and 2048 (bottom) nozzles. The radial pressure gradient in the supersonic exhaust upstream of the Mach disk is significantly stronger for the 2058 nozzle. This hypothesis was further substantiated by considering the model problem of a 2D planar supersonic jet. Numerical experiments show that the shape of the Mach disk is particularly sensitive to radial pressure gradients, and Mach disk curvature also occurs in the planar case. Figure 7 compares flow fields of a jet with constant static pressure (top) and a jet with a prescribed static pressure gradient (bottom). The results show the same qualitative behavior as observed in the axisymmetric nozzle flows.

4 Conclusion and Outlook

The nozzle geometry, and in particular the design Mach number, has shown to have an effect on the shock system of overexpanded TIC nozzles. At low NPR values, the Mach reflection of nozzles with high design Mach number is bended inward. The deformation features a high curvature, almost triangular. The axial amplitude of the deformation decreases with increasing NPR values. This effect corresponds to the passing of the Mach reflection through regions of high radial pressure gradients in the flow. The nozzle with the lower design Mach number presented smaller pressure gradient and showed a classical Mach disk configuration for the whole NPR range of the study.

To pursue this investigation, three additional nozzle geometries have been designed and manufactured. Design Mach numbers between 7 and 11 have been chosen, and the nozzle models will be tested in the next months.

References

1. A. Hadjadj, M. Onofri, Nozzle flow separation. Shock Waves **19**, 163–169 (2009)
2. F. Nasuti, M. Onofri, Shock structure in separated nozzle flows. Shock Waves **19**, 229–237 (2009)
3. R. Stark, B. Wagner, Experimental study of boundary layer separation in truncated ideal contour nozzles. Shock Waves **19**(3), 185–191 (2009)
4. C. Génin, R. Stark, Experimental investigation of cold flow TIC nozzles, a spectral analysis, AIAA Paper 2016-4668, 2016
5. R. Stark, C. Génin, Optimisation of a rocket nozzle side load reduction device. J. Propuls. Power **32**(6), 1395–1402 (2016)
6. S. Langer, A. Schwöppe, N. Kroll, The DLR Flow Solver TAU – Status and Recent Algorithmic Developments, AIAA Paper 2014-0080, 2014
7. P.R. Spalart, S.R. Allmaras, A One-Equation Turbulence Model for Aerodynamic Flows, AIAA-Paper 92-0439, 1992

Numerical Investigation of a Planar Shock Wave Interacting with an Acentric Water Ring

Gaoming Xiang and Bing Wang

Abstract The droplet breakup and the bubble collapse are typical flow phenomenon involving complicated pressure and density variation as well as interface evolution. In this paper, the numerical simulation of a planar shock wave interacting with an acentric water ring is studied. In order to simulate the spatiotemporal interface evolution of the water ring impinged by a planar shock wave, a quasi-conservative interface capturing method is employed, in which the governing equations consist of the conservative Euler equations and the scalar transportation equations, together with the stiffened gas equation of state of the two phases. An incremental stencil adapted WENO scheme with fifth order in the smooth regions is employed for the spatial reconstruction. The numerical results show that the bubble collapses under different incident Mach number shock waves due to the strong pressure gradients. The strong transverse jets form because of the Richtmyer-Meshkov instability. The jet tip and its impaction on the downward wall of the cavity are extracted by analyzing the isolines of γ representing the two-phase interface. The jet tip speed and the pressure at the impaction point nonlinearly increase with the incident shock wave strength.

1 Introduction

The shock interaction with droplets and bubbles is widely involved in nature and industrial application, such as supernova explosion, ultrasound lithotripsy, fuel atomization in the scramjet combustor [1], and cavitation collapse in hydromachines [2]. The physical mechanism of those processes has been especially emphasized. Therefore, it is of importance to study the disintegration of two-phase interfaces impacted by the shock wave.

G. Xiang · B. Wang (✉)
School of Aerospace Engineering, Tsinghua University, Beijing, China
e-mail: wbing@tsinghua.edu.cn

A. Sasoh et al. (eds.), *31st International Symposium on Shock Waves 2*,
https://doi.org/10.1007/978-3-319-91017-8_70

Regarding the liquid droplet breakup by a shock wave impaction, Pilch et al. [3] summarized five different regimes based on the *We* number, which are vibrational breakup, bag breakup, bag-and-stamen breakup, sheet stripping, and wave crest stripping, followed by catastrophic breakup. However, they did not show the wave interaction with the interface once the shock waves propagate inside the droplet. The breakup scenario of catastrophism cannot be well explained and has become one of the controversial conclusions. In the recent experimental investigation, the cavitation was found inside a water column when it was impinged by a high-strength shock wave [4]. Therefore, the interaction between shock waves and a droplet embedded with a cavity has inspired the researcher's interests. As for the bubble collapse, the formation mechanism and quantitative characterization of the transverse jet were studied through the numerical [5] and the experimental method [6]. Moreover, the collapse of the bubble was proposed to be potential way in targeted drug delivery [7]. However, there is lack of investigation about the interaction of shock wave with droplets embedded with an air cavity.

Due to the limitation of experimental technologies and measurement approaches, numerical simulation has become one of the important approaches to demonstrate the flow structures and wave evolution in the interaction of shock wave with droplets/bubbles. The main difficulty for the numerical method lies in precisely capturing the shock and interface discontinuities existing in such compressible two-phase flows. Several strategies have been tried in decades, such as the level-set method, the front-tracking method, the volume of fraction method, and the γ transportation method [8], which are related to quantities in the advection equation and the schemes treating the governing equations. Considering the computation efficiency and implementation for the code, the γ transportation method is employed.

In this paper, the shock and interface capturing method is used for the numerical simulation. The two-phase interface is represented and transported by resolving the specific heat ratio (γ) equation. An acentric cavity embedded inside a two-dimensional cylindrical water column is then numerically studied. The paper is organized as follows. In Sect. 2, a brief description of the numerical method and the problem setup is presented. In Sect. 3, the results obtained by the numerical simulation are analyzed. Finally, a summary is given in Sect. 4.

2 The Numerical Method and the Problem Setup

2.1 The Numerical Method

In this paper, the compressible two-phase flow is described by the conservative Euler equation and the advection equation of two material-property coefficients,

$$\frac{\partial \boldsymbol{w}}{\partial t} + \frac{\partial \boldsymbol{f}(\boldsymbol{w})}{\partial x_j} = 0 \tag{1}$$

where $\boldsymbol{w} = (\rho, \rho u_i, E)^T$ and $\boldsymbol{f} = (\rho u_j, \rho u_i u_j + p\delta_{ij}, (E + p)u_j)^T$, which correspond to the conservative variables and fluxes. The scalar transport equation is

$$\frac{\partial \boldsymbol{\phi}}{\partial t} + u_j \frac{\partial \boldsymbol{\phi}}{\partial x_j} = 0 \tag{2}$$

where $\boldsymbol{\phi}$ is given by

$$\boldsymbol{\phi} = (\phi_1, \phi_2)^T = \left(\frac{1}{\gamma - 1}, \frac{\gamma P_\infty}{\gamma - 1} \right)^T$$

A stiffened gas EOS is used to close the above governing equations,

$$\frac{p + \gamma P_\infty}{\gamma - 1} = \rho e = E - \frac{1}{2} \rho u_i u_i \tag{3}$$

where ρ is density; u_i is velocity; p is pressure; E is total energy; γ is heat specific ratio; and P_∞ is the reference pressure. The sound speed is defined as $c = \sqrt{\gamma (p + P_\infty)/\rho}$. The Euler equations together with the scalar transport equations form the quasi-conservative model.

In this paper, the finite volume framework is employed to discretize the governing equations. A 5th-order incremental WENO scheme is introduced to reconstruct the primitive variables in characteristic space. This space scheme has a wider range of accuracy order when solving large density ratio compressible flow with high Mach numbers. The HLLC approximate Riemann solver based on the Godunov-type method is applied to solve the flux at the cell edge. The 3rd-order TVD Runge-Kutta scheme is used for the time discretization.

2.2 Problem Setup

In this paper, a planar shock wave interacting with an acentric water ring is studied. The computational setup is shown in Fig. 1. c_0 and c_b are the initial center of the water column and the cavity, $c_0 = (8.8,0)$ mm and $c_0 = (9.4,0)$ mm, respectively. The initial diameter (d_0) of the water column is 4.8 mm, and the cavity diameter is 2.4 mm. The computational domain extends from $[-6d_0, 6d_0] \times [-3d_0, 3d_0]$. The nomenclature UW, DW, CUW, and CDW is used to represent the upstream water column wall, the downstream water column wall, the upstream cavity wall, and the downstream cavity wall, as shown in Fig. 1.

For all the simulation cases, the specific heat ratio (γ) and the material parameter (P_∞) of the air are 1.4 and 0 Pa and for the water γ is 6.12 and P_∞ is 3.3×10^8 Pa. A planar shock wave moves from the left to the right side and the initial parameters behind the shock are given in Table 1. Three different incident Mach numbers are chosen for the present numerical study. The initial parameters of the pre-shock air

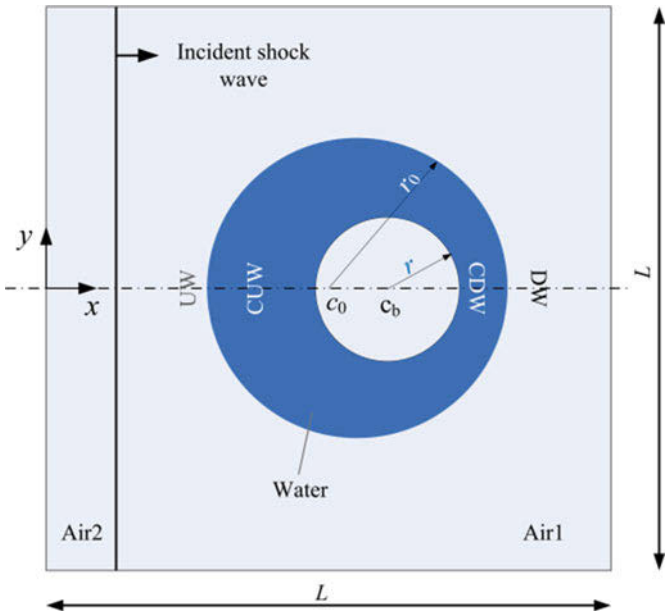

Fig. 1 The computational setup

Table 1 Setup parameters for the initial post-shock

Ms	ρ_{air2} [kg/m^3]	u_{air2} [m/s]	p_{air2} [MPa]
2.0	3.200	429.78	0.456
2.4	3.854	568.26	0.664
2.8	4.396	699.92	0.910

and the air bubble inside the water column are (ρ_{air1}, u_{air1}, p_{air1}) = (1.2 kg/m^3, 0 m/s, 0.1 MPa) and the corresponding parameters for the water column are (ρ_{water}, u_{water}, p_{water}) = (10^3 kg/m^3, 0 m/s, 0.1 MPa). The computational domain is chosen large enough to prevent reflection off the boundary from polluting the area we are concerned. The extrapolation boundary condition is applied for all the domain boundaries. The grid resolution is 333 per column diameter. The CFL number is set as 0.5 for all the simulation cases.

3 Discussion and Analysis

As presented in Sect. 2, an acentric water ring interacting with a high-intensity incident shock wave is studied through numerical simulations. The three incident shock wave Mach numbers are 2.0, 2.4, and 2.8. As the typical wave patterns and interface shape are similar for the three chosen incident Mach numbers, only the case of $Ms = 2.4$ is presented in this paper, as shown in Fig. 2. The top half of

each subfigure shows the numerical Schlieren contours, and the bottom half shows the pressure contours. The non-dimensional time is introduced for the following analysis, which is expressed as

$$t^* = \frac{t u_{\text{air2}}}{d_0} \sqrt{\frac{\rho_{\text{air2}}}{\rho_{\text{water}}}} \tag{4}$$

where t is the physical time; u_{air2} is the initial x-component velocity behind the shock; d_0 is the initial diameter of the water column; and ρ_{air2} and ρ_{water} are the densities, respectively.

$t^* = 0$ is chosen at the time when the incident shock wave (ISW) just impacts on the upstream water column wall (UW) of the water ring. Later on, the ISW is transmitted into the water ring and be reflected into the air, forming the transmitted wave (TW) and the reflected shock wave (RSW). When the TW arrives at the upstream cavity wall (UCW), it will be transmitted into cavity, forming the re-transmitted wave (RTW), and be reflected into the liquid, forming the 2nd reflected wave (2nd RW). As the TW is transmitted and reflected inside the water ring repeatedly, the pressure experiences significant changes. At later time stages, as shown in Fig. 2f–h, the cavity inside the water column deforms, and a transverse jet is formed. The transverse jet propagates downstream and impacts on the downstream cavity wall (CDW). Finally, the jet pierces the cavity, and an extreme high-pressure region occurs near the impaction point.

In the numerical simulation, the cavity is acentricly embedded inside the water column, and cavity center is closer to the downstream water column. Thus, the transmitted/reflected waves between the UW and the CUW take longer time to be transmitted or reflected once again when compared to the coaxial water ring. In addition, it makes sense that the wave structures are altered when the cavity is acentric. The pressure profiles change as well when compared with the coaxial cavity, though the results of which are not presented in this paper.

The formation mechanism and the parameters of the transverse jet are important for the bubble collapse. From Fig. 2f–h, it is observed that the incident shock wave has passed through the water ring at the time when the cavity begins to deform. The pressure gradient inside the water ring is the main reason for the bubble collapse. As shown in Fig. 3, four monitor points are mounted inside the water ring, including three mounted in the upstream side and one in the downstream side. The pressure curves of the four monitor points are shown in Fig. 4. Since the water ring deforms at later time stages, only at the early stage the pressure curves are shown. When the TW arrives at the monitor *M1*, the pressure increases sharply. In case of $Ms = 2.8$, the pressure reaches as high as 4 MPa. The pressure decays gradually as the TW propagates downstream, which is obvious for the pressure curves of the monitor *M2* and *M3*. When the TW is reflected at the CUW, the reflected wave propagates upstream, the pressures of monitor 3 to monitor 1 drop down in sequence. For the monitor *M4*, the pressure increases when the TW arrives. Since the wave strength decays gradually as it propagates, the pressure of the monitor *M4* is much lower than that of *M1* to *M3*.

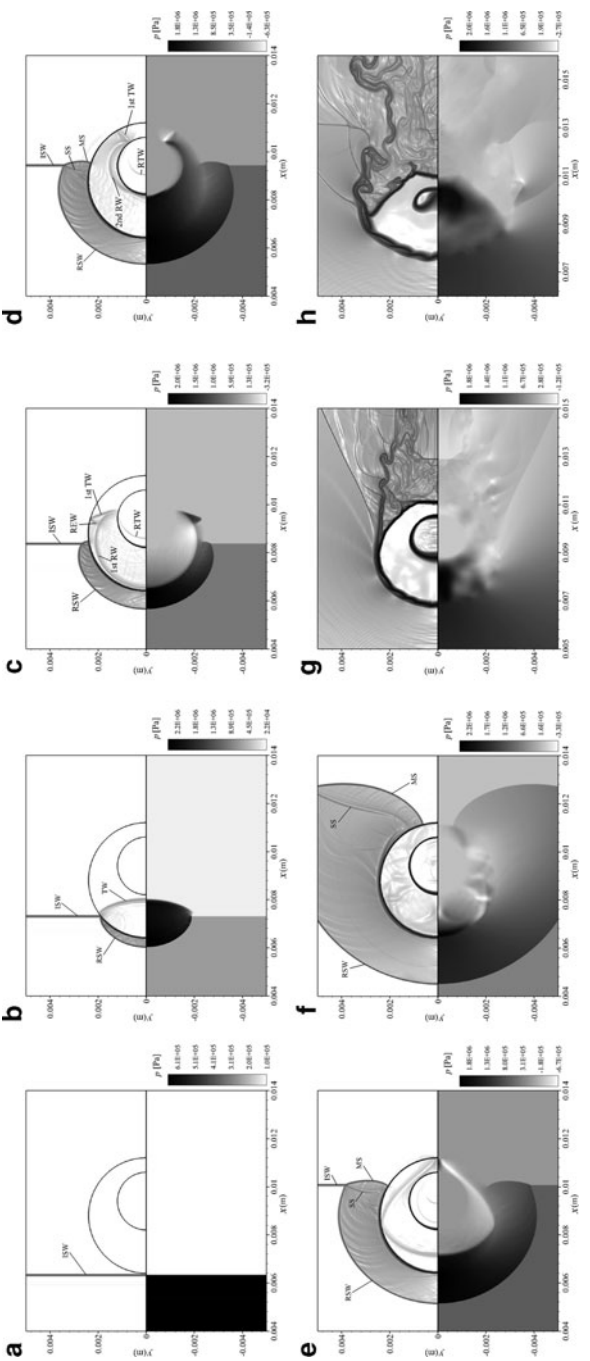

Fig. 2 The numerical Schlieren (top) and the pressure contours (bottom) at different time instants in case of $Ms = 2.4$

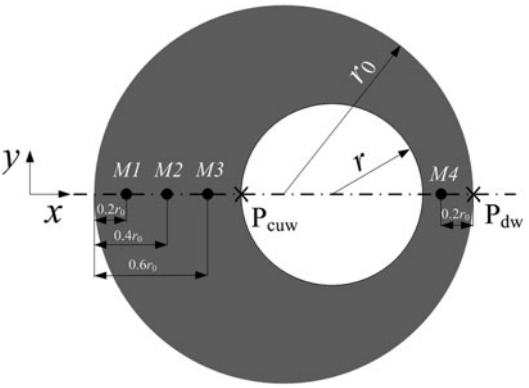

Fig. 3 The monitor point positions in the numerical simulations

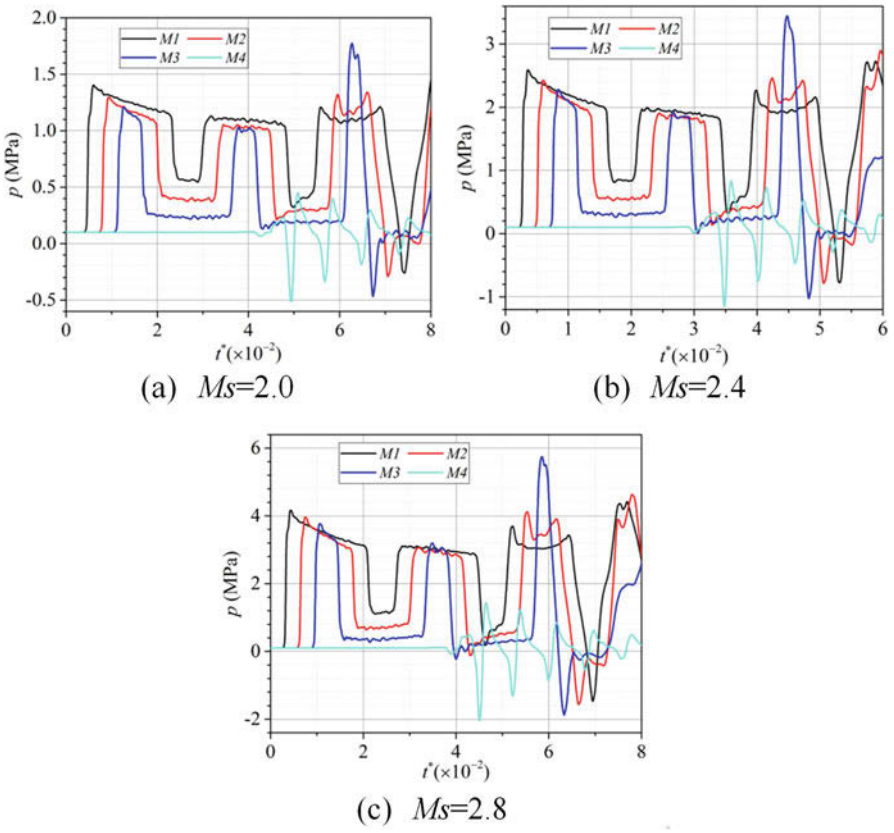

Fig. 4 The pressure curves at the four monitor points for the three chosen Mach numbers

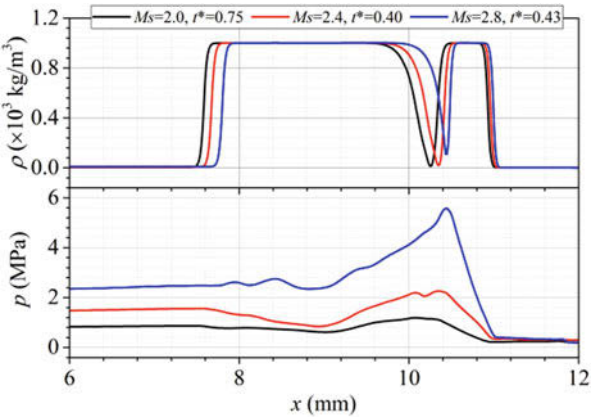

Fig. 5 The centerline density and pressure when the transverse jet impacts on the CDW

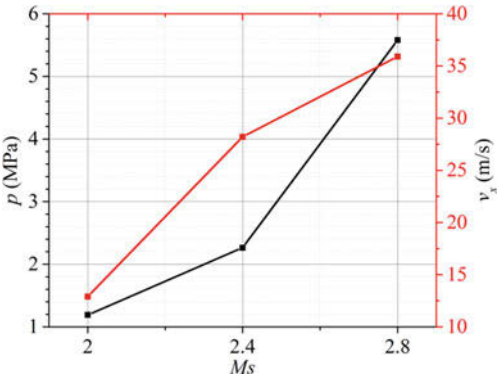

Fig. 6 The jet tip pressure and velocity at the impaction point

As we know, the air inside the cavity is much easier to be compressed than the liquid of the water ring, and the liquid is driven into the air due to the pressure gradient. With the curvature effect of the water ring, the fluid close to the centerline moves faster than the fluid far from the centerline. Thus, the transverse jet observed from Fig. 2 can be explained. The Richtmyer-Meshkov instability also explains the formation mechanism of the transverse jet. When the shock wave interacts with the interface, the heavy fluid is driven into the light fluid, and the curvature of the interface facilitates the formation of the jet.

When the jet impacts on the CDW, the pressure increases near the impaction region. The centerline pressure and density are extracted when the transverse jet impacts on the CDW. From the density profiles, the positions of the impaction point are easy to be identified, as shown in Fig. 5. When the incident Mach number increases, the pressure at the impaction region increases as well. Figure 6 shows the pressure at the impaction point and the x-component velocity of the jet tip at the impaction point. In case of $Ms = 2.0$, the pressure at the impaction point is 1.2 MPa, and the x-component velocity is 12.9 m/s. When the incident Mach number is 2.8, the pressure is 5.6 MPa, and the x-component velocity is 36 m/s. As the jet impacts on the CDW, the kinetic energy is transferred into the pressure potential energy.

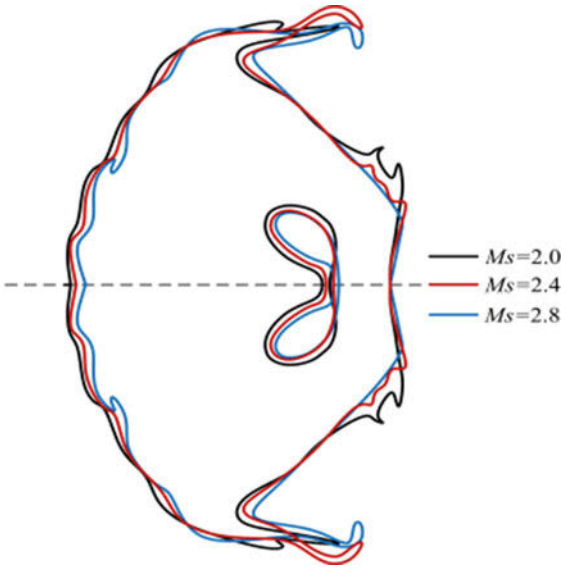

Fig. 7 The extracted two-phase interface when the transverse jet impacts on the CDW

Therefore, the pressure at the impaction point increases dramatically for even higher incident Mach number.

The qualitative properties also have significant differences of the transverse jet for different incident Mach numbers. The interface is extracted based on the numerical results to analyze the effect of the incident shock intensities. In the numerical simulation, the specific heat ratio γ is a scalar transport variable and is used to identify the interface between the liquid and the air. Figure 7 shows the extracted two-phase interface when the transverse jets impact on the CDW for the three chosen Mach numbers. It is observed that the width of the jet is larger for higher incident Mach number. This is consistent with the result in [5], which studied the problem of a planar shock wave interacting with a centric air cavity in liquid. The remaining cavity inside the water column is highly compressed, and the interface of the water ring becomes unstable. The liquid is stripping off the lateral pole of the water ring.

4 Conclusion

In this paper, the interaction of a planar shock wave with an acentric water ring is investigated from the numerical aspect. The finite volume method is employed to discretize the governing equations, which consist of the Euler equations and the scalar transport equations. An incremental WENO scheme is introduced for the space reconstruction, and the HLLC approximate Riemann solver is employed to solve the flux at the cell edges. The 3rd-order TVD Runge-Kutta scheme is applied for the time advancing.

The numerical results show that the reflection and transmission process repeatedly after the incident shock wave transmitting into the water ring. The cavity inside the water column collapses and forms the transverse jet because of the Richtmyer-Meshkov instability. The intensity of the incident shock wave has an effect on both the tip-width and speed of the transverse jet. An extreme high pressure occurs at the impaction region when the jet impacts on the downstream cavity wall.

References

1. E.A. Kush, J.A. Schetz, Liquid jet injection into a supersonic flow. AIAA J. **11**(9), 1223–1224 (1973)
2. C.E. Brennen, *Cavitation and bubble dynamics* (Cambridge University Press, New York, 2013), pp. 79–107
3. M. Pilch, C.A. Erdman, Use of breakup time data and velocity history data to predict the maximum size of stable fragments for acceleration-induced breakup of a liquid drop. Int. J. Multiphase Flow **13**(6) (1987)
4. S. Sembian et al., *Plane shock wave interaction with a cylindrical water column*. Phys. Fluids. **28**, 5 (2016)
5. N.A. Hawker, Y. Ventikos, Interaction of a strong shockwave with a gas bubble in a liquid medium: A numerical study. J. Fluid Mech. **701** (2012)
6. O. Supponen et al., Scaling laws for jets of single cavitation bubbles. J. Fluid Mech. **802** (2016)
7. O. Shpak et al., Acoustic droplet vaporization is initiated by superharmonic focusing. PNAS **111**, 5 (2014)
8. V. Coralic, T. Colonius, Finite-volume WENO scheme for viscous compressible multicomponent flows. J. Comput. Phys. **274** (2014)

A Compact High-Order Finite Volume Method for Computing Shock Waves on Arbitrary Grids

L. Li, H. Luo, and Yuxin Ren

Abstract A cell-centered finite volume method based on a variational reconstruction, termed FV(VR) in this paper, is developed for compressible flows on 3D arbitrary grids. In this method, a linear polynomial solution is reconstructed using a newly developed variational formulation. Like the least-squares reconstruction, the variational reconstruction has the property of 1-exactness. Unlike the cell-centered finite volume method based on the least-squares reconstruction, termed FV(LS) in this paper, the resulting FV(VR) method is stable even on tetrahedral grids, since its stencils are intrinsically the entire mesh. However, the data structure required by FV(VR) is the same as FV(LS) and is thus compact and simple. A nonlinear WENO reconstruction is used to suppress nonphysical oscillations in the vicinity of strong discontinuities. A variety of the benchmark test cases are presented to assess the accuracy, efficiency, robustness, and flexibility of this finite volume method. The numerical experiments indicate that the developed FV(VR) method is able to maintain the linear stability, attain the designed second order of accuracy, and outperform the FV(LS) method without a significant increase in computing costs and storage requirements.

1 Introduction

In recent years, significant progress has been made in developing finite volume methods to solve the compressible Euler and Navier-Stokes equations on unstructured grids. These methods have gained widespread acceptance in recent years for their robustness, their intuitive formulation, and their computational advantages. There exist two major classes of finite volume methods: cell-centered

L. Li · H. Luo (✉)
North Carolina State University, Raleigh, NC, USA
e-mail: hong_luo@ncsu.edu

Y. Ren
Tsinghua University, Beijing, China

A. Sasoh et al. (eds.), *31st International Symposium on Shock Waves 2*,
https://doi.org/10.1007/978-3-319-91017-8_71

and vertex-centered finite volume methods. Although the debate that which one has an edge over the other will probably never be settled, the cell-centered finite volume formulation can be easily extended to higher-order (>2nd) approximation. In the cell-centered finite volume method, the mesh cells serve directly as control volumes, and the flux integrals are evaluated on the boundary of the cells. Since the boundary of the four most common element types, tetrahedra, prisms, pyramids, and hexahedra, consists of either triangular or quadrilateral faces, the boundary flux integrals can be readily approximated by a numerical integration scheme, e.g., by a quadrature rule. Furthermore, the cell-centered finite volume formulation is preferred in the context of arbitrary grids, which may contain hanging nodes. The existence of several cell types in a hybrid grid poses a great challenge to numerical methods. Although it is unavoidable to treat different cell types differently during the pre- and post-processing stages, it is undesirable that an algorithm depends on the mesh topology during the flow solution stage. The required conditional statements not only lead to an untidy code but also adversely affect the program speed. Therefore, it is desirable to design an algorithm that treats different cell types in the same way. Such an algorithm is termed grid-transparent in the literature, which does not require any information on the local cell topology. A grid-transparent scheme has a number of advantages: firstly of all it can significantly reduce the discretization stencils compared to a non-grid-transparent scheme; secondly it can increase the speed of the program; and lastly it can facilitate the implementation of implicit schemes and parallelizations.

The objective of the efforts presented in this work is to develop an accurate, efficient, and robust cell-centered finite volume method for solving compressible flow problems on arbitrary grids. The novelty of this finite volume method is to use a newly developed variational formulation [1] to reconstruct a linear polynomial solution. The solution gradients are obtained by solving an extreme value problem, which minimizes jumps of the values of the reconstructed polynomial solutions and their spatial derivatives at cell interfaces and therefore maximizes smoothness of the reconstructed polynomial solutions. Like the least-squares reconstruction, the variational reconstruction has the property of 1-exactness. Unlike the cell-centered finite volume method based on the least-squares reconstruction, the resulting FV(VR) method is stable even on tetrahedral grids, since its stencils are intrinsically the entire mesh. However, the data structure required by FV(VR) is the same as FV(LS) and is thus compact and simple. A variety of the benchmark test cases are presented to assess the accuracy, efficiency, robustness, and flexibility of this finite volume method. The numerical experiments demonstrate that the developed FV(VR) method is able to maintain the linear stability, attain the designed second order of accuracy, and outperform the FV(LS) method without a significant increase in computing costs and storage requirements.

2 Numerical Method

The system of the governing compressible Euler equations is discretized in space using a cell-centered finite volume method. In a finite volume method, the computational domain Ω is divided by a set of nonoverlapping control volumes Ω_i, which can be one or combination of the four most common element types: tetrahedral, prisms, pyramids, and hexahedra. On each control volume, the integral form of the governing equations is required to be satisfied.

$$\int_{\Omega_i} \frac{\partial \mathbf{U}}{\partial x} dV + \int_{\partial\Omega_i} \mathbf{F}_j \mathbf{n}_j d\Gamma = 0 \tag{1}$$

By taking the unknowns to be the cell-averaged conservative variable vector $\mathbf{U}_i$ defined by

$$\mathbf{U}_i = \frac{1}{V_i} \int_{\Omega_i} \mathbf{U} dV \tag{2}$$

and approximating the boundary integration in Eq. (1) using one point quadrature at the midpoint of the face, the semi-discrete form of the equations may be written as

$$V_i \frac{d\mathbf{U}_i}{dt} + \sum_j \mathbf{F}_{ij} \cdot \mathbf{n}_{ij} \Gamma_{ij} = 0 \tag{3}$$

where V_i is the volume of the control volume i, and the flux function gives the flux through the face ij separating the control volume i from the adjacent control volume j.

Equation (3) represents a system of ordinary differential equations. A fully implicit time scheme is employed to integrate Eq. (3) to reach steady-state solutions. An approximate Newton method is used to linearize the equations arising from the implicit discretization. A fast, matrix-free implicit method, LU-SGS method, is then used to solve the resultant system of linear equations [2].

The inviscid flux discretization consists of integrating a numerical flux over a face separating the cells i and j. In this work, HLLC scheme [3] is used to compute interface fluxes $\mathbf{F}_{ij}$. The finite volume formulation for the discretization of the inviscid fluxes leads to only a first-order accuracy in space to the compressible Euler equations, when an upwind scheme is used to compute the numerical fluxes at the cell interface via simple cell-averaged flow variables. A second order of accuracy can be achieved using a reconstruction scheme where a piecewise linear polynomial

solution is reconstructed at the interface using the neighboring cells. This simply requires the evaluation of the derivatives in the cell for the flow variables. One of the most commonly used and simplest reconstruction schemes is the least-squares reconstruction [4], where the computation of gradients is performed in the form of a minimization problem. This least-squares reconstructed finite volume method FV(LS) can be successfully used to solve the 2D compressible Euler equations for smooth flows on arbitrary grids and is able to achieve the designed second order of accuracy and significantly improves the accuracy of the underlying first-order FV method. However, when extended to solve the 3D compressible Euler equations on tetrahedral grids, the FV(LS) suffers from the so-called linear instability, which occurs even for the linear hyperbolic equation [5]. This linear instability is attributed to the fact that the reconstruction stencils only involve von Neumann neighborhood, i.e., adjacent face-neighboring cells. Alternatively, a recently developed variational reconstruction [1] can be used to obtain the solution gradients by solving an extreme value problem, which minimizes jumps of the values of the reconstructed polynomial solutions and their spatial derivatives at cell interfaces, and therefore maximizes smoothness of the reconstructed polynomial solutions. The resultant finite volume method, FV(VR), can achieve the linear stability, since the stencils for this implicit variational reconstruction are intrinsically the entire mesh. In order to maintain the so-called nonlinear stability, i.e., to suppress nonphysical oscillations in the vicinity of strong discontinuities, the solution gradients on cell i are finally obtained using a nonlinear WENO reconstruction [6] as a convex combination of the least-squares reconstructed first derivatives at the cell itself ($k = 0$) and its face-neighboring cells ($k = 1$, .., nface),

$$\frac{\partial \mathbf{U}}{\partial x_n}\Big|_i^{\mathrm{WENO}} = \sum_{k=0}^{nface} w_k \frac{\partial \mathbf{U}}{\partial x_n}|_k \tag{4}$$

where nface is the number of the face-neighboring cells for cell i and the normalized nonlinear weights w_k are computed as

$$w_k = \frac{\tilde{w}_k}{\sum_{i=0}^{nface} \tilde{w}_k} \tag{5}$$

The non-normalized nonlinear weights $\tilde{w}_k$ are functions of the linear weights λ_i and the so-called oscillation indicator o_i.

$$\tilde{w}_i = \frac{\lambda_i}{(\varepsilon + o_i)^\gamma} \tag{6}$$

where ε is a small positive number used to avoid division by zero, and γ an integer parameter to control how fast the nonlinear weights decay for non-smooth stencils. The oscillation indicator for the reconstructed second-order polynomials is simply defined as

$$o_k = \sqrt{\left(\left. \frac{\partial U}{\partial x_n} \right|_k \right)^2}$$

The linear weights λ_i can be chosen to balance the accuracy and the non-oscillatory property of the FV method. Note that the least-squares reconstructed polynomial at the cell itself serves as the central stencil, and the least-squares reconstructed polynomials on its face-neighboring cells act as biased stencils in this WENO reconstruction.

3 Numerical Results

A few examples are presented in this section to demonstrate the high accuracy and robustness of our FV(VR) method for compressible flow problems on arbitrary grids. The first test case is chosen to demonstrate that the developed FV(VR) method is able to achieve the designed second order of convergence for smooth flows. The last two test cases are presented to illustrate the applicability of the FV(VR) method to solve problems of scientific and industrial interests for complex configurations.

3.1 Test Case 1: Subsonic Flow Past a Sphere

A subsonic flow past a sphere at a Mach number of $M_\infty = 0.5$ is considered to assess if the FV(VR) method can achieve a formal order of the convergence rate on tetrahedral grids. A sequence of the four successively refined tetrahedral grids are used in the grid convergence study. The numbers of tetrahedral elements, grid points, and boundary faces for the four grids are (535, 167, 124), (2426, 598, 322), (16,467, 3425, 1188), and (124,706, 23,462, 4538), respectively. The cell size is halved between consecutive meshes. Note that only a quarter of the configuration is modeled due to the symmetry of the problem and that the number of elements on a successively refined mesh is not exactly eight times the coarse mesh's elements due to the nature of unstructured grid generation. The computations are conducted on the four grids using the FV(VR) method. Since the FV(LS) method is unstable for this test case, the results obtained by a second-order DG(P1) method on the first three grids are also presented for the purpose of comparison. Figure 1 illustrates the mesh with 16,467 tetrahedral and the computed velocity contours obtained by

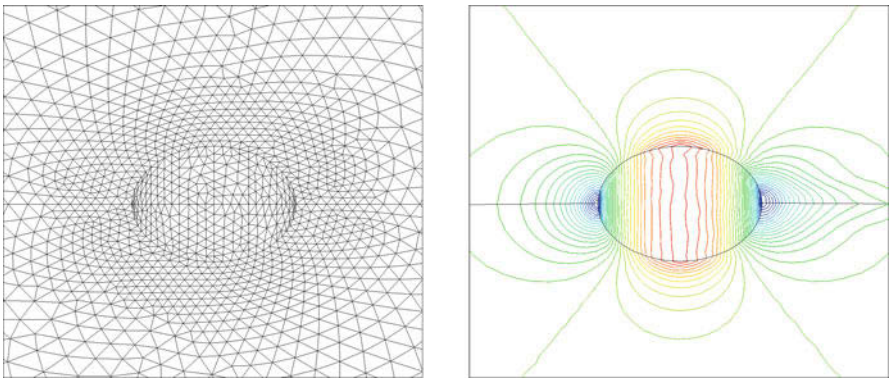

Fig. 1 Unstructured surface mesh and computed Mach number contours for subsonic flow past a sphere (nelem = 16,467, npoin = 3425, nface = 1188) at $M_\infty = 0.5$

Table 1 L2-error and order of convergence for the FV(VR) and DG(P1) methods

Log(length scale)	FV(VR) – log(L2-error)	Order	L2-error – DG(P1)	Order
−1.1283	−0.210001E + 01		−0.252941E + 01	
−1.40554	−0.267299E + 01	2.067	−0.313107E + 01	2.170
−1.69863	−0.321460E + 01	1.848	−0.372355E + 01	2.021
−1.99507	−0.382841E + 01	2.071		

the FV(VR) method on this grid. The errors and the convergence rates for both FV(VR) and DG(P_1) methods are reported in Table 1. It shows the mesh size, the L2-error of the error function, and the order of convergence. Note that L2-norm of the entropy production is used as the error measurement. Figure 2 provides the details of the spatial convergence of the FV(VR) and DG(P1) methods for this numerical experiment. Both FV(VR) and DG(P1) achieve the expected second order of convergence rates, being 1.995 and 2.096, respectively. Clearly, the second-order DG(P1) method is far more accurate than the second-order finite volume method on the same grids. However, the FV(VR) solution is almost as accurate as the DG(P1) solution for the same number of the degrees of freedom, convincingly demonstrating the high accuracy of this FV(VR) method.

3.2 Test Case 2: Transonic Flow Past an ONERA M6 Wing

A transonic flow over the ONERA M6 wing at a Mach number of $M_\infty = 0.84$ and an attack angle of $\alpha = 3.06^\circ$ are considered in this example. This test case is chosen to demonstrate that the FV(VR) method is able to obtain a stable solution for transonic flows using a WENO limiter. The mesh used in this computation consists of 593,169 tetrahedral cells, 110,282 grid points, and 39,770 boundary

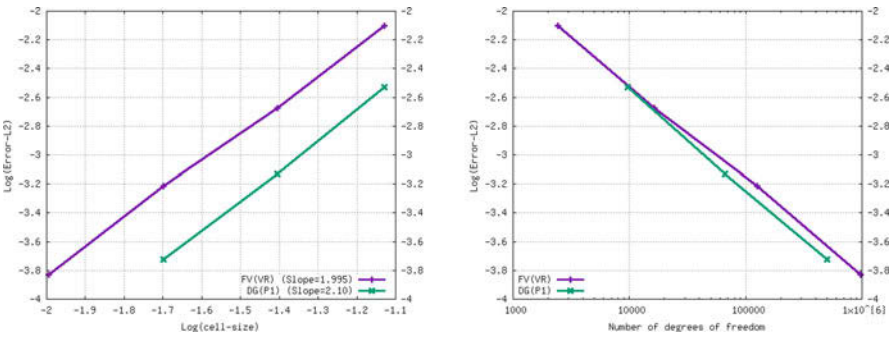

Fig. 2 Accuracy summary for an inviscid subsonic flow past a sphere obtained using the FV(VR) and DG(P1) methods

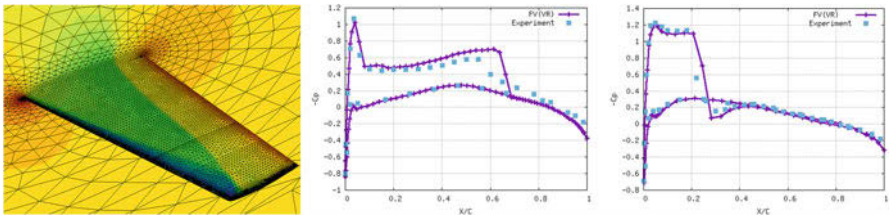

Fig. 3 Computed pressure contours on the unstructured surface mesh (left) and comparison of the computed pressure coefficient distributions obtained by the FV(VR) method with experimental data at 20% (middle) and 95% (right) spanwise locations

faces. Figure 3 shows the computed pressure contours on the upper wing surface and the comparison of the computed pressure coefficients obtained by the FV(VR) method with experimental data [7] at 20% and 95% spanwise stations in Fig. 3. The results obtained by the FV(VR) method compare closely with the experimental data, except at the root stations, due to the lack of viscous effects. The shocks are captured sharply essentially without any oscillations, clearly demonstrating the high accuracy and non-oscillatory property of our FV(VR) method, when combined with a WENO limiter.

3.3 Test Case 3: Transonic Flow Past a Boeing 747 Aircraft

Finally, a transonic flow past a complete Boeing 747 aircraft is presented in this test case. The 747 configuration includes the fuselage, wing, horizontal and vertical tails, underwing pylons, and flow-through engine nacelle. The mesh used in this test case contains 188,822 grid points, 1,0251,702 tetrahedral cells, and 11,802 boundary faces for the half-span airplane. The solution is computed at a free stream of Mach number of 0.85 and an angle of attack of 2°. The computed Mach number contours

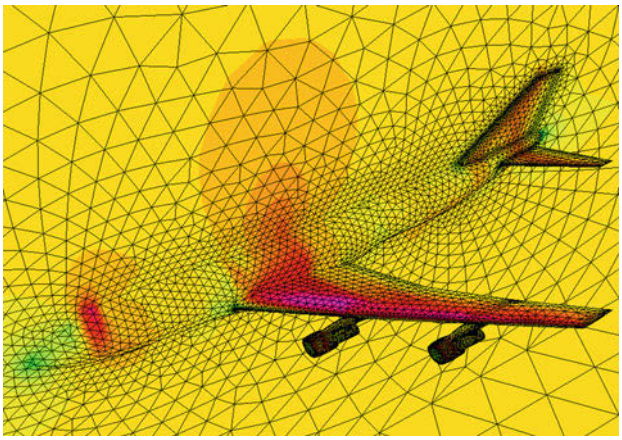

Fig. 4 Computed Mach number contours for transonic flow past a complete B747 aircraft at $M_\infty = 0.85$ and $\alpha = 2°$

on the surface of the airplane, along with the surface mesh, are shown in Fig. 4. This example demonstrates that the developed FV(VR) method can be used to compute complicated flows of practical importance for complex configurations.

4 Conclusions

A cell-centered finite volume method based on a variational reconstruction, FV(VR), has been developed for solving the compressible Euler equations on 3D arbitrary grids. The variational reconstruction can be viewed as an extension of the compact schemes on unstructured grids and has the property of 1-exactness. The resulting FV(VR) method is linearly stable, since its stencils are intrinsically the entire mesh. However, the data structure required by the FV(VR) method is compact and simple. A variety of the benchmark test cases have presented to assess the performance of this FV(VR) method. The numerical experiments indicate that the developed FV(VR) method is able to maintain the linear stability, attain the designed second order of accuracy, and outperform the FV(LS) method without a significant increase in computing costs and storage requirements.

References

1. Q. Wang et al., Compact high order finite volume method on unstructured grids III: Variational reconstruction. J. Comput. Phys. **337** (2017)
2. H. Luo et al., A Fast, Matrix-free Implicit Method for Compressible Flows on Unstructured Grids. J. Comput. Phys. **146** (1998)

3. P. Batten et al., Average-state Jacobians and implicit methods for compressible viscous and turbulent flows. J. Comput. Phys. **137** (1997)
4. T. Barth, Recent development in high-order K-exact reconstruction on unstructured meshes, AIAA Paper 93-0668, 1993
5. D. Haider et al., Stability analysis of the cell centered finite-volume MUSCL method on unstructured grids. Numirische Mathematik **113** (2009)
6. H. Luo et al., A Hermite WENO-based limiter for DG methods on unstructured grids. J. Comput. Phys. **225** (2007)
7. V. Schmitt et al., Pressure distributions on the ONERA M6-Wing at transonic Mach Numbers, Experimental Data Base for Computer Program Assessment, AGARD AR-138, 1979

Numerical Modelling of the Effects of Surface Roughness on Blunt Body Heat Transfer

D. Kim, G. Park, and E. Avital

Abstract The paper presents the numerical modelling of the effects of surface roughness on heat transfer of high Mach number flow to a blunt body. Computational fluid dynamics (CFD) is pursued using our in-house Clithium2 code for axisymmetric flow of $M = 6$ impinging on a flat-faced circular cylinder. Laminar and ideal gas conditions are assumed due to the short flow time and low stagnation temperature (<2000 K). Good to excellent agreement is achieved with known results of stagnation flow over flat smooth surface. The heat flux is indirectly calculated using CFD results of boundary layer edge condition due to the layer's thin thermal thickness. A peak at the cylinder's face centre is found, where roughness initially causes a decline in the heat flux but an increase at 1000 micron or above. The stand-off distance of the bow shock wave behaved inversely to the heat flux. Real gas effects and the breakdown of the continuum assumption are also discussed for further analysis.

1 Introduction

Estimation of heat transfer experienced by a vehicle re-entering atmosphere is exacerbated by the combination of aerodynamic and radiative transport properties. It is a common practice to estimate the heat transfer based on high enthalpy flow of dissociated gas, neglecting low enthalpy effects [1, 2]. In this research we check whether the ideal gas model can accurately predict the effects for the temperatures below 2000 K while also exhibiting considerable reduction in computational costs as compared to real gas models. If the effects of surface roughness on convective heat transfer are understood in the low enthalpy flow, the real gas modelling can be

D. Kim · G. Park
Korea Advanced Institute of Science and Technology, Daejeon, Republic of Korea

E. Avital (✉)
Queen Mary University of London, London, UK
e-mail: e.avital@qmul.ac.uk

A. Sasoh et al. (eds.), *31st International Symposium on Shock Waves 2*,
https://doi.org/10.1007/978-3-319-91017-8_72

further implemented as the way forward for higher temperatures effects (as in [3]) and inclusion of other heat fluxes [2].

2 Computational Modelling

2.1 Conservation Algorithm

The computational modelling is based on our in-house Clithium2 code that solves the Navier-Stokes equations for compressible flow for the flat-faced rigid body with the axially symmetrical flow domain [4]. The FORCE scheme is used as the elementary scheme for the convection term, which is an average between the first-order Lax-Friedrichs (LF) scheme and the second-order Lax-Wendroff (LW) scheme. The conservative FORCE formulation for the convection terms was modified from triangular element [4] to quadrilateral element to fit within our structured grid used for planar or in this case axisymmetric simulations. Table 1 and Table 2 demonstrate, respectively, the shock tube conditions and the simulation specification used in the study.

The computational domain was designed so to prevent the outflow conditions affecting the stagnation flow developing on the cylinder's face due to disturbances that may propagate upstream through the boundary layer developing on the cylinder's side. The computational domain is presented in Fig. 1 with the following

Table 1 Flow conditions

Parameter	Value
Design Mach number (-)	6
Total pressure (MPa)	2.94
Total temperature (K)	293
Static pressure (Pa)	1868
Static temperature (K)	208
Freestream velocity (m/s)	1697.8
Body temperature (K)	293

Table 2 Simulation specifications

Parameter	Value
Simulation (-)	Transient
Time step max (-)	100,000
Simulation time (s)	4.d-4
Gas (-)	Air, standard composition
Thermal conductivity coefficient (g/mol)	0.024
Dynamic viscosity (kg/m s)	1.827×10^{-5}
Transient scheme (-)	Lax-Friedrichs (LF) and Lax-Wendroff (LW)

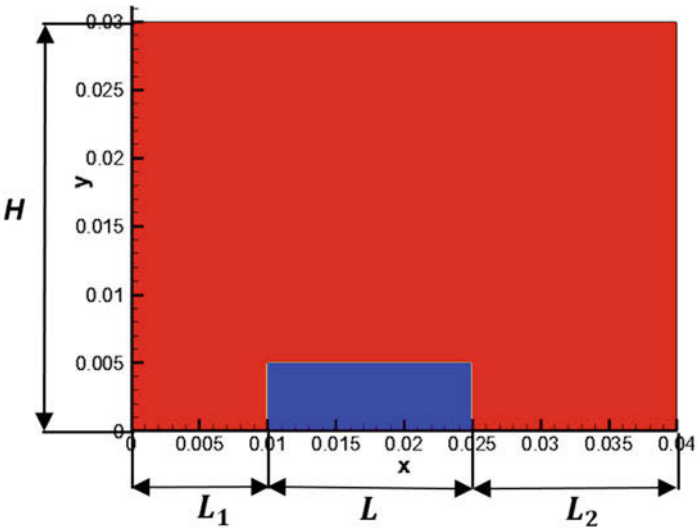

Fig. 1 Computational domain

dimensions: radius R is 5 mm; length L is 1.5 mm; distances before and after the models L1 and L2, respectively, is 10 mm; and vertical domain H is 3 mm.

A MINBEE TVD flux correction form was added to achieve second-order accuracy far from shock waves by changing the balance between the LF and LW fluxes above the wall. The grid generation is automatically embedded in the code and was controlled to capture the boundary layer thickness. The grid points were varied between 22,801 and 811,801. The corners of the cylinder in the model are sharp due to the cylindrical co-ordinates being used. In addition, the cylinder's walls coincide with the grid lines. The heat conduction and dynamic viscosity coefficients are approximated using Sutherland's law. The rigid finite circular cylindrical body is captured using a second-order ghost point ensuring second-order accuracy of no-slip and isothermal wall conditions. The cylinder is laid streamwise. Due to the very short time scales of the flow, it was assumed to be laminar. Illustration of the mesh near the wall is given in Fig. 2, where only second point in each direction is plotted as in all following contour plots.

Steady-state condition was achieved by running the simulation for several times and comparing the results, i.e. velocity, temperatures, and most importantly heat fluxes.

2.2 Roughness Modelling

Since surface roughness is naturally a highly unstructured phenomenon as shown in Fig. 3a, for the computational modelling, it was decided to use an idealised surface

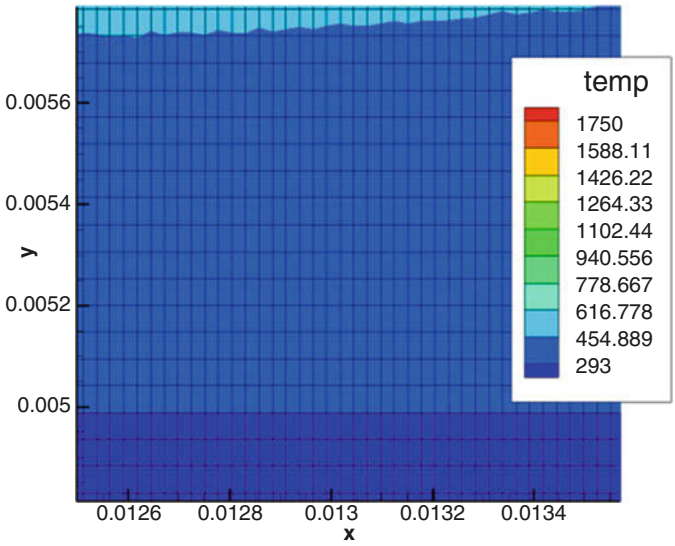

Fig. 2 Mesh size at the surface of the cylinder flat base and temperature variation (K)

roughness. Surface roughness on its face is modelled as an idealised topology by construction of corrugated rings as illustrated in Fig. 3.

3 Code Validation

The results were verified for the developed boundary layer, stand-off distance of the detached shock wave and angle [5]. This is demonstrated in Figs. 4a and b, showing excellent agreement with experimental results for the stand-off distance.

4 Results and Discussion

Preliminary calculation based on boundary layer (bl) theory showed the heat flux to be about 1.2 MW/m2 at the stagnation point [1]. This means a bl thermal thickness of less than 0.2 mm; thus our numerical resolution was insufficient to properly resolve it. Nevertheless, the good agreement in the global flow field as in Fig. 4b and good agreement in the pressure distribution along the impinged surface led to calculating the heat flux using the CFD's boundary layer edge results and an integral bl thickness approximation [6]. The results are shown in Fig. 5, where Fig. 5a is of lower numerical resolution, hence its lower heat flux q at the stagnation point.

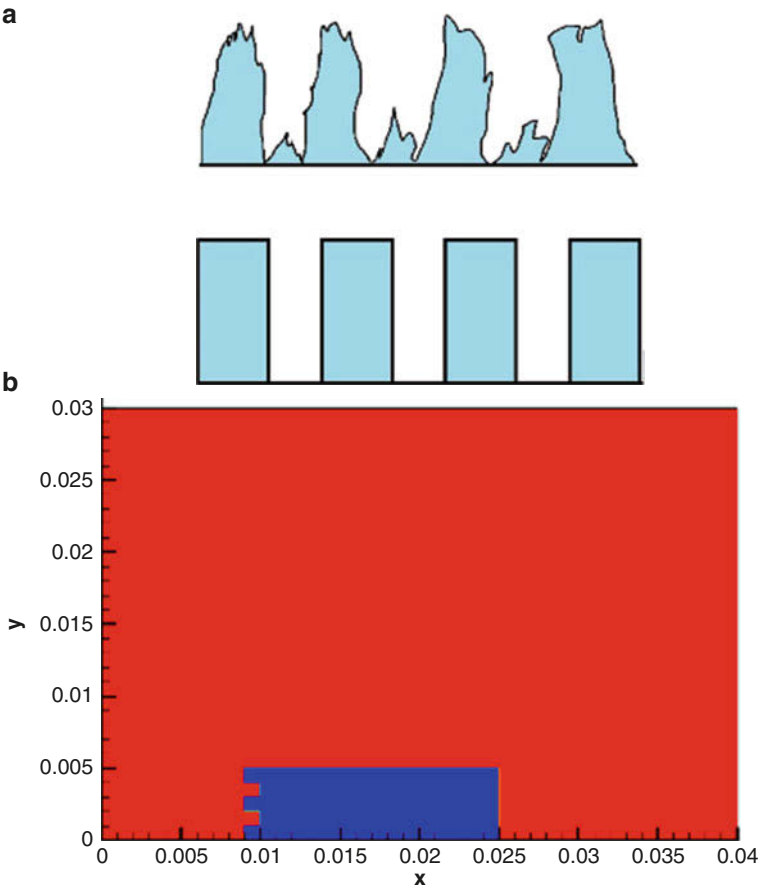

Fig. 3 (**a**) Real and idealised roughness rings. (**b**) Modelling of rough surface

The maximum heat flux is at the stagnation point ($y = 0$) followed by a decline and then increase with the radius y towards the cylinder's edge. Numerical experimentation showed the decline near y was sensitive to grid resolution and TVD limiter type, but this overall behaviour is physical. The roughness height is seen to generally reduce the stagnation heat flux for $h < 1000$ micron and the opposite for $h > 1000$ micron. This can be associated with the stand-off distance of the bow wave that behaved inversely, i.e. increased with h for $h < 1000$ micron and reduced with h for $h > 1000$ micron.

Figure 6 reveals a more detailed view of the streamwise velocity field pointing to the detached shock wave structure, the tangential boundary layer over the cylinder's side, and the wake behind it. The tangential boundary layer has shown a close to linear velocity profile and thickness growth as expected from a laminar layer, but it

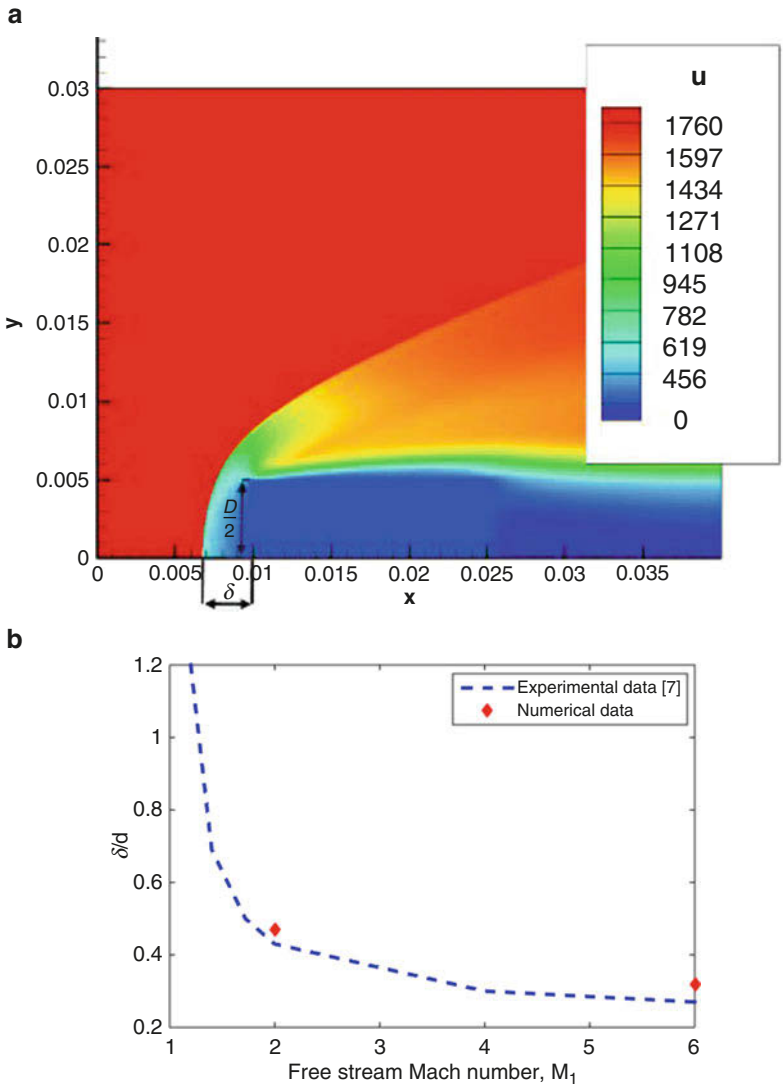

Fig. 4 (**a**) Contour plot of the streamwise velocity (m/s) near the body's front face for $M = 6$. (**b**) Shock wave detachment distance as calculated by the CFD code

has started from a rather thick normal boundary layer of about 3 mm on the front edge of the cylinder.

Further illustration is given in Fig. 7, where one can see subsonic flow developing in front of the body. Thus the detached shock wave acts as a normal wave. On the other hand, far from the body supersonic flow is developing where the detached

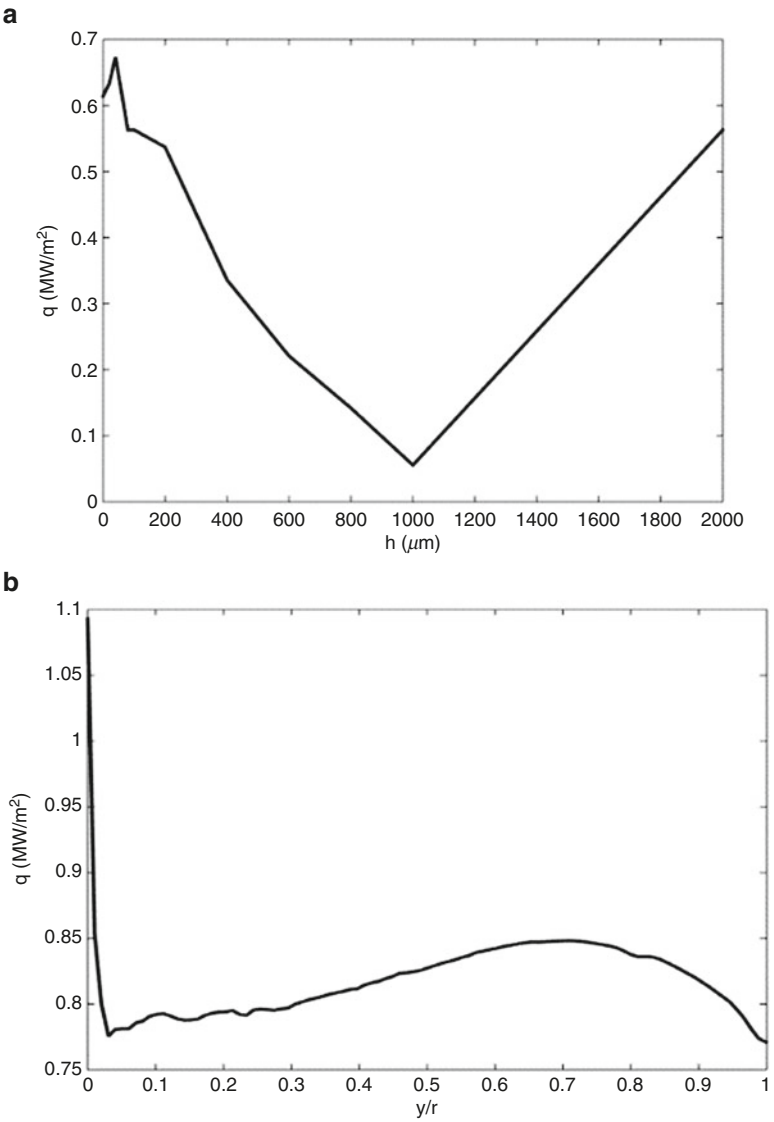

Fig. 5 (**a**) Heat flux for different level of roughness along the leading edge. (**b**) Heat flux along the leading edge for Mach 6, smooth wall

shock wave becomes conical. The variation of the Mach number along the axis of symmetry is given in Fig. 7b.

While for the hypersonic flow with real gas effects, the velocity and thermal boundary layer might have different profiles, when comparing the thermal boundary layer to the velocity boundary layer, it has a similar boundary layer thickness which

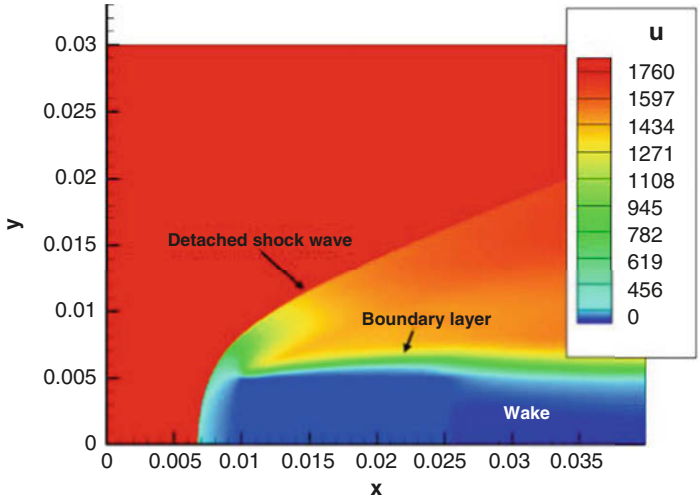

Fig. 6 Contours of streamline velocity u (m/s) showing the development of a boundary layer over the body

is about 0.003 m (see Fig. 8a). The temperature profile in Fig. 8b is typical of stagnation flow, but it misses a maximum blip before its decline towards the wall, indicating a higher grid resolution is needed [7].

When comparing the heat flux along the leading edge of the body, the highest value corresponds to 0 height roughness and 1 micron (Fig. 5a). This is explained by the larger surface area serving for a higher conduction. One should note that the current grid resolution cannot capture 1 micron resolution, and thus the grid generator oscillated the roughness up to about 50 microns. When looking at Fig. 9a, it is easy to understand that flow around rough surface is dominated by inertia forces which cause vortices, chaotic eddies, and other flow instabilities. This, in turn, leads to higher heat transfer. Above 92 km, the continuum flow assumption fails instead bringing the kinetic theory into action as described in [7, 8]. As demonstrated in Fig. 9b, molecules reaching the cavity speed up due to the conservation of energy. By the time the molecules reach the upper surface, they obtain V_2 with $V_2 < V_1$. Therefore, v_1 has less time to pass the cavity. For such a short time, molecule v_1 can increase its temperature by a small increment. Therefore, $T_1 < T_2$. When analysing why 1-micron roughness height provide smaller heat transfer at the stagnation than the 1-mm roughness, it is clear that there is no time for molecule to travel around the cavity. It directly obtains velocity V_2. Thus the effect of roughness is expected to be similar to when the continuum flow assumption becomes questionable.

It should be considered that when the compression shock wave passes by, the air obtains high p and ρ. After time Δt it achieves a streamline behaviour; some fluid momentum is trapped in gaps causing continual flow recirculation. Heat is trapped because of the small "cavity"-like phenomena occurring between the gaps. To check the theory, it is suggested to simulate different M. It is possible

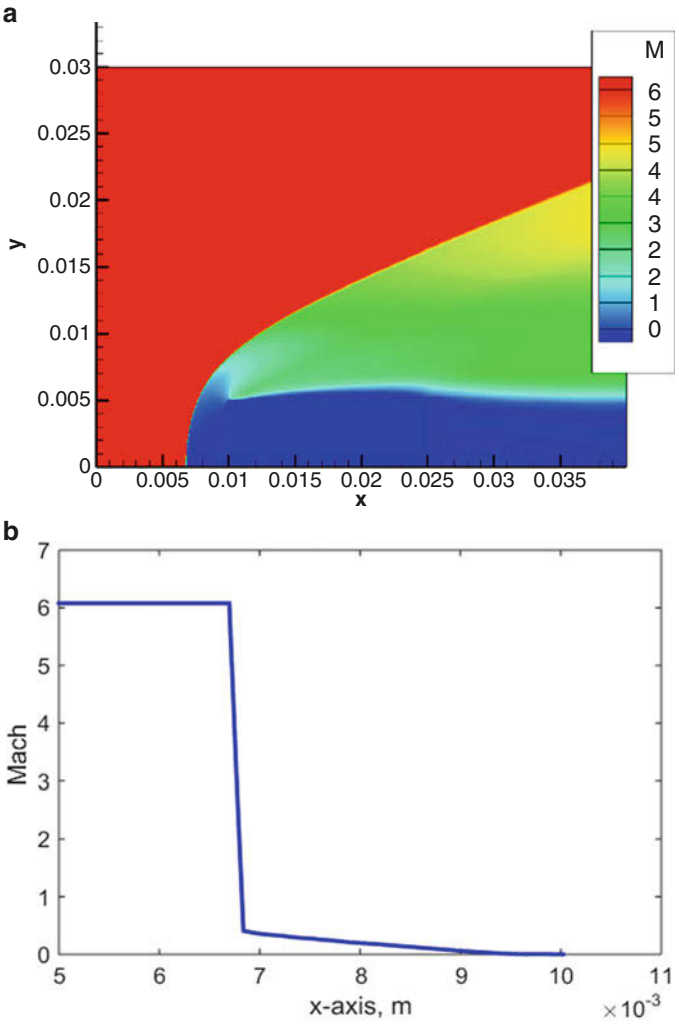

Fig. 7 (**a**) Mach number distribution. (**b**) Mach number across shock wave at the axis of symmetry

that the density formation is affected by the conservation of mass, meaning the distance is technically compensating for ρ. Moreover, the explanation may lie in the temperature limitation. The system can lose, distribute, and radiate T, based on the cost of V molecules and the p of the system, but it cannot generate T. Meaning, once the system starts to generate its own T, the system is no longer conserved. This behaviour requires further investigation.

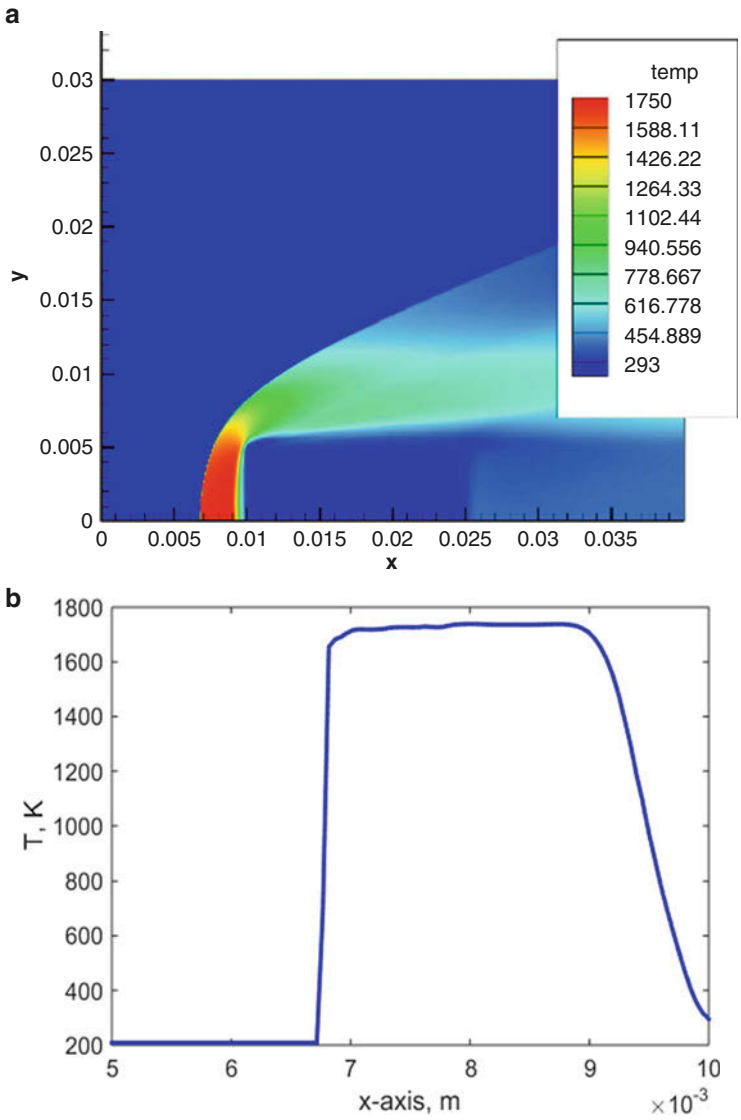

Fig. 8 (**a**) Temperature distribution (K). (**b**) Temperature across shock wave at long axis of symmetry

5 Conclusion

This study conducted numerical modelling and analysed the effects of surface roughness on heat transfer of blunt body at $M = 6$ and very low ambient pressure. Using ideal gas assumption and indirect calculation based on the boundary layer

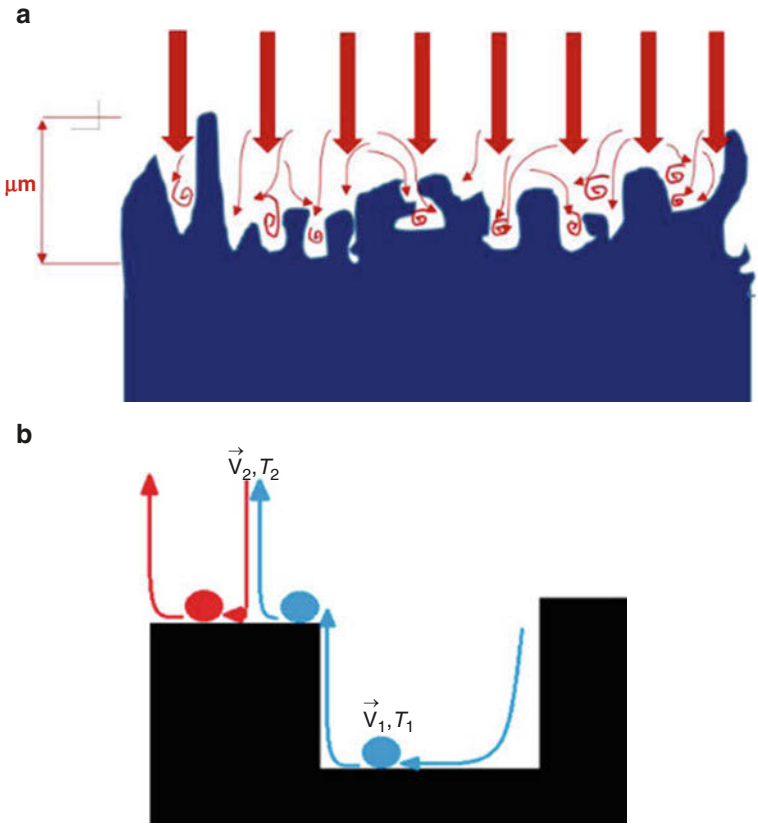

Fig. 9 (**a**) Flow around rough surface. (**b**) Behaviour of molecules

theory and its edge conditions taken from the CFD, it was found that idealised roughness higher than 1000 micron level increases the heat flux, while a lower level of roughness decreases. This can be related to the stand-off distance of the detached shock wave that behaved inversely to the heat flux. Arguments based on rarefied gas dynamics point to similar flow behaviour for higher altitudes where the continuum flow assumption fails. However, further investigation is required as well as closer assessment of grid resolution and splitting the tasks between capturing the global flow field and the fine details of the normal boundary layer.

Acknowledgement This research publication is supported by BK21 Plus Program under the National Research Foundation of Korea (NRF). The computational power is provided by clusters located at Queen Mary University of London.

References

1. J.A. Fay, F.R. Riddell, J Aeronaut Sci. **25**, 2 (1958)
2. R. Goulard, J Jet Propul. **28**, 11 (1958)
3. G. Park, J Spacecr Rocket. **50**, 3 (2013)
4. E.J. Avital et al., Fluid Dyn Res. **49**, 4 (2017)
5. H.W. Liepmann, A. Roshko, *Elements of Gas Dynamics* (Wiley, London, 1963), pp. 104–105
6. H. Schlichting, K. Gersten, *Boundary-Layer Theory* (Springer, New York, 2003), pp. 285–311
7. J.D. Anderson, *Hypersonic and High Temperature Gas Dynamics* (AIAA Education, Reston, 2006), pp. 21–22
8. I.G. Brykina et al., J. of Appl Math Mech. **70**, 6 (2006)

Numerical Study of Shock Propagation in Liquid/Gas Media

N. Apazidis

Abstract A semi-conservative, stable, interphase-capturing numerical scheme for shock propagation in heterogeneous systems is applied to the problem of shock propagation in liquid-gas systems. The scheme is based on the volume fraction formulation of the equations of motion for liquid and gas phases with separate equations of state. The semi-conservative formulation of the governing equations ensures the absence of spurious pressure oscillations at the material interphases between the constituents. Interaction of a planar shock in water with a single spherical bubble as well as twin adjacent bubbles and a bubble array is investigated. Several features of the interaction process are studied, including propagation and focusing of the transmitted (refracted) shock within the deformed bubble, creation of a water hammer by a diffracted shock in water, and generation of high-speed liquid jet due to induced flow vorticity in the later stages of the process.

1 Introduction

The problem of shock-induced bubble collapse has been investigated theoretically and numerically by a large number of researchers, among others by [1–11], during the past two decades. An extensive overview of shock-bubble interaction for various combinations of heavy/light and light/heavy fluids may be found in [11]. As pointed out by [1], one of the main challenges in the numerical treatment of multi-fluid models is ensuring pressure equilibrium at the interface separating the constituents. The same researcher reported that the schemes develop spurious pressure oscillations at the interfaces. These oscillations are not due to higher order terms but exist already in the first-order approximations and usually appear when the governing equations are put in the conservative form. A semi-conservative model based on volume fraction with the total density of the mixture as one of the

N. Apazidis (✉)
Mechanics, KTH Royal Institute of Technology, Stockholm, Sweden
e-mail: nap@mech.kth.se

A. Sasoh et al. (eds.), *31st International Symposium on Shock Waves 2*,
https://doi.org/10.1007/978-3-319-91017-8_73

main variables was proposed by Shyue [6–9]. In the semi-conservative formulation, the evolution of the volume fraction is given by the advection equation. Such volume fraction semi-conservative formulation of the governing equations resolves the problem of the spurious pressure oscillations at the interface between the constituents of the mixture and is adopted in the present study.

2 Problem Formulation

We will here consider the problem of shock propagation in a tube with circular cross section filled with water. A spherical air bubble placed symmetrically at the tube axis will be subjected to the action of a propagating shock in water. In the present study, we will adopt the similar approach to that of [7, 8]. We assume that the mixture consists of two immiscible fluid components each characterized by its own ratio of specific heats γ_1 and γ_2 with subscripts 1 and 2 for air and water, respectively. The mixture density $\rho = \alpha\rho_1 + (1-\alpha)\rho_2$ is introduced by means of volume fraction of air α. The total system of governing equations for the mixture flow is formulated in a semi-conservative form. The semi-conservative form of the equations has been discussed in several investigations [4, 8], where the authors argued that a conservative formulation of the volume fraction-based model leads to incorrect pressure condition at the interphase of the mixture constituents resulting in spurious pressure oscillations and a non-stable behavior of the numerical scheme. These authors argue that a semi-conservative formulation of governing equations with evolution equations for some of the variables written in non-conservative form eliminates this problem and ensures correct pressure conditions at the interface. We are here using a volume fraction-based model in which the evolution equation is formulated for α and the ratio of specific heats is then computed by the relation:

$$\frac{1}{\gamma - 1} = \frac{\alpha}{\gamma_1 - 1} + \frac{1-\alpha}{\gamma_2 - 1} \tag{1}$$

The resulting system of governing equations for the mixture consists of a system of Euler equations in conservative form combined with the evolution equation for the volume fraction written in non-conservative form and formulated as an advection equation. For the time-dependent 2D axisymmetric case with x denoting the axial coordinate and r the radial distance, the Euler equations are formulated in vector form as

$$\frac{\partial \mathbf{U}}{\partial t} + \frac{\partial \mathbf{F}}{\partial x} + \frac{1}{r}\frac{\partial\,(r\mathbf{G})}{\partial r} = 0 \tag{2}$$

with the vector variables according to

$$\begin{aligned} \mathbf{U} &= [\rho \quad \rho u \quad \rho v \quad \rho e]^T \\ \mathbf{F} &= [\rho u \quad \rho u^2 + p \quad \rho u v \quad (\rho e + p)\, u]^T \\ \mathbf{G} &= [\rho u \quad \rho u v \quad \rho v^2 + p \quad (\rho e + p)\, v]^T \end{aligned} \tag{3}$$

The system of Euler equations for the mixture is extended by the evolution equation of the volume fraction α which is given by the advection equation

$$\frac{\partial \alpha}{\partial t} + u \frac{\partial \alpha}{\partial x} + \frac{v}{r} \frac{\partial (r\alpha)}{\partial r} = 0 \tag{4}$$

This system of Euler equations for the mixture together with the evolution equation for the volume fraction is then closed by the equation of state (EOS) and the equation for the ratio of specific heats of the mixture. Following [4, 7–9] we use the Tait equation of state for compressible liquids,

$$p(\rho) = (p_0 + B) \left(\frac{\rho}{\rho_0} \right)^{\gamma_2} - B \tag{5}$$

with ρ_0 and p_0 being the reference density and pressure, respectively, and B a pressure-like constant describing the stiffness of the liquid. Here we adopt the values $B = 4050$ atm and $\gamma_2 = 6.68$. The equation of state combining the internal energy, pressure and density of the mixture takes the form

$$p(\rho, e) = (\gamma - 1)\, \rho \left(e + \frac{B}{\rho_0} \right) - \gamma B \tag{6}$$

where ρ is the mixture density and γ the ratio of the specific heats for the mixture and are related to the density and ratio of the individual specific heats of the constituents through the volume fraction α by

$$\rho = \alpha \rho_1 + (1 - \alpha)\, \rho_2 \tag{7}$$

and Eq. (1).

3 Results

The set of 2D axisymmetric Euler equations together with the equation describing the evolution of the volume fraction α are solved numerically by a central flux vector splitting scheme [12], implemented on a rectangular mesh. The scheme is second-order accurate in space and uses a sixth-order accurate Runge-Kutta integration in time [13].

3.1 Validation

Experimental studies on liquid shock-bubble interaction are rather scarce. Substantially more experimental work has been done on interaction of plane shock in a carrier gas with gas columns or bubbles of a different gas, lighter or heavier than the carrier medium. Interaction of weak shocks in air with cylindrical and spherical cavities filled with helium or R22 gas was investigated in an early experimental study by Haas and Sturtevant [14]. In another classical study by Jacobs [15], the author investigates interaction with a plane shock in air with a column of helium and CF6 gas injected perpendicularly in the flow field. Recently an extensive experimental study of an interaction of plane shock in air with spherical helium, nitrogen, and krypton bubbles was conducted by Layes et al. [16]. We will therefore test the predictions of our numerical model by comparison with the experimental results in these studies. In case of two gases, the Tait equation of state for compressible liquids (5) is replaced by an ordinary ideal thermal EOS for gases. Figure 1 shows the results of numerical computations of shock interaction with light (helium in air) and heavy (CF6 in air) bubbles. The parameters are chosen to match the experimental studies [14, 15].

Figure 2 shows comparison of numerical results with experimental measurements in [15, 16]. Figure 2a shows comparison of the numerical calculations of the ration of bubble length L to initial bubble diameter D_0 as function of time with

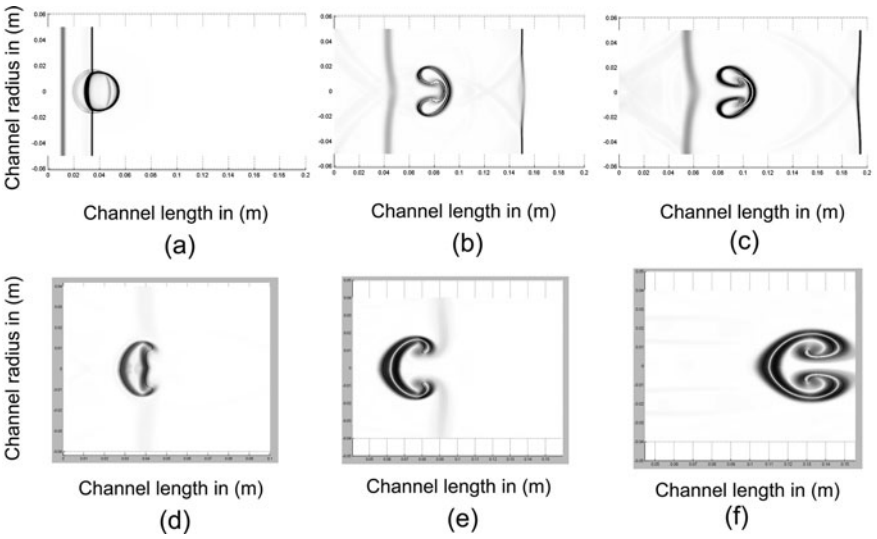

Fig. 1 Numerical schlieren of time evolution of the cylindrical helium cavity interacting with an incident shock of $M = 1.22$ moving from left to right in air (**a**–**c**) and SF6 cylinder interacting with a shock of $M = 1.09$ moving from left to right in air (**d**–**f**)

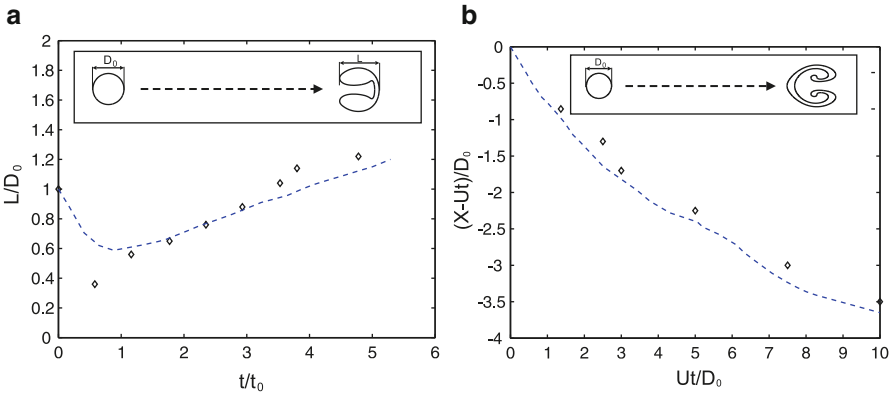

Fig. 2 (**a**) Dimensionless time evolution of the helium bubble length. Comparison with experimental values ◇ of [16]. (**b**) Displacement of the centroid of SF6 column. Comparison with the experimental values ◇ of [15]

experimental values of [16], while Fig. 2b is a comparison of the calculated centroid displacement of the SF6 column at shock Mach number $M = 1.09$ with experimental values from [15].

3.2 Single Air Bubble in Water

We will now apply the numerical model on the problem of blast wave interaction with initially spherical air bubble in water. Figure 3a shows the initial configuration with a 20 mm spherical bubble placed at the axis of a cylindrical tube filled with water. A blast wave is initiated at the left end of the tube by imposing an impulsive pressure of 2 GPa in a thin layer adjacent to the wall. Blast wave profiles of shock propagating in water are shown in Fig. 3b, while density profile along the tube axis at the moment of shock impingement on the bubble is illustrated in Fig. 3c.

The impulsive pressure produces a blast wave with initial Mach number of $M = 1.4$ in water. Note a substantial decrease of shock strength due to the blast wave profile with pressure behind the shock reduced to 0.45 GPa as it arrives at the bubble interface. The density of water at the bubble interface is 1200 kg/m^3 at the same moment with a density ratio water/air of ca 833. Such extreme conditions of discontinuities over the shock and water/air interface require a high degree of robustness and stability of the numerical scheme. Numerical charts over pressure, density, and vector field during shock-bubble interaction are illustrated in Fig. 4.

Figure 4 illustrates several stages of shock-bubble interaction. In (a) a transmitted shock in the bubble is seen to be bent by the interface and lags behind the incident shock in water. Water hammer shock, right behind the downstream bubble interface, is seen in (b). Note also the expansion wave marked by the yellow circle as

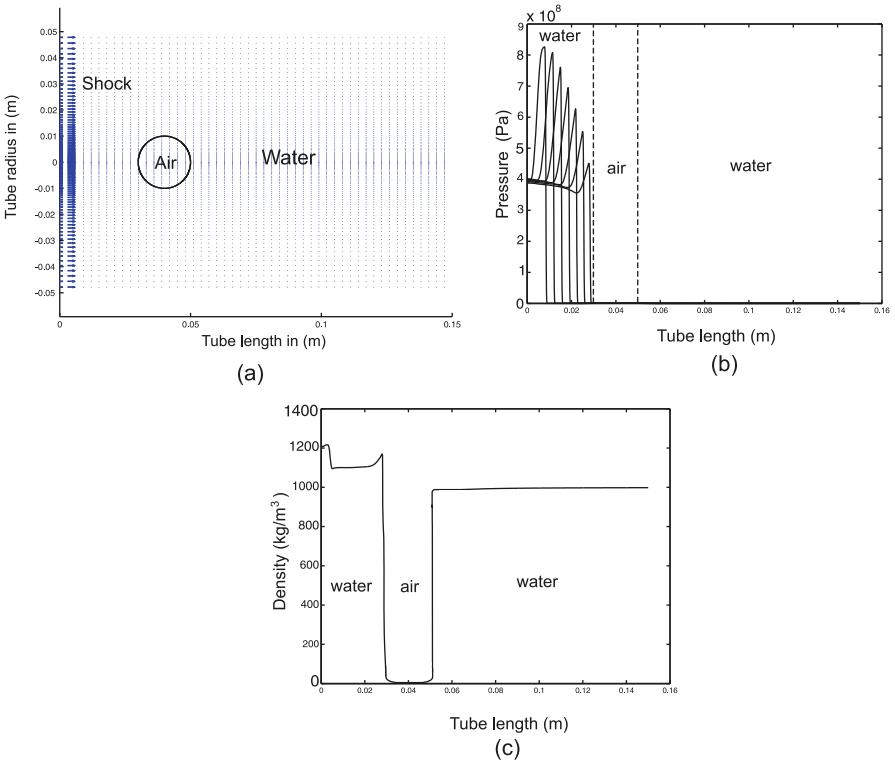

Fig. 3 (**a**) Problem definition. (**b**) Blast wave pressure profiles of the advancing from left to right plane shock in water. (**c**) Density profile along the a tube axis at the instant of shock impingement on the air bubble

well as two small high-pressure regions at the triple-point location close to the bubble interface. Figure. 4c shows the focusing of the shock reflected from the downstream bubble interface resulting in the elongated high-pressure region on the axis stretching from the focal region to the water hammer shock. Deformation of the bubble into two separate regions with counter-rotating vortices and creating a high-speed water jet is with maximum velocities of 1100 m/s illustrated in Figs. 4d.

3.3 Twin Adjacent Air Bubbles in Water

As we have seen, the interaction of the initial shock with a single bubble creates a powerful water hammer shock and high-speed liquid jet in the direction of propagation. How will these as well as other features influence a second bubble placed right behind the first one? Figure 5 shows the features of shock interaction with two twin bubbles with a separation distance of 0.1 bubble radius. Water hammer shock

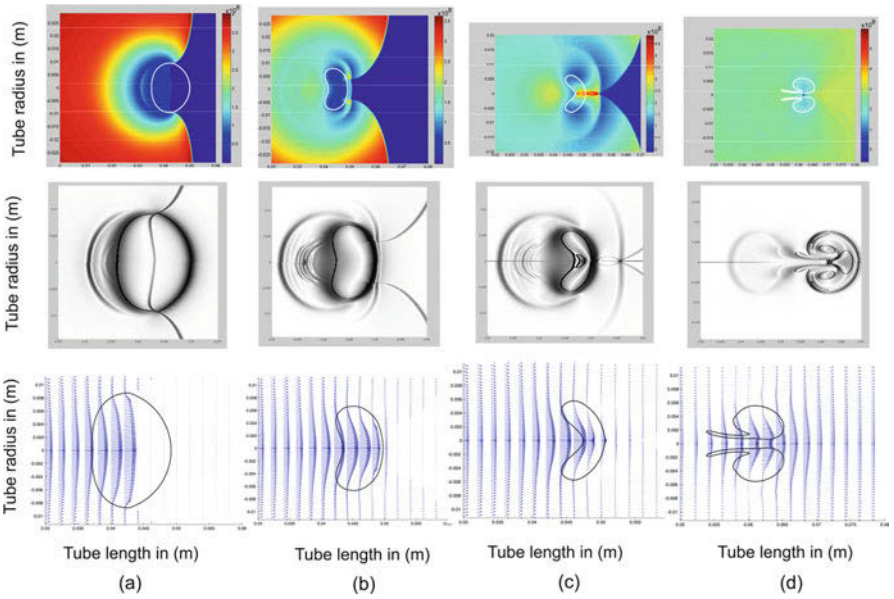

Fig. 4 Numerical pressure field, schlieren and velocity vector field, and contour flow images (first, second, and third row) of interaction of plane $M = 1.4$ shock in water moving from left to right with initially spherical 20 mm air bubble. (**a**) Transmitted and initial shock. (**b**) Water hammer shock. (**c**) Focusing. (**d**) Jetting

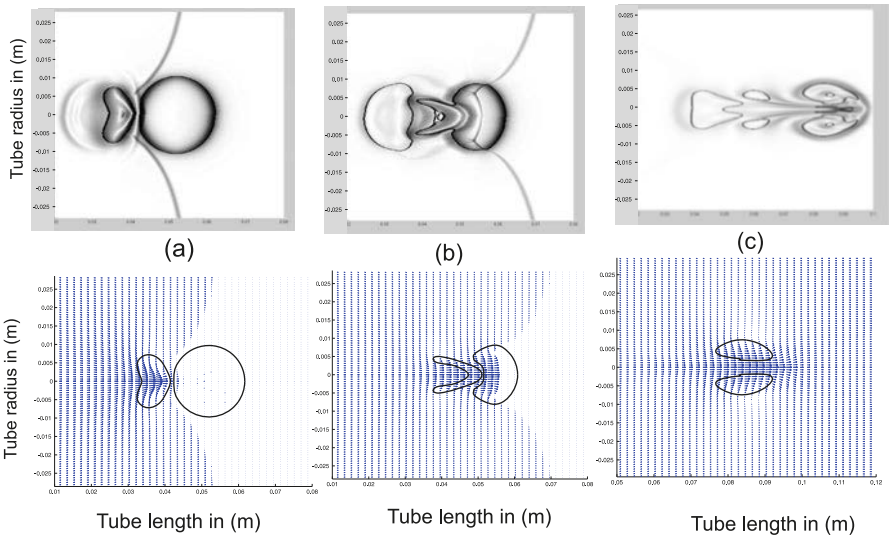

Fig. 5 Numerical schlieren, velocity vector field, and contour flow images (upper and lower rows) of interaction of plane $M = 1.4$ shock in water moving from left to right with two adjacent initially spherical 20 mm air bubbles initially at a distance of 0.1 bubble radius. (**a**) Water hammer shock impinging on the second bubble. (**b**) Propagation of the transmitted shock. (**c**) Jetting

created by the first bubble amplifies the compression and deformation of the second bubble. The transmitted shock in the second bubble shown in Fig. 4b differs from the transmitted shock in a single bubble in its shape and two triple points, above and under the axis created as a result of front and side action of the water hammer shock. The velocity of high-speed liquid jet is enhanced by 30% as compared to a single bubble and reaches maximum values of about 1450 m/s.

Acknowledgment The financial support of Vetenskapsrådet (VR) (the Swedish Research Council) is gratefully acknowledged.

References

1. R. Abgrall, S. Karni, J. Comput. Phys. **169** (2001)
2. G. Allaire, S. Clerc, S. Kokh, J. Comput. Phys. **181** (2002)
3. D. Igra, K. Takayama, Int. J. Numer. Methods Fluids **38** (2002)
4. E. Johnsen, T. Colonius, J. Fluid Mech. **629** (2009)
5. M. Ozlem, D.W. Schwendeman, A.K. Kapilla, W.D. Henshaw, Shock Waves **22** (2012)
6. K.M. Shyue, J. Comput. Phys. **142** (1998)
7. K.M. Shyue, J. Comput. Phys. **200** (2004)
8. K.M. Shyue, Shock Waves **15** (2006)
9. K.M. Shyue, J. Comput. Phys. **229** (2010)
10. J. Quirk, S. Karni, J. Fluid Mech. **318** (1996)
11. J.H.J. Niederhaus, J.A. Greenough, J.G. Oakley, D. Ranjan, M.H. Anderson, R. Bonazza J. Fluid Mech. **594** (2008)
12. M. Sun, K. Takayama, J. Comput. Phys. **189** (2003)
13. H.A. Luther, Math. Comput. **22** (1968)
14. J.F. Haas, B. Sturtevant, J. Fluid Mech. **18** (1987)
15. J.W. Jacobs, Phys. Fluids A **5** (1993)
16. G. Layes, G. Jourdan, L. Houas, Phys. Fluids **21** (2009)

CFD Models of Shocks and Flow Fields Associated with Decelerating Spheres in Terms of Flow History and Inertial Effects

H. Roohani, I. M. A. Gledhill, and B. W. Skews

Abstract The bow shock stand-off distances of a sphere decelerating in air under its own drag were determined through numerical simulations using Fluent. Three cases were investigated with three different initial velocities. These results were then compared to steady-state numerical results obtained from the same CFD code in order to identify differences between the steady and unsteady cases at given Mach numbers. The initial Mach numbers used were 1.13, 1.19 and 1.25. A two-dimensional axisymmetric model was used in conjunction with a viscous turbulence model suitable for analysing transonic external aerodynamic problems. Numerically determined shock stand-off distances were compared to previous experimental results from literature for the steady and unsteady cases. There is a very good agreement between the steady-state numerical and experimental results, which confirms that a suitable numerical model was used. In the unsteady scenario, the numerical results follow the same trend as the experimental results, but the agreement is not as good. Some explanation for this is given. It was found that the shock stand-off distance for the unsteady cases was generally smaller than for the steady-state cases. Also, for the unsteady cases, a bow shock that was formed in supersonic flight transforms into a wave and persists well into the subsonic regime. In the steady-state cases, it is of course well known that no such phenomenon exists in flow at sonic and subsonic Mach numbers. The differences in the flow field and consequently in the drag in the steady and unsteady cases are explained using the concepts of flow history and fluid inertia.

H. Roohani · B. W. Skews
Flow Research Unit, School of Mechanical, Industrial and Aeronautical Engineering, University of the Witwatersrand, Johannesburg, South Africa

I. M. A. Gledhill (✉)
Flow Research Unit, School of Mechanical, Industrial and Aeronautical Engineering, University of the Witwatersrand, Johannesburg, South Africa

Aeronautic Systems Competence Area, DPSS, CSIR, Pretoria, South Africa
e-mail: Igle.Gledhill@wits.ac.za

A. Sasoh et al. (eds.), *31st International Symposium on Shock Waves 2*,
https://doi.org/10.1007/978-3-319-91017-8_74

1 Introduction

The aerodynamics of objects accelerating in the transonic regime are of growing interest as the accelerations of aerodynamic bodies rise to hundreds of g, where g is the acceleration due to gravity. The aerodynamic loads and flow fields associated with accelerating transonic objects differ substantially from those in steady-state flight [1].

The effects can be described in terms of flow history and inertial effects. The flow history concept was introduced by Basset [2] for boundary layers only and is now defined as the difference between the flow field of an accelerating object at a given velocity and the steady flow field of the same object at the same velocity. An instantaneous flow field around an accelerating object often appears to lag the expected fully developed steady flow field. An example occurs on an accelerating airfoil [3]: shocks appear to be displaced by acceleration from expected steady flow positions towards positions associated with an earlier time.

Theory and computational methodologies for arbitrarily accelerating frames have been introduced [4]. However, very few validation test cases are available in the transonic regime in which significant acceleration or deceleration is applied. It has been demonstrated experimentally [5] that the drag on a sphere launched at initial speeds M_0 in the Mach number range 1.13 to 1.25 is sufficient to cause acceleration effects on bow shock stand-off distance δ, and computational fluid dynamics (CFD) models in the relative frame attached to the projectile confirmed [5] that δ decreases during deceleration and that a shock-like structure may be observed at subsonic speeds.

In this paper, we present results from a modified version of Fluent [6] in which the acceleration source terms in the momentum and energy conservation equations in the relative frame have been added and in which velocity-dependent drag (VDD) is incorporated. A transonic CFD capability with at least one degree of translational freedom should be able to model deceleration by drag through the transonic range. The case published by Saito et al. [5] is the only relevant case with public domain experimental data that has been found to date.

1.1 Experiment and CFD

The experiment was conducted at the ballistic range at Tohoku University [5]. The test section length is 12 m; the internal diameter is 1.7 m, but this is reduced to 0.6 m by an insert near the observation window. A 30 mm diameter sphere with a mass of 0.127 kg is launched using a sabot. The medium in the dump tank is air at ambient temperature and a pressure of 99,000 Pa. Shadowgraphs of the flow fields at the second observation window [5] allow the shock stand-off distance δ to be

measured. The speed is measured by the interruption of a series of laser beams. An in-house code based on the weighted average flux scheme [5], second order in both space and time, with source terms included for the rectilinear acceleration, gave good comparison with the experimental results; the insert wall at a diameter 0.6 m was modelled for part of the length of the simulation domain.

1.2 Theory

The Navier-Stokes equations solved by Fluent can be written for rectilinear acceleration with source terms for the momentum equation

$$S_1 = \rho \frac{\partial \boldsymbol{v}}{\partial t} \tag{1}$$

and energy equation

$$S_2 = \rho \boldsymbol{v} \frac{\partial \boldsymbol{v}}{\partial t} \tag{2}$$

where ρ is density, t is time, and $\boldsymbol{v}$ is the velocity of the ground frame relative to the sphere frame, where the ground frame is an inertial frame. The transformation of the Navier-Stokes equations to arbitrarily moving frames has been covered by Gledhill et al. [4].

2 Numerical Model

A relative frame implementation was used, with source terms S_1 and S_2 specified by user-defined functions in Fluent. For shock capture, a second-order upwind scheme was used; the solver is a finite-volume cell-centred unstructured AUSM algorithm. The temperature is assumed to be 300 K and the pressure 99,000 Pa. For free stream cases, turbulent viscous models were used with Local Reynolds numbers at the sphere wall of $30 < y^+ < 100$ for the Spalart-Allmaras turbulence scheme. For models with the pipe insert, Euler models were used. A velocity-dependent drag (VDD) scheme is used, where at each time step, the axial forces on the projectile are calculated and the velocity of the projectile is updated. A time step of 10^{-5} s was found to capture the dynamics of the experiment. Results presented in this paper are for initial velocities of $M_0 = 1.13$, 1.19 and 1.25.

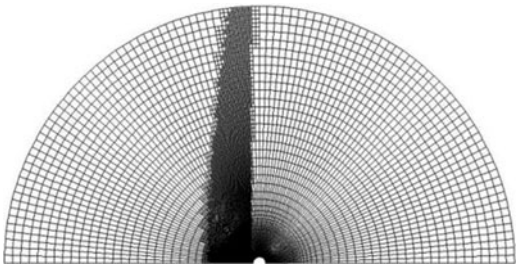

Fig. 1 Entire meshed domain for free stream cases showing grid adaption at M = 1.01

2.1 Grid and Geometry

The initial two-dimensional structured grid was based on approximately 100 points over the sphere wall surface from nose to tail. Grid adaption was used to capture flow field effects at the bow shock. The zone of refinement is confined to the fluid upstream of the projectile to prevent changes to y^+ in the vicinity of wall surfaces. Refinement depends on gradients Δ of pressure, temperature, density and velocity. The mesh is refined when for any parameter $\Delta > 0.5\%$ of a specified maximum gradient. The refined grid is coarsened when $\Delta < 0.3\%$.

The simulation geometry was axisymmetric; this simplifies the wake structure considerably but is justified by the success of Saito et al. [5] in capturing δ in an axisymmetric model. Effects at the end of the driver tube, including the puff of driver gas and the sabot separation, are neglected. Under free stream conditions, the Fluent pressure far-field boundary condition is used for far-field boundaries. A no-slip wall is applied at the sphere surface, and the x-axis is specified as an axis of symmetry. The radius of the free stream grid is 0.6 m (Fig. 1).

3 Results

A flow field showing the bow shock in front of a sphere decelerating from $M_0 = 1.25$, using the free stream boundary, is shown in Fig. 2. The stand-off distance δ is the distance between the bow shock and the nose of the sphere and is non-dimensionalised with the radius R of the sphere. Steady-state results were compared with previous data, including the ballistic range data of Starr et al. [7] are shown in Fig. 3. Very good agreement is obtained for free stream boundaries.

Steady-state data from Fluent are represented by a line for clarity. In Fig. 4, the transient data from Fluent show smaller shock stand-off distances than the steady-state cases. The experimental data of Saito et al. [5] show a very significant difference from steady-state data. Unsteady Fluent cases, compared with the unsteady data of Saito et al., exhibit smaller differences from steady state.

In Fig. 4 the transient data obtained from Fluent and all other sources are compared. The purpose is, first of all, to obtain a comparison between steady and

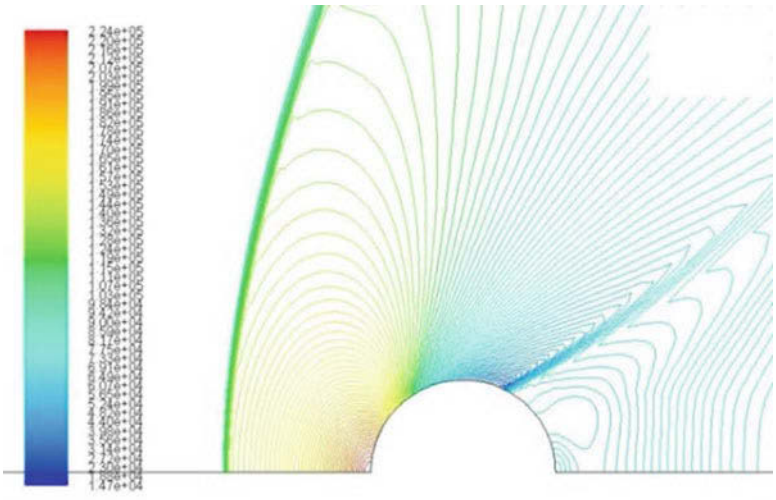

Fig. 2 Contours of static pressure in Pascal at Mach 1.15 while decelerating

Fig. 3 Steady-state results from all sources

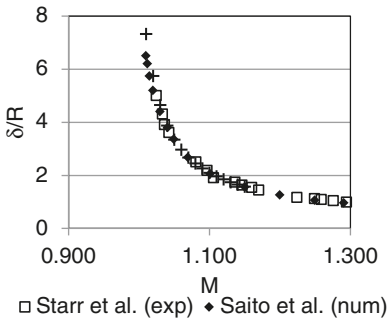

unsteady data in Fluent, and then to compare the unsteady data from Fluent with unsteady data from Saito et al. [5].

In Fig. 5, shock profiles are plotted for the transient case in which $M_0 = 1.25$, for successive times. The coordinate x is the distance from the centre of the sphere. For example, at Mach 1.15 in this case, the distance of the inflection point of the shock from the centre of the sphere is 0.0383 m, and the shock stand-off distance is 0.0233 m. The shocks become weaker as time passes and the Mach number is reduced.

At later times, shown in Fig. 6, an acoustic disturbance propagates (M = 0.989, M = 0.970). Inspection of the Mach number profiles confirms that flow in the region upstream of the sphere is subsonic relative to the sphere. In Fig. 7 the x coordinate of the inflection point of the first wave (Fig. 6) is plotted in terms of δ/R against Mach number. The filled black circles represent shocks and the empty circles represent pressure waves.

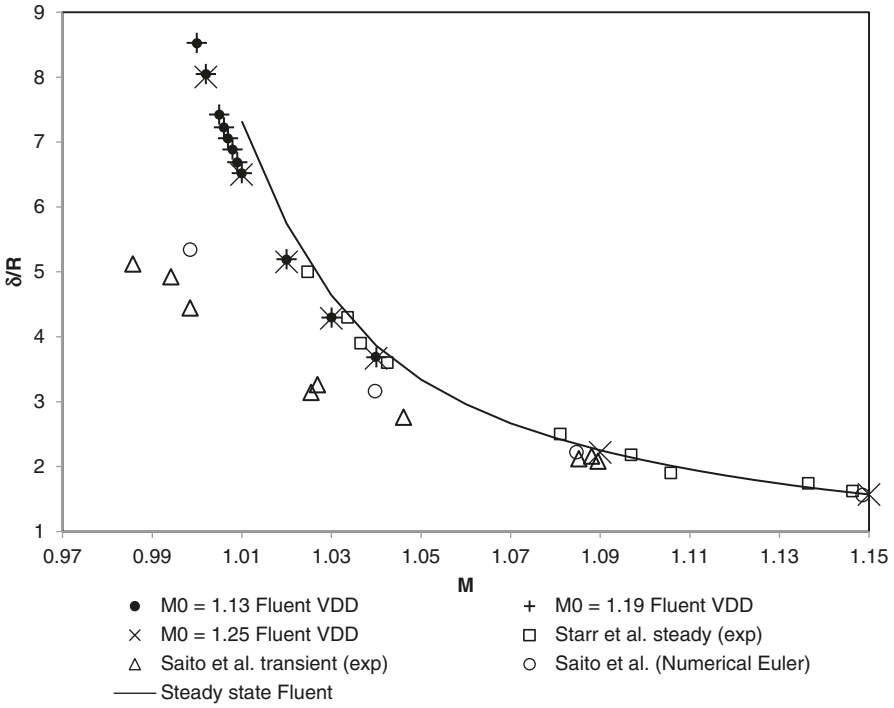

Fig. 4 Comparison of transient and steady-state data from Fluent and all other sources

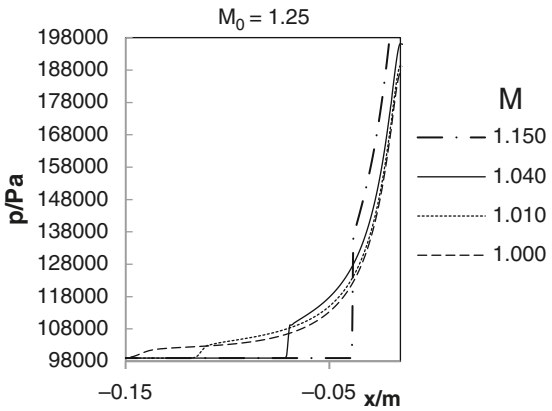

Fig. 5 Pressure profiles at different times for $M_0 = 1.25$, for supersonic M

4 Discussion

The difference in the Fluent results and those of Saito et al. [5] might be attributable to several factors. First of all, in the ballistic range, the radius of the test section is 0.3 m in the region of the observation window. In the simulation of Saito et al.

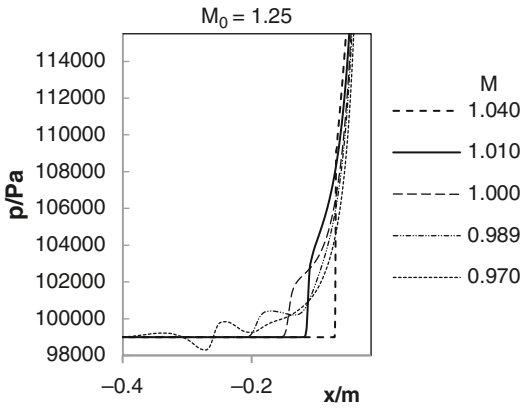

Fig. 6 Pressure profiles at different times for $M_0 = 1.25$, low and subsonic M

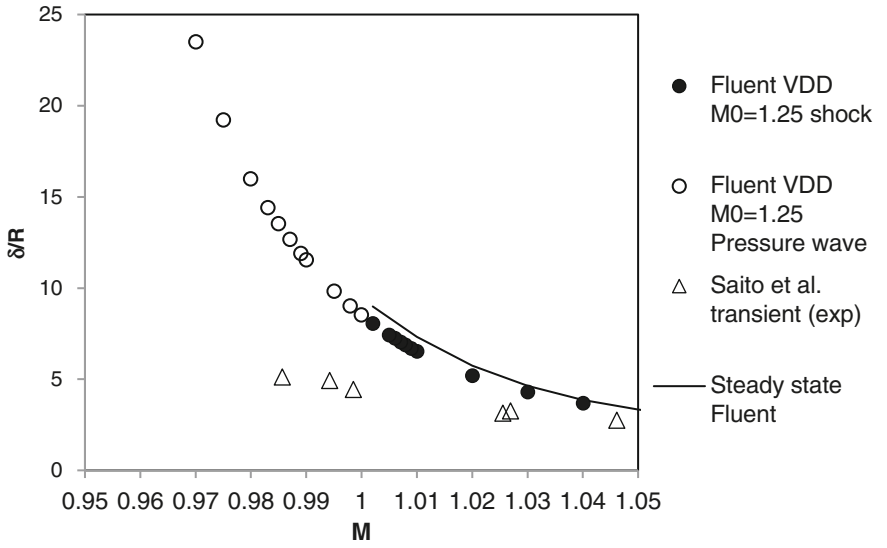

Fig. 7 Positions of pressure waves propagating ahead of the sphere for initial $M_0 = 1.25$

[5], a solid wall was included at 0.3 m from the axis. While the x-axis of the domain extended for 0.54 m, the wall was specified only for a length of 0.27 m. In the Fluent models, free stream conditions are modelled using a nonreflecting pressure far-field boundary condition instead.

Secondly, the internal radius of the ballistic range dump tank is 0.85 m, which is reduced to 0.30 m at the observation window. The sudden change of boundary conditions, and the transition as the bow shock enters the pipe, will affect the parameters of the shock, and this should affect the stand-off distance between the shock and the sphere.

In comparison with the expected steady-state condition at a given Mach number, the bow shock stand-off distance δ under deceleration is reduced in the free stream Fluent model. The smaller δ can be attributed to a flow history effect. The flow history concept indicates that an instantaneous transient flow field will have some of the features of the flow field from an earlier time. In the case of deceleration, the earlier flow field is related to higher Mach numbers and would be expected to exhibit a smaller stand-off distance δ.

If the deceleration of a projectiles is very slow, the flow field may be in a regime where it approaches steady-state conditions. It would be expected that the effect of the deceleration on stand-off distance would be very small. For a sphere at transonic speeds, the drag is high enough for the effect to be measurable. The deceleration in these cases is of the order of 50 g and produces significant flow history effects.

When the sphere speed has dropped below Mach 1, the wave at the supersonic shock position deteriorates into a series of compression waves. These propagate upstream at the speed of sound, while the sphere slows down and falls further behind the waves as its speed drops below the speed of sound.

Lilley et al. [8] have given a relevant method for constructing the wave envelope for an arbitrarily moving source with a speed that is near the speed of sound. In an example for a decelerating supersonic particle, the waves generated in the early history of the source continue to propagate ahead of the decelerating source.

5 Conclusions

Shock stand-off distance has been modelled in the body-fixed frame, with free stream conditions, in Fluent for a sphere decelerating under its own drag. Reduction of the stand-off distance due to deceleration was observed and has been explained in terms of flow history.

It has been noted that in free stream cases, when the sphere velocity has dropped below Mach 1 under deceleration, pressure disturbances continue to propagate ahead of the sphere.

The difference between transient and steady-state stand-off distance values is smaller than that observed in a ballistic range and captured in the numerical model of Saito et al. [5]. In the experiment, a cylindrical insert surrounds the sphere flight path at the observation window. A reflecting wall of the same radius as the insert was included in the numerical model of Saito et al. In the Fluent model, free stream conditions are used which do not include the cylindrical insert. Interaction of the shock with the insert may be responsible for further reduction of the stand-off distance.

References

1. H. Roohani, B.W. Skews, 26th ISSW A3551 (2007)
2. B.A. Basset, *Treatise on Hydrodynamics* (Deighton, Bell and Co., Cambridge, 1888)
3. H. Roohani, B.W. Skews, Shock Waves **19**, 297 (2009)
4. I.M.A. Gledhill, H. Roohani, K. Forsberg, P. Eliasson, B.W. Skews, J. Nordström, Theor. Comput. Fluid Dyn. **30**, 449 (2016)
5. T. Saito, K. Hatanaka, H. Yamashita, T. Ogawa, S. Obayashi, K. Takayama, Shock Waves **21**, 483 (2011)
6. ANSYS ® Inc., *Fluent User's Guide* (2014)
7. R.F. Starr, A.B. Bailey, M.O. Varner, AIAA J. **14**, 537 (1976)
8. G.M. Lilley, R. Westley, A.H. Yates, J.R. Busing, J. R. Soc. Aeronaut. **57**, 396 (1953)

Conjugate Heat Transfer Analysis in a Hypersonic Flow

Ravi K. Peetala

Abstract Transient heat transfer analysis is very significant and has scientific relevance to understand the flow in hypersonic applications. The present studies mainly focus on the effects of experimental time scale and substrate properties on the thermal penetration of the heat into the aerodynamic surfaces. The problem is addressed though conjugate heat transfer (CHT) analysis. The main observation of present analysis is that near the sensor region (stagnation point), heat penetration is less as compared to SiC and carbon-carbon region. Temperature rise is more significant in the sensor region. Stagnation-point heat flux is seen to be largely decreased due to maximum rise in the wall temperature in that region. The CHT analysis has the capability of predicting heating rates at any locations on the aerodynamic surfaces with multiple wall materials and can be used as tool for selection material and design of hypersonic configurations.

1 Introduction

Higher surface heating rate is the major design constraint in hypersonic flow regime. Hence prediction of wall heating rates is always a challenging task for the design engineers. Generally, heat transfer measurements are carried out in short-duration impulse facilities and actual flight experiments, such as the thin-film gauges in the hypersonic experiments [1, 2]. Thin-film sensors are typically used to record the rate of change of temperature with a time. These thin-film sensors are made from sputtering or painting a sensing material (platinum, nickel, gold, etc.) on a backing/insulating material (quartz, Macor, etc.) as shown in Fig. 1. Moreover, they are flush mounted on the aerodynamic surfaces experiencing high-enthalpy flows. In view of this, a CHT solver is developed to predict penetration of the heat into the aerodynamic surfaces in cylinder. Various researchers around the

R. K. Peetala (✉)
Department of Mechanical Engineering, Visvesvaraya National Institute of Technology (VNIT), Nagpur, India

A. Sasoh et al. (eds.), *31st International Symposium on Shock Waves 2*,
https://doi.org/10.1007/978-3-319-91017-8_75

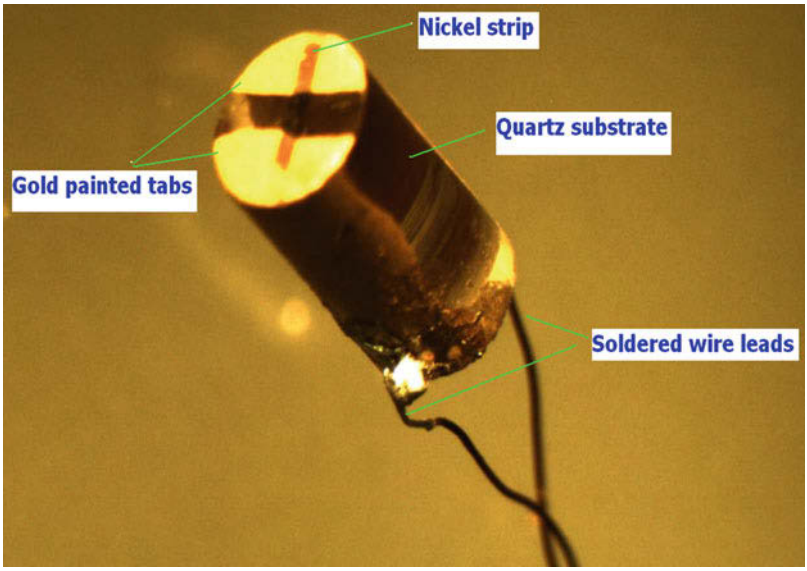

Fig. 1 Thin film sensor [1]

globe have performed CHT analysis for estimation of surface properties on the way to design hypersonic flights. Hassan et al. [3] presented an iterative loose coupling between a finite volume method (FVM) computational fluid dynamics code and a finite element material thermal response code and used it to study the ablation of a reentry vehicle flying through a ballistic trajectory. Liu et al. [4] developed numerical schemes for strongly coupled fluid and solid solver through the constant computation of the heat flux at the fluid-solid interface. The coupled field problem addressed in this paper deals with coupling of convective heat transfer external to the solid body with the conduction heat transfer within the solid body. Thus conjugate heat transfer applies to any thermal system in which multimode convective/conduction heat transfer is of particular importance to thermal design. Hence CHT arises naturally in most instances where external and internal temperature fields are coupled [5]. He et al. [6] adopted the boundary element method (BEM)/FVM approach in further studies of CHT in incompressible flow in ducts subjected to constant wall temperature and constant heat flux boundary conditions. Kontinos [7] also adopted the BEM/FVM coupling algorithm to solve the CHT over metallic thermal protection panels at the leading edge of the X-33 in a Mach 15 hypersonic flow regime.

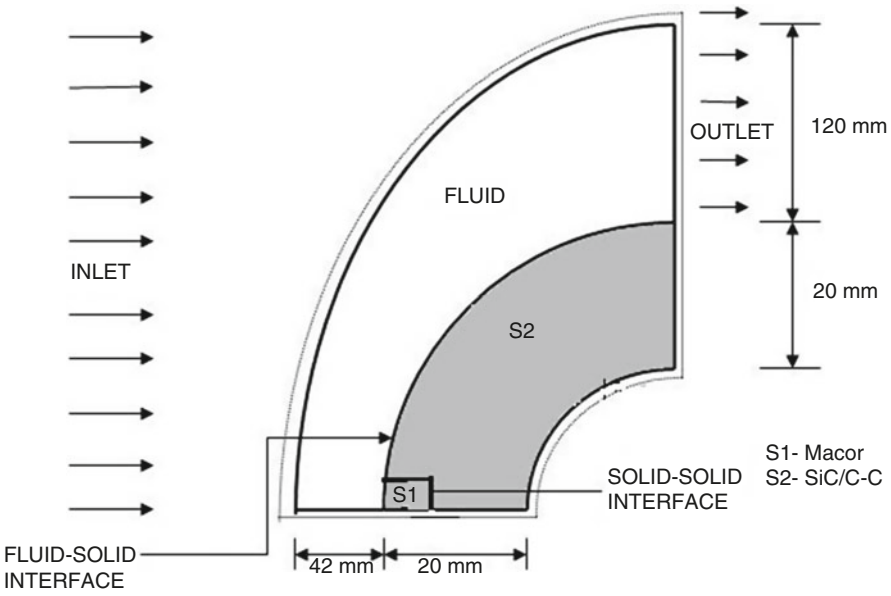

Fig. 2 Geometrical configuration of flow domain for CHT study

The present studies mainly focus on the effects of experimental time scale and substrate properties on the thermal penetration of the heat into the aerodynamic surfaces. The problem is addressed through conjugate heat transfer (CHT) analysis of fluid and solid domain for a quarter cylinder configuration as shown in Fig. 2. The thermal sensor "S1"of typical size (2 mm diameter and 4 mm length) is placed at the stagnation location. Finite-volume framework and explicit time stepping have been implemented for both the compressible Navier-Stokes fluid flow solver and the solid-domain conduction solver. This 2-D fluid flow solver considers AUSM-δ [8] scheme for inviscid flux calculations. Viscous flux computations are carried out using area-weighted gradients at the nodes. The freestream conditions are taken from Mallinson and Milthorpe [9] with Mach 9.2, static pressure of 690 Pa, and static temperature of 155 K, while the initial wall temperature is kept at 300 K. Other desired assumptions like top-wall heat flux boundary and bottom of the wall, an isothermal boundary (i.e., substrate is of infinite length, and the temperature rise at infinity is zero), are also considered.

2 Mathematical Formulation of CHT Studies

The governing equations for a laminar compressible flow are described by the conservation of mass, momentum, and energy equations [10]. The governing equations in nondimensional form fluid domain are

$$\frac{\partial \rho}{\partial t} + \frac{\partial (\rho u)}{\partial x} + \frac{\partial (\rho v)}{\partial y} = 0 \tag{1a}$$

$$\frac{\partial (\rho u)}{\partial t} + \frac{\partial \left(\rho u^2 + p\right)}{\partial x} + \frac{\partial (\rho u v)}{\partial y} = \frac{\partial (\tau_{xx})}{\partial x} + \frac{\partial \left(\tau_{yx}\right)}{\partial y} \tag{1b}$$

$$\frac{\partial (\rho v)}{\partial t} + \frac{\partial (\rho u v)}{\partial x} + \frac{\partial \left(\rho v^2 + p\right)}{\partial y} = \frac{\partial \left(\tau_{xy}\right)}{\partial x} + \frac{\partial \left(\tau_{yy}\right)}{\partial y} \tag{1c}$$

$$\frac{\partial (\rho E)}{\partial t} + \frac{\partial (\rho u H)}{\partial x} + \frac{\partial (\rho v H)}{\partial y} = \frac{\partial \left(u\tau_{xx} + v\tau_{yx} - \dot{q}_x\right)}{\partial x} + \frac{\partial \left(u\tau_{yx} + v\tau_{yy} - \dot{q}_y\right)}{\partial y} \tag{1d}$$

Where

$$\tau_{xx} = \frac{1}{\mathrm{Re}_\infty}\left\{\lambda\left[\frac{\partial u}{\partial x} + \frac{\partial v}{\partial y}\right] + 2\mu\frac{\partial u}{\partial x}\right\} \tag{2}$$

$$\tau_{yy} = \frac{1}{\mathrm{Re}_\infty}\left\{\lambda\left[\frac{\partial u}{\partial x} + \frac{\partial v}{\partial y}\right] + 2\mu\frac{\partial v}{\partial y}\right\} \tag{3}$$

$$\tau_{xy} = \tau_{yx} = \frac{1}{\mathrm{Re}_\infty}\left\{\lambda\left[\frac{\partial u}{\partial y} + \frac{\partial v}{\partial x}\right]\right\} \tag{4}$$

$$\dot{q}_x = \frac{-\mu}{(\gamma - 1)\, M_\infty^2 \mathrm{Re}_\infty \,\mathrm{Pr}}\frac{\partial T}{\partial x} \tag{5}$$

$$\dot{q}_y = \frac{-\mu}{(\gamma - 1)\, M_\infty^2 \mathrm{Re}_\infty \,\mathrm{Pr}}\frac{\partial T}{\partial y} \tag{6}$$

In the above equations, Re_∞ is the free stream Reynolds number, Pr_∞ is the Prandtl number, and M_∞ is freestream the Mach number. Since the number of unknowns is more than the number of equations, the closure problem is solved by using an additional equation, which is nothing but the nondimensional form of the equation of state that is given by,

Table 1 Material properties used in the simulation by Holman [12]

Material	Thermal conductivity (k) (W/m.K)	Density (ρ) (kg/m^3)	Specific heat (c_p) (J/Kg.K)
Macor	1.46	2520	790
Carbon-carbon	4.79	1655	645
Silicon carbide (SiC)	120	3100	750

$$p = \rho \overline{R} T, \quad \text{where} \quad \overline{R} = \frac{1}{\gamma M_\infty^2} \tag{7}$$

Governing equation for heat transfer analysis alone is the unsteady heat conduction equation which is given as

$$\rho c \frac{\partial T}{\partial t} = \frac{\partial}{\partial x}\left[k \frac{\partial T}{\partial x}\right] + \frac{\partial}{\partial y}\left[k \frac{\partial T}{\partial y}\right] + S \tag{8}$$

Sutherland's formula is used for viscosity calculation in fluid domain, while thermal conductivity of solid is considered as constant. FVM-based cell-centered explicit formulation is used for fluid-domain computations. Solid-domain computations are carried out using technique mentioned by Veersteeg and Malalasekera [11]. Explicit formulation is used for the solid domain and fluid flow using fluid-domain-based time-step calculations. The properties of these wall and sensor materials used are given in Table 1.

3 Results and Discussion

Conjugate heat transfer analyses are carried out in flow over a cylinder for finding heat flux and temperature along the surface. The heat penetration rate in various wall materials is studied, at different time scales, using fluid flow solver (isothermal wall boundary conditions) and CHT solver. The results are discussed in this section. The investigations follow the observations like thermal penetration of heat with experimental times of 10 ms, 100 ms, 200 ms, and 1 s. Also, the effect of wall and substrate material properties on thermal penetration of heat is studied. The wall materials (solid wall S2) used for the present analysis are carbon-carbon composite (C-C) and silicon carbide (SiC), while the gauge material (solid wall S1) is taken as Macor.

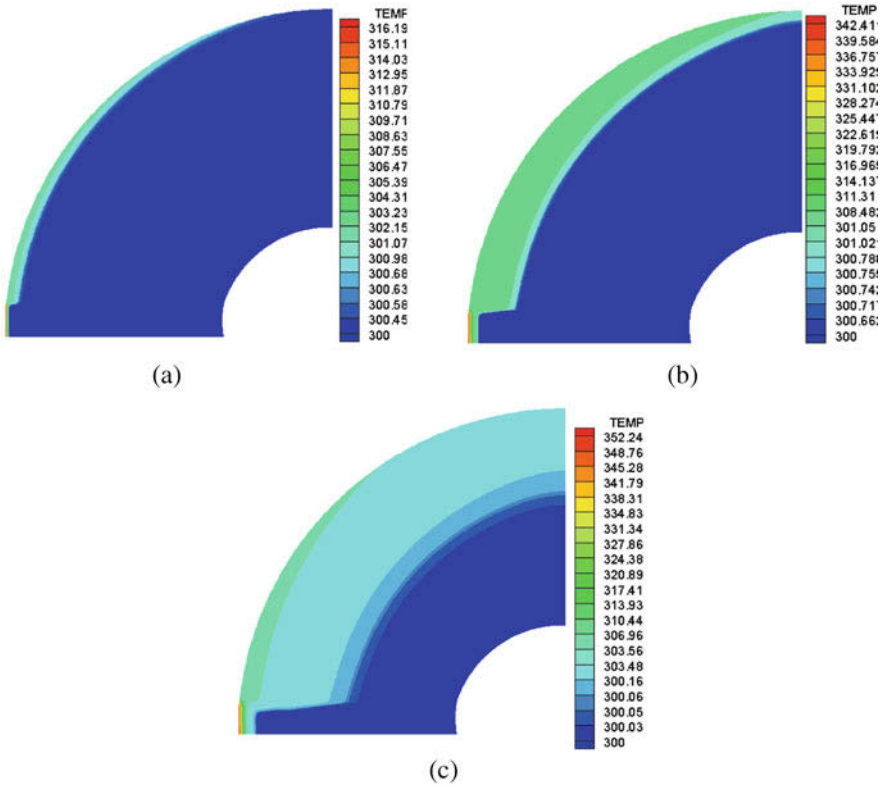

Fig. 3 Solid domain used in CHT: (**a**) Macor – SiC at 10 ms; (**b**) Macor – SiC at 100 ms; (**c**) Macor – SiC at 200 ms

The results are shown in Fig. 3a–c. The thermal penetration increases with time in silicon carbide (SiC), and similarly observations are drawn in carbon-carbon composite (C-C) as shown in Fig. 4a–c. Temperature rise is more in sensor-located region (stagnation region) of the cylinder, and thermal penetration is less in that region. The thermal penetration is seen to be higher for SiC as compared to carbon composite. For better understanding of the interaction, surface heat flux variation along the length of the cylinder is plotted in Fig. 5a, b. Surface heat transfer gradually decreases with increase with theta. These figures clearly show that surface

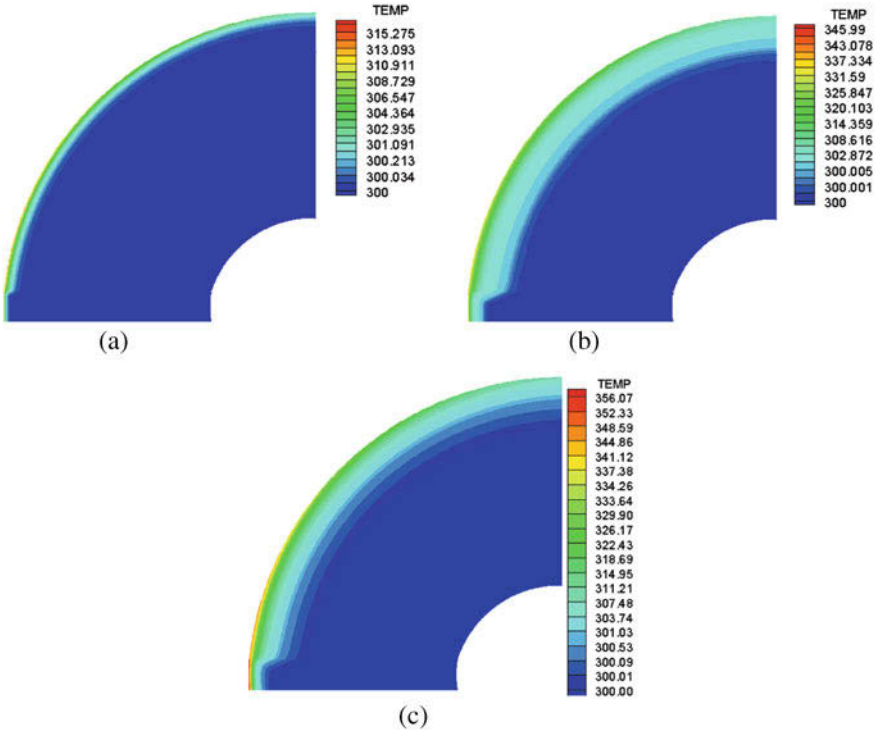

Fig. 4 Solid domain used in CHT: (**a**) Macor – C-C at 1 ms; (**b**) Macor – C-C at 100 ms; (**c**) 1 s

heat flux is less near the sensor region (stagnation-point region) compared to the other regions. Same observations are found in temperature distribution over the surface of the cylinder. Temperature rise is more in sensor region compared to other portions as shown in Fig. 6. Sensor region temperature rise is more because of less heat penetration. From these analyses thermal protection is more important in sensor region. Moreover, the CHT analysis has the capability of predicting heating rates at any locations on the aerodynamic surfaces with multiple wall materials and can be used as a tool for selection of material and design of hypersonic configurations.

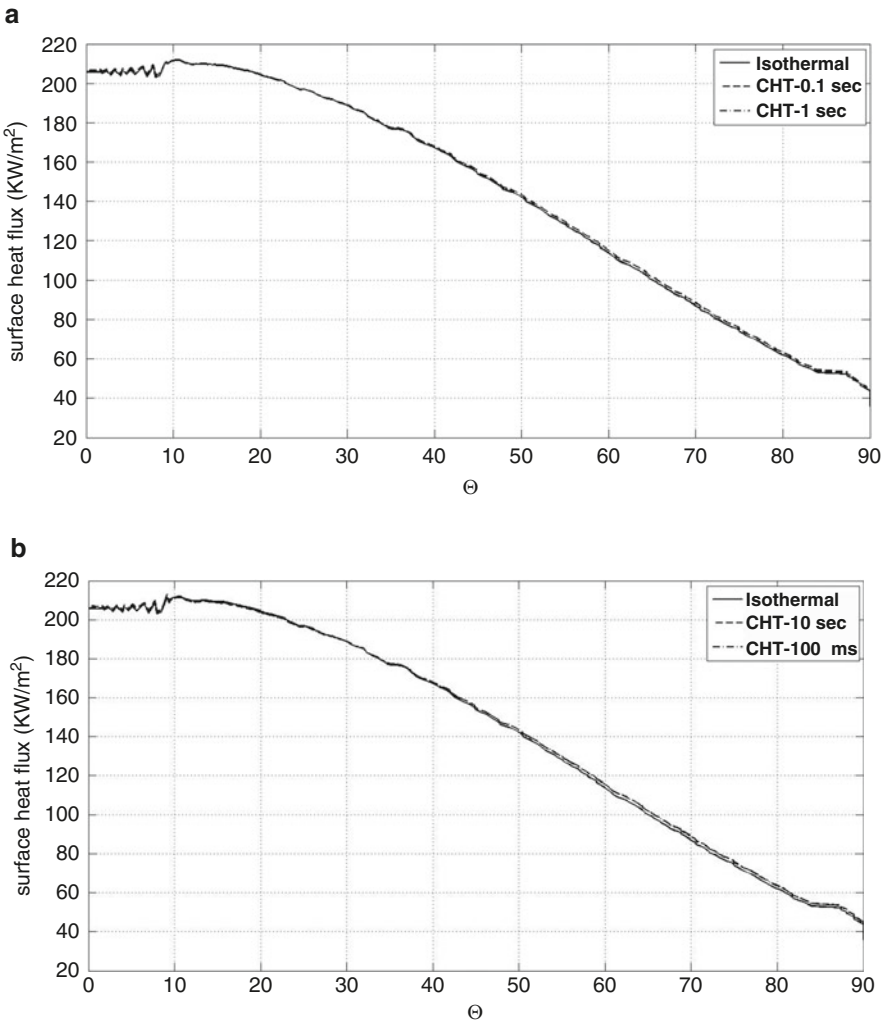

Fig. 5 Surface heat flux distribution: (**a**) Macor – C-C at 1 ms; (**b**) Macor – SiC

4 Conclusion

An in-house CHT solver has been successfully implemented in cylinder configuration for various wall materials. The author has critically examined on conjugate heat transfer (CHT) techniques for flow over a cylinder configuration. It has been observed that wall heat flux decreases along with theta. Similar observations are

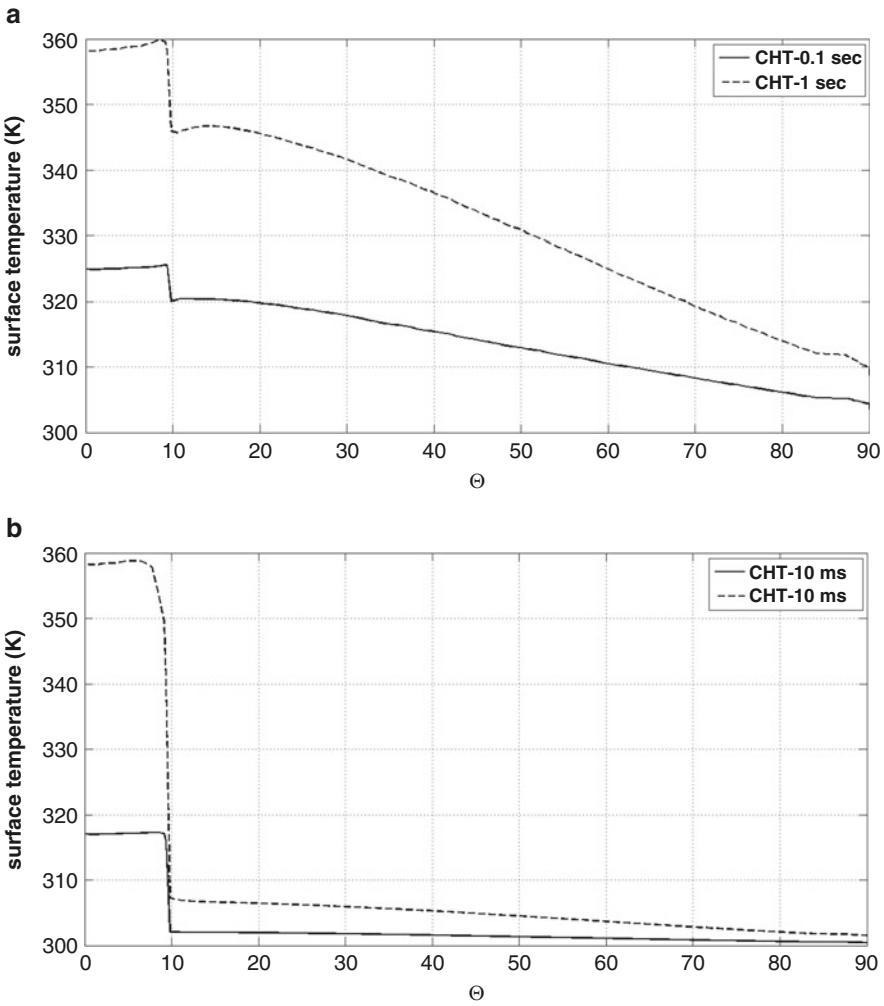

Fig. 6 Surface temperature distribution: (**a**) Macor – C-C; (**b**) Macor – SiC

evident from the aspects of solid where more temperature rise has been observed at the stagnation point. The main observation of present analysis is that near the sensor region (stagnation point), heat penetration is less as compared to SiC and carbon-carbon region. Temperature rise is more significant in the sensor region. Stagnation-point heat flux is seen to be largely decreased due to maximum rise in the wall temperature in that region. CHT analysis has been encountered as a good tool for preexperimental estimations and design of experiments.

References

1. N. Sahoo, Simultaneous measurement of aerodynamic forces and convective surface heat transfer rates for large angle blunt cones in hypersonic shock tunnel, PhD Thesis, Department of Aerospace Engineering, Indian Institute of Science, Bangalore, India (2003)
2. V. Kulkarini, K.P.J. Reddy, Effect of supersonic counter flow jet on blunt body heat transfer rates for oncoming high enthalpy flow. J. Eng. Phys. Thermophys. **8**(1), 3–7 (2008)
3. B. Hassan, D. Kuntz, D. L. Potter, Coupled fluid/thermal prediction of ablating hypersonic vehicle, 36th AIAA Aerospace Sciences Meeting and Exhibit, Reno, NV, Paper No. 98–0168, 12–15 January (1998)
4. F.B. Liu, A modified genetic algorithm for solving the inverse heat transfer problem of estimating plan heat source. Int. J. Heat Mass Transf. **51**, 3745–3752 (2008)
5. F. Pietro, D. Domenic, A numerical method for conjugate heat transfer problems in hypersonic flows, 40th AIAA Thermophysics Conference, pp. 4247, (2008)
6. M. He, P. Bishop, A.J. Kassab, A. Minardi, A coupled FDM/BEM solution for the conjugate heat transfer problem. Numer. Heat Transf. Part B Fundam. **28**(2), 139–154 (1995)
7. D.A. Kontinos, Coupled thermal analysis method with application to metallic thermal protection panels. J. Thermophys. Heat Transf. **11**(2), 173–181 (1997)
8. M.S. Liou, A sequel to AUSM: AUSM+. J. Comput. Phys. **129**, 364–382 (1996)
9. S.G. Mallinson, J. F. Milthorpe, An experimental and numerical study of hypersonic study of hypersonic flat plate flow, 12th Australasian fluid mechanics conference, The University of Sydney, Australia (1995)
10. J. Blazek, *Computational Fluid Dynamics: Principles and Applications* (Elsevier Science Ltd., Oxford, 2006)
11. H.K. Veersteeg, W. Malalasekera, *An Introduction to Computational Fluid Dynamics (Finite Volume Method)* (Longman Scientific and Technical and Wiley & sons Inc., New York, 1995)
12. J.P. Holman, *Heat Transfer*, 6th edn. (McGraw-Hill, Inc, New York, 1989), p. 139

Laser-Induced Shock Waves in Micro Tubes

U. Teubner, Y. Kai, T. Schlegel, and W. Garen

Abstract This work presents fundamentals of the laser-induced micro shock waves (LIMS). The shock wave generation mechanism and the subsequent propagation process of the shock in a micro capillary are investigated. In particular, emphasis is put on well-defined and controllable conditions which also offer the opportunity for potential applications in the future. LIMS are induced by an intense 150 fs laser pulse. In succession, they propagate in the strongly confined 2D geometry of a micro tube. Contactless diagnostic tools are applied to investigate the evolution of density and velocity profiles of the shock waves in the tubes. The initial conditions of LIMS are simulated by the hydrocode MULTI-fs.

1 Introduction

Since the first laser-generated shock wave experiments in the 1980s, a lot of investigations have been performed, mostly concentrating on shocks in solids and plasmas at free or slightly confined (e.g., due to a retainer layer) propagation conditions. However, common shock wave generation and propagation in gases based on blasts and performed in macroscopic tubes become not further applicable when the tube size is strongly decreased – it gets stuck for tube diameters in the sub-mm or micron range (within the present work, the term "tube" is used for any kind of pipe, channel, etc., independently of its size). Hence, new concepts and developments for the miniaturization of shock tubes (down to micrometers) are

U. Teubner (✉) · Y. Kai
Hochschule Emden/Leer, University of Applied Sciences, Institute for Laser and Optics, Emden, Germany

Carl von Ossietzky University of Oldenburg, Institute of Physics, Oldenburg, Germany
e-mail: ulrich.teubner@hs-emden-leer.de

T. Schlegel · W. Garen
Hochschule Emden/Leer, University of Applied Sciences, Institute for Laser and Optics, Emden, Germany

A. Sasoh et al. (eds.), *31st International Symposium on Shock Waves 2*,
https://doi.org/10.1007/978-3-319-91017-8_76

required. Using LIMS [1] in the confined geometry of such miniaturized tubes, a novel suitable physical method is set off and discussed in detail within the present work. It demonstrates that the well-developed macroscopic shock wave theories cannot be directly applied to the micro shock waves. For example, experimental results show that the reflected expansion waves strongly influence the shock propagation in the smallest tubes and the flow becomes laminar, which is different to the turbulent motion in conventional tubes.

2 Experiments

2.1 LIMS Method

In contrast to shock wave generation with macroscopic tubes, which have a high-pressure part and a low-pressure section, the present LIMS method makes use of a tube filled with an initially homogenous fluid in its whole volume.

The principle of the LIMS is shown in Fig. 1. The setup consists of a 1-mm-thick glass plate located very closely to the entrance of the tube, namely, at a distance which is at least one order of magnitude smaller than the tube diameter, even for the smallest tube. Thus, the laser-initiated shock is almost completely lanced into the tube. The present work includes experiments, where the opposite side of the tube was open.

An intense laser pulse is focused through the glass plate onto a thin layer of aluminum deposited on the rear side of the plate (i.e., the target; note: such thin layers can be partly oxidized), where it generates almost instantaneously a laser-produced plasma (LPP). The sudden occurrence of a high-pressure high-temperature LPP represents an extreme non-equilibrium, which runs down in the emission of a shock wave. This LPP acts as the driver for a shock wave, which propagates into a tube positioned in the immediate vicinity (less than 5 μm from the target).

For the present work, linearly polarized pulses of a Titanium: sapphire laser system with a wavelength of 775 nm, an adjustable pulse energy (maximum 1 mJ), and a pulse duration of 150 fs (FWHM) were focused with an achromatic lens of

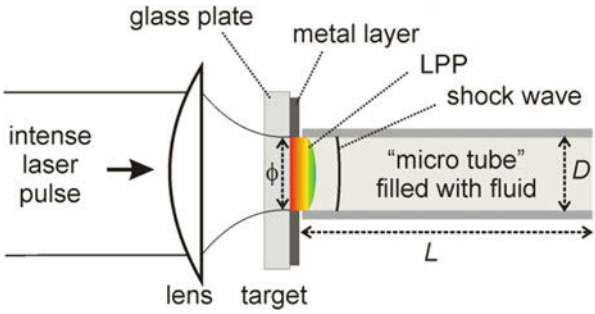

Fig. 1 The LIMS method. The target is a 50-nm-thin Al layer on the rear side of a glass plate. The glass substrate is 1-mm thick, where the LPP shall not be generated

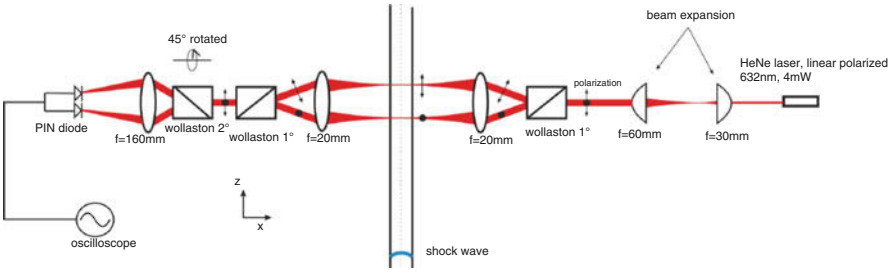

Fig. 2 Laser differential interferometer as the diagnostic. The spacing between the two beams is 370 μm. The distance x_1 from the LPP to the first interferometer beam is varied during experiments

rather long focal length at normal incidence. This yields a large focus but provides still a sufficiently high intensity, which is kept constant as $I = 2 \times 10^{13}$ W/cm^2.

2.2 Setup

The experiments are performed with different commercially acquired glass tubes (CM scientific) with inner widths of $D = 50$ μm, 100 μm, 200 μm, and 300 μm, respectively. The length of all tubes is $L = 50$ mm; the tube wall is half the thickness of the inner diameter of the tube. The shock wave propagation in the tube is investigated by a laser differential interferometer (LDI), which is a modification of the arrangement published earlier in [1]. The diagnostic setup is presented in Fig. 2. Primarily, the trajectory (propagation distance x as a function of time delay t) of the shock wave is measured.

The shock velocity can be obtained through time-of-flight method using the LDI. The hereby determined shock velocity is thus the average value between the two LDI beams.

3 Results

Figure 3 shows that shock waves generated with the same laser intensity in bigger tubes propagate faster (are stronger) than those in smaller tubes. Here, velocities are plotted in absolute values. This may be explained by the fact that a bigger tube indicates less influence of friction and heat transfer than a smaller one.

The observed behavior of the shock wave velocity decline along the tube can be explained by two processes. The first one is the core flow expansion behind the created shock wave which is caused by the initial pressure ratio and a very short driver. The second one is the development of the wall boundary layer which interacts with the core flow. These two processes lead to a decrease of the shock wave velocity [1].

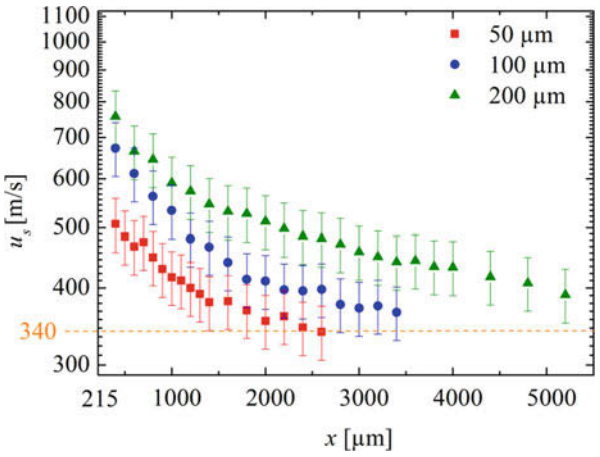

Fig. 3 Shock wave attenuation determined experimentally by the time-of-fight method (scattered points with 10% error bars). The same fs-laser intensity is applied for all tubes. The coordinates $x_{sw} = 1888$, 2707, and 7913 µm for the tubes with diameters $D = 50$, 100, and 200 µm, correspondingly, are the distances where the shocks become sound waves

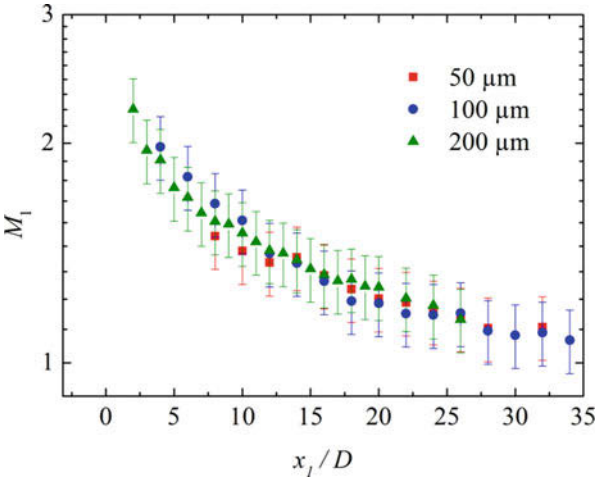

Fig. 4 Normalized shock wave attenuation

However, the shock wave Mach numbers will not differ significantly, if the propagation distance is normalized to the tube diameter (see Fig. 4). It means that a "normalized" LIMS in a smaller tube can be as strong as that in a bigger tube. However, less input energy is needed in case of a smaller tube, since the fs-laser intensity is constant, and thus a smaller tube cross-section corresponds to less energy.

4 MULTI-fs Simulations

The one-dimensional hydrocode MULTI-fs [2] is applied to get a principal insight in the short-pulse laser-target heating and the subsequent propagation of a shock wave in the adjacent medium. This Lagrangian hydrodynamic code with multigroup radiation transport simulates the laser pulse propagation in the plasma region up to the critical surface by solving the wave equation. As the result, light reflection

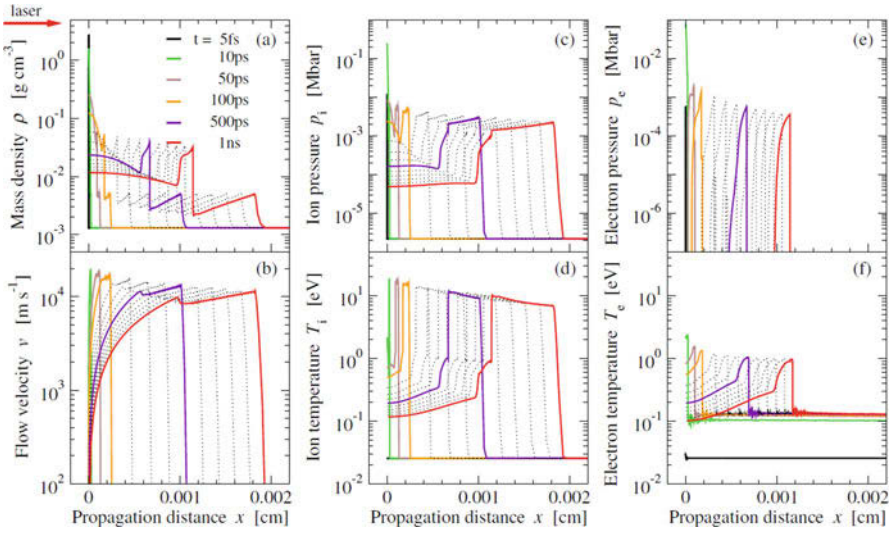

Fig. 5 Mass density ρ; ion and electron pressures p_i, p_e; temperatures T_i, T_e; and flow velocity v as functions of the shock propagation distance x. MULTI-fs simulation for the initial conditions of LIMS. The simulation uses the actual experimental parameters of the fs-laser and the aluminum sample

in plane geometry is modeled correctly and provides realistic absorption values. Hence, we avoid an overestimation of the gas dynamic pressure by excessive absorption in the aluminum layer. The laser absorption coefficient extracted from simulations was in the range of the experimentally measured value 0.3.

Spatial profiles of the mass density, the ion and electron pressures, the corresponding temperatures, and the flow velocity at several instants $t \gg 10$ ps (see the legend in panel (a)) are shown in Fig. 5, for propagation in an air medium.

Time is counted starting from the arrival of the laser pulse at the left boundary of the aluminum layer (conterminous to the glass support in the experiment). Dotted curves correspond to multiples of 100 ps beside the curve for half a nanosecond (solid violet curve). The front of the first mass density bump on each curve marks the aluminum-air boundary (see Fig. 5a).

The bordering region in aluminum at this interface exhibits a strong electron pressure as well as an electron temperature in the eV-range (see panels (e) and (f), respectively), which are missing in the adjacent air volume. Ion pressures in this bordering region are larger by an order of magnitude than the corresponding data for electrons at the same positions. Furthermore, in the whole aluminum plasma, we observe similar temperature distributions for electrons and ions after approximately 100 ps because of electron-ion relaxation. In the compressed air, however, the low density and the strong ion heating by the shock preserve the thermodynamic non-equilibrium. In addition, we realize a slight deceleration of the shock front in air already at this early propagation stage (see, e.g., panel (b)).

5 Conclusion

A novel method to generate shock waves in small tubes with diameters down to the micrometer range has been developed, namely, laser-induced micro shock waves (LIMS). This method makes use of plasmas generated in thin-layered targets by means of intense femtosecond laser pulses. It opens up a new possibility for the experimental shock wave research at micro scales. It has been shown that a carefully designed laser-produced plasma driver enables strong shock wave generation in air. Different scenarios of this process have been investigated. In particular, shock wave generation in free air and under confined conditions of small tubes, both in point-like and in planar driver geometry, were tested. As expected, planar laser plasmas are the most suitable drivers and offer the opportunity for the propagation of strong shock waves in tubes with sub-mm or micrometer diameter. In such a confined geometry, propagation lengths up to several mm become available, before the wave attenuates to a sound wave. Experimental results have been complemented by hydrocode simulations.

Acknowledgment This work is supported by the German research foundation DFG (Deutsche Forschungsgemeinschaft DFG; grand No. TE 190/8-1 and GA 249/9-1).

References

1. U. Teubner, Y. Kai, T. Schlegel, D.E. Zeitoun, W. Garen, Laser-plasma induced shock waves in micro shock tubes, New.J.Phys. **19**, 103016 (2017)
2. R. Ramis, K. Eidmann, J. Meyer-ter-Vehn, S. Hüller, Multi-fs a computer code for laser plasma interaction in the femtosecond regime. Comput. Phys. Commun. **183**(3), 637–655 (2012)

Study of MHD Effects in the High-Enthalpy Shock Tunnel Göttingen (HEG) Using a 30 T-Pulsed Magnet System

J. Martinez Schramm and K. Hannemann

Abstract The interaction between high-enthalpy partially ionized gas flows and magnetic fields, mostly called magnetohydrodynamics (MHD), is regarded as a potential way to manipulate flows. One example is the wall heat-flux mitigation during spacecraft re-entry or entry into an atmosphere. However, the theoretical background and the practical application are still discussed controversially. One way to enhance the knowledge in this field is to utilize advanced computational fluid dynamics (CFD) tools in combination with experimental studies providing suitable validation data. The German Aerospace Center, DLR, has assembled an experiment for the high-enthalpy shock tunnel Göttingen (HEG) to provide data for verification and validation of numerical predictions. A 30 T-pulsed magnet, driven by a 100 kJ capacitor bank, generates the required field. This paper outlines the experimental requirements to obtain magnetohydrodynamic effects in high-enthalpy partially ionized gas flows and the final realization of the experiment. Selected results of experiments using flow stagnation enthalpies of 22 MJ/kg are presented.

1 Introduction

The interaction between electrically conducting flows and magnetic fields, commonly referred to as magnetohydrodynamics (MHD), is regarded as a unique way to exert directed volume forces on the fluid. The potential for flight control, heat flux reduction and in particular phenomena of fundamental interest for applications like shock-less deceleration of super- and hypersonic flow has been reported [1]. For years experimental MHD investigations suffered from drawbacks in engineering: mass and volume of classical magnets and power supplies and limited capabilities in measuring flow parameters. Recent developments in superconductors and semiconductors and new materials helped to overcome many technical difficulties.

J. Martinez Schramm (✉) · K. Hannemann
German Aerospace Center, DLR, Institute for Aerodynamics and Flow Technology, Spacecraft Department, Göttingen, Germany
e-mail: Jan.Martinez@dlr.de

A. Sasoh et al. (eds.), *31st International Symposium on Shock Waves 2*,
https://doi.org/10.1007/978-3-319-91017-8_77

Advanced numerical tools, capable of handling the coupled Navier Stokes/Maxwell equations, still lack experimental verification and validation. Ambitious proposals revived the general interest in MHD and call for the availability of reliable experimental reference data, focussing, e.g., on manipulating the gas-dynamic bow shocks of spacecraft for heat-flux reduction [2]. In this paper we outline an experiment designed for the high-enthalpy shock tunnel Göttingen (HEG) of the German Aerospace Center (DLR). The experiment, which is suitable to investigate MHD effects, will provide experimental background for theoretical analysis and is designed to be a reference case for verification and validation purposes. The experiment consists of a liquid nitrogen-cooled 30 T-pulsed magnet, which is driven by a 100 kJ capacitor bank. The coil is installed in a spherical model. Modifications of the bow shock distance and shape can indicate changes in flow conditions and are easily accessible by nonintrusive optical measurement methods. To characterize MHD-relevant flow conditions, the standard set of non-dimensional flow quantities, like Mach number, Reynolds number, etc., has to be extended. The magnetic interaction parameter, or Stuart number Θ, relates the force exerted on the conducting fluid by the coil field to the inertia force of the flow and is calculated as $\Theta = \varepsilon B2l/(\rho u)$, ε denoting the electrical conductivity of the gas, B the magnetic flux density generated by the coil, l a characteristic length, ρ the flow density and u the flow speed. Empirically, $\Theta \geq 1$ ensures detectable effects of the magnetic field on the flow. In our case, an increase of the shock distance with increasing B is expected. The magnetic Reynolds number Re_m relates the magnetic field generated by the moving charged flow to the coil field. The magnetic Reynolds number is defined as $Re_m = \mu_0 \varepsilon ul$, with μ_0 as the vacuum permittivity. For $Re_m \ll 1$, the coil field clearly dominates the field generated by moving charges. In the case of $Q \geq 1$ and $Rem \ll 1$, both the theoretical treatment and the interpretation of experiments are simplified in various ways. But when viewed in more general terms, the roles of Θ and Re_m and the interaction mechanisms between conducting flow and magnetic field via Lorentz forces and secondary electric and magnetic fields are complex and still not completely understood nor investigated [2].

2 The High-Enthalpy Shock Tunnel Göttingen, HEG

The HEG is one of the major European hypersonic test facilities. This free-piston-driven shock tunnel (Stalker type [3]) was commissioned for use in 1991 and has been utilized extensively since then in a large number of national and international space and hypersonic flight projects. HEG was designed to study the influence of high-temperature effects such as chemical and thermal relaxation on the aerothermodynamics of entry or re-entry space vehicles [4–7]. The HEG condition used for the experiments described in this paper is the condition I with a stagnation flow enthalpy of 22 MJ/kg.

The ionization induced in the shock layer of a blunt body in HEG at this flow condition produces a significant gas conductivity, which is an advantage

Table 1 Pre- and post-shock flow conditions for HEG condition I

M	8.2	
u_1	5900	m/s
ρ_1	1.7	g/m^3
T_1	1140	K
u_2	675	m/s
ρ_2	13.1	g/m^3
T_2	9770	K
ε_2	1730	S/m

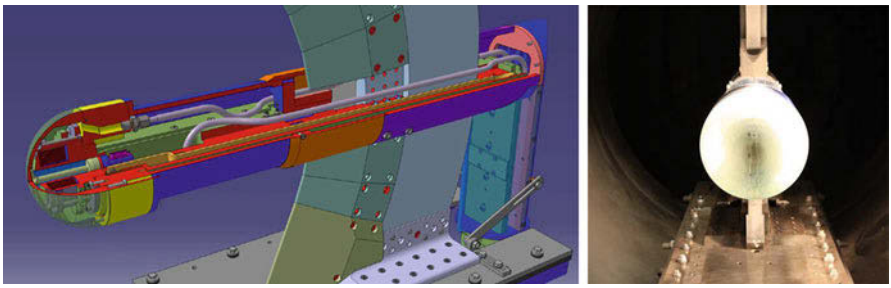

Fig. 1 Schematic of the wind tunnel model in HEG on the left side and a photograph of the model installed in the HEG test section on the right side

for MHD experiments over alternatives like seeding the flow with alkali metals, electron-beam ionization or arcjet heating; these produce contamination or less well-defined freestream conditions. The pre- and post-shock flow conditions are given in Table 1.

3 Experimental Setup

To tailor the experiment to a systematic investigation of MHD phenomena, the following requirements were specified: The wind tunnel model is a hemisphere cylinder with its axis aligned to the flow, having a diameter of $D = 160$ mm. This configuration has been tested to quite some extent in HEG, and experimental as well as numerical reference data are available. The shock stand-off distance Δ is used as a reference length to evaluate the relevant Stuart number Θ (Fig. 1).

To achieve a Steward number $\Theta \geq 1$ with the post-shock conditions in Table 1 and a shock stand-off distance of $\Delta = 9$ mm (sphere with $D = 160$ mm), a magnetic field of $B \geq 1$ T is necessary at the shock location. A higher magnetic field is desirable, which helps to overcome the general uncertainties, the inhomogeneous flow field and the fact that Θ decreases rapidly with distance from the ideal interaction point. The corresponding magnetic Reynolds number amounts to $Re_m = 0.014$, which is a tolerable result. The coil is installed within the model in order to minimize the distance to the interaction region ahead of the hemisphere. The model

diameter is sufficiently small to prevent tunnel flow blockage; at the same time, the optical path length through the shock layer for advanced nonintrusive laser methods is found to be acceptable. The rise time of the magnetic field must not exceed $t \approx 3$ ms with good reproducibility (low jitter) to suit trigger constraints during the tunnel operation. The coil power supply must be mobile; coil, model, cabling and cooling must be demountable and sufficiently robust to withstand several experiment campaigns. Further details on the power supply have to remain for future publications. The effective measurement time using HEG operating condition I is in the order of $t \approx 1$ ms; therefore the coil operation follows a corresponding time scale and has to produce the maximum field only for a similar short interval.

In principle it is possible to generate a field of one tesla fairly easily using permanent magnets; however, preliminary studies showed that the magnetic field of permanent magnets falls off very quickly with distance. Also, it is desirable to generate a higher magnetic field as the effects should scale with the Stuart number which is proportional to B^2. In general, fields higher than a few tesla are generated using electromagnets. The most economical way of generating high magnetic fields is doing this pulse, which lends itself for this experiment as the field is only required for about a millisecond. Pulsed magnets are usually driven by a capacitor bank, which leads to a half-sinusoidal pulse. This is common practice for condensed matter physics research; a number of facilities worldwide offer fields in excess of 60 T routinely [8, 9]. The performance of a pulsed magnet is usually determined by two factors: the first is the mechanical strength of the employed materials, which limits the peak magnetic field which can be achieved. High-strength materials are required due to the Lorentz force, which gives rise to a large magnetic pressure. The second important parameter is the electrical conductivity of the conductor material, which limits the pulse length. The better the electrical conductivity, the longer the pulse can be. Given that the material is crucial for a pulsed magnet, the material chosen for the present coil is Cu-Ag7-Zr0.05. Among the Cu-based conductor materials, the family of Cu-Ag alloys shows the highest conductivity at a given strength (or vice versa) at room temperature [10]. The performance is better at low temperatures; this is why the wind tunnel model was designed to include a liquid nitrogen cooling system for the coil. An unusual challenge for the magnet design lies in the fact that the field is not required at the centre of the magnet but rather far away from it in the fringe field region. Therefore, a monolithic coil geometry with an inner diameter of 40 mm, an outer diameter of 80 mm and a length of 30 mm was chosen. The coil was designed in cooperation with the high magnetic field lab in Oxford, UK, and manufactured there. A technical drawing and a photograph of the coil are given in Fig. 2. Of importance is the exact knowledge of the magnetic field distribution that the magnetic coil will generate when it is energized. A lot of effort was put into the exact measurement of the distribution of the magnetic field around the wind tunnel model, as it is of importance to the exact modelling of the interaction with CFD. Figure 3 shows a result of these measurements. Even though a lot of metal pieces belonging to the model and liquid nitrogen tubing system are necessarily disturbing the magnetic field, it is homogenous and axisymmetric.

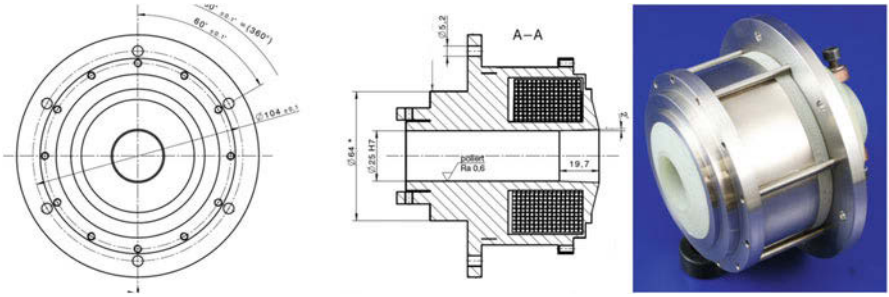

Fig. 2 Technical drawing of the coil used in the wind tunnel model and photograph

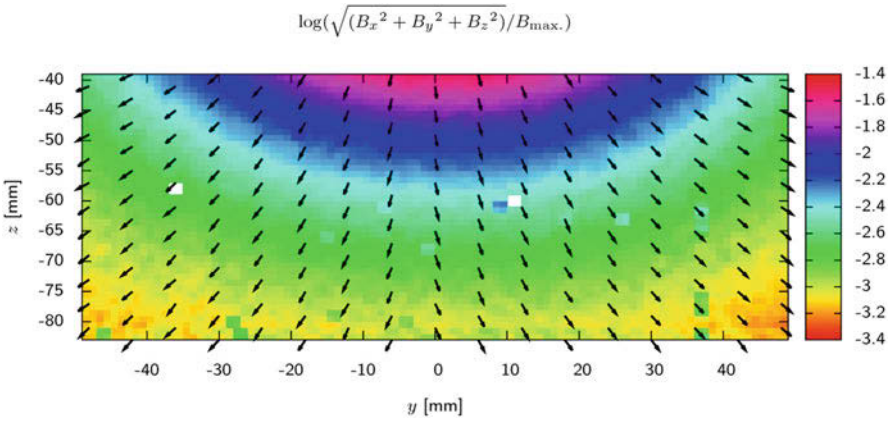

Fig. 3 Measurements of the magnetic flux density field around the coil using a low-energy measurement technique. The origin of the z-coordinate is at the maximal magnetic flux density on the axis of the coil

4 Experiment and Results

The experiments in HEG were performed with varying magnetic flux densities of the magnetic field around the hemisphere-cylindrical model. The varying magnetic flux density was changed by charging the capacitor bank that drives the coil with different energy levels. Prior to the run, the magnetic coil installed in the wind tunnel model was cooled by pumping liquid nitrogen through its core. The inner resistance of the coil dropped typically from 130 mΩ down to 60 mΩ. Once the resistance measurements equilibrated, the coil was regarded to be cooled down homogenously. This process, performed under the tunnel vacuum, usually took about 2 hours. The coil was then energized by discharging the capacitor bank into the coil. The maximum voltage of the half-sinusoidal pulse was at 3.5 kV having a current of 13 kA. The charging process of the capacitor bank had to be finalized a few seconds before the run. The discharge of the capacitor bank into the coil was synchronised

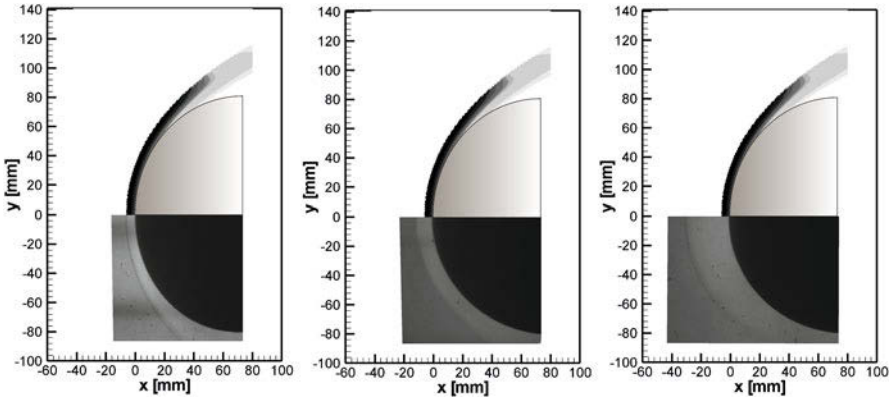

Fig. 4 Comparison of numerical modelling of the flow around the sphere for HEG condition I always on top (density) to the experimental data obtained with Schlieren visualization for the cases of (B = 0 T, B = 1 T and B = 4.5 T) from left to right

to the run to obtain a steady magnetic field during the test time. Figure 4 shows the results obtained. A numerical modelling result of the flow around the spherical part of the model for no magnetic field is shown on the top of each image. The density distribution of the CFD data is shown in false colours. On the bottom side, the Schlieren images obtained from the experiments are given. The experimental results are given for the case of no magnetic field, the case with B = 1 T magnetic flux density in the middle and B = 4.5 T on the right. The magnetic flux density is given at the axial position, where the shock wave stands for the measurement without any magnetic interaction. The change in shock stand-off distance is clearly visible. In the case of the strongest magnetic field, the shock stand-off distance is increased by a value of 4.6. Not only is the shock stand-off distance influenced, but the complete flow field. The changes of shock shape are drastic and are observable through the complete flow field. The exact description of the changes will be given in future publications.

5 Conclusions

Experiments demonstrating the interaction with high-enthalpy partially ionized gas flow and magnetic fields of varying magnetic field flux have been presented. The interaction has been shown by presenting measurements of density gradients with Schlieren visualisations. The change in shock shape and shock stand-off distance with acting magnetic field is clearly visible. The design and layout of the wind tunnel model holding the liquid nitrogen-cooled magnetic field coil have been discussed. The basic ideas to design the experiment as a validation and verification test case have been sketched. The next steps in the process of the establishment

of a real test case will be to perform additional experiments and compare these to numerical modelling results with coupled Navier Stokes/Maxwell equations.

References

1. E. Resler, W. Sears, The prospects for magneto aerodynamics. J. Aeronaut. Sci. **4**, 235–245 (1958)
2. J. Poggie, Numerical modeling of electro-magnetic control techniques for high-speed flows, in *Introduction to Magneto-Fluid-Dynamics for Aerospace Applications, VKI Lecture Series 2004–01*, ed. by O. Chazot, M. Huber, (von Karman Institute, Rhode Saint Genese, 2004), pp. 1–21
3. R.J. Stalker, A study of the free-piston shock tunnel. AIAA J. **5**(12) (1967)
4. K. Hannemann, J. Martinez Schramm, S. Karl, Recent extensions to the high enthalpy shock tunnel Göttingen (HEG), in *Proceedings of the 2nd International ARA Days "Ten Years after ARD"*, Arcachon, France, 21–23 October 2008
5. K. Hannemann, R. Krek, G. Eitelberg, Latest calibration results of the HEG contoured nozzle, in *Proceedings of the 20th International Symposium on Shock Waves, Pasadena, CA, USA, July 1995*, ed. by B. Sturtevant, J. E. Sheperd, H. G. Hornung (Eds), (World Scientific, 1996), pp. 1575–1580
6. K. Hannemann, J. Martinez Schramm, High enthalpy, high pressure short duration testing of hypersonic flows, in *Springer Handbook of Experimental Fluid Mechanics*, ed. by C. Tropea, J. Foss, A. Yarin (Eds), (Springer, Berlin Heidelberg, 2007), pp. 1081–1125
7. K. Hannemann, High enthalpy flows in the HEG shock tunnel: experiment and numerical rebuilding, 41st AIAA aerospace sciences meeting and exhibit, Reno, Nevada, 6–9 January 2003
8. F. Herlach, Pulsed magnets for strong and ultrastrong fields. IEEE Trans. Magn. **32**(4), 2438–2443 (1996)
9. N. Miura, F. Herlach, Pulsed strong and ultra-strong magnetic fields, Technical Report of ISSP Ser. A, No. 1471, The Institute for Solid State Physics, University of Tokio, Roppongi, Minkato-Ku, Tokyo 106, Japan (1984)
10. J. Freudenberger, N. Kozlova, A. Gaganov, L. Schultz, H. Witte, H. Jones, Magnetoresistance up to 50 T of highly strengthened CuAg conductors for pulsed high field magnets. Cryogenics **46**, 724–729 (2006)
11. A. Gülhan, B. Esser, U. Koch, F. Siebe, J. Riehmer, D. Giordano, D. Konigorski, Experimental verification of heat-flux mitigation by electromagnetic fields in partially-ionized-argon flows. J. Spacecr. Rocket. **46**(2), 274–283 (2009)
12. J.S. Shang, Shared knowledge in computational fluid dynamics, electromagnetics, and magneto-aerodynamics. Prog. Aerosp. Sci. **38**(6–7), 449–467 (2002)

An Electrodynamic Aerobraking Experiment in a Rarefied Arc-Heated Flow

H. Katsurayama, N. Fukuda, T. Toyodome, Y. Katoh, K. Tomita, and M. Matsui

Abstract Our previous numerical study (Katsurayama et al. AIAA Paper 2008-4016) has predicted that an insulating boundary in a flow is necessary to activate electrodynamic braking in a rarefied flow: the insulating boundary can prevent the Hall effect from dissipating the current which is necessary for the electrodynamic braking. In order to validate this numerical prediction, the present study measures the total drag on a test model in a rarefied arc flow whose insulating boundary (that is an arc plume boundary) location is variable and compares the measured electrodynamic increases of the total drag with the computed values. As a result, the measured and computed total drags increase by applying the magnetic field, but contrary to the computational prediction, the measured electrodynamic increase of the total drag is insensitive to the insulating boundary location.

1 Introduction

Reentry vehicles are exposed to serve convective heating attributable to a high-enthalpy flow past them. A passive system with a heat-resistant or ablative material has been employed to protect the vehicles from aerodynamic heating. However, the lack of reusability and low reliability of such a thermal protection system persist as obstacles to cost and risk reductions of space transportation system.

An alternative to existing thermal protection systems can be achieved by actively controlling a weakly ionized flow past the vehicle through the electrodynamic force. The system is called electrodynamic braking [1] (Fig. 1).

H. Katsurayama (✉) · N. Fukuda · T. Toyodome · Y. Katoh
Yamaguchi University, Ube, Yamaguchi, Japan
e-mail: katsura@yamaguchi-u.ac.jp

K. Tomita
Kyushu University, Kasuga, Fukuoka, Japan

M. Matsui
Shizuoka University, Hamamatsu, Shizuoka, Japan

A. Sasoh et al. (eds.), *31st International Symposium on Shock Waves 2*,
https://doi.org/10.1007/978-3-319-91017-8_78

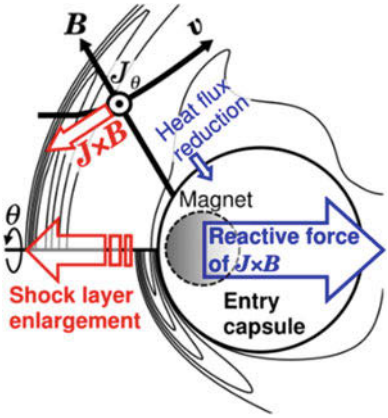

Fig. 1 Electrodynamic braking

The system expands a dipolar magnetic field $\boldsymbol{B}$ around the body using an on-board magnet and induces a circumferential current J_θ according to the electrodynamic interaction between $\boldsymbol{B}$ and the weakly ionized flow behind the bow shock. The electrodynamic effect generates the Lorentz force $\boldsymbol{J} \times \boldsymbol{B}$ against the flow direction, and the force enlarges the shock layer. This effect reduces aerodynamic heating and increases aerodynamic drag because of the effective increase of the radius of curvature of the body (in practice, $\boldsymbol{J} \times \boldsymbol{B}$ acting on the fluid exerts a reaction force on the magnet).

Past experimental [2–5] and numerical [6] studies have reported that the electrodynamic braking is effective in dense flows at low altitudes. And several recent numerical [7, 8] and experimental [9, 10] studies have investigated its effectiveness in rarefied flows at high altitudes. However, the effectiveness in rarefied flows is not yet fully clarified, although the slow-speed entry from high altitude will enable a drastic reduction of aerodynamic heating through the whole entry trajectory.

2 Role of an Insulating Boundary in a Rarefied Flow

In order to demonstrate the electrodynamic braking, Kawamura et al. [11] have measured the drag on a test model which is located in a rarefied arc flow (Fig. 2). The Knudsen number Kn and Hall parameter β of the flow are approximately $Kn \approx 0.05$ and $\beta \approx 30$. The experiment has reported that the electrodynamic drag increase is 1.5 times when the magnet of 0.5 T is used.

In order to validate this experiment, we conducted a simple computational fluid dynamics (CFD) analysis [12], in which the test model is assumed to be located in a uniform ionized flow (Fig. 3a). This computation failed to reproduce

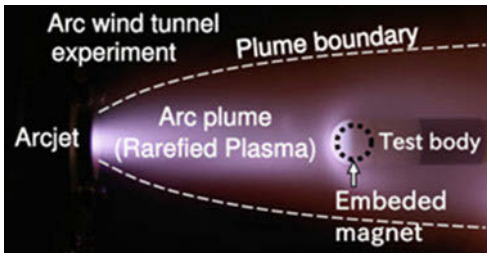

Fig. 2 Arc experiment [2]

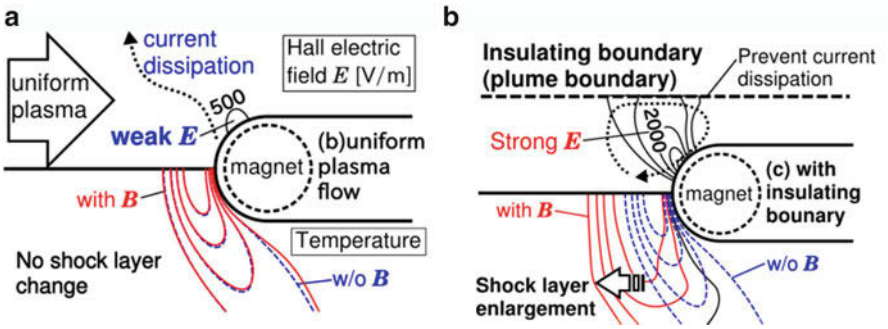

Fig. 3 The role of an insulating boundary [3]. (**a**) No insulating boundary. (**b**) With insulating boundary

the measurement because the Hall effect dissipates current along the magnetic flux and the dissipation results in no electrodynamic force. However, the real arc flow (Fig. 2) has a plume boundary which can serve as an insulating boundary preventing the current dissipation. Therefore, we conducted the CFD analysis in which an artificial insulating boundary is located in the flow for imitating the plume boundary (Fig. 3b). In the computation, the insulating boundary prevents the current dissipation, and the strong Hall electric field $\boldsymbol{E}$ is induced. The J_θ resulting from $\boldsymbol{E} \times \boldsymbol{B}$ drift generates the large electrodynamic force.

As a result, this computation predicted that an insulating boundary in the flow is necessary to generate the electrodynamic force in rarefied flows. Moreover, the insulating boundary location closer to the body will result in the stronger $\boldsymbol{E}$ and the larger electrodynamic force.

To validate this computational prediction, the present study measures the total drag on a test model in a rarefied arc flow whose insulating boundary (i.e., an arc plume boundary) location is variable. And it compares the measured electrodynamic increase of the drag with those of the new computation [13], which can enable more realistic simulation as compared with the previous simple computation [12].

3 Rarefied Arcjet Wind Tunnel Experiment

Figure 4 shows the overall experimental system. The system produces a weakly ionized argon flow (Fig. 4a) using a constrictor type arcjet, whose input power is 1.5 kW. Table 1 shows the numerical prediction [13] of the arc flow characteristics.

A test model (Fig. 4b) is located at 110 mm downstream from the arcjet nozzle exit. The model head, whose diameter is 22 mm, is made of ceramics (Macor), and it is capable of mounting a neodymium magnet whose magnetic flux density at the stagnation point B_0 is 0.365 T. The test model is attached to a pendulum device (Fig. 4c). The pendulum design is almost the same as that of Kawamura et al. [11], and its measurable drag range is 0–500 mN.

A vacuum chamber (Fig. 4d) is evacuated using a vacuum pump system with the maximum exhaust capability 2100 m^3/h. The back pressure in the vacuum chamber p_b is controllable in the range of 15–100 Pa by adjusting a butterfly valve. The diameter of the plume boundary (i.e., insulating boundary) decreases with increasing p_b. Figure 5 shows the photographs in the cases of $p_b = 20$ and 100 Pa. The plume diameter in the former is much larger than that of the latter.

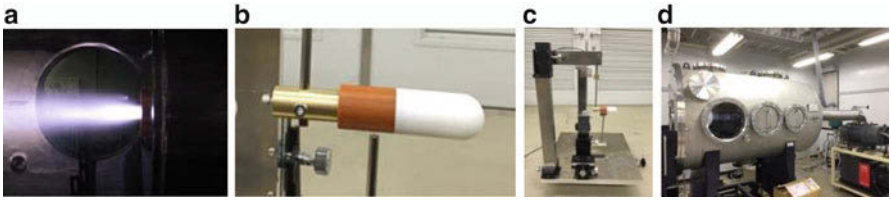

Fig. 4 The arc wind tunnel system of Yamaguchi Univ. (**a**) Arcjet. (**b**) Test model. (**c**) Pendulum system. (**d**) Vacuum chamber

Table 1 Table 1

Working gas	Ar
Test body diameter d	22 mm
Knudsen number Kn	0.05
Mach number M	1.7
Flow speed v	1097 m/s
Heavy particle temperature T	1200 K
Electron temperature T_e	≈6100 K
Neutral particle density n_n	2.05×10^{21} m^{-3}
Electron density n_e	$\approx 1 \times 10^{19}$ m^{-3}
Ionization degree α	≈0.5%
Static pressure p	34 pa
Max magnetic flux density B_0	0.365 T
Electric conductivity σ	731 S/m
Hall parameter β	164

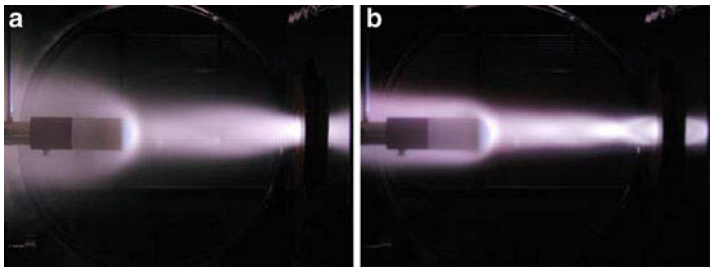

Fig. 5 The arc plume boundary displacement in the experiment. (**a**) $p_b = 20$ Pa. (**b**) $p_b = 100$ Pa

4 Numerical Prediction of the Arcjet Wind Tunnel Experiment

Prior to the experimental drag measurement, we predicted the influence of the plume boundary location on the electrodynamic braking using the arc wind tunnel simulation code [13]. In this calculation, the chamber back pressure was varied in the range of $p_b = 15$ to 60 Pa.

The present study intends to investigate the influence of the insulating boundary location on the electrodynamic force generation. However, there is a suspicion that the increase of p_b might change the flow characteristics to conditions in which the electrodynamic force generates more easily. To dispel this suspicion, we calculated the maximum Hall parameter $\beta_{\max}$ in the shock layer and the magnetic interaction parameter Q:

$$Q = \frac{\boldsymbol{J} \times \boldsymbol{B} D}{\rho_\infty v_\infty^2} = \frac{\sigma_{\max} B_0 D}{\rho_\infty v_\infty} \tag{1}$$

which is the expected ratio of the electrodynamic force to the inertia force when the Hall effect is neglected. Here, J is the induced current, ρ_∞ and v_∞ are the representative density and velocity of the flow, and D is the characteristic length (i.e., model diameter). Figure 6 shows the back pressure dependences of $\beta_{\max}$ and Q. The $\beta_{\max}$ and Q parameters are almost constant, which means that the increase of p_b does not affect the flow characteristics which govern the electromagnetic force generation.

Figure 7 shows the distribution of the electric conductivity σ in the cases of $p_b = 15$ and 60 Pa. In these cases, the locations of $\sigma = 50$ S/m were regarded as an insulating boundary. The plume radius (i.e., insulating boundary location) r_i decreases from 58 mm to 42 mm with increasing p_b.

Figure 8 shows the back pressure dependences of the maximum $\boldsymbol{E}$ and axial Lorentz force $(\boldsymbol{J} \times \boldsymbol{B})_z$. As was expected, the $|\boldsymbol{E}|$ and the resulting axial Lorentz force increase with the decrease of r_i (i.e., the increase of p_b).

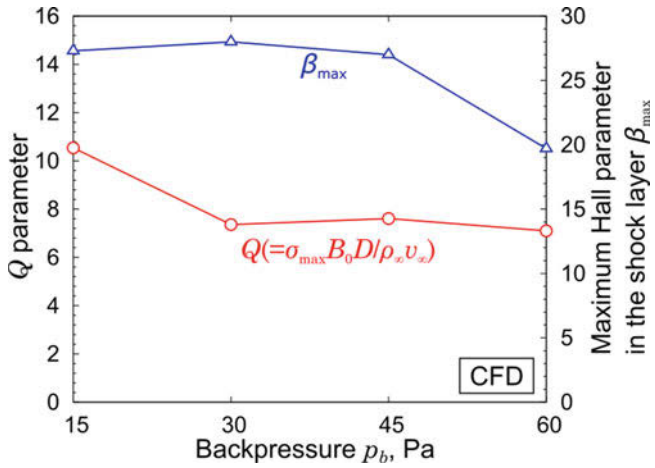

Fig. 6 The back pressure dependences of maximum Hall parameter β_{max} and Q parameter

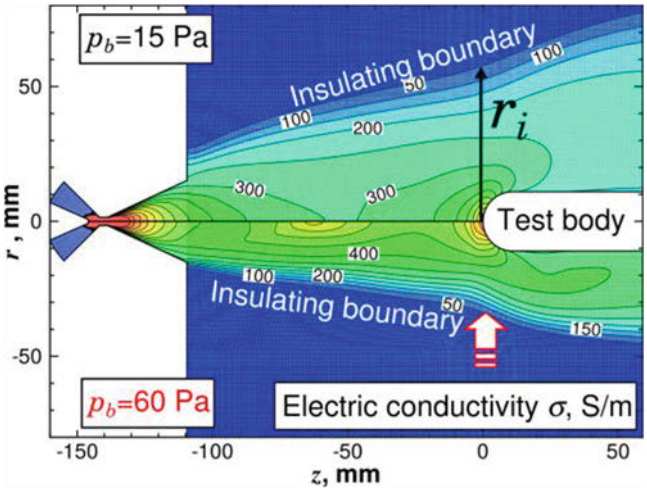

Fig. 7 Computed electric conductivity σ and the insulating boundary location

5 Comparison between the Measured and Computed Total Drags

Figure 9 shows the measured and computed back pressure dependency of D_t (with and without $\boldsymbol{B}$) and its increase rates by applying $\boldsymbol{B}$, which is defined as $\Delta D_t{}^{\text{with } B}/D_t{}^{\text{w/o } B}$.

As shown in Fig. 9a, the values of D_t in all the cases increase by applying $\boldsymbol{B}$, but the measured D_t is larger by 30–40 mN than those of the computation. The

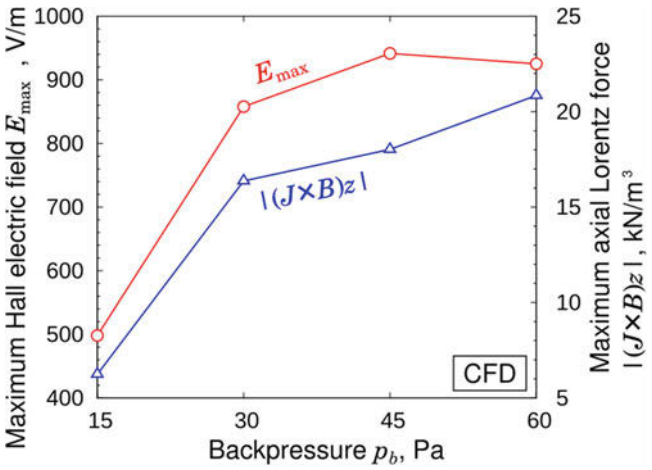

Fig. 8 The back pressure dependences of the maximum values of the Hall electric field $E_{\max}$ and axial Lorentz force $(\boldsymbol{J} \times \boldsymbol{B})_z$

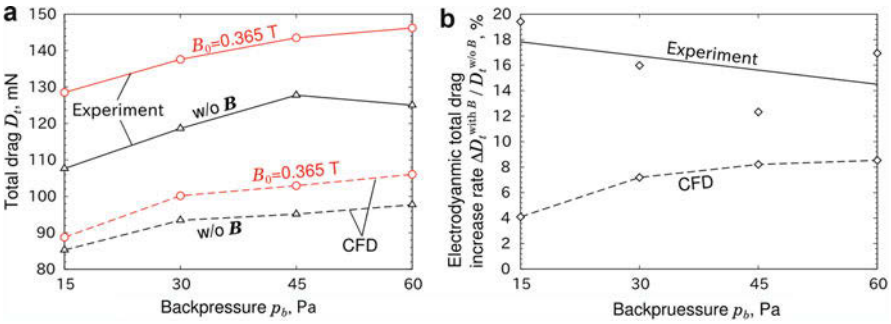

Fig. 9 The measured and computed back pressure dependency of the total drag (with and without $\boldsymbol{B}$) and its increase rate by applying $\boldsymbol{B}$. (**a**) Total drag D_t vs. p_b. (**b**) The electrodynamic total drag increase rate $\Delta D_t^{\text{with } B}/D_t^{\text{w/o } B}$ vs. p_b

electrodynamic increase of D_t in the measurement is approximately 20 mN in all p_b, which is also much larger than the values of 5–10 mN in the computation.

Moreover, contrary to the CFD prediction that $\Delta D_t^{\text{with } B}/D_t^{\text{w/o } B}$ will increase with p_b because the insulating boundary is closer to the body, the measured $\Delta D_t^{\text{with } B}/D_t^{\text{w/o } B}$ is almost constant or has a decreasing tendency with p_b, as shown in Fig. 9b.

The reason of these disagreements between the measurement and the computation is not clear. A possible reason is the CFD prediction error of the arc flow characteristics: the flow in the experiment might have a larger Q or smaller β (i.e., denser) than that of the CFD prediction.

In the future study, we will measure the electron density and electron temperature of the arc flow using the laser Thomson scattering (LTS) method in order to know

the characteristics of the flow. And we will conduct the direct measurement of the Lorenz drag by measuring the force on the magnet.

6 Conclusion

The CFD predicted that the plume radius (i.e., insulating boundary location) r_i decreases with increasing p_b, and the decrease of r_i increases the $|\boldsymbol{E}|$ and the resulting axial Lorentz force.

In all the cases of the experiment and CFD, the values of D_t increase by applying $\boldsymbol{B}$, but the measured D_t is larger by 30–40 mN than those of the computation. The electrodynamic increase of D_t in the measurement is approximately 20 mN in all p_b, which is also much larger than the values of 5–10 mN of the CFD.

Contrary to the CFD prediction that the electrodynamic increase rates of D_t, which is defined as $\Delta D_t{}^{\text{with } B}/D_t{}^{\text{w/o } B}$, will increase with p_b because the insulating boundary is closer to the body, the measured $\Delta D_t{}^{\text{with } B}/D_t$ is almost constant or has a decreasing tendency with p_b.

References

1. A.R. Kantrowitz, Proc. Conf. High Speed Aeronaut., 335–339 (1955)
2. R.W. Ziemer, W.B. Bush, Phys. Rev. Lett. **1**, 58 (1958)
3. R.W. Ziemer, Am. Rocket Soc. J. **29**, 642 (1959)
4. R. Nowak, M.C. Yuen, AIAA J. **11**, 1463 (1973)
5. R.J. Nowak et al., J. Spacecr. Rockets **4**, 1538 (1967)
6. J. Poggie, D.V. Gaitonde, Phys. Fluids **14**, 1720 (2002)
7. H. Otsu et al., AIAA J. **48**, 2177 (2010)
8. T. Fujino et al., J. Spacecr. Rocket. **43**, 63 (2006)
9. Y. Takizawa et al., Phys. Fluids **18**, 117105 (2006)
10. A. Matsuda et al., Phys. Fluids **18**, 027102 (2008)
11. M. Kawamura et al., J. Spacecr. Rocket. **46**, 1171 (2009)
12. H. Katsurayama et al., AIAA Paper 2008-4016 (2008)
13. H. Katsurayama, T. Abe, J. Appl. Phys. **113**, 053304 (2013)

Blast Wave Propagation Affected by Ground Characteristics

A. Lipshtat and S. Pistinner

Abstract Blast waves are being formed by aerial, surface, or subsurface explosions. The waves propagate in the surrounding media – air and\or ground. In cases of aerial or surface explosion, blast waves are being formed in the ambient air. The waves hit the ground and form a ground shock wave. Ground contraction due to high pressure coming from above followed by rapid expansion may produce a new shock wave, going upward from ground surface. The original wave propagation may be affected as well. Ground movements may also cause fracturing and fragmentation, thus contributing to dust lofting. Suspended dust mitigates aerial wave propagation. All these phenomena, accompanied by ground deformation, make the ground an active agent affecting the aerial shock propagation.

In this study we examine the mechanism of ground wave interaction by means of numerical simulations. To this aim we employ a homemade ALE code, named ParaSALE, which includes a variety of equations of state, strength models, and other material-dependent parameters. Dust lofting scheme is based on Mirels' analysis and assumptions (AIAI J. 22:1582–1589, 1984). Above some threshold friction velocity, vertical momentum dissipation of the horizontal momentum is converted into a vertical mass flow of dust. If the turbulent mass flux is stronger than the gravitational force, the lofted dust particles are coupled to the flow field and being carried by it (Shao, Physics and modeling of wind erosion, Springer, New York, 2008). Changing ground characteristics affects both the ground dynamics and aerial wave. We simulate both sub- and above-surface explosions with various ground specifications. Effects on crater formation and wave propagation will be presented and analyzed.

A. Lipshtat (✉) · S. Pistinner
Soreq Nuclear Research Center, Yavne, Israel
e-mail: eliezerli@soreq.gov.il

A. Sasoh et al. (eds.), *31st International Symposium on Shock Waves 2*,
https://doi.org/10.1007/978-3-319-91017-8_79

1 Introduction

Large explosions may be responsible to massive destruction mainly due to the blast waves following the explosion. Blast waves are formed at the explosion foci (Ground Zero, GZ) and propagate in ambient media. Thus, the measured effect at large distance from GZ is a composition of the blast source with the propagation function. In cases of underground explosions, where propagation takes place mainly within ground, it is obvious that ground characteristics play a major role in shaping the propagated wave. However, ground effects are less evident in cases of surface or aerial explosions. In these cases there may be several routes in which ground characteristics may interfere with wave formation and propagation [3], and this study examines the extent to which each of these mechanisms affects the overall phenomena.

1.1 Ground Effect at Subsurface Explosions

Underground explosions may form compression, shear, and surface waves. Propagation of these waves and its dependence on ground characteristics are well studied in context of seismicity. Phenomenological location-dependent velocity models [4, 5] as well as global theoretical models [6] are in common use. For the purpose of this study, it would suffice to note that as long as uniform media is assumed, ground characteristics affect propagation via its equation of state (EOS). The EOS of granular material and minerals under compression conditions are qualitatively and quantitatively similar to those of solids. Under tension conditions the situation may be quite different as granular material has a stronger resemblance to fluids rather than to solid minerals. Therefore, in cases where the pressure is negative, ideal gas EOS can be used in order to model the fluidized soil. In reality, beyond a limited radius, the ground cannot be considered as uniform. Continuous or abrupt changes in density, acoustic impedance, and other characteristics cause reflections, mitigation, and other deviations from the naïve route of propagated wave.

1.2 Ground Effect at Surface and Aerial Explosions

The main focus of this study is ground effect on aerial explosion blast waves. Blast wave formed by above-surface explosions propagates mainly in ambient air. However, there are several ways in which existence of ground below the explosion point can affect the blast wave propagation.

Direct effect of ground can be mediated by process of dust lofting. Initial surface explosion produces blast waves which propagate in both air and ground. Ground wave runs faster than the air wave. Depending on ground composition and structure, the running wave may granulate the ground. Thus, at the time in which the aerial wave arrives, the ground is made of small grains that can easily be carried by the aerial wave. This way, the amount of lofted dust depends on soil

and ground coverage. It is already known that propagation in pure air is different than propagation in dust-air suspension [7], and this way, ground characteristics interfere with aerial wave propagation.

Another mechanism is due to crater formation. Based on ground characteristics, blast wave approaching the ground may be reflected or transmitted into the ground. The typical case is partial reflection, whereas some fraction of the energy deforms the air-ground boundary. Thus, the amount of energy which is released to the air and form the aerial blast wave depends on ground characteristics.

2 Numerical Simulations

In order to investigate blast wave propagation and its sensitivity to ground characteristics, we have employed a homemade numeric code named ParaSALE [8]. ParaSALE includes variety of material-dependent parameters such as equations of state and strength models and thus is adequate for this type of research. It is the 3-D code and 2-D axisymmetric phenomena are modeled with wedge geometry. The 3-D nature of the code allows sufficient flexibility that allows 2-D plane geometry as well.

We start with demonstrating results of simulating an underground spherical charge buried under dry soil (Fig. 1). We present density, pressure, and velocity of both ground and gaseous phases. Comparing these results to those of similar simulation with aluminum replacing the dry soil, we see that the opening is much wider in the soil case than in the aluminum grounding. This is due to the much stronger tendency to fluidization of the soil. The fluidized matter slows down the flow velocity, and thus the velocities in this simulation are slower than velocities in the aluminum ground case. We conclude that both crater dimensions and blast wave propagation following underground explosions depend on ground characteristics.

As opposed to underground explosions, blast wave due to surface explosions travels mainly in ambient air. However, there is also a significant fraction of energy that hits the ground and penetrates into it. This is why a crater is observed at the GZ. Explosions of sufficient energy produce body waves in the ground, which can be detected by seismometers located large distances away. It is well known that seismic waves are materially dependent. Here we claim that directed and reflected wave propagating in ambient air may be affected by ground characteristics as well. Partial support to this statement can be found in the underground explosion results presented above. We've shown that lofted dust affects wave propagation. This effect is expected to hold true for either sub- or above-surface explosions. Since dust lofting depends on ground characteristics, we conclude that ground characteristics should be taken into account in all cases.

Theoretical foundation can be given to the dependence of aerial wave on ground characteristics, which may provide some quantitative predictions as well.

Following dust lofting, the medium in which wave propagation takes place is a dust-air suspension. For every material dispersed-phase volume, the governing equation written in terms of mass loading is

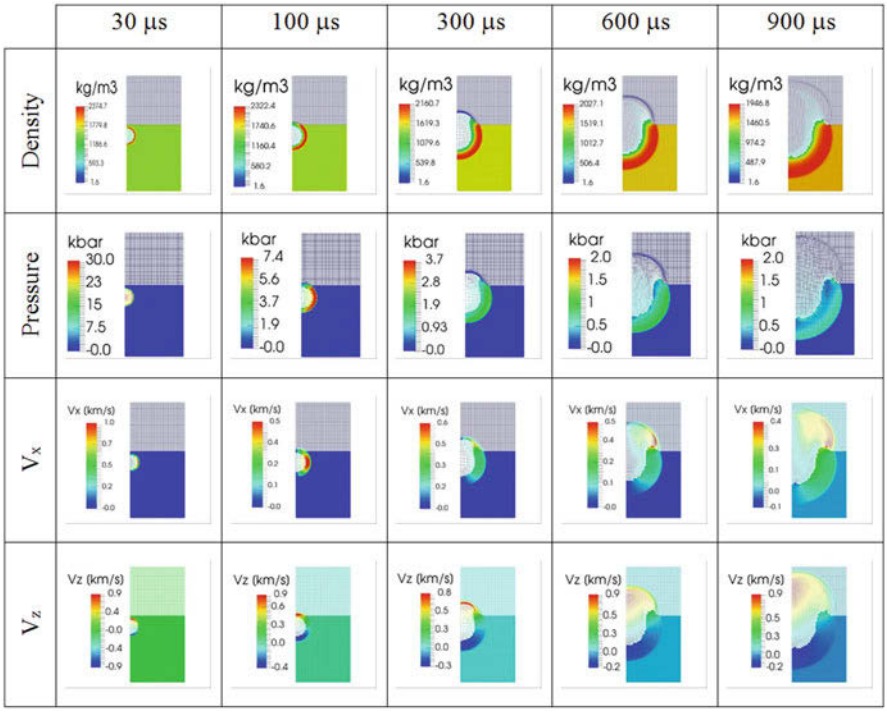

Fig. 1 Evolution of an underground spherical charge explosion buried in dry soil

$$\frac{d_m\left(\rho_m c_\alpha\right)}{dt} + \left(\rho_m c_\alpha\right)\nabla\cdot\left(u_m\right) = -\nabla\cdot\left(\rho_m c_\alpha u_{m\alpha}\right) \tag{1}$$

where $\frac{d_m}{dt} \equiv \frac{\partial}{\partial t} + u_m\cdot\nabla$ is the mixture Lagrangian derivative, c_α is the mass fraction of phase α, and $u_{m\alpha}$ is the relative velocity between phase α and the mixture. Dust particles of different particle radii can be viewed as different phases. Formally, one could now carry an ensemble average of Eq. (1), and assuming that there are no fluctuations in the mixture density and mixture velocity, one would get an additional term which is the turbulent transport term, namely

$$\frac{d_m\left(\rho_m c_\alpha\right)}{dt} + \left(\rho_m c_\alpha\right)\nabla\cdot\left(u_m\right) = -\nabla\cdot\left(\rho_m c_\alpha u_{m\alpha}\right) - \nabla\cdot\left(\rho_m\overline{c'_\alpha u'_{m\alpha}}\right) \tag{2}$$

where the over bar denotes ensemble averaging. This fluctuating term is approximated via the Boussinesq hypnosis of eddy viscosity (of the mixture).

We now turn our attention to the non-fluctuating term in Eq. (2). More specifically, we analyze this term in the turbulent boundary layer in the vicinity of the granular surface. The region of the boundary layer in our simulations is underresolved (about 5–50 cm for a single grid cell), and one must study the subgrid scales analytically. Typical velocities are of order of 100 m/s so that the time scale

to flow through a grid cell is O (1 ms). An individual particle relaxation time scale is given by [9, 10]:

$$\tau \approx \frac{\rho_p d_d^2}{\rho_f 18\nu} \approx 0.3 \times 10^{-2} \left(\frac{d_p}{1\mu}\right)^2 ms \tag{3}$$

which is O(0.01 ms) for 1 μm diameter particles and O(1 ms) for 10 μm particles. In Eq. (3) the subscripts p and f denote particle and fluid, respectively, ν is the air kinematic viscosity, and d_p is a typical particle diameter. Thus, for sufficiently small particles, one can assume that $u_{m\alpha} \approx 0$ and obtain

$$\rho_m \frac{d_m u_m}{dt} \approx \nabla P_m - \rho_m \overrightarrow{g} \tag{4}$$

$$\frac{d_m \left(\rho_m c_\alpha\right)}{dt} + \left(\rho_m c_\alpha\right) \nabla \cdot \left(u_m\right) \approx 0 \tag{5}$$

whereas for larger dust grain, the terms $\nabla \cdot \tau_{turb}$ and $-\nabla \cdot \left(\rho_m \overline{c'_\alpha u'_{m\alpha}}\right)$ become significant and affect propagation dynamics. These terms are treated analytically within the boundary layer.

In addition to shock mitigation by dust-air suspension, ground composition may affect wave propagation via the cratering process. Different ground compositions have different strength models and may react in various ways to the hitting shock. An ideal reflecting ground would reflect all the incoming energy back to the air, strengthening and intensifying the propagated wave. In Fig. 2 we present the wave front location for the two scenarios. The fully reflected wave propagates faster. This result is not surprising as in this case all the energy is directed to the propagating wave rather than into the ground.

In Fig. 3 we present the blast wave resulting from a large explosion. The presented wave is defined as the area in which overpressure is measured ($P > 1$ bar). In

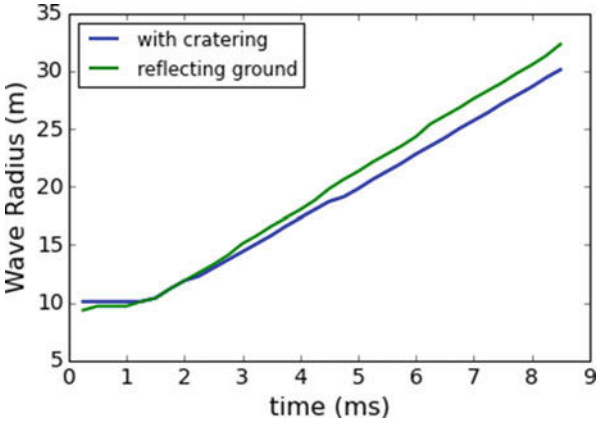

Fig. 2 Wave front propagation with (blue) and without (green) cratering

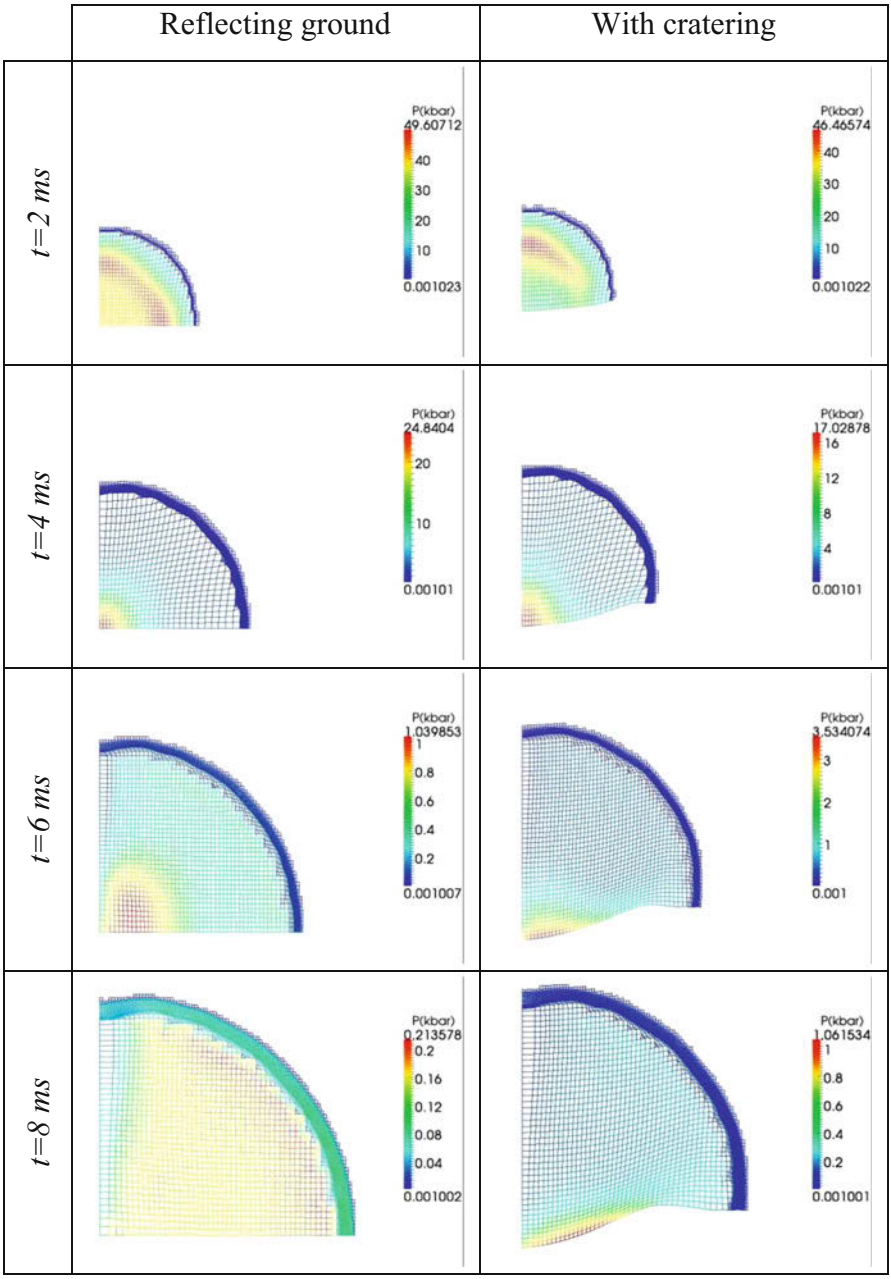

Fig. 3 Pressure maps of blast wave with (right) and without (left) cratering

one case cratering was allowed, whereas ideal reflecting ground was assumed for the other case. It can be seen that the resulting pressure maps are different. Reflecting ground delivers the propagated wave away in an approximately radial symmetric manner, whereas ground flexibility significantly amplifies the overpressure in crater vicinity and exhibits much higher-pressure maxima. These findings may affect the damage expectations that are predicted to follow such an explosion.

3 Summary and Discussion

Even though aerial and ground waves are studied as independent phenomena, in reality they may be strongly coupled [3]. Here we demonstrate how changes in ground characteristics may affect propagation of aerial blast waves. We outline various mechanisms by which such coupling may be implemented. These include wave mitigation by dust lofting [7] and changes in energy partition between aerial and ground waves. In addition, in cases of non-isotropic ground composition, ground waves may be directed back to surface and form new aerial waves, even though these are not expected to be as strong as the blast wave.

All these phenomena require detailed quantitative description and mathematical modeling which are beyond the scope of this study.

References

1. H. Mirels, Blowing model for turbulent boundary layer dust ingestion. AIAI J. **22**, 1582–1589 (1984)
2. Y. Shao, *Physics and Modeling of Wind Erosion* (Springer, New York, 2008)
3. S.J. Arrowsmith, J.B. Johnson, D.P. Drob, M.A.H. Hedlin, The seismoacoustic wavefield: A new paradigm in studying geophysical phenomena. Rev. Geophys. **48**, RG4003 (2010)
4. H. Magistrale, S. Day, R.W. Clayton, R. Graves, The SCEC Southern California reference three-dimensional seismic velocity model version 2. Bull. Seismol. Soc. Am. **90**(6B), S65–S76 (2000)
5. D. Eberhart-Phillips, M. Reyners, S. Bannister, M. Chadwick, S. Ellis, Establishing a versatile 3-d seismic velocity model for New Zealand. Seismol. Res. Lett. **81**(6), 993 (2010)
6. D. Komatitsch, J. Tromp, Spectral-element simulations of global seismic wave propagation-II. Three-dimensional models, oceans, rotation and self-gravitation. Geophys. J. Int. **150**(1), 303 (2002)
7. A. Lipshtat, S. Pistinner, Blast mitigation by dust lofting – Theoretical perspective, in *ISSW-30 Proceedings*, (2016)
8. D. Sidilkover, *ParaSALE – A plasto-dynamic sale code*, private communication (2011)
9. K. Hiltunen, A. Jasberg, et al., *Multiphase Flow Simulations* (VTT Publication, Helsinki, 2009), p. 722
10. S. Kallio, A. Akademi, *On the Mixture Model of Multiphase Flow* (VTT Publication, Helsinki, 1996), p. 288

Multiple Reflected Shock Wave in Closed Volume with Granular Screen

O. Mirova, S. V. Golovastov, A. Kotelnikov, V. Golub, and T. Bazhenova

Abstract Pressure decrease of the shock wave is investigated at reflection from the end of the shock tube channel passing through a sand layer. The influence of the layer location on the pressure pulse extension and on the decrease of the maximal pressure amplitude behind the shock wave is studied. A shock tube was consisted of high-pressure and low-pressure chambers in 72×72 mm^2 square cross sections. The high-pressure chamber represented a "short" section, 25 cm long, to create the shock wave with the decreasing profile. The impact of a shield made of granulated material on attenuation of the shock wave multiply reflected from walls is investigated at an explosion inside a closed volume. We performed the experiments in the shock tube with a short high-pressure chamber. The low-pressure chamber was filled with air at atmospheric pressure. The flat blast wave with the reducing pressure profile was created. We discover the dependency of the pressure reduction at the reflected wave front on the distance between the protecting shield and the closed end of the shock tube.

1 Introduction

At the shock wave propagation inside a closed volume, additional temperature and pressure increase take place behind the reflected shock waves [1, 2]. The presence indoors of the combustible gas mixture might cause burning and detonation. In order to attenuate the action of the reflected (from the walls) shock wave, the use of shields made of lightly degradable material is recommended in [3–5]. It was shown in [3–5] that the thinner the shield thickness, the less the impulse of the wave reflected from the shield. It is valid for both short [3, 4] and long [5] shock waves. When attenuation of the shock wave reflected from the wall is stronger, the velocity of the protecting material dispersion is greater [3]. With the layer thickness decrease, the shield

O. Mirova · S. V. Golovastov (✉) · A. Kotelnikov · V. Golub · T. Bazhenova
Joint Institute for High Temperatures of the Russian Academy of Sciences (JIHT RAS), Moscow, Russia

A. Sasoh et al. (eds.), *31st International Symposium on Shock Waves 2*,
https://doi.org/10.1007/978-3-319-91017-8_80

material dispersion velocity increases under the shock wave impact. Attenuation of the shock wave reflected from the sand shield takes place predominantly due to the rarefaction wave catching it up; this rarefaction wave occurs at the refracted shock wave coming from the protecting layer on the back surface of the shield.

The shock wave passing through the shield is reflected from the solid wall and catches up the shock wave reflected from the shield. The maximal amplitude of the second reflected wave is several times less than at reflection of the nondeformed shock wave, as was shown in [4]. In the multifraction gas suspension with particles, the wave-structure dissipation and wave-structure dispersion take place [6], thus contributing to their attenuation.

In the present work, we investigate the influence of the protecting shield location on the shock wave attenuation coefficient behind the reflected shock wave and after the multiple reflection from the shock tube end.

2 Experimental Facility

The shock tube consisted of high-pressure (HPC) and low-pressure (LPC) chambers (Fig. 1) in 72 × 72 mm^2 square cross sections. In the LPC, the atmosphere pressure air was present; we pumped air into the HPC up to pressure of ∼5 atm. Then, the diaphragm was broken and the shock wave propagated over the LPC to the closed-end side. The Mach number of the shock wave was within 1.65–1.75. The measurement procedure of parameters of the shock wave is described in detail in [7].

The high-pressure chamber represented a "short" section, 25 cm long, to create the shock wave with the decreasing profile. At the low Mach numbers of the shock wave, in the HPC, the rarefaction wave "head" rapidly caught up the shock wave and the characteristic pressure profile occurred behind it, similar to the pressure profile behind the blast wave. The distance from the wave front to the point where the pressure dropped to 1 atm equaled 48 cm, that is, in the point of the G3 gauge location. In the side LPC wall, we installed three pressure gauges (G1, G2, G3); the fourth gauge (G4) was installed at the end. The presence of the three gauges made

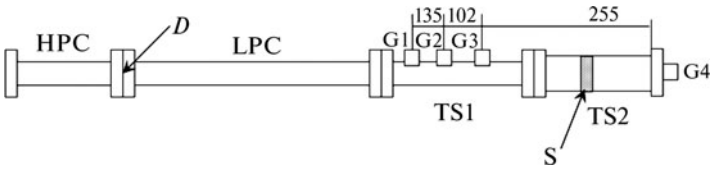

Fig. 1 Layout of the experimental facility to study the effect of the protecting shield made of lightly destructed material (one-dimensional case): HPC, high-pressure chamber; LPC, low-pressure chamber (the given distances between them – in mm); TS1, TS2, test sections; G1–G4, pressure gauges; D, diaphragm; S, shield

it possible to determine not only the pressure in the given tube section but also the velocity and direction of the passing-by shock wave.

In the TS2 cross section, we installed the different thickness protecting shields (S) consisting of the pressed natural sand.

3 Experimental Results and Discussion

3.1 Pressure at the Closed End

We used the oscillograms of the pressure gauge in the end of the test section TS2 to measure the pulse of the shock wave passing to the end of the test section after its interaction with the shield. We installed the shields with different thicknesses (20, 30, 40, and 50 mm) at different distances *S* from the TS2 end. In each experimental set, the distance from the end (and, respectively, from the G4 gauge) varied from 0 (the sand wall was installed closely to the end) to 120 mm.

We defined the pressure attenuation coefficient *K* as the ratio of the pressure on the front of the shock wave reflected from the unprotected end of the shock tube to the maximal pressure at the end after the reflection of the shock wave passing through the sand layer.

At the interaction with the shield, the shock wave decays into two waves: reflected and transmitted. The last reflects from the end and propagates following the wave reflected from the shield. To estimate the effect of the second reflected wave on the increase of the pressure in the chamber, we measured the pressure in the tube end after the shock wave interaction with the shield, at different distances from the shield to the end.

Typical pressure oscillograms from the gauge located behind the shield, at the shock wave end, at two shield thicknesses (40 mm and 50 mm) can be found in [7]. On the base of pressure oscillograms after the shock wave interaction with the sand shield, the parameters of the pressure pulse extension (duration increases and the maximal amplitude decreases) were measured. For example, the maximal pressure amplitude decreases from 8 atm to 2 atm and 1.5 atm for the shield thicknesses of 40 mm and 50 mm, respectively.

Figure 2 shows the dependence of the shock wave attenuation coefficient behind the reflected shock wave on the distance between the sand layer and the end. Data are given for three thicknesses: 20 mm, 30 mm, and 40 mm. As can be seen from the Fig. 2, the dependence of the coefficient has a nonmonotonic character. The minimum value of the attenuation coefficient is recorded for the 40–80 mm. For the greater distances from the closed end, the value of the attenuation coefficient sufficiently increases. Maximal registered values are 2.0–3.5.

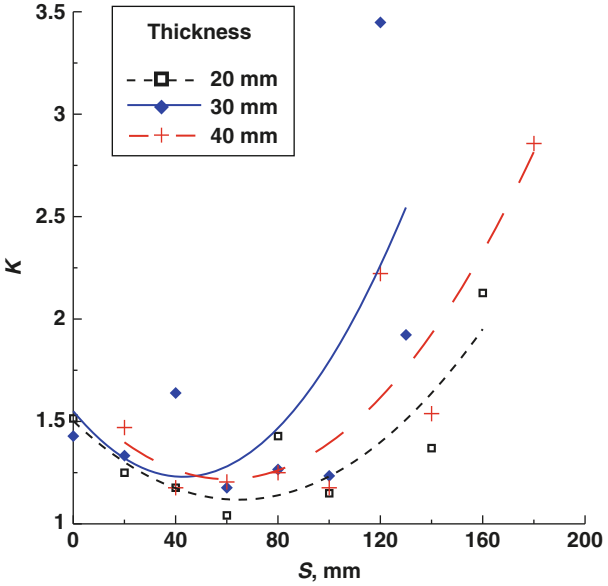

Fig. 2 Dependencies of the shock wave attenuation coefficient K on the distance between the protecting shield and the right end of the shock tube for three thicknesses: 20, 30, and 40 mm

3.2 Pressure after Multi-reflection

In the experiments with multi-reflection of the shock wave, we installed the shields inside the LPC; the shields were 20 mm thick, made of pressed natural sand. We placed the sand wall at different distances from the shock tube end: $S = 0$–15 mm.

The upper part of Fig. 3 shows the X–T diagram of the subsequent blast wave reflections in the shock tube. The time scale is broken in order to show the shock wave movement with higher resolution. The shock wave partly reflected from the sand obstacle and partly passed through it. In the obstacle destruction process, the shock wave deformed, its amplitude decreased, and the positive phase duration increased. Figure 3 shows the trajectories of incident shock wave (1), and of the shock wave reflected from the right end (2), and then from the left end (3), and once more from the right end of the shock tube (4). The dotted line represents the shock wave trajectory after its interaction with the destructed sand wall; the arrows show the shock wave direction within each section.

The procedure for determination of the pressure attenuation is similar above. In more detail for multi-reflected shock waves, this procedure is given in [8]. The characteristic oscillograms on time are presented in Fig. 4. The pressure oscillograms obtained by means of the gauges installed in the LPC illustrate the process of subsequent reflections, during 60 ms of the blast wave from the shock tube ends (its total length being 8.5 m). Figure 4 shows the pressure oscillograms

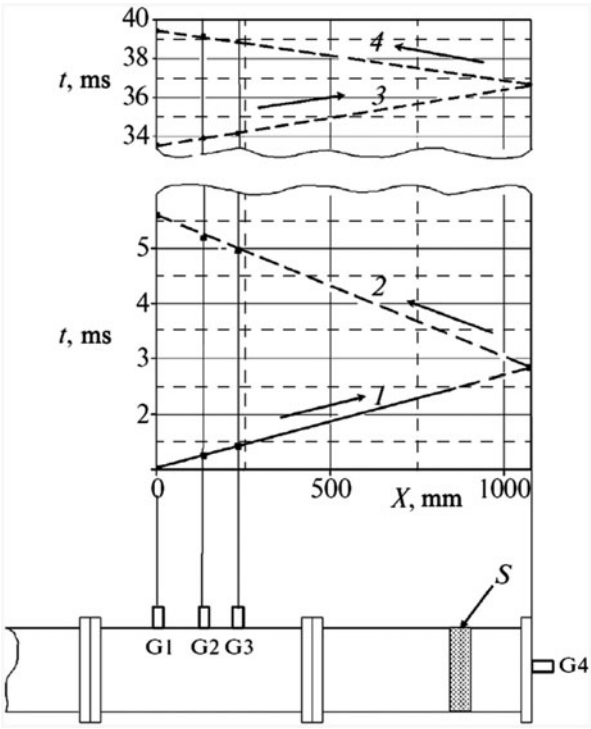

Fig. 3 Low-pressure chamber of the shock tube and X–T diagram of the shock wave movement: G1–G4, pressure gauges; S, protecting shield made of pressed sand

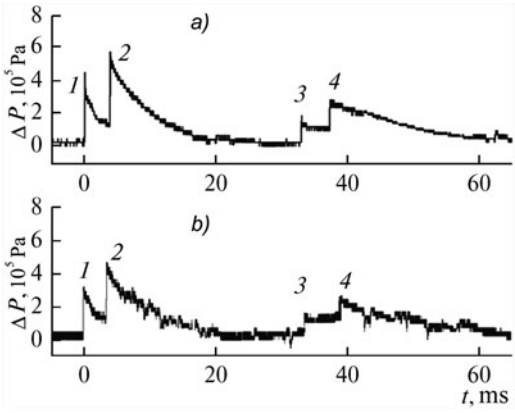

Fig. 4 Pressure oscillograms at the position of G3 gauge when the left end of the shock tube is unprotected (**a**) and when the protecting shield, 20 mm thick, is installed at a distance of 5 cm from the left end (**b**). 1, incident shock wave; 2, wave reflected from the right end of the shock tube; 3, wave reflected from the left shock tube end; 4, the secondary wave reflected from the right shock tube end

(the G3 gauge) obtained in the experiments without the protecting shield (Fig. 4a) and with the protecting shield, 20 mm thick, installed at a distance of 5 cm from the right end of the shock tube (Fig. 4b).

The maximal amplitude of the secondary reflected (from the right end) shock wave, 4, is higher than the same of the wave 3 reflected from the left end but four times less than that of the wave, 2, the first reflected from the left end of

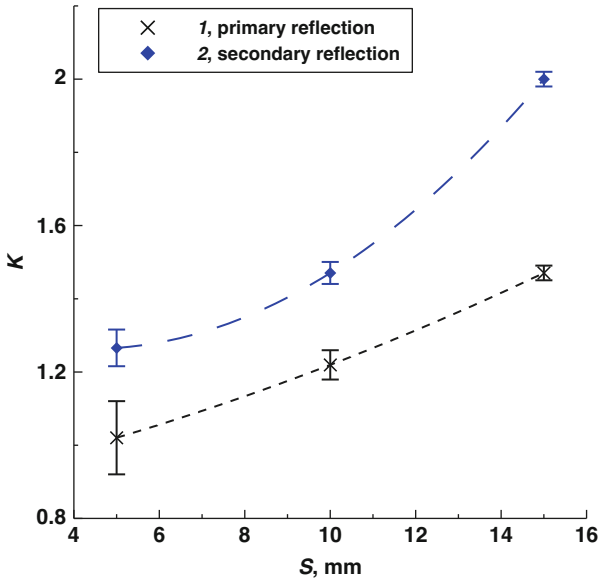

Fig. 5 Dependency of the shock wave attenuation coefficient, K, on the distance between the protecting shield and the right end of the shock tube for primary reflection (*1*) and secondary reflection (*2*)

the shock tube. The following two factors influence the pressure value behind the nonstationary shock wave: the pressure decreases when propagating along the channel, and the pressure increases at the reflection from the ends. In our experimental conditions, the first factor dominates. As a result, the maximal pressure behind the shock wave decreases during its propagation. With the protecting shield presence (Fig. 4b), the amplitudes of the respective disturbances are less than in the nonprotected chamber (Fig. 4a).

From the pressure oscillograms obtained by means of the G3 gauge at the different locations of the protecting shield in respect to the closed shock wave end, we determined the values of the pressure behind the shock wave and the coefficient of its attenuation. Figure 5 shows the coefficient K of the amplitude attenuation of the shock wave reflected from the right shock tube end for the primary, 1, and the secondary, 2, reflections.

An increase of the distance from the shield to the end enhances the decrease of the maximal pressure behind the reflected waves because, at the larger shield-end distance, the path of the wave passing through the shield to the reflecting surface is respectively larger and the wave undergoes larger deformation. The pressure decreases with the distance increase from 5 cm to 15 cm. Further increase of the shield-end distance is nonconstructive as it causes the channel encumbering and requires an increase of sand mass. The above-determined pressure attenuation

coefficient, K, for the protecting shield location at the distance of 5–15 cm from the right shock tube end equals 1.01–1.4 for the first reflection and 1.28–2.0 for the second reflection.

4 Conclusions

The sand shield located at a certain distance from the protected surface reduces the pressure by several times. The higher the distance from the shield to the end, the higher the pressure decrease, the higher the shock wave attenuation coefficient. If a similar shield is attached tightly to the surface, the pressure behind the shock wave remains the same as at reflection from the rigid metal wall.

The protecting action of the sand shield reduces the maximal pressure at the explosion in the closed channel under the multiple reflection of the blast wave from the channel ends.

The above-determined pressure attenuation coefficient K for the protecting shield location at the distance of 5–15 cm from the right shock tube end equals 1.01–1.4 for the first reflection and 1.28–2.0 for the second reflection.

Acknowledgments The work is supported by the Russian Science Foundation, Project no. 14-50-00124.

References

1. S.V. Onufriev, Temperature of products of a hydrogen-air mixture explosion in conical cavity. High Temp. **50**, 244 (2012)
2. B.E. Gel'fand, S.P. Medvedev, S.V. Khomik, V.L. Agafonov, Self-ignition of hydrogen-air mixtures behind reflected explosive waves. High Temp. **48**, 436 (2010)
3. T.V. Bazhenova, V.V. Golub, O.A. Mirova, et al., Attenuation of impact of the reflected shock wave upon an explosion inside a vessel with granular material walls. High Temp. **50**, 447 (2012)
4. A.L. Kotel'nikov, O.A. Mirova, V.V. Golub, et al., Study of an interaction of a blast wave with a destructible screen made of a granular material. High Temp. **52**, 708 (2014)
5. O.A. Mirova, A.L. Kotel'nikov, V.V. Golub, T.V. Bazhenova, Shock wave effect on protective sand screens of different thicknesses. High Temp. **53**, 155 (2015)
6. D.A. Gubaidullin, E.A. Teregulova, D.D. Gubaidullina, Acoustic wave propagation in multi-fraction gas suspensions. High Temp. **53**, 713 (2015)
7. O.A. Mirova, A.L. Kotel'nikov, V.V. Golub, T.V. Bazhenova, Protecting shield influence on pressure decrease at shock wave interaction with the wall. High Temp. **54**, 905 (2016)
8. O.A. Mirova, A.L. Kotel'nikov, V.V. Golub, T.V. Bazhenova, Multiple shock wave reflections at an explosion in a closed volume with shielded walls. High Temp. **55**, 315 (2017)

Some Aspects of the Numerical Modeling of Shock Wave–Dense Particle Bed Interaction Using Two-Fluid Approach

P. Utkin

Abstract The work is dedicated to the parametric numerical study of the shock wave with the dense particle bed interaction. The problem is solved using two-fluid approach when both gaseous and dispersed phases are considered to be compressible media nonequilibrium on velocities and pressures. The determinative system of equations has the hyperbolic type and is solved using HLL numerical scheme. The statement of the problem corresponds to the natural experiment. The main features of the process are obtained in the calculations, namely, the formation of the transmitted and reflected waves and the motion of the particle cloud with sharp front edge and smearing trailing edge. The comparison of the amplitudes of the reflected and transmitted waves as well as the dynamics of the cloud motion with the experimental data is carried out. The investigation of the influence of the dispersed phase equation of state parameters and some properties of the numerical methods on the process is carried out.

1 Introduction

A lot of both experimental and theoretical investigations of two-phase flows with shock waves (SW) deal with dusty gas. But not much work addresses to the dense two-phase flows, although there are a lot of applications such as internal ballistic problems, convective burning in heterogeneous media, dust layer dispersion, and so on.

So the up-to-date problem is the construction of numerical procedures efficient for the calculation of two-phase flows with wide range of possible regimes – from dilute with low dispersed-phase volume fraction to the dense with the dispersed-

P. Utkin (✉)
Institute for Computer Aided Design of the Russian Academy of Sciences, Moscow, Russian Federation

Moscow Institute of Physics and Technology, Moscow Region, Russian Federation
e-mail: pavel_utk@mail.ru

A. Sasoh et al. (eds.), *31st International Symposium on Shock Waves 2*,
https://doi.org/10.1007/978-3-319-91017-8_81

phase volume fraction close to the packing limit. The analysis of recent papers [1–4] shows that most of such approaches are based on two models. The first one is the two-fluid Baer–Nunziato model [5], and the second one is the kinetic theory of granular media [6].

A canonical problem that can be used to study modeling issues related to the dense high-speed multiphase flows is a SW impacting a planar particle cloud [7, 8]. The goals of the paper are (i) the formulation of the mathematical model and the numerical algorithm for the description of dense two-phase flows on the basis of two-fluid approach, (ii) its verification using known experiments on SW–dense particle cloud interaction, and (iii) investigation of the influence of some hard interpreted from natural experiments' point of view parameters of the numerical approach on the results of modeling.

2 Statement of the Problem

The statement of the problem corresponds to the natural experiments [9]. The one-dimensional frame Ox is considered. The beginning of the frame corresponds to the left boundary of the computational area with the length 2.8 m. The coordinate of the left boundary of the glass spherical particle cloud is 1.39 m; the coordinate of the right boundary is 1.41 m. The diameter of the particles is 1.5 mm; the real density is 2500 kg/m^3. The initial dispersed-phase volume fraction in the cloud is 0.65. At the initial time moment, SW is located near the right boundary of the cloud and moves to the left. The gas pressure is measured using three sensors in the points with the coordinates 0.692 m (sensor No. 1), 1.367 m (sensor No. 2), and 1.520 m (sensor No. 3).

At the initial time moment, the area in front of the SW is filled with the quiescent air under normal conditions. In the rest part of the computational area, the parameters behind the SW with the Mach number 1.3 which moves in the negative direction of Ox axis are set.

The nonpenetrating condition is imposed on the left boundary; the inflow condition is imposed on the right boundary. The total simulation time is 4 ms in accordance with the duration of the SW compression stage in the experiments [9].

3 Mathematical Model and Numerical Algorithm

Mathematical model is based on the system of equations from [10] which describes two-fluid compressible flows:

$$\mathbf{u}_t + \mathbf{f}_x(\mathbf{u}) = \mathbf{h}(\mathbf{u})\,\alpha_{1x} + \mathbf{p} + \mathbf{s},$$

$$\mathbf{u} = \begin{bmatrix} \alpha_1 \\ \alpha_1\rho_1 \\ \alpha_1\rho_1 v_1 \\ \alpha_1\rho_1 E_1 \\ \alpha_2\rho_2 \\ \alpha_2\rho_2 v_2 \\ \alpha_2\rho_2 E_2 \end{bmatrix}, \mathbf{f} = \begin{bmatrix} 0 \\ \alpha_1\rho_1 v_1 \\ \alpha_1\left(\rho_1 v_1^2 + p_1\right) \\ \alpha_1 v_1\left(\rho_1 E_1 + p_1\right) \\ \alpha_2\rho_2 v_2 \\ \alpha_2\left(\rho_2 v_2^2 + p_2\right) \\ \alpha_2 v_2\left(\rho_2 E_2 + p_2\right) \end{bmatrix}, \mathbf{h} = \begin{bmatrix} -v_i \\ 0 \\ p_i \\ p_i v_i \\ 0 \\ -p_i \\ -p_i v_i \end{bmatrix},$$

$$\mathbf{p} = \begin{bmatrix} \mu\left(p_1 - p_2\right) \\ 0 \\ 0 \\ \mu p_i\left(p_2 - p_1\right) \\ 0 \\ 0 \\ \mu p_i\left(p_2 - p_1\right) \end{bmatrix}, \mathbf{s} = \begin{bmatrix} 0 \\ 0 \\ -f \\ -f \cdot v_i \\ 0 \\ f \\ f \cdot v_i \end{bmatrix},$$

$$\alpha_1 + \alpha_2 = 1, E_1 = \frac{v_1^2}{2} + \frac{p_1 + \gamma_1 P_0}{\rho_1\left(\gamma_1 - 1\right)}, E = \frac{v_2^2}{2} + \frac{p_2}{\rho_2\left(\gamma_2 - 1\right)},$$

$$p_i = \alpha_1 p_1 + \alpha_2 p_2, v_i = \frac{\alpha_1\rho_1 v_1 + \alpha_2\rho_2 v_2}{\alpha_1\rho_1 + \alpha_2\rho_2}.$$

Here the notations are standard: α is the volume fraction and ρ is the real density. Parameters with the index 1 correspond to the dispersed phase and with the index 2 to the gaseous phase. The stiffened-gas equation of state (EOS) with the parameters γ and P_0 is used for the dispersed phase. For the calculation of interphase force f, the closing relations from [3, 6] are used.

Parameter μ is the dynamic compaction viscosity coefficient which was introduced in [5] for the description of the pressure relaxation at the phase interfaces. Vector $\mathbf{p}$ is the correction of one-dimensional model taking into account the multidimensional processes at the interphase boundaries. In this paper the interphase condition $p_1 = p_2$ is used. This condition is taken into account in the pressure relaxation procedure. Note that the phase's pressure equilibrium is not the prior assumption that can lead to the non-hyperbolicity of the determinative system but the additional condition which is applied at the interphase boundaries.

The numerical algorithm in general follows [10] and is based on the splitting approach. Computational algorithm for one time-step integration consists of three stages. At first the hyperbolic step is carried out with $\mathbf{p} = 0$ and $\mathbf{s} = 0$, then pressure relaxation procedure [11], and then integration of the algebraic right-hand side term $\mathbf{s}$. Hyperbolic step is carried out using the numerical scheme HLL (Harten-Lax-van Leer) taking into account the consistent approximation of the right-hand side term $\mathbf{h}(\mathbf{u})\alpha_{1x}$ (the condition "a two-fluid system, uniform in velocity and pressure at t = 0 will be uniform on the same variable during its temporal evolution" [12] should be fulfilled). The time step is chosen dynamically from the stability criterion. For

the numerical algorithm approximation order increase, the minmod reconstruction of the conservative vector components in the computational cell is used.

4 Results of the Numerical Experiments

4.1 General Characteristics of the Process

For the determinative system of equations to be hyperbolic in all computational cells, both phases should exist so it is imposed $\alpha_1 = 10^{-7}$ at the initial time moment out of the bounds of the bed. The parameters of the dispersed-phase EOS that are used in the computations are presented in Table 1. Their influence on the characteristics of the process is investigated in Sect. 4.2. All computations are carried out on the mesh with the cell number 22,400. CFL number is equal to 0.5.

Consider the results of the numerical experiment No. 1 (see Table 1). Interaction of the incident SW with the dense bed leads to the formation of two waves – reflected wave (RW) and transmitted wave (TW) – and the bed moves due to the interphase friction force and the pressure difference to the left and to the right of the bed. RW ($x \approx 1.9$) and TW ($x \approx 0.85$) are clearly visible in Fig. 1a on pressure distribution. Gas dynamic parameters behind the waves are not constant, that is, partially connected with the cloud motion with the velocity up to the 10 mm/s. As the dispersed phase is considered to be compressible fluid, its density varies during the cloud motion. The maximum density variation is about 0.08%. In the problem in consideration, the formal compressibility of the particles as well as the existence of the pressure in the dispersed phase should be considered as part of the numerical approach that provides the robust simulations in the presence of the interphase boundaries.

During the motion of the cloud, the profile of the dispersed-phase volume fraction changes. The significant smearing of the boundaries of the cloud occurs. The backward boundary is smeared more than the front one; see blue lines in Fig. 1b. In [9] the experimental (green lines in Fig. 1b) and calculated (red line in Fig. 1b) data are presented. The obtained results are in reasonable agreement but demonstrate

Table 1 Parameters of the numerical experiments

Numerical experiment number	P_0, Pa	γ_1	Numerical scheme spatial approximation order
1	10^8	2.5	2
2	10^9	2.5	2
3	10^{10}	2.5	2
4	10^7	2.5	2
5	10^8	2.0	2
6	10^8	3.0	2
7	10^8	2.5	1

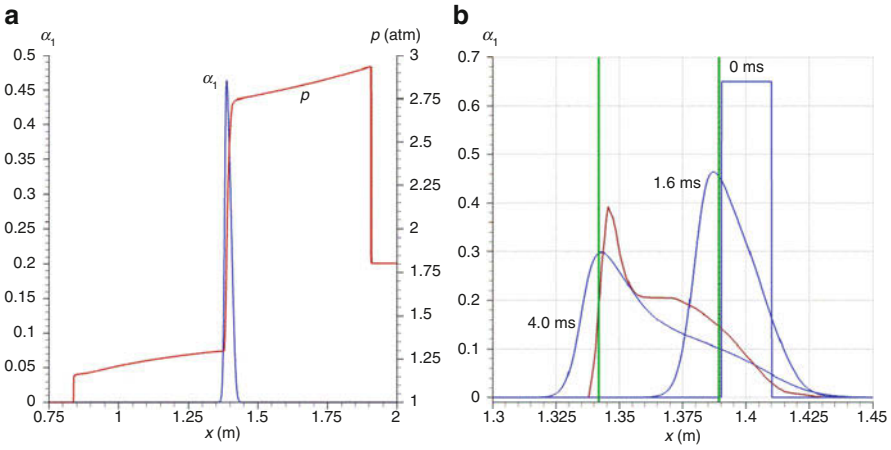

Fig. 1 Predicted spatial distributions in the calculation No. 1 (see Table 1): (**a**) dispersed-phase volume fraction and pressure at the time moment 1.6 ms and (**b**) dispersed-phase volume fraction at three successive time moments (blue lines), calculated distribution from [9] (red line) at the time 4.0 ms, and experimental bound of the bed at the time 4.0 ms [9] (green lines)

that less dissipative numerical scheme should be used. The statement corresponded to the natural experiments [9] was also investigated numerically in [3, 10] but none of these works contains the spatial profiles of α_1 to compare. In [3, 10] the problem of SW–particle bed interaction is used as one of the tests which demonstrate the principal applicability of the numerical approach without parametric study and the recommendations about the choice of the parameters of the mathematical model.

Figure 2a illustrates the quantitative comparison of the calculated and experimental pressure curves for three sensors. Sensor No. 3 is placed upstream and registers RW. Sensors No. 1 and 2 are placed downstream and show the dynamics of TW. The closing relations for the interphase force f affect both the speeds and the amplitudes of RW and TW. The maximal relative error between the calculated and experimental values is ∼7% for sensor No. 1 (on the falling part of the curve), ∼23% for sensor No. 2 (on the part from 2.5 up to 3.5 ms), and ∼5% for sensor No. 3. The largest error for the sensor No. 2 is due to the inaccuracy in the particle cloud motion description. Nevertheless the model reproduces correctly the important feature of the problem, namely, the changes of the pressure curve growth rate at the sensor No. 2 at the time moments 2.5 and 3.5 ms. The changes are conditioned by the motion of the particles cloud over the point where the sensor is placed.

The comparison of the experimental and the calculated pressure curves for the sensor No. 3 demonstrates the pulsations on the falling part of the curve in the experiment that are absent in the calculations. Among the possible reasons for that are the measurement errors in the experiment and the fact that the incident SW is not ideally flat. In the experimental data [9], one can see the pressure pulsations behind the incident SW. The order of the pulsations is the same as behind the RW, about 2–3%. Another reason is the multidimensional effects in the natural experiments due

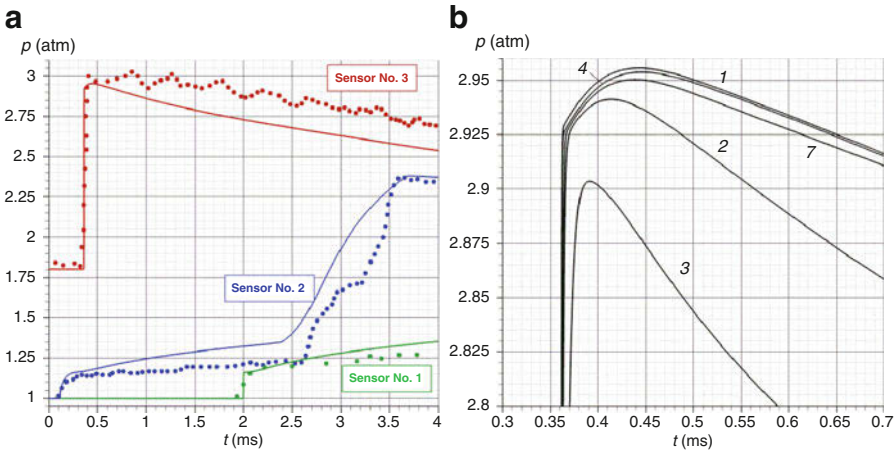

Fig. 2 (**a**) Comparison of the calculated (solid lines) and experimental (points) pressure curves at the sensors in calculation No. 1, (**b**) the effect of EOS parameters and algorithm's approximation order, calculated pressure curves at sensor No. 3, and numbers of curves corresponding to Table 1

to the multiple reflections of the incident SW from the particles. The scale of such effects can be estimated from [7]. In [7] two-dimensional case, that is, for the array of cylinders not the spheres for the similar incident SW strength (Mach number 1.67) and the dispersed-phase volume fraction 0.15, the pulsations on the curve of planar-averaged pressure for the RW are about the same 2% of the amplitude. One more reason of multidimensional effects which is noted in [9] is the existence of boundary layer near the tube walls that leads to the visible curvature of the particle cloud shape near the walls on the experimental snapshots. The analysis of such effect is possible using multidimensional extension of the described numerical approach.

4.2 Effect of the Parameters of the Dispersed-Phase Equation of State and Numerical Scheme Approximation Order

In order to use the described numerical approach for the mathematical modeling of the practical applications, it is necessary to realize the influence of the dispersed-phase EOS parameters to the results of modeling. The parametric studies of the influence of hard interpreted in natural experiments γ and P_0 parameters as well as the numerical algorithm approximation order were carried out (see Table 1). The influence of the mentioned parameters is investigated on the example of pressure curve at sensor No. 3 behavior (see Fig. 2b).

In the first four calculations, the influence of parameter P_0 was investigated. It is obtained that the increase of P_0 in comparison with the basic value 10^8 Pa up to two orders of magnitude leads to the worse agreement between the experimental and

calculated data. At the same time, the increase of P_0 leads to the integration time-step decrease and so to the significant computational costs. The value $P_0 = 10^7$ Pa provides the same results as the basic value with error of fractions of percent. Analogously in the numerical experiments No. 5 and 6, the value of γ_1 was varied. It is obtained that the decrease of γ_1 down to 2.0 and the increase up to 3.0 don't lead to the significant change of the results (curves No. 5 and 6 in Fig. 2b are situated between curves No. 1 and 4 and are not plotted). So the results of modeling are insensitive to the variation of dispersed-phase EOS parameters at least in the range $P_0 = 10^7$–10^8 Pa, $\gamma_1 = 2.0$–3.0. The conclusion seems to be important as for a number of practical application, for example, internal ballistics problems, the parameters of the dispersed-phase EOS are priory unknown.

The influence of the approximation order is investigated in calculation No. 7. Against expectation the influence of higher approximation order is small; see curves No. 1 and No. 7 in Fig. 2b. This means that the main efforts on improving the numerical algorithm properties should be connected with the usage of less dissipative numerical flux in comparison with HLL and the corresponding consistent approximation of non-conservative differential right-hand side terms; see, for example, [13].

5 Conclusions

The parametric numerical investigation of the problem of SW–dense particle bed interaction in the statement of [9] is carried out. In the numerical simulations, the main characteristics of the process are obtained, namely, the formation of TW and RW and the motion of the particle cloud with the backward boundary more smeared than the front one. The dynamics of cloud motion reasonably correlates with the experimental and calculated data from [9]. The maximal relative error between experimental and numerical pressure curves for the different sensors varies from 5 up to 23%. The principal effect of the pressure curve growth rate changes at the sensor due to the particle cloud motion obtained.

As the determining system of equations, the model [10] is used with the closing relations for the interphase force [3, 6]. The numerical algorithm is based on the physical process splitting approach and uses HLL method for the numerical flux calculation and for the nonconservative right-hand side-term approximation [10] and pressures relaxation algorithm for the robust calculation process in the presence of interphase boundaries [11] and minmod reconstruction for the second approximation order achievement.

The investigations of the influence of dispersed-phase EOS parameters and some properties of the numerical algorithm on the characteristics of the process are carried out. It is shown that the results of modeling are insensitive to the variation of dispersed-phase EOS parameters at least in the range $P_0 = 10^7$–10^8 Pa, $\gamma_1 = 2.0$–3.0.

The reported study is partially funded by grant of the President of the Russia Federation for ypung PhD scientists (contract No 14.W01.16.6756-MK) and partially by the Federal Agency for Scientific Organizations.

References

1. T.A. Khmel', A.V. Fedorov, Combust. Explos. Shock Waves. 50, 2 (2014)
2. T. Khmel, A. Fedorov, J. Loss Prev. Process Ind. **36**, 223 (2015)
3. R.W. Houim, E.S. Oran, J. Fluid Mech. **789**, 166 (2016)
4. T.P. McGrath II, J.G. St Clair, S. Balachandar, J. Appl. Phys. **119**, Paper 174903 (2016)
5. M.R. Baer, J.W. Nunziato, Int. J. Multiph. Flow **21**, 861 (1986)
6. D. Gidaspow, *Multiphase Flow and Fluidization* (Academic Press, 1994)
7. J.D. Regele, J. Rabinovitch, T. Colonius, G. Blanquart, Int. J. Multiph. Flow **61**, 1 (2014)
8. V.M. Boiko, V.P. Kiselev, S.P. Kiselev, A.N. Papyrin, S.V. Poplavsky, V.M. Fomin, Shock Waves **7**, 275 (1997)
9. X. Rogue, G. Rodriguez, J.F. Haas, R. Saurel, Shock Waves **8**, 29 (1998)
10. R. Saurel, R. Abgrall, J. Comp. Phys. **150**, 425 (1999)
11. R. Saurel, O. Lemetayer, J. Fluid Mech. **431**, 239 (2001)
12. R. Abgrall, J. Comp. Phys. **125**, 150 (1996)
13. S. Liang, W. Liu, L. Yuan, Comp. Fluids. **99**, 156 (2014)

To the Complex Approach to the Numerical Investigation of the Shock Wave: Dense Particle Bed Interaction

D. Sidorenko and P. Utkin

Abstract The problem of planar shock wave–dense particle cloud interaction is solved using two approaches. In the first one, the two-dimensional gas dynamics modeling of the interaction of the planar shock wave with Mach number 1.67 with the set of cylinders is carried out. The original author's numerical algorithm of the Cartesian grid method is used. The set of cylinders models the dense particles cloud with the volume fraction 0.15. As a result of interaction, the collective reflected and transmitted waves are formed. In the second approach, the one-dimensional system of equations for the description of the dense two-phase flows is solved. Results of one-dimensional modeling are matched with the cross-section averaged pressure distribution from the two-dimensional calculation. The quantitative agreement is achieved. The specific features of the process are discussed. We formulate the idea of complex approach to the investigation of the shock wave–dense particle cloud interaction that is based on the getting of the drag coefficient of the particles bed from the results of the multidimensional calculations and the comparison of those results with the calculation using the two-phase model.

1 Introduction

A canonical problem that can be used to study modeling issues related to the dense high-speed multiphase flows is a shock wave (SW) impacting a planar particles cloud [1, 2]. The problem is of interest from several points of view. First of all there are some particular applications such as blast waves attenuation during the accidents in the mining industries [3]. On the other hand, the statement is close to the fundamental Riemann problem for the two-phase flows. Even the formulation

D. Sidorenko · P. Utkin (✉)
Institute for Computer Aided Design of the Russian Academy of Sciences, Moscow, Russian Federation

Moscow Institute of Physics and Technology, Moscow Region, Russian Federation
e-mail: pavel_utk@mail.ru

A. Sasoh et al. (eds.), *31st International Symposium on Shock Waves 2*,
https://doi.org/10.1007/978-3-319-91017-8_82

of the basic equations of the mathematical model for the description of two-phase flows applicable from dense to dilute particle environments using the approach of the heterogeneous media mechanics is an opened question up to now (see, e.g., the recent paper [4, 5]).

For the clarification of the features of the process SW–particle cloud interaction, the multidimensional gas dynamics simulations are used [1, 6, 7]. In [6] the array of motionless cylinders that were arranged transversally to the flow was considered. The types of the interactions of the reflected waves were classified. It was also demonstrated that the wave patterns for the flows around the cylinder and the sphere are essentially different. In [7], two motionless spheres (two-dimensional (2D) calculations in the axisymmetric statement) arranged along the flow direction were considered. The curves for drag coefficients variations in time for both spheres against the distance between the spheres are obtained. In [1] the two-dimensional gas dynamics numerical simulations are used to capture qualitatively the multi-dimensional behavior of three-dimensional cloud. The obtained solution is also used as the "exact" solution to compare with the one-dimensional volume-averaged models. The results of simulations show the importance of multidimensional effects connected with Reynolds stress terms inside the particle cloud and in its turbulent wake.

The very important issue which significantly affects to the possibility of such multidimensional gas dynamics modeling is the numerical algorithm in use because the computational domain is multiply connected and couldn't be covered by the structured computational grid. In [6, 7] the simulations were carried out using ANSYS Fluent. In two-dimensional simulations, the computational cells were quadrilateral; the details about grid structure and the numerical algorithm are unknown. In [1] the authors use Cartesian grid and the general Riemann-type solver. So the geometry of the cylinder boundaries is steplike that can lead to artificial effects during shock reflections. The results presented in this paper are based on the special numerical algorithm of the Cartesian grid method [8] which provides the numerical integration of gas dynamics equations in the shaped form domains.

The goal of the paper is the comparison of 2D gas dynamics simulations of the SW passing through the array of motionless cylinders that qualitatively reproduces the initial stage of the SW–particle cloud interaction process with the one-dimensional (1D) simulations of the same problem using two-phase approach [9].

2 Statement of the Problem and the Numerical Approaches

The statement of the 2D problem corresponds to that in [1] (see Fig. 1, lower part). The extended computational domain is the rectangular $[-2.5; 3.5] \times [-0.5; 0.5]$. We impose inflow condition with set parameters on the left boundary $X = -2.5$, zero-order extrapolation on the right boundary $X = 3.5$ (calculations last up to the moment of transmitted shock arrival to the right boundary), and periodic conditions

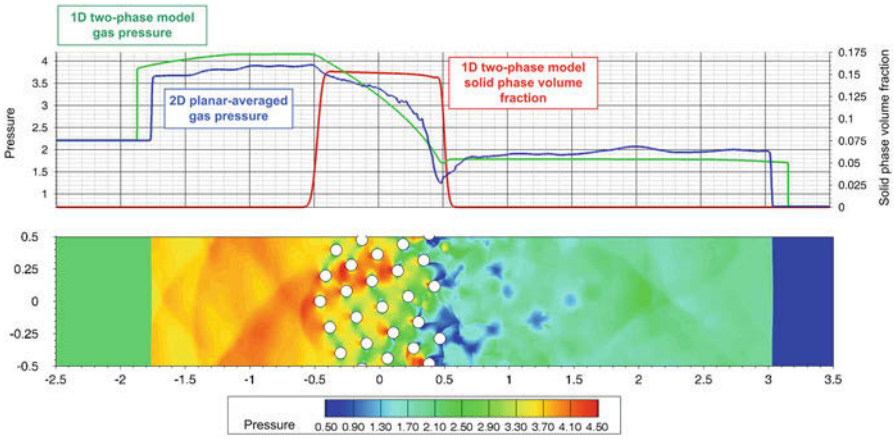

Fig. 1 Comparison of 2D gas dynamics simulation with 1D two-phase model simulation

on the upper and lower boundaries $Y = -0.5$ and $Y = 0.5$ to simulate an infinitely long array of cylinders. The inflow parameters correspond to that behind the SW with Mach number 1.67. The "cloud" located between $X = -0.5$ and $X = 0.5$ is modeled by 26 cylinders which are fully (within the domain) or partially (at the boundaries) placed on the extended computational domain. As it was derived in [1], the cylinder arrangement from Fig. 1 lower part provides the more uniform distribution of the planar-averaged cross sections of the "cloud" in comparison with a number of common regular arrangements. The average solid-phase volume fraction of the considered cylinder configuration is 0.15. The main computational domain is obtained by the subtraction of the inner part of the cylinders from the extended rectangular area.

We solve the Euler equations in the main computational domain. The determinative system of equations is transformed to the dimensionless form using character scales from [1]. The original numerical algorithm of the Cartesian grid method [10] for the integration of 2D gas dynamics equations in the domains with curvilinear boundaries which is based on the idea of "h-boxes" from [8] is used. The algorithm consists of the following stages:

1. The building of simple uniform Cartesian computational grid with square cells for the extended domain with the division of all computational cells into inner, cut, and outer ones. The last ones (in our case the cells inside the cylinders) don't take part in the calculation at all. One of the restrictions of the method in consideration is that the element of curvilinear boundary within the cell is approximated by the straight line segment. However the situation is quite typical for the majority of the methods (including general boundary fitted methods) and is conditioned by the degree of discretization in process of boundary approximation. So the cut cell has one of three possible shapes: triangle, tetragon, or pentagon.

2. The usage of the common explicit finite volume scheme [11] for the numerical integration of the determinative system in both regular and cut cells. Integration time step is chosen dynamically from the stability criterion but based on the parameters in the inner cells only. The stable calculation process is obtained by the usage of special approach for the numerical flux calculation through the edges of the cut cells.
3. Numerical flux calculation through the edges of the inner cells using classical Godunov scheme in the realization [11].
4. Numerical flux calculation through the edges of cut cells using specially constructed h-boxes. H-boxes are the parallelograms with the bases on the cut cell edges and constructed in each of four directions which are defined by the orientation of the boundary edge of the cell (two perpendicular and two parallel directions). The vector of conservative variables in the h-box is defined as the weighted arithmetic mean of the vectors of conservative variables in cells that the h-box intersects. The weights correspond to the relative areas of intersections. Some of h-boxes can be in part or in whole beyond the main computational domain. For the parts of such h-boxes which are beyond the main computational domain, we build the correspondent "mirror" h-boxes with changed normal component of gas velocity. As the parameters in h-boxes are known, the numerical fluxes through the edges of cut cells can be calculated. The rotated grid method [12] is used here.

Computational cell size is equal to 1/800. Note that it is possible to consider the particle "clouds" from the dilute ones with the dispersed-phase volume fraction about several hundredths up to the dense ones using the described statement and the Cartesian grid method. The usage of Cartesian grid method provides the automatic statement and calculation of each configuration with variation of cylinders number and their size as well as the shape of the cylinders (almost arbitrary contours in almost arbitrary amount are superimposed on the uniform Cartesian grid) and don't demand the rebuilding of the computational grid. The numerical algorithm is verified on the problems of SW – wedge [13] and SW – one cylinder [14] interactions as a result of comparison of experimental and calculated pressure or density distributions along the bodies.

The problem in the same statement was considered using two-phase 1D model [9]. The phases are considered to be compressible and non-equilibrium on velocities and pressures. The dispersed phase is described using stiffened-gas equation of state with the parameters $\gamma = 2.5$, $P_0 = 10^8$ Pa. The 1D frame Ox is considered. The beginning of the frame corresponds to the center of the particles cloud with the length 1.0 (see Fig. 1, upper part). The coordinate of the left boundary of the spherical particles cloud is -0.5, and the coordinate of the right boundary is 0.5. The diameter of the particles is 0.089. The initial dispersed-phase volume fraction in the cloud is 0.15. At the initial time moment, SW is located near the left boundary of the cloud and moves to the right. At the initial time moment, the area in front of the SW is filled with the quiescent air under normal conditions. In the rest part of the computational area, the parameters behind the SW with the Mach

number 1.67 which move in the positive direction of Ox axis are set. The zero-order extrapolation condition is imposed on the right boundary, and the inflow condition is imposed on the left boundary. As the closing relationships for the interphase force the correlations from [15] for the array of cylinders were used that are similar to the Ergun formula for the drag force in the porous bed of spherical particles [16]:

$$f = \left[\alpha_1 \frac{\alpha_s \mu}{\alpha d^2} + (\alpha_2 + \alpha_3 \alpha_s) \frac{\alpha_s}{\alpha} \frac{\rho |v_s - v|}{d}\right] (v_s - v)\,, \quad \alpha_1 = 106.7, \alpha_2 = 0.59, \alpha_3 = 4.84. \tag{1}$$

Here, α and α_s are the volume fractions for the gaseous and the dispersed phases correspondingly, v and v_s are the velocities for gaseous and the dispersed phases, μ is gas viscosity coefficient, d is the diameter of cylinders, and ρ is the real density of the gas.

3 Results of the Numerical Experiments

At the initial stage of the process of SW–array of cylinders interaction, the reflected wave consisting of several parts due to the incident SW reflection from the single cylinders forms (see Fig. 2). The strength of the reflected wave increases in time because of the additional contribution of the disturbances coursed by the interaction of the leading SW with the cylinders downstream. As a result after some time, the almost flat collective reflected wave ($X \approx -1.8$ in Fig. 1, lower part) and transmitted wave ($X \approx 3.0$) form. The flow in the wake of the "cloud" is highly perturbed with the formation of the structures like Karman vortex street. In case of inviscid model in use, the effects of turbulence are conditioned by the artificial scheme viscosity. For the possibility of the comparison of the results of 2D gas dynamics modeling with the results of 1D two-phase modeling, the planar-averaged parameters in 2D simulations are calculated. The corresponding pressure profile is depicted in Fig. 1, upper part, blue line.

In both simulations the pressure behind the reflected wave is not constant due to the contribution of the additional disturbances downstream. One can see the feature which is discussed in [1], namely, the clearly visible gap on pressure profile on the right boundary of the cloud in 2D simulation which is almost absent in 1D case. This 2D effect is connected with the Reynolds stress tensor within the cloud and in the turbulent wake. For its correct simulation in 1D case, the special right-hand side term in determinative system of equations was introduced in [1].

The correlation of pressure profiles in Fig. 1 upper part is more qualitative. Note that the closing relation (1) was obtained in [15] for much more slow flows of incompressible fluid, and its usage strictly speaking is not well argued for the problem in consideration although it is written in terms of dimensionless Reynolds number. At the same time, there is a lack of closing terms for the high-speed flows in literature. The idea of the complex approach is to obtain new data or make

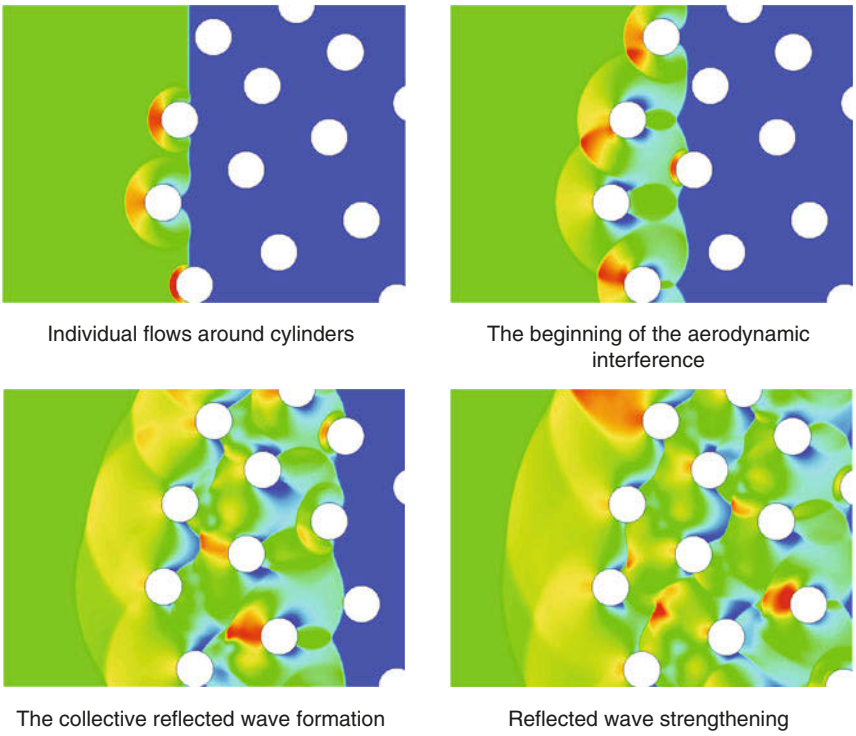

Fig. 2 The stages of the SW–array of cylinders interaction. Pressure distributions at the successive time moments

more precise existing one (e.g., in terms of coefficients α_1, α_2, α_3 in (1)) for the drag coefficient of the particles bed as a result of the above-described comparison of results of detailed multidimensional gas dynamics modeling with the results of modeling using two-phase models.

4 Conclusions

The complex numerical investigation of the problem of SW–particle "cloud" interaction is carried out. The results of gas dynamics modeling using Euler equations and Cartesian grid method demonstrate the formation of collective reflected and transmitted waves after several stages of the process (individual flows around cylinders, the aerodynamic interference, the strengthening of the reflected wave). The principal difference of the described statement in comparison with [6, 7] is the usage of 2D arrangement of the cylinders, so the cylinders downstream are flown with essentially different parameters in comparison with the forward ones. The results of 2D gas dynamics modeling are compared with the results of 1D two-

phase calculations. The qualitative agreement between the pressure profiles using the drag coefficient for the array of cylinders from [15] is achieved. The following work on the adjusting of drag coefficient law is to be done.

The reported study is partially funded by grant of the President of the Russia Federation for young PhD scientists (contract No 14.W01.16.6756-MK) and partially by the Federal Agency for Scientific Organizations.

References

1. J.D. Regele, J. Rabinovitch, T. Colonius, G. Blanquart, Int. J. Multiphase Flow **61**, 1 (2014)
2. V.M. Boiko, V.P. Kiselev, S.P. Kiselev, A.N. Papyrin, S.V. Poplavsky, V.M. Fomin, Shock Waves **7**, 275 (1997)
3. S.N. Medvedev, S.M. Frolov, B.E. Gel'fand, J. Phys. Eng. **58**, 924 (1990)
4. R.W. Houim, E.S. Oran, J. Fluid Mech. **789**, 166 (2016)
5. T.P. McGrath II, J.G.St. Clair, S. Balachandar, J. Appl. Phys. **119**, Paper 174903 (2016)
6. I.A. Bedarev, A.V. Fedorov, V.M. Fomin, Comb., Expl. Shock Waves. **48**, 446 (2012)
7. I.A. Bedarev, A.V. Fedorov, J. Appl. Mech. Tech. Phys. **56**, 750 (2015)
8. M. Berger, C. Helzel, SIAM J. Sci. Comp. **34**, A861 (2012)
9. R. Saurel, R. Abgrall, J. Comput. Phys. **150**, 425 (1999)
10. D.A. Sidorenko, P.S. Utkin, Num. Meth. Programm. **17**, 353 (2016)
11. E.F. Toro, *Riemann Solvers and Numerical Methods for Fluid Dynamics*, 3rd ed. (Springer, 2009)
12. Y.-X. Ren, Comput. Fluids **32**, 1379 (2003)
13. H.M. Glaz, P. Colella, I.I. Glass, R.L. Deschambault, Proc. Royal Soc. London A. **298**, 117 (1985)
14. K. Takayama, K. Itoh, Proc. 15th Int. Symp. on Shock Waves and Shock Tubes **439** (1985)
15. Y. Tanino, H.M. Nepf, J. Hydraul. Eng. **134**, 34 (2008)
16. S. Ergun, Chem. Eng. Prog. **48**, 89 (1952)

Numerical Study of Dusty Shock Reflection over a Double Wedge

Jingyue Yin, Juchun Ding, and Xisheng Luo

Abstract The shock reflection over a double wedge in dusty gas is numerically investigated in the present paper by the VAS2D (two-dimensional and axisymmetric vectorized adaptive solver) program which solves the compressible two-phase Euler equations with second-order accuracy in space and time. The non-equilibrium effects on the reflection wave configuration are emphasized. The reflection process for a shock wave propagating in dusty gas greatly differs from the pure gas case, and the wave configuration is found to depend on the distance traveled by the incident shock. The reflection wave structures with a short scale are different from that with a large scale. The non-equilibrium effects related to the particle relaxation change the transition criterion and complicate the shock reflection process.

1 Introduction

Shock reflection problem occurs in supersonic and hypersonic flows, and the related studies are of benefit for a large number of man-made applications such as aircraft design and detonation control. Mach was the first to discover two different shock configurations in shock reflection problem: regular reflection (RR) and Mach reflection (MR). The transition between MR and RR has attracted increasing attention since it may affect the flow structure and further the flow performance. Shock reflection has been intensively studied experimentally, numerically, and theoretically [1]. Previous studies on the shock reflection are mainly focused on the case of pure gas. In many real applications such as the explosive safety in coal mines [2], the environmental gas is often filled with small particles, which is referred to as dusty gas. As a shock wave penetrates into a dusty gas, the particles become in equilibrium with the gas except for a transition region behind the shock wave where the non-equilibrium effect manifest. As time proceeds, the non-equilibrium region

J. Yin (✉) · J. Ding · X. Luo
Advanced Propulsion Laboratory, Department of Modern Mechanics, University of Science and Technology of China, Hefei, China
e-mail: jyyin@mail.ustc.edu.cn

A. Sasoh et al. (eds.), *31st International Symposium on Shock Waves 2*,
https://doi.org/10.1007/978-3-319-91017-8_83

of the mixture develops gradually into an equilibrium state through the transfer of momentum and heat between the gas and particles. Due to such complicated mechanisms of dusty flow, the transition criteria for pure gas are never applicable.

In 1962, Saffman derived the equations describing the motion of a gas carrying small dust particles [3], and effects of two parameters for the dusty flow are emphasized including the concentration of the particles and the relaxation time. The mechanisms of heterogeneous flow were reviewed by Marble [5] with an assumption that the volume fraction of the particles and the interaction between them are ignored. Also, some other related problems such as point source dusty flow [6], dusty flow in variable cross-sectional tube [7], and shock-induced dusty flow [8] were reported. In 1983, Miura performed a systematical study on the passage of a shock wave in pure gas through a dusty gas layer [9], and the criteria for the wave reflection at the contact surface separating the pure gas and dusty layer were obtained. However, that work is based on the idealized equilibrium gas that ignores the transition region behind the shock. Saito et al. numerically studied the one-dimensional dusty flow in a shock tube, and the RR configuration transits to MR structure as a planar shock propagates along a single wedge [10]. Effects of the particle size and the mass fraction on the shock reflection problem were investigated in detail by Igra [2].

Shock reflection over a double wedge is a classical problem, and the related studies are helpful for supersonic flows. Ben-Dor had investigated the shock reflection over a double wedge in pure gas and found seven complex types of reflection structures [11]. So far, the non-equilibrium effects caused by particle relaxation on the shock reflection over a double wedge have seldom been analyzed, which motivates the present work.

2 Numerical Methods

Assuming all the particles are spherical and share the same size and specific heat as well as neglecting particle gravity and the collision between particles, dilute particle-gas flows can be governed by continuum medial model, written as:

$$\frac{\partial \mathbf{U}}{\partial t} + \frac{\partial \mathbf{F}}{\partial x} + \frac{\partial \mathbf{G}}{\partial y} = \mathbf{S} \tag{1}$$

$$\mathbf{U}=\begin{pmatrix}\rho\\ \rho u\\ \rho v\\ \rho E\\ \rho_p\\ \rho_p u_p\\ \rho_p v_p\\ \rho_p E_p\end{pmatrix};\ \mathbf{F}=\begin{pmatrix}\rho u\\ \rho u^2+p\\ \rho uv\\ (\rho E+p)\,u\\ \rho_p u_p\\ \rho_p u_p^2\\ \rho_p u_p v_p\\ \rho_p E_p u_p\end{pmatrix};\ \mathbf{G}=\begin{pmatrix}\rho v\\ \rho uv\\ \rho v^2+p\\ (\rho E+p)\,v\\ \rho_p v_p\\ \rho_p u_p v_p\\ \rho_p v_p^2\\ \rho_p E_p v_p\end{pmatrix};$$

$$\mathbf{S}=\begin{pmatrix}0\\ -D_x\\ -D_y\\ -\left(D_x u_p+D_y v_p+Q\right)\\ 0\\ D_x\\ D_y\\ D_x u_p+D_y v_p+Q\end{pmatrix}$$

Here, ρ, p, and u and v represent the density, pressure, and velocity components in x and y directions for the gas phase, respectively. ρ_p, u_p, and v_p are the corresponding physical quantities for particle phase. E and E_p denote specific total energy for gas and particle phases, respectively,

$$E=\rho C_p T+\frac{1}{2}\rho\left(u^2+v^2\right),\ E_p=\rho_p C_d T+\frac{1}{2}\rho_p\left(u_p^2+v_p^2\right),$$

C_d and C_p stand for the specific heat for particle and for gas under constant pressure, respectively. D_x and D_y stand for acting force between gas and particle in x and y directions, respectively, Q for the thermal conductivity between the two phases, which are expressed as,

$$D_x=\frac{3}{8}\rho C_d\frac{\rho_p}{\rho_d r_d}\left(u-u_p\right)\sqrt{\left(u-u_p\right)^2+\left(v-v_p\right)^2}$$

$$D_y=\frac{3}{8}\rho C_d\frac{\rho_p}{\rho_d r_d}\left(v-v_p\right)\sqrt{\left(u-u_p\right)^2+\left(v-v_p\right)^2}$$

$$Q=\frac{3}{2}\frac{\rho_p}{\rho_d r_d^2}\frac{C_p\mu Nu}{\mathrm{Pr}}\left(T-T_p\right).$$

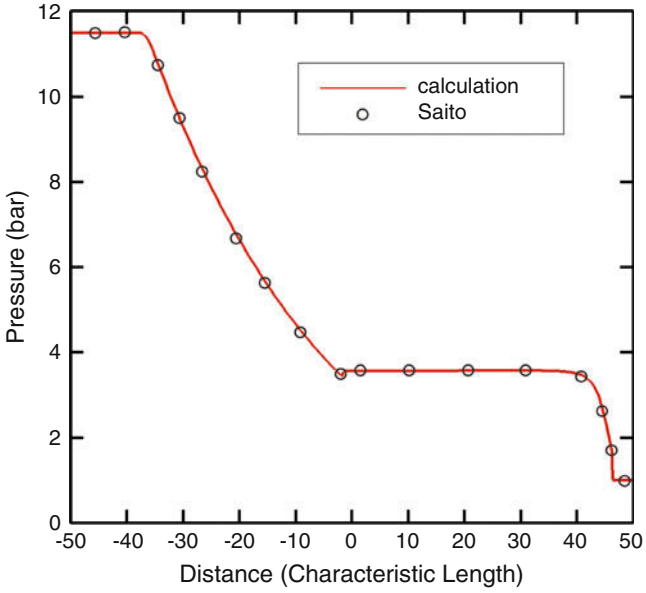

Fig. 1 Dusty gas shock tube problem steady solution simulated by Saito and VAS2D, $P_{41} = 11.5$

Here, T and T_p are the temperature for gas and particles, respectively, ρ_d is the material density, r_d is the particle radius, μ is the viscosity coefficient, Nu is the Nusselt number, and Pr is the Prandtl number.

The numerical solver VAS2D (two-dimensional and axisymmetric vectorized adaptive solver) is employed in this work, which has been well validated in simulating dusty gas flows such as particle injection in a tube [12]. The multiphase compressible Euler equations (1) are solved by finite-volume method based on adaptive unstructured mesh technique. The mesh is refined adaptively at regions with large density gradient for capturing the complex wave patterns with high resolution. The MUSCL-Hancock scheme is adopted to achieve second-order accuracy in both temporal and spatial scales.

For validating the present solver, the dusty shock tube problem considered by Saito is simulated here, and the initial configurations are the same as those of Saito. As shown in Fig. 1, good agreements are achieved between the present numerical solutions with previous ones.

3 Dusty Gas Shock Reflection Over a Double Wedge

The shock reflection type of a shock in ideal gas is determined by γ, M_s, and the angle of wedge θ_w [1]. But in dusty gas flows, it is not only related to the three parameters but also depends on the traveling distance of the incident shock due

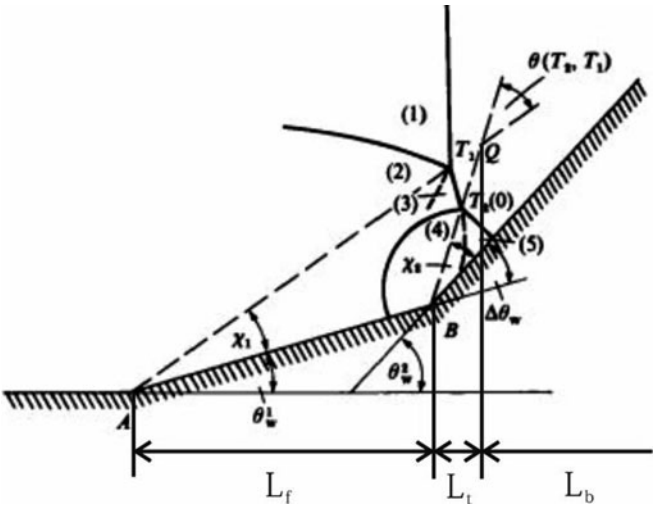

Fig. 2 The coefficient sketch map of shock reflection over a double wedge

to the existence of non-equilibrium effects. For a dusty shock, the strength of the frozen and equilibrium shock are different as well as the fluid properties behind them. Specifically, $M_{sf} < M_{se}$, thus the detachment angle of frozen shock θ_f is less than that of the equilibrium shock θ_e.

Therefore, the non-equilibrium effects play an important role in the configuration of shock reflection, which has been intensively studied for the case of a single wedge. However, a dusty shock reflection over a double wedge has been seldom studied, which is more complicated than the single wedge case. For well exploring the non-equilibrium effects, in the current research, $M_{sf} = 1.05$ is specified for all the cases, corresponding to the detachment angles of $\theta_f = 31^\circ$ and $\theta_e = 47^\circ$. It should be noted that when $M_{sf} > 1.4$, the detachment angle of dusty shock is approaching that of the pure gas.

Figure 2 presents a sketch of shock reflection over a double wedge, where θ_{wb}, θ_{wf}, and $\Delta\theta_w$ represent the angle of back wedge, former wedge, and angle between the two wedges, respectively. L_b and $L_f$are the length along the x axis of the former wedge and back wedge, respectively, and L_t is the distance between two triple points above the former and back wedges. Differing from the existing RR and MR structures in pure gas, the non-equilibrium effects in dusty gas would affect the reflection type. In the present study, a double wedge with $\theta_{wf} = 20^\circ$ and $\theta_{wb} = 40^\circ$ is adopted to illustrate the non-equilibrium effects on the reflection process, which are related to the particle relaxation.

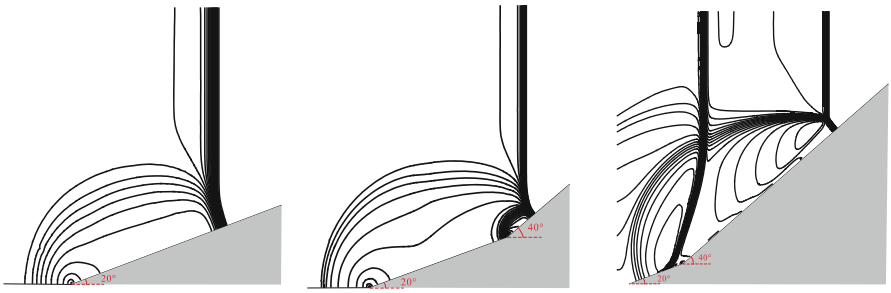

Fig. 3 The computation plot of shock reflection as shock propagating over a double wedge in equilibrium dusty gas with $\theta_{wf} = 20^{\circ}$ and $\theta_{wb} = 40^{\circ}$

3.1 *Dusty Shock Reflection Over a Double Wedge with a Long Scale*

Though the shock reflection over a double wedge in pure gas has been studied [11], this phenomenon in dusty gas is seldom investigated. Because of the non-equilibrium effect, the reflection phenomena must have a closed relation with the length scale traveled by the wave. For a dusty shock moving along a double wedge at $L_f \gg L_{eq}$, the equilibrium shock reflection dominates the flow phenomena, and the transition criteria differ from the pure gas case. Specifically, the variable θ_f in the transition prediction for pure gas should be replaced by θ_e. If the angles satisfy $\theta_e > \theta_{wb} > \theta_{wf}$, MR occurs at the former wedge, forming a Mach stem. As the Mach stem generated propagates to the back wedge, MR occurs again for $\theta_e > \Delta\theta_w$. Then, the two triple points get together gradually. Finally, MR occurs on the back wedge because of $\theta_e > \theta_{wb}$. This type of reflection is called MR-MR-MR. The shock structure is shown in Fig. 3. Clearly, the equilibrium shock reflection structures are greatly different from pure gas case.

3.2 *Dusty Shock Reflection Over a Double Wedge with a Short Scale*

Similarly, for a dusty shock moving along a double wedge at $L_f \ll L_{eq}$, the reflection waves are different from the long-scale case. When L_f is comparable to L_t, the reflection at the former wedge before the two triple points getting together is similar to the frozen shock case, and it is similar to equilibrium shock case when shock travels a long distance at the back wedge. If the angles satisfy $\theta_e > \theta_{wb} > \theta_f > \theta_{wf}$ and $\Delta\theta_w < \theta_f$, the reflection over a double wedge is initially identical to frozen shock, i.e., MR occurs on the former wedge, and the Mach stem propagates to the back wedge leading to a RR structure at the back wedge for the relation of

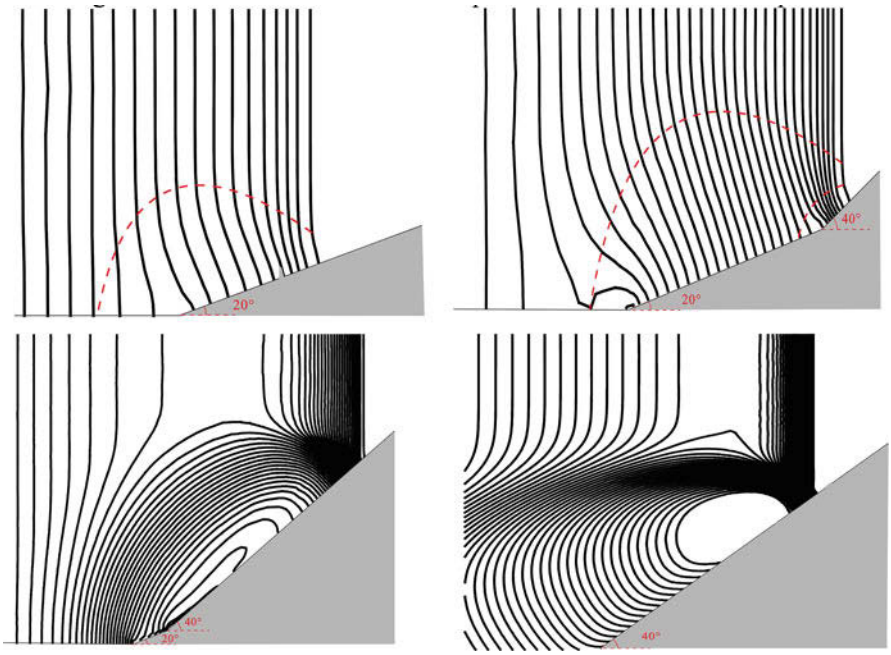

Fig. 4 The computation plot of shock reflection as shock propagates over a short-scale double wedge in dusty gas with $\theta_{wf} = 20^{\circ}$ and $\theta_{wb} = 40^{\circ}$

$\theta_{wb} > \theta_f$. Finally, RR transits again to MR configuration at the back wedge as equilibrium shock case for $\theta_e > \theta_{wb}$. This reflection type is called MR-MR-(RR-MR). The shock structure is plotted in Fig. 4. The non-equilibrium effects related to the particle relaxation change the transition criterion and complicate the shock reflection process.

4 Conclusion

The dusty shock reflection over a double wedge is numerically investigated in the present paper. The VAS2D program is adopted to solve the compressible two-phase flows, and its validity is well examined by simulating the shock tube problem with dusty gas.

Due to the non-equilibrium effects on the wave patterns, the reflection process considerably differs from the pure gas case, and the wave configuration depends on the distance traveled by the incident shock. For a dusty shock moving along a double wedge at $L_f \gg L_{eq}$, the equilibrium shock reflection dominates the flow phenomena. If the angles satisfy $\theta_e > \theta_{wb} > \theta_{wf}$, MR occurs at the former wedge, forming a Mach stem. As the generated Mach stem propagates to the back wedge,

MR occurs again for $\theta_e > \Delta\theta_w$. Then, the two triple points get together gradually. Finally, MR occurs on the back wedge because of $\theta_e > \theta_{wb}$. However, for a dusty shock moving along a double wedge at $L_f \ll L_{eq}$, the reflection waves are different from the long-scale case. If the angles satisfy $\theta_e > \theta_{wb} > \theta_f > \theta_{wf}$ and $\Delta\theta_w < \theta_f$, the reflection over a double wedge is initially closed to frozen shock, i.e., MR occurs on the former wedge, and the Mach stem propagates to the back wedge leading to a RR structure at the back wedge for the relation of $\theta_{wb} > \theta_f$. Finally, RR transits again to MR configuration at the back wedge as equilibrium shock case for $\theta_e > \theta_{wb}$.

References

1. G. Ben-Dor, *Shock Wave Reflection Phenomena*, vol 2 (Springer, 2007)
2. O. Igra, G. Hu, J. Falcovitz, B.Y. Wang, Shock wave reflection from a wedge in a dusty gas. Int J Multiphase Flow **30**(9), 1139–1169 (2004)
3. P.G. Saffman, On the stability of laminar flow of a dusty gas. J Fluid Mech **13**(01), 120–128 (1962)
5. F.E. Marble, Dynamics of dusty gases. Annu Rev Fluid Mech **2**(1), 397–446 (1970)
6. B.Y. Wang, A.N. Osiptsov, M.A. Teverovshii, Flow properties of a dusty-gas point source in a supersonic free stream. Appl Math Mech **24**(8), 821–826 (2003)
7. B.Y. Wang, Q.S. Wu, Shock-induced two-phase flows in a variable cross-section tube. Acta Aerodynamica Sinica **10**(3), 355–361 (1992)
8. V.M. Boiko, V.P. Kiselev, S.P. Kiselev, A.N. Papyrin, S.V. Poplavsky, V.M. Fomin, Shock wave interaction with a cloud of particles. Shock Waves **7**(5), 275–285 (1997)
9. H. Miura, I.I. Glass, On the passage of a shock wave through a dusty-gas layer, in *Proceedings of the Royal Society of London A: Mathematical, Physical and Engineering Sciences*, vol 385 (The Royal Society, 1983), pp. 85–105
10. T. Saito, M. Marumoto, K. Takayama, Numerical investigations of shock waves in gas-particle mixtures. Shock Waves **13**(4), 299–322 (2003)
11. G. Ben-Dor, J.M. Dewey, K. Takayama, The reflection of a plane shock wave over a double wedge. J Fluid Mech **176**, 483–520 (1987)
12. J.Y. Yin, X.S. Luo, Numerical study on unsteady wave patterns produced by particle injection in pipe flows. Chin J ComputPhys **33**(4), 391–398 (2016)

Shock and Blast Wave Interaction with Hard Sand Pan

R. T. Paton and B. W. Skews

Abstract The effect of the passage of blast and shock waves over sand on a hard substrate as well as a hard pan was explored. While the initial entrainment by a blast wave is similar to that by a shock wave, there is a reduction in entrainment after the passage of the negative pressure phase which may reduce the overall estimate of entrained mass. Problems with apparatus and visualization mean that further tests will be required to develop meaningful quantitative data.

1 Introduction

1.1 Background

While most studies of shock and blast waves consider ideal surfaces, the reality of the situations in which these waves occur is that there is often interaction with uneven, permeable or dusty surfaces. A typical example of this would be the explosion of an IUD in a desert setting, such as many of the current theatres of war, where the blast wave will move over a hard desert surface upon which there may also be loose sand and dust.

Early work in the field, such as that by Saffman [1], White and Schulz [2] and Merzkirch and Bracht [3], focused on the mechanism by which particles become entrained in a post-shock flow. Shear with the passing air initiates the entrainment although the Magnus effect can contribute to the lifting of the particles away from the surface. In general, the particles have significant shear with the gas, and this results in a two-stage flow.

R. T. Paton (✉)
Flow Research Unit, University of the Witwatersrand, Johannesburg, South Africa
e-mail: Randall.Paton@wits.ac.za

B. W. Skews
Flow Research Unit, School of Mechanical, Industrial and Aeronautical Engineering, University of the Witwatersrand, Johannesburg, South Africa

A. Sasoh et al. (eds.), *31st International Symposium on Shock Waves 2*,
https://doi.org/10.1007/978-3-319-91017-8_84

More recent work by Skews and Doyle [4] explored these dynamics at a larger particle scale and for longer test periods. This resulted in the identification of surface waves formed at the interface between the entrained particles and the bulk post-shock flow. This work has continued with a recent study by Chowdhury et al. [5] examining the particle entrainment after a shock wave with higher temporal resolution using high-speed imaging.

All studies to date appear to have focused on the entrainment of free particulates by post-shock flow. However, in the example given previously, it was clear that there is a different configuration of sand and dust which may be routinely subjected to shock wave loading, namely, hard pans. These pans share the porous composition of loose sand beds but have greater mechanical cohesion due to the cementation that occurs during the drying of the pan.

The current research project explores the effect of shock and blast waves on the breakup of hard pan surfaces and subsequent dust entrainment. This work is motivated in part by the development of the Bloodhound Supersonic Car (SSC), which will be tested on the Hakskeenpan in the Northern Cape of South Africa with the intention of setting a new land speed record of 1000 mph (1603 kph).

1.2 Apparatus

Two separate shock tubes were configured to produce either a conventional shock wave or a blast wave simulation by a shortened driver section. A schematic of the arrangement of the blast wave simulator is shown in Fig. 1. A mirror was mounted directly above each of the test sections to allow simultaneous visualization of the flow field in elevation and plan to assess the two-dimensionality of the flow field. The test section cross-section of the blast wave simulator has dimensions of

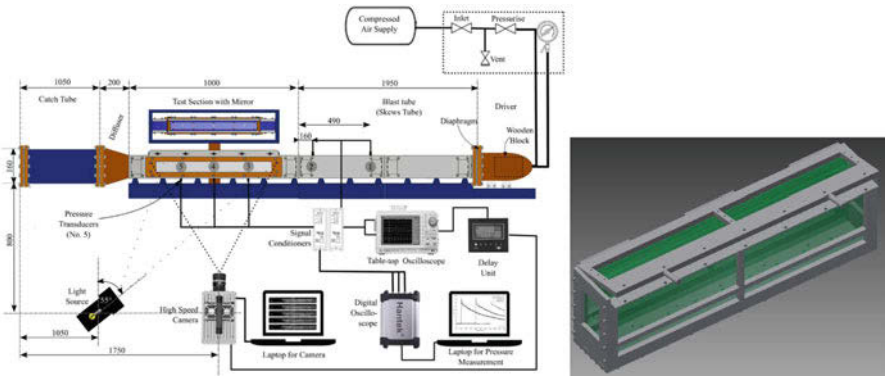

Fig. 1 Schematic of the general arrangement as indicated for the blast wave simulator (*left*) and the test section of the shock tube test section (*right*)

$3'' \times 3''$ (76 × 76 mm) while that of the shock tube is approximately $4'' \times 6''$ (107 × 157 mm). Each of the test sections was designed with a hinged top to easily reset the test section after each test.

The sand entrainment was visualized using a Photron SA5-775 K-C1 operating at speeds between 5000 and 7500 fps. The visualization system was triggered by high-frequency PCB M113A21 pressure transducers upstream of the test section. The desert pan was simulated by drying slurries of plaster sand with a particle size distribution similar to that measured at the Hakskeenpan in trays which could be inserted into the floor of the shock tube. The shock wave strength tested was approximately Mach 1.3, the Mach number which the Bloodhound SSC is expected to achieve. Comparison tests were also made of thin layers (<1 mm) of loose sand on impermeable plates to identify the particular effect of penetration of the surface by the shock wave.

2 Results

2.1 Interaction on an Impermeable Substrate

While the entrainment of a dust layer over a hard substrate by a passing shock wave is well established in literature, little information is available on the same process for the passage of a blast wave. The fundamental difference between the effect of the two is due to the rapidly changing pressure behind a blast wave. This rapid decay is due to a rarefaction caused by the fact that for most blast sources, there is a centre of the blast originator (generally an explosive), and while the production of gas by combustion can allow for some continued flow in the direction of the wave front, eventually the flow behind a blast wave must return to the original condition. The effect of this is to retard and eventually stop the flow behind the blast wave. Thus it can be expected that the dust entrainment behind a blast wave would rapidly diminish and eventually stop.

As can be seen in Fig. 2, the entrainment by a blast wave is similar to that by a shock wave over an impermeable surface and does not appear to demonstrate a significant damping over the time scales studied. Although the total height of the entrained material at the upstream end of the test section decreased through the duration of the test (such as in the third frame in Fig. 2), this could be due to the reduction in material available for entrainment there rather than a change in the shear exerted by the flow on the sand. The continued entrainment at later times suggests that this may not be the case but rather a reduction in flow shear.

It is notable that surface waves develop in the upper regions of the entrained sand as identified in [4] but that they do not have the coherent form seen in that work. Rather, the waves developed are consistent with the trajectories for the randomly packed samples in that work. This could be due to the variation of the particle size for the scattered sand. It is also notable that there are clumps of material entrained whole in the flow.

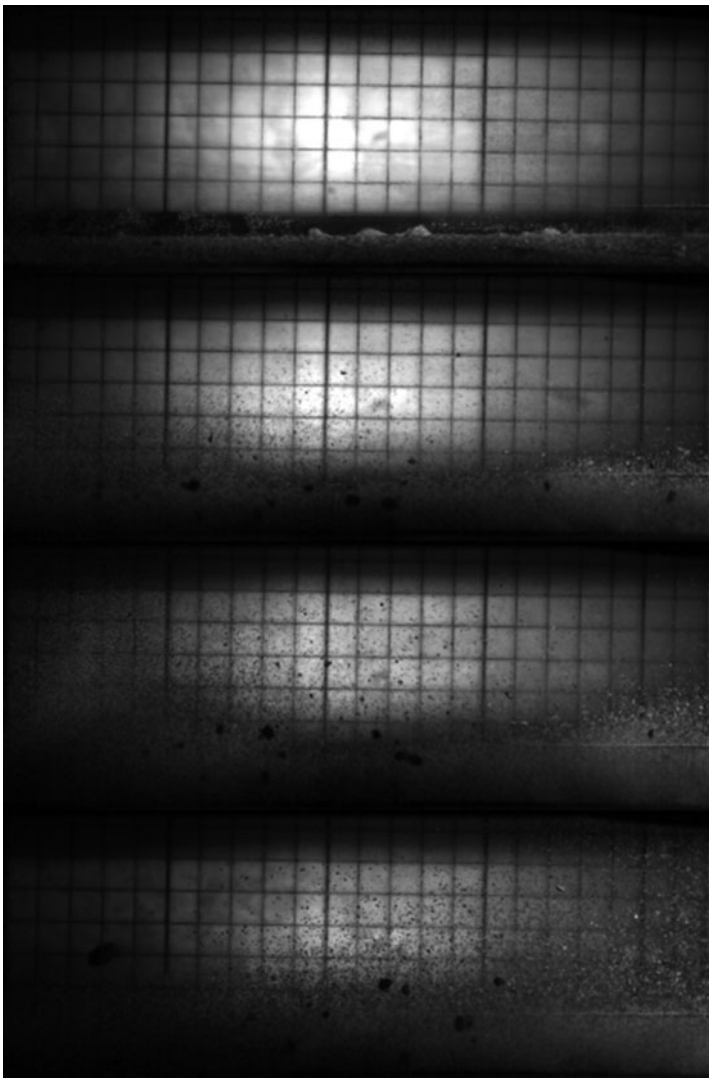

Fig. 2 Development of sand entrainment on an impermeable surface by a blast wave (*from top to bottom*) when the wave arrives in the test section and approximately 20 ms, 35 ms, and 50 ms, respectively, after the arrival of the wave in the test section

2.2 Interaction with a Hard Sand Pan

Hard pans were produced for each of the test sections by two means: natural drying and baking. Due to issues with the temperature control of the autoclave used to bake the samples, the sand was discoloured, and the results obtained with these samples

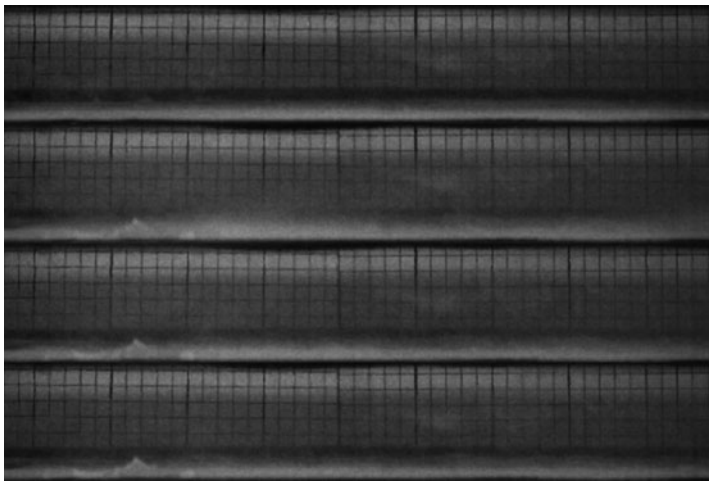

Fig. 3 Development of sand entrainment on a hard pan surface by a shock wave (*from top to bottom*) when the wave arrives in the test section and approximately 20 ms, 35 ms, and 50 ms, respectively, after the arrival of the wave in the test section

Fig. 4 Hard pan after the passage of a shock wave (upstream to the left of the image)

were discarded as it was unknown what effect this overheating may have had on the mechanical properties. Additionally, the blast wave results for the hard pan were not clearly visible and so could not be included here.

The images in Fig. 3 show the entrainment for a Mach 1.3 shock wave travelling over a naturally cured hard pan. Clearly a significant amount of sand is entrained by the passage of the shock wave when compared to the flow over a steel plate. Again, there are some surface waves visible in the sand plume, but these die down as the test ends. These results are, however, considered questionable as the condition of the test sample after the test, as shown in Fig. 4, shows severe degradation.

Given that the Thrust SSC, which travelled at Mach 1.03, drove over a pan of this sort before without causing damage this severe (albeit for a much weaker shock wave), it is clear that the samples as developed for this apparatus are not accurately representing the real surface. There are several possible causes for this.

First, the samples are quite shallow (approximately 25 mm thick) in a thin steel pan. While the mean thickness of the surface of the Hakskeenpan is approximately

25 to 40 mm, the pan material lies on top bedrock which is significantly stiffer due to its bulk than a thin steel pan supported on several adjustable struts. Second, the pans are of a finite width (107 mm) and clamped between test section walls. This installation may introduce stress into the sample not present in the natural hard pan. This could increase the chance of surface breakup. Additionally, when installing the pans, there was some initial cracking due to twisting of the sample pan.

The third and most significant possible difference is in the composition of the pan itself. The samples were made using clean plaster sand and fresh water. While the particle size distribution of the plaster sand was comparable to the Hakskeenpan and would thus have undergone similar cementation as the sample dried, the soil in Hakskeenpan also contains a significant salt content since it was originally flooded with ocean water. This salt may complement the mechanical cohesion of the sand particles by acting as an adhesive. The overall effect would be a mechanically stronger surface than those produced in the current tests. Modification to the test apparatus and sample composition would thus both be necessary for meaningful results.

3 Conclusion

While the nearly simultaneous lift-off of the sand particles identified in previous works was confirmed here, the entrainment is somewhat retarded by the negative pressure phase of the blast wave while it continues with the shock wave. Thus, the entrainment by a vehicle such as the Bloodhound SSC may be less than originally expected by considering only a simple shock wave. Chunks of the hard pan are also occasionally entrained but only if the surface was initially cracked.

Further experiments are required considering the effect of existing surface cracking as well as the effect that producing samples using water of various salinity may have. The former may exacerbate the surface breakup and hence the mass entrained because it allows the shock wave to penetrate deeper into the surface and produce a higher pressure at those depths because of internal reflections. The latter may improve surface mechanical strength as the salinity increases, and thus testing such samples would be better representative of the actual pan which is known to have a significant salt content.

Better visualization is also needed to quantitatively assess the entrainment differences between shock and blast waves. Given the significant differences in the test section sizes, the shock tube apparatus should be modified to also produce blast waves.

Acknowledgements The results presented here were gathered by Ikhlaas Raoof and Neo Sambo as part of their undergraduate work.

References

1. P. Saffman, The lift on a small sphere in a slow shear flow. J. Fluid Mech. **22**(2), 385 (1965)
2. B.R. White, J.C. Schulz, Magnus effect in saltation. J. Fluid Mech. **81**(3), 497 (1977)
3. W. Merzkirch, K. Bracht, The erosion of dust by a shock wave in air: Initial stages with laminar flow. Int. J. Multiphase Flow **4**(1), 89 (1978)
4. B.W. Skews, G.K. Doyle, Fluid Dyn Prop, HSF-09-01 (2001)
5. A.Y. Chowdhury et al., Effect of shock strength on dust entrainment behind a moving shock wave. J. Loss Prevent Proc **36**, 202 (2015)

Unsteady Dynamics of Particles Accelerated by a Shock Wave

A. Bordoloi, A. Martinez, and K. Prestridge

Abstract The dynamics of shock-accelerated nylon microparticles ($d_p = 4$ um) are studied in the post-shock relaxation zone for incident Mach numbers, $M_s = 1.2$, 1.3, 1.4, and 1.5. Particle motion is imaged using a multi-pulse laser and a high-speed camera system. The velocity, acceleration, and the coefficient of drag for an individual particle are estimated based on its recorded trajectory. The absolute shock location is obtained using a shadowgraph system. Results show significant difference from earlier empirical relationships in the variation of C_D with respect to particle Reynolds number (Re_p).

1 Introduction

Shock-particle interactions in multiphase flows result in complex unsteady dynamics, such as unconventional drag force, evaporation and breakup of the dispersed particles, as well as modulation of the carrier fluid turbulence [1–3]. When a shock wave passes through a gas/particle mixture, the gas phase is immediately shocked to a higher pressure, temperature, and velocity. The time scale of shock passage, on the other hand, is too small to create immediate change in the mechanical and thermal state of the particle [4]. The difference in states between the two phases initiates interphase transfer of momentum and energy until the particles relax into an equilibrium with the carrier phase. The understanding of particle dynamics during the relaxation phase is important for many applications such as expansion flow of a gas turbine, detonation, and various seeding techniques such as particle image velocimetry (PIV).

Most of earlier studies on particle dynamics during the relaxation phase have been limited to particle clouds [5–10]. Inegbo [5] measured drag on particles injected into a steady stream. Rudinger [6] measured particle drag from bulk particle

A. Bordoloi (✉) · A. Martinez · K. Prestridge
Physics Division, Los Alamos National Laboratory, Los Alamos, NM, USA
e-mail: ankur@lanl.gov

A. Sasoh et al. (eds.), *31st International Symposium on Shock Waves 2*,
https://doi.org/10.1007/978-3-319-91017-8_85

Table 1 Summary of empirical relationship between drag coefficient (C_D) and particle Reynolds number (Re_p)

Reference	Relation	Measurement on	Range of Re_p
Ingebo, 1956	$C_D = 27{Re_p}^{-0.84}$	Particle cloud	$6 < Re_p < 400$
Rudinger, 1970	$C_D = 6000{Re_p}^{-1.7}$	Particle cloud	$10 < Re_p < 700$
Outa et al., 1981	$C_D = 2216{Re_p}^{-1.47}$	Particle cloud	
Sommerfeld, 1985	$C_D = 112{Re_p}^{-0.98}$	Particle cloud	$50 < Re_p < 500$
Igra & Takayama, 1993	$\log_{10}(C_D) = (7.82 - 5.81\log_{10}(Re_p) + 1.41 \log_{10}(Re_p)^2 - 0.115 \log_{10}(Re_p)^3$	Individual particle	$6000 < Re_p < 101{,}000$
Jourdan, 2008	$\log_{10}(C_D) = (-0.696 + 1.26\log_{10}(Re_p) - 0.465 \log_{10}(Re_p)^2 + 0.05 \log_{10}(Re_p)^3$	Individual particle	$500 < Re_p < 10^4$

trajectories and found that the coefficient of drag is at least two orders of magnitude larger than that predicted by standard drag equation. Based on Laser Doppler Anemometry measurements on a homogenous gas/particle mixture, Sommerfeld [10] proposed an empirical correlation for drag as $C_D = 112{Re_p}^{-0.98}$ in the range of incident Mach number, $1 < M_s < 1.7$. Here, the Reynolds number (Re_p) is based on the slip velocity of the particle. The only studies that considered drag on individual particle are Igra & Takayama and Jourdan et al. [11, 12]. However, these studies only considered the beginning of the relaxation zone and were not extended until the particle reaches mechanical equilibrium with the post-shock fluid. Table 1 summarizes various empirical C_D vs. Re_p relationships between ranges of Reynolds numbers considered in various studies.

We report measurements of particle velocity (u_p), acceleration (a_p), and coefficient of drag (C_D) for micron-sized particles accelerated by a normal shock. Experiments are designed to precisely track the motion of individual particles shortly after the passage of the shock until the particle relaxes into an equilibrium with the carrier gas.

2 Experimental Facility and Methods

2.1 Horizontal Shock Tube

We conduct the experiments in the horizontal shock tube (HST) facility at Los Alamos National Laboratory. The facility consists of a 6.5 m long shock tube with 76.2 mm × 76.2 mm cross section (see Fig. 1). The shock tube is capable of

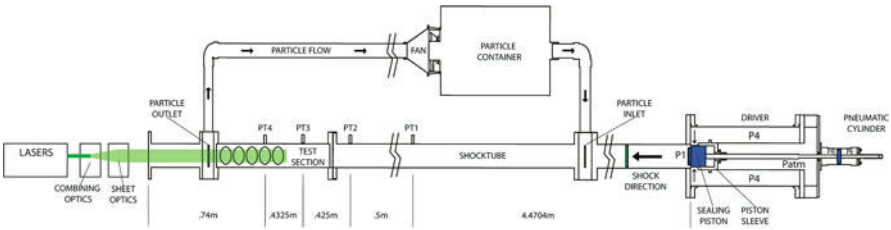

Fig. 1 Schematic of horizontal shock tube facility. Shock moves from right to left. Inset shows a cartoon of field of view with an example shock wave and scattered light from particles within the laser sheet

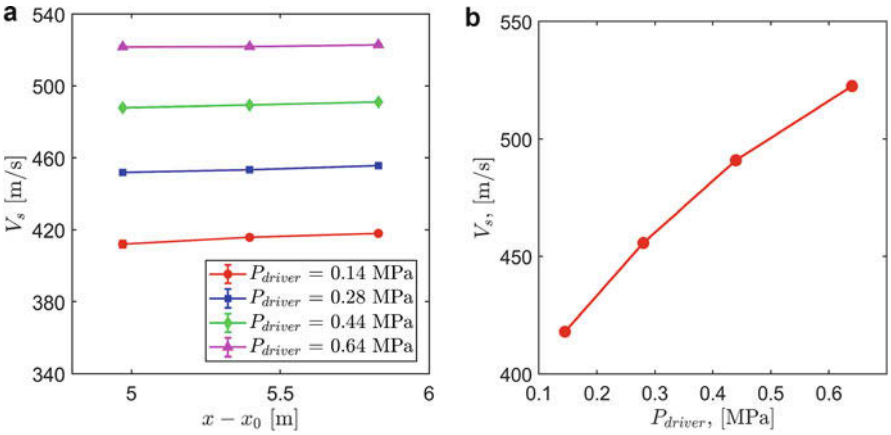

Fig. 2 (**a**) Variation of shock speed (Vs) at different location along the tube. The distance (x-x_0) is measured from the driver cross section. (**b**) Shock speed at the measurement section with respect to input driver pressure (P_{driver})

generating repeated shock waves using a fully automated diaphragmless pneumatic driver. The measurement section is located at 5.83 m from the driver. Since there is no diaphragm involved in the system, the flow is devoid of contamination by a fragmented diaphragm during each test [13, 14].

To verify that the shock wave has stabilized well before the measurement section, we estimate the shock speed (V_s) at different axial locations before and at the measurement section using pressure traces from multiple pressure transducers (PT1-PT4, PCB Piezotronics Inc. Model 113B27) along the tube using a method described in [14]. The driver gas pressure can be regulated between $0.14 < P < 1.4$ MPa to provide resultant incident shock Mach number between $1.1 < M_s < 2$. The measured shock speeds at three different axial locations for four different driver set pressures (P_{driver}) are shown in Fig. 2a. For each P_{driver}, V_s becomes nearly constant before reaching the measurement section. The variation of shock speed at the measurement section with respect to the set driver pressure (P_{driver}) is shown in Fig. 2b. The driver pressure is maintained at 0.14, 0.28, 0.44, and 0.64 MPa to obtain an incident

Table 2 Experimental parameters

Parameter	Value
Shock Mach numbers, M_s	1.2,1.3,1.4,1.5
Particle Reynolds no., Re_p	0.14–65
Post-shock gas density ρ_g(kg/m^3)	1.253,1.415,1.578, 1.748
Post-shock gas viscosity, μ_g(kg/m.s)	2.0×10^{-5}, 2.1×10^{-5}, 2.2×10^{-5}, 2.3×10^{-5}
Post-shock gas phase velocity, u_g (m/s)	108.3, 160.7, 206.2, 245
Particle volume fraction, C	10^{-7}

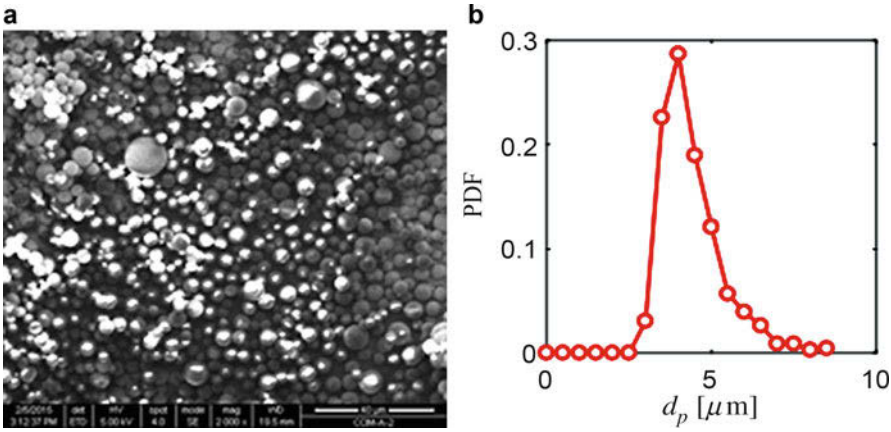

Fig. 3 (**a**) Sample electron microscope image showing the distribution of nylon microparticles and (**b**) the corresponding size distribution

shock Mach number, $M_s \approx 1.2$, 1.3, 1.4, and 1.5, respectively. The experimental parameters for this study are summarized in Table 2.

2.2 Particles

For the current measurements, we use nylon particles (TSI 10084) with mean diameter $d_p = 4$ μm and mass density $\rho_p = 1140$ kg/m^3. We characterize the size distribution of these particles within a range of 2–7 μm using a scanning electron microscope. A sample microscopic image and the corresponding size distribution are shown in Fig. 3.

The particles are introduced into the shock tube using a feeder mechanism shown in Fig. 1. The feeder mechanism consists of a high-speed jet of particles entering the particle container through an air blaster that uses the Venturi effect that allows an even dispersion of particles in the container minimizing the clumps that may have formed in the reservoir due to electrostatic forces, moisture content, and compaction. The particles are driven through a pipe from the container and

introduced to the shock tube through an inlet port with area 484 mm^2 located near the driver and are exited through a similar port located near the end of the tube. The size and location of these ports are chosen carefully to prevent perturbation to the shock. The fan is regulated at a speed such that the average pre-shock speed of a particle is 0.6 m/s. This speed is insignificant compared to the speed of the shock and the post-shock gas, so the particles are assumed to be stationary at the time of shock interaction. The particles are introduced in dilute concentration ($C \sim 1.0 \times 10^{-7}$) to avoid collision among themselves.

2.3 Image Diagnostics

Four dual-head Quantel Twins CFR300 Nd:YAG 532 nm lasers with repetition rate of 15 Hz are used to illuminate the particles in the measurement section. Each of the eight heads is timed independently to produce a single pulse during each experimental run. The light sheets, with a width of 1 mm, are aligned using polarizing beam splitters and a combination of optics. Particles and shock are imaged simultaneously using a SIMD high-speed framing camera capable of 8 frames with 5 ns minimum exposure at rates of 7 million frames per second (fps) over 8 frames or 1 billion fps over 4 frames. Each CCD in the camera has resolution of 1280x960 pixels with each pixel on the CCD 6.45 μm. The camera has a K2 Distamax microscopic lens with magnification 2.06x to 3.05x. The camera is positioned orthogonal to the laser sheet to capture Mie scattering from particles in the eight frames. The particle images are calibrated using a precision chrome-on-glass cross-hair grid (Edmund Optics FA79E-58509) with 0.065 mm diameter spaced 0.125 mm apart. The image resolution is 2.14 μm/pixel at a magnification of almost 3, and the total field of view is 2.74 mm × 2.05 mm. The depth of field of 3/4 mm is measured using a DOF 5–15 target with the camera aperture set at f/22. The shock wave is simultaneously imaged in the second image frame with a shadowgraph from a backlit illumination using a Photo-Systeme Nano-lite driver with a spark flashlamp (KL-L). The absolute shock location (x_s) is obtained at time (t_s) from the shadowgraph image.

3 Results and Discussion

To obtain particle trajectories across the relaxation zone, we acquire multiple measurements at different post-shock times. For any given particle, usually four to seven post-shock trajectory images are captured. To track each candidate particle along its trajectory, the pre-shock particle location is manually registered from the first frame, and the particle is identified in the successive frames using an image cross-correlation algorithm.

For one-dimensional flows, the relationship between C_D and the physical and kinematic properties of a particle and the post-shock gas can be expressed as:

$$\frac{a_p}{\left(u_g - u_p\right)^2} = \frac{3\rho_g C_D}{4\rho_p d_p} = A \tag{1}$$

Here, u_p and a_p are velocity and acceleration of the particle; ρ_p and ρ_g are the densities of the particle and the post-shock gas. To calculate velocity and acceleration from individual tracks, we adopt a method of piecewise fitting of the measured particle locations [15]. Integrating Eq. 2.1 twice with initial conditions $u_p = 0$ and $x_p = x_0$ at $t = 0$, we obtain:

$$x_p = x_0 + u_g\,(t - t_0) - \frac{\log\left(A u_g\,(t - t_0) + 1\right)}{A} \tag{2}$$

Three successive particle locations are piecewise fitted to the fifth order Taylor series expansion of Eq. (2) with fitting parameters x_0, t_0, and A. Before performing each fit, the time axis is shifted to the reference time $t_0 = t_s - \frac{x_x - x_p}{V_s}$, the time when the shock location coincides with the particle location x_0. The particle velocity u_p is obtained by invoking parameter A into the first integral of eq. (1):

$$u_p = \frac{u_g^2 A\,(t - t_0)}{1 + u_g A\,(t - t_0)}, \tag{3}$$

and the acceleration is obtained from Eq. (1). The particle drag coefficient C_D at time t for each trajectory is obtained from parameter A.

Figure 4a shows particle locations for four example trajectories for incident Mach number, M_s = 1.2, 1.3, 1.4, and 1.5, and their corresponding piecewise fits. The accuracy of each fit is within a least square error of 1 pixel. The particle velocity and acceleration for these trajectories are shown in Fig. 4b and c, respectively. Figure 4b shows that the particle velocity continuously increases and asymptotically approaches the post-shock fluid velocity (u_g) shown with a dashed line for each M_s. The acceleration (Fig. 4c) reaches a peak immediately after the shock and decreases as the particle relaxes into equilibrium.

The drag coefficients (C_D) for multiple particle trajectories for the four incident Mach numbers (M_s = 1.2, 1.3, 1.4, and 1.5) are shown with respect to Re_p in Fig. 5. The empirical relations (see Table 1) from earlier studies are also shown for comparison. Results show that none of the existing relationships predicts the drag coefficient observed in this study. C_D in the present experiment increases sharply with decreasing Re_p in the beginning of the relaxation zone ($Re_p > 10$), to more than an order of magnitude larger than the standard drag prediction. However, as the particle relaxes into equilibrium with the surrounding gas, the rise in C_D becomes relatively moderate. A small dependence of C_D on the incident Mach number is

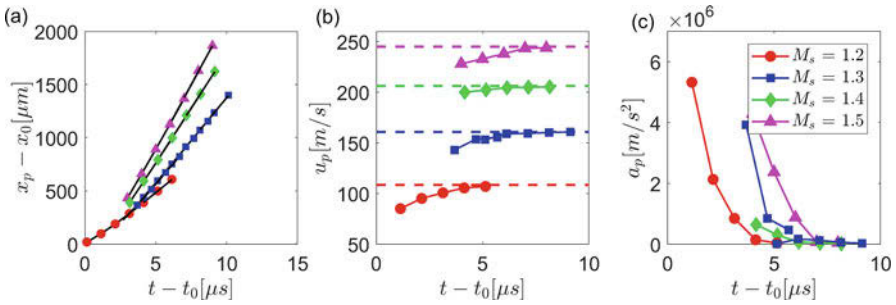

Fig. 4 Examples of (**a**) particle location ($x_p - x_0$) obtained from particle tracking and the corresponding piecewise fit, (**b**) velocity u_p and (**c**) acceleration a_p for $M_s = 1.2$, 1.3, 1.4, and 1.5. The dashed lines in (**b**) represent the corresponding post-shock fluid velocities (u_g)

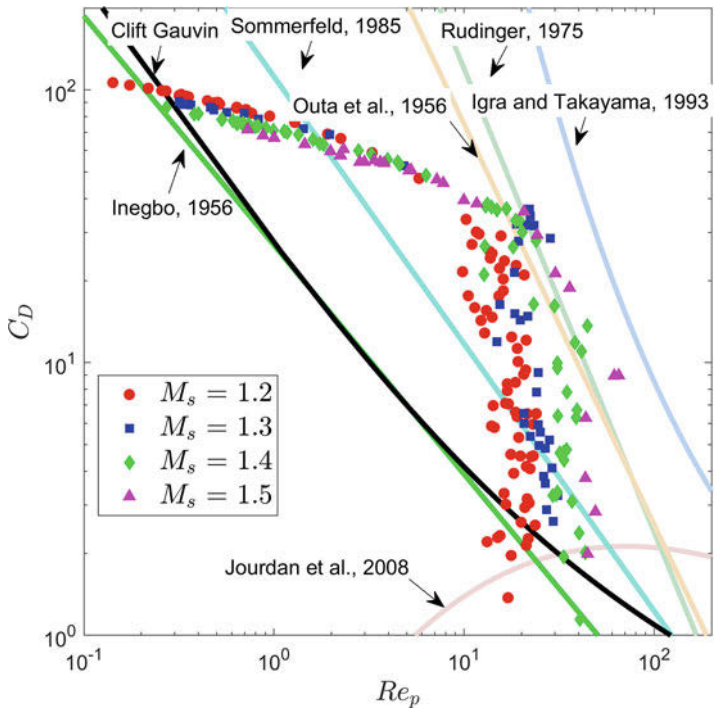

Fig. 5 Coefficient of drag (C_D) with respect to Reynolds number (Re_p) for four incident Mach number ($M_s = 1.2$–1.4). The solid lines show various empirical C_D-Rep relationships based on past experiments (see Table 1)

observed towards the end of the relaxation zone. For a fixed Re_p, C_D decreases with increasing M_s.

4 Conclusions

Dynamics of shock-accelerated micron-sized particles are examined through the relaxation period using high-speed laser visualization and shadowgraph imaging for a range of incident Mach number, $M_s = 1.2$–1.4. Soon after the passage of a shock, particles attain a peak acceleration. The acceleration of a particle gradually decreases as the particle relaxes into mechanical equilibrium with the carrier phase. The unsteady drag coefficient increases at a fast rate with decreasing Re_p immediately after the passage of the shock for $Re_p > 10$. As Re_p decreases further, the increase in C_D becomes moderate. The coefficient of drag is weakly dependent on Ms for the range considered; for a fixed Re_p, C_D is smaller for a larger M_s. The variation of C_D with respect to Re_p does not follow empirical relationships based on earlier experiments.

References

1. H.J. Smolders et al., Shock Waves **2**(4), 255–267 (1992)
2. R. Gore, C. Crowe, Int. J. Multiphase Flow **15**, 279 (1989)
3. J.J.F. Strecker et al., Part. Part. Syst. Charact. **11**, 222–226 (1994)
4. Butler and Schmitt, Powder Technology **63**, 229–240 (1990)
5. R.D. Ingebo, NACA TN **3762** (1956)
6. G. Rudinger, ASME J Basic Eng **92**, 165–172 (1970)
7. E. Outa et al., Bull. JSME **19**, 384–394 (1976)
8. H. Miura, I.I. Glass, Proc. Roy. Soc. Lond. A **385**, 85–105 (1983)
9. V.M. Boiko et al., Shock Waves **7**, 275–285 (1997)
10. M. Sommerfeld, Exp. Fluids **3**, 197–206 (1985)
11. O. Igra, K. Takayama, Proc R Soc A **442**, 231–247 (1993)
12. G. Jourdan et al., Proc R Soc **463** (2008)
13. R. Mejia-Alvarez et al., Shock Waves **25**(6), 635–650 (2015)
14. A. Martinez et al., Exp. Fluids **56**, 1854 (2015)
15. A. Bordoloi et al., J. Fluid Mech. **823**, R4 (2017)

Shock Focusing Effect upon Interaction of a Shock with Low-Density Dust Cloud

O. Sutyrin, V. Levin, and P. Georgievskiy

Abstract A propagation of Mach 2 and 3 plane shock wave through the air containing cylindrical cloud of low-concentration quartz dust is numerically modeled using Euler's equations. One-velocity single-temperature model of dust-air mixture is used. A refraction of incident shock and formation and focusing of transversal shocks are described. Two qualitatively different interaction patterns – external and internal – are found to take place for different dust concentration values. A dependence of peak shock focusing point position and relative shock focusing intensity on volume concentration of dust in range from 0.01 to 0.15% is determined. With increase of dust concentration peak focusing point draws near the cloud edge and moves inside the cloud, while focusing intensity non-monotonically rises.

1 Introduction

Shock propagation through dust-filled gas takes place in a wide range of applications, including such important examples as interstellar shock expansion, explosion safety of coal mines, dusty layer wall shielding against blast waves, and pulse explosive methods of powder coating deposition. The key role is played by interaction of shock waves with local clouds of suspended particles. Experimental data show that during such interaction a reflected shock is formed and dust cloud is significantly distorted and unevenly accelerated [1]. Heterogeneous dust streams and jets are formed, and significant role is played by initial cloud shape [2]. Incident shock part that bends around the cloud outside outruns the shock inside the latter, which leads to formation and mutual reflection of transversal shock waves [3]. This effect of "focusing" of incident shock wave may induce an initiation of combustion and detonation of flammable dust particles [4]. The present paper

O. Sutyrin (✉) · V. Levin · P. Georgievskiy
Institute for Mechanics of Lomonosov Moscow State University, Moscow, Russia
e-mail: sutyrin@imec.msu.ru

A. Sasoh et al. (eds.), *31st International Symposium on Shock Waves 2*,
https://doi.org/10.1007/978-3-319-91017-8_86

continues and expands the study [5] of incident shock focusing effect and impact of dust concentration on qualitative and quantitative flow features.

2 Mathematical Model and Problem Formulation

A model based on Euler's equations for two-component mixture of perfect gases is used to simulate unsteady two-dimensional dust-gas mixture flows. An equilibrium mixture approximation is applied: dust particles have the same velocity and temperature as ambient gas. Equations for two-dimensional plane flows have the following form:

$$\frac{\partial}{\partial t}\begin{pmatrix}\rho^g\\ \rho^d\\ \rho u\\ \rho v\\ H-p\end{pmatrix}+\frac{\partial}{\partial x}\begin{pmatrix}\rho^g u\\ \rho^d u\\ p+\rho u^2\\ \rho uv\\ Hu\end{pmatrix}+\frac{\partial}{\partial y}\begin{pmatrix}\rho^g v\\ \rho^d v\\ \rho uv\\ p+\rho v^2\\ Hv\end{pmatrix}=0,$$

where ρ^g, ρ^d, and $\rho=\rho^g+\rho^d$ are densities of background gas, dust "gas," and mixture density correspondingly, u and v are gas velocity components along Cartesian axes x and y correspondingly, and p and H are total pressure and enthalpy of the mixture:

$$p=\frac{\rho^g}{\mu^g}R_0T+\frac{\rho^d}{\mu^d}R_0T,\qquad H=\frac{\rho\left(u^2+v^2\right)}{2}+\rho^g c_p^g T+\rho^d c_p^d T.$$

Here μ^g, μ^d, c_p^g, c_p^d are molar masses and specific heat capacities of background and dust gases, R_0 is universal gas constant, and T is mixture temperature.

For numerical simulation, an explicit MacCormack "predictor-corrector" method of second order of spatial and temporal accuracy [6] is used. To prevent nonphysical oscillations, total variation diminishing property is ensured by introducing Davis artificial viscosity [7].

Air ($\mu^g=28.98$ g/mol, $c_p^g=1.006$ kJ/kg·K) under $T=293$ K, $p=101\ 325$ Pa is used as a background gas. Dust cloud density is set by volume percentage η^d of dust component, modeled by gas with very high molar mass, which is chosen so that density of pure dust "gas" ($\eta^d=100\%$) under the same T, p would be equal to density of crystal quartz (SiO_2, 2.65 g/cm3): $\mu^d=63700$ g/mol. Specific heat capacity of dust component is assumed equal to quartz heat capacity: $c_p^d=0.74$ kJ/kg·K.

For verification of adopted approach, an interaction of a shock wave with rectangular cloud of Plexiglas particles (material density 1.2 g/cm3, particles concentration $\eta^d=1\%$) [3] has been reproduced. In the study [3], a developed

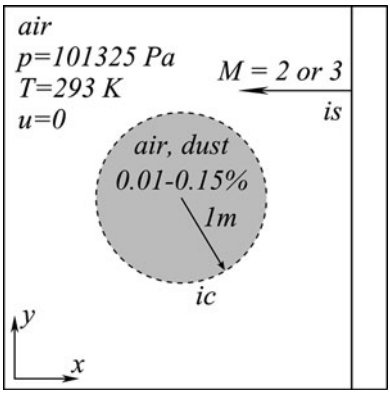

Fig. 1 Initial condition schematic: Mach 2 or 3 shock *(is)* propagates from right to left over a 2 m-wide cylindrical cloud *(ic)* of SiO_2 dust (volume concentration 0.01–0.15%) suspended in motionless air at normal conditions

continual-discrete nonequilibrium model of the dust cloud has been applied, which allowed effective simulation of both shock refraction and motion of shock-accelerated dust particles. Despite the simplicity of equilibrium dust-filled gas model used in the present work, simulations have shown good agreement with respect to depicting incident shock refraction and formation of secondary shock waves. The aim of the present study is to describe the refraction and focusing of shock wave upon interaction with dust cloud of low concentration ($\eta^d \leq 0.15\%$), so the adopted equilibrium model is expected to have sufficient accuracy.

Figure 1 shows the schematic of initial condition. Plane shock wave (compression jump) propagates from right to left through uniform air that contains cylindrical dust cloud of circular cross section. Incident shock intensity is set by Mach number M, cloud radius equals to 1 m, and at the time moment $t = 0$ shock wave touches rightmost point of the cloud. Computations are performed using uniform square mesh of 375 cells per meter. The problem is symmetrical about horizontal plane, so all the following figures show only the top half of the corresponding computational domain region.

3 Interaction of a Shock with a Cloud

Figure 2 shows dust density flood and pressure contour for early and intermediate stages of the interaction for $\eta^d = 0.05\%$, which correspond to effective mixture Atwood number 0.355. Initial position of the cloud is marked by dashed line. Upon transition of the shock into the cloud, a convex shock *rs* is reflected off the cloud edge. Part *ts* of the shock inside the cloud propagates significantly slower than undisturbed shock *is* and has concave shape. With time, it is "overturned": a transversal shock *tts* that propagates toward the symmetry plane, and triple point *tp*, which also moves to the symmetry plane, are formed. Bent part *bis* of incident shock is connected to transversal shock *tts* and skirts the cloud outside.

Qualitatively different shock-cloud interaction patterns take place depending on the governing parameters of the problem. For parameter range of M=2 or

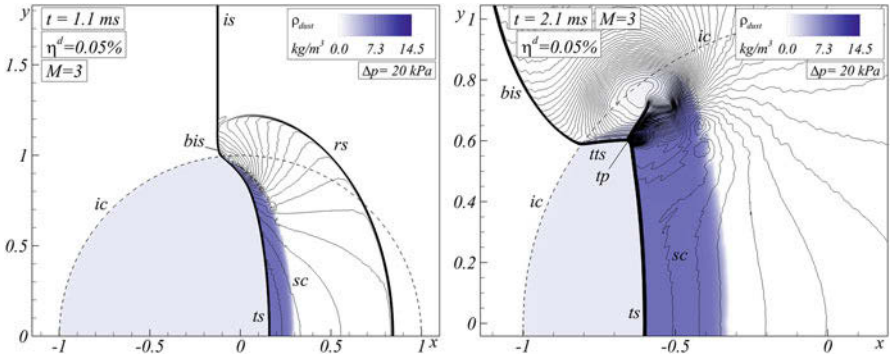

Fig. 2 Early (left) and intermediate (right) stages of the interaction for $M = 3$, $\eta^d = 0.05\%$: upper half of the domain, dust density flood, pressure contour. *rs*, *ts*, reflected and transmitted shocks; *bis*, bent part of the initial shock; *sc*, shocked dust cloud edge; *tp*, triple point; *tts*, transversal secondary shock

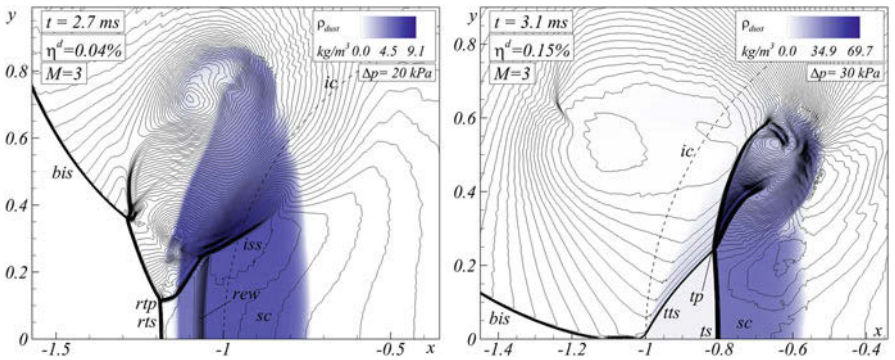

Fig. 3 Interaction patterns for $M = 3$: external (left, $\eta^d = 0.04\%$) and internal (right, $\eta^d = 0.15\%$): time moments shortly before shock focusing peak. *rts*, *rtp*, retransmitted shock and triple point; *iss*, internal secondary shock; *rew*, reflected expansion wave

3, $\eta^d = 0.01 - 0.15\%$ (effective Atwood number 0.099–0.622), for which the simulations were performed, two interaction patterns occurs. For lower dust concentrations, shock *ts* and triple point *tp* that propagate inside the cloud reach the leeward edge of the cloud and emerge from it before the enveloping shock *bis* reaches the symmetry plane (Fig. 3, left). Later on, the retransmitted triple point *rtp* continues to move toward the symmetry plane. During the transition of shock *ts* through the cloud edge, rarefaction wave *rew* is reflected inside the cloud. When transversal shock is reflected from the symmetry plane, a sharp local pressure rise is registered; the highest pressure is reached when triple point reaches the symmetry plane. In this way, the gas in the shock focusing area suffers two consecutive compressions: first by passage of retransmitted shock *rts*, then by reflection of transversal shock.

For higher values of volume dust concentration, the wave inside the cloud propagates even slower, and shock *bis* have enough time to reach the symmetry plane before the waves inside the cloud hit its leeward edge (Fig. 3, right). As a result, at the moment when shock *bis* touches the symmetry plane, a local area of undisturbed dust-air mixture is bounded by shocks *ts* and *tts*. Shortly after, it collapses due to countermovement of the shocks, and sharp local pressure rise is registered as well. Qualitatively similar shock refraction patterns are observed for interaction of a shock with oblate cylindrical area of high-density gas [8]. Unlike external flow pattern, the gas in the shock focusing area is dust-filled and suffers compression by simultaneous collapse and reflection of transmitted and transversal shocks.

A process of transversal shock reflection off the symmetry plane – shock focusing – also has different nature depending on dust concentration in the cloud. For lower concentration values, peak gas pressure is reached in the immediate vicinity of the triple point *rtp* at the moment when it hits the symmetry plane outside the distorted cloud – an external focusing pattern takes place (a moment shortly before the focusing outside the cloud is shown in Fig. 3, left). Upon dust concentration increasing, shock focusing point moves near the cloud edge and shifts inside of it – a transition to internal shock focusing pattern takes place. The dependence of X_{foc} – the distance between peak shock focusing point position and initial cloud center – on dust concentration for $M = 2$ and 3 is shown in Fig. 4 (left scale). A transition between external and internal focusing patterns occurs at $\eta^d = 0.09 - 0.10\%$ for $M = 2$ and at $\eta^d = 0.11 - 0.12\%$ for $M = 3$. The time interval between the start of interaction and peak shock focusing moment monotonically rises from 4.3 ms to 5.2 ms for $M = 2$ and from 3.0 ms to 3.4 ms for $M = 3$.

Peak gas pressure P_{foc} reached at focusing point also depends significantly on η^d (Fig. 4, right scale): it monotonically rises till the certain point as the focusing point moves toward the cloud edge, then drops slightly in the closest proximity

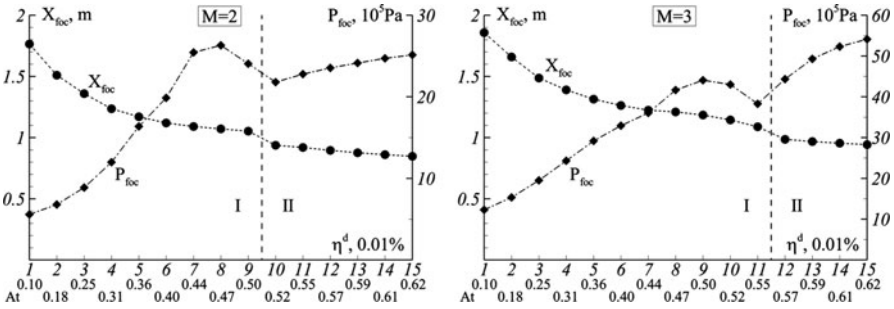

Fig. 4 Dependence of X_{foc} (circles, left scale) and P_{foc} (diamonds, right scale) on η^d for $M = 2$ (left figure) and $M = 3$ (right figure). Effective Atwood numbers for each η^d values are shown below the horizontal axis. Dashed vertical line separates regions of external (I) and internal (II) interaction patterns

of the edge, and rises again upon the transition to internal focusing pattern. The non-monotony of P_{foc} is most probably caused by a competition of two effects: First, with dust concentration increase, the intensity of transversal shock rises, thus increasing peak pressure reached upon reflection off the symmetry plane. Second, the closer the shock focusing point gets to the cloud edge, the more oblique becomes transversal shock (similarly to shock *tts* in Fig. 3, right), thus decreasing the pressure reached upon reflection off the symmetry plane. The latter effect is most significant for external shock focusing patterns that are very close to transition to internal pattern, thus leading to aforementioned non-monotony.

Similar yet much more pronounced focusing intensity rise upon flow type transition is observed for interaction of a shock with axisymmetric bubble of high-density gas [9], and it is shown that beside density crucial role is played by bubble shape. Similarly, dust cloud shape here is expected to significantly influence qualitative and quantitative features of shock focusing process as well.

4 Conclusion

Interaction of a shock with dust cloud has been simulated using equilibrium dusty gas model based on Euler's equations for perfect gas mixture. It is shown that interaction of a shock with dust cloud leads to qualitative flow restructuring, i.e., to incident shock refraction and formation and mutual reflection – focusing – of transversal shocks waves. Two distinct interaction patterns – external and internal shock focusing – are observed. Dust volume concentration has a crucial influence on shock focusing pattern and intensity: lower concentrations lead to mostly relatively weak external focusing, while higher concentrations result in generally more intense internal focusing patterns. The peak pressure reached upon shock focusing non-monotonically rises with dust concentration increase.

This study is performed in the Institute for Mechanics of Moscow State University using computational resources of Moscow State University "Lomonosov" cluster with financial support of Russian Foundation for Basic Research (project 16-29-01092) and the Council for Grants of the President of the Russian Federation (NSh-8425.2016.1).

References

1. V.M. Boiko, V.P. Kiselev, S.P. Kiselev, A.N. Papyrin, S.V. Poplavsky, V.M. Fomin, Shock wave interaction with a cloud of particles. Shock Waves **7**(5), 275–285 (1997)
2. G.B. Jacobs, W.S. Don, T. Dittmann, High-order resolution Eulerian–Lagrangian simulations of particle dispersion in the accelerated flow behind a moving shock. Theor. Comput. Fluid Dyn. **26**, 37–50 (2012)
3. V.P. Kiselev, S.P. Kiselev, E.V. Vorontsov, Interaction of a shock wave with a particle cloud of finite size. Shock Waves **16**(1), 53–64 (2006)

4. K. Benkiewicz, A. Koichi Hayashi, Aluminum dust ignition behind reflected shock wave: Two-dimensional simulations. Fluid Dynamics Research. **30**, 269–292 (2002)
5. P.Y. Georgievskiy, V.A. Levin, O.G. Sutyrin, Shock focusing upon interaction of a shock with a cylindrical dust cloud. Tech. Phys. Lett. **42**(9), 936–939 (2016)
6. R.W. MacCormack, The effect of viscosity in hypervelocity impact cratering, AIAA Paper. No. 69–354 (1969)
7. S.F. Davis, A simplified TVD finite difference scheme via artificial viscosity. SIAM J. Sci. Stat. Comput. **8**(1), 1–18 (1987)
8. J. Ray, R. Samtaney, N.J. Zabusky, Shock interactions with heavy gaseous elliptic cylinders: Two leeward-side shock competition modes and a heuristic model for interfacial circulation deposition at early times. Phys. Fluids **12**(3), 707–716 (2000)
9. P.Y. Georgievskiy, V.A. Levin, O.G. Sutyrin, Interaction of a shock with elliptical gas bubbles. Shock Waves **25**(4), 357–369 (2015)

Shock-Induced Motion of a Spherical Particle Floating in Air

Y. Sakamura, M. Oshima, K. Nakayama, and K. Motoyama

Abstract Shock tube experiments were conducted to investigate the shock-induced motion of spherical solid particles and the flow structure around them. In each shot, a spherical particle initially placed on the shock tube floor was tossed into the air and then collided with a planar shock wave with a Mach number of 1.3 when it reached the top of its trajectory almost at rest. The shock-induced motion of the particle and the flow field around it were visualized by the shadowgraph technique coupled with a high-speed video camera. It was found that (1) the separation points and wakes noticeably fluctuated, (2) the shocked particles moved not only in the horizontal (shock propagating) direction but also in the vertical direction, and (3) the drag coefficients obtained from the present experiments were larger than those from the standard drag curve at the same particle Reynolds numbers.

1 Introduction

When a shock wave propagates in a suspension of solid particles in a gaseous medium, the interaction between the shock wave and the solid particles occurs. The elapsed time for the shock wave to pass through a particle is usually much smaller than the velocity (or Stokes) relaxation time ($\tau_V = \rho_p d_p^2/(18\mu_g)$, where ρ_p and d_p are the density and the diameter of the particle, respectively, and μ_g is the viscosity of the gas behind the shock wave [1, 2]), and the particle velocity hardly changes during the shock passage. The gas velocity, on the other hand, impulsively increases behind the shock wave, so that there exists a large velocity difference between the gas and solid phases immediately behind the shock wave. Such large interphase differences in flow velocities cause rapid momentum transfer; thus the deviations from equilibrium conditions decay with time.

Y. Sakamura (✉) · M. Oshima · K. Nakayama · K. Motoyama
Department of Mechanical Systems Engineering, Toyama Prefectural University, Toyama, Japan
e-mail: sakamura@pu-toyama.ac.jp

A. Sasoh et al. (eds.), *31st International Symposium on Shock Waves 2*,
https://doi.org/10.1007/978-3-319-91017-8_87

The relaxation phenomena mentioned above play an important role in high-speed flows of gas-particle systems with shock waves [3] such as flows in solid rocket nozzles [4] and dust explosions in coal mines and process industries [5]. In order to understand the dynamics of the solid particle immersed in the highly transient flows induced by a shock wave, a number of shock tube experiments have been conducted so far. Among them are Igra and Takayama [6], Suzuki et al. [7], and Jourdan et al. [8]. One of the most important results from these studies is that the drag coefficients of particles accelerating behind a shock wave were larger than the drag coefficients of a sphere moving steadily in a fluid at the same relative Reynolds numbers. In these works, the increased drag was attributed to flow unsteadiness. Recently, Wagner et al. [9] carried out shock tube experiments of particle response to the shock wave passage and then concluded that the increased drag was caused by compressibility rather than flow unsteadiness based on a recent model for the unsteady force acting on a particle during shock-particle interaction [10].

As stated above, there is still no conclusive explanation for the increased drag of a particle in shock-induced flows. This is partly due to the fact that we have little knowledge about flow physics around the shocked particles, including boundary-layer separation, vortex shedding, and wakes [11–13]. The present work is the first step of our plan to investigate the shock-induced motion of a spherical particle and the flow structure around the shocked particle. In each experiment, a spherical solid particle initially placed on the floor of a shock tube was tossed into the air with an injecting device and then collided with a planar shock wave, so that shock wave interactions with a particle without any supports were realized. The shock-induced motion of the particle and the flow field around it were visualized by the shadowgraph technique coupled with a high-speed video camera.

2 Experimental Facilities and Method

2.1 Shock Tube

The experiments were conducted in a horizontally placed shock tube of Toyama Prefectural University, which consists of a 1.46-m-long driver section with 120 mm inner diameter, a 4.6-m-long driven section with 30 mm × 100 mm rectangular cross section, and a dump tank. A test section with a pair of optical viewing windows of 90 mm × 200 mm was installed between the driven section and the dump tank. Two piezoelectric pressure gauges (Kistler, 601A) were flush mounted on a sidewall of the driven section both for recording pressure histories in the driven section and for measuring the propagating speed of an incident shock wave.

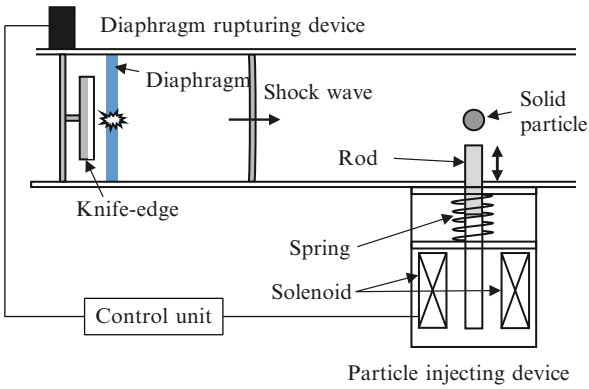

Fig. 1 Particle-injecting system

2.2 Particle-Injecting System

A newly developed particle-injecting device [14] was mounted on the floor of the test section 3.8 m away from the diaphragm location. It was electronically connected to a diaphragm-rupturing device through a control unit. Figure 1 shows a schematic diagram of the present system. The particle-injecting device is composed of a cylindrical rod, a spring, and a solenoid. The spring-loaded rod was initially pulled flush with the shock tube floor by the solenoid, and a spherical particle was placed on the top of the rod. When an electrical signal from the control unit released the rod, the spherical particle was injected into the air. After injecting the particle, the rod was quickly pulled back to its initial position by the solenoid so as not to disturb the flow in the test section.

The diaphragm-rupturing device consists of a spring-loaded plunger with a knife-edge and a solenoid. By a trigger signal from the control unit, which is synchronized with the initiation of the particle-injecting device, the solenoid and thus the plunger were activated to break the diaphragm to create a planar shock wave in the shock tube. Tuning the delay of the trigger signal after the initiation of the injecting device made the shock wave interact with the particle floating in the air almost at rest without any supports.

2.3 Visualization System

The shock-induced motion of the particle and the flow field around it were visualized using the shadowgraph technique and recorded by a high-speed video camera (Photron, APX RS205K) with a camera lens (Nikon, Nikkor 105 mm, F1.8). The frame rate and the exposure time of the recording were set at 20,000 fps and 1/500,000 s, respectively, and an acquired image had 512 $\times$ 256 pixels (1 pixel = 0.317 mm). A mercury lamp (Ushio, UI-100) was used as the light source

Table 1 Properties of spherical particles used

Classification	Range of d_p [mm]	Range of ρ_p [kg/m^3]	Material
Sphere1	12.67 – 12.68	1366 – 1377	Polyoxymethylene
Sphere2	5.86 – 5.90	1018 – 1048	Polystyrene
Sphere3	5.53 – 5.54	1372 – 1389	Polyoxymethylene

of the shadowgraph system. A concave mirror with a focal length of 200 mm was used to collimate the light from the mercury lamp, and the other one was used to focus the light passed through the test section on the camera lens.

2.4 Test Conditions

The working gas was air, and the gas in the test section was initially at atmospheric pressure and at room temperature. The Mach number of the incident shock wave was set to 1.3, and the speed of the post-shock flow was estimated at about 150 m/s. Owing to the arrival of expansion waves from the dump tank, the flow duration time was limited to about 6 ms. It should be noted here that the Mach number of the shock-induced flow was about 0.4 and the effect of compressibility on the drag coefficient of a spherical particle may be negligible [15].

The properties of spherical particles used in the present work are summarized in Table 1. The particles are classified into three types (Sphere1, Sphere2, and Sphere3) according to the diameter and density (i.e., material). Each shot was numbered consecutively and designated with the type of particle such as Sphere1-*x*, where *x* is the shot number, in this paper.

3 Experimental Results and Discussion

3.1 Flow Visualization

Typical shadowgraph images obtained for Sphere1–7 and Sphere3–1 are shown in Fig. 2, where t is the time after the incident shock wave moving from left to right passed the center of the particle. It can be seen from these images that the particle scarcely moved about 1 ms after the shock passage even though large forces caused by shock wave reflections from the particle's surface might temporally act on the particle. The shadows of vortex rings produced by shock diffraction can be observed from the shadowgraphs taken at $t = 0.138$ ms for Sphere1–7 and at $t = 0.107$ and 0.157 ms for Sphere3–1. With passage of time, the vortices collapsed, and the boundary-layer separation and wake appeared as seen in the shadowgraphs.

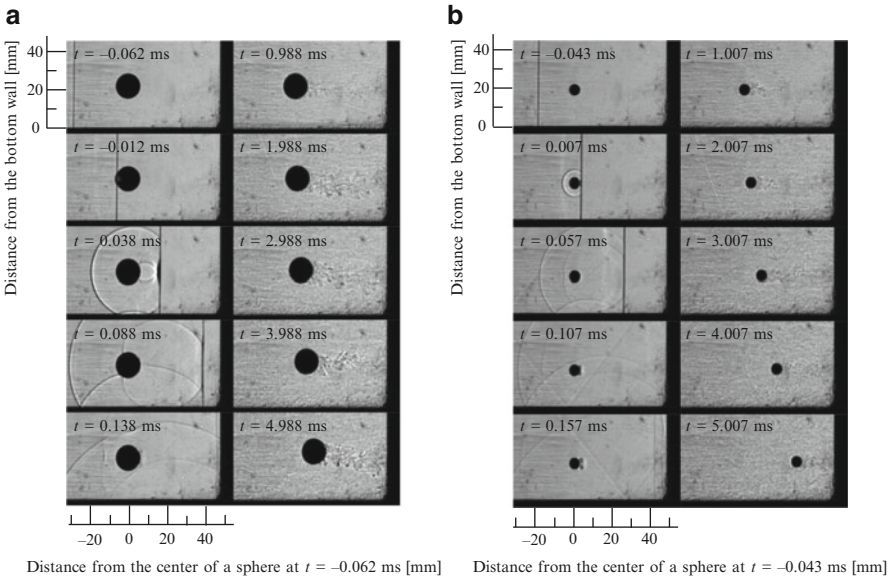

Fig. 2 Representative shadowgraph images obtained from the present experiments (**a**) Sphere1–7 and (**b**) Sphere3–1

It should be mentioned here that some shocked particles moved not only in the flow direction but also in the direction normal to the flow as seen in Fig. 2a (Sphere1–7) even though the vertical speeds were much smaller than the horizontal ones. This is probably due to vertically asymmetric boundary-layer separations on the shocked particles.

It is also found from the temporally resolved images that the wakes noticeably fluctuate behind the particles. Such unsteadiness of the flow field around the particle is likely to influence the particle's motion. According to Achenbach [11], strong periodic fluctuations in the wake flow behind a sphere are observed in the Reynolds number range from 6×10^3 to 3×10^5. The flows around the shocked particles shown in Fig. 2 seem to be in this flow regime. In fact, the particle Reynolds numbers defined as [16]

$$\mathrm{Re_p} = \frac{\rho_\mathrm{g} d_\mathrm{p}}{\mu_\mathrm{g}} \left| \frac{u_\mathrm{g} - u_\mathrm{p}}{\mathrm{d}u_p/\mathrm{d}t} \right| \sqrt{\left(\frac{\mathrm{d}u_\mathrm{p}}{\mathrm{d}t} \right)^2 + \left(\frac{\mathrm{d}v_\mathrm{p}}{\mathrm{d}t} + g \right)^2}$$

where 1.6×10^5 and 0.7×10^5 for Sphere1–7 and Sphere3–1, respectively, and both are within the range mentioned above. Here ρ_g and u_g are the density and velocity of the gas behind the shock wave, respectively, g is the acceleration of gravity, and u_p and v_p are the horizontal and vertical components of the particle velocity, respectively.

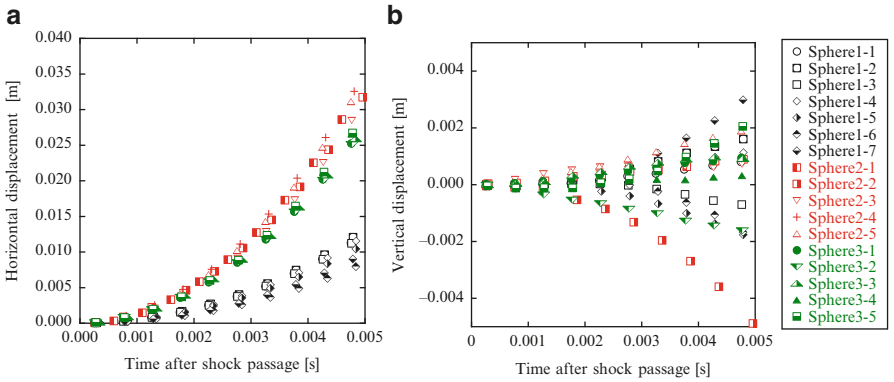

Fig. 3 Temporal variations of the horizontal and vertical displacements of shocked particles (**a**) Horizontal displacement and (**b**) vertical displacement

Figure 3 illustrates the temporal variations in the horizontal and vertical displacements of shocked particles for each shot. The results of horizontal motion of the particles of the identical classification clearly show the same trend, but those of vertical motion differ from shot to shot although the vertical displacement is much smaller than the horizontal one. The irregular motion in the vertical direction suggests that the locations of boundary-layer separation were vertically asymmetric and irregular.

3.2 Drag Coefficients

From the particle trajectories shown in Fig. 3, the drag coefficients of spheres, C_D, were calculated as [16]

$$C_D = \frac{3}{4}\frac{\rho_p}{\rho_g} d_p \frac{\left(\frac{du_p}{dt}\right)^2}{(u_g - u_p)^2 \sqrt{\left(\frac{du_p}{dt}\right)^2 + \left(\frac{dv_p}{dt} + g\right)^2}}$$

The time-averaged values of C_D during 5 ms after shock passage as a function of Re_p are shown in Fig. 4 with the standard drag curve from Henderson [15]. As expected from the previous works [6–9], the drag coefficients obtained from the present experiments were larger than those from the standard drag curve. It should be noted that the Mach number of the shock-induced flow was about 0.4, so the effect of compressibility on the drag coefficient of a spherical particle seems to be small. It is also found that a large scatter of data exists only for the cases of Sphere1. One of the possible reasons for this result is the flow unsteadiness enhanced by the elevated particle Reynolds numbers [11]. Another possible reason is the effect of

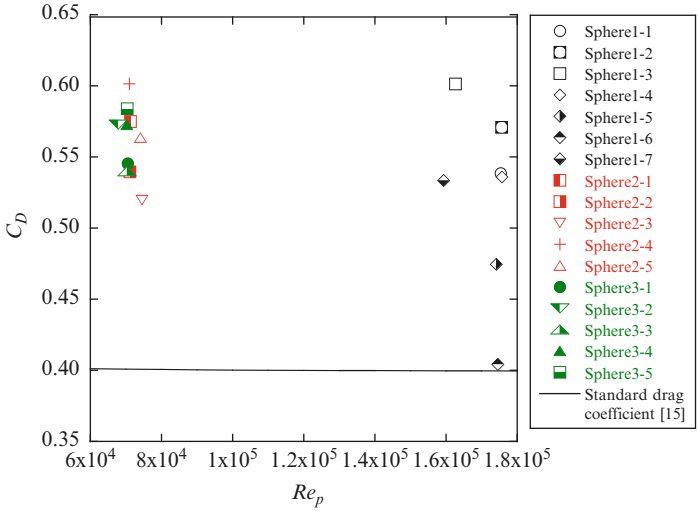

Fig. 4 Drag coefficient versus particle Reynolds number

"tunnel blockage" [13]; the blockage ratio defined as d_p/w, where w is the width of the test section (30 mm in the present experiments), was about 0.43 for the cases of Sphere1 and more than two times larger than those for other cases.

4 Concluding Remarks

A series of shock tube experiments was conducted to investigate the shock-induced motion of a spherical solid particle and the flow structure around it. In each experiment, a planar shock wave with a Mach number of 1.3 interacted with a particle floating in the air at atmospheric pressure and room temperature without any supports. The main conclusions are summarized as follows:

- The separation points on the shocked particles and wakes behind them noticeably fluctuated.
- The shocked particles moved not only in the horizontal direction but also in the vertical direction probably due to vertically asymmetric separations.
- The drag coefficients obtained from the present experiments were larger than those from the standard drag curve at the same particle Reynolds numbers.

References

1. G. Rudinger, *Fundamentals of Gas-Particle Flow* (Elsevier, Amsterdam, 1998), p. 9
2. L.-S. Fan, C. Zhu, *Principles of Gas-Solid Flows* (Cambridge University Press, Cambridge, 1998), p. 93
3. O. Igra, G. Ben-Dor, Appl. Mech. Rev. **41**, 379 (1988)
4. R.F. Hoglund, J. Am. Rocket Soc. **32**, 662 (1962)
5. R.K. Eckhoff, *Explosion Hazards in the Process Industries*, 2nd edn. (Elsevier, Amsterdam, 2016), pp. 253–383
6. O. Igra, K. Takayama, Proc. R. Soc. A **442**, 231 (1993)
7. T. Suzuki et al., Meas. Sci. Technol. **16**, 2431 (2005)
8. G. Jourdan et al., Proc. R. Soc. A **463**, 3323 (2007)
9. J.L. Wagner et al., Phys. Fluids **123301**, 24 (2012)
10. M. Parmar et al., Shock Waves **19**, 317 (2009)
11. E. Achenbach, J. Fluid Mech. **54**, 565 (1972)
12. E. Achenbach, J. Fluid Mech. **62**, 209 (1974)
13. E. Achenbach, J. Fluid Mech. **65**, 113 (1974)
14. M. Oshima et al., Proc. of the 22nd Int. Shock Interaction Symp. **73** (2018)
15. B.C. Henderson, AIAA J. **14**, 707 (1976)
16. S. Temkin, S.S. Kim, J. Fluid Mech. **96**, 133 (1980)

Exploring the Capability of a New Shock Tube Facility to Investigate Shock Interaction with Inert Particle Columns

M. G. Omang, K. O. Hauge, and J. K. Trulsen

Abstract In this paper we present work in progress and preliminary results from experimental studies of shock propagation through particle-laden gas columns. The experiments are conducted in a double-driver shock tube. The tube has a total length of 8.6 m. A setup with a double-driver chamber is chosen, as results clearly demonstrate high degree of repeatability. In order to obtain relatively short shock durations, the total length of the driver section is only 0.12 m. Pressure gauges and high-speed cameras are used to measure the results. A specially designed window section together with high-speed video cameras equipped with telecentric lenses and illuminators allows the shock-particle interaction in directions perpendicular to each other to be captured.

1 Introduction

This paper presents work in progress and preliminary results from experimental and numerical studies of shock propagation through particle clouds. A test center has been built up at Østøya, Horten in Norway, and the experimental facility has been further developed the last years. The present results are based on experiments performed in April and represent the state of the art at this point.

M. G. Omang (✉)
Norwegian Defence Estates Agency, Oslo, Norway

Institute of Theoretical Astrophysics, University of Oslo, Oslo, Norway
e-mail: momang@astro.uio.no

K. O. Hauge
Norwegian Defence Estates Agency, Oslo, Norway

J. K. Trulsen
Institute of Theoretical Astrophysics, University of Oslo, Oslo, Norway

A. Sasoh et al. (eds.), *31st International Symposium on Shock Waves 2*,
https://doi.org/10.1007/978-3-319-91017-8_88

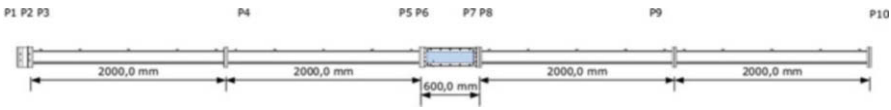

Fig. 1 Shock tube sketch with sensor positions given. The blue-colored area is the window section. This is also where the dust is injected

2 Experimental Setup

The shock tube is constructed to simulate short duration blast waves and consists of two driver sections of length 0.09 and 0.03 m, respectively. The driver sections are separated from each other and the driven section by Mylar Dupont membranes. The tube is rectangular with dimensions 108 × 48 mm. The driven section has a length of 8.6 m, with a window section of length 600 mm, mounted 4.12 m from the left wall of the tube. The experimental setup is illustrated in Fig. 1. Both driver and driven sections are equipped with adapters for pressure and temperature measurements. Kulite XT190 and thermocouple Type K sensors are used to measure the pressure and temperature in the driver chambers, whereas Kistler 603B pressure gauges are used to measure the pressure-time history in the driven section. The window section is specially constructed to allow high-speed video to be recorded simultaneously in directions perpendicular to each other. Two Phantom v2012 high-speed video cameras are used for the recordings, with 41,298 frames per second and an exposure time of 0.303 μs. Each picture has a resolution of 768 × 576 pixels, with a conversion factor of 7.8 pixels per millimeter.

High-resolution telecentric lenses from Opto Engineering TC4MHR080-F are mounted on both cameras. On the opposite sides of the window section, relative to the two cameras, telecentric illuminators HP LTCLHP0808-R are mounted as illustrated in Fig. 2. A calibration cylinder is positioned in the field of view, outside the tube, to illustrate the dimensions of the pictures. The cylinder has dimensions 20x5 mm. A sketch and a photo of the optical setup are presented in Fig. 2.

3 Numerical Method

Smoothed particle hydrodynamics (SPH) has been used for the numerical simulations. SPH is a Lagrangian interpolation method where particles are used to simulate a continuous fluid flow [1]. In the current work, an extension to the method called regularized smoothed particle hydrodynamics (RSPH) has been used. In RSPH, a piecewise constant resolution is introduced, giving particles different resolution, called smoothing length, throughout the computational domain. At regular time intervals, the spatial resolution is optimized through a particle regularization, in which the particles are redistributed. The new particle distribution inherits its properties from the old particle set, to ensure conservation of mass, momentum, and energy.

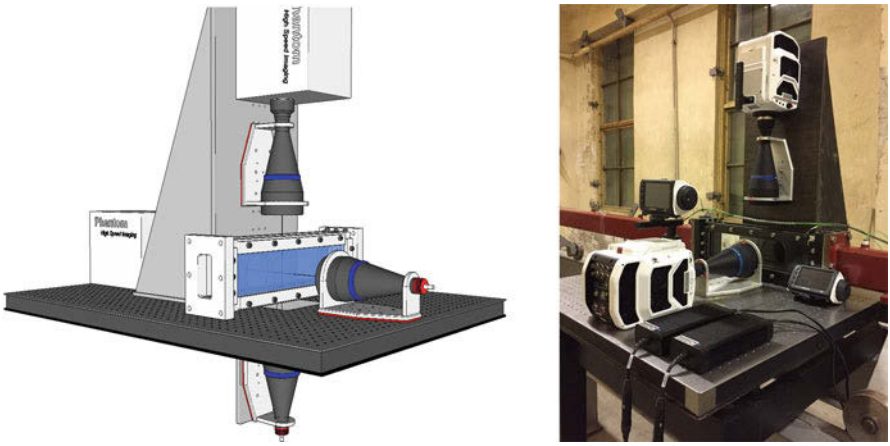

Fig. 2 Left panel shows sketch of the optical setup. Right panel shows a photo of the actual test equipment

A detailed description of the formulation is given in [2]. In recent years the code has been developed further to include a multiphase description [3]. Here each phase is described with a separate set of simulation particles and a separate set of equations of motion. The equations are coupled through the source terms. For nonreactive particles the source terms included are heat exchange and drag terms.

The simulation particles are given properties such as mass, density, pressure, temperature and velocity, and a void fraction defined to describe the diluteness of the gas-dust mixture. The total void fraction for of all phases should sum up to unity. In the current simulations, the dust void fraction is assumed to be small, which implies that particle-particle collision can be neglected.

4 Result Presentation and Conclusions

The aim of this study is to look at the interaction of planar shock waves with columns of dust. The dust is injected into the window section from below at a distance 4.443 m from the left-hand wall. The volume of the injected inert dust particles is measured prior to injection. An amount of either 3.5 mm^3 or 7 mm^3 was used in the current test series. The particles are injected with a spark generator, and accurate timing is necessary to ensure that the particles are in suspension before the shock arrives. The dust particles applied for these tests are aluminum-coated retroreflective barium titanate solid glass spheres, manufactured by Cospheric. The glass spheres have a density of 4490 kg/m^3. The spheres have a distribution in size with a mean diameter of 40–50 μm. For the numerical work, a diameter of 45 μm was chosen, assuming only one-size particles.

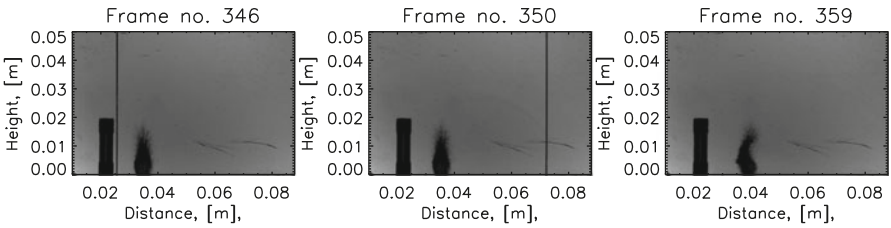

Fig. 3 Pictures from the high-speed video for three different frame numbers

Table 1 Pressure sensor positions

	P1	P2	P3	P4	P5	P6	P7	P8	P9	P10
x[m]	0.015	0.105	0.22	2.22	4.02	4.22	4.62	4.82	6.62	8.62
h[m]	0.1	0.1	0.1	0.1	0.1	0.1	0.1	0.1	0.1	0.1

Table 2 Initial conditions used in the numerical simulations

	P_0 [kPa]	P_1 [kPa]	P_2 [kPa]	ρ_0 [m/kg^3]	ρ_1 [m/kg^3]	ρ_2 [m/kg^3]	ρ_d [m/kg^3]	d_d [μm]
1	100.	194.31	1035.29	1.203	2.31068	12.2822	4490	45
2	100.	196.75	1060.84	1.203	2.33495	12.6167	4490	45

The initial conditions for the numerical and experimental tests are given in Table 2. Suffix 0 is used for the atmospheric conditions, whereas suffix 2 and 1 are used for the two driver section parts as given from left to right.

Results from the horizontally mounted high-speed camera are presented in Fig. 3. In the left panel, the shock is observed to the left of the cloud, as a solid vertical line. The mid-panel shows the situation where the shock has passed through the cloud and is about to leave the field of view. In this frame the cloud has hardly been moved, whereas in the right frame the dust has clearly been displaced. Also the shape of the cloud has been altered and now appears slightly curved.

As presented in Table 1, pressure sensors were also included in the shock tube. Based on the initial pressures measured in the different chambers, numerical simulations were performed with RSPH. Comparison of numerical and experimental pressure sensors for a given position is illustrated in Fig. 4. The experimental and numerical positions are synchronized at this point. The unfiltered pressure signal is presented, but pressure level and shape of the two pressure curves are similar.

The main objective of this work is to obtain high-quality quantitative experimental data that will allow for verification and calibration of the numerical models used in the simulation of shock interaction with both inert and reactive particle clouds.

The work presented shows the status of the current the project. Closer comparison between numerical and experimental results still remains to be performed, but the preliminary results are promising.

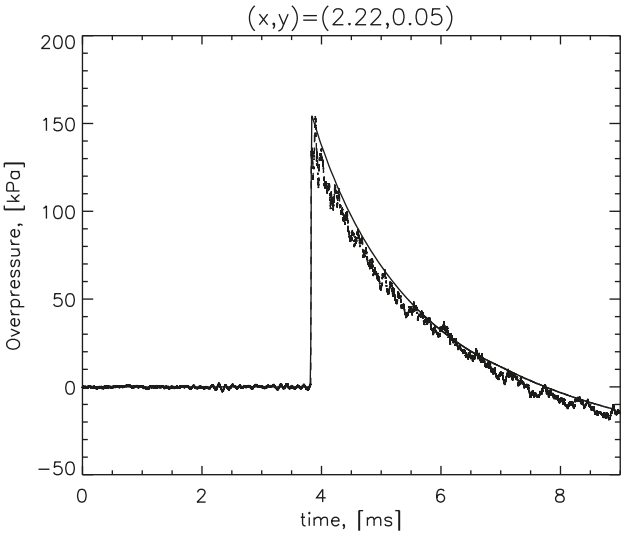

Fig. 4 Comparing numerical and experimental results for a chosen pressure sensor position corresponding to measure point P4

References

1. J.J. Monaghan, Rep. Prog. Phys. **68**(8), 1703–1759 (2005)
2. S. Børve, M. Omang, J. Trulsen, J. Comput. Phys. **208**(1), 345–367 (2005)
3. M.G. Omang, J.K. Trulsen, Shock Waves **24**(5), 521–536 (2014)

Mitigation of Blast in a Water Mist

T. Schunck, M-O. Sturtzer, J. Mory, D. Eckenfels, and J-F. Legendre

Abstract The purpose of this work was to study blast mitigation in a water mist and more specifically the effects of the droplet size and of the water mist loading on blast mitigation. A tunnel has been equipped with a water mist fire suppression system. By using this facility, experiments of detonation were carried out in the air and in different water mists. The blast effects were evaluated by means of four pressure gauges placed on the tunnel walls and one pressure gauge placed at the end of the tunnel. The transmission factor of the initial overpressure in the water mist was around 0.8 when four nozzles were used to produce the mist, whatever the size of the droplets. The transmission factor of the initial overpressure was smaller, about 0.6, with eight nozzles generating the mist, either for small or large droplets. The shock wave was delayed by the presence of the mist. The maximum impulse was reduced by about 20% when four nozzles were used to produce the mist, whether the droplets were small or large. The maximum impulse was more reduced with eight nozzles generating the mist, i.e., by about 30% for both droplet sizes.

1 Introduction

It is well known that explosion effects can be significantly mitigated by surrounding a detonating charge with a layer of water. Water can be used in various physical forms, bulk water [1], spray, or mist [2]. Numerous studies have described the mitigation of dust, hydrocarbon mist, and vapor/gas cloud explosions by using water mist [2–5]. In contrast, the use of water mist to mitigate the blast effect from a high explosive has been less studied, and only a small number of papers have been published [6–11]. Nevertheless, it has been shown that the overpressure, the impulse, as well as the quasi-static pressure of an explosion are reduced by the presence of mist.

T. Schunck (✉) · M.-O. Sturtzer · J. Mory · D. Eckenfels · J.-F. Legendre
ISL, French-German Research Institute of Saint Louis, Saint Louis, France
e-mail: therese.schunck@isl.eu

A. Sasoh et al. (eds.), *31st International Symposium on Shock Waves 2*,
https://doi.org/10.1007/978-3-319-91017-8_89

It has been assumed in the previous studies [9–12] that the factors strongly influencing the explosion attenuation are the droplet size and the water load. But most of the time in these studies, the water mist was not characterized precisely and consequently, it was difficult to evaluate the mitigation efficiency according to the type of water mist. Therefore, a facility and a method of evaluating the mitigation properties of a water mist and its characteristics were developed. A tunnel was built and equipped with a water mist fire suppression system. By using this facility, experiments of detonation were carried out in air and in water mists. The water load of the mist in the tunnel as well as the droplet size was varied. The water mists effects on the blast wave overpressure and impulse loading generated by the detonation of Composition B spheres were assessed.

2 Experimental

The tunnel has the following dimensions: a length of 4.50 m, a width of 2 m, and a height of 3 m. The tunnel was equipped with a water mist fire suppression system consisting of a high-pressure pump (SEM-SAFE®, Danfoss, 114 liters per minute, 120 bar) and nozzles. Three types of nozzles were used: the first and the second ones (types F500.147.37.04 and F500.143.37.04, DEF, France) generate fine droplets (diameter of the order of 25–100 μm), and the third one (type 17 90 05, DEF, France) generates large droplets (diameter of the order of 200–300 μm). Two arrangements of nozzles in the tunnel were investigated; they are presented in the Fig. 1 (left).

The flow of each nozzle was determined by collecting the whole ejected mass of water in a plastic barrel for a given period of time. The water distribution on the floor

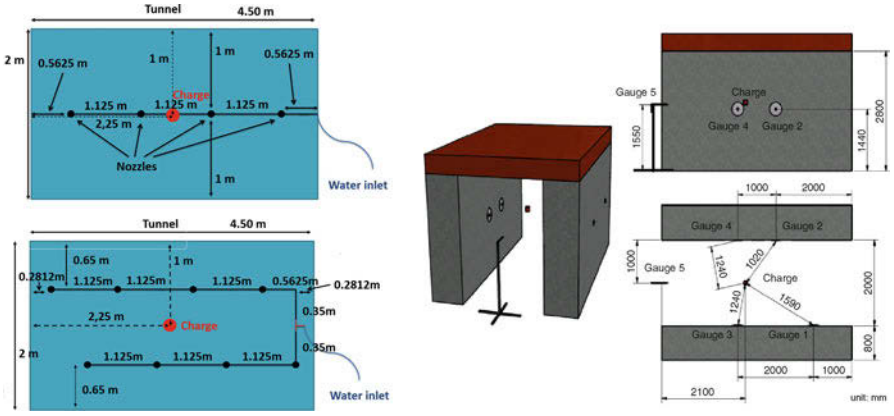

Fig. 1 (Left) The two arrangements of nozzles. (Right) Gauge positions inside the tunnel and charge position with respect to the gauges

was measured in a similar way: an array of 100 × 100 mm plastic boxes collected water for a certain length of time.

The charges used were homogeneous spherical charges of Composition B. The sphere mass was 57 g. They were ignited by means of a high-voltage cap and 5 g of C4. The position of the charge in the tunnel and with respect to the pressure gauges is presented in Fig. 1. Blast effects were evaluated by using four reflected pressure gauges (PCB 113B28) placed on the tunnel walls and one side-on pressure gauge (PCB 137 A 23) placed at the end of the tunnel.

3 Results

3.1 Water Mist Characteristics

It was observed that the nozzles generating small droplets restricted the flow; indeed, for the two nozzle configurations, the nozzle flow was approximately the same. Such was not the case for the nozzles generating large droplets, the nozzle flow being much higher when four nozzles were used, compared with eight. The water distribution on the floor was measured for each configuration. The time of flight (TOF) of droplets from top to bottom in the tunnel was estimated. From these water distributions and from the TOF, it was possible to estimate the water load. First of all it was observed that for small droplets, the water distribution was affected by drafts, which was less the case for large droplets. The small droplets were volatile and escaped from the tunnel. When four nozzles were used, whether for small or large droplets, the water distribution was very inhomogeneous. When four nozzles ejecting small droplets were used, the mean water load was about 200 g/cm^3, and with eight nozzles the value increased to 300 g/cm^3. When four nozzles ejecting large droplets were used, the mean water load was about 150 g/cm^3, but with eight nozzles the value decreased to 120 g/cm^3. This is due to the higher flow of the nozzle in the case of a four-nozzle configuration.

3.2 Detonation Tests

Thirty four detonation tests were performed, 8 detonations in the air and 26 in a water mist. Five tests were carried out with four nozzles generating small droplets, and six tests were performed with four nozzles generating large droplets. Eight tests were made with eight nozzles generating small droplets, and seven were performed with eight nozzles generating large droplets. Figure 2 presents the overpressure as a function of time for all the tests obtained with the five gauges. The red curves correspond to blast tests in the air, the light blue ones correspond to blast tests in water mist composed of small droplets generated by four nozzles, the dark blue

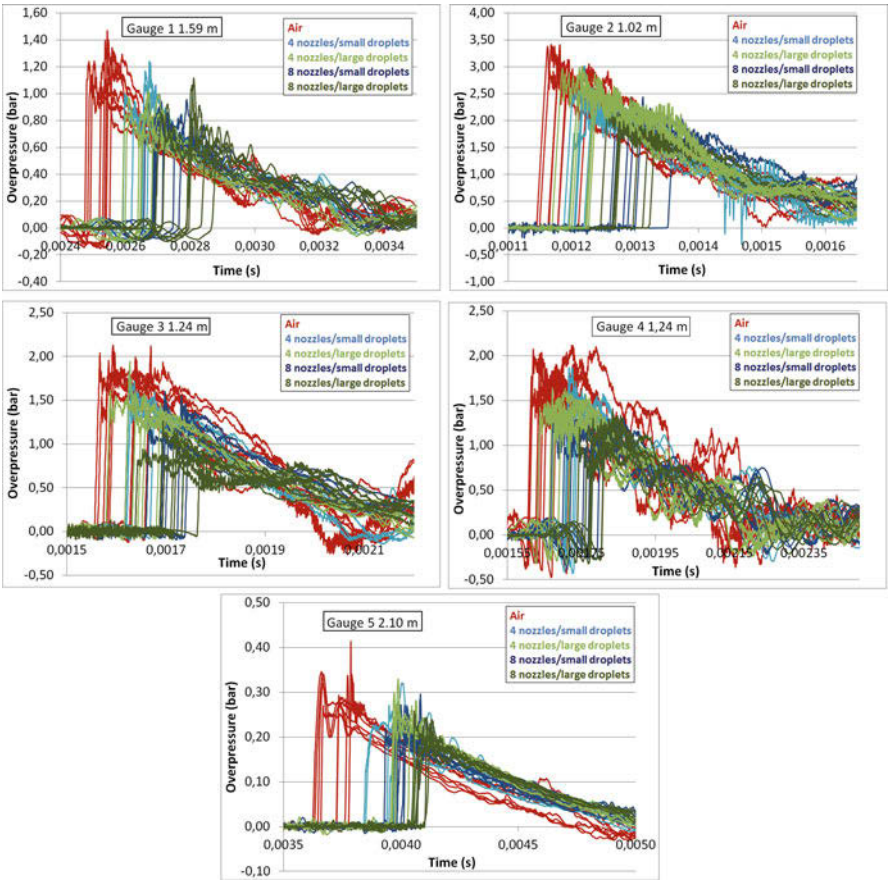

Fig. 2 Overpressure versus time obtained with gauges 1, 2, 3, 4, and 5

ones correspond to blast tests in a water mist made of small droplets generated by eight nozzles, the light green ones relate to blast tests in a water mist made of large droplets generated by four nozzles, and the dark green ones correspond to blast tests in a water mist made of large droplets generated by eight nozzles. The overpressure was reduced by the presence of the water mist, and this could be observed on all the gauges. Moreover, the shock wave was delayed by the presence of the mist.

Figure 3 (left) shows the average initial overpressure as a function of the distance to the charge for the tests in the air and the tests in a water mist. The uncertainty of the initial overpressure was estimated at 10%. The transmission factor of the initial overpressure that corresponds to the initial overpressure in a water mist divided by the initial overpressure in the air was computed. It was around 0.8 for this range of distance (from 1 to 2.10 m) when four nozzles were used to produce the mist, whether there were small or large droplets. The transmission factor of the initial overpressure was smaller when eight nozzles were used to generate the

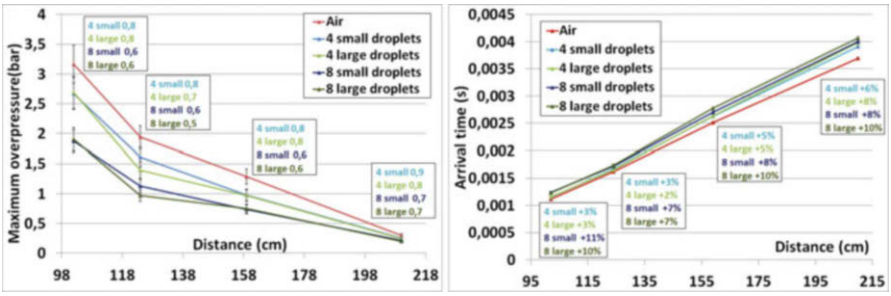

Fig. 3 (Left) Initial overpressure as a function of the distance to the charge for the tests in the air and the tests in a water mist. The transmission factor of the initial overpressure is given. (Right) Arrival time as a function of the scaled distance for the tests in the air and the tests in a water mist. The increase in the arrival time compared to the tests performed in the air is given in percent

mist. Whether for small or large droplets, the transmission factor of the initial overpressure was around 0.6 for a distance ranging from 1 to 2.10 m. Figure 3 (right) presents the average arrival time as a function of the scaled distance for the tests in the air and the tests in the water mist. The value of uncertainty of the arrival time was estimated at 20 μs. The shock wave was delayed by the mist, and this delay increased with the distance to the charge, and thus with the quantity of water mist the shock wave passed through. Moreover, the delay was longer when eight nozzles were used compared with four, and this was also probably due to the greater amount of mist on the shock-wave path.

Figure 4 shows the impulse versus time obtained with gauges 1, 2, 3, 4, and 5. The impulse corresponds to the overpressure signal integrated over time. The red curves correspond to blast tests in the air, the light blue ones correspond to blast tests in a water mist generated by four nozzles ejecting small droplets, the dark blue ones correspond to blast tests in a water mist generated by eight nozzles ejecting small droplets, the light green ones relate to blast tests in a water mist generated by four nozzles producing large droplets, and the dark green ones correspond to blast tests in a water mist generated by eight nozzles ejecting large droplets. The impulse was reduced by the presence of the water mist, and this was visible on the five gauges. The reduction was less significant on gauge 2, as this gauge was the nearest to the charge and the measurements were affected by the fireball. Moreover, it could also be supposed that if the impulse was less reduced by the presence of mist, this was due to the smaller amount of mist on the shock-wave path. The maximum impulse was averaged over the different tests for each configuration; the results are given in Table 1. The difference in percentage in comparison with the tests performed in the air is also given. The maximum impulse was reduced by about 20% when four nozzles were used to produce the mist, whether for small or large droplets, except for gauge 2 where the decrease was less pronounced. Whether for small or large droplets, the maximum impulse was reduced by about 30% with eight nozzles generating the mist.

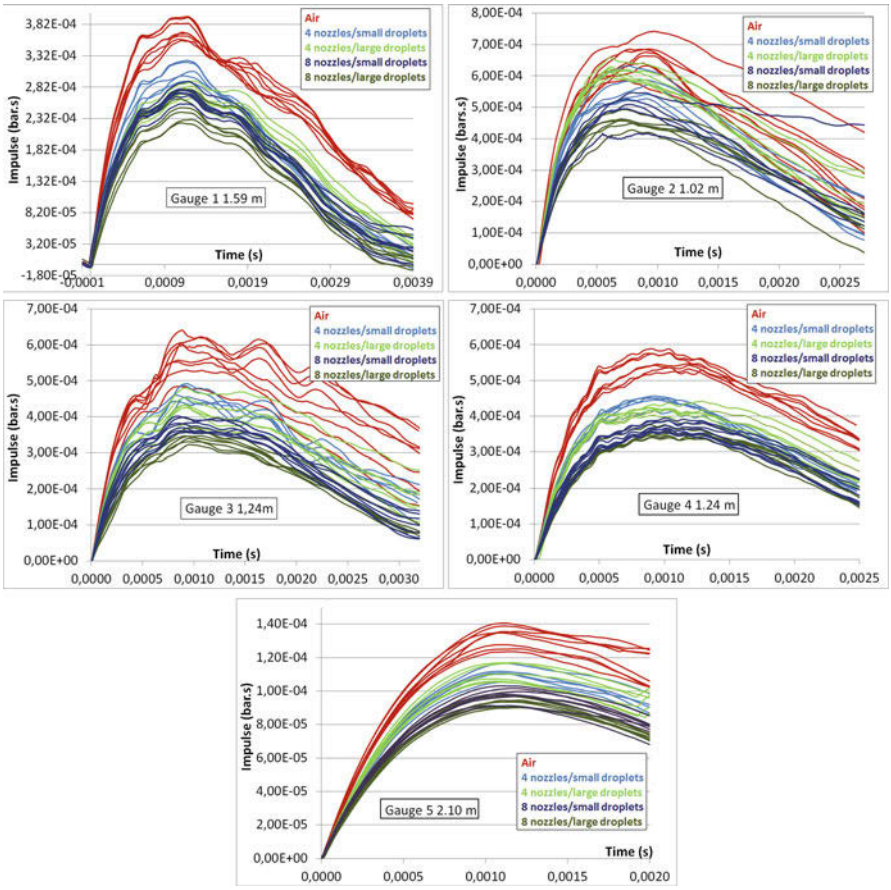

Fig. 4 Impulse versus time obtained with gauges 1, 2, 3, 4, and 5

4 Conclusion

The aim of this work was to assess the mitigation of an explosion by a water mist generated by a water mist fire suppression system. We attempted to study the mitigation efficiency as a function of the droplet size and the water loading of the mist. For this purpose, nozzles generating two different sizes of droplets were used as well as two nozzle configurations (either four or eight nozzles). The initial overpressure was reduced by the presence of the mist. The transmission factor of the initial overpressure in the water mist was around 0.8 for a distance ranging from 1 to 2.10 m when four nozzles were used to produce the mist, whatever the size of the droplets. The transmission factor of the initial overpressure was smaller, around 0.6, with eight nozzles generating the mist, whether for small or large droplets. The shock wave was delayed by the presence of the mist, and this delay increased

Table 1 Maximum impulse averaged over the different tests for each configuration. The difference compared to the tests performed in the air is also given in percent

		Air	Four nozzles/small droplets	Four nozzles/large droplets	Eight nozzles/small droplets	Eight nozzles/large droplets
Gauge 1 (1.59 m)	Impulse (bar.s)	3.73E-4	3.09E-4	2.78E-4	2.74E-4	2.52E-4
	Difference with air (%)		17	26	27	33
Gauge 2 (1.02 m)	Impulse (bar.s)	6.64E-4	5.72E-4	6.22E-4	5.07E-4	4.61E-4
	Difference with air (%)		14	6	24	31
Gauge 3 (1.24 m)	Impulse (bar.s)	5.75E-4	4.67E-4	4.33E-4	3.47E-4	3.79E-4
	Difference with air (%)		19	25	40	34
Gauge 4 (1.24 m)	Impulse (bar.s)	5.57E-4	4.44E-4	4.22E-4	3.55E-4	3.74E-4
	Difference with air (%)		20	24	36	33
Gauge 5 (2.10 m)	Impulse (bar.s)	1.33E-4	1.11E-4	1.10E-4	9.70E-5	9.33E-5
	Difference with air (%)		16	17	27	30

with the distance to the charge, and thus with the quantity of water mist, the shock wave passed through. This delay was also longer with eight nozzles, compared with four, and this was due to the greater amount of mist on the shock-wave path. The maximum impulse was reduced by about 20% with four nozzles used to produce the mist, whatever the size of the droplets. The maximum impulse was more reduced with eight nozzles generating the mist, i.e., by about 30% for both droplet sizes. For small droplets, when the number of nozzles increased, the water load increased as well as the mitigation efficiency. Consequently, it may be assumed that the mitigation efficiency increases with the quantity of water contained in the mist and probably with the homogeneity of the mist. By contrast, for large droplets when the number of nozzles increased, the water load slightly decreased. However, the blast mitigation improves with eight nozzles. It can be assumed that the uniformity of the water load has an impact. The shock wave was also more delayed with eight nozzles. With respect to the effect of the droplet size on the mitigation efficiency, we have obtained a similar mitigation with a smaller water load with large droplets, compared with small droplets. It can be supposed that the droplets of a diameter of 200–300 μm are more effective for attenuating the blast produced by a high explosive. This observation has to be confirmed.

The next steps will be first to study the mitigation efficiency when the explosive charge explodes outside the water mist and to close the tunnel ends and to assess the mitigation efficiency in a confined environment.

References

1. A. A. Buzukov, Combust. Explos. and Shock Waves **36**, 395 (2000)
2. A. Jones, G.O. Thomas, Trans. IChem E **71**, 41 (1993)
3. V.H.Y Tam et al., J. Loss Prev. Process Ind. **16**, 81 (2003)
4. G.O. Thomas, Trans. IChem E **78**, 339 (2000)
5. C.A. Catlin et al., Trans. IChemE **71**, 101 (1993)
6. E. Mataradze, et al., Shock energy absorber for protection underground structure from internal explosions, in 15th *International Symposium on Interaction of the Effects of Munitions with Structures Proceedings*, Postdam (2013)
7. R. Tosello, et al., Shock wave attenuation using watermist, in *International Symposium on Military Aspects of Blast and Shock Proceedings*, Bourges (2012)
8. R. Ananth et al., Fire. Technol **48**, 641 (2012)
9. H.D. Willauer et al., J. Hazard. Mater. **165**, 1068 (2009)
10. J.L. Bailey, et al., NRL report: NRL/MR/6180- -06-8933 (2006)
11. A.D. Resnyansky, T.G. Delaney, DSTO report: DSTO-TR-1944 (2006)
12. D.A. Schwer, K. Kailasanath, NRL report: NRL/MR/6410- -06-8976 (2006)

Shock Wave Propagation Through a Series of Perforated Plates

O. Ram, G. Ben-Dor, and O. Sadot

Abstract A simplified analysis can be employed to predict the pressure buildup behind a porous barrier fairly accurately without resorting to numerical modeling. A macroscopic approach is used in which the pressure buildup behind the porous barrier is analyzed in relation to the load inflicted on its front face thus allowing finding the effects of the different parameters of the porous barrier. This method was successfully employed to study the impingement of shock waves and blast waves on stiff silicon carbide foams and more recently on buildings that had enough internal divisions as to be considered as a low porosity medium. In this study, the methodology is employed to study a porous barrier comprised from an array of perforated plates with various porosities to determine the parameters affecting the pressure buildup behind it. Perforated plates were chosen since the geometry of the barriers assembled from the plates is simple enough so it can be exactly defined, and still the shock structure and the developing fields are so complicated that only few studies attempted to deal with similar scenarios in the past. In fact, previous studies were limited to one or two perforated plates. In the experiments presented, 3 mm plates were placed 8 mm apart inside a 32 mm by 32 mm shock tube. The last plate was mounted 10 mm from the end wall. The plates were drilled to accommodate various blockage ratios (defined as blocked to open area ratio) ranging from 50% to 80%. It was found that the volume of air confined inside the porous medium undergoes an adiabatic process, and thus the pressure buildup time at the end wall depends on the volume to the power of the heat capacities ratio.

1 Introduction

Porous barriers have the potential of mitigating the loads that develop behind them following the impingement of shock or blast waves. Due to this potential, the propagation of shock waves through porous barriers and the developing loads behind

O. Ram (✉) · G. Ben-Dor · O. Sadot
Shock Tube Laboratory, Protective Technologies R&D Center, Beer-Sheva, Israel
e-mail: Omrir@bgu.ac.il

A. Sasoh et al. (eds.), *31st International Symposium on Shock Waves 2*,
https://doi.org/10.1007/978-3-319-91017-8_90

them has been the focus of many studies in recent years. Various porous barriers have been proposed and studied before. Among these are silicon carbide filters [1–4], sets of columns with various geometries [5, 6], sets of buffers [7, 8], packed granular media [9, 10], perforated plates [11–16], and more. Most of these studies employed an experimental investigation into the effects of the various porous barrier properties on the propagation of a shock wave through them, its attenuation, and the developing flow field behind them. A specific case was considered in some studies where the porous medium was placed in a tunnel with a standoff distance to the end wall thus forming a confined volume of air behind it. This scenario is complicated since the conditions behind the porous medium do not remain constant. The transmitted shock wave propagates into the confined volume, impinges on the end wall, reflects upstream toward the porous barrier, and reverberates back and forth inside the confined volume. Its strength declines with each encounter with the back wall until it subsides. In parallel to this feature, the pressure gradients that form on the two faces of the porous medium drive a fast mass flow into the confined volume causing its pressure to increase. The flow into the confined volume continues until pressure equalization occurs and the pressure in the confined volume reaches the pressure on the front face of the porous medium. The mass flow into the confined volume is high at the beginning, but it subsides as the pressure subsides; the relation between the two is inherently nonlinear. The unsteady mass flow through the porous medium increases the difficulty of predicting the pressure buildup and, in turn, also inhibits the ability to study the effects of various parameters such as the volume, the length of the porous barrier, and the properties of the porous barrier itself. This paper presents a part of an ongoing study into the parameters that govern the pressure buildup behind the porous barrier. Perforated plates were suggested before as means of mitigating shock and blast waves in tunnels and were proven effective by experiments. However, while being one of the simplest porous media, the shock interaction with the perforated plates, the transmitted shock between the plates, and the resulting flow through them are so complex. To the best of our knowledge, no study had studied the pressure buildup behind a set of more than two perforated plates. A macroscopic approach is used to examine this scenario in which the pressure buildup behind the porous barrier is analyzed in relation to the load inflicted on its front face thus allowing finding the effects of the different parameters of the porous barrier. This method was successfully employed to study the impingement of shock waves and blast waves on stiff silicon carbide foams [2, 3] and more recently on buildings that had enough internal divisions to be considered as low porosity media [17]. Since the methodology that is described above does not require the solution of the microscopic interaction between the fluid and the plates, a set of many perforated plates with various properties can be studied.

2 Experimental Setup

The experimental investigations were performed in a shock tube located at the Protective Technologies R&D Center of the Ben-Gurion University of the Negev (BGU-PTR&DC). A horizontal, 6-m long shock tube with an internal square cross section of 32 mm by 32 mm was used. A schematic description of the experimental apparatus is depicted in Fig. 1.

The basic configuration of pressure measurements consisted of three Endevco 8530b-500 pressure transducers (PT): two were located along the shock tube spaced by 600 mm, and a third pressure transducer was mounted on the end wall. The pressure transducers along the shock tube were used to monitor the shock speed. The shock wave velocity that was generated in the shock tube was very repeatable and varied by no more than 2% between experiments performed with the same conditions. A number of perforated plates (examples are shown in Fig. 2) were mounted in the test section in grooves that formed a tight fit and were held in place by pins running through the outer frame of the test section. The grooves that were not used in the experiments were filled by spacers that completed the shock tube inner surface so not to disturb the flow. The entire shock tube operation was computer controlled, and an in-house designed trigger box was used to trigger a Lecroy WaveJet 314 oscilloscope that recorded the pressure profiles. The driver section was filled with compressed air to a predetermined pressure and was separated by a KB-40 fast-opening valve manufactured by ISTA Inc. According to the manufacturer specifications, the fast-opening valve has an opening time of 1–2 ms. The test section entrance was more than 100 diameters from the fast-opening valve, a distance that enabled for any irregularities caused by the valve opening to subside. The shock wave was also monitored in order to make sure that it is sharp and plane in the test section entrance and is not affected by the opening of the valve. In order to analyze the effects of porosity and perforation size on the pressure buildup behind the plates array, several models were manufactured from Perspex by CNC (Fig. 2).

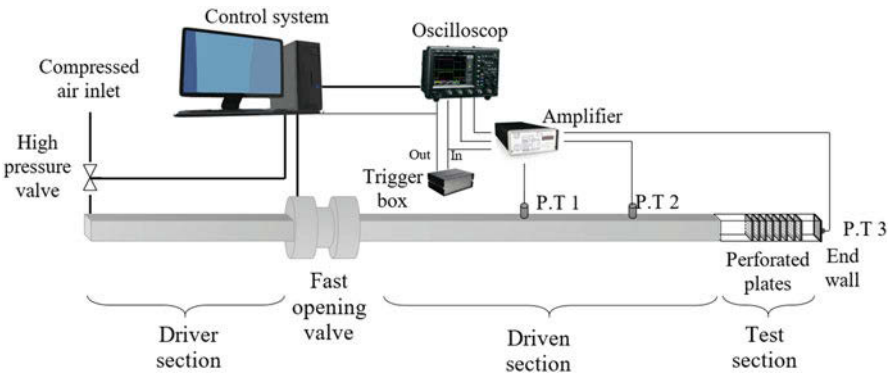

Fig. 1 A schematic description of the shock tube used in the experiments

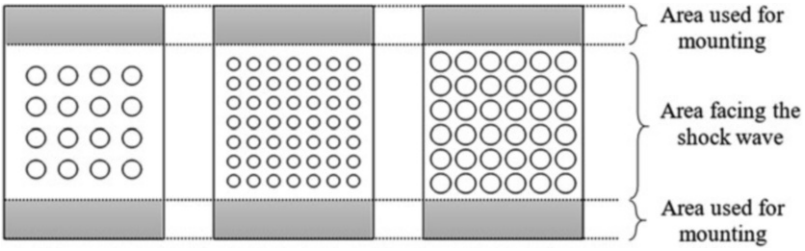

Fig. 2 Illustration of some of the perforated plate models that were used in this study. The hole diameter and number of holes were varied to acquire various porosities and various hole diameters

In addition to the area of the plate that faces the flow, each plate was extended in two directions to allow mounting them in grooves machined in the shock tube walls. The models were all manufactured out of a 3 mm plate. Porosities were chosen ranging from 11% open area to 44.2% open area. All of the perforations used in the experiments were round and were evenly distributed inside the 32 mm by 32 mm cross section of the shock tube.

3 Results

Figure 3 depicts the end-wall pressure recordings from a set of experiments performed with three porosities. As can be expected, the pressure buildup duration highly depends on both the porosity of the plate and on the number of plates. It is shown in Fig. 3 that as the number of plates increases, in addition to prolonging the pressure buildup duration, the shock wave that reaches the end wall gets significantly attenuated. For example, in experiments performed with a porosity of 23.4% and more than five perforated plates, a sharp shock front was not recorded at the end wall.

As seen in previous studies of shock propagation through porous barriers that have a confined volume behind them, Fig. 3 shows that the pressure profiles have a behavior that follows the exponential decaying pressure buildup presented in Eq. (1):

$$P(t) = P_5\left(1 - e^{-At}\right) \tag{1}$$

where each experiment has a different constant A and P_5 is the same reflected pressure that would have been developed at the end wall without a porous barrier. A previous study [2, 3] showed that the pressure buildup behind a stiff porous medium could be essentially studied as a lumped mechanical system in which the porous medium and the confined volume of air in it could be modeled as a low-pass filter.

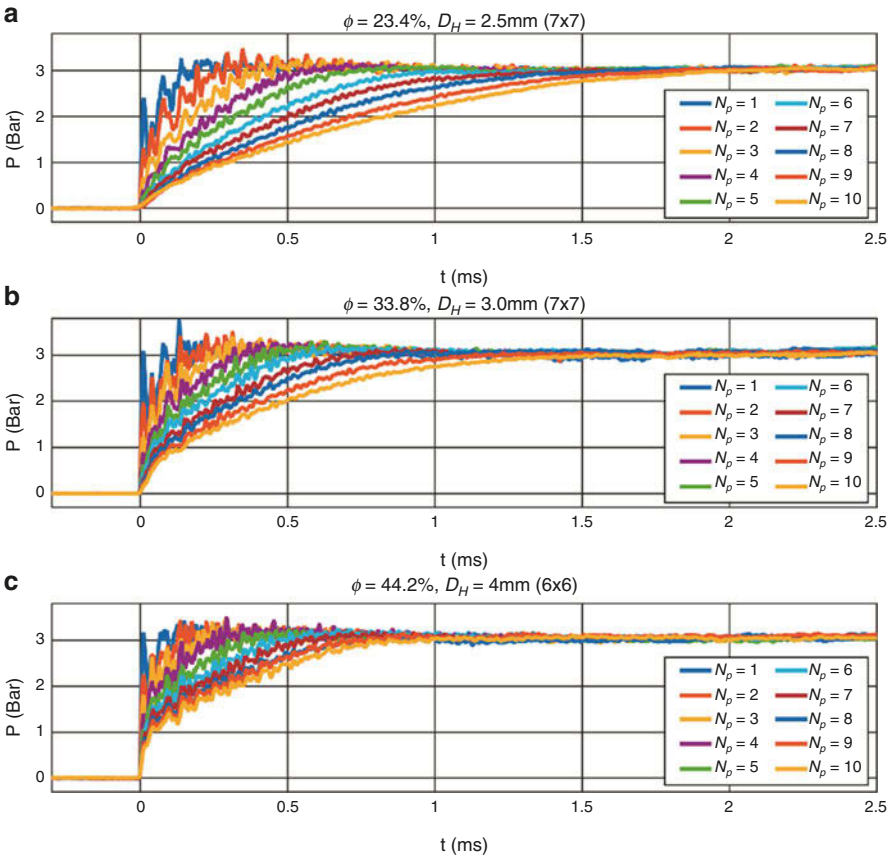

Fig. 3 End-wall pressure from experiments performed with increasing number of perforated plates performed with (**a**) porosity of 23.4%, 7 x 7 hole matrix, and perforation diameter of 2.5 mm; (**b**) porosity of 33.8%, 7 × 7 hole matrix, and perforation diameter of 3 mm; (**c**) porosity of 442%, 6 × 6 hole matrix, and perforation diameter of 4 mm

It was shown that essentially, the porous medium and the confined air mitigated the propagation of fast-changing pressure pulses and the pressure buildup on the end wall. This model incorporated an experimental parameter, α, which was porous medium specific. This experimental parameter lumped the properties of the porous medium that affected the pressure buildup. Since SiC filters whose geometry was random and difficult to characterize were used, the previous study did not provide the dependence of α on the specific properties of the porous medium. A fit of Eq. (1) to the experimental results shown in Fig. 3a using a least square method is shown in Fig. 4a. The results show that Eq. (1) gives a good representation of the pressure profiles recorded on the end wall.

The volume of gas that is confined within the porous plate array can be calculated as

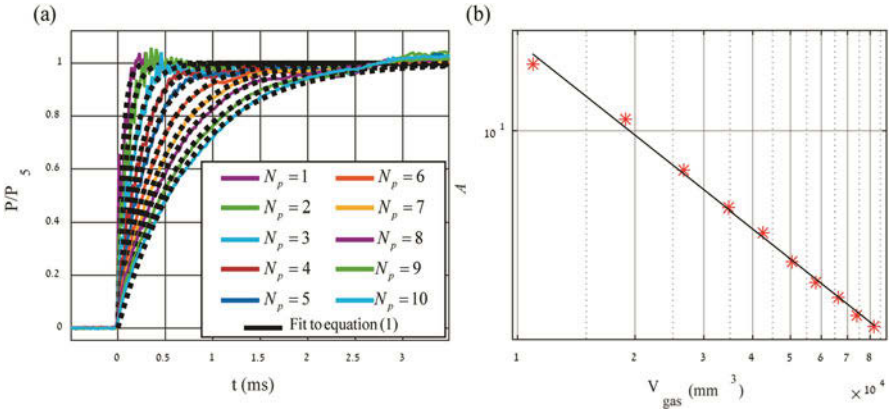

Fig. 4 (**a**) Least-square fit of Eq. (1) to the experiments performed with porosity of 23.4%, 7 × 7 hole matrix, and perforation diameter of 2.5 mm. (**b**) Parameter A in Eq. (1) acquired from the fitting vs. the volume that is confined within the porous plate array

$$V_{\text{gas}} = \left(S_0 + \sum_{i=1}^{N_p - 1} S_i + \sum_{i=1}^{N_p} \phi \cdot s \right) A_{ST} \tag{2}$$

where N_p is the number of plates, A_{ST} is the surface area of the shock tube, S_i is the distance between the plate i and plate $i-1$, $i=0$ is the end wall, ϕ is the porosity calculated from $\phi = A_{\text{open}}/A_{ST}$, and s is the thickness of *i-th* plate.

The parameter A in Eq. (1) was obtained by a linear fitting to the log-log plot of A vs. the volume of gas that is confined within the porous plate array (Eq. 2). The linear fitting is shown in Fig. 4b. Figure 4 shows that A depends on the volume of the gas confined within the perforated plate array by the power of -1.393 (the slope of the linear regression line).

An explanation of the slope found in Fig. 4b is based on the analysis presented by Ram and Sadot [2]. We assume that after the initial reflection of the shock wave, the gas that flows between the plates undergoes an adiabatic compression process that follows the relation

$$\frac{P}{P_0} = \left(\frac{\rho}{\rho_0} \right)^{\gamma} = \left(\frac{m_{\text{gas}}}{\rho_0 V_{\text{gas}}} \right)^{\gamma} \tag{3}$$

where γ is the heat capacity ratio (1.4 for air) and V_{gas} is the volume of the air contained by the porous medium which is calculated by Eq. (2).

Equation (3) shows that

$$P(t) \propto V_{\text{gas}}^{-\gamma} \tag{4}$$

These results explain the linear regression line slope shown in Fig. 4b and in fact shows that the perforated plates array can be analyzed as a porous medium.

4 Conclusions

The problem of shock wave propagation through a large array of perforated plates is difficult to model since there are multiple scales involved in the developing flow field (perforations diameter, shock tube's cross section area, etc.). Furthermore, the fast flow that propagates through the perforated plates array undergoes a large number of contractions and expansions generating a complex flow field that requires a viscous solution that also correctly models the flow interaction with the multiple shock reflections inside the porous medium. This study adopts a macroscopic experimental approach to find the effects of the different parameters of the perforated plates array. This approach does not concern with the fine features of the flow field and internal shock reflections inside the porous barrier but rather focuses on the pressure buildup profile that develops behind the plates array. This method allows studying the influence of the different parameters with a reduced complexity. The initial results presented in this paper show that the pressure buildup time behind the porous barrier is highly effected both by the porosity of the plates and by the number of plates. While the fact that decreasing the plates' porosity increases the resistance to the flow and subsequently increases the pressure buildup time is not surprising, the effects of increasing the barrier length by adding more plates are not so intuitive. It was shown that increasing the number of plates effectively increases the volume confined in the porous medium. It was found that the pressure buildup time depends on the confined volume to the power of the heat capacity ratio γ, i.e., 1.4 in the case of air. This dependency was shown to stem from the fact that the flow into the confined volume following the initial shock impingement is adiabatic.

References

1. A. Levy, G. Ben-Dor, B.W. Skews, S. Sorek, Head-on collision of normal shock waves with rigid porous materials. Exp. Fluids **15**, 183–190 (1993). https://doi.org/10.1007/BF00189885
2. O. Ram, O. Sadot, A simple constitutive model for predicting the pressure histories developed behind rigid porous media impinged by shock waves. J. Fluid Mech. **718**, 507–523 (2013). https://doi.org/10.1017/jfm.2012.627
3. O. Ram, O. Sadot, Analysis of the pressure buildup behind rigid porous media impinged by shock waves in time and frequency domains. J. Fluid Mech. **779**, 842–858 (2015). https://doi.org/10.1017/jfm.2015.463
4. A. Levy, S. Sorek, G. Ben-Dor, J. Bear, Evolution of the balance equations in saturated thermoelastic porous media following abrupt simultaneous changes in pressure and temperature. Transp. Porous Media **21**, 241–268 (1995). https://doi.org/10.1007/BF00617408
5. A. Chaudhuri, A. Hadjadj, O. Sadot, G. Ben-Dor, Numerical study of shock-wave mitigation through matrices of solid obstacles. Shock Waves **23**, 91–101 (2012). https://doi.org/10.1007/s00193-012-0362-2

6. H. Naiman, D.D. Knight, The effect of porosity on shock interaction with a rigid, porous barrier. Shock Waves **16**, 321–337 (2007). https://doi.org/10.1007/s00193-007-0077-y
7. S. Berger, O. Sadot, G. Ben-Dor, Experimental investigation on the shock-wave load attenuation by geometrical means. Shock Waves **20**, 29–40 (2010). https://doi.org/10.1007/s00193-009-0237-3
8. S. Sha, Z. Chen, X. Jiang, J. Han, Numerical investigations on blast wave attenuation by obstacles. Procedia Eng **45**, 453–457 (2012). https://doi.org/10.1016/j.proeng.2012.08.185
9. G. Ben-Dor, A. Britan, T. Elperin, O. Igra, J.P. Jiang, Experimental investigation of the interaction between weak shock waves and granular layers. Exp. Fluids **22**, 432–443 (1997). https://doi.org/10.1007/s003480050069
10. A. Britan, G. Ben-Dor, Shock tube study of the dynamical behavior of granular materials. Int. J. Multiphase Flow **32**, 623–642 (2006). https://doi.org/10.1016/j.ijmultiphaseflow.2006.01.007
11. B.W. Skews, K. Takayama, Flow through a perforated surface due to shock-wave impact. J. Fluid Mech. **314**, 27 (1996). https://doi.org/10.1017/S0022112096000225
12. A. Britan, A.V. Karpov, E.I. Vasilev, O. Igra, G. Ben-Dor, E. Shapiro, Experimental and numerical study of shock wave interaction with perforated plates. J. Fluids Eng. **126**, 399 (2004). https://doi.org/10.1115/1.1758264
13. H. Onodera, Shape of a shock wave front diffracting on a perforated wall. Exp. Fluids **24**, 238–245 (1998). https://doi.org/10.1007/s003480050170
14. K. Kontis, R. An, H. Zare-Behtash, D. Kounadis, Head-on collision of shock wave induced vortices with solid and perforated walls. Phys. Fluids **20** (2008). https://doi.org/10.1063/1.2837172
15. S. Seeraj, B.W. Skews, Dual-element directional shock wave attenuators. Exp. Thermal Fluid Sci. **33**, 503–516 (2009). https://doi.org/10.1016/j.expthermflusci.2008.11.002
16. B. Skews, Shock wave interaction with porous plates. Exp. Fluids **39**, 875–884 (2005). https://doi.org/10.1007/s00348-005-0023-7
17. O. Ram, E. Nof, O. Sadot, Dependence of the blast load penetrating into a structure on initial conditions and internal geometry. Exp. Thermal Fluid Sci. **78**, 65–74 (2016). https://doi.org/10.1016/j.expthermflusci.2016.05.012

Experimental Investigation of Strong Shock-Heated Gases Interacting with Materials in Powder Form

Jayaram Vishakantaiah

Abstract A novel method is developed in our laboratory to use shock tube for heating the test gases to extremely high temperature and to interact with the materials in the form of fine powder for millisecond time scale. As a case study, we present the results obtained on nitridation of TiO_2 compound. Material shock tube (MST) is used to heat Ar and N_2 gas mixture to 3750 K–6725 K with reflected shock pressure of about 25–50 bar for about 1–2 ms duration; at these shock conditions, nitrogen gas experiences real gas effect. This nitrogen gas interacts with the rutile TiO_2 at the reaction chamber of the MST. The surface morphology, crystal structure, surface composition and electronic structure of the rutile TiO_2 sample were examined before and after exposure to shock waves using scanning electron microscopy (SEM), X-ray diffraction (XRD) and X-ray photoelectron spectroscopy (XPS).

The results obtained from the experimental investigations show the formation of new titanium oxides and oxynitride compounds when exposed to multiple shocks. Formation of new compounds like Ti_2O_5 and $TiN_{0.74}O_{0.34}$ is due to noncatalytic reaction occurred during the shock treatment. The result shows that the nitridation of TiO_2 is possible in millisecond time scale. MST is an important tool to study catalytic/noncatalytic surface reaction on high-temperature materials near the surface of the re-entry space vehicles.

1 Introduction

Three different polymorphs of TiO_2 occur in nature, namely, rutile, anatase and brookite structure. Rutile is thermodynamically most stable phase, and anatase is more kinetically favoured phase. Titanium dioxide (TiO_2) is one of the most prominent materials used in space, energy and environmental application [1]. After

J. Vishakantaiah (✉)
Shock Induced Materials Chemistry Laboratory, SSCU, Indian Institute of Science, Bengaluru, India
e-mail: jayaram@sscu.iisc.ernet.in

A. Sasoh et al. (eds.), *31st International Symposium on Shock Waves 2*,
https://doi.org/10.1007/978-3-319-91017-8_91

the discovery of photocatalytic splitting of water [2] and solar energy conversion device [3], TiO_2 considered as good photo-functional material. Considerable efforts have been devoted to enhance the photocatalytic activity of TiO_2 by doping of nitrogen atoms [4, 5]. Doping of anions like nitride (N^{3-}) and carbide (C^{4-}) in anatase TiO_2 (like $TiO_{2-x}N_x$ or $TiO_{2-x}C_x$) shows decrease in the band gap of TiO_2 to achieve higher photocatalytic activity [6]. In recent years, synthesis, modification and phase transformation of TiO_2 were studied using shock waves under extreme thermodynamic conditions. Shock-induced chemical reaction due to high strain rate for very short duration causes change in material properties [7]. Laser-induced shock is another method used to study semiconductor materials [8]. Nitrogen-doped titania photocatalysts were synthesized using shock waves [9]. Transformation of anatase TiO_2 to N-doped rutile TiO_2 structure was studied using free piston-driven shock tube [10].

In this paper we used shock-heated N_2 gas to interact with TiO_2, which enables us to understand noncatalytic reactions. We present the detailed experimental setup of MST and its application for the synthesis of titanium oxynitride. A similar experimental work on the reversible phase transformation of rutile to anatase TiO_2 on shock dynamic loading in presence of argon gas was also reported in the literature [11]. Material shock tube (MST) was used to heat Ar + N_2 gas mixture to a very high temperature and at medium reflected shock pressure for short duration. At this thermodynamic condition, N_2 goes to non-equilibrium state with vibrational, rotational excitation and dissociation state. We explore the possible phase transformation of rutile TiO_2 to monoclinic phase in the form of titanium oxide and oxynitride compounds.

2 Experimentation

2.1 Shock Tube Arrangement and Experimental Procedure

A simple shock tube consists of two sections: the driver section and the driven section. The outer and inner diameters of the shock tube are 115 mm and 80 mm, respectively. The length of the driver and driven sections is 2.1 m and 5.1 m long. The driver section is separated from the driven section by an aluminium diaphragm of required thickness. The thickness of the diaphragm dictates its bursting pressure which will affect the shock strength and thereby increases the shock Mach number, reflected shock temperature and pressure. The shock tube employed here is specifically designed for the interaction of fine powders with shock waves. The schematic diagram of MST is shown in Fig. 1. A manually operated ball valve is fixed at the end of the driven section right after the powder sample holder and the 0.6 m long TiO_2 reaction chamber assembled after the sample holder. Shock tube experiments were performed by placing 99.99% pure TiO_2 rutile powder of 0.2 gm on the sample holder. This arrangement is made so that when the shock reaches

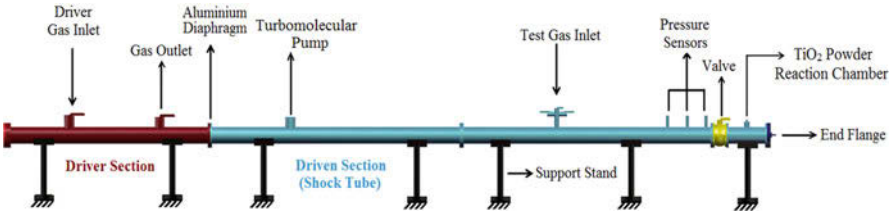

Fig. 1 Schematic diagram of MST showing the position of pressure transducers

the sample holder, it reacts with the TiO_2 fine powders in the reaction chamber. The sample experiences reflected shock pressure (P_5) and temperature (T_5) at the end flange of the shock tube. As soon as the diaphragm bursts, the ball valve is closed to retain the reacted sample left inside the TiO_2 reaction chamber.

Experimental procedure starts by placing the aluminium diaphragm between driver and driven section and mounting the powder sample of required quantity (0.2 gm) in the sample holder. Turbomolecular pumping system is used to evacuate the shock tube to high vacuum. Rough pumping of the shock tube is done using rotary pump up to 5×10^{-2} mbar at a very slow rate so that the sample does not get disturbed or pumped out. After rough pumping, the turbomolecular pumping system is used to evacuate the shock tube to high vacuum (5×10^{-5} mbar). After reaching this vacuum, the driven section is purged with ultrahigh pure (UHP) argon (99.999%) for three to four times to remove residual gas present inside the shock tube. Further the shock tube is filled with equal partial pressure of 0.025 bar UHP argon and N_2 gas. The driver section is filled with high-pressure helium until the diaphragm bursts and generates the shock wave. The shock-heated nitrogen gas interacts with the rutile TiO_2 powder, and the chemical reactions occur inside the reaction chamber. A similar procedure is followed to perform multiple shock treatments of rutile TiO_2 sample at different temperatures. The shock speed and reflected shock pressure are measured by dynamic pressure sensors (Model 113B22, PCB Piezotronics Ltd., USA), and the data acquired is stored using a Tektronix digital storage oscilloscope (TDS2014B). The reflected shock temperature (T_5) for a given shock Mach number can be estimated using 1D normal shock relations [12]. The estimated temperature (T_5) of the test gas behind the reflected shock is a function of shock Mach number, specific heat ratio of gas γ and the ambient temperature T_1 of the test gas. Pristine TiO_2 is exposed to shock waves at reflected shock pressure of ~25–50 bar and temperature of 3750–6725 K in presence of argon and nitrogen gas mixture for 1–2 ms. The powder sample left inside the TiO_2 reaction chamber is collected for further investigation using different experimental techniques.

2.2 Characterization

Pristine rutile TiO_2 powder of high purity (99.99%) was obtained commercially from Sigma-Aldrich Chemical Company, Inc. Experimental techniques like X-ray diffraction (XRD), scanning electron microscopy (SEM) and X-ray photoelectron spectroscopy (XPS) were used to characterize TiO_2 sample before and after shock-heated nitrogen gas. SEM micrographs and energy-dispersive spectroscopy (EDS) spectra were obtained to study the surface morphology and the elemental analysis of the samples before and after shock treatment (ULTRA 55 with GEMINI technology) at a working distance of 7.5 mm operating at 5 kV accelerating voltage. The XRD patterns were recorded for all samples before and after shock exposure using the CuKα ($\lambda = 1.5418$ Å) radiation at a scan rate of 2° min^{-1} with a step size of 0.013° for 2θ from 20° to 75° (PANalytical Empyrean). XPS study is carried out using Al Kα (1486.6 eV) radiation to understand the chemical composition and electronic structure of TiO_2 before and after shock treatment (AXIS Ultra DLD, Kratos Analytical). Low-energy electron flood gun was used to nullify the charge accumulation on the surface of insulating sample. The position of C1s peak at 284.6 eV is taken as reference with an accuracy of ±0.1 eV for calibrating, if any shift in the binding energy (BE). All the spectra were obtained with pass energy of 40 eV. XPS spectra were recorded by mounting the powder samples on a carbon tape.

3 Results and Discussions

Before and after exposure to shock waves, experimental investigation was carried out on TiO_2 fine powder using SEM, XRD, XPS, etc. SEM micrographs are recorded at 100000x magnifications for pristine rutile TiO_2 and shock-treated sample are shown in Fig. 2. SEM micrograph of rutile TiO_2 before exposure to shock shows acicular morphology with particle size varying from 3 to 0.2 μm as shown in Fig. 2a. Four and two shock-treated TiO_2 powder in presence of N_2 test gas shows change in microstructure is shown in Fig. 2b and c, respectively. SEM micrograph shows particle size ranging from 20 nm to 120 nm due to melting, nucleation and recrystallization of reacted sample at different temperature. The spherical shape of the particles present in this compound is due to superheating and cooling process occurred at the rate of $\sim 10^6$ K/s. EDS analysis shows the presence of 20–40% atomic percentage of N_2 in the shock-treated sample.

XRD pattern of rutile TiO_2 powder before shock and multiple shock-treated samples at different temperature are shown in Fig. 3. The diffraction peaks at 27.47° and 25.34° are characteristic peaks corresponding to rutile TiO_2 (110) and anatase TiO_2 (101), respectively [13]. XRD of pristine rutile TiO_2 shows the tetragonal crystal structure (SG: $P4_2/mnm$, JCPDS No. 01-078-1508) with lattice parameters $a = b = 4.592$ Å and $c = 2.959$ Å. The diffraction lines correspond to major peaks

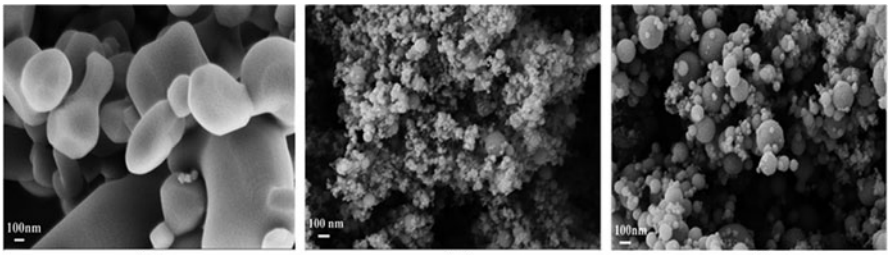

Fig. 2 SEM micrographs of rutile TiO_2. (**a**) Pristine. (**b**) After four shock treatments in presence of N_2 test gas at 3750 K. (**c**) After two shock treatments in presence of N_2 test gas at 6725 K

of rutile phase are represented as 'R', and the impurity in the form of anatase phase is marked as 'A' as shown in Fig. 3a. After the fourth shock treatment at 3750 K and the second shock treatment at 6725 K in presence of N_2 test gas, the powder XRD pattern shows the presence of new titanium oxide (Ti_3O_5) and oxynitride ($TiO_{0.34}$ $N_{0.74}$) compounds. Shock-treated sample shows development of new diffraction peaks (marked with *) for monoclinic Ti_3O_5 compound with lattice parameters $a = 9.828$ Å, $b = 3.7766$ Å and $c = 9.898$ Å. The titanium oxynitride ($TiO_{0.34}$ $N_{0.74}$) compound also shows monoclinic structure with lattice parameters $a = 9.961$ Å, $b = 3.796$ Å and c = 9.802 Å, and the corresponding diffraction lines are shown in Fig. 3b and c. There are also few diffraction peaks which are not matching with any of the new compounds formed.

Titania undergoes melting, nucleation and recrystallization due to superheating and cooling during shock treatment. The XRD spectra shows intense peak for rutile phase, but after multiple shock treatment, FWHM changes for the titanium oxynitride compound, which shows the formation of fine nanoparticles on shock treatment. Scherrer's formula is used to estimate the average crystallite size. The pristine TiO_2 rutile samples had a crystallite size of about 520 nm but after four and two shocks, it was about 29 and 26 nm. The microstrain present in the rutile TiO_2 before shock and the microstrain developed after exposure to shock wave in presence of N_2 gas were estimated using the Williamson-Hall equation. The microstrain of the TiO_2 rutile sample is about 7.3×10^{-3}, but the microstrain developed after multiple shock exposure is about $4.9–5.2 \times 10^{-3}$. Due to the repeated shock treatment, both the crystallite size and microstrain decrease. The phase transformation of TiO_2 exhibits due to the variation in lattice defects and the relaxation of the lattice strain due to multiple shock treatments.

XPS studies were performed to investigate oxidation state of shock-treated rutile TiO_2. BE of Ti $2p_{3/2}$ electron for no shock rutile TiO_2 was observed at 458.3 eV as shown in Fig. 4a due to Ti^{4+} state, which matches well with BE of Ti(2p) electron as reported in the literature [14]. The two- and four -shock-treated sample shows the formation of new compounds, and their Ti(2p) BE was observed at about 460.5 eV due to the presence of Ti^{4+} and Ti^{3+} state in the nitride compound as shown in

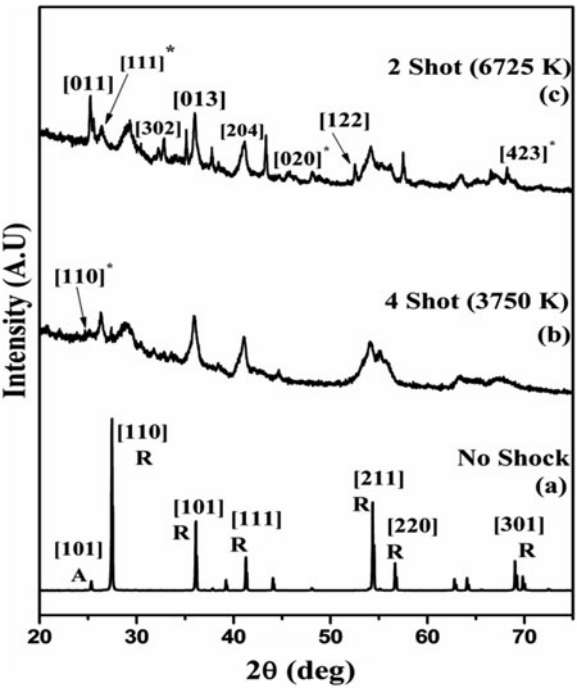

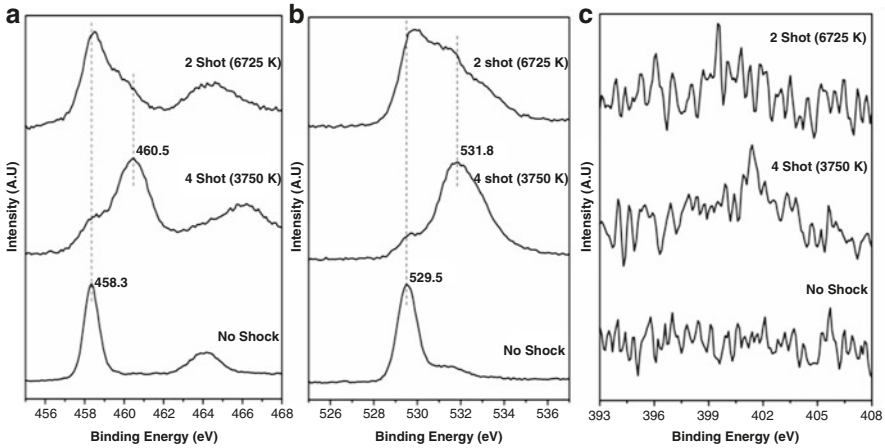

Fig. 3 Powder XRD pattern of rutile TiO_2. (**a**) Pristine. (**b**) After four shock treatments in presence of N_2 test gas at 3750 K. (**c**) After two shock treatments in presence of N_2 test gas at 6725 K

Fig. 4 XPS spectra of rutile TiO_2 before and after multiple shock treatment (**a**) Ti(2p), (**b**) O1s, and (**c**) N1 s

Fig. 4a. Thus XPS result which shows slight shift at higher binding energy in Ti(2p) peak confirms the formation of nitride compound.

XPS spectra of O1s of rutile TiO_2 samples before and after shock treatment are shown in Fig. 4b. The O1s peak at 529.5 eV BE is due to the presence of Ti^{4+}

or Ti^{3+} species in rutile phase. A prominent O1s peak developed as a shoulder at 531.8 eV is attributed to presence titanium oxynitride and Ti_3O_4 after four and two shock treatments as shown in Fig. 4b. Shoulder peak developed towards higher binding energy may be due to chemisorbed oxygen.

After four and two shock exposures, the N(1 s) peak at 397.5 eV shown in Fig. 4c confirms that N is present in the N^{3-} ion, but in the pristine samples, the presence of N is not detected by XPS (Fig. 4c). Titanium nitride compound shows broad N(1 s) peak between 396 to 403 eV which was assigned to N-Ti bonding [5, 15]. In higher nitrogen doping, the BE of the N(1 s) shifts towards lower electron BE. The presence of 398 eV due to N atoms in the TiO_2 crystal lattice is due to the formation of oxynitride compound due to Ti-N and N-O bonds [16]. N(1 s) peak at 398 eV confirms the presence of O-Ti-N bond. The XPS data confirms nitridation of rutile TiO_2 sample when interacted with shock-heated nitrogen gas. It is possible to assign the exact number of peaks and their positions only after the deconvolution of the XPS spectra.

4 Conclusions

Material shock tube (MST) is used to produce moderate reflected shock pressure of 25–50 bar and temperature of 3750–6725 K (estimated) for short duration (1–2 ms). Shock-heated N_2 test gas interacts with the rutile TiO_2 fine powder which results in the formation of new compound and phase transformation. During shock treatment materials undergo melting, nucleation/growth and recrystallization process. Effect of superheating and cooling at the rate of 10^6 K/s shows the variation in crystallite size, lattice defects and relaxation of the lattice strain on the materials. This high-temperature nitrogen gas reacting with rutile TiO_2 results in the formation of new titanium oxide and oxynitride compounds. Formation of these new compounds was confirmed using different experimental techniques like SEM, XRD, XPS, etc. Formation of new compounds and crystallographic phase transformation occur simultaneously. In the present shock tube experiments, materials in fine powder form are subjected to high-temperature gas impact, which is a unique method developed in our laboratory. This novel experimental technique is essential to study chemistry of materials under extreme thermodynamic conditions for high-temperature applications.

Acknowledgements Financial supports for this study from the DRDO, ISRO-IISc Space Technology Cell and DST, Government of India, are gratefully acknowledged. Thanks to Professors K P J Reddy and G Jagadeesh of Aerospace Engineering Department, IISc, Bangalore, for their fruitful discussion and encouragements.

References

1. M.R. Hoffmann, S.T. Martin, W. Choi, D.W. Bahnemann Chem, Review **95**, 69–96 (1995)
2. A. Fujishima, K. Honda Nature. **238**, 37–38 (1972)
3. B.O. Regan, M. Gratzel, Nature **353**, 737–740 (1991)
4. R. Asahi, T. Morikawa, T. Ohwaki, K. Aoki, Y. Taga Science **293**, 269–271 (2001)
5. H. Irie, Y. Watanabe, K. Hashimoto, J. Phys, Chem. B. **107**, 5483 (2003)
6. X. Chen, S.S. Mao Chem, Review **107**, 2891–2959 (2007)
7. N. N. Thadhani Prog. Mater. Sci. **37,** 117–226, (1993)
8. V. Yakovyna, N. Berchenko, K. Kurbanov, I. Virt, I. Kurilo, Y. Nikiforov, Phys. Status Solidi C **0**(3), 1019–1023 (2003)
9. X. Gao, J. Liu, P. Chen Mater, Res. Bull. **44**, 1842–1845 (2009)
10. V. Jayaram, P. Singh, K.P.J. Reddy Adv, Ceram. Sci. Engn. **2**(1), 40–46 (2013)
11. V. Jayaram, Shock-induced reversible phase transformation from rutile to anatase in TiO_2 powders, SAMPE – 2016 – Long Beach, (2016)
12. A.G. Gaydon, I.R. Hurle, *The Shock Tube in High-Temperature Chemical Physics* (The Reinhold Publishing Corporation, New York, 1963)
13. Q. Zhang, L. Gao, J. Guo Appl, Catal. B: Environ. **26**, 207–215 (2000)
14. V.V. Atuchin, V.G. Kesler, N.V. Pervukhina, Z. Zhang, J. Electr, Spectros Relat. Phenom. **152**, 18–24 (2006)
15. N.C. Saha, H.G. Tompkins, J. Appl, Physics **72**, 3072 (1992)
16. O. Diwald, T.L. Thompson, T. Zubkov, E.G. Goralski, S.D. Walck, J.T. Yates Jr., J. Phys. Chem. B **108**, 6004 (2004)

Selective Shock-Refraction Properties in Non-ideal Fluids

E. Touber and N. Alferez

Abstract The interaction between a low-density spot and a compression shock in non-ideal fluids is studied using the linear interaction theory. Unlike in ideal fluids, the spot can be made to generate powerful sound or extreme shear rates. This is a general property of any substance featuring a local minimum in its sound speed. The selectivity of the refracted field may offer novel strategies to enhance mixing or for sound mitigation in high-speed flows.

1 Motivation

Shocks in ideal gases are known to generate thermo-acoustic modes when subjected to upstream perturbations. For example, turbulence intensities as low as 0.1% have been found to generate 120 dB noise levels at a shock in engine exhausts [1]. Similarly, hot/cold blobs of fluid can generate vorticity at the shock and increase the efficiency of high-speed combustion [2]. However, current knowledge on shock-refraction properties is limited to ideal fluids. Yet, environments such as combustion chambers, supersonic turbines operating in dense vapors, or ionizing shocks in reentry systems give rise to complex shocked fluids severely departing from the ideal gas law. The present work investigates the refraction of an entropic (density) perturbation at a shock in arbitrary substances.

E. Touber (✉) · N. Alferez
Mechanical Engineering, Imperial College London, London, UK
e-mail: e.touber@imperial.ac.uk

A. Sasoh et al. (eds.), *31st International Symposium on Shock Waves 2*,
https://doi.org/10.1007/978-3-319-91017-8_92

2 Methodology

2.1 Linear Interaction Analysis

The linear interaction analysis (LIA) formalism introduced by Ribner [1] for an ideal gas and extended by McKenzie et al. [3] to an arbitrary equation of state is used here. A formulation employing the primitive variables has been favored over the original formulation (see [4] for details). The LIA is built from the elementary interactions of incident plane waves with the shock (Fig. 1a), the response of which serves as building blocks for the general interaction problem (in the limit of small perturbations so as to neglect nonlinear interactions).

The Euler equations are linearized both upstream and downstream of the shock position and the perturbation projected onto Kovasznay's eigenmode basis (i.e., entropy, vortical, and acoustic modes) [3, 5]. A transmission condition is provided by the system of linearized Rankine-Hugoniot conditions at the shock position. It is then possible to deduce the downstream-mode amplitudes (i.e., generated acoustic, χ_{a^+}, and vorticity, χ_Ω, transmitted entropy, χ_s) knowing the upstream amplitudes (classical refraction problem). The refracted amplitudes have non-zero imaginary parts beyond a critical angle [1, 3] and produce non-propagating modes in the refracted field. For a general equation of state, the shock adiabat can satisfy the D'yakov-Kontorovich criteria [4, 6] and make the transmission problem singular, a circumstance not considered in this paper. The acoustic- and vortical-mode generation coefficients are shown in Fig. 2 for the flows considered in the paper (see Sect. 3 and Fig. 1b).

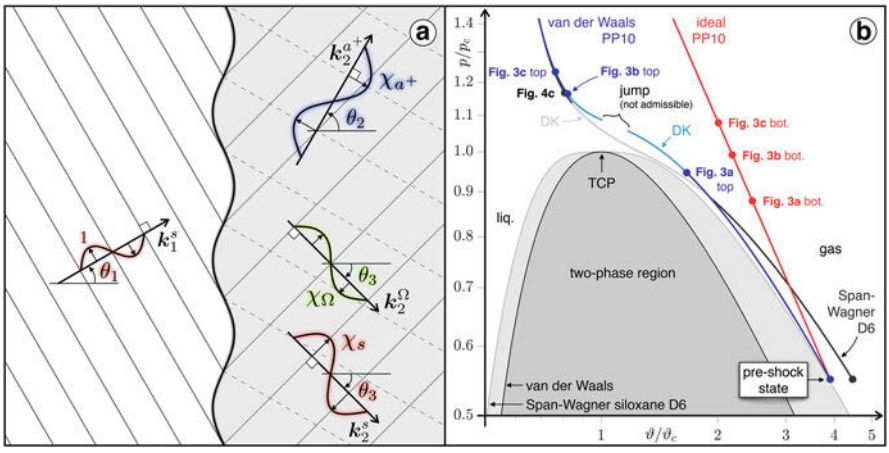

Fig. 1 Schematic of a plane-wave refraction on a normal shock. (**a**) Operating points on the pressure/specific volume (ϑ) phase diagram of the shocks considered in the paper. (**b**)

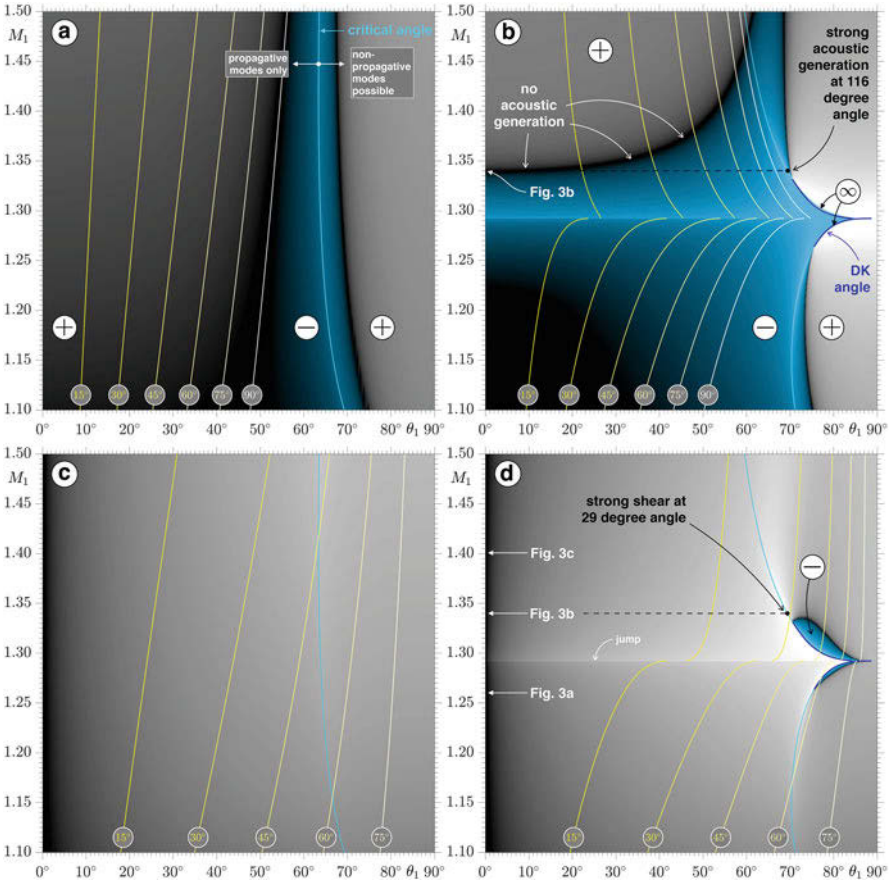

Fig. 2 Maps of the generation factors (χ_{a^+}, χ_Ω) for the acoustic (**a**, **b**) and vortical (**c**, **d**) modes for both the ideal (**a**, **c**) and van der Waals (**b**, **d**) gases over a narrow range of shock speeds (M_1) along the adiabats shown in Fig. 1b as functions of the incidence angle (θ_1). The generation factors are shown in gray scale (in log of the absolute value of their real parts), and the blue regions highlight where the real part of the generation factor is negative. All figures are shown with the exact same contour levels. The light blue lines correspond to the critical angle beyond which the imaginary part is non-zero (the post-shock perturbation has a non-propagative contribution). The dark blue lines in (**b**, **d**) correspond to the D'yakov-Kontorovich angle [6] (the linear theory is singular at this angle). The lines in shades of yellow correspond to the wave-vector angles θ_2 (**a**, **b**) and θ_3 (**c**, **d**) defined in Fig. 1

Analytical solutions to the pulse/shock-interaction problem are obtained by decomposing the pulse into plane waves (Fourier transform) in the wave-number space. A semi-analytical solution was derived for shock/vortex [7] and shock/Gaussian-entropy spot [8] interactions and extended here to arbitrary equations of state.

2.2 Numerical Simulations

The linear analysis results are compared with direct numerical simulations (DNS) of the Euler equations obtained with an in-house flow solver (employing a third-order TVD Runge-Kutta scheme for time integration and fourth-order centered finite-differences schemes for spatial derivatives). Large stencils (13 points) are used to optimize dispersion errors (up to 4 points per wavelength). Stability is ensured using a 13-point eighth-order explicit filter (with a cutoff at 5 points per wavelength). The shock is captured using a localized artificial diffusivity, whose coefficients are fixed so as to diffuse the shock over 25 grid points (see [9] for more details). This approach limits the wiggles amplitude to 0.01% of the amplitude of the density perturbation studied. Finally, grid stretching in the shock-normal direction is applied so that the thickness of the numerical shock represents 2% of the density perturbation wavelength.

3 Flow Configuration

A calorically perfect gas with a high number of active degrees of freedom is considered. The ratio of the isochoric specific heat capacity with the gas constant, C_v/R, is set to 78.2 (PP10). The non-ideal thermal equation of state is set to follow that of a van der Waals gas. The pre-shock temperature and pressure (T_1, p_1) are set relative to their values at the critical point (T_c, p_c): $p_1/p_c = 0.55$ and $T_1/T_c = 1.00$. This choice is driven by the possibility of observing "silent" shocks (see [4] for details) along the adiabat (shown in Fig. 1b). In log scales the ideal adiabat is a straight line, whereas the van der Waals one curves owing to the existence of a saddle point on the nearby isotherm and the high number of active degrees of freedom in the molecule (the adiabat converges to the isotherm when C_v/R is infinitely large [4]). Three particular shock speeds are considered: $M_1 = 1.26$ (Fig. 3a), $M_1 = 1.34$ (Fig. 3b), and $M_1 = 1.40$ (Fig. 3c), where M_1 is the pre-shock Mach number in the reference frame attached to the shock. Finally, to investigate the sensitivity of the results to the choice of thermodynamic model, the 12-parameter Span-Wagner equation of state for siloxane D6 [10] is applied to a shock with $p_1/p_c = 0.55$, $T_1/T_c = 0.98$, and $M_1 = 1.39$. Throughout the paper, the DK label refers to a region on the adiabat which satisfies the D'yakov-Kontorovich criteria [4, 6].

4 Results

A low-density spot (Gaussian profile as in [8], with maximum dip set to 1% of the pre-shock density) is introduced in a fluid at rest and impinged by compression shocks of varying speeds (see Fig. 1b and Sect. 3 for details about the pre-shock

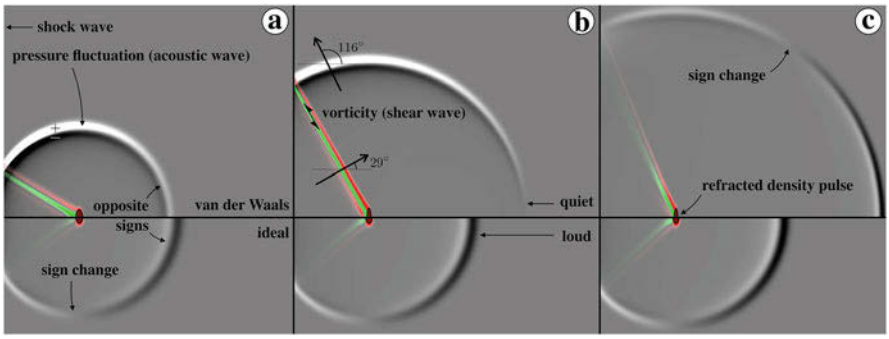

Fig. 3 Refraction of a low-density spot as predicted by LIA for the van der Waals (top row) and ideal (bottom row) gases for the three shock speeds considered in Fig. 1b: $M_1 = 1.26$ (**a**), $M_1 = 1.34$ (**b**), and $M_1 = 1.40$ (**c**). The pressure fluctuations are shown in gray scale (white for positive, black for negative), and the vorticity appears in color (green for positive, red for negative). All subfigures have identical scales (lengths and contour levels) and are shown at times corresponding to the same post-shock distance traveled by the refracted density pulse

state and shock speeds). Behind the shock the low-density spot is compressed in the shock-normal direction (giving it an elliptic shape) and accompanied by a cylindrical acoustic wave and parallel shear waves connecting the elliptical spot with the perturbation traveling along the shock (see Fig. 3). While the post-shock field always consists of a compressed spot together with acoustic and shear waves, their properties (e.g., propagation speed, directivity, and amplitude) can substantially vary.

4.1 Selective Properties as Predicted by the Linear Interaction Analysis

Figure 3 presents the refracted fields obtained by the LIA (Sect. 2.1). The main features are readily seen from the generation coefficient maps (Fig. 2) since the axisymmetric property of the Gaussian spot precludes forcing any particular incidence angle (θ_1). The nearly unchanged fields along the bottom row of Fig. 3 (obtained for varying shock speeds) reflect the uniformity (in M_1) of the generation coefficients (Fig. 2a,c). In effect, for a perfect gas, the ability of an entropy perturbation to generate acoustic and shear waves is set by the choice of specific heat ratio and shock speed and is insensitive to moderate variations in shock speeds.

In contrast, the van der Waals case offers an additional degree of freedom: the relative position of the pre-shock state with respect to the thermodynamic critical point. The top row in Fig. 3 demonstrates that the magnitude and directivity of the post-shock acoustic and shear waves can be altered over a narrow range of shock speeds.

The operating conditions were primarily selected for their ability to eliminate the acoustic wave in the direction normal to the shock, as may be seen from the pressure fluctuations in Fig. 3b. This is consistent with the zero-valued ridge emerging from the $M_1 = 1.33$ mark in the acoustic generation map (Fig. 2b). Indeed, a quiet wedge extending to about 30 degrees is expected. Conversely, the map also suggests that perturbations impinging the shock near the critical angle (beyond which the refracted field contains non-propagative modes) will refract into strong acoustic waves at about 116°, consistent with the pronounced wave front propagating along the shock in Fig. 3b. Finally, the generation coefficient being negative at all incidence angles up to the critical angle; the resulting pressure wave in Fig. 3b consists of a white-black front, which contrasts with the ideal gas where a black-white pattern switches to a white-black pattern around 90° (as anticipated from Fig. 2a).

Remarkably, reducing the magnitude of the cylindrical acoustic wave is found to come with the production of distinct shear waves. This is expected from the map given in Fig. 2d, where a region near a triple point between the critical and DK angles is found to exhibit particularly large (and in fact arbitrarily large – from the linear theory viewpoint) values of χ_Ω. For the Mach 1.33 case, sharp shear waves are expected with a wave-number angle of about 29°, consistent with the results in Fig. 3b. It is also possible to produce the opposite effect (i.e., energetic acoustic waves and weak shear waves), as shown to some extent in Fig. 3a, or obtain results similar to that of the ideal gas (still within a narrow range of shock speeds).

4.2 Comparison with the Direct Numerical Simulations

The selective refraction properties of the van der Waals shocks under conditions similar to those of Sect. 4.1 have been demonstrated using direct numerical simulations (DNS); see, for example, Fig. 4 of [9]. Evidence that the LIA recovers the DNS results is provided in Fig. 4a and Fig. 4b. Note that the DNS results include all nonlinear terms. The impinging density perturbation was set to 1% of the pre-shock density and is amplified to 5% of the post-shock density, making the agreement of the LIA particularly remarkable. Naturally, shear waves are inherently unstable and eventually roll up, an aspect which cannot be captured by the linear theory. Nevertheless, the LIA remains predictive if one is concerned with the manner in which the energy of the incoming perturbation is redistributed across the eigenmodes (acoustic, entropy, and shear waves). The ability of the linear theory to predict the post-shock turbulence kinetic energy in the context of ideal gases is well established [11], and the present results suggest that this is expected to hold true in non-ideal gases. However, this may no longer be valid for admissible shocks satisfying the DK "instability" criterion, for which the plane-wave solution becomes singular (see Fig. 2b,d).

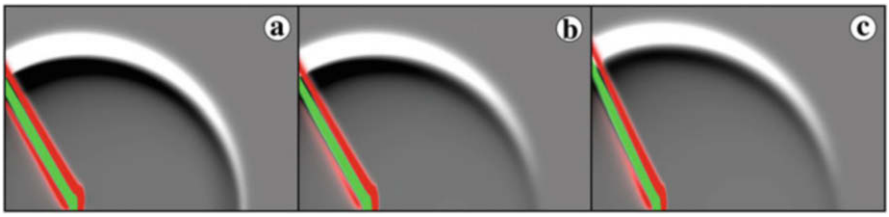

Fig. 4 Refraction of a low-density spot as predicted by DNS (**a**) and LIA (**b**, **c**). The quantities shown here are exactly the same as in Fig. 3 (but shown at an earlier time following the shock impingement time). Flow configurations (**a**) and (**b**) are the same as Fig. 3b, whereas (**c**) corresponds to the Span-Wagner case shown in Fig. 1b

4.3 Sensitivity of the Results to the Choice of Thermodynamic Model

The LIA results applied to siloxane D6 modeled using the 12-parameter Span-Wagner equation of state, and restricted to a region where the molecule is expected to be thermally stable, are provided in Fig. 4c. The corresponding shock adiabat is given in Fig. 1b. The deficiencies of the van der Waals model in the vicinity of the critical point are well acknowledged in the literature (and to some extent visible from Fig. 1b). Yet, the refracted fields in Fig. 4b and Fig. 4c are strikingly similar. This demonstrates that the peculiar shock-refraction properties are not an artifact of the van der Waals model but a universal feature associated with the convexity (or lack of) of the isentropes in parts of the pressure/specific volume phase diagram. Therefore, the present results are not restricted to the thermodynamic critical point but will apply to any substance with a local dip in the speed of sound.

5 Conclusion

The interaction between an entropy perturbation and a compression shock in a non-ideal fluid has been studied on the basis of the linear interaction theory. This extends the authors' recent results in one dimension [4] by confirming the possibility of severely damping the acoustic wave generated by the entropy perturbation in the direction normal to the shock. Moreover, an associated feature (not accessible with the 1D analysis) is the production of extremely large shear rates. These peculiar shock-refraction properties, unique to non-ideal fluids, could offer novel flow control strategies such as enhanced mixing in supersonic combustion or reducing jet noise. This is theoretically possible in any substance whose sound speed can be locally reduced under isentropic compression (e.g., critical-point phenomena, combustion, plasmas).

References

1. H. Ribner, *Shock-turbulence interaction and the generation of noise*, NACA Tech. Rep. 1233**,** (1955)
2. F. E. Marble, et al., *Shock enhancement and control of hypersonic mixing and combustion*, AIAA Paper 1981 (1990)
3. J.F. McKenzie, K.O. Westphal, Interaction of linear waves with oblique shock waves. Phys. Fluids **11**, 2350–2362 (1968)
4. N. Alferez, E. Touber, One-dimensional refraction properties of compression shocks in non-ideal gases. J. Fluid Mech. **814**, 185–221 (2017)
5. L.S.G. Kovasznay, Turbulence in supersonic flow. J. Aeronaut. Sci. **20**, 657–674 (1953)
6. J.W. Bates, The D'yakov-Kontorovich instability of shock waves in real gases. Phys. Rev. Lett. **84**, 1180–1183 (2000)
7. H. Ribner, Convection of a pattern of vorticity through a shock wave. NACA Tech. Rep. **1164**, 199–215 (1954)
8. D. Fabre et al., Linear interaction of a cylindrical entropy spot with a shock. Phys. Fluids **13**(8), 2403–2422 (2001)
9. N. Alferez, E. Touber, Shock-induced energy transfers in dense gases. J. Phys. Conf. Ser. **821**, 012019 (2017)
10. R. Span, *Multiparameter Equations of State: An Accurate Source of Thermodynamic Property Data* (Springer Science and Business Media, Berlin, 2000)
11. R. Quadros et al., Turbulent energy flux generated by shock/homogeneous-turbulence interaction. J. Fluid Mech. **796**, 113–157 (2016)

A Numerical Investigation of Oblique Shock Waves in Non-ideal Compressible Fluid Flows

G. Gori, D. Vimercati, and A. Guardone

Abstract Non-ideal compressible fluid dynamics effects are predicted to occur in flows of fluids characterized by moderate to high molecular complexity, such as heavy hydrocarbons, siloxanes, or perfluorocarbons, by state-of-the-art equation of states. These fluids are of utmost importance in many applications, and non-ideal effects must be taken into account to improve the efficiency of industrial plants (P. Colonna, J. Propuls Power 24:282–294, 2008). This paper is focused on two relevant non-ideal phenomena expected to occur across oblique shock waves for pre-shock states in the close proximity of the liquid-vapor saturation curve. The first one is the possible Mach number increase across the shock wave. This effect is due to the sound speed decrease, for increasing shock strength, along the compressive branch of the shock adiabat. This behavior contrasts with its ideal gas counterpart, for which the post-shock Mach number monotonically decreases with increasing shock strength. For the speed of sound to decrease in a compressive process, the so-called fundamental derivative of gas dynamics Γ must be lower than one (P.A. Thompson, Phys. Fluids 14:1843–1849, 1971). The second non-ideal effect is the dependency of the maximum flow deflection angle across an oblique shock on the pre-shock state. Indeed, in the ideal regime, the maximum turning angle depends on the pre-shock Mach number only. To highlight fundamental features, numerical results are presented for a set of exemplary fluid flows. The present findings are expected to be relevant for the design of devices involving supersonic or transonic flow of molecular complex fluids.

G. Gori (✉) · D. Vimercati · A. Guardone
Department of Aerospace Science and Technology, Politecnico di Milano, Milano, Italy
e-mail: giulio.gori@polimi.it

A. Sasoh et al. (eds.), *31st International Symposium on Shock Waves 2*,
https://doi.org/10.1007/978-3-319-91017-8_93

1 Introduction

In most of theoretical and practical applications, researchers and engineers are legitimated to model the behavior of a given gas using the well-known equation of state (EoS) for ideal gases, $Pv = RT$, hereinafter simply referred to as the ideal gas law or ideal EoS.

The ideal gas law has a proven reliability for most fluids, in a wide range of different circumstances.

Even since before the early work of van der Waals, scientists and engineers have been aware of the existence of effectiveness boundaries to the ideal EoS.

Indeed, under particular circumstances of high pressure and high temperature, the long-range molecular interactions among atoms begin to play a key role.

In such circumstances, more general and refined EoS is required in order to manage and to accurately describe the thermodynamic behavior of the gas.

The application of EoS that is capable of dealing with molecular complex gases in dense conditions, for instance, the van der Waals or the Peng-Robinson fluid models, opens the path to a set of physical phenomena that would not be predicted just by using the ideal EoS.

For instance, the van der Waals model may already predict a non-monotonic variation of the speed of sound, with respect to the temperature of the gas, while the law for ideal gases yet implies a monotone behavior.

Since such phenomena occur outside the limit of validity of the ideal gas law, they are referred to as non-ideal effects.

As a rough criterion to discern whether the regime of the flow can be classified as ideal or non-ideal, the fundamental derivative of gas dynamics Γ [2] may be evaluated:

$$\Gamma = \frac{v^3}{2c^2}\left(\frac{\partial^2 P}{\partial^2 v}\right)_s$$

If Γ is larger than one, then the flow is considered to be ideal, while if its value is smaller than 1, the regime may be referred to as non-ideal.

If Γ is negative, we talk about nonclassical regime, i.e., nonclassical phenomena such as rarefaction shock waves may occur.

This work is limited to non-ideal yet classical flows only; thus nonclassical phenomena are not considered hereinafter, and Γ is always positive.

This paper is focused on showing two non-ideal phenomena that may arise in practical applications, in particular, in ORC turbomachinery.

In the following, a brief introduction of the main features of non-ideal oblique shock waves is carried out (Sec. 2). In Sec. 3 exemplary flow configurations are presented to highlight non-ideal phenomena that may occur in flows of complex fluids.

The presented configurations include a regular shock reflection through a supersonic channel and a diamond-shaped airfoil at a large angle of attack plunged into a supersonic stream.

2 Mathematical Modeling

This section briefly resumes the main features and the critical aspects that characterize oblique shock waves. This is carried out to underline and explain the physical process to which results presented in this work are due; further details may be found in [3].

In the simplest case, a straight shock wave splits the domain into two uniform regions, A and B, namely, the pre- and the post-shock zone.

Given a fluid having a speed $\mathbf{u_A}$ whose magnitude is larger than the speed of sound resulting from the asymptotic stream state, the flow is turned abruptly by a finite angle θ across the discontinuity, which forms an angle β with respect to the flow upstream direction.

Locally, vectorial quantities can always be split into two different components: one normal to the shock (pointed out by subscript n) and one aligned along the direction of the discontinuity (we will refer to such direction as tangential, t, in the following).

Shock waves are discontinuous solutions that can be managed by means of the well-established Rankine-Hugoniot jump relations.

Beside this, the speed-ordering condition [4, 5] must be satisfied to ensure the stability of the shock and to abide by the second principle of thermodynamics.

The speed-ordering condition states that the following relation must always be satisfied

$$\frac{|u_{A,n}|}{c_A^2} \geq 1 \geq \frac{|u_{B,n}|}{c_B^2}$$

while the magnitude of the tangential component of the flow velocity $\mathbf{u}_t$ is always conserved.

If one considers the P-v plane, the shock adiabat commonly refers to the locus of thermodynamic states that can possibly be connected by a shock wave.

Given that for fluids having $\Gamma < 1$ the speed of sound do no longer increase monotonically with increasing density along the shock adiabat, the magnitude of the Mach number related to the tangential component of the speed may possibly increase across the shock.

If such increase is larger than the Mach number decrease in the normal direction, then also the flow overall Mach number increases across the shock.

An analytical relation may be retrieved to determine the post-shock Mach number, for shock of small strength and small value of θ:

$$M_B = M_A + \frac{M_A^3}{\sqrt{M_A^2 - 1}} \left(1 - \Gamma_A - \frac{1}{M_A^2}\right) \theta + O\left(\theta^2\right)$$

Though the latter relation doesn't have a general validity, it can be used to point out some of the crucial aspects that characterize a non-ideal shock wave.

In particular, the equation shows that the value of the Mach number after the shock depends on the value of Γ, which ultimately is a marker of the sound speed derivative.

As a consequence, this non-ideal effect results to be largely related to the non-monotonic variation of the speed of sound across the shock, which in turn strongly depends on the flow turning angle θ and on the fluid pre-shock state.

Differently than a purely ideal flow, there exists a tight bound between the Mach number variation across the shock and the asymptotic state of the fluid.

Moreover, for a fixed value of the flow turning angle θ and for a fixed upstream Mach number, the pre-shock thermodynamics conditions are found to have a remarkable influence on the value of the shock angle β.

When a more accurate description of the fluid thermodynamic behavior is taken into account, the value of Γ varies according to the upstream state of the fluid, thus introducing a further dependency factor.

Therefore, as soon as the intermolecular forces start playing a substantial role, two different non-ideal effects may occur: a Mach number increase across the shock and a dependency of the shock angle on the upstream thermodynamic state.

In the following, a set of exemplary cases are presented to show and investigate such phenomena.

3 Results

In this section we present two exemplary test cases, namely, a regular shock reflection within a converging nozzle and a diamond-shaped airfoil plunged in to a supersonic stream.

Test cases are aimed at reproducing scenarios that may possibly occur in practical applications.

To this extent, numerical simulations were carried out using SU2 [6, 7], an open-source suite which includes a computational fluid dynamics solver for non-ideal flows.

A few different EoS for gases are available within the SU2 framework. Moreover, the FluidProp library [8] can be employed to exploit state-of-the-art EoS.

In each case presented in the following, the thermodynamic behavior of the fluid is indeed reconstructed using the EoS included within the FluidProp library.

The fluid is toluene (or methylbenzene, C_7H_8), an aromatic hydrocarbon whose properties are reported in Table 1.

Table 1 Physical properties of toluene

R [J/KgK]	Γ [−]	T_{cr} [K]	P_{cr} [Pa]	ρ_{cr} [Kg/m^3]
90.24	1.09	591.75	4,126,300	291.99

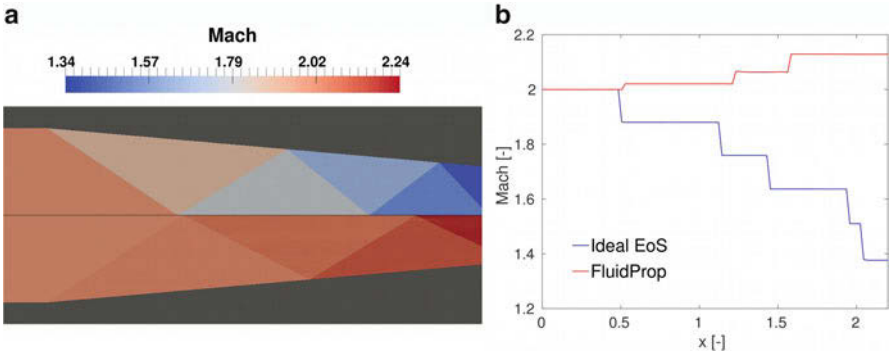

Fig. 1 (**a**) Mach field as computed using the ideal EoS (upper side) and FluidProp (lower side). (**b**) Mach number trends along the nozzle. Trends are extracted at a distance from the axis corresponding to half of inlet cross section

All the simulations were carried out using second-order accurate schemes, assuming that the fluid is inviscid and neglecting thermal conductivity.

A mesh adaptation procedure, up to six different level of refinement, depending on the case, was implemented to improve the resolution and the accuracy of the solution.

3.1 Regular Reflection

The geometry basically resembles a converging nozzle. The domain, along with the Mach number field retrieved using the ideal gas law (upper side) and FluidProp (lower side), is depicted in Fig. 1a.

The flow Mach number at the inlet, left-hand side, is equal to 2. The static pressure at the inlet is set to $0.5P_{CR}$, while temperature is $0.932T_{CR}$.

Since the slope of the nozzle wall varies, the flow is turned abruptly, and a shock wave is therefore generated. The shock propagates into the domain until it reaches the axis of the nozzle, which is a symmetry plane. There, the wave is reflected into the nozzle and continues to propagate until it is reflected again against the wall. The shock keeps bouncing alternately between the wall and the axis of the nozzle until it is eventually discharged into an infinite-acting reservoir (right boundary) at a very low pressure.

Figure 1a shows the resulting flow field. On the upper half, the Mach number field retrieved using the ideal gas law is depicted. On the lower side, the solution computed using an accurate fluid model (included in FluidProp) is reported.

A direct comparison between the two counterparts highlights notable differences. In particular, results reveal that the thermodynamic law largely affects the resulting flow configuration. Indeed, though the shock pattern is qualitatively similar, significant differences are obvious by observing the position of each reflection point, along the symmetry axis.

Moreover, while the Mach number decreases every time the fluid flows through a shock, for a gas modeled with the ideal EoS, the very reversed behavior is observable for the solution related to FluidProp. In this latter case, the Mach number increases across each shock. Mach number trends are plotted in Fig.1b for a more definite comparison.

3.2 Diamond-Shaped Airfoil

A diamond-shaped airfoil is exposed to a supersonic stream of toluene at a high angle of attack (15°).

The airfoil is symmetrical with respect to its diagonals, it has a chord c equal to 0.1 units, and the geometrical angle at the leading and trailing edges corresponds to 15°.

In this test case, the shock wave pattern is studied by varying the value of the freestream static pressure which spans from $0.1P_{CR}$ to $0.6P_{CR}$. The freestream static temperature is kept constant, and it is equal to T_{CR} while the Mach number is 1.5.

The flow field corresponding to each of the different values of pressure is reported in Fig. 2a–f. Simulations show that the resulting shape of the leading shock wave changes significantly if the upstream thermodynamic state varies. For low values of pressure, a detached, curved shock is formed ahead of the trailing edge (Fig. 2a, b and c). By further increasing the value of the freestream pressure, the shock gradually shifts toward the airfoil until it reaches the leading edge and the shock becomes planar (Fig. 2d).

The solution thus largely depends on the upstream conditions of the fluid; this is essentially a non-ideal phenomena. Indeed, for an ideal flow, the solution of this particular problem depends on the value of the upstream Mach number only. As the pressure is further increased, also a non-ideal Mach number growth is observed across the leading shock (Fig. 2f).

Over the airfoil pressure side, a similar, though complementary, phenomenon is observed as well. There, a non-ideal expansion occurs producing a Mach number decrease. It is worth to point out that, in the ideal regime, a supersonic expansion over an edge always results in a Mach number increase.

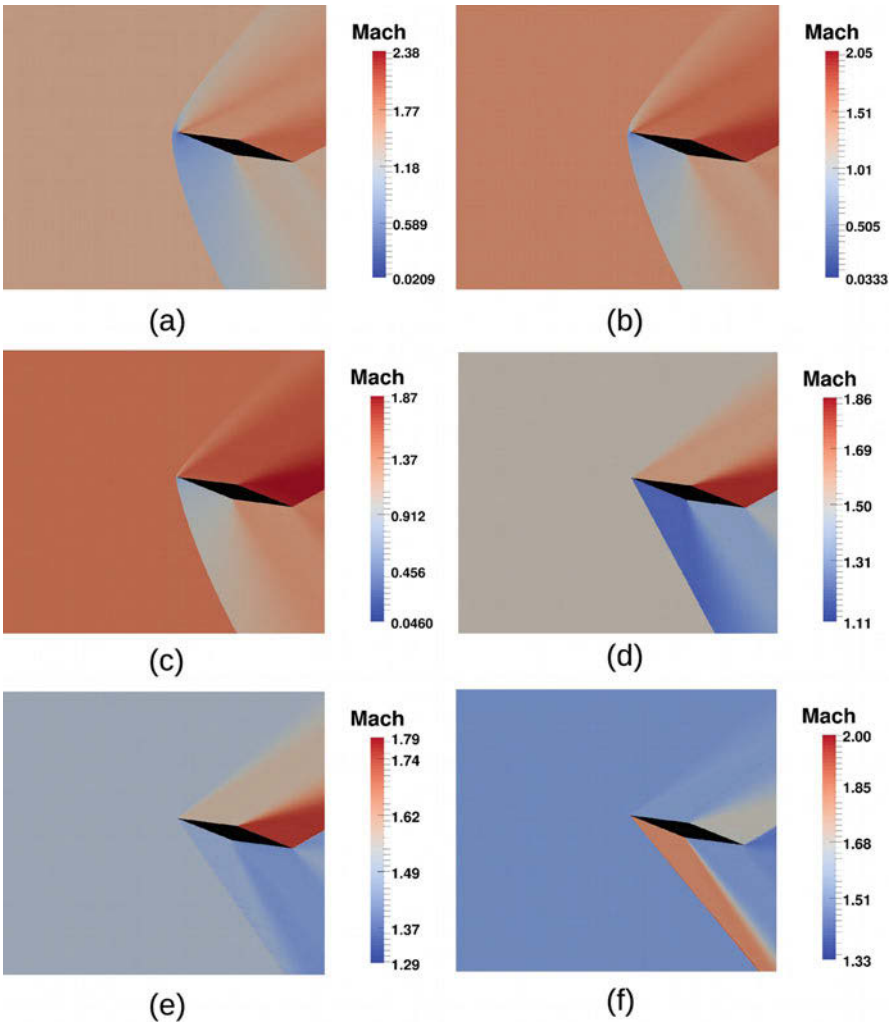

Fig. 2 Mach field around a diamond-shaped airfoil. Upstream Mach number is 1.5, while flow temperature is equal to T_{cr} for toluene. Upstream pressure varies: (**a**) $0.1P_{cr}$, (**b**) $0.2P_{cr}$, (**c**) $0.3P_{cr}$, (**d**) $0.4P_{cr}$, (**e**) $0.5P_{cr}$, and (**f**) $0.6P_{cr}$

4 Conclusions

In this paper a numerical investigation of oblique shock waves in non-ideal compressible fluid flows is presented.

These works investigate two different non-ideal effects: the first one is a possible Mach number increase across oblique shock waves, while the second one is the shock angle dependency on the flow upstream thermodynamic state.

Two exemplary test cases were presented to highlight such phenomena, namely, a supersonic converging nozzle, where a regular shock reflection takes place, and a diamond-shaped airfoil at a high angle of attack, where the shock pattern is proved to vary by changing the upstream flow pressure.

The non-ideal phenomena investigated in this work are expected to play a key role in practical applications such as those involving organic Rankine cycle systems.

References

1. P. Colonna et al., Real-gas effects in organic Rankine cycle turbine nozzles. J. of Propulsion and Power **24**(2), 282–294 (2008)
2. P.A. Thompson, A fundamental derivative in Gasdynamics. Phys. Fluids **14**(9), 1843–1849 (1971)
3. G. Gori et al., Non-Ideal compressible-fluid effects in oblique shockwaves. J. of Physics: Conference Series **821, 1** (2017)
4. P.D. Lax, Hyperbolic systems of conservation laws II. Commun. Pure Appl. Math. **10**, 537–566 (1957)
5. O. Oleinik, Uniqueness and stability of the generalized solution of the Cauchy problem for a quasi-linear equation. Usp. Mat. Nauk **14**, 165–170 (1959)
6. F. Palacios, et al., Stanford University Unstructured (SU2): An open-source integrated computational environment for multi-physics simulation and design. AIAA paper 2013–0287, 2013
7. S. Vitale, et al., Extension of the SU2 open source cfd code to the simulation of turbulent flows of fluids modelled with complex thermophysical laws. AIAA paper 2015–2760, 2015
8. P. Colonna, T.P. van der Stelt, FluidProp: a program for the estimation of thermo physical properties of fluids. Tech. Rep. 2005

Assessment of Real Gas Effects on S-CO_2 Flows with Shock Waves

Senthilkumar Raman and Heuy Dong Kim

Abstract When the CO_2 flows through the passages such as compressor or turbine, the state of CO_2 changes from S-CO_2 to G-CO_2 or vice versa. At these conditions, the equation of state (EOS) which predicts one property is failed to calculate the other properties at one temperature and pressure. Hence, it is necessary to assess each EOS available before any computations have been started. In this present work, S-CO_2 flow through an overexpanded nozzle is analyzed theoretically and computationally. For the theoretical study, one-dimensional gas dynamics equations were considered along with individual EOS. For the computational study, the 2-D Euler equations were considered. In comparison with flow field along the axis, it is found that consideration of different EOSs has so much deviation in flow properties due to different real gas effects.

1 Introduction

Carbon dioxide above its critical point attains a supercritical state and exhibits certain peculiar properties such as higher density as a liquid but with a lower viscosity comparable to a gas. This supercritical carbon dioxide (S-CO_2) has a wider range of engineering applications such as in the enhanced oil recovery, caffeine extraction, drying aerogels, textile dying, dry cleaning, etc. S-CO_2 has become a subject of vital research interest for investigators all over the world mainly due to its interesting characteristics as well as its potential applications [1, 2]. In thermodynamic power cycles, the high-density property of S-CO_2 is utilized to reduce compressor work, thereby augmenting the effective power output of the cycle. This property also helps to achieve a similar level of output power by using only a smaller sized compressor. Nakagawa et al. [3] studied an application of S-CO_2 as a refrigeration fluid and found that the efficiency of the refrigeration cycles

S. Raman · H. D. Kim (✉)
Andong National University, Andong, South Korea
e-mail: kimhd@anu.ac.kr

A. Sasoh et al. (eds.), *31st International Symposium on Shock Waves 2*,
https://doi.org/10.1007/978-3-319-91017-8_94

utilizing S-CO_2 increases considerably. Moreover, easy availability of CO_2 makes it cheaper to procure and operate inside a power cycle, compared to most of the other types of working fluids. The most crucial factor about S-CO_2 is that it can attain supercritical state relatively easily, close to the standard ambient temperature, without employing any powerful heating systems. Hence, the research on the power cycles based on S-CO_2 as a working fluid has substantially increased in the last few years.

The thermophysical properties of CO_2 such as density, local speed of sound, and specific heat capacity vary abruptly above the critical point which will, in turn, affect the performance of fluid machinery. Computational tools have difficulty in predicting these real gas effects of S-CO_2 due to lack of proven EOS. Despite the availability of many EOS, not many EOS were tested and explored for their applicability to S-CO_2. The performance of the compressor is mainly affected by shock waves occurring near blade section at high temperature and pressure. The formation of these shock waves was affected by the real gas effects, and hence it is vital to understand the quality and behavior of the each equation of state, and it is also necessary to examine how these influence the flow field and its behavior in shock formation. Detailed study on the effect of real gas effects on flow properties inside shock wave is carried out using Becker's solution [4, 5]. To the best knowledge of the author, there is no comparative study on this case with different EOS at the same conditions available. Ahn et al. [2] state that for the power cycles based on the S-CO_2, the turbine inlet temperature approximately varies from the range of 700 K–100 K. To carry out high-speed flow experiment at very high pressure and temperature is practically difficult. So it is indispensable to study the predictions of each EOS on supercritical CO_2 compressible flow. Hence, for this work, the condition for S-CO_2 is considered with the temperature at 1100 K and pressure 500 bar. The present work explores the real gas characteristics of S-CO_2 flow through a convergent-divergent nozzle with the different equation of state (EOS) at different conditions. The EOSs developed by Aungier, 1995 (ARK); Peng and Robinson, 1976 (PR); Boston and Mathias, 1980 (PRBM); Plocker, 1978 (LKP); Benedict, Webb, and Rubin, 1940 (BWR); and Span and Wagner, 1996 (SW), are considered. For the calculation of thermophysical properties of CO_2, NIST REFPROP utilizes SW EOS, and hence throughout this work, SW EOS is represented as NIST. The real gas effects in the shock front of S-CO_2 at different upstream Mach numbers are studied with varying pressure ratios.

A computer code is written based on the series of one-dimensional equations and the equations of states, to examine the compressible flow of S-CO_2 through a convergent-divergent nozzle. The behavior of compressible flow of supercritical CO_2 is also computationally analyzed with different EOSs for the same pressure ratio. Most of the flow and fluid properties predicted with various EOSs significantly vary with each other.

2 Methodology

2.1 Real Gas Equations of State

At standard atmospheric pressure and temperature, the CO_2 behaves as an ideal gas, and its compressibility factor equals to unity. However, at high temperature and pressure, the compressibility factor varies from unity, due to real gas effects. In order to predict this real gas effects, six different EOSs are considered for analysis of the real gas effects in the compressible S-CO_2 flow. The details about various equations of states that are adopted for this study, along with their critical fluid properties, can be found in the references [6–9].

2.2 Governing Equations

In order to approximate the behavior of real gas, all the properties (isentropic exponent, viscosity, density, and local speed of sound) required in the standard gas dynamics equations are substituted after calculating with each EOS.

Jhonson [10] derived an exact one-dimensional solution to the equations of fluid dynamics which analytically captures the profile of shock fronts. For analysis of velocity distribution, a nondimensional shock front the Eq. (1) derived by Jhonson [10] is adopted. Morduchow and Libby [11] derived solutions for the viscous, heat conducting and compressible gas and obtained expressions for calculating the properties distribution through the shock front. For calculations of distribution of the various properties in the shock wave, the work done by Morduchow and Libby [11] is adopted as shown in the Eqs. (2)–(4).

$$\xi = \frac{2}{\kappa+1}\ln\left[(u_1-u)^{\left(\frac{u_1}{u_1-u_2}\right)}(u-u_2)^{\left(\frac{-u_2}{u_1-u_2}\right)}\right] \tag{1}$$

$$\frac{\rho}{\rho_1} = \frac{u_1}{u} = \frac{1}{V} \tag{2}$$

$$\frac{P}{P_1} = \frac{1}{V}\left[1+\frac{\kappa-1}{2}M_1^2\left(1-V^2\right)\right] \tag{3}$$

$$\frac{S-S_1}{C_v} = \left\{\left[1+\frac{\kappa-1}{2}M_1^2\left(1-V^2\right)\right]V^{\kappa-1}\right\} \tag{4}$$

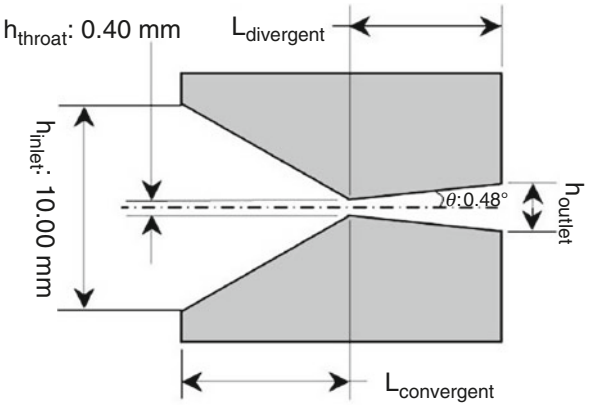

Fig. 1 Dimensions of the two-dimensional converging-diverging nozzle

2.3 Theoretical Analysis

Nozzle geometry considered by Nakagawa et al. [12] is extensively studied for the two-phase CO_2 compressible flow. Similar nozzle geometry with shortened divergent sectional length of 8.38 mm as shown in Fig. (1) is considered for the present work.

For the study of flow properties inside the normal shock wave, a region with a continuous change in flow properties is considered within the shock wave called shock front. For the S-CO_2 initial pressure of 500 bar and temperature of 1100 K were considered. The initial conditions are carefully taken into consideration such that no phase change occurs anywhere inside the nozzle.

3 Results and Discussion

The influence of variation in the fluid properties predicted from different EOS on the flow properties of a nozzle at various conditions is summarized in this section.

3.1 Real Gas Effects in Nozzle Flow Without Shock Wave

For a choked nozzle, the ratio between the pressure at the throat (P_{th}) and the inlet stagnation pressure (P0) is called throat critical pressure ratio, $P_{th,cr}$. Table 1 shows the variation in prediction of $P_{th,cr}$ for S-CO2 while using different EOS. For the same nozzle geometry, the difference in the critical pressure ratio between S-CO2 and G-CO2 is mainly due to the variation in the κ value and due to the high temperature and pressure of S-CO2. The second critical pressure ratio, $P_{super,cr}$, is the ratio between the static pressure at the nozzle exit section (Pe) and the total pressure at the inlet (P_0) during the flow in which the divergent section is completely

Table 1 Flow conditions for the isentropic and chocked nozzle flow

State	EOS	$P_{th,cr}$	$P_{sub,cr}$	$P_{super,cr}$	$M_{super,e}$
S-CO_2	Ideal gas	0.568	0.863	0.238	1.65
	PR EOS	0.563	0.86	0.232	1.66
	NIST	0.56	0.859	0.231	1.66
	PRBM	0.566	0.862	0.235	1.65
	BWR	0.567	0.863	0.235	1.65
	LKP	0.569	0.863	0.238	1.65
	ARK	0.572	0.866	0.241	1.64
G-CO_2	Ideal	0.553	0.859	0.205	1.7

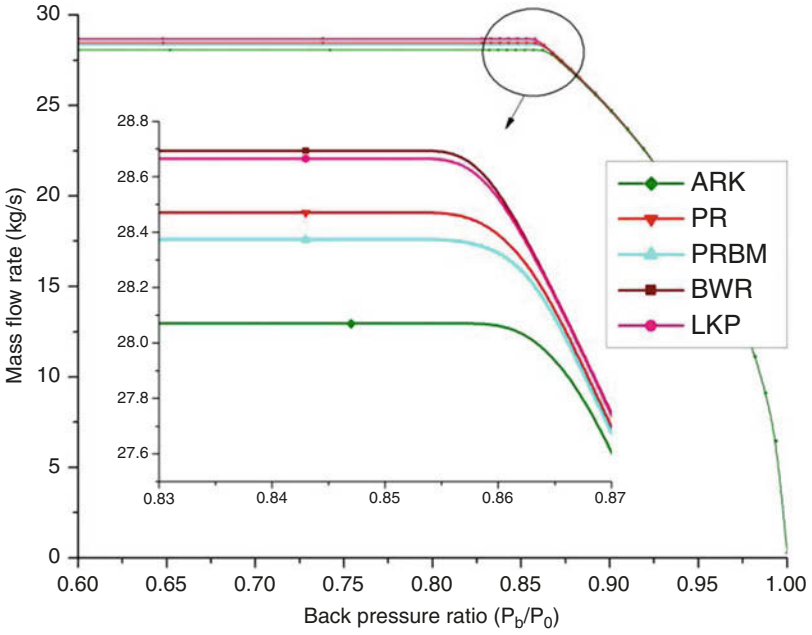

Fig. 2 Mass flow rate and the variation of back pressure ratio in nozzle

supersonic without any shock waves. The expansion of G-CO2 flow through the nozzle is 16% more than S-CO2 for same nozzle geometry which results in higher $M_{super,e}$ for G-CO2 than S-CO2 as tabulated in Table 1. Hence, the exit Mach number decreases due to the real gas effects.

Mass flow is another important flow factor in a choked nozzle flow. From Eqs. (12), it can be observed that the mass flow rate mainly depends upon κ and M for the constant Pt, T_{th}, and A_{th}. While keeping the total pressure as constant at inlet and decreasing the back pressure, before the chocking condition, the different EOS predicts the mass flow rate as the same. But for the choked nozzle, the mass flow rate predicted by various EOS is found to vary, and maximum difference in prediction is found between BWR EOS and ARK EOS as shown in Fig. 2. This indicates that

the variation in the real gas effects due to the different EOS is negligible before the chocking condition. While predicting the pressure distribution theoretically in EOSs, the pressure value suddenly decreases, reaching a value of nearly 0.57 for all EOS. The critical pressure ratio calculated with the CFD calculation shows a higher value than theoretical calculation as 0.7. Near the exit of the nozzle, the static pressure calculated with theoretical calculation and CFD becomes equal as seen in Fig. (2b).

3.2 Real Gas Effects in the Nozzle Flow with Shock Wave

For fully isentropic flow through the nozzle, it is found that values of static pressure at the exit to the total pressure at the inlet (P_e/P_0), calculated by each EOS, are different from the other for the same nozzle geometry. The back pressure ratio (BPR) is a primary governing factor for an exit Mach number, and it is defined as the ratio between the back pressure and inlet total pressure.

In order to analyze the real gas effects on pressure distribution along the axial length, the back pressure (P_b) is increased from the $P_{super,cr}$ tabulated in Table 1. Increasing the back pressure (P_b) while keeping the inlet total pressure (P_0) constant, in order to compensate the rise in the back pressure, a normal shock forms inside the nozzle. The normal shock wave occurs at a different length from throat section for various EOS for the same pressure ratio as shown in Fig. (3). Normal shock location for G-CO_2 is always ahead of the S-CO_2 as shown in Fig. 3. The prediction of normal shock location by LKP EOS is much behind other EOS for both lower and higher back pressure ratios. Further increasing the back pressure ratio will result in a condition when sonic speed is attained at the throat, but with subsonic exit Mach number without any normal shock. The pressure ratio between P_b and P_0 at this condition is called the first critical pressure ratio, $P_{sub,cr}$. This phenomenon occurs at BPR of nearly 0.86 for both S-CO_2 and G-CO_2 and with 0.5 exit Mach number for all six EOSs considered. This indicates that at the lower subsonic Mach number, the variation in the flow characteristics due to real gas effects is invariant with different EOS. However, there is appreciable variation in the Mach number and the pressure ratio for the supersonic flow case.

3.3 Effect of Real Gas in the Shock Front

The equations based on Becker's solution are used to analyze the change in properties inside the shock front. The various real gas effects are introduced in shock front analysis by substituting the values of specific heat capacity, viscosity, and thermal conductivity predicted from different real gas EOSs. As the BPR increases, shock wave moves toward the throat, and pre-shock Mach number decreases which results in increasing shock thickness as shown in Fig. (4a). Dissipative loss is the principal mechanism for pressure loss in shock. For lower BPR, the pressure loss

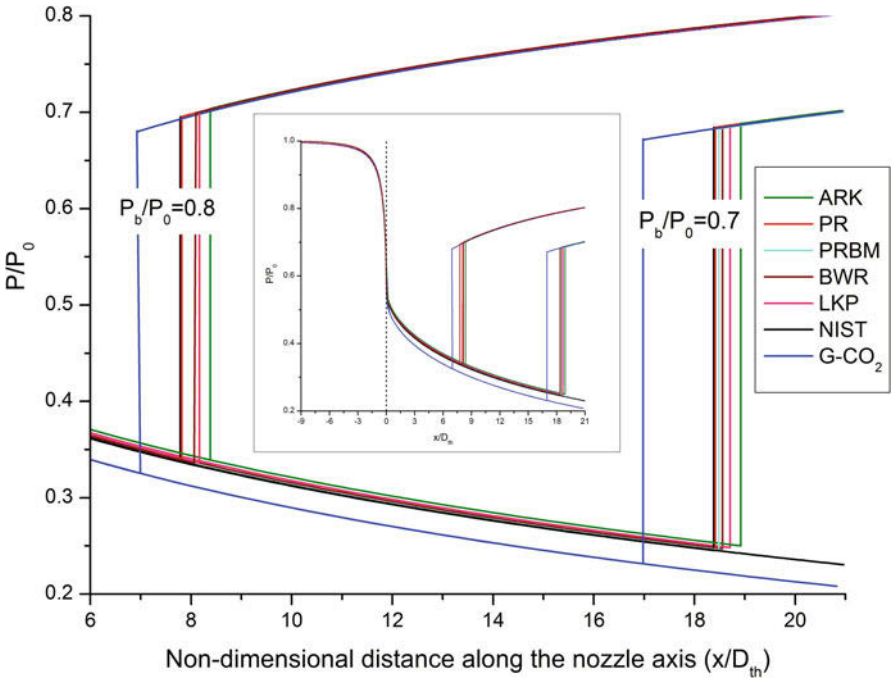

Fig. 3 Pressure distribution for the back pressure ratio (BPR) of 0.7 and 0.8

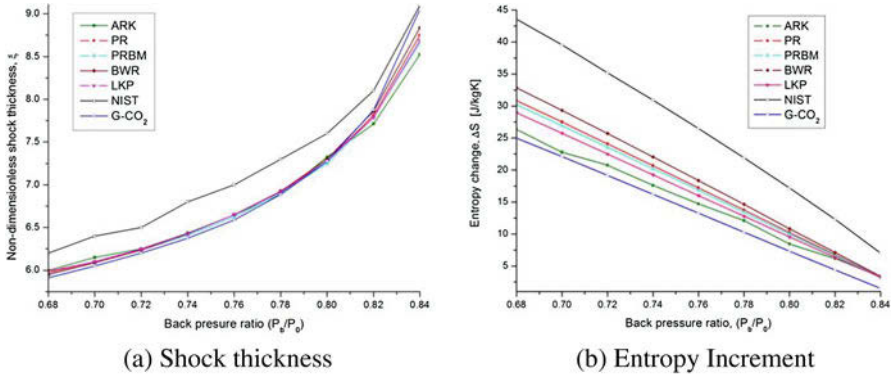

(a) Shock thickness (b) Entropy Increment

Fig. 4 Variation of the shock thickness and entropy increment for different back pressure ratio

predicted by SRK EOS is relatively higher than other EOS, while the prediction of BWRS EOS is relatively lower. This difference in total pressure loss shown in Fig. 4b directly corresponds to the variation in prediction of shock wave location as shown in Fig. 3. Except NIST, all other EOS has higher pressure loss compared to G-CO_2 for different ranges of pressure ratio. Interestingly at a pressure ratio of 0.80,

the pressure loss due to NIST suddenly decreases and becomes the same as that of G-CO_2 which is based on the ideal gas EOS.

Figure (4a) and (b) shows the variation of shock thickness and entropy across shock. Regarding the various EOS, it can be concluded that, in contrast with what one may expect, the flow property prediction by NIST is not different from other EOS. The difference in the shock properties between G-CO_2 and S-CO_2 is more pronounced at lower BPR than at higher BPR.

4 Conclusion

The flow properties are calculated for S-CO_2 at various nozzle pressure ratios with ideal gas EOS, Peng-Robinson EOS, Peng-Robinson-BM, SW, LKP, BRWS, and SRK. The flow field is compared with the same nozzle pressure ratio for G-CO_2 flow. The deviation in specific heat ratio prediction by different EOSs is known to be the main reason for the change in the flow property in the supercritical CO_2. In fact, variation in the flow properties is qualitatively similar to one another even though the fluid properties predicted by different EOS are not. Some fluid and flow properties are virtually unchanged for different EOS. The difference in the value of properties predicted by different EOS is minor. The pressure distribution, shock thickness, and entropy distribution in the shock front are also calculated for varying viscosity and thermal conductivity. The prediction of shock strength and the shock thickness varies from one EOS to another. The shock properties like entropy and total pressure loss are found to vary linearly for both G-CO_2 and G-CO_2 for changes in back pressure ratio. However for the first time in the present work, the variation of properties inside shock front has been explained in terms of various EOS.

Acknowledgment This work was supported by the National Research Foundation of Korea (NRF) grant funded by the Korean government (MSIP) (No. NRF-2016R1A2B3016436).

References

1. N.D. Baltadjiev, C. Lettieri, Z.S. Spakovszky, J. Turbomach. 137, 91003 (2015)
2. Y. Ahn, S.J. Bae, M. Kim, S.K. Cho, S. Baik, J.I. Lee, J.E. Cha, Nucl. Eng. Technol. 47, 647 (2015)
3. M. Nakagawa, A.R. Marasigan, T. Matsukawa, A. Kurashina, Int. J. Refrig. 34, 1604 (2011)
4. M.A. Khidr, M.A.A. Mahmoud, Astrophys. Space Sci. **113**, 289 (1985)
5. R.K. Anand, H.C. Yadav, Acta Phys. Pol. A 129, 28 (2016)
6. U. Plocker, H. Knapp, J. Prausnitz, Ind. Eng. Chem. Process. Des. Dev. **17**, 324 (1978)
7. R.H. AungierJ. Fluids Eng., **117**, 277, 281 (1995)
8. R. Span, W. Wagner, J. Phys. Chem. Ref. Data 25, 1509 (1996)
9. M. Benedict, G.B. Webb, L.C. Rubin, J. Chem. Phys. **8**, 334 (1940)

10. B.M. Johnson, J. Fluid Mech. 726, R4 (2013)
11. M. Morduchow, P.A. Libby, J. Aeronaut. Sci. **16**, 674 (1949)
12. Nakagawa, M., Serrano, M. S., Harada, A., in *International Refrigeration and Air Conditioning Conference*, 2165, Prude, (2008)

Structure of Shock Waves in Noble Gases Under High-Density Conditions

Z. A. Walenta and A. M. Słowicka

Abstract In the present paper, we show the dependence of the shock structure in a dense, noble gas on each of the three non-dimensional parameters: non-dimensional initial density, non-dimensional initial temperature, and non-dimensional shock velocity. It will also be demonstrated that the length scale, most suitable for measuring the thickness of the shock wave in a dense gas, is the sum of the mean free path (calculated the same way as for a dilute gas) and the diameter of a single gas molecule.

1 Introduction

The research reported presently is a continuation of our earlier work on shock waves in dense media. In our paper [1] we argued that for description of the shock-wave structure in a dense, noble gas, the following three non-dimensional parameters should be used:

- The non-dimensional density, $\rho = n\sigma^3$ (n is the number density of the molecules in the medium ahead of the shock wave, and σ is some linear scale parameter connected with magnitude of the molecule, here assumed equal to the parameter in the Lennard-Jones interaction potential called "diameter of the molecule").
- The non-dimensional temperature, $\theta = TB/\varepsilon$ (T– temperature of the medium in front of the shock, ε– depth of the well of the interaction potential of the molecules, B– universal gas constant).
- The non-dimensional velocity, $\omega = U/c^*$ (U– shock velocity with respect to the medium in front of it, c^* – most probable molecular speed in the medium ahead of the shock).

Z. A. Walenta · A. M. Słowicka (✉)
Institute of Fundamental Technological Research, Polish Academy of Sciences, Warszawa, Poland
e-mail: zwalenta@ippt.pan.pl

A. Sasoh et al. (eds.), *31st International Symposium on Shock Waves 2*,
https://doi.org/10.1007/978-3-319-91017-8_95

In the present paper, we show the dependence of the shock structure on each of these parameters separately. The results, for argon gas, were obtained numerically with the molecular dynamics technique [2]. For computations, the suitably modified program MOLDY [3] was used.

2 Molecular Dynamics Simulation

The program MOLDY [3], used in the present research, was originally designed for investigation of stationary phenomena. For the present research, it was supplemented with additional procedures for calculation of the phenomena occurring in the medium in motion.

For description of the interactions between the molecules of the medium (single atoms), the Lennard-Jones potential [2] was applied.

The assumed shape of the calculation domain was that of a parallelepiped, whose length (in the x-direction) was equal to 50 or 100 average distances between the centers of the molecules in the undisturbed medium.

Before the actual simulation, the medium was first equilibrated for a period equal to at least 10 picoseconds (10,000 time steps). After that it was set in motion by adding the assumed macroscopic velocity V to the x-component of the thermal velocity of each molecule. At the same time two impermeable, reflecting planes were inserted into the flow at the left and right borders of the calculation domain, thus generating the shock wave moving from the right border to the left and a rarefaction wave moving from the left border to the right.

The number of molecules taken for each simulation run ranged from 125,000 to 500,000. The time step assumed for simulation was equal to 0.001 picosecond. Each simulation run was finished after time period sufficiently long to evaluate the shock velocity and structure.

3 Results

3.1 Influence of the Initial Density

The influence of the initial density of the medium upon the structure of the shock has been presented in Figs 1 and 2. Figure 1, left, shows this influence upon density increase inside the shock for two different shock intensities, Fig. 1 – right – shows the same for temperature increase, and Fig. 2 shows this influence upon the shock thickness.

From Fig. 1 it is evident that the initial density influences strongly both the density and temperature increases inside the shock. The reason seems to be the following: the molecules, whose volume practically cannot be compressed, with increasing density occupy relatively larger and larger part of the total volume of the

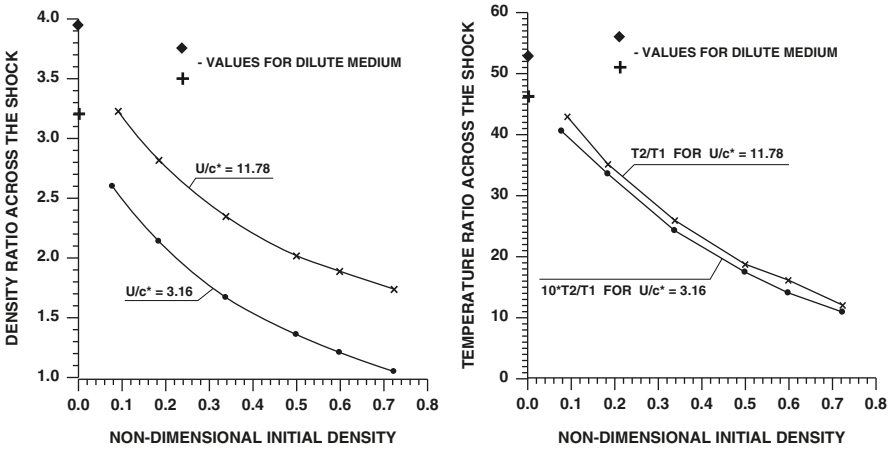

Fig. 1 Density ratios (left) and temperature ratios (right) across the shock in argon, in terms of the non-dimensional initial density, $\rho = n\sigma^3$, for the non-dimensional initial temperature $\theta = 2.5042$ ($T_1 = 300K$) and two non-dimensional velocities: $\omega = \frac{U}{c^*} = 3.16 \pm 0.04$, ($U \approx 1118m/s$) and $\omega = \frac{U}{c^*} = 11.78 \pm 0.28$ ($U \approx 4163m/s$). Note that the temperature ratios for $\omega = 3.16$ were multiplied by the factor 10

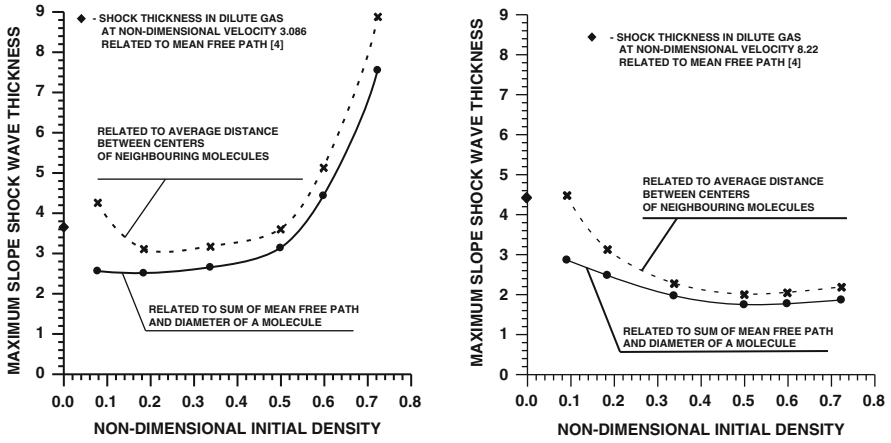

Fig. 2 Maximum slope shock thicknesses in argon, in terms of the non-dimensional initial density $\rho = n\sigma^3$, for the non-dimensional initial temperature $\theta = 2.5042$ ($T_1 = 300K$) and two non-dimensional velocities: left, $\omega = 3.16 \pm 0.04$ ($U \approx 1118m/s$) and right, $\omega = 11.78 \pm 0.28$ ($U \approx 4163m/s$). Broken lines – shock thicknesses related to $\sqrt[3]{n}$ (where n, number density of the molecules). Solid lines – shock thicknesses related to the sum of the mean free path and the diameter of a molecule. Values of shock thickness in dilute gas taken from [4]

medium. At the same time, at increasing density, part of the kinetic energy of the thermal motion of the molecules is transmitted into potential energy of the molecular interactions.

Each of the diagrams in Fig. 2 contains two lines: the broken one, presenting shock-wave thickness related to the average distance between the centers of the neighboring molecules (following suggestion of Bridgman [5], taken equal, approximately, to $\sqrt[3]{n}$, where n – number density of the molecules), and the solid line, presenting shock-wave thickness related to the sum of the mean free path and the diameter of a molecule. Both lines are approximately parallel at initial densities above about $\rho = 0.2$; however, at densities lower than that, the broken line turns unexpectedly up. To explain such behavior, one should note that at densities higher than $\rho = 0.2$, the distances between the neighboring molecules are smaller than the diameter of a molecule, and therefore collisions may occur only between the closest neighbors. At lower densities the moving molecule may squeeze between its closest neighbors and collide with some molecule at larger distance. Under such circumstances the absolute value of the shock-wave thickness will be correspondingly larger; however, this value related to the sum of the mean free path and the diameter of a molecule may remain constant. It seems therefore obvious that the average distance between the centers of the neighboring molecules may be used as the dimension characteristic for the shock-wave structure only for the most dense media, at non-dimensional densities $\rho \geq 0.2$. The sum of the mean free path and the diameter of a molecule seems to be applicable in this respect in much broader range of densities. In the subsequent considerations, the shock thickness will always be related to this sum of the mean free path and the diameter of a molecule.

One additional point should be noted here: for weaker shocks, ($\omega = 3.16 \pm 0.04$), in the density range $\rho \leq 0.5$, the variation of the shock thickness is very weak. For $\rho > 0.5$, however, with increasing density, the shock thickness increases relatively fast. Such increase of shock thickness is characteristic for very weak shocks, which suggests that for initial densities $\rho > 0.5$ and velocities $\omega \approx 3$, the shocks are indeed very weak. Confirmation of this fact may be found in Fig. 1 – the ratios of density and temperature across such shocks are very close to unity.

3.2 Influence of the Initial Temperature

The influence of the initial temperature of the medium upon the structure of the shock has been presented in Fig. 3. Figure 3 – left – shows this influence upon the density and temperature increase inside the shock; Fig. 3 – right – shows this influence upon the shock thickness.

In the considered temperature range (from 137.75 K to 300 K), the influence of the initial temperature upon structure of the shock wave in argon under high-density conditions is weak. With increasing temperature, the density ratio across the shock increases from 1.345 to 1.44 (about 7 per cent) only. The temperature ratio increases from 2.14 to 2.34 (about 9 per cent). The non-dimensional value of the maximum slope shock thickness decreases from 3.17 to 2.24 (about 30 per cent), which is a bit more significant.

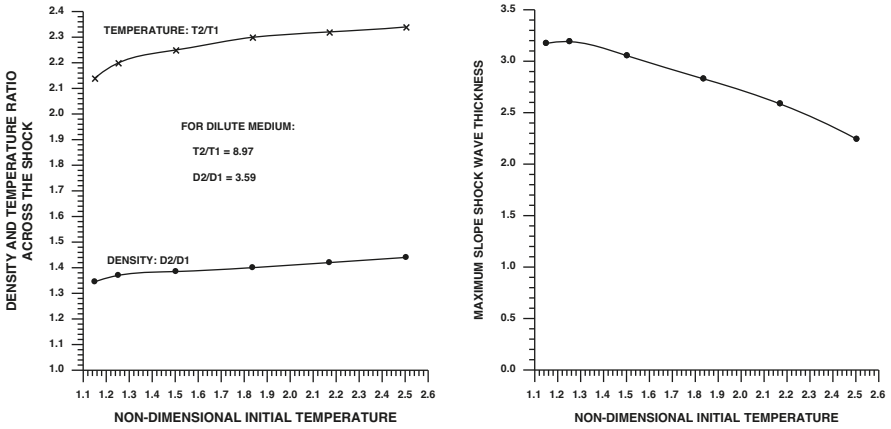

Fig. 3 Density and temperature ratios across the shock (left) and the maximum slope shock thicknesses (right) in argon, in terms of the non-dimensional initial temperature $\theta = T_1 B/\varepsilon$, at initial density $\rho = 0.5978$ (mass density of argon equal to mass density of water), and non-dimensional velocity $\omega = 4.66 \pm 0.07$ ($U \approx 1648$ *m*/*s*)

It should be noticed that in dilute argon, at the same non-dimensional velocity, the density ratio across the shock equals 3.59, independently of initial density and temperature. Similarly, the temperature ratio equals 8.97. Both values are much higher than those at high-density conditions.

3.3 Influence of the Shock Velocity

The influence of the shock velocity upon its structure has been presented in Figs. 4 and 5. Figure 4 – left – shows this influence upon the density increase inside the shock, Fig. 4, right, upon the temperature increase. The curves for dense medium are similar to those for dilute argon (also shown in the figures); only the values of density and temperature ratios at the same shock velocities in dense medium are lower.

Figure 5 – left – shows the dependence of the "reciprocal shock-wave thickness" (inverse of the non-dimensional maximum slope shock thickness) on shock velocity. Similarly to the case of dilute gas, the slow (weak) shock is thick. With increasing velocity the non-dimensional thickness of the shock decreases and seems to tend to some asymptotic value

In a dilute gas (Fig. 5 – right), this dependence has a minimum around the Mach number $Ms = 3$ [6] (non-dimensional velocity $\omega = 2.74$). Such minimum is not visible in dense gas.

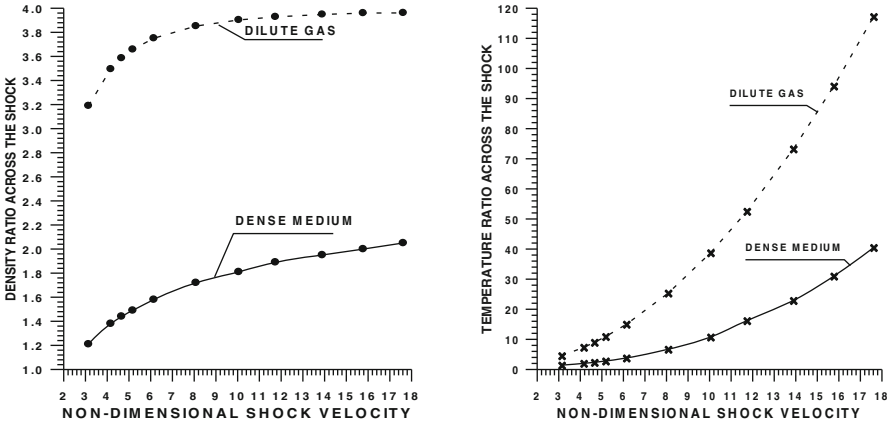

Fig. 4 Solid lines – density ratio (left) and temperature ratio (right) across the shock in argon, in terms of non-dimensional velocity $\omega = U/c^*$, at non-dimensional initial density $\rho = 0.5978$ (mass density of argon equal to mass density of water), and non-dimensional temperature $\theta = 2.5042$ ($T_1 = 300K$). Broken lines – corresponding values for dilute gas

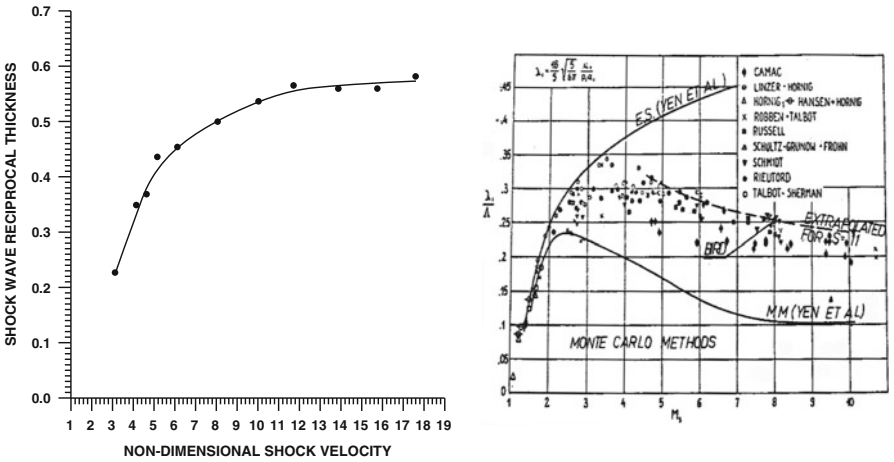

Fig. 5 Left: inverse shock-wave thickness in dense argon in terms of the non-dimensional velocity $\omega = U/c^*$, at non-dimensional initial density $\rho = 0.5978$ (mass density equal to that of water), and non-dimensional temperature $\theta = 2.5042$ ($T_1 = 300K$). Right: inverse shock-wave thickness in dilute argon in terms of the shock Mach number [6]

4 Conclusions

- It has been found that the average distance between the centers of the neighboring molecules (as suggested by Bridgman [5]) may be used as a measure of shock thickness in the case of the highest densities only. The measure, which is

appropriate in much broader range of parameters, is the sum of the mean free path (calculated in a standard way) and the diameter of a single molecule.

- Increase of the initial density causes decrease of density and temperature ratios across the shock propagating in the dense medium, in spite of the fact that the shock velocity remains constant. The above follows from the fact, that at higher densities the molecules, which have finite and practically constant volume (cannot be compressed), occupy larger part of the total volume of the medium. At the same time, at increasing density, part of the kinetic energy of the thermal motion of the molecules is transmitted into potential energy of the molecular interactions.
- The initial temperature has little influence upon the structure of the shocks in dense media. The increase of this temperature causes only slight increase of the density and temperature ratios across the shock, as well as decrease of the non-dimensional shock thickness.
- Influence of velocity of the shock upon its structure in a dense medium is qualitatively similar to that in a dilute gas. However the ratios of densities and temperatures across the shock, for the same non-dimensional shock velocities are smaller for dense medium than for dilute gas. Apart from that, the dependence of the shock thickness in a dilute gas on its velocity has a minimum for the shock Mach number about 3, while in a dense medium, no minimum is present. When velocity of the shock is increased, its thickness tends to some asymptotic value.

References

1. Z.A.Walenta, A.M. Slowicka, Similarity parameters for shock waves in dense fluids. Presented at ISSW30, Tel Aviv, Israel (2015)
2. M.P. Allen, D.J. Tildesley, *Computer Simulation of Liquids* (Clarendon Press, Oxford, 1987)
3. K. Refson, Moldy: A portable molecular dynamics simulation program for serial and parallel computers. Comput. Phys. Commun. **126**(3), 309–328 (2000)
4. H. Alsmeyer, Messung der Struktur von Verdichtungsstossen in Argon und Stickstoff, Ph.D. thesis, University of Karlsruhe, Karlsruhe, 1974
5. P.W. Bridgman, The thermal conductivity of liquids under pressure. Proc. Amer. Acad. Arts and Scie **59**, 141–169 (1923)
6. W. Fiszdon, R. Herczynski, Z. Walenta, The structure of a plane shock wave of a monatomic gas. Theory and experiment, in *Proceedings of the Ninth International Symposium on Rarefied Gas Dynamics*, ed. M. Becker, M. Fiebig, DFVLR-Press, Porz-Wahn, vol. 2, 1974

Shock Train Structures in Rectangular Ducts

F. Gnani, H. Zare-Behtash, C. White, and K. Kontis

Abstract The deceleration of a supersonic flow to subsonic velocity inside a high-speed engine occurs through a series of shock waves, known as a shock train. The generation of such a flow structure is due to the interaction between the shock waves and the boundary layer inside a long duct. This phenomenon is frequently encountered in a variety of internal flow fields where a shock wave interacts with the boundary layer including air-breathing engines, high-speed wind tunnel diffusers, and supersonic compressors and ejectors. The present study investigates the complex SBLI phenomenon encountered in a Mach 2 shock train through numerical analysis.

1 Introduction

The study of scramjet/ramjet intakes is vital for future space transportation and hypersonic flight applications. Since the peculiarity of air-breathing engines consists in the absence of any moving parts, the compression is achieved by means of a shock wave structure called a shock train. The characteristics of such a shock system depend on a number of variables including: the duct geometry, wall friction, Mach number, Reynolds number, boundary layer thickness, and pressure conditions at the two extremities of the duct [1, 2].

At low shock Mach numbers, a very weak shock/boundary layer interaction takes place, but as the flow Mach number increases, the formation of multiple shock waves leads to a lower pressure recovery and increment of the overall length of the wave structure [3]. For Mach numbers between approximately 1.5 and 2, the flow configuration consists of a series of normal shocks in the centre of the duct that are split into a series of oblique shocks due to the interaction with the boundary layer near the wall, as illustrated in Fig. 1. As the Mach number increases, between 2

F. Gnani (✉) · H. Zare-Behtash · C. White · K. Kontis
School of Engineering, University of Glasgow, Glasgow, UK
e-mail: f.gnani.1@research.gla.ac.uk

A. Sasoh et al. (eds.), *31st International Symposium on Shock Waves 2*,
https://doi.org/10.1007/978-3-319-91017-8_96

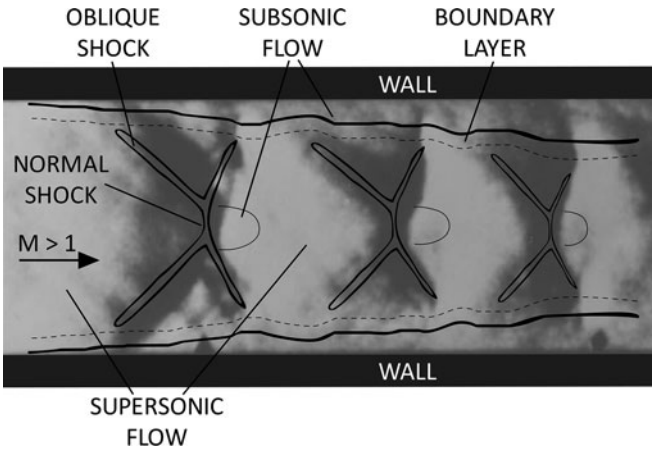

Fig. 1 Shock wave/boundary layer interaction

and 3, the stronger interaction with the boundary layer leads to a change in the flow pattern, which is composed of oblique shocks [4]. Above Mach 3 some difficulties in detecting a shock train have been reported, and the flow no longer has a defined structure [5, 6].

The numerous variables which contribute to generating a complicated interaction between the shocks and the boundary layer make a comprehensive analysis of the flow field extremely challenging. Understanding the flow physics in the presence of the interaction of multiple shock waves with the boundary layer in internal flows is particularly difficult but essential to developing methods and control strategies. Analytical models are capable to outline the general behaviour of the pressure rise through the shock train; however, they rarely match with experimental data. Another approach to study shock trains is by numerically solving the Navier-Stokes (NS) equations. CFD enables a detailed analysis of the flow field, but few satisfactory results have been found in literature.

The choice of the turbulence model that closes the NS equations depends on the flow regime under investigation and is guided by the need for an accurate solution which opposes fastness requirements [7]. Sun et al. [8] claimed to have obtained good agreement with experimental data using the Baldwin-Lomax model turbulence model. However, the experimental data were satisfactorily replicated only in one tested case. Knight [9] reported that the Baldwin-Lomax model does not precisely predict the recovery of a turbulent boundary layer downstream of a strong two-dimensional shock interaction. Carroll et al. [10] compared the experimental data of a Mach 1.6 shock train in a rectangular duct and the RANS equations closed with the Baldwin-Lomax and the k-ω Wilcox-Rubesin models. As Fig. 2 shows, both models fail to provide an accurate prediction of the shock train. The Baldwin-Lomax model is not capable to even capture the general features of the shock train.

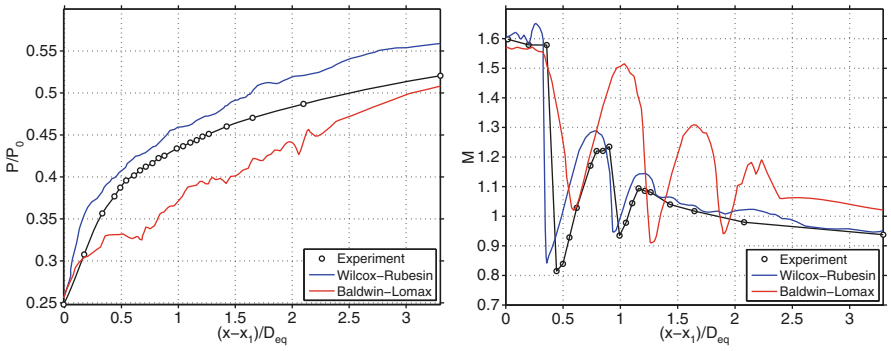

Fig. 2 Wall static pressure and centreline Mach number distribution shifted for common pressure rise, normalised to the equivalent diameter [10]

Compared to other turbulence models, the k-ω model seems to be the most appropriate choice to model shock trains. This model is able to reproduce subtle features close to the solid boundary and is more accurate for two-dimensional boundary layers with both favourable and adverse pressure gradients and in the presence of separation induced by the interaction with a shock wave [11]. Om et al. [3] showed that in case of attached boundary layer, the details of a normal shock interacting with the boundary layer are well predicted. On the other hand, when flow separation is present, the discrepancies of the simulated results with experiments increase as separation becomes larger.

The objective of the present study is to numerically investigate and corroborate the experimental findings of Sun et al. [8] in a square duct with a Mach 2 shock train with the RANS equations closed by the Wilcox k-ω turbulence model.

2 Numerical Method and Physical Setup

Numerical simulations were carried out solving two- and three-dimensional coupled implicit Reynolds-Averaged Navier-Stokes (RANS) equations in STAR-CCM+ with the Wilcox k-ω turbulence model. The RANS equations are discretised using a cell-centred finite-volume method. Inviscid and viscous fluxes are evaluated using, respectively, Liou's AUSM+ flux-vector splitting scheme based on the upwind concept and second-order central differences. The temporal term has been discretised with a second-order accuracy interpolation scheme.

For all simulations the experimental configuration and flow conditions described by Sun et al. [8] are investigated. A Mach 2 shock train is studied in a test section of a square cross-sectional area of 80 mm × 80 mm and 1500 mm long. The boundary and geometrical conditions are reported in Table 1. The working fluid is treated as an ideal gas. The viscosity and thermal conductivity are evaluated using Sutherland's

Table 1 Boundary and geometry conditions of the computational domain. The subscript 0 refers to the total condition

M	T_0 [K]	P_0 [kPa]	H [mm]	W [mm]	L [mm]	L/D_{eq}
2	300	196	80	80	1500	18.75

law. Adiabatic and no-slip boundary conditions are imposed on the walls along the duct. Initial conditions are set with an inviscid normal shock at the exit of the computational domain. Stagnation conditions are imposed at the inlet with uniform flow properties. At the outlet boundary, the flow variables except the pressure are extrapolated from the adjacent cell value using reconstruction gradients. The back pressure was determined from the experimental results and assumed to be constant at the exit plane with a value of $P_b = 92.2$ kPa.

The effect of the flow confinement δ/h at the inlet of the computational domain plays a fundamental role on the location of the shock train. In this study a computational domain with $L/D_{eq} = 23$ has been used to allow the boundary layer to develop. Only the portion of duct with length 11 times the height was taken to process the data, with the inlet located at δ/h equal to approximately 0.25 [8]. Due to the symmetry of the problem, half of the region of the flow field is computed in the two-dimensional case and one quarter in the three-dimensional case. A mesh refinement is carried out in proximity of the wall to resolve the behaviour of the turbulent boundary layer.

3 Results and Discussion

3.1 Effect of Mesh Resolution

For the grid independence study, a coarse mesh that meets the criteria of convergence is used as a starting point to gradually increase the number of cells in the computational domain. The six grids employed are tabulated in Table 2.

The static pressure with different grid sizes are compared in Fig. 3. It is observed that, as the mesh resolution increases, the shock train moves upstream towards the inlet and increases in length. Fine grids better match with the experimental data because the representation of the flow field is more accurate. Since the back pressure is prescribed as a boundary condition, the pressure at the end of the shock train tends towards the experimental value.

The general behaviour of the shock train is similar in the six cases; however, a very coarse mesh fails to capture fine structures such as the boundary layer. In such flows, where the ratio of the thickness of the boundary layer to the duct height is a key parameter in determining the shock characteristics, an error of only a few percent in resolving the boundary layer can result in a considerable divergence from experiments. The difference between Grid 5 and Grid 6 in Fig. 3

Table 2 Number of cells for different grids employed

Grid name	Grid 1	Grid 2	Grid 3	Grid 4	Grid 5	Grid 6
Grid size	62 × 368	116 × 921	154 × 2454	276 × 4601	314 × 6134	350 × 9200

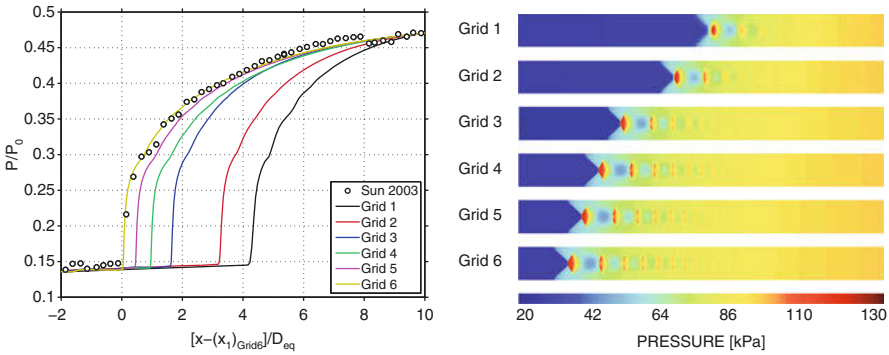

Fig. 3 Effect of grid resolution on pressure. (**a**) Wall pressure; (**b**) Numerical distribution

is not significant and the relative error is less than 3%. As a consequence, the results with a finer grid are expected to be very close to Grid 6 which is adequate to achieve grid-independent results. Taking into account both the accuracy of the grid with the computational cost, Grid 2 is used to perform the simulations reported in this work.

3.2 Effect of Back Pressure

The effect of the back pressure P_b is investigated by applying a periodic wave with an amplitude of 10% the initial value and frequency f = 2 Hz. The different time steps are $\Delta T_1 = 0.1T_c$, $\Delta T_2 = 0.5T_c$, $\Delta T_3 = 0.025T_c$, and $\Delta T_4 = 0.0125T_c$, where T_c is the characteristic time defined as L/U_∞.

Figure 4 shows the response of the first shock to the imposed back pressure change. The Mach number behind the first shock wave is characterised by a large oscillation due to the forcing and a small oscillation due to the unstable nature of the flow. With an increase in back pressure, the shock train responds with a decrease in the flow speed meaning that the first shock is stronger and the flow is more strongly decelerated. On the contrary, when the back pressure is decreased, the first shock becomes weaker and the flow speed is higher.

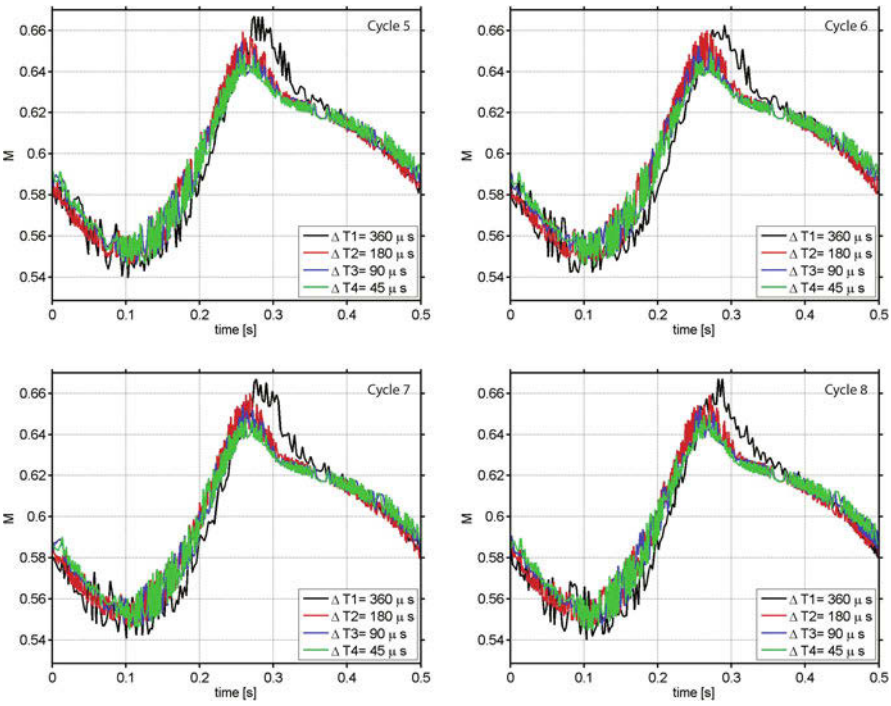

Fig. 4 Mach number behind the first shock wave under back pressure forcing with different time step

3.3 Effect of Sidewalls

Two-dimensional simulations have the advantage of being efficient since the inclusion of the third dimension costs additional computational time. The presence of sidewalls cannot be neglected in the current study since the duct aspect ratio is unity. Although the accuracy of Grid 2 is limited, the qualitative understanding of the flow behaviour when the sidewall effects are included can be outlined. Figure 5 illustrates the Mach number and pressure distribution for 2D and 3D domains.

Compared to the 2D case, in 3D the shock train moves upstream by 12.75 L/D_{eq}. The reason of this difference is caused by the effect of the boundary layer on the side walls and the corners. As Morgan et al. [12] reported, the flow confinement plays the greatest role in determining the location of the initial shock. In 2D the boundary layer occupies 25% of the duct height, whereas by including the boundary layer on the side walls, the reduction of the effective area is amplified. The core flow is reduced by 44%, which is almost double the 2D case. The shape of the shock train also changes and in particular the first shock wave. Each peak in the pressure plot identifies a wave composing the shock train that are gradually damped along the duct. The flow behind the first shock is decelerated more strongly, as the deeper trough in the pressure plot illustrates.

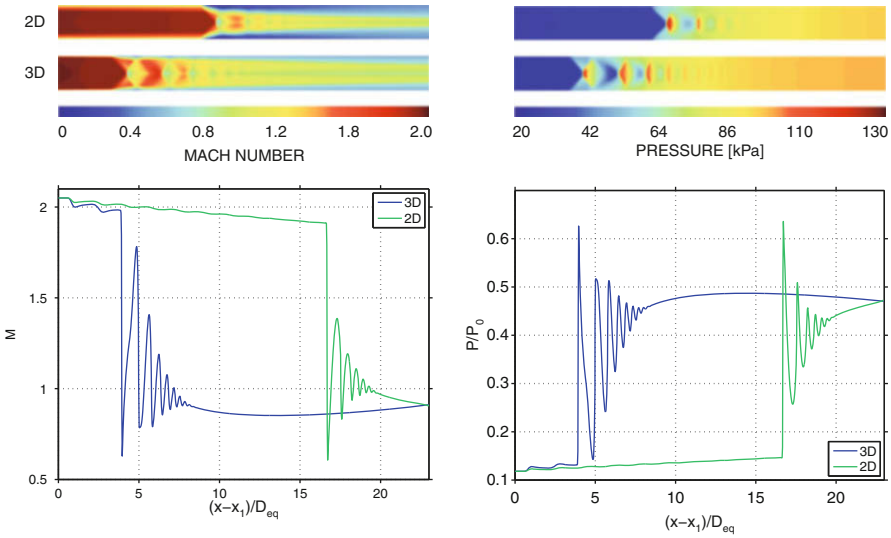

Fig. 5 Mach number and pressure distribution with 2D and 3D domain

It can also be noticed that in the 3D case, the pressure recovery behind the last shock wave reaches a maximum value higher than the back pressure. This trend is evident in the wall pressure collected by Sullins [13] studying a shock train in a Mach 2 flow in a rectangular duct with an aspect ratio of 2.5. The same behaviour however is not visible in the data from Sun et al. [8] in Fig. 3, but the reason is not clear.

4 Conclusions

The characteristics of a shock train at Mach 2 in a rectangular duct have been investigated. Numerical simulations are carried out with RANS equations closed by the Wilcox k-ω turbulence model.

Grid analysis has shown that the location and shape of the shock train are highly sensitive to the mesh resolution. Additionally a drastic difference in the location of the shock train takes place from the 2D to the 3D case. In the presence of a periodic variation of the back pressure, a large oscillation is established as a response of the forcing. An additional small oscillation is observed due to the unstable nature of the flow.

References

1. E.T. Curran, W.H. Heiser, D.T. Pratt, Fluid phenomena in scramjet combustion systems. Annu. Rev. Fluid Mech. **28**, 323–360 (1996)
2. F. Gnani, H. Zare-Behtash, K. Kontis, Pseudo-shock waves and their interactions in high-speed intakes. Prog. Aerosp. Sci. **82**, 36–56 (2016)
3. D. Om, M.E. Childs, J.R. Viegas, Transonic shock-wave/turbulent boundary-layer interactions in a circular duct. AIAA J. **23**(5), 707–714 (1985)
4. W.H. Heiser, D.T. Pratt, *Hypersonic Airbreathing Propulsion* (American Institute of Aeronautics and Astronautics, Washington, DC, 1994)
5. I. Hataue, Computational study of the shock-wavey/boundary-layer interaction in a duct. Fluid Dyn. Res. **5**(3), 217–234 (1989)
6. H. Sugiyama, R. Minato, K. Mizobata, A. Tojo, Y. Muto, Experimental and numerical analysis of the structure of pseudo-shock systems in Laval nozzles with parallel side walls. J. Therm. Sci. **15**(1), 37–42 (2006)
7. T.J. Barber, G.B. Cox, Hypersonic vehicle propulsion – a computational fluid dynamics application case study. J. Propuls. Power **5**(4), 492–501 (1989)
8. L.Q. Sun, H. Sugiyama, K. Mizobata, K. Fukuda, Numerical and experimental investigations on the mach 2 pseudo-shock wave in a square duct. J. Vis. **6**(4), 363–370 (2003)
9. D.D. Knight, Calculation of three-dimensional shock/turbulent boundary-layer interaction generated by sharp fin. AIAA J. **23**(12), 1885–1891 (1985)
10. B.F. Carroll, P.A. Lopez-Fernandez, J.C. Dutton, Computations and experiments for a multiple normal shock/boundary-layer interaction. J. Propuls. Power **9**(3), 405–411 (1993)
11. W.Y.K. Chan, P.A. Jacobs, D.J. Mee, Suitability of the $k - \varepsilon$ turbulence model for scramjet flowfield simulations. Int. J. Numer. Methods Fluids **70**(4), 493–514 (2012)
12. B. Morgan, K. Duraisamy, S.K. Lele, Large-eddy simulations of a normal shock train in a constant-area isolator. AIAA J. **52**(3), 539–558 (2014)
13. G. Sullins, Experimental results of shock trains in rectangular ducts. AIAA-92-5103 (1992)

Effect on Shock Train Behaviour of the Addition of a Cavity for Supersonic Intakes

A. Russell, H. Zare-Behtash, and K. Kontis

Abstract One of the key research areas related to high-speed flight is the ramjet/scramjet propulsion systems. These appear to have the most potential for development into reliable high-speed air-breathing propulsion system. These propulsion systems function by using simple geometries to decelerate the flow through a series of shock waves, a shock train, before entering the combustion chamber. The isolator is an important feature of the propulsion system that is necessary to house this shock train. A significant issue with the operation of ramjet/scramjet engines that this research targets is unstart in isolators. Unstart is the phenomenon that occurs when the isolator experiences an increase in back pressure from the combustion chamber, which itself can be a result of numerous events, resulting in the shock train being expelled out of the propulsion system intake.

This research examines the use of a cavity in the wall of the isolator to delay unstart. However the cavity flow must be actively controlled so as to mitigate the negative impact, drag increase, of the cavity addition. Therefore first the cavity flow dynamics must be examined and the active flow control technique, ns-DBD plasma actuators in this case, demonstrated. This paper presents initial work on the baseline facility flow and the impact that the addition of a cavity will have on it.

The numerical results presented illustrate that the tunnel and cavity model design performs as expected and that the cavity geometry has little impact on the facility flow field as a whole. The experimental work to follow will validate this study and examine the cavity flow field and its control.

1 Introduction

Supersonic/hypersonic flight is currently a highly discussed area of research. One of the key factors limiting current flight speeds is the propulsion system. One promising technology is the ramjet/scramjet type of propulsion system. These

A. Russell (✉) · H. Zare-Behtash · K. Kontis
School of Engineering, University of Glasgow, Glasgow, UK
e-mail: a.russell.2@research.gla.ac.uk

A. Sasoh et al. (eds.), *31st International Symposium on Shock Waves 2*,
https://doi.org/10.1007/978-3-319-91017-8_97

remove the need for a typical compressor in propulsion system and instead use ram air force to compress air before reaching the combustion chamber. There are currently a number of issues surrounding the operation of a ramjet/scramjet. One such issue that this research is interested in tackling is unstart; this can occur when a sudden pressure increase occurs at the combustion chamber. If this pressure increase is large enough, the internal shock structure can be forced upstream out of the inlet. This results in all of the supersonic compression occurring instantaneously, upstream of the inlet. In comparison to the efficient normal working mode, this compression is extremely inefficient and results in a massive loss in pressure recovery. This therefore results in a large inlet pressure drop and thus overall engine thrust [1].

Clearly it is desirable to avoid engine unstart. The area of the propulsion system where it may be possible to prevent/delay this phenomenon is called the isolator, generally a short duct located upstream of the combustion chamber. The isolator houses the flow features responsible for compression within the ramjet/scramjet known as a shock train. The shock train is a series of oblique/normal shock waves resulting from the boundary layer separation upstream of the combustion chamber [2]. It is this shock train that can be forced upstream of the inlet as a result of, for example, a pressure increase in the combustion chamber. It is thought that one method of delaying unstart is to use a cavity housed in the wall of the isolator to "trap" the shock train [3]. The issue with including a cavity in the isolator is the drag rise associated with it. To avoid this drag rise, active flow control must be employed in order to minimise the shear layer deflection into the cavity, reducing the drag increase, until the cavity is required to delay unstart. At this point the flow control is turned off, and the shear layer is allowed to deflect into the cavity.

However before active flow control can be implemented, the cavity itself must be examined and the frequencies at which it resonates at measured. This is what will be covered by the current numerical research and the experimental research to follow.

Cavity flows have been a popular research topic for decades due to their prominence in various applications. They are generally split into three categories: closed, transitional and open. The latter is the category that this research is interested in. Open cavities display resonance in primarily the longitudinal direction, oscillating at frequencies that are often known as Rossiter modes [4]. This longitudinal resonance is a result of a feedback loop driven by acoustic waves, generated as the cavity shear layer impinges on the trailing edge, propagating upstream within the cavity and perturbing the shear layer. These perturbations grow as a result of the Kelvin-Helmholtz instability and entrain fluid within in the cavity up into the shear layer, resulting in a pressure drop within the cavity itself [5]. This results in the shear layer deflecting down into the cavity (it is this deflection into the cavity that may explain why a cavity can "trap" a shock train formation). The resonant frequency of these oscillations depends on a number of factors and can be predicted to a good degree of accuracy through the empirical formula defined by Rossiter [4] and later modified to better match supersonic flows by Heller et al. [6]. Equation (1) is the modified version of the Rossiter equation:

$$Sr_m = \frac{f_m L}{U_\infty} = \frac{m - a}{\frac{M_\infty}{\sqrt{1+\left[\frac{(\gamma-1)M_\infty^2}{2}\right]}} + \frac{1}{k_c}} \tag{1}$$

where f_m is the oscillation frequency, L is the cavity length, U_∞ is the free stream velocity, m is the mode number, a is a phase difference between vortex and related acoustic wave location, M_∞ is the free stream Mach number and k_c is the vortex convection speed relative to the free stream.

For cavity control these predicted frequencies are key as they determine what frequency the active flow control should be applied at. If the cavity is weakly resonating, then it is suggested that active flow control can be used to enhance the resonance when desired by being applied at the frequency of the dominant Rossiter mode. If the cavity is strongly resonating, then it is suggested that the active flow control should be applied at some frequency between two Rossiter modes to weaken the cavity resonance.

However first the Rossiter modes of the cavity have to be determined numerically (CFD) and/or experimentally as the modified Rossiter equation is not completely accurate. The reason for the inaccuracy is that a and k_c are empirical values. It has been shown that values of k_c can range anywhere from 0.5 to 0.75 between Mach numbers 0.4 and 2.5 [7]. a is often taken to be 0.25 but is also subject to variation depending on test conditions. This paper will examine numerical simulations of two model test cases and discuss future experimental work to compare predicted and actual Rossiter mode frequencies and also control the cavity flow using ns-DBD plasma actuators.

2 Model Setup

There are two related parts to this study: the baseline wind tunnel and the wind tunnel with the cavity installed. It is an in-draft supersonic wind tunnel facility designed to operate at, for the current configuration, Mach 2. The test section is a straight rectangular duct 0.7 m in length with a cross section of 101.6 × 54 mm.

The second, more interesting test case is the tunnel with the inclusion of the cavity model. The cavities examined had a length to depth ratio (L/D) of 6, 7 and 8. These values should result in an open cavity based on previous research [8]. This is imperative as open cavities exhibit Rossiter mode resonance. It is this resonance that is hoped can be controlled by active flow control for application to ramjet/scramjet isolators. The physical dimensions of the cavity were driven by the predicted Rossiter mode frequencies. Future work will examine active flow control of the cavity using nanosecond dielectric barrier discharge (ns-DBD) plasma actuators. The generator that drives these actuators has a maximum frequency of 3 kHz; therefore the cavity dimensions were chosen so that the first four predicted Rossiter modes had frequencies equal to or lower than this value. The result was that

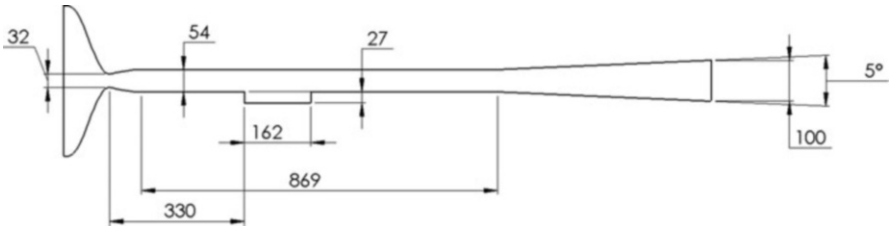

Fig. 1 Schematic diagram of in-draft wind tunnel facility (in mm)

the cavity depth is 27 mm (0.5H where H is the test section height) and cavity length is 162, 189 and 216 mm for L/D of 6, 7 and 8, respectively. For future applications to shock "trapping," it was thought sensible to locate the cavity at a location upstream of the shock train formation. Therefore the cavity is located at the furthest upstream position within the test section that is still optically accessible, 330 mm downstream of the nozzle throat. A schematic of the in-draft facility is shown in Fig. 1, with a cavity (L/D = 6) included.

3 Numerical Modelling Approach

The numerical modelling of the aforementioned test cases was carried out using STAR-CCM+. Two-dimensional simulations were conducted since for both test cases, the important flow features of interest are 2D in nature in this case.

The Reynolds-averaged Navier-Stokes (RANS) equations are solved using a coupled implicit finite volume approach. The computations are 2nd order accurate in time and space. The two-equation k-ω Wilcox turbulence model was used to solve the RANS closure problem. This model solves for turbulent kinetic energy, k, and specific dissipation rate, ω. This specific turbulence model was chosen as it has been previously suggested that it deals well with adverse pressure gradients [9]. While not overly important for this study, later work related to this will involve strong adverse pressure gradients. Therefore it was sensible to use a turbulence model that could be used for later work allowing the separate studies to be related to one another. The fluid is modelled as an ideal gas and uses Sutherland's law for viscosity calculations.

The simulation geometry is as shown in the schematic in Fig. 1 (for the baseline case, there is no cavity, but the tunnel geometry remains unchanged). The domain is discretised using a polyhedral mesh. This may be seen as unusual for a flow that is principally axial in direction as it would be commonplace to use a structured mesh aligned with the principal flow direction. The reason behind the use of the unstructured polyhedral mesh was computational power. When meshing for a 2D simulation in STAR-CCM+, there are two options: 2D meshing and 3D meshing followed by a 3D to 2D conversion. The problem being that there is no option to use a structured mesh when using 2D meshing. The issue with meshing first in 3D

and then converting to 2D is that the computational power available limited the maximum cell number that could be created. 2D meshing provides the opportunity to achieve that maximum cell number in the final mesh. However when converting a 3D mesh to a 2D mesh, the largest final 2D mesh is significantly smaller due to the limitation of having to create a 3D mesh first which is always considerably larger than the associated 2D mesh. Therefore with the available computational power, a finer unstructured polyhedral mesh was achievable in comparison to a structured mesh. The base size of the polyhedral mesh was chosen based on a mesh independency study. This independency was determined based on examination of two relevant physical quantities: nozzle exit Mach number and diffuser exit Mach number. This study resulted in a base size for the polyhedral mesh of 0.0037 m.

The flow physics setup of the problem is very straightforward. The inlet is set as a stagnation inlet with atmospheric pressure as the total pressure. The outlet is a pressure outlet with pressure set to vacuum pressure. The wind tunnel walls are no slip, adiabatic walls. The baseline test facility is started with ambient initial conditions, while the cavity model case is started with the initial conditions as the final result of the baseline test facility.

4 Overview of Experimental Setup

4.1 Facility

As touched on previously, the facility is an in-draft wind tunnel. It is driven by a 34 m^3 vacuum tank that is evacuated by a Busch R5-400 vacuum pump. The tank is connected through a series of pipework to a 100-mm-diameter spring-driven, fast-response ball valve. The baseline test section is made from aluminium with the central 560 mm of the test section having full optical access from the side and two separate regions of optical access 61.6 $\times$ 228.4 mm above the test section. The replacement test section floor that houses the cavity geometry and the converging-diverging nozzle was manufactured from polyurethane modelling board. The nozzle is designed to accelerate the stagnant upstream air to Mach 2 in the test section.

4.2 Experimental Model

There are two models for this study: the baseline tunnel (touched upon briefly as the tunnel has never been used prior to this study) and the cavity model. The baseline tunnel is simply a straight rectangular duct. The cavity model replaces the floor of the test section with two parts designed to house a cavity of various dimensions. The cavity itself fits inside the two sections that make up the tunnel floor. This modular design of the cavity model allows for multiple cavity sizes and geometries to be examined simply and inexpensively.

4.3 Experimental Campaign

The experimental campaign is currently in the process of being carried out. There are three stages to the experimental campaign: baseline test facility characterisation, uncontrolled cavity model characterisation and examination of effect of ns-DBD plasma actuator control on cavity flow. These test cases will be examined using Schlieren, pressure measurements and particle image velocimetry (both streamwise and spanwise). The overall aim being to determine how ns-DBD plasma actuators can control a supersonic cavity flow.

5 Numerical Results

The results presented are numerical results of the baseline test facility and the cavity model. Figure 2 shows the Mach number contour for the baseline test facility. Figure 3 shows the Mach number contour for the cavity model in the test facility after the solution has reached a steady solution (not accounting for shear layer fluctuations). At the entrance to the constant-area test section, both exhibit a centreline Mach number of approximately 2 as expected with the nozzle design. At the diffuser both are expected to remain supersonic as there is no converging section. The slightly lower speeds observed in the cavity case is sensible due to the thicker boundary layer downstream. This will result in a smaller "core" flow area, decelerating the flow to a slower speed before it reaches the diffuser. Figure 3 also illustrates that the cavity is an open cavity with the current flow conditions. This is clear as the cavity shear layer reattaches to the trailing edge of the cavity instead of the floor of the cavity as is the case in a closed cavity flow. It is important for the future experimental study that the cavity design was open so that the longitudinal resonance mode was present. This will enable the cavity to be actively controlled by ns-DBD plasma actuators. Figure 4 illustrates the expected leading edge and trailing edge shocks that should be present in an open cavity flow confirming the statement made previously.

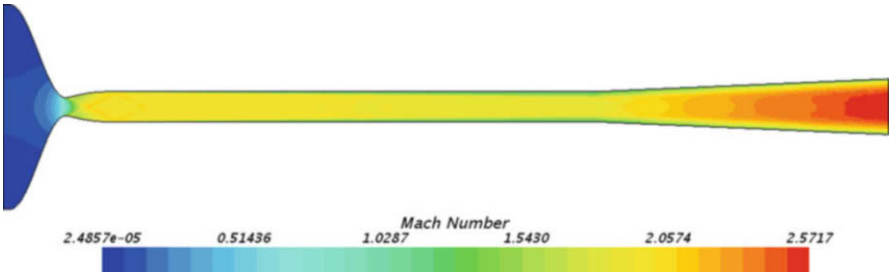

Fig. 2 Mach number contour of baseline facility test case

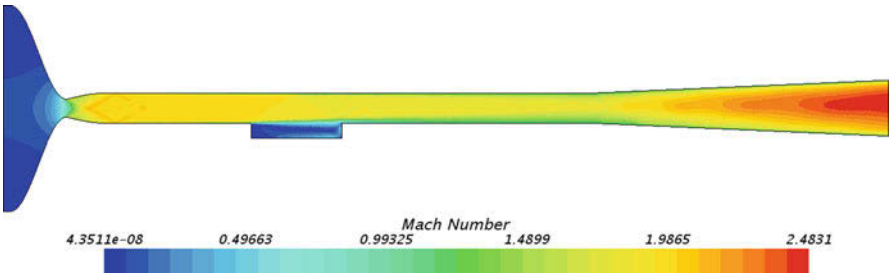

Fig. 3 Mach number contour of cavity model test case

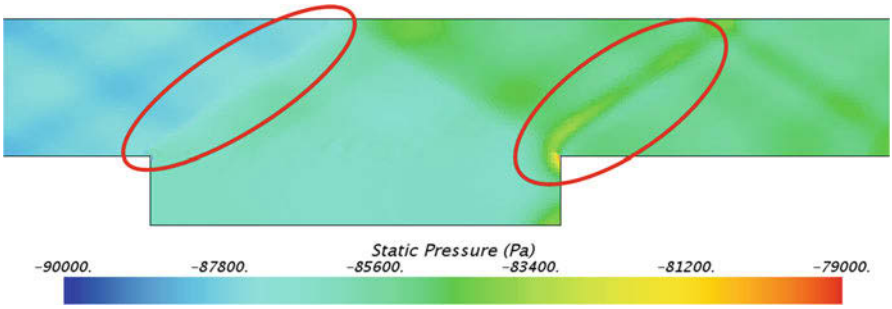

Fig. 4 Gauge static pressure (relative to atmosphere) in vicinity of cavity model (red rings indicate shock waves expected in a typical open supersonic cavity flow)

6 Conclusion

The results presented in this study show the predicted flow field through the baseline test facility alongside the model geometry of interest, cavity with an L/D = 6. These show that the flow field is as expected following the design of the test facility and the introduction of the cavity. The particular results presented are shown in order to provide some confidence that the numerical solutions are sensible results for the cases examined.

The current/future work is to experimentally examine the same flow fields and provide validation for these simulation results. The experimental work will provide insight into the Rossiter modes of the cavity geometry and also examine the effect of active flow control applied to the cavity geometry.

References

1. M.A. Bolender, H. Wilkin, Flight dynamics of a hypersonic vehicle during inlet unstart, in *16th AIAA International Space Planes and Hypersonic Systems and Technologies Conference*, 2009
2. F. Gnani, H. Zare-Behtash, K. Kontis, Pseudo-shock waves and their interactions in high-speed intakes. Prog. Aerosp. Sci. **82**, 36–56 (2016)

3. N.Webb, M.Samimy, Shock-trapping capability of a cavity in supersonic flow, in *46th AIAA Plasmadynamics and Lasers Conference*, 2015
4. J.E. Rossiter, *Wind-tunnel experiments on the flow over rectangular cavities at subsonic and transonic speeds*, Aeronautical Research Council Reports and Memoranda. 3438, (1964)
5. N. Zhuang, F.S. Alvi, M.B. Alkislar, C. Shih, *Supersonic Cavity Flows and Their Control*. AIAA J. **44**(9), 2118–2128 (2006)
6. H.H. Heller, D.G. Holmes, E.E. Covert, Flow-induced pressure oscillations in shallow cavities. J. Sound Vib **18**(4), 545–553 (1971)
7. O.H. Unalmis, N.T. Clemens, D.S. Dolling, Cavity oscillation mechanisms in high-speed flows. AIAA J **42**(10), 2035–2041 (2004)
8. R.L. Stallings, F.J. Wilcox, *Experimental cavity pressure distributions at supersonic speeds*, NASA Technical Paper 2683, (1987)
9. STAR CCM, *STAR CCM User Guide v11.02*, (2017)

Experiments in Supersonic Gaseous Ejector Using 2D-PIV Technique

S. K. Karthick, Srisha M. V. Rao, Gopalan Jagadeesh, and K. P. J. Reddy

Abstract Supersonic gaseous ejector is practically a supersonic confined jet, where the primary supersonic jet flows through the confined passage and thereby entrains the secondary flow from the ambient. In this paper, the flow field of the supersonic gaseous ejector is investigated prominently using 2D-PIV measurement technique to study the mixing progression between the primary and the secondary flow at different operating conditions. A rectangular supersonic gaseous ejector (air-air) of low area ratio (AR = 3.7) is used in this study. Two separate supersonic primary flow nozzles of design, Mach number (M_{PD}) 2.0 and 2.5, are considered in this experimentation. Differences between the supersonic free jet and the supersonic ejector or confined jet on the aspects of flow mixing are brought out clearly regarding flow kinematics. Centerline velocity decay, vorticity field, and wall static pressure distribution are used in parallel to explain the mixing progression in the ejector. Influence of the nozzle operating conditions on the gaseous mixing process is found to be prominent. Even a moderately underexpanded primary jet in a low AR supersonic ejector is observed to mix faster due to larger vorticity generation and early interaction of the mixing layer with the confined passage.

1 Introduction

Supersonic gaseous ejector or supersonic confined jet [1–3] is a simple gas-dynamic device to entrain the secondary jet into the confined passage by the primary supersonic jet alone without any additional work. Applications of the supersonic gaseous ejector in aerospace industries are wide, ranging from high-altitude (HAT) testing facilities to thrust augmentations in propulsive devices. A supersonic confined jet experiences complex shock patterns, wall boundary layer interaction with developing mixing layer, and a rapid transport of mass, momentum, and energy with the secondary flow. Fundamentally, the mechanism of entrainment

S. K. Karthick (✉) · S. M. V. Rao · G. Jagadeesh · K. P. J. Reddy
Department of Aerospace Engineering, Indian Institute of Science, Bangalore, India

A. Sasoh et al. (eds.), *31st International Symposium on Shock Waves 2*,
https://doi.org/10.1007/978-3-319-91017-8_98

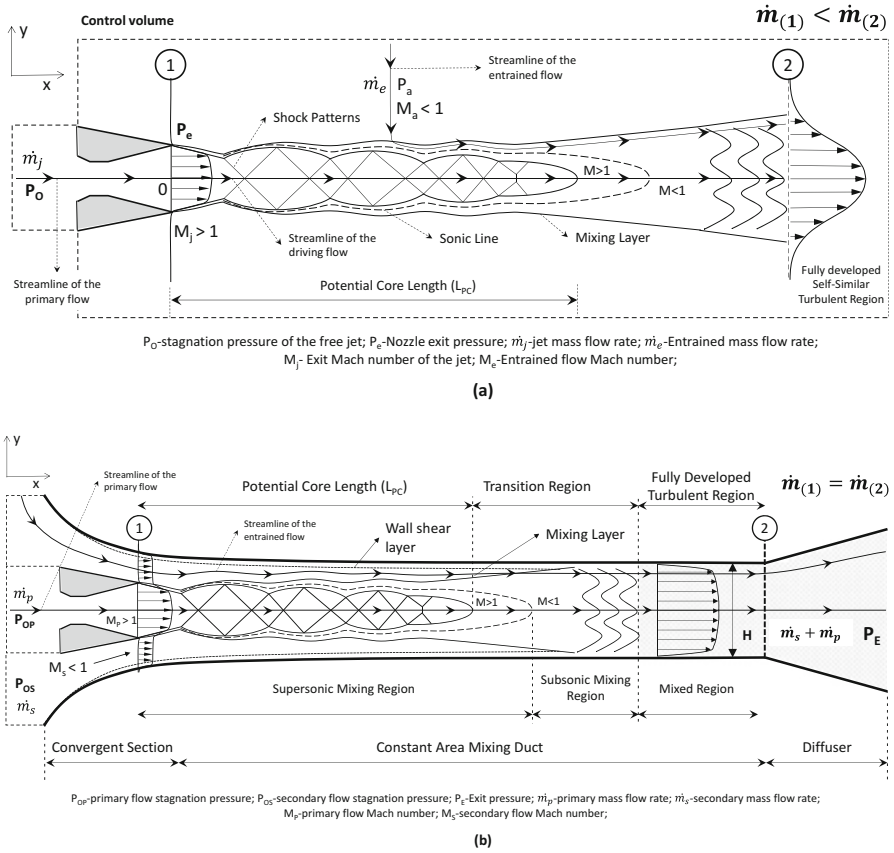

Fig. 1 Schematic describing the flow kinematics encountered in a typical (**a**) supersonic free jet and (**b**) supersonic ejector or supersonic confined jet

and mixing of secondary flows needs to be understood which is not clearly discussed in the earlier literature. Previous studies [4] have used equal measures to study flow mixing like the non-mixed length (L_{NM}) and potential core length of the primary flow (L_{PC}), from planar laser Mie scattering (PLMS) images [5] to infer regarding the mixing processes within the ejector. Quantitative velocity measurements have been difficult owing to the confined nature of the flow. Considering that momentum mixing is the predominant phenomenon in the cases considered here, velocity field measurements are crucial to comment on the flow physics, in particular on the mixing progression. Thus, the use of nonintrusive optical flow diagnosis like two-dimensional planar image velocimetry (2D-PIV) technique becomes imperative. In this study, the mixing progression encountered in the supersonic gaseous ejector is studied prominently using 2D-PIV. The flow kinematics leading to fluid mixing in the supersonic free jet and the supersonic ejector or confined jet is shown clearly in Fig. 1.

2 Experimental Techniques

Experiments are carried out in the supersonic rectangular gaseous ejector, established in LHSR, IISc – Bangalore [6]. More details regarding the specifications and the flow passage dimensions can be found in the previous work of the authors [4]. The exit of the supersonic nozzle is kept at 15 mm ahead of the constant-area mixing duct. The primary flow is supersonic, and the secondary flow is subsonic. Air is used as the working fluid in both flows. The layout of the experimental facility can be seen in Fig. 2.

2.1 Wall Static Pressure Measurement

Wall static pressure measurements are carried out to access the gross flow physics inside the supersonic ejector. Piezo-resistive type pressure sensors (Freescale Semiconductors, MPX 5700 ASX) are used to measure the wall static pressure (P/P_a) distribution. Details regarding the spatial locations of the sensors on the top wall of the supersonic ejector can be found in the previous work of the authors [4]. A typical distribution of [P/P_a] measured in the supersonic ejector can be seen in Fig. 5. The uncertainty in the [P/P_a] measurements is found to be ±5% from the measured values.

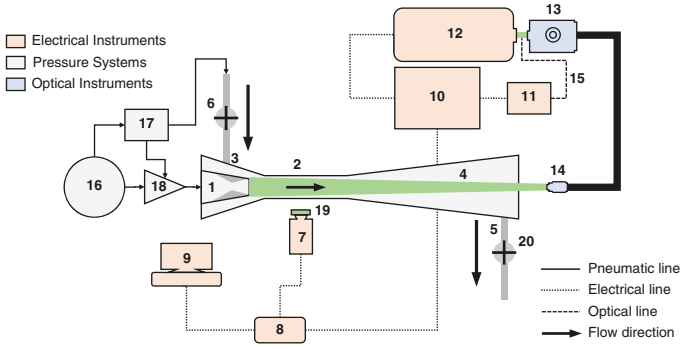

1.Primary super sonic flow nozzle (C-D); 2. Constant area mixing duct; 3. Convergent section; 4. Diffuser; 5. Mixed flow exhaust;
6. Entrained flow entry; 7. Phantom Miro 110 PIV camera; 8. High speed controller; 9. High performance computer; 10. Laser controller/Chiller;
11. Laser time stabilizer; 12. Dual Cavity, Litron: Nd-YLF laser (537nm); 13. Laser guiding arm; 14. Sheet making optics;15. Optic fiber;
16. High pressure air storage tanks; 17. Particle seeding unit; 18. Primary flow stagnation chamber; 19. 527 nm band pass filter; 20. Ball valve

Fig. 2 Schematic of the 2D-PIV arrangement for the supersonic ejector studies

2.2 Two-Dimensional Particle Image Velocimetry (2D-PIV)

Using the dual-cavity Nd-YLF laser (527 nm, 24 mJ per pulse at 1 kHz, 190 ns pulse width), 2D-PIV experiments are carried out in a plane along the flow direction by seeding both flows with the refined sunflower oil particles (particle size, 0.6–1.2 μm; response time, 0.8–3.0 μs). Phantom Miro 110 camera (1280 × 800 pixels, 20 μm pixel width) is used to capture the scattered light from the particles, and it is operated in the PIV straddle mode with the minimum "dt" (inter-frame time) of 0.7 μs. A laser time stabilizer unit is used to ensure the time difference between the pair of laser pulses, consistently at 0.7 μs. Nikon AF-S DX Micro 40 mm prime lens is used at f/2.8 to capture the small flow passage with better spatial resolution in the camera. The investigation area of the considered flow field is about 50 mm × 30 mm with the spatial resolution of about 0.05 mm/pixel. A 527 nm band-pass filter is used to remove the background light and parasite reflections from the laser. Particles are introduced into the stagnation chamber of the primary flow with an overpressure of 2 bar to seed the primary flow. However, the secondary flow is seeded under ambient conditions only. An in-house particle-seeded unit is used in this process. Characteristics of the generated particles and the particle production methodology can be found in the previous work of Karthick et al. [7]. DaVis 8.3 software is used as the interfacing system. An adaptive cross-correlation algorithm with the decreasing window size (from 64 × 64 pixels to 32 × 32 pixels) is employed. Nearly, 800 image pairs are captured per second, and they are used to represent the time-averaged flow field. The maximum uncertainty encountered in the 2D velocity field of the considered experiments is not larger than ±3%, which includes the uncertainty arising from particle seeding and the computation of velocity vectors. The arrangement of the 2D-PIV technique for the supersonic ejector studies is shown clearly in Fig. 2.

3 Results and Discussions

The experimental observations are represented in the form of non-dimensionalized parameters like SPR (stagnation pressure ratio [P_{OP}/P_{OS}]), ER or ω (entrainment ratio [$\dot{m}_s/\dot{m}_p$]), fully expanded jet Mach number [M_{PJ}], and Mach number ratio [M_{PD}/M_{PJ}]. Details regarding the nomenclature and the derivations can be found in the previous work of the authors [4]. Throughout the discussions, experiments are carried out at M_{PD} 2.0 and 2.5. The corresponding experimental conditions can be found in Table 1.

Table 1 Experimental conditions observed in the supersonic gaseous ejector

M_{PD}	P_{OP} (bar)	NPR	SPR	ER or ω	M_{PJ}	M_{PD}/M_{PJ}
2.0	5.89	7.480	7.019	0.455	2.001	1.000 (PE)
	6.89	8.601	8.209	0.359	2.088	0.958 (UE)
	7.89	9.673	9.202	0.306	2.157	0.927 (UE)
2.5	7.89	10.321	9.357	0.535	2.211	1.131 (OE)

M_{PD} design Mach number of the primary nozzle; P_{OP} total pressure of the primary flow; *NPR* nozzle pressure ratio; *SPR* stagnation pressure ratio; *ER* or ω entrainment ratio; M_{PJ} fully expanded jet Mach number of the primary nozzle; M_{PD}/M_{PJ} Mach number ratio; *PE* perfectly expanded; *UE* underexpanded; *OE* Overexpanded

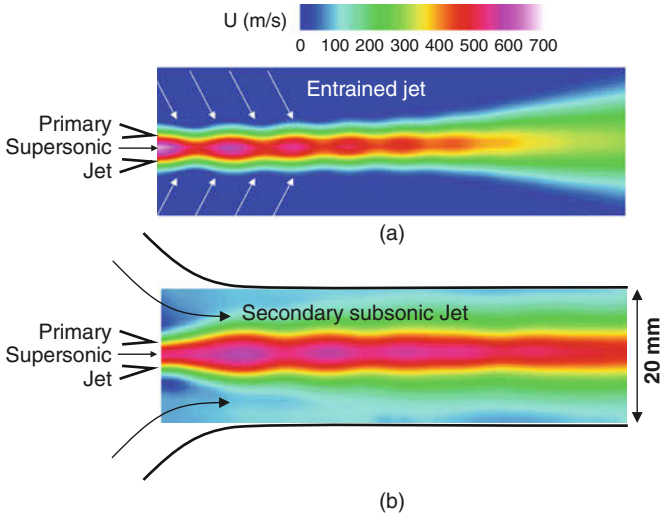

Fig. 3 Typical time-averaged 2D-PIV image acquired for (**a**) supersonic free jet and (**b**) supersonic ejector or supersonic confined jet. Conditions: $M_{PD} = 2.0$; P_O=$P_{OP} = 7.89$ bar; SPR = 9.202; ω = 0.306

3.1 Time-Averaged 2D Velocity Field

The typical time-averaged 2D velocity field is shown in Fig. 3 for the supersonic free jet (Fig. 3a) and the supersonic ejector or the supersonic confined jet (Fig. 3b). In Fig. 3a, the supersonic free jet is expanded into the ambient conditions ($P_a = 0.89$ bar). As the total pressure (P_O) is only 7.89 bar, the supersonic C-D (convergent-divergent) nozzle, whose M_{PD} is 2.0, will be OE. Because of the low M_{PJ}, the jet is thin, and the potential core (L_{PC}) terminates early. Till the location of L_{PC}, the mixing layer (marked in green contour) can be seen thin. Downstream the L_{PC}, one can see the rapid growth in the mixing layer, as the flow enters the fully developed turbulent jet regime. Also, from the figure, it is evident that the streamline dives into the flow as described in Fig. 1a. By looking at Fig. 3b, the

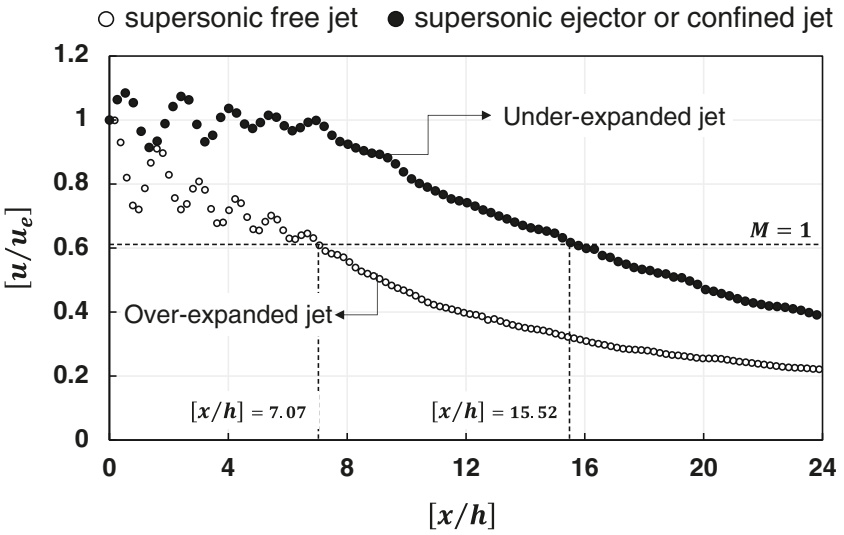

Fig. 4 Graphical representation of the normalized centerline velocity decay observed in the supersonic free jet (circles, outline) and the supersonic confined jet (circles, filled). Conditions: $M_{PD} = 2.0$; P_O=$P_{OP} = 6.89$ bar; SPR = 8.209; $\omega = 0.359$

supersonic jet in the confined passage, for the similar P_{OP}, expands rapidly up to a velocity of 600 m/s. From the $[P/P_a]$ measurements, the NPR can be calculated as 9.73, which suggests that the nozzle is UE. The local pressure drop created by the high-speed primary jet flowing through the confined passage creates a huge drop in static pressure. It in turn makes the supersonic jet to expand more. The growing mixing layer further entrains fluid from the ambient. The entrained flow runs in parallel with the primary jet. The parallel running streamlines of the primary and the secondary flow as depicted in Fig. 1b lead to the production of lower convective Mach number (M_C) in the mixing layer, which leads to the elongation of the sonic line (M = 1).

3.2 Centerline Velocity Decay

Typical variation of the normalized centerline velocity decay for both the supersonic free jet and the supersonic ejector is shown in Fig. 4. From the figure, it can be clearly seen that the supersonic ejector flow is UE and the supersonic free jet is OE. Also, the rapidly decaying OE field is clearly marked by the centerline velocity variations. On the other hand, in the supersonic ejector, due to the low static pressure environment, the jet underexpands, leading to a rise in the centerline velocity. Added to that, the decay rate of the primary jet is almost zero till the L_{PC} of the primary jet. After that, as the primary and the secondary flow lose their distinct characteristics, the flow mixes, and the mixed flow enters into the fully developed turbulent regime.

In this process, the decay in the centerline velocity is almost linear. Figure 4 also sheds details regarding the extent of the sonic line in the flow field. For the free jets, the sonic line lies at [x/h] of 7.07, whereas in the case of the supersonic ejector, it is found to be at [x/h] of 15.52. As described in earlier discussions, this two times difference between the occurrence of the sonic line in the free jet and the ejector is primarily due to the confined passage. This extension of sonic line contributes predominantly to the differences observed between the supersonic free jet and ejector.

3.3 Mixing Progression in Supersonic Ejector

The progression ofmixing in the supersonic ejector can be studied to a certain extent by corroborating the [P/P_a] distribution and the centerline velocity decay. A typical variation in the normalized centerline velocity decay and the normalized [P/P_a] distribution is shown in Fig. 5. From Fig. 5, it can be seen evidently that the spatial resolution of the [P/P_a] distribution is poor compared with the velocity distribution. The larger form factor of the pressure sensors is the major reason. The bumps in the velocity distribution correspond to the location of the middle portion of the shock cell, which is thick, and the trenches correspond to the thinning region of the shock cell. Because of this curvy external profile of the shock cell, the secondary flow faces a constricted flow passage, where the secondary flow accelerates, leading to the observation of lower [P/P_a]. It can be clearly seen in Fig. 5, where the first point

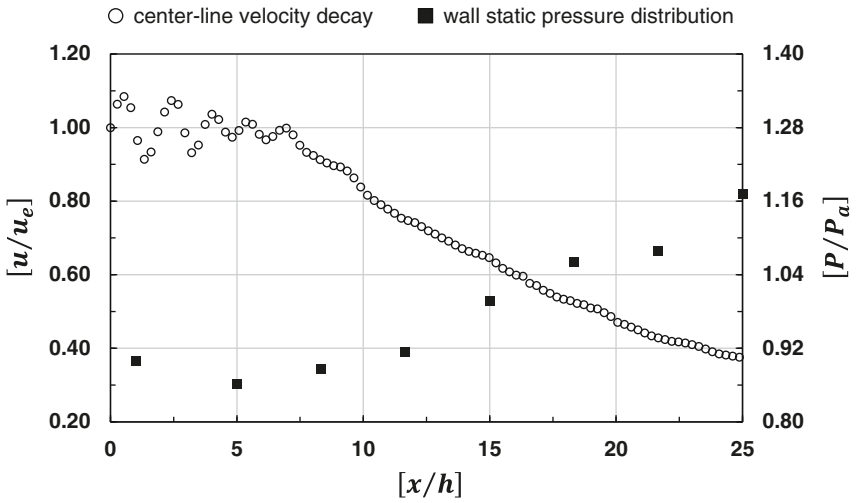

Fig. 5 Graphical representation of the normalized centerline velocity decay (circles, outline) and the normalized wall static pressure distribution (square, filled). Conditions: $M_{PD} = 2.0$; $P_O = P_{OP} = 6.89$ bar; SPR = 8.209; $\omega = 0.359$

in the [P/P_a] measurement is observed to be lesser than the atmospheric pressure. As the mixing layer progresses, it entrains more fluid into it and offers further smaller passage to the secondary flow. The persistent second shock cell of similar strength is indeed evident in Fig. 5, where the minimum [P/P_a] is encountered. Further downstream, as both flows start to mix rapidly, [P/P_a] increases gradually. In the same region, the centerline velocity profile is also observed to be decaying linearly, indicating gaseous mixing.

3.4 Vorticity Field

The effect ofprimary flow Mach number or the primary flow nozzle operating conditions can be easily understood by looking into the vorticity field of the supersonic gaseous ejector through 2D-PIV measurements. A typically normalized vorticity field observed in two different primary nozzles (M_{PD} = 2.0 and 2.5) for similar conditions (SPR ≈ 9) is shown in Fig. 6. The higher velocity observed in

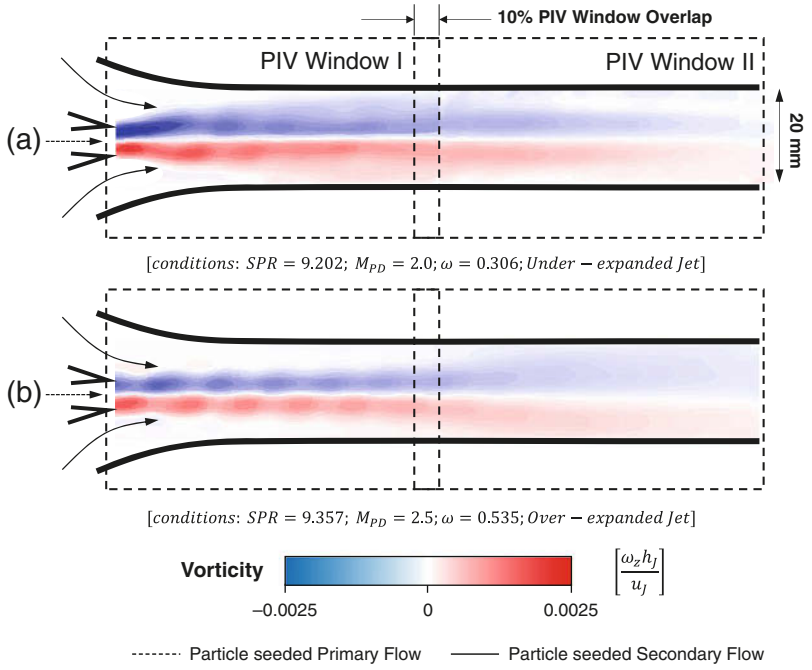

Fig. 6 Non-dimensionalized time-averaged vorticity contours for different flow conditions observed through 2D planar PIV experiments. (**a**) UE supersonic primary jet (conditions: SPR = 9.202, M_{PD} = 2.0, ω = 0.306) (**b**) OE supersonic primary jet (conditions: SPR = 9.357, M_{PD} = 2.5, ω = 0.535). Planar field data taken at two different locations are stitched together with an overlap of 10% to represent larger spatial field variations

the UE primary flow (Fig. 6a) leads to the production of vorticity of larger strength compared with the lower velocity field seen in the OE primary flow (Fig. 6b). The large vorticity generation and the larger effective jet width (h_J) – almost in the order of the mixing duct height (H) – lead to an earlier gaseous mixing in the UE flow field. Earlier experiments of the authors [4, 8, 9] also confirm this argument through the non-mixed length (L_{NM}) observations using the PLMS technique. Also, on looking at the ER or ω of the UE flow, it is observed to be lower than that of the OE flow. This in turn attributes to the observation of lower vorticity in the OE flow field.

4 Conclusions

Progression of mixing in the supersonic gaseous ejector is explained in detail in terms of flow kinematics using the 2D-PIV technique. The differences between the supersonic free jet and the confined jet have been brought out in detail. The nozzle operating conditions are found to be important in the gaseous mixing process of the supersonic ejector. Severely UE flows are observed to produce large vorticity leading to better mixing, however, with the lower entrainment of the secondary flow.

Acknowledgment Ministry of Human Resource Development (MHRD), India; Defence Research and Development Organization (DRDO), India; and Council for Scientific and Industrial Research (CSIR), India

References

1. W.L. Chow, A.L. Addy, AIAA J. **2**, 4 (1964)
2. K. Matsuo et al., B. JSME **29**, 256 (1986)
3. D. Papamoschou, J. Propuls. Power **12**, 4 (1996)
4. S.K. Karthick et al., Phys. Fluids **28**, 7 (2016)
5. S.K. Karthick et al., PSFVIP-10, Naples, Italy, 8 (2015)
6. S.M.V. Rao, Ph.D. Thesis, IISc, Bangalore, India (2013)
7. S.K. Karthick et al., J. Indian Inst. Sci. **96**, 1 (2016)
8. S.K. Karthick et al., ISSW-30, Tel-Aviv, Israel, 6 (2015)
9. S.M.V. Rao, G. Jagadeesh, Phys. Fluids **26**, 3 (2014)

Numerical Analysis of Surface Heat Flux in a Forward-Facing Cavity

B. Sudarshan and S. Saravanan

Abstract Passive, semi-passive and active techniques are in active research to tackle the range of heat loads encountered by the hypersonic vehicles. The forward-facing cavity is one of the effective passive techniques explored for hypersonic short-duration vehicles in low-altitude atmospheric conditions. Studies show that the shape of the cavity plays a major role in reducing surface heat flux of the vehicle. To understand comprehensively the surface heat flux characteristics, we have considered the important cavity geometrical parameter, cavity length (L)/cavity diameter (D) ratio, from 0.5 to 5 and compared with and without cavity conditions. The transient simulation results showed that around 10–28% of heat flux reduced over the outer body surface. The variation of pressure and temperature at the cavity base and along the cavity wall for different L/Ds is also discussed.

1 Introduction

The hypersonic projectile configuration is particularly discussed herein. These projectiles propel at low altitudes; efficient passive thermal protection system should be designed with decreased aerothermal loads on the nose cone of the vehicle. In the flight regime 2–4 km/sec, the projectile nose tip experiences severe heat rates, and shape change due to ablation can occur. Consequently, to extend the flight regime above 2 km/s, there is a need to develop active or passive techniques to reduce tip heating rates.

With the motivation of understanding the forward-facing cavity passive technique and its heat flux characteristics, the current numerical study has been carried

B. Sudarshan (✉)
Department of Aerospace Engineering, Indian Institute of Science, Bangalore, KA, India

B.M.S. College of Engineering, Bangalore, KA, India

S. Saravanan
Department of Aerospace Engineering, Indian Institute of Science, Bangalore, KA, India

A. Sasoh et al. (eds.), *31st International Symposium on Shock Waves 2*,
https://doi.org/10.1007/978-3-319-91017-8_99

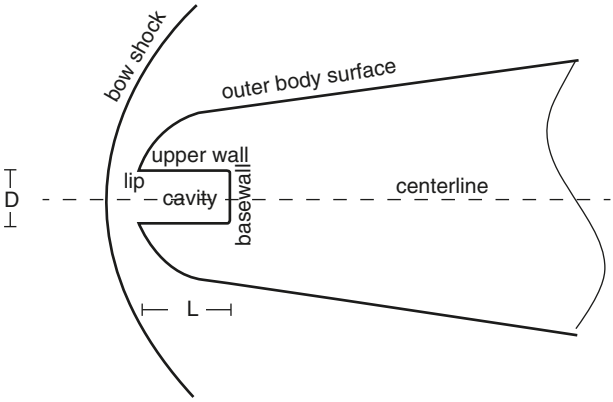

Fig. 1 Schematic of the geometry

Table 1 Different geometries

Sl No	D (in mm)	L (in mm)	R (in mm)	L/D	Sl no	D (in mm)	L (in mm)	R (in mm)	L/D
1	12	6	30	0.5	5	12	48	30	4
2	12	12	30	1	6	12	60	30	5
3	12	24	30	2	7	12	24	15	2
4	12	36	30	3	8	18	72	4	4

out. The schematics of the geometry and different geometries considered for the analysis are shown in Fig. 1 and Table 1, respectively.

1.1 Background and Brief Review

A deep forward-facing rectangular or cylindrical cavity in hypersonic flow acts like an organ pipe, and the flow oscillation of the stagnant cavity fluid causes the oscillation of the bow shock wave, which in turn produces the cooling effect. Sambamurthi et al. [1] and Heubner and Utreja [2] studied the oscillation of the bow shock and the corresponding heat transfer rates for blunt cones with cylindrical cavities at Mach 10. It was found that the bow shock oscillates at the natural frequency of the cavity and there is a significant reduction in stagnation-point heat transfer rates. Silton and Goldstein [3] found that for sufficiently deep cavities, the local heat fluxes were reduced over the surface when the strong longitudinal pressure oscillations are induced leading to large bow shock oscillations. Engblom et al. [4] investigated the surface heating rates of a blunt body with medium depth cavity cases (L/D = 0.75) and deep cavity cases (L/D = 2) by numerical code and compared with infrared camera results. Saravanan et al. [5] observed a reduction of 35 to 40% in surface convective heat transfer rates for a missile-shaped body at a free stream Mach number of 8. Lu and Liu [6] showed numerically that the deeper

the cavity, the smaller the heat flux and the mean heat flux increases along the body surface to reach a peak value near the sharp edge and then falls sharply.

Most of the investigations are focussed over the outer body surface, and studies related to the inside of the cavity are very few in literature. In this background, the objective of the present study is to determine the surface heat flux characteristics influenced by L/Ds for a spherical nosed body with cylindrical cavity including the pressure, temperature and heat flux variations inside the cavity.

2 Methodology

2.1 Computer Code Description

This paper presents results from a numerical study using the commercial code FLUENT 15.0 version. Unsteady analysis done using the 'pressure-based' solvers, 2D double precision with axisymmetric conditions, is applied to capture the strong shocks to represent the actual configuration. 'Coupled' pressure-velocity coupling scheme, 'Least Squares Cell-Based' spatial discretisation with 'Second-Order Upwind Scheme' for pressure, density, momentum and energy, has been used. For transient formulation 'Second-Order Implicit' technique has been used.

2.2 Numerical Assumptions

The free stream conditions and stagnation conditions considered for the analysis are shown in Table 2. The flow is assumed axisymmetric because pressure oscillations at the cavity base in experiments are typically planar. Flow is assumed laminar because of the small scale of the flow field (i.e. nose region). Since the characteristic flow lengths are smaller and a favourable pressure gradient is present, transition is not expected to occur within the cavity unless the oscillations within the cavity cause the flow to trip. An isothermal wall constraint ($T_{wall} = 300K$) is used when surface heat rates are of interest. The minimum and maximum flow temperatures in the simulations remain within 143 K and 1800 K. Hence the flow is assumed ideal gas.

Table 2 Free stream and stagnation conditions

Free stream conditions				Stagnation conditions	
Mach number	8	Re no/m	0.98×10^6	Pressure	1940 Pa
Pressure	205.2 Pa	Temperature	143 K	Temperature	1955.154 K

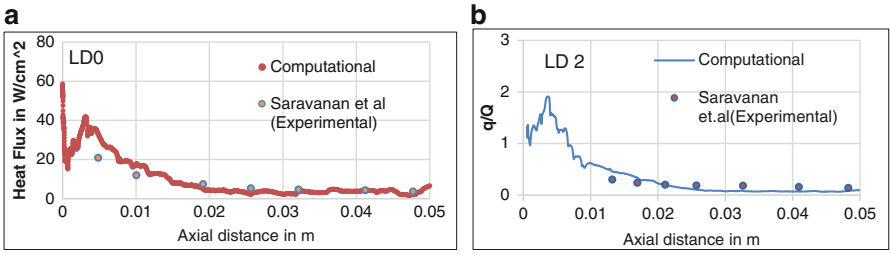

Fig. 2 (**a**) Validation for L/D 0 case, (**b**) validation for L/D 2 case

2.3 Numerical Procedure

Heat flux calculation for unsteady flow fields is obtained with a relatively finer grid of 0.05 mm cell thickness near the body surface. The cell thickness was determined from the literature. The time step of 1×10^{-8} second and 20 subiterations per time step has been taken for all the cases. The simulations are well converged with a residual ranges from 1×10^{-3} to 1×10^{-5}.

2.4 Grid Independency Study

The grid size of 289,874 elements with 288,040 nodes has been compared with the 347,056 elements and 345,030 nodes grid which is approximately 20% higher. The base pressure and temperature oscillations and the surface-averaged and point heat flux terms are compared. It's found that grid results are in good agreement.

2.5 Code Validation

The numerical results are compared with the literature experimental results for the same geometry and flow conditions. Figure 2a and b shows that the heat flux over the body surface numerical results is in good agreement and variations are within the allowable limits.

3 Results and Discussions

3.1 Cavity Base Pressure and Temperature Variations

Figure 3 shows for L/D = 0.5, base pressure values (in kPa) vary from minimum range of 7 kPa to 19 kPa to maximum range of 4 kPa to 28 kPa and cycle time nearly

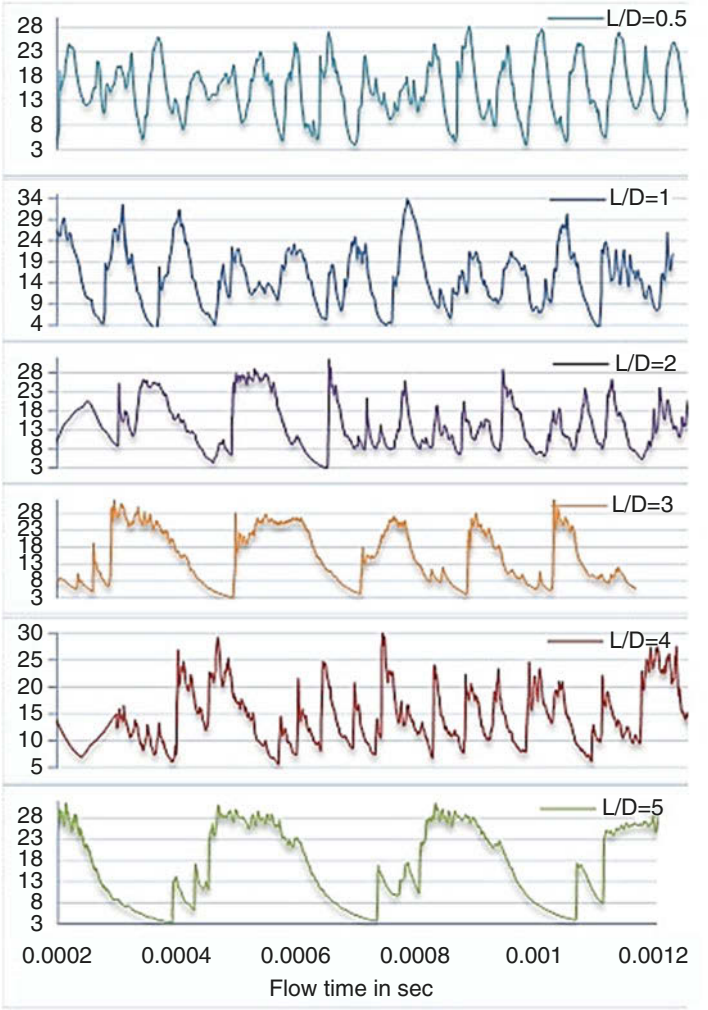

Fig. 3 Base pressure variations

equal to 50 μs. Similarly for L/D = 1, it varies from minimum range of 10 kPa to 22 kPa to maximum range of 4 kPa to 32 kPa, and cycle time will be 60 μs. In the order of pressure range of 5kpa to 30kpa, the cycle time for L/D = 2, 3, 4 and 5 increases roughly to 100 μs, 130 μs, 270 μs and 350 μs, respectively.

Using the theoretical formula, considering average shock standoff distance, shock oscillation frequency has been calculated and drawn with respect to L/D in Fig. 4. It shows that, as the L/D increases, the number of cycles decreases and therefore the frequency (f) of shock oscillations decreases. The curve matches with the open literature trend.

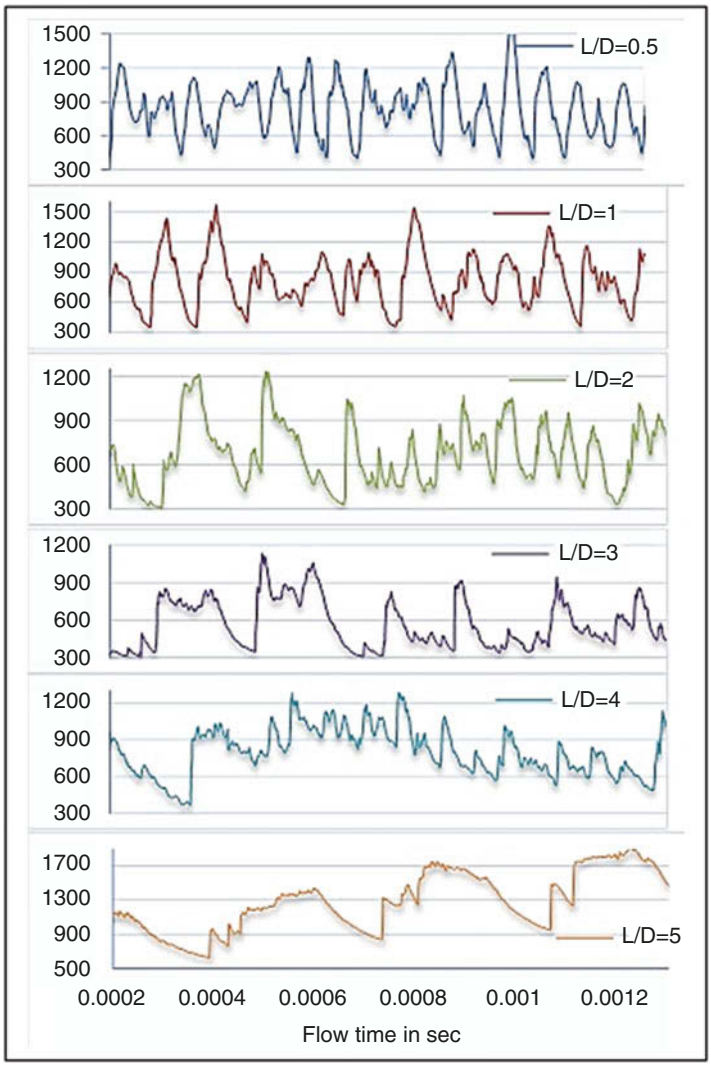

Fig. 4 Frequency v/s L/D

In a similar way, Fig. 4 shows the base temperature variations (in K) v/s flow time for different L/Ds. For L/D = 0.5 case, temperature varies from minimum 400 K to maximum 500 K with a cycle period of 60 μs. Similarly for L/D = 1,2,3,4 and 5, in the range of temperature varying from minimum 300 K to maximum 1700 K, cycle time varies to 70 μs, 120 μs, 150 μs, 300 μs and 345 μs, respectively. All the cycle time was approximated between the flow duration of 0.6 ms to 1.2 ms.

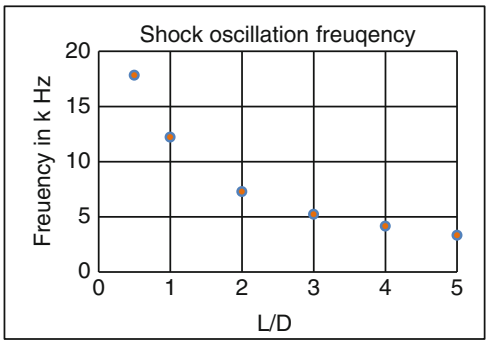

Fig. 5 Base temperature variations

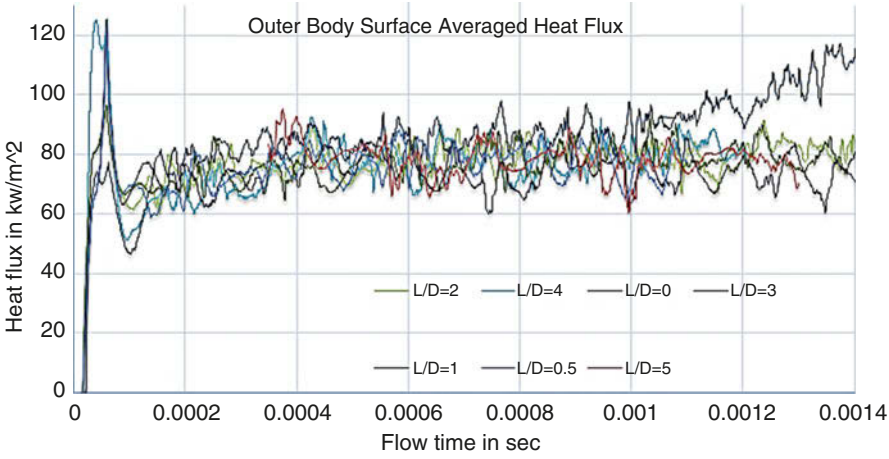

Fig. 6 Surface-averaged heat flux variation

3.2 Averaged Surface Heat Flux Variation over a Time and Length

Figure 6 shows the area-weighted average heat flux values over the outer body surface for each time step. The area covered by the heat flux curves for different L/Ds was compared with and without cavity (L/D = 0) case using the trapezoidal rule. It was found that the averaged surface heat flux is reduced by 10.23%, 13.42%, 9.10%, 10.53%, 10,091% and 9.93% for L/D = 0.5,1,2,3,4 and 5, respectively.

Similarly, Fig. 7 shows the heat flux distribution over the curved surface points averaged over the number of iterations. In reference to the axial distance, it was found that the heat flux distribution is reduced by 20.59%, 28.38%, 16.48%, 25.8%, 22.33% and 10.71% for L/D = 0.5, 1, 2, 3, 4 and 5, respectively, with respect to the L/D = 0 (without cavity) case. Comparison has been done for the time period of 0.2 ms to 1.2 ms excluding the effects of starting unstable variations. It shows that heat flux is very high for the axial distance 2.5 mm–5 mm (i.e. between 23.5° and

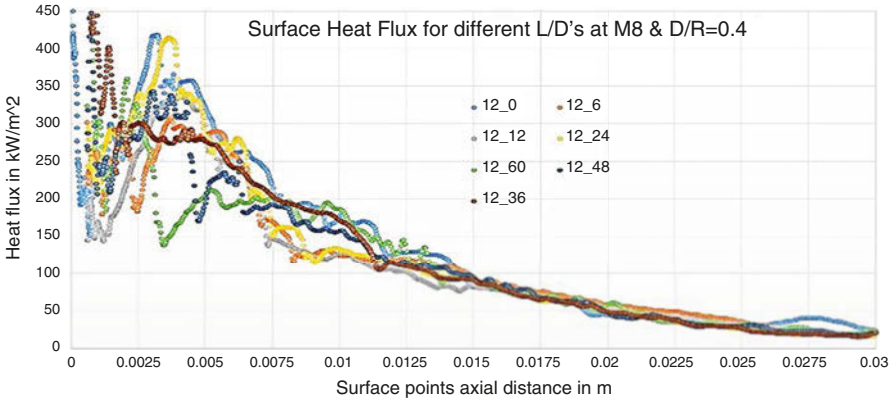

Fig. 7 Surface heat flux variation

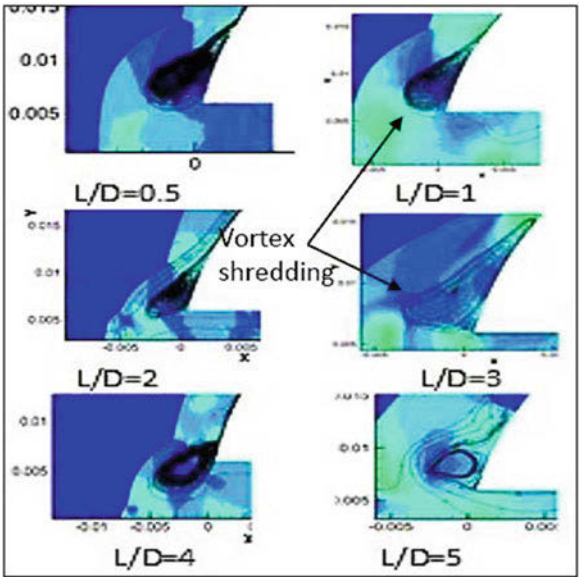

Fig. 8 Pressure contours with streamlines near the lip

33.54° angle from the stagnation point). As L/D increases the peak value lowers, and the peak point moves towards the nose. This is because the shock stays near to the cavity lip region for more time as L/D increases.

The reduction of heat flux is more in L/D = 1 and 3 because of flow periodic oscillations able to drive out the fluid and creating bigger and longer vortex shredding over the surface as shown in Fig. 8.

4 Effects Inside the Cavity

4.1 Cavity Wall: Pressure, Temperature and Heat Flux Variation

Based on the cavity length, a number of probing points or rake are being created over the cavity wall and data acquired using 'monitors' for each time step. Figures 9 and 10 show the temperature (in K) and pressure (in kPa) variation over the cavity wall, respectively.

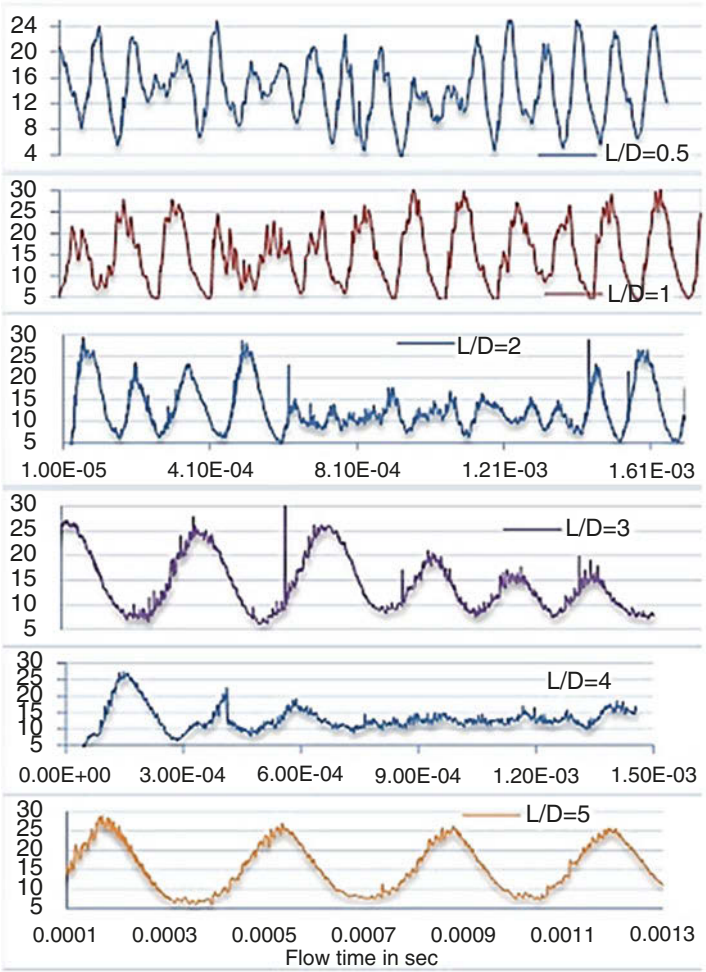

Fig. 9 Wall-pressure variations

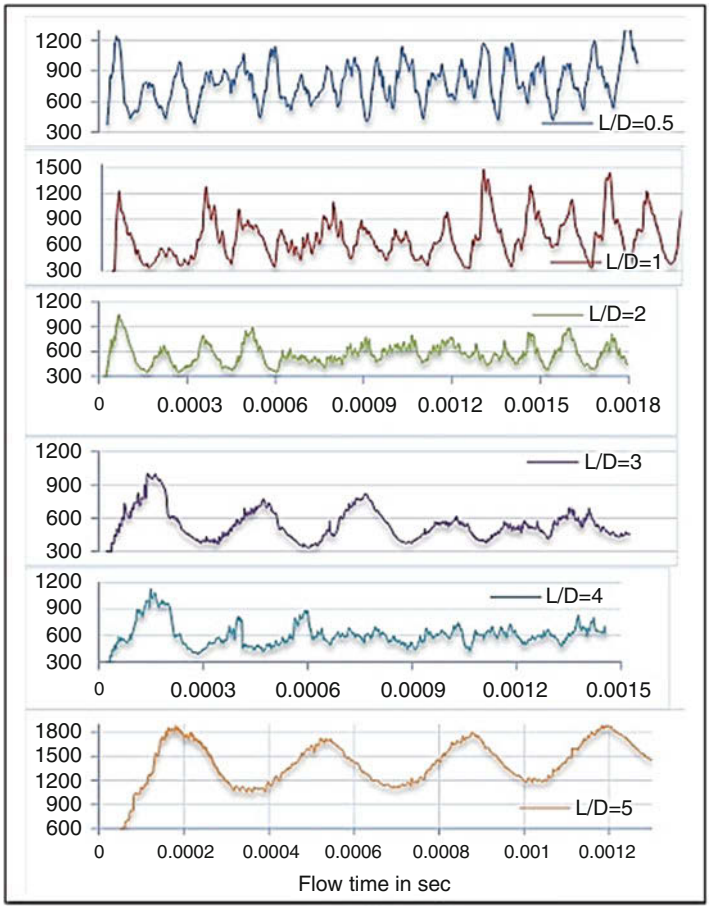

Fig. 10 Wall-temperature variations

For L/D = 0.5 case, the pressure increases from 4 kPa to 24 kPa; accordingly temperature increases from 300 K to 1200 K. For L/D = 1 the pressure varies from 5 kPa to 30 kPa; correspondingly temperature varies from 300 K to 1400 K. From L/D = 2 pressure and temperature variation is minimal from 600 μs to 1.4 ms and again increases to 25 kpa from 10 kPa; similarly temperature increases from 600 K to 900 K. It indicates that the cycle maintains more time with lower pressure and temperature inside the cavity, i.e. shock is away from the nose and suddenly increases to the higher values. Same thing happens for L/D = 4 where the dwell time is more than the L/D = 2.

While for L/D = 3, the cyclic variation of pressure and temperature decreases steeply and raises to repeat the cycle where the dwelling time is minimal, for L/D = 5, the temperature and pressure in a cyclic variation increase gradually with a maximum range of 6 kPa to 25 kPa and temperature from 1100 K to 1850 K.

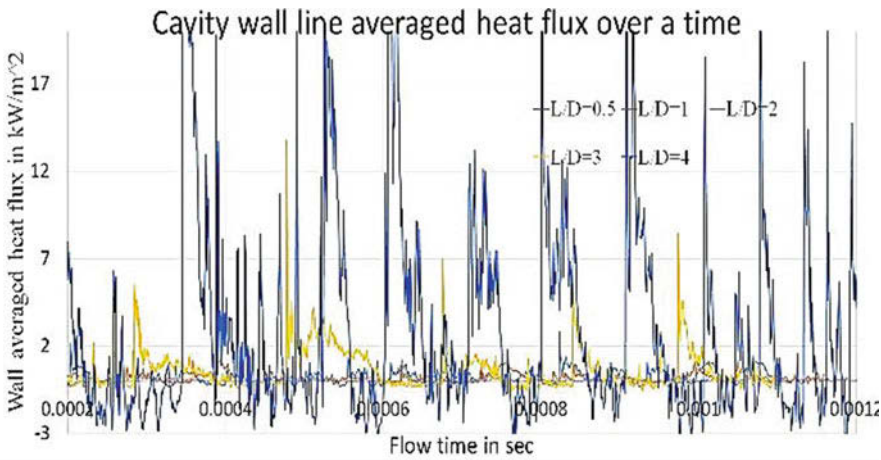

Fig. 11 Cavity wall heat flux variation

Figure 11 shows the variation of area-weighted average value of wall heat flux which varies minimally from L/D = 0.5 to 2, but later heat flux increases very drastically after L/D = 2.

5 Conclusions

1. The unsteady simulation well captured the pressure and temperature oscillations at the cavity base and wall and also their heat flux characteristics.
2. The pressure and temperature oscillation frequency decreases as L/D increases for both the cavity base and cavity wall.
3. For the given flow and geometry configurations, the L/D = 1 and 3 cases are giving higher and L/D = 2 and 5 giving lower heat flux reduction in both point-averaged and surface-averaged studies.
4. The cavity wall temperature and pressure data depict the oscillation behaviour of the cavity fluid clearly. As the L/D increases, the wall heat flux values and its staying time increase inside the cavity.

6 Scope, Applications and Extensions

Simulation for higher flow time with three-dimensional study will help to understand the cyclic nature and shock oscillation behaviour. With an optimised geometry of cavity, greater heat flux reduction can be achieved. It can be extended to blunt body re-entry vehicle configurations.

References

1. J.K. Sambamurthi, L.D. Huebner, L.J. Utreja, AIAA, 87-1193, June 1987
2. L.D. Heubner, L.J. Utreja, J. Spacecr. Rocket. **30**(3), 291–297 (1993)
3. S.I. Silton, D.B. Goldstein, J. Fluid Mech. **528**, 297–321 (2005)
4. W.A. Engblom, D.B. Goldstein: AIAA, 96-0354, 1996
5. S. Saravanan, G. Jagadeesh, K.P.J. Reddy, J. Spacecr. Rocket. (2009)

Large Eddy Simulation of Expansion Wave Diffraction

Z. Shaikh and B. W. Skews

Abstract A computational analysis of expansion wave diffraction was conducted using a large eddy simulation solver. The investigation was aimed at resolving particular flow features following a diffracting expansion wave which were previously identified experimentally through shadowgraph imaging but unresolved in the accompanying RANS computational analysis. The features included large-scale turbulent structures within the separation bubble at the apex, a large wake region downstream of the bubble, shear layer instability and vortex shedding. The analysis was made feasible by combining the embedded LES and wall-modelled LES hybrid RANS-LES techniques in ANSYS Fluent. The larger-scale turbulence within the separation bubble was resolved, and vortex shedding was identified in the LES solution. Evidence of the wake region was noted but remained largely unresolved due to the relatively small-scale turbulent motion. An oblique shock, found towards the rear end of the separation bubble, resolved at higher initial diaphragm pressure ratios ($PR > 9$) in the RANS analysis, was observed from $PR = 7.7$ in the LES analysis. A strong indication of this shock was seen in the shadowgraph images for $PR = 7.7$.

1 Introduction

1.1 Background

Studies involving expansion wave diffraction had been first considered by Mohamed and Skews [1]. The study considered both an experimental and a computational analysis of expansion wave diffraction around a 90-degree corner. The major flow features observed experimentally (shown in Fig. 1) included a shear layer resulting

Z. Shaikh (✉) · B. W. Skews
Flow Research Unit, School of Mechanical, Industrial and Aeronautical Engineering, University of the Witwatersrand, Johannesburg, South Africa
e-mail: zahra.shaikh@students.wits.ac.za

A. Sasoh et al. (eds.), *31st International Symposium on Shock Waves 2*,
https://doi.org/10.1007/978-3-319-91017-8_100

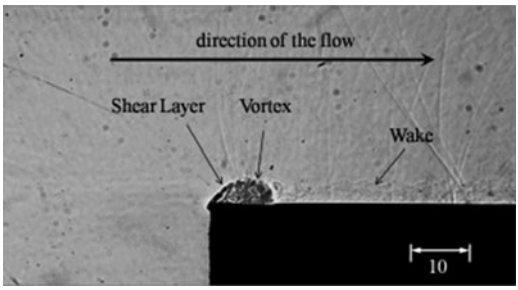

Fig. 1 High-speed shadowgraph image of the diffraction corner

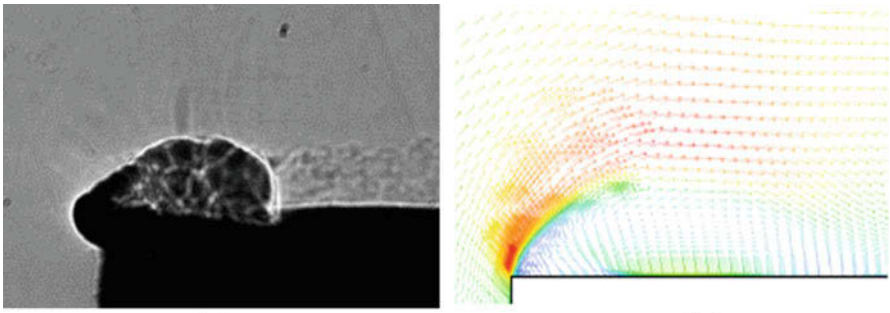

Fig. 2 (**a**) Shadowgraph image (**b**) RANS velocity vector plot. Initial diaphragm pressure ratio, $PR = 5.6$. Time delay from when the expansion wave reaches the corner, $t = 350$ μs

from flow separation at the corner, a separation bubble which remained attached to the wall and a large wake region downstream of the bubble. Shadowgraph imaging indicated the presence of large-scale turbulent structures within the separation bubble and wake region as well as shear layer instability and vortex shedding. The computational analysis involved a Reynolds-averaged Navier-Stokes (RANS) solver. Turbulence was modelled using the shear-stress transport k-ω model. Results from the computational analysis corresponded well with the experimental analysis in terms of the bubble's size and positioning but failed to resolve any of the turbulent characteristics and vortex shedding. Figure 2 shows a comparison between the shadowgraph image and the RANS CFD results. Further numerical analysis using large eddy simulation (LES) is proposed to resolve and investigate the experimentally determined turbulence to further characterise the separation bubble and other major flow features following the diffracting expansion wave.

1.2 Large Eddy Simulation

Large eddy simulation is a solution technique that aims to resolve all large-scale turbulent motion while modelling only smaller 'sub-grid' scales. The LES rationale

is based on larger-scale motion accounting for majority of the transfer of turbulent energy and momentum and on the smaller scales being largely universal and consequently easier to model. Sub-grid scale (SGS) models drastically increase the feasibility of LES in comparison with direct numerical simulation which attempts to resolve the full range of turbulent scales. Unlike ensemble averaging in RANS, LES equations result from applying a numerical filter, with a particular length scale Δ, to the velocity field. The length scale distinguishes between large- and small-scale motions. LES involving mixing layers in the compressible regime is still quite rare [2], and the available SGS models would need further development to accurately describe the flow. The current study attempts an analysis using available models as only qualitative insight into the turbulent flow features is sought.

2 Computational Method

To reduce the computational intensity of the simulation to a feasible level, hybrid RANS-LES techniques were employed. Embedded LES (ELES) is a method which allows for the computational domain to be split and an LES or RANS solver specified for each region. In the current analysis, an LES solver was considered for the area enclosing the separation bubble and wake region, and the rest of the domain was covered using RANS. Due to the turbulent scales being significantly smaller in the near-wall portion of the boundary layer, a classical wall-resolved LES at high Reynolds numbers would demand high-grid resolution requirements and significantly small time step sizes. The wall-modelled LES (WMLES) scheme allows the solver to switch from LES to RANS in the inner part of the logarithmic layer where the grid resolution is not fine enough to resolve the turbulent scales. The sub-grid scale model used in the WMLES formulation is a combination of the mixing length model and the modified Smagorinsky model (Fig. 3).

The resolution requirements for WMLES are $N_x \approx 10$, $N_y \approx 30 - 40$ and $N_z \approx 20$ cells per boundary layer thickness. A value of $\Delta y^+ \sim 1$ is recommended for WMLES although higher values are tolerated if this cannot be achieved. The current mesh resolution used was $\Delta y^+ = 2$, $\Delta x^+ = 4$ and $\Delta z^+ = 4$ in the separation bubble and wake region. A time step size of 1e-6 s was found necessary to resolve the turbulent features and fell below the viscous condition requirement. All simulations were run using the ANSYS Fluent 16.2 commercial package.

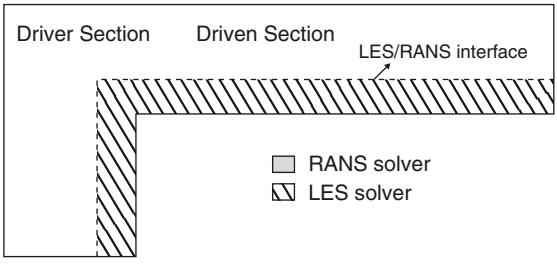

Fig. 3 Embedded LES computational domain

3 Results and Discussion

3.1 Comparison with Experimental Results

The images in Fig. 4 show a comparison between the shadowgraph images and LES results. The presence of turbulent structures within the separation bubble is clearly observed in the density plots. The wake region was still largely unresolved possibly due to the relatively small scale eddies. An attempt at resolving the wake region would require reducing the grid resolution as well as the time step significantly. Another factor that could be considered is the possible over-dissipation by the SGS model which may have dampened the turbulence in the wake.

The shear layer in the $PR = 7.7$ case is well defined in the LES image although a large break in the shear layer appears towards the centre of the bubble. An indication of this break is evident in the shadowgraph image and is expected to be present at some distance through the bubble.

3.2 The Oblique Shock

The RANS analysis by Mohamed and Skews found that an oblique shock would develop at the rear end of the separation bubble under certain conditions. The shock is thought to develop as a result of the acceleration of the flow around the bubble induced by the bubble's curvature. The shock would develop to satisfy immediate downstream conditions and was identified as an oblique shock as is was completely

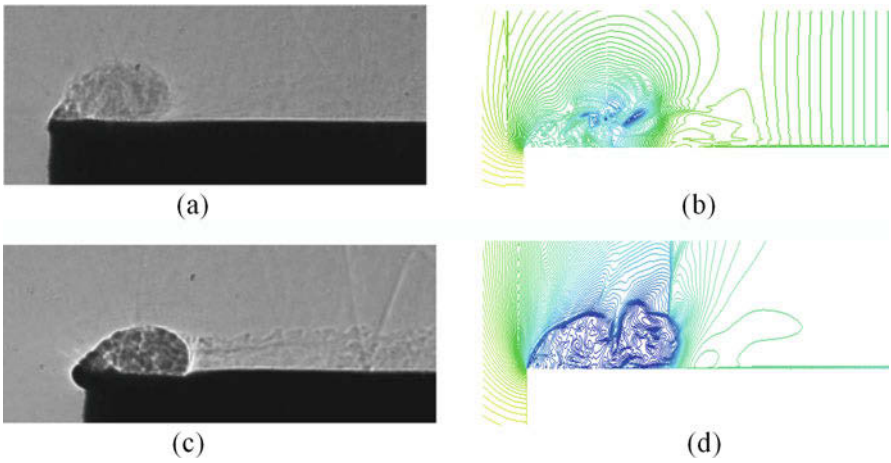

Fig. 4 Comparison between shadowgraph imagery and LES density contour plots at $t = 400$ μs (**a**), (**b**) $PR = 3.2$, (**c**), (**d**) $PR = 7.7$

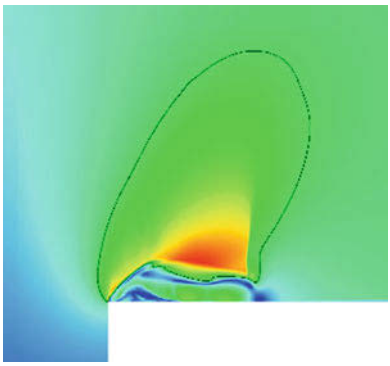

Fig. 5 Mach number plot indicating the oblique shock enclosed by a supersonic region. $PR = 7.7$ and $t = 200\ \mu s$

enclosed within a *supersonic region.* The oblique shock was resolved at $PR = 9$ in the RANS analysis. Shadowgraph imaging however had indicated the presence of the oblique shock at $PR = 7.7$, but the shock was not resolved due to the low-resolution imaging. In the LES analysis, the shock was resolved at $PR = 7.7$ possibly as a result of the three-dimensional nature of the simulation. Figure 5 is a Mach number plot through the centre of the domain illustrating the shock. The boundary of the supersonic region is defined by the Mach 1 trace marked on the plot.

3.3 Viscous Vortices Within the Separation Bubble and Vortex Shedding

RANS simulation results indicated the presence of a large primary vortex within the separation bubble. A smaller secondary vortex was also identified near the diffraction corner embedded within the primary separation bubble. The vector velocity plots in Fig. 6b and c show the primary and secondary vortices obtained using the RANS solver. The primary and secondary vortices can be identified in the LES solution, shown in Figures 6b and d although they are not as well defined due to the three-dimensional nature of the flow.

Vortex shedding originating at the rear end of the separation bubble was made evident from the shadowgraph imaging (Fig. 7) but remained unresolved in the RANS simulations. Shed vortices are clearly visible on the LES vector plots in Fig. 6.

3.4 Mean Flow Velocity

The mean flow velocity through the separation bubble was considered for the RANS and LES cases. The results are shown in Fig. 8 where x_s is the stagnation point (defining the length of the separation bubble) and U_e is the velocity following

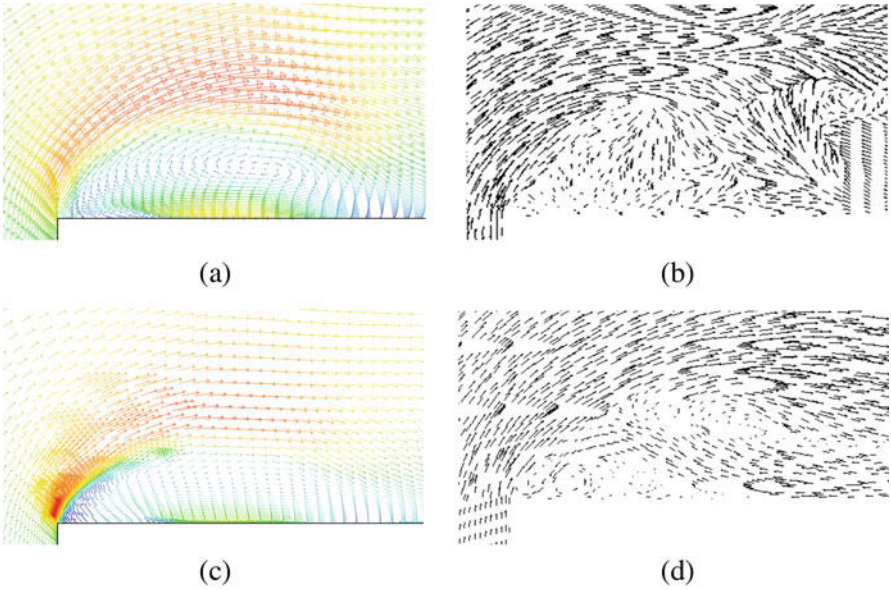

Fig. 6 Velocity vector plots for RANS and LES comparison. (**a**), (**b**) $PR = 3.2$, (**c**), (**d**) $PR = 7.7$

Fig. 7 Shadowgraph image of the separation bubble at $PR = 7.7$ and $t = 300$ μs emphasising vortex shedding

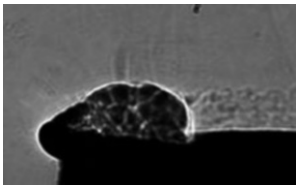

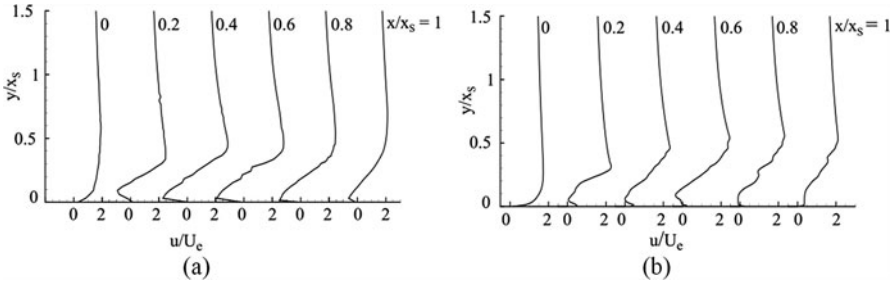

Fig. 8 Time-mean longitudinal velocity distribution through the separation bubble. $PR = 3.2$, $t = 200$ μs. (**a**) RANS (**b**) LES

the expansion wave (at a midline between the wall and the top of the tube). The RANS and LES results correlate fairly well validating the LES analysis. The RANS velocities are overestimated to a certain extent due unresolved turbulence as well as the large grid resolution used in the region of the bubble.

4 Conclusions

An LES solver was used to analyse expansion wave diffraction around a 90-degree corner. Turbulence within the separation bubble was resolved using an LES solver and the embedded LES and wall-modelled LES hybrid RANS-LES techniques. The structure and shape of the bubble agreed reasonably well with experimental shadowgraph imagery. The large turbulent wake region behind the bubble, evident in the experimental results, was unresolved in LES results, although a fair indication of the region was present. This was attributed to the grid resolution not being fine enough to resolve the very small eddies contained in the wake region.

The oblique shock which was found at the rear end of the separation bubble in the previous RANS analysis was captured well by the LES solver at $PR = 7.7$. Experimental images strongly indicated the presence of this shock at $PR = 7.7$, but it was only captured by the RANS analysis at $PR = 9$. The mean velocity profile through the bubble was compared for the RANS and LES solvers, and the results correlated reasonably well.

To better capture the turbulent dynamics of the system, employing more accurate models like the dynamic Clark model [2] could be considered.

References

1. I. Mohamed, B.W. Skews, Expansion wave diffraction over a 90 degree corner. J. Fluid Mech. **757**, 649–664 (2014)
2. E. Garnier, N. Adams, P. Sagaut, *Large Eddy Simulation for Compressible Flows* (Springer, London, 2009)

In-Pipe Aerodynamic Characteristics of a Projectile in Comparison with Free Flight for Transonic Mach Numbers Between 0.5 and 1.5

R. Hruschka and D. Klatt

Abstract The transient shock dynamics and drag of a transonic projectile flying through a pipe 3.55 times larger than its diameter are analyzed by means of time-of-flight and pipe wall pressure measurements as well as computational fluid dynamics (CFD). In addition, free-flight drag of the 4.5-mm-pellet-type projectile was also measured in a Mach number range between 0.5 and 1.5, providing a means for comparison against in-pipe data and CFD. For nearly incompressible flow, the presence of the pipe has little influence on the drag. There is a strong increase, however, between Mach 0.3 and 0.8, to a value of about two times the free-flight drag. This is exactly where the nose-to-base pressure ratio of the projectile becomes critical, and henceforth drag can be estimated by supersonic nozzle theory. For even higher Mach numbers, the drag decreases again and finally drops below the free-flight drag. This behavior is explained by five different flow regimes that the in-pipe projectile experiences, as opposed to only two for the free-flying one (subsonic and supersonic, respectively). 2-D axisymmetric CFD simulations agree well with measured values for drag and shock speeds.

1 Introduction

Studies of projectile aerodynamics from subsonic up to low supersonic velocities, either in wind tunnels, in free flight, or by means of CFD, usually avoid any interference from walls or close boundaries [1, 2]. In the current study, however, wall effects are introduced deliberately by choosing the duct or tunnel diameter in the same order of magnitude as the projectile itself.

The 4.5-mm projectile with a base cavity used in this study, as schematically shown in Fig. 1, is first analyzed experimentally and numerically in free-flight mode, because of the lack of literature data on similar configurations.

R. Hruschka (✉) · D. Klatt
French-German Research Institute of Saint Louis, Saint Louis, France
e-mail: robert.hruschka@isl.eu

A. Sasoh et al. (eds.), *31st International Symposium on Shock Waves 2*,
https://doi.org/10.1007/978-3-319-91017-8_101

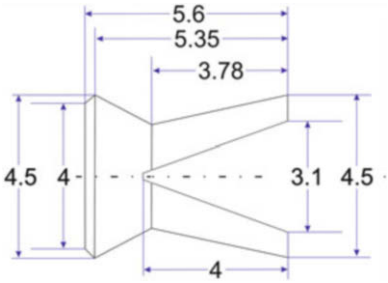

Fig. 1 Dimensions of the projectile used (in mm)

CFD methods using steady-state Reynolds-averaged Navier-Stokes (RANS) methods have been used successfully to calculate drag, lift forces, and also dynamic derivatives of projectiles in the transonic regime [2–4].

2 Theoretical Considerations

The current work describes the passage of a blunt, cylinder-like projectile through a pipe 3.55 times larger in diameter. When the projectile velocity v_p, which is considered constant during the tube passage, is increased in successive experiments, the flow physics can be categorized into five different regimes, which are schematically shown in Fig. 2. In the incompressible flow regime ($M < 0.3$, case A in Fig. 2), only a small effect of the pipe is expected. With increasing v_p, a shock wave is formed in front of the projectile. Propagating forward at the speed of sound at low v_p, this shock wave becomes stronger and faster as v_p increases; however the difference between leading shock speed and v_p is decreasing, shown in in Fig. (2B). From a fluidmechanical point of view, the projectile acts as a local cross-sectional reduction in the tubular duct, and in a projectile-fixed coordinate system, the local flow is similar to the one through a convergent-divergent (Laval) nozzle. As v_p increases, the ratio of projectile nose pressure to base pressure p_n/p_b increases also. When a critical ratio of p_n/p_b is reached (for air, $p_n/p_{b,crit} = 1.9$), the flow behind the projectile becomes supersonic with respect to the projectile, even though v_p has not reached supersonic values yet. Now p_n/p_b no longer depends on the ambient pressure at the tube entry point. The local supersonic flow behind the projectile also leads to a trailing recompression shock wave with a velocity $v_{s,t}$ lower than v_p; hence the projectile head start with respect to the recompression wave is increasing during the pipe passage (Fig. 2C). As opposed to a projectile in free flight, v_p exceeding the speed of sound before entering the pipe does not change the flow characteristics. At a certain supersonic value of v_p, however, the advancing shock in the tube can no longer propagate faster than v_p – instead it remains static in front of the projectile, similar to the corresponding free-flight situation. The shock now reflects on the tube wall and interferes with the local flow field around the projectile, which in turn can have an increasing effect on base pressure. The flow is now quasi-steady

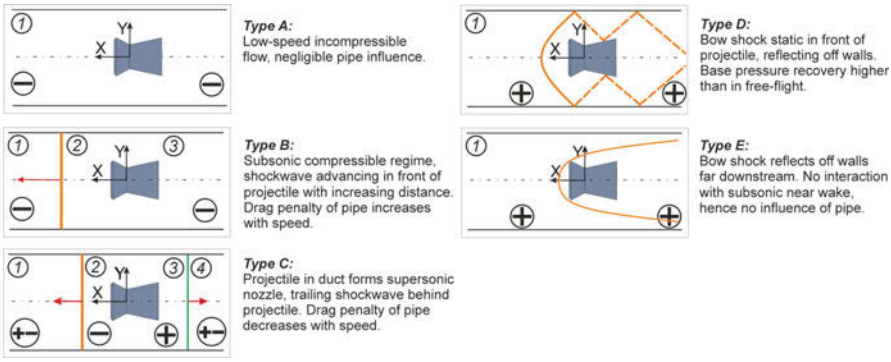

Fig. 2 Velocity-dependent flow regimes experienced by the projectile inside the pipe. The (+) symbol indicates local supersonic flow, while the (−) symbol indicates subsonic flow. Numbers indicate the location of indices used for local quantities

in a projectile-fixed coordinate system, as shown in Fig. 2D. The fifth and final regime, which the projectile enters at very high Mach numbers (Fig. 2E), describes the case where the bow shock wall reflection occurs so far downstream that the locally subsonic part of the projectile flow field and wake is not affected at all any longer and the presence of the pipe is no longer important for the physics of the flow and the projectile drag.

3 Experiments Measuring Drag and In-Pipe Wall Pressure

The projectile (Fig. 1) was launched by an air gun through a series of five light barriers distributed along a 4.5 m-long flight track to obtain downrange distance x vs. time t. By fitting a second-order polynomial to the data of each shot, velocity as well as mean acceleration was determined; this implies the assumption of constant drag over time. The projectile velocity was adjusted by varying the effective barrel length of the gun. Additionally, free-flight drag was also determined by time-of-flight and radar measurements.

For the in-pipe drag measurements, velocity was measured before and after the projectile passed through a 3-m-long pipe of 16-mm inner diameter, as schematically shown in Fig. 3A. In addition to drag, the time histories of wall pressure inside the pipe were recorded using six PCB pressure transducers distributed along an otherwise identical 2-m-long transparent pipe, sketched in Fig. 3B. For the in-pipe-measurements, using setup A, one third of the flight track occurs outside the pipe; thus the initial drag measurements are biased toward the free-flight values. Having measured these as well, however, the effect could be calculated and corrected for. Using the transparent pipe of setup B with a light barrier in the center, this type of correction was not necessary.

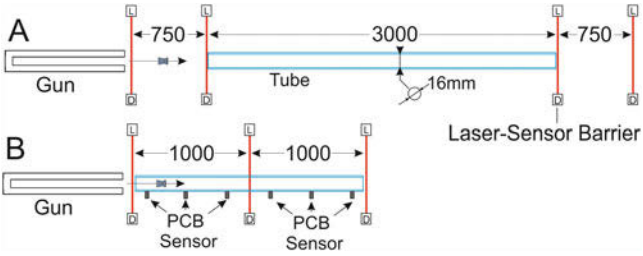

Fig. 3 Experimental setup to measure in-pipe drag and wall pressure histories

4 Numerical Simulations

Two-dimensional axisymmetric, steady, as well as time-resolved simulations were conducted using ANSYS FLUENT (V13). The k-ω SST turbulence model and a second-order upwind scheme were employed on grids with densities of 0.01, 0.04, 0.169, 0.69, and 2.76 million hexahedral cells for the free-flying case and 0.3 and 1.2 million for the in-pipe case. For the free-flight simulations, the diameter of the circular domain was chosen at 90 times the projectile diameter to avoid unwanted far-field boundary influence.

5 Results and Discussion

5.1 Free-Flying Projectile

The free-flight drag measurements are compared against simulations in Fig. 4. They agree well with the measurements up to $M = 0.9$, however slightly overpredicted the drag at transonic and supersonic Mach numbers, most likely caused by the RANS model underpredicting base pressure. The comparison bears similarity to the results presented by [4].

The influence of the grid resolution is shown by also displaying results obtained on a gird four times coarser (0.69 mil. cells). The difference between the two grids is less than two percent for all Mach numbers simulated.

5.2 In-Pipe Projectile Drag in Comparison with Free Flight

The unsteady 2-D axisymmetric RANS simulations were mostly able to reproduce the measured in-pipe drag, as demonstrated in Fig. 5, although for $M > 0.8$, the simulations are at the lower end of the experimental value distribution. To quantify the sensitivity to numerical parameters, a simulation with a coarse grid with 0.3

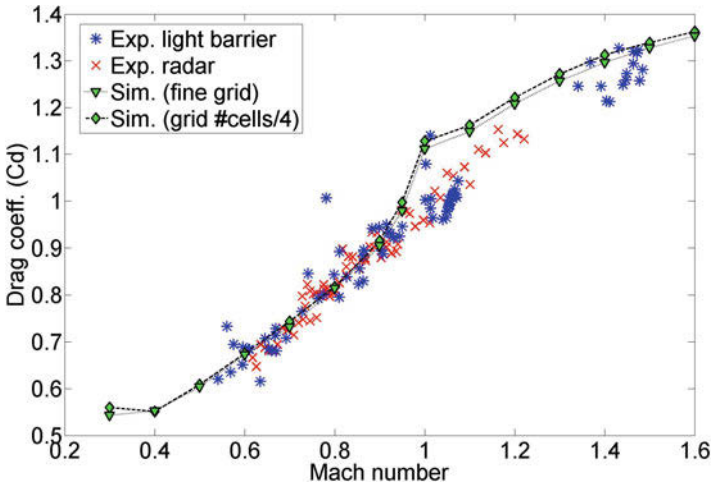

Fig. 4 Free-flight drag, comparison of measurement and simulations

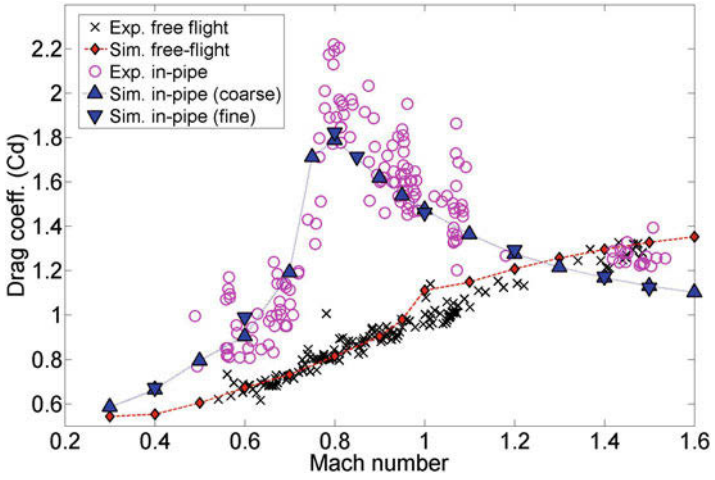

Fig. 5 In-pipe and free-flight drag, comparison of measurement and simulations

million cells and a time step of $1{\cdot}10^{-6}$ s was compared to one with 1.2 million cells and a time step of $5{\cdot}10^{-7}$ s. The fine simulation shows slightly higher drag coefficients for $M = 0.6$ and 0.8 but apart from that nearly identical values. The values for C_d show a distinct peak around Mach 0.8, at more than two times the drag of a free-flying pellet at the same speed. It can be shown by using normal shock relations and supersonic nozzle theory to calculate air flux past the projectile that at exactly this value the critical pressure ratio between the space ahead of projectile with respect to the one behind is reached. At higher Mach numbers, drag decreases again, and the simulations indicate that it even drops below the corresponding free-flight value.

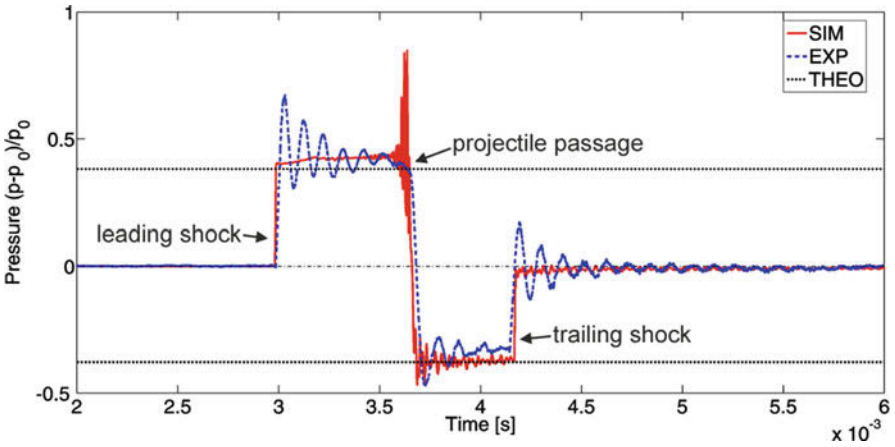

Fig. 6 Measured (EXP) and simulated (SIM) pressure histories on pipe wall

It should be mentioned that the drag reaches a nearly constant value after a short initial settling period for all Mach numbers investigated. This is due to the nearly constant conditions between leading shock and projectile, independent of the shock position. It needs to be noted that the pipe entry process of the projectile was not modeled in CFD. Instead, the simulation was initialized with uniform flow around the projectile, which is, however, expected to result in similar times until locally steady flow is established.

5.3 Wall Pressure History in the Pipe

One representative pipe wall pressure sensor signal of the sensor 1.19 m downrange of pipe entry for a projectile Mach number of 0.97 is compared to simulation and theoretically calculated values in Fig. 6. The initial pressure jump caused by the leading shock agrees well with the theoretical value and the CFD simulation. When the projectile passes the sensor, a sudden pressure drop to about half the forebody pressure results – which is accordance with theory and simulation. Strength and position of the trailing shock, characteristic for flow regime C, are also well predicted by the simulations. The spurious oscillations in the measured signal are most likely due to the recess mounting of the sensors, resulting in local Kelvin-Helmholtz instabilities.

Using all pressure signals, an *x*-*t*-diagram for each experiment can be plotted, and fitting functions through the data points allows determination of shock velocities and for the projectile its velocity and its deceleration, hence drag coefficient. The projectile velocity drop during pipe passage of setup B was of the order of $15 m/s$ and hence small enough to warrant the constant-velocity modeling in the simulation.

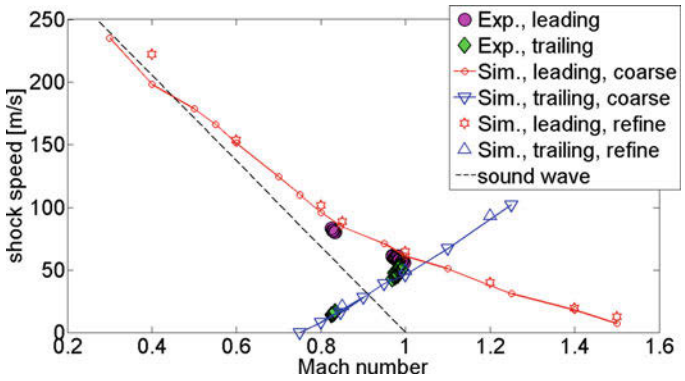

Fig. 7 Measured (EXP) and simulated (SIM) pressure histories on pipe wall

5.4 Shock Speeds Dependent on Projectile Mach Number

Shock speeds in a projectile-based coordinate system are shown in Fig. 7, dependent on projectile Mach number M_p. The measured speeds at $M_p = 0.83$ and 0.97 agree well with simulated data. The simulations show that the leading shock velocity plus with respect to the projectile decreases from sound speed at low velocity to zero at about Mach 1.5, that is, where the flow transitions from regime C to D. For Mach numbers larger than 0.8, the transition point from regime B to C, the trailing shock comes into existence, vanishing again at Mach 1.3 due to zero pressure difference between region 3 and 4 indicated in Fig. 2 C.

6 Conclusion

It has been proposed that the transonic flight of a projectile through an oversized pipe could be categorized into five different flow regimes. Experimental and CFD studies have shown that the pipe causes a maximum drag penalty on the projectile when the critical pressure level for sonic flow in the constricted area between the projectile and the pipe wall is reached. At higher speeds, the drag was shown to decrease again. At supersonic Mach numbers around 1.5, the simulations indicated that the pipe had a small reducing effect on the drag due to an increased base pressure recovery compared to free flight, although the accuracy of the current measurements was insufficient to prove this relatively small effect. Steady-state, axisymmetric CFD simulations were able to predict free-flight drag prediction. For the in-pipe case, unsteady simulations proved adequate to reproduce the experimentally measured drag, shock speeds, and pipe wall pressure signals.

References

1. J. Sahu, *Drag Predictions for Projectiles at Transonic and Supersonic Speeds*, Tech. Rep. BRL-MR-3523, (1986)
2. C.J. Nietubicz W.B. Sturek, *Navier-Stokes Code Verification for Projectile Configurations at Supersonic and Transonic Velocities*, AIAA-Paper 88-1995 (1995)
3. S. Silton, Navier-stokes computations for a spinning projectile from subsonic to supersonic speeds. J. Spacecr. Rocket. **42**(2), 223–231 (2005)
4. J. DeSpirito, S. Silton, P. Weinacht, Navier-stokes predictions of dynamic stability derivatives: Evaluation of steady-state methods. J. Spacecr. Rocket. **46**(6), 1142–1154 (2009)

Experimental Investigation of Shock Wave Characteristics in Small-Scale Circular Channel

R. Singh, E. F. Médici, and K. Tajiri

Abstract Shock wave propagation through small-scale circular channel is studied using two fast-response pressure transducers. The shock wave is generated by a modified Split-Hopkinson pressure bar shock tube. Pressure profile measured in the channel indicated the sharp increase followed by gradual decrease with fluctuations and several small peaks. Values of peak pressure increase with channel wall temperature, but the shock tube pressure has no significant impact. On the other hand, the intervals between peak pressures decrease with increased shock tube pressure, while the wall temperature has marginal impact.

1 Introduction

Studies of high-speed flows and shock waves in small channels are of increasing interest in engineering and science. A number of applications, such as micro-propulsors [1, 2], gas compression [3], and drug delivery systems [4, 5], make use of millimeter-scale compressible fluid flows.

Characteristics unique to the small-scale shock waves include [6, 7]:

- Viscous stresses in the flow cause smoothing of the shock wave and attenuation in the gas velocity.
- Continuous pressure increase behind the shock wave is observed, rather than a step change.
- High heat transfer rates between fluid and solid walls prohibit the adiabatic flow approximation.
- ReD/L can be used as a scaling parameter for small-scale shock wave propagation where Re based on the speed of sound, D the hydraulic diameter of the channel, and L the axial extent of the shock region.

R. Singh · E. F. Médici · K. Tajiri (✉)
Michigan Technological University, Houghton, MI, USA
e-mail: ktajiri@mtu.edu

A. Sasoh et al. (eds.), *31st International Symposium on Shock Waves 2*,
https://doi.org/10.1007/978-3-319-91017-8_102

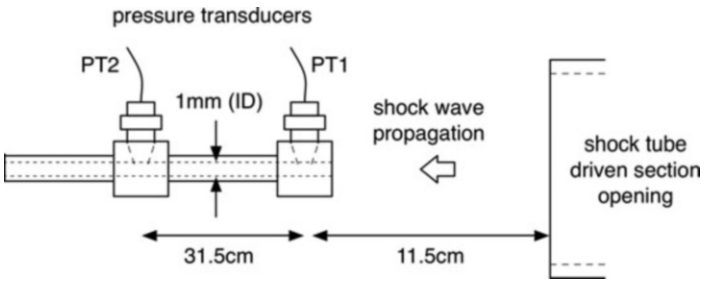

Fig. 1 Schematic diagram of experimental setup (not scaled)

The characteristics of the shock waves in micro-devices are, however, not yet well understood, and this fact is limiting the practical application of small-scale shock waves. The objective of this study is to understand the characteristics of propagating shock wave in a cylindrical channel with small diameter (∼1 mm), particularly the impact of shock strength and wall heating.

2 Experimental Setup

The Atmospheric Shock Facility at Michigan Tech is unique in that a modified Split-Hopkinson pressure bar actuated by a high-speed servo valve is used to generate shock waves [8]. The advantage of using a Split-Hopkinson pressure bar as a driver section is a fast-acting piston that replaces the diaphragm used in conventional shock tubes, which allows for a quick reload and a safer operation.

In this study, precisely constructed circular channel test section with 1 mm inner diameter is placed at 7.7 cm distance from the driven section opening of the shock tube so that the shock wave is introduced into the channel. Two fast-response pressure transducers (PCB Piezotronics, model 113B22) are located at 3.8 cm and 35.3 cm from the channel inlet in order to characterize the pressure signature of the shock wave for the channels (Fig. 1). Four different channel wall temperatures (20 °C, 40 °C, 80 °C, and 120 °C) and two different pressures of the shock tube driver section (34 and 51 atm) are tested.

3 Results and Discussion

First the shock wave and the flow in the open space between shock tube and the circular channel are visualized using shadowgraph, and the wave propagation speeds are estimated from the captured high-speed camera image. Mach numbers of the wave propagation when entering the microchannel are Ma ∼1.1 and 1.05 for the shock tube driver section pressure of 51 and 34 atm, respectively.

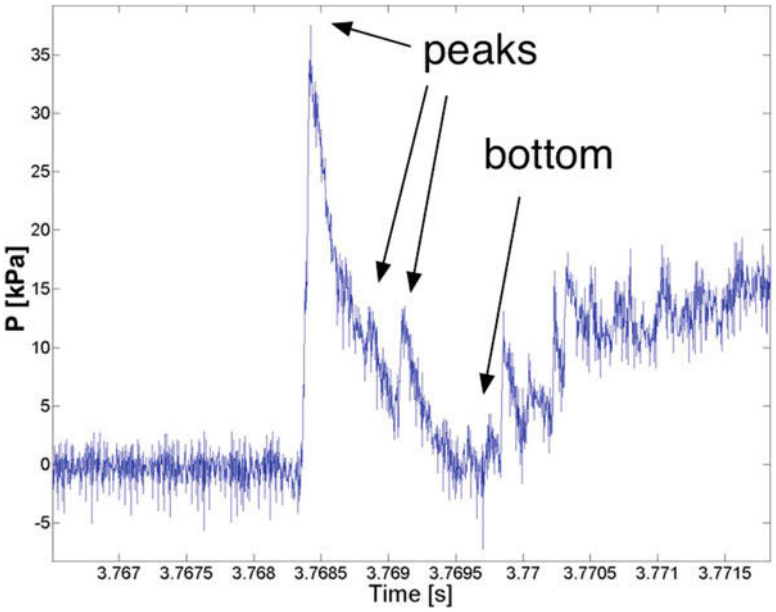

Fig. 2 Typical result of pressure profile at PT2 with 120 °C wall temperature and 51 atm shock tube driver section pressure

Figure 2 shows a typical result of pressure profile measured at a pressure transducer PT2 located at 35.3 cm from inlet. The experimental condition for this particular result is with tube wall temperature of 120 °C and shock tube driver section pressure of 51 atm. Figure 2 shows the pressure profile near the shock entrance into the circular channel. As seen in Fig. 2, the pressure first jumps up and then gradually decreases with several fluctuating peaks. The average pressure wave propagation speed in the channel was obtained from the delay between the signals of two pressure transducers and estimated as 395 m/s (Mach number ∼1.0 at 120 °C).

3.1 Impact of Wall Temperature and Shock Tube Pressure

In Fig. 2 the pressure fluctuations and several peaks are observed. In the following discussion, these pressure peaks are compared with different experimental conditions. For the tests with shock tube driver section pressure of 51 atm, three peak pressures are selected (see Fig. 2). For 34 atm cases, only two peaks are clearly observed, and therefore those two peaks are selected. Figure 3 shows the effect of wall temperature on pressure peak values. As a general trend, the first peak pressure increases with wall temperature, but the second and third peaks have minor variations as the wall temperature increases.

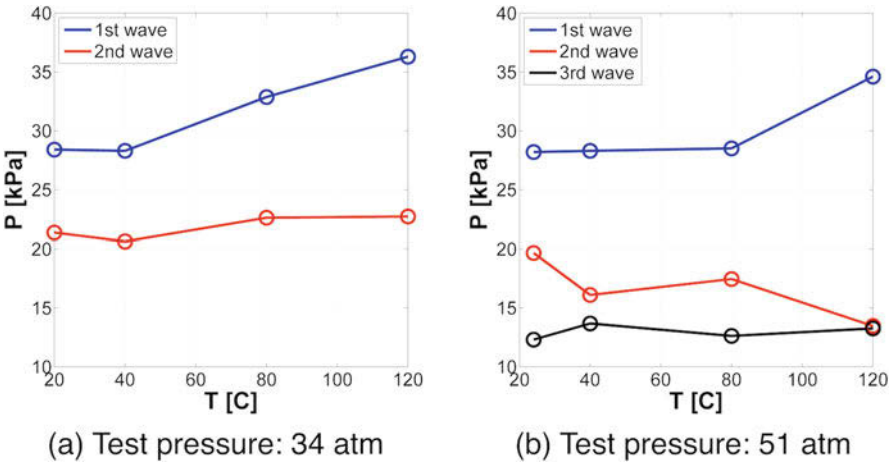

Fig. 3 3 Effect of wall temperature on pressure peak values. (**a**) 34 atm, (**b**) 51 atm

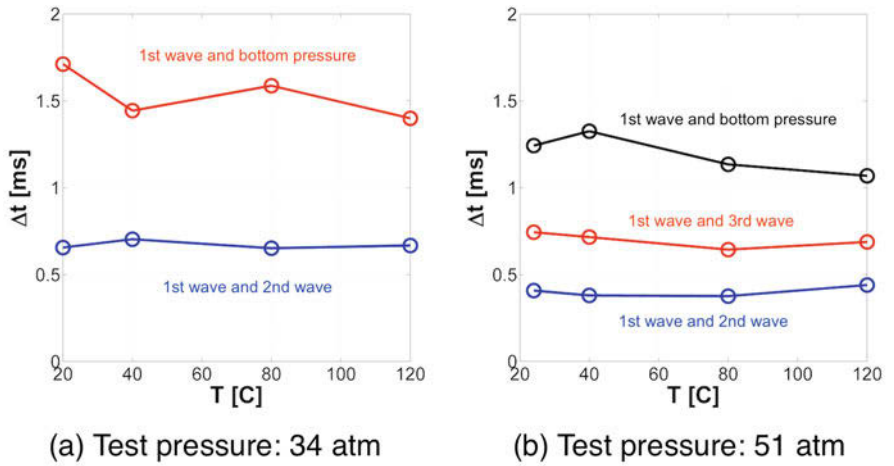

Fig. 4 Effect of wall temperature on time intervals between pressure peaks. (**a**) 34 atm, (**b**) 51 atm

The time intervals between the pressure peaks are also compared with different test conditions in Fig. 4. In Fig. 4a, the time interval between the first peak and second peak and the interval between the first peak and the bottom pressure are plotted. In Fig. 4b, three lines indicate the time intervals between the first peak and second peak, first peak and third peak, and first peak and the bottom pressure. It is clearly observed that for higher test pressure (51 atm), the time intervals become shorter in general. On the other hand, time intervals are incentive to variation on the wall temperature.

4 Conclusion

Shock wave propagation in small-scale circular channel was studied using two fast-response pressure transducers. Pressures at shock tube driver section (34 and 51 atm) and channel wall temperature (20 °C, 40 °C, 80 °C, and 120 °C) were varied to see their impact on the pressure profiles. The following specific conclusions were drawn from this study.

1. Wave propagation speed in 1 mm diameter channel was 395 m/s (Mach number ∼1) for 51 atm and 120 °C case.
2. The pressure profile measured at second transducer (35.3 cm from inlet) indicated the sharp increase followed by a gradual decrease with fluctuations and several small peaks.
3. Pressure peak value increases with channel wall temperature, but the shock tube pressure has no significant impact on the pressure peak value.
4. The time intervals between peaks decrease with shock tube pressure, but the wall temperature shows marginal impact.

References

1. D.L. Hitt et al., Smart Mater. Struct. **10**, 1163 (2001)
2. B.J. Greenfield et al., 49th AIAA Aerospace Sciences Meeting. AIAA 2011–189 (2011)
3. F. Iancu, N. Muller, Microfluid. Nanofluid. **2**, 50 (2006)
4. N.J. Quinlan et al., Investigations of gas and particle dynamics in first generation needle-free drug delivery devices. Shock Waves **10**, 395 (2001)
5. V. Menezes et al., Shock wave driven microparticles for pharmaceutical applications. Shock Waves **18**, 393 (2008)
6. G. Mirshekari, M. Brouillette, One-dimensional model for microscale shock tube flow. Shock Waves **19**, 25 (2009)
7. G. Mirshekari et al., J. Fluid Mech. **724**, 259 (2013)
8. E.F. Médici, G.P. Waite, Geophys. Res. Lett. **43**, 85 (2016)

Shock Oscillations in a Supersonic Diffuser Flow with Varying Stagnation Pressure

Jintu K. James and T. M. Muruganandam

Abstract The flow in supersonic wind tunnel diffusers is usually transonic in nature, and the formation of a normal shock just downstream of the diffuser throat region is required for power economy. The behavior of this starting normal shock decides the start or unstarts of a supersonic wind tunnel. The earlier shock oscillation studies were limited to either divergent or constant-area flow situations. In the present work, experimental studies were conducted in a fully transparent Mach 1.7 blowdown tunnel. The experimental investigations included schlieren visualization using a high-speed camera and unsteady pressure measurements. Experiments with increasing and decreasing stagnation pressures indicate a behavior similar to intermittency near bifurcations. Higher stagnation pressure was required in the upstream motion compared to that in the downstream motion. The experiments with different rates of operation are conducted to understand the rate dependency of shock oscillation. The size of the separated flow region determines the shock structure, and the behavior is rate dependent. Hence an optimum starting operation of a wind tunnel can be by increasing the stagnation pressure fast and decreasing it slowly to bring the shock near the diffuser throat.

1 Introduction

Flows in supersonic intakes in high-speed propulsion systems and wind tunnel diffusers are usually transonic in nature and are characterized by a normal shock just downstream of the throat region. The shock wave is known to oscillate, and the flow in the diffuser is unsteady. The unsteadiness in the flow may become self-excited or can result in small-scale fluctuation to large-amplitude motion of shock waves. The problem of shock oscillation in diffuser flow or cavity flow has gained significance since in many practical applications, it can lead to the failure of the system. The

J. K. James (✉) · T. M. Muruganandam
Department of Aerospace Engineering, Indian Institute of Technology Madras (IIT-M), Chennai, India

A. Sasoh et al. (eds.), *31st International Symposium on Shock Waves 2*,
https://doi.org/10.1007/978-3-319-91017-8_103

typical examples of shock oscillation present include ducts, pipelines, supersonic wind tunnels, airfoils, supersonic inlets of aircraft engines, supersonic ejectors, etc. Shock-wave/boundary-layer interaction (SBLI) is a fundamental phenomenon observed in most of the gas dynamics applications, and this is formed by an external shock wave impinging onto a surface on which there is a boundary layer. These SBLIs are the reason [1] for unsteadiness in the flow, and the boundary layer separation leads to a highly unsteady flow field resulting in inlet instability, aircraft buffeting, and aerostructure fatigue. When the strength of shock is enough to separate the boundary layer, the shock is bifurcated, and there appear one or more shocks downstream of the bifurcated shock [2]. A series of shock structure, thus formed, is called "shock train." If the duct is long enough, generally it is followed by an adverse pressure gradient region. Thus the effect of the interaction extends over a considerable distance, and the flow is decelerated from supersonic to subsonic through this region. Wong [3] has summarized the key mechanism or processes that governed the shock wave movement. These mechanisms included (a) pressure-gradient-induced separation (PGIS) and shock-induced separation (SIS), (b) turbulent boundary-layer and shear-layer instability, and (c) periodic shock motion and acoustic resonance. Experimental and numerical studies on oscillating transonic shock in ducts were conducted by Bruce and Babinski [4, 5]. The aim of their study was to understand the fundamental mechanism of shock wave dynamics and how the information is transmitted from perturbations to shock wave. The result of this work states that the mechanism by which shocks respond to back pressure variations is to change their relative strength, and their relative Mach number matches the pressure jump. This change in shock strength changes the boundary layer separation and SBLI structure.

In the present study, the oscillation characteristics of the shock wave in a supersonic diffuser with varying stagnation pressure have been investigated experimentally. Schlieren pictures and pressures on the diffuser surface have been used for the investigation. The shock motion across the diffuser throat during the starting process is studied in detail here. Effect of shock motion on the separation is also investigated.

2 Description of Experiments

2.1 Wind Tunnel and Test Conditions

The experiments were carried out in the wind tunnel facility in the Gas Dynamics Lab at IIT Madras. This intermittent blowdown facility is capable of handling a stagnation pressure up to 10 bar in the settling chamber. The compressed air is supplied to the tunnel from a common reservoir and is controlled using the valve ahead of the tunnel. Figure 1 displays the photograph of the tunnel.

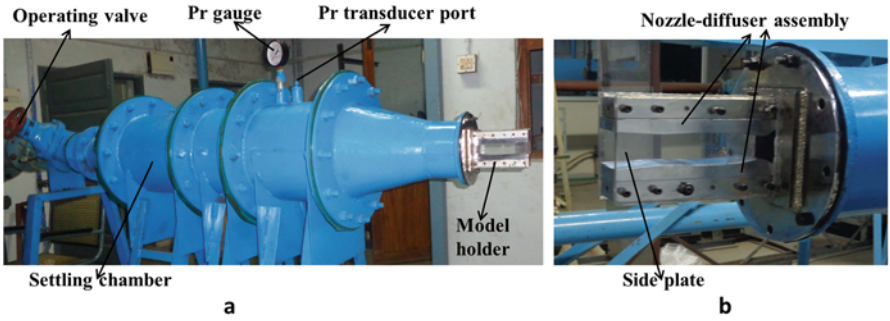

Fig. 1 (**a**) Complete tunnel and test section and (**b**) model holder with a model kept inside

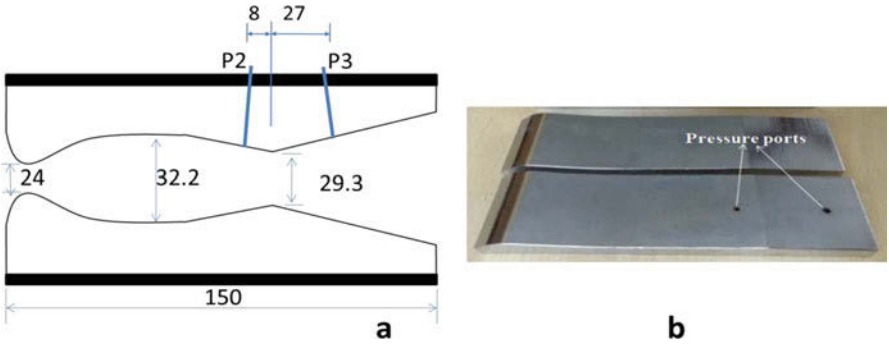

Fig. 2 (**a**) Schematic of the nozzle-diffuser assembly. All dimensions are in mm. P2 and P3 are the piezoelectric transducers. (**b**) Photograph of the model showing the transducer location

2.2 Model and Measurements

The model holder is attached to the exit of settling chamber through one flange, and it consists of two fixed blocks on top and bottom having 40 mm width and 150 lengths as shown in Fig. 1b. The model used in the experiments consists of convergent-divergent (c-d) nozzle followed by a c-d diffuser. The nozzle section was designed using the method of characteristics (MOC) to get a Mach number of 1.7, while the diffuser was a simple straight-line section as shown in Fig. 2. The nozzle followed by test section and diffuser was made as an integral piece from a single MS block, for each of top and bottom walls. The models are electroplated to have a smooth flow over the profiles. This model is attached to the upper and lower plate of the model holder and forms a symmetric passage as shown in Fig. 2a. The nozzle geometry has an area ratio of 1.341 with a throat height of 24 mm, which produces a Mach number of 1.7 at the test section. The width of the flow duct is 40 mm. The second throat height is kept as 29.3 mm and exit height as 36 mm. Piezoelectric transducers P2 and P3 are mounted on the convergent and divergent portion of the diffuser, respectively, to measure the fluctuating pressure during experiments.

Schlieren photography was performed to qualitatively visualize the movement of shock across the second throat of the diffuser. The instantaneous schlieren visualization was conducted using a Newport Corporation light source (50 W halogen lamp), and a slit is positioned in front of the light source, effectively creating a point source of light. The images are recorded using IDT NX4-S3 camera which can acquire images at 3000 fps at a maximum resolution of 1024 × 1024. The pictures were taken at a frame rate of 3000 fps and having a size of 545 × 250 pixels with an exposure time of 10 μs. The image resolution of acquisition was measured approximately to be 0.17 mm/pixel. The schlieren images were processed using Matlab code to identify the shock locations.

The stagnation pressure in the settling chamber is measured using a GE DRUCK PMP-4110 piezo-resistive transducer ranging 0–14 bar with an accuracy of ±0.4% full scale (FS). The fluctuating pressure in the diffuser is measured using two piezoelectric transducers (PCB-113B28) positioned at a distance of 8 mm upstream and 27 mm downstream from the diffuser throat. The pressure data was taken at a sampling frequency of 17,389 and camera synchronization signal also acquired to correlate the image and pressure data using LabVIEW software.

3 Results and Discussions

The movement of starting normal shock during the shock swallowing process in the starting of the wind tunnel was studied using pressure measurements and high-speed schlieren imaging. Two types of experiments were conducted. Stagnation pressures were increased and decreased such that the flow fully establishes. The second part was to vary this rate of increase and decrease of stagnation pressure and study its effect.

3.1 Stagnation Pressure Variation

The first set of experiments were to increase and decrease the diffuser pressure ratio (PR) which is defined as the ratio of stagnation pressure (P_o) to the back pressure (P_b). As the flow is expanded to the atmosphere, the back pressure can be assumed constant and equal to the atmospheric pressure. In a single run, PR was increased up to a value where the shock is fully in the divergent portion of the diffuser and then returned to almost zero value. Shock location was derived from the high-speed images of the shock movement by threshold-based image processing.

Figure 3 plots the temporally varying shock location with respect to the change in stagnation pressure for two different experimental runs with almost same conditions. Xs, the shock location, is assumed to be zero at the diffuser throat and increases along the flow direction. It is clearly seen that as the stagnation pressure is increased, the shock moves downstream. The shock wave moves through the diffuser till the exit portion of the diffuser and returns to the test section in a single run.

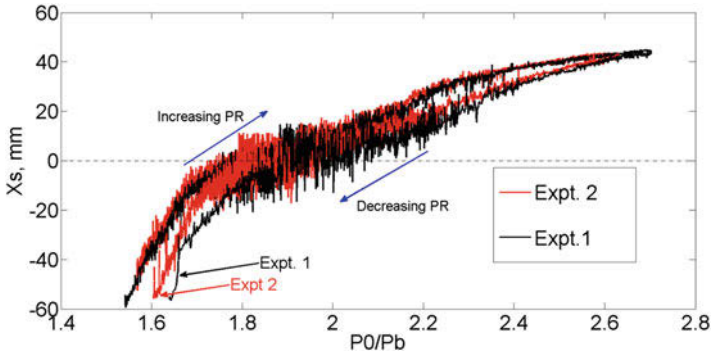

Fig. 3 Variation of shock location with a change in PR for different rates of operation

During the pressure increase phase, the shock moves downstream from the test section, and when it nears the throat, it crosses the throat several times, and this continues till the pressure reaches a threshold value. After this point onwards, the shock oscillation amplitude is decreased, and the relative position of the shock reaches the exit of the diffuser. Once the maximum shock location is reached, the pressure ratio was decreased continuously, and the shock moves upstream. The shock starts to oscillate across the throat with large amplitude when it nears the throat. It could be observed that the return path represented by "decreasing PR" line is slightly shifted from the "increasing PR" line. In both the lines, when the shock is near the throat, it starts to oscillate with large amplitude, and once it crosses the throat, only small-amplitude oscillations are present. It is evident that for the same shock location, the pressure ratio needed is larger for the return phase compared to the increasing phase. While this type of behavior can be easily attributed to hysteretic behavior, on closer scrutiny, it could be observed that the behavior is *against hysteresis*. These data sets were repeated three times each for every model and were found to give similar data and trends. Thus the behavior is repeatable.

3.2 Effect of Rate of Change of PR

There were experimental constraints for the rates at which the opening and closing of the valves are operated. The rates of increasing and decreasing PR are not equal and not constant in the experiments. This might be a parameter which causes this "reverse hysteresis" which is unknown in literature. To understand the dependency of the rate of operation, experiments were conducted at different rates for a given model. Figure 4 presents the temporal variation of stagnation pressure for two runs with different operating rates having same flow conditions as in Fig. 3. The triangular marker represents the pressure at which the shock starts to oscillate across the second throat in the increasing PR branch, while the diamond markers represent

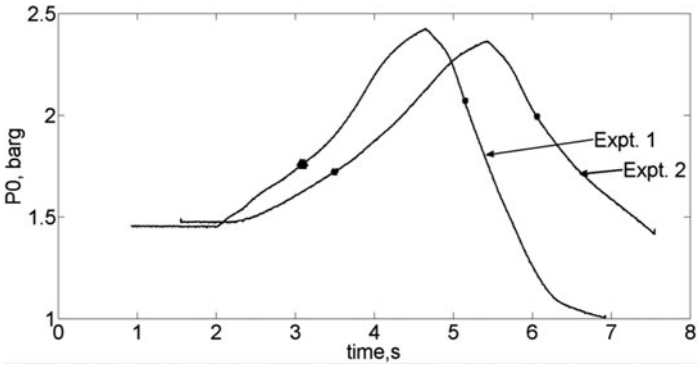

Fig. 4 Variation of stagnation pressure at different operating rates. The triangular and diamond marker represent the point at which the shock starts oscillate across the second throat

Table 1 The variation of pressure values and slope for increasing and decreasing PR

	Increasing PR (pressure ratio)	Decreasing PR (pressure ratio)	Slope (s^{-1}) (increasing PR)	Slope (s^{-1}) (decreasing PR)
Expt. 1	1.757	2.07	2.2187	−4.4699
Expt. 2	1.729	1.992	0.5608	−0.3162

the same during decreasing PR branch. It could be noted that the rate of operation is different for all the runs and these experiments were done one after the other; thus the atmospheric conditions were not very different. The rates of pressure change were different for these runs both in the increasing and decreasing phases, and the time derivative of PR at each of these runs is given in Table 1.

From the table, it could be noted that run 1 has more slope than run 2 at the critical PR value. The two hysteresis curves behave similar to earlier observations, with lower amplitude of oscillation at far upstream and far downstream of the throat, and both the curves have large amplitude of oscillation near the throat. On the increasing PR branch, both the curves almost fall on top of each other, and there is a very slight differentiation between them. But on the return branch, the shock location corresponding to run 1 jumps upstream at higher PR. The rate of operation for run 1 is higher than the rate of operation for run 2. This indicates that as the rate decreases, the two branches of the hysteresis curve come closer. The difference between the paths is reduced as the rate at which the tunnel operated is reduced. Thus the apparent reverse hysteresis behavior is, in fact, a rate-dependent hysteresis behavior. Due to experimental limitations, we could not run with the same rate as the decreasing rate in the increasing phase. Thus we always observed a shift in the return PR from the PR for a downstream jump of shock.

From the above analysis, it could be concluded that as the rate of decrease of PR is decreased, the two branches of the hysteresis curves tend to merge. Thus the behavior of the shock location vs. pressure ratio plot is rate dependent, and thus the observed “reverse” hysteresis behavior can be termed as “rate-dependent

hysteresis." Each of these experiments was repeated three times, and all the three runs exhibited the same behavior, repeatably. Further investigations may be required to understand the dependence of the rate on surface roughness, boundary layer thickness, etc.

4 Conclusions

Experimental studies were conducted in a fully transparent Mach 1.7 blowdown tunnel to find the effect of stagnation pressure variation on shock oscillation across the second throat of a supersonic diffuser. The method of observations included schlieren flow visualization and unsteady pressure measurements. The time series analysis of shock location and the unsteady pressure measurements were carried out. The results indicated that the path traced by the shock wave in forward motion when the pressure ratio is increased is different from that in the backward motion when the pressure ratio is decreased. The higher stagnation pressure was required in the upstream motion compared to that in the downstream motion, which is against the usual hysteresis behavior. It is also observed that as the decreasing rate of PR decreases, the gap between the two branches of hysteresis decreases. Thus the behavior of the shock location vs. pressure ratio plot is rate dependent, and thus the hysteresis behavior can be termed as "rate-dependent hysteresis." Further investigations are required to understand the behavior.

References

1. H. Babinsky et al., *Shock Wave-Boundary-Layer Interactions* (Cambridge University Press, Cambridge, 2011)
2. K. Matsuo et al., Shock train and pseudo-shock phenomena in internal gas flows, Shock Waves. Prog. Aerosp. Sci. **35**(1), 33–100 (1999)
3. H.Y.W. Wong, Overview of flow oscillations in transonic and supersonic nozzles. J. Propuls. Power **22**(4), 705–720 (2006)
4. P.J.K. Bruce, H. Babinsky, Unsteady shock wave dynamics. J. Fluid Mech. **603**(5), 463–473 (2008)
5. P.J.K. Bruce, H. Babinsky, Experimental and numerical study of oscillating transonic shock waves in ducts. AIAA J. **49**(8), 1710–1720 (2011)

Measurement of Shock Wave Attenuation in a Micro-channel

J. Giordano, P. Perrier, L. Meister, and M. Brouillette

Abstract This work presents optical measurements of shock wave propagation in a glass micro-channel. This transparent facility, with a section ranging from 1 mm × 150 μm to 1 mm × 500 μm, exploits a high-speed schlieren videography to visualize the propagation of a shock wave within the micro-channel and to quantify velocity and boundary effects. In this paper, we focus on the Mach waves induced by wall roughness in the supersonic flow behind the wave.

1 Introduction

With the development of micro-devices such as micro-compressors [1, 2], micro-propulsors [3], drug delivery systems [4], and micro-explosives [5], the study of the effects of gas-wall interactions at these scales remains a domain of strong interest for the scientific community, in particular when fluid flows reach high speeds where shock waves can be present. In this context, some experiments were proposed to characterize shock wave behavior in microsystems, particularly to evaluate the attenuation induced by wall shear. However, the spatial resolution of these previous experiments is not efficient to correctly describe phenomena. Thus, we have designed a new device coupled to a high-speed schlieren videography able to provide the visualization of flow in micro-channel with a great spatial and temporal resolution. This device allows us to visualize different characteristics of the fluid flow, such as the attenuation of an incident shock wave moving in micro-channel or Mach waves induced by wall roughness.

J. Giordano (✉) · P. Perrier · L. Meister
Aix Marseille University, CNRS, IUSTI, Marseille, France
e-mail: jerome.giordano@univ-amu.fr

M. Brouillette
Shock Wave Laboratory, Université de Sherbrooke, Sherbrooke, QC, Canada

A. Sasoh et al. (eds.), *31st International Symposium on Shock Waves 2*,
https://doi.org/10.1007/978-3-319-91017-8_104

2 Experimental Device

The device is schematized in Fig. 1. A classical shock tube, with a cross section of 8 mm x 8 mm and 200 mm for high- and low-pressure chambers, is coupled to a glass micro-channel with a section ranging from 1 mm $\times$ 150 μm to 1 mm $\times$ 500 μm and a length ranging from 65 mm to 100 mm.

To generate the shock wave, the pressure in the high-pressure section is increased until diaphragm rupture; nitrogen or helium is used as the driver gas, while ambient air or sulfur hexafluoride (SF6) is used as the test gas. Two pressure sensors, 90 $\pm$ 0.1 mm apart, are located in the low-pressure chamber to measure the incident shock velocity Mi. After propagating through the low-pressure section, this shock wave is then transmitted into the micro-channel, which is clamped to the downstream end wall of the shock tube.

A classical schlieren technique with a high-speed digital video recorder is used to image shock wave propagation within the micro-channel [6]. This system uses a collimated white LED source, with a diameter of 20 mm, along with a negative achromatic lens (diameter = 25 mm and focal length f = -40 mm) and two positive achromatic lenses (diameter = 75 mm and f = 200 mm). The knife edge is a simple razor blade, and an additional achromatic lens can also be used to modify the field of view. Video recording is achieved with a Photron FASTCAM SA1.1 camera equipped with a Sigma 28–70 mm, f/2.8 lens.

The set of sensitivity and the speed of the camera shutter are the main issues of the measure. In our case, we set the shutter at the minimum time, equals to 1 μs and the frame acquisition in the range of 270–500 kHz. However, with the speed of the shock wave that can reach $\approx$ 1000 m/s in the present apparatus, the shock wave can move 1 mm during the shutter time, which is the dimension of the canal height, leading to the loss of any measurable light variations. Conversely, if we set the shutter time too small, the signal is too weak to be observed. Thus, we have to pay a great attention to have a good ratio between the shutter speed and the amount of light signal to see the shock wave and to correctly measure its speed. Besides, we have to consider the loss of picture resolution with the increasing of the acquisition frequency that does not help to have a good detection.

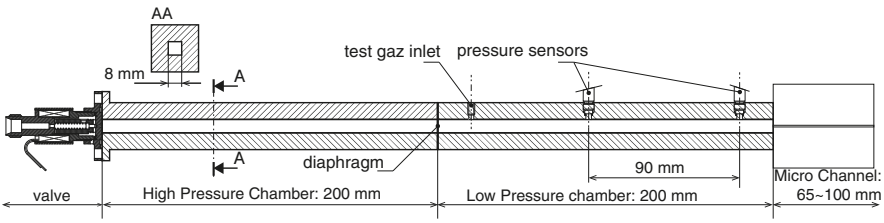

Fig. 1 Experimental device

3 Results

The aim of this section is to present an overview of the results we have obtained through a representative experiment. This experiment was realized with the following characteristics. First, the dimensions of the micro-channel are L = 65 mm, h = 1 mm, and w = 150 μm. The test gas was SF6 at ambient conditions of temperature T1 = 299 ± 2 K and pressure p1 ≈ 105 Pa. We use a micro-leakage regulating valve to fill continuously the low-pressure chamber with the SF6 by the inlet schematized on the Fig. 1. The SF6 is free to go out of the device through the micro-channel outlet and thus remains at ambient pressure. In this experiment, the driver gas He reached a pressure p4 ≈ 10^6 Pa when the diaphragm bursts. The incident shock wave velocity was measured at 312 ± 4.5 m.s − 1 in the low-pressure chamber thanks to the pressure sensors. This shock celerity gives a Mach number equal to ≈ 2.3 ± 0.04 in the SF6. This is in good agreement with the theoretical values from the Rankine-Hugoniot relations with an initial pressure ratio of 10.

Figure 2 shows the propagation of the shock wave into the micro-channel, where one image out of five is presented. For all experiments, we set the time origin when the shock wave exits the micro-channel and the space origin at the micro-channel outlet. The shock speed at the micro-channel inlet is approximately 350 m/s. Indeed, the variation of tube section between the low-pressure chamber (Fig. 1) and micro-channel induces the local amplification of the shock wave strength. In this experiment, this amplification can be evaluated with the analytical approach of Laporte [7] at 120% resulting in an inlet velocity in the micro-channel close to 375 m/s. This analytical value is in good agreement with the experimental one, and we can explain the deviation by difference between the real conditions compared to the model hypothesis, by losses induced by leaks and a slight default of alignment at the micro-channel junction. At the channel outlet, the shock wave is transmitted to the outside gas at ambient pressure and temperature and becomes a blast wave. This gas is actually a mixture of SF6 and air, with a greater proportion of SF6 near the outlet than further away. Thus, the blast wave velocity (≈120 m/s) is about the celerity of sound in SF6 at ambient conditions (≈135 m/s) and increases with the air ratio in the gas. The deviation between the measured velocity and the sound speed

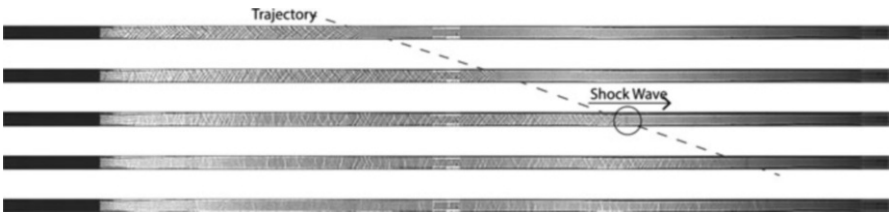

Fig. 2 Mach waves generated by wall roughness behind the incident shock wave in the case of supersonic flow. L = 65 mm, h = 1 mm, and w = 150 μm. Incident shock wave at Mi =2.2 ± 0.03, test gas SF6. Shutter speed 1 μs, pixel resolution 256 × 80

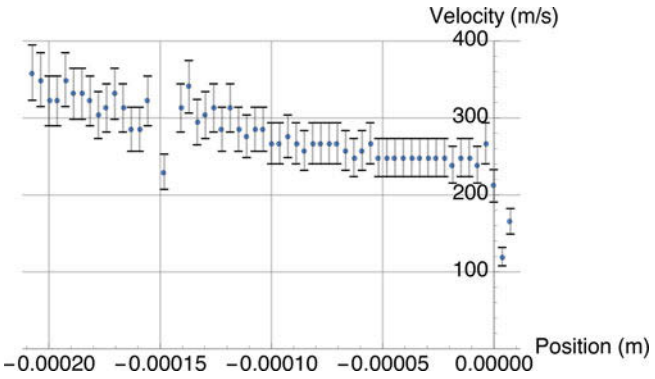

Fig. 3 Evolution of shock wave velocity along the micro-channel. L = 65 mm, h = 1 mm, and w = 150 μm. Incident shock wave at Mi =2.2 ± 0.03, test gas SF6

are due to the difficulty of correctly identifying and locating the blast wave in this open domain.

The measurement of shock wave velocity attenuation is plotted in Fig. 3. The space origin is set at the end of the micro-channel. We can observe in this figure that the shock velocity is decreasing by almost 30%.

4 Mach Waves in Supersonic Flow Behind the Shock

In the case of a strong incident wave, such as in the presented experiment, we observe a supersonic flow behind the shock. This supersonic flow propagating over wall roughness elements generates Mach waves. This phenomenon can be seen on Fig. 2 and more precisely in Fig. 4 where an optical magnification is proposed. The rectangular channels are confined by wall surfaces comprising polished or machined glass where the mean roughness of the polished (front and back) surfaces can be estimated to be lower than 10 nm. The top and bottom channel surfaces, however, are delimited by the machined edges of glass slides that have not benefited from the same polishing process as the front and back surfaces. We have measured this roughness using a STIL™ confocal micromesure with CL1-MG140 pen at 600 nm with peaks in the range of [2 μm; 6 μm].

These Mach waves present a straight part far from the walls and a curved one close to them. Moreover, we can note that the Mach wave angle is changing in time and space. These two events can be explained by the relation of the Mach angle and the fluid flow Mach number. Indeed, at the wall, the fluid flow velocity is equal to zero (in the present conditions no slip can be observed), and with the attenuation occurring in the micro-channel, the flow speed decreases with time. This fluid flow velocity decreasing induces the reducing of the flow Mach number and as consequence generates a Mach wave with an angle closer to 90°. Then, if the attenuation leads to a subsonic flow, the Mach waves are vanishing.

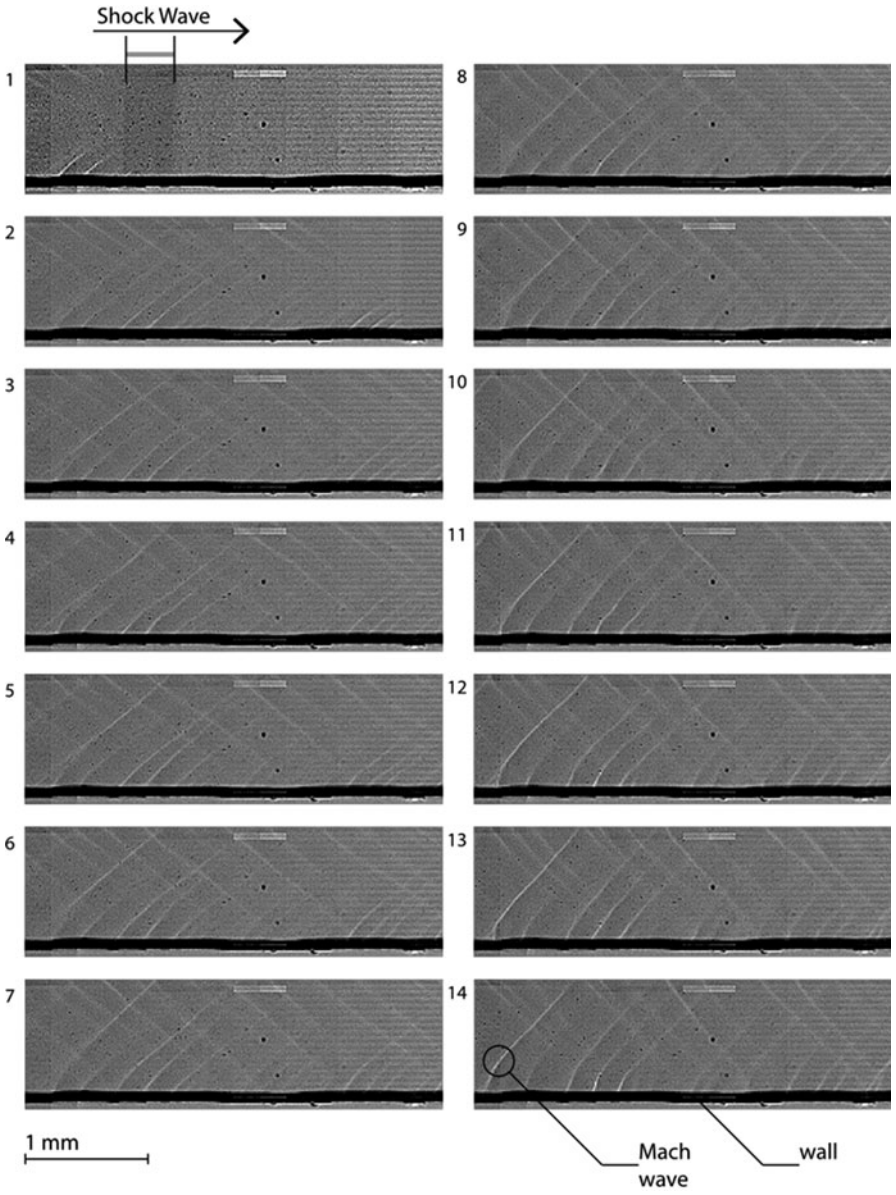

Fig. 4 Mach waves generated by wall roughness behind the incident shock wave in the case of supersonic flow. L = 65 mm, h = 1 mm, and w = 150 μm. Incident shock wave at Mi =2.2 ± 0.03, test gas SF6. Shutter speed 1 μs, pixel resolution 256 × 80

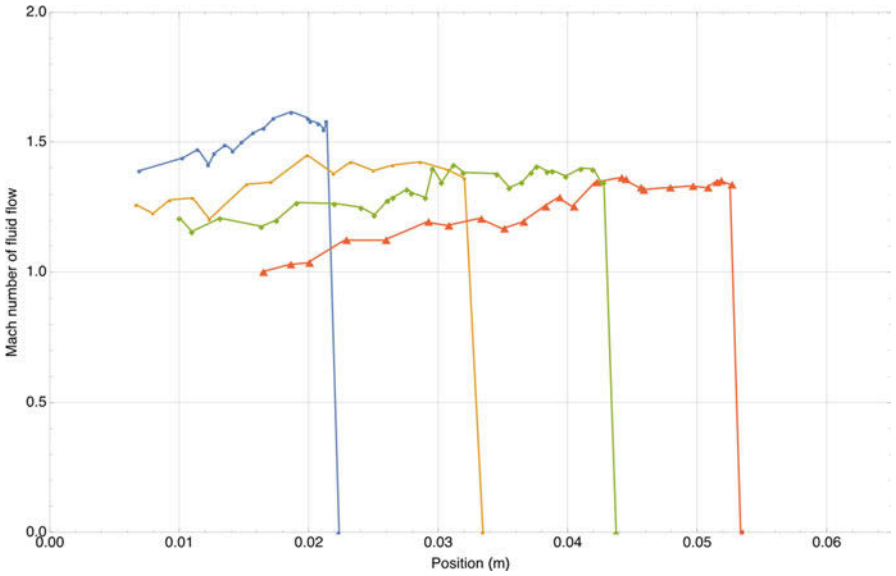

Fig. 5 Mach number distribution of the fluid flow at different locations of shock wave, micro-channel: L = 65 mm, h = 1 mm, and w = 150 μm. Incident shock wave at Mi = 2.31 ± 0.03; test gas SF6. The uncertainty each Mach number is estimated to ±0.15

Thus the measurement of the time evolution of the Mach wave angle gives the estimation of the fluid flow Mach number. We are not able to estimate the velocity because we do not know the temperature evolution and as a consequence the local sound velocity. Figure 5 presents the flow Mach number distribution along the micro-channel center axis at four positions of the incident shock wave for the present experiment. It is seen that the flow Mach number is globally decreasing with the forward motion of the incident shock. This deceleration is due to the flow attenuation induced by the wall friction and heat transfer.

At the first upstream location of the shock wave (filled dots in Fig. 4), we observe a local increase in flow Mach number right behind the shock which may be caused by micro-channel entrance effects. Then, as the shock wave moves into the micro-channel, the flow Mach number gradually decreases in time at a given location and in space behind the shock wave. Under sufficient attenuation, the flow behind the shock wave can ultimately become subsonic, as seen in Fig. 4 for the most forward shock position.

5 Conclusion

The work presents the visualization and measurement of shock wave behavior at micro-scales. With the design of a new device, we were able to provide images of an incident shock wave moving in a micro-channel. This high-speed video recording

allowed us to significantly improve the space and time resolution of the shock attenuation measurement. Moreover, we observed Mach wave generated by the wall roughness in the case of supersonic flows. With the measurement of the Mach wave angle, we proposed an evaluation of the fluid flow Mach number behind the shock wave. We believe these measurements will be useful to validate theoretical and numerical approaches dealing with high-speed flows at micro-scales.

References

1. F. Iancu, N. Muller, Microfluid. Nanofluid. **2**, 1 (2006)
2. F. Iancu, X. Zhu, Y. Tang, D. Alsam, N. Müller, Microsyst. Technol. **14**, 1 (2008)
3. E. Martel, M. Brouillette, Comput. Fluid Dyn. J. **12**, 2 (2003)
4. K. Takayama, Proceeding of the 22nd ISSW (1999)
5. D.S. Stewart, Shock Waves J. **11** (2002)
6. G.S. Settles, *Schlieren and Shadowgraph Techniques: Visualizing Phenomena in Transparent Media* (Springer Science & Business Media, Berlin, 2001)
7. O. Laporte, *Los Alamos Scientific Laboratory of the University of California* (Los Alamos Scientific Laboratory, Los Alamos, 1954)

Surface Jets Produced from an Underwater Shock Wave

B. W. Skews and H. Karnovsky

Abstract Surface effects resulting from the impact of an underwater shock wave have previously mainly been studied as a consequence of underwater chemical or nuclear explosions. Of the many complex features that occur, one is the development of surface jets or plumes. This particular aspect is examined by applying a shock wave impulse to the bottom of a circular disk submerged in a water bath. Different strength shocks are used with different depths of water. It is demonstrated that a wide variety of jets and plumes may be generated.

1 Introduction

An underwater explosion results in a number of complex fluid dynamic phenomena depending on a variety of factors such as depth and charge energy release. First of all there is the shock wave generated from the release of energy at the source which passes up to the surface which it deforms. As it reflects from the interface, a rarefaction propagates back down due to the difference in acoustic impedance. This results in the development of cavitation which itself can generate further compressions as it collapses. Thirdly, a large gas bubble is formed at the source which also exhibits complex dynamic features of successive enlargement and collapse with associated wave systems, also resulting in plumes at the surface. Refraction effects can also occur as well as wave reflection off the ground. Many of these phenomena have been described in detail [1, 2]. Thus there will be a series of pressure pulses propagating toward the surface as shown in Fig. 1. A description of many of the processes is given in [3] (Fig. 2). The effect of the loading of the shock wave, cavitation, and bubble collapse is also relevant in medical processes [4] and volcanic eruptions [5].

B. W. Skews (✉) · H. Karnovsky
Flow Research Unit, School of Mechanical, Industrial and Aeronautical Engineering, University of the Witwatersrand, Johannesburg, South Africa
e-mail: beric.skews@wits.ac.za

A. Sasoh et al. (eds.), *31st International Symposium on Shock Waves 2*,
https://doi.org/10.1007/978-3-319-91017-8_105

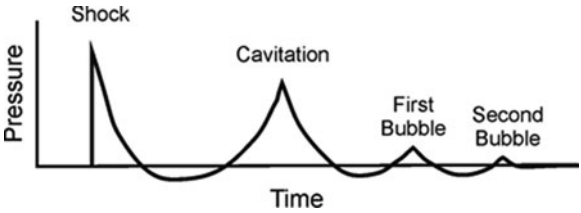

Fig. 1 Schematic of pressure pulse propagation

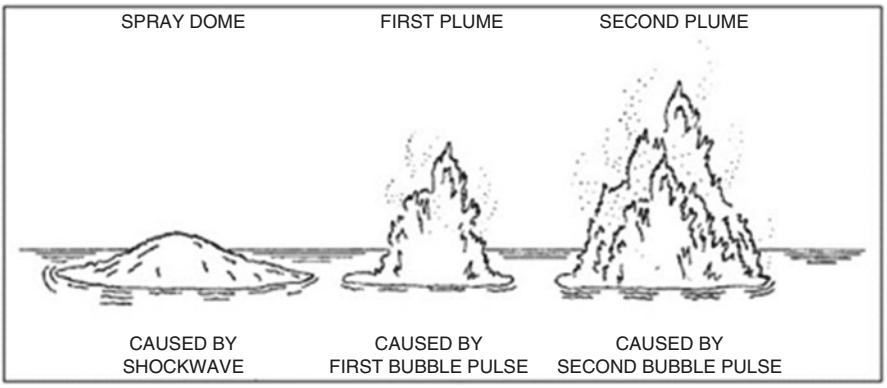

Fig. 2 Typical plume profiles [3]

The first effect on the surface is a bell-shaped dome, sometimes developing into a jet surrounded by spray. This is then followed by a column of spray as the flow breaks up into a plume. The water then falls back to the surface.

Free-surface water jets can be formed by rapidly accelerating a plate positioned below the surface in a water bath producing similar effects to that of an explosion. The correspondence is useful in that it does identify some fundamental processes, including those with a focused wave which occur in the medical procedure of lithotripsy.

Some earlier work using a plate accelerated using an electromagnetic acoustic source, EMAS, reports such studies with a high plate impulse [6]. The device consists of a coil energized with a high-current and high-voltage pulse, with a thin insulating surface above it followed by a thin metal plate which is accelerated rapidly upward in a water bath. In some cases the coil and disk can be made concave so as to generate a focusing wave. Typical results are given in Fig. 3 for the concave focusing EMAS, referred to as a FEMAS.

Initially liquid particles are shed from the surface at a velocity of about 4 m/s followed by deformation of the surface and the development of a column of liquid moving at about 0.4 m/s. When using the plane EMAS disk, the initial behavior is similar, but at later times a more complex jet is developed as shown in Fig. 4.

The current paper uses a similar approach but with the disk accelerated by a shock wave from below. It examines wave interactions at a water/air interface through an idealized set of experiments with emphasis on shock wave effects and the surface jets and plumes that result when struck by the underwater wave.

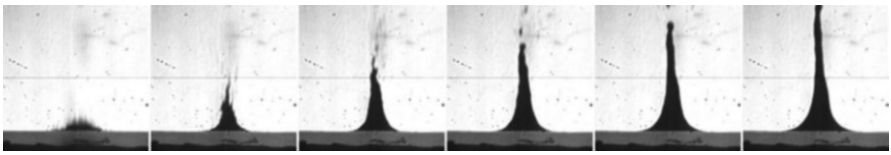

Fig. 3 Jet development from a concave FEMAS, 61 mm water depth, 9 kV supply, 10 ms between frames

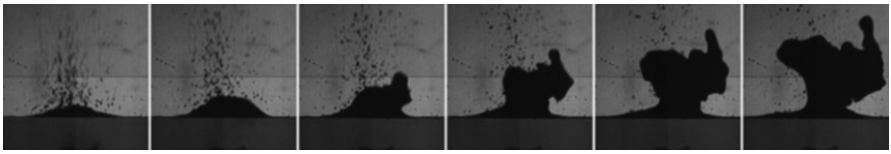

Fig. 4 Jet development from a plane disk EMAS. 61 mm water depth, 10 kV supply, 10 ms between frames

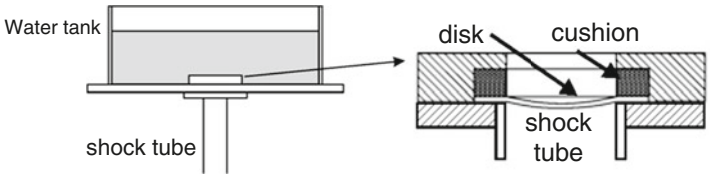

Fig. 5 Experimental arrangement showing the water tank above the shock tube and methods of mounting the disk, allowing it to move

2 Apparatus

The facility used has a circular disk impacted from the bottom by a shock wave generated in a simple shock tube, situated below a water tank, as shown in Fig. 5 [7], which also shows a detail of the disk-mounting system. In order to allow the disk to move, it was positioned against a foam cushion as shown. Three different disk shapes were used: a spherical surface with a diameter of 58 mm and a depth of 10 mm, a parabolic surface 52 mm in diameter and focal length of 50 mm, and a plane disk. A variety of driver pressures were employed, ranging from 2.5 to 4 bars, so as to generate different pressures on the underside of the disk. A range of water depths were used, generally 45 and 55 mm from the disk surface. Imaging was with a split frame CCD camera resulting in a separation between the four recorded frames in the final image. Frame rate was 300 fps.

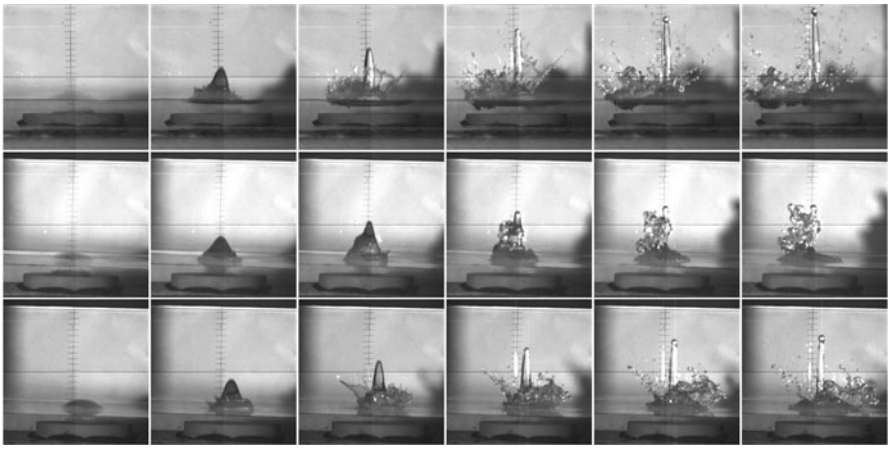

Fig. 6 Jets from the spherical (top), parabolic (middle), and plane (bottom) disks, with a driver pressure of 3 bar, 45 mm water depth. 20 ms between frames

3 Results

Selected frames from the videos are given below. It should be noted that the light source was offset to the left of the optical axis and a sheet of white paper placed behind the rig. This occasionally resulted in a shadow of the developing jet on the paper and a light reflection off the jet itself, which can also be visible in the images. Because of the number of test cases examined, only representative results are presented.

The first set of results indicate the effect of the shock tube driving pressure and thus the strength of the shock and the resulting force on the base of the disk after it reflects from the disk undersurface, for the three disk profiles. Shock tube driver pressures of 3 bar (Fig. 6) and 4 bar (Fig. 7) were used.

The first indication of surface effects is a rounded dome which then develops into a smooth surfaced conical mound. Thereafter a narrow columnar spike develops propagating directly upward. This is most marked for the spherical disk profile and least for the parabolic case. The focal length of the parabola is larger than the water depth. A circular ring of splashes around the jet then develops. In the spherical case where the optical axis is parallel to the liquid surface, unlike the other cases where it is inclined, it is noted the surrounding water surface becomes depressed due to the flow into the jet. At later times the columnar jet continues to rise in the spherical and plane disk cases and eventually starts to fall under the influence of gravity. The effect of surface tension then results in the separation of a spherical drop of liquid at the top. The jet flow in the parabolic disk case is much more irregular, indicating a complex wave system being generated in the water gap.

For the higher driver pressure of 4 bar, Fig. 7, the main features are similar to the lower pressure case, except the jet development occurs earlier, and the splash is

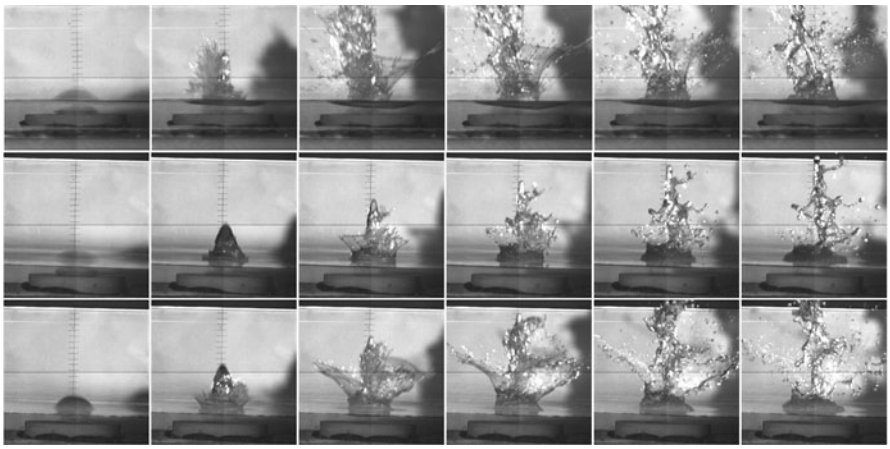

Fig. 7 Jets from the spherical, parabolic, and plane disks, with a driver pressure of 4 bar, 45 mm water depth. 20 ms between frames

much more vigorous. It emerges as a conical sheet before starting to break up into individual drops due to surface tension. At late times the jets and splash break reach maximum elevation and move back toward the liquid surface.

It is to be expected that as the water depth increases, so the jetting effects will become less marked as the pressure pulse through the liquid expands and diffracts sideways. The effect of depth is demonstrated in Fig. 8, with depths of 35, 55, and 85 mm which can also be compared with the results above at 45 mm. The effect is significant, indicating a very rapid attenuation of the pressure wave with distance from the plate. A columnar jet is still produced but is much weaker and emerges much later as water depth increases, as expected. There are strong indications of a cloud of cavitation bubbles, which is discussed below.

Figure 8 shows the area between the disk and surface as well as the developing surface mound and splash for a 45 mm water depth and 3.5 bar driver pressure. There is a very slight indication of a more cloudy area above the disk in the first frame, which in the second frame has developed into a cavitation cloud. There is a slight indication of an effect on the surface, but this does not have the smooth nature which develops later so is likely to be mist. By the third frame the cavitation cloud is half the height of the water depth and the surface distortion has a fully developed surface. The following row of images shows the cloud rising toward the surface and starting to also become conical in shape corresponding to the surface mound due to the direction of flow into the mound from below, besides the natural buoyancy of the cavitation bubbles. In the third row they reach the position of the original surface and start spreading outward at the same time as the surface splash becomes apparent. In the last row the cloud becomes more diffuse and individual cavitation bubbles become visible (Figs. 9 and 10).

Some tests were conducted with a different disk arrangement, without the foam cushion. The disk was mounted on the top of the support with a thin layer of

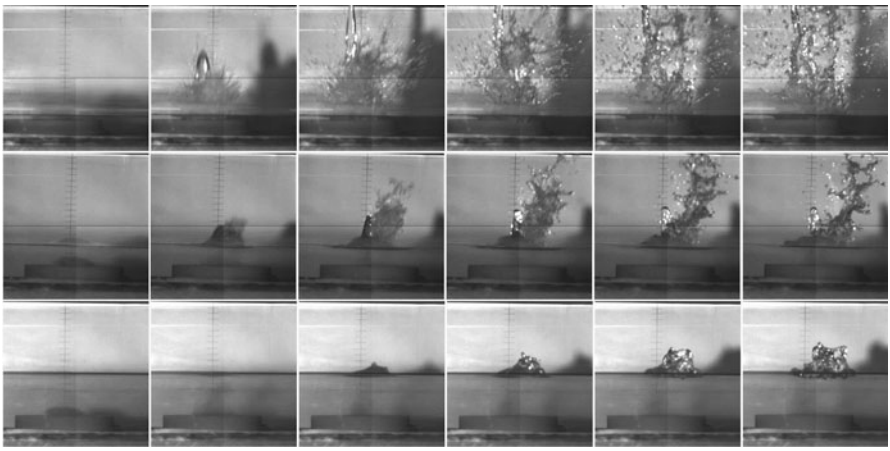

Fig. 8 Jet effects at similar times with water depths of 35, 55, and 85 mm using the spherical disk and a driver pressure of 3.5 bar

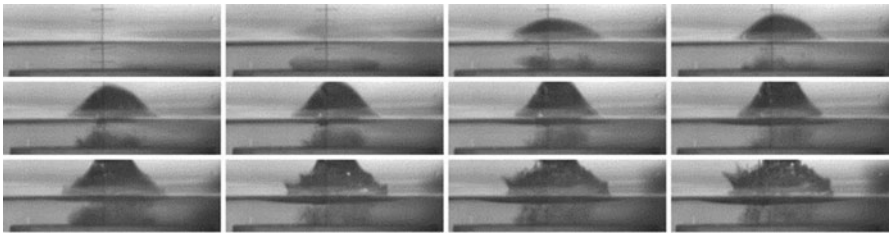

Fig. 9 Development of cavitation above the disk. Parabolic disk, 45 mm water depth and 3.5 bar driver pressure. Time between frames 3.3 ms

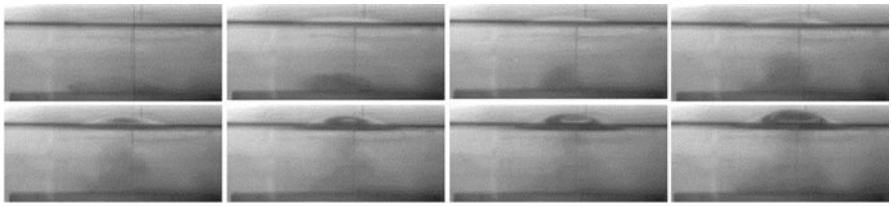

Fig. 10 Development of cavitation above the disk. Spherical disk, 70 mm water depth and 3.5 bar driver pressure. Time between frames 3.3 ms

flexible silicone adhesive holding it in place allowing an adjustable movement up to a stopping plate. In some cases the adhesive did not seal, and gas from the shock tube escaped. Although not the same as the gas bubble from an explosion, its trajectory is still of interest as similar mechanisms are at play. It starts with a smooth distortion of the water surface followed by breakdown into spray (Fig. 11).

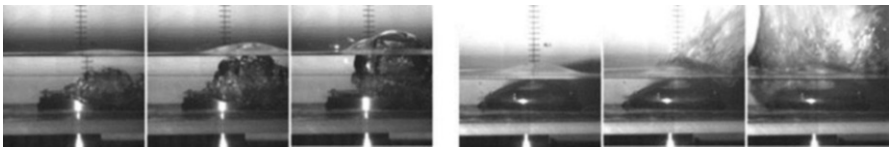

Fig. 11 Gas bubble movement. 3.5 bar driver pressure. Left: 85 mm water depth, movement limited to 0.5 mm. Right: 60 mm depth, 2 mm movement

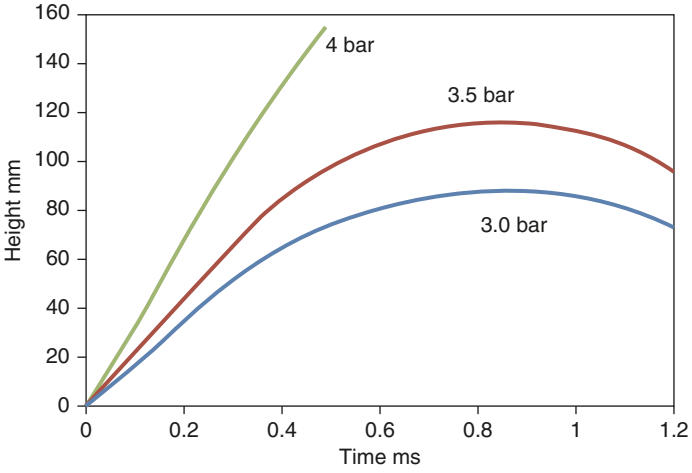

Fig. 12 Jet trajectory dependence on supply pressure

The height of the jet is strongly dependent on the driver pressure in the shock tube as shown in Fig. 12. The jet reaches a maximum height and then falls back under gravity. As shown above it is also strongly affected by the shape of the diaphragm.

4 Conclusion

A simple set of experiments are conducted in the generation of jets arising from an impulse supplied through an underwater disk driven by a shock wave from below. The behavior has features similar to those exhibited from an underwater explosion. The size, shape, and magnitude of the jet are influenced by the shape of the disk and the driving pressure.

References

1. R.H. Cole, *Underwater Explosions* (Princeton University Press, Princeton, 1948)
2. V.K. Kedrinskii, *Hydrodynamics of Explosion* (Springer, Berlin, 2005)
3. F.A. Costanzo, Underwater explosion phenomena and shock physics, in *Proceedings of IMAC-XXVIII, Society for Experimental Mechanics Inc*. (2010)
4. K. Takayama, K. Ohtani, Applications of shock wave research to medicine, Computational Methods and Experimental Measurements XII, 653–661 (2005)
5. M. Ichihara, M. Ripepe, A. Goto, H. Oshima, H. Aoyama, M. Iguchi, K. Tanaka, H. Taniguchi, Airwaves generated by an underwater explosion: Implications for volcanic infrasound. J. Geophys. Res. **114**(b03210) (2009)
6. B.J.P. Mortimer, M. Draxl, B.W. Skews, The interaction of a shock pulse and a liquid-air boundary. J. South African Acoustic Institute **7**, 1–6 (2000)
7. B.W. Skews, H. Karnovsky, Surface jets resulting from a shock-accelerated submerged surface, *3rd ISISWR*, Kleine H. (Ed.), Canberra (2006), Abstract only

Pressure Sensors for Hostile Environments

H. Fortier-Topping, M. Brouillette, V. Suponitsky, and D. Plant

Abstract We present sensor concepts eventually able to measure pressure pulses traveling in liquid metal, for example, for nuclear fusion applications. Two promising solutions have been tested and validated in water: a fast-response piezoelectric transducer mounted in a custom liquid-cooled housing and a stress bar where mechanical waves produced by the pressure pulse are dynamically measured using strain gauges.

1 Introduction

General Fusion's technology involves placing a highly magnetized toroidal plasma into a cavity surrounded by a liquid metal alloy. A large radially convergent pressure pulse is then focused onto the plasma-containing cavity [1]. The pressure pulse is generated by a number of radial hammers that, with computer control, impact a constellation of anvils. The anvils are in direct contact with liquid metal and transfer the kinetic energy of the striking hammers into the liquid metal as a short and intense pressure pulse. The design of the liquid metal compression system is based on detailed computer modeling. These models must be validated against smaller-scale prototypes that can generate the extreme pressure conditions that will be needed in a viable reactor. A key component of model validation is accurate measurement of fast pressure pulses in liquid metal.

These pressure impulses are expected to have an amplitude up to 700 MPa for 160 microseconds in liquid metal at temperatures between 330 °C to 540 °C. Ideally the entire pressure profile of the pulse should be captured, so the sensor's frequency

H. Fortier-Topping · M. Brouillette (✉)
Shock Wave Laboratory, Université de Sherbrooke, Sherbrooke, QC, Canada
e-mail: martin.brouillette@usherbrooke.ca

V. Suponitsky · D. Plant
General Fusion Inc., Burnaby, Canada

A. Sasoh et al. (eds.), *31st International Symposium on Shock Waves 2*,
https://doi.org/10.1007/978-3-319-91017-8_106

response must be over 100 kHz. Lastly, the sensor is to be compact enough to fit within a small opening at the bottom of the liquid metal chamber.

There is no known technology available to accurately measure extremely short, very large, pressure pulses propagating in high-temperature liquid metal. It is the intent of this project to develop a suitable technology and a functional prototype sensor.

2 Sensor Concepts

We present sensor concepts eventually able to measure pressure impulses traveling in liquid metal for nuclear fusion applications. Specifically, two promising solutions have been identified: (1) the use of a fast-response piezoelectric transducer mounted in a custom liquid-cooled housing and (2) the use of a stress bar [2], where mechanical waves are dynamically measured using strain gauges.

2.1 Cooled Piezoelectric Transducer Concept

For the first prototype, a commercially available PCB Piezotronics Model 119B12 piezoelectric sensor was selected, and a housing was designed to protect it from the hostile environment (Fig. 1). Except for the sensing extremity of the sensor, an insulating ceramic layer is put around a water-cooled stainless steel casing into which the sensor is installed. In the casing, 20 1 mm diameter holes are placed around the sensor. Water flows through the 20 holes to keep the sensor below its maximum operating temperature of 200 °C. The holes are connected in parallel, so the water flows downward in ten channels and flows upward in the other ten. The water flows in a closed loop which provides water at 20 °C and ∼4 bars at the inlet of the casing.

For the sensing extremity, a 17–4 PH stainless steel protective diaphragm is added in front of the sensor diaphragm. To ensure a direct contact between both diaphragms, a protective plate, made of nitrile butadiene rubber, is added. Water circulates in the cavity between the protective diaphragm and the protective plate. Because the cavity in front of the diagram acts like a low-pass filter, the channel length is designed to minimize the impact on the frequency response.

The sensor thermal protection is sized to keep the sensor under 200 °C over the operating temperature range of 330 °C to 540 °C. Heat transfer simulations were performed to ensure a design within the operating temperature of the sensor while simultaneously preventing metal solidification on the outside of the cooled housing. To achieve this, it was found that a minimal convection coefficient of 3000 W/(°Cm^2) is required inside the cooling channels, along with an extracted power of around 10 kW.

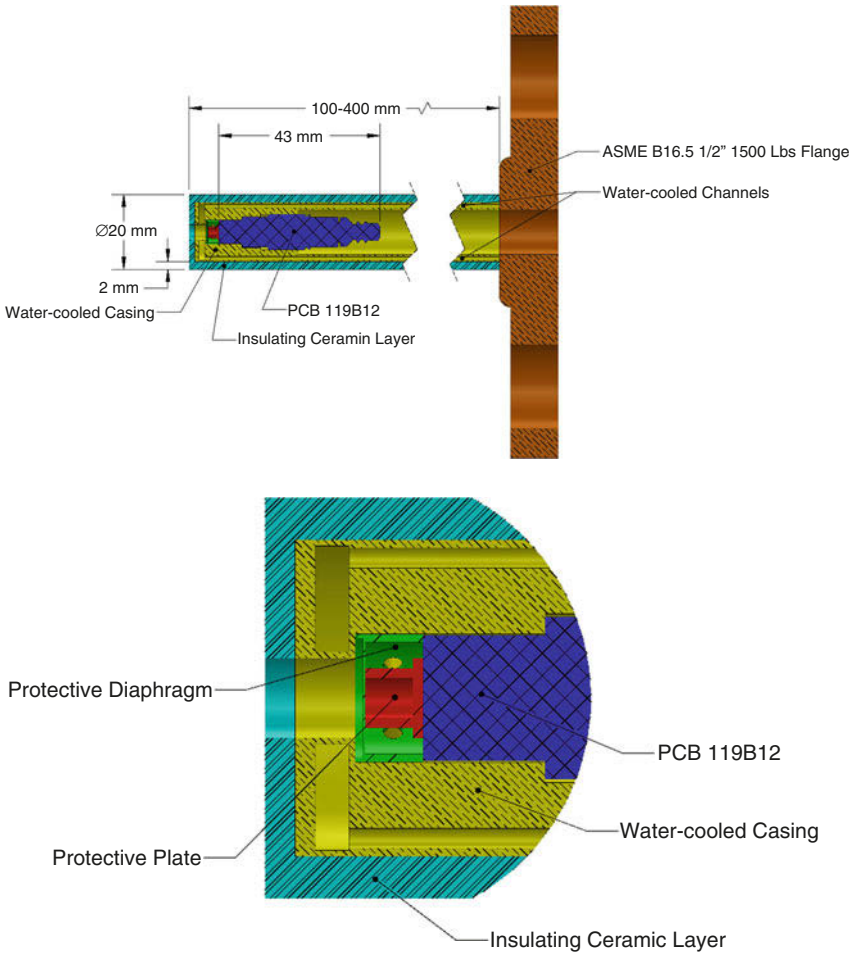

Fig. 1 Embedded piezoelectric pressure transducer with cooling housing. Top: general arrangement. Bottom: detail of the transducer tip assembly

Figure 2 shows the temperature profile of the analysis with the assumed minimal convection coefficient; we see that all the walls inside the casing and the sensor diaphragm are kept below the target temperature of 200 °C, while the outside of the casing is maintained above the fusion temperature of the liquid metal. It is estimated that a water flow rate of approximately 1.5 l/min is necessary to get the required cooling effect, with an estimated turbulent forced convection coefficient of around 8000 W/(°C m^2) resulting in a temperature rise of the water of approximately 10 °C between the entrance and the exit of the channels.

Obviously, the embedded transducer in such a housing may change its calibration and frequency response, and these issues are addressed in the Experimental Validation section below.

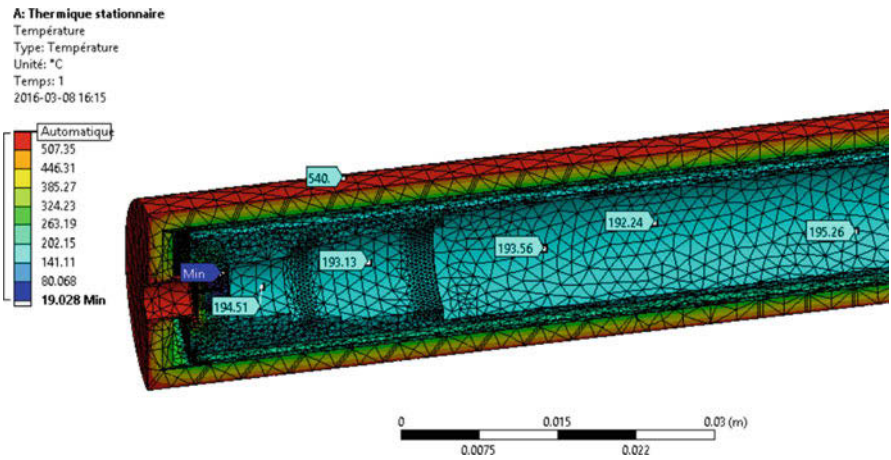

Fig. 2 Temperature distribution for the embedded piezoelectric pressure transducer with cooling housing. Exterior temperature set at 540 °C and inlet cooling water set at 25 °C

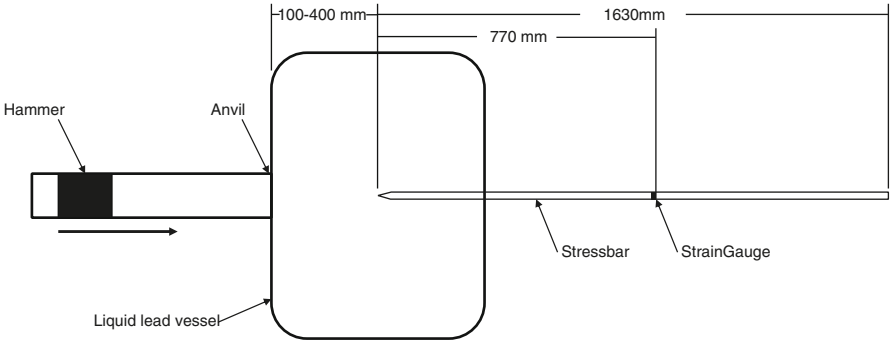

Fig. 3 Schematic of stress wave transducer system used to measure pressure pulses produced by hammer motion within liquid lead vessel

2.2 Stress Wave Transducer Concept

For the second concept, a simple metallic bar is inserted into the wave propagation medium, and strain gauges, located on the bar outside the medium away from the high-temperature environment, are used to measure the stress wave produced by the pressure pulse (Fig. 3). The length of the stress bar and the location of the strain gauges are optimized from a simple 1-D acoustic wave analytical model for the propagation of the waves produced by the pressure pulse within the bar. The stress bar actually comprises a solid conical tip attached to the proximal end of a hollow tube (Fig. 3). As for the previous concept, careful system calibration is required to ensure meaningful results, as described below.

3 Experimental Validation

A laboratory test rig was designed and built to produce representative pressure pulses in water to test the proposed sensor concepts. This pressure pulse is produced by the impact of a hammer on piston immersed in a water tube (Fig. 4). A critical step in testing is to determine the calibration between the actual pressure-time history experienced by the sensor systems and their output. This is achieved by using a calibration method whereby the actual pressure is measured using a different piezoelectric pressure transducer immersed in the flow next to the tested sensor, i.e., the "PCB Input Sensor" in Fig. 4. The calibration is performed in a single run by comparing the actual measured pressure-time history either from the cooled piezoelectric transducer or the stress wave transducer with the PCB Input Sensor value. The calibration obtained from this run is thereafter used to infer actual pressure histories for different experimental conditions.

The graphs on the left of Fig. 5 show an example of a calibration run, where the top graph is the actual pressure-time history measured with the PCB Input Sensor, the middle graph is the response of the cooled piezoelectric transducer, and the bottom graph is the deconvoluted output of the cooled piezo, showing excellent agreement with actual values, indicative of the proper identification of the system calibration.

The graphs on the right of Fig. 5 show a similar experiment, performed at different conditions, demonstrating the use of the calibration obtained from the data on the left to perform the sensor output deconvolution. The agreement between the actual (top right graph) and deconvoluted (bottom right graph) signals is again excellent, demonstrating that the single calibration step is sufficient to capture the correct pressure-time history for the cooled piezoelectric transducer concept. The same approach was used with the stress wave transducer system, and similar results were obtained over a wide variety of pulse durations and amplitudes.

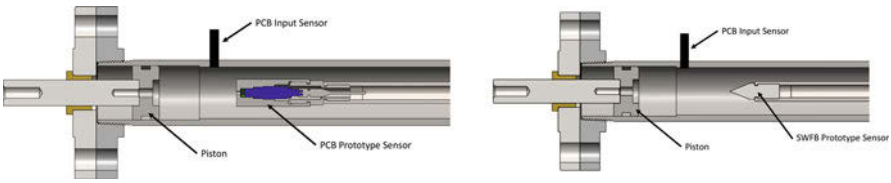

Fig. 4 Laboratory test rig for sensor calibration and concept validation. Left: cooled piezoelectric transducer concept. Right: stress wave transducer concept

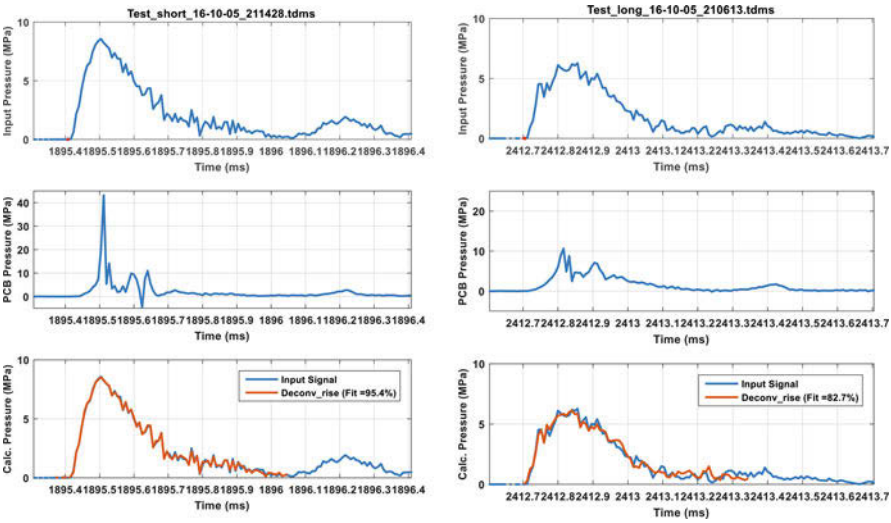

Fig. 5 Left: calibration run with cooled piezoelectric transducer concept. Top left: actual pressure-time history measured with the PCB Input Sensor. Middle left: response of cooled piezoelectric transducer. Bottom left: deconvoluted output (red) of the cooled piezo compared to actual pressure-time history (blue). Right: test run with cooled piezoelectric pressure transducer, reusing the calibration obtained from data on the left. Top right: actual pressure-time history measured with the PCB Input Sensor. Middle right: response of cooled piezoelectric transducer. Bottom right: deconvoluted output (red) of the cooled piezo compared to actual pressure-time history (blue)

4 Conclusion

The project proposed to base the required sensor on devices already successfully used for pressure and force measurement in impulsive flow facilities such as shock tubes and shock tunnels and adapt them for the liquid metal environment. Promising designs were prototyped and validated with representative high-pressure impulses produced in water on a specially built test bench. Liquid metal is not a common medium in which pressure/force measurement is done: the innovative nature of the methodology is the adaptation of shock tube measuring techniques to such an environment.

References

1. D. Richardson et al., Status of progress towards acoustic magnetized target fusion at general fusion, in *Proceedings of the 34th Annual Conference of the Canadian Nuclear Society* (2013)
2. D.J. Mee, Dynamic calibration of force balances for impulse hypersonic facilities. Shock Waves **12**, 443 (2003)

Visualization of Inception, Propagation, and Collapse Process of Underwater Positive Streamer

T. Sato, R. Kumagai, T. Nakajima, K. Ohtani, A. Komiya, S. Kanazawa, and T. Kaneko

Abstract Visualization of a whole process of underwater positive primary streamers is difficult because the time scales among inception and propagation of streamers, collapse of streamer gas channels, and formation of residual fine bubbles are different and the spatial scale is a micrometer scale. This study succeeded in successive visualization of the whole process of the streamer with a frame rate of 10 Mfps.

1 Introduction

Underwater streamers are pre-breakdown phenomena and are propagated with ∼2 km/s for a primary streamer and ∼20 km/s for a secondary streamer [1–3]. At an inception of the primary streamer, protrusion-shaped bubbles are formed and increase electric field strength in the vicinity of the tip of the electrode. When the strength is over a threshold, the streamer starts to propagate. The streamer forms gas channels, and small bubbles are generated after collapse of the channels. If the process for generation of these residual small bubbles is clarified, it will be helpful to understand the formation mechanism of smaller bubbles of less than microscale, because these residual bubbles have potential to generate nanoscale bubbles. However, it was difficult to visualize a whole process of streamer phenomena due to different time scales for inception, propagation, and collapse. In this study, we aimed at visualization of the process for one streamer discharge.

T. Sato (✉) · R. Kumagai · T. Nakajima · K. Ohtani · A. Komiya
Tohoku University, Sendai, Japan
e-mail: sato@ifs.tohoku.ac.jp

S. Kanazawa
Oita University, Oita, Japan

T. Kaneko
Tohoku University, Sendai, Japan

A. Sasoh et al. (eds.), *31st International Symposium on Shock Waves 2*,
https://doi.org/10.1007/978-3-319-91017-8_107

2 Experimental Setup

A single-shot pulsed positive high voltage with duration of 10 μs was applied to a needle electrode with tip radius of around 40 μm. A capacitance was 666 pF. The discharge reactor was filled with 3 ml of ultrapure water. Streamer propagation was visualized at 10 Mfps using a high-speed camera (Shimadzu, Hyper Vision HPV-X2) with a microscope lens (Keyence, VH-Z50L). The synchronized waveforms of the applied voltage and the discharge current were monitored on the oscilloscope with the camera gate timings. Further details of the experimental methods are described in reference [1–3].

3 Results and Discussion

Figure 1 shows a series of images of the primary streamer process for inception, propagation, and collapse. At $t = 0.2$ μs, a microscale channel-like bubble is formed, and then it grows. After 0.6 μs, several channel-like bubbles are formed and elongate. At around 1.4 μs, these bubbles form a bubble cluster and grow continuously. The electrical charges can be accumulated in the bubbles, and a protrusion-shaped bubble is formed at 3.0 μs. These accumulated charges are concentrated in the protrusion-shaped bubble and the streamer incepted when the electric field strength becomes greater than the threshold of 23 MV/cm [3]. The propagation stops in several μs, but the gas channels grow. At around 7 μs, the gas channels start to collapse, and they collapse at around 25 μs.

Figure 2 shows a series of images of the propagation of the shock wave of the primary streamer. To make clear the location of the shock wave, the difference is emphasized in the images against the one at $t = 2.1$ μs. At $t = 2.3$ μs, the primary streamer started to propagate and stopped the propagation at 2.6 μs. The shock wave was generated at the starting time of the propagation of the primary streamer because the propagation velocity is around 2 km/s, and the shock wave expanded after stopping the propagation. This result showed that the shock wave was not generated in the inception period. The reason why multiple shock waves were generated during the primary streamer was propagated is that the shock waves were generated along the filaments of the primary streamer [1].

4 Conclusion

We have succeeded in visualizing a series of a whole process for streamer phenomena such as the bubble formation process for the inception of the primary streamer at the tip of the electrode, the propagation of the primary streamer with the shock wave, the formation and collapse of streamer gas channels, and generation of residual fine bubbles.

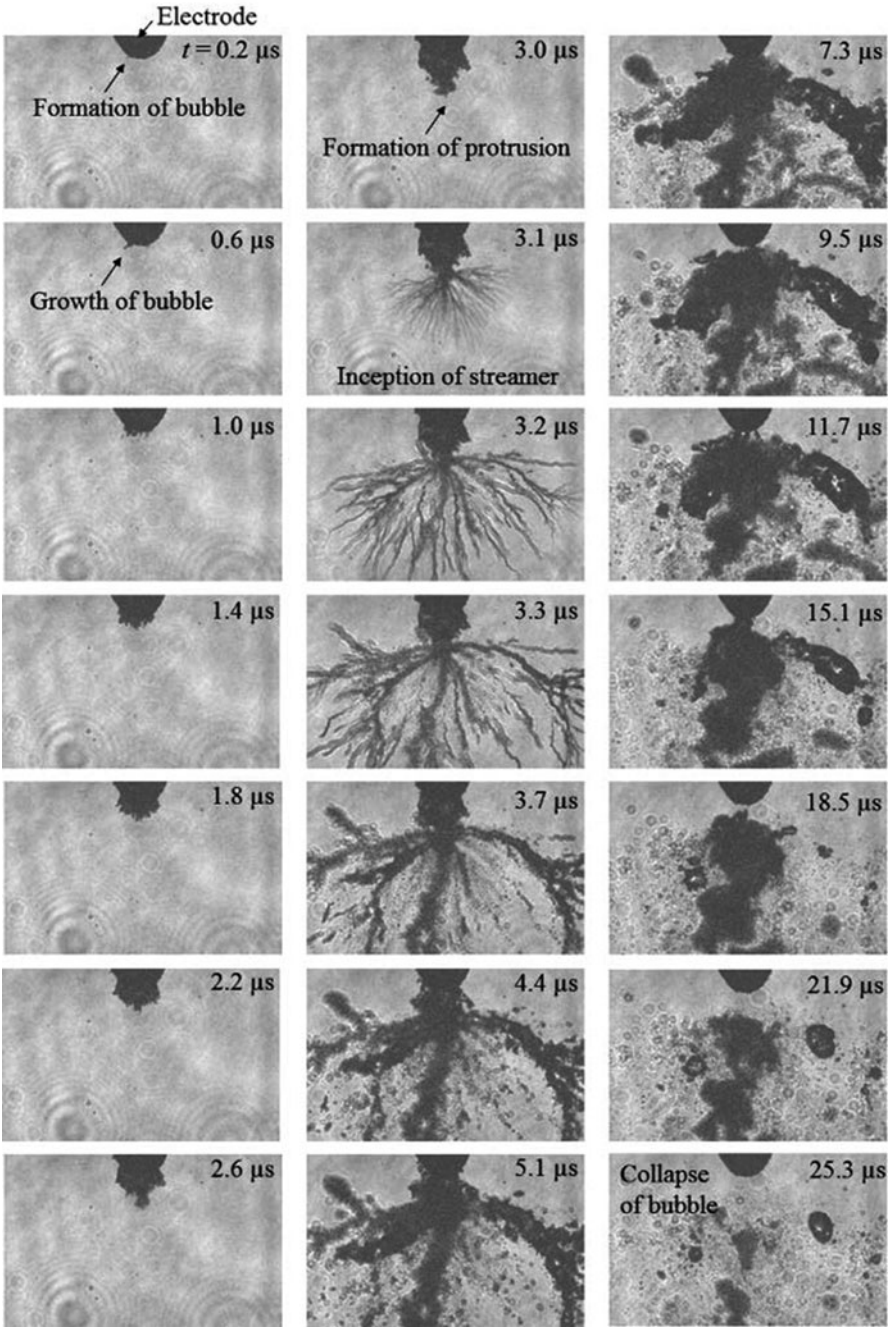

Fig. 1 A series of images of the primary streamer process for inception, propagation, and collapse. The width of the image is 690 μm

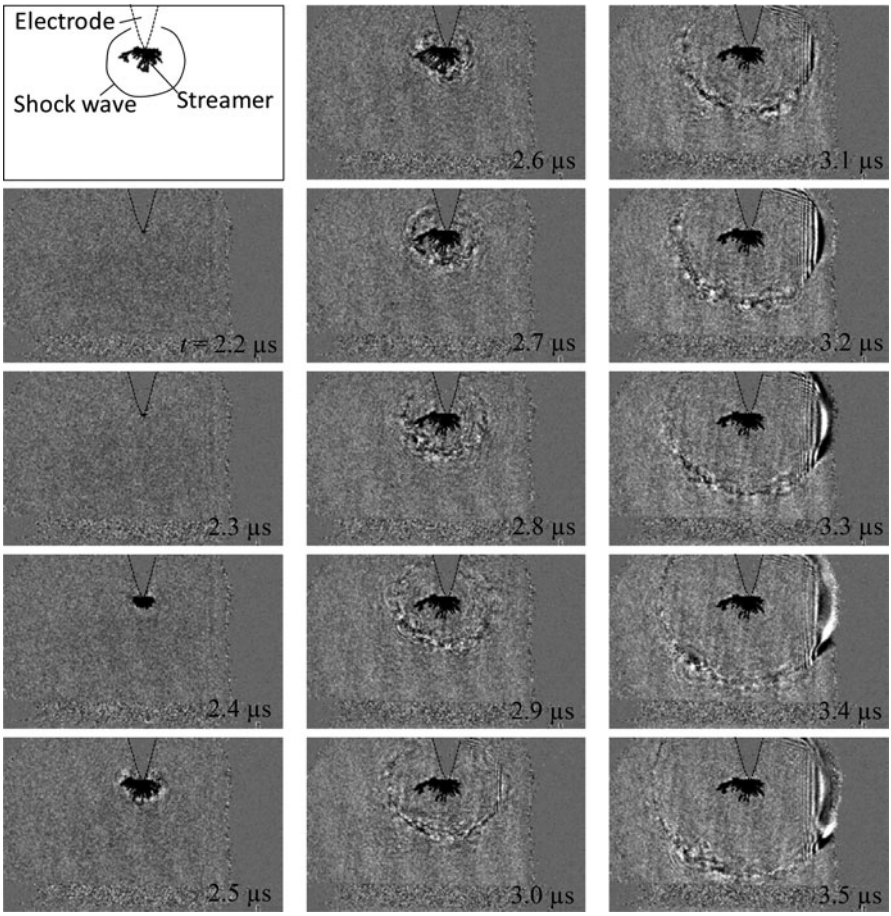

Fig. 2 A series of images of the propagation of the shock wave of the primary streamer. The width of the image is 5.9 mm

Acknowledgments This work was supported by JSPS KAKENHI Grant Number 16H02311 and 24108004 and the Collaborative Research Project of the Institute of Fluid Science, Tohoku University.

References

1. H. Fujita et al., Spatiotemporal analysis of propagation mechanism of positive primary streamer in water. J. Appl. Phys. **113**, 113304 (2013)
2. H. Fujita et al., Fast propagation of an underwater secondary streamer by the appearance of a continuous component in the discharge current. EPL **105**, 15003 (2014)
3. H. Fujita et al., Initiation process and propagation mechanism of positive streamer discharge in water. J. Appl. Phys. **213301**, 116 (2014)

Optimization and Design of a Fully Instrumented Mach 12 Nozzle for the X3 Expansion Tube

P. Toniato, D. E. Gildfind, P. A. Jacobs, and R. G. Morgan

Abstract This paper describes the optimization and design of a new Mach 12 hypersonic nozzle to be used in the X3 expansion tube. The contoured nozzle has been designed and built to accommodate large-scale models and reproduce constant Mach 12 flows to allow for scramjet testing. The requirements for this nozzle were a core flow of at least 300 mm and exit flow angles below 2°. A new optimization process has been developed, using a parallel Nelder-Mead method, and a new shape has been calculated where CFD analysis indicates the design objectives were successfully met. Off-design performance has been evaluated, and the nozzle has been shown to retain good core flow size, Mach number and low flow divergence for different inflow conditions.

1 Introduction

At the Centre for Hypersonics at the University of Queensland (UQ), a variety of scramjet engines have been tested and analysed in the T4 reflected shock tunnel (RST). While this facility (and RSTs at this scale in general) can achieve test times of $\sim 0.7 - 1.0$ ms [1] at Mach 10 conditions, they are limited by two factors: the flow total pressure that needs to be structurally contained in the facility and the amount of dissociation in the test gas generated by the stagnation process, where the gas reaches temperatures of several thousands of degrees.

A 1:2 model of the Mach 12 REST (rectangular to elliptical shape transition) engine designed by Smart [2] has been tested in T4 at a Mach 10 condition with a Mach 12 equivalent enthalpy, assuming the flow generated is equivalent to the one behind the shock generated from a forebody shock. However, correct pressure length scaling was not achieved, as the total pressure requirements were not attainable by the facility.

P. Toniato (✉) · D. E. Gildfind · P. A. Jacobs · R. G. Morgan
School of Mechanical and Mining Engineering, University of Queensland, St Lucia, Brisbane, QLD, Australia
e-mail: p.toniato@uq.edu.au

A. Sasoh et al. (eds.), *31st International Symposium on Shock Waves 2*,
https://doi.org/10.1007/978-3-319-91017-8_108

The X3 expansion tube facility at the UQ has been recently used to successfully investigate scramjet combustion in Mach 10 pressure-length scaled conditions [3], showing that expansion tubes can be used to examine scramjet performance when correct pressure-length scaled conditions are targeted. Test flows in expansion tubes are never stagnated, thus removing both the total temperature and pressure limitations of RSTs.

To extend the operating envelope of the X3 expansion tube to enable Mach 12 scramjet testing, a variety of upgrades are necessary, amongst which is the design of a new hypersonic nozzle to work at Mach 12.

2 Nozzle Design

In an expansion tube, the flow is already hypersonic at the entrance of the nozzle, whereas in classical convergent-divergent supersonic nozzles, supply region the flow is subsonic; thus hypersonic nozzles for expansion tunnels are characterized by the absence of a throat (where the Mach is unitary) and being only divergent. Previous work on hypersonic nozzles has been undertaken by Craddock [4] and Scott [5], where the latter developed a Mach 10 nozzle for the X2 expansion tube. This nozzle subsequently has been scaled up and built for X3, where currently it is the only nozzle available for the facility. Although the Mach 10 nozzle has been shown to be capable of producing Mach 10 scramjet conditions, its exit diameter (ø 440 mm) and the scramjet sensitivity to inflow Mach numbers and flow divergence make it unsuitable for operating at higher Mach numbers.

Initial work on a Mach 12 nozzle was started by Wei et al. [5], targeting high enthalpy conditions, but it was decided to modify the target to a denser, scramjet condition. The optimization process has been largely modified and improved. The nozzle profile has been determined by an optimization process whose features are detailed in the rest of this study.

2.1 Contour Description

The nozzle contour in the optimization process has been defined by means of 11 Bezier nodes defining a 2.8-meter-long Bezier curve. In the literature other modelling choices were possible, such as the use of cubic spline polynomials [6], or use of a hyperbolic section profile, or a high-order polynomial [7]. Bezier curves have been chosen as they produce smooth profiles, guaranteeing that the curve is tangent to the control polygon at the endpoints, ensuring smooth transition at the acceleration tube connection. The initial diameter is fixed to that of the acceleration tube, 182.6 mm. The length of the nozzle has been fixed to 2.8 m, to integrate with the new test section and to allow for models to be aligned with windows for optical access.

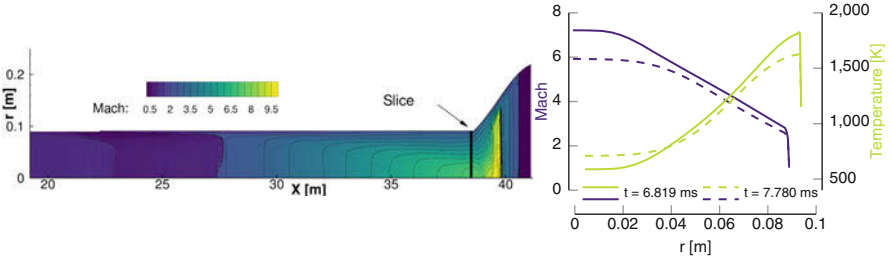

Fig. 1 Axisymmetric simulation of Mach 10 scramjet condition in X3 expansion tube (left). Mach number and temperature at the nozzle inlet across the test slug (right) at start and end of test time

2.2 Nozzle Inflow

The flow in an expansion tube is time-varying and radially nonuniform, and full facility simulations are necessary to provide detailed insight into the nozzle inflow properties. Work towards full facility simulations of X3 is currently being carried out in a separate study, where hybrid simulations of a Mach 10 condition have been used to estimate the flow through the acceleration tube and nozzle. These simulations, while for a different condition, are similar to a future Mach 12 condition. As shown in Fig. 1 (right), the boundary layer is significant and varies between 30 mm and 50 mm through the test gas, compared to the tube radius, 91.3 mm.

Properties in the test gas are not steady, but, due to the computational cost associated with simulating transient flows, it has been assumed that the inflow is steady with averaged properties of the test gas. The nozzle inflow has been computed assuming that the axial velocity follows a 1/7th boundary layer power law (i.e. fully turbulent) and that the boundary layer thickness is 30 mm radially. The inflow profile has been determined assuming an inflow pressure of 10 kPa, constant across the radius, velocity of 3650 m/s and temperature of 600 K, for a calculated inflow Mach of 7.5, all chosen to closely reproduce the free-stream design condition of the Mach 12 REST engine (dynamic pressure of 50 kPa at 36 km altitude, for a velocity of 3.7 km/s, pressure of 500 Pa and temperature of 240 K).

In previous studies, the nature of the tube boundary layer of the expanded test gas has been found to be directly correlated with the test flow quality observed. It has been noted [8] that laminar boundary layers produce flows of good quality, and fully turbulent ones produce still reasonable flow quality, but if the boundary layers are transitional, the quality is unacceptable.

Prediction of hypersonic boundary layer transition in expansion tubes has been difficult to establish, with only few correlations being established [8, 9]. The simplest method, often used at the HYPULSE facility, suggests that if the unit Reynolds number, Re_l, $\geq 1.4 \cdot 10^6$ 1/m, the flow will be fully turbulent. Therefore, for the nozzle inflow condition shown above with $Re_l \sim 6.5 \cdot 10^6$ 1/m, the inflow will be assumed as fully turbulent.

2.3 Contour Optimization

The goal of the design is to obtain a nozzle profile that produces a uniform Mach 12 core flow and that, the same time, minimizes the flow exit angle at the nozzle exit. This multi-objective problem has been reduced to a single objective problem by means of linear weighting of the different objectives. The optimization problem is therefore defined as follows:

$\overrightarrow{X} = [x_0, x_1, \ldots, xi]$ with $0 \leq i \leq 11$ Bezier points.

Objective function:

$$f\left(\overrightarrow{X}\right) = \left(f_\theta + f_{\text{Mach}} + f_{\text{pressure}}\right)^2$$

With $f_\theta, f_{\text{Mach}}, f_{\text{pressure}}$ given by:

$$f_\theta = \frac{\phi_\theta}{N} \sum_{j=1}^{N} \left(\theta_j\left(\overrightarrow{X}\right) - \theta_{\text{design}}\right)^2$$

$$f_{\text{Mach}} = \frac{\phi_{\text{Mach}}}{N} \sum_{j=1}^{N} \left(M_j\left(\overrightarrow{X}\right) - M_{\text{design}}\right)^2$$

$$f_{\text{penalty}} = \begin{cases} 0 & 0 < y_i < y_{i+1} \\ Z & \text{otherwise} \end{cases}$$

where θ_j and M_j are, respectively, Mach number and flow angle in the exit plane, with N the number of the radials cells in the core flow. ϕ_θ, ϕ_{Mach}, are weights, tuned to balance the relative importance of each terms of the objective function. y_i indicates the evaluated nozzle profile. f_{penalty}, in which Z is a large number, is used to prevent the optimization algorithm to converge to a solution in which the nozzle profile curves inwards.

Function evaluations are conducted by means of a complete simulation of the nozzle, using UQ's EILMER3 CFD code [10] for 2D and 3D Navier Stokes compressible flow. The simulations have been carried out using NENZFR-R [11], a block-marching code built on top of EILMER3 in order to save computational time. Simulations included viscous effects and as mentioned above were fully turbulent using the $k - \omega$ turbulence model [12]. The test gas has been modelled as five-species air, fully reacting, using the Gupta reaction scheme [13]. Alternative methods, like the method-of-characteristics plus displacement corrections, had been considered but discarded because the presence of a thick boundary layer invalidated their assumptions.

This optimization problem falls into the category of optimization of expensive black-box functions, as each of the function evaluation takes a few hours. The algorithm of choice for this optimization was a modified, parallel Nelder-Mead simplex algorithm [14], in which the evaluation of the different points of the simplex

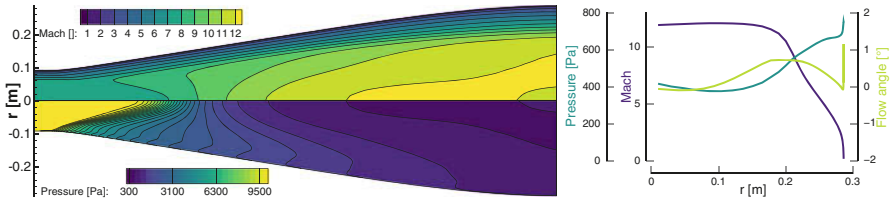

Fig. 2 Optimized Mach 12 nozzle Mach number and pressure contours (left). Exit Mach number, flow angle and pressure for optimized Mach 12 nozzle (right)

occurs in parallel. This algorithm represents a compromise between the necessity of parallel function evaluations, the computational capability available at the time, simple algorithm implementation and the empirical observation that the objective function is well behaved. The optimization was considered converged once the variations in the locations Bezier Points were below 0.1 mm on average.

2.4 Results

The final nozzle profile is shown in Fig. 2 (left), showing Mach and pressure contour plots. Attention has been dedicated to ensure that the profile generated is shock-free. Exit flow properties are shown in Fig. 2 (right), and they show an excellent profile in terms of Mach number, with a core flow diameter in excess of 360 mm and exit flow angle in average $\sim 0.3^{\circ}$.

On the other hand, a less satisfactory pressure profile is present, which is due to recompression effects that take place in the last 0.3 m, as a side effect of the flow redressing process. This is an intentional result of the weights chosen for the different parts of the objective function, as it has been decided to prioritize flow exit angle against pressure. It has also been observed that if an additional pressure term was introduced to the objective function, it would have a detrimental effect on flow exit angle and would create stronger waves centered at the nozzle edge, thereby reducing the total core flow diamond available for model testing. A final comparison with the current Mach 10 nozzle is available in Fig. 3.

3 Nozzle Off-Design Performances

The nozzle has been designed to target the specific Mach 12 condition (mentioned above), but it will often operate at off-design conditions. A sensitivity study has been undertaken, and a partial summary of the results is shown in Fig. 4. Inflow velocity, inflow Mach number and boundary layer thickness have been varied. Exit flow angle was found to be largely invariant to the inflow properties with a

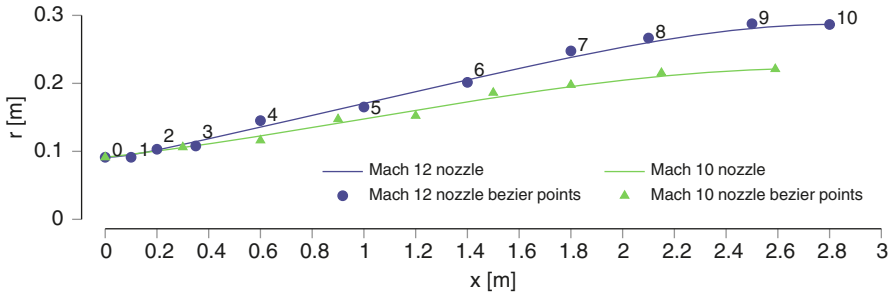

Fig. 3 Comparison of Mach 12 nozzle and current Mach 10 nozzle profile

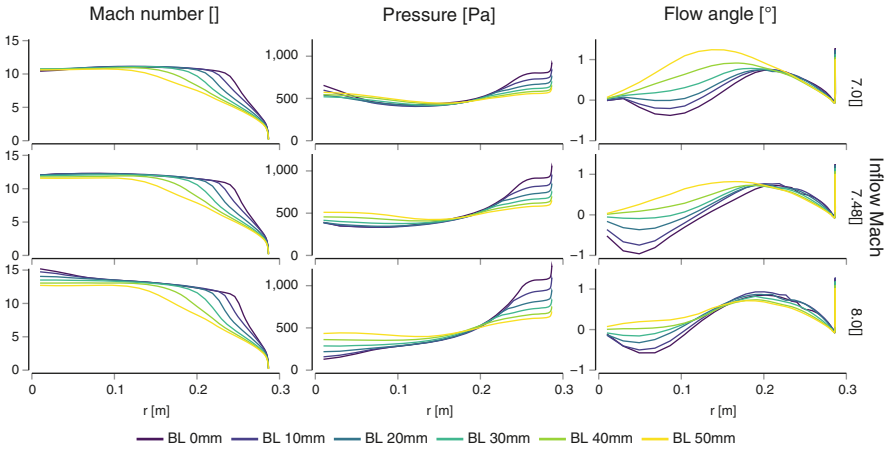

Fig. 4 Nozzle performance with varying inflow Mach number and boundary layer (BL) thickness for an inflow velocity of 3650 m/s

variation of $\pm 1^{\circ}$. Exit pressure and exit Mach number exhibit a certain sensitivity to inflow Mach number. If inflow Mach number is >7.5,the gas is overexpanded in the nozzle centreline, resulting in a less uniform core flow. The nominal boundary layer thickness was 30 mm, but the analysis has shown that acceptable Mach number exit profiles are maintained above 20 mm. With lower thickness, exit flow quality is decreased.

4 Nozzle Manufacturing

The mechanical design has been carried out and the nozzle has been built. The nozzle will have a new connection system to the acceleration tube, which allows for a pitot rake to be inserted at the nozzle inlet to measure radial variation in impact

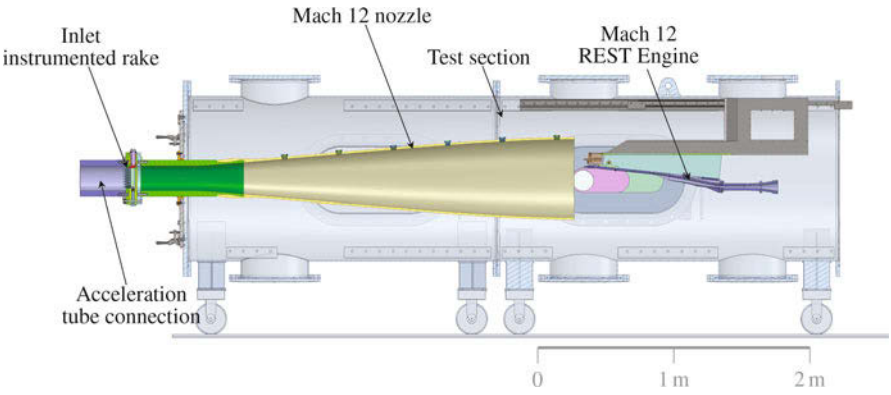

Fig. 5 Mach 12 nozzle inside X3 test section

pressures at nozzle inflow. The nozzle wall will host six wall sensor mounts, able to simultaneously house pressure transducers and heat transfer gauges.

The nozzle was filament-wound from fibre glass around a foam mandrel. A steel insert, which contains the initial part of the nozzle profile, was machined and inserted on the mandrel. Then, the fibre glass was wound around the mandrel-steel insert assembly. After the winding process, the nozzle has been removed and polished. The nozzle sits inside the dump tank and is connected to the acceleration tube by means of the steel insert. Adequate sealing is provided by O-rings around the polished external surface of the steel part. A CAD representation of nozzle installed in the test section is shown in Fig. 5.

5 Discussion

The validity of the parallel Nelder-Mead method has been proven by means of multiple restarts from different initial profiles, which showed (local) convergence to the same profile. Alternative global optimization methods have been considered, like evolutionary/genetic algorithms, or global optimization using surrogate modelling/response surfaces [15], but they have been shown to converge slower, requiring a higher number of function evaluations. In addition, they have shown to be sensitive to tuning parameters, and the high cost of function evaluations resulted in a reduced capability to modify the parameters specific to each algorithm. Black-box optimization is an active field of research, and further work could investigate the capability of newer algorithms to converge to a solution reducing the number of total function evaluations.

A number of simplifying hypotheses have been made to complete this optimization, amongst which the most significant is the steady-state assumption for the inflow; however no feasible alternatives are currently available to optimize for a fully transient inflow condition.

6 Conclusions

An expansion tube hypersonic nozzle has been designed to target Mach 12 scramjet conditions. The optimized nozzle profile has shown to produce excellent results for on-design condition and good results in off-design condition if the entry Mach number of the test flow can be maintained around 7–7.5. Exit flow angle has proven to be insensitive to all inflow parameters.

The nozzle has been manufactured, and its nozzle performance will be analysed experimentally once it is commissioned. New instrumentation will allow for a full characterization of the performance of this hypersonic nozzle, with new hardware built to obtain experimental measurements of nozzle transient inflow, allowing to determine the test gas free stream properties and significantly reducing uncertainties on them.

Acknowledgements This research is supported by an Australian Government Research Training Program (RTP) Scholarship and the Cooperative Research Centre for Space Environment Management (SERC Limited) through the Australian Government's Cooperative Research Centre Programme. This research was undertaken with the assistance of resources from the National Computational Infrastructure (NCI), which is supported by the Australian Government. The authors finally wish to thank F. De Beurs and N. Duncan for technical assistance with the X3 hardware.

References

1. Doherty, L.J., Smart, M.K., and Mee, D.J. Experimental Testing of an Airframe Integrated 3-D Scramjet at True Mach 10 flight Conditions. in *19th AIAA International Space Planes and Hypersonic Systems and Technologies Conference*. American Institute of Aeronautics and Astronautics (AIAA)
2. Wise, D., *Experimental Investigation of a Three Dimensional Scramjet Engine at Hypervelocity Conditions*. (University of Queensland, 2015). pp. 197–197
3. Sancho Ponce, J., *Scramjet Testing at High Total Pressure*. (University of Queensland, 2016)
4. Craddock, C.S., *Computational Optimization of Scramjets and Shock Tunnel Nozzles*. (University of Queensland, 1999)
5. Scott, M.P., *Development and Modelling of Expansion Tubes*. (University of Queensland, 2007)
6. Shope, F. Contour design techniques for super/hypersonic wind tunnel nozzles. in *24th AIAA Applied Aerodynamics Conference*. American Institute of Aeronautics and Astronautics (AIAA)
7. R.S.M. Chue et al., Design of a Shock-Free Expansion Tunnel Nozzle in Hypulse. Shock Waves **13**(4), 261–270 (2003)
8. Erdos, J.I. and Bakos, R.J. Prospects for a quiet hypervelocity shock-expansion tunnel. in *25th Plasmadynamics and Lasers Conference*. American Institute of Aeronautics and Astronautics
9. McGilvray, M., *Scramjet Testing at High Enthalpies in Expansion Tube Facilities*. (University of Queensland, 2008)
10. R.J. Gollan, P.A. Jacobs, About the formulation, verification and validation of the hypersonic flow solver Eilmer. Int. J. Numer. Meth. Fluids **73**(1), 19–57 (2013)

11. Jacobs P. A., G.R.G.a.Z.F., Still Using Nenzf? That's So 1960s, in *International Workshop on Shock Tube Technologie*. (Brisbane, 2011)
12. Wilcox, D. Formulation of the K-Omega turbulence model revisited, in *45th AIAA Aerospace Sciences Meeting and Exhibit*. AIAA
13. Gupta, R. N., et al., A review of reaction rates and thermodynamic and transport properties for an 11-species air model for chemical and thermal nonequilibrium calculations to 30000 K, Technical Report NASA-RP-1232, NASA, (1990)
14. D. Lee, M. Wiswall, A parallel implementation of the simplex function minimization routine. Comput. Econ. **30**(2), 171–187 (2007)
15. R.G. Regis, C.A. Shoemaker, Constrained global optimization of expensive black box functions using radial basis functions. J. Glob. Optim. **31**(1), 153–171 (2005)

Heat Flux Measurement of Flat Delta Plate Using Phosphor Thermography Technique in Gun Tunnel

Han Shuguang, Jia Guangsen, Bi Zhixian, and Wen Shuai

Abstract Phosphor thermography technique (PTT) is a global optical heat flux measurement method. Phosphor thermography system based on the temperature-sensitivity material has been developed in China Academy of Aerospace Aerodynamics (CAAA), and a brief introduction of PTT is made; the basic parts of this system include phosphor material, calibration systems, UV systems, image acquisition system, and date reductions. CAAA FD-20 gun tunnel is also introduced in this paper. A series of experiments of flat delta plate is performed in FD-20. Global heat flux distribution of the model which shows flow transition is discussed, and a comparison result which is obtained by using traditional heat flux measurement method (thin-film heat transfer sensors) is made; an evaluation on phosphor thermography technique has been made.

1 Introduction

Phosphor thermography technique is a global optical heat flux measurement method in hypersonic wind tunnel. The phosphor material fluoresces when excited by ultraviolet radiation, and their emission intensity is dependent on their temperature. Contrasted with the traditional measurement methods (e.g., thin-film heat transfer sensors, the thermal couples), the thermography is a noncontact method which could quantitatively obtain the global distribution of the heat flux and capture the high heat flux region; furthermore, it also could measure the heat flux of region which has limit space to place the gauges.

CAAA carried out PTT which is used in hypersonic gun tunnel in 2006 [1]. In this article, an overview of phosphor thermography method is first presented; then, results of a flat delta plate which is fabricated with ceramic are given to show the heat flux distributions at different Reynolds number in CAAA FD-20 gun tunnel. High heat flux region induced by flow transition is presented.

H. Shuguang (✉) · J. Guangsen · B. Zhixian · W. Shuai
China Academy of Aerospace Aerodynamics, Beijing, China

A. Sasoh et al. (eds.), *31st International Symposium on Shock Waves 2*,
https://doi.org/10.1007/978-3-319-91017-8_109

2 Phosphor Thermography Technique

2.1 Basic Theory and System

The phosphor material is developed based on the lanthanum. Prior to excitation, the material's electronic levels are populated in the ground state, and the excitation sources (ultraviolet) deposit the energy in the material, which result in a higher electronic state, and this process is accomplished by exposure to electromagnetic radiation, which includes visible light (Fig. 1). The atomic configuration won't remain permanently excited but will return to its ground state or assume an intermediate level. With the change of environment temperature, the intensity of visible light changes in inverse proportion. Base on this phenomenon, the temperature distribution of model surface can be calculated out by the transformation which relies on the intensity-temperature relationship [2].

Phosphor thermography system was shown in Fig. 2, before the test, model coated with phosphor material is fixed in the wind tunnel, the radiant visible light from the phosphor coating was excited by the UV light source, and the visible light is received by the CCD camera placed at the optic window. During the test, the intense change of visible light caused by aeroheating is captured by the high-speed camera, and the images are switched to the surface heat flux distribution after the test.

2.2 Phosphor Material

The phosphor material belongs to the lanthanum. Before the test it is mixed with the binder with a certain proportion and is sprayed uniformly on the model surface in the test. Diameter of the granules in the material is about 1 micron; thickness of the phosphor coating is about 20–30 microns observed by electron microscope (Fig. 3). Figure 4 is phosphor powder's behavior with/without UV light irradiation (left side, normal state without UV; right side, excited state with UV).

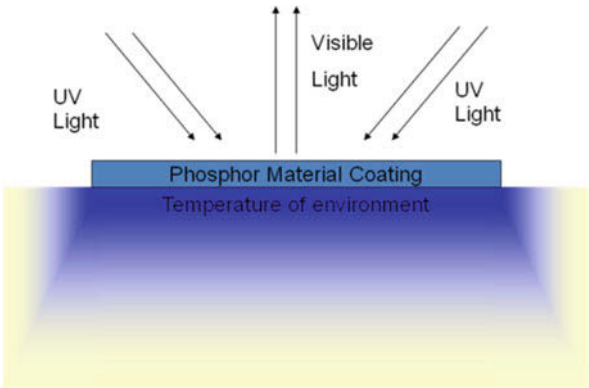

Fig. 1 Thermography principle

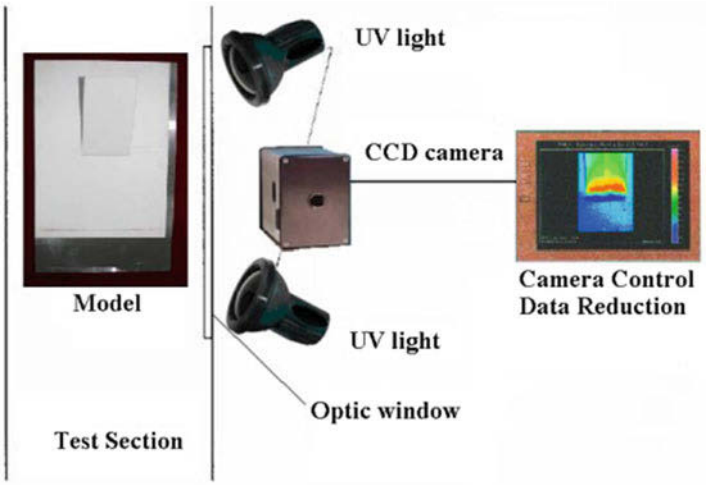

Fig. 2 Phosphor thermography system

Fig. 3 Phosphor coating

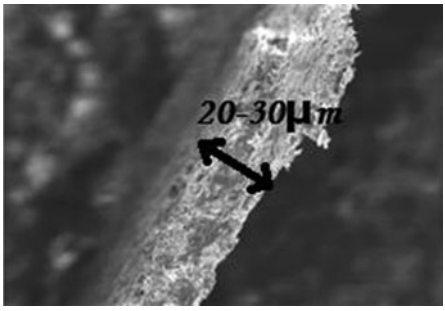

Fig. 4 Phosphor powder

2.3 Calibration

The light intensity-temperature relationship is obtained by calibration (Fig. 5), a ceramic plate with phosphor coating is heated by a temperature controller, and then the light intensity is captured by CCD camera; repeat this step at different temperature points selected, and then a relationship of temperature and light intensity can be fitting out. Figure 6 is the calibration curves.

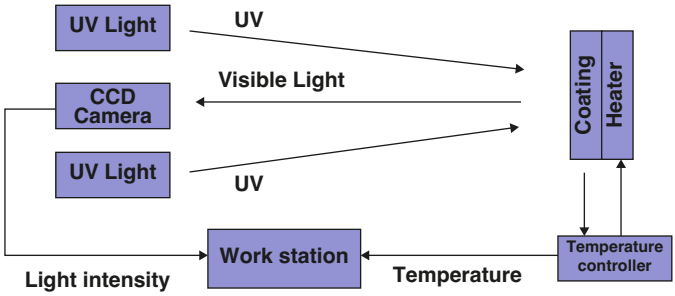

Fig. 5 Calibration system

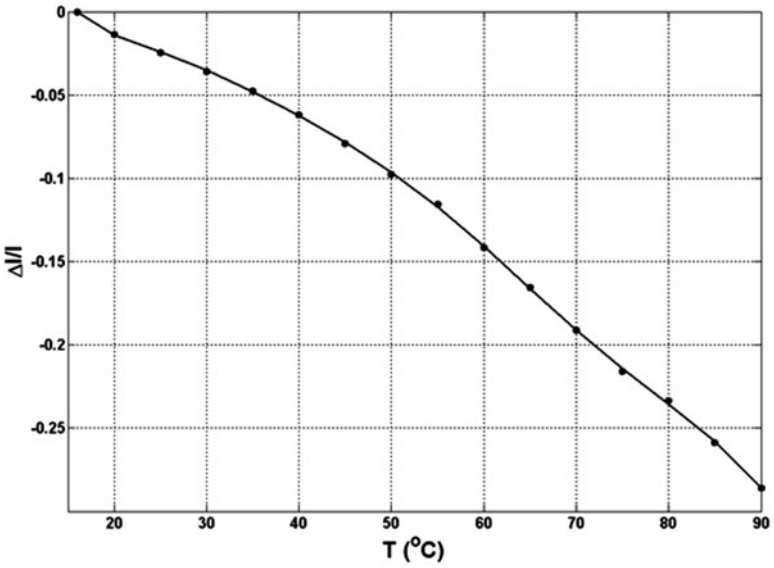

Fig. 6 Calibration curves

2.4 UV Light and Image Acquisition

The short duration of gun tunnel requires high-intensity UV light to keep the coating emission stable during the test; the intensity of UV light is 14,000 $\mu w/cm^2$ (distance, 15 inches). The wavelength of the UV light is 365 nm. The power of the UV light is 35 W.

Light intensity change on the surface of the model is recorded by the image acquisition system in the tests. The frame rate of the system should be fast enough for the short run time of the wind tunnel. This system is composed of a high-speed video camera with a zoom lens, a work station with a digitizer.

2.5 Data Reduction

Assuming the model is a semi-infinite flat plate, the transient one dimensional heat conduction can be used as the surface temperatures govern equation in isotropic, homogeneous material. Then, heat flux is discretized by regarding the local linearization approximation of temperature [3]:

$$q(t) = \sqrt{\frac{\rho ck}{\pi}} \sum_{i=1}^{m} \frac{T(i) - T(i-1)}{(t_m - t_i)^{1/2} + (t_m - t_{i-1})^{1/2}} \tag{1}$$

Heat transfer distribution can be obtained from Eq. (1).

3 Experiment Setup

3.1 Wind Tunnel

The present experiments have been performed in FD-20, an impulse hypersonic wind tunnel at CAAA. The facility is a piston shotgun tunnel with a nozzle exit of 380 mm in diameter. Free stream Mach number is set with different Laval contour nozzles from 5 to 15. All the transition experiments are made at Mach 8. The typical stable flow period varies from 25 to 60 milliseconds.

3.2 Model Material

In order to obtain higher measurement accuracy, the change of visible light intense from the coating should be larger, and it needs higher temperature at unit heat flux. Therefore, models need to be made of the material with lower thermal diffusivity properties. Ceramic material whose thermal diffusivity is far lower than the stainless steel was chosen.

3.3 Model (Flat Delta Plate)

A flat delta plate model is fabricated by ceramic (Fig. 7). Length of the model is 470 mm, the sweepback angle is 70 deg., and the radius of the leading edge is 6 mm.

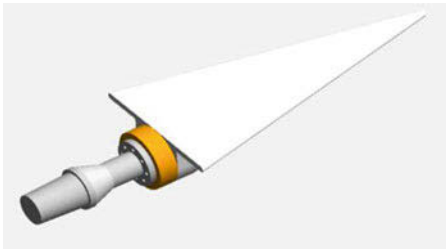

Fig. 7 Flat delta plate model

Table 1 Nominal tunnel flow conditions (AoA = 0 deg)

	Ma	Re(1/m)	T_0(K)	P0(MPa)
Condition 1	7.97	4.9×10^6	1128	4.43
Condition 2	7.97	2.3×10^7	960	15.96

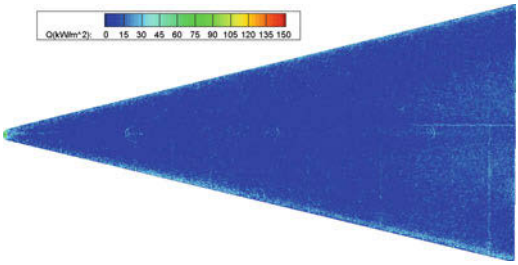

Fig. 8 Heat flux at condition 1

4 Results and Discussion

The experiment condition is shown in Table 1. Two conditions are chosen for this experiment; two different Reynolds numbers are selected to obtain the laminar flow and turbulent flow on the model surface.

At condition 1 (Fig. 8), the heat flux distribution is less than 10 kW/m^2 at the front of the model, which is a typical laminar flow, and the heat flux rises at 340 mm from the tip of the model, the transition occurs, and the heat flux is about 15 kW/m^2.

At condition 2 (Fig. 9), the heat flux distribution is markedly higher than condition 1. Transition occurs forward at 170 mm from the tip of the model, and the turbulent flow region presents a triangle form, and the leading edge of turbulent regions is parallel with the leading edge of the model. A low heat flux region appears at the central line. The heat flux of turbulent region is around 30 kW/m^2, which is two or three times higher than the laminar region.

Thin-film heat transfer sensors are plated on the central line; the data is shown agree with PTT results (Figs. 10 and 11).

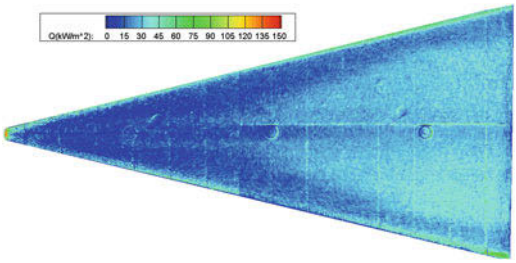

Fig. 9 Heat flux at condition 2

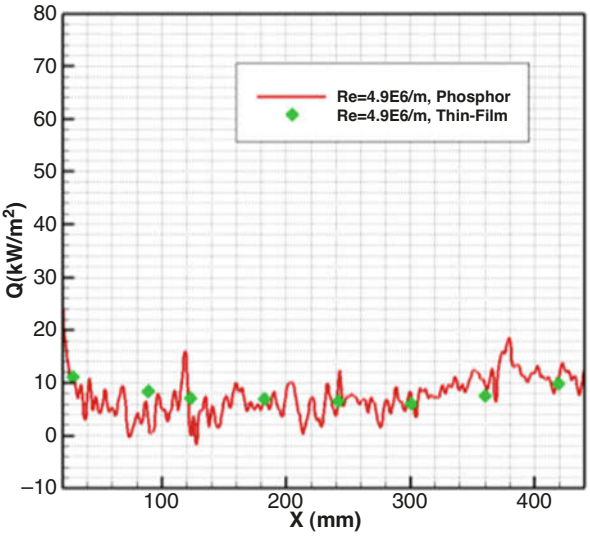

Fig. 10 Central-line heat flux at condition 1

5 Conclusion

By using PTT, thermal environment of flat delta plate can be shown; because of the relation between the flow structure and the heat transfer, the heat flux distribution can be used in flow structure studies effectively.

PTT is used to obtain the heat flux of the model under the hypersonic flow; furthermore, a hypersonic vehicle model can be fabricated, and PTT could measure the heat flux of the model with a complicated shape.

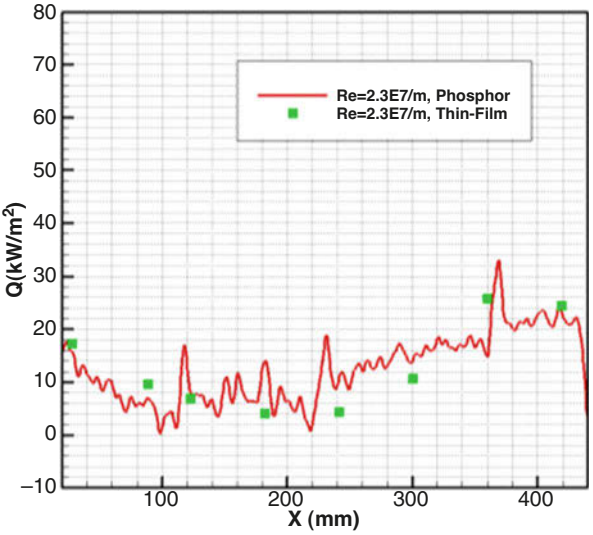

Fig. 11 Central-line heat flux at condition 1

References

1. C.H. Wu, Study on Phosphor Thermography Technique in Gun Tunnel, in *15st China Hypersonic Aerodynamic/Aeroheating Meeting*, 2006
2. T. Liu, J.P. Sullivan, *Pressure and Temperature Sensitive Paints* (Springer, Berlin/Heidelberg, 2005), p. 16
3. W.J. Cook, E.J. Felderman, Reduction of data from thin-film heat-transfer gages: A concise numerical technique. AIAA J. **4**(3) (1966)

Hypersonic Boundary Layer Tripping to Turbulence on a Conical Body

Tarandeep Singh and K. P. J. Reddy

Abstract A low Reynolds number hypersonic flow boundary layer tripping on a conical body is studied. The experiments are performed in a conventional shock tunnel at conditions providing flight realistic combination of Reynolds number and Mach number. It is observed that it is difficult to trip such a flow even with diamond trip heights as much as five times the local boundary layer thickness. Heat flux measurements over the cone indicate that though trip causes local disturbance in the flow field, the boundary layer seems to relaminarize toward the end of the cone.

1 Introduction

The aerodynamics of vehicles moving at hypersonic speeds is always affected by the boundary layer behavior at such speeds. In most cases, for realistic vehicle length scales, boundary layer transition from laminar to turbulent is a critical phenomenon that can drastically affect the heat flux to the vehicle wall. Though this increase in heat flux when the boundary layer goes to turbulent needs to be avoided, in certain cases having a turbulent boundary layer becomes necessary. This is the case for SCRAMJET inlets where a turbulent boundary layer is preferred to avoid the problem of laminar separation due to shock impingement that can lead to unstart of the engine [1]. For this reason, such inlet studies work on tripping the boundary layer into transition to get the required turbulent boundary layer [1, 2].

Tripping of boundary layer in hypersonic flow has been studied in some detail using either distributed roughness or isolated three-dimensional elements [3]. These studies show that effectiveness of the trips is strongly dependent on the boundary layer edge Mach number M_e, and few studies address this problem at hypersonic values of M_e. The general trend is that the higher the M_e, the more drastic the trip

T. Singh (✉) · K. P. J. Reddy
Department of Aerospace Engineering, Indian Institute of Science, Bangalore, India

A. Sasoh et al. (eds.), *31st International Symposium on Shock Waves 2*,
https://doi.org/10.1007/978-3-319-91017-8_110

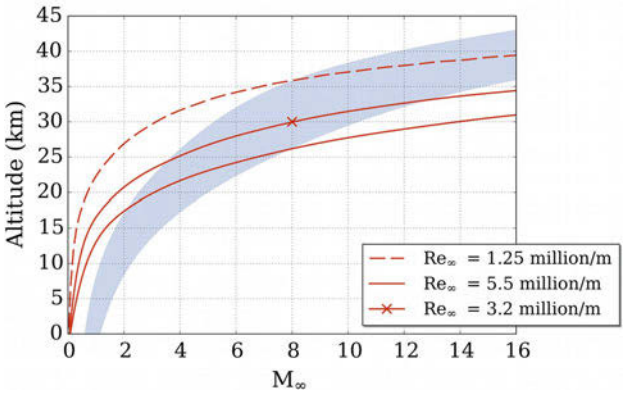

Fig. 1 Flight corridor for hypersonic vehicle taken from Heiser and Pratt [4] with constant Re_∞ curves overlapped

height needs to be, to be critical at all. This poses an issue on the effectiveness of the trip at hypersonic M_e where the trip height to boundary layer height ratio k/δ requirements can be as high as 2 [2].

Apart from M_e, free-stream Reynolds number also affects this phenomenon though it is usually taken into account as the parameter Re_k, which is the Reynolds number based on trip height and conditions at the trip height. Again at hypersonic M_e, the Re_k requirements are much higher than for supersonic M_e [3] which makes for further complicated correlations that need more data at hypersonic speeds. To add to that, most studies have high enough Re_∞, or the unit length Reynolds number in the free stream to study the transition caused by roughness, but very little data is produced at the actual Re_∞ that vehicles moving at hypersonic speeds at the corresponding altitudes may have. Figure 1 shows a plot redrawn from Heiser and Pratt [4], which shows an example of a flight corridor, for a range of dynamic pressures that the vehicle is allowed to experience in flight, as the shaded region. On that, constant Re_∞ curves have been overlapped to show that most hypersonic flight has low Re_∞ to contend with at such altitudes. This makes hypersonic boundary layer tripping studies at lower, more realistic Reynolds numbers, imperative.

With this background, the current study aims to study tripping of such a condition at free-stream Mach number of 8 with a Re_∞ of 3.2 million/m. This condition falls in the flight corridor shown in Fig. 1, though only in terms of Mach number and unit length Reynolds number. This corresponds to Mach 8 flow at 30 km altitude. An axisymmetric model is chosen to further provide a challenging (though still realistic) scenario as compared to flat plate, the latter being more well studied as well as easier to trip the flow on. Heat flux measurements have been employed to track the tripped boundary layer behavior in a hypersonic shock tunnel at LHSR.

2 Experimental Setup

2.1 Test Model

The experiments on hypersonic boundary layer tripping have been performed on a 12 deg. half-angle right circular cone with 800 mm axial length. The cone is shown in Fig. 2 along with an example of fixing trips on the cone surface. The cone has an array of flush-mounted MACOR inserts on the top surface which have platinum thin-film sensors mounted onto them. Data from the sensors on the second half of the cone have been used to study the boundary layer behavior. Wall heat flux measurements have not been made in the vicinity of the trips.

The cone, made of Duralumin, has a surface smooth finish and the cone tip is sharp, made of stainless steel with a machining tolerance of ± 0.05 mm. This study is focused only on tripping the boundary layer using diamond trips as they have been found to work best for such flows [1]. Cubes of edge lengths 1.5 mm, 3 mm, 4 mm, and 5 mm have been used to create different heights of the trips at the appropriate locations. To fix the trip to any location, a small piece of Kapton tape, that is, 150 μm thick, is attached to the surface of the cone, and the required trip is fixed onto the tape using a thin layer of super glue such that there is no spilling of the glue around the trip. By using this method trips could be placed at any location on the cone surface.

2.2 Experimental Facility and Test Conditions

All experiments were done in the hypersonic shock tunnel 4 (HST4) at LHSR. The facility is a gas-driven shock tunnel that has a nozzle exit diameter of 1 m with interchangeable Mach 7 and 8 throat inserts. The shock tube diameter is 165 mm,

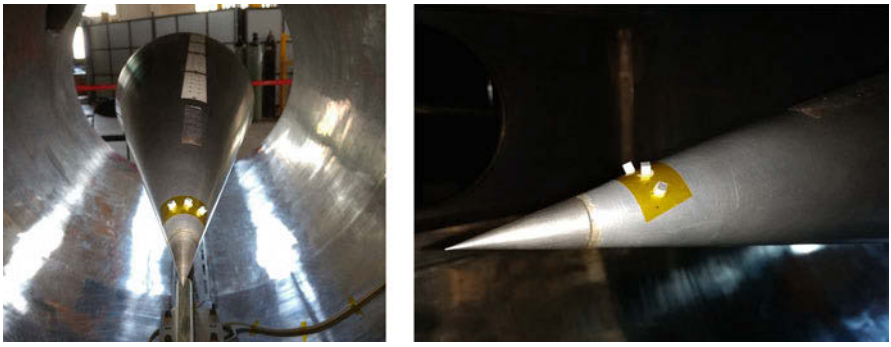

Fig. 2 800-mm-long cone model with MACOR inserts housing thin-film sensors (left) and a close-up of the trips (right)

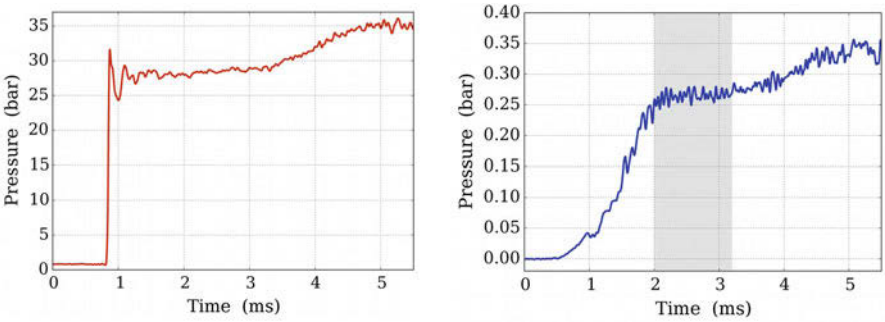

Fig. 3 HST4 reservoir pressure (left) and pitot pressure signal (right, shaded region shows test time)

Table 1 Flow parameters for the condition used in HST4

P_o (bar)	28.17	M_∞	7.81
T_o (K)	1178.5	Re_∞ (million/m)	3.24
H_o (MJ/kg)	1.184	M_e	5.8
P_∞ (Pa)	338	Re_e (million/m)	4.98
T_∞ (K)	89.3		

the driven length is 10 m, and the driver is 3 m long. A sample signal from the nozzle inlet reservoir sensor and the corresponding pitot sensor signal inside the tunnel for a condition used in the current study are shown in Fig. 3.

Figure 3 shows the reservoir supply pressure to be steady for more than 2 ms, and the pitot pressure shows the test time of around 1.2 ms. The flow parameters obtained for this condition are tabulated in Table 1.

3 Results and Discussion

3.1 Case Without Trips

The main measurement for the present study is the wall heat flux estimated by employing the thin-film sensors. This provides a good indication if the boundary layer goes into transition and turbulent heat flux would be much higher than its laminar counterpart. Figure 4 shows the heat flux measurements on the 800 mm cone for a shot without the trips, and clearly the given condition has laminar boundary layer. The number of heat flux data points per shot is limited to 12 given a change in equipment during the course of the campaign.

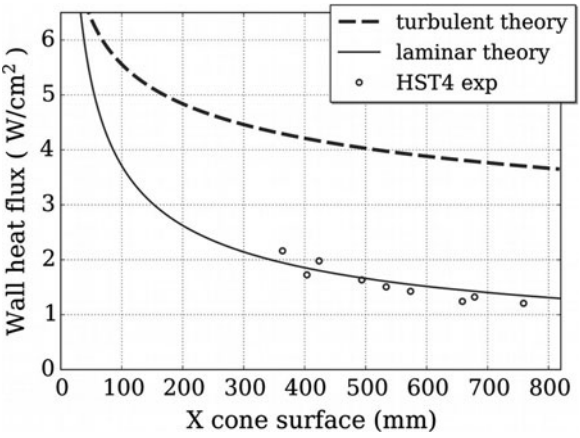

Fig. 4 Heat flux measurements for case with no trips – laminar boundary layer

3.2 Case with Trips

For boundary layer flow in a shock tunnel with hypersonic M_e, it has been found that k/δ of roughly 2 is required for the trip to be effective and of roughly 1 to be critical [2]. This is a trend that is commonly observed [3] for flat plates. But for conical bodies very less data is present at hypersonic M_e with low Reynolds numbers.

The HIFiRE 1 conical model was tested at Mach 6 with a single trip element at a low Reynolds number [5], but the M_e was supersonic such that a k/δ of 0.5 was sufficient for effective tripping. In this context, various k/δ ratios were tried, starting with more than critical values reported in the literature. Figure 5 shows the behavior of the wall heat flux in the presence of various k/δ ratios for a single element and a trip with three elements of diamond trip placed in line perpendicular to the flow direction. The separation of the elements is more than three times the cube face diagonal for the trip as proposed by Whitehead [6] (Fig. 2 shows lower separation case, which is from earlier shots). From Fig. 5 it is not very clear if multielement trip is much different from single 3D element. Also for a k/δ comparable to the case of flat plate [2], there looks to be a lot of fluctuation of heat flux between 300 mm and 600 mm, but the heat flux does not tend toward turbulent values downstream. This is also clear from the laminar nature of the heat flux signal toward the end of the cone which is not observed to be unsteadily fluctuating, as in the case of transitional or turbulent boundary layer. Next, the trip heights were increased to beyond two times the local boundary layer height; results of the heat flux are shown in Fig. 6.

It can be readily observed from Fig. 6 that trip height criterion is no more a critical factor at lower Reynolds numbers. Though the heat flux shows a lot of fluctuations in the midsection of the cone, all cases settle down to a narrow range of heat flux which hints at relaminarization of the boundary layer. The higher k/δ ratio cases show lower heat flux in the midsection owing to the greater spread of the vortex wake that misses the sensors directly in line with the central trip element. Finally, for all cases there is no evident departure from orderly temperature rise,

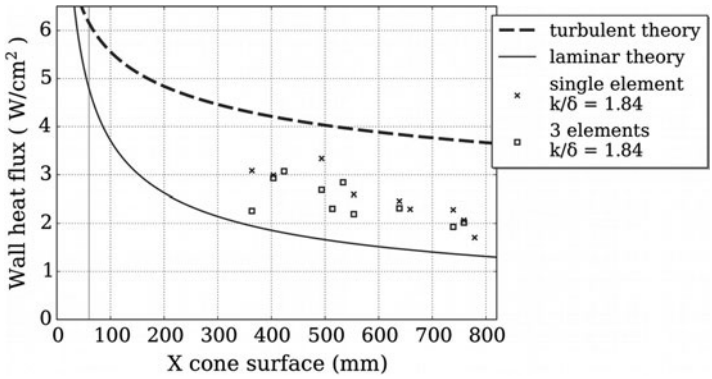

Fig. 5 Heat flux measurements behind diamond trip with k/δ of 1.84 for single and 3 elements – vertical line at 60 mm shows trip location

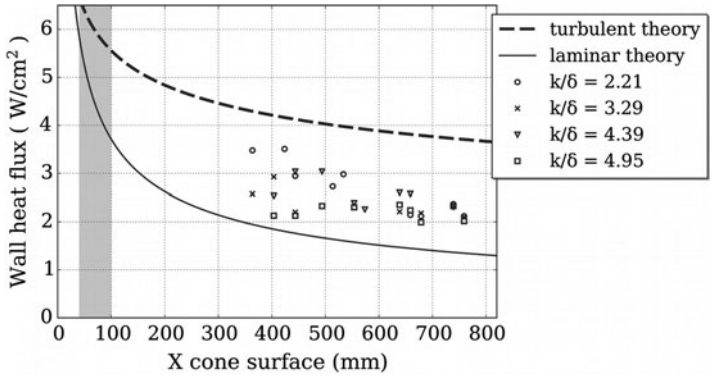

Fig. 6 Heat flux measurements behind diamond trips of various heights – shaded band represents region of tripping for the 4 cases

with no heat spikes or fluctuations to point toward turbulent spots or trip wake breakdown, also hinting at no clear transitional behavior in the boundary layer.

4 Conclusion

A study on tripping of boundary layer with high edge Mach number and low free-stream Reynolds number is carried out on an axisymmetric body. It was observed that the trips, earlier reporter to be effective for flat plate cases, cause only local disturbance to the boundary layer in the case of this conical body. Increasing trip height to as much as five times the local boundary layer height does not lead to clear transition. In fact, much of the data hints at relaminarization toward the rear end of the cone. This behavior may be attributed to more stable trip wake at higher

Mach numbers along with the disturbance relaxation caused by the axisymmetric flow nature, both of which are known effects in this area of investigation. This study brings forward the issues in tripping hypersonic boundary layer over axisymmetric bodies at flight realistic Reynolds numbers. More investigations must be conducted in different tunnels at such conditions to clarify such phenomenon and address it for applications such as the SCRAMJET inlets where these studies become exceedingly important.

References

1. S.A. Berry, A.H. Auslender, A.D. Dilley, J.F. Calleja, Hypersonic boundary-layer trip development for hyper-X. J. Spacecr. Rocket. **38** (2001)
2. D.J. Wise and M.K. Smart, Forced transition of hypervelocity boundary layers, in *18th AIAA/3AF International Space Planes and Hypersonic Systems and Technologies Conference*, 2012
3. S.P. Schneider, Effects of roughness on hypersonic boundary layer transition. J. Spacecr. Rocket. **45** (2008)
4. W.H. Heiser and D.T. Pratt, *Hypersonic Airbreathing Propulsion*, (AIAA, 1994), pp. 37–39
5. Roger L. Kimmel, Roughness considerations for the HIFiRE-1 vehicle, in *AIAA 38th Fluid Dynamics Conference and Exhibit*, 2008
6. Allen H. Whitehead Jr., Flow-field and drag characteristics of several boundary-layer tripping elements in hypersonic flow, NASA TN D-5454

Hypersonic Flow Computations by Using an Equivalent Gas Model

S. Shitrit and E. Arad

Abstract The aerodynamics of hypersonic vehicles is highly affected by enthalpy or "real gas" effects. The purpose of the current study is to assess the proper formulation of computational fluid dynamics required for simulation of high-enthalpy flows. Under the assumption of chemical and thermal equilibrium, a functional representation has been employed for specific heat at constant pressure, thermal conductivity, and viscosity coefficients for air at 500 to 30,000 K and pressure range of 10^{-4} to 100 atm. The proposed approach is evaluated using double-cone configuration at hypersonic flow. It is shown that the equivalent gas model is capable of capturing the main features of these flow fields and compares well with experiments.

1 Introduction

Numerical simulation of fluid flow is currently an integral part in the design process of a flight vehicle. The extreme conditions experienced in hypersonic flight are difficult to reproduce in an experimental facility. The cost of such hypersonic experimental studies is higher than low-speed flow because of the immense amount of energy that is required to reproduce the flight conditions. Furthermore, the number of facilities which are equipped and capable to perform such experiments is very limited. The computational fluid dynamics (CFD) application can reduce the number of costly experiments by providing deep insight into the flow field. The high speed of hypersonic flows causes many physical phenomena that are not modeled by the common perfect gas form of the Navier-Stokes equations. Such particular phenomena include caloric and chemical effects, additional aerodynamic forces, plasma effects, and thermal and chemical non-equilibrium and ionization [1, 2]. A pioneering computation of multidimensional flow field including thermochemical

S. Shitrit (✉) · E. Arad
Aeronautical Systems, RAFAEL Advanced Defense Systems LTD., Haifa, Israel
e-mail: shlomis1@rafael.co.il

A. Sasoh et al. (eds.), *31st International Symposium on Shock Waves 2*,
https://doi.org/10.1007/978-3-319-91017-8_111

non-equilibrium and ionization was performed by Candler [3] who solved a set of equations that coupled thermal and chemical non-equilibrium equations to the fluid dynamic equations. Another CFD code for entry flows called LAURA (Langley Aerothermodynamic Upwind Relaxation Algorithm) was developed by Gnoffo [4] at NASA Langley Research Center. This code solves a set of equations developed by Lee [5]. However, such complicated codes and flow field calculations based on either of these approaches (or similar) brings about a significant loss in efficiency. Simplification can be obtained by assuming a chemical equilibrium without elemental separation. This allows the governing equations to be written in a functional form, so that the specific heat at constant pressure C_p, thermal conductivity K, and molecular viscosity μ are defined as total properties. Meaning that the energy equation does not contain the species production rate term appearing in the viscous-shock-layer form of the energy equation for a chemically reacting multicomponent gas mixture. As a result, the energy equation has the same form as the perfect gas equations. That way the equations for an equilibrium reacting gas mixture can be solved in a manner similar to that of a perfect gas [6].

The current study focuses on the implementation of an equivalent gas model (EGM) for weakly ionized hypersonic flows in thermochemical equilibrium into compressible flow solver around complex configurations. The derivation presented here is based on the 11-species air model published by Gupta [6]. This report presents an accurate curve fits for the computed values of enthalpy, total specific heat, compressibility factor, viscosity, and total values of thermal conductivity and Prandtl number, for equilibrium air from 500 to 30,000 K over a pressure range of 10^{-4} to 100 atm. The model is based on the assumption of chemical equilibrium without elemental separation. The main motivation for taking this course for solving hypersonic flow problems and not the full thermally and chemically non-equilibrium Navier-Stokes equations is computational efficiency. Solving a reacting Navier-Stokes equations may produce better physical results but with significantly higher cost. The remainder of this paper presents the thermodynamic coefficients computation and model developed by Gupta. A double-cone configuration was tested includes comparison to experimental results.

1.1 Curve-Fit Temperature Intervals

In Gupta's model [6], the entire temperature and pressure range are broken down to two or more intervals. In order to ensure a smooth variation of the curve-fit properties over the complete temperature range, the curve-fit coefficients are linearly averaged at the temperature interval boundaries over a specified overlap region. As an example, curve-fit of the total specific heat at constant pressure C_p is defined as follows [1, 7]:

$$C_p = \left(\frac{\partial h}{\partial T}\right)_p = \sum_{i=1}^{NS} C_i C_{p,i} + \sum_{i=1}^{NS} h_i \left(\frac{\partial C_i}{\partial T}\right)_p, \quad (1)$$

where C_i is the mass fraction of species i $\left(\frac{\rho_i}{\rho}\right)$ obtained from the free-energy minimization calculation method described in [8] and $\left(\frac{\partial C_i}{\partial T}\right)_p$ is evaluated numerically by differentiating the data from this calculation. The following expression is employed to curve-fit the $C_p$values, following the form presented by Gupta [6]:

$$C_p = \exp\left(A_{C_p}\chi^4 + B_{C_p}\chi^3 + C_{C_p}\chi^2 + D_{C_p}\chi + E_{C_p}\right), \quad (2)$$

with $\chi = \ln\left(\frac{T}{10{,}000}\right)$. The polynomial coefficients are given in [6] as function of temperature and pressure values. Once C_p, μ, and K have been computed, it is possible to compute Prandtl number, $\Pr = {\mu C_p}/{K}$. For temperature values lower than 500 K and pressure value of 1 atm, the Lemmon [9] polynomial approximation is used for the specific heat at constant pressure, C_p.

The model for the transport properties, thermal conductivity, and viscosity coefficients has a similar form with the appropriate coefficients. As for the thermal conductivity and viscosity coefficients, for temperature values lower than 500 K, the Sutherland law is applied.

1.2 Thermodynamic Coefficients Table

The current study focuses on the computational EGM effectiveness compared to the calorically perfect gas model and the calorically imperfect gas model (C_p= C_p (T)). Three physical models were evaluated:

- **Calorically Perfect Gas:** The specific heat at constant pressure has a constant value of 1006, J/KgK. Both the thermal conductivity and viscous coefficients are computed using the Sutherland law.
- **Calorically Imperfect Gas:** The case of a calorically imperfect gas, C_p= C_p (T), has a polynomial representation. Both the thermal conductivity and viscous coefficients are computed by the Sutherland law.
- **Equivalent Gas Model:** The thermodynamic coefficients C_p, μ, and K depend on temperature and pressure as well. This model is more realistic and permits the analysis of stronger shocks for practical gases. The gas is still considered to be thermally perfect and diatomic.

The EGM model was implemented into a compressible Navier-Stokes solver. Two approaches were considered for the EGM implementation: functional curve-

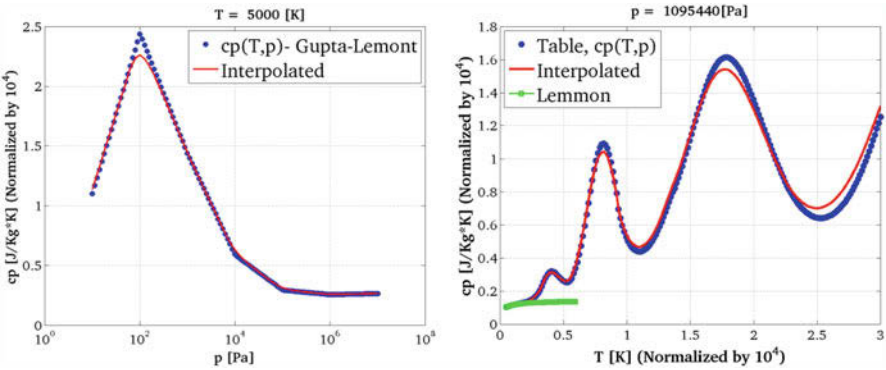

Fig. 1 Right: values of C_p as function of temperature, at constant pressure of 10 atm
Left: C_p, as function of pressure, at constant temperature of 5000 K

fit approach and thermodynamic coefficient table look-up. The functional curve-fit formulation provides continues definition of the coefficients through all the temperature and pressure range. However, since the application range of temperature and pressure is wide, and the variation of C_p in extreme conditions, i.e., high temperature and low pressure, is dominant, a significant mismatch is produced between the functional fit and Gupta's [6] table. In addition, a multi-term functional formulation is computationally expensive. This load is significant since the coefficients need to be evaluated at each mesh cell for each iteration or time step. Consequently, significant rise of CPU time and efficiency reduction were observed when this functional fit was applied. This led us to look for a more efficient approach. The second approach consists of a thermodynamic coefficient table look-up. The entire temperature and pressure range are broken down to several small intervals, with a minimum temperature interval of 50 K. During the iterative process in each cell, the thermodynamic coefficients are evaluated using a logarithmic interpolation process. Since the table's resolution (temperature and pressure intervals), in terms of the tabulated terms, is known a priori and defined during the coefficient table construction phase (prior solving the flow equations), the identification of the relevant "area" in the table, according to a given temperature and pressure, is done by a simple linear transformation. That is to say, no searching procedure is involved, and the property discrete computation is extremely fast. The interpolated curve-fit (red line) and Gupta's original values (blue circles) for C_p at a constant pressure of about 10 atm are presented in Fig. 1. Also shown for comparison is the Lemmon curve-fit [9]. This curve-fit is part of the model in this particular temperature range of 300–600 K, since its simpler formulation and the relatively smooth variation of the curve-fit properties over the Gupta-Lemmon models. A preprocessor stand-alone algorithm, which is based on the methodology described above, is used to construct the thermodynamic coefficient tables as function of the local pressure and temperature.

1.3 Numerical Setup and Boundary Conditions

The flow field computations were performed using a compressible Navier-Stokes solver. The discretization of the governing equation is done by finite volume approach with a central formulation over structured meshes. The convective terms are computed by Roe flux splitting upwind scheme with Van Albada limiter. Viscous fluxes are computed to second-order accuracy using a central difference approach. The residual smoothing is made by employing an explicit fifth-order multistage Runge-Kutta algorithm. In addition, the turbulent viscosity is computed by the Spalart-Allmaras single-equation turbulence model.

Due to the short test duration time (i.e., in HIEST a typical experiment takes about 10 msec), the model temperature does not vary significantly during the shot; therefore an isothermal wall is assumed, with a constant temperature of 300 K for all cases. Free stream conditions are enforced at the far-field boundaries. The stagnation and free stream conditions were obtained from Tissera [10] for the double-cone model.

Left: C_p, as function of pressure, at constant temperature of 5000 K

2 Test Case Configuration

The well-known calibration model is a sharp tip $25^o - 55^o$ double-cone configuration (Fig. 2). This model is a suitable test case to evaluate the EGM due to presence of complicated flow features such as interaction between a shock wave and a separated flow. The research facilities at Caltech, Calspan (CUBRC), and Princeton University were used to produce a large experimental database for this test case [11].

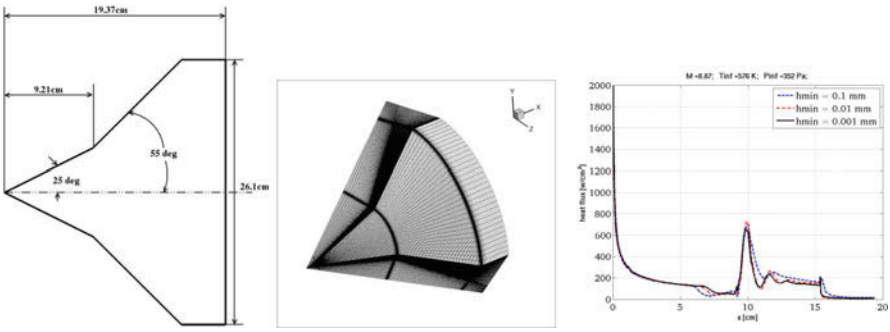

Fig. 2 Left: sharp double-cone model scheme. Middle: computational mesh of the double-cone model. Right: grid convergence

In order to properly capture the heat transfer over the surface, a sufficiently refined computational mesh was built. The accuracy of the heat transfer predicted near the wall is strongly dependent on the quality of the grid (Fig. 1) and the clustering near the wall. For this purpose several levels of grid refinement have been checked to assess the effect on the numerical accuracy, while the total number of grid cells ranges from 200 K to 1 M cells. The minimum cell's height on the wall was changed from 100 μm to 1 μm.

3 Results

The flow conditions for the double-cone configuration validation were taken according to run 43 presented in [10]. This case involves high-enthalpy conditions (approximately 10 MJ/kg) and is simulated using calorically perfect gas, calorically imperfect gas, and EGM. The heat transfer distributions from the numerical simulations are compared with the experimental and computed data presented in [10]. The flow structure typical of the double cone is presented in the visualization of the temperature contours (Fig. 3), identifying the shock positions, the details of the separation region, and the underexpanded jet along the second cone. The first cone generates an incident shock which is close to the cone's surface (Fig. 4). The incident shock interacts with the second shock generated by the second cone. The shocks interactions causes a pressure rise and flow separation. Again, the EGM prediction for the temperature rise in the shock layer is smaller than that obtained by the two other models. Furthermore, the shock location that is identified by the EGM model is closer to the solid surface that obtained by the other models.

4 Conclusions

Self-consistent models have been used for total specific heat at constant pressure, thermal conductivity, and viscosity coefficients of equilibrium air from 500 K to 30,000 K and pressure range of 10^{-4}–100 atm. The derivation presented here of the EGM is based on the 11-species air model published by Gupta [6]. Practically, the thermodynamic coefficients were computed and arranged in form of a table model, while a logarithmic interpolation relation is provided to obtain values at a given temperature and pressure. A double-cone test case was compared with data at enthalpy levels of up to 10 MJ/kg in an ambient air. The agreement between the EGM computations and experiment values is reasonable for the surface pressure, but there is a discrepancy in the predicted heat transfer rates for the three physical models. The computations agree best for the EGM in Run 43 (10 MJ/Kg). The heat transfer rate is remarkably good, with all of the flow features captured. The EGM algorithm and its implementation in a compressible Navier-Stokes solver are far from being optimal. However, it already appears to be very instrumental

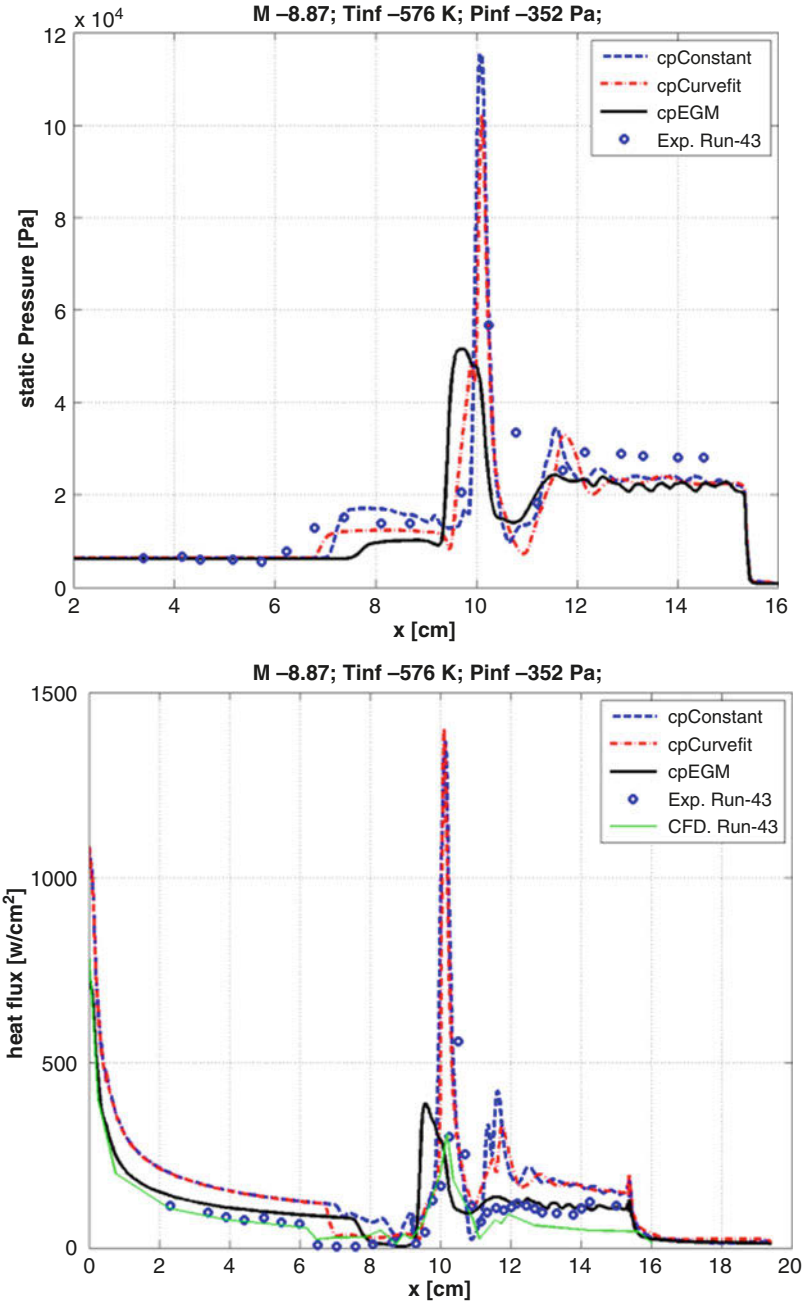

Fig. 3 Heat flux (right) and static pressure (left) of the double-cone model for perfect gas (blue), imperfect gas (red), and EGM (black) for $H_0 = 10$ MJ/Kg}, $M_\infty = 8.87$

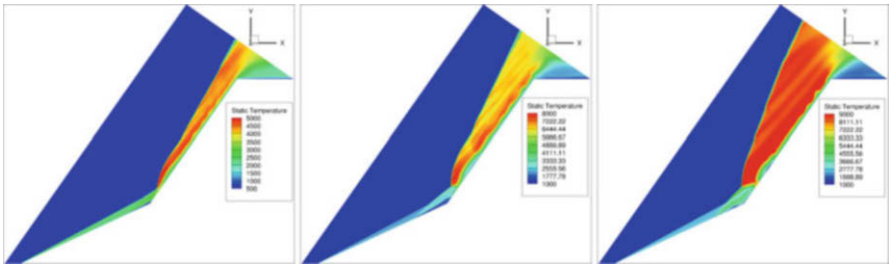

Fig. 4 Static temperature contours of the double-cone model for perfect gas (right), imperfect gas (middle), and EGM (left) for H0 = 10 MJ/kg, $M_\infty = 8.87$

in solving complicated configurations in hypersonic flow, as is presented in this work. Although the EGM offers realistic predictions, more development is needed to achieve better quantitative agreement with measurements.

References

1. J.D. Anderson, *Hypersonic and High Temperature Gas Dynamics.* s.l. (McGraw-Hill, New York, 1989)
2. D.G. Fletcher, *Fundamentals of Hypersonic Flow-Aerothermodynamics.* s.l. Technical Report RTO-EN-AVT-116 (von Karman Institute, Belgium, 2004)
3. G.V. Candler, *The Computational of Weakly Ionized Flow in Nonequilibrium.* s.l. PhD Thesis, Stanford University, 1988
4. P.A. Gnoffo, R.N. Gupta, J.L. Shin, *Conservation Equations and Physical Models for Hypersonic Air Flows in Thermal and Chemical Nonequilibrium.* Virginia: Technical Report 2867 (NASA, Langley, Hampton, Virginia, 1989)
5. J.H. Lee, Basic governing equations for the flight regimes of aeroassisted orbital transfer vehicles. s.l., in *19th Thermophysics Conference, Fluid Dynamics and Co-located Conferences*, 1984. https://doi.org/10.2514/6.1984-1729
6. R.N. Gupta, K.-P. Lee, R.A. Thompson, J.M. Yos, *Calculations and Curve Fits of Thermodynamic and Transport Properties of Equilibrium Air to 30000K.* s.l. (NASA, 1991), p. 1260
7. C. Frederick Hansen, *Approximations for the Thermodynamic and Transport Properties of High-Temperature Air.* s.l. NASA TR R-50, 1959
8. K.L. Brinkley, C.W. Stroud, *Chemical Equilibrium of Ablation Materials.* s.l. Technical report, NASA, technical note. D-539, 1969
9. E.W. Lemmon, R.T. Jacobsen, S.G. Penoncello, D.G. Friend, Thermodynamic properties of air and mixtures of nitrogen, argon, and oxygen from 60 to 2000 K at pressures to 2000 MPa. s.l. J. Phys. Chem. Ref. Data **29**(3), 331–385 (2000)
10. S. Tissera, *Assessment of High Resolution Methods in Hypersonic Real-Gas Flows.* Cranfield, UK: s.n., 2010
11. M. Holden, T. Wadhams, *Code Validation Study of Laminar Shock/Boundary Layer and Shock/Shock Interaction Hypersonic Flow Part A: Experimental Measurements,* 2001. AIAA 2001-1031

DNS of Hypersonic Ramp Flow on a Supercomputer

I. Klioutchnikov, S. Cao, and H. Olivier

Abstract The main goal of this paper is to study the hypersonic flow over a compression ramp by highly resolved direct numerical simulations. The results obtained with a grid of 4096 × 512 × 512 points show a very good resolution in the region of the separation shock, the separation bubble, and up to the region of the appearance of Görtler vortices. The development and the detailed structure of Görtler vortices downstream of the reattachment region are shown. The Görtler vortices produce strong spanwise heat transfer variations with significant peak heating. The results for different Reynolds numbers are thoroughly analyzed to show the influence on the vortex-induced spanwise heat flux variations. The comparison of numerical results with experimental data yields a good agreement.

1 Introduction

Hypersonic ramp flows show a lot of unsteady phenomena such as local separation regions, shock-boundary layer interaction, boundary layer transition, and turbulence. The state of the boundary layer, laminar or turbulent, strongly influences the thermal state of the ramp surface. These facts necessitate the investigation of the presence of hydrodynamic instabilities for hypersonic ramp flows. Görtler instability is one among the centrifugal instabilities which is caused by centrifugal forces associated with the change in direction of fluid motion over a concave wall or a shear layer near reattachment of a separated ramp flow. The streamwise-oriented, counterrotating Görtler vortices can produce strong heat transfer variations in the ramp flow reattachment region. The most important consequence of the nonlinear effects connected with Görtler instability is known as secondary instability leading to transition and turbulent flow. Two types of secondary instabilities of Görtler

I. Klioutchnikov (✉) · S. Cao · H. Olivier
RWTH Aachen University, Shock Wave Laboratory, Aachen, Germany
e-mail: klioutchnikov@swl.rwth-aachen.de

A. Sasoh et al. (eds.), *31st International Symposium on Shock Waves 2*,
https://doi.org/10.1007/978-3-319-91017-8_112

Table 1 Numerical cases

Case	Grid	Ramp angle	M	Re_L
1	$1056 \times 256 \times 256$	15°	7.7	4.1×10^5
2	$4096 \times 512 \times 512$			4.1×10^5
3				1.5×10^6
4				3.0×10^6

vortices appear: sinuous mode and horseshoe or varicose mode [1]. The sinuous mode grows stronger for shorter wavelengths, while the varicose mode does for large wavelengths.

2 Numerical Method

Numerical methods for direct numerical simulation (DNS) of hypersonic ramp flows require a robust shock capturing feature, as well as minimal dissipation and dispersion errors to resolve small scales of turbulent fluctuations.

An in-house DNS solver [2] was applied with a fifth-order WENO (Weighted Essentially Non-Oscillatory) scheme for the convective terms, a sixth-order central scheme for viscous terms, and a fourth-order Runge-Kutta scheme for the time integration. DNS of three-dimensional hypersonic ramp flows were conducted using a high-resolution mesh with $4096 \times 512 \times 512$ grid points, with $\Delta x^+ < 8$, $\Delta y^+ < 1$ and $\Delta z^+ < 10$ inside the boundary layer for all cases. More than 2×10^5 time steps are needed for a converged solution. To obtain an optimal performance, 262,144 cores on the JUQUEEN supercomputer were used.

The three-dimensional computational domain consists of a flat plate ($L = 100$ mm) with sharp leading edge and a ramp (100 mm length) with 15° ramp angle. Both, flat plate and ramp have a spanwise width of 30 mm. Isothermal wall boundary conditions are used for all calculation and periodic boundary conditions in spanwise direction.

Four cases are considered, as described in Table 1.

3 Results

For all cases a separation bubble is formed near the ramp, consequently generating a separation shock, as it is shown for case 3 in Fig. 1. The flow is then deflected by the separation and the ramp and features a reattachment region as well as a corresponding reattachment shock. The free shear layer along the reattachment region has a strong concave curvature, which induces the Görtler instability.

Cases 1 and 2 at $M = 7.7$ and $Re_L = 4.1 \times 10^5$ correspond to experiments performed at the Shock Wave Laboratory. The surface pressure coefficient (c_p),

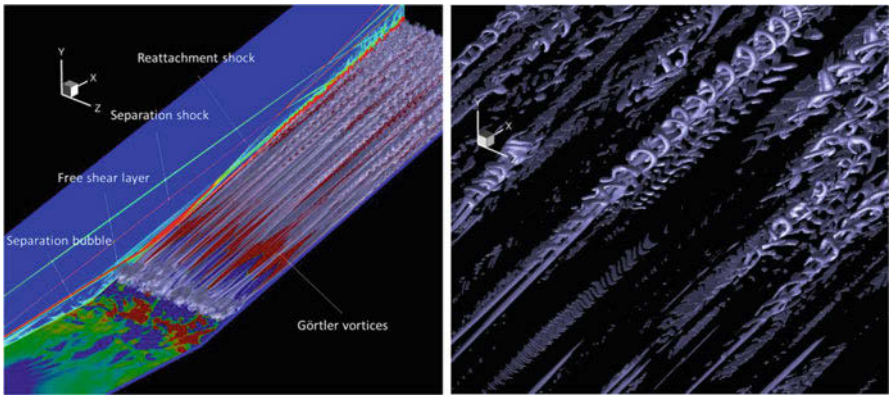

Fig. 1 Hypersonic ramp flow at $M = 7.7$ and $\mathrm{Re}_L = 1.5 \times 10^6$, Görtler vortices (case 3)

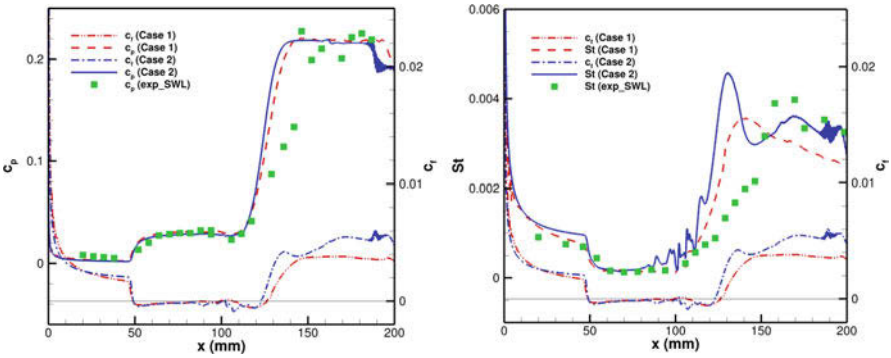

Fig. 2 Surface pressure coefficient, skin-friction coefficient and Stanton number distribution

skin-friction coefficient (c_f), and Stanton number (St) distribution along the x-direction are plotted in Fig. 2. Both of the two grid resolutions show good agreement with experimental data. The reason why in the recompression zone a systematic deviation between experimental and numerical results occurs is subject of ongoing research.

Due to centrifugal forces in the reattaching free shear layer, Görtler instability occurs, which results in the generation of counterrotating pairs of streamwise vortices, the so-called Görtler vortices. According to the condition of $c_f = 0$, the reattachment region starts between $x = 120$ mm and $x = 130$ mm. The evolution of Görtler vortices also starts in this region.

In Fig. 3, Görtler vortices (case 2) are visualized by a iso-surface of the Q-criterion ($Q = 10$). The zoom of Fig. 3 shows details of the secondary instabilities of Görtler vortices. For this case the varicose mode of instability appears. This instability type is typical for lower Reynolds numbers and large wavelengths [1].

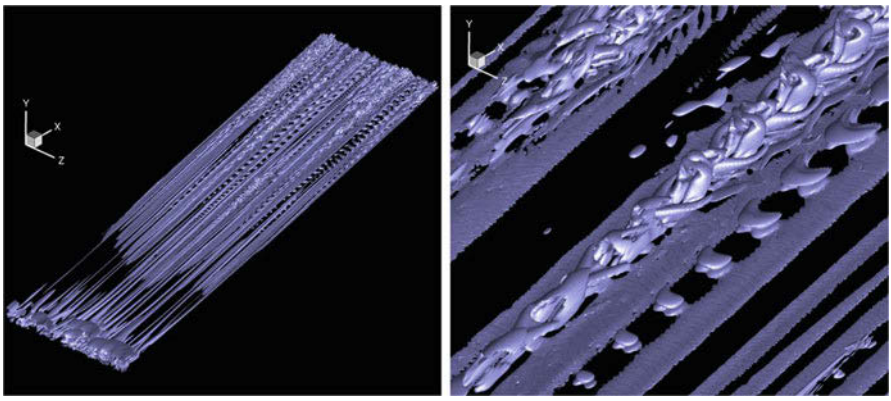

Fig. 3 Görtler vortices, snapshot of Q-criterion iso-surface, $Re_L = 4.1 \times 10^5$ (case 2)

Table 2 Görtler numbers for three different Reynolds numbers

Cases	R (mm)	λ (mm)	G_{δ_2}	Λ	θ_s (°)
2	72.3	1.9	24.2	1263	3.9
3	33.4	1.2	45.9	3200	3.5
4	21.9	1.0	68.9	6701	3.0

The Görtler number is an important parameter to analyze the Görtler instability and is classically defined as

$$G_{\delta_2} = \mathrm{Re}_{\infty,\delta_2}(\delta_2/R)^{0.5} \tag{1}$$

where δ_2 is the boundary layer momentum thickness at the beginning of the curvature of the shear layer at reattachment and R is the corresponding radius of curvature of the shear layer, which can be estimated by the following formula:

$$R = \delta/\left[\tan(\theta_r - \theta_s)\sin(\theta_r - \theta_s)\right] \tag{2}$$

where δ is the free shear layer thickness measured at the same position as δ_2, θ_r is the ramp angle, and θ_s is the separation angle.

Another Görtler number Λ is given based on the wavelength of the vortices in spanwise direction, defined as

$$\Lambda = \mathrm{Re}_{\infty,\lambda}(\lambda/R)^{0.5} \tag{3}$$

Table 2 list all the calculated results for three Reynolds numbers.

It is obvious that with increasing Görtler number, the wavelength decreases.

One of the most obvious phenomena related to hypersonic ramp flow is the heat transfer variation caused by Görtler vortices in spanwise direction (see Fig. 4). It can be observed that the highest temperatures are located just downstream of the

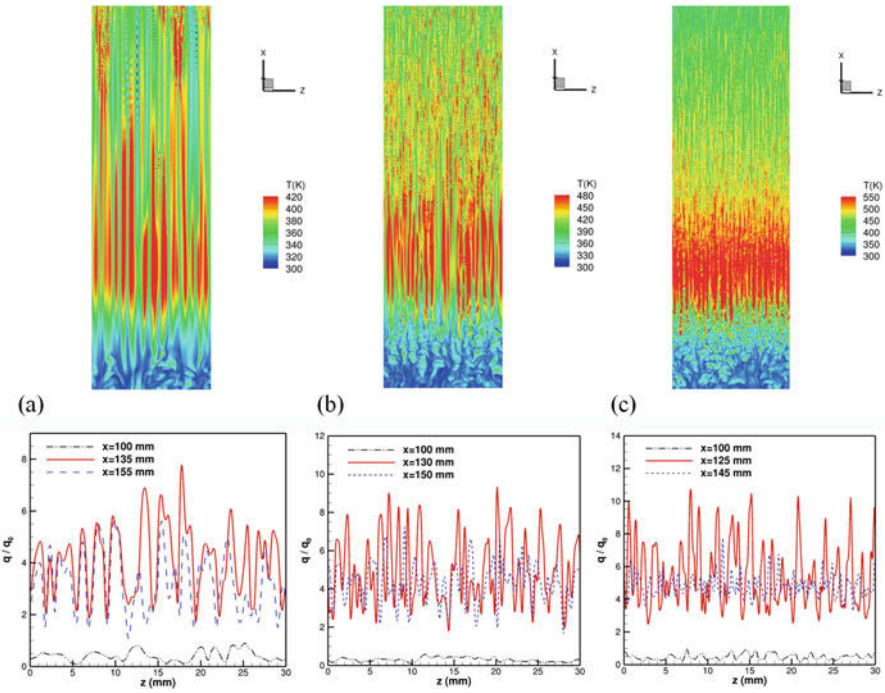

Fig. 4 Instantaneous temperature and heat flux spanwise distribution: (**a**) $Re_L = 4.1 \times 10^5$, (**b**) $Re_L = 1.5 \times 10^6$, (**c**) $Re_L = 3.0 \times 10^6$, q_o – heat flux before separation

reattachment region. The remarkable streak patterns give evidence of the presence of vortex pairs. Dark streaks indicate a flow toward the wall and bright streaks indicate a flow away from wall. The results prove that the vortices evolve with quasi constant wavelength.

The surface temperature increases with increasing Reynolds number, but the wavelength of the vortices decreases with increasing Görtler number. The surface temperature distributions indicate that the Görtler vortices are more unstable with increasing Görtler number. Different Reynolds numbers result in different boundary layers, leading to different sizes of the separation bubble. Figure 5 shows the surface pressure coefficient and heat flux distribution for three Reynolds numbers (cases 2, 3, and 4). The separation point relocates upstream with increasing Reynolds number, and the reattachment region shows the same behavior. As a consequence, the change of the separation bubble size doesn't show a monotonic trend. Additionally, a higher Reynolds number corresponds to a higher heat flux at the reattachment region and a smaller separation angle (see Table 2).

Figure 6 shows the vortex structures of the ramp flow for the highest Reynolds number (case 4). The flow becomes more unstable downstream of the reattachment region. An increase of Reynolds number causes a change of the secondary instability mechanism for Görtler vortices from the varicose mode to the sinuous mode, which is typical for shorter wavelengths (see Figs. 1 and 3 for comparison).

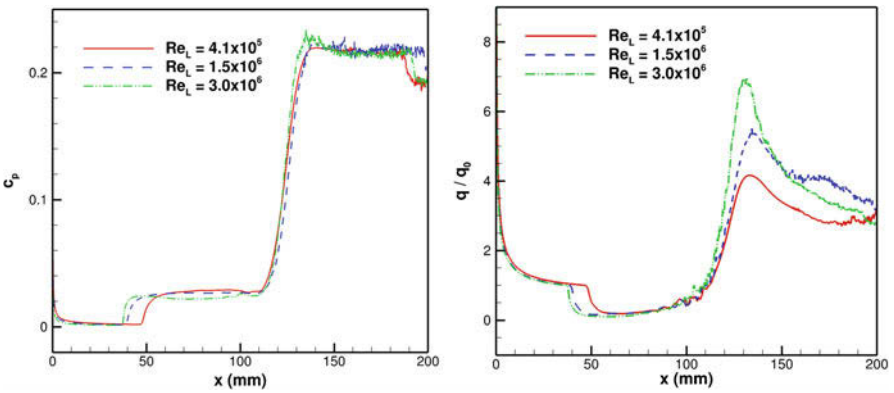

Fig. 5 Surface pressure coefficient and heat flux distribution for different Reynolds numbers

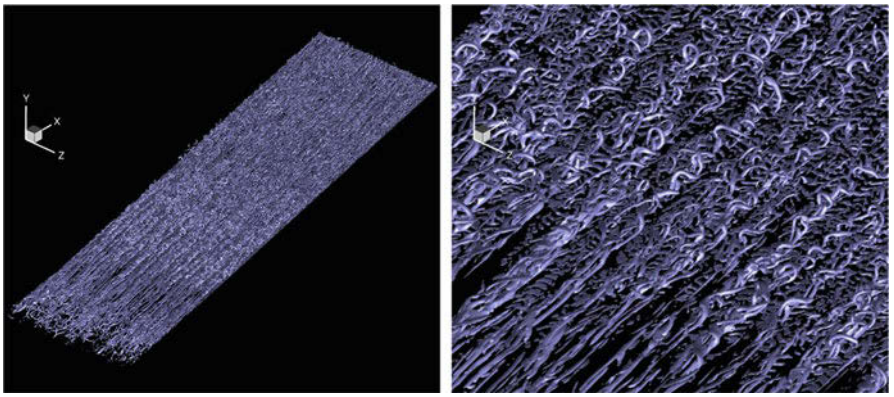

Fig. 6 Görtler vortices, $Re_L = 3.0 \times 10^6$ (case 4)

In order to gain a better understanding of the influence of the Görtler vortices on the heating, an air jet impingement model was developed. Figure 7 shows three selected vortex pairs (case 2), here B is the width of the impinging flow, and H denotes the height of the smallest flow cross section of the impinging flow from the wall. An empirical correlation based on experimental data was determined of the form [3]:

$$Nu_0 = 0.726\mathrm{Re}^{0.53}(H/B)^{-0.191} \tag{4}$$

where Nu_o is the Nusselt number at the stagnation region and Re is the local Reynolds number of the wall normal air jet. The Nusselt number for this case is defined as follows:

$$Nu = \frac{hL}{\lambda} = \left(\frac{\partial T}{\partial y}\right)_w B(T_\infty - T_w)^{-1} \tag{5}$$

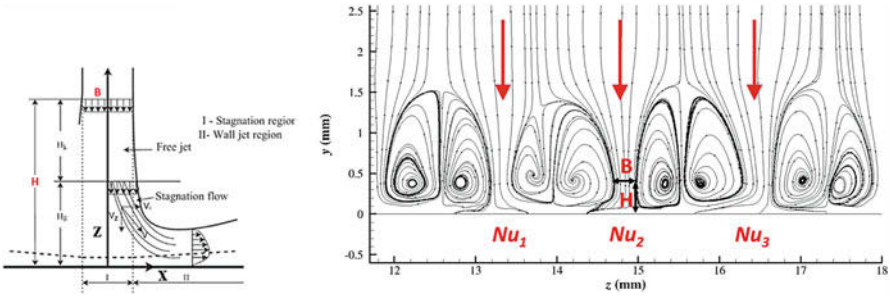

Fig. 7 Air jet impingement model and vortex structure

Table 3 Calculated Nusselt number based on air jet impingement model

Approaches	Nu_1	Nu_2	Nu_3
Wall jet model, Eq. (4)	6.15	6.82	7.12
Numerical solution, Eq. (5)	6.42	6.26	5.90

which denotes the ratio of the convective to conductive heat transfer with B as reference length L.

The deduced Nusselt numbers for the three vortex pairs shown in Fig. 7 are given in Table 3 and indicate a reliable application of the air jet impingement model.

4 Conclusion

The hypersonic flow for various Reynolds numbers over a compression ramp is studied using highly resolved direct numerical simulations. An increase of the Reynolds number or Görtler number, resp., causes a change of the secondary instability mechanism for Görtler vortices from the varicose to the sinuous mode that grows stronger for shorter wavelengths accompanied by an increase of the heat transfer in the reattachment region. A new formulation of radius of curvature of the shear layer for the Görtler number calculation was used, and a jet impingement-heating model for Görtler vortices was developed and validated.

References

1. F. Li, M.R. Malik, Fundamental and subharmonic secondary instability of Görtler vortices. J. Fluid Mech. **297**, 77 (1995)
2. M. Gageik, I. Klioutchnikov, H. Olivier, Comprehensive mesh study for a direct numerical simulation of the transonic flow at $Re_c = 500{,}000$ around a NACA 0012 airfoil. Comp. Fluids **122**, 153 (2015)
3. D. Lytle, B.W. Webb, Air jet impingement heat transfer at low nozzle-plate spacings. Int. J. Heat Mass Transf. **37**(12), 1687 (1994)

The Role of Three-Dimensional Shock Wave Interaction in the Complex Hypersonic Heating

Chun Wang, Gaoxiang Xiang, Zonglin Jiang, Xudong Li, and Zengmin Shi

Abstract The phenomena of complex gasdynamic heating exist in the hypersonic interaction region, such as the interaction region of body and wing of hypersonic aircraft. The main mechanism is the interaction of three-dimensional shock waves and boundary layer. This paper explored the role of three-dimensional (3D) shock wave interaction in the complex hypersonic heating based on the theory of 3D shock/shock interaction (SSI). The results show that complex 3D SSI configuration exists in the hypersonic interaction regions in different flight conditions, both regular interaction and irregular interaction. The contact surface induced by the 3D SSI represents the flow jet inclines to the boundary layer of aircraft surface, which always causes the high local heating flux. In the flight condition with a certain attack angle, complex 3D Mach interaction of shock waves in the interaction region of body/wing exists, which induces the complex flow around the wing; the jet bounded by two contact surfaces inclines to the surface of wing and causes the local heating peak, similar to the IV-type heating mechanism in two-dimensional interaction of shock wave and boundary layer.

1 Introduction

Since the development of hypersonic aircraft technology in the last century, the problem of hypersonic heating is one of the most important problems of hypersonic aerodynamics; there is a great deal of theoretic, experimental, and numerical work conducted to overtake the heat barrier of hypersonic aviation. Based on the theory of hypersonic boundary layer, the mechanism of gasdynamic heating in the nose

C. Wang (✉) · G. Xiang · Z. Jiang
SKL of High-temperature Gas dynamics, Institute of Mechanics, Beijing, China

Department of Aerospace Engineering Science of UCAS, Beijing, China
e-mail: wangchun@imech.ac.cn

X. Li · Z. Shi
Beijing Institute of Aerospace Long March Vehicle, Beijing, China

A. Sasoh et al. (eds.), *31st International Symposium on Shock Waves 2*,
https://doi.org/10.1007/978-3-319-91017-8_113

of aircraft and that in the large area region of simple configuration of hypersonic vehicles has been clarified, several prediction formulae of hypersonic heating rely on the parameters of free stream, and wall incline angle and wall pressure have been built and well applied in the engineer practices. However, in the interaction regions of hypersonic vehicle, such as the interaction zones of body/wing and body/rudder, the gasdynamic heating is rather complex, the mechanism has not been well understood, and there is no generally accepted prediction formula. Plenty of experimental work is still necessary to simulate the complex gasdynamic heating, and it has been a critical problem for the design of new-type hypersonic aircraft. While the hypersonic aircraft flights in different conditions of flight Mach number and attack angle, the local heat flux in the interaction regions shows great difference which cannot be fully predicted in ground tests. Obviously, the hypersonic complex gasdynamic heating in the interaction region comes from the interaction of three-dimensional (3D) shock waves and boundary layer, which has not been well understood in the current hypersonic gasdynamics. Also the problem of steady 3D shock/shock interaction (SSI) is a key fundamental problem in hypersonic gasdynamics.

2 Theory of 3D Steady SSI Problem

3D steady SSI means the steady interaction of two shock wave planes, which can be widely observed in hypersonic inlet and wing regions. The problem of 3D steady SSI deals with the shock interaction configuration of two shock wave planes, which is different from the problem of shock reflection that often deals with steady or pseudo-steady shock wave reflecting on a wall surface.

According to our recent theoretic work on 3D steady SSI problem, the mechanism of 3D steady SSI is same as that of moving two-dimensional (2D) shock/shock interaction. Each shock configuration of 3D steady SSI problem has its correspondent shock configuration of 2D moving SSI problem [1, 2]. It has been known that there are several complex configurations in 3D steady SSI, for example, regular interaction and irregular interaction. In the irregular interaction configurations of 3D steady SSI problem, simple Mach interaction, complex Mach interaction, and weak interaction exist.

Figure 1 shows numerically simulated regular interaction and simple Mach interaction configuration in 3D steady SSI induced by two intersecting wedges, in which pressure contours show the 3D steady wave structures in both regular interaction and simple Mach interaction.

The above problem of 3D steady SSI can be transformed into that of 2D moving SSI, and then it can be theoretically analyzed with the shock dynamics in a two-dimensional plane. It should be noted that in the irregular 2D moving SSI, the theoretic approach of shock polar is not so applicable since it cannot be transformed to a fully steady problem; the theory of 2D moving SSI and shock dynamics is necessary.

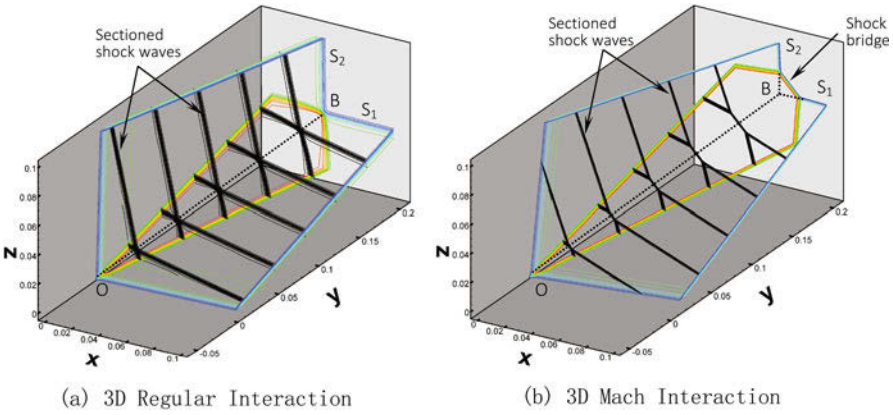

Fig. 1 3D steady SSI induced by two intersecting wedges (S_1 and S_2 denote the two planar shock waves and OB is the interaction line of S1 and S2)

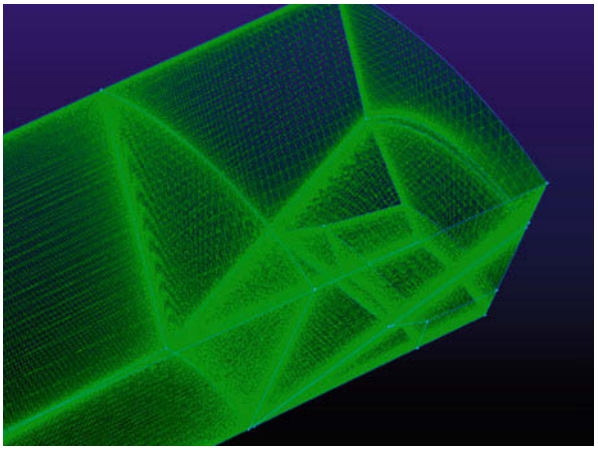

Fig. 2 Meshes of numerical simulation

3 Complex Flows in Hypersonic Interaction Region

Figure 2 shows the numerical meshes of the interaction model of hypersonic body/wing. The interaction of 3D shock waves and boundary layer is mainly concerned. In numerical simulation, 3D Navier-Stokes equations with high-temperature reaction were solved; the fluid media is air. Turbulence simulation adopts the dual equation k-ε model, and fully turbulent inflow at the entrance is adopted. The high-temperature reaction model of air adopts the seven-species model proposed by Park [3], the species including O_2, N_2, O, N, NO, NO^+, and e^-.

The Mach number of the free stream is 10.11, and the cases of attack angles of 0° and 20° are simulated and discussed.

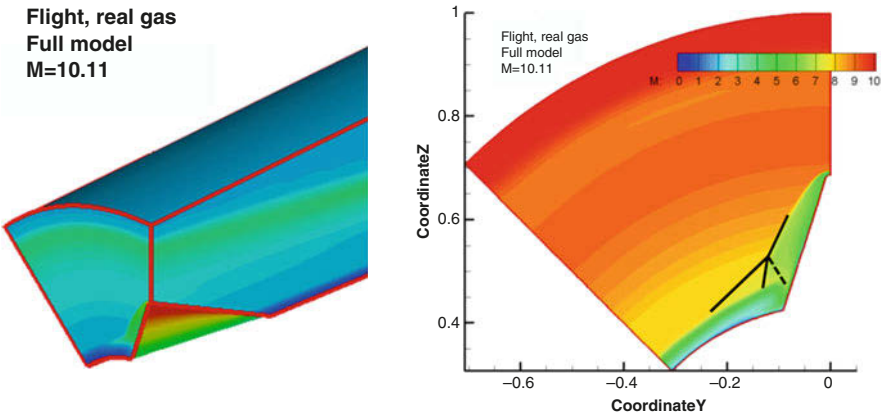

Fig. 3 The flow mechanism of interaction region with 0° attack angle

Figure 3 shows the numerical results of the case of 0° attack angle. In the case of 0° attack angle, 3D interaction of wing shock and boundary layer of body surface can be observed. The flow configuration exhibits 3D λ-type interaction of shock wave and boundary layer. The contact surface induced by 3D shock interaction represents the flow jet inclines to the wing surface, and it makes the boundary layer thin. We can deduce that the position on wing surface impinged by the contact surface has higher heating flux.

Figure 4 shows the numerical results of the case of 20° attack angle. In the case of 20° attack angle, the interaction of body shock and wing shock takes places. The 3D SSI further interacts with the boundary layers of body and wing and causes the complex flow mechanism in the interaction region of body and wing.

In the leading edge of the wing, the interaction of body shock and wing shock is near 3D regular interaction, which causes the appearance of contact surfaces behind the shock interacting point. The direction of contact surface means the flow direction of local flow, that is, the contact surface represents a local flow jet. The local flow jet further impinges on the boundary layer of the leading edge of the wing and makes the boundary layer thinner. Inevitably, the position of flow jet impinging on the boundary layer is a region with higher local heating flux. In the case of 3D SSI, there is always a contact surface representing a local flow jet, so the region with the higher local heating flux always exists.

In the lateral region of the wing, the interaction of body shock and wing shock is near 3D Mach interaction, so there are two tripoints on the both ends of the Mach stem. Also, there are two contact surfaces are formed due to the appearance of 3D Mach interaction. The flow bounded by the two contact surfaces means the flow jet impinging on the boundary layer of wall surface. It will inevitably make the local boundary layer thinner and cause the wall surface region with higher local heating flux.

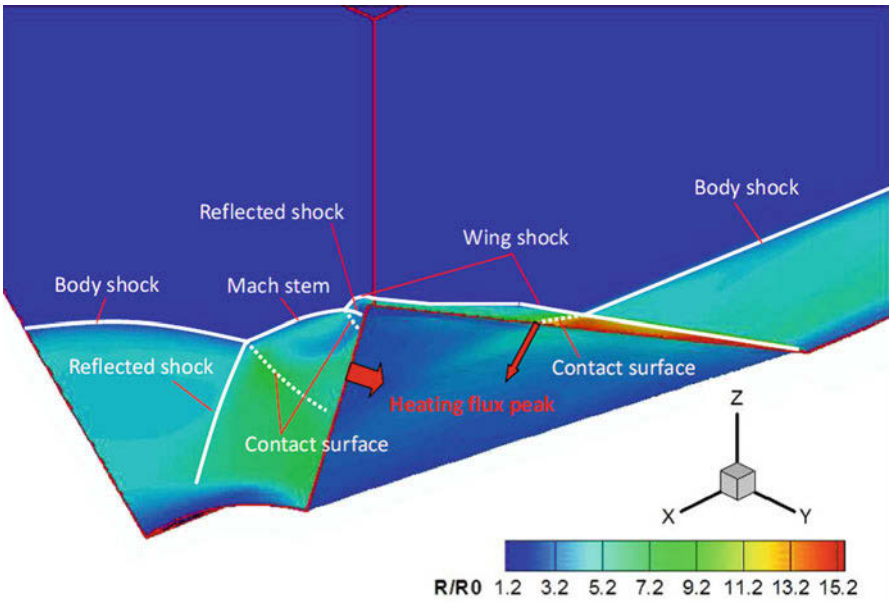

Fig. 4 The flow mechanism of interaction region with 20° attack angle

According to the theory of 3D steady SSI and the numerical flow filed of hypersonic interaction region, we can find that the 3D steady SSI configuration plays an important role on the complex gasdynamic heating in the hypersonic interaction region. As the direction of contact surfaces induced by the 3D steady SSI just represents the local flow direction, the contact surface in the flow field always means a flow jet impinging on the boundary layer of wing surface. The flow jet bounded by the contact surfaces makes the boundary layer thinner and further causes the local heating flux peak. The gasdynamic heating mechanism in the above situations is similar to the IV-type heating mechanism in two-dimensional interaction of shock wave and boundary layer.

Due to the pressure distribution on the wing surface cannot be used to distinguish the contact surface of 3D steady SSI, it is not suitable for the correlation of heating flux distribution. Also, in numerical simulation, the capture of contact surfaces is of great importance to find the local heating flux peak.

4 Concluding Remarks

Three-dimensional steady SSI plays an important role on the 3D steady SSI configuration which plays an important role on the complex gasdynamic heating in the hypersonic interaction region. Theoretical analysis and numerical results show

that complex 3D SSI configuration exists in the hypersonic interaction regions in different flight conditions, both regular interaction and irregular interaction. The contact surface induced by the 3D SSI represents the flow jet inclines to the boundary layer of aircraft surface, which always causes the high local heating flux. In the flight condition with a certain attack angle, complex 3D Mach interaction of shock waves in the interaction region of body/wing exists, which induces the complex flow around the wing; the jet bounded by two contact surfaces inclines to the surface of wing and causes the local heating peak, similar to the IV-type heating mechanism in two-dimensional interaction of shock wave and boundary layer.

References

1. Yang Y., *The investigations on complex flow of three-dimensional shock/shock interaction*, Ph.D. Thesis of Institute of Mechanics, CAS, 2012. (in Chinese)
2. Wang C., Xiang G., Jiang Z., Yang Y., Analytical approach to the problem of three-dimensional steady shock wave interactions, in *Proceedings of the 30th International Symposium on Shock Waves*, Tel Aviv, Israel, 19–24 July, 2015
3. Pack C., On convergence of computation of chemistry reacting flows, in *AIAA 23rd Aerospace Sciences Meeting*, Reno, Nevada, 1985

Numerical Simulation of Effect of Angle of Attack on a Supersonic Parachute System

X. Xue, S. Luo, and C. Y. Wen

Abstract In the present study, a detailed investigation of unsteady supersonic flows around rigid parachute models is performed by numerically solving three-dimensional compressible Navier-Stokes equations at a freestream Mach number of 1.5. The parachute system employed here consists of a capsule and a canopy. The cases with different capsule angles of attack (α) are simulated. The objective of this study is to examine the effects of capsule angle of attack on the flow fields and investigate ways to suppress the complicated aerodynamic interactions around the parachute models. As a result, it is found that as α is increased, the unsteady pulsation flow mode is weaken, and it almost disappears at α =10 deg.

1 Introduction

In the Mars missions, a supersonic parachute has been used to decelerate the spacecraft to the Mars surface. However, in recent studies, on MSL supersonic parachute, it was found that the aerodynamic interference between the capsule wake and canopy shock wave around the parachute system causes the drag decrease and the flow instability increase, which depends on the Mach number, the capsule shape, and the proximity to the capsule [1]. To understand the complexity of the unsteady flow field around a supersonic parachute, a rigid parachute model was employed by Barnhardt et al. [2] and Gidzak et al. [3, 4] to investigate the effect of such wake/shock interaction on the unsteady flow instability. The current research group has conducted the numerical and experimental studies on the rigid parachute models, investigated the effects of the trailing distance (*X/d*) and the ratio

X. Xue (✉) · S. Luo
School of Aeronautics and Astronautics, Central South University, Changsha, P.R.China
e-mail: xuexiaopeng@csu.edu.cn; luoshibin@csu.edu.cn

C. Y. Wen
Department of Mechanical Engineering, The Hong Kong Polytechnic University, Hung Hom, Hong Kong

A. Sasoh et al. (eds.), *31st International Symposium on Shock Waves 2*,
https://doi.org/10.1007/978-3-319-91017-8_114

of the capsule diameter to the canopy diameter (*d/D*) on the supersonic parachute performance [5, 6], and found four unsteady flow modes occur under the effect of *X/d* and the pulsation mode responds to the most unstable flow mode [6].

A new computational fluid dynamics study will further investigate the complicated aerodynamic interactions around the parachute, where the effect of angle of attack (α) is examined on the flow instability.

2 Methods of Simulation

2.1 Parachute Model

The parachute system employed here consists of a capsule and a canopy. Here the rigid parachute model consists of a capsule and a canopy, and the capsule is connected with canopy by a rod (see Fig. 1), which is the same with the experimental model at JAXA [5]. Here *X/d* is 2.38, *d/D* is 0.2, and α is 0, 5, and 10 degrees.

2.2 Numerical Method

The calculations are conducted by solving the three-dimensional compressible Navier-Stokes equations to simulate the supersonic flow fields around parachute model. The simple high-resolution upwind scheme (SHUS) [7] is adopted to computer the inviscid fluxes. The accuracy of this scheme is improved using the 3rd MUSCL scheme with the Van Albada flux limiter. On the other hand, the viscous terms are computed using the usual 2nd order central differencing scheme. The 3rd total variation diminishing Runge-Kutta scheme is used to obtain time accurate

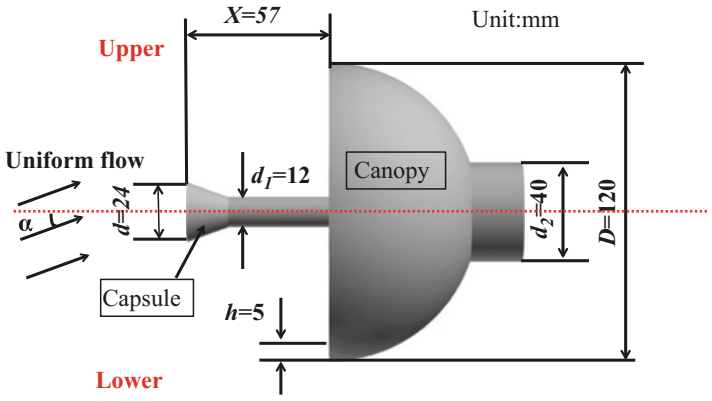

Fig. 1 Parachute model used in the present computation, which is reproduced from [5]

Table 1 Freestream flow conditions in the present study

M_∞	Re	P_0	P_∞	T_0
1.5	2.04×10^{-7} m^{-1}	166 kPa	21.0 kPa	298 K

results in unsteady calculations. In addition, each variable takes its free stream value (see Table 1) for the initial conditions, while nonslip and adiabatic conditions are imposed at body surfaces for the boundary conditions. No turbulence model was used in this study, because in the previous studies [5, 6], the laminar numerical simulations of a rigid parachute model were performed at a freestream Mach number of 2, where a satisfactory agreement was obtained between the computational and experimental data. The extended form of the numerical method used in [5, 6] is employed for the current study.

The freestream conditions used in this study are same with [5], except for the freestream Mach number is 1.5 here, which is listed in Table 1.

2.3 Grids

The 3D rigid parachute model was generated by using a structured, single-block grid, which was created by a meridional plane, due to the axisymmetric configuration of the parachute system. The 3D view and the validity test of the grid convergence were demonstrated in the previous study [5], and a similar grid density was adopted for the present study.

3 Results and Discussion

At $\alpha = 0$ deg., it was found that the flow field around the parachute system exhibits the pulsation mode (see Fig. 2) [5, 6]. When the capsule wake interacts with the canopy shock, the pressure inside the canopy reaches the peak value, the pressure around the capsule frontal surface reaches to the lowest value (see the arrows of Fig. 3), and the pressure difference causes the interaction system to move upstream; as the capsule shock interacts with the canopy shock, the pressures around the capsule and canopy both reach the peak values (see the ellipse of Fig. 3), and the high pressure causes the shock/shock interaction system to expand laterally. The similar pressure changes occur at $\alpha = 5$ deg. (see Fig. 3); however, the unsteady pulsation flow mode becomes much weaker, as shown in Fig. 2. In addition, when $\alpha = 10$ deg., only the weak interaction between the capsule wake and canopy shock is the main characteristics of the flow field around the parachute system (see Fig. 2), and the pressure has a different change trend with the formers, and the pressure difference between the capsule and canopy is small (see Fig. 3), which reveals that the pulsation mode disappears.

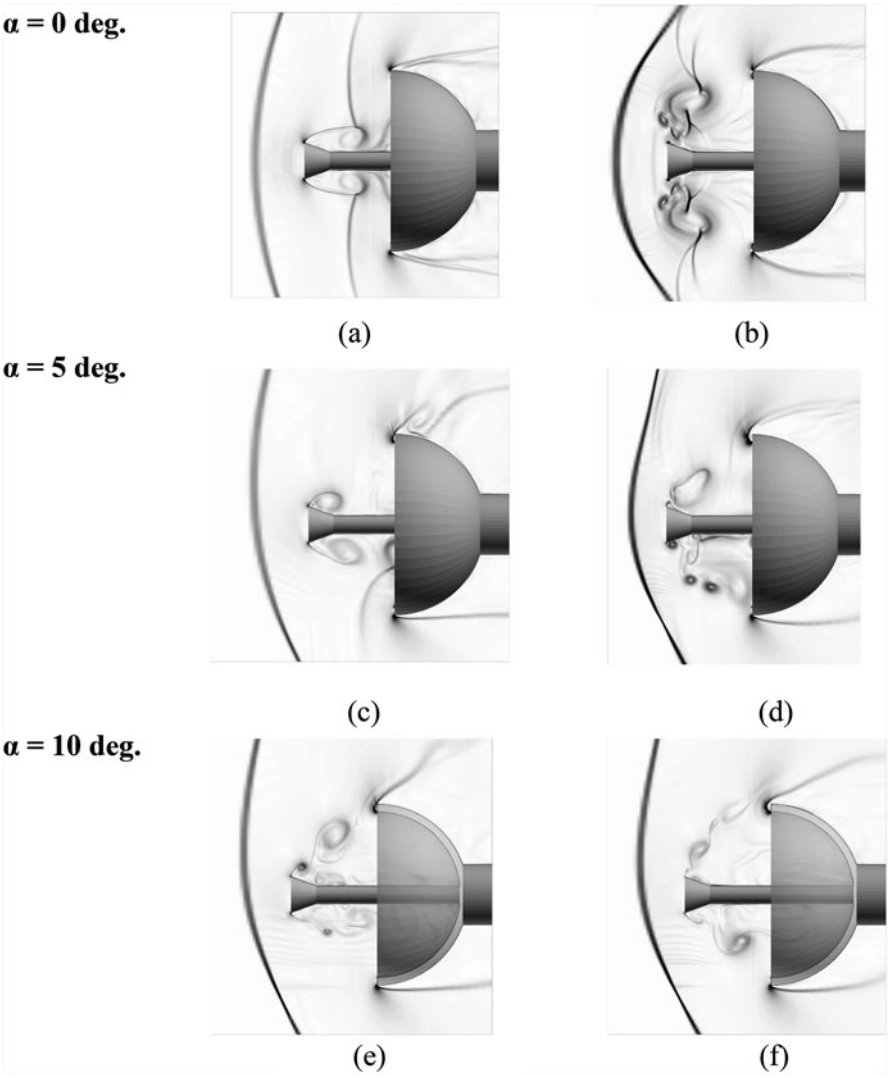

Fig. 2 Comparison of the density gradient contours for the cases of $\alpha = 0{\sim}10$ deg. in two representative instantaneous flow fields of aerodynamic interaction. T is the time period for the unsteady flow mode, and the subscripts 0, 5, and 10 indicate the angle of attack cases: (**a**) $t = 5\ T_0/24$, (**b**) $t = 13\ T_0/24$, (**c**) $t = 5\ T_5/24$, (**d**) $t = 15\ T_5/24$, (**e**) $t = 5\ T_{10}/22$, (**f**) $t = 14\ T_{10}/22$

In addition, when $\alpha \neq 0$ deg. and $M_\infty = 2$, the aerodynamic interactions around the parachute system exhibit apparent asymmetric flow features with the same flow pulsation mode [8]. However, in this study, at $\alpha = 10$ deg., the pulsation mode disappears, and a new flow mode is present.

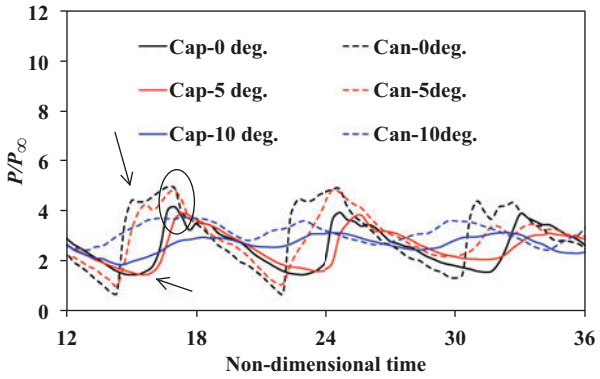

Fig. 3 Pressure histories of the center point of the capsule frontal surface and the intersection point of the connecting rod and canopy inner surface; here nondimensional time refers to [5]

4 Conclusion

The flow instability of the supersonic parachute system originates from the aerodynamic interference between the canopy shock/capsule wake and the canopy shock/capsule shock. Moreover, it was found that Mach number and angle of attack have important effects on the flow instability around parachute system, and when Mach number is 1.5, the pulsation mode may disappear at $\alpha = 10$ deg.

References

1. A. Sengupta, Fluid structure interaction of parachutes in supersonic planetary entry, AIAA-2011-2541 (2011)
2. M. Barnhardt, T. Drayna, I. Nompelis, C.V. Candler, W. Garrard, Detached eddy simulations of the MSL parachute at supersonic conditions, AIAA-2007-2529 (2007)
3. V. Gidzak, M. Barnhardt, T. Drayna, I. Nompelis, C.V. Candler, W. Garrard, Simulation of fluid-structure interaction of the Mars Science Laboratory parachute, AIAA-2008-6910 (2008)
4. V. Gidzak, M. Barnhardt, T. Drayna, I. Nompelis, C. V. Candler, W. Garrard, Comparison of fluid-structure interaction simulation of the MSL parachute with wind tunnel tests, AIAA-2009-2971 (2009)
5. X. Xue, H. Koyama, Y. Nakamura, Numerical simulation on supersonic aerodynamic interaction of a parachute system. Trans. JSASS Aerospace Tech. Japan. **11**, 33–42 (2013)
6. X. Xue, H. Koyama, Y. Nakamura, K. Mori, C.Y. Wen, Parametric study on aerodynamic interaction of supersonic parachute system. AIAA J. **53**, 2796–2801 (2015)
7. E. Shima, T. Jounouchi, Roe of CFD in Aeronautical Engineering (No.14)-AUSM Type Upwind Schemes-, NAL-SP30, in *Proceedings of 13th NAL symposium on Aircraft Computational Aerodynamics*, 1996, pp. 41–46
8. X. Xue, Y. Nakamura, K. Mori, C.-Y. Wen, H. Jia, Numerical investigation of effects of angle-of-attack on a parachute-like two-body system. Aerosp. Sci. Technol. **69**, 370–386 (2017)

Experimental Study of High-Altitude Environment Simulation for Space Launch Vehicles

Sungmin Lee and Gisu Park

Abstract In this work, a high-altitude environment simulation of space launch vehicle has been examined experimentally. One flow condition was used to replicate Mach 6 flight condition for the Korean Space Launch Vehicle (KSLV-II) at an altitude of 65 km. Flow verification was carried out by measuring stagnation pressure, heat flux, and shock standoff distance. Four different configurations of scaled models were used, respectively, to simulate a particular region of the launch vehicle. The models considered examined the shock wave patterns around the launch vehicle, the aerothermodynamic properties on the forebody flow, the aspects of obtaining shock-free technique, and an interaction between nozzle plume and shear layer emanated from the incoming boundary layer of the model.

1 Introduction

Experimental studies on space launch vehicles should be preceded for the successful completion of missions and cost reduction of space launch vehicles. Such experimental research is linked to national security, so it is not possible to obtain relevant data from advanced research institutes [1–5]. In Korea, on the other hand, only an analytical study on high-altitude environment simulations of space launch vehicles including propulsion systems has been carried out in various research institutes based on the Korea Aerospace Research Institute (KARI) [6–8]. There are no experimental studies on the high-altitude environment simulations conducted by domestic research institutes.

In this study, it was conducted to secure the high-altitude environment simulation technique for the independent development of domestic space launch vehicle and to build an experimental database. As the basis, high-altitude atmospheric conditions of KSLV-II exceeding Mach number 6 at 65 km are used in KAIST K1 shock

S. Lee · G. Park (✉)
Korea Advanced Institute of Science and Technology, Daejeon, Republic of Korea
e-mail: gisu82@kaist.ac.kr

A. Sasoh et al. (eds.), *31st International Symposium on Shock Waves 2*,
https://doi.org/10.1007/978-3-319-91017-8_115

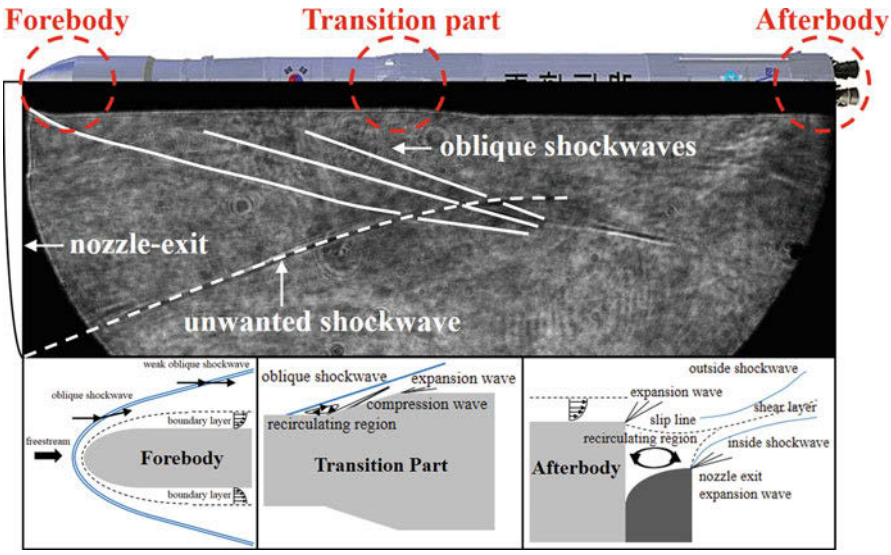

Fig. 1 Region of interests for aerodynamic analysis of KSLV-II: (**a**) forebody, (**b**) transition part, (**c**) afterbody

tunnel. Figure 1 is a schematic diagram of several key phenomena occurring in the forebody, transition part, and afterbody of KSLV-II. The flow development and shock wave patterns were confirmed by visualization technique for each part, and quantitative analysis was performed by pressure and heat flux measurement. Especially a reasonable experiment was performed by applying a shock-free shape to recover the freestream through the cancelation of the compressive wave and the expansion wave in a scaled down transition part and afterbody model requiring freestream formation on the model surface.

2 Flow Condition

Target altitude atmospheric pressure, temperature, and density data are applied to calculate the specific heat (C_p), sound speed (a_1), viscous coefficient (μ_1), and specific heat ratio (γ_1) through the CEA program, and Mach number (M_1), velocity (u_1), and Reynolds number (Re_1) of freestream flow condition can be calculated (Fig. 2). Then, the enthalpy and the pitot pressure can be calculated through the enthalpy relation and the Rayleigh pitot formula.

Using the calculated H_t and P_{pitot} values, the temperature (T_2), density (ρ_2), viscosity (μ_2), and Reynolds number (Re_2) of the post-shock condition are obtained. The density ($\rho_{2,model}$) of the 100:1 scaled down model of KSLV-II head shape is obtained through binary scaling (fixed density (ρ) times model diameter (D)). To

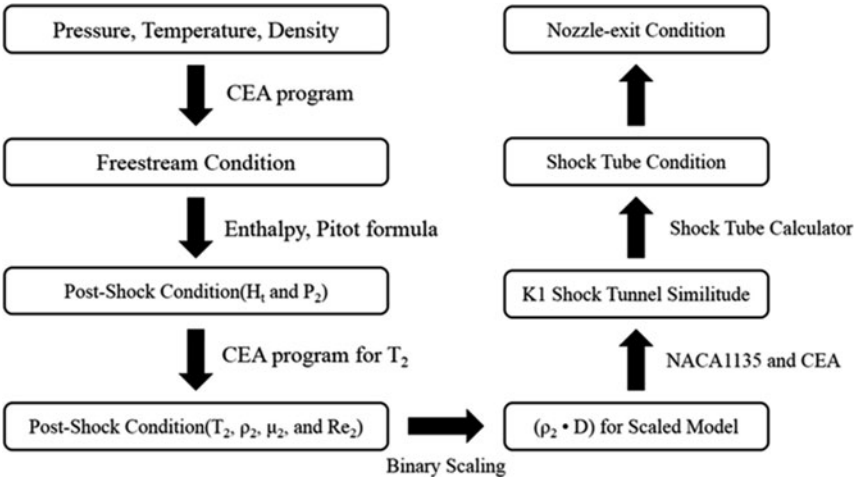

Fig. 2 Flowchart for calculation of flow condition

Table 1 Freestream flow condition

Property	Value
$M_\infty[-]$	6
$T_\infty[K]$	231
$\rho_\infty[kg/m^3]$	0.016
$R_\infty[J/kg{\cdot}K]$	289
$u_\infty[m/s]$	1833

calculate the nozzle exit freestream condition of the K1 shock tunnel used in this study, the freestream density (ρ_1) is calculated through the one-dimensional vertical shock wave relation assuming ideal gas. Finally, by using NASA technical report NACA1135, CEA program, and shock tube calculator, K1 shock tunnel pressurizing and nozzle exit freestream conditions are calculated. The results are summarized in Table 1.

Stagnation pressure was measured through both methods of pitot pressure sensor installation, flush mount and recessed mount. The flush mount uses a pitot probe with a flat surface on which the sensor surface is directly exposed to the flow, and the recessed mount retracts the sensor from the surface and forms a cavity in a small radius nose cone. The flush mount method confirmed a reasonable flow development with an error of $\pm 1\%$ (Fig. 3a) and confirmed that the cavity and grease effects for recessed mount sensor surface noise damping had an error of about $\pm 8\%$. Furthermore, we used our in-house thermocouple to measure the stagnation heat flux and compare it with Fay and Riddell's theoretical data of hypersonic flow stagnation heat flux [9]. Using the measured temperature difference, the heat flux was calculated to be about 1.33 MW/m^2, which is within only $\pm 1\%$ of the theoretical value (Fig. 3b). Shockwave standoff distance was measured in steady-state condition of the flow. The standoff distance (δ) was measured to be about

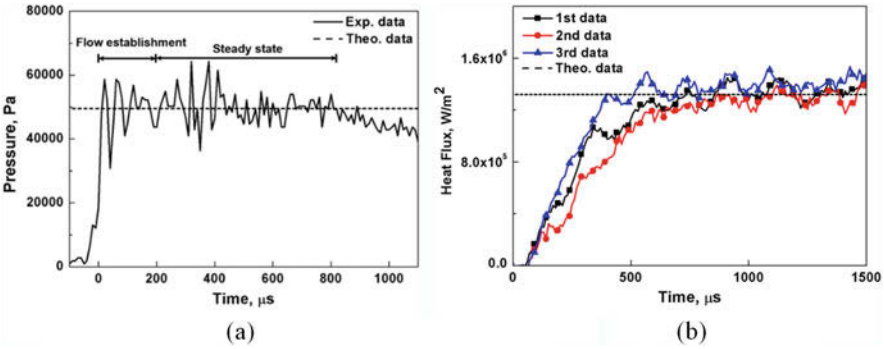

Fig. 3 Stagnation pressure and heat flux measurement results: (**a**) a flush mount pressure data, (**b**) heat flux measurement data

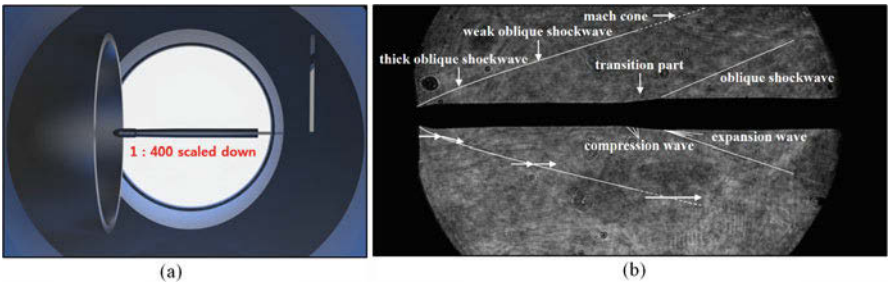

Fig. 4 KSLV-II entire shape model test result: (**a**) schematic of a test section, (**b**) shadowgraph measurement result

2.26 mm, and the ratio δ/d to the hemispherical model diameter (d) was 0.075, which is consistent with the experiment of Mach 6 flow conditions [10].

3 Results and Discussion

3.1 KSLV-II Entire Shape

Shadowgraph measurement for scaled down entire shape of KSLV-II was performed (Fig. 4a). Thick shock wave, weak shock wave, and Mach cone in supersonic and hypersonic environments were identified, and each of the resulting flows is shown in Fig. 4b. It was confirmed that a compression wave and an expansion wave occurred due to the diameter change of the transition part at the center of the model and a secondary oblique shock wave was formed.

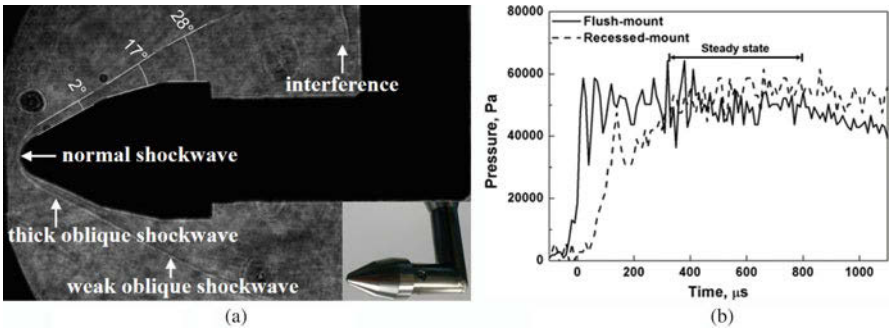

Fig. 5 Forebody test model and results: (**a**) forebody shadowgraph image, (**b**) two methods of pressure measurement

3.2 Forebody

The shape of the oblique shock wave formed on the forebody model was confirmed (Fig. 5a), and a recessed mount was used to form the cavity by retracting the sensor from the surface in a small radius nose cone for pressure measurement. It was confirmed that the cavity and grease effects for recessed mount sensor surface noise damping had an error of about ±8% (Fig. 5b). In addition, it was confirmed through the stagnation heat flux measurement of the forebody that a reasonable flow within about ±1% was developed compared with the theoretical data of hypersonic flow stagnation heat flux (Fig. 3b).

3.3 Transition Part

For the scaled down model of the transition part located at the middle point of the KSLV-II, a shock-free shape with a symmetrical inflection point was used to cancel the compression wave and the expansion wave (Fig. 6a). The static pressure and inclination angle measurement verified that a reasonable freestream recovery was achieved on the model side surface through the shock-free shape (Fig. 6b). The static pressure measurement results had an error within ±10%, due to the noise phenomenon in the low-pressure range, as compared with the theoretical value of 1057 Pa. The inclination angle measurement was compared with the theoretical inclination angle 9.59°, where Mach number is maintained even after the oblique shock wave at Mach number 6 flow with the plate model having a zero angle of attack. The inclination angle was 9.42°, which indicates an error of about 1.8%.

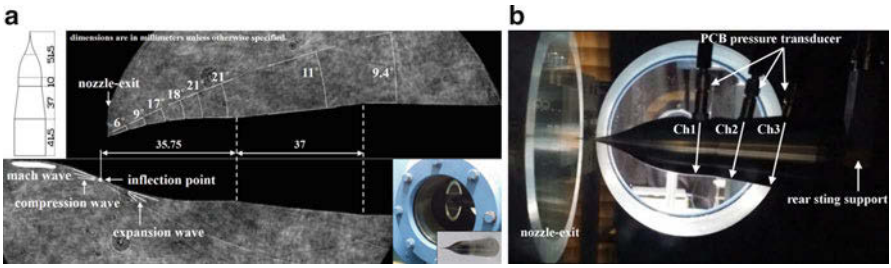

Fig. 6 Transition part model with shock-free shape: (**a**) shock-free shape and principle, (**b**) pressure and inclination angle test

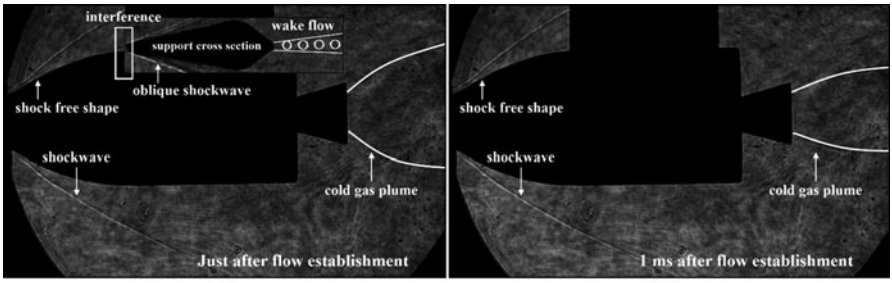

Fig. 7 Cold gas thruster visualization results: (**a**) with underexpansion plume, (**b**) with changing to the overexpansion plume

3.4 Afterbody

A single cold gas conical nozzle was installed at the base plane of the model. The plume from the thruster showed the flow development process in a high-altitude environment. Immediately after the intersection of freestream and cold gas plume, an underexpansion plume was formed (Fig. 7a). It was confirmed that after about 1 ms beyond the steady-state flow, the back pressure increase causes overexpansion plume (Fig. 7b). In order to minimize the effect of interference and the influence of the shape of the model support, the wake flow thickness at the end of model has been measured according to the shape of the support.

4 Conclusions

As a preliminary study of high-altitude environment simulations, the atmospheric condition of KSLV-II at an altitude of 65 km and the Mach number 6 was selected. The pressurizing conditions for the target flow condition were theoretically calculated, and flow verification was performed at the exit of the K1 shock tunnel

nozzle. Using the entire shape model of KSLV-II, we confirmed several phenomena including the oblique shock wave, compression and expansion waves between the flow and the model surface in hypersonic environment. Through the forebody model test, more detailed shock wave pattern, the stagnation pressure, and the heat flux were measured. By using the transition part model, the shock-free shape is proved to be effective for the freestream recovery of the scaled down model used in ground shock wave tests. Finally, afterbody model experiments confirmed the shock-shock interaction between freestream and cold gas plume and shape change of plume due to back pressure increase. In the near future, a study on the heating gas thruster test for actual exhaust gas simulation and support shape for minimizing external flow disturbance will be carried out.

Acknowledgment This work was supported by the Korea Space Launch Vehicle (KSLV-II) funded by the Ministry of Science, Information and Communications Technology, and Future Planning (MSIP, Korea) as well as the BK21 plus program.

References

1. S. Stephan, R. Radespiel, and R. Muller-Eigner, Jet simulation facility using the Ludwieg tube principle, 5th Eur. Conf. Aerosp. Sci. pp. 1–15 (2013)
2. S. Stephan, J. Wu, and R. Radespiel, Propulsive jet influence on generic launcher base flow, CEAS Sp. J. **7**, 4 (2015)
3. A. Justin, R. James, S. Panicker, A. N. Subash, and S. Kumar, Development of high altitude test facility for cold jet simulation, J. Res. Aero. M. Eng. **2**, 9 (2014)
4. R. Nallasamy, M. Kandula, L. Duncil, and P. Schallhorn, Numerical simulation of the base flow and heat transfer characteristics of a four-nozzle clustered rocket engine, 50th Therm. Conf. pp. 1–28 (2008)
5. D. Saile, and A. Gulhan, Plume-induced effects on the near-wake region of a generic space launcher geometry, in *32nd AIAA Applied Aerodynamics Conference*. AIAA 2014–3137 (2014)
6. J. H. Lee, H. Ok, Y. Kim, and I. Kim, A numerical analysis of aerodynamic characteristics and loads for KSLV-II configuration at the system design phase. Aerosp. Eng. Tech. **12**, 1 (2013)
7. W. Jeon, S. Baek, J. Park, and D. Ha, Rocket plume analysis with DSMC method. J. Kor. Soci. Prop. Eng. **18**, 5 (2014)
8. S. J. Ahn, N. Hur, and O. J. Kwon, Numerical investigation of plume-induced flow separation for a space launch vehicle. J. Comp. Fl. Eng. **18**, 2 (2013)
9. G. Park, Oxygen catalytic recombination on copper oxide in tertiary gas mixtures. J. Spacecr. Rocket. **50**, 3 (2013)
10. H. W. Liepmann, and A. Roshko, *Elements of Gas Dynamics* (Wiley, New York, 1993), pp. 102–106

Characteristics of Self-Sustained-Shock Pulsation

Toshiharu Mizukaki and Kazuhiko Yamada

Abstract Shock wave visualization around a circular cylinder with aerospike has been conducted to reveal characteristic of shock pulsation around supersonic parachute. The frequency of shock pulsation has been changed by valuing the ratio of the depth to the diameter, L/D, of the circular model that was valued from zero to two. Pressure history at the bottom of the circular cylinder model was recorded to analyze frequency of the shock pulsation. The characteristic of shock pulsation has strongly been affected by L/D in flow with strong disturbance.

1 Introduction

In general, parachutes are employed to decrease the speed of the aircraft after landing, the object dropped from aircraft, and the personnel evacuating from a malfunctioned vehicle. Furthermore, not only for aircrafts but also for spacecraft, parachutes are employed to decelerate their speed at the entry stage into other planets (ex. Mars) or the reentry into the Earth because parachutes have less weight and space for storage than other devices. The parachute used for planetary probing is often called "supersonic parachute" because the vehicles would be at supersonic speed when the parachute would be deployed.

At supersonic speeds, aerodynamic phenomena including bow shock, separation flows, and vortices appear around a parachute. The bow shock in front of the parachute would be influenced by the disturbances in the subsonic region that appears behind the bow shock and inside the parachute because all the phenomena

T. Mizukaki (✉)
Department of Aeronautics and Astronautics, Tokai University, Tokyo, Japan
e-mail: mizukaki@keyaki.cc.u-tokai.ac.jp

K. Yamada
Institute of Space and Astronautics Science, JAXA, Sagamihara, Japan

A. Sasoh et al. (eds.), *31st International Symposium on Shock Waves 2*,
https://doi.org/10.1007/978-3-319-91017-8_116

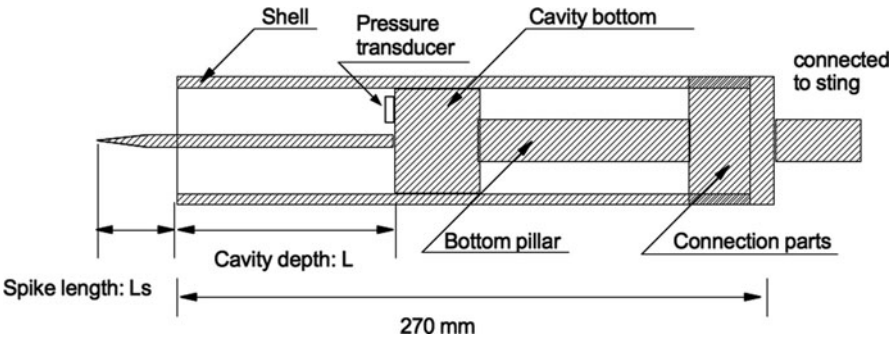

Fig. 1 A schematic diagram of the cavity model; the aerospike with semi-apex angle of 10°

appeared in the subsonic region shall affect over the subsonic region. Therefore, all the disturbance inside the supersonic parachutes at supersonic speeds needs to be investigated in detail.

In this study, experimental and numerical investigation on the characteristics of oscillation of shock waves in front of a cylindrical cavity model with an aerospike has been performed.

2 Experimental Method

The model examined was the cylindrical cavity with 50-mm in diameter, made of stainless steel. The aerospike with 40 mm for Mach 2.0 or 60 mm for Mach 3.0 was attached at the bottom of the cavity (Fig. 1). The ratio of the depth L to the diameter D, L/D, varied from 0.0 to 2.0. A strain gauge-type pressure transducer (Kyowa PS-5KC) was placed at the bottom of the cavity for measurement of resonant frequency. A strain gauge amplifier (TEAC SA-59) was employed for bridge excitation and signal amplification. The pressure history was recorded with an oscilloscope (Yokogawa DL-750) by 50,000 Sa/s. The experiment was conducted at Mach number 2.0 or 3.0. The experiments were performed in the 600 × 600 mm supersonic wind tunnel of JAXA/ISAS. Ordinary schlieren method with a high-speed video camera was employed to visualize behavior of the shock waves around the cylindrical cavity model. The images were recorded with 40,000 frames per second and 20 microsecond for exposure time (Fig. 2).

3 Numerical Method

Supersonic flow field, at Mach 2 and 3, around a cylindrical cavity model is numerically simulated with a two-dimensional axisymmetric flow solver. This study assumes that gases are viscid and follow the equation of state for perfect

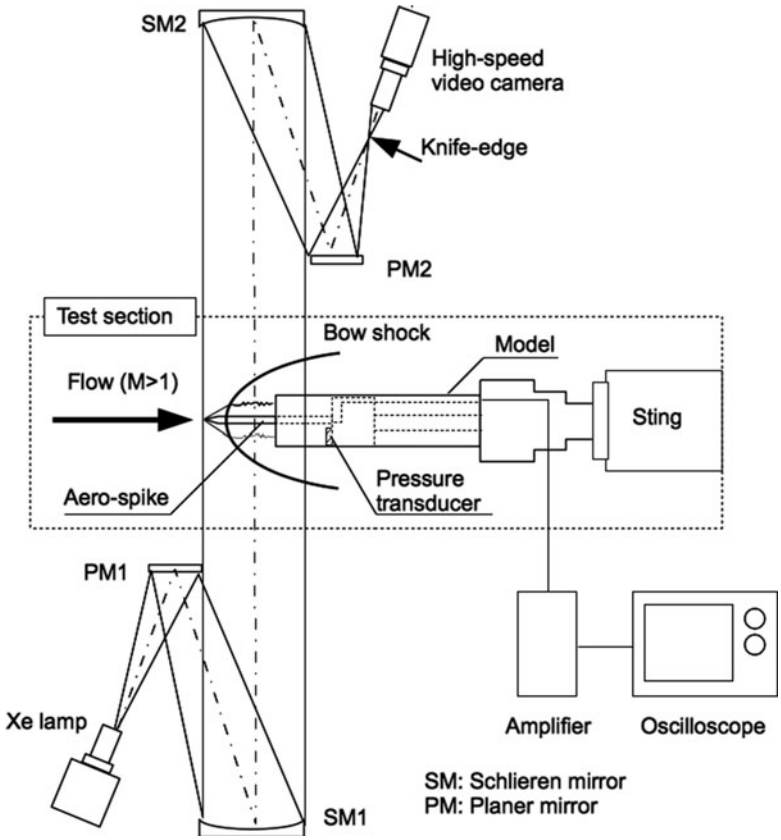

Fig. 2 Schematic diagram of experimental setup for shock oscillation. *PM*, plane mirror; *SM*, schlieren mirror

gases. The weighted average flux scheme (WAF) is used to solve higher-order extended Godunov scheme with second-order accuracy both in time and space. It is constructed as a finite-volume method using the integral form of the governing equations. The HLLC approximate Riemann solver with a TVD limiter function is utilized for inner cell flux evaluation. The adaptive mesh refinement (AMR) is used to capture the shock waves around the cylindrical cavity.

4 Result

Figures 3 and 4 show results of shock waves visualization by the high-speed camera on L/D = 0.50, for Mach 2 (Fig. 3) and Mach 3 (Fig. 4). The value, L/D = 0.5, is the same ratio for supersonic parachutes because shape of typical parachute

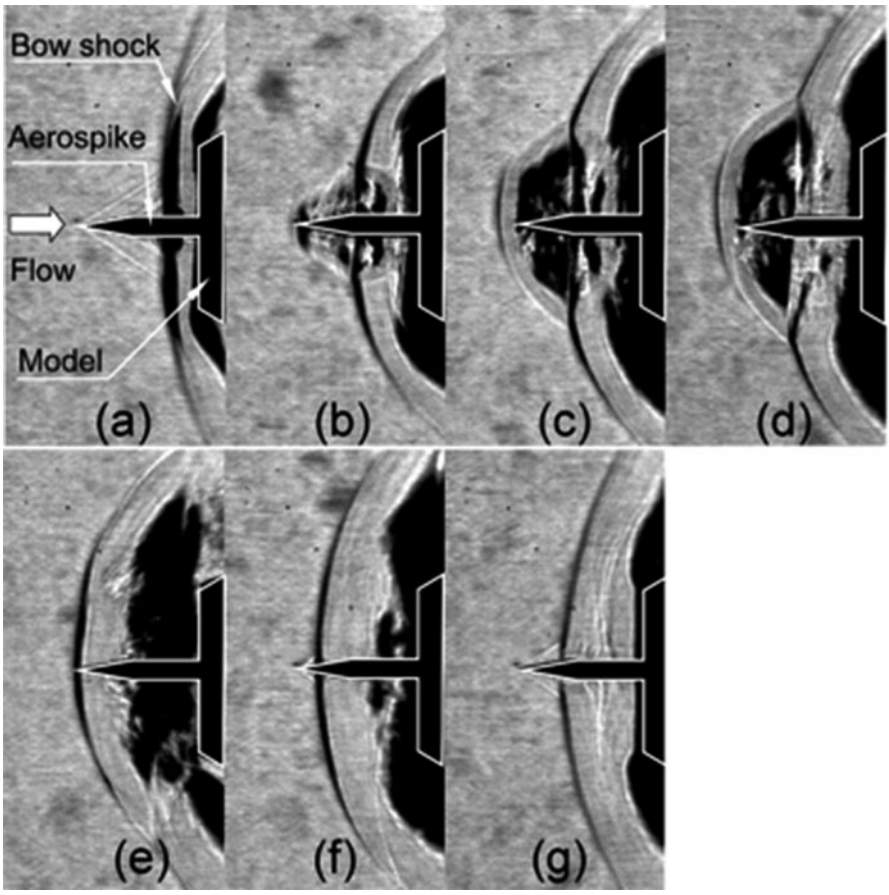

Fig. 3 Sequential schlieren image around the model; time interval t_{int}, 100 μs; exposure time t_{ex}, 20 μs. Flow and model configuration, M = 2.0, L/D = 0.50

is hemisphere. The disturbances produced by aerospike induce large-scale shock oscillation between the tip of the aerospike and the cylindrical cavity model. The frequency of the oscillations is revealed to be approximately 1410 Hz and 1480 Hz for Mach 2 and Mach 3, respectively.

Figure 5 shows the pressure histories at the bottom of the cylindrical cavity model. Both visualization images and the pressure histories indicate that the oscillation of the shock waves is affected not only by flow Mach number but also by cavity depth because the frequency of the oscillation has less dependence on flow Mach number.

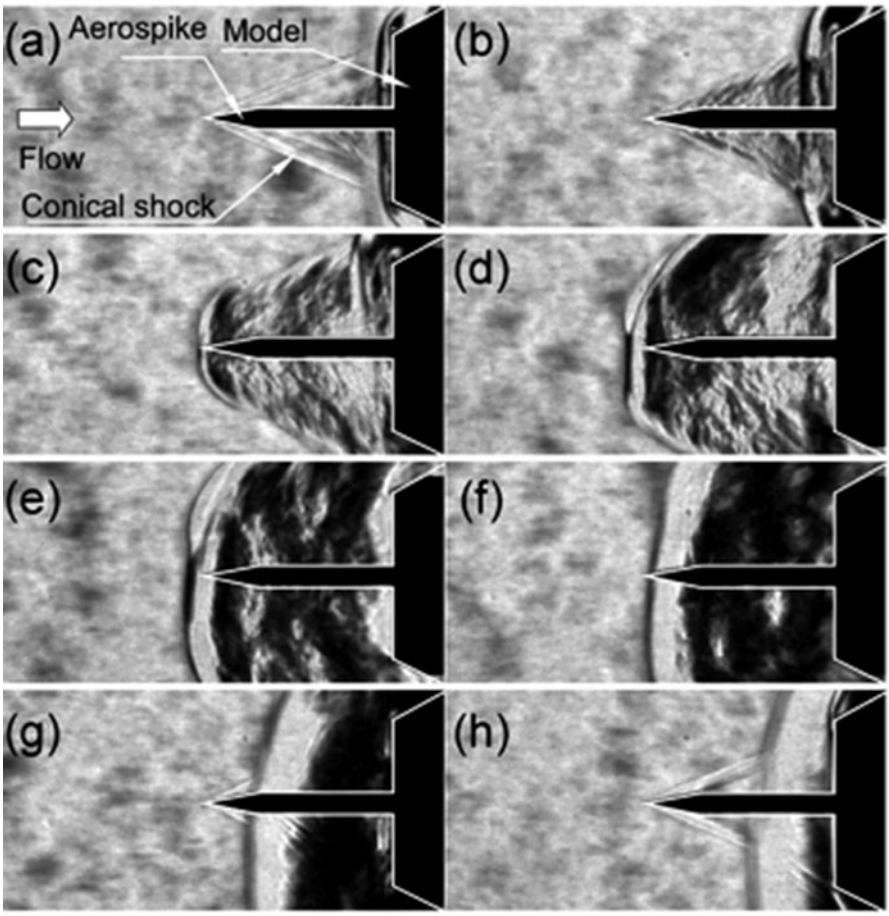

Fig. 4 Sequential schlieren image around the model; time interval t_{int}, 100 μs; exposure time t_{ex}, 20 μs. Flow and model configuration, M = 3.0, L/D = 0.50

5 Conclusion

To determine the predominant factor of BOW shock oscillation ahead of a forward-facing concave in supersonic turbulence, the BOW shock behavior and pressure history have been examined with Helmholtz's resonator model equipped with spike. The conclusions are shown below:

- Thirty-four configurations including contrast one have been examined and clearly visualized.
- Predominant factor, the critical L/D: (L/D)*, above which Helmholtz frequency dominants the BOW sock behavior, has been determined: 0.5 for M2.0 and 1.0 for M3.0.

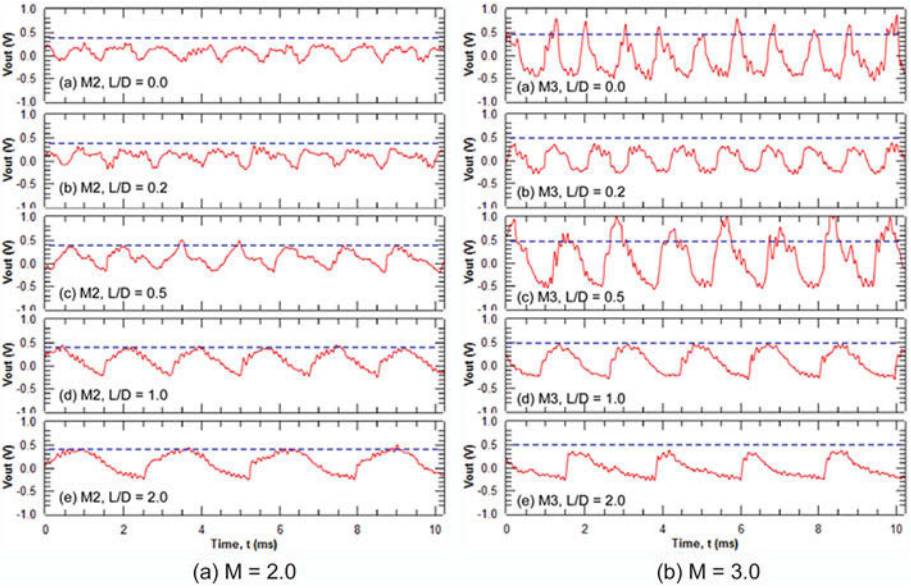

Fig. 5 Histories of the pressure at the bottom of the cylindrical cavity model at Mach 2 and 3 (**a**) $M = 2.0$ (**b**) $M = 3.0$

- Numerical analysis excluding acoustic dumping rate could not reproduce the experimental results. It suggests that acoustic dumping rate acts important role at L/D<(L/D)*.
- Supersonic parachute, which L/D = 0.5, would be in critical condition at its deployment.

References

1. Rudi J. Berndt: Supersonic Parachute Research. ASD-TDR-62-236 (1962)
2. H. Hiraki, Y. Takakura, N. Arai: Flow Characteristics around a Concave Body in Supersonic Flows, Japan Symposium on Shock Waves 18-C-1-3 (2008) (in Japanese)
3. Air Force Flight Dynamics Laboratory: Recovery System Design Guide. AFFDL-TR-78-151 (1978)

Free Flight Experiment Investigation of AOA Effect on Cone Boundary Layer Transition at Mach 6

Zonghao Wang, Sen Liu, and Jie Huang

Abstract To investigate the angle of attack (AOA) effect of hypersonic boundary layer transition on slightly blunted cone, China Aerodynamics Research and Development Center has conducted a series of ballistic free flight experiments on 5° half angle circular cones. The projectile is 110 mm long with surface roughness between 0.46 μm and 0.77 μm. Six shots were taken under Mach 6 and separated unit Reynolds numbers, and the AOA varied between 0.2° and 7.9°. Results showed that the transition shifted upward to the nose tip on the leeside and afterward to the bottom on the windside within small AOA of less than 3°. When the angle got further increased, the moving direction of the transition on the windside reversed toward the nose tip but will not exceed the leeside in present results with nose tip radius of less than 0.4 mm. The transition Reynolds number without AOA was about 4.7×10^6, and there was a noticeable decrement with AOA, which may relate with both pressure gradient and wall heating difference.

1 Introduction

Boundary-layer transition has always been hotspot of aerodynamic theory and experimental research, because of the important effects of boundary-layer to wide range of aerodynamic problems, especially for hypersonic vehicles. Since the famous Reynolds' water tube test in 1983, which found laminar and turbulence, researches on transition problems never stopped. For low-speed flow, semi-engineer method based on linear stability theory (LST) can predict the transition well. However, for supersonic and hypersonic flow, strong compression, high temperature, ablation, and real-gas effect make the boundary layer flow extremely complex. On one side, the environment disturbance differences reduce the ground test accuracy, and on the other side, most of the measurement technologies become useless or

Z. Wang · S. Liu (✉) · J. Huang
Hypervelocity Aerodynamics Institute, China Aerodynamics Research and Development Center, Mianyang, People's Republic of China
e-mail: liusen@cardc.cn

A. Sasoh et al. (eds.), *31st International Symposium on Shock Waves 2*,
https://doi.org/10.1007/978-3-319-91017-8_117

unreliable in hypersonic condition. That is why the test results of a circular cone model, which is simple in shape but complicated in transition phenomena, differ from one facility to another.

For the effect of AOA, most present research results show that transition moves toward the nose tip on the leeside and moves opposite direction on the windside [1–8], while other tests show transition reverse [9–14]. This reveals the complexity of transition experiments, especially for blunted cone, and how to obtain consistent and reliable data becomes very important. Fly test is ideal, but it costs a lot and the test cycle is long. As a compromise, free flight test in ballistic range presents a new efficiency and effective approach.

Ballistic range, different from other wind tunnels, avoids the influence of support structures and background noise. The projectiles, accelerated to hypervelocity by a two-stage light-gas gun, fly freely in the test chamber, where the wall to stagnation temperature ratio and real-gas effect can be the same as the real flight. Recently, CARDC upgraded the shadowgraph imaging system of its ballistic range and applied in boundary layer flow visualization [15]. This paper will present a preliminary AOA effect study on circular cone at Mach 6 and try to improve the understanding of hypersonic boundary layer transition by qualitative and quantitative analysis.

2 Experiment Method

The experiment was carried out in the aerophysics range of Hypervelocity Aerodynamics Institute, CARDC. This facility consists of launch system, measurement system and test chamber, shown in Fig. 1. The launch system is a two-stage light-gas gun with 28 mm launch tube and maximum 7.2 km/s launch velocity. The measurement system contains three laser detect devices for velocity measurement, a set of high-resolution shadowgraph imaging station, and a central computer. The test chamber can simulate a flight environment of up to 60 km atmosphere by changing the vacuum level.

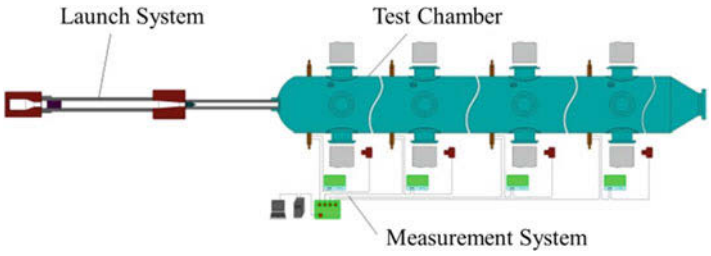

Fig. 1 Schematic diagram of CARDC aerophysics range

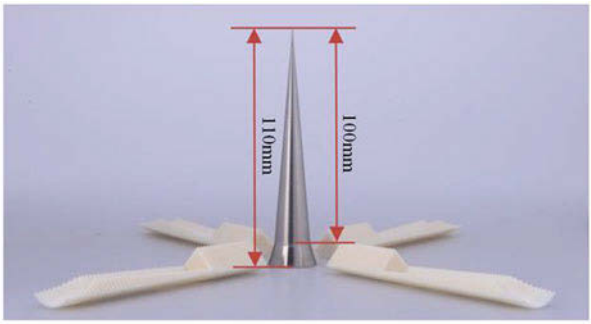

Fig. 2 The cone model and sabot

The 5° half angle circular cone model and sabot are shown in Fig. 2. It is about 110 mm long with skirt, and the radius of the nose tip is under 0.4 mm. It is made of steel and weight around 79 g. The surface roughness is between 0.46 μm and 0.77 μm. The projectile must stand high acceleration load in the launch tube. Own to the soft launch technology [17], the launch load was notably reduced, and the successful launch rate was improved.

Mach number and Reynolds number are mainly simulated by controling launch velocity and environment pressure separately in the ballistic range test. The Mach number is selected as 6 which is equal to about 2 km/s at the normal temperature.

3 Test Result

The conditions and results, including 6 shots, are shown in Table 1. The transition point X stands for the coordinate value of x axis started from the nose of the model. The tests were carried out under room temperature, and the wall to stagnation temperature ratio T_w/T_0 was about 0.12. The transition Reynolds number is defined as $Re_{tr} = X \times Re_\infty/L$. Test ZL-15, ZL-16, and ZL-29 had almost the same unit Reynolds number of about 6.5×10^7 m^{-1}, while the other three tests had a higher unit Reynolds number of about 8.5×10^7 m^{-1}, and their transition points were relatively earlier than the former group.

Figures 3 and 4 showed the shadowgraph images of test ZL-13 and ZL-30. They had nearly the same unit Reynolds number but different AOA of 7.9° and 0.2° separately. There were vast of spokewise acoustic waves, which were induced by turbulence, among the main shock and the cone surface. The pressure gradient from the windside to the leeside may cause cross flow and made the thickness of the boundary layer on the leeside greater than the windside. The transition points on both sides of the cone seemed equal in test ZL-30 as the cone flied with almost zero AOA. Turbulent spots and intermittent turbulence can be seen on the surface of the model.

Table 1 Test conditions and results

	Nose tip radius R (mm)	Ma_∞	Re_∞/L (m^{-1})	AOA (deg)	Transition point X (mm)		Re_{tr}	
					Windside	Leeside	Windside	Leeside
ZL-13	0.25	5.77	8.56×10^7	7.9	30	13	2.57×10^6	1.11×10^6
ZL-15	0.31	5.80	6.52×10^7	8.5	47	18	3.06×10^6	1.17×10^6
ZL-16	0.18	5.83	6.82×10^7	2.3	76	66	5.18×10^6	4.50×10^6
ZL-29	0.33	5.65	6.48×10^7	2.6	68	64	4.41×10^6	4.15×10^6
ZL-30	0.24	5.76	8.82×10^7	0.2	53	53	4.67×10^6	4.67×10^6
ZL-35	0.16	5.72	8.75×10^7	1.2	55	44	4.81×10^6	3.85×10^6

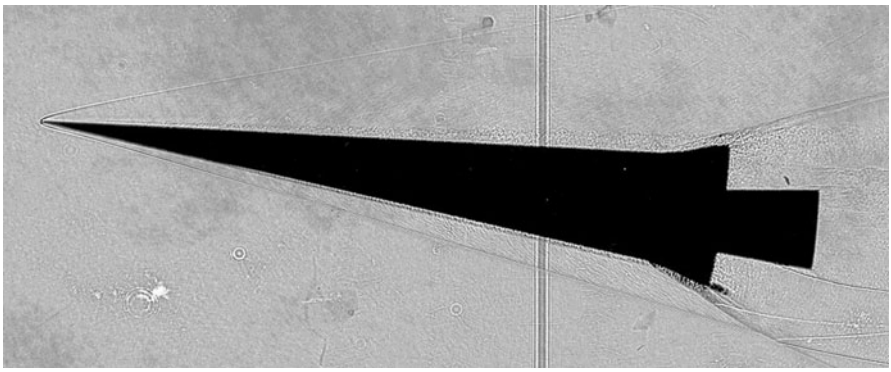

Fig. 3 The shadowgraph image of test ZL-13 (Ma = 5.77, Re/L = 8.56×10^7 m^{-1}, $\alpha = 7.9°$)

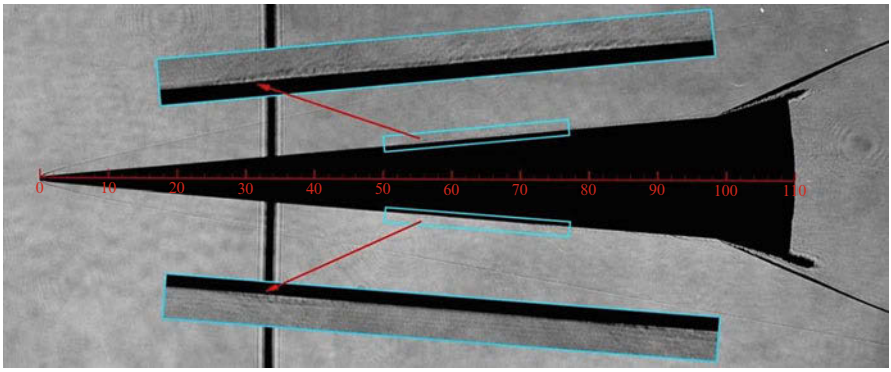

Fig. 4 The shadowgraph image of test ZL-30 (Ma = 5.76, Re/L = 8.82×10^7 m^{-1}, $\alpha = 0.2°$)

There were vortexes in the transition and turbulent area of the boundary layer, and they presented gray level changes in the image. The eddy scale distribution of the boundary layer was computed by FFT spectrum analysis, and it reflected the transition process from laminar to turbulence clearly. As an example, Fig. 5 shows bar charts of the eddy scale distribution on the windside and leeside of the cone of test ZL-30. In the laminar flow area, the eddy scale is under 0.2 mm with small fluctuation. At the transition point, one or more sharp bars stand out, and that corresponds to the turbulent spots. Some re-laminar areas between turbulent spots could be identified too. According to the eddy scale distribution, the transition could be located accurately.

The transition points on both leeside and windside of each test were compared in Fig. 6. Higher unit Reynolds number led to earlier transition. The transition shifted upward on the leeside and afterward on the windside within small AOA of less than 3°. When the angle gets further increased, the moving direction of the transition on the windside reversed toward the nose tip but will not exceed the leeside in the present results with nose tip radius of less than 0.4 mm.

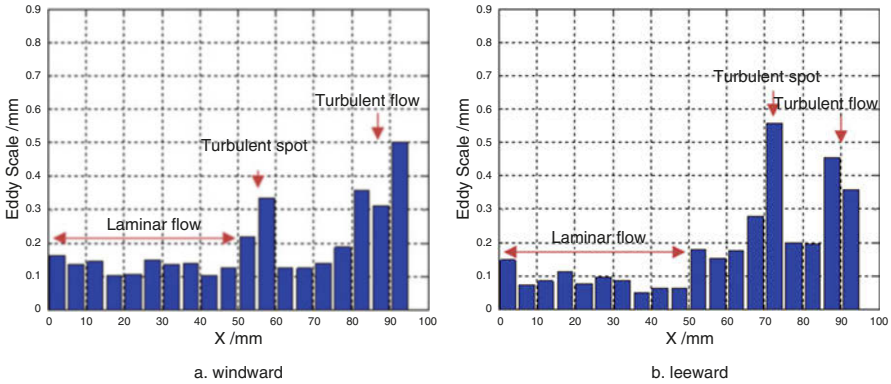

Fig. 5 The eddy scale distribution on the model of test ZL-30

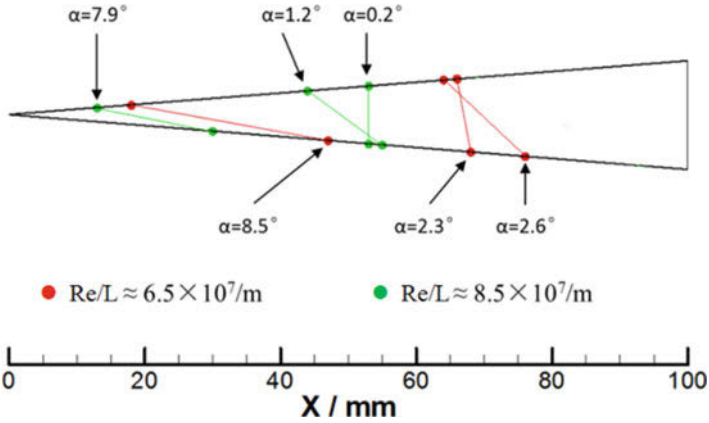

Fig. 6 Distribution of the transition point of different AOA and unit Reynolds number

For the slightly blunted cone, the main shock can be assumed to be sticked to the wall; therefore, it is easy to calculate the local parameters of basic flow theoretically. It seems the flow on the windside had a higher enthalpy and lower Mach number, and that resulted in unbalance transition on the cone's surface with AOA.

4 Discussion

Some references ascribed the moving direction reverse of the transition to the crossflow increased by AOA. It is doubtable why there are so many differences between results of different facilities. At least, the crossflow effect is not the only mechanism to dominate transition process.

It is generally recognized that wind tunnel transition occurred at lower Reynolds numbers than in flight due to wind tunnel noise. However, the transition test result comparison of HiFIRE-1 on ground and in flight showed that there was noticeable decrement in transition Reynolds number with AOA from 5° to 13°, even in some case, wind tunnel windward transition occurred at a higher Reynolds number than in flight [18]. Ballistic range test also showed same differences in transition Reynolds number between small and big AOA.

It is noticed that there is a non-negligible change of wall to stagnation temperature ratio between wind tunnel ($T_w/T_0 = 0.56$) and in flight ($T_w/T_0 = 0.18$ for HiFIRE-1 fly test and $T_w/T_0 = 0.12$ for ballistic range test). Therefore, the destabilizing effects of wall cooling may outweigh the effect of background noise and play an important role in the transition problems. A recent paper of Tsinghua University reported that favorite pressure gradient will stabilize the first and second unsteady modes; however, a new mode may arise when wall heating added in the high-speed boundary layer [19]. This theory may help to study the AOA effect to the cone transition in further research.

5 Conclusion

The cone has a simple shape but quite complicated transition phenomenon in hypersonic flow. To investigate the AOA effect to the slightly blunted circular cone, CARDC carried out a series of free flight test in the ballistic range.

Results showed that the transition location shifted upward on the leeside and afterward on the windside within small AOA. When the angle gets further increased, the moving direction of the transition on the windside reversed toward the nose tip but will not exceed the leeside in present results with nose tip radius of less than 0.4 mm. There is noticeable decrement in transition Reynolds number with AOA, which may related with both pressure gradient and wall heating. Further theoretical and experimental research is necessary.

Acknowledgments This work was supported by National Program on Key Research Project (Grant No. 2016YFA0401201).

References

1. E.J. Softley, Boundary layer transition of hypersonic blunt, slender cones, AIAA Paper 69-0705 (1969)
2. V. Dicristina, Three-dimensional laminar boundary layer transition on a sharp 8-deg, Cone at Mach 10. AIAA J. **8**(5) (1970)
3. M.C. Fischer, An experimental investigation of boundary layer transition on a 10-deg Half-angle cone at Mach 6.9, NASA TN-D-5766 (1970)

4. L.E. Sakell, *An Experimental Investigation of Boundary Layer Transition over Three Axially Symmetric Bodies at M_∞=6.0*. Ph.D Thesis, New York University, New York (1972)
5. J.F. Muir, A.A. Trujillo, *Experimental Investigation of the Effects of Nose Bluntness, Free-Stream Unit Reynolds Number, and Angle of Attack on Cone Boundary Layer Transition at a Mach Number of 6*, AIAA Paper 72–216 (1972)
6. K.F. Stetson, Mach 6 experiments of transition on a cone at angle of attack. J Spacecrt. **19**(5) (1982)
7. K.F. Stetson, E.R. Thompson, J.C. Donaldson, L.G. Siler, Laminar boundary layer stability experiments on a cone at Mach 8 part 3 sharp cone at angle of attack. AIAA Paper, 85–0492 (1985)
8. J. Perraud, D. Arnal, L. Dussillols, F. Thivet, Studies of laminar turbulent transition in hypersonic boundary layers at ONERA, in *European Symposium on Aerothermodynamics for Space Vehicles,* 1998
9. A. Martellucci, R.S. Neff, W.H. Truelll, An experimental investigation of boundary layer transition on a cone at angle of attack, NASA TR-69-0383 (1969)
10. V. DiCristina, Three-dimensional laminar boundary-layer transition on a sharp 8° cone at Mach 10. AIAA J. **8**(5) (1970)
11. J.F. Muir, A.A. Trujillo, Experimental investigation of the effects of nose bluntness, free-stream unit Reynolds number and angle of attack on cone boundary layer transition at a Mach number of 6, AIAA Paper 72-0216 (1972)
12. L.E. Sakell, *An experimental investigation of boundary layer transition over three axially symmetric bodies at Mach 6*, Ph.D. Thesis, New York University, School of Engineering and Science, (1972)
13. M.R. Malik, Numerical method for hypersonic boundary layer stability. J. Comput. Phys. **86** (1990)
14. J.E. Gronvall, H.B. Johnson, G.V. Candler, Hypersonic three-dimensional boundary layer transition on a cone at angle of attack. AIAA Paper, 2011–3561 (2011)
15. Z. Wang, S. Liu, A. Xie, J. Huang, Shadowgraph imaging and post-processing for hypersonic boundary layer transition in ballistic range, in *13th Asian Symposium of Visualization*, 154 (2015)
16. S.A. Stanfield, R.L. Kimmel, D. Adamczak, Boundary-layer transition experiment during reentry of HIFiRE-1. J. Spacecr. Rocket. **52**(3) (2015)
17. S.-c. Liang, J. Huang, Y. Li, et al., The effect of waves rupture diaphragm on acceleration loads of projectile. Proc. Inst. Mech. Eng. Part G: J. Aerosp. Eng. **228**(10) (2014)
18. S.A. Stanfield, R.L. Kimmel, D. Adamczak, et al., Boundary-layer transition experiment during reentry of HIFiRE-1. J Spacecr. Rocket **52**(3) (2015)
19. J. Ren, S. Fu, *Instability of hypersonic boundary layer is caused by favorable pressure gradient and wall-heating*, AIAA Paper 2017-2134 (2017)

Review on Film Cooling in High-Speed Flows

K. Fujiwara, R. Sriram, K. Kontis, and T. Ideta

Abstract This review presents the state of the art in film cooling applied to high-speed flows. Film cooling is a promising technique to reduce heat transfer and shield a surface that is exposed to high-temperature core stream. The technique applies cold pneumatic injection into a hot core stream, and while the film cooling in gas turbines is generally subsonic, it has also been a success in high-speed environment such as an extension nozzle of liquid rocket engines. The present paper aims to bring together the main results from experiments and numerical simulation on film cooling in high-speed flow. Parameters from not only fluid dynamical conditions but also gas properties and geometric features of injection affect the cooling performance.

1 Introduction

Film cooling involves introduction of secondary fluid injected into a core stream, which functions as a thermal sink and protective thermal layer to shield a surface from the core [1]. This cooling technique has been a huge success especially in gas turbines whose performance, defined quantitatively as film cooling effectiveness defined by Eq. (1), rises with turbine inlet temperature. For this application, a large number of investigations have been conducted over the past 50 years [2].

$$\eta = \frac{T_w - T_\infty}{T_c - T_\infty} \tag{1}$$

K. Fujiwara (✉) · R. Sriram · K. Kontis
School of Engineering, University of Glasgow, Glasgow, UK
e-mail: k.fujiwara.1@research.gla.ac.uk

T. Ideta
IHI Corporation, Yokohama, Japan

A. Sasoh et al. (eds.), *31st International Symposium on Shock Waves 2*,
https://doi.org/10.1007/978-3-319-91017-8_118

where T_w, T_c, and T_∞ represent wall, coolant, and core stream temperature, respectively. While flow in gas turbines is generally in subsonic regime, film cooling also finds applications in high-speed flows. Some applications include extension nozzle of a modern rocket engine [15] and thermal protection system (TPS) for a blunt body at high speed [3]. The technique of cooling based on fluid injection is also called "effusion cooling" when multiple blowing holes are arranged closely together or called "transpiration cooling" when coolant is supplied from a porous material. To evaluate the cooling performance in high speed, the effectiveness is redefined by replacing the temperatures with recovery temperatures to account for the compressibility Eq. (2) or in terms of heat fluxes in few cases (isothermal walls).

$$\eta = \frac{T_w - T_{r,\infty}}{T_{r,c} - T_{r,\infty}} \tag{2}$$

Because the cooling performance is dictated by inherent heat transfer process in the flow field, it is important to investigate the transport mechanism with coolant injection in high-speed flow, while the heat transfer data at high speeds is also important concerning design of various configurations. To that end, a numbers of experimental and computational investigation have been conducted and reported in the literature, and the present paper attempts to bring together the main features and results on film cooling in the high-speed flow regime.

2 Tangential Blowing

Film cooling by tangential slots involves continuous injection of secondary fluid parallel to the core stream. Stollery and El-Ehwany [5] differentiated three separate regions in the flow field as illustrated in Fig. 1. Just downstream of the slot exit is the "potential core" region wherein the wall temperature remains close to the coolant. Following this region is a zone where velocity profile is similar to that of wall jet and fully developed turbulent boundary layer farther downstream. Interaction between the core and coolant is dictated by the shear layer which penetrates down to the wall to degrade cooling performance.

The cooling effectiveness is affected by the geometric and fluid dynamical features [1]. The former involves slot height which is rather found to have insignificant or secondary effect on cooling [7, 8], whereas the latter involves blowing ratio$\left(BR = \frac{\rho_j u_j}{\rho_\infty u_\infty}\right)$, momentum ratio$\left(MR = \frac{\rho_j u_j^2}{\rho_\infty u_\infty^2}\right)$, density ratio$\left(DR = \frac{\rho_j}{\rho_\infty}\right)$, core stream Reynolds number$\left(\mathrm{Re} = \frac{uL}{\nu}\right)$, turbulent intensity ($Tu$), boundary layer thickness(δ/L) , and gas properties. Effects of these parameters are extensively investigated through experiments as well as numerical simulations. For engineering purposes, it is useful to obtain correlations for cooling performance with the nondimensional parameters. When the same gas is used as core and coolant and

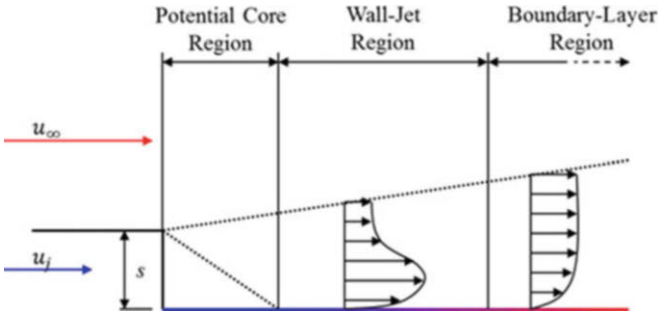

Fig. 1 Three regions formed by the injection (Redrawn from [5])

the same pressure is also maintained between them, the effectiveness is a function of fluid-fluid dynamical parameters and position for a given injection geometry,

$$\eta = f\,(\mathrm{Re}, \mathrm{Pr}, BR, DR, Tu, \delta/L) \tag{3}$$

In [5], analytical expression for effectiveness in the form

$$\eta = (const)\left(\frac{x}{BR \cdot s}\right)^{-0.8} \tag{4}$$

was derived to correlate their experimental data. Seban and Back [6] presented experimental results for film cooling by tangential slots and found power-law region for the effectiveness.

Flow structure and behavior of the effectiveness in high speed more or less appears to be similar to subsonic cases when the injection and freestream pressure are maintained the same. In one of the early experimental work [7] at free stream at Mach number of 3.01, regardless of the gas injected through the tangential slot (air or helium), two separate regions were reported similar to subsonic flows: a region with complete coverage (film cooling effectiveness of unity) up to a certain point and the other region where cooling performance drops abruptly (Fig. 2).

The extent of the region of complete coverage from the point of injection is referred to as "cooling length" [9], after which the effect of turbulent shear mixing between core and coolant penetrates down to the surface (Fig. 1). Others reporting this type of behavior include Parathasarathy and Zakky [9] and Bass et al. [10]. In [7]–[10], correlations for the cooling performance of a tangential slot after the cooling length are proposed, relating the performance with the blowing ratio and the distance from the point of injection in the form:

$$\eta = a\left(\frac{x}{s}\right)^{b} BR^{c} \tag{5}$$

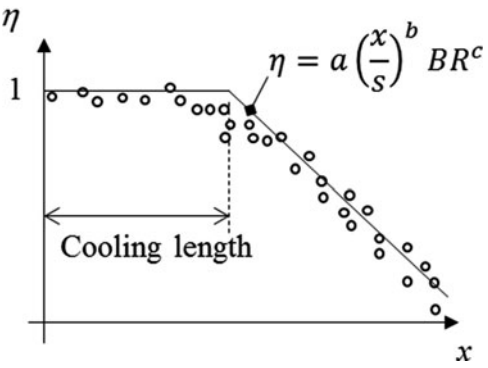

Fig. 2 Schematic of curve of cooling effectiveness

where a, b, and c are constants that are determined experimentally and x and s are distances from the point of injection and slot height, respectively. More injection generally results in enhanced cooling; the performance however is strongly dependent on other factors too. Bass et al. [10] pointed out the difficulty in ascertaining the constants in the correlation since they may be affected by the wide range of other parameters, including total temperature ratio, pressure ratio, Reynolds number, lip thickness coolant injection angle, boundary layer, surface roughness, turbulence, and heat capacity. In the range of their study, they nonetheless suggested that correlation parameter of $(x/s)BR^{-0.8}$ collapsed the data on a single log-log line to a reasonable accuracy. Recently, Hombsch and Oliver [11] theoretically developed a correlation factor from a simple heat balance model for laminar flow, having a more complex form than Eq. (5).

Advances in computational resources as well as numerical techniques have enabled and inspired researchers to investigate the details of film cooling mechanism in high-speed flow, which is not always available in experiments. Features that are common to experiments and numerical simulations for rear-facing tangential slots include better cooling performance at increased injection rates, correlation for cooling effectiveness after "cooling length," and the lesser importance of the (tangential) slot height. O'Connor and Haji-Sheikh [12] conducted two-dimensional RANS computations (with *k-kl* turbulence model) at core stream Mach number of 3.0 where slot geometry was based on the work by Goldstein et al. [7]. Results fell within the accuracy of Goldstein's experimental campaigns using $x/(BR \bullet s)$ as a correlation factor. Flow structure such as behavior of recompression shock and expansion on varying the injection rate were also investigated.

The pressure ratio between core stream and injection affects the jet penetration and trajectory in jet in a supersonic crossflow (JISC) [16], and the importance of pressure ratio rather than blowing ratio appears more obvious in tangential slot cases as illustrated in the detailed analysis using direct numerical simulation (DNS) by Keller and Kloker [13]. Their simulation included three different pressure ratios of core to injection (p_j/p_∞=1.1, 2.2, and 3.3) resulting into underexpanded gas injection at core stream Mach number of 2.60. The characteristic wave patterns formed by the underexpanded coolant depend on the pressure ratio. For the case of

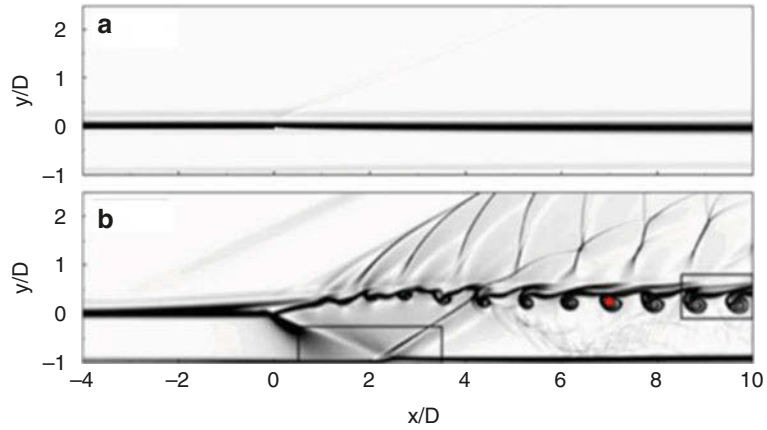

Fig. 3 Numerical schlieren images for (a) $p_j/p_\infty = 1$ and (b) $p_j/p_\infty = 3.3$ [13]

low pressure ratio of $p_j/p_\infty = 1.1$, only weak expansion can be observed, whereas for the highest pressure ratio of $p_j/p_\infty = 3.3$, an undesirable, film-dissolving, self-excited unsteadiness developed showing vortex shedding in the shear layer region (Fig. 3). Such wave patterns are unique to high-speed flows and are obviously absent in subsonic flows; they significantly affect the local and global cooling performance.

The effect of difference in gas properties between the core fluid and coolant is also discussed. The ratio of heat capacity of core and injection $c_{p\infty}/c_{pj}$ was also included to the correlation [8]. Helium injection resulted in higher cooling performance because of its larger heat capacity than air, while ratio of thermal conductivity and heat capacity $(k_j c_{p\infty})/(k_\infty c_{pj})$ was also proposed due to the fact that gases with high heat capacity often possesses high thermal conductivity as well [11]. For a laminar flow, Hombsch and Oliver [11] considered also the diffusivity, density, and viscosity and proposed a new correction parameter. Keller et al. [15] however concluded from their experimental and numerical campaign that the diffusion coefficient virtually had no influence on the cooling performance in the case of turbulent flows. Some of these parameters are also of importance in the cases with non-tangential injection, which is discussed in the subsequent section.

3 Non-tangential Injections

Although a simple flow configuration for analytical purposes, the inclusion of tangential slots in fluid dynamic applications complicates the surface geometry resulting in a step, which often results in detrimental fluid dynamic effects. Non-tangential injection for film cooling has been widely discussed and applied in the case of turbine blades at subsonic speeds. The jet penetrates into the core at higher momentum ratio rather than flowing along the surface for thermal shielding. The

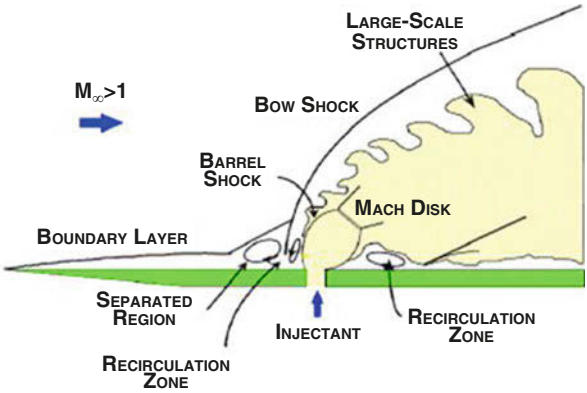

Fig. 4 Jet in a crossflow at high speed [18]

injection from hole rather than slots (even with tangential injection) creates complex vortex structure such as jet shear layer vortices, horseshoe vortices, and counter-rotating vortex pair (CRVP) [17]. CRVP tends to lift the coolant into the core and entrain the hot core to the surface, degrading film cooling performance. For the case of subsonic turbine blade cooling, many novel film cooling geometries have been proposed (e.g., shaped holes [2]) to reduce the jet penetration and CRVP effect. In the case of high-speed flows, the study of non-tangential injection is often motivated by fuel mixing enhancement, a purpose completely opposite to film cooling requirement. Investigations on jets injected normally into a compressible crossflow have been ongoing since the 1960s in connection with the scramjet projects [18]. Flow structure of JISC is characterized by shock structures such as bow shock just in front of injection, barrel shock, and Mach disk and recirculation region, as shown in Fig. 4. While the penetration can possibly shield the surface below the recirculation zone, peak heating at the reattachment could be detrimental. Unsteadiness caused by wave patterns and vortex shedding may degrade cooling performance. Wide spectrum of research concerns jet penetration depth and is correlated with momentum ratio.

The strong dependence of the flow structure on the non-tangential injection geometry has been well demonstrated at subsonic speeds [4]. In high-speed regime, Hobsch and Oliver [11] experimentally compared film cooling with injection through different blowing geometries. In general, more injection meant more cooling, but non-tangential injection into laminar core can cause transition to turbulence and can enhance heating. It was also concluded that tangential slot result in better cooling performance than non-tangential slots, which in turn perform better than blowing holes. Linn and Kloker [14] numerically investigated injection through non-tangential slots and blowing holes in super/hypersonic core stream. Two rows of slots, one slot, two rows of in-line holes, and two rows of staggered holes were compared in their DNS. It was concluded that the slots performed better in terms of film cooling than the blowing holes because injection velocity was lower for the same mass flow rate given. At lower blowing ratio, coolant is in contact with

the surface. The aligned holes were found to induce a strong spanwise variation of the surface temperature and less cooling effectiveness compared to the staggered holes. The complexities in non-tangential injection require further investigations to improve the understanding of the details of the flow filed and cooling performance.

4 Summary

Although film cooling is a key technique in mitigating surface heating due to convection, successfully employed in a number of low- and high-speed applications, a number of complexities persist in understanding the flow field and the associated heat transfer with injection. A reasonable understanding of the flow phenomena has developed in the case of tangential slot injection. Blowing ratio is the foremost parameter, and the film cooling effectiveness is often empirically correlated with slot height and blowing ratio in the form given in Eq. (5). The common consensus observed is the enhanced cooling and extended "cooling length" with increasing injection and negligible effect of slot geometry. However, additional parameters considered in previous investigations include other fluid dynamical conditions such as pressure and temperature ratio between the core and injection fluids, gas properties, and geometric features of injectors. In a high-speed flow field, pressure difference between core and injected flows results in wave structures in the flow field which can induce unsteadiness and film-dissolving vortex shedding. Gas properties such as heat capacity, thermal conductivity, and diffusivity are other influential parameters, and correction factors to account for the differences in gas properties have been proposed. However, the existence of multiple factors affecting the flow field makes it impossible to obtain a universal correlation. Further complications arise when the injection is non-tangential and through holes rather than slots.

Some of the intricate flow feature has been resolved by means of numerical computations. DNS studies reveal unsteady vortex shedding in the shear layer between the core and tangentially injected coolant through slot, especially in the case of high pressure ratio. Vortical structure in multiple cooling was also captured and resolved using DNS, while experiments have a limitation in resolving many details of such features. CRVP was identified in both aligned holes and staggered holes. The aligned holes demonstrated stronger variation in surface temperature and degraded cooling performance when compared to staggered arrangement. Not many detailed experimental studies with non-tangential injection at high speeds are reported. Noncircular shaped holes can possibly generate higher cooling performance by suppressing CRVP and interaction with core stream at high speed. There is a need for detailed investigations on various geometrical and dynamical parameters involved in non-tangential (slot as well as holes) injection and the associated flow physics that can help in identifying optimal design for cooling system in various high-speed flow applications.

References

1. R.J. Goldstein, Film cooling. Adv. Heat Tran. **7**, 321–379 (1971)
2. R.S. Bunker, A review of shaped hole turbine film cooling technology. J. Heat Transf. **127**, 441–453 (2005)
3. R. Sriram, G. Jagadeesh, Film cooling at hypersonic Mach numbers using forward facing array of micro-jets. Int. J. Heat Mass Transf. **52**, 3654–3664 (2009)
4. B.A. Haven, M. Kurosaka, Kidney and anti-kidney vortices in crossflow jets. J. Fluid Mech. **352**, 27–64 (1997)
5. J.L. Stollery, A.A.M. El-Ehwany, A note on the use of a boundary-layer model for correlating film-cooling data. Int. J. Heat Mass Transf. **8**, 55–65
6. R.A. Seban, L.H. Back, Velocity and temperature profiles in turbulent boundary layers with tangential injection. J. Heat Transf. **84**, 45–54 (1962)
7. R.J. Goldstein et al., Film cooling with air and helium injection through a rearward-facing slot into a supersonic air flow. AIAA J. **4**(6), 981–985 (1966)
8. X. Yang et al., A numerical study of hypersonic laminar film cooling. Aeronaut. J., 479–486 (2003)
9. K. Pathasarathy, V. Zakkay, An experimental investigation of turbulent slot injection at Mach 6. AIAA J. **8**(7), 1302–1307 (1969)
10. R.W. Bass et al., Supersonic Film Cooling, AIAA second. Int. Aero. Planes Conf., 1–16 (1990)
11. M. Hombsch, H. Oliver, Film cooling in laminar and turbulent supersonic flows. J. Spacecr. Rocket. **50**(4), 742–753 (2013)
12. J.P. O'Connor, A. Haji-Sheikh, A Numerical Study of Film Cooling in Supersonic Flow, AIAA Paper (1991), AIAA-91-4010
13. M. Keller, M.J. Kloker, Direct numerical simulations of film cooling in a supersonic boundary-layer flow on massively-parallel supercomputers, Sustained Simulation Performance (2013), pp. 107–128
14. J. Linn, M.J. Kloker, Direct numerical simulation of film cooling in hypersonic boundary-layer flow, High Performance Computing in Science and Engineering, (2008), pp. 171–189
15. M.A. Keller et al., Influence of cooling-gas properties on film-cooling effectiveness in supersonic flow. J. Spacecr. Rocket. **52**(5), 1443–1455 (2015)
16. K. Mahesh, The interaction of jets with crossflow. Annu. Rev. Fluid Mech. **45**, 379–407 (2013)
17. T.F. Fric, A. Roshko, Vortical structure in the wake of a transverse jet. J. Fluid Mech. **279**, 1–47 (1994)
18. A.R. Karagozian, Transverse jets and their control. Prog. Energy Combust. Sci. **36**, 531–553 (2010)

Ballistic Range Experiment and Numerical Simulation of Shock Stand-Off Distances Over Spheres in CO_2

Dongjun Liao, Sen Liu, Jie Huang, Hexiang Jian, Aimin Xie, and Zonghao Wang

Abstract To provide experimental data for validation of numerical simulations, measurement of shock stand-off distances over spheres in CO_2 has been made in the hypervelocity ballistic range of Hypervelocity Aerodynamics Institute, China Aerodynamic Research and Development Center. The models were spheres with a diameter of 10 mm. The flight speeds were between 2.122 km/s and 4.220 km/s, with ambient pressures between 2.42 kPa and 12.3 kPa. The shock stand-off distance was measured using shadowgraph. Results revealed that high-temperature gas effect is more obvious in CO_2 than in air, while two-temperature nonequilibrium model can basically reproduce the shock stand-off distances over spheres under present test conditions. The flow over spheres of present test is speculated to be mainly nonequilibrium. The accuracy and capability of two-temperature nonequilibrium model in CO_2 may differ with different flow speeds and pressures, which need to be further investigated.

1 Introduction

Mars exploration has becoming an important part of global deep space exploration. Numbers of Mars exploration activities have been planned [1], which will definitely require large amount of aerodynamic data of Mars entry vehicles. Flight test, ground test, and numerical simulation are three major approaches to obtain the aerodynamic data of hypersonic vehicles. One of the goals of the ground test is to provide reliable data for the validation of the numerical simulation.

Various aerodynamic parameters can be adopted for the validation of numerical simulation, of which shock stand-off distance is commonly used. Not being able to correctly predict the shock stand-off distance over a sphere means not being able to correctly describe the shock shape and pressure distribution over a flying

D. Liao (✉) · S. Liu · J. Huang · H. Jian · A. Xie · Z. Wang
Hypervelocity Aerodynamics Institute, China Aerodynamics Research and Development Center, Mianyang, People's Republic of China
e-mail: hai@cardc.cn

A. Sasoh et al. (eds.), *31st International Symposium on Shock Waves 2*,
https://doi.org/10.1007/978-3-319-91017-8_119

object, which can influence the prediction of aerodynamic characteristics for a flying object [2]. Measurement experiments of shock stand-off distances over spheres were mainly performed in air related to Earth entry conditions [3–5]. The Martian atmosphere, however, includes about 95.3% CO_2 [6], which is quite different from Earth. Test data of shock stand-off distances over spheres in CO_2 are therefore necessary for the validation of the numerical simulation under Mars entry conditions.

Ballistic range is a facility in which a model is launched into quiescent gas at required speed and flies freely in the test section to simulate the real flight environment. No chemical reactions in free stream need to be considered for the ballistic range tests. This makes the data of shock stand-off distance obtained in ballistic range more reliable than that obtained in pulse tunnels [7]. It is therefore significant to measure the shock stand-off distance over spheres in CO_2 in a ballistic range.

Two-temperature (2-T) nonequilibrium model [8] has been widely used for the numerical calculation of different aerodynamic parameters including shock stand-off distance over spheres. However the two-temperature model was developed for the Earth's atmosphere and may not be fully applicable to CO_2 conditions. The applicability of two-temperature model CO_2 should be validated with test data of shock stand-off distances over spheres to provide more evidence for the numerical study of nonequilibrium flow under Mars entry conditions.

Measurement of the shock stand-off distance over spheres in CO_2 has been made in the hypervelocity ballistic range of Hypervelocity Aerodynamics Institute (HAI), China Aerodynamic Research and Development Center (CARDC). Data of shock stand-off distances and shock shapes over spheres in CO_2 were obtained to compare with test data in air with same flow conditions and numerical results calculated using two-temperature model.

2 Test Methods and Conditions

2.1 Test Facility

Tests were performed in one of the hypervelocity ballistic ranges of HAI, CARDC [9] (Fig. 1). A 16 mm two-stage light-gas gun was used to accelerate the test models to required speeds. Flight speeds of models were measured by the measurement and control system, which also sent trigger signal to the shadowgraph. The chamber, which includes detonation section and test section, provided space for sabots separation and shock stand-off distance measurement. The vacuum system provided required ambient pressures for the tests. Pressure and temperature in the test section were measured by an electronic thermometer and an electronic vacuum gauge. The test flow field was visualized by transient shadowgraph using a YAG laser with a 10 ns pulse duration as light source.

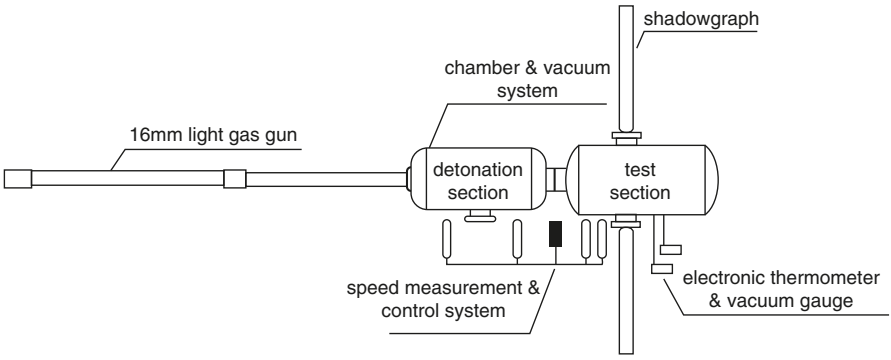

Fig. 1 Schematic of the hypervelocity ballistic range of HAI, CARDC

Fig. 2 Models and sabots

2.2 Test Models and Conditions

The test models were spheres made of alumina, weight 2.1 g with a diameter of 10 mm. The models were held by four petals of sabots, which were shown in Fig. 2.

Flight speeds of the models for present tests referenced the entry speed of Viking entry vehicle at height between 25 km and 40 km, which is from about 2 km/s to 4 km/s [10]. The ambient pressures were designed to be between 2 kPa and 12 kPa. The tests were performed in both CO_2 and air to compare the differences between shock stand-off distances over spheres in CO_2 and air.

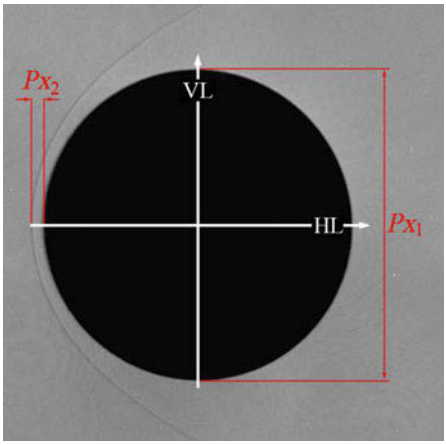

Fig. 3 Schematic of measurement for shock stand-off distance

2.3 Measurement Method

Shock stand-off distances over spheres of present tests were measured based on the shadowgraph of flow field as schematically shown in Fig. 3. Number of pixels of the sphere diameter was measured along vertical axis of symmetry (VL) of the model as Px_1. Number of pixels of the distance between outer edge of the shock layer and model surface was measured along horizontal axis of symmetry (HL) of the model as Px_2. Then, the shock stand-off distance (Δ) could be related to the sphere diameter (D) as Eq. (1).

$$\Delta = \frac{Px_2}{Px_1} D \tag{1}$$

For further analysis, Δ was normalized by sphere radius as Δ/R. Errors of sphere diameter, Px_1 and Px_2, were taken into consideration for the overall test error.

3 Numerical Method

Two-dimensional axial symmetrical Navier-Stokes equations are used as governing equations. The chemical reactions of the flow are described by Park's chemical reaction model for five species (CO_2, CO, O_2, O, C) and eight reactions [11], as shown below.

$$
\begin{aligned}
&CO_2 + m_1 \leftrightarrow CO + O + m_1\\
&CO_2 + m_2 \leftrightarrow CO + O + m_2\\
&CO + m_1 \leftrightarrow C + O + m_1\\
&CO + m_2 \leftrightarrow C + O + m_2\\
&O_2 + m_1 \leftrightarrow 2O + m_1\\
&O_2 + m_2 \leftrightarrow 2O + m_2\\
&CO + O \leftrightarrow O_2 + C\\
&CO_2 + O \leftrightarrow O_2 + CO
\end{aligned}
$$

where m_1 (O_2, CO_2, CO) and m_2 (C, O) are catalysts. Reaction constants of the equations above are given by reference [11].

4 Results and Discussion

Four tests were performed in CO_2. Figure 4 shows the shadowgraph of test C10–1. Table 1 presents the measured shock stand-off distances and corresponding test conditions of four tests. Figure 5 compares the shadowgraph of test C10-1 and a test performed in air numbered A10-1 with similar test conditions. It is obvious that the shock stand-off distance over sphere in CO_2 is smaller than that in air, indicating the high-temperature gas effect is more obvious in CO_2 than in air.

Figure 6 compares the calculated shock stand-off distances using two-temperature nonequilibrium model and the test data. The dash lines, given as indication of flow state, represent the shock stand-off distances calculated for $\rho R = 1.1 \times 10^{-4}$ kg/m^2 using two-temperature nonequilibrium model and ideal gas

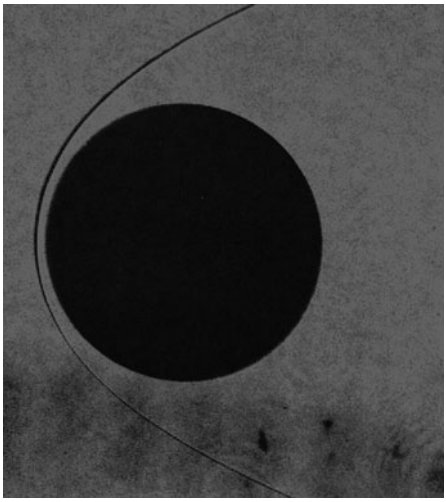

Fig. 4 Shadowgraph of test C10–1 $D = 10$ mm, $V = 2.122$ km/s, $P = 12.300$ kPa $\rho R = 1.1 \times 10^{-3}$ kg/m^2

Table 1 Shock stand-off distances and test conditions

Test	Diameter D(mm)	Flight speed V(km/s)	Ambient pressure P(kPa)	Ambient temperature T(K)	Binary scaling ρR(kg/m^2)	Normalized shock stand-off distance Δ/R	Test error
C10-1	10	2.122	12.300	292.1	1.1E-03	0.0795	±3.89%
C10-2	10	2.845	7.425	293.2	6.7E-04	0.0705	±4.37%
C10-3	10	3.810	4.210	292.7	3.8E-04	0.0553	±10.59%
C10-4	10	4.220	2.420	293.7	2.2E-04	0.0618	±4.88%

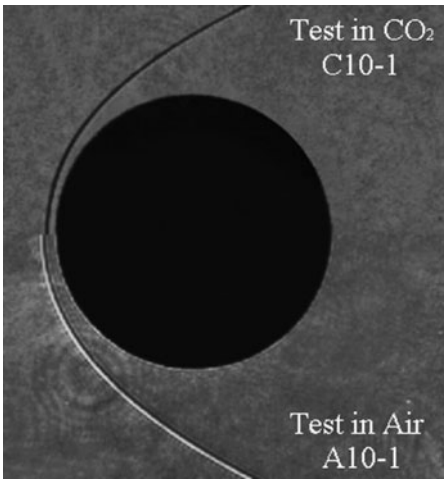

Fig. 5 Comparison between shadowgraph of test in CO_2 and in air C10–1: $D = 10$ mm, $V = 2.122$ km/s, $P = 12.300$ kPa A10–1: $D = 10$ mm, $V = 2.363$ km/s, $P = 12.300$ kPa

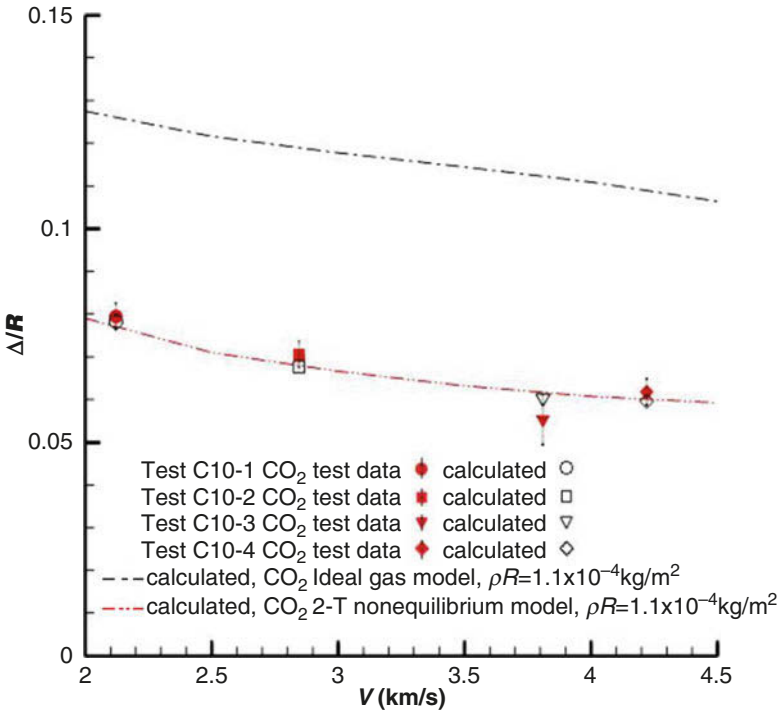

Fig. 6 Comparison of the calculated and test results of shock stand-off distances

Table 2 Differences between test and calculated results of shock stand-off distances

Test	Normalized shock stand-off distance test results Δ/R	Normalized shock stand-off distance calculated results Δ/R	Test error	Differences between calculated and test results
C10-1	0.0795	0.0783	±3.89%	−1.51%
C10-2	0.0705	0.0676	±4.37%	−4.11%
C10-3	0.0553	0.0604	±10.59%	9.22%
C10-4	0.0618	0.0596	±4.88%	−3.56%

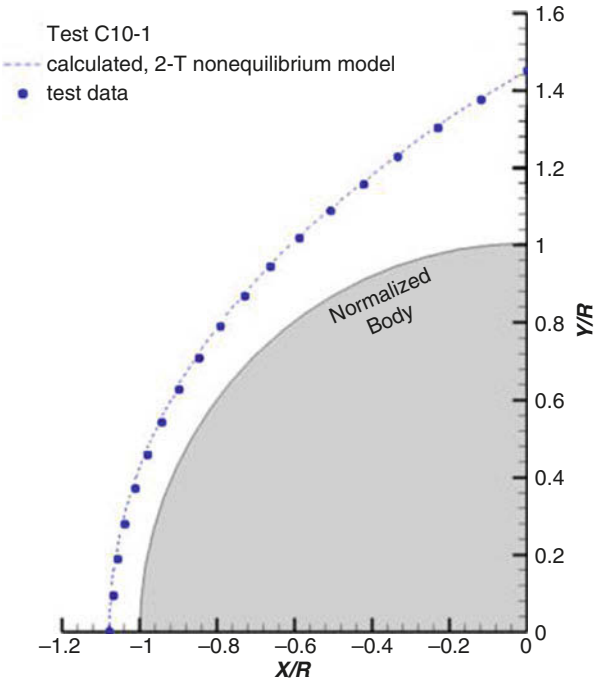

Fig. 7 Comparison between calculated and test results of shock shape of test C10-1

model. It is shown that the calculated results basically match the test data. Table 2 presents the specific differences between calculated results and test data. The differences between calculated and test results are smaller than the corresponding test error, indicating the two-temperature nonequilibrium model can basically reproduce the shock stand-off distances over spheres under present test conditions.

Figure 7 compares calculated and measured shock shape of test C10–1. The calculated shock shape generally matches the test data. It is therefore speculated from the calculated results that the flow over spheres under present test conditions is mainly nonequilibrium.

Some previous researches showed that, however, the two-temperature model obviously underestimates the shock stand-off distance for an entry vehicle model in shock tunnel [12, 13], differing from the results of present study. Besides test error and discrepancies between facilities, it is speculated that the capability of two-temperature model in CO_2 may also differ under different flow conditions. More test data of shock stand-off distances over spheres in CO_2 with different speeds and pressures will be needed to further investigate the accuracy and capability of two-temperature nonequilibrium model in CO_2.

5 Conclusion

Measurements of shock stand-off distances over spheres in CO_2 have been made in the hypervelocity ballistic range of HAI, CARDC. The flight speeds of test models are between 2.122 km/s and 4.220 km/s, with ambient pressures between 2.42 kPa and 12.3 kPa. Conclusions for present test conditions are drawn as follows:

1. High-temperature gas effect is more obvious in CO_2 than in air.
2. Two-temperature nonequilibrium model can basically reproduce the shock stand-off distances over spheres, while the flow over spheres of present test is speculated to be mainly nonequilibrium.
3. The accuracy and capability of two-temperature nonequilibrium model in CO_2 may differ under different flow conditions, which need to be further validated with more test data.

Acknowledgment The authors would like to express sincere thanks to Prof. Andrew Higgins for his valuable comments and suggestions. Special thanks are also given to the personnel who have participated in the tests.

References

1. D.J. McCleese, Mars exploration strategy 2009–2020, Mars Science Program Synthesis Group, (2003)
2. C. Park, The limits of two-temperature model, AIAA 2010-911 (2010)
3. S. Nonaka, H. Mizuno, K. Takayama, C. Park, Measurement of shock standoff distance for sphere in ballistic range. J. Thermophys. Heat Transf. **14**(2), 225–229 (2000)
4. J. Liu, A.H. Shi, G.S. Yang, Measurement of shock standoff distances for sphere in nonequilibrium flow in ballistic range, in *11th National Conference on Shock Wave and Shock Tube* (2004)
5. F. Zander, R.J. Gollan, P.A. Jacobs, R.G. Morgan, Hypervelocity shock standoff on spheres in air. Shock Waves **24**(2), 171–178 (2014)
6. J.K. Shi, Z.M. Zhang, Z.X. Liu, Y.J. Wang, An analysis of results of the Martian environment exploration. Prog. Geophys. **12**(4), 98–108 (1997)
7. S.P. Sharma, C. Park, Survey of simulation and diagnostic techniques for hypersonic nonequilibrium flows. J. Thermophys. Heat Transf. **4**(2), 129–142 (1990)
8. C. Park, Assessment of two-temperature kinetic model for dissociating and weakly-ionizing nitrogen. J. Thermophys. Heat Transf. **2**(1) (1988)
9. S. Liu, J. Huang, Y. Li, Z.X. Zhou, Z.X. Ma, Recent advancement of hypervelocity impact tests at HAI. J Manned Spacecraft **17**(6), 17–23 (2011)
10. S. Mark, D. Artern, B. Pieter, B. Scallion, J.V. Norman, Aerodynamic challenges for the Mars Science Laboratory entry descent and landing, AIAA 2009-3914 (2009)
11. C. Park, J.T. Howe, R.L. Jaffe, G.V. Candler, Review of chemical-kinetic problems of future NASA missions, II: Mars entries. J. Thermophys. Heat Transf. **8**(1), 9–23 (1994)
12. M. Maclean, M. Holden, Catalytic effects on heat transfer measurements for aerothermal studies with CO_2, AIAA 2006-0182 (2006)
13. S. Doraiswamy, D. Kelley, V.G. Candler, Vibrational modeling of CO_2 in high-enthalpy nozzle flow. J. Thermophys. Heat Transf. **24**(1), 9–17 (2010)

Prediction of Stagnation-Point Radiative Heating for FIRE II

Sung Min Jo, Gisu Park, and Oh Joon Kwon

Abstract In the present study, modeling of radiative shock layer for predicting stagnation-point heating environment was conducted for a FIRE II configuration. For the analysis of the one-dimensional flow in thermochemical nonequilibrium, a viscous shock layer method with a two-temperature model was utilized including radiative cooling. To estimate the effect of radiative cooling, the flow and radiation fields were analyzed in a loosely coupled manner. To estimate the radiative heating with the effect of non-Boltzmann state population distributions, SPRADIAN14 was utilized. To improve the accuracy of non-Boltzmann modeling, three new electron impact rate models for atomic N and one for O were developed by adopting the state-of-the-art quantum mechanical results for transitions from low-lying electronic levels. The methodologies were verified by applying them to benchmark problems. It was shown that the results are accurate and physically reliable in comparison with available data. Then, two of the trajectory points of FIRE II were analyzed, and the effects of new electron impact rate models were validated by comparing the results with those from the previous rate model. It was found that most of the discrepancies in the previous rate model from the flight data were resolved by introducing the new models, particularly by the "Frost-Tayal" model.

1 Introduction

Accurate prediction of radiative heating is one of the most important factors in designing a thermal protection system (TPS) for atmospheric entry vehicles. This is because high-temperature gas in the shock layer is excited and ionized by the collisional processes and high-lying electronic levels emit radiative energy that

S. M. Jo · G. Park · O. J. Kwon (✉)
Department of Aerospace Engineering, Korea Advanced Institute of Science and Technology (KAIST), Daejeon, Republic of Korea
e-mail: ojkwon@kaist.ac.kr

A. Sasoh et al. (eds.), *31st International Symposium on Shock Waves 2*,
https://doi.org/10.1007/978-3-319-91017-8_120

heats the surface. Therefore, analysis of the collisional-radiative (CR) processes is required to model the radiative heating environment in high-speed entries, such as for lunar return conditions.

The FIRE II flight experiment was conducted in 1965 [1] to obtain radiative heating data during Earth reentry. The measured data has been widely used to validate the accuracy of developed air radiation models. The related numerical studies conducted in the past were reviewed by Johnston et al. [2]. Recently, Park [3] utilized a viscous shock layer (VSL) method [4] and the NEQAIR96 [5] with the CR processes modeled by solving a quasi-steady state (QSS) master equation with the CR parameters in NEQAIR96. However, Johnston et al. [6] and Panesi et al. [7] stated that the atomic CR parameters produce overpopulated high-lying electronic states for compression flows, especially for atomic N and O. Recent state-of-the-art studies [7–9] modeled the nonequilibrium rate processes by developing new CR models. Most of these advancements were achieved by improving the accuracy of atomic electron impact rate models. The electron impact process is dominant when the flow is highly dissociated and ionized as for the lunar return conditions.

In the present study, modeling of radiative shock layer was conducted along the stagnation line of FIRE II. To calculate the one-dimensional flow, the VSL method [4] with a two-temperature model [10] was utilized. The radiation code, SPRADIAN14 [11], which has been developed based on the SPRADIAN07 [12], was utilized to model the non-Boltzmann state populations and the radiative spectra. To model the radiative cooling effect, a flow-radiation coupled analysis was conducted in a loosely coupled manner. Three new electron impact rate models for atomic N and one for O were proposed and were implemented in SPRADIAN14 to improve the accuracy of modeling and to secure the physical reliability. The involved methodologies were validated by applying them to benchmark simulations. Then, they were applied to FIRE II, and two flight trajectories of 1634s and 1636s cases were analyzed. The predicted radiative and total heating on the stagnation point was compared with the flight data and those of other available numerical calculations.

2 Numerical Method

2.1 Viscous Shock Layer Method

For the assessment of the flow properties, conservative equations of mass, momentum, and global energy were solved by adopting the viscous shock layer (VSL) method [4] along the one-dimensional stagnation region. To characterize the nonequilibrium relaxation processes, a two-temperature model of Park [10] was implemented. The finite rate parameters for chemical reaction and the related kinetic data for 11-species air system were adopted from the work by Park et al. [13]. The fully catalytic wall boundary condition for the recombination of atomic N and O was

Table 1 Calculated trajectory points of the FIRE II cases

Time t, [s]	Altitude H, [km]	Density ρ_∞, [kg/m^3]	Velocity V_∞, [km/s]	Temp. T_∞, [K]	Wall Temp. T_w, [K]	Radius R_N, [m]
1634	76.42	3.72^{-5}	11.36	195	615	0.935
1636	71.02	8.57^{-5}	11.31	210	810	0.935

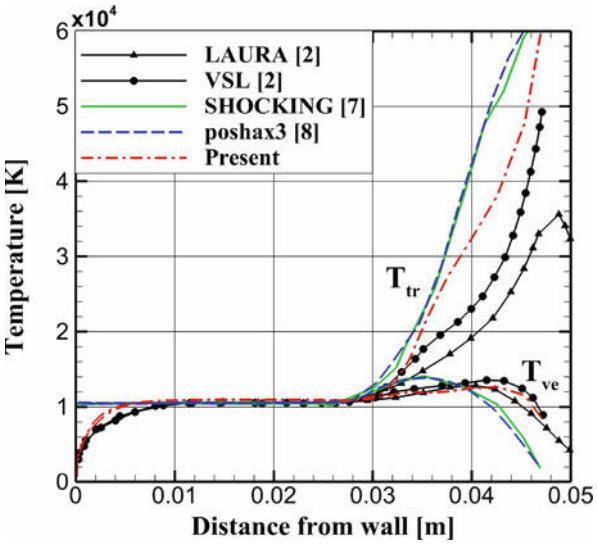

Fig. 1 Comparison of calculated temperature fields with related calculations [2, 7, 8] along stagnation line for $t = 1634$s

implemented. The radiative cooling effect modeled by SPRADIAN14 was included in the energy equation. The change of temperature during the coupled iterations was used as the convergence criterion for the coupled procedure.

For the validation of the VSL method, FIRE II 1634s trajectory point was examined. The flow conditions for the trajectory points, 1634s and 1636s cases, considered in the present study are summarized in Table 1. In Fig. 1, comparison of the simulated temperature distributions with the related calculations [2, 7, 8] is presented. The temperatures deduced from the present method are bounded by the previous studies. The vibrational-electronic-electron temperature that is the governing temperature of radiation is especially enveloped by the results obtained from the VSL [2] and LAURA [2] of the NASA Langley research center.

2.2 SPRADIAN14 with Improved Electron Impact Rate Models

SPRADIAN14 [11] is a line-by-line radiation code, which has been upgraded to extend the modeling capability to the infrared (IR) wave range. The radiative transitions of the contained species are modeled in the wave range of ultraviolet (UV), visible, vacuum UV (VUV), and IR. The radiative transport was modeled

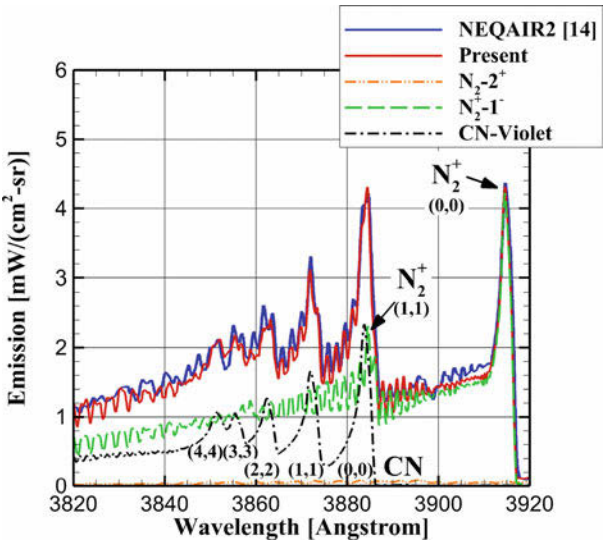

Fig. 2 Comparison of simulated spectra emitted from a plasma torch with other predictions [14]

by adopting a spherical cap model. In Fig. 2, comparison of the simulated spectra with other predictions [14] is presented. The composite spectra calculated by SPRADIAN14 are in reasonable agreement with the benchmark solution deduced from NEQAIR2.

To characterize the non-Boltzmann electronic state populations, a quasi-steady state (QSS) master equation was solved. For diatomic species, the CR parameters of Park [15, 16] were utilized. Three new electron impact rate models for N and one for O were developed in the present study. This is because Park's atomic electron impact rate model [10] is known to predict overpopulated high-lying electronic states for compression flows, such as in post-shock conditions. The major objective of developing these new models is to implement recent quantum mechanical (QM) results considering excitation and ionization from low-lying states of N and O. At first, the atomic line data, which consists of 38 levels for N and 32 levels for O, for conducting nonequilibrium calculations were newly constructed. This is because the previous ones with 22 and 19 levels for N and O, respectively, were too lumped to utilize the recent subdivided QM results. For atomic N, three different models were investigated. First, the "Frost" model was formulated based on the study by Frost et al. [17] for the transitions from the first three states. The second model, "Tayal," utilizes the results of Tayal [18] for the transitions from the first six states. The third model, "Frost-Tayal," is a hybrid of "Frost" and "Tayal" models, using the values by Frost for the first three levels and those of Tayal for the next three levels. For the transitions from high-lying states, Park's model [10] was maintained because the hydrogenic assumption of the model was found to be reasonable in those cases. All other transitions were modeled by adopting the semiempirical models by Drawin

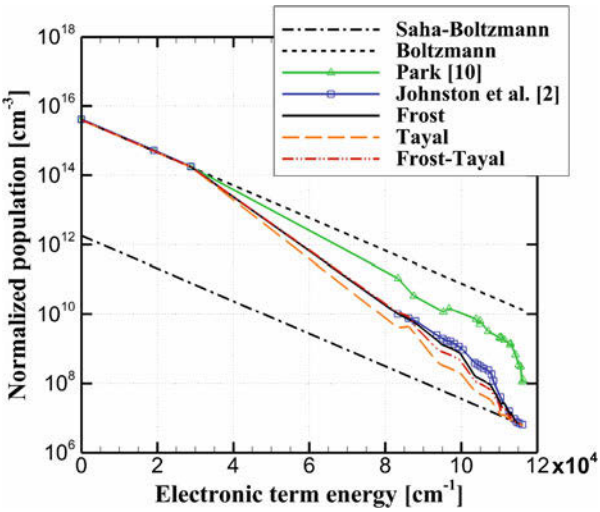

Fig. 3 Comparison of electron impact rate models for populations of atomic N at a post-shock condition [2]

[7] and Gryzinski [10]. For atomic O, the transitions from the first three levels were modeled by utilizing the results of Zatsarinny and Tayal [19] wherever available. All other transitions were modeled in the same way as for atomic N. For electron impact ionization, the models by Kunc and Soon [20] and Soon and Kunc [21] were adopted for the first three levels of atomic N and O, respectively. Drawin's formula proposed by Johnston et al. [6] was utilized for all remaining ionization processes. All rate parameters obtained from Refs. [17–19] were compiled as curve fit parameters in the modified Arrhenius form.

In Fig. 3, comparison of the electron impact rate models for the populations of atomic N at a post-shock condition [2] is presented. The results from the three new models are in reasonable agreement with those of Johnston et al. [2] and are shown to capture the depletion of the high-lying electronic states from the Boltzmann distributions due to the CR processes. However, the model of Park [10] overestimates the population of the high-lying levels. This is mainly due to the lack of accuracy for modeling excitation and ionization from the ground and first two metastable states.

3 Results and Discussion

At first, the three developed rate models for N were compared with the model of Park [10]. Then, comparison of the present calculations with the flight data and the related numerical studies was presented to estimate the accuracy of the developed

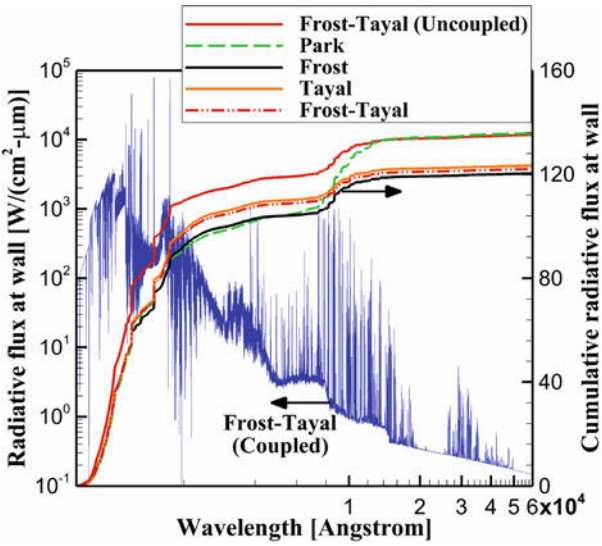

Fig. 4 Spectral and cumulative radiative flux distributions at wall obtained from four electron impact rate models at $t = 1636$s

rate models. In Fig. 4, the spectral and cumulative radiative flux distributions at the wall obtained from the four rate models are presented at t = 1636s. It is noted that the most increments of the cumulative flux come from the atomic line radiation. Also, the effect of flow-radiation coupling is shown by comparing the cumulative flux distributions obtained from the "Frost-Tayal" model by decreasing the wall heat flux about 10%. It is noted that Park's model presents highly overestimated results even for the coupled case. In Fig. 5, spatial distributions of the wall directed radiative heat flux are presented with the effect of non-Boltzmann modeling. It was found that the overestimation of Park's model mostly comes from the region directly behind the shock where the electronic temperature is high. The effects of non-Boltzmann modeling are presented by means of the uncoupled simulations using the "Frost-Tayal" model. The Boltzmann calculation, tagged as "(B)," produced excessive amount of radiation in comparison with the case of non-Boltzmann. Therefore, the non-Boltzmann population distributions should be considered and modeled in a proper way for the conditions considered in the present study.

In Figs. 6, 7, and 8, comparisons of the calculated values with the flight data [1] and other simulations [2, 3, 22–24] are presented for the two trajectory points. The results obtained from the "Tayal" model are not presented in these figures, because they are almost identical with those of the "Frost-Tayal" model, although the "Frost-Tayal" model shows slightly more accurate predictions. In Fig. 6, the spectrally integrated wall intensities for two wave ranges, which are 0.3 to 0.6 and 0.2 to 4 μm, are presented. For both ranges, Park's model overestimates the intensity at t = 1636s as underlined in Figs. 4 and 5. Other models developed in the present study are in

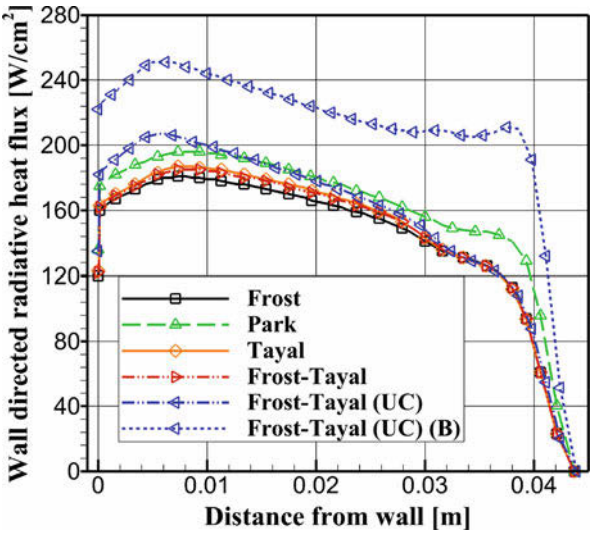

Fig. 5 Wall-directed radiative heat flux calculated by means of the four rate models with the effect of non-Boltzmann modeling for $t = 1636$s

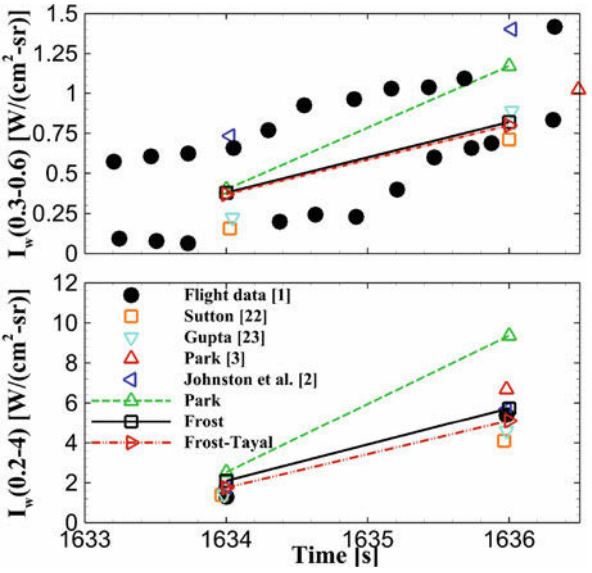

Fig. 6 Comparison of calculated wall intensity with the flight data [1] and the related simulations [2, 3, 22, 23] for the wave ranges of 0.3–0.6 and 0.2–4 μm

reasonable agreements with measurements, while the "Frost-Tayal" model shows the most accurate results. In Figs. 7 and 8, the partially integrated radiative and total heat flux are shown, respectively. Again, the "Frost-Tayal" model shows the best agreements with measurements as shown in Fig. 7. The total heat flux values calculated by the models developed in the present study are almost identical with the recent calculations by Johnston et al. [2] as presented in Fig. 8, although the radiative heating was predicted with an improved accuracy as shown in Figs. 6 and 7. It is observed that certain uncertainties still exist in modeling the radiative shock

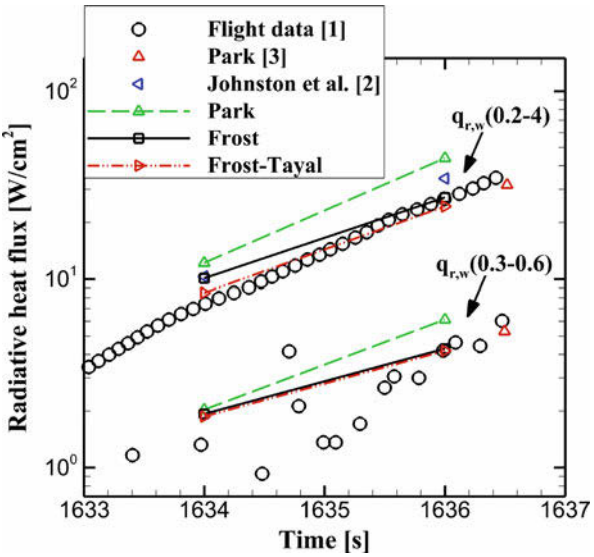

Fig. 7 Comparison of simulated radiative heat flux with measurements [1] and related calculations [2, 3] for two wave ranges

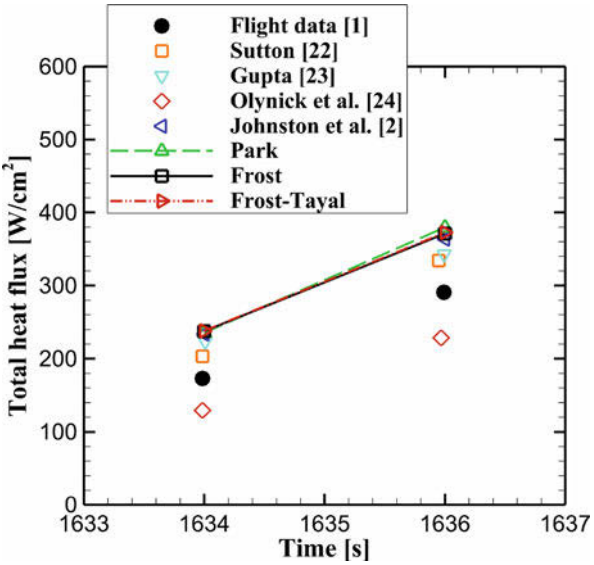

Fig. 8 Comparison of simulated total heat flux with measurements [1] and related calculations [2, 22–24]

layers, because some discrepancies were captured in the total heating in comparison with the flight data. One of the possible causes of the error is in the accuracy of the thermochemical nonequilibrium models for the flow fields that affects the convective heating.

4 Conclusions

In the present study, modeling of the radiative shock layer was conducted. To model the thermochemical nonequilibrium flow in the shock layer, the VSL method with Park's two-temperature model was utilized along with the radiative cooling effect deduced from SPRADIAN14. Accuracy of the VSL method and SPRADIAN14 was validated by solving benchmark problems. To improve the accuracy of the non-Boltzmann modeling for atomic N and O, three new electron impact rate models for N and one for O were developed by utilizing the recent QM results. The accuracy of the models was assessed by solving the test problem for atomic N. It was shown that the methodology utilized in the present work is able to predict physically reliable results. As an application, two of the FIRE II flight trajectories were analyzed. It was observed that the tendency of overestimation of the previous model is resolved by adopting the state-of-the-art QM data in the present new rate models. It was found that the "Frost-Tayal" model produces the most accurate results in comparison with the flight data.

Acknowledgment The authors gratefully acknowledge funding for this work through ADD Grant UD150034.

References

1. D.L. Cauchon, NASA TM X-1402 (1967)
2. C.O. Johnston et al., Nonequilibrium stagnation-line radiative heating for fire II. J. Spacecr. Rocket. **45**(6) (2008)
3. C. Park, J. Thermophys. Heat Transf. **18**, 3 (2004)
4. C. Park, H.K. Ahn, J. Thermophys. Heat Transf. **13**, 1 (1999)
5. E.E. Whiting et al., NEQAIR96, nonequilibrium and equilibrium radiative transport and spectra program: User's manual, NASA RP-1389 (1996)
6. C.O. Johnston et al., Non-Boltzmann modeling for air shock-layer radiation at lunar-return conditions. J. Spacecr. Rocket. **45**(5) (2008)
7. M. Panesi et al., Fire II flight experiment analysis by means of a collisional-radiative model. J. Thermophys. Heat Transf. **23**, 2 (2009)
8. D. Potter, Doctoral Thesis, University of Queensland, 2011
9. B. Lopez et al., Improved non-Boltzmann modeling for nitrogen atoms, in *AIAA 2016–4431, 46th AIAA Thermophysics Conference*, Washington, DC (2016)
10. C. Park, *Nonequilibrium Hypersonic Aerothermodynamics* (Wiley, New York, 1990), pp. 119–143
11. H.J. Nam, O.J. Kwon, Infrared Phys. Technol. **67** (2014)
12. S.Y. Hyun, Doctoral Thesis, KAIST, Daejeon, 2009
13. C. Park et al., Chemical-kinetic parameters of hyperbolic earth entry. J. Thermophys. Heat Transf. **15**, 1 (2001)
14. C.O. Laux, *High Temperature Gas Dynamics Lab Report T-288* (Stanford University, Stanford, 1993)
15. C. Park, in *AIAA 2008-1206, 46th AIAA Aerospace Sciences Meeting and Exhibit*, Reno, 2008
16. C. Park, in *AIAA 2008-1446, 46th AIAA Aerospace Sciences Meeting and Exhibit*, Reno, 2008

17. R.M. Frost et al., Calculated cross sections and measured rate coefficients for electron-impact excitation of neutral and singly ionized nitrogen. J. Appl. Phys. **84**(6) (1998)
18. S.S. Tayal, Astrophys. J. Suppl. Ser. **163** (2006)
19. O. Zatsarinny, S.S. Tayal, Astrophys. J. Suppl. Ser. **148** (2003)
20. J.A. Kunc, W.H. Soon, Phys. Rev. A **40**, 10 (1989)
21. W.H. Soon, J.A. Kunc, Phys. Rev. A **41**, 2 (1990)
22. K. Sutton, AIAA Paper 84-1733 (1984)
23. R.N. Gupta, AIAA Paper 87-1576 (1987)
24. D.R. Olynick et al., Comparisons of coupled radiative Navier-Stokes flow solutions with the project fire II flight data. AIAA Paper, 94–1955 (1994)

Characterisation of Curved Axisymmetric Internal Shock Waves

A. A. Filippi and B. W. Skews

Abstract Understanding the shape of curved axisymmetric shock waves in supersonic intake-type conditions allows one to better design for downstream compression and heating requirements. Numerical results were obtained for ring wedge models with varying internal surface curvatures and wedge entry angles at different flow Mach numbers. Experimental results were obtained to validate the numerical method. A general power law fit which describes the shape of continuously curved axisymmetric shock wave segments was determined via curve fitting numerical results. The relationships between the curve fit constants in the general curved shock wave shape equation were shown for the models with a wedge entry angle of $\alpha = 4°$ between Mach 2.9 and 3.6. The curve fit constants were found to be self-similar in nature which promoted the process of characterising them with respect to normalised internal radius of curvature and flow Mach number. This resulted in a proposed empirical model which could predict the shape of the continuously curved axisymmetric shock wave segments within particular justified parameter limitations.

1 Introduction

The cardinal aspects of supersonic and hypersonic propulsion axisymmetric intake design involve understanding the internal shock wave structures forming therein. Varying the geometry of the internal surface in the said intakes allows for the control of the shock waves that are utilised for compression and heating purposes. By characterising the influence of geometrical and flow parameters, one can model the shape of the curved axisymmetric shock waves that form. This then gives an indication on the suitability of the intake via calculating the resulting shock wave shape. By using curved shock theory proposed in [1] and the methods outlined in [2], one has a means to analyse curved shock waves on the basis of only their shape. The

A. A. Filippi (✉) · B. W. Skews
Flow Research Unit, School of Mechanical, Industrial and Aeronautical Engineering, University of the Witwatersrand, Johannesburg, South Africa

A. Sasoh et al. (eds.), *31st International Symposium on Shock Waves 2*,
https://doi.org/10.1007/978-3-319-91017-8_121

characterisation of curved shock waves provides understanding as to how their shape is altered and if there are underlying relationships which control their formation. This paper aims to characterise the shape of the continuously curved shock wave segments in axisymmetric internal flow fields with respect to the internal surface curvature and Mach number and display evidence of self-similarity between the defining shape parameters.

2 Experimental Testing

Axisymmetric ring wedges were manufactured with varying internal radii of curvature and wedge entry angles for experimental testing. A schematic of a typical ring wedge model is displayed in Fig. 1. The blowdown supersonic wind tunnel facility within the Flow Research Unit at the University of the Witwatersrand was used to test the ring wedge models. Results were captured using shadowgraph techniques which provided a basis to validate the numerical modelling from which the curved shock wave characterisation was derived. All the dimensions of the ring wedge have been normalised with respect to the leading edge radius, R_{le} (see Fig. 1), and are a ratio thereof where R_c denotes the normalised internal radius of curvature, L_w the normalised ring wedge length and α the wedge entry angle. Experimental validation tests were completed at Mach numbers between Mach 2.8 and 3.6. With the wind tunnel test cross-sectional dimensions being limited to 101.6 mm by 101.6 mm and after initial parameter studies, models with a leading edge radius of 20 mm and wedge length of 10 mm were selected to deal with spatial constraints. Due to the axisymmetric nature of the ring wedges, only the flow field behind each model could be captured.

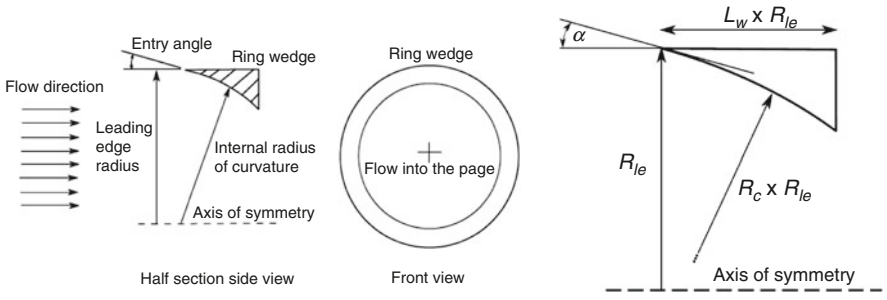

Fig. 1 Axisymmetric ring wedge schematic with experimental parameters

3 Numerical Modelling

Numerical modelling was required to visualise the internal curved shock wave segments that are hidden from view during experimental tests. CFD simulation results were obtained using Euler equation formulations in ANSYS Fluent 15.0. Two-dimensional axisymmetric computational domains were created for each ring wedge in question, and simulation results were obtained between Mach numbers of Mach 2.4 and 3.6. The computational domain was discretised using the standard CFD meshing algorithms built into ANSYS 15.0 with uniform quadrilateral cell sizing being applied to the domain. Dynamic adaptive meshing techniques were employed to locate and refine the shock structures using refinement levels and thresholds which were found to produce sufficiently resolved flow features. Solutions were continued until their iterative convergence fell within acceptable standards. Figure 2 displays comparative overlaid CFD and experimental results for the two different ring wedges.

The continuously curved shock wave segments that were curve fitted, represented by the dashed boxes in Fig. 2, are bounded by the leading edge of the ring wedge model and the influence of the trailing edge expansion fan. These axisymmetric curved shock wave segments are only affected by the internal geometry of the ring wedge and flow speed. CFD results were post processed using Tecplot 360 EX 2014 Release 1. The shock shape was then extracted and curve fitted using image processing techniques in MATLAB R2009b after the data was normalised with respect to the leading edge radius.

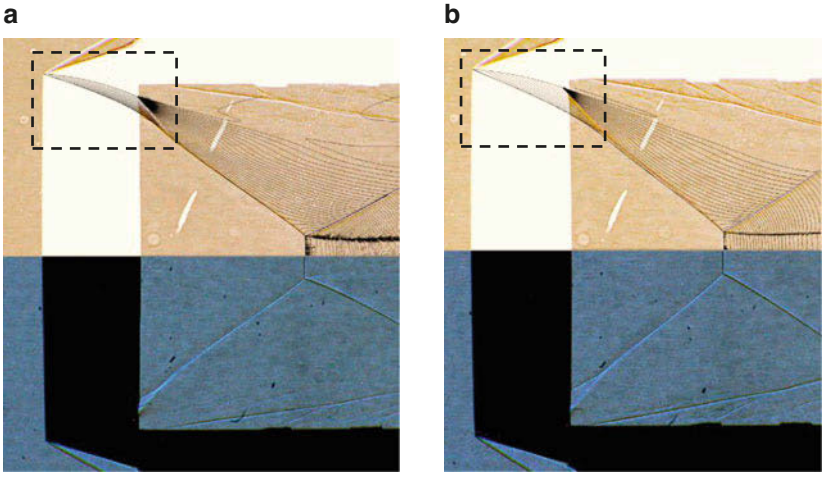

Fig. 2 (**a**) $R_c = 1.5$, $\alpha = 4°$, $L_w = 0.5$ model at Mach 3.6 (**b**) $R_c = 2$, $\alpha = 4°$, $L_w = 0.5$ model at Mach 3.0

4 Results and Discussion

4.1 Curved Shock Wave Shape Equation

Ring wedges with $R_c = \{1, 1.5, 2\}$ and $\alpha = \{0°, 4°, 8°\}$ were tested between Mach 2.4 and 3.6, and it was found that the continuously curved shock wave segment was very closely described by Eq. (1) with R^2 correlation values near unity:

$$y_s = \left(\frac{x_s - \lambda}{\varepsilon}\right)^{\frac{1}{\eta}} \tag{1}$$

Therefore a general equation was determined that accurately describes the shape of the continuously curved shock wave segments generated in axisymmetric internal flow fields, which are curved in both the flow and flow-normal planes. The curve fit constants ε, η and λ then vary depending on the flow Mach number, internal surface radius of curvature and wedge entry angle. When $\alpha = 0°$, the leading edge is parallel to the flow, meaning that the internal curved surface experiences an isentropic compression which eventually coalesces into a shock wave. The $\alpha = 8°$, $R_c = 1$, model only experienced non-choked flow past Mach 4.2 which is above the maximum testing Mach number of Mach 3.6 so no data was available. Therefore the $\alpha = 4°$ ring wedge cases have been chosen to showcase the shock wave shape relationship between the curve fit constants ε, η and λ and the parameters that determine them. For $R_c = 1$, $\alpha = 4°$, model, data is only present after Mach 2.9 since the exit area contraction is too large to allow attached flow to exist below the said limit. The remainder of the data points is then plotted under the same Mach number range of Mach 2.9 to 3.6. As a result of being able to capture data for all the values of R_c with $\alpha = 4°$, and with a full shock wave being present instead of an isentropic compression, additional CFD cases were simulated. Normalised internal radii of curvature ratios of $R_c = 1.25$ and $R_c = 1.75$ were selected to fit between the original datasets. Figure 3 shows the varying values of ε, η and λ for the wedge entry angle $\alpha = 4°$ models as well as maximum x-axis value and horizontal shock length for the $\alpha = 4°$ shock waves.

Both values of ε and λ seem to remain almost constant with a very gradual linear relationship as Mach number increases. The values of η however follow a sharper gradient baring a linear increasing relationship. It can be seen that the first three Mach number data points for the $R_c = 1$ series in all constant and maximum length cases follow a differing relationship to the remaining data points. They increase in the case of ε, η and x_{max} or decrease in the case of λ more rapidly in comparison to the data points ahead of them before joining a more linear type trend. The reason this occurs is due to their stage in shock wave progression. The curved shock wave segment's length is initially determined by the start of the reflection point and eventually moves into the expansion fan region where it remains as Mach number increases. For the $\alpha = 0°$ constants, it was found that they were more erratic and vertically scattered due to the isentropic compression that was forming and later

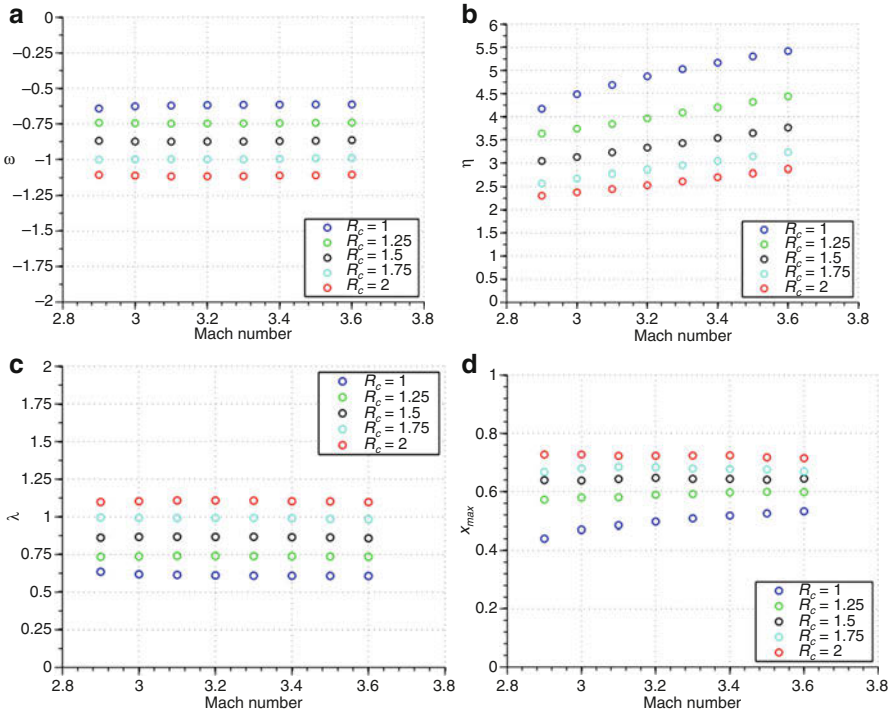

Fig. 3 (**a**) ε for Eq. (1) where $\alpha = 4°$, (**b**) η for Eq. (1) where $\alpha = 4°$, (**c**) λ for Eq. (1) where $\alpha = 4°$, (**d**) x_{max} for Eq. (1) where $\alpha = 4°$

coalescing to create a shock wave. Since the internal curved surface is now placed at an angle, due to the increase in α from 0° to 4°, the flow is initially deflected through a larger angle. A shock wave is present so the decrease in flow Mach number behind the initial shock compression is larger than in the isentropic compression case. The decrease in flow speed then means that the following compressions occur at a steeper angle. For a lower Mach number and constant deflection, the shock angle increases. Therefore the infinitesimally present compressive Mach waves or characteristics, which alter the shape of the shock wave, occur with a steeper angle. The shape of the curved shock wave formed through this mechanism becomes more regular than in the case of an isentropic compression. The determination of the shape and curve fitting data becomes more consistent, and hence the constants follow suit with a uniform trend.

4.2 Curved Shock Wave Characterisation

In order to find an underlying relationship between the experimental parameters and the curved shock wave shape they produce, an attempt was made to characterise the constants used in Eq. (1). Only the $\alpha = 0°$ and $\alpha = 4°$ cases contained R_c values of 1 through 2. The $\alpha = 0°$ case however did not represent a true shock wave but rather the frontal surface of an isentropic compression which later transitioned to a shock wave. Therefore only the $\alpha = 4°$ data was considered for characterisation purposes as an attached leading edge shock wave was present with available simulation data below Mach 3.6. Referring to Fig. 3, it is evident that self-similar trends are present with each value of R_c. Each trend looks to show the same general relationship and is only separated by a particular ratio as R_c increases. Since this occurs, an attempt was made to collapse the curves and possibly characterise them by a set of functions which could describe the curved shock wave shape given a set of input parameters. To try to collapse the curves for each set of constants, they were normalised with respect to those of the $R_c = 1$ case. Therefore a set of curve fitting constant ratios were created, symbolised by ϕ, where the numerator represents ε, η or λ for the set $R_c = \{1, 1.25, 1.5, 1.75, 2\}$ and the denominator ε, η or λ for $R_c = 1$. The said ratios are depicted in Eqs. (2)–(4):

$$\phi_\varepsilon = \frac{\varepsilon_{Rc}}{\varepsilon_1} \tag{2}$$

$$\phi_\eta = \frac{\eta_{Rc}}{\eta_1} \tag{3}$$

$$\phi_\lambda = \frac{\lambda_{Rc}}{\lambda_1} \tag{4}$$

Since each ϕ value will be coupled to a particular Mach number, they must be averaged for each R_c dataset to find their correlation with change in R_c. Figure 4 displays the average ϕ for each constant where $\alpha = 4°$.

Linear curve fits were applied to the ϕ_ε and ϕ_λ data points, and a power law was applied to the ϕ_η data producing R^2 correlation values near unity. The ϕ fits for the curve fit constants ε, η and λ are displayed in Eqs. (5)–(7), respectively, as a function of R_c:

$$\phi_\varepsilon = 0.7934 R_c + 0.2100 \tag{5}$$

$$\phi_\eta = 1.2131 {R_c}^{-0.7194} - 0.2118 \tag{6}$$

$$\phi_\lambda = 0.8037 R_c + 0.1991 \tag{7}$$

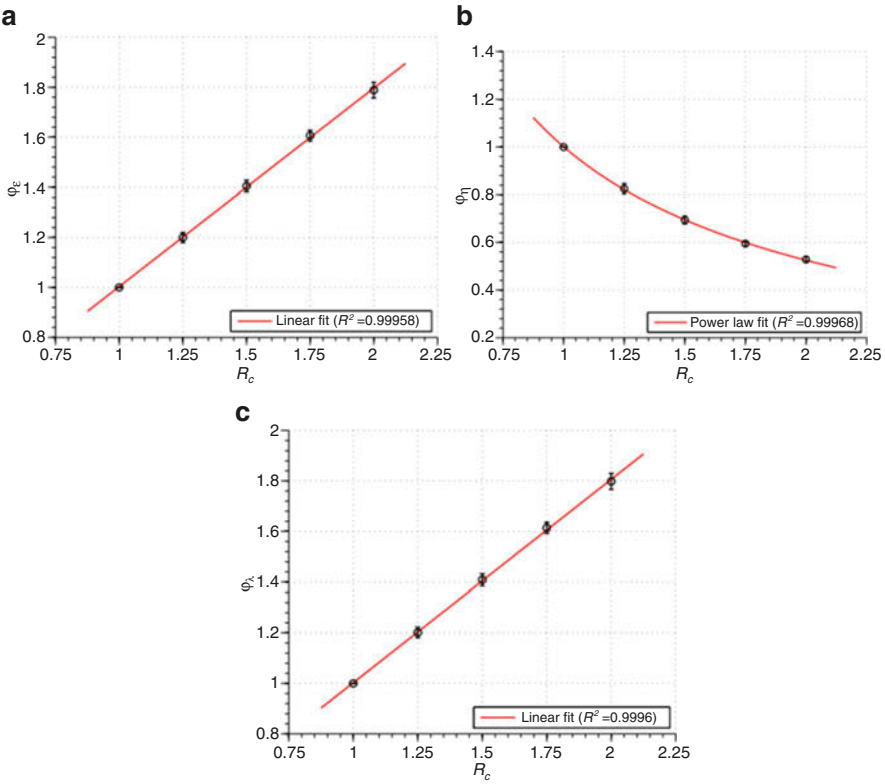

Fig. 4 (**a**) Average ϕ_ε values for all the $\alpha = 4°$ cases (**b**) Average ϕ_η values for all the $\alpha = 4°$ cases (**c**) Average ϕ_λ values for all $\alpha = 4°$ cases

Since the values of ϕ are generated by normalising the curve fitting constants by those of $R_c = 1$, it implies that the regression fits' lower limits are that of the $R_c = 1$ data point. Any model with $R_c < 1$ would immediately experience choking due to the reduction in flow exit area and increased flow turning as a result of a smaller internal radius of curvature. It would therefore be impossible for an attached shock wave to exist at a Mach number for models where $R_c < 1$ if one is not present at $R_c = 1$. Predicting values of ϕ via extrapolating the regression fits would not be valid unless done so where $R_c \geq 1$ and $\alpha = 4°$. Applying regression methods to the relationships between ε, η and λ against Mach number (M) for $R_c = 1$ produces Eqs. (8)–(10). This supplies a means to estimate the shock shape curve fitting constants where $R_c = 1$ and $\alpha = 4°$:

$$\varepsilon_1 = \frac{1.688 - 0.6084M}{M - 2.781} \tag{8}$$

$$\eta_1 = \frac{7.092M - 16.54}{M - 1.937} \tag{9}$$

$$\lambda_1 = \frac{0.603M - 1.685}{M - 2.801} \tag{10}$$

The regression fits for the different ϕ terms can be multiplied by the functions that predict the values for ε, η and λ. This provides a series of functions which can calculate ε, η and λ where $R_c \geq 1$ for Mach numbers greater than 2.9. Substituting them in Eq. (1) produces the shape of the continuously curved shock wave segment via empirical methods in Eq. (11):

$$y_s = \left(\frac{x_s - \phi_\lambda \lambda_1}{\phi_\varepsilon \varepsilon_1}\right)^{\frac{1}{\phi_\eta \eta_1}}, \quad \text{for} \quad R_c \geq 1 \quad \text{and} \quad M \geq 2.9 \quad \text{where} \quad \alpha = 4^\circ \tag{11}$$

Equation (11) therefore determines the shape of the continuously curved shock wave segment as a function of normalised internal radius of curvature, R_c, and Mach number, M. The simulation model wedge lengths used to develop the relationship were however only half the length of the leading edge radius ($L_w = 0.5$). This implies another constraint on Eq. (11) to curved internal surfaces where $L_w \leq 0.5$. If the empirical model is applied to curved surfaces where $L_w > 0.5$, it will assume that the same curvature conditions, which affect the shock wave, remain constant. This may be the case for the flow plane curvature induced by the internal surface but not the flow-normal plane transverse curvature induced by the axisymmetric nature of the ring wedges. Therefore extrapolating the curved shock wave for $L_w > 0.5$ will produce a shape that is less curved towards the axis of symmetry than what it should. For $L_w > 0.5$, additional characteristics which emanate from the internal curved surface will too curve the shock wave to a greater extent as they merge with it, altering its shape. Interpreting the trends seen in the values of ϕ one can gain a sense of self-similarity evident in the changing values of ε, η and λ. The linear fits of Fig. 4a and c show how the values of ε and λ change by equal incremented amounts for each R_c dataset. Therefore as R_c increases, the values of ε and λ will change by the same constant proportion, which can be seen in Fig. 3a and c. The power law fit of Fig. 4b is expected as the η makes up part of the exponential component of Eq. (1). It gives an indication to the role of R_c in determining η, and with increasing R_c, the power law fit in Fig. 4b seems to approach an asymptotic value of ϕ_η. Figure 5 shows the empirical shock waves using Eq. (11) for $R_c = 2$ and $M = 3.6$, as white lines, overlaid on the experimental results for the $R_c = 2$, $\alpha = 4°$, $L_w = 0.5$ model at Mach 3.6. They extend from the leading edge until the influence of the trailing edge expansion fan and follow the visible experimental shock waves very closely.

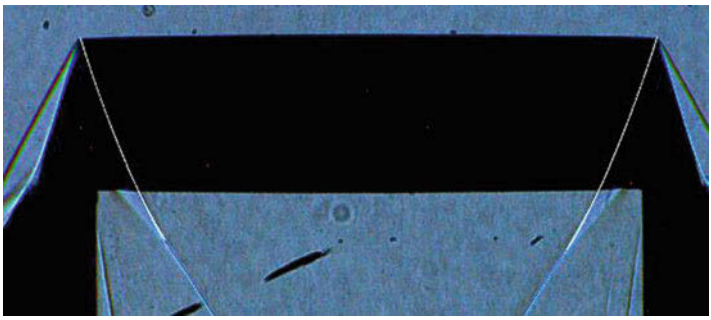

Fig. 5 Overlaid experimental and empirical results where $R_c = 2$, $L_w = 0.5$ and $\alpha = 4°$ at Mach 3.6

5 Conclusions

A general curved shock wave shape was determined for the continuously curved shock wave segment bounded by the leading edge and downstream influence effects. A curve-fitted shock shape relationship is presented in Eq. (1). The curve fit constants which are used in the curved shock wave shape equation were found to be self-similar in nature with varying experimental parameters. The relationships for the $\alpha = 4°$ models were then characterised into an empirical model represented by Eq. (11) which is a function of normalised internal radius of curvature and Mach number. The induced curvatures and wall emanating characteristics curve the shock and change its shape such that it cannot be extrapolated to cases where $L_w > 0.5$.

References

1. S. Mölder, Curved shock theory. Shock Waves **26**(4) (2016)
2. S Mölder, Flow behind concave shock waves, Shock Waves., **[Online]** (2017)

Comparative Heat Flux Measurement of a Sharp Cone Between Three Hypersonic Test Facilities at LHD

Q. Wang, P. Lu, J. W. Li, S. Wu, J. P. Li, W. Zhao, and Z. L. Jiang

Abstract Comparative heat flux measurements for a sharp cone model were conducted by utilizing a high Reynolds number shock tunnel JF8A, a high-enthalpy shock tunnel JF10, and a large-scale shock tunnel JF12 at the Key Laboratory of High Temperature Gas Dynamics (LHD), Institute of Mechanics, Chinese Academy of Sciences, which were responsible for providing the nonequilibrium or perfect gas flows. Through the assessment of data accuracy and consistency between each facility, we aim to compare the heat transfer data of a sharp cone taken in them under a totally different kind of freestream conditions. A parameter, defined as the product of the Stanton number and the square root of the Reynolds number, was found to be more characteristic for the aerodynamic heating phenomena encountered in hypersonic flight under laminar flows. This parameter can almost eliminate the variability caused by the different flow conditions, and it should be a more preferable parameter for the reduction of the ground experimental data and the extrapolation to flight.

1 Introduction

Reliable prediction of heat transfer rates is a major issue for researchers and developers working within the current space program. For the high costs of flight tests, most aerodynamic heating experiments are still completed in the ground facilities, where shock tunnels show their advantages for the accommodation of

Q. Wang (✉) · J. W. Li · S. Wu · J. P. Li
State Key Laboratory of High Temperature Gas Dynamics, Institute of Mechanics, Chinese Academy of Sciences, Beijing, China
e-mail: wangqiu@imech.ac.cn

P. Lu · W. Zhao · Z. L. Jiang
State Key Laboratory of High Temperature Gas Dynamics, Institute of Mechanics, Chinese Academy of Sciences, Beijing, China

School of Engineering Science, University of Chinese Academy of Sciences, Beijing, China

A. Sasoh et al. (eds.), *31st International Symposium on Shock Waves 2*,
https://doi.org/10.1007/978-3-319-91017-8_122

relatively large-sized models and low operational costs. And the development of experimental technique has made it possible to realize hypersonic flows ranging from 2.5 to 45 MJ/kg, which corresponds to velocities from 2 to 10 km/s, respectively [1, 2]. However, no single ground test facility can fully simulate the many aspects of hypersonic flights; similarity parameters, such as Reynolds number and Mach number, are somewhat different from each other for different facilities due to their capability difference, which makes it difficult for the analysis, extrapolation, comparison, using of the experimental data [3]. Therefore, database or principles obtained from original models are necessary to be considered, which can provide guidance for comparison between different ground facilities or from ground to flight extrapolation. And cones are often the object of investigations for their relative simplicity of the flow fields and widespread use in missile designs.

In the present study, heat transfer measurements of a spherically sharp cone were conducted in three shock tunnels at LHD, which were responsible for providing the nonequilibrium (JF10) or perfect gas flows (JF8A and JF12), respectively. Different Reynolds numbers are also considered. The surface temperature is measured by using the E-type coaxial thermocouples or thin film gauges. And numerical analysis using the CFD technique has also been conducted. Through the assessment of data accuracy and consistency between each facility, we aim to establish practical guidelines for the complementary use of these ground-based test facilities and provide reliable database for CFD validation.

2 Experimental Setup

2.1 Facilities

The experimental program was conducted in the JF8A, JF10, and JF12 shock tunnels, which were reflected shock tunnels using high-pressure air or detonation driving technique. These facilities are common in the sense that they cover hypersonic speed regime, but there exist large differences regarding the flow properties and the tunnel specifications. JF8A is a middle-sized shock tunnel, and several times of experiments per day are possible. This is favorable as for data productivity, but the flow enthalpy is much lower and attainable. Reynolds number is much higher compared to the other two facilities. JF10 is a high-enthalpy shock tunnel which can provide high-temperature gas conditions for hypersonic flight, and real gas effect can also be studied. JF12 is the largest shock tunnel in the world with the nozzle exit diameter of 2.5 m, capable of replicating flight conditions for Ma5∼9 at altitude of 25 ∼ 50 km, and integrated vehicle/engine is possible to test. The major specifications of the three shock tunnels are shown in Table 1, and details can be seen in literature [4, 5]. Hence these facilities should be the compliments of each other, taking advantage of a merit of one facility and compensating a shortcoming of the others.

Table 1 Facility comparison

	JF8A	JF10	JF12
Operation mode	High-pressure air	Forward detonation	Backward detonation
Flow duration time	30 ms	5 ms	130 ms
Nozzle shape	Contoured	Conical	Contoured
Nozzle diameter	0.8 m	0.5 m	2.5 m
Maximum H_0	1.3 MJ/kg	20 MJ/kg	5 MJ/kg
Maximum Re	4.2×10^7/m		4×10^6/m

2.2 Sensors

Thin film resistance gauges, with a diameter of 2.2 mm, were installed in the JF8A test model due to their short rise times and high electrical output per degree rise in temperature. However, they are prone to thermal damage and rapid erosion by small particles in high-enthalpy flows of JF10 and JF12, and the lifetime of each gauge is limited to one or two shots. Thus, homemade E-type (chromel-constantan) coaxial thermocouples, 1.4 mm in diameter, were installed in these two shock tunnel models, which turned to have fast response times and can be flush-mounted. From the measured surface temperature T, the heat flux is calculated according to Schults and Jones [6] as follows:

$$\dot{q}\left(t_n\right) = 2\sqrt{\frac{\rho c k}{\pi}} \sum_{i=1}^{n} \frac{T\left(t_i\right) - T\left(t_{i-1}\right)}{\sqrt{t_n - t_i} - \sqrt{t_n - t_{i-1}}} \tag{1}$$

where ρ, c, and k are the density, heat capacity, and heat conductivity of the sensor material and T and t are the temperature and time, respectively.

2.3 Models

A relatively simple model configuration was selected to alleviate uncertainties coming from the model geometry complexity. It was shown in Fig. 1 a 7 deg half-angle spherically sharp cone. Considering the nozzle exit diameter of the facilities, the model with an overall length of 590 mm was chosen for the JF10 shock tunnel and 1100 mm for the JF8A and JF12 shock tunnels.

2.4 Test Conditions

Reservoir pressure was measured using a piezoelectric pressure transducers mounted at the end of the shock tube. Other reservoir parameters were computed using the measured shock tube filling pressure, shock speed, and nozzle reservoir

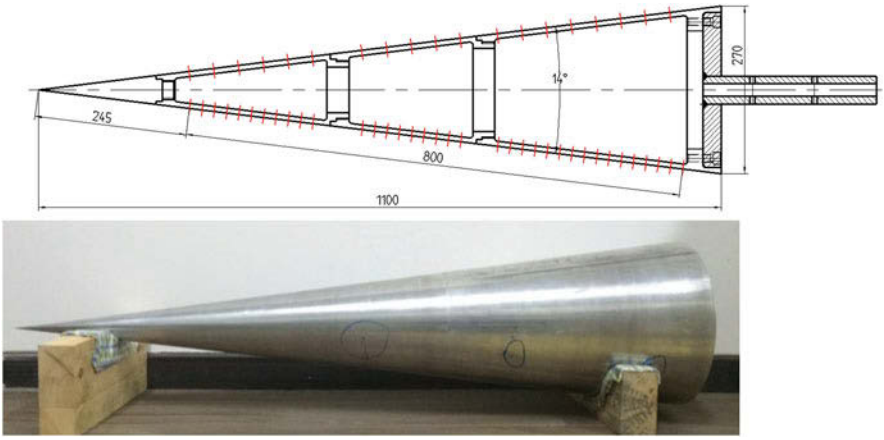

Fig. 1 Experimental models in JF8A

Table 2 Test conditions

	JF8A	JF10	JF12
P_0 (MPa)	1.2	13.5	2.2
H_0 (MJ/kg)	0.6	16	3.3
T_∞ (K)	67.5	435	293
ρ_∞ (kg/m^3)	2.7×10^{-2}	7.0×10^{-4}	5.0×10^{-3}
u_∞ (m/s)	1054	4979	2343
Re/L (/m)	6.4×10^6	1.5×10^5	6.5×10^5

pressure. Based on the reservoir conditions, the freestream was subsequently determined by numerical rebuilding of nozzle flow [7]. The accuracy of CFD analysis of the nozzle flow had also been judged by experiments taken in the freestream, such as static pressure, pitot pressure, and stagnation point heat flux. The reservoir and freestream conditions in our test were shown in Table 2. Subscript "0" represents the reservoir condition and "∞" for freestream condition. Reynolds number $\mathrm{Re} = \frac{\rho_\infty u_\infty L}{\mu_\infty}$, with the characteristic length L, represents for model length. In addition, the experiments were conducted at the surface temperature of 290 K (room temperature). And the angle of attack was set to zero in all the experiments.

3 Numerical Method

As a valuable complement for the analysis of experimental results, such as boundary layer parameter determination, numerical simulations were used in the paper. And calculating heat transfer had also been compared with the experiments under laminar flows. The governing equations employed were the axisymmetric, compressible Navier-Stokes equations. Considering the test conditions of the three shock tunnels

and the computing cost, two sets of computation procedure were used in this paper. Calorically perfect gas was chosen for the JF8A and JF12 flow conditions, while thermal chemical nonequilibrium for the JF10 conditions. Beyond that, they were both based on the finite difference method of AUSMPW+ Scheme [8], and point implicit scheme of LU-SGS [9] was used. On the solid wall, the no-slip condition for velocity is considered, and the temperature is prescribed to the room temperature. The chemical composition on the body surface is considered either fully catalytic or non-catalytic to chemical reactions. The numerical heat flux is calculated by summing three contributing parts: translational temperature model flux, vibrational temperature model flux, and diffusion model flux as follows (only translational temperature model flux is considered for JF8A and JF12 condition):

$$q_w = k\frac{\partial T}{\partial n} + k_v\frac{\partial T_v}{\partial n} + \sum_{i=1}^{ns} h_i \rho D_i \frac{\partial c_i}{\partial n} \tag{2}$$

4 Results and Discussion

In the paper, the experimental results of the sharp cone in three different shock tunnels were explored and compared with each other. Since the sharp cone results in JF10 and JF12 could be found in the literature [10], we mainly focus on the results in JF8A and its comparison with the other two. The typical stagnation pressure and sensor curves were shown in Fig. 2, with an effective test time from 19 to 26 in the legend. Since the Reynolds number in JF8A was 6.4×10^6/m, transition and turbulent flow existed on the sharp cone surface, where it can also be distinguished by the different signal to noise ratio of the curves, whereas the other two shock tunnels were only laminar flow due to their much lower Reynolds number.

In order to be able to compare the results between different conditions, such as results from flight and ground tests or from different shock tunnel conditions, it is necessary to reduce the data to a suitable nondimensional form. Heat transfer rate is typically normalized into a Stanton number (St). It is known that heat transfer is the effect of boundary layer parameters to the wall, which would be affected by the freestream flows, such as shock strength or dissociation. Therefore, it is necessary to normalize the heat transfer using the boundary layer parameters rather than the freestream flows while trying to compare the experimental data from different ground facilities. Fortunately, the boundary layer parameters are easily to be obtained with the help of numerical simulation, but not for the heat flux which is relatively difficult with accurately calculation. St and Re_x are defined in Eq. (3). Subscript e represents for the boundary layer edge parameters and w for the wall parameters. r is the recovery factor, where $r = \sqrt{\Pr}$ for laminar flows [11]. Pr is the Prandtl number, which is assumed to be constant, a fair approximation for most conditions of interest:

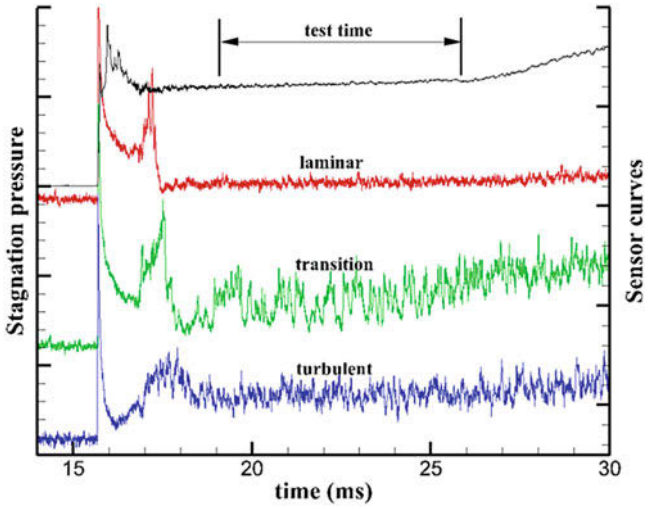

Fig. 2 Stagnation pressure and sensor curves in JF8A

$$St = \frac{q_w}{\rho_e u_e \left(H_0 - 0.5 \times u_e^2 (1 - r) - H_w\right)} \qquad \mathrm{Re}_x = \frac{\rho_e u_e x}{\mu_e} \tag{3}$$

In the previous literature [10], we developed a parameter, defined as the product of the Stanton number and the square root of the Reynolds number, which was found to be more characteristic for the aerodynamic heating phenomena encountered in hypersonic flight under laminar flows. This parameter can almost eliminate the variability caused by the different flow conditions, whether or not the flow is in dissociation or the boundary condition is catalytic. That was:

$$St = \frac{G\left(Ma_e, \mathrm{Pr}, \gamma, {}^{T_w}\!/_{T_e}\right)}{\sqrt{\mathrm{Re}_x}} = \frac{0.73}{\sqrt{\mathrm{Re}_x}} \tag{4}$$

And Hornung [12] developed the similar relations for turbulent flows:

$$St == \frac{0.191}{\mathrm{Pr}^{2/3} \left(\ln\left(0.046\mathrm{Re}_x\right)\right)^2} \tag{5}$$

Gas condition under laminar flows for JF8A was a perfect gas, and heat transfer on a sharp cone can be obtained by solving boundary layer equations easily [11]. And the turbulent results were obtained using Eq. (5). Comparison between Exp and theory in Fig. 3 showed that the experiment was 10% smaller than the theoretical value. The reason was still in analysis. However, it was acceptable for heat transfer measurements in hypersonic flows.

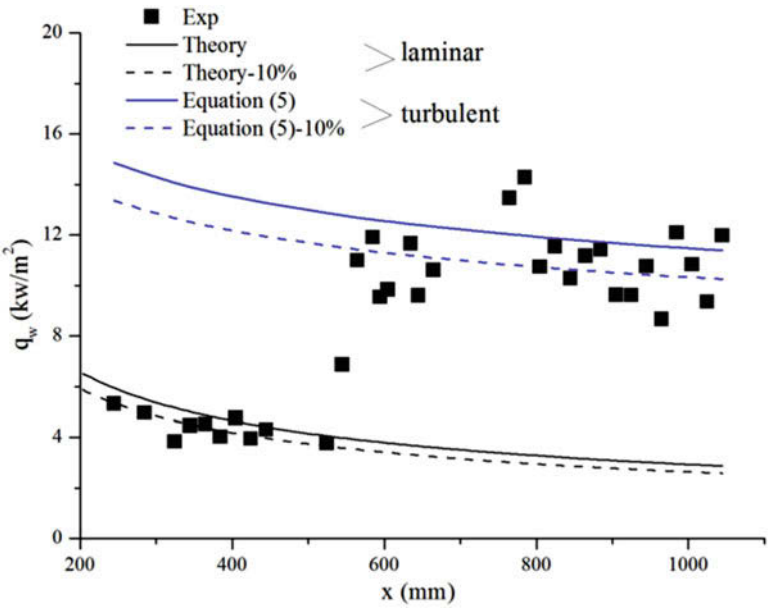

Fig. 3 Heat transfer data comparison between Exp and theory in JF8A

Figure 4 showed the Stanton number-Reynolds number relationship for the three shock tunnels, including experimental data, CFD, and a fitting line. And it needed to be emphasized that St and Re_x were defined using the boundary layer parameters in Eq. (4). Logarithmic coordinates were used to give an intuitive expression of constant A, which was 0.73 for laminar flows. It can be seen from Fig. 4 that although the Reynolds numbers were quite different from each other, the magnitude of 10^4 for JF10, 10^5 for JF12, and 10^6 for JF8A, the laminar heat transfer along the sharp cone showed the same regularity under parameter A, whether or not the flow is in dissociation. Flow chemistry of JF10 condition had small effect on it.

5 Conclusion

A comparative study had been conducted to investigate the hypersonic aerodynamic heating using a sharp cone model configuration between the three hypersonic facilities at LHD. From the experimental and numerical results obtained, the following conclusions were drawn. Parameter A, defined as the product of St and the square root of Re_x, was found to be a useful similarity parameter, where Stanton number-Reynolds number relationship shows almost the same regular in the three shock tunnel laminar conditions. It is noted that St and Re_x should be normalized using the boundary layer parameters. Work is presently underway to perform uncertainty analysis of the experimental data in JF8A shock tunnel and to extend the present study to higher Reynolds number flows.

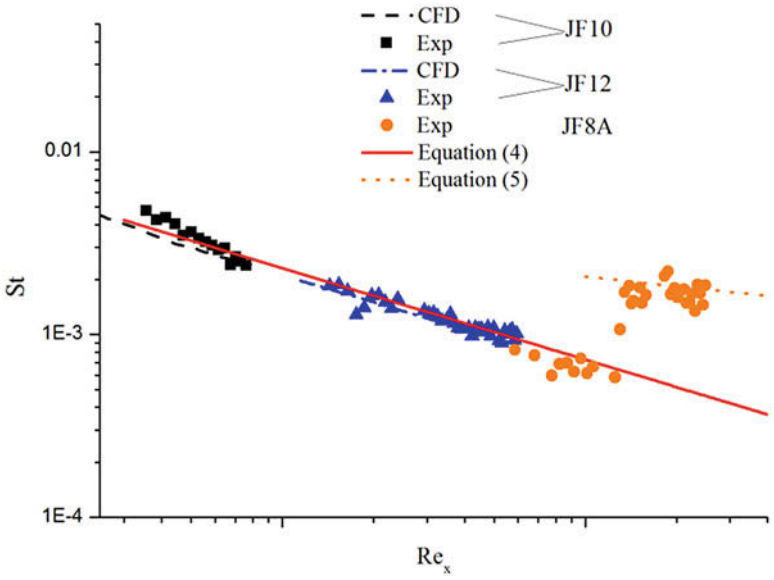

Fig. 4 Stanton number-Reynolds number relationships in the three shock tunnels

Acknowledgments This work was supported by the National Natural Science Foundation of China (Grant Nos. 11402275 and 11472280).

References

1. S.L. Gai et al., Stagnation point heat flux in hypersonic high enthalpy flows. Shock Waves **2**, 1 (1992)
2. T. Kishimoto et al., *High Enthalpy Flow Computation and Experiment Around the Simple Bodies* (Special Publication of National Aerospace Laboratory SP-29, Tokyo, 1996)
3. W.Z. Dong et al., Numerical analysis for correlation of standard model testing in high enthalpy shock facility and flight test. Exp. Meas. Fluid. Mech. **16**, 2 (2002)
4. Z. L. Jiang et al., Experiments and development of the long-test-duration hypervelocity detonation-driven shock tunnel (LHDst), AIAA 2014-1012
5. F.K. Lu et al., Advanced hypersonic test facilities, in *Progress in Astronautics and Aeronautics*, 2002
6. D.L. Schultz et al., Heat transfer measurements in short duration facilities, AGARD-AG-165, 1973
7. Q. Wang, *Experimental Study on Characteristics of Heat Transfer and Electron Density in High Enthalpy Flow* (Institute of Mechanics, Chinese Academy of Sciences, Beijing, 2013)
8. K.H. Kim et al., Methods for the accurate computations of hypersonic flows: I. AUSMPW+ scheme. J. Comput. Phys. **174**, 1 (2001)
9. A. Jameson et al., Lower-upper implicit schemes with multiple grids for the Euler equations. AIAA J. **25**(7) (1987)

10. Q. Wang et al., Comparative study on aerodynamic heating under perfect and nonequilibrium hypersonic flows. Sci. China Phys. Mech. **59**(2) (2016)
11. F.M. White, *Viscous Fluid Flow*, 2nd edn. (McGraw-Hill, New York, 1991)
12. P. Germain, et al., Transition on a sharp cone at high enthalpy: new measurements in the shock tunnel T5, AIAA 93-0343

Near-Field Pressure Signature over Mach 1.7 Free-Flight Bodies

Y. Aoki, D. Yoshimizu, A. Iwakawa, and A. Sasoh

Abstract The shock wave induced by the supersonic flight model and the turbulent flow induced by the free-falling grid were interacted using the time-synchronized launch operating system of the aero-ballistic range. The time-synchronized launch system was successfully done. However, the clear effect of the turbulence on the pressure signature has not been obtained because of the mismatch of the shock Mach number and the induced turbulent Mach number. D-SEND#2, which is similar to the aircraft, scale model was launched with high-precise attitude control by the rectangular-bore core aero-ballistic range, and the near-field pressure around the model was measured. The obtained pressure signature was compared with the numerical simulations, and these pressure signatures agreed well except for the pressure wave originating from the main wing. From these experiments, the experimental capability of the aero-ballistic range was extended.

1 Introduction

The pressure change around the supersonic flight model is integrated during the propagation to the ground; the loud noise is observed at the ground. This loud noise, named the sonic boom, is still one of the aerodynamic issues for re-realizing the supersonic transportation. To reduce the sonic boom noise, some researchers conducted the investigations for more than six decades [1]. Some investigations conducted the field experiment and proved the low-boom concept design such as Quiet Spike™ [2] or Drop test for Simplified Evaluation of Non-symmetrically Distributed sonic boom (D-SEND) [3] project. These field experiments are able to clearly show the effectiveness of the model geometry modification on the sonic boom, but these experiments need extremely high cost, and it is impossible to always examine by field experiment. Another point of view, the field experiment often

Y. Aoki · D. Yoshimizu · A. Iwakawa (✉) · A. Sasoh
Department of Aerospace Engineering, Nagoya University, Nagoya, Japan
e-mail: iwakawa@nuae.nagoya-u.ac.jp

A. Sasoh et al. (eds.), *31st International Symposium on Shock Waves 2*,
https://doi.org/10.1007/978-3-319-91017-8_123

includes the atmospheric turbulence which cannot be controlled, and it is difficult to evaluate the effect of the turbulence. D-SEND#2 is the second phase experiment of the D-SEND project. The low-boom concept design is adapted to the three-dimensional flight model, and the field experiment has been successfully conducted in July 2015 at Esrange Space Center in Sweden. From this experiment, the far-field pressure signature at Mach 1.39 was measured. The measured pressure signature of this experiment did not completely correspond to the pressure waveform predicted by the wind tunnel experiment and the numerical analysis. This discrepancy was caused by the existence of the atmospheric turbulent; hence, it is necessary to evaluate the effect of the turbulence on the pressure signature. The field experiment has the large advantage to obtain the real-scale far-field pressure signature, but there are still some problems to overcome to do the experiment.

In this paper, two experiments, the shock-turbulence interaction experiment and the free-flight experiment of D-SEND#2 scale model, using the aero-ballistic range, were conducted, and the near-field pressure signature was measured. The objective of this study is to demonstrate the shock-turbulence interaction using the aero-ballistic range and comparison between the near-field pressure signature around three-dimensional model obtained by the free-flight experiment and the numerical simulation.

2 Experimental Apparatus

All experiments were conducted in a rectangular-bore aero-ballistic range installed in Nagoya University; the detail was already described by past studies [4–6]. For conducting the shock-turbulence interaction, some minor modification was adapted, and the time-synchronized launch operation method was established. Near-field pressure signature was measured by piezoelectric pressure transducers (113B28, PCB Piezoelectric, Inc.). These transducers were flush-mounted on a steel plate at both longitudinal and lateral direction at 150 mm apart from the nominal flight path. During the free-flight in the test section, the flow field around the projectile was visualized by a shadowgraph system with a high-speed framing camera (HPV-1, Shimadzu Co.) and a flash ramp (200 J/Flash maximum, SA-200F, Nissin Electronics Co., Ltd.).

3 Result of Shock-Turbulence Interaction Experiment

3.1 Grid Turbulence and Test Section Facility

The grid turbulence and the shock wave induced by the supersonic flight model were interacted, and the effect of the turbulence on the pressure signature was measured. The grid was made of steel and the shape was circular. The diameter, grid distance

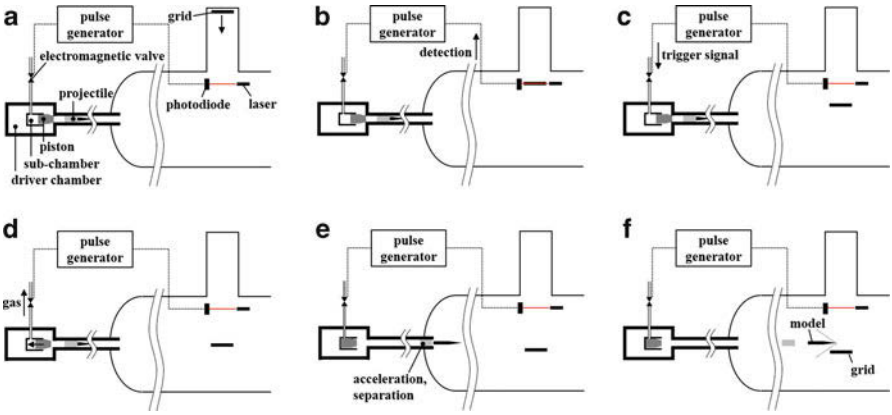

Fig. 1 Schematic illustration of procedure of time-synchronized launch operation. (**a**) Grid free-fall starting (**b**) Grid position detection (**c**) Trigger signal delivery (**d**) Piston removal (**e**) Acceleration/separation (**f**) Interaction

L, length of one side of a corner *d*, and aperture ratio of the grid are 184 mm, 20 mm, 4 mm, and 0.64, respectively. To maintain the attitude of the grid, the grid dropped along the guiding rod, and the linear bearing was used for reducing the friction between the grid and the guiding rod. Before experiment, this grid has been held at the upper flange of the test section by four electromagnets, and the grid started to drop to the test section when the current of the electromagnets turned off. The height from the nominal flight path to hold position was 1630 mm and it takes 50 ms. This dropping duration is longer than the model launch duration from the initial position to the test section. Therefore, the grid drop must start before the model launch signal.

The time-synchronized launch operation method has been established to conduct the turbulence-shock interaction experiment. The procedure of the time-synchronized launch operation is shown in Fig. 1. The current supply to the electromagnets holding the grid turned off, and the grid starts to fall as shown in Fig. 1a. The set of the laser and the photodiode detected the height of the grid, and the detection signal was delivered to the pulse generator, as shown in Fig. 1b. The trigger signal with appropriate delay time from the pulse generator was delivered to the electromagnetic valve as shown in Fig. 1c. The electromagnetic valve opened, and the high-pressure gas in the sub-chamber was removed; then the piston, which sealed the high-pressure helium in the driver chamber to the launch tube, was moved, and the helium propagates to the launch tube as shown in Fig. 1d. The helium propagating to the launch tube accelerated the sabot and the model as shown in Fig. 1e. The sabot and the model were separated by the in-tube catapult launch method [7]. Finally, the model passed the test section after grid falling as shown in Fig. 1f. To establish this operation method, the characteristics of the aeroballistic range were calibrated, and the standard deviation of the launch duration was less than 1.83 ms. The standard deviation of the grid position corresponding to the standard deviation of the launch duration was 8.4 mm. The launch signal was

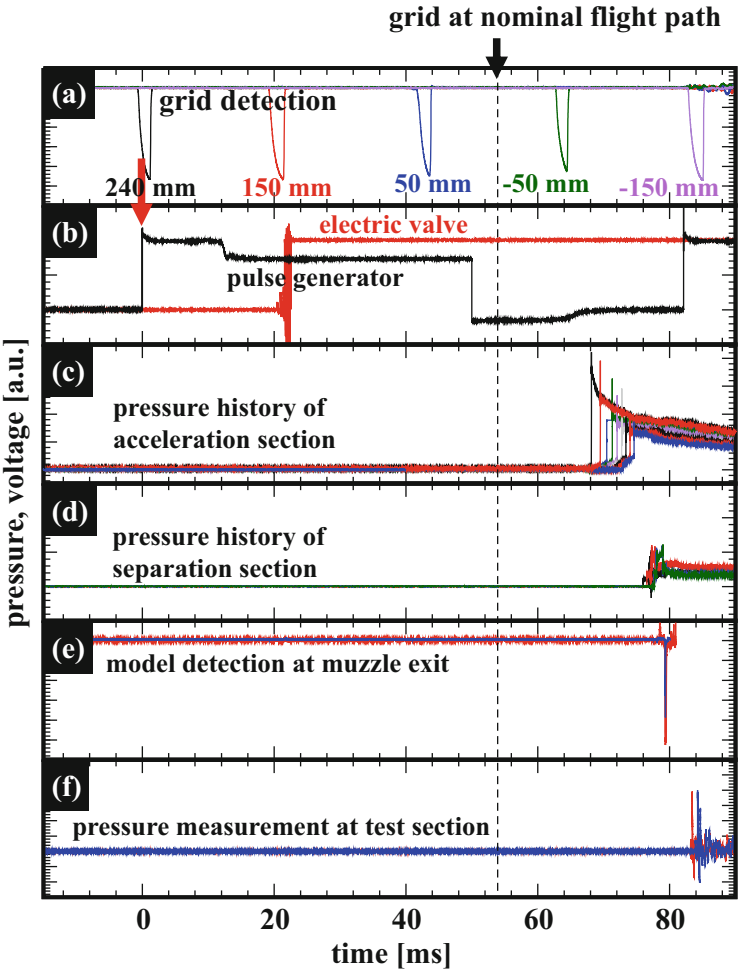

Fig. 2 Experimental result of the time-synchronized launch operation

delivered when the grid position was 142 mm below from the nominal flight path to prevent colliding to the grid.

Figure 2 shows the signals obtained by a time-synchronized launch experiment. First, the grid falling has started manually, and the height of the grid was detected by the laser and the photodiode, as shown in Fig. 2a. In this figure, the distance shows the height of the grid from the nominal flight path; the positive distance means higher, and the negative distance means lower than the nominal flight path. The grid arrived at a certain position, the pulse generator delivered the launch signal to the electric valve, and then the electric valve was opened, as shown in Fig. 2b. The model and the sabot were accelerated in the launch tube; the time history of the acceleration can be obtained by the pressure transducers installed at the launch

tube, as shown in Fig. 2c and d. The instant of the model arriving at the muzzle exit can be obtained by the laser and the photodiode located at the exit of the launch tube, as shown in Fig. 2e. Finally, the model arrived at the test section and the overpressure histories induced by the model can be measured by the pressure transducers. In this experiment, the time of the grid arriving at the nominal flight path was 50 ms; the time is shown by the vertical dashed line in Fig. 2. Then, the time when the model passed the flow induced by the grid was 82 ms. At that time, the grid already passed the nominal flight path and is located at the 147 mm lower than the nominal flight path. In this way, the time-synchronized launch operation was able to be successfully done.

3.2 Free-Flight Experiment of Three-Dimensional Model

The rectangular shape of the launch tube is suitable for the model shaped like aircraft. As the demonstration of the three-dimensional model like aircraft, D-SEND #2 scale mode was launched, and the whole near-field pressure signature was measured. In this experiment, both horizontal and vertical shadowgraph images during the flight were obtained. The model and the sabot are shown in Fig. 3. In this series of experiment, four models were launched, and the results of the experiments were shown in Table 1. The flight attitude shown in this table was evaluated by the visualized images. Although one of the difficulties of the aero-ballistic range experiment is the flight attitude control, this series of experiment was able to suppress the angle of attack within $\pm 1.5°$, the yaw angle within $\pm 1.0°$ using the rectangular launch tube, and the in-tube catapult launch system. The roll angle was evaluated by the horizontal visualized image; if the main wing has not been seen in the visualized image, the roll angle was less than $11.6°$ by the geometrical relation.

The visualized image of experiment #3 is shown in Fig. 4. The vertical image and horizontal image are shown in Fig. 4a and b, respectively. The nominal flight path in these figures shows the center axis of the test chamber. The flight attitude was estimated by these visualized images.

Figure 5a shows the horizontal direction of the near-field pressure signature obtained by experiment #3. From Figs. 4 and 5, the pressure signature of the

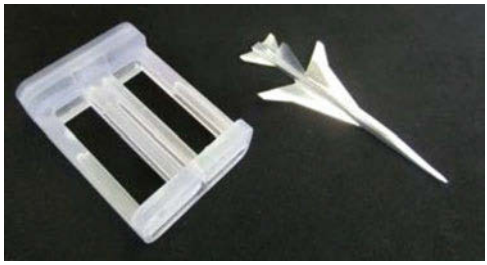

Fig. 3 D-SEND#2 scale model

Table 1 Experimental results

#	Model mass [g]	Mach number [−]	Flight attitude		
			AoA	Yaw	Roll
1	3.99	1.69	+1.3°	3.9°	<11.6°
2	4.17	1.68	+0.5°	1.0°	<11.6°
3	4.17	1.66	+0.7°	0.95°	<11.6°
4	4.16	1.64	−0.7°	0.70°	34°

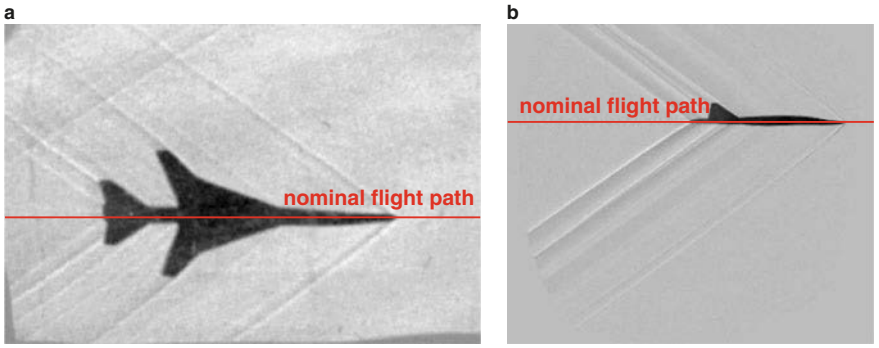

Fig. 4 High-speed framing schlieren images of experiment #3. (**a**) Vertical image (**b**) Horizontal image

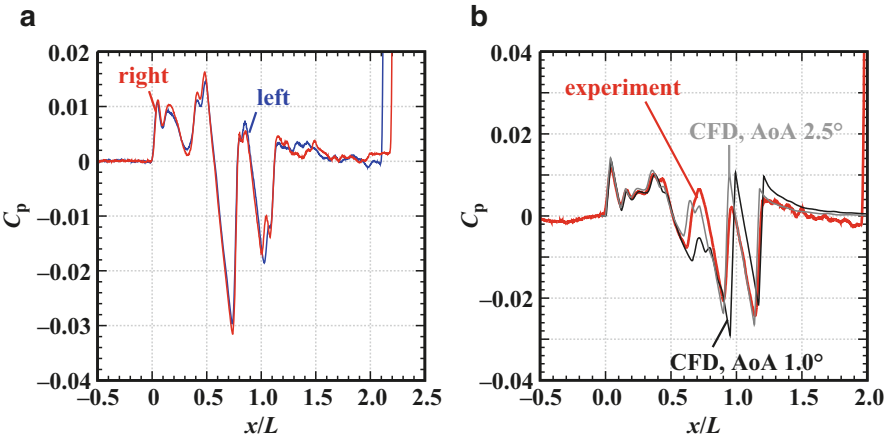

Fig. 5 Near-field pressure signature. (**a**) Side (**b**) Undertrack

horizontal direction well agrees with each other; thereby, the yaw and roll angle during the free-flight can be regarded as small. Fig. 5b shows the pressure signatures of the undertrack obtained by both the experiment and numerical simulation. The numerical simulation has been conducted by JAXA using TAS code and UPACS. The conditions of the simulation are Mach 1.69 and angle of attack of 1.0° and 2.5°.

From Fig. 5b, the overall pressure signature, the number of the shock waves, and the expansion fans agreed, but there are some discrepancies from $x/L = 0.5$ to 1.3. The pressure signature from $x/L = 0.5$ to 1.0 was originated at the main wing. From the results of the simulation, the angle of attack affects the pressure signature of the main wing. The compression/shock wave at the main wing of the experiment was relatively stronger than that of the simulation. This discrepancy was likely to be caused by the experimental limitation, because this stronger tendency was always observed by experiment #1 to #4. There are some possible reasons of the cause of this difference, which are the machining limitation of the wing thickness and the estimation of the flight attitude of the visualization.

4 Conclusion

The time-synchronized launch operation system of the aero-ballistic range was established, and the shock-turbulence interaction experiment was demonstrated. After the turbulent flow is induced in the test section by the free-falling grid, the model was launched and flew in the test section at supersonic speed. The pressure signature induced by the supersonic flight model was measured, and the signature with and without turbulence was obtained by the same launch. The obvious difference was not found because there is a large difference between the shock Mach number and the turbulent Mach number. The experimental conditions should be improved; however, the supersonic flight model has not collided with the free-falling grid, and the launch procedure was successfully done.

D-SEND#2 scale model was launched as a three-dimensional model using the aero-ballistic range. From the results of the high-speed visualization image, the discrepancy of the flight attitude was suppressed, such as the angle of attack less than $\pm 1.5°$ and the yaw angle less than $\pm 4.0°$. This high-precision control of the flight attitude enables to obtain the pressure signature of horizontal direction to well agree with each other, and the measured pressure of horizontal direction agreed very well. The pressure signature of the undertrack was also measured and compared with the numerical simulations. The overall pressure signature obtained by the experiment and the simulations agreed well, but there was discrepancy at the pressure wave originating the main wing. The possible reasons of this discrepancy are the method of the flight attitude evaluation by the visualization and the machining limitation of the model manufacturing. Still some issues of the experimental limitation remain; however, the high-precise control of the flight attitude is valid to evaluate the wake pressure signature.

From these series of experiment, the experimental capability of the aero-ballistic range was extended as follows: the pre-induced flow can be interacted to the model, and the interaction can be controlled by the time-synchronized launch operation; the pressure signature of the three-dimensional model like aircraft can be obtained without the large variation of the flight attitude because the rectangular-bore core and in-tube catapult launch systems enable to launch the model with suppressing the discrepancy of the flight attitude.

Acknowledgments The authors would like to gratefully thank Messrs. N. Shiraki, M. Nakakimura, and K. Yamamoto, Technical Division, Nagoya University, for their assistance. This research was supported by JSPS KAKENHI, Grants-in-Aid for Scientific Research (A), No. 15H02321.

References

1. D.J. Maglieri, P.J. Bobbitt, K.J. Plotkin, K.P. Shepherd, P.G. Coen, and D.M. Richwine, Sonic boom: Six decades of research, NASA SP-2014-622, (2014)
2. N.D. Spivey, C.Y. Herrera, R. Truax, C. Pak, and D. Freund, Quiet spike TM build-up ground vibration testing approach, NASA Technical Report, (2007)
3. M. Honda and K. Yoshida, D-SEND Project for Low Sonic Boom Design Technology, in *28th International Congress of Aeronautical Science*, (2012), pp. 1–8
4. D. Furukawa, Y. Aoki, A. Iwakawa, A. Sasoh, Moderation of near-field pressure over a supersonic flight model using laser-pulse energy deposition. Phys. Fluids **28**(5), Article ID 51701 (2016)
5. A. Sasoh, S. Oshiba, Impactless, in-tube sabot separation technique useful for modest-sized supersonic ballistic ranges. Rev. Sci. Instrum. **77**(10) (2006)
6. A. Toyoda, K. Suzuki, T. Imaizumi, A. Sasoh, Staged aft body for alleviation of tail boom. AIAA J. **52**(12), 2899–2901 (2014)
7. A. Sasoh, T. Imaizumi, A. Toyoda, T. Ooyama, In-tube catapult launch from rectangular-bore aeroballistic range. AIAA J.**53**(3), 2781–2874 (2015)

Experimental Study of Radiation Behind Reflected Air Shock Waves

S. Yamazaki, A. Harasawa, and M. Funatsu

Abstract In our laboratory, the characteristics of radiation behind air shock waves have been studied systematically by using a shock tube. In this study, shock waves with different incident shock Mach number were produced under conditions where pressure in low-pressure chamber was kept at constant value and pressure in high-pressure chamber was increased. The radiation behind those reflected shock waves was visualized temporally and spatially by high-speed video camera. In addition, the radiation originated from the chemical species was analyzed by using narrow band-pass filters. Nitrogen and oxygen which are the main components of air were focused; therefore, narrow band-pass filters corresponding and not corresponding to these components were used in order to investigate the amount of radiation intensity. As a result, radiation intensity obtained using the narrow band-pass filters that correspond to the components is stronger than radiation intensity obtained using other filters. Thus, there is a possibility that the radiation intensity obtained using the narrow band-pass filters which correspond to the atomic lines is derived by the atomic lines itself.

1 Introduction

When spaceplanes, for example, HAYABUSA, return into Earth's atmosphere, a strong shock wave is generated in front of the spaceplanes, and it is heated by aerodynamic heating. Aerodynamic heating consists of convection and radiation heating where the faster the speed of the spaceplanes, the bigger proportion of effect the spaceplanes received from the radiation heating. Therefore, in order to design

S. Yamazaki (✉) · A. Harasawa
Department of Mechanical Science and Technology, Graduate School of Science and Technology, Gunma University, Gunma, Japan
e-mail: t13302112@gunma-u.ac.jp

M. Funatsu
Division of Mechanical Science and Technology, Graduate School of Science and Technology, Gunma University, Gunma, Japan

A. Sasoh et al. (eds.), *31st International Symposium on Shock Waves 2*,
https://doi.org/10.1007/978-3-319-91017-8_124

spaceplanes that are able to resist the heat, it is very important to make clear the characteristics of radiation behind the shock wave [1].

In our laboratory, the characteristics of radiation behind air shock waves have been studied systematically [2–5]. In previous studies, shock Mach number was produced under conditions where pressures in high-pressure chamber and low-pressure chamber were changed, and radiation behind the reflected air shock wave was observed by a high-sensitivity cooled CCD camera [2]. In this study, air shock waves with different incident shock Mach number were produced under conditions where pressure in low-pressure chamber was kept at constant value and pressure in high-pressure chamber was increased. The radiation increased behind reflected shock waves was obtained by a high-speed video camera. In addition, chemical species related to the radiation increased behind the reflected shock waves were obtained by using several kinds of narrow band-pass filters that correspond to nitrogen and oxygen atomic lines.

2 Experimental Setup

Schematic of experimental setup is shown in Fig. 1. In this study, a diaphragm-type shock tube was used, and it consists of a high-pressure chamber (1000 mm in length) and a low-pressure chamber (4000 mm in length) that has an inner diameter of 80 mm. Helium was used as the driving gas, and air (volume ratio $N_2/O_2 = 79:21$) was used as the sample gas. Polyethylene terephthalate (PET) was used as the diaphragm between the high-pressure chamber and the low-pressure chamber. When pressure of high-pressure chamber is increased, the diaphragm will break; thus, shock wave is generated. The pressure of the high-pressure chamber was adjusted by total thickness of overlaying diaphragm. Figure 2 shows a detail of measuring section (A) in Fig. 1. In the measuring section, two pressure sensors were set up as channel 1 (Ch. 1) and channel 2 (Ch. 2). Channel 1 was set at 3560 mm from the diaphragm (440 mm from the tube end); channel 2 was set at 3900 mm from the diaphragm (100 mm from the tube end). From these pressure sensors, a signal was inputted to an oscilloscope via an amplifier, and a pressure waveform was acquired. The radiation generated inside the shock tube was obtained by a high-speed video camera through the observation window.

3 Results and Discussion

3.1 Measurement of Shock Mach Number

In this study, pressure in low-pressure chamber P_1 was kept at constant value of 760 Pa, and pressure in high-pressure chamber was increased. The relationship between

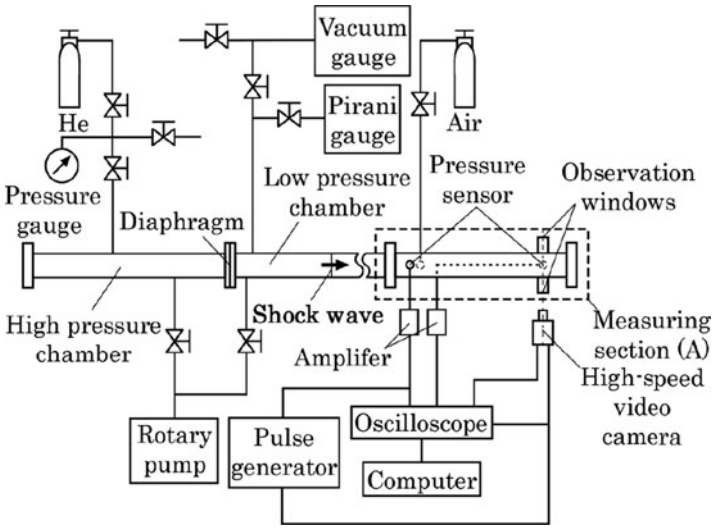

Fig. 1 Schematic view of experimental setup

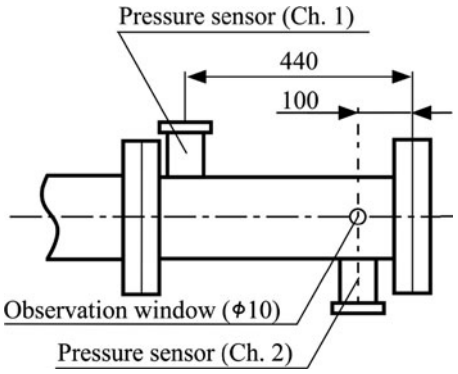

Fig. 2 Detail of measuring section (A)

pressure in high-pressure tube and incident shock Mach number is shown in Fig. 3. In the figure, the horizontal axis shows pressure in high-pressure chamber, and the vertical axis shows the incident shock Mach number. The plotted circles in the figure show the experimental value, and the solid line shows the theoretical value [2]. Pressure values in both high-pressure and low-pressure chambers were expressed in absolute pressure. As shown in Fig. 3, it can be seen that as the pressure in the high-pressure chamber increases, the incident shock Mach number also increases.

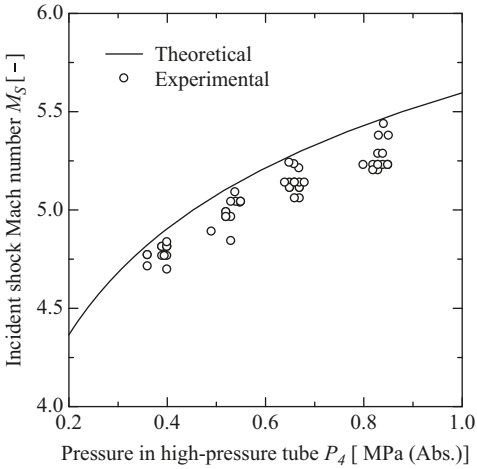

Fig. 3 Relationship between pressure in high-pressure tube and incident shock Mach number

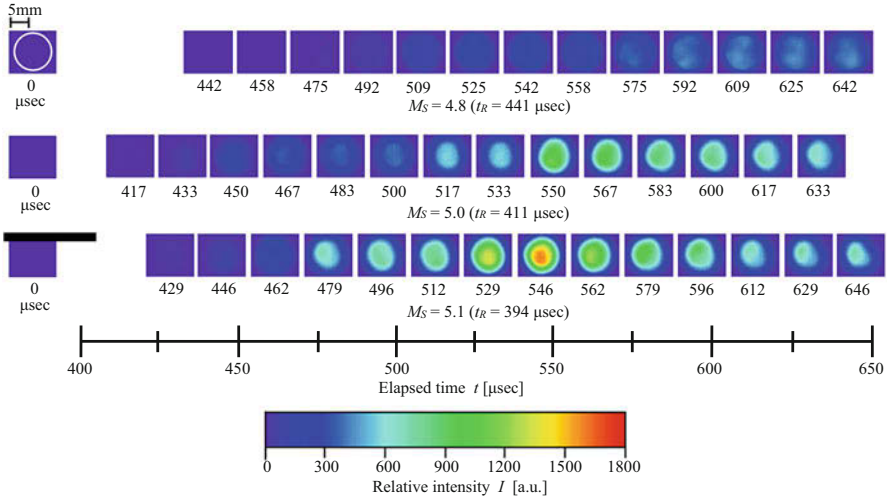

Fig. 4 Time change of relative intensity distribution behind shock waves ($P_1 = 760$ Pa)

3.2 Time Change of Relative Intensities

Time change of relative intensities behind reflected shock waves was obtained by a high-speed video camera. Shutter speed of the high-speed video camera was 60,000 frames/sec, and the exposure time was 16.7 µsec. Pseudo color of experimental result is shown in Fig. 4. Incident shock Mach numbers of 4.8, 5.0, and 5.1 are shown from the top of Fig. 4.

The radiation intensity corresponds to the color bar. The time below the figure shows the elapsed time after the incident shock wave was detected by pressure

Table 1 Characteristics of narrow band-pass filters

Filter name	Central wavelength [nm]	FWHM [nm]	Transmittance [%]	Corresponding systems
MC650	648.75	12.50	89.7	N I (648.27 nm)
MC750	747.00	10.00	68.5	N I (746.83 nm)
MC780	779.25	10.50	80.2	O I (777.19 nm)
MC870	869.25	11.50	67.1	N I (868.03 nm)

sensor of Ch. 1. A white line circle at 0 μsec shows the position of the observation window. t_R is the time when the pressure sensor of Ch. 2 detects the reflected shock wave, which means the time where the reflected shock wave arrives at the position of the observation window. As shown in Fig. 4, it can be seen that the radiation intensity increases behind the reflected shock wave and then decreases along with elapsed time at all incident shock Mach number. Moreover, it can be seen that as the incident shock Mach number increases, the radiation intensity increases in whole radiation intensity, and the maximum radiation intensity of each shock Mach number also increases.

3.3 Radiation Measurements by Using a High-Speed Video and Narrow Band-Pass Filters

The chemical species behind the shock waves were analyzed using the high-speed video camera and narrow band-pass filters. Exposure time of the camera is increased because of the narrow band-pass filters that attenuate the radiation. Therefore, shutter speed of the high-speed video camera was set to 30,000 frames/sec, and the exposure time was set to 33.3 μsec. For an example, MC650 narrow band-pass filter has a central wavelength of 648.75 nm, a full width at half maximum of 12.50 nm, and a transmittance of 89.7% and corresponds to nitrogen atomic lines of 648.27 nm. As shown in Table 1, MC650, MC750, and MC870 correspond to nitrogen atomic lines, and MC780 corresponds to oxygen atomic lines.

It was found that radiation can also be observed by using narrow band-pass filters and high-speed video camera. From visualized images taken by the high-speed video camera and narrow band-pass filters, time change of radiation intensity that occurred at the center of observation window was acquired. Figure 5 shows the time change of the radiation intensity obtained from the center point of observation window at each incident shock Mach numbers 4.8, 5.0, and 5.1. In the figure, the horizontal axis shows the elapsed time after the pressure sensor of Ch. 1 detects the incident shock wave, and the vertical axis shows the relative intensity. Black, red, and green dashed lines in the figure are the results obtained by using narrow band-pass filters corresponding to nitrogen atomic lines of MC650, MC750, and MC870, respectively, and blue solid line is the result obtained by using MC780 narrow band-pass filter corresponding to oxygen atomic lines. “Incident” in the

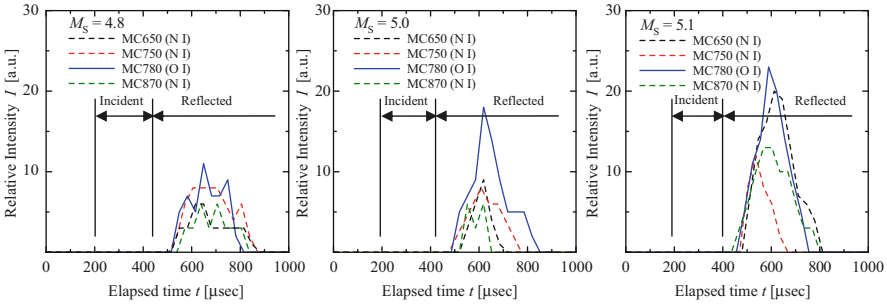

Fig. 5 Profile of relative intensities behind shock waves ($P_1 = 760$ Pa)

Table 2 Characteristics of narrow band-pass filters

Filter name	Central wavelength [nm]	FWHM [nm]	Transmittance [%]	Corresponding systems
MC520	521.00	10.00	83.0	–

figure shows the time taken between incident shock wave and reflected shock wave to arrive at the observation window, while "Reflected" shows the time domain after the shock wave is reflected. At all shock Mach number, radiation intensity is hardly seen at "Incident," but at "Reflected" the radiation intensity rapidly increases and then decreases. As shown in Fig. 5, it can be seen generally that as the incident shock Mach number increases, the radiation intensity obtained at each of the narrow band-pass filters also increases. Also, from the experimental result obtained using MC780 (solid line in the figure) which corresponds to oxygen atomic lines, it can be seen that the maximum radiation intensity becomes stronger as the incident shock Mach number increases. On the other hand, the maximum radiation intensity obtained from MC650, MC750, and MC870 (dashed line in the figure) which correspond to nitrogen atomic lines at incident shock Mach numbers 4.8 and 5.0 did not have a remarkable change, but at incident shock Mach number 5.1, the maximum radiation intensity appeared to be stronger than the other conditions. From these results, it can be concluded that the radiation intensity tends to increase with increase of the incident shock Mach number, but the change of the amount of radiation intensity depends on the chemical species.

In order to investigate whether the radiation obtained using narrow band-pass filters which correspond to nitrogen and oxygen atomic lines was because of the chemical species or not, a narrow band-pass filter that does not correspond to nitrogen and oxygen atomic lines was used, and the radiation that occurred behind the reflected shock wave was studied. MC520 narrow band-pass filters which do not correspond to nitrogen and oxygen atomic lines were used, and the characteristics of this filter are shown in Table 2.

This experiment using a narrow band-pass filter that does not correspond to nitrogen and oxygen atomic lines was concluded at incident shock Mach number 5.2. As a result, radiation was observed when using all the narrow band-pass filters.

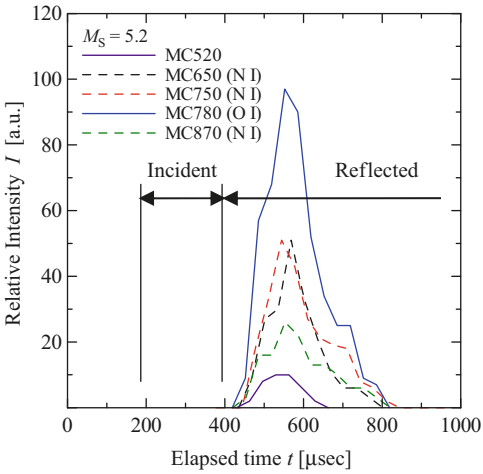

Fig. 6 Profile of relative intensities behind shock waves ($P_1 = 760$ Pa)

Time change of radiation was acquired using the same method to acquire the time change of radiation in Fig. 5. Figure 6 shows the time change of the radiation intensity from the center point of observation window. In the figure, the horizontal axis shows the elapsed time after the pressure sensor of Ch. 1 detects the incident shock wave, and the vertical axis shows the relative intensity. The black dashed lines and blue solid line are the results obtained by using narrow band-pass filters that correspond to nitrogen and oxygen atomic lines, and the purple solid line is the result of MC520 which does not correspond to nitrogen and oxygen atomic lines. The "Incident" and "Reflected" are the same as shown in Fig. 6. As shown in Fig. 6, it can be seen that the radiation intensity of all narrow band-pass filters was increased at "Reflected." Also, the radiation intensity obtained using MC520 is weaker than the radiation intensity obtained using other narrow band-pass filters, which was about half of the radiation intensity obtained using MC870. From the experiment result, it can be concluded that there is a possibility that the radiation intensity obtained when using MC520 does not relate to nitrogen and oxygen atomic lines, and radiation intensity obtained from MC650, MC750, and MC780 which are stronger than radiation intensity obtained from MC520 was derived from the nitrogen and oxygen atomic lines.

4 Conclusions

1. The radiation intensity behind the reflected shock wave rapidly increases and then decreases.
2. As incident shock Mach number increases, the radiation intensity becomes stronger.

3. The radiation intensity tends to increase with the increase of the incident shock Mach number, but the increment of the radiation intensity depends on the chemical species.
4. The radiation intensity obtained using the narrow band-pass filter that does not correspond to nitrogen and oxygen atomic lines is weaker than the radiation intensity obtained using other narrow band-pass filters.
5. Radiation intensity obtained using the narrow band-pass filters that do not correspond to the atomic lines is weaker than radiation intensity obtained using narrow band-pass filters that correspond to atomic lines. Thus, there is a possibility that the radiation intensity obtained using the narrow band-pass filters which correspond to the atomic lines is derived by the atomic lines itself.

References

1. G. Yamada, T. Suzuki, H. Takayanagi, K. Fujita, Development of shock tube for ground testing Reentry aerothermodynamics. Proc. Trans. Japan Soc. Aero. Space Sci. **54**(183) (2011)
2. S. Aoki, T. Okamoto, E. Go, M. Funatsu, Fundamental study of radiation behind reflected air shock waves, in *Proceedings of the 46th fluid dynamics conference*. JSASS-2014-2044.pdf (in Japanese) (2014)
3. S. Aoki, A. Harasawa, M. Funatsu, Experimental study of radiation behind reflected air shock waves with narrow band-pass filters, in *Proceedings of the 47th fluid dynamics conference*. JSASS-2015-2105-F/A.pdf (in Japanese) (2015)
4. A. Harasawa, S. Aoki, Y. Shimpo, M. Funatsu, Experimental study of radiation behind reflected air shock waves-radiation measurements with narrow band-pass filters, in *Proceedings of the 48th fluid dynamics conference*. JSASS-2016-2064.pdf (in Japanese) (2016)
5. S. Yamazaki, A. Harasawa, M. Funatsu, Visualization behind reflected air shock waves with narrow band-pass filters, in *Proceedings of the Hitachi visualization symposium 2016*, Trans. Visualization Soc. Japan. **36**(Suppl. 2), D106.pdf (in Japanese) (2016)

Flow Field for an Accelerating Axisymmetric Body

I. Mahomed, H. Roohani, B. W. Skews, and I. M. A. Gledhill

Abstract This study numerically investigates the compressible flow field near an axisymmetric body that is influenced by constant acceleration at 100 g where the motion is straight and level flight. Selected, instantaneous acceleration and deceleration results are compared to steady-state flow at corresponding projectile Mach numbers. The geometries tested were sharp 10° and 30° half-angle cone-cylinders with constant cylindrical aft section. Significant differences in the behavior of the flow field were found for the transonic Mach number range when compared with steady-state results. This was largely due to relative movement of the shock systems and their influence on the near flow field around the projectile. In particular, acceleration was found to delay the complete development of the bow shock and alter the expansion region at the cone-cylinder interface. Deceleration caused all shock structures to propagate upstream relative to the body and influence the nature of the flow field in a different manner compared to acceleration. The flow history concept was evident in both geometries and is demonstrated using simulation results from acceleration cases.

I. Mahomed (✉)
University of the Witwatersrand, Flow Research Unit, Johannesburg, Gauteng, South Africa
e-mail: imahomed@live.co.za

H. Roohani · B. W. Skews
Flow Research Unit, School of Mechanical, Industrial and Aeronautical Engineering, University of the Witwatersrand, Pretoria, Johannesburg, South Africa

I. M. A. Gledhill
Flow Research Unit, School of Mechanical, Industrial and Aeronautical Engineering, University of the Witwatersrand, Johannesburg, South Africa

Aeronautic Systems Competence Area, DPSS, CSIR, Pretoria, South Africa

A. Sasoh et al. (eds.), *31st International Symposium on Shock Waves 2*,
https://doi.org/10.1007/978-3-319-91017-8_125

1 Introduction

The compressible flow field is well documented for objects in steady-state motion such as aerofoils, wings, and missile-shaped geometries, including their resulting aerodynamic forces and moments. More recent work is focused on unsteady (accelerated) motion of finite volume objects as opposed to a point source [1]. The motion is characterized by large-scale, center of mass displacement generating significant, accelerated motion that is imposed upon a dynamic, compressible flow field.

The objective of the present work is the behavior and response of shock wave dynamics and their influence on the flow field around a sharp-nosed slender body during acceleration and deceleration, in the transonic Mach number range. This paper is qualitative and will focus on the overall flow field behavior for acceleration and deceleration cases.

2 Geometry and Test Cases

The typical geometry is illustrated in Fig. 1 with constant aft cross-sectional area and 0° incidence. The selected cone half-angles were 10° and 30°. The first case was *acceleration* from steady-state Mach 0.5 to Mach 1.5, and the second case was *deceleration* from steady-state Mach 1.5 to Mach 0.5. The acceleration magnitude is 100 g. Comparison to steady-state cases corresponding to select, instantaneous Mach numbers is reported in this paper.

By Taylor-Maccoll theory for supersonic cones, the 10° half-angle cone generates an attached conical shock while $M_\infty \geq 1.05$, whereas there is an attached bow shock for the 30° half-angle cone while $M_\infty \geq 1.49$. Typically, the projectile

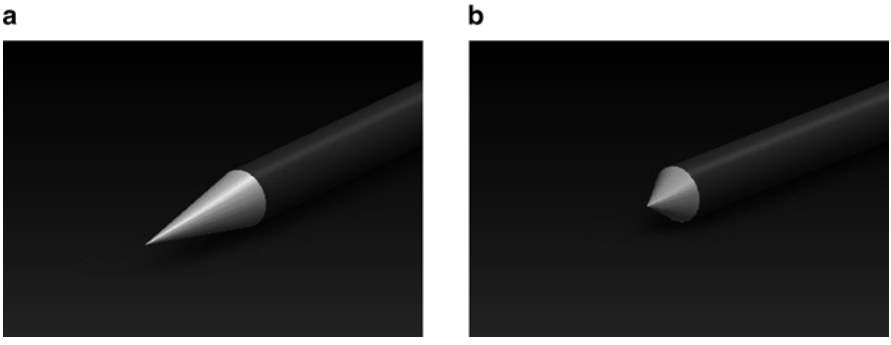

Fig. 1 Illustration of cone-cylinder geometry used in Fluent simulations, slenderness ratio (L/D) = 8. (**a**) 10° half-angle cone-cylinder and (**b**) 30° half-angle cone-cylinder, both models with constant cross-sectional area for the cylinder

characteristic length is the diameter (D = 50 mm), whose dimension was selected to ensure turbulent free-stream Reynolds number in the transonic Mach number range. Free-stream Reynolds number based on model diameter varied from a minimum of 0.55E6 ($M_\infty = 0.5$) to a maximum of 1.7E6 ($M_\infty = 1.5$).

3 Methodology

3.1 Numerical Method

All simulations were performed using (ANSYS) Fluent with a two-dimensional (2D) unstructured, axisymmetric solver and kω-SST turbulence model ($y+ \approx 1$).

The acceleration technique used for this study keeps the object stationary and simultaneously accelerates each fluid element in the flow domain and at the fluid boundary. This technique is documented and validated in [2] for two-dimensional accelerating aerofoils.

3.2 Solver and Mesh Validation

After mesh independence studies, additional confidence for using the selected mesh and solver setup was needed. Different approaches were used to address this requirement.

A slender body, at zero incidence, must generate finite axial drag and zero lift force; this was noted for all axisymmetric simulation results. In steady, supersonic flow, an attached bow shock is formed for the 10° half-angle cone, where the ratio of P_1/P_c (free-stream pressure over cone surface pressure) was found to agree with Taylor-Maccoll theory within 1% absolute error. A second indicator was the free-stream Mach number that agreed to the specified boundary condition within ≈1% absolute error. These checks were performed at various Mach numbers.

To further validate the Fluent solver setup and to establish confidence in the turbulence model, steady-state experimental data [3] was compared with results from Fluent where excellent agreement was found using the kω-SST turbulence model.

4 Discussion and Results

4.1 Cone-Cylinder 10° (Half-Angle)

Acceleration data identified no significant variation for subsonic and supersonic flow, compared to corresponding steady-state Mach numbers. Significant flow field differences were observed during the transonic Mach number range, of which some notable differences are described below.

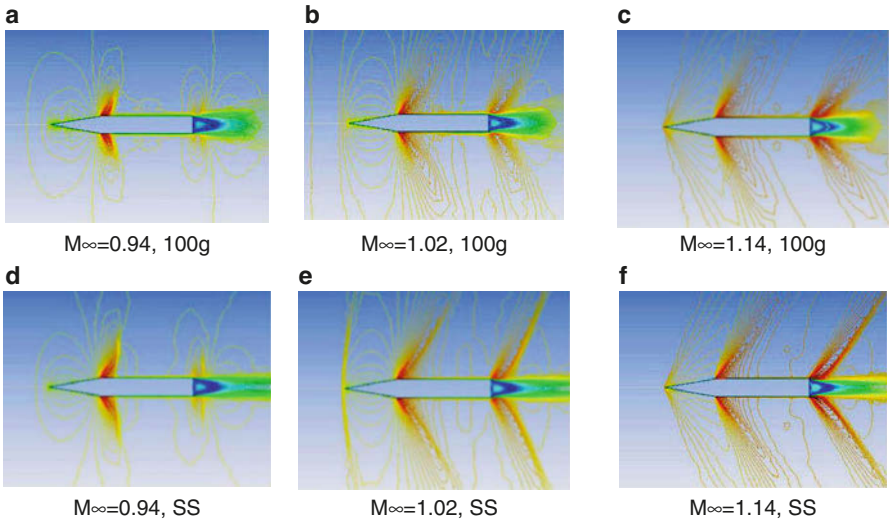

Fig. 2 Comparison of instantaneous transonic Mach contours for acceleration at 100 g with corresponding steady-state (SS) results. Acceleration results (**a**–**c**) and steady state (**d**–**f**)

4.1.1 Shockwave Dynamics

For $M_\infty > 1$, there is a progressive reduction in cone shock angle during acceleration. From Fig. 2, the bow shock angle for steady-state is slightly reduced when compared with acceleration. The bow shock is developed at steady-state $M_\infty = 1.02$ and is not present during acceleration at this same Mach number. Further, the overall flow field is more developed for steady-state than in the corresponding acceleration cases. These observations highlight the flow history concept. The accelerated flow is not permitted with sufficient time to stabilize and aspects of the flow such as the bow shock are representative to steady state at an earlier point in time. The instantaneous, accelerated flow field is influenced by its history as relative motion occurs between flow structures and the solid body. This was more discernable during deceleration and for the 30° cone-cylinder.

During deceleration, there is a progressive increase in cone shock angle until a subsonic Mach number is reached whereby the bow shock detaches and propagates ahead of the cone apex, shown in Fig. 3. The trailing shock waves appear to follow a similar pattern except they dissipate once $M_\infty < 1$. This is different to the 2D biconvex aerofoil case [2] where the trailing shock waves propagated over the aerofoil at 106 g and deceleration from $M_\infty = 1.5$. The axisymmetric case is effectively a simplified representation of a three-dimensional (3D), symmetric flow field about one axis. For steady-state 3D flow, the additional dimension introduces a pressure-relieving effect. More investigation is needed on this aspect for acceleration and deceleration flows.

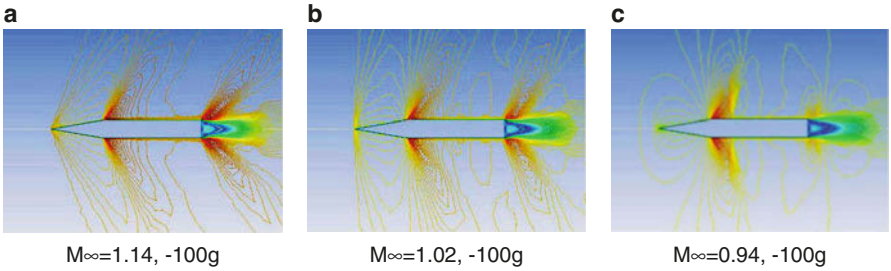

Fig. 3 Instantaneous transonic Mach contours for deceleration at 100 g

4.1.2 Flow in the Vicinity of the Cone-Cylinder Interface

For $M_\infty > 1$, there is a centered expansion fan followed by isentropic compression until constant flow properties are achieved along the cylinder length. For $M_\infty < 1$, further boundary layer thickening coupled with supersonic flow through the centered expansion fan generates compression waves, and these coalesce into a normal, disk-shaped shock. This normal shock extends outward into the flow field, and the foot of the normal shock terminates at the boundary layer on the cylinder. This general behavior appears similar and was observed for acceleration and deceleration cases (Figs. 2 and 3).

4.2 Cone-Cylinder 30° (Half-Angle)

This geometry produced results that are different compared to the previously discussed 10° cone-cylinder. The key difference is the presence of a detached bow shock and the greater flow turning angle at the cone-cylinder interface based on the selected cone angle and Mach number range.

4.2.1 Shockwave Dynamics

Referring to Fig. 4, while the projectile accelerates for $M_\infty < 1$, a smooth, separated shear layer develops from the cone-cylinder interface, with a terminating shock above the shear layer extending a finite distance into the free-stream. In contrast to the corresponding steady-state Mach number, there is no shear layer, and a terminating shock is present immediately after the expansion region. It appears insufficient time is available during acceleration to suppress the shear layer. Acceleration for $M_\infty > 1$ resulted in a bow shock, no separated shear layer, and a terminating shock that emanates from the tail end of the expansion fan. During supersonic acceleration, the bow shock strengthens and moves closer to the projectile nose. All shock angles orient toward the projectile body.

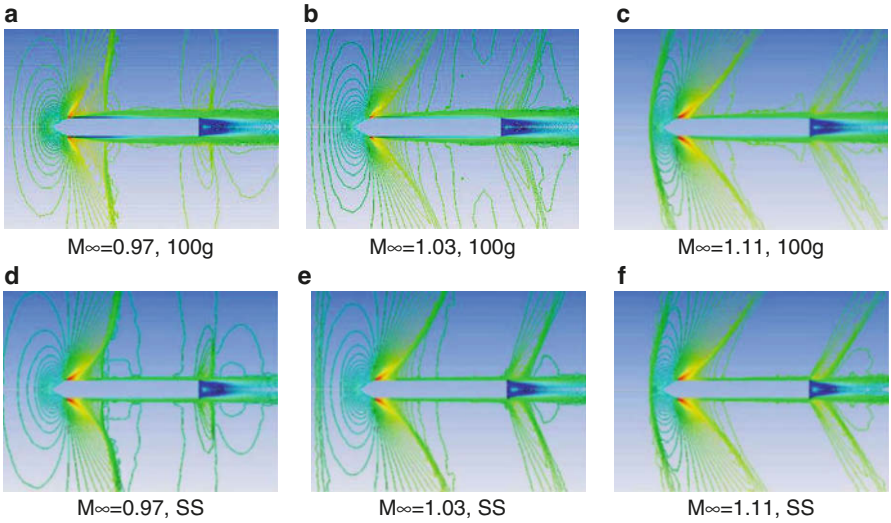

Fig. 4 Comparison of instantaneous transonic Mach contours for acceleration at 100 g with corresponding steady-state (SS). Acceleration results (**a**–**c**) and steady-state (**d**–**f**)

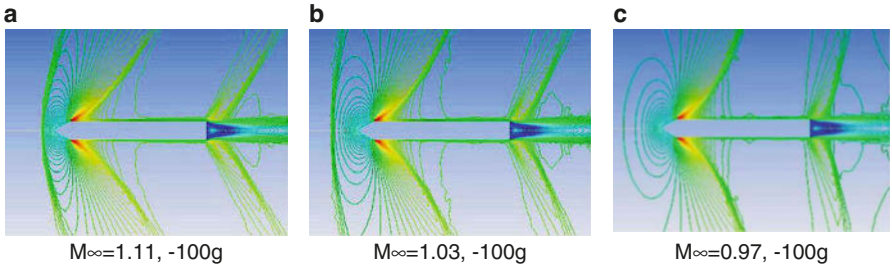

Fig. 5 Instantaneous transonic Mach contours for deceleration at 100 g

Referring to Fig. 5, during deceleration, all shock angles orient away from the projectile body. The bow shock propagates ahead of the projectile nose and weakens by a reduction in shock curvature; the bow shock has propagated out of the image in Fig. 5c. The oblique trailing shock waves at the base adjusted their angle in response to the deceleration and dissipate once $M_\infty < 1$. There is an embedded terminating shock near the outer tail end of the centered expansion fan which extends significantly outward into the free-stream. The outer region of this shock wave was observed to propagate forward but does not overtake the projectile nose, while the lower region remains with the expansion fan. This shock progressively weakened as M_∞ approaches 1.

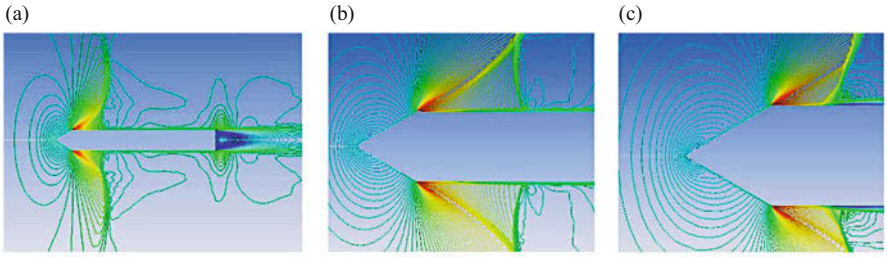

Fig. 6 Overall flow field for deceleration at 100 g (**a**), a zoomed-in section of the flow aft of the expansion fan (**b**), and the corresponding steady-state case (**c**). All images are Mach contours at $M_\infty = 0.91$

4.2.2 Flow in the Vicinity of the Cone-Cylinder Interface

Slight boundary layer thickening contributes to compression immediately after the centered expansion fan. The compression waves do not coalesce until the projectile has decelerated below $M_\infty < 1$ where the compression waves coalesce into a shock, as appears in Fig. 6a. Referring to Fig. 6b and c, this shock has a curved profile near the cylindrical surface. From the corresponding steady-state case, a lambda shock structure develops in the presence of a separation bubble. It is not immediately certain, for the instantaneous deceleration case, whether this curved shock profile near the cylindrical surface represents the aft section of the lambda shock.

5 Conclusion

The flow field around an accelerating projectile is different compared to steady state at corresponding instantaneous Mach numbers and, similarly, for deceleration.

There exists relative movement of all shock systems around the projectile body during acceleration and deceleration. From this, we infer aerodynamic loads will differ compared to steady-state flow and will be investigated further.

Results for the 30° half-angle cone-cylinder was different compared to the 10° case, where diameter and body length were kept identical. At this stage, differences for the 30° case are attributed to the presence of significant flow separation at the cone-cylinder interface and formation of a detached bow shock over the selected Mach number range. These flow mechanisms were found to be greatly influenced by the presence of acceleration and deceleration. The flow history concept was evident for both geometries and was demonstrated using simulation results from acceleration cases.

6 Future Work

Based on the flow history concept, tests at lower acceleration magnitudes will cause the flow field to evolve at a different rate and will provide further insight for the flow features highlighted in this paper.

References

1. G.M. Lilley, R. Westley, A.H. Yates, J.R. Busing, Some aspects of noise from supersonic aircraft. J. R. Aeronaut. Soc. Coll. Aeronaut. Rep. **71**, 396–414 (1953)
2. H. Roohani, B.W. Skews, The influence of acceleration and deceleration on shock wave movement on and around aerofoils in transonic flight. Shock Waves **19**, 297–305 (2009)
3. M.A. Ramaswamy, G. Rajendra, Experimental investigation of transonic flow past a blunt cone-cylinder. J. Spacecr. Rocket. **15**(2), 120–123 (1978)

Modeling of 3-DOF Launch Dynamics in Transonic and Supersonic Regime Using Navier-Stokes Equation

Anupam Purwar and Gopalan Jagadeesh

Abstract The modeling of rigid body dynamics including the trajectory estimation of a launch vehicle is essential to investigate the effects of various flow interactions with vehicle for possible instabilities encountered in the transonic and supersonic regime. This work presents a systematic formulation for simulation of the vehicle trajectory under aerodynamic forces, which are calculated by solving the Navier-Stokes equations using the open-source software package SU2. A closed-loop computational framework consisting of computational fluid dynamics (CFD) and kinematic equation solver has been developed. This framework (**Fdynam**) has been used to estimate typical properties of launch trajectory, viz., Mach number vs. time and dynamic pressure vs. altitude, under the effect of thrust, gravity, and aerodynamic loads. A maximum dynamic pressure of 70 kPa and terminal launch phase Mach number of 4.7 have been estimated for National Launch System (NLS1.5) configuration during powered ascent to an altitude of 30 km.

1 Introduction

The modeling of rigid body dynamics including the trajectory estimation of a launch vehicle is important to identify the effect of flow interactions with vehicle for possible instabilities encountered in different high-speed flow regimes. Efforts to model flow around the launch vehicles undergoing forced coupled oscillation have been carried out earlier to simulate transient motions in both the longitudinal and lateral directions [1]. Guruswamy et al. reported large-scale computations for stability analysis of launch vehicles using cluster computers to generate aerodynamic database for static stability analysis of launch vehicles [2]. Computational structural dynamics (CSD) to perform dynamic transient structural sub-domain analysis using single-image supercomputers has also been reported [3]. Conventionally, aerodynamic force coefficients are used to calculate the aerodynamic forces during

A. Purwar (✉) · G. Jagadeesh
Centre of Excellence in Hypersonics, Indian Institute of Science, Bangalore, India

A. Sasoh et al. (eds.), *31st International Symposium on Shock Waves 2*,
https://doi.org/10.1007/978-3-319-91017-8_126

the launch phase, which essentially ignore the effect of shocks and fluid-structure interaction [4–6]. Recent work by Wang et al. [7] modeled incompressible flow by solving Euler equations. However, in launch phase, transonic and supersonic flow regime is encountered, which makes it imperative to model the compressible flow phenomenon to accurately compute shock-induced loads. In this perspective, the current work adopts a coupled methodology where fluid flow around the vehicle body has been modeled using computational fluid dynamics (CFD) along with the kinematic analysis to estimate the flight trajectory. The CFD and kinematic analysis modules have been integrated together to develop a framework which seamlessly estimates the vehicle trajectory at each time step. Another important highlight of this work is the use of open-source CFD package SU2 [8], which provides great flexibility in modifying the developed framework for a variety of problems including incompressible and compressible fluid flow. The work has been divided into four sections. Section 1 (Introduction) provides a brief overview of prior work. Section 2 describes the methodology and its implementation. Section 3 elaborates on the results of CFD and kinematic analysis for NLS 1.5 configuration, and Sect. 4 summarizes the salient findings of this work and plan for future work.

2 Computational Methodology

The computation consists of estimating aerodynamic forces by performing CFD analysis using SU2 CFD package [8] based on freestream flow conditions for NLS 1.5 configuration (see Fig. 1). The estimated aerodynamic forces, viz., lift and drag, are then used to perform 3 degrees of freedom kinematic analysis, using Eqs. 1, 2, and 3. The kinematic analysis is carried out using a FORTRAN90 code, which calculates lifting, dragging, and pitching moment using Cl, Cd, and X_{cp} values estimated by SU2 code. The seamless interfacing between SU2 and FORTRAN90 code is done by a shell script (.sh file), which updates the flow conditions in SU2 configuration file (.cfg file) based on launch vehicle velocity and altitude estimated by FORTRAN90 code. In particular, the estimated velocity and altitude of launch vehicle are used to estimate freestream pressure, temperature, and Mach number for subsequent CFD analysis. These calculations are done iteratively, as shown in Fig. 2, till the final altitude of 30 km is achieved. The following considerations have been made in performing the kinematic analysis:

1. Constant thrust (T) of 1500kN with maximum thrust vector angle of 5 degrees with vehicle axis has been modeled.
2. Altitude dependence of acceleration due to gravity (g) has been modeled; latitude- and rotation-based effects on “g” have been neglected.
3. Variation of moment of inertia and center of mass of launch vehicle has been modeled by considering a constant propellant burn rate of 5.5 mm/s.
4. Earth atmospheric model [9] has been used to calculate freestream pressure and temperature as a function of launch vehicle altitude.

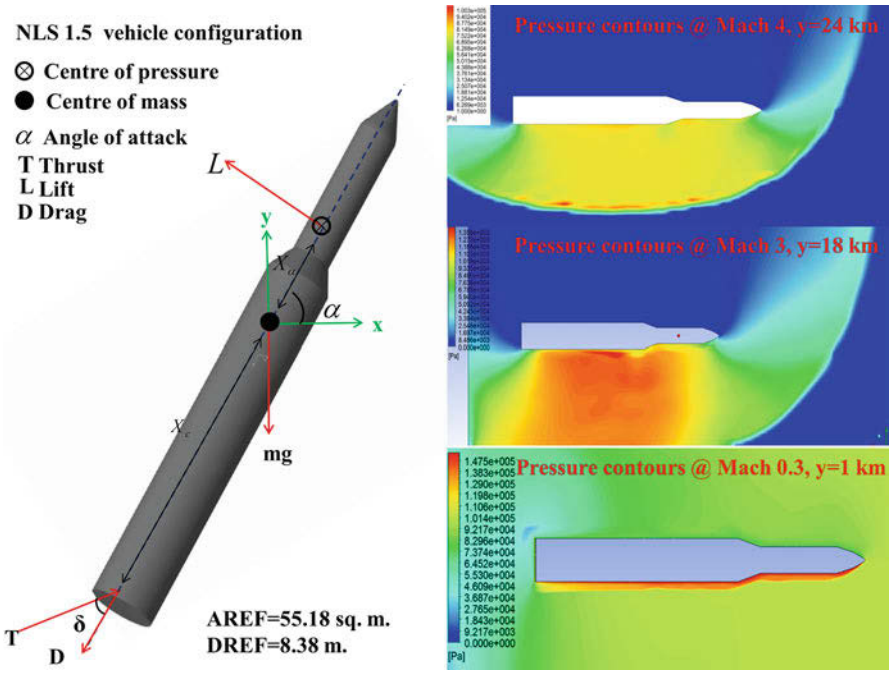

Fig. 1 NLS 1.5 model [13] free body diagram, indicating thrust, drag (D), lift (*L*), and gravitational force (mg) at an angle of attack (α) acting during the flight [14] and representative pressure contours estimated from SU2 at different altitude and flow conditions

5. NLS1.5 configuration and payload mass have been taken to be 800 tons [10] and 22.65 tons [11], respectively.
6. Variation in moment of launch vehicle moment of inertia and center of mass has been modeled by considering the mass loss due to booster burnout for realistic estimation.

2.1 CFD Analysis

The flow field around the NLS 1.5 configuration has been modeled by solving Reynolds-averaged Navier-Stokes (RANS) governing equations with Spalart-Allmaras (SA) turbulence model using SU2. A two-dimensional cross section of NLS1.5 configuration has been considered for the sake of simplicity with pressure far field as inlet and pressure outlet as boundary conditions along with isothermal wall at 300 K temperature. Sutherland viscosity model has been used to estimate the freestream viscosity. Unstructured mesh with highly refined mesh near the wall, to accurately model boundary layer, has been generated using open-source

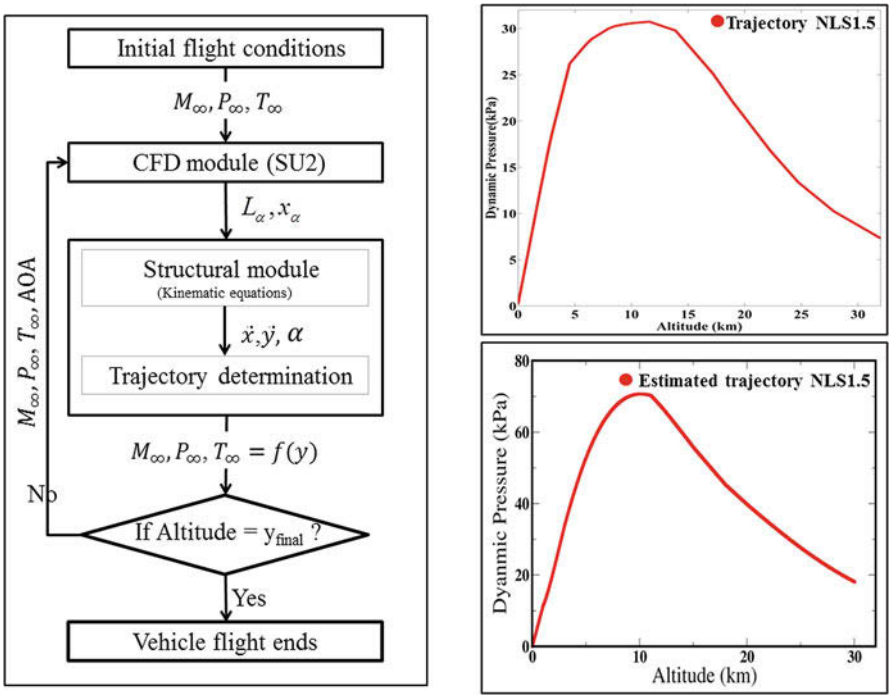

Fig. 2 **Fdynam** computational framework (left), comparison of actual and estimated trajectory of NLS1.5 configuration (right)

meshing package GMSH [12] and exported in .SU2 format to SU2 solver. GMSH can be run noninteractively in batch mode through shell script. Flow conditions including pressure, temperature, velocity component, and angle of attack are defined in the input configuration file of SU2 solver. Files containing the results, viz., Cl, Cd, and X_α, are written upon reaching convergence before exiting SU2, and the flow solutions have been exported in ParaView (.vtk) and Tecplot (.dat for ASCII) format for visualization and post processing. The physical time step for progressing kinematic analysis has been estimated from CFD time step based on characteristic length of NLS1.5 and local sound speed.

$$I\ddot{\alpha} = LX_\alpha + T\sin(\delta)\cdot X_c \tag{1}$$

$$m\frac{d^2x}{dt^2} = T\cos(\alpha-\delta) - L\sin(\alpha) - D\cos(\alpha) \tag{2}$$

$$m\frac{d^2y}{dt^2} = T\sin(\alpha-\delta) + L\cos(\alpha) - mg - D\sin(\alpha) \tag{3}$$

3 Results and Discussion

The launch phase trajectory for vehicle has been estimated using **Fdynam** framework, as shown in Fig. 2. Qualitative match is obtained between reported [13] and estimated dynamic pressure (q) values for NLS1.5; it increases up to 12 km altitude and then reduces with further increase in altitude. The difference in maximum q can be explained by the approximations made in thrust profile and gross weight of NLS1.5, used in trajectory estimation. The variation of launch vehicle Mach number and altitude with time is shown in Fig. 3a and Fig. 3b, respectively. The vehicle touches speed of Mach 4.7 near the end of launch phase at an altitude of 30 km. In particular, the vehicle speed increases more steeply after 45 s due to decrease in drag as affected by a decrease in q beyond 45 s.

Similarly, the Mach number increases almost linearly with altitude (Fig. 3c). But the dynamic pressure varies nonlinearly with altitude and time; it increases up to 12 km altitude and then reduces with further increase in altitude (Fig. 3d and Fig. 3e). This can be explained by the decrease in air density with altitude. Lift which is a function of dynamic pressure also shows similar nonlinear behavior, and maximum lift of 260kN is recorded at 12 km altitude (Fig. 3f).

4 Conclusions

The present work outlines the methodology for carrying out dynamic analysis of a launch vehicle. A framework for carrying out coupled CFD and kinematic analysis (**Fdynam**) has been developed for the same, and typical properties of launch vehicle, viz., Mach number vs. altitude and dynamic pressure vs. altitude, have been estimated. The main novelty of developed framework is the integration of open-source CFD code SU2 with FORTRAN90-based kinematic analysis code using a shell script to estimate launch vehicle flight trajectory. This provides greater flexibility in modifying **Fdynam** for a variety of problems involving compressible and incompressible flow. This framework would also aid the designers in analyzing the launch vehicle dynamics and the effect of variation of thrust and vehicle body geometry in transonic as well as supersonic flow regime. **Fdynam** can serve as a design tool for aerodynamicists and controls engineers alike in aerospace vehicle design and control algorithm formulation and testing. In the future, this framework will be extended to perform estimation of time accurate structural displacements using the Newmark's time integration scheme and solve fluid-structure interaction problems for investigating aeroelastic phenomenon, namely, flutter and divergence.

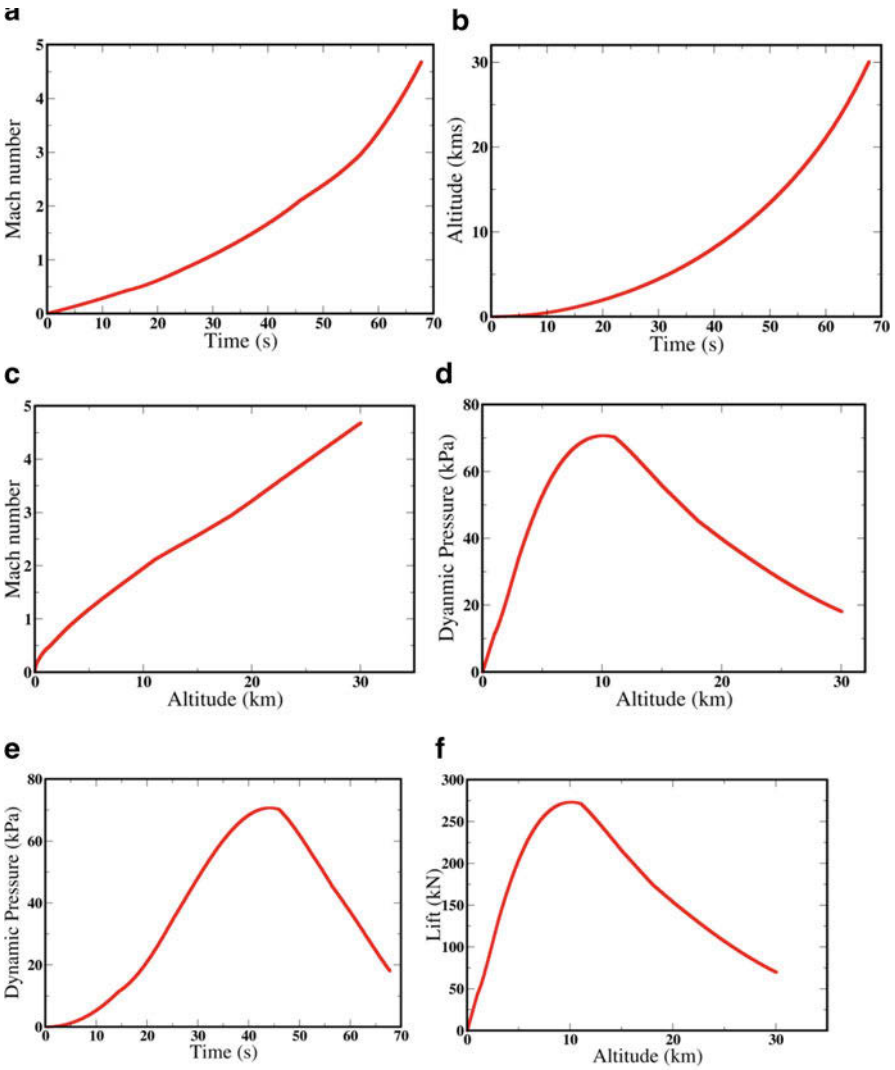

Fig. 3 Variation of trajectory properties of NLS1.5 launch vehicle with altitude and time, estimated using **Fdynam** computational framework

Acknowledgments The authors express thanks to the Centre of Excellence in Hypersonics for providing infrastructural support toward this work.

References

1. G.P. Guruswamy, Navier-stokes based unsteady aerodynamic computations of launch vehicles undergoing forced coupled oscillations. J. Spacecr. Rocket. **52**, 299–302 (2015)
2. G.P. Guruswamy, Large-scale computations for stability analysis of launch vehicles using cluster computers. J. Spacecr. Rocket. **48**(4), 584–588 (2011)
3. A. Striz, C. Byun, G.P. Guruswamy, High Fidelity Dynamic Analysis of Launch Vehicles on Single Image Supercomputers, in *AIAA-2005-1940, AIAA Structural Dynamics Conference*, Austin Texas, April 2005
4. V.C. Guilherme da Silveira, A six degrees-of-freedom flight dynamics simulation tool of launch vehicles. J. Aerosp. Technol. Manag., São José dos Campos. **7**(2), 231–239 (2015)
5. W. Du et al., *Dynamic modeling and ascent flight control of Ares-I Crew Launch Vehicle*, Graduate Theses and Dissertations, 11540, 2010
6. D. Jeyakumar, K.K. Biswas, B. Nageswara Rao, Stage separation dynamic analysis of upper stage of a multistage launch vehicle using retro rockets. Math. Comput. Model. **41**, 849–866 (2005)
7. J. Wang, Coupled CFD and rigid body dynamics analysis for the launch vehicle stage separation, in *33rd Joint Propulsion Conference and Exhibit*, American Institute of Aeronautics and Astronautics, 1997
8. SU2-Open Source CFD (2017). Available: http://su2.stanford.edu/index.html
9. Earth Atmospheric Model NASA (2017). Available: https://www.grc.nasa.gov/www/k-12/airplane/atmosmet.html
10. NLS Heavy Lift Version (2016). Available: http://www.astronautix.com/n/nlshlv.html
11. M.T. Lyons, National Launch System and its potential application to the launch of Geosynchronous Satellites, (PDF), AIAA, 18–22 (1992)
12. C. Geuzaine, J.-F. Remacle, Gmsh: A three-dimensional finite element mesh generator with built-in pre- and post-processing facilities. Int. J. Numer. Methods Eng. **79**(11), 1309–1331 (2009)
13. A.M. Springer, D.C. Pokora, Aerodynamic Characteristics of the National Launch System (NLS) 1.5 Stage Launch Vehicle, NASA Technical Paper, 3488, 1994
14. M.J.L. Turner, *Launch Vehicle Dynamics*, *Rocket and Spacecraft Propulsion: Principles, Practice and New Developments.* (Springer Berlin Heidelberg, 2005), pp. 115–144

Skin Friction Measurement Based on SSLCCs in Hypersonic Wind Tunnel

Xing Chen, Bi Zhixian, Wen Shuai, Dapeng Yao, and Junjie Pan

Abstract This paper describes a creative application of global skin friction measurement based on shear-sensitive liquid crystal coatings (SSLCCs) for delta wing in hypersonic wind tunnel. The system of optical skin friction measurement is built, and some wind tunnel experiments are performed in China Academy of Aerospace Aerodynamics (CAAA). Global skin friction distribution of the model which shows complicated flow structures is discussed, and a brief mechanism analysis and an evaluation on optical measurement technique have been made. The experiments prove this method practicable, and it valuably solves the hard problem of skin friction measurement in hypersonic flow condition.

1 Introduction

In hypersonic fluid dynamics, skin friction has a great influence on the aerodynamic performance and heating, and as a fundamental research of fluid dynamics, great attention has been paid on friction measurement. But the prediction of friction is rather difficult by both wind tunnel experiments and numerical simulations. These difficulties are due to the small absolute value of the friction and the complexity of the flow.

There are varieties of techniques for friction measurements, such as friction gauge, optical methods, Preston tube, and MEMS technology [1–3]. As an optical noncontact measurement technique, the shear-sensitive liquid crystal coatings (SSLCCs) method can quantitatively measure both the magnitude and direction of shear stress. In the past 20 years, NASA Ames Research Center, Niigata University of Japan, and other institutions have made a thorough study on this technique [4–7]. But those studies are focused on subsonic and supersonic conditions. Here, we aim to explore an experimental method for skin friction measurement in hypersonic wind tunnel.

X. Chen · B. Zhixian · W. Shuai (✉) · D. Yao · J. Pan
China Academy of Aerospace Aerodynamics, Beijing, China

A. Sasoh et al. (eds.), *31st International Symposium on Shock Waves 2*,
https://doi.org/10.1007/978-3-319-91017-8_127

2 Theory and System

Because of some particular optical properties of the SSLCCs, the shear stress vector distribution can be quantitatively measured by the SSLCCs. The liquid-crystal materials are sprayed to the model surface and then a coating is formed. When a certain shear stress is applied on the coating, a color-change response can only be observed. A friction gauge is used for calibration, and the relationship between color-change response and stress, Hue-τ curve, could be obtained. For quantitative measurement, images of the coating are recorded from multiple in-plane view angles encompassing all shear vector directions. After image processing, hues at each point of the coating gained from different angles are obtained. The color-change response to a constant shear stress vector is a Gaussian function of the relative in-plane view angle between the observer and the vector orientation. The optical measurement system includes illumination, image acquisition, and control subsystems (Fig. 1).

3 Experiment Setup

Experiments are performed in FD-07 wind tunnel at CAAA (China Academy of Aerospace Aerodynamics). The equipment, FD-07, is a conventional free stream blow down hypersonic wind tunnel, equipped with a contoured nozzle, whose exit diameter is 500 mm. The detail test condition is shown in Table 1.

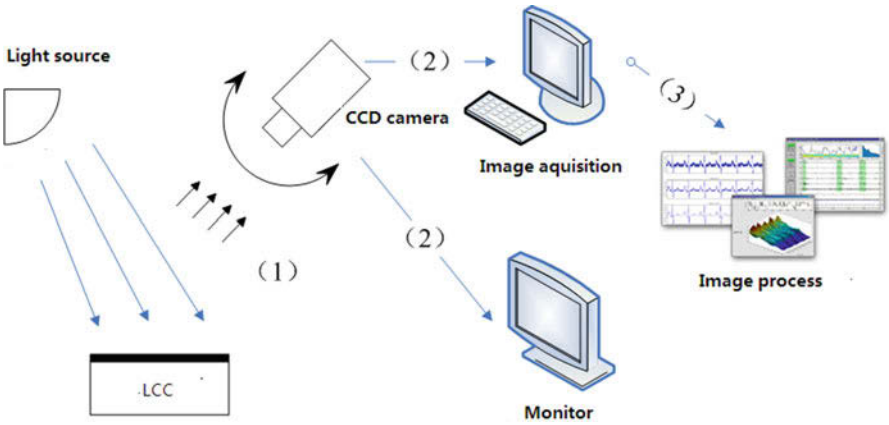

Fig. 1 Optical skin friction measurement system

Table 1 Nominal tunnel flow conditions

M_∞	Re_∞(1/m)	P_0(MPa)	T_0(K)
5	1.1 × 107	0.5	353

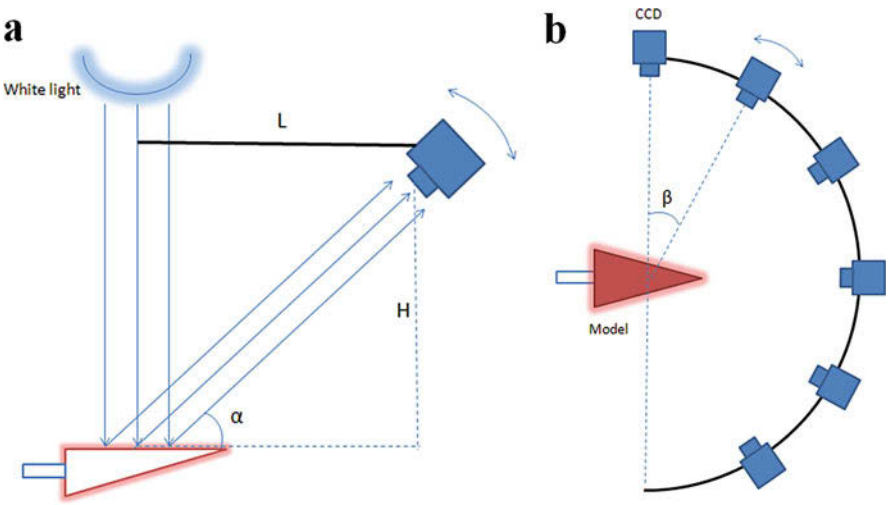

Fig. 2 Schematic illustration of optical system. (**a**) Side view. (**b**) Vertical view

Fig. 3 Optical system

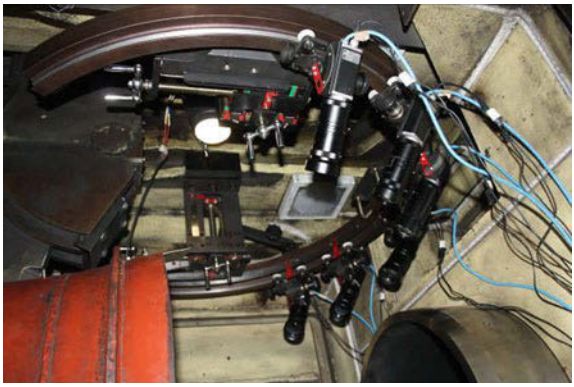

Color change on the model surface is recorded by the image acquisition system in the tests. Six color CCD cameras (frame rate, 30 fps; resolution, 1600x1200 pixels) are set on a circular sliding guide with different view angle (Figs. 2 and 3).

The length of the flat-plate delta wing model is 350 mm. Its head triangle angle is 30°and the head diameter is φ3.5 mm. The model with LCCs shows dark red color at wind-off condition (Fig. 4).

Original color-change pictures are captured by CCD cameras at different viewing angle. A series of image processing methods are utilized to obtain more precise results, distortion correction for eliminating lens distortion, image registration for matching image at different viewing angle, and color correction for cameras' color uniformity. After that the Hue-τ conversion and vector fitting are calculated to achieve skin friction distribution according to calibration curve (Fig. 5).

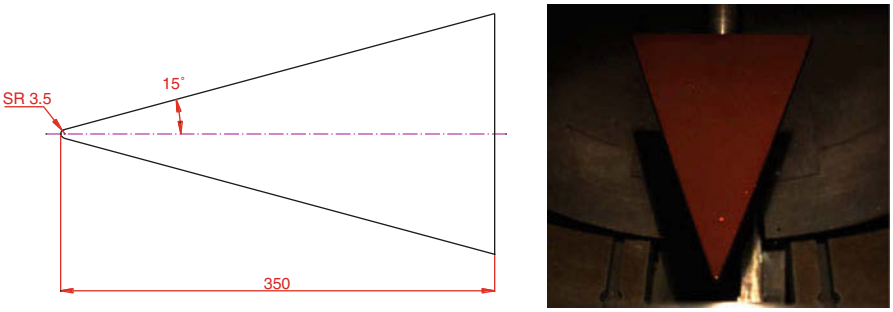

Fig. 4 Flat-plate delta wing model

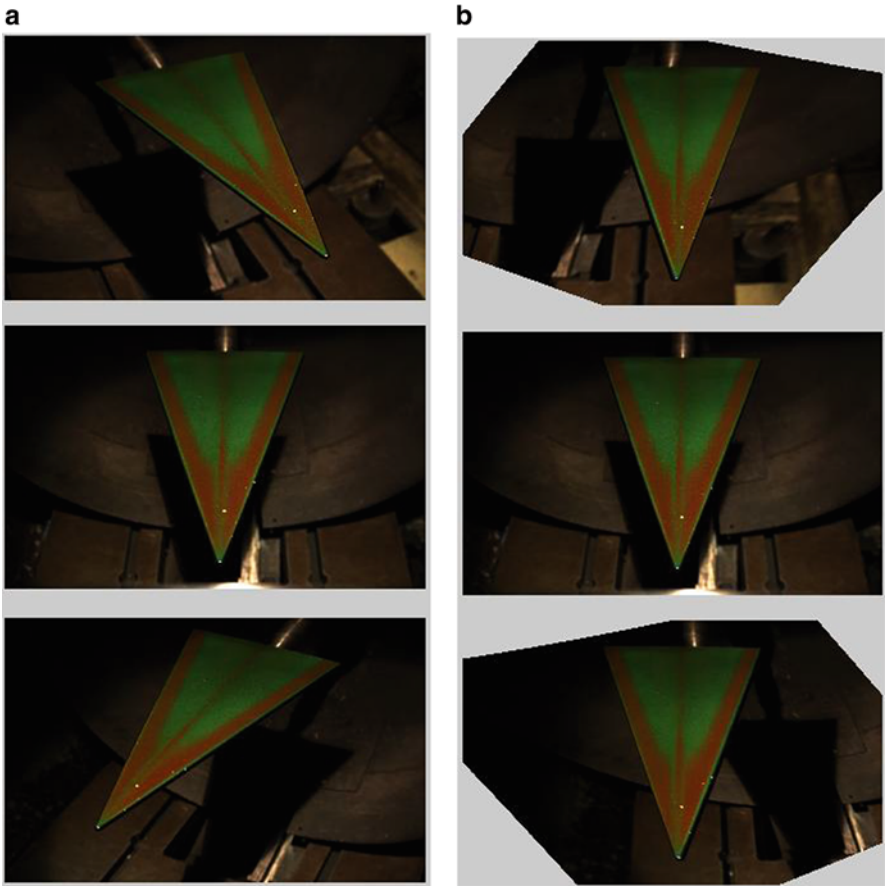

Fig. 5 Schematic illustration of image registration. (**a**) Source image at different viewing angle. (**b**) Image after registration

4 Results and Discussion

Stress distribution can be preliminarily inferred from the color variation shown in Fig. 6a. In the front of the model it almost shows a dark red, and then changes to green downstream, indicating that shear stress is tiny in the front region, grows downstream, and implies that the boundary layer transition has occurred. Both the magnitude and direction distribution of the shear stress are quantitatively shown in Fig. 6b. The location of boundary layer transition is exhibited with clarity. The shear stress in the front of wing centerline increases because of bluntness effect and then becomes lower downstream until transition onset. Meanwhile, the boundary layer transition on the wing sides is probably promoted by the leading edge disturbance. The shear stress increases obviously at $\alpha = 10$ than $\alpha = 0$ (Fig. 7). As a result, the transition onset location of the wing sides is ahead of the wing centerline. This is a typical "W" shape delta wing transition phenomenon.

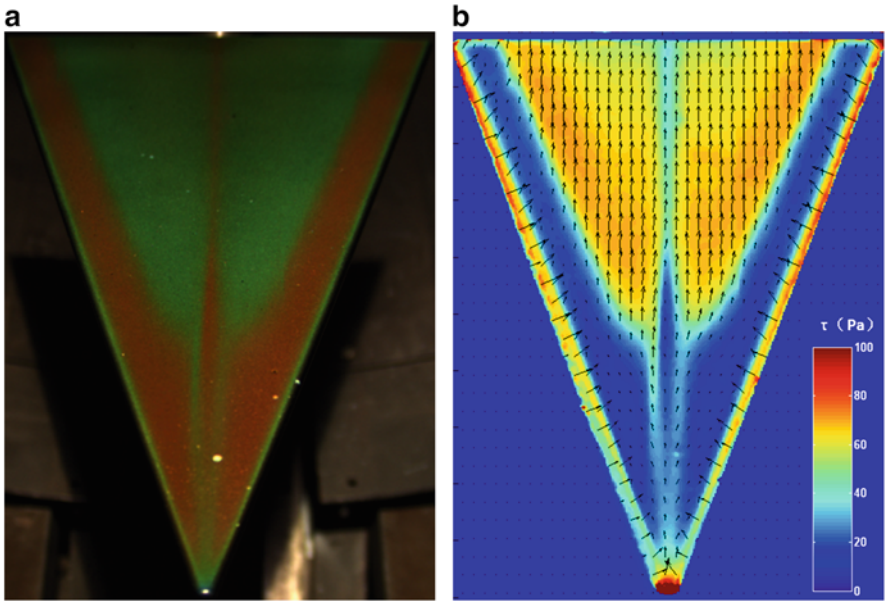

Fig. 6 Skin friction distribution of flat-plate delta wing ($\alpha = 0$). (**a**) LCCs' color-change image. (**b**) Shear stress vector distribution

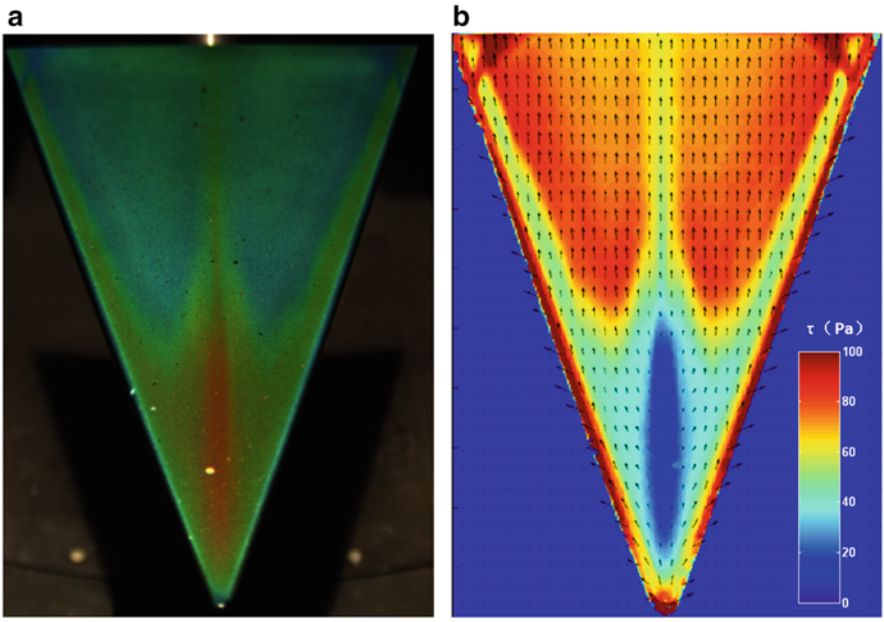

Fig. 7 Skin friction distribution of flat-plate delta wing ($\alpha = 10$). (**a**) LCCs' color-change image. (**b**) Shear stress vector distribution

5 Conclusions

The optical skin friction measurement technique based on LCCs does not damage the model surface while obtaining far more skin friction information than conventional friction gauge. The variation of skin friction reveals vivid details and structures of surface flow, and indicates the transition onset location, which provides a new perspective for flow analysis, flow state diagnostics, and transition research in hypersonic wind tunnel. It valuably solves the difficult technological problem of skin friction measurement at hypersonic flow condition.

References

1. P. Reddeppa, G. Jagadeesh, M.S. Bobji, Measurement of direct skin friction in hypersonic shock tunnels, AIAA 2005-1412 (2005)
2. T. Liu, J.P. Sullivian, Luminescent oil film skin friction meter. AIAA 97-2216 (1997)
3. J.W. Naughton, M. Sheplak, Modern skin friction measurement techniques description, use, and what to do with the data. AIAA 2000-2521 (2000)
4. D.C. Reda, M.C. Wilder, Uncertainty analysis of the liquid crystal coating shear vector measurement technique. AIAA 98-2717 (1998)

5. N. Fujisawa, A. Aoyama, S. Kosaka, Measurement of shear-stress distribution over a surface by liquid-crystal coating. Meas. Sci. Technol. **9**, 1655–1661 (2003)
6. Xing Chen, Dapeng Yao, Shuai Wen, Jian Gong, and Zhixian Bi, Optical skin friction measurement in hypersonic flow utilizing LCCs, in *Eleventh International Conference on Flow Dynamics*, Japan, pp. 638–639, 2014
7. P.T. Ireland, T.V. Jones, Liquid crystal measurements of heat transfer and surface shear stress. Meas. Sci. Technol. **11**(7), 969–986 (2000)

Thermo-structural Design of Hypersonic Vehicle Sharp Leading Edges for Thermo-erosive Stability Using Finite Element Modelling

Anupam Purwar

Abstract Hypersonic vehicle structural components with sharp geometries, namely, strut, cowl and nose, experience high pressure and heat flux due to flow stagnation. Besides the heat flux and pressure, high-temperature erosive environment is also experienced by such structures. Thus, evaluation of high-temperature wear becomes crucial to design of such sharp structural components. In present work, thermo-structural analysis along with evaluation of damage due to wear-induced mass loss has been carried out by using wall temperature-dependent pressure and heat flux estimated from computational fluid dynamics analysis. Critical design parameters, namely, temperature, stress and mass loss due to erosion, have been estimated considering non-linear material behaviour of ZrB_2-SiC-based ultrahigh-temperature ceramic. Multiple temperature-dependent erosion models for ZrB_2-SiC have been developed, and maximum mass loss of 74 milligrams has been estimated for ZrB_2-SiC strut subjected to heat flux of 6.08 MW/m^2 and 753 kPa pressure in Mach 3 flow for 300 seconds duration.

1 Introduction

Sharp leading edges are crucial for superior aerodynamic performance of hypersonic vehicles [1–3]. In a typical hypersonic vehicle, the nose, the cowl and the strut-based flameholder form the sharp structural components. During hypersonic flight, such structural components experience shock-induced heat flux (1–6 MW/m^2) coupled with pressure loads (1–50 bars) and high-temperature erosion for extended durations. This necessitates careful selection of material [4] and thermo-structural analysis to ensure their survivability. In particular, the erosion at such high temperature of 2500 K needs to be evaluated to prevent damage due to structural mass loss. In this perspective, the current work proposes a novel computational approach

A. Purwar (✉)
Indian School of Business, Hyderabad, India

A. Sasoh et al. (eds.), *31st International Symposium on Shock Waves 2*,
https://doi.org/10.1007/978-3-319-91017-8_128

for thermo-structurally reliant and damage-tolerant design of sharp leading edges, which integrates erosion modelling with thermo-structural analysis.

2 Design and Modelling

A typical hypersonic flight trajectory (Mach 7, 30 km altitude) has been considered, and thermo-structural loads experienced by strut-based flameholder have been estimated using computational fluid dynamics (CFD) analysis. The dimensions of strut-based flameholder have been selected based on the principle of minimizing flow blockage for scramjet combustor of 4 × 6 cm cross section, such that the width of strut base is 14% of combustor width with a semiangle of 4 degrees (nose radius of 2.5 mm). Ultrahigh-temperature ceramics (UHTC), namely, ZrB_2-SiC-based ceramics, have excellent high-temperature properties and are potential candidates for protecting hypersonic vehicle leading edges [5–8]. Hence, it has been selected as the material for strut.

2.1 High-Temperature Erosion Modelling

Erosion at high temperature can result in loss of material, thereby changing structural dimensions and degrading overall structural stability. For ceramics, the erosion (E, mm^3/kg) is modelled by considering "Eq. (1)", where A is a proportionality constant, m is −1.3 and n is −0.25 [9]. Accordingly, erosion behaviour of ZrB_2-SiC layer has been modelled by using Eq. 1. The erosion E quantifies the volume of material lost (V) due to erosion per unit mass of erodent particles (m). For strut the mass flow rate of the erodent particle has been estimated based on the impingement speed and concentration of particulate matter in atmosphere at 30 km altitude. It has been reported that the maximum concentration (C) of particulate matter is 129.6 μg/kg of air [10].

$$E = A * K_{IC}^{m} * H^{n} \tag{1}$$

$$\dot{m} = \rho * A * v * C \tag{2}$$

In "Eq. (2)", $\dot{m}$ is the mass flow rate of impinging erodent particles, v is air flow speed (950 m/s) and A is the cross-sectional area of exposed leading edge. The erosion behaviour of ZrB_2-SiC layer has been modelled by considering high-temperature hardness and fracture toughness data available in literature [11]. Based on this, a second-order polynomial function has been derived to model the mass loss due to erosion, M_e ($=\rho_{ZrB2-SiC} * E$) as a function of temperature (see Fig. 1).

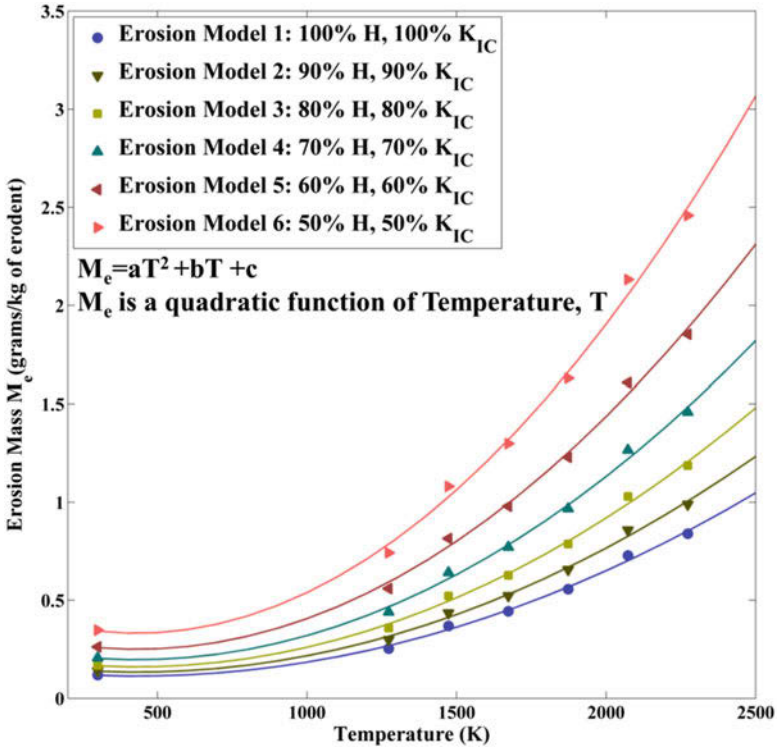

Fig. 1 Different erosion models to estimate sensitivity of mass erosion to temperature-dependent H and K_{IC}

ZrB_2-SiC-based ceramics are generally processed using sintering route, and processing of sintered ceramics varies based on sintering conditions and type of starting powders [5]. Hence, it is imperative to model this variation in hardness and toughness to investigate the sensitivity of erosion behaviour to ceramic processing method. This has been modelled by creating hardness (H) and fracture toughness (K_{IC})-dependent material erosion models (1–6), with H and K_{IC} varying from 100 per cent to 50 per cent of the original value (see Fig. 1).

2.2 Supersonic Flow Around Flameholder

The flameholder has been designed for a 2-D scramjet engine designed to operate at Mach 7 hypersonic flow at an altitude of 30 km. The scramjet has been designed with multi ramp air intake system, which converts the Mach 7 hypersonic flow into supersonic flow. This supersonic flow enters the scramjet combustor, exposing the strut-based flameholder to high-speed flow of Mach 3.3 [6]. The supersonic flow

stagnates around the strut creating subsonic regions at the rear of the strut, where liquid kerosene fuel is injected. The release of heat due to kerosene combustion along with the flow stagnation exposes the strut to heat flux as high as 6.08 MW/m^2. The scramjet engine considered here is designed to operate at fuel equivalence ratio of 0.65 [6]. Also, the kinetic energy deposited per unit area of ceramic surface has been calculated by considering complete loss of velocity of impinging particles on striking the vehicle flying at Mach 7. This kinetic energy deposition is converted into an equivalent heat flux boundary condition, according to "Eq. (3)":

$$\frac{\dot{q_{KE}}}{A} = \frac{1}{2} * \rho * v^3 * C \tag{3}$$

In the above equation, v is the velocity of impinging erodent particles, A is the cross-sectional area of exposed leading edge (strut) and C is particulate concentration.

2.3 Computational Fluid Dynamics Modelling

CFD analysis has been done using ANSYS Fluent. Semi-structured grid for fluid domain has been generated using ANSYS. Density-based solver has been used to account for compressible effects which become significant for supersonic flow. Boundary layer has been captured by providing multiple layers of refined mesh around the strut (solid domain). Spalart-Allmaras turbulence model has been used, as it has demonstrated to give good results for supersonic flow [12]. Steady-state solutions have been calculated with absolute convergence criterion, till residuals have dropped to the order of 10^{-4}. Heat flux and pressure values have been estimated at different wall temperatures of 300 K, 600 K, 900 K, 1200 K, 1500 K and 1800 K to ensure realistic temperature estimation during thermal analysis. Maximum heat flux value of 6.08 MW/m^2 and static pressure of 753 kPa have been estimated at wall temperature of 300 K, as shown in Fig. 2.

3 Finite Element Model

The thermo-structural analysis has been performed by employing the commercial code ANSYS which has been previously used by other researchers for similar analysis [6, 7]. The 3-D model mesh of the strut assembly is shown in Fig. 3. Refined mesh has been generated around the strut nose (radius = 2.5 mm) to accurately estimate temperature and strain. Similarly, multiple elements have been placed along the thickness direction to capture the temperature variation across different material interface. Second-order elementswith midside nodes, SOLID90

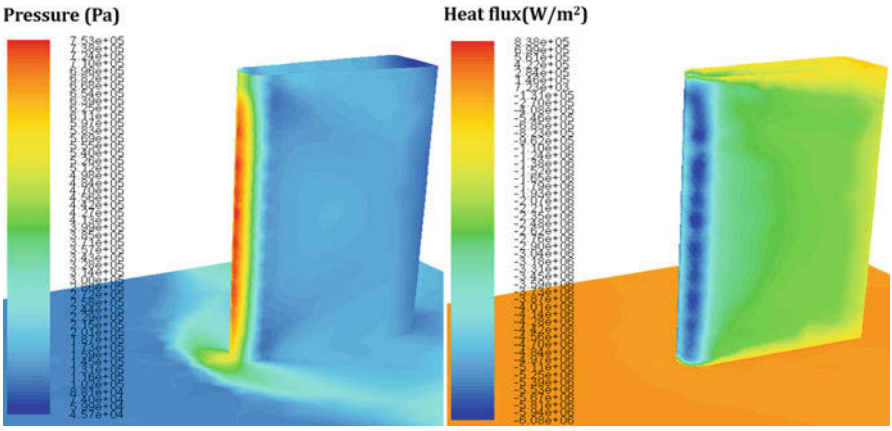

Fig. 2 Heat flux and pressure contours at wall temperature of 300 K as estimated by CFD analysis

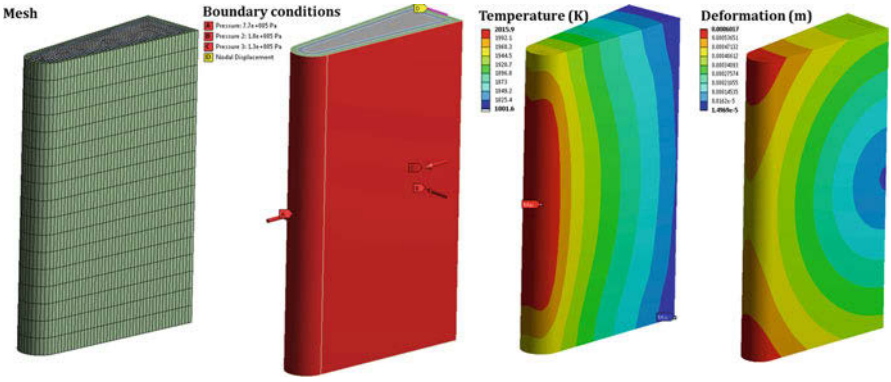

Fig. 3 Strut-based flameholder design: Strut finite element mesh depicting multiple elements along thickness; thermo-structural boundary conditions, spatially varying pressure and heat flux applied on strut external surface; thermo-structural response for 300 seconds scramjet operation: Temperature (in Kelvin) and deformation (in metres)

"3D 20-node thermal solid" and SOLID 186 "3D 20-node hexahedral structural solid" have been used to discretize the structural domain. CONTA174 "3D 8-node surface to-surface contact" elements have been used to take into account contact phenomena between the joined components. The following boundary conditions have been considered:

(a) Transient thermal fluxes, simulating the test conditions and calculated from CFD analysis along with deposited kinetic energy equivalent heat flux ($\frac{q_{KE}}{A}$) , have been applied on the exposed strut external surface.
(b) Radiation to supersonic flow at 1016 K has been applied to exposed surface of strut-based flameholder with emissivity of 0.75.

(c) The initial temperature of the model, namely, the temperature at the beginning of scramjet operation, has been assumed to be equal to 295 K.
(d) Temperature-dependent material properties have been used for ZrB_2-SiC.

3.1 Finite Element Modelling: Coupled Thermo-structural Analysis

Finite element modelling has been done using ANSYS Mechanical. Structured grid with second-order elements (SOLID186) for higher accuracy has been generated to discretize the solid domain. After discretization, wall temperature-dependent pressure and heat flux calculated from CFD analysis have been mapped from fluid to structural domain. Transient thermal analysis is performed to estimate nodal temperature of the structure. Then, the nodal temperatures are mapped from thermal to structural domain. This is followed by coupled thermo-structural analysis, which involves solving "Eq. (4)" to calculate stress and strain:

$$\begin{bmatrix} M & 0 \\ 0 & 0 \end{bmatrix} \begin{Bmatrix} \ddot{u} \\ \ddot{T} \end{Bmatrix} + \begin{bmatrix} C & 0 \\ 0 & C^{t} \end{bmatrix} \begin{Bmatrix} \dot{u} \\ \dot{T} \end{Bmatrix} + \begin{bmatrix} K & 0 \\ 0 & K^{t} \end{bmatrix} \begin{Bmatrix} u \\ T \end{Bmatrix} = \begin{Bmatrix} f + f^{th} \\ q \end{Bmatrix} \tag{4}$$

In above equation, $[M]$ = element mass matrix, $[C]$ = element structural damping matrix, $[K]$ = element stiffness matrix, $\{f\}$ = sum of element nodal force and pressure, $\{f^{th}\}$ = thermal strain force vector, $[C^t]$ = element specific heat matrix, $[K^t]$ = element diffusion conductivity matrix, $\{T\}$ = temperature vector, $\{q\}$ = sum of element heat generation load and element convection surface heat flow and $[u]$ = displacement vector.

4 Results and Discussion

4.1 Thermo-Structural Analysis

Coupled thermo-structural analysis of strut has been carried out by using heat flux, pressure and displacement boundary conditions, as shown in Fig. 3. Thermo-structural integrity of most optimum strut design has been analysed in terms of maximum temperature and pressure experienced by the strut. Maximum deformation and maximum temperature of 0.61 mm and 2016 K have been estimated at the nose of strut, respectively, as shown in Fig. 3. Maximum stress regions (von Mises stress = 88 MPa) have developed towards the rear face of UHTC layer, where displacement constraints have been applied. The maximum temperature and stress have been found to be well within material strength limits of ZrB_2-SiC [13].

Table 1 Total mass loss due to erosion for different erosion models

Erosion model	M1[a]	M2	M3	M4	M5	M6
Mass loss (mg)	21.75	31.87	39.35	50.76	61.36	74.17
Percentage of strut mass lost (%)	0.073	0.103	0.127	0.164	0.198	0.240

[a]M1, erosion model 1, strut original mass, 31 grams

4.2 Thermo-Erosive Behaviour

The material loss due to high-temperature erosion for ZrB_2-SiC-based strut has been estimated by considering the six erosion models (Erosion models: M1-M6). Material mass loss (M) has been calculated using "Eq. (5)" for exposure time (t) of 300 s, with temperature-dependent E value calculated for each element of exposed surface. The mass loss due to erosion increases quadratically as temperature rises and falls with increase in H and K_{IC} values of the material. Maximum erosion is estimated near the strut nose and minimum erosion near the strut rear, where temperature is maximum and minimum, respectively (Table 1):

$$M = E * \rho * A * v * C * \rho_{ZrB2-SiC} * t \tag{5}$$

5 Conclusion and Further Work

ZrB_2-SiC-based sharp leading edges are capable of enduring extreme thermo-structural loads for extended durations. These sharp leading edges also experience erosion in high-temperature environment. In present work, thermo-structural design of strut-based flameholder has been carried out, and procedure for investigating its thermo-erosive stability has been proposed. Multiple erosion models of ZrB_2-SiC ceramics have been formulated, and thermo-erosive behaviour of the strut has been analysed. The loss in mechanical properties, viz., hardness and fracture toughness at high temperature, has been effectively modelled using analytical relations, and maximum material loss of 74 mg has been estimated for ZrB_2-SiC, considering 50% loss in material properties due to variation in processing conditions. Currently, experimental investigation of high-temperature erosion of ZrB_2-SiC is being carried out, and the proposed erosion models will be compared with the experimental data in the near future.

Acknowledgement The author expresses thanks to the Centre of Excellence in Hypersonics for providing infrastructural support towards this work.

References

1. W. Sandra, S. Brian, *Sharp Refractory Composite Leading Edges on Hypersonic Vehicles*. (American Institute of Aeronautics and Astronautics, 2004)
2. W.F.N. Santos, Leading-edge bluntness effects on aerodynamic heating and drag of power law body in low-density hypersonic flow. J. Braz. Soc. Mech. Sci. & Eng. **27**, 236–242 (2005)
3. F.M. Wang, H.Q. Han, M.F. Lei, J. Zhang, Aerodynamic and aerothermal performance of power-law shaped leading edge of hypersonic waveriders. Procedia Eng **67**, 207–217 (2013)
4. M.L. Hill, Materials for small radius leading edges for hypersonic vehicle. J. Spacecr. Rocket. **5**, 55–61 (1968)
5. P. Anupam, R. Krishnamurthy, S. Ariharan, K.G. Nagarajan, B. Bikramjit, Development of ZrB_2–SiC–Ti by multi stage spark plasma sintering at 1600°C. J. Ceram. Soc. Jpn. **124**, 393–402 (2016)
6. A. Purwar, Thermo-structural design of strut based flame holder for scramjet combustor, ICoRD'17, Springer, 2017, vol. 1, pp. 105–115
7. A. Purwar, B. Basu, Thermo-structural design of ZrB_2–SiC-based thermal protection system for hypersonic space vehicles. J. Am. Ceram. Soc. **100**, 1618–1633 (2017)
8. A. Purwar, V. Thiruvenkatam, B. Basu, Experimental and computational analysis of thermo-oxidative-structural stability of ZrB_2–SiC–Ti during arc-jet testing. J. Am. Ceram. Soc. **100**, 4860–4873 (2017)
9. I.M. Hutchings, *Tribology: Friction and Wear of Engineering Materials*. (Edward Arnold, 1992)
10. I. Tegen, I. Fung, Modeling of mineral dust transport in the atmosphere: Sources, transport, and optical thickness. J. Geophys. Res. **99**, 22897–22914 (1994)
11. E.W. Neuman, *Elevated temperature mechanical properties of zirconium diboride based ceramics*. (Missouri University of Science and Technology, 2014)
12. H.Y. Wong, One-equation turbulence model of Spalart and Allmaras in supersonic separated flows. AIAA J. **37**, 391–393 (1999)
13. R. Loehman, *Ultra High Temperature Ceramics for Hypersonic Vehicle Applications*. (SANDIA National Laboratory, 2006)

Computational Study on Rigid Disk-Gap-Band Supersonic Parachute Aerodynamics

K. Takabayashi, K. Fukumoto, and K. Kitamura

Abstract In Mars, supersonic parachutes have been used as a decelerator at around Mach 2. In order to stabilize the parachute, NASA proposed a supersonic parachute equipped with a gap and a vent, called disk-gap-band (DGB) supersonic parachute. However, it is not fully investigated how its surrounding flow field and its aerodynamics are affected by the gap and the vent (a small ventilation hole at a stagnation point). In this study, a computational study has been carried out on the aerodynamics of rigid-body-modeled parachutes. Results indicate that computed drag coefficient is in good agreement with the experimental data. Moreover, it is observed that reduction of drag per opening area by the vent is greater than that by the gap. Two factors are considered for this reduction: (1) the vortices around the jet from the gap and (2) the vent location at a stagnation point.

1 Introduction

In Mars, supersonic parachutes have been used as a decelerator at around Mach 2. Researches on supersonic parachutes have been conducted by NASA, JAXA, and others since Viking plan (1975) [1]. Among them, shocks and their interactions are characteristic of the supersonic parachutes, causing instabilities such as area oscillations [2]. In order to stabilize the parachute, NASA proposed a disk-gap-band (DGB) supersonic parachute equipped with a gap and a vent (a small ventilation hole at a stagnation point) (Fig. 1), in which stagnated air escapes from a canopy through the gap and the vent, in expense of reduced drag. This type of parachute is widely used for many years, and then, many experiments related to this have been carried out [3]. However, its opening mechanism and stability are still unknown, and thus, experiments employing "rigid body" parachute models (rather than more realistic, "flexible body" parachutes) will be important from the standpoint of basic research.

K. Takabayashi (✉) · K. Fukumoto · K. Kitamura
Yokohama National University, Yokohama, Kanagawa, Japan
e-mail: takabayashi-koki-fp@ynu.jp

A. Sasoh et al. (eds.), *31st International Symposium on Shock Waves 2*,
https://doi.org/10.1007/978-3-319-91017-8_129

The rigid body can remove a large number of other causes of the instability (than the shock-induced ones), e.g., cloth flexibility, permeability, suspension line, and accessory objects such as a capsule. As a representative research on a rigid body model, Sengupta et al. (2011) conducted experiments in a supersonic wind tunnel to clarify the influence of Mach number on the DGB parachute [4].

Nevertheless, it is not fully investigated from the experiments how the parachute's surrounding flow field and its aerodynamics are affected by the gap and the vent, which will be examined here. In this study, a computational study will be carried out on the aerodynamics of rigid-body-modeled parachutes, which do not take into account their deformation.

2 Numerical Methods and Models

The flow is governed by unsteady, compressible, 3D Navier-Stokes equations. To solve these equations, we use FaSTAR [5] developed at JAXA. Inviscid fluxes were solved using SLAU [6], in which spatial accuracy is improved through use of the 2nd-order MUSCL scheme [7] with Hishida limiter. Turbulent term is solved by SA-noft2 [8] or DDES [9]. Time integration method is 2nd-order LU-SGS [10].

A targeted parachute model is a DGB parachute used in Mars exploration by NASA's Mars Science Laboratory (MSL) (Fig. 1). Uniform flow velocity is Mach 2, and Reynolds number (based on a diameter of the canopy) is 1.6×10^6. Table 1 summarizes the shapes of the parachutes – Case 1, a hemispherical shell shape ("canopy," baseline); Case 2, canopy with gap ("gap"); Case 3, canopy with vent ("vent"); and Case 4, canopy with gap and vent ("DGB"). The porosity in Table 1 stands for an opening area per Case 1's nominal area. Figure 1 shows the grid structure around Case 4. This grid is unstructured and generated for +z half-body only because of flow symmetry. Each case has approximately 3 M–5 M cells.

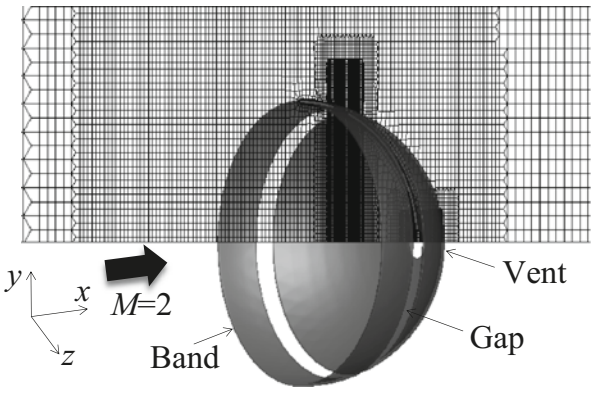

Fig. 1 Grid of the rigid parachute model (DGB)

Table 1 Shapes of parachute

Case	1	2	3	4
Shape	Canopy	Gap	Vent	DGB
porosity(%)		12.1	0.6	12.7

Table 2 Comparison of C_D between SA model and DDES model, along with the experiment in [11]

Case 4	Calculation	Experiment
C_D (SA model)	0.82	0.78
C_D (DDES model)	0.79	

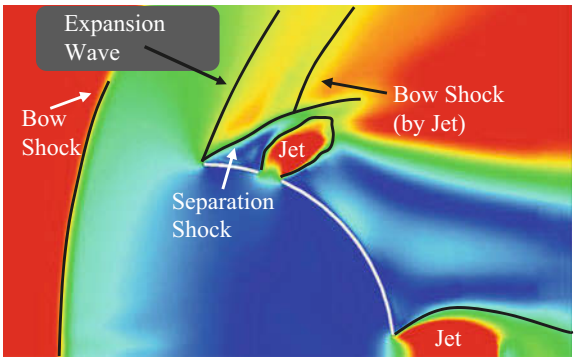

Fig. 2 Visualization of Mach number flow field (Case 4)

3 Results

First we will consider the effect of turbulence models. Table 2 shows the comparison of calculated C_D in the cases of SA model and DDES model (Case 4). Here, we also show the experimental data obtained under the similar condition [11]. As can be seen from the table, the DDES model showed a better agreement with the experiment than the SA model. This is because the DDES model better resolves small vortices compared to the SA model.

In the flow around the supersonic parachute, the vortices of various scales are generated as described later. This is why the DDES model which can capture vortices more precisely gave a reasonable result. Note that, in the DDES model, it is necessary to prepare fine grids so that vortices can be resolved in detail. In this paper, the grid convergence has been confirmed for both SA model and DDES model, and the DDES results will be used for consistency with the experimental values.

In all cases, a bow shock in front of the canopy settled to steady position after breath movements. Figure 2 shows the flow field at the steady state (Mach distribution) in the x-y section of Case 4.

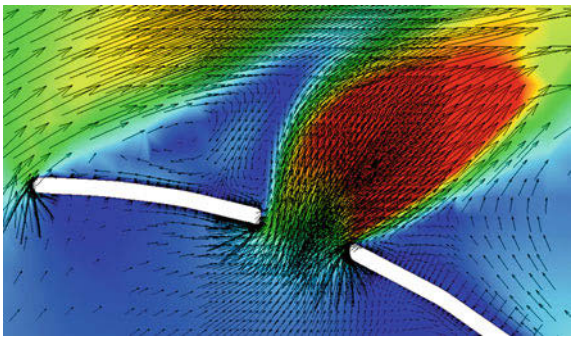

Fig. 3 Visualization of pressure flow field with velocity vectors (Case 4)

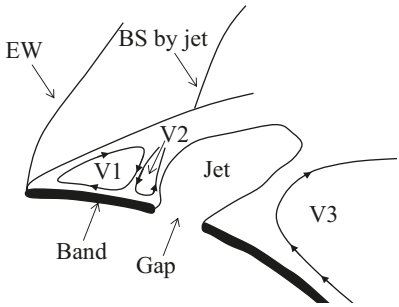

Fig. 4 Schematic diagram of flow field (Case 4): EW, expansion wave; BS, bow shock; SS, separation shock; V1, separation vortex; V2, horseshoe vortex; V3, recompression vortex

Bow shock occurs ahead of the canopy, and expansion wave occurs at the edge part of the canopy. Also, a boundary layer is separated at the edge, and as a result, separation shock is formed. Furthermore, air which stagnated inside the canopy leaks from the gap and compressed. Then, it forms bow shock (by jet). Likewise, jet is also generated at the vent.

Figure 3 shows the pressure contours around the gap with the velocity vectors. Also, Fig. 4 shows its corresponding schematic diagram. These figures show that vortices V1 (separation vortex) and V2 (horseshoe vortex) are generated in the region where the boundary layer separates. Moreover, V3 (recompression vortex) is also formed downstream the jet from the gap. The flow field shows qualitatively good agreement with past studies [4, 12].

Next, we will consider how the gap and the vent contribute to aerodynamic characteristics. Table 3 summarizes drag coefficient C_D, ΔC_D, $\Delta C_D S_0/S$, where ΔC_D (gap or vent) $= C_D$ (canopy with gap or vent)-C_D (canopy), S_0 is a projected area viewed from inflow direction, and S is the opening area (gap or vent). Thus, ΔC_D means drag coefficient created by the gap and the vent. Also, $\Delta C_D S_0/S$ is ΔC_D per opening area.

Again, C_D in Case 4 is in good agreement with the experiment. ΔC_D $(= -0.10)$ by the gap (Case 2) is less than that by the vent, -0.02 (Case 3). On the other hand, in terms of $\Delta C_D S_0/S$, $\Delta C_D S_0/S$ $(= -3.96)$ by the vent (Case 3) is less than that by the gap, -0.85 (Case 2). Therefore, it can be said that the vent decreases drag per opening area by five times, compared to the gap. Two factors are considered for

Table 3 Comparison of drag coefficient C_D (compared with the experiment [11])

Case	1(Canopy)	2(Gap)	3(Vent)	4(DGB)	Exp.(DGB)
C_D	0.90	0.80	0.88	0.79	0.78
ΔC_D		-0.10	-0.02	-0.12	
$\Delta C_D S_0/S$		-0.85	-3.96	-0.92	

this reason: (1) the gap does not greatly decrease drag owing to the vortices around the jet from the gap, and (2) the vent located at a stagnation point greatly decreases drag.

4 Conclusions

A computational study on a flow around disk-gap-band (DGB) supersonic parachute and its drag characteristics has been conducted.

- Computed drag coefficient is in good agreement with the experiment.
- Flow field around the rigid DGB parachute is revealed in this study.
- Reduction of drag per opening area by the vent is greater than that by the gap. This is due to (1) vortices around the gap and (2) the vent located at the stagnation point.

References

1. H. Takayanagi, T. Suzuki, K. Yamada, Y. Maru, S. Matsuyama, K. Fujita, Development of supersonic parachute for Japanese Mars Rover Mission: 30th ISTS, Paper No. 2015-e-08, (2015)
2. K. Karagiozis, R. Kamakoti, F. Cirak, C. Pantano, A computational study of supersonic disk-gap-band parachutes using large-Eddy simulation coupled to a structural membrane. J. Fluids Struct. **27**, 175–192 (2011)
3. A. Sengupta, M. Wernet, J. Roeder, R. Kelsch, A. Witkowski, T. Jones, Supersonic testing of 0.8 m Disk Gap Band Parachutes in the Wake of a 70 deg Sphere Cone Entry Vehicle, in *20th AIAA Aerodynamic Decelerator Systems Technology Conference and Seminar AIAA 2009–2974*, Washington, 4–7 May, 2009
4. A. Sengupta, Fluid structure interaction of parachutes in supersonic planetary entry, in *21st AIAA Aerodynamic Decelerator Systems Technology Conference and Seminar*, 2011
5. A. Hashimoto, K. Murakami, T. Aoyama, K. Ishiko, M. Hishida, M. Sakashita, P. Lahur, AIAA-2012-1075, (2012)
6. E. Shima, K. Kitamura, Parameter-free simple low-dissipation AUSM-family scheme for all speeds. AIAA J. **49**(8), 1693–1709 (2011)
7. B.V. Leer, Towards the ultimate conservative difference scheme. IV. A new approach to numerical convection. J. Comput. Phys. **23**(3), 276–299 (1977)

8. P. Spalart, S. Allmaras, A one-equation turbulence model for aerodynamic flows, AIAA-paper1992-439, 1992
9. M.L. Shur, P.R. Spalart, M.K. Strelets, A.K. Travin, A hybrid RANS-LES approach with delayed-DES and wall modelled LES capabilities. Int. J. Heat Fluid Flow **29**, 1638–1649 (2008)
10. S. Yoon, A. Jameson, Lower-upper Symmetric-Gauss-Seidel method for the Euler and Navier-Stokes equations. AIAA J. **26**(9), 1025–1026 (1988)
11. V. Gidzak, M. Barnhardt, T. Drayna, I. Nompelis, G.V. Granham, W. Garrard, Comparison of fluid-structure interaction simulations of the MSL Parachute with Wind tunnel tests, Paper No. AIAA-2009-2971, (2009)
12. M.K. Ibrahim, T. Nakamura, K. Kitamura, K. Mori, Y. Nakamura, The role of vortices in side Jet/Blunt body interaction at hypersonic speed. Trans. JSASS Space Tech. Japan **7**, 1–10 (2009)

Numerical Simulation of Laser Ablation Propulsion Performance for Spherical Capsule

C. Xie, D. T. Tran, and K. Mori

Abstract The purpose of this research is to study the performance of laser ablation propulsion with a numerical method based on computational fluid dynamics (CFD). We focus on the propulsion performance when pulsed laser beam is irradiated on a 10-mm-diameter spherical model. In this paper, 1.3 mm pulsed laser beam and a so-called donut-mode laser beam were both done to validate a simple numerical method without laser ablation model under 10 kPa – 100 kPa ambient pressure. The flow field quantities were solved with three-dimensional Euler equation by finite volume method. Blast wave energy conversion efficiency η_{bw} and momentum coupling coefficient C_m were both investigated by comparing between numerical simulation and experiment. Specifically, a so-called explosion source model is used to simplify laser ablation process and estimate blast wave energy conversion efficiency η_{bw} in this numerical method. Relatively good results of η_{bw} and C_m are obtained with this method. Finally, results of donut-mode laser beam simulation are presented about blast wave expansion and C_m.

1 Introduction

Laser propulsion is a concept proposed by Kantrowitz [1] in order to realize low-cost launch for sending spacecraft into space in 1970s. Comparing with chemical-fuel rocket, laser propulsion can proceed in long distance with ground-based laser. Atmospheric gases can be used as a propellant during flight in a dense atmosphere. So it is possible to reduce the weight of chemical fuel of rocket or spacecraft to obtain a higher payload ratio and decrease launch cost. Since laser technology develops in recent decades, the laser power can meet the requirement of practical launching. Many propulsion systems have been proposed and investigated experimentally and numerically. Several flights were done by Myrabo et al. during

C. Xie (✉) · D. T. Tran · K. Mori
Department of Aerospace Engineering, Nagoya University, Nagoya, Japan
e-mail: xie.chongfa@a.mbox.nagoya-u.ac.jp

A. Sasoh et al. (eds.), *31st International Symposium on Shock Waves 2*,
https://doi.org/10.1007/978-3-319-91017-8_130

1998 to 2001 [2–4]. The world record flight of laser-powered launching is 71 meters using 10 kW CO_2 pulsed laser that is demonstrated by Myrabo on October 2, 2000 [4]. Other researchers [5–7] also estimated the performance of a laser-powered launch system in numerical way. Most of them mainly focus on pulsed laser performance about induced impulse or momentum coupling coefficient C_m instead. For laser-powered orbital launching, launching trajectory is also proposed in Katsurayama's research [8]. However, stability problem is one of the factors that affect the flight height of launched lightcraft, which is significant and unsolved in view of current technology level.

Common laser launching system utilizes atmospheric gases as a propellant in dense atmosphere. But at high altitude or in vacuum environment, ambient air is not enough to provide sufficient thrust in air-breathing processes. Additional propellant, such as extra fuel carried with the vehicle, or vapor induced by laser ablation (LA), is required in those cases. In our study, we are more interested in the latter one. Laser ablation is the material removing process when irradiating a solid or occasionally liquid surface with a laser beam. The material absorbs the laser energy and evaporates or sublimates. Then a vapor jet will be generated above the target surface. At high laser fluence, the material jet is typically converted to a plasma jet. The ablated material efficiently attenuates the incoming laser radiation and reduces the ablation rate that is expressed as the amount of removed material per laser pulse, so-called plasma shielding effect [9]. The vapor jet absorbs laser and induces thrust to propel the vehicle. The thrust scales linearly with laser power [10]. Laser ablation propellant performance has been studied by many researchers by experiment [11–14] or simulation [15–18]. The crucial factors are, including but not limited to, the ablation rate, energy conversion efficiency η_{bw} expressed as the fraction of laser energy E_L conversed into blast wave energy E_{bw}, and momentum coupling coefficient C_m expressed as the impulse provided by unit energy laser beam.

We considered a launching system that the vehicle obtains thrust from vapor jet induced by laser ablation in dilute atmosphere or vacuum. Also, we hope to solve the stability problem mentioned above with this launching system. The normal laser beam pattern, spot, shows little stability in propulsion. One proposal put forward by Mori [19] is to use a so-called donut-mode laser beam; see Fig. 1. We are specially interested in the feasibility of a donut-mode laser-guided spherical capsule launching system about the gas dynamics and energy efficiency in propulsion.

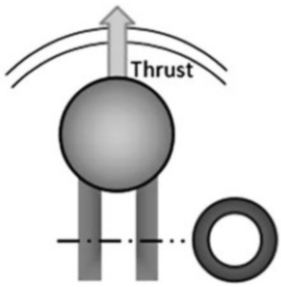

Fig. 1 Donut-mode laser beam-based launching system

However, as mentioned above, laser-powered flight tests are difficult and high cost in current technology level, especially supersonic ones. Our purpose is to use numerical methods based on computational fluid dynamics (CFD) to investigate the performance of laser ablation propulsion for donut-mode laser beam-based launching system.

In this paper, simulation of laser ablation process is not discussed. A simple model, explosion source model, is used to simplify laser ablation process in numerical simulation. This method was also used in several numerical studies [7, 20] and gave good results in energy conversion efficiency estimate and impulse computing.

2 Numerical Method

2.1 Governing Equations and Numerical Schemes

Three-dimensional compressible Euler equations are used to simulate gas dynamics of laser ablation propulsion. Air is treated as ideal gas. The governing equations are given as follows:

$$\frac{\partial \mathbf{Q}}{\partial t} + \frac{\partial \mathbf{E}}{\partial x} + \frac{\partial \mathbf{F}}{\partial y} + \frac{\partial \mathbf{G}}{\partial z} = 0 \tag{1}$$

with

$$\mathbf{Q} = \begin{bmatrix} \rho \\ \rho u \\ \rho v \\ \rho w \\ E \end{bmatrix} \quad \mathbf{E} = \begin{bmatrix} \rho u \\ \rho u^2 + p \\ \rho uv \\ \rho uw \\ (E + p)\, u \end{bmatrix} \quad \mathbf{F} = \begin{bmatrix} \rho v \\ \rho uv \\ \rho v^2 + p \\ \rho vw \\ (E + p)\, v \end{bmatrix} \quad \mathbf{G} = \begin{bmatrix} \rho w \\ \rho uw \\ \rho vw \\ \rho w^2 + p \\ (E + p)\, w \end{bmatrix}$$

where ρ is density; u, v, and w are velocity components; p is pressure; and E is total energy. In addition, E and the state equation are defined as

$$E = \frac{p}{\gamma - 1} + \frac{\rho\left(u^2 + v^2 + w^2\right)}{2} \tag{2}$$

$$p = \rho RT \tag{3}$$

where γ is the specific heat ratio and R is the gas constant.

The Euler equations are discretized spatially by vortex-centered finite volume method and integrated in time with three-stage Runge-Kutta method. The HLLC Riemann solver is used to evaluate the inviscid fluxes with 3rd-order MUSCL high-resolution approach and Van Albada limiter.

2.2 Computational Grid and Computational Conditions

The diameter of spherical target is fixed as 10 mm in simulation. Figure 2 shows the computational grid with 1,500,000 cell numbers. To make resulting thrust independent of the grid resolution, the grid convergence was checked via C_m (see Table 1), where ξ, η, and ς are parameters in computational coordination. Minimum cell width is set as $\Delta r = 31\mu$m in of next wall cells. Although cell number of 375,000 also shows relatively good result of C_m, the cell number is still set as 1,500,000 in order to obtain better results of blast wave propagation especially in target surface direction.

The outer boundary is set as Riemann invariant boundary condition that is able to suppress nonphysical wave reflecting from the outer boundary. On target surface, the boundary is set as slip wall boundary, and pressure values are extrapolated from next cells. The computation is performed under CFL = 0.5.

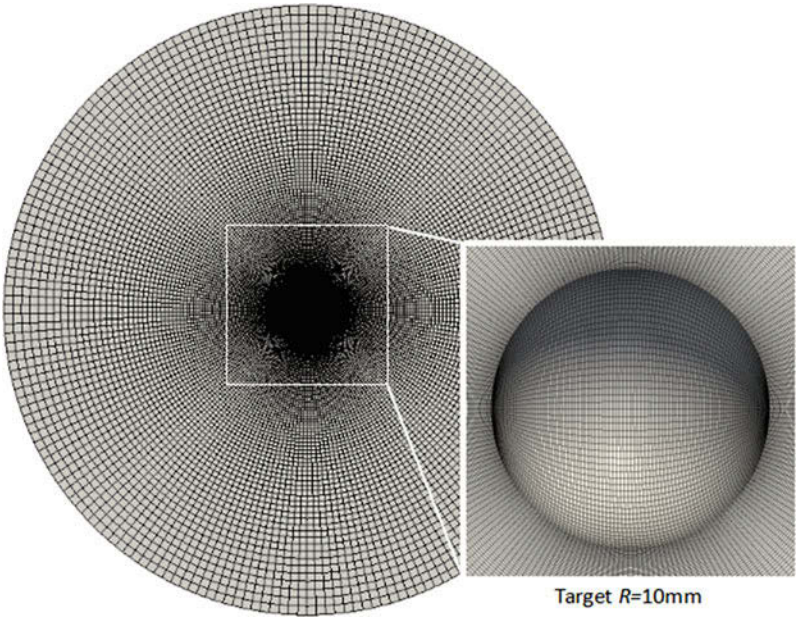

Fig. 2 Computational grid

Table 1 Grid convergence of C_m

Cell number ($\xi \times \eta \times \zeta$)	C_m, N/MW
125,000 ($50 \times 50 \times 50$)	13.11
250,000 ($50 \times 50 \times 100$)	48.36
375,000 ($50 \times 50 \times 150$)	57.11
843,750 ($75 \times 75 \times 150$)	56.06
1,500,000 ($100 \times 100 \times 150$)	55.66

Table 2 Computational parameters

Ambient pressure	10 kPa–100 kPa
Blast wave energy E_{bw}	0.15–0.5 J
Laser type	Nd-YAG laser
Spot laser diameter D_L	1.3 mm
Donut laser diameter D_i–D_o	3.1 mm–6.5 mm
Laser pulse energy E_L	0.7 J

In current simulation program, explosion source model is used to replace the effects of chemical reactions and electric excitation of laser ablation process. What we are really concerned about is the energy conversion efficiency η_{bw}. Blast wave energy E_{bw} is defined as the bulk energy of gas motion in the volume of the blast wave V_{bw} [20]:

$$E_{bw} = \int_{V_{bw}} \left(\frac{p - p_a}{\gamma - 1} + \frac{\rho u^2}{2} \right) dV_{bw} \tag{4}$$

where p_a is ambient pressure. We consider pressure is uniform in explosion source in initial condition, and then blast wave energy E_{bw} can be treated as

$$E_{bw} = \frac{p_0 - p_a}{\gamma - 1} V_0 \tag{5}$$

In computation, blast wave energy E_{bw} is assumed from 0.15 J to 0.5 J with laser pulse energy E_L of 0.7 J. With explosion source volume V_0, initial pressure p_0 can be decided under different blast wave energy. Histories of the blast wave volume V_{bw} can be obtained in different cases, and then blast wave energy E_{bw} can be decided comparing results of simulation and experiment, which will be discussed in the following. Thrust is also computed with estimated E_{bw}. In addition, the diameter of initial explosion source in cross laser incidence direction is determined according to laser beam size. The thickness h of explosion source can be estimated according to schlieren photography of experiment. h is set as about 1.0 mm, 20 cells of computational grid, in simulation. The value of h effects the thrust computation.

Calculation parameters are determined according to experiment parameters that are shown in Table 2.

2.3 Blast Wave Energy and Impulse

On the basis of blast wave energy E_L defined in Eq. (4), blast wave energy conversion efficiency η_{bw} is used to describe the energy conversion, which is defined as

$$\eta_{bw} = \frac{E_{bw}}{E_L} \tag{6}$$

The impulse produced by pulsed laser beam is computed by integrating pressure on model surface in time, that is,

$$\overrightarrow{I}_m = \int_t \int_{\overrightarrow{S}} p d\overrightarrow{S}\, dt \tag{7}$$

where p, S, and t are surface pressure, surface area, and time of one laser pulse period, respectively. The surface pressure value is affected by the numerical method of simulation, including flux-solving scheme, spatial and temporal computational accuracy, solid wall boundary condition, and so on. Furthermore, momentum coupling coefficient C_m is used to describe the impulse provided by unit energy laser beam as

$$C_m = \frac{I_m}{E_L} \tag{8}$$

3 Results and Discussion

The results will be discussed of the propulsion performance of pulsed laser on a spherical target. Single-spot pulsed laser is first present, comparing simulation results with experiment results, to validate the explosion source model. Both the blast wave propagation and energy conversion efficiency are discussed in this part. Then C_m is investigated on the basis of energy conversion efficiency for both of single-spot laser beam and the donut-mode laser beam.

3.1 Spot Laser

Blast Wave Propagation

Figure 3 shows an example in which we can compare blast wave propagation between experiment (top) and simulation (bottom) in the case of 1.3 mm circle laser spot and 100 kPa ambient pressure with 0.7 J incidence laserpulse. Initial E_{bw} is set

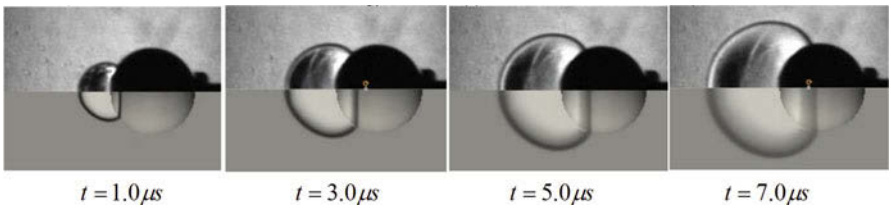

Fig. 3 Blast wave expansion of experiment (top) and simulation (bottom)

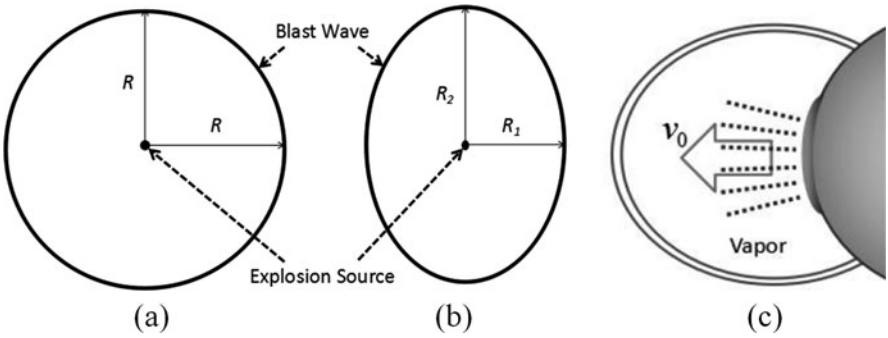

Fig. 4 (**a**) Spherical blast wave. (**b**) Elliptical blast wave. (**c**) Vapor jet's effect on blast wave

as 0.35 J in simulation. Pressure inside blast wave is higher than ambient pressure. As blast wave is expanding outward, gas is put backward and induces thrust on the target.

Blast Wave Energy and Energy Conversion Efficiency

According to the definition of blast wave energy in Eq. (4), blast wave expands in different speed with different E_{bw}. The change of V_{bw} is an important factor to estimate the blast wave energy. According to a former study done by Mori, K. et al. [20], the blast wave can be divided into two kinds, spherical blast wave and elliptical blast wave. The volume of blast wave is determined geometrically as

$$V_{bw,\text{spherical}} = 4\pi R^3(t)/3 \tag{9}$$

$$V_{bw,\text{elliptical}} = 4\pi R_1(t) R_2^2(t)/3 \tag{10}$$

where R, R_1, and R_2 are shown in Fig. 4a, b.

In the experiment, blast wave expands nonuniformly in each direction, that is, elliptical blast wave. The main reason is the effect of vapor jet induced by laser beam in early stage; see Fig. 4c. In laser ablation process, the target material is

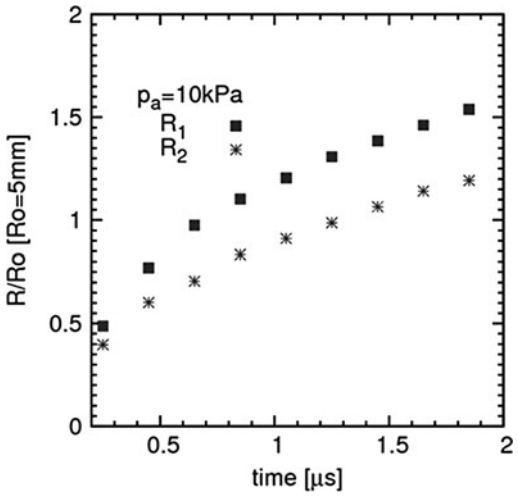

Fig. 5 Difference between R1 and R2 in 10 kPa ambient case

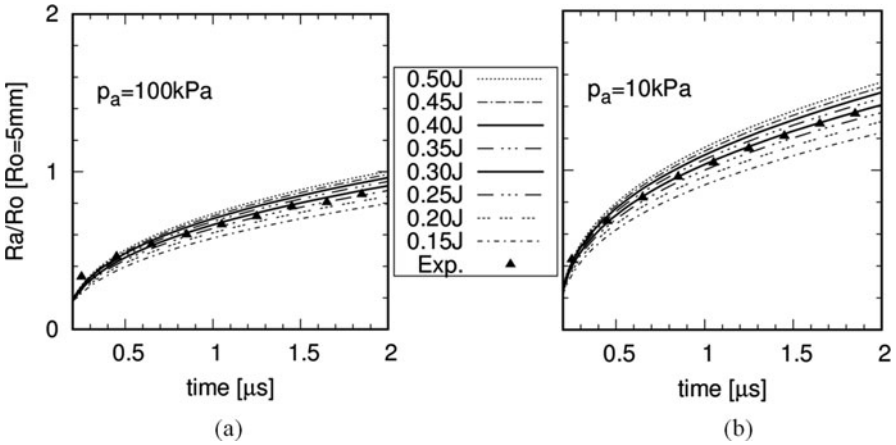

Fig. 6 Comparison of blast wave volume between simulation (line) and experiment (point). (**a**) 100 kPa ambient pressure, (**b**) 10 kPa ambient pressure

melting and vapor jet with high speed and temperature is induced. The jet expands out and compresses ambient air. Blast wave is induced with initial speed in vapor jet direction. In contrast, the blast wave always expands uniformly in the simulation, that is, spherical blast wave, because the initial velocity of blast wave due to vapor jet is not considered with explosion source model.

Based on Eqs. (9) and (10), R of spherical blast wave and $\sqrt[3]{R_1 R_2^2}$ of elliptical blast wave can represent blast wave volume; transformation is needed to deal with spherical and elliptical blast wave.

Figure 5 showsthedifference between R_1 and R_2 in 10 kPa ambient case. To determine E_{bw}, Fig. 6a and b, as examples, shows the comparison between

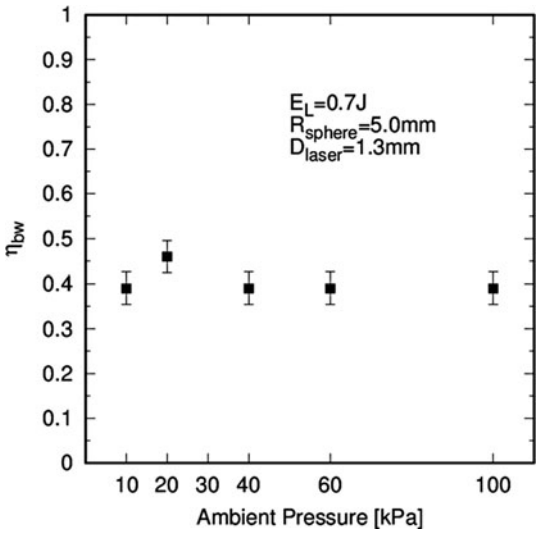

Fig. 7 Energy conversion efficiency

experiment and simulation of 100 kPa and 10 kPa, respectively, where R_a is the value to represent R of simulation or $\sqrt[3]{R_1 R_2^2}$ of experiment. Eight cases of simulation are shown to compare with experiment. The blast wave expands more quickly with higher E_L. In both cases, the blast wave energy is estimated to be 0.25–0.30 J. The cases of 20 kPa, 40 kPa, and 60 kPa ambient were analyzed in the same way.

η_{bw} can be obtained in different ambient pressure based on Eq. (6). Figure 7 shows the relation between blast wave energy conversion efficiency η_{bw} and ambient pressure p_a. Blast wave energy conversion efficiency is about 0.36–0.43.

Momentum Coupling Coefficient

As discussed above, the thrust computation, as well as C_m, is affected by several factors in numerical method, including boundary conditions, initial condition, numerical scheme, and so on. What we expect to study in numerical way is to find a general rule that can describe the relation between C_m and ambient pressure p_a. C_m is shown to increase with the increase in ambient pressure. With the variation E_L and p_a, the plot of C_m was shown to be [14]

$$C_m = \beta \left(\frac{R_{\text{sphere}}}{R_{bw}} \right)^n \tag{11}$$

In spherical target, where R_{bw} is defined as $(E_L/p_a)^{1/3}$, R_{disk} is the diameter of target disk, and β, n are the coefficients determined by E_L and p_a. Figure 8a shows momentum coupling coefficient C_m obtained in simulation (line) and experiment

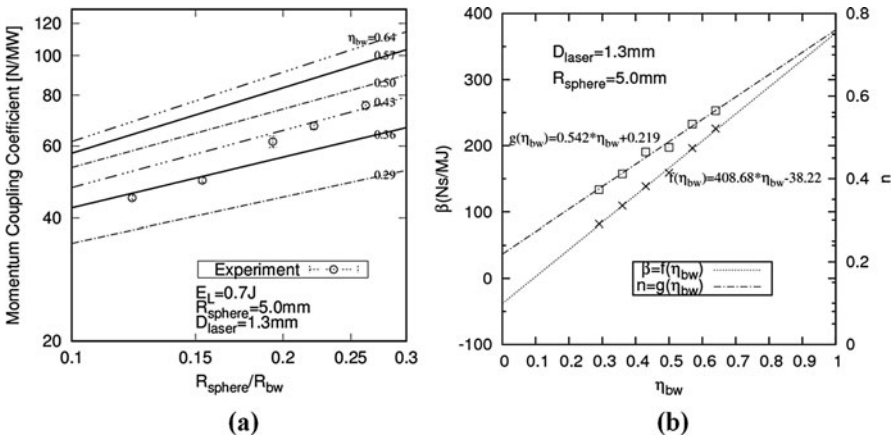

Fig. 8 C_m of single spot laser pulse. (**a**) comparison of C_m between simulation (line) and experiment (point); (**b**) β, n values obtained by simulation and their function via η_{bw}

Table 3 β, n values via η_{bw}

η_{bw}	β(N s/MJ)	n
0.64	225.87	0.5646
0.57	196.32	0.5323
0.50	158.98	0.4757
0.43	138.47	0.4648
0.36	109.32	0.4118
0.29	81.92	0.3736

(point), respectively. Figure 8b and Table 3 show β, n values obtained by simulation and their function via η_{bw}. They are shown to change linearly in η_{bw} value of 0.29–0.64. With those results, it is able to estimate C_m according to η_{bw}, $E_{L,}$ and p_a in 10 mm sphere target.

3.2 Donut-Mode Laser

Figure 9 shows simulation results of the blast wave propagation induced by donut-mode laser pulse. The blast wave was ring shape in early stage. Interaction of shock wave happened and gas was compressed in the ring center of laser beam when blast wave propagates there. In donut-mode laser beam cases, we are also interested in the relation among C_m, η_{bw}, $E_{L,}$ and p_a. Simulation results of C_m can be found in Table 4 and Fig. 10.

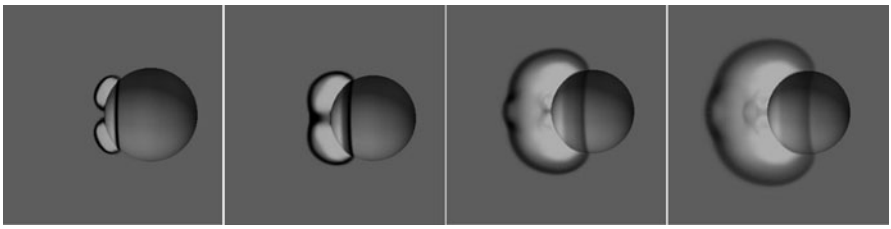

Fig. 9 Blast wave expans$_i$on with donut-mode laser beam in simulation

Table 4 β, n values via η_{bw}

η_{bw}	β(N s/MJ)	n
0.43	279.99	0.68
0.29	187.37	0.63
0.14	90.46	0.54

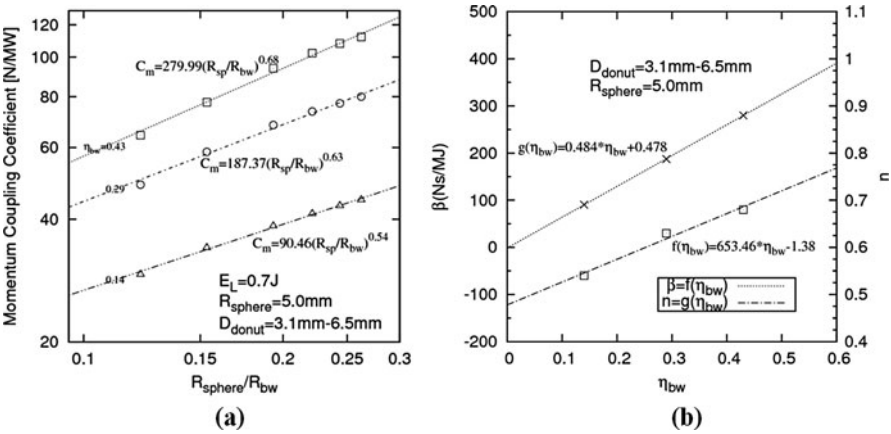

Fig. 10 C_m of single spot laser pulse. (**a**) comparison of C_m between simulation (line) and experiment (point); (**b**) β, n values obtained by simulation and their function via η_{bw}

4 Conclusion

In this paper, a simple numerical method, using explosion source model, was adapted to estimate the performance of laser ablation propulsion in spherical target. It provided a relatively easy way to compute η_{bw} and C_m under ambient pressure from 10 kPa to 100 kPa. Both approaches, blast wave volume V_0 and C_m, show η_{bw} to be 0.36–0.43. The results of C_m estimated by the numerical method are also give the relation among C_m, η_{bw}, $E_{L,}$ and p_a in 10 mm sphere target. For donut-mode laser beam, C_m is also investigated with the numerical method mentioned above.

References

1. A. Kantrowitz, Propulsion to orbit by ground based lasers. Aeronaut. Astronaut. **10**, 74–76 (1972)
2. L. Myrabo, D. Messitt, F. Mead, Jr., Ground and flight tests of a laser propelled vehicle, in *36th AIAA Aerospace Sciences Meeting and Exhibit*, 1998
3. D. Messitt, L. Myrabo, F. Mead, Jr., Laser initiated blast wave for launch vehicle propulsion, in *36th AIAA/ASME/SAE/ASEE Joint Propulsion Conference and Exhibit*. 2000
4. L. Myrabo, World record flights of beam-riding rocket lightcraft-Demonstration of "disruptive" propulsion technology, in *37th Joint Propulsion Conference and Exhibit,* 2001
5. S. Kim, I.-S. Jeung, J.-Y. Choi. Numerical Study on Thrust Performance Evaluation of Laser Propulsion during Supersonic/Hypersonic Flight, in *AIP Conference Proceedings*. Eds. Andrew V. Pakhomov, and Leik N. Myrabo. Vol. 766. No. 1. AIP, 2005
6. H. Chen et al., Numerical simulation of air-breathing nanosecond laser propulsion considering subsonic inflow and multi-pulse. Optik-Int J Light and Electron Opt. **125**(14), 3444–3448 (2014)
7. H. Katsurayama et al., Numerical analyses of exhaust and refill processes of a laser pulse jet. J. Propuls. Power **24**(5), 999–1006 (2008)
8. H. Katsurayama, K. Komurasaki, Y. Arakawa, A preliminary study of pulse-laser powered orbital launcher. Acta Astronaut. **65**(7), 1032–1041 (2009)
9. J.M. Vadillo et al., Effect of plasma shielding on laser ablation rate of pure metals at reduced pressure. Surf. Interface Anal. **27**(11), 1009–1015 (1999)
10. C. Phipps et al., Review: Laser-ablation propulsion. J. Propuls. Power **26**(4), 609–637 (2010)
11. N. Farid et al., Emission features and expansion dynamics of nanosecond laser ablation plumes at different ambient pressures. J. Appl. Phys. **115**(3), 033107 (2014)
12. S.-B. Wen et al., Expansion of the laser ablation vapor plume into a background gas. I. Analysis. J. Appl. Phys. **101**(2), 023114 (2007)
13. S.-B. Wen et al., Laser ablation induced vapor plume expansion into a background gas. II. Experimental analysis. J. Appl. Phys. **101**(2), 023115 (2007)
14. K. Mori, R. Maruyama, K. Shimamura, Energy conversion and momentum coupling of the sub-kJ laser ablation of aluminum in air atmosphere. J. Appl. Phys. **118**(7), 073304 (2015)
15. S.H. Jeong, R. Greif, R.E. Russo, Numerical modeling of pulsed laser evaporation of aluminum targets. Appl. Surf. Sci. **127**, 177–183 (1998)
16. A. Bogaerts et al., Laser ablation for analytical sampling: What can we learn from modeling? Spectrochim. Acta B At. Spectrosc. **58**(11), 1867–1893 (2003)
17. Z. Chen, A. Bogaerts, Laser ablation of Cu and plume expansion into 1 atm ambient gas. J. Appl. Phys. **97**(6), 063305 (2005)
18. T. Sakai, Impulse generation on Aluminum target irradiated with Nd: YAG laser pulse in ambient gas. J. Propuls. Power **25**(2), 406–414 (2009)
19. K. Mori, R. Maruyama, Launch capability of a conceptual laser-launch system of a spherical vehicle and a dunut-mode beam, in *54th AIAA Aerospace Sciences Meeting,* 2016
20. K. Mori, K. Komurasaki, Y. Arakawa, Energy transfer from a laser pulse to a blast wave in reduced-pressure air atmospheres. J. Appl. Phys. **95**(11), 5979–5983 (2004)

Investigation of the Heat Transfer in Hypersonic Flow on Modified Spike-Blunt Bodies

N. Gopalakrishna and S. Saravanan

Abstract Hypersonic vehicles experience high levels of drag and aerodynamic heating during flight which has to be considered during the vehicle's development phase. For this purpose, the high-speed community has been studying various techniques to minimize these effects, which in turn leads to longer range, lower fuel consumptions, and safer flight. In the last seven decades, one of the most reliable techniques developed was spikes. A spike mounted on the nose of high-speed vehicles modify the external flow field by pushing the bow shock away and causing flow separation zones ahead of the body where the pressure and heating rates are lower. In this study we have performed experimental and computational investigation of heat transfer over hemispherical blunt body with a modified spike protrusion in front which is termed as "double spike." Further, we have compared this double spike with the single spike configuration along with the blunt body case.

1 Introduction

To reduce the heat transfer to the hypersonic vehicle, the preferred shape is hemispherical blunt body. At high speed the blunt body has a bow shock in front of it, which leads to high drag. Also it is critically loaded by thermal stresses at the nose (stagnation point). Therefore, it is utmost importance to find techniques to reduce the heat at the nose tip of a hypersonic flight. Due to this there is a constant need to develop feasible, cost-effective, and innovative active or passive technique in comparison with other conventional techniques to reduce tip heating rates and enhance the lift to drag ratio of a model. Hence, in this backdrop the present work has been carried out to understand the complexity of gas dynamics in the near stagnation region of a model with double aerospikes at hypersonic flows.

N. Gopalakrishna (✉) · S. Saravanan
Department of Aerospace Engineering, Indian Institute of Science, Bangalore, KA, India

A. Sasoh et al. (eds.), *31st International Symposium on Shock Waves 2*,
https://doi.org/10.1007/978-3-319-91017-8_131

1.1 Literature Review

Hypersonic flow over a spike-blunt body has been extensively studied from the 1940s. Ahmed and Qin [1] gave detailed survey of studies on spiked body. Few relevant significant studies have been discussed here. Using spikes for hypersonic flow was first suggested by Alexander [2] in 1947 for the reduction of drag on blunt bodies at supersonic speeds. Crawford in 1959 [3] conducted an extensive experimental investigation of drag and aerodynamic heating on a spiked hemisphere cylindrical model at Mach 6.8. He concluded that the heat transfer to a spiked nosed cylinder was greatly influenced by the nature of flow field over the separated boundary layer. It was also found that the heat transfer rates are reduced as compared to the un-spiked body only if the Reynolds number is low enough for the existence of laminar flow at the reattachment point. Gerdroodbary and Hosseinalipour [4] observed that the spikes with hemispherical tips are the best for the reduction of heat fluxes, and L/D ratio of 1 (L/D = length of the spike to diameter of blunt body) is the optimum choice for both heat and drag reduction. Viren [5] made measurements with different tipped spikes fixed over 120-degree blunt cone and found that aerospike is most effective in reducing drag. Notably, Yadav R, Guven's [6, 7] computational studies compared single-disk versus double-disk spikes of the same overall length and hemispherical cap size and suggested that double-disk spikes are superior in reducing peak heating of the main body as well as drag.

1.2 Flow Characteristic of Spiked Body

Picture shows the Schlieren image of a double spike compared with the computation density gradient in front of a hemispherical blunt body. The typical flow characteristics of a spike body are indicated in (Fig. 1).

2 Experimental and Computational Setup

2.1 Model Design and Experimental Setup

Experiments were carried out on hemispherical blunt body of diameter D = 80 mm, with slots to place the insertion of Macor strips over which platinum thin film sensors were painted for measurement of surface heat transfer rate. The platinum thin film gauges for sensing convective heating rates to the model forebody in a shock tunnel flow were first developed by Vidal [8]. Figure 2 shows the dimension of the blunt body and double spike. The double spike has an overall length of L = 80 mm, change it to proper sentence.

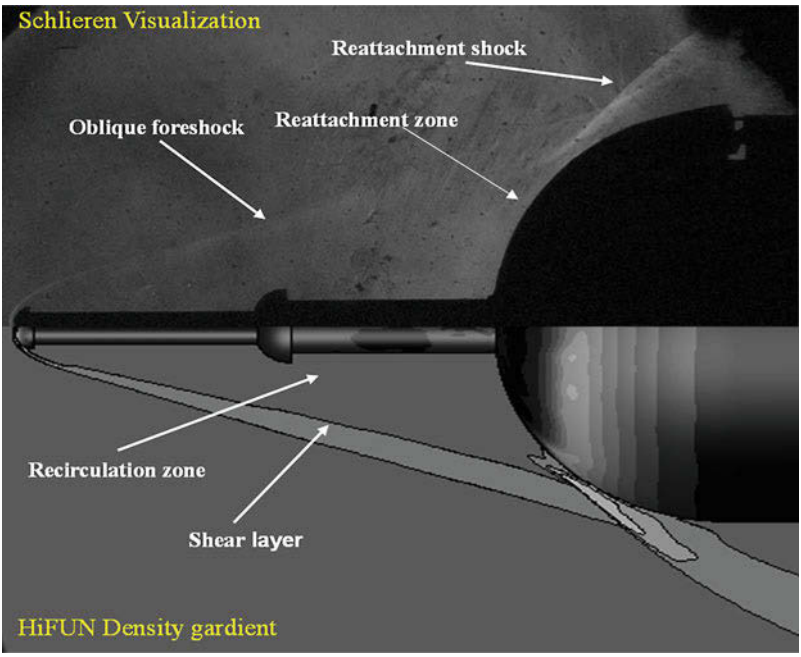

Fig. 1 Typical flow characteristics of a spike body

The **HST2**(hypersonic shock tunnel) happens to be the second one in the series of hypersonic shock tunnels at Aerospace Engineering Department at Indian Institute of Science. The shock tube is a stainless steel tube of 70 mm outer diameter and 50 mm inner diameter separated into driver and driven sections by an aluminum diaphragm. The 2.5-m-long driver section is equipped with an arrangement to feed the driver gas from high-pressure helium cylinders. The driven section is 5.12 m long. Typical test time is of the order of 1 ms. Free stream conditions obtained in test section are provided in Table 1.

2.2 Computational Details

The HiFUN (high-resolution flow solver on unstructured meshes) solver is an unstructured data-based cell-centered finite volume solver developed at computational aerodynamics' lab and is the current solver product of Simulation and Innovation Engineering Solutions (SandI).The computations for the present study have been made using the Roe flux formula. A diamond path-based Green-Gauss procedure has been used for both linear solution reconstruction and viscous flux computations. Solution monotonicity was preserved using the limiter proposed by Venkatakrishnan. Convergence acceleration to steady state was obtained using a

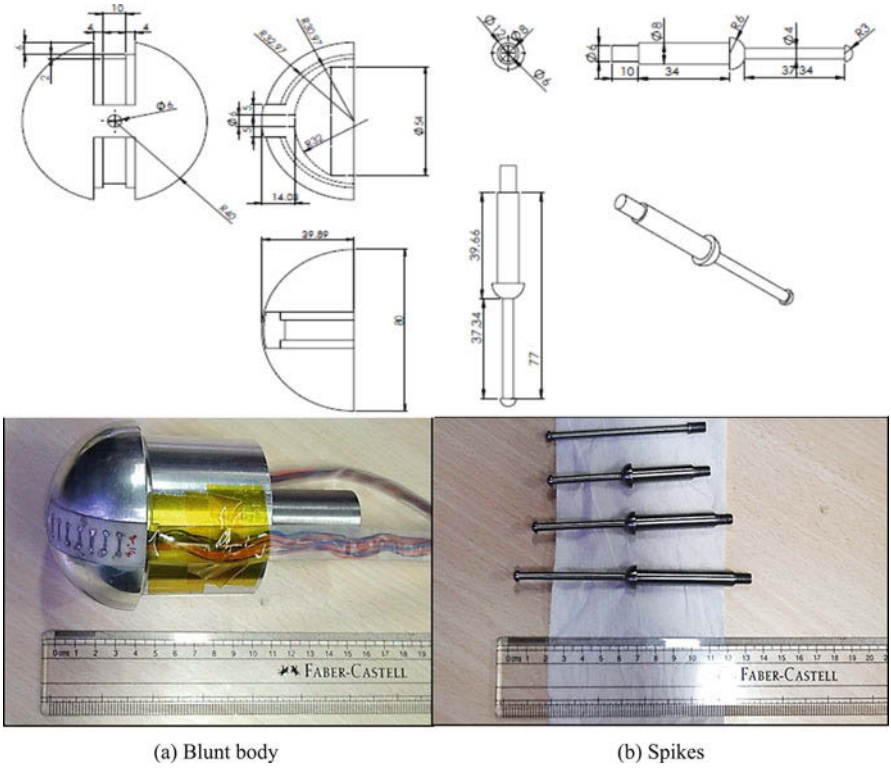

(a) Blunt body (b) Spikes

Fig. 2 Dimensions and representative images of the model made from Duralumin. (**a**) Blunt body, (**b**) Spikes

Table 1 Free stream conditions

Mach number M_∞	5.68
Temperature T_∞ (K)	149.26
Pressure P_∞ (kPa)	2.24
Density ρ_∞ (kg/m^2)	0.052
Velocity U_∞ (m/s)	1390
Reynolds number Re_∞ (m^{-1})	1.14
Stagnation enthalpy H_o (MJ/kg)	1.133

matrix-free implicit procedure based on symmetric Gauss-Seidel iterations. The effect of turbulence was modeled using the standard Spalart-Allmaras one-equation turbulence model (SA model). The HiFUN solver was known to scale over several thousand processor cores and requires as small as 10,000 volumes per processor core for achieving over 95% parallel efficiency. Convergence was declared after 4 decade fall in relative residue the change in force coefficients (1 C_L count $= 10^{-3}$, 1 C_D count $= 10^{-4}$) over 100 iterations was less than one count. All the computations

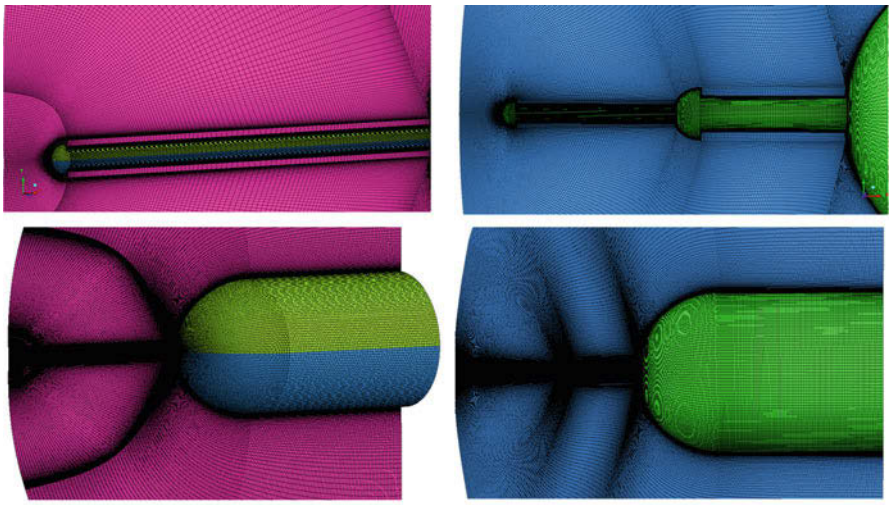

Fig. 3 Structured mesh of single and double spike

Table 2 Grid details

			Double spike		
Grid type	Blunt	Single spike	Coarse	Medium	Fine
Field cells	6 million	8 million	3 million	6 million	12 million
First cell (mm)	0.0003	0.0003	0.0003	0.0003	0.0003
No of cells close to the wall	34	34	34	34	34

presented have been carried out using structured grids. These grids have been generated in Ansys ICEMCFD using blocking mythology.

A sequence of medium and fine grids for double spike configurations were generated for the grid convergence study (Fig. 3), details of which is given in Table 2. All three categories of grids meet the y + requirement typically needed for RANS computations.

3 Results and Discussion

3.1 Experimental Heat Flux

The heat transfer measurements are carried out on a blunt body with single and double spikes. Model size would influence the unsteadiness of the flow field by increasing the number of body passes the fluid would have over the model in the test

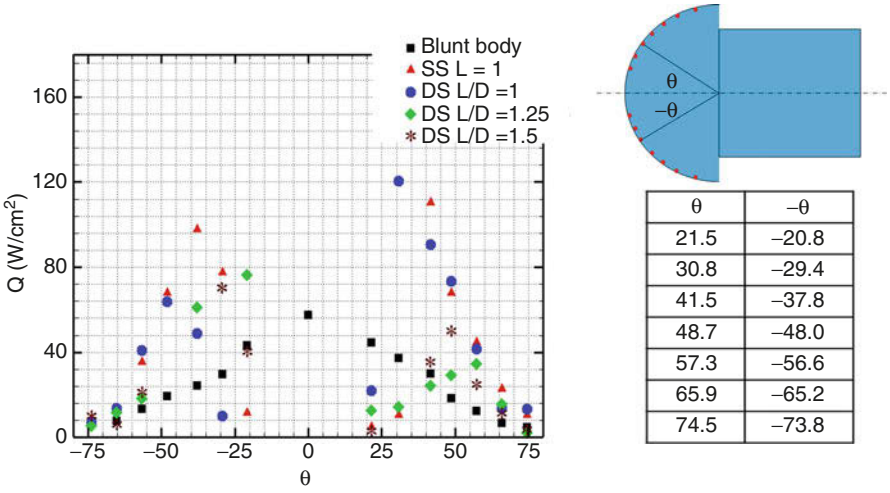

θ	–θ
21.5	–20.8
30.8	–29.4
41.5	–37.8
48.7	–48.0
57.3	–56.6
65.9	–65.2
74.5	–73.8

Fig. 4 Heat flux measured using platinum thin film sensor indicating location of a gauge

section within the given test time. Fourteen thin film gauges were accommodated along a ray on a Macor strip on this model surface. Around 30% reduction in heat transfer of double spike in comparison to single spike was observed (Fig. 4). Indicated heat transfer is an average of the eight to ten repeatable experiments. The measured heat transfer rates exhibit scatter near the reattachment zone of the model indicating flow unsteadiness. Though the fluctuation in some gauges was large, based on the uncertainties associated with the gauge characteristics, circuitry, data acquisition systems, reduction techniques, and the tunnel-free stream conditions, the measured values of heat transfer rates were believed to be accurate to ±8.09%. The figure contains heat flux data of double spike L/D = 1.25 and 1.5 indicating increase in the length of the spike leads to lesser heat flux. More extensive studies are to be carried out on the latter. Keeping within the scopes of the current study, we constrain our work to understand spikes with L/D = 1.

3.2 HiFUN Simulation

This section presents a discussion on the results obtained from simulations of hemispherical blunt body, grid convergence study of double spike, and comparison of the single and double spike for medium category grids along with the experimental model in CFD. All simulations are steady and performed for laminar case and also with the use of SA turbulence model. Figure 5 shows that for hemispherical blunt body, HiFUN simulation predicted the heat flux values by around 15% compared to the experimental values, although a very similar trend was observed. Also, no changes in turbulence and laminar simulation were seen;

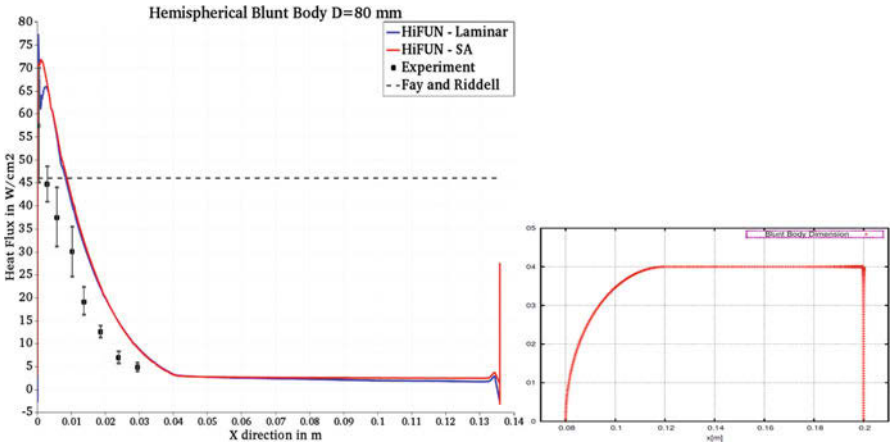

Fig. 5 HiFUN and experimental comparison of the blunt body

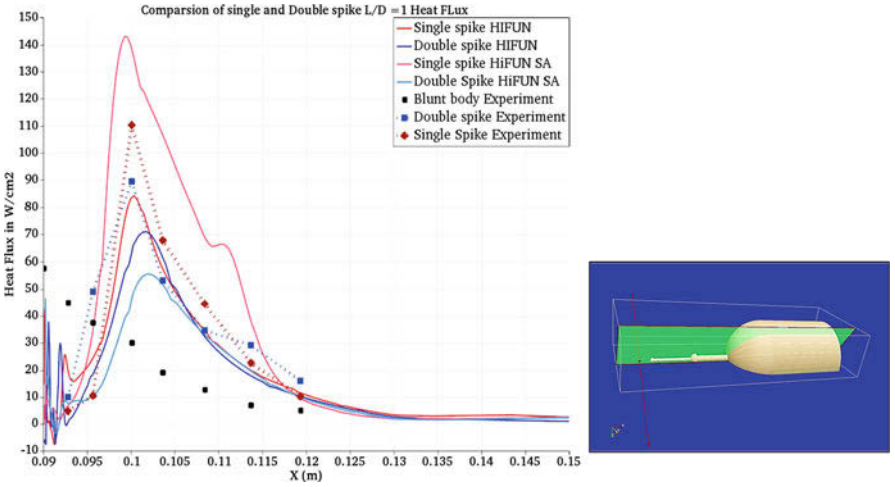

Fig. 6 HiFUN and experimental comparison of the single and double spike

except at the stagnation point, the laminar simulation showed a shift in peak heat flux value. This can be attributed to the stiffness of the grid or resolving the large change in gradient at this location.

The grid convergence study for the double spike L/D = 1 is shown in Fig. 6. The heat flux and pressure of the different grids showed the curves to be closer to the experimental values except for the medium and fine grid of HiFUN SA simulations. This is because the solution has not been converged. Since it is high-speed flow simulation, the convergence had to be monitored with careful control of CFL. Figure 7 shows that the HiFUN simulation captures the trend in both single

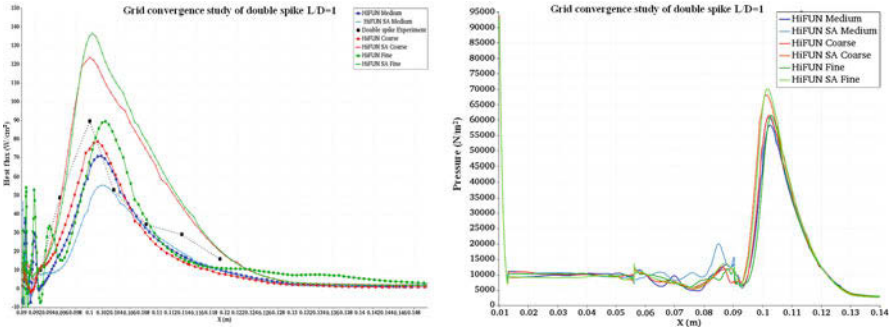

Fig. 7 Grid convergence for double spike, L/D = 1. Left, heat flux (W/cm^2); right, pressure (N/m^2)

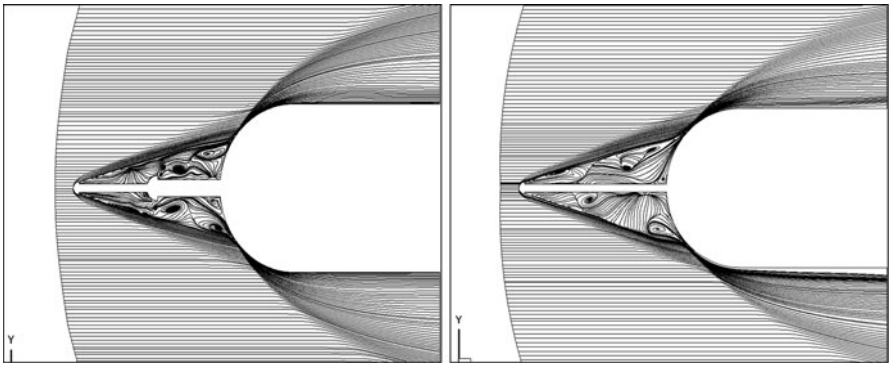

Fig. 8 Streamline comparison between double spike (left) and single spike (right)

and double spikes, as seen in the experiments. The lesser heat flux of double spike compared to single spike is also seen in the simulations.

From Fig. 8, it was observed that the oblique shock structure remained the same for both double and single spikes. The double spike separation bubble structure and activity was more compared to the single spike. This could be the reason for the lesser heat flux for double spike as compared to single spike. Also, we observed an asymmetry in the bubble structure. As of now, the physics behind this is not well understood, and more studies have to be performed.

The drag coefficients for HiFUN laminar simulation are the following: blunt body $C_D = 0.4569$, single spike $C_D = 0.2787$, and double spike $C_D = 0.2735$. Double spike shows 2% reduction in drag compared to single spike. Our future study includes drag measurement.

4 Conclusion

This investigation contains comparison of double disk spiked with the single spike. From the experiments we observed that double spike (L/D = 1) produces 25–30% reduction in heat transfer as compared to single spike. Good trend in heat transfer data between experiments and HiFUN computations are clearly visible. The double spike drag obtained from HiFUN simulation shows 2% reduction as compared to that of single spike. Quantitative analysis would require more experiments, and optimum double-disk configurations need to be obtained through future studies.

References

1. Ahmed, Qin, Prog. Aerosp. Sci. **47**, 425–449 (2011)
2. S.R. Alexander NACA RM L6K08 (1947)
3. D.H. Crawford NASA TN-D-118 (1959)
4. M.B. Gerdroodbary, S.M. Hosseinalipour, Acta Astraonaut **67**, 180–193 (2010)
5. PhD Thesis: VirenMenezes. Indian Insitutute of Science (2003)
6. R. Yadav, V. Guven, Aeronaut. J. **117**, 913–928 (2013)
7. S. Joshi, R. Yadav, Int. J. Appl. Eng. Res. **11**(1), 366–376 (2016)
8. R.J. Vidal, Cornell Aeronautical Laboratory Report WADC TN.56-315 (1956)

Numerical Investigation on the Effects of Air Dissociation upon Hypersonic Projectile in Standard Atmospheric Air

Hirotaka Kasahara and Akiko Matsuo

Abstract In this paper, the aerodynamic and thermal effects on hypersonic projectile which is launched by ground-based railgun are investigated. Air dissociation effect, which is the typical chemical reaction in hypersonic regime, is focused due to this influence to aerodynamic coefficient and temperature. Around projectile tip, strong dissociation reaction is generated due to high pressure and temperature. Also, there are dissociation region in the back part because of recirculation region. While the effect of dissociation to aerodynamic coefficient is small, surface temperature is affected by dissociation reaction.

1 Introduction

In recent years, many researches of railgun were conducted for the application of supersonic or hypersonic launcher [1, 2]. Lorentz force, which is generated by interaction between two parallel conductors, accelerates projectile, while traditional launcher which driven gas is light gas or combustion gas of solid propellant gains acceleration by fluid force. In conventional launcher, there is restriction about maximum projectile velocity in accelerating phase due to initial sonic speed of driven gas. Then, high-pressure light gas is required in order to reach hypersonic regime at muzzle velocity. In contrast, there are not any restrictions from fluid dynamics to maximum projectile speed in railgun. Utilizing no-pressure limitation and sonic speed, railgun has been developed in various research institutions [3, 4].

In traditional hypersonic analysis, the flight or inlet condition was set as rarefied gas since hypersonic flow occurs only in space craft reentry or near orbit [5]. As a result, various phenomena were obtained through experiments and numerical

H. Kasahara (✉)
Nagoya University, Nagoya, Japan
e-mail: kshrx4a@keio.jp

A. Matsuo
Keio University, Yokohama, Japan

A. Sasoh et al. (eds.), *31st International Symposium on Shock Waves 2*,
https://doi.org/10.1007/978-3-319-91017-8_132

calculations. Air dissociation is one of these knowledges. Dissociation means the chemical reaction of air which N_2 or O_2 molecules separate into atoms in this paper. It was clear that the dissociation reaction affects not only pressure and temperature distribution but flow field structure including shock shape in hypersonic flow. Therefore, in numerical simulation of reentry plane, this chemical reaction must be considered for calculating more valid solution. Similarly, the effect of projectile geometry has been considered for heat durability and optimum aerodynamic coefficient in hypersonic projectile.

Nevertheless, there are few researches about hypersonic projectile in standard atmospheric air, since there is no such flight condition without ground-based railgun [6, 7]. Then, the effects of chemical reactions to flow field and the relationship between projectile shape and aerodynamics or heat damage are not clear, which are substantial parameter for determining projectile geometry. In order to maintain initial high flight velocity or stable flight, the geometric characteristic of these projectile and details of flow field are extremely essential.

In this paper, the effects of air dissociation are investigated by using 2D computational fluid dynamics. For evaluating the effect of chemical reaction, changes of aerodynamic coefficient, two types of simulation with and without dissociation were conducted, and the difference of aerodynamic coefficient, temperature, and flow field structure was estimated.

2 Calculation Setup

2.1 Numerical Method

Projectile steady calculations are conducted by using two computational grids and methods. Governing equations are two-dimensional Navier-Stokes equations considering five chemical species, N_2, O_2, N, O, and NO, and source term of chemical reactions. Third-order SLAU2 (simple low-dissipation AUSM) with MUSCL method for discretization of convection term and second-order accurate central differential scheme for viscous term are applied. LU-ADI scheme (lower-upper alternating direction implicit) is adopted to time integration method. As turbulence model to calculate flow field of turbulent boundary layer, k-ω model is used. In this calculation, Park's reaction model [8] is employed to determine reaction rate and reaction rate coefficient in N_2-O_2 dissociation, and MTS (multi-time scale) method is applied to time integration of source term.

Figure 1 shows equilibrium state of air just behind shock for various Mach numbers by using zero-dimensional calculation with original Park's reaction model. Air starts to be dissociated around Mach number 7. Moreover, within the range of Mach number in this calculation, ion molecules and electron are not generated, because temperature behind shock is not so high that ionization is not induced. Hence, these species, NO^+, N_2^+, O_2^+, N^+, O^+, e^-, are ignored, and five neutral

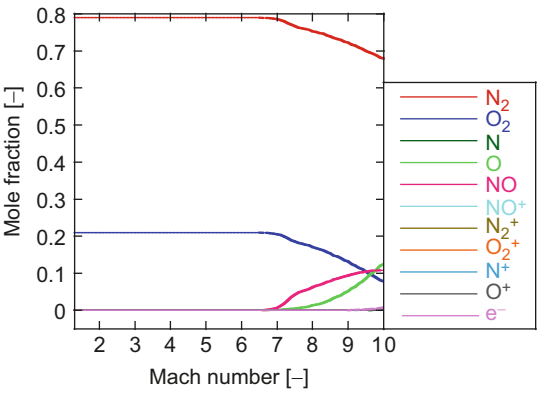

Fig. 1 Equilibrium behind shock (upstream condition: $P = 0.1013$ MPa, $T = 300$ K)

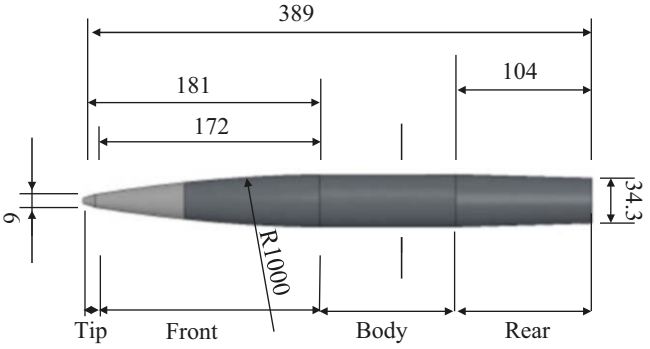

Fig. 2 Projectile shape

air species, N_2, O_2, N, O, NO, are considered for the numerical simulation at flight condition.

2.2 *Calculation Target*

The target of calculation is hypersonic projectile with blunt head as shown in Fig. 2, which geometry is determined by empirical methods for optimum shape. The length of projectile is 389 mm and diameter is 40 mm. The projectile consists of 181 mm front area, 104 mm body part, and 104 mm back part. The front part has R1000 curvature toward projectile tip and connected tip part which is cut off vertically. Inlet condition is set as standard atmospheric condition, that is, pressure is 0.1013 MPa, temperature is 300 K, and chemical species are 23.3 vol.% O_2 and 76.7 vol.% N_2 by mass. In this calculation, inlet Mach number is set as 7–10.

3 Result and Discussion

3.1 Flow Field Around Projectile ($M = 7$)

Inlet Mach number is set as 7 which is reproduced in some experiments. In Fig. 3, distributions of pressure and flow Mach number around the projectile are shown. Shock wave, which is generated in front of projectile tip, is detached bow shock, since there is a vertical cutoff on the tip. Also, expansion waves are generated at the joint of front, body, and rear parts, and the flows are accelerated by expansion. Especially, flow speed is larger than main flow speed $M = 7$ due to strong expansion wave of projectile end. This expansion wave also changes flow direction to axis line. This turned flow generates recompression region and recompression shock wave, which raise pressure and reduce flow velocity, as it collides on the axis line owing to axial symmetry property. There is backflow to projectile bottom caused by adverse pressure gradient. Then, these flow fields result in creating large recirculation region behind the projectile.

In Fig. 4, pressure distribution and streamline around projectile bottom are shown. In this region, two recirculation regions can be confirmed. There are several pressure and expansion waves on larger circulation regions. Thus, the recirculation region turns direction of flow several times as it were a solid wall. Figure 5 shows the distributions of pressure and temperature around the recirculation region. Discontinuous pressure rise takes place in the vicinity of the projectile bottom. This results from backflow speed which is accelerated by adverse pressure gradient and supersonic regime. Therefore, backflow shock is generated in this calculation condition. Similarly, temperature rises discontinuously for the same reason as lower of Fig. 5 shows. Temperature is also high value in the recirculation region, since flow speed is little and kinetic energy is converted into internal energy.

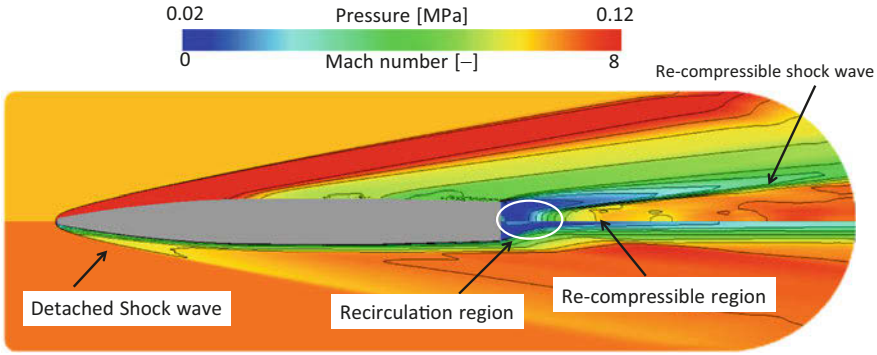

Fig. 3 Pressure and Mach number distribution

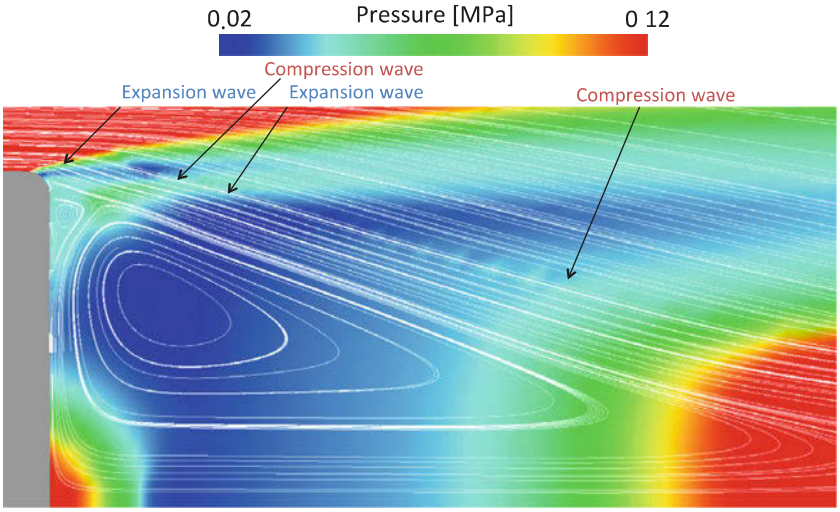

Fig. 4 Pressure distribution and streamline

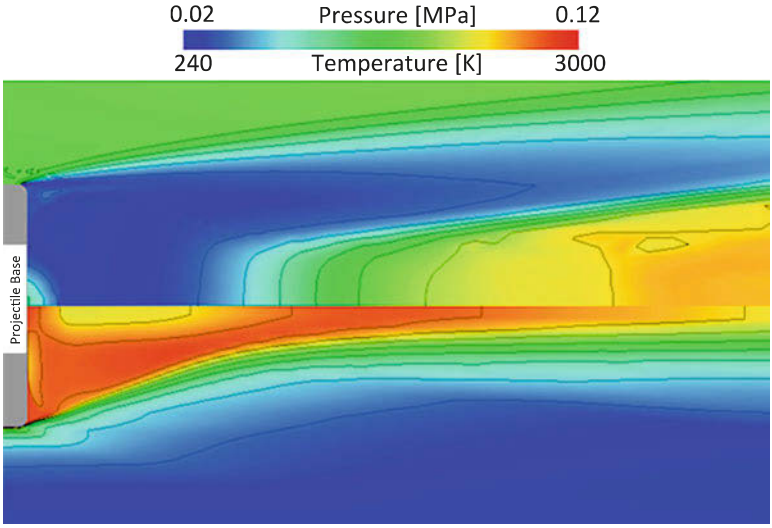

Fig. 5 Pressure and temperature distribution

3.2 The Effect of Air Dissociation

Four conditions, $M = 7$, 8, 9, and 10, are applied. Figure 6 shows the distribution of oxygen molecular mole fraction in each case. The contour line above the projectile corresponds to the domain of influence of velocity boundary layer. While product materials disappear in $M = 7$ due to expansion wave around projectile tip,

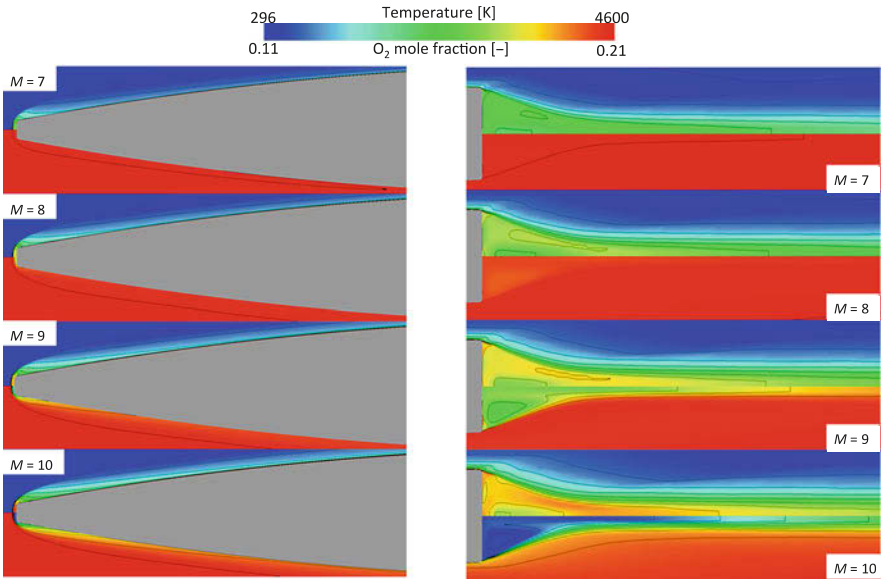

Fig. 6 Temperature and mole fraction distribution of O_2 around projectile

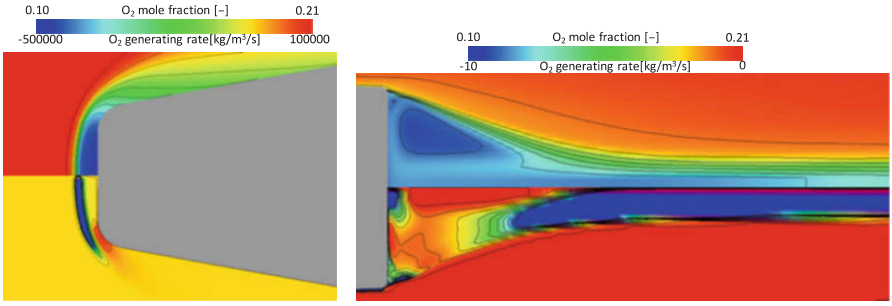

Fig. 7 O_2 mole fraction and generation rate around projectile tip (**a**) and rear part (**b**) in $M = 10$

dissociation reaction maintains in boundary layer in $M = 10$, where temperature is high due to the increase of Mach number. Then, mole fraction on the projectile surface is changed from standard atmospheric condition because of rise of Mach number.

Around the tip part, the similar dissociation reaction as $M = 7$ is generated in all conditions. Figure 7 shows mole fraction and generating rate of oxygen molecule in $M = 10$. Although there are similar distributions, the reaction region is narrowed and the chemical reaction reaches constant equilibrium near the projectile tip. Therefore, larger Mach number increases the equilibrium of reactive flow. Also, strong backward reaction is generated around the corner of the tip.

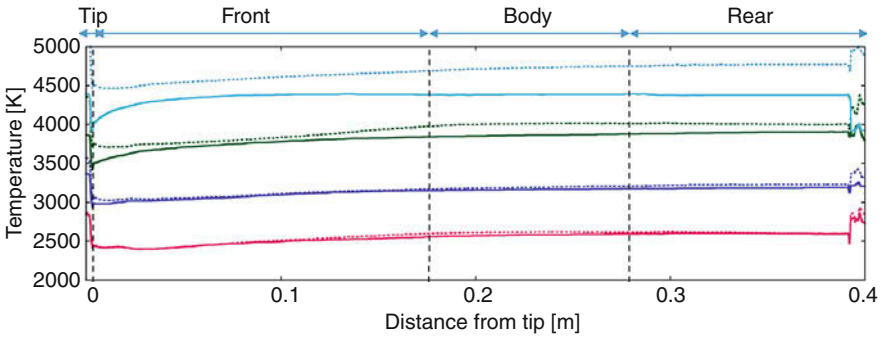

Fig. 8 Temperature distribution on the projectile surface (solid line, w/ reaction; broken line, w/o reaction)

In $M \geq 9$ conditions, dissociation arises not only in front of the projectile but also behind as Fig. 6 shows. Figure 7 indicates the mole fraction and generating speed of oxygen molecule behind the projectile in $M = 10$. What makes it clear from this figure is that the regions with large generating rate are re-compressible region and backflow shock. In this region, the high temperature and pressure are generated by adiabatic compression of shock wave like the tip part. On the other hand, dissociation does not occur on the axis line due to lower temperature, since backflow accelerates to supersonic. While oxygen mole fraction is small, generating rate in recirculation region is also small. In this region, temperature keeps high and flow reaches equilibrium since flow loses velocity.

Figure 8 shows temperature distribution on the projectile surface. Temperature on the side wall between with and without reaction is not changed in $M = 7$ and 8. In contrast, there is a little difference in $M = 9$ and is 300 K difference in $M = 10$. Furthermore, temperature on the front part is extremely affected by dissociation. In $M = 10$ case, there is 1000 K difference around the axis line. Temperature on the tip part is susceptible to dissociation. Then, consideration about air dissociation is indispensable in hypersonic projectile.

Finally, drag force is considered. Table 1 shows aerodynamic coefficient. The error of chemical reaction is under 1% in all inlet condition, and dissociation does not affect the evaluation of aerodynamic coefficient in this velocity regime.

4 Conclusion

In this paper, the numerical simulation about hypersonic projectile launched by ground-based railgun with considering dissociation effect is carried out. In intermediate hypersonic sonic condition $7 \leq M \leq 10$, air dissociation is generated around the tip and front part. In $M \geq 9$, chemical reaction also occurs behind the projectile due to the high temperature at recirculation region. The influence of

Table 1 Aerodynamic coefficient result

M	Dissociation	Pressure drag [$\times 10^{-2}$]	Viscous drag [$\times 10^{-2}$]
7	w/o	8.76	2.19
7	w/	8.77	2.21
8	w/o	7.26	1.99
8	w/	7.28	1.99
9	w/o	6.94	1.81
9	w/	6.99	1.83
10	w/o	6.70	1.69
10	w/	6.77	1.73

dissociation on temperature is proportional to the projectile velocity. By contrast, pressure distribution is still independent of dissociation reaction.

From these results, the consideration about air dissociation is indispensable for estimating heat load in standard atmospheric condition and has little effect on calculating aerodynamic character of the projectile.

References

1. S. Humdertmark, D. Lancelle, A scenario for a future European shipboard railgun. IEEE Trans. Plazma Sci. **43**(5), 1194 (2015)
2. C. Robert et al., The Feasibility of Railgun Horizontal-Launch Assist, Technical Report KSC-13597, KSC-2010-010, NASA, 2011
3. M.M. Tower et al., Hypervelocity impact testing using an electromagnetic railgun assist. Int. J. Impact Eng. **5**(1–4), 635–644 (1987)
4. V.E. Fortov, Railgun experiment and computer simulation of hypervelocity impact of lexan projectile on aluminum target. Int. J. Impact Eng. **33**, 253–262 (2006)
5. Furudate et al., Behavior of two-temperature model in intermediate hypersonic flow, in *Aero space Nunmerical Simulation Technology Symposium*, vol. 41, 1999
6. Jorg Behrens et al., Hypersonic and electromagnetic Railgun Technology as a future alternative for the launce of suborbital payloads, in *Proceedings of the 16th ESA Symposium on European Rocket and Balloon Programes and Related Research*, 2–5, 2003
7. O. Bozic, P. Giese, Aerothermodynamic aspects of railgun-assisted launches of projectiles with sub and low-earth-orbit payloads. IEEE Trans. Magn. **43**(1), 474 (2007)
8. C. Park, *Nonequilibrium Hypersonic Aerothermodynamics* (Awielyey Interscience Publication, New York, 1990)

Shockwave Oscillation Under Critical Starting Mach Number in Hypersonic Inlet

Pengfei Xiong, Hanchen Bai, Xiaofei Zhai, Jun Chen, and Zhenfeng Wang

Abstract The motivation of this paper was to study the characteristics of start-up and the feature of shockwave under low Mach number in hypersonic inlet. The characteristics of flow field and shockwave at the critical starting Mach number ($Ma3.8$) without back pressure were numerically studied in the hypersonic inlet in which the design condition was Ma6. The results showed that the flow field and shockwave were unstable, and they were under some certain periodic oscillation state at the critical starting Mach number ($Ma3.8$). The total mass flow rate between inflow and outlet, the mass flow of throat, and the mass average Mach number of outlet all also showed periodic oscillation. Unmatched mass flow that passed through the throat that could not all pass through the exit of isolator was the induced reason of periodic oscillation. The block of the max mass flux flow through the area of throat was the main factor that caused the periodic oscillation of flow field and shockwave. The unmatched mass flux in internal channel leads to periodic "split out" and "swallow in" of "separation bubble" from the internal channel, which formed the periodic oscillation of flow field and shockwave.

1 Introduction

The conditions of start and unstart are common problems in hypersonic inlets. There are many reasons that led to unstart of hypersonic inlets such as high back pressure, big attack angle, and low Mach number. The unstart inlet often caused the pressure load of compressing surface increased sharply, the coefficient of resistance increased, and the heat load changed [1–3]. All these changes could make damage of the component structure and the stable fly condition of the vehicles. Also the decreased captured mass flow for unstart inlet could not supply the enough oxidant

P. Xiong (✉) · H. Bai · X. Zhai · J. Chen · Z. Wang
Science and Technology on Scramjet Laboratory of Hypervelocity Aerodynamics Institute, CARDC, Mianyang, China

A. Sasoh et al. (eds.), *31st International Symposium on Shock Waves 2*,
https://doi.org/10.1007/978-3-319-91017-8_133

into the combustor; thus, the engine could not work effectively. Thus the unstart characteristics of hypersonic inlets have been widely focused, and many scholars have made studies in this area.

The flow field oscillation and unstable characteristics of the unstart inlet caused by anti-pressure were experimentally studied by Tan [4, 5]. The results showed that the flow field could oscillate when the anti-pressure was strong enough. Also the characteristics of flow field were measured by PIV (particle image velocimetry) by Wagner [6, 7]. Results showed that the shock chain was moved forward in isolator, and there were some flow vibration at a frequency of 124 Hz. The instantaneous velocity of shock wave was measured by Rodi [8] and Weiting [1]. The study conducted by Hawkins [9] indicated that the vibration of pressure could increase, and the vibration frequency could be more than 100 Hz when the inlet was under unstart. McDaniel [10] pointed out that the separation of boundary layer which induced by ignition of fuel on the sidewall of combustor could lead to unstart of inlet. The characteristics of unstart/restart of hypersonic inlets caused by variations of attack angle of freestream were numerically studied by Chang [11].

In the above, a lot of work about the unstable characteristics of hypersonic inlets were mainly focused on the influence of anti-pressure. Few studies were emphasized on the critical starting Mach number or low Mach number without anti-pressure. We are still confused with the reason and mechanism of flow oscillation in hypersonic inlets under low Mach number without anti-pressure. In order to explore this reason and mechanism of flow oscillation, the characteristics of flow field and the shockwave during the period of flow oscillation under the critical starting Mach number were discussed in detail.

2 Numerical Model

Physical model of the hypersonic inlet as shown in Fig. 1 was used to study the characteristics of flow field and the shockwave under the critical starting Mach number ($Ma3.8$) while the designed mach number was 6.

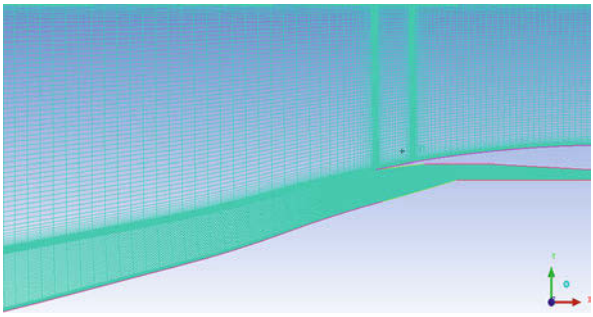

Fig. 1 Model of hypersonic inlet

Table 1 Flow conditions at the entrance

Ma	*T*/K	*P*/pa
3.8	216.65	10,353

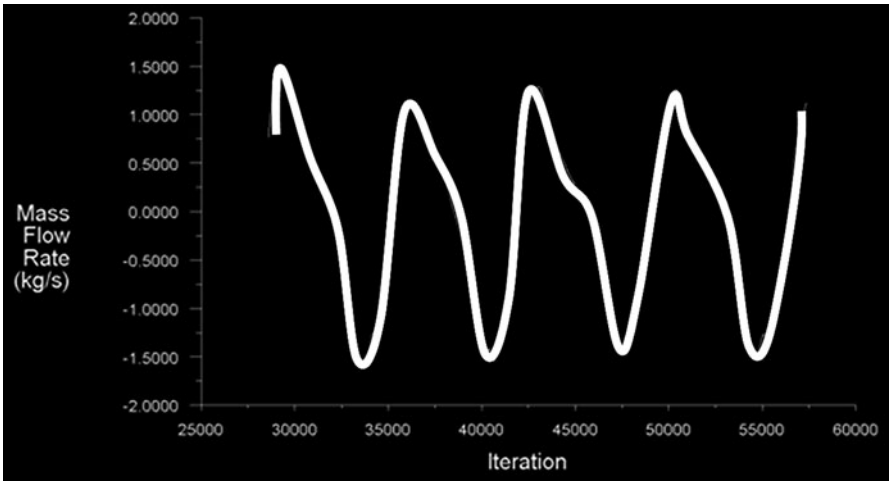

Fig. 2 Total mass flow rate between inflow and outlet

Numerical simulations were conducted using the Reynolds-averaged Navier-Stokes (RANS) equation. The structured mesh of quadrilateral cells was generated around the physical models with a grid size of 400(x-direction) by 400(y-direction) cells. Mesh refinement tests have been carried out on a finer mesh of 500 by 500 cells, and grid independence has been found. Grid stretching is applied to near-center body surface to increase the resolution of the boundary layer.

The initial far-field flow condition was shown in Table 1. An adiabatic wall condition was assumed. The pressure of outlet was set to zero.

3 Results and Analysis

3.1 Total Characteristics of Flow Field

The total mass flow rate between inflow and outlet and the mass average Mach number of outlet showed in Figs. 2 and 3 indicate that flow field of hypersonic inlet was under periodic oscillation at the critical starting Mach number.

As shown in Fig. 4a, there was a small "separation bubble" near the shut in the flow field which is defined as the initial condition of one period under the critical Mach number(*Ma*3.8) while the designed Mach number was 6. According to the capture mass flux and the flow field, the hypersonic inlet was started under this initial condition. Also we could see that the separation shockwave interacted with

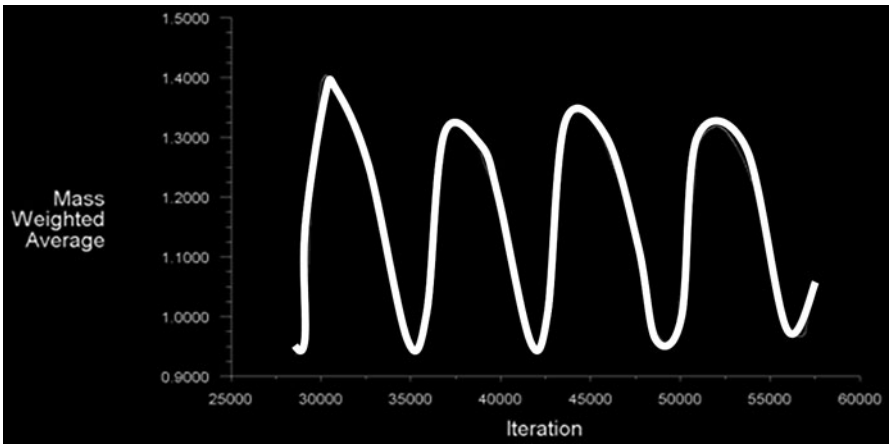

Fig. 3 Mass-weighted average Mach number of outlet

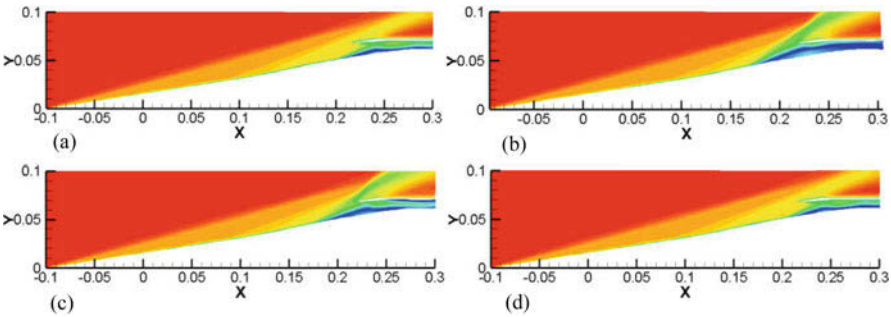

Fig. 4 Mach number contour in one oscillation period. (**a**) $t = 0$, (**b**) $t = 1/4$ T, (**c**) $t = 1/2$ T, (**d**) $t = \mathrm{T}$

the lip shockwave, and the end point of separation shockwave was in the internal compressing channel. As the compute step moved on, when the flow field was under one fourth period as shown in Fig. 4b, the "separation bubble" was so large that only few mass flows into the internal channel were captured. The separation shockwave could not interact with the lip shockwave anymore, but interact with the external compression shockwave and then form a strong shockwave which is apart from the lip. As the compute step kept moving on, when the flow field was under two fourth period as shown in Fig. 4c, the "separation bubble" became smaller than that in Fig. 4b. It was showed that the captured mass flows increased under this condition. The separation shockwave still interacted with the external compression shockwave and then form a strong shockwave. However, the strong shockwave was moving toward the lip. Just as the compute step is going on, when the flow field was under one period as shown in Fig. 4d, the "separation bubble" and the flow field became same as that in Fig. 4a. It suggested that the flow field and shockwave have completed one oscillation period.

From the simulation results above, many unsteady characteristics could also be obtained by steady method. Thus the steady numerical method at some certain extent could be used to obtain some unsteady characteristics of the oscillation flow of hypersonic inlet from the numerical stratagem. Yu [12] has also proved that many of the shockwave oscillation features with anti-pressure of hypersonic inlet could be realized by steady numerical method.

3.2 Detailed Analysis of the Periodic Oscillation of Flow Field

In order to fully understand the oscillation process and find the oscillation mechanism, we have made more detailed analysis about the change of flow field, the shockwave, the mass flow of throat and outlet, and the "separation bubble" under every compute step of one oscillation period.

As shown in Fig. 5, the captured mass flux in the throat and outlet also showed the periodic oscillation of the flow field. The max and minimum captured mass flux of throat were 0.55 and 0.18. The inlet experienced start, unstart, and restart periodic processes. However, it showed that the max and minimum captured mass flux of outlet were 0.5 and 0.24.

From Fig. 5, the change of captured mass flux at the throat and outlet was not same with each other. The change of captured mass flux at the outlet was later than that at the throat. At some certain time step, both conditions arrived at the same point. However, this condition could not be maintained. The mass flow would be blocked at the area of the throat when the captured mass flux at the entrance of the inlet was large than the max captured mass flux at the throat. At this time, the "separation bubble" would be increased gradually by this "blocking" factor, and the separation shockwave would be splitted out from the lip. Thus the spillage of flow out from the internal channel is realized and the captured mass flow is decreased. Though the mass flux flow through the outlet was increased, the max flux released was always less than the max captured at the entrance. So the effect of "blocking" could not be solved.

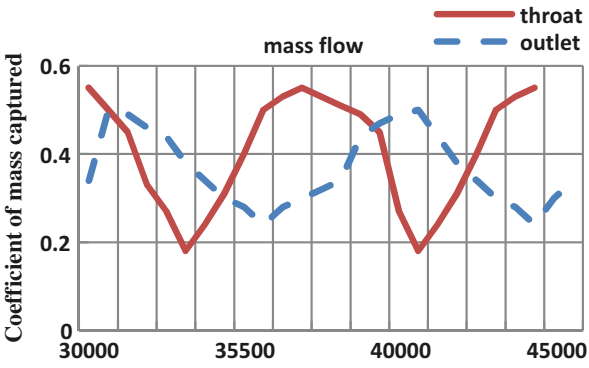

Fig. 5 Coefficient of mass captured at the throat and outlet

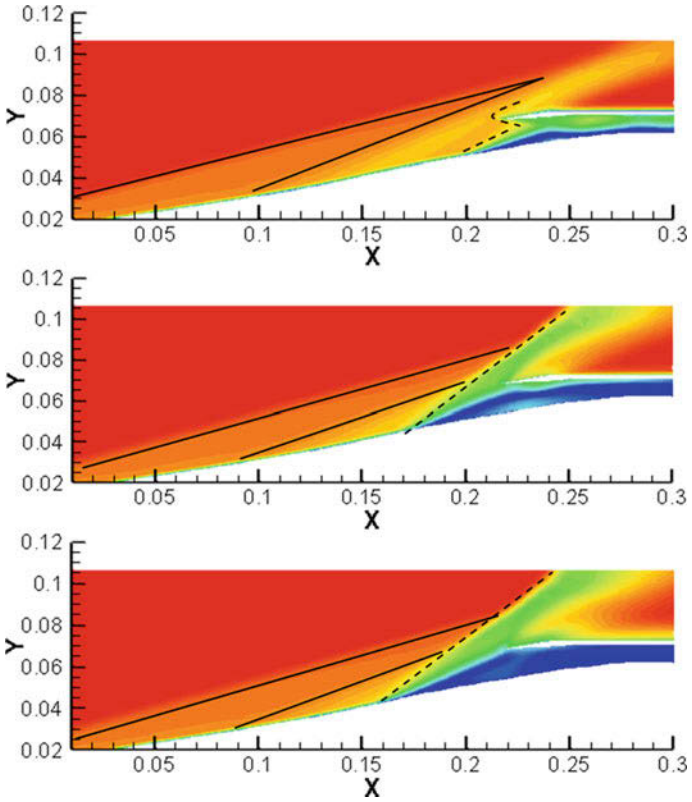

Fig. 6 "Separation bubble" became larger at the first half period

From Fig. 6, the "separation bubble" became larger and larger due to the mass flow that is captured from the entrance at initial condition that could not all pass through the throat. The captured flow would spill some out from the entrance of the inner channel to meet the passing of the mass flux that accumulated at the throat through the outlet. The separation shockwave became far away from the position of the lip. The captured mass flow could all pass through the outlet when the "separation bubble" was large enough; the "separation bubble" and separation shockwave would not move forward anymore. However, the instantaneous capability of the inlet became very strong.

From Fig. 7, the "separation bubble" became smaller and smaller due to the strong capability of the mass captured in the internal channel at the second period. The captured mass flow became max at the throat again when the flow field of inlet experienced one period. The "separation bubble" became smallest again. The separation shockwave again moved in the internal channel. The flow field and shockwave experienced one oscillation period.

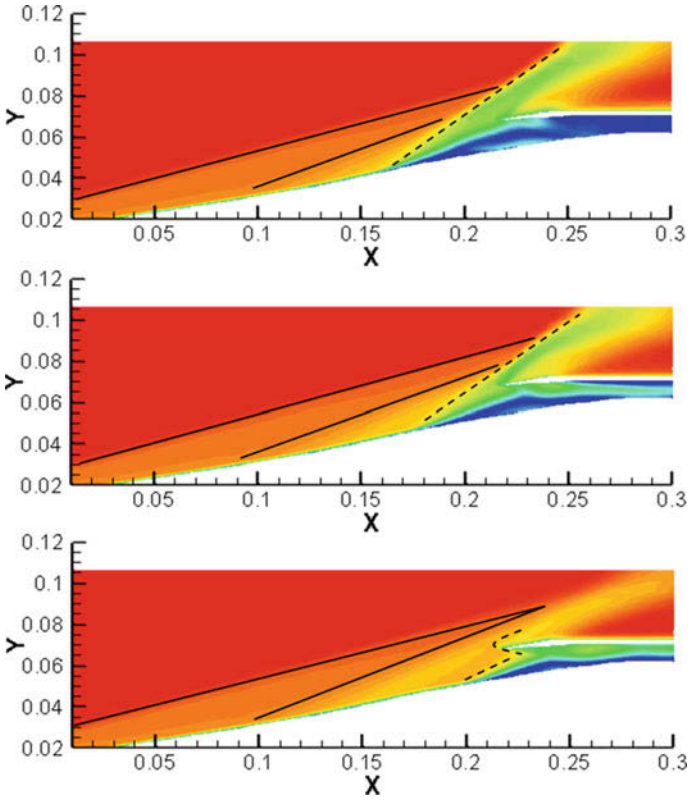

Fig. 7 "Separation bubble" became smaller at the second period

4 Conclusion

(a) If there was a periodic oscillation of the flow field under the critical starting Mach number of hypersonic inlet, the inlet would experience start-unstart-restart process.
(b) The blocking of captured mass flow at the throat and the unmatched mass flux in internal channel were the main factors that lead to the periodic oscillation of flow field and shockwave.
(c) The steady numerical method at some extent could be used to obtain some important unsteady characteristics of the oscillation flow of hypersonic inlet from the numerical stratagem.

Acknowledgment This work was supported by Grant No. 51606212 of the National Natural Science Foundation of China.

References

1. A.R. Weiting, *Exploratory study of transient unstart phenomena in a three-dimensional fixed-geometry scramjet engine*[R], NASA TND-8156, 1976
2. T. Shmura, T. Mitani, N. Sakuranaka, et al., *Load oscillations caused by unstart of hypersonic wind tunnels and engines*[J]. J. Propuls. Power **14**(3), 348–353 (1998)
3. C.R. McClintion , J.L. Hunt, R.H. Ricketts, et al., *Airbreathing hypersonic technology vision vehicles and development dreams*[R], AIAA-1999-4978, 1999
4. H.J. Tan, S. Sun, Z.L. Yin, *Oscillatory flows of rectangular hypersonic inlet unstart caused by downstream mass-flow choking*[J]. J. Propuls. Power **25**(1), 138–147 (2009)
5. H.J. Tan, R.W. Guo, *Experimental study of the unstable unstarted condition of a hypersonic inlet at Mach 8*[J]. J. Propuls. Power **23**(4), 783–788 (2007)
6. J.L. Wagner, K.B. Yuceil, N.T. Clemens, *PIV measurements of unstart of an inlet-isolator model in a Mach 5 flow*[R], AIAA-2009-4209, 2009
7. J.L. Wagner, A. Valdivia, K.B. Yuceil, et al., *An experimental investigation of supersonic inlet unstart*[R], AIAA-2007-4352, 2007
8. P.E. Rodi, S. Emami, C.A. Trexler, *Unsteady pressure behavior in a ramjet/scramjet inlet*[J]. J. Propuls. Power **12**(3), 486–493 (1996)
9. W.R. Hawkins, E.J. Marquart, *Two-dimensional generic inlet unstart detection at Mach2.5-5.0*[R], AIAA-95-6016, 1995
10. K.S. McDaniel, J.R. Edwards, *Three-dimensional simulation of thermal choking in a model scramjet combustor*[R], AIAA-2001-0382, 2001
11. J.T. Chang, D.R. Yu, W. Bao, *Characteristic analysis of unstart/restart of hypersonic inlets caused by variations of attack angle of freestream*[J]. J. Aerospace Power **23**(5), 816–821 (2008)
12. A.Y. Yu, D.W. Yang, J. Wu, *A numerical research on forecasting shock oscillations of scram-inlets*[C], in The Fifteenth National Conference of Shock and Shock Tube, Anhui, China, 2010

Variation in Spanwise Direction of Transonic Buffet on a Three-Dimensional Wing

Y. Kojima, M. Kameda, A. Hashimoto, and T. Aoyama

Abstract Transonic buffet is a self-induced oscillation of shock wave appearing at high angles of attack. We simulated the transonic buffet over the NASA-CRM wing with a zonal detached eddy simulation (ZDES). We found that the frequency characteristics of the surface pressure fluctuation are varied in the spanwise direction and are categorized into three patterns. In the inboard region, the buffet exhibits a periodical oscillation with a single dominant frequency equivalent to the 2D wing. At the mid-span of the wing, although the buffet frequency is equal to the inboard, the wave front of shock moves in the spanwise direction. In the outboard, the spectrum exhibits two dominant modes. One is a periodical oscillation similar to the 2D wing. The other is a high-frequency fluctuation propagating in spanwise direction.

1 Introduction

Shock wave/boundary layer interaction on the suction side of the wing at high Mach number and/or high angle of attack leads to large-scale self-sustained motion of the shock wave. This phenomenon is called transonic buffet. The buffet potentially leads to dangerous structural vibrations so that it constrains the flight envelope of commercial aircraft.

Many groups have investigated the transonic buffet experimentally. Most studies on the transonic buffet phenomenon focus on the buffet of two-dimensional (2D) wing [1, 2]. Here, the 2D wing is defined as the wing which cross-sectional shape at arbitrary spanwise position is equal to root sectional shape. The characteristics of the 2D buffet are well known. As described by several authors, the 3D buffet has

Y. Kojima (✉) · M. Kameda
Tokyo University of Agriculture and Technology, Koganei, Tokyo, Japan
e-mail: y-kojima@st.go.tuat.ac.jp

A. Hashimoto · T. Aoyama
Japan Aerospace Exploration Agency, Chofu, Tokyo, Japan

A. Sasoh et al. (eds.), *31st International Symposium on Shock Waves 2*,
https://doi.org/10.1007/978-3-319-91017-8_134

different characteristics from the 2D one [3, 4]. In the 2D case, the oscillation of the buffet is periodical and has a well-marked peak of spectrum. According to Lee [5], frequency of 2D buffet is $St = 0.08$. Here, the Strouhal number, St, is defined as $St = fc/U$. The U and c are the uniform flow speed and the local chord length, respectively. In the 3D case, spectrum of the buffet is more broadband. Koike et al. [6] tested a NASA Common Research Model (CRM) equipped with 24 unsteady pressure sensors and observed a broad spectral around $St \approx 0.3$. In addition to the difference of spectrum, a few authors reported an existence of a propagation phenomenon in the spanwise direction from wing root side to wing tip side. Koike et al. and Dandois [7] reported the pressure fluctuation propagates in the spanwise direction, and its speed is about 0.19 $0.30a_\infty$ with a_∞ the speed of sound in the freestream.

Iovnovich et al. [8] simulated the 3D buffet with unsteady Reynolds-averaged Navier-Stokes (URANS) method, whereas Brunet et al. [9] and Sartor et al. [10] simulated it with detached eddy simulation (DES) method. Brunet et al. and Sartor et al. observed a broad spectrum, which is a similar tendency with the experiments. Iovnovich et al. simulated rectangular wing with sweep angle and studied its effect. The frequency of the buffet increases from $St = 0.07$ to 0.27 with increasing the sweep angle from 0° to 30°. Moreover, Iovnovich et al. and Sartor et al. reported a propagation phenomenon in the spanwise direction. Few studies focused on the buffet phenomenon on the realistic aircraft shape, and its mechanism and characteristic are not clear.

The purpose of this study is to clarify the characteristic and sustaining mechanism of 3D buffet on the realistic aircraft shape. This paper reports the results of simulation of the buffet on the NASA-CRM wing and its characteristic.

2 Numerical Setup

2.1 NASA Common Research Model (CRM)

This study focuses on NASA-CRM wing (see Fig. 1). The wing in this simulation is the same geometry as the wind tunnel model by Koike et al. [6]. The mean aerodynamic chord (MAC) is $c_{mac} = 151.31$ mm. The wing span is $b = 570.31$ mm,and the sweep angle is $\Lambda = 35^\circ$. This model does not take into account the effect of body and aeroelastic deformation.

Experiments are carried out at the 2m $\times$ 2m transonic wind tunnel in Chofu Aerospace Center of Japan Aerospace Exploration Agency (JAXA). The buffet on NASA-CRM wing-body model is tested at freestream Mach number $M_\infty = 0.85$, free stream total temperature $T_\infty = 323$ K , free stream total pressure $P_\infty = 80$ kPa , Reynolds number based on c_{mac}, $Re_c = 1.515 \times 10^6$, and angle of attack $\alpha = 5.37^\circ$.

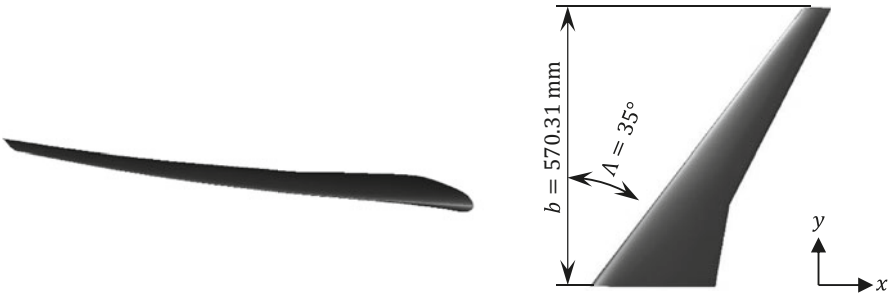

(a) Overall view (b) Top view

Fig. 1 Wing of NASA Common Research Model. (**a**) Overall view. (**b**) Top view

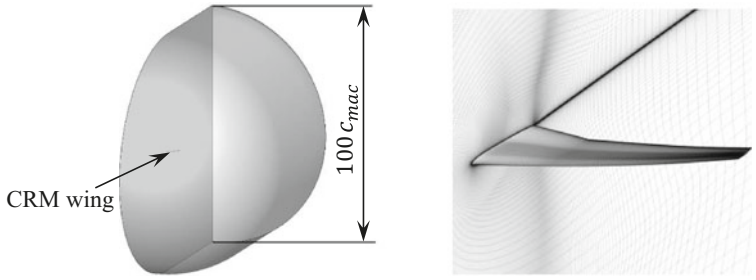

(a) Overall view (b) Mesh around the CRM wing

Fig. 2 Grid condition. (**a**) Overall view. (**b**) Mesh around the CRM wing

2.2 Grid

The topology of grid is C-O type (see Fig. 2). The domain of upper side of airfoil contains 171 × 351 × 122 points in chordwise, spanwise, normal direction of wall, respectively. A total number of grid points are equal to 2.8×10^7. The far-field condition is imposed at 100 times the MAC length.

2.3 Numerical Setup

An unstructured mesh-based flow solver, FaSTAR developed by JAXA, is employed in this study. In FaSTAR, the three-dimensional compressible Navier-Stokes equations are discretized by finite volume method. Velocity and length are nondimensionalized by speed of sound in the freestream and MAC length, respectively. A simple low-dissipation AUSM (SLAU) scheme is employed to evaluate the numerical inviscid flux. Gradient at cell center is evaluated by a Gauss-based weighted least squares method (GLSQ). Venkatakrishnan-like limiter extended for unstructured mesh is used. For time integration, LU-SGS implicit method is employed.

These calculations were performed on JAXA Supercomputer System generation 2 (JSS2).

2.4 Turbulence Model

As a turbulence model, we employ Spalart-Allmaras zonal detached eddy simulation (ZDES) [11] which is one kind of RANS/LES hybrid method suggested by Deck. In ZDES, the RANS mode is applied in wall vicinity region and the LES mode is applied elsewhere. The switching into LES mode occurs at a given distance from wall, d_w, prescribed by the user. According to Deck [12], it is possible to simulate 2D buffet accurately if the value of d_w is chosen suitably. In this study, we employ a unique value as d_w, which is defined by the boundary layer thickness just ahead of the shock. More specifically, it is the simple mean thickness of three different spanwise positions $\eta = 0.2$, 0.5, and 0.8. η is dimensionless coordinate in span direction, $\eta = y/(b/2)$.

3 Results and Discussion

3.1 Root Mean Square (RMS) of Pressure Fluctuation

We plot the position of maximum RMS value at each span direction y using the dot-and-dash line. The shock position is shifted upstream at the mid-span location. In Fig. 3b, we plotted the chordwise distribution of Cp RMS at two different spanwise positions ($\eta = 0.443$ and 0.555). Associated with the numerical results, we plotted the experimental data obtained by Koike et al. [6]. As shown in Fig. 3b, the shock position at $\eta = 0.555$ is located further upstream than at $\eta = 0.444$, whose trend

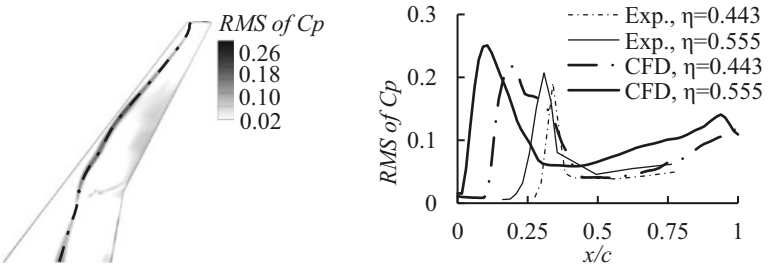

(a) Distribution on upper side of wing (b) Comparison with the experimental data

Fig. 3 RMS of C_p fluctuation. (**a**) Distribution on upper side of wing. (**b**) Comparison with the experimental data

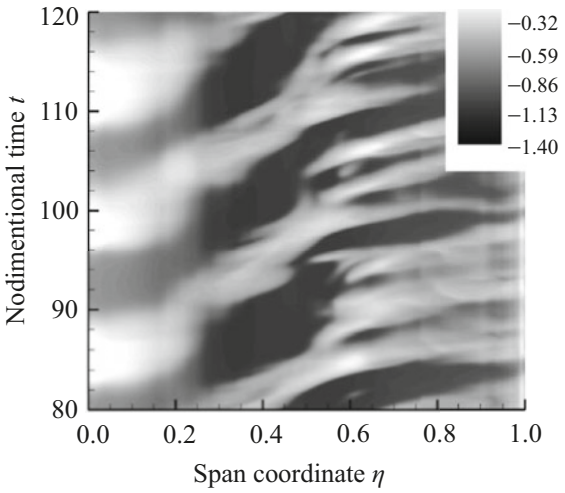

Fig. 4 Time-space contour of surface pressure coefficient

is observed both in CFD and wind tunnel test. The peak values of RMS of CFD are almost equal to the experiment. Although the shock position of CFD is different from the experiment, we can conclude that the transonic buffet on NASA-CRM wing is successfully captured in the present ZDES computation.

3.2 Time-Space Contour of Surface Pressure Coefficient

Figure 4 shows the time-space contours of the surface C_p fluctuation along the dashed-dotted line shown in Fig. 3. As shown in Fig. 4, the oscillation of the buffet is varied in spanwise direction which is categorized into three patterns.

In the inboard region ($\eta < 0.25$), the buffet exhibits a periodical vibration and appears to have a single dominant frequency. At the mid-span of the wing ($0.25 \leq \eta < 0.55$), the pressure fluctuation has a phase velocity in the spanwise direction because the shock wave front is moving. This phenomenon is a characteristic of 3D buffet, which is reported by Iovnovich et al. [8], Dandois, Koike et al. [6], and Sugioka et al. [13]. In outboard region ($0.55 \leq \eta$), buffet exhibits complicated oscillation, and the pressure fluctuation has a phase velocity in the spanwise direction.

3.3 Power Spectrum Density (PSD) of Pressure Fluctuation

The power spectral density of the pressure fluctuation shown in Fig. 4 was calculated in order to investigate the frequency characteristics of the oscillation of the buffet.

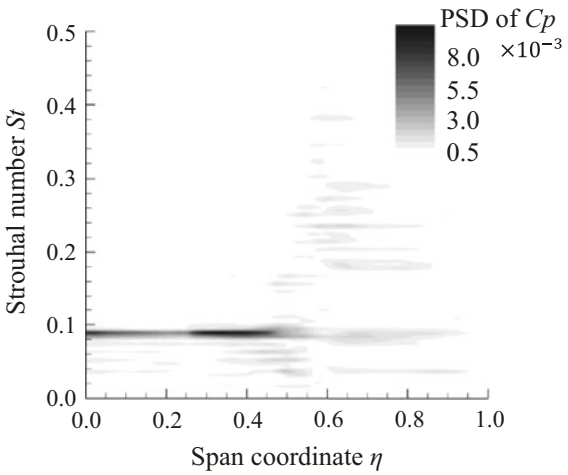

Fig. 5 PSD of pressure fluctuation

The PSD of pressure fluctuation is shown in Fig. 5. Here, the Strouhal number, St, is defined as $St = fc_{mac}/U_\infty$. As shown in Fig. 5, the oscillation in $\eta < 0.55$ has a single dominant frequency $St = 0.09$, and the oscillation in $\eta \geq 0.55$ is broadband. $St = 0.09$ is almost the same as $St = 0.08$ of the buffet frequency indicated by Lee. This agreement indicates that the buffet within $\eta < 0.55$ is sustained by mechanism proposed by Lee [5]. In the $\eta \geq 0.55$, the oscillation of the buffet has multiple dominant frequencies. Excluding the vibration of $St = 0.09$, the frequency is distributed in the range of $St = 0.2 - 0.4$. According to Koike et al. [6], the oscillation of the buffet in CRM has a frequency distributed around $St = 0.3$, which is the same as the simulated result in this study.

3.4 Phase Velocity of Shock Wave Front in Spanwise Direction

We calculate the phase velocity of the shock wave front in spanwise direction described in Section 3.2. Figure 6 shows a frequency-wavenumber spectrum of the pressure fluctuation in Fig. 4. Figure 6 is a frequency analysis results in the range of $0.25 \leq \eta < 1.0$. The phase velocity of the shock wave front is equal to the phase velocity of pressure propagation. The phase velocity is calculated by $v_p = \omega/k$. Here, $\omega = 2\pi StU_\infty/c_{mac}$ is angular frequency, and k is wavenumber.

The distribution of peak in the range of $St = 0.2 - 0.4$ indicates that the phase velocity in this frequency band is equal to $v_p = 0.4a_\infty$. Since this frequency band was observed in $0.55 \leq \eta$, the propagation phase velocity in this region is equal to $0.4a_\infty$. Also, the phase velocity calculated by the peak existing at $k = 3$, $St = 0.09$, is equal to $v_p = 0.2a_\infty$. In addition, the peak existing at $k = 0$, $St = 0.09$, indicates uniform vibration in the span direction.

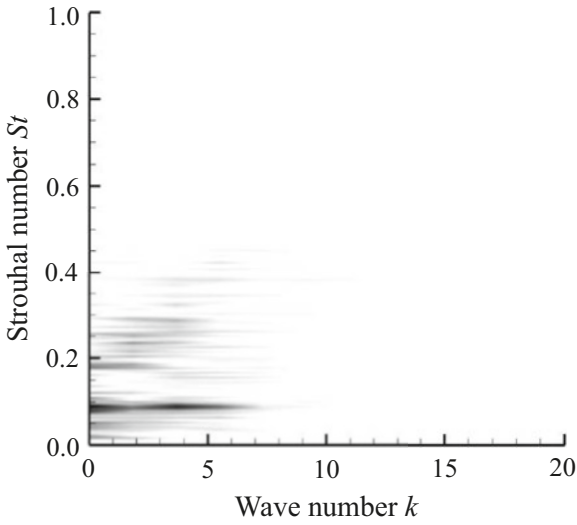

Fig. 6
Frequency-wavenumber spectrum of pressure fluctuation in Fig. 4

In the experimental data of Dandois [7], the phase velocity of the pressure in the span direction is $0.19a_\infty$, and in the data of Koike et al. [6], it is $0.30a_\infty$, which is the same order of the phase velocity in the simulation of this study.

4 Conclusion

This paper presents an investigation of transonic buffet on the NASA-CRM wing by means of zonal-DES. We compared the simulation results with the experimental data of Dandois [7] and Koike et al. [6] and showed that the 3D wing buffet phenomenon was qualitatively reproduced.

We performed frequency analysis of the surface pressure fluctuation and showed that the shock oscillation of the buffet was varied in the spanwise direction. The frequency characteristics were categorized into three patterns. In the inboard region ($\eta < 0.25$), the buffet exhibits a periodical oscillation with a single dominant frequency of $St = 0.09$, equivalent to the 2D wing. At the mid-span of the wing ($0.25 \leq \eta < 0.55$), the wave front of shock moves in the spanwise direction, and its phase velocity is equal to $0.2a_\infty$. In the outboard ($0.55 \leq \eta < 1.0$), the spectrum exhibits two dominant modes. One is a periodical oscillation similar to the 2D wing with a single dominant frequency of $St = 0.09$. The other is a high-frequency fluctuation of $St = 0.2 - 0.4$ propagating in the span direction.

References

1. J. McDevitt, A. Okuno, Static and dynamic pressure measurements on a NACA 0012 airfoil in the Ames High Reynolds Number Facility, NASA Technical Paper 2485 (1985)
2. B. Benoit, I. Legrain, Buffeting prediction for transport aircraft applications based on unsteady pressure measurements, in *5th Applied Aerodynamics Conference*, Monterey, CA, AIAA-1987-2356, 1987
3. D. Caruana et al., Buffeting active control in transonic flow, in *21st AIAA Applied Aerodynamics Conference*, Orlando, Florida, AIAA-2003-3667, 2003
4. P. Molton et al., Control of buffet phenomenon on a transonic swept wing. AIAA J. **51**, 761 (2013)
5. B.H.K. Lee, Self-sustained shock oscillations on airfoils at transonic speeds. Prog. Aerosp. Sci. **37**, 147 (2001)
6. S. Koike et al., Unsteady pressure measurement of transonic buffet on NASA common research model, in *34th AIAA Applied Aerodynamics Conference*, Washington, DC, AIAA 2016-4044, 2016
7. J. Dandois, Experimental study of transonic buffet phenomenon on a 3D swept wing. Phys. Fluids **28**, 016101 (2016)
8. M. Iovnovich et al., Numerical study of shock buffet on three-dimensional wings. AIAA J. **53**, 449 (2015)
9. V. Brunet et al., Zonal-Detached Eddy simulation of transonic buffet on a civil aircraft type configuration, in *38th Fluid Dynamics Conference and Exhibit*, Seattle, Washington, AIAA-2008-4152, 2008
10. F. Sartor et al., Delayed detached eddy simulation of shock buffet on half wing body configuration, in *22nd AIAA Computational Fluid Dynamics Conference*, Dallas, Texas, AIAA-2015-2607, 2015
11. S. Deck, Recent improvements in the zonal detached Eddy simulation (ZDES) formulation. Theor. Comput. Fluid Dyn. **26**, 523 (2012)
12. S. Deck, Numerical simulation of transonic buffet over a supercritical airfoil. AIAA J. **43**, 1556 (2005)
13. Y. Sugioka et al., experimental analysis of transonic buffet on a three-dimensional wing using fast-responding pressure-sensitive paint, in *48th FDC/34th ANSS*, JSASS-2016-2129, 2016

Critical Condition of Bow-Shock Instability Around Edged Blunt Body

N. Ohnishi, Y. Inabe, K. Ozawa, and K. Ohtani

Abstract Critical condition of a bow-shock instability was experimentally investigated for a low specific heat ratio flow in a ballistic range with different gas species and Mach numbers. Unstable shock surfaces were observed in front of an edged blunt body by shadowgraph images as predicted in advance by numerical simulations, and a disturbed flow appeared in the downstream even if the flow condition was close to the critical one. A numerically predicted critical curve in a parameter space of specific heat ratio and Mach number indicated that the instability can be found in a low specific heat ratio and high Mach number flow, being consistent with the present experiments. The density ratio of 10.5 across the shock front is similar to the critical curve; therefore, larger one may be an ingredient to make a bow-shock wave unstable.

1 Introduction

A bow-shock instability was observed in a ballistic range filled with chlorofluorocarbon [1] though a detached shock wave around a blunt body is usually stable in a uniform flow. From their experiments under various conditions, it was concluded that the occurrence of the instability depends on the Mach number, ambient gas pressure, and curvature of the blunt body. It has also been suggested that the instability is caused by chemical reactions within the shock layer [2]. However, because it is difficult to experimentally analyze the flow field behind the shock wave, the mechanism of the instability is still controversial.

We previously investigated the instability through three-dimensional numerical simulations and concluded that edged bodies, such as circular cones, induce the

N. Ohnishi (✉) · Y. Inabe
Department of Aerospace Engineering, Tohoku University, Sendai, Japan
e-mail: ohnishi@rhd.mech.tohoku.ac.jp

K. Ozawa · K. Ohtani
Institute of Fluid Science, Tohoku University, Sendai, Miyagi, Japan

A. Sasoh et al. (eds.), *31st International Symposium on Shock Waves 2*,
https://doi.org/10.1007/978-3-319-91017-8_135

shock instability observed in the experiments [3–5]. A parametric study was also conducted for the specific heat ratio γ and Mach number M and presented a critical curve of the instability in $\gamma - M$ parameter space [3]. Moreover, we also confirmed that two-dimensional simulations rarely reproduce the instability even with the chemical reactions, and the asymmetric features were obtained in three-dimensional simulations, indicating that purely hydrodynamic, asymmetrically unstable modes are responsible for the onset of the bow-shock instability rather than the chemical reactions such as dissociations in our conditions unlike the suggestion by the previous study [6]. The critical condition must reveal the mechanism of the instability but have been only examined by inviscid numerical simulations without chemical reactions [3] because of high computational loads for non-equilibrium three-dimensional computations. Therefore, it should be investigated by the appropriate experiments in the $\gamma - M$ space.

In this study, the numerically predicted critical curve was assessed by experiments with several conditions chosen based on our previous work. The dependence of the deformed shock front on the $\gamma - M$ relation was investigated under different experimental conditions, and the corresponding numerical simulations were then compared with the experimental results.

2 Ballistic Range Experiments

The experiments were conducted in a ballistic range at the Institute of Fluid Science, Tohoku University [7], as shown in Figs. 1 and 2. The ballistic range consists of propellant chamber, the launch tube (15-mm diameter, 3-m length), and test section (1.6-m diameter, 12-m length). The optical windows (600-mm diameter) are located at the sides of the test section, enabling optical measurements. The optical measurements were done by the shadowgraph method. The sequential snapshots

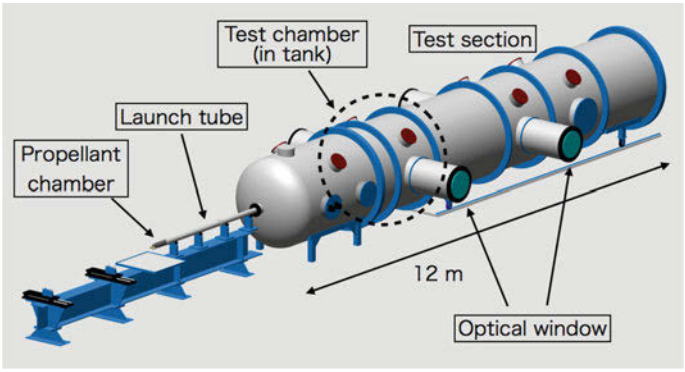

Fig. 1 Schematic view of the ballistic range

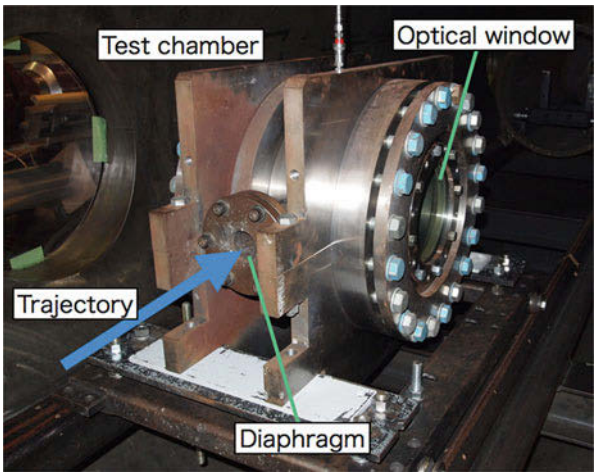

Fig. 2 Photograph of the test chamber

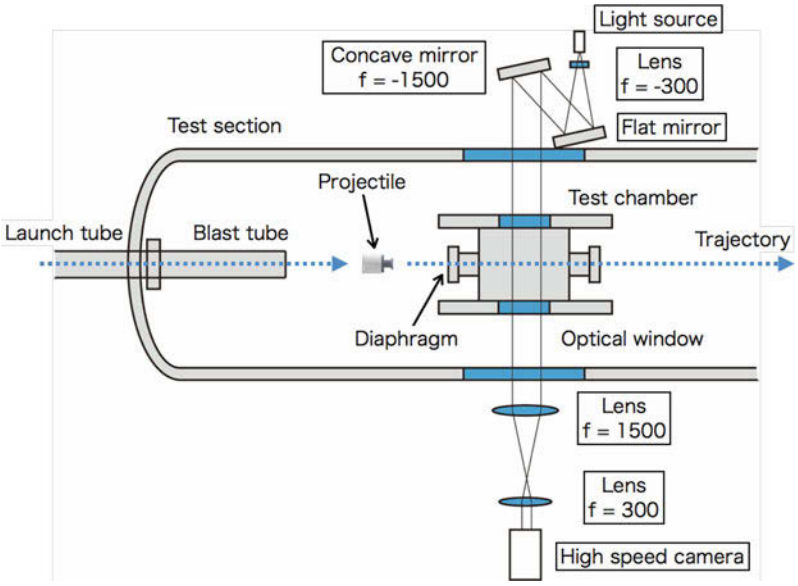

Fig. 3 Schematic illustration of experimental setup and optical systems

were obtained by a high-speed camera (Shimadzu Hyper Vision HPV-X, max. 5,000,000 fps, 400 × 250 pixels) with an optical system as illustrated in Fig. 3. A metal halide lamp (SUMITA LS-M210) was used as the light source.

The hydrofluorocarbon HFC-134a and its mixtures with air were utilized as the test gas and filled only a test chamber ($400 \times 400 \times 200$ mm^3) as shown in Fig. 2 for reducing the amount of the required gas. Entrance and exit holes of the test chamber along the trajectory were initially covered by diaphragms of Miler film. The specific

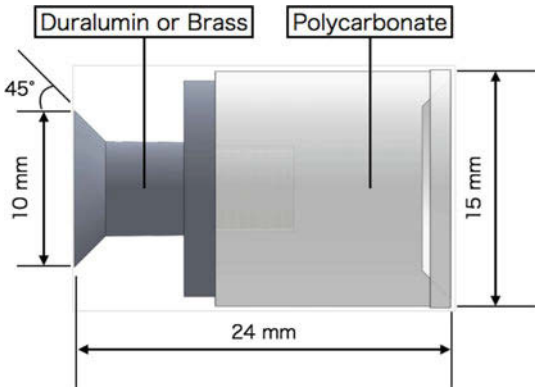

Fig. 4 Schematic view of the projectile

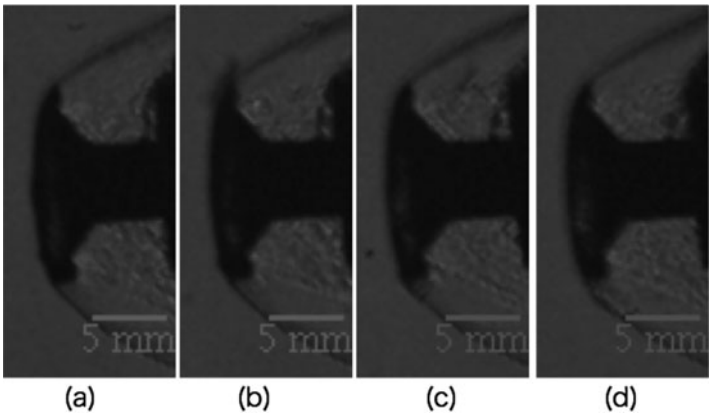

Fig. 5 Sequential images of the deformed bow-shock wave (Shot #1224). (**a**) 0 μs, (**b**) 8 μs, (**c**) 16 μs, (**d**) 24 μs

heat ratio for HFC-134a is 1.12, while those for the mixtures take1.15−1.12. A circular cone was employed as the head shape for the projectiles. The diameter of the circular cone was 10 mm, and the edge angle was 45°, which is the same as the previous work [6], as shown in Fig. 4. The mixed gas was made in the test chamber by adjusting the pressure ratio of air and HFC-134a.

3 Results and Discussion

The bow-shock instability was observed as a deformed shock front and disturbances in downstream behind the shock wave. Figure 5 shows the sequential shadowgraph images in Shot #1224 under the condition of $M = 5.9$ and $\gamma = 1.12$, which is unstable in the previous numerical simulation. One can find that the deformed shock front varies with time, and bumps are emitted from the edge of the projectile to

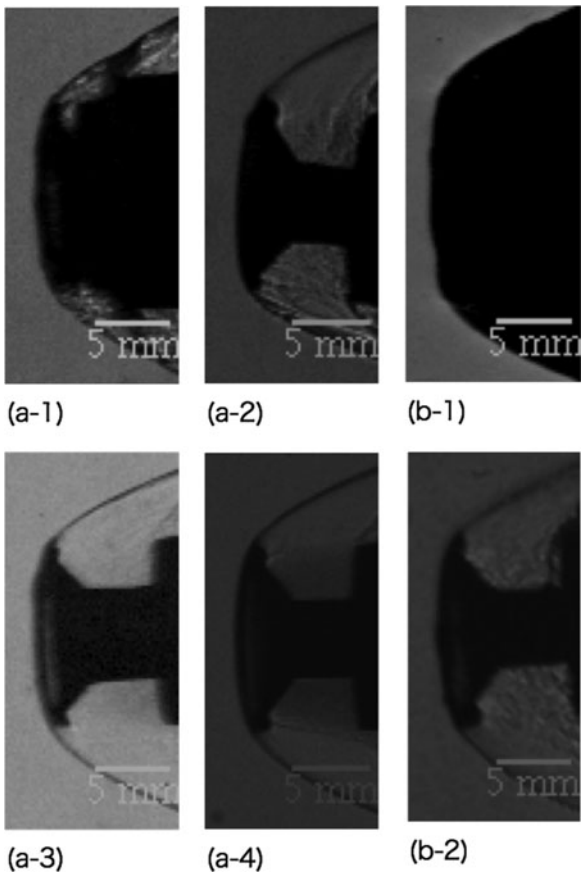

Fig. 6 Dependency of the shock deformation on the parameters of γ and M. (**a-1**) Shot #1208 ($M = 9.6$, $\gamma = 1.16$), (**a-2**) Shot #1212 ($M = 9.3$, $\gamma = 1.17$), (**a-3**) Shot #1210 ($M = 8.9$, $\gamma = 1.18$), (**a-4**) Shot #1214 ($M = 8.7$, $\gamma = 1.19$), (**b-1**) Shot #1205 ($M = 11.1$, $\gamma = 1.12$), (**b-2**) Shot #1224 ($M = 5.9$, $\gamma = 1.12$)

the downstream, resulting in the wavy structures. The shock standoff distance is relatively short due to the low γ, and the disturbed flow in the shock layer pollutes the shadowgraph image so that the projectile head is unclear compared with an image of a stable bow-shock wave appearing in a low-M and high-γ flow.

The comparison among different conditions clearly indicates that the high-M and low-γ condition easily induce the instability (see Fig. 6). The flow under the stable condition shows the sharp structures and no wavy structure, while the nearly stable condition makes wavy structures in the downstream even though the deformation of the shock front cannot be identified by the resolution of the images. Therefore, we judged the flow stability with the wavy structures in the downstream.

Figure 7 shows the stability diagram in the $\gamma - M$ parameter plane. The filled symbols were obtained by the inviscid three-dimensional simulations without chemical reaction. The experiments were done under the conditions around the numerically predicted critical curve. The experimentally observed critical boundary clearly lies close to the predicted one. This result suggests that the numerical

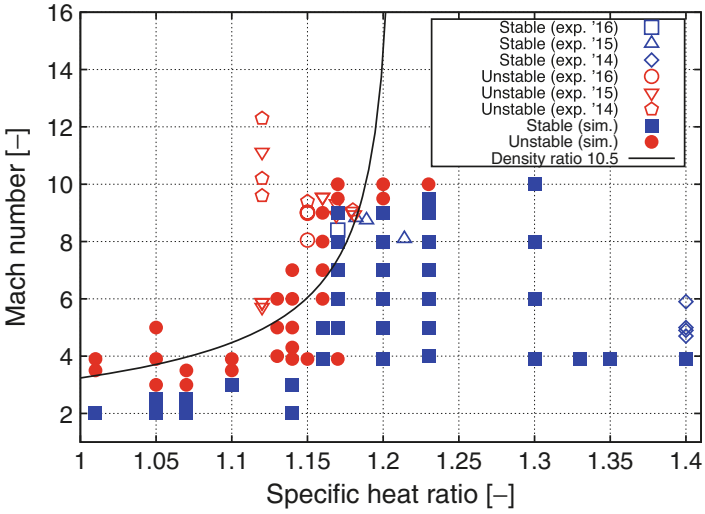

Fig. 7 Stability diagram in the $\gamma - M$ parameter plane

simulations can reproduce the bow-shock instability in these conditions, while shock capturing scheme may have an inherent instability.

The solid line in Fig. 7 indicates a density ratio of 10.5 estimated by the Rankine-Hugoniot relation assuming a normal shock. Some authors have pointed out that the density ratio across a shock wave is one of the important factors on flow stability related to the shock wave [1, 2, 8]. Actually, the density ratio of 10.5 seems to be a threshold for this case; however, the discrepancies from the numerically predicted curve are not negligible. In particular, the high-γ region is unstable for $M > 10$, and the predicted curve steeply rises at γ 1.17. These features should be confirmed in the forthcoming experiments.

4 Conclusion

We have experimentally investigated the critical condition of the bow-shock instability under the flow conditions around the critical curve predicted by our previous numerical study. The obtained critical boundary is consistent with the predicted one, while more elaborate research is needed for drawing a measured critical curve which may reveal the mechanism of the instability. Moreover, the stability analysis on the numerical solution must give a useful clue for understanding this instability.

References

1. A.S. Baryshnikov, A.P. Bedin, V.G. Maslennikov, G.I. Mishin, Stability of a bow shock. Sov. Tech. Phys. Lett. **5**, 113–114 (1979)
2. A.S. Baryshnikov, Baroclinic turbulence of dissociating gas as a reason for instability of bow shock wave. Phys. Scr. **T132**, 014007 (2008)
3. N. Ohnishi, Y. Sato, Y. Kikuchi, K. Ohtani, K. Yasue, Bow-shock instability induced by Helmholtz resonator-like feedback in slipstream. Phys. Fluids **27**, 066103 (2015)
4. Y. Sato, K. Yasue, N. Ohnishi, Numerical simulation of bow-shock instability around circular cone, in *Proceedings of 20th International Shock Interaction Symposium*, 2012, pp. 157–160
5. Y. Sato, Y. Suzuki, K. Yasue, N. Ohnishi, Three-dimensional simulation of bow-shock instability using discontinuous Galerkin method, in *Proceedings of 28th International Symposium on Shock Waves,* ed. by K. Kontis, vol. 1 (Springer, New York, 2012), pp. 1027–1033
6. Y. Kikuchi, N. Ohnishi, K. Ohtani, Experimental demonstration of bow-shock instability and its numerical analysis. Shock Waves **27**, 423–430 (2017)
7. D. Numata, K. Ohtani, M. Anyoji, K. Takayama, M. Sun, Experimental study of hypervelocity impacts at low temperatures. Shock Waves **18**, 169–183 (2008)
8. J.H.G. Hornung, P. Lemieux, Shock layer instability near the Newtonian limit of hypervelocity flows. Phys. Fluids **13**, 2394–2405 (2001)

Experimental Study on Hypersonic Pitch-Up Anomaly in Shock Tunnel

H. Tanno, T. Komuro, K. Sato, and K. Itoh

Abstract Abnormal pitch-up phenomenon of winged reentry vehicles at hypersonic gliding was experimentally studied in the high-enthalpy free-piston shock tunnel JAXA-HIEST. The novel multicomponent force measurement technique "Free-flight in wind tunnel" was implemented, which involved the test model being completely non-restrained for the duration of the test and thus experiencing free-flight conditions for a period on the order of milliseconds. The test model was a 10%-scaled HYFLEX Japanese lifting body reentry vehicle. Sixteen miniature piezoelectric accelerometers and eight piezo-resistive pressure transducers were instrumented in the model with three onboard miniature data recorders to store measured data. During the test campaign, the model angle of attack was varied from 30° to 50° with elevon (body flap) deflection angle of 0° and 20°. To derive the high-temperature real-gas effect, the comparison was conducted on the aerodynamic coefficients between perfect gas condition and the high-temperature real-gas condition. The following two test conditions were selected: (1) low-enthalpy test flow condition in which no oxygen molecules were dissociated and (2) high-enthalpy test flow condition in which 40% of oxygen molecules were dissociated. The comparison revealed that the lift-drag ratio agreed quite well in both of the above conditions. However, a significant difference of trim angle was detected at a flap deflection of 0°. The high-temperature real-gas effect was believed to be the major cause of the difference.

1 Introduction

In the first flight of the Space Shuttle, unexpected pitch-up was found in the hypersonic gliding phase, which is well known as the hypersonic pitch-up anomaly [1]. The following numerical analysis [2, 3] implied that a major cause of this anomaly

H. Tanno (✉) · T. Komuro · K. Sato · K. Itoh
Japan Aerospace Exploration Agency, Kakuda Space Center, Kakuda, Miyagi, Japan
e-mail: tanno.hideyuki@jaxa.jp

A. Sasoh et al. (eds.), *31st International Symposium on Shock Waves 2*,
https://doi.org/10.1007/978-3-319-91017-8_136

Fig. 1 Free-piston high-enthalpy shock tunnel HIEST

was forward movement of the pressure center on the vehicle as a high-temperature real-gas effect in partially or fully dissociated hypersonic free-stream. However, experimental validation in wind tunnels has not been conducted in these couple of decades, because of immature experimental skills of ground testing. Although high-enthalpy impulsive facilities those can duplicate high-temperature real-gas flow are available, their short test duration was a serious drawback for aerodynamic force measurement. During a decade of research on new force measurement techniques in the free-piston high-enthalpy shock tunnel HIEST (Fig. 1) [4], a new free-flight technique was successfully developed in JAXA Kakuda Space Center [5]. The free-flight technique is based on onboard instruments instead of conventional optical tracking techniques. Through a previous wind tunnel test campaign [6] with a generic model, the technique showed that it had the potential to detect the pitch-up anomaly as pitching-moment coefficient variation.

To determine the pitch-up anomaly of lifting reentry vehicles on the ground, an aerodynamic test campaign applying this free-flight force measurement technique was conducted in HIEST. A Japanese lifting body vehicle HYFLEX [7] was selected as the test model, in which the vehicle successfully performed hypersonic gliding flight in 1997. In this report, accuracy of the measurement technique was estimated at the beginning, followed by discussion of the HYFLEX pitching characteristics under the high-temperature real-gas condition.

2 Free-Flight Force Measurement Technique

Free-flight force measurement techniques have been implemented by the previous researcher. Instead of the conventional free-flight optical tracking technique described by Bernstein [8], a new technique with a completely free-flight model was developed in JAXA-HIEST. In this technique, test models are released from a magnetic holder installed on the wind tunnel ceiling so that it lies in the nozzle

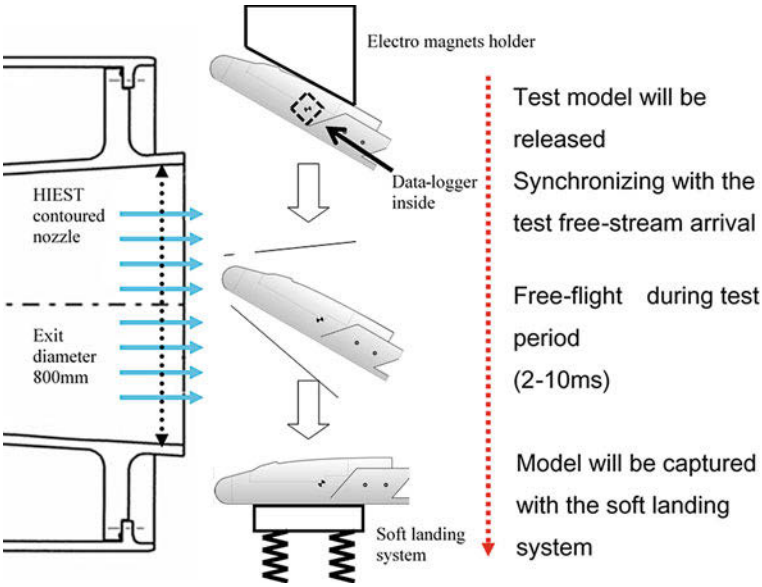

Fig. 2 Sequence of events in the free-flight technique

core synchronized with the arrival of the test flow. Thus, throughout the entire test, the model is completely unrestrained by any support system and is not interfered aerodynamically or mechanically. Since a comparatively heavy model can be used using this technique, variation in model position and attitude can be virtually eliminated during the test period even high free-stream dynamic pressure in HIEST. Moreover, acceleration measurement accuracy can be ensured with onboard accelerometers, the outputs of which were stored on an onboard miniature data recorder. After the termination of the test flow, the model falls into a soft landing system placed on the floor, enabling the model and instruments to be reused. This sequence of events is shown in Fig. 2.

2.1 Free-Flight Test Model

The HYFLEX is a Japanese lifting body reentry test vehicle, which successfully conducted hypersonic flight in 1996. The special feature of the HYFLEX test flight was a hypersonic maneuver with two elevons aft of the fuselage. The flight data was the unique benchmark for the error analysis of the force measurement technique in HIEST.

For the present HIEST wind tunnel test, a 1:10 scale HYFLEX model was manufactured as shown in Fig. 3. The specifications of the model are described in Table 1. In the table, the moment of inertia around y-axis I_{yy} is an important

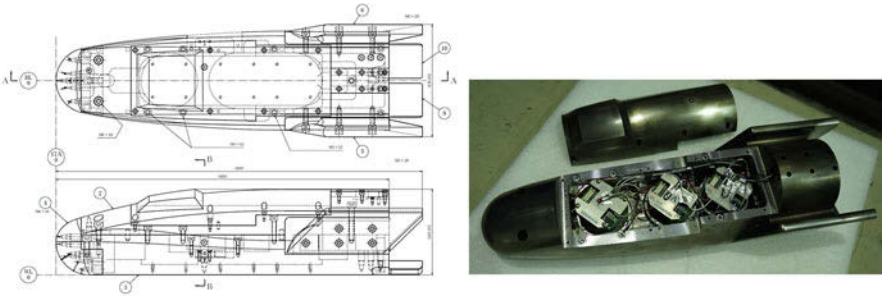

Fig. 3 (Left) Schematic of HYFLEX free-flight test model. (Right) Three data recorders instrumented in the HYFLEX free-flight model

Table 1 Specification of HYFLEX 1:10 scale model

Total mass (including sensors and data recorders)	16.78 kg
Total length	0.440 m
Moment of inertia *I*yy	0.226 kg m^2
Center of gravity X_G (from the nose tip)	0.241 m
Center of gravity Y_G (from the bottom surface)	0.0463 m

parameter for measurement accuracy of pitching moment. The two-support wire torsional pendulum method was applied to determine the *I*yy of the present HYFLEX model.

In the free-flight technique in HIEST, electromagnets were used to hold and release the model; the model was hence made of SUS420 magnetic stainless steel. Stainless steel was also effective to increase the model weight. Inside a model, three JAXA in-house data recorders and 16 miniature piezoelectric-type accelerometers (PCB352A07) are on board, with which the aerodynamic force applied to the model is measured as acceleration. Furthermore, in order to measure model surface pressure, eight high-speed piezo-resistive pressure transducers (Kulite XCQ-093) were instrumented. In the whole wind tunnel test, the elevon (body flap) deflection angle was fixed to 0° or 20°. The angle of attack of the model was varied from 30° to 50°.

2.2 Test Condition

In this test campaign, two free-stream test conditions in HIEST were selected: low-enthalpy conditions ($H_0 = 3$ MJ/kg) and high-enthalpy conditions ($H_0 = 14$ MJ/kg). The first test condition was perfect gas condition, and the second one was high-temperature real-gas conditions, under which condition approximately 40% of oxygen molecules were dissociated. Both free-stream conditions, shown in Table 2, which conditions were obtained through calculation with the one-dimensional

Table 2 HIEST test free-stream condition

	HIEST low H_0	HIEST high H_0	ONERA S4MA
	Perfect gas	Real gas	Reference
Stagnation temperature (K)	3.0×10^3	7.3×10^3	1.1×10^3
Stagnation pressure (MPa)	16	32	6.1
Stagnation enthalpy (MJ/kg)	3.7	13.6	N.A.
Static temperature (K)	2.8×10^2	1.4×10^3	5.5×10^1
Static pressure (kPa)	1.3	4.7	1.7×10^{-1}
Free-stream density (kg/m^3)	1.6×10^{-2}	1.1×10^{-2}	1.1×10^{-2}
Free-stream velocity (km/s)	2.6	4.7	1.5
Free-stream Mach number	7.6	6.0	9.7
Free-stream unit Reynolds number (1/m)	2.4×10^6	1.0×10^6	8.7×10^5
O mass fraction	3.3×10^{-4}	6.9×10^{-2}	N.A.
O_2 mass fraction	2.1×10^{-1}	1.4×10^{-1}	N.A.

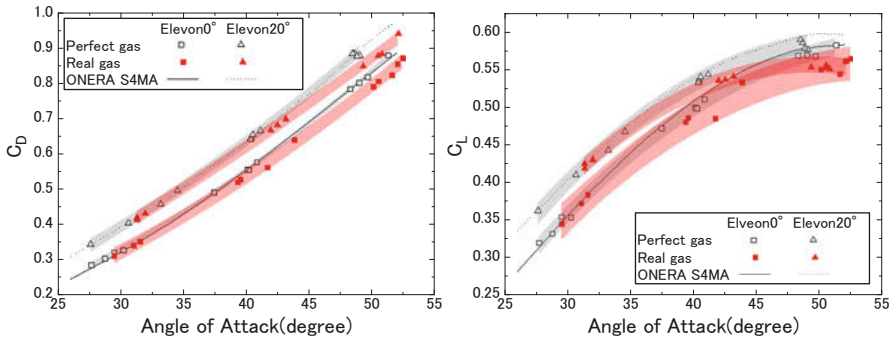

Fig. 4 Drag coefficient (left) and lift coefficient (right) of the HYFLEX test model at angle of attack from 30° to 50°. Results measured in the conventional blow down wind tunnel ONERA S4MA were superimposed

thermochemical non-equilibrium nozzle code [9, 10]. In the table, the free-stream condition in ONERA S4MA was also shown.

3 Test Results

3.1 Drag and Lift Coefficient

Measured drag coefficient, lift coefficient, and lift-drag ratio related to angle of attack were shown in Figs. 4 and 5. In all the figures, the open items and closed items were the results under perfect gas conditions and high-temperature real-gas conditions, respectively. Moreover, the results measured in the conventional hypersonic wind tunnel ONERA S4MA were also overlaid in all the figures as the

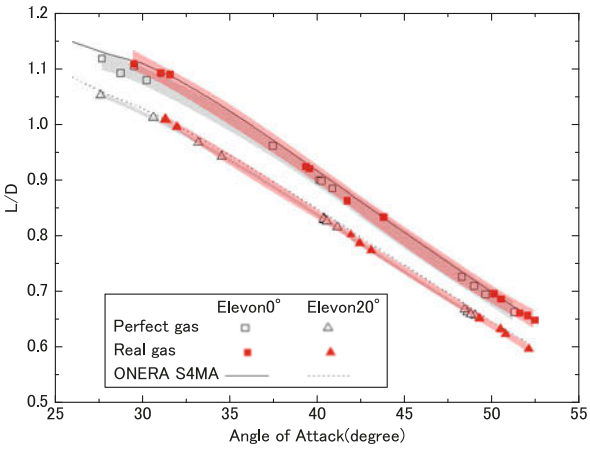

Fig. 5 Lift-drag ratio of HYFLEX test model at angle of attack from 30° to 50°. Results measured in the conventional blow down wind tunnel ONERA S4MA were superimposed

solid (elevon 0°) and dotted lines (elevon 20°) to estimate the accuracy of the present free-flight force measurements in HIEST. To estimate the uncertainty of the HIEST measurements, 95% (2-σ) prediction bands for the HIEST perfect gas condition and high-temperature real-gas condition were also plotted as the hatched area in the figures.

As shown in these figures, all the measurements in HIEST agreed quite well with those of S4MA. These results revealed that drag force and lift force are insensitive to a stagnation enthalpy, namely, flight speed in hypersonic flow. These results also demonstrated the high accuracy and precision of the present HIEST force measurement technique. However, as shown in Fig. 4, there was a tendency that the CD and CL under high-temperature real-gas condition were slightly lower than those under perfect gas condition. This tendency became remarkable when the angle of attack increased. The cause is still unknown; however, same tendency was also observed in the previous aerodynamics test [11] in HIEST with a blunt cone model.

3.2 Pitching Moment

Figure 6 showed the pitching moment coefficients with elevon deflection angles of 0° and 20°. In the present discussion, HIEST measurements with an elevon deflection angle of 0° are the focus. The fitted regression lines indicated that the trim angle for HIEST perfect gas condition was about 45°. In contrast, it increased to about 55° for the high-temperature real-gas condition. An advance of the pressure center as a high-temperature real-gas effect was believed to be the cause of the increment of angle of attack.

It should be noted that pitching moment coefficient obtained in ONERA S4MA was remarkably larger than those of the HIEST perfect gas condition, especially at a high angle of attack (40° or larger). The trim angle of S4MA was accordingly

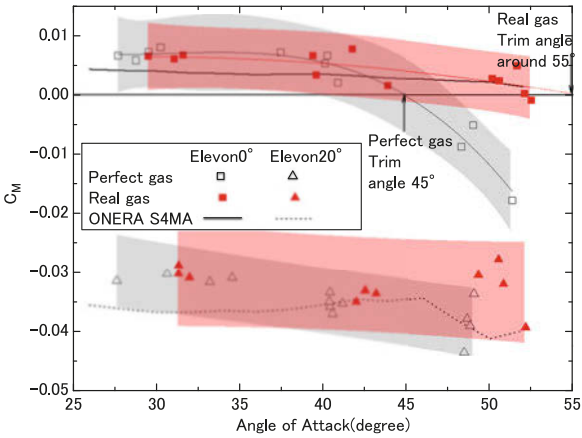

Fig. 6 Pitching moment coefficient of HYFLEX test model at angle of attack from 30° to 50°. Results measured in the conventional blow down wind tunnel ONERA S4MA were overlapped

larger (approximately 55°) than that of HIEST perfect gas condition. A report for the HYFELX flight test [12] said that body flap deflection angle was far less than the pre-flight prediction at Mach 8 or higher. Since the pitching stability of HYFLEX was designed based only on the S4MA wind tunnel results, the discrepancy between S4MA and HIEST should be deeply discussed.

4 Conclusion

The three-component aerodynamics measurement test of the HYFLEX lifting body model was carried out under high-temperature real-gas condition in the high-enthalpy shock tunnel HIEST. The measurement evidently showed that there was a significant real-gas effect on the pitching moment, which causes pitching anomaly recognized as a major problem for the design of winged reentry vehicles. The present measurement results also demonstrated the high precision of the present force measurement technique, which was sufficient to estimate designs of reentry vehicles. However, numerical studies are required for detailed analysis of the effects due to Mach number and Reynolds number.

References

1. J.C. Young, L.F. Perez, P.O. Romere, D.B. Kanipe, *Space Shuttle Entry Aerodynamic Comparison of Flight 1 with Preflight Predictions*, AIAA Paper No. 81-2476, 1981
2. J.R. Maus, B.J. Griffith, K.Y. Szema, J.T. Best, Hypersonic Mach number and real gas effects on space shuttle orbiter aerodynamics. J. Spacecr. Rocket **21**(2), 136–141 (1984)
3. B.J. Griffith, J.R. Maus, B.M. Majors, J.T. Best, Addressing the hypersonic simulation problem. J. Spacecr. Rocket **24**(4), 334–341 (1987)

4. K. Itoh, S. Ueda, H. Tanno, T. Komuro, K. Sato, Hypersonic aerothermodynamic and scramjet research using high enthalpy shock tunnel. Shock Waves **12**, 93–98 (2002)
5. H. Tanno, T. Komuro, K. Sato, K. Itoh, M. Takahashi, *Miniature Data-Logger for Aerodynamic Force Measurement in Impulsive Facility*, AIAA Paper No. 10-4204, 2010
6. H. Tanno, T. Komuro, K. Sato, K. Fujita, S.J. Laurence, Free-flight measurement technique in the free-piston high-enthalpy shock tunnel. Rev. Sci. Instrum **85**, 045112 (2014)
7. M. Shirouzu, M. Yamamoto, *Overview of the HYFLEX Project*, AIAA Paper No. 96-4524, 1996
8. L. Bernstein, *Force Measurement in Short-duration Hypersonic Facilities*, AGARD-AG-214, ed. by R.C. Pankhurst (Technical Editing and Reproduction, London), 1975.
9. R.K. Prabhu, W.D. Erickson, *A Rapid Method for the Computation of Equilibrium Chemical Composition of Air to 15000K*, NASA TP-2792, 1988
10. J.A. Lordi, R.E. Mates, J.R. Moselle, *Computer Program for the Numerical Simulation of Non-Equilibrium Expansion of Reacting Gas Mixtures*, NASA CR-472, 1966
11. K. Sato, T. Komuro, H. Tanno, K. Itoh, *The Acceleration Measurement Aerodynamics Test of the Blunt Cone Model in a High Temperature Shock Tunnel*, shock wave symposium lecture collected papers, 2007, pp. 353–356
12. S. Watanabe, S. Ishimoto, Y. Yamamoto, *Aerodynamic Characteristics Evaluation of Hypersonic Flight Experiment (HYFLEX) Vehicle Based on Flight Data*, AIAA Paper No. 96-4527, 1996
13. H. Tanno, T. Komuro, K. Sato, K. Itoh, M. Takahashi, *Miniature Data-Logger for aerodynamic Force Measurement in Impulsive Facility*, AIAA Paper No. 10-4204, 2010

Pressure Measurements Around an Electric Discharge Produced on a Wedge in a Supersonic Flow

P. Gnemmi, C. Rey, B. Sauerwein, and M. Bastide

Abstract An original mean for the steering of supersonic projectiles is proposed since several years. Now, the deflection of the trajectory of such a projectile by generating electric discharges producing plasma on its surface becomes very realistic facing the experimental results got previously. The present paper deals mainly with academic pressure measurements carried out on a wedge, the transducers being located very near the electrodes of the electric discharge actuator. The experiments are carried out in a shock tunnel at the Mach number of 4.5 under realistic conditions present at 8 km of altitude. The research is motivated by expectations to be confirmed or not about physical effects producing the motion of the projectile under electric discharge actuation. Several series of tests prove that the electric discharge generating plasma produces a local overpressure around the electrodes. This result is in coherence with the motion of a projectile submitted to electric discharges observed in a wind tunnel and a shock tunnel.

1 Introduction

The flow control around aerial vehicles by using plasma is one of the concerns of the fluid dynamics flow control community for over two decades. The most popular plasma actuator, which mechanism is well understood and widely in use in different laboratories, is based on a dielectric barrier discharge (DBD) mechanism. This plasma actuator is mainly used in numerous subsonic and transonic applications. The use of electric discharge actuators is encountered in supersonic applications. A review on these kinds of flow control is given by Gnemmi and Rey [1].

An original application for the steering of supersonic projectiles is proposed since several years [2]. Now, the deflection of the trajectory of a supersonic projectile by generating plasma on its surface becomes very realistic facing the experimental

P. Gnemmi (✉) · C. Rey · B. Sauerwein · M. Bastide
French German Research Institute of Saint-Louis (ISL), Saint-Louis, France
e-mail: patrick.gnemmi@isl.eu

A. Sasoh et al. (eds.), *31st International Symposium on Shock Waves 2*,
https://doi.org/10.1007/978-3-319-91017-8_137

results got previously [1, 3]. The application aims with guided anti-aerial projectiles launched by a 40-mm gun and designed to increase their precision when faced with increasingly agile aerial vehicles flying up to a few kilometers of altitude [4, 5]. The objective of the proposed concept consists in generating one long or several short plasma discharges so that the asymmetry is large and long enough to cause the deviation of the projectile with respect to its initial trajectory. The plasma discharge on the projectile surface is produced by an electric arc discharge between electrodes embedded in the projectile.

All these experimental results [1–3] were produced to demonstrate the feasibility of the concept. However, physical effects producing the motion of the projectile under electric discharge actuation must be clarified. Therefore, academic pressure measurements are necessary to help the understanding of the interaction effects of the electric discharge with the cross flow of a projectile. These measurements also contribute to the validation of a computation code newly under development [6].

The present paper deals with pressure measurements carried out on a wedge, transducers being placed around the electrodes of the electric discharge actuator. Chapter "Experimental Setup and Instrumentation" presents the experimental setup and the instrumentation and chapter "Results" shows the most interesting results.

2 Experimental Setup and Instrumentation

2.1 Shock Tunnel and Model

Many experiments are carried out in the shock tunnel STA of ISL in order to investigate the pressure distribution around the electrodes of the electric discharge actuator embedded in a wedge (Fig. 1). The wedge has an angle of 30° and a width of 120 mm, and it is located 10 mm in front of the nozzle exit. The electrodes are flush mounted in an electrically insulating plate of 60-mm long and 40-mm wide. The plate made of polyethylene is embedded in the lower part of the wedge at 60 mm from its leading edge. The wedge has no angle of attack. Before these tests, the measurement section is pressurized at 6000 Pa to avoid unexpected discharges which could easily occur under vacuum. When the membranes of the shock tunnel burst, the nitrogen flow is accelerated up to the desired pressure, temperature, and flight velocity, leading to the Mach number of 4.5 for altitude conditions present at 8 km. The electric discharge generating plasma is produced by using the low-voltage actuator located inside the wedge.

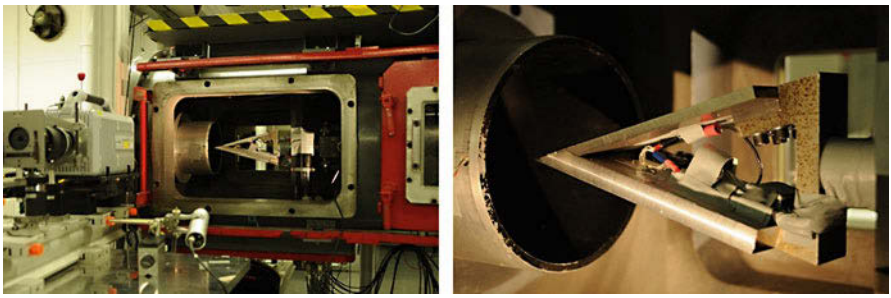

Fig. 1 Wedge in the measurement section of the shock tunnel

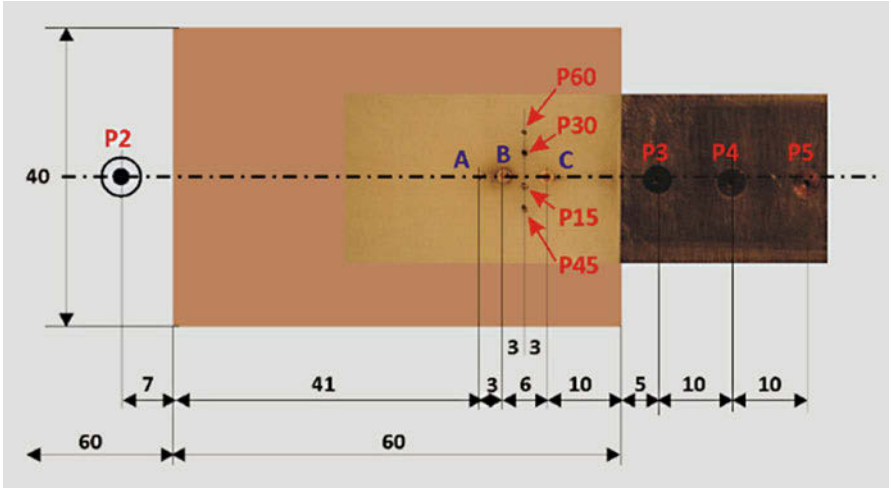

Fig. 2 Electrodes and pressure transducers in the polyethylene plate

2.2 *Electric Discharge Actuator*

The way of generating a plasma discharge on the projectile surface consists in producing an electric arc discharge between electrodes embedded in the projectile. Therefore, a low-voltage electric discharge actuator, largely detailed in [7], has been developed in order to satisfy the requirements for a use in atmospheric conditions. The actuator is composed of three parts: a high-voltage low-energy activating system, a low-voltage high-energy plasma generator, and a low-voltage supply which is common to the previous two parts. The high-voltage low-energy activating system, called discharge trigger, is connected to an electrode pair (A-B) and is able to break the dielectric barrier present between the electrodes (Fig. 2).

The low-voltage high-energy electric discharge generator, called low-voltage generator, is able to produce an electric discharge by the mean of a capacitor

connected to another electrode pair (B-C). The electrodes are in the middle of the wedge and aligned parallel to the incoming flow

2.3 Measurement Techniques

Eight pressure transducers located 2 mm above the surface are embedded in the wedge according to Fig. 2. Transducers P2, P3, P4, and P5 are aligned with the electrodes, so they are parallel to the incoming flow. Transducers P15, P30, P45, and P60 are perpendicular to the electrodes: P15, P30, P45, and P60 are 1.5, 3.0, 4.5, and 6.0 mm distant from the electrode alignment, respectively.

All transducers are from the Kulite Semiconductor company; they have a diameter of 2 mm, and they are compensated in temperature within a 298–353 K range. The model XCL-080-7BARA is used for locations P2, P3, P4, P5, P45, and P60, and the model XCQ-080-7BARA is used for location P30: the rated absolute pressure is 7 bar. The model XCL-080-3.5BARA is used for location P15: the rated absolute pressure is 3.5 bar. The accuracy of the measurement is 0.1% of the rated absolute pressure. The natural frequencies are 300 and 380 kHz for transducers having the rated absolute pressure of 3.5 and 7 bar, respectively. The dielectrically isolated piezoresistive technology of these pressure sensors has the great advantage that they are not susceptible to electromagnetic interference (EMI) as there are no P-N junctions, which is mandatory in these experiments.

The data acquisition is carried out by using amplifiers IMD DMF 15-R-B (gain 10) and a transient recorder ELSYS AG TPC (14 bits, 2.5 MHz) controlled by TRANSAS software. The complete wedge equipped with pressure transducers and their acquisition chains are calibrated at rest in the shock tunnel test chamber; indeed, the shock tunnel is airtight when the installation is closed, and a defined pressure is set from 5 to 10^5 Pa to calibrate the measurement chains.

The electric discharge is produced on the projectile surface when the flow is quasi-steady around the model. A differential interferometer (DI) is used to visualize the flow-field structure [8] by means of a high-speed CCD camera. The DI is based on the density-gradient field, and it is adjusted in order the interferogram pictures make the density changes visible. Interferograms of 1024 pixels per 408 pixels are recorded at a frequency of 30,000 frames per second.

The measurements of the voltage and current during the electric discharge are recorded. The voltage measured at the electrode bounds indicates the lifetime of the electric discharge. The current measurement gives a representation of the impulsiveness of the discharge.

3 Results

A typical experiment consists in generating an electric discharge between the electrodes creating a plasma discharge on the wedge when the flow is constant. Simultaneously, the pressure measured by the sensors and the interferograms of the flow behavior are recorded.

A reference test is presented in Fig. 3 in which there is no electric discharge. The pressure at the nozzle exit is 6000 Pa before the test. A sharp pressure increase occurs during the flow establishment. Six hundred μs after the membrane bursting, the flow at a pressure of 1.5 bar is completely steady over the wedge during 2 ms.

Another test is conducted by masking the transducers by a polyimide tape in order to show the influence of the electric discharge on pressure measurements. The capacitor of 1000 μF is loaded under 450 V leading to a stored energy of 101 J. Figure 4a shows how the current is distributed in the discharge and how the voltage behaves. The electric discharge is triggered at the instant $t = 0$. After 16 μs the current increases rapidly to reach a maximum of 460 A after around 380 μs, whereas the voltage drops from 450 V to 110 V after around 38 μs. After 1.18 ms the plasma

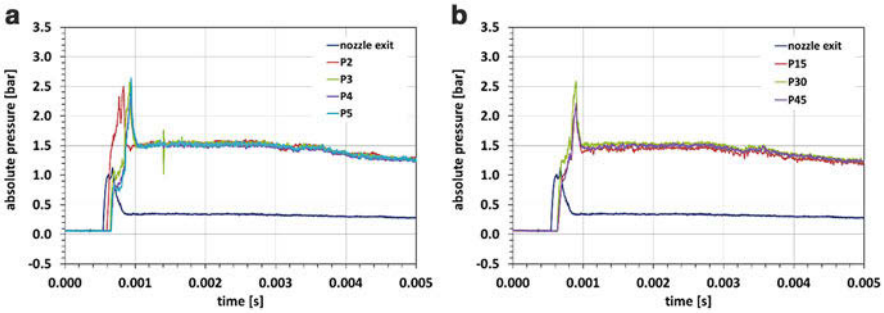

Fig. 3 Pressure measurements without electric discharge, test 63_161109_02. (**a**) Along the longitudinal axis, (**b**) Along the transverse line

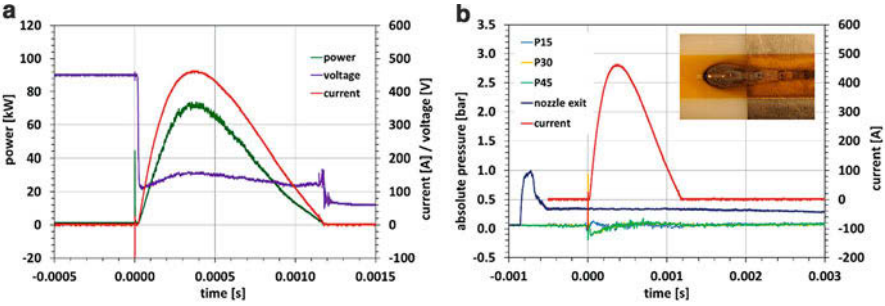

Fig. 4 Transducers protected by a polyimide tape, $E = 101$ J, test 62_161109_01. (**a**) Voltage and current in the discharge, (**b**) Pressure measurements along the transverse line

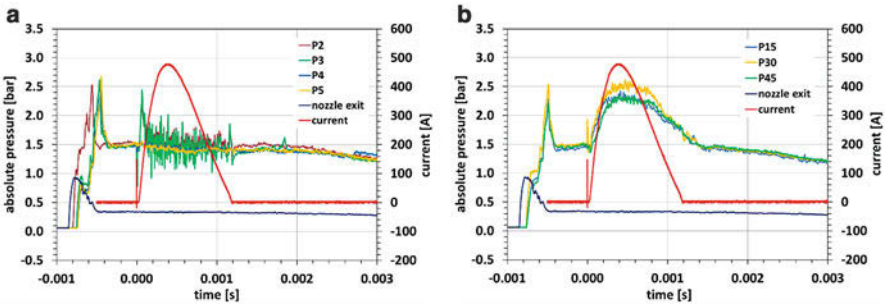

Fig. 5 Voltage, current, and pressure measurements, $E = 101$ J, test 61_161108_02. (**a**) Pressure measurements along the longitudinal axis, (**b**) Pressure measurements along the transverse line

discharge extinguishes. Figure 4a also depicts the power in the discharge reaching a maximum of 70 kW. The calculated consumed energy in the discharge is 46 J corresponding to 46% of the stored energy.

The comparison of Fig. 3b with Fig. 4b proves that the influence of the electric discharge is mostly visible on the pressure measurements during the disruption of the dielectric barrier. The picture taken after the test shows the trace of the plasma effects left on the tape: it clearly depicts the horseshoe pattern around the common cathode indicating the interaction of the plasma with the incoming flow.

The next test is carried out for the same conditions as the ones of the previous test. There is no measurable influence on the transducers located along the longitudinal axis (Fig. 5a), whereas the interaction of the plasma with the incoming flow is really clear along the transverse line (Fig. 5b). The overpressure reaches 0.75–1 bar depending on the pressure location. As shown in Fig. 5a, signals provided by P2 and P3 transducers are very noisy in each test, and they cannot be analyzed without filtering.

The last presented test is carried out with a stored energy of 202 J. Figure 6a shows the current, voltage, and power in the discharge: the power reaches a maximum of 100 kW. After 1.79 ms the plasma discharge extinguishes. The calculated consumed energy in the discharge is 82 J corresponding to 40% of the stored energy. Figure 6b, c presents pressure profiles along both directions. As in the previous test, there is no influence on the transducers located along the longitudinal axis, contrarily to the one along the transverse line. The overpressure reaches 1–1.5 bar depending on the pressure location. The overpressure amplitude and duration depend on the distance from the longitudinal axis. Figure 6d presents the interferogram taken at $t = 0.911$ ms; thus, after the maximum overpressure, the interaction of the plasma with the incoming flow is clearly visible.

Figure 6d shows the picture taken after the test: the trace of the plasma effects left on the wedge clearly depicts the horseshoe pattern around the common cathode indicating the interaction of the plasma with the incoming flow. This result also confirms that the overpressure is concentrated around the electrodes and that there are no counter effects like an under pressure behind the plasma as it is the case in lateral jet.

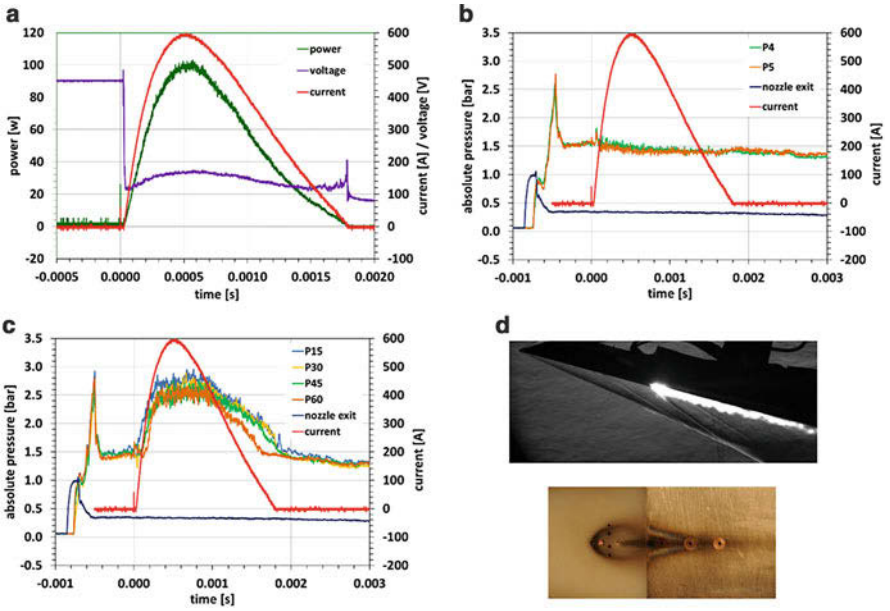

Fig. 6 Voltage, current, and pressure measurements, $E = 202$ J, test 72_161117_01. (**a**) Voltage and current in the discharge, (**b**) Pressure measurements along the longitudinal axis, (**c**) Pressure measurements along the transverse line, (**d**) Pattern on the wedge due to the interaction of the plasma with the incoming flow

4 Conclusion

Experiments are carried out in a shock tunnel at the Mach number of 4.5 under realistic conditions present at 8 km of altitude in which pressure is measured on a wedge very near the electrodes of an electric discharge actuator. Tests prove that the electric discharge does not affect the pressure measurements by electromagnetic interferences. Other experiments demonstrate that the electric discharge generating plasma produces an overpressure just localized around the electrodes. This result is in coherence with the motion of a projectile submitted to electric discharges observed in a wind tunnel and a shock tunnel. So, expectations on physical effects producing the motion of the projectile under electric discharge actuation are confirmed. These measurements will be used for computation validations, which are in progress.

References

1. P. Gnemmi, C. Rey, *Experimental Investigations on a Free-Flying Supersonic Projectile Model Submitted to an Electric Discharge Generating Plasma*, 30th International Symposium on Shock Waves 2, ISSW30 Volume 2, 2017
2. P. Gnemmi, R. Charon, J.P. Dupéroux, A. George, Feasibility study for steering a super-sonic projectile by a plasma actuator. AIAA J. **46**(6), 1308–1317 (2008)
3. P. Gnemmi, C. Rey, Plasma actuation for the control of a supersonic projectile. J. Spacecr. Rocket. **46**(5), 989–998 (2009)
4. P. Wey, C. Berner, E. Sommer, V. Fleck, H. Moulard, *Theoretical Design for a Guided Supersonic Projectile*, 22nd International Symposium on Ballistics, Vancouver, BC, Canada, 14–18 November, 2005
5. P. Wey, *Performance Analysis of the ISL's Guided Supersonic Projectile*, 23rd International Symposium on Ballistics, Tarogona, Spain, 16–20 April, 2007
6. A. Nekris, P. Gnemmi, C. Mundt, *Multi-Species Simulations of Plasma Discharges in NLTE State in Supersonic Flows*, 51st 3AF International Conference of Applied Aerodynamics, Strasbourg, France, 4–6 April, 2016
7. P. Gnemmi, C. Rey, Guidance of a supersonic projectile by plasma-actuation concept. *Wind tunnels and experimental fluid dynamics research* (Dr. Jorge Colman Lerner and Dr. Ulfilas Boldes), July, 2011
8. G. Smeets, Interferometry, Lecture Series 1990–05 on measurement techniques for hypersonic flows, von Kàrmàn Institute for Fluid Dynamics, Rhode-St-Genèse, Belgium, May 28–June 1, 1990

Thermal Spike Conception for Wave Drag Reduction of Blunt Bodies at Different Supersonic Speeds

P. Georgievskiy and V. Levin

Abstract A computational study of supersonic flow past blunt bodies in the presence of energy deposition localized in very small regions of upstream flow is carried out. The effect of front separation zone formation due to the interaction of a bow shock wave and a shock layer with "thermal spike" (a high-temperature wake downstream of the energy deposition region) is investigated. The universal similarity condition for effective wave drag reduction of bodies due to localized energy deposition and front separation zone formation is determined.

1 Introduction

The effect of wave drag reduction of blunt bodies in the presence of an energy deposition localized in upstream supersonic flow was initially noticed in computational studies in frames of Euler equations [1–3]. Later it was proved experimentally by Tret'yakov et al. [4] (energy deposition was realized in argon using high-power repetitive pulsing laser spark). The computational studies in frames of Navier-Stokes equations were performed for blunt axisymmetric bodies by Gromov et al. [5] and Riggins et al. [6]. We have proved [7] that wave drag reduction by localized upstream energy deposition was effective both for blunt and streamlined bodies. Reviews of early year's studies of aerodynamic drag reduction and supersonic flow control by energy deposition were presented by Knight [8] and Shneider et al. [9]. Recent results of experimental and numerical investigations are presented by Schülein et al. [10], Erdem et al. [11], and Sasoh et al. [12].

From the very beginning, localized energy deposition was considered as an instrument for controlling a supersonic flow past large bodies and wave drag reduction due to formation of separation zones ahead of fore surface of bodies. Appearing of front separation zones in case of localized upstream energy deposition

P. Georgievskiy (✉) · V. Levin
Institute for Mechanics of Lomonosov Moscow State University, Moscow, Russia
e-mail: georgi@imec.msu.ru

A. Sasoh et al. (eds.), *31st International Symposium on Shock Waves 2*,
https://doi.org/10.1007/978-3-319-91017-8_138

was a result of interaction of an arbitrary thin high-temperature wake with a bow shock wave and a shock layer – "thermal spike conception." In practice thermal spike can be realized as plasma filament initiated by subcritical microwave energy deposition controlled by laser pulses (Kolesnichenko et al. [13]) or by laser beam ionization (Michael et al. [14]). Computational studies of effect of flow reorganization due to interaction of heated plasma filament with a shock layer were performed by Azarova, Anderson, and Knight in [15, 16].

According to Guvernyuk et al. [17], the basic principle behind thermal spike conception is that a static pressure inside a blunted front separation zone should be equal to a total dynamic pressure in a temperature wake (downstream of a normal shock for supersonic wake). In [18] we have explained the appearance of front separation zones transversal pulsations by periodical capturing of high-enthalpy jet and have applied a method of transformation of the energy deposition regions to obtain quasi-stationary isobaric front separation zones in numerical experiments.

In the present study, a numerical simulation of supersonic flow past blunt bodies in the presence of energy deposition localized in very small regions of upstream flow is performed. The influence of Mach number of upstream flow, energy source intensity, and size on front separation zones shape is examined. The conditions for effective wave drag reduction of bodies are determined.

2 Formulation of the Problem

Euler equations and energy source model were used for numerical simulation of unsteady two-dimensional axisymmetric flow past bodies in the presence of localized energy deposition. The equations in cylindrical coordinate z, r are:

$$\frac{\partial}{\partial t} r \begin{pmatrix} \rho \\ \rho u \\ \rho v \\ e \end{pmatrix} + \frac{\partial}{\partial z} r \begin{pmatrix} \rho u \\ p + \rho u^2 \\ \rho u v \\ (e + p)\, u \end{pmatrix} + \frac{\partial}{\partial r} r \begin{pmatrix} \rho v \\ \rho u v \\ p + \rho v^2 \\ (e + p)\, v \end{pmatrix} = \begin{pmatrix} 0 \\ 0 \\ p \\ r \rho Q \end{pmatrix} \tag{1}$$

Here p is a pressure, ρ is a density, u, v are velocity components along z, r directions correspondingly, and e is a total energy per volume unit. For the ideal perfect gas with constant specific heat ratio, $e = p/(\gamma - 1) + \rho(u^2 + v^2)/2$ (in this study a specific heat ratio is $\gamma = 1.4$).

The energy source was assumed to be predetermined function of coordinates and time. The specific power input per mass unit Q was set by the relationship:

$$Q = Q_0(t) \exp\left(- \left(r/\Delta r(t)\right)^2 - \left((z - z_0)/\Delta z(t)\right)^2 \right) \tag{2}$$

The formulation was dimensionless. Physical scales for coordinates and distances were a middle section radius of a body R_B, pressure $p - p_\infty$, density $\rho - \rho_\infty$,

velocities u, $v - (p_\infty/p_\infty)^{1/2}$, time $t - R_B(p_\infty/p_\infty)^{-1/2}$, and power input per mass unit $Q - {R_B}^{-1}(p_\infty/p_\infty)^{3/2}$ (index ∞ corresponds to parameters in ambient flow).

Explicit MacCormack scheme [19] of second-order accuracy with coordinates and time was used. Discontinuities (shock waves and tangential surfaces) were calculated using regular algorithm, and FCT-type monotonization procedure [20] was applied. Courant-Friedrich-Levy stability condition was used to determine a time step.

3 Energy Source in a Supersonic Flow at Different Mach Numbers

The similarity criteria can be formulated for the problem of a supersonic flow past an energy source as a direct consequence from dimension analyses. Supersonic flows past sources of different size (index I and II) are similar if the following conditions are satisfied:

$$\gamma^{\mathrm{I}} = \gamma^{\mathrm{II}}, \quad {M_\infty}^{\mathrm{I}} = {M_\infty}^{\mathrm{II}}, \quad {Q_0}^{\mathrm{I}}\Delta r^{\mathrm{I}} = {Q_0}^{\mathrm{II}}\Delta r^{\mathrm{II}}, \quad \frac{\Delta r^{\mathrm{I}}}{\Delta z^{\mathrm{I}}} = \frac{\Delta r^{\mathrm{II}}}{\Delta z^{\mathrm{II}}}; \tag{3}$$

A total power input W depends not only on specific power input distribution function Eq. (2) but also on density distribution. The input power coefficient ξ is defined as a ratio of an input power W and an enthalpy flux H through the energy source effective cross section $S_Q = \pi\ \Delta r^2$:

$$W(t) = \int \rho\ Q\, dV, \quad H = \rho_\infty u_\infty S_Q \frac{\gamma p_\infty}{(\gamma - 1)\,\rho_\infty}, \quad \xi = \frac{W}{H} \tag{4}$$

We have examined basic features of supersonic flows past energy sources in [7, 18]. A high-temperature wake with reduced density, total pressure, and Mach numbers but increased longitudinal velocity appears behind the energy deposition region (a static pressure increases locally). For spherical energy sources $\Delta r = \Delta z$ of "supercritical" intensity $Q_0 > Q_0^*$, the "flow choking" effect was noticed: a local subsonic zone and a bow shock wave were formed, and the larger the intensity Q_0 the higher a pressure peak behind a bow shock. For "subcritical" intensity a hanging shock wave was formed on the periphery of a flow. Simplified analytical model for determination of the critical intensity Q_0^* was formulated and verified in numerical simulation in [7]. The result was:

$$Q_0^*\Delta r = \frac{\gamma^{3/2}M_\infty^3}{\sqrt{\pi}\,(\gamma^2 - 1)}\left(1 - \frac{1}{M_\infty^2}\right)^2 \tag{5}$$

In the present study, we have analyzed supersonic flow past spherical energy sources $\Delta r = \Delta z$ at different Mach numbers. We have proposed additional condition

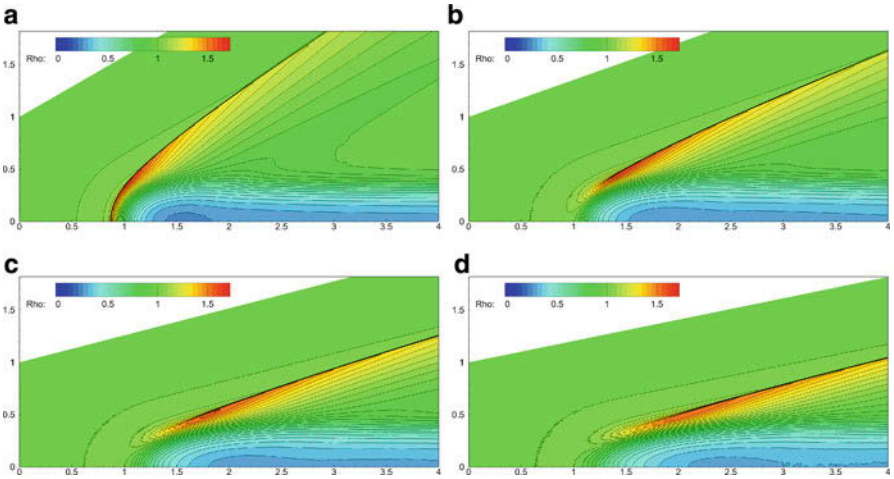

Fig. 1 Supersonic flow past energy sources at different Mach numbers (density isolines) $\Delta r = 0.2$, $z_0 = 1$ (**a**) $M_\infty = 2$, $Q_0 = 60$, (**b**) $M_\infty = 3$, $Q_0 = 90$, (**c**) $M_\infty = 4$, $Q_0 = 120$, (**d**) $M_\infty = 5$, $Q_0 = 150$

Table 1 Input power coefficient ξ and some parameters (Mach number, pressure, density, velocity ratio u/u_∞, temperature ratio T/T_∞, total pressure after normal shock wave $p_s^*/p_{s\infty}^*$) in a temperature wake at symmetry axes ($z = 4$)

M_∞	Description	ξ	M	p	ρ	u/u_∞	T/T_∞	$p_s^*/p_{s\infty}^*$
2	$Q: 60 \times 0.2 \times 0.2$	2.46	1.40	0.979	0.283	1.30	3.46	0.527
3	$Q: 90 \times 0.2 \times 0.2$	2.57	1.96	0.939	0.292	1.18	3.22	0.423
4	$Q: 120 \times 0.2 \times 0.2$	2.57	2.53	0.895	0.293	1.10	3.06	0.370
5	$Q: 150 \times 0.2 \times 0.2$	2.57	3.09	0.882	0.296	1.07	2.98	0.346

that energy source intensity is proportional to Mach number of upstream flow $Q_0 \sim M_\infty$. Physically this condition means that each fluid particle during motion through the energy deposition region at different speed gets just the same additional portion of energy ΔQ. The results are presented in Fig. 1 and Table 1.

The input power coefficient ξ remains just the same for different Mach numbers. According to Eq. (5) critical Mach number is proportional to Mach number in third degree $Q_0^* \sim M_\infty^3$. The flow is supercritical at $M_\infty = 2$ (bow shock wave) and subcritical for $M_\infty \geq 3$ (hanging shock waves) (Fig. 1). The higher the Mach number, the lesser the velocity increase u/u_∞ in the wake, and the more are relative total pressure losses behind the normal shock wave $p_s^*/p_{s\infty}^*$ (Table 1). Pressure approaches to $p = 1$ in the temperature wake downstream the energy deposition region – the higher is Mach number, the longer is distance. The most important conclusion is that for all cases temperature wake is just the same both in qualitative aspect (Fig. 1) and quantitative aspect (Table 1). According to thermal spike conception [17, 18], density cross distribution in the wake is a key factor for

determining the isobaric front separation zone shape and hence wave drag reduction of bodies.

4 Efficiency of Wave Drag Reduction at Different Mach Numbers

Wave drag coefficient c_x was defined as a ratio of a wave drag force F_x and a dynamic impact on a body midsection $S_B = \pi R_B^2$. The efficiency coefficient for wave drag reduction η was defined as a ratio of a saved propulsion power and a total power input W:

$$c_x = \frac{F_x}{0.5\rho_\infty u_\infty^2 S_B}; \quad \eta = \frac{U_\infty \Delta F_x}{\xi H} = \frac{(\gamma - 1)\, {M_\infty}^2 S_B \Delta c_x}{2\xi S_Q} = \frac{(\gamma - 1)\, {M_\infty}^2 \Delta c_x}{2\xi \Delta r^2}; \tag{6}$$

According to Eq. (6), wave drag reduction efficiency coefficient is proportional to Mach number in second degree M_∞^2 and proportional to ratio of a body midsection and an energy deposition region midsection $S_B/S_Q = 1/\Delta r^2$. At first sight this conclusion is not more than mathematical trick because even if input power coefficient ξ remains constant then wave drag reduction Δc_x could depend on both Mach number and energy source size.

In the present study, we have analyzed supersonic flow past a sphere of a radius $R_B = 1$ in the presence of energy sources localized in very small regions of upstream flow at different Mach numbers. We have proposed that energy source intensity is inversed proportional to energy source radius (Eq. (3) similarity conditions) and proportional to Mach number (additional condition) $Q_0 \sim M_\infty/\Delta r$. The results are presented in Table 2 and Fig. 2.

To avoid transversal pulsations of front separation zones, we applied a process of quasi-stationary transformation of an energy deposition region proposed in [18]. Initially for each Mach number, steady flow was computed for relatively large energy source $\Delta r = 0.2$. Then the energy source radius Δr was decreased linearly with time from $\Delta r = 0.2$ down to $\Delta r = 0.02$ in such a manner that the similarity criteria Eq. (3) were satisfied. Finally for each Mach number quasi-stationary

Table 2 The efficiency of wave drag reduction of sphere for different Mach numbers

M_∞	Description	Start $\Delta r = 0.2$, $\Delta z = 0.2$			Finish $\Delta r = 0.02$, $\Delta z = 0.02$		
		ξ	$\Delta c_x/c_x^0$	η	ξ	$\Delta c_x/c_x^0$	η
2	Q: 60–600	2.46	37.6%	2.60	2.46	25.6%	177
3	Q: 90–900	2.57	36.1%	5.38	2.57	33.2%	495
4	Q: 120–1200	2.57	31.1%	8.37	2.57	34.9%	939
5	Q: 150–1500	2.57	26.2%	11.0	2.57	30.0%	1260

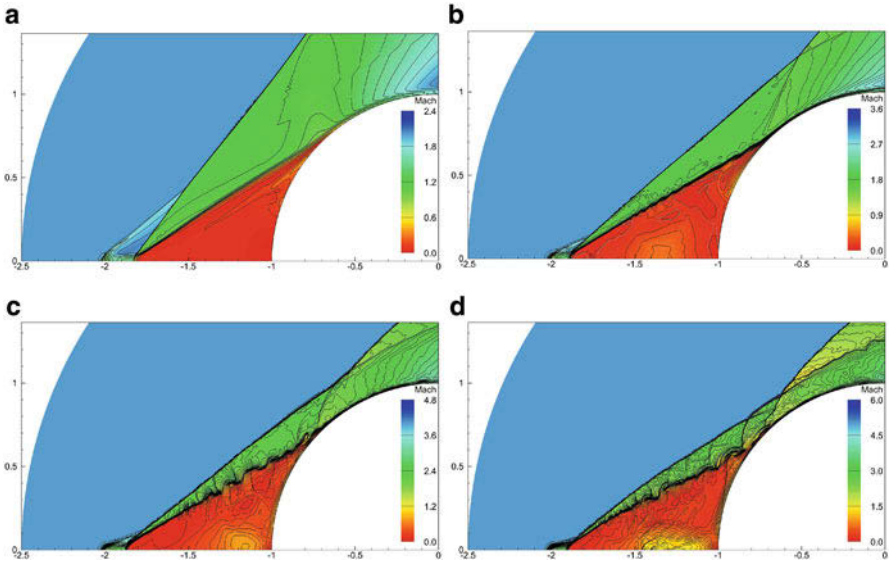

Fig. 2 Supersonic flow past a sphere in the presence of energy sources of very small size (Mach numbers isolines) $\Delta r = 0.02$, $z_0 = -2$ (**a**) $M_\infty = 2$, $Q_0 = 600$. (**b**) $M_\infty = 3$, $Q_0 = 900$. (**c**) $M_\infty = 4$, $Q_0 = 1200$. (**d**) $M_\infty = 5$, $Q_0 = 1500$

isobaric front separation zone of blunted cone shape were formed (Fig. 2). The very important conclusion is that for different Mach numbers, final virtual shape bodies (sphere together with separation zone according to [9] terminology) were just the same. This result is more or less understandable because as we have mentioned above in each case temperature wake downstream the energy deposition region was just the same.

During transformation process, dimensionless parameters in the wake were the same in geometrically similar points. Therefore according to thermal spike conception [17, 18], a static pressure inside front separation zone and consequently a wave drag reduction Δc_x remained approximately the same (Table 2 – rows). Moreover for different Mach numbers, wave drag reduction Δc_x is also just the same because virtual shape bodies are just the same (Table 2 – columns).

So the condition $Q_0 \sim M_\infty/\Delta r$ is a kind of universal synthetic similarity condition for wave drag reduction by localized energy deposition. If this condition is satisfied than input power coefficient ξ and wave drag reduction coefficient Δc_x are just the same and according to Eq. (6), the efficiency coefficient η is proportional to M_∞^2 and inverse proportional to Δr^2.

5 Conclusions

A computational study of supersonic flow past blunt bodies in the presence of energy deposition localized in very small regions of upstream flow is performed. The effect of front separation zone formation due to the interaction of a bow shock wave and a shock layer with "thermal spike" (a high-temperature wake downstream of the energy deposition region) is investigated. The universal similarity condition for effective wave drag reduction of bodies due to localized energy deposition and front separation zone formation is determined. The energy source intensity should be proportional to Mach number of upstream flow and inverse proportional to energy source size. If this condition is satisfied, then input power coefficient (a ratio of input power and an enthalpy flux through an energy source cross section) and wave drag reduction coefficient Δc_x are just the same for different Mach numbers and energy source size. In this case the efficiency coefficient (a ratio of a saved power and an input power) is proportional to Mach number in second degree and inverse proportional to energy source radius in second degree.

Acknowledgments The investigations were carried out according to research plan of the Institute of Mechanics of Lomonosov Moscow State University with partial financial support of Russian Foundation for Basic Research (projects 16-29-01092 and 18-01-00793).

References

1. P.Y. Georgievsky, V.A. Levin, Supersonic flow over bodies in the presence of external heat release sources. Pisma v Zhurnal Tekhnicheskoi Fisiki **14**(8), 684–687 (1988). (in Russian)
2. V. Borzov, I. Rybka, A. Yuriev, The estimation for power input using for wave drag reduction of a body in a supersonic flow. Inzhenerno – Phizicheski Zhurnal **63**(6), 659–664 (1992). (in Russian)
3. L.N. Myrabo, Yu.P. Raizer, AIAA Paper 1994–2451 (1994)
4. P.K. Tret'yakov, A.F. Garanin, V.L. Krainev, V.I. Yakovlev, et al., Control of supersonic flow around bodies by means of high-power recurrent optical breakdown. Dokl. Phys. **41**(11), 566–567 (1996)
5. V.A. Levin, N.A. Afonina, V.G. Gromov, AIAA Paper 1999–4967 (1999)
6. D. Riggins, H.F. Nelson, E. Johnson, AIAA J. **37**(4), 460–467 (1999)
7. P.Y. Georgievskii, V.A. Levin, Control of the flow past bodies using localized energy addition to the supersonic oncoming flow. Fluid Dyn. **38**(5), 154–167 (2003)
8. D. Knight, J. Propuls. Power **24**(6), 1153–1167 (2008)
9. M.N. Shneider, S.O. Macheret, S.H. Zaidi, I. Girgis, R.B. Miles, J. Propuls. Power **24**, 900–915 (2008)
10. E. Schülein, A. Zheltovodov, Shock Waves **21**, 383–396 (2011)
11. E. Erdem, K. Kontis, L. Yang, Shock Waves **23**, 285–298 (2013)
12. A. Sasoh, J.-H. Kim, K. Yamashita, T. Sakai, Shock Waves **24**, 59–67 (2014)
13. Y. Kolesnichenko, D. Khmara, V. Brovkin, S. Afanas'ev, AIAA Paper 2007-1228 (2007)
14. J.B. Michael, A. Dogariu, M.N. Shneider, R.B. Milesa, J. Appl. Phys. **108**, 093308 (2010)
15. O. Azarova, D. Knight, Y. Kolesnichenko, ShockWaves **21**(5), 439–450 (2011)
16. K. Anderson, D. Knight, Shock Waves **21**(2), 149–161 (2011)

17. S.V. Guvernyuk, K.G. Savinov, Isobaric separation structures in supersonic flows with a localized inhomogeneity. Dokl. Phys. **52**(3), 151–155 (2007)
18. P. Georgievsky, V. Levin, AIAA Paper 2007-1232 (2007)
19. R.W. MacCormack, AIAA Paper 1969-354 (1969)
20. A. Zhmakin, A. Fursenko, On a monotonic shock-capturing difference scheme. USSR Comput. Math. Math. Phys. **20**(4), 218–227 (1980)

Experimental Investigations of a Diffuser Start/Unstart Characteristics for Two Stream Supersonic Wind Tunnel

S. Manoj Prabakar and T. M. Muruganandam

Abstract The present paper aims to clarify the starting characteristics of two stream diffusers. Two types of diffusers are examined for a two-stream supersonic wind tunnel: constant area and C-D diffuser. Experiments are conducted at five different secondary Mach numbers (1.8–2.6) by keeping primary at constant Mach number 2. High-speed schlieren and pressure measurements are used to understand the performance of the diffuser. This study reveals encouraging results in performance of this tunnel with optimum diffuser geometry. This work also highlights the visualized unsteady complex flow fields with significant boundary layer separation during the transient period for a different Mach number and diffuser conditions. Hysteresis is apparent in a transient process of start/unstart of a tunnel; it is used to decrease the operating starting pressure of the tunnel.

1 Introduction

Efficient recovery of kinetic energy into pressure energy is important in designing wind tunnels with low-power requirements. Recovery of high-speed flow kinetic energy poses many problems of interest to designers of gas dynamic lasers [1, 2], super ejectors [3], high-altitude test facilities [4], and air-augmented rockets. When the flow entering the passage is supersonic, the diffusion process is particularly difficult. Performance of two stream supersonic diffusers is very different from single stream ones, especially when the Mach number difference is large [5]. A quick survey of literature shows that no systematic study on two stream supersonic wind tunnel diffusers has been conducted [6]. There is very little knowledge on nonuniform flows in diffusers or ejectors. Flows in the test section of hypersonic wind tunnels, and in the cavity of gas dynamic laser systems, are known to be significantly complex, with wakes, shear layers, mixing layers, recirculation

S. Manoj Prabakar (✉) · T. M. Muruganandam
Department of Aerospace Engineering, Indian Institute of Technology Madras (IIT-M), Chennai, India

A. Sasoh et al. (eds.), *31st International Symposium on Shock Waves 2*,
https://doi.org/10.1007/978-3-319-91017-8_139

regions, and wall boundary layers, interacting with each other and with shock waves and expansions. In such cases, understanding the behavior of flow becomes critical to efficient design and operation. Therefore, a systematic study on nonuniform flows in supersonic diffusers is required.

Two types of diffusers are examined for a two stream supersonic wind tunnels: constant area and convergent-divergent (C-D) diffuser. In a constant area diffuser, the duct is parallel, i.e., cross-sectional area is constant, and pressure recoveries similar to those across normal shock waves are obtainable with the pressure rise being attributable to a complex series of shocks which may extend over an axial distance equal to several channel widths. While deceleration of a supersonic stream to subsonic speeds with lower losses requires, ideally, C-D ducts, it is known that the flow has a tendency to separate from the passage walls in the divergent region [7]. Consequently, diffusion to subsonic speeds becomes difficult in this case and further, excessive losses result due to eddies in the separated region.

Despite several studies dealing with two stream supersonic wind tunnels [8–10], many aspects of their starting procedures are not clearly described, particularly when one seeks quantitative data of the starting stagnation pressure. The present paper aims to study the starting characteristics of two stream supersonic diffuser, with primary stream fixed at Mach 2 and secondary stream with $1.8 \leq M \leq 2.6$. The occurrences of hysteresis, during the process of start/unstart, were also targeted. Flow is investigated using schlieren visualization, wall pressure measurements, and exit plane stagnation pressures.

2 Experimental Setup and Procedures

2.1 Experimental Setup

Experiments were conducted at IIT Madras transparent supersonic blow-down wind tunnel. Figure 1 shows a schematic of the facility. Compressed air from a common settling chamber was used for both the streams. A 1-mm-thick 125-mm-long aluminum splitter plate separates the two supersonic flows created by two supersonic nozzles. Nozzles were designed using MOC to get the supersonic flow. The nozzle and diffuser were made as two different pieces. Side walls were made of transparent polycarbonate sheet for optical access.

Five different 2D diffusers are used in this study to understand the geometric influence of the diffusers and the detailed parameters shown in Table 1. The diffuser has three sections, converging mixing section of length (L_2) followed by constant area throat of length (L_3) and subsonic diffuser of length (L_4). Notice that Diffuser 1 is a constant area diffuser and has given same dimensional parameter i.e., contraction ratio $= H_{in}/H_{throat}$. The converging angle (θ) and subsonic diffuser angle (β) are fixed at 6 and 7°, respectively.

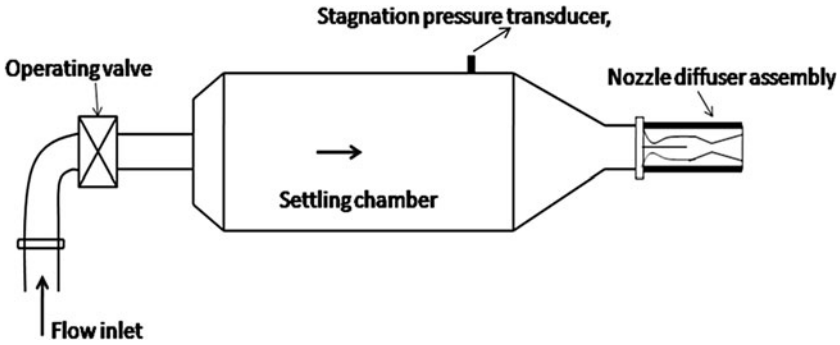

Fig. 1 Schematic of the test facility

Table 1 Geometric parameters of the diffusers

Diffuser number	H_m (mm)	Contraction ratio H_{in}/H_{sth}	L_3 (mm)
Diffuser 1	50	1.0	175
Diffuser 2	50	1.1	80
Diffuser 3	50	1.2	80
Diffuser 4	50	1.3	80
Diffuser 5	50	1.4	80

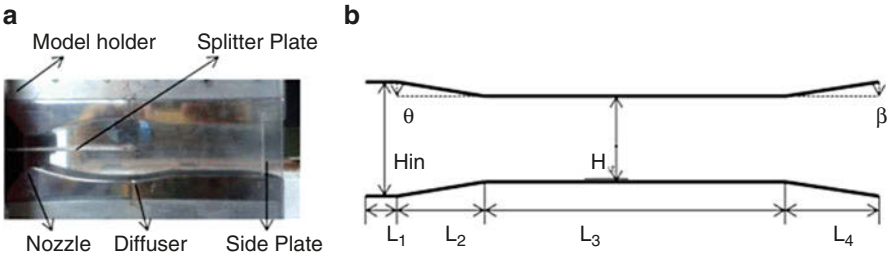

Fig. 2 (**a**) Nozzle-diffuser setup (**b**) Supersonic diffuser schematic

The side walls of the test section are transparent acrylic sheets to have clear optical access for schlieren visualization. Maximum viewing is of approximately 80 mm high and 287 mm long. Figure 2a, b shows nozzle-diffuser setup schematics of supersonic diffuser, respectively. This supersonic-supersonic apparatus provides two planar and uniform supersonic streams entering into the supersonic diffuser. The diffuser has constant area mixing tube instrumented with static pressure taps and a total pressure rake in the diffuser exit plane.

The high-speed schlieren images (with horizontal knife edge) were captured using IDT N4-S3 high-speed CMOS camera, at sampling rates (500 to 2000 fps). Piezo-resistive transducers (GE DRUCK PMP-4110) were used to measure stagnation pressure (P_0) in the settling chamber, static pressure at entry, and exit of the diffuser with an accuracy of 0.05% full scale. Total pressures at the exit of the

diffuser and diffuser wall static pressure distributions were measured with a 16-channel DSA 3217 Scanivalve Corp. transducer with a range of 0–750 psi. Data was acquired from 16 channels simultaneously a 500 fps. Zero correction and calibration correction were performed before using the data. The accuracy of the transducer is specified to be 0:05% full scale. Multiple experiments were done to check the repeatability.

2.2 Experimental Procedure

To analyze the experimental data with an accurate time base, the starting characteristics of a tunnel are investigated by correlating the stagnation chamber pressure, diffuser entry, and exit pressure with the schlieren images. In order to achieve this, a reference time has been fixed as follows. Data acquisition (DAQ) is started first, acquiring pressure changes due to operation of valves. Camera acquisition starts next, and its sync out signal is also recorded in the DAQ. The stagnation pressure in the tunnel is increased by opening the control valve. It can be shown as the peak has been marked as the reference time ($t = 0$) for all the experiments. This is shown in Fig. 3a, where the voltage signals from sensors and camera are plotted with respect to flow time. The procedure shown in Fig. 3 illustrates the schematic of acquired voltage data details from the experiments.

The symbols, P_o and p_b, represent the stagnation pressure of the settling chamber and back pressure (atmospheric pressure), respectively. Figure 3b gives the better picture of the progress of driving stagnation pressure and wall pressures at the diffuser entry (p_i) and exit (p_e) during the lifetime of tunnel operation. Several values of constant P_0 cases were taken for each Mach number at the tunnel started condition. The variation in flow Mach number is achieved by changing the nozzle blocks. Mach number upstream of the diffuser was estimated by both pressure and image processing, and they were in good agreement with each other and theoretical value. Sample schlieren pictures of C-D diffuser and constant area diffuser of the same length in a started condition are shown in Fig. 4. The position of the terminal shock was controlled by varying the stagnation pressure.

3 Results and Discussion

3.1 Operational Characteristics

Experiments were conducted to visualize operational characteristics of two stream supersonic flow in a supersonic diffuser and to get pressure recovery at the exit of the diffuser, static pressure rise, and schlieren flow visualization of the shock dynamics.

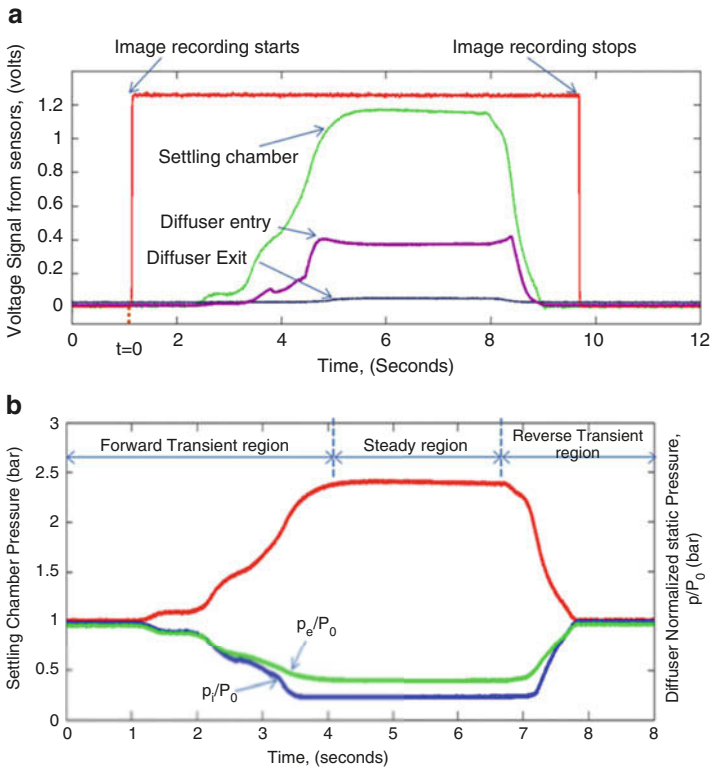

Fig. 3 (**a**) Voltage signals from the sensors and camera with reference condition. (**b**) Evolution of driving stagnation pressure and diffuser entry and exit pressures during the process of wind tunnel operation

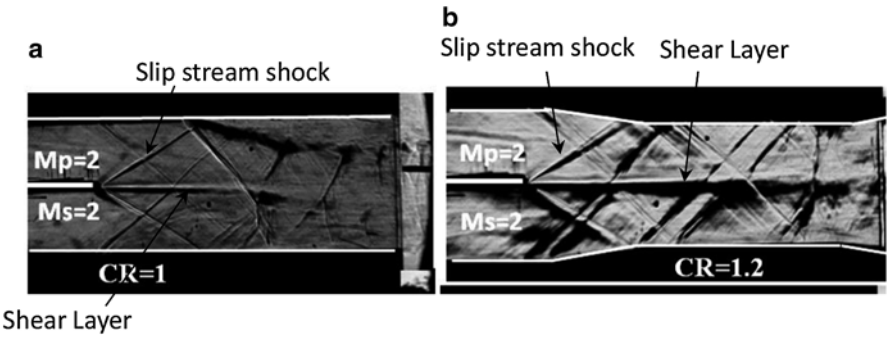

Fig. 4 (**a**) Convergent-divergent diffuser (**b**) Constant area diffuser

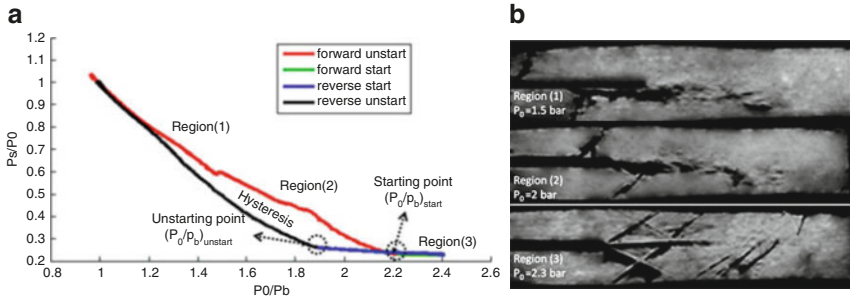

Fig. 5 (**a**) Performance curve of a tunnel between open (forward) and close (reverse) operation. (**b**) Flow evolution starting characteristics of a two stream tunnel, Ms = 1.8, Mp = 2, CR = 1.1

The performance curve of the two stream tunnel is illustrated shown in Fig. 5a. The normalized stagnation pressure (P_o/p_b) was plotted against the normalized secondary pressure (p_s/P_o). When the flow through this tunnel is started by opening valve in settling chamber, high-pressure air from the chamber acts as the piston pushes the starting normal shocks emanating between the low-pressure expanding air and ambient air through the tunnel.

In the region (1), the front part of the diverging section of nozzles becomes supersonic and aft part becomes subsonic with a starting normal shock demarcating these two flow regions, while both the nozzle and diffuser remain unstarted. As a result, subsonic mixing occurs between the primary and secondary flows in the entire mixing section of diffuser. In region (2), the starting normal shock in the primary side is swallowed through the diffuser creating supersonic flow in the primary side, since lower Mach number requires less (P_o/p_b). But the secondary side normal shock remains in the divergent portion of the secondary nozzle. Therefore, the supersonic-subsonic mixing occurs in the entire mixing chamber. Further increase in (P_o/p_b) beyond starting pressure in the region (2) causes the tunnel to attain region (3) where tunnel is started with the shock structure fully established as shown in Fig. 5b. The tunnel is said to be "started" if flow at the exit of the two nozzles is supersonic and at the Mach number obtained in calibration runs. At the region (3), the tunnel is fully started, and the supersonic-supersonic mixing occurs in the mixing chamber, and the corresponding pressure ratio (P_o/p_b) is the minimum starting pressure ratio $(P_o/p_b)_{Start}$. If the tunnel pressure ratio decreased below the unstart pressure ratio from the Fig. 5b, the tunnel becomes unstarted. In a reverse process, it is noted that tunnel remains started at pressure ratio below the minimum starting pressure ratio $(P_0/p_b)_{Start}$. The difference between the starting pressure ratio and unstart pressure ratio shows that there is hysteresis phenomenon in start/unstart of a two stream tunnel.

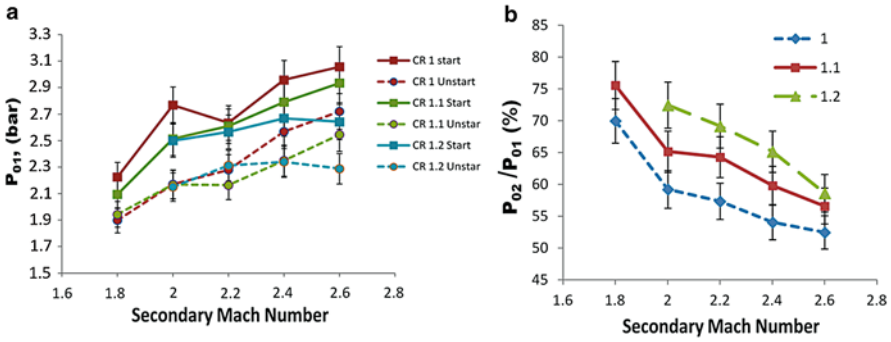

Fig. 6 (**a**) Effect of contraction ratio on starting pressure ratio, (**b**) effect of contraction ratio on pressure recovery

3.2 Influence of Diffuser Contraction Ratio on Pressure Recovery

For each combination of Mach number, tests were run to find optimum second-throat area starting with the wide open throat position (Diffuser 1). As the throat opening was reduced gradually, the shock system remains in the nozzle; thus wind tunnel unstarts above 1.2 contraction ratio. Thus the last two diffusers were not useful in this study, up to stagnation pressures of 5 bar. It very much evident from the Fig. 6a effect of contraction ratio decreases minimum starting pressure ratio to start a wind tunnel. It is also evident the unstart pressure is always lesser than the starting pressure, showing that there is hysteresis in all the diffusers that started.

The ratio between the exit stagnation pressures (P_{02}) and the settling chamber pressure (P_{01}) just prior to the start of the supersonic wind tunnel is referred to as the maximum obtainable stagnation pressure recovery for the particular combination of the diffuser and inlet Mach numbers. Diffusers with contraction ratio of 1.2 give slightly higher pressure recovery than the corresponding diffuser of 1.1, and the diffusers with contraction ratios above 1.2 unstart the tunnel. Thus it can be summarized that the pressure recovery is better for higher contraction ratios of the diffuser, but beyond some CR, the diffuser will not start fully. But the increase in secondary Mach number results in an increase in P_{01} and lower recovery because more pressure is needed to accelerate more mass flow rate in a fixed second-throat diffuser. This may also be related to the single settling chamber arrangement in this facility. Further study will involve different stagnation pressures for the two streams.

4 Conclusions

Performance characteristics of two stream supersonic wind tunnel are experimentally investigated. It is observed at started condition, two stream supersonic flows are decelerated by a series of shock trains. At started condition shock

oscillations were found with shock-induced separation of the boundary layer. A certain pressure is required to start the diffuser, and the starting pressure decreases as the contraction ratio of the diffuser increases. The lowest stagnation pressure required for diffuser starting is itself a function of the geometry of the second-throat diffuser. Experiments show that behavior of one stream is influenced by the presence of the other stream. Hysteresis separates the start and unstart pressure ratio of the tunnel. Experiments show that the starting condition of a given diffuser configuration primarily depends on the stagnation pressure of the settling chamber.

References

1. V.A. Amatucci, J.C. Dutton, A.L. Addy, Pressure recovery in a constant-area, two-stream supersonic diffuser. AIAA J. **20**, 1308–1309 (1982)
2. R.J. Driscoll, L.F. Moon, Pressure recovery in chemical lasers. AIAA J. **15**, 665–673 (1977)
3. J.C. Dutton, D. Mikkelsen, A.L. Addy, A theoretical and experimental investigation of the constant area, supersonic-supersonic ejector. AIAA J. **20**, 1392–1400 (1982)
4. R.M. Kumaran, T. Sundararajan, D.R. Manohar, Performance evaluation of second-throat diffuser for high-altitude-test facility. J. Propuls. Power **26**, 248–258 (2010)
5. D. Papamoschou, Diffuser performance of two-stream supersonic wind tunnels. AIAA J. **27**, 1124–1127 (1988)
6. J.A. Johnson III, B.J. Wu, Pressure Recovery And Related Properties In Supersonic Diffusers: A Review. AFOSR Report, (April), 1974
7. J. Lukasiewicz, Diffusers for supersonic wind tunnels. J. Aeronaut. Sci. **20**, 617–626 (1953)
8. D. Papamoschou, A. Roshko, The compressible turbulent shear layer: An experimental study. J. Fluid Mech. **197**, 453 (1988)
9. J.P. Renie, J.C. Dutton, H. Krier, N.L. Messersmith, S.G. Goebel, Investigation of supersonic mixing layers. J. Propuls. Power **6**, 353–354 (1990)
10. N. Chinzei, G. Masuya, T. Komuro, A. Murakami, K. Kudou, Spreading of two stream supersonic turbulent mixing layers. Phys. Fluids **29**, 1345 (2005)

Experimental Investigation of Film Cooling Technique over a Blunt Body in Hypersonic Flow

J. L. K. Sindhu, S. Mohammed Ibrahim, and K. P. J. Reddy

Abstract As an alternative to conventional TPS (thermal protection system), film cooling technique has been previously extensively studied. The aim of the current work is to inject new coolants, i.e., mist (atomized water particles) and N_2-CO_2 mixture, and study the heat transfer variation over the surface of a blunt body in hypersonic flow.

1 Introduction

Exceedingly high temperatures are experienced by a spacecraft during reentry. Thus, the design of thermal protection system is very crucial to ensure flight vehicle safety. The TPS commonly used on Earth and other planetary entry spacecrafts is ablative cooling system. Although ablative cooling has been successfully employed, it has certain drawbacks. Especially when reusability of the spacecraft is concerned, it can be very expensive. This drove us to explore alternate techniques for TPS.

Film cooling is one such technique, where a coolant gas is injected from the body surface into the shock layer, with the injected coolant modifying the boundary layer characteristics and minimizing the heat transfer rate to the body. The evolution of coolant jet, various parameters affecting the film cooling effectiveness, and the performance of different coolant gases like N_2, CO_2 ,and He are well studied and established over the past decades [1–3]. Exploration of new coolants for the purpose of film cooling is the objective of current study. Water has a heat capacity of 4.2 KJ/Kg K and a high latent heat of vaporization of 2442 J/Kg making it a potential coolant. In the present study, liquid water is atomized using an in-house seeder to create mist particles of size of the order of a few micrometers. Atomization not only makes water injection feasible but also increases the surface area available for heat absorption. Mist injection has been carried out at different pressures, and

J. L. K. Sindhu (✉) · S. Mohammed Ibrahim · K. P. J. Reddy
Laboratory for Hypersonics and Shock Wave Research, Department of Aerospace Engineering, Indian Institute of Science, Bangalore, India

A. Sasoh et al. (eds.), *31st International Symposium on Shock Waves 2*,
https://doi.org/10.1007/978-3-319-91017-8_140

Table 1 Free stream flow conditions

M_∞	5.69
U_∞ (m/sec)	1481.538
P_0 (KPa)	992.8744
T_0 (K)	1261.533
P_∞ (KPa)	0.874631
T_∞ (K)	168.9213
ρ_∞ (kg/m^3)	0.018001
Re_∞ (million/m)	2.3243
H_0 (MJ/kg)	1.267209

its effects on the flow field and surface heat transfer rates were observed. Another coolant currently under study is N_2-CO_2 mixture. Ibrahim et al. [4] reported that the near-resonant transfer of vibrational energy from N_2 to the asymmetric stretching mode v3 of CO_2 as the possible explanation for enhanced performance of nitrogen as coolant in high enthalpy CO_2 flows. Studies are ongoing to test this phenomenon using a mixture of composition of 79% N_2 and 21% CO_2 by weight.

1.1 Experimental Facility

The experiments were carried out in hypersonic shock tunnel (HST2), at a flow enthalpy of 1.26 MJ/kg and the flow conditions generated for the current set of experiments are presented in Table 1.The driver and driven side of the shock tube are filled with 40 bar helium and 200 mm hg of air, respectively. A pneumatically operated rapid opening sleeve (i.e., the diaphragm-less valve) ISTA KB-40 separates the driver and the driven section. Fast opening act of the diaphragm-less valve results in generation of shock wave which travels along the length of the driven section rupturing the paper diaphragm and resulting in expansion of test gas to hypersonic velocities in the nozzle. As shown in Fig. 1, the model is mounted inside the test section and the dump tank is equipped with ports to connect the inlet of the model to the external cylinder to facilitate injection.

1.2 Model and Mist Injection Setup

The test model is a large angle blunt cone with an apex angle of 60°, a nose radius of 35 mm, and a base diameter of 80 mm. Platinum thin-film sensors are fabricated on the Macor strip and flush mounted on to the surface of model to measure the convective heat transfer rates (Fig. 2).

A total of 8 thin-film sensors, 4 on each side of the stagnation point, are used in the present investigation. The coolant is injected through the micro jet plate (dia 300 μm) housed in the nose portion of the model.

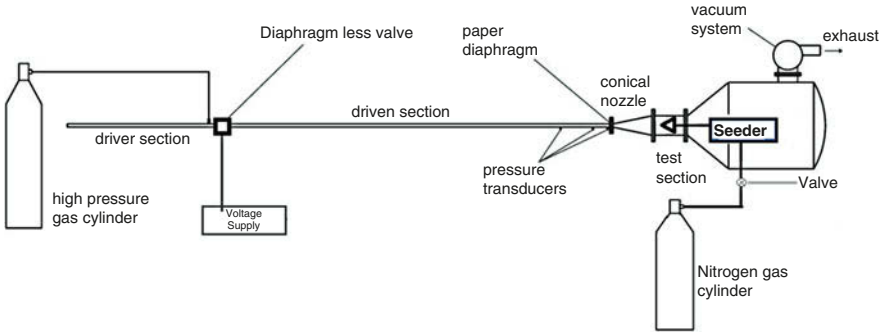

Fig. 1 Schematic of HST2 facility

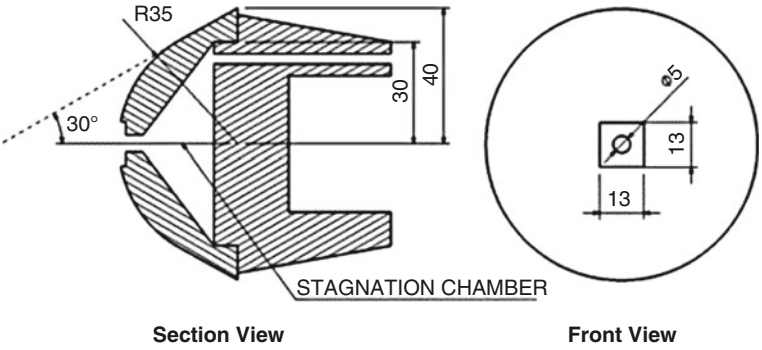

Fig. 2 Schematic of the test model

Mist particles are generated thorough an in-house built seeder [5]. The seeder chamber is pressurized through a cylindrical strut immersed in water as shown in Fig. 3. The bottom of the strut has four 1 mm dia holes on its periphery through which the high-pressure gas disperses into water producing a mixture of the high-pressure gas and mist particles in the size range of 0.8–1 μm. The nose portion of the model is directly connected to the outlet of seeder using a flexible polyurethane pipe to avoid condensation of mist particles on the walls of the model chamber. However, in case of N_2-CO_2 mixture injection experiments, the model stagnation chamber is connected to the external cylinder through the solenoid valve.

1.3 Experimental Procedure

The vacuum chamber of the tunnel is evacuated to 10^{-5} m bar. To avoid the drop in vacuum when the injected coolant is released into the chamber, a timing circuit was designed as shown in Fig. 4. The switch supplies voltage to open the diaphragm-

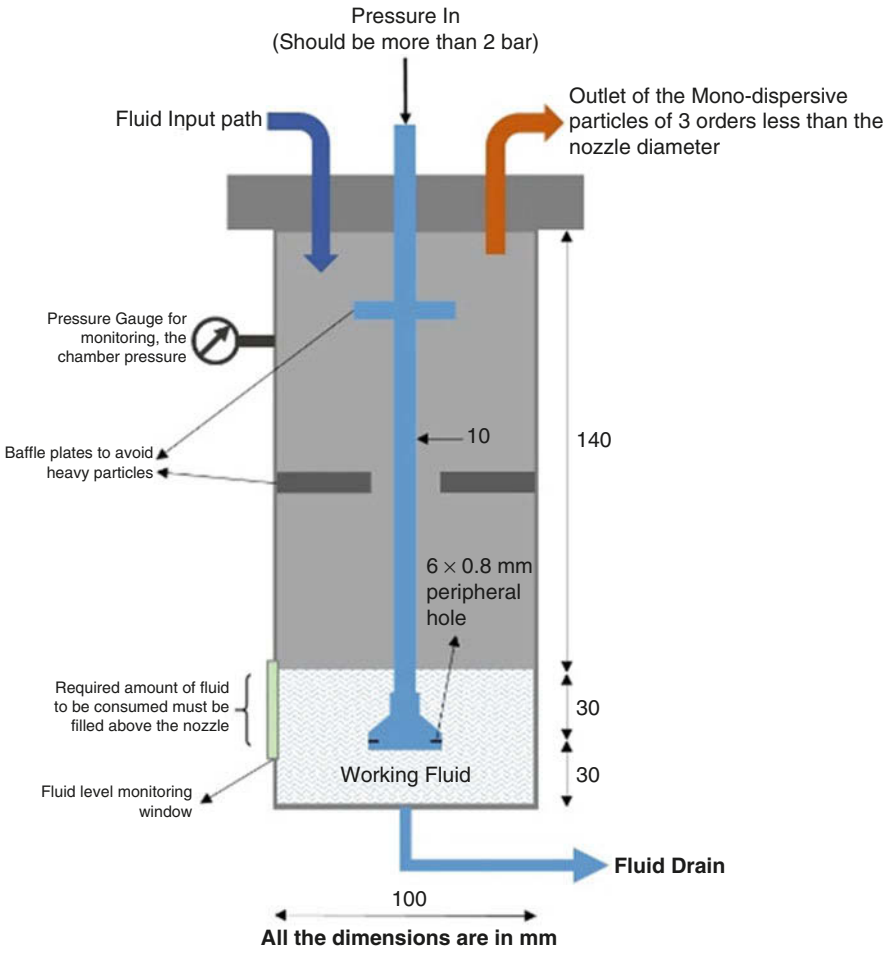

Fig. 3 In-house built seeder

less valve and simultaneously sends an impulse signal to the delay pulse generator (DPG), which in-turn opens the solenoid valve after the set delayed time. The solenoid valve is connected in between the model and the seeder and upon opening releases the injected coolant into the model. In case of N_2-CO_2 mixture injection, the solenoid valve is connected in between the mixture cylinder and the model.

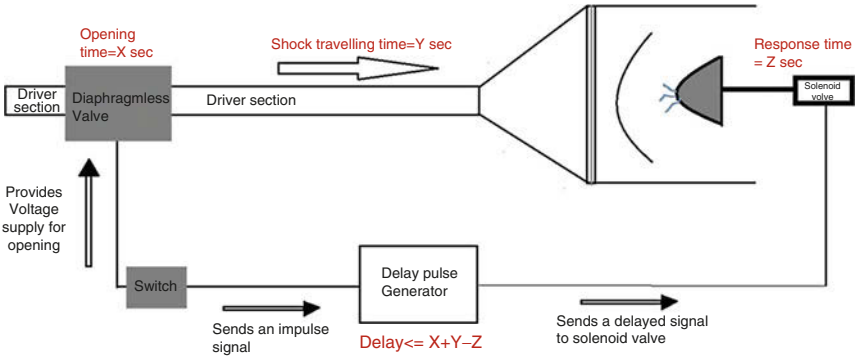

Fig. 4 Timing the simultaneous arrival of shock and injected coolant

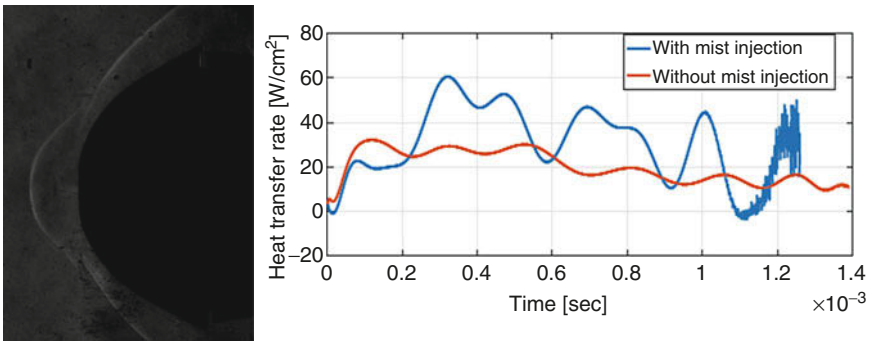

Fig. 5 Left: Schlieren visualization of the flow field for the case of mist injection for a supply pressure of 4 bar. Right: Typical heat transfer rate signals for the gauge closest to nose region of model for the cases of with and without mist injection

2 Results and Discussion

2.1 Mist Injection

2.1.1 Injection Disturbing the Flow Field

The mist was injected at a cylinder supply pressure of 4 bar disturbing the shock ahead of the model. Figure 5 shows the heat transfer rate signals for the cases of with and without mist injection for the gauge closest to the nose region of the model. It can be observed that the heat transfer rate for the case of with injection is fairly high compared to the case of without injection throughout the steady test time.

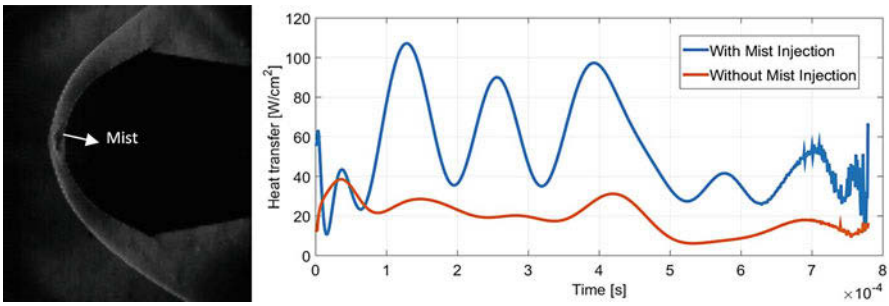

Fig. 6 Left: Schlieren visualization of the flow field for the case of mist injection for a supply pressure of 1.37 bar. Right: Typical heat transfer rate signals for the gauge closest to nose region of model for the cases of with and without mist injection

2.1.2 Injection Without Disturbing the Flow Field

In this case the mist was injected at a cylinder supply pressure of 1.37 bar without disturbing the shock ahead of the model. Figure 6 shows the heat transfer rate signals for the cases of with and without mist injection for the gauge closest to the nose region of the model. In spite of reducing the supply pressure of mist from 4 bar to 1.37 bar and not disturbing the bow shock like in the previous case (3.1.1), the heat transfer rate for the case of mist injection continues to be high compared to the case of without injection. Also the unsteadiness in heat transfer rate is higher for 1.37 bar case compared to the 4 bar supply pressure case.

2.2 N_2-CO_2 Mixture Injection

The mixture was injected from the stagnation point of the model at a cylinder supply pressure of 1.37 bar, and the schlieren flow field was visualized as shown in Fig. 7. The surface convective heat transfer rate measurements are currently ongoing.

3 Conclusion

Injection from the stagnation point of a blunt body model was carried out using two coolants, i.e., mist and N_2-CO_2 mixture. The flow field visualization for the case of mist injection (at supply pressures of 4 bar and 1.37 bar) and for the case of N_2-CO_2 mixture injection (at a supply pressure of 1.37 bar) has been performed.

The heat transfer rates for the thin-film gauge closest to the stagnation point of the model have been obtained for the case of mist injection for both the supply pressures of 4 bar and 1.37 bar.

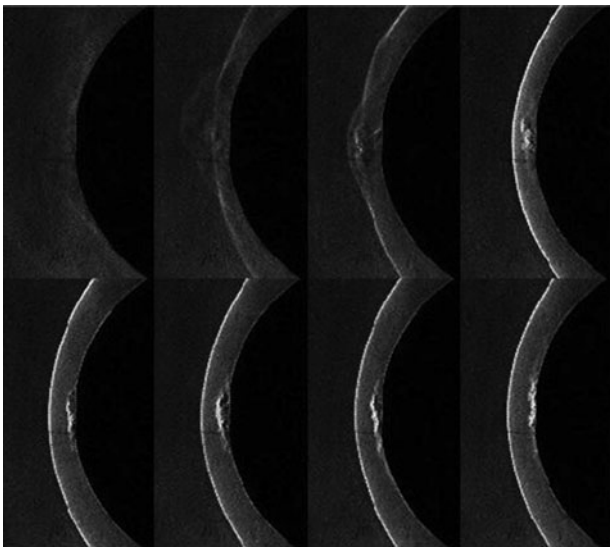

Fig. 7 Schlieren images showing the diffusion of the injected coolant from the stagnation point during the flow buildup and steady test time

The heat transfer rate for both the supply pressures is higher compared to the no-injection case.

Further studies are planned at supply pressures lower than 1.37 bar to verify the effectiveness of mist injection and N_2-CO_2 mixture injection for the purpose of reduction of heat transfer, the results of which will be presented during the poster presentation.

References

1. R. Sriram, G. Jagadeesh, Film cooling at hypersonic Mach numbers using forward facing Array of micro-jets. Int. J. Heat Mass Transf. **54**, 3654–3664 (2009)
2. P.J. Finley, The flow of a jet from a body opposing a supersonic free stream. J. Fluid Mech. **26**(2), 337–368 (1966)
3. N. Sahoo, V. Kulkarni, S. Saravanan, G. Jagadeesh, K.P.J. Reddy, Film cooling effectiveness on a large angle blunt cone flying at hypersonic speed. Phys. Fluids **17**, 036102 (2005)
4. S. Mohammed Ibrahim, R. Sriram, K.P.J. Reddy, Experimental investigation of heat flux mitigation during Martian entry by coolant injection. J. Spacecr. Rocket. **51**(4), 1363–1368 (2014)
5. S.K. Karthick, G. Jagadeesh, K.P.J. Reddy, Visualization of supersonic free and confined jet using planar laser mie scattering technique. J. Indian Inst. Sci. **96**, 29–46 (2016)

Wavefront Aberration in a Laser Beam Induced by Supersonic Flow Field Around a Wedge

Sangyoon Lee, Mancheol Jeong, Minwook Chang, In-Seuck Jeung, and Hyoung Jin Lee

Abstract Aero-optical experiment is conducted in Mach 7 shock tunnel. To investigate the influence of shock wave and boundary layer on the optical wave, 12° wedge model with window on the surface is designed and used. Vibration of the facility is reduced by isolating the test section table from the facility. Also the nozzle shear layer is avoided by installing another wedge structure on the incident laser beam. Diode laser beam with 635 nm wavelength is shot through the flow field, and two-dimensional Shack-Hartmann sensor measured the wavefront of the laser beam. The flow characteristics are acquired by shadowgraph image and pressure measurement. The angle of the laser beam is varied to study the effect of the line of sight. From the measured wavefront, point spread function is calculated to quantify the bore sight error and Strehl ratio. As the line of sight is lowered, bore sight error increased, and Strehl ratio decreased. Thus, lower line of sight is influenced more by the flow.

1 Introduction

Propagation of optical wave is determined by the index of refraction (n) of the propagating medium. Since index of refraction of a flow is linearly related with density by Gladstone-Dale equation as in Eq. (1), compressible flow influences the propagation of the optical wave and distorts the wave.

$$n = 1 + \mathrm{K_{gd}}\rho \tag{1}$$

S. Lee · M. Jeong · M. Chang · I.-S. Jeung (✉)
Department of Mechanical and Aerospace Engineering, Seoul National University, Seoul, Republic of Korea
e-mail: enjis@snu.ac.kr

H. J. Lee
Department of Aerospace Engineering, Inha University, Incheon, Republic of Korea

A. Sasoh et al. (eds.), *31st International Symposium on Shock Waves 2*,
https://doi.org/10.1007/978-3-319-91017-8_141

Here, ρ denotes density, and K_{gd} denotes Gladstone-Dale constant, which is related to the composition of the flow and wavelength of the optical wave. Aero-optics studies this interaction between flow and optical wave, especially the flow developed near the optical system.

Density varying element around the supersonic flight vehicle is mainly shock wave, boundary layer, and shear layer. These elements affect the propagation of optical wave and degrade the performance of the optical system installed inside the flight vehicle, such as camera or laser. Thus, research have been conducted to quantify the aero-optical phenomena, which occurred by these density varying elements [1, 2].

The important parameter that quantifies aero-optical phenomena is bore sight error (BSE), Strehl ratio, and blur. BSE is defined as the shift of the source position of the optical wave, Strehl ratio represents the total quality of the image, and blur shows the diverging property of the optical wave. These parameters can be acquired from the measurement of the wavefront. Thus aero-optical experiments focus on the measurement of the wavefront.

This study experimentally investigates the aero-optical effect due to the shock wave and boundary layer in supersonic flow. Wind tunnel experiment is conducted with the wedge model. The wavefront of the laser beam, propagating through the flow field developed around the wedge model, is measured using the Shack-Hartmann wavefront sensor.

2 Experimental Setup

2.1 Test Facility

Wind tunnel experiment is conducted using AST-2 shock tunnel at Seoul National University. Figure 1 shows the overview of the test facility. Total length of the facility is 16 m, length of the driver section is 3 mm, and the length of the driven section length is 8 m. Maximum designed pressure for the driver section is 30Mpa. To measure stagnation flow condition, six PCB piezoelectric sensors are installed along the tube. The nozzle attached to the driven section is Mach 7 contoured nozzle with exit diameter 340 mm. Test section has a 1 m diameter and 3 m length. To maximize the test section size, vacuum chamber and test section are united. Nitrogen (N_2) is used for driver gas and steady-state test time is around 3 msec.

To reduce the vibration of the facility, which may affect the optics installed inside the test section, test section table is isolated with the test section chamber by installing the leg of table directly on the laboratory floor. Rubber O-ring is installed between the test section and the leg to seal the test section. There are two windows on the side for flow visualization and one flange on the top, which is used for various applications, such as path for the laser.

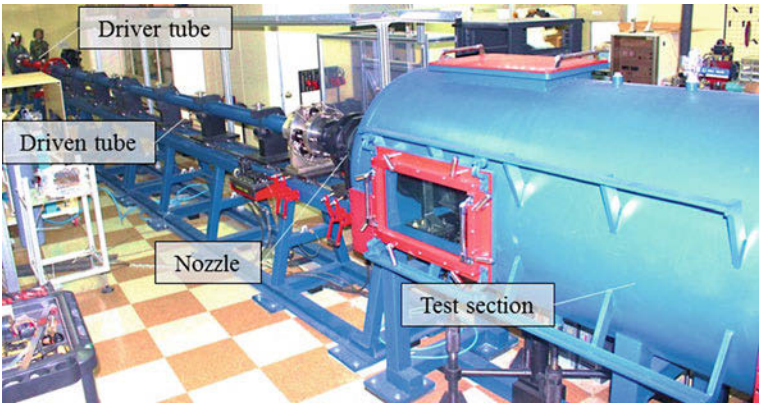

Fig. 1 Overview of AST-2 at Seoul National University

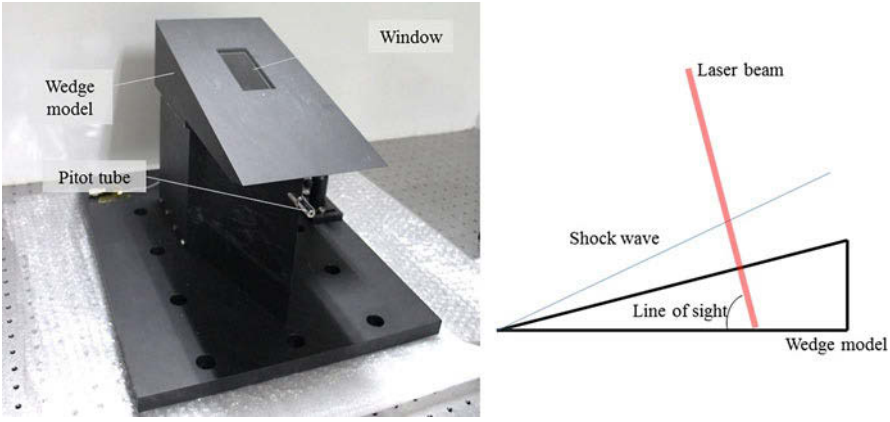

Fig. 2 Wedge model with window

2.2 Experiment Model

To study the influence of shock wave and boundary layer on the optical wave, 12° wedge model is designed. Manufactured model and the strut are shown in Fig. 2. Strut is designed to protect the optics from the flow. Window is installed on the middle of the wedge surface for the laser beam to propagate through and to be measured by the wavefront sensor. The size of the window is 40 mm × 100 mm, and the material is Nikon synthetic silica glass (SiO_2). Window size is designed to have enough space for different incident angle of the laser beam. The incident laser beam angle is defined as line of sight (LOS) as in Fig. 2. To measure the test section flow condition, two pressure sensors are used. PCB piezoelectric pressure sensor is installed inside the pitot tube below the wedge model, and Kulite pressure sensor is installed right before the wedge window.

2.3 Optical Setup

Laser beam is propagated through the flow field, to investigate the aero-optical phenomena around the wedge model. Overview of the optics is shown in Fig. 3. Laser, beam expander, mirror, beam shield, beam reducer, and wavefront sensor are used for the experiment. Diode laser with wavelength of 635 nm is expanded to 25 mm diameter parallel beam by the beam expander, which consists of 100 mm focal length positive achromatic lens and lens tube system. Since the shear layer developed at the boundary of the nozzle exit flow influences the laser beam, beam expander protector is installed, surrounding the beam expander. Protector has the window made of Schott borofloat 33 for the laser beam to propagate. The laser beam which passed through the flow field is reflected by the mirror installed inside the strut. The reflected laser beam goes through the beam shield, which protects laser beam from the nozzle flow, and passes through the test section window. Finally, the laser beam arrives to the beam reducer and the wavefront sensor. For the wavefront sensor, Lumetrics CLAS-XP, a two-dimensional Shack-Hartmann wavefront sensor is used. Since the Shack-Hartmann sensor has 30 fps, only one image can be acquired during experiment.

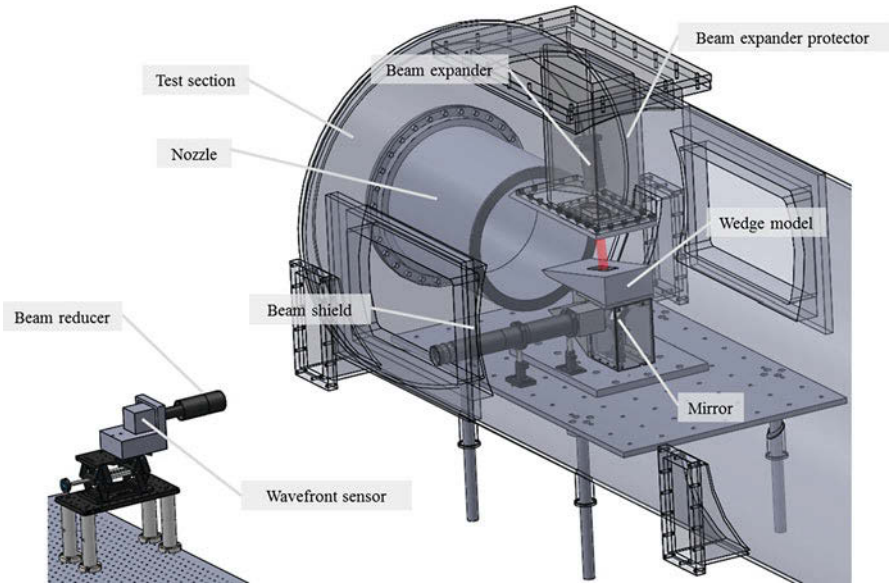

Fig. 3 Optical setup for laser beam wavefront measurement

3 Result and Discussion

3.1 Flow Measurement

In the wind tunnel experiment, flow and wavefront measurements are acquired in the same time. Shadowgraph image is acquired and pressure is measured to investigate the flow property. Figure 4 shows the shadowgraph result of the wedge model. As in Fig. 4, shock wave with 18.5° angle and the boundary layer are established. The analytic solution of the shock angle for 12° wedge in Mach 7 flow is 18.4°, which is similar to the measured shock wave angle.

The density of the flow, which is important in aero-optical experiment, could not be measured directly. Thus, assuming free stream flow as an ideal gas, ideal gas law is used to estimate the density. Pressure is measured using pressure sensor, and temperature is calculated using shock speed of shock tube. Thus, estimated free stream density is 2.0966×10^{-2} kg/m^3, which matched the density of the 29 km altitude.

3.2 Wavefront Measurement

Since only one wavefront measurement data can be acquired, trigger signal is adjusted to acquire the data at the middle of the steady-state condition inside the test section. The acquired wavefront optical path difference (OPD) map of the laser beam is shown as in Fig. 5. Figure 5 shows one of the measured wavefront data at LOS 78°, and coordinate of the wavefront is drawn with the reference picture of the wedge model. From the OPD map, the wavefront pattern, which is influenced by the flow field, is analyzed. In Fig. 5, the OPD map is gradually changing in the direction of the shock wave.

Bore sight error (BSE) and Strehl ratio are calculated by acquiring point spread function (PSF) from the OPD map. Bore sight error is calculated by the displacement of the PSF peak, and Strehl ratio is calculated by the ratio of irradiance

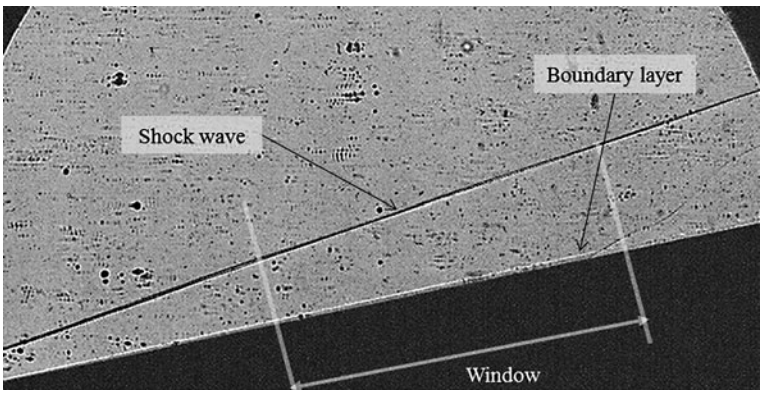

Fig. 4 Shadowgraph image of the wedge model at Mach 7 flow

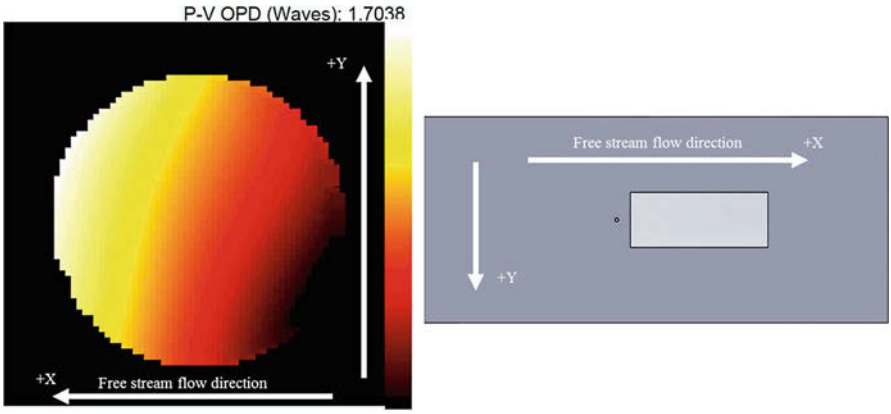

Fig. 5 Wavefront of the laser beam (LOS 78°)

Table 1 Averaged results depending on the line of sight

	OPD_{rms}	BSEx (μrad)	BSEy (μrad)	Strehl ratio
LOS 70	0.1122λ	−165.69	15.27	0.6566
LOS 78	0.1075λ	−144.07	26.90	0.6331

value at the PSF peak. The averaged value for each parameter, depending on the line of sight (LOS), is shown in Table 1. The smaller LOS, which is 70°, has bigger OPD_{rms}, BSE. Also, BSE along the x direction is larger than y direction, which is the direction of the shock wave. LOS 70° is more shifted from the original position regarding the BSE, and total optical performance is degraded more regarding the Strehl ratio. Thus, laser beam propagating with lower incident angle experiences more distortion on the wavefront.

4 Conclusion

Influence of shock wave and boundary layer on the optical wave propagation is studied by wind tunnel experiment. 12° wedge model is installed inside the test section to laser beam propagated through the model. Flow and wavefront are measured simultaneously to analyze the aero-optical phenomena. The incident angle of the laser beam, which is defined as line of sight, is varied to study different area of the flow field. The measured wavefront data shows that, as the line of sight became smaller, the optical wave experiences more distortion or aberration.

References

1. E.J. Jumper, E.J. Fitzgerald, Prog. Aerosp. Sci. **37**, 3 (2001)
2. C.M. Wyckham, A.J. Smits, AIAA J. **47**, 9 (2009)

Boundary Layer Transition Measurements on Sharp and Blunt Cones in the T4 Stalker Tube

David J. Mee and Sreekanth Raghunath

Abstract The process via which a hypersonic boundary layer transitions from laminar to turbulent flow is important in determining the length of transitional flow regions which is important information for designers of hypersonic vehicles. The effects of bluntness of the leading edge of the hypersonic body on the unsteady processes in the transitional region have not received much attention in the literature. This paper compares the unsteady processes in the transitional region for a slender cone with both a sharp and a blunted tip at hypersonic flow conditions in the T4 Stalker Tube. Fewer, more isolated turbulent spots were observed for the blunted than for the sharp cone when tested at similar or higher Reynolds number conditions.

1 Introduction

The levels of aerodynamic heating and skin frictional drag on slender hypersonic vehicles are influenced strongly by the state of the boundary layers formed on the surfaces [1]. Designers of such vehicles require details of the location and extent of the region in which the boundary layer transitions from laminar to turbulent flow [2]. This is important to ensure that vehicles can maintain structural integrity and so that designers can predict the overall levels of aerodynamic forces, particularly the drag force, on the vehicles. Transition from laminar to turbulent flow is not instantaneous but occurs over a region referred to as the transitional region. The length of the transitional region can be a substantial portion of the entire vehicle length [3]. Therefore, knowledge of not just where transition starts but of how long the transitional region extends is of importance. The aim of the present study is to understand how bluntness influences the unsteady transitional process on a slender conical model in a hypervelocity flow.

D. J. Mee (✉) · S. Raghunath
Centre for Hypersonics, School of Mechanical and Mining Engineering, The University of Queensland, Brisbane, Australia
e-mail: d.mee@uq.edu.au

A. Sasoh et al. (eds.), *31st International Symposium on Shock Waves 2*,
https://doi.org/10.1007/978-3-319-91017-8_142

Experiments to measure heat transfer rates to a 5° semi-angle cone with both sharp and blunt leading edges over a range of oncoming flow Reynolds numbers for Mach numbers of 6 and 6.6 are reported. Heat transfer rates were measured using fast-response thin-film heat transfer gauges that permit both the transient signals and mean levels during the test time to be observed.

2 Experiments

The experiments were performed in the T4 Stalker Tube at The University of Queensland [4, 5]. Tests were performed at flow Mach numbers of nominally 6.0 and 6.6. These Mach numbers were achieved by using T4's Mach 6 nozzle and operating the facility at different nozzle-supply enthalpies. With this nozzle installed in T4 and air as the test gas, a Mach number of 6.0 is achieved at a nozzle-supply enthalpy of approximately 7 MJ/kg and Mach 6.6 is achieved at a nozzle-supply enthalpy of approximately 3 MJ/kg.

The test model was a 5° semi-vertex angle right cone which was originally designed and tested in the T4 shock tunnel by Porter [6]. Two nose bluntnesses were tested. The nominally sharp tip had a nose radius estimated to be smaller than 0.2 mm and the blunt tip had a nose radius of 5.4 mm. The cone has a base radius of 50 mm resulting in an axial length for the model with sharp tip of 572 mm. The surface length for the model with sharp tip was 574 mm.

Surface static pressures were measured at five locations along a streamwise ray using PCB model 112A22 transducers located in a small cavity fed by a pressure tapping of 2 mm diameter and one to several mm long. The first tapping was located 273 mm from the tip of the cone when the sharp tip was installed. Subsequent gauges were located at 65 mm intervals along the streamwise ray. The signals from these gauges gave confidence in the quality of the flow.

Two rows of thin-film heat transfer gauges (TFGs) were aligned along streamwise rays diametrically opposite each other in a plane rotated 90 degrees from that containing the static pressure tappings. There were 19 TFGs in one of the rows (designated row F) and 20 in the other row of TFGs (designated row M). To allow for installation and wiring of the instrumentation, the conical body of the model was hollowed out, and the cone splits into two halves. The two parts of the body of the model were held together by two clamping rings, one at the base and the other 356 mm from the base. The latter ring also supported a threaded rod to which the nose tips were attached.

The thin-film heat transfer gauges, manufactured in-house, were based on a quartz substrate approximately 3 mm long and 2.1 mm in diameter. The face of the quartz was polished until it was optically flat. The temperature-sensitive element was either platinum, hand painted onto the surface, or nickel that was vacuum deposited. The films were approximately 0.2 mm wide and 1 mm long. They were connected to gold leads painted on the sides of the substrate, over the corner and

partway across the face of the gauge. A layer of SiO_2, 1000 angstroms thick, overlaid the gauge to insulate it from potential ionization effects in the freestream.

Before the T4 tests, the thin-film gauges were calibrated in an air calibration oven. The complete model was placed in this oven, and the oven temperature was cycled from ambient to 100 °C and back to ambient, and the gauges' resistances were recorded. A linear fit was then found for how each gauge's resistance varied with temperature. The method of Schultz and Jones [7] was used to infer the heat transfer rate from the surface temperature of the quartz as indicated by the TFG during a shot in the tunnel. Signals were sampled at 1 or at 2 μs intervals.

The first thin-film gauge in each row was located 264 mm from the tip of the cone when the sharp tip was installed. Subsequent gauges were located at 15 mm intervals along the two streamwise rays. This test campaign was part of a collaborative project in which the same model was tested in facilities in Australia, Germany, and Russia. The present tests were the last in the series and some of the gauges had failed before the tests. Some more gauges failed during the campaign. Therefore, signals were not obtained from all gauges for every test.

The thickness of the primary diaphragm in T4 was varied for each flow Mach number and cone tip. Appropriate changes in the tube filling pressures were made to maintain an approximately constant nozzle-supply enthalpy as the pressure levels in the tunnel changed. This enabled the freestream Reynolds number of the flow to be varied, while the mainstream flow speed and temperature were kept approximately constant, so that the location of natural transition could be varied. Air was the test gas for all tests.

Photographs of the model installed in the test section are shown in Fig. 1. The test campaign comprised a total of 16 shots. The flow conditions for the shots are summarized in Table 1. M is the Mach number, H is the enthalpy, p is the pressure, T is the temperature, ρ is the density, and Re is the Reynolds number. The subscript ∞ refers to the mainstream flow, and s refers to the condition in the nozzle-supply region. t_d is the thickness of the primary diaphragm.

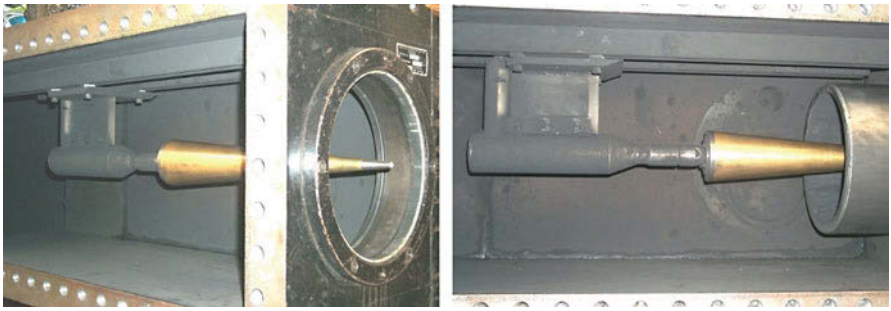

Fig. 1 Blunt cone model in the test section with nozzle removed and with nozzle in position before a shot. Note that the nozzle recoils by up to 120 mm during a shot

3 Results

The ratio of the measured Pitot pressure in the test section to the nozzle-supply pressure was used to identify establishment of nozzle flow. A further time for the flow to pass a distance equivalent to 2.5 model flow lengths was allowed for the flow over the model to become established. The designated end of the steady-flow period was based on the test flow remaining uncontaminated by driver gas [8] or by p_s remaining constant to within 10%. This gave test windows starting approximately 1.0 and 1.5 ms after flow arrival for the high and low enthalpy conditions, respectively. The steady test flow durations were 1.0 ms and 1.5 ms, respectively.

Plots of the heat transfer distributions along the two lines of TFGs were obtained by taking averages of the heat transfer rates during the test period. The theoretical laminar and turbulent levels were calculated using the flow conditions in Table 1. The method of Taylor and Maccoll [9] was used to find conditions behind the conical shock at the "edge" of the boundary layer. For the present calculations, the effects of bluntness on these boundary layer edge conditions were not included. The laminar heat transfer levels were calculated using the reference-enthalpy method given in Simeonides [10]. The turbulent levels were calculated using the method of van Driest [11] with a factor of 1.1 to account for conical effects [12]. For both laminar and turbulent calculations, the origin of the layer is taken to be the tip of the sharp cone. Sample heat transfer distributions are shown in Fig. 2a for a test in which

Table 1 Flow conditions for the T4 experiments. Air is the test gas

Shot No.	Tip	M_∞	t_d (mm)	H_s (MJ/kg)	p_s (MPa)	p_∞ (kPa)	T_∞ (K)	ρ_∞ (kg/m^3)	Re_∞/m ($\times 10^{-6}$)
7144	Sharp	6.1	3	6.5	3.8	6.8	740	0.032	3.9
7141	Sharp	6.0	4	7.2	5.2	9.1	850	0.037	4.3
7142	Sharp	6.0	4	7.0	5.2	9.1	820	0.038	4.5
7143	Sharp	6.1	5	6.8	7.0	11.5	800	0.050	5.9
7145	Sharp	6.0	6	6.9	8.4	13.5	810	0.058	6.8
7146	Blunt	6.1	6	6.7	8.4	13.1	780	0.059	7.0
7147	Blunt	6.0	6	7.3	8.4	13.7	880	0.054	6.1
7149	Sharp	6.5	1	3.7	1.2	2.2	390	0.020	2.9
7136	Sharp	6.6	2	3.3	2.4	3.7	330	0.039	5.9
7137	Sharp	6.6	2	3.2	2.4	3.6	330	0.039	6.0
7138	Blunt	6.7	2	3.3	2.4	3.7	320	0.041	6.4
7150	Sharp	6.7	3	3.0	3.8	5.1	300	0.059	9.5
7140	Blunt	6.6	3	3.3	3.8	5.5	340	0.057	8.8
7151	Sharp	6.6	4	3.3	5.2	7.4	340	0.076	11.6
7139	Blunt	6.6	4	3.3	5.2	6.9	330	0.073	11.2
7148	Blunt	6.6	5	3.2	7.0	9.3	330	0.098	15.1

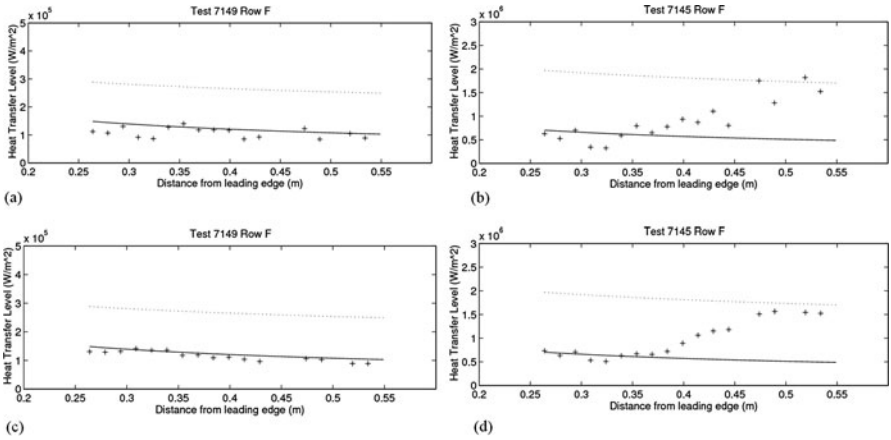

Fig. 2 Sample heat transfer distributions for laminar and transitional signals. (**a**) Shot 7149 – raw data. (**b**) Shot 7145 – raw data. (**c**) Shot 7149 – Shot calibrated data. (**d**) Shot 7145 – Shot calibrated data

the flow is primarily laminar and in Fig. 2b for a test in which the flow undergoes transition in the measurement region.

It can be seen from Fig. 2a, b that there is some spatial scatter in the heat transfer levels and that some gauges seem to read consistently lower than nearby gauges and some read higher. This trend was consistent across all tests and is attributed to two possibilities. The sensitivities of the gauges could have changed since their calibration or the gauges may not have been perfectly aligned with the surface when they were installed so that they may be slightly protruding or recessed and, correspondingly, read consistently high or low. For transition detection, this scatter is problematic, particularly if an intermittency detector is to be used.

A method to reduce the scatter was trialed and found to work well. It is referred to as "shot calibration." It has been found in previous tests that the laminar heat transfer levels can be well predicted in tunnels such as T4 using reference temperature methods [13]. A shot in which there were few or no turbulent spots was identified, and the measured heat transfer levels at each gauge location were averaged over the periods of laminar flow during the test time. A "shot calibration" factor for each gauge was then identified by finding the ratio of the measured to theoretical laminar heat transfer level. This factor was then used in all tests to correct the heat transfer level for each gauge. Shot 7144 was used as the calibration shot. Sample results of applying the correction for the two shots in Fig. 2a, b are shown in Fig. 2c, d. It can be seen that this significantly reduces the scatter and that the rise in heat transfer level through the transition region for shot 7151 is much clearer. This correction was applied to all shots in the remainder of the results presented in this paper.

The results indicated the previously observed phenomenon that boundary layer transition is delayed by introducing a small bluntness to the tips of cones [1]. The turbulent spot activity showed interesting results. The results for two shots at

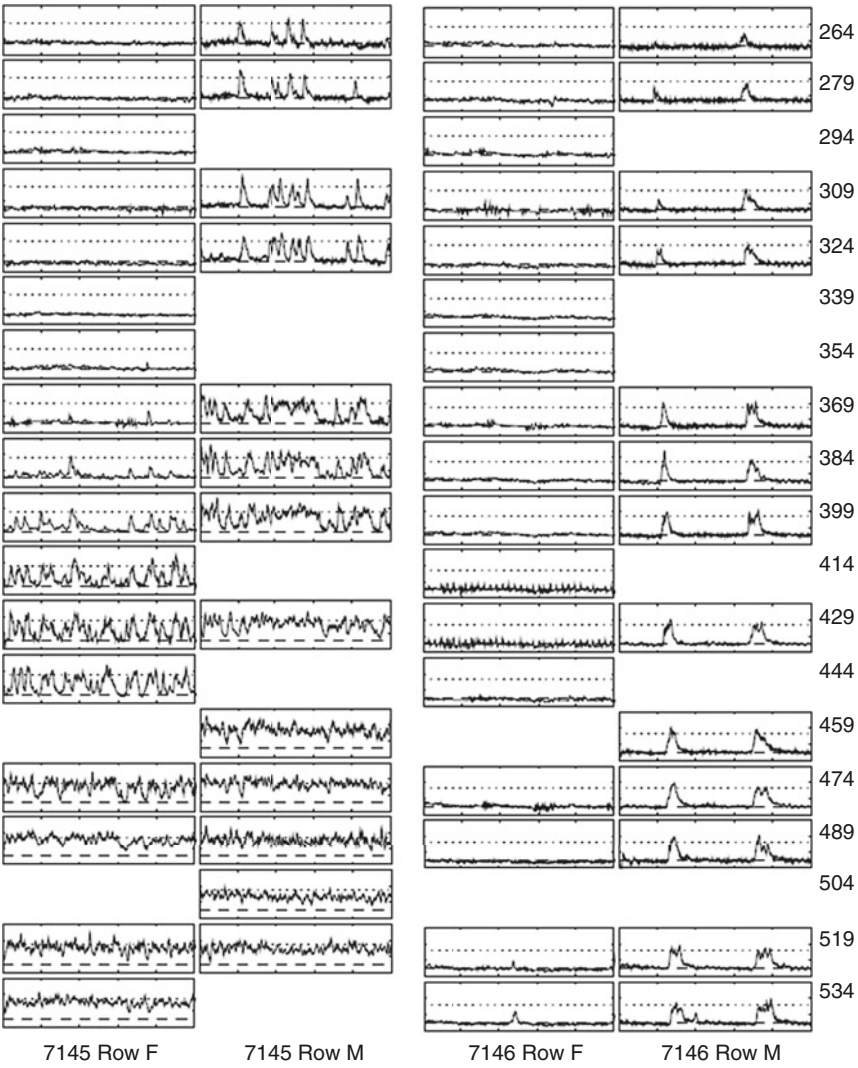

Fig. 3 Sample signals from the rows of gauges (F and M) for sharp (7145) and blunt (7146) at the same nominal flow condition. Each window shows the heat transfer signals during the 1.0 ms test period. The vertical axis is heat transfer rate from 0 to 3 MW/m^2. The long dashed lines indicate the laminar level and the short dashed line the turbulent level. The numbers at the right indicate the location of the gauge from the tip with the sharp tip attached

nominally the same Mach 6 flow condition for a sharp and a blunt tip are shown in Fig. 3. They show how the heat transfer varies transiently along each of the rows of measurements. It can be seen that turbulent spots (identified by rapid increases from the laminar toward the turbulent level) for the sharp tip are generally formed earlier

on each row than for the blunt tip. It is possible to trace the growth of the spots as they propagate past the gauges. There are two spots that form early on row M for the blunt tip and these grow, but no new spots are formed until the last gauge. In contrast, the spots form at a higher rate for the sharp tip and the transition process is completed earlier. Similar results (initiation of few, isolated spots for a blunt tip) were observed for shots 7150 (sharp) and 7140 (blunt) for a Mach 6.6 condition.

One possible conclusion is that the spots form with a lower spot initiation rate for the blunt tip than for the sharp tip. This would lead to longer transition lengths for the blunt cones. Another possibility is that some isolated spots are formed on the blunt cone due to particulates in the flow striking the model, as has been observed by Jewell et al. [14] in the T5 Stalker Tube. This looks to be the more likely reason because the distribution of intermittency for the blunt cones when these early, isolated spots appear is very different from that observed in other experiments [15, 16]. Further research is required to clarify this.

4 Conclusions

Turbulent spot activity, detected by thin-film heat transfer gauges, has been compared for experiments on a slender cone with both sharp and blunt tips over a range of conditions. The method of "shot calibration" of the heat transfer signals improved the quality of the traces and enabled clearer identification of the transitional phenomena. There is evidence that spot initiation rates may be lower for the blunted cones but more research is required to clarify this.

References

1. S.P. Schneider, Hypersonic laminar-turbulent transition on circular cones and scramjet Forebodies. Prog. Aerosp. Sci. **40**(1–2), 1–50 (2004)
2. K.Y. Lau, Hypersonic boundary-layer transition: Application to high-speed vehicle design. J. Spacecr. Rocket. **45**(2), 176–183 (2008)
3. S. Frauholz, B.U. Reinartz, S. Müller, M. Behr, Transition prediction for scramjets using γ-Reθt model coupled to two turbulence models. J. Propuls. Power **31**(5), 1404–1422 (2015)
4. R.J. Stalker, R.G. Morgan, Free piston shock tunnel T4 – Initial operation and preliminary calibration, CR 181721, NASA, 1988
5. Jacobs, P. A., Morgan, R. G., Stalker, R. J., and Mee, D. J., Use of argon-helium driver-gas mixtures in the T4 shock tunnel, shock waves @ Marseille, Proceedings of the 19th International Symposium on Shock Waves, ed. by R. Brun and L. Dumitrescu, Springer, Berlin, 1993, pp. 263–268
6. L.M. Porter, High enthalpy, hypersonic drag measurements on blunt cones in an impulse facility, Ph.D. thesis, The University of Queensland, 1996
7. D.L. Schultz, T.V. Jones, Heat transfer measurements in short duration hypersonic facilities, AGARDograph 165, AGARD, 1973
8. K.A. Skinner, Mass spectrometry in shock tunnel experiments of hypersonic combustion, Ph.D. thesis, The University of Queensland, 1994

9. G.I. Taylor, J.W. Maccoll, The air pressure on a cone moving at high speed – II. Proc. R. Soc. Lond. A Math. Phys. Sci. **139**(A838), 278–311 (1932)
10. G. Simeonides, Generalized reference enthalpy formulations and simulation of viscous effects in hypersonic flow. Shock Waves **8**(3), 161–172 (1998)
11. E.R. Van Driest, Turbulent boundary layers in compressible fluids. J. Aeronaut. Sci. **18**, 145–160 (1951)
12. F.M. White, *Viscous Fluid Flow* (McGraw-Hill, New York, 1991)
13. D.J. Mee, Boundary-layer transition measurements in hypervelocity flows in a shock tunnel. AIAA J. **40**(8), 1542–1548 (2002)
14. J.S. Jewell, N.J. Parziale, I.A. Leyva, J.E. Shepherd, Effects of shock-tube cleanliness on hypersonic boundary layer transition at high enthalpy. AIAA J. **55**(1), 332–338 (2017)
15. D.J. Mee, C.P. Goyne, Turbulent spots in boundary layers in a free-piston shock-tunnel flow. Shock Waves **6**, 337–343 (1996)
16. S. Raghunath, D.J. Mee, R. Narasimha, Estimating turbulent spot initiation rates from transition lengths in hypersonic boundary layers. AIAA J., 2017, to appear

Estimation of the Particle Drag Coefficients for Compressible and Rarefied Flows Using PIV and MTV Data

T. Handa, S. Koike, and K. Imabayashi

Abstract In the present study, the particle drag coefficients in compressible and rarefied flows are estimated experimentally. In the experiments, the particle and gas velocities in an underexpanded jet are measured using PIV and MTV techniques. The drag coefficients are calculated from the equation of the particle motion using the PIV and MTV data. The resulting coefficient is situated in the region where compressibility and rarefaction effects are believed to be remarkable. The results reveal that the estimated drag coefficients do not agree with those calculated from a well-known empirical relation including the both effects, but the data fit to a relation similar to the form of the Stokes drag law. That is to say, the experimental drag coefficient is inversely proportional to the particle Reynolds number although the coefficient has been believed to obey the empirical relation.

1 Introduction

Particle motion and traceability in high-speed flows are important in several engineering issues, e.g., cold spray, ashes in gas turbine, deposit of droplets in clouds on the surface of a supersonic aircraft, PIV and LDV measurements in supersonic flows, and so on. In order to analyze the particle motion in these engineering issues, the drag coefficients of the particles in compressible and rarefied flows are necessary. Several empirical relations are proposed to estimate the particle drag coefficient for compressible and rarefied flows [1–3], and numerous researchers currently use these relations. However, these relations were constructed although the

T. Handa (✉)
Toyota Technological Institute, Tempaku-Ku, Nagoya, Japan
e-mail: handa@toyota-ti.ac.jp

S. Koike
Japan Aerospace Exploration Agency, Chofu, Japan

K. Imabayashi
Kyushu University, Kasuga, Japan

A. Sasoh et al. (eds.), *31st International Symposium on Shock Waves 2*,
https://doi.org/10.1007/978-3-319-91017-8_143

experimental data were limited in a region where compressible and rarefied flows appear around a particle. In this study, we estimate the particle drag coefficients in such a region using the experimental data of the particle and gas velocities in an underexpanded freejet.

2 Experiments

An underexpanded jet discharged into an expansion chamber from an orifice was selected for testing. The orifice was placed at the downstream end of the stagnation chamber. The pressures in the stagnation and expansion chambers were 81 and 10.1 kPa, respectively; i.e., the pressure ratio is 8.0. The temperature in the stagnation chamber is maintained at 293 ± 1.5 K for both flows.

The particle velocities were measured using particle image velocimetry (PIV). The experimental setup used in this study was the same as that of Sakurai et al. [4] who investigated the particle traceability in transonic and supersonic flows. In the PIV experiments, we used a double-pulsed Nd:YAG laser (Quantel, CFR400) operated with a second harmonic mode of 532 nm as a light source. A laser sheet was injected into the flow. The sheet was located to a central plane of the jet. Scattered light from the particles was detected by a charge-coupled device camera (LaVision, Image Pro Plus 4 M) through a lens (Nikon, f/200 mm) and then recorded by a personal computer. A PIV image was captured in synchrony with a laser pulse using a programmable timing unit (LaVision). The time between two successive laser pulses is set to 110 ns. A pair of images is captured at a rate of 4 Hz. 250 pairs of images were captured in a single experimental run. Eight experimental runs were conducted. The velocity vectors were then calculated based on the image data correlating 32×32 pixel^2 windows with a 50% overlap.

The tracer particles of dioctyl (DOS) were produced through the Laskin nozzles in a mist generator. The nitrogen gas is introduced into a balloon made of vinyl chloride through the mist generator. The gas reserved in the balloon was supplied into a stagnation chamber and discharged into the expansion chamber through the orifice. The averaged particle size was measured using equipment based on the principle of the laser diffraction (Malvern, SPRAYTEC), and the averaged particle size was 1.1 μm. The particle density was 0.913 kg/m^3.

The gas velocities in the jet were measured using a MTV technique. In this technique, acetone was used as the molecular tracer. The detailed descriptions of the MTV system are provided by Handa et al. [5]. The laser was a Nd:YAG laser (Spectra Physics, 130-10) operated with a fourth harmonic mode (266 nm). Located in the central axis of the orifice, the laser beam was focused by a spherical lens (1000-mm focal length) and was irradiated into the jet perpendicularly to the jet axis. The resulting LIF (laser-induced fluorescence) signal was collected through a lens and was detected by the CCD camera with an image intensifier (Hamamatsu C7772S). The image intensifier's gate was set to be open during 20–30 ns. The time delay between tag and interrogation was varied between 400 ns and 800 ns by

using the delay pulse generator (Stanford System, DG645). In a single experimental run, 50–200 images were captured and averaged. Eight experimental runs were conducted at each measurement location.

3 Results and Discussion

Figure 1 shows the maps of particle and gas velocities measured using the PIV and MTV techniques, respectively. It is clear from the figure that particles cannot trace the flow; i.e., the barrel shock wave, Mach disk, and reflected shock wave are not clear in the map of particle velocity although these are clearly seen in the map of gas velocity.

Figure 2 shows the distributions of particle and gas velocities along the central axis of the jet. It is found from the figure that the particles cannot trace the flow either upstream or downstream from the Mach disk. The particle drag coefficient was estimated from the velocity data shown in Fig. 2. The method how to estimate the coefficient is explained in the following paragraphs.

We estimated the particle drag coefficient from the following equation that was derived by Koike et al. [6]:

$$u_{pj}\frac{\partial u_{pi}}{\partial x_i} = \frac{3}{4} C_D \frac{\rho_g}{\rho_p}\frac{1}{d_p}\left|\boldsymbol{u}_g - \boldsymbol{u}_p\right|\left(u_{gi} - u_{pi}\right) \tag{1}$$

In this equation, d_p is the particle diameter, ρ is the density, $\boldsymbol{u}$ is the velocity vector, and x is the position. The subscripts g and p denote variables of the gas and particle, respectively. Einstein summation convention is used for the terms having subscripts i and j. Equation (1) was derived from the Basset-Boussinesq-Oseen (BBO) equation assuming that the flow was steady and that the term of the particle

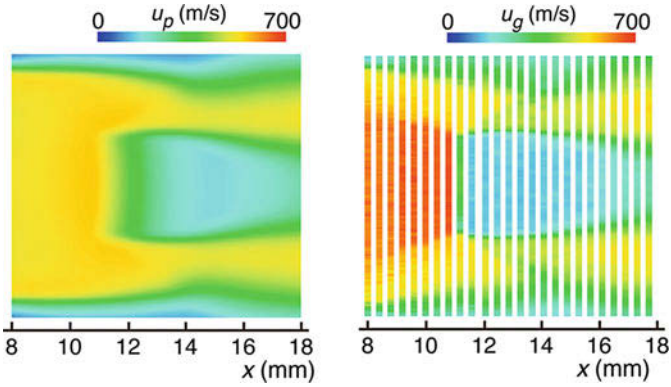

Fig. 1 Maps of particle (left) and gas (right) velocities

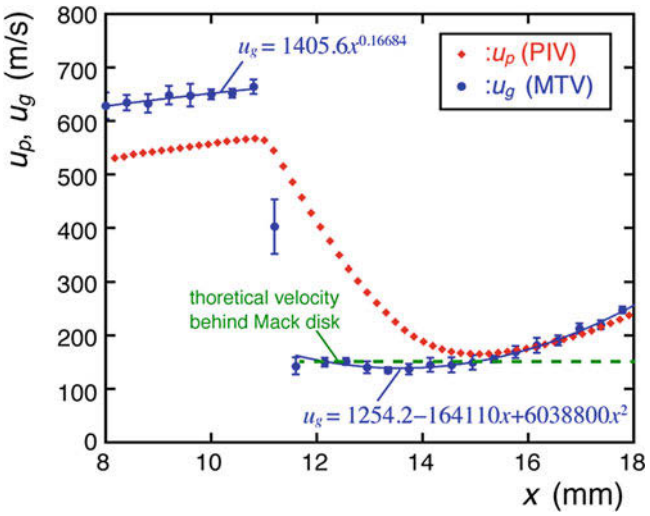

Fig. 2 Distributions of particle and gas velocities along the central axis of the jet

drag resulting from the difference between the gas and particle velocities was much higher than the other terms corresponding to the pressure gradient, added mass, and unsteady motion. Consequently, the particle drag coefficient can be calculated from the other form of Eq. (1):

$$C_D = \frac{4}{3}\, u_{pj}\, \frac{\partial u_{pi}}{\partial x_j}\, \frac{\rho_p}{\rho_g}\, \frac{d_p}{|\boldsymbol{u}_g - \boldsymbol{u}_p|\,(u_{gi} - u_{pi})} \tag{2}$$

In use of Eq. (2), we encounter the problem that the MTV data (gas velocity data) are limited although the gas velocities relevant to the PIV data are necessary. In order to solve this problem, we estimate the gas velocity u_g by fitting the MTV data into appropriate equations. That is to say, the MTV data upstream and downstream from the Mach disk are fitted, respectively, into the following equations:

$$u_g = 1405.6x^{0.1884} \tag{3}$$

$$u_g = 1254.2 - 16110x + 6038800x^2 \tag{4}$$

It should be noted that u_g and x in the above equations have units of meter per second (m/s) and meter (m), respectively. The fitting results are shown by the solid lines in Fig. 2. It is clear that Eqs. (3) and (4) agree quite well with the experimental data.

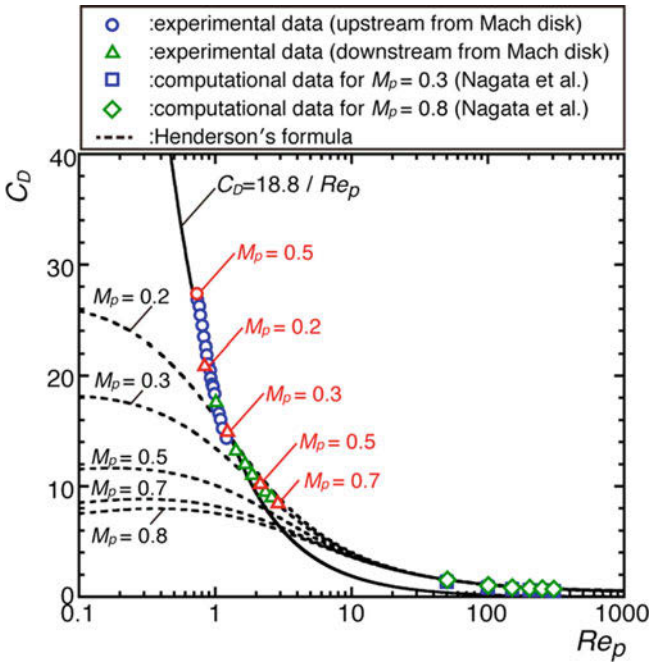

Fig. 3 Plots of particle drag coefficient C_D versus particle Reynolds number Re_p

Now we can calculate the particle drag coefficient from Eq. (2) using the experimental data shown in Fig. 2. The calculated drag coefficients are plotted against the particle Reynolds number Re_p as shown in Fig. 3. Here, the particle Reynolds number Re_p is defined as:

$$\mathrm{Re}_p = \frac{\rho_g \left|\boldsymbol{u}_g - \boldsymbol{u}_p\right| d_p}{\mu_g} \tag{5}$$

where μ_g is the viscosity of the gas. The well-known empirical relation of Henderson [2] is also plotted in Fig. 3 for each relative Mach number defined as:

$$M_p = \frac{\left|\boldsymbol{u}_g - \boldsymbol{u}_p\right|}{a_g} \tag{6}$$

Nagata et al. [7] performed numerical simulation of the compressible flows around a sphere and estimated the drag coefficient for $50 \leq Re_p \leq 300$. Their computational data are also plotted in Fig. 3. As shown in the figure, the empirical relation can reproduce their computational data. The open circles and triangles shown in Fig. 3 correspond to the present experimental data measured in the regions upstream and downstream from the Mach disk, respectively. The data measured

in the two regions connect smoothly with each other as shown in Fig. 3. The drag coefficient C_D decreases remarkably with the particle Reynolds number Re_p although the relative Mach number does not change practically upstream from the Mach disk (i.e., $0.47 < M_p < 0.50$). The data corresponding to $M_p = 0.2$, 0.3, 0.5, and 0.7 are denoted by red color. It is clear from Fig. 3 that the empirical relation cannot reproduce the experimental data, whereas the data can be fitted well to the relation having a form similar to the Stokes drag's law $C_D = 24/Re_p$. That is to say, the data can be fitted well to the following relation:

$$C_D = \frac{18.8}{\mathrm{Re}_p} \tag{7}$$

In general, the previous empirical relations [1–3] were constructed so that the drag coefficient approaches the free molecular limit [8] for high Knudsen numbers. However, the experimental data do not approach the limit although the Knudsen numbers are relatively high in the present experiment (Knudsen numbers range between 0.3 and 1.0).

4 Conclusions

The particle drag coefficients in compressible and rarefied flows were estimated experimentally. In the experiments, the particle and gas velocities in an underexpanded jet were measured using PIV and MTV techniques. The drag coefficients were calculated from the equation of particle motion using the PIV and MTV data. The results revealed that the estimated drag coefficients did not agree with those calculated from the well-known empirical relation but fit to a relation similar to that of the Stokes drag's law. That is to say, the experimental drag coefficient is inversely proportional to the particle Reynolds number in a region where compressibility and rarefaction effects have been believed to be remarkable.

References

1. C.T. Crowe, AIAA J. **5**, 1021 (1967)
2. C.H. Henderson, AIAA J. **14**, 707 (1976)
3. E. Loth, AIAA J. **46**, 2219 (2008)
4. T. Sakurai et al., J. Vis. **18**, 511 (2015)
5. T. Handa et al., Exp. Fluids **55**, 1725 (2014)
6. S. Koike et al., AIAA J. **45**, 2770 (2007)
7. T. Nagata et al., Phys. Fluids **28**, 056101 (2016)
8. J.R. Stadler, V.J. Zurick, NACA TN, 2423 (1951)

RANS Simulation of Over- and Under-expanded Beveled Nozzle Jets Using OpenFOAM

B. Zang, Vevek U S, and T. H. New

Abstract The present study numerically investigates supersonic jet flows issued at M = 1.45 from a beveled nozzle with 60° inclination. Utilizing *rhoCentralFoam* solver in OpenFOAM, unsteady Reynolds-averaged Navier-Stokes (RANS) simulations were performed with two nozzle pressure ratios (NPRs) of 2.8 and 4, corresponding to over- and under-expanded exit conditions, respectively. The Mach distributions reveal a more organized near-field shock formation for the over-expanded jet with smaller and periodic shock cells, as compared to those of the under-expanded one. Moreover, the jet flows are deflected in opposite directions for the two different NPRs, indicating a strong dependence of jet vectoring on NPR in addition to the bevel angle. Last but not least, reasonably good agreements can be observed for both qualitative and quantitative comparisons between simulation and experimental results, supporting the notion that the compressible *rhoCentralFoam* solver in OpenFOAM is suitable to model such supersonic jet flows.

1 Introduction

Trailing-edge modified nozzles are known to provide improved mixing characteristics and high-speed jet noise reduction performance when designed appropriately [1]. One good example is the chevron-shaped engine nacelles used in modern commercial airliners, which seek to attenuate jet mixing noises for quieter flights. Thus, they have sparked extensive interests from both research and industrial communities for their potential applications [2]. Beveled nozzles are among the several promising configurations, due to ease in their manufacture and their effectiveness in manipulating noise radiation directivity [3]. In their experimental investigations of beveled rectangular nozzles, Rice and Raman [1] observed notable deflections of jet core for single beveled nozzle at under-expanded conditions. Furthermore,

B. Zang · Vevek U S · T. H. New (✉)
School of Mechanical and Aerospace Engineering, Nanyang Technological University, Singapore, Singapore
e-mail: dthnew@ntu.edu.sg

A. Sasoh et al. (eds.), *31st International Symposium on Shock Waves 2*,
https://doi.org/10.1007/978-3-319-91017-8_144

their microphone measurements revealed a shift in the jet mixing noise to higher frequencies. Viswanathan et al. [3] performed large-eddy simulations (LES) of single- and dual-stream beveled nozzles with inclination angles of 24° and 45°, respectively, and concluded that the noise reduction of the jet flows was due to the modifications of noise emitted from the large-scale turbulent structures. Later, Aikens et al. [4] confirmed that there exist azimuthal variations of turbulent kinetic energy in the asymmetric beveled jets with 35° inclination, which contribute to asymmetry in the far-field jet broadband noise.

Since experiments on high-speed jet flows are not always feasible and full-scale LES are computationally very demanding, Reynolds-averaged Navier-Stokes (RANS) simulation has been explored as a useful alternative to evaluate and understand the fundamental flow behaviors and noise characteristics associated with the resulting jet flows [5–7]. This is especially the case when different combinations of trailing-edge modifications and operating conditions are investigated as part of the optimization process or when solutions are required over a short "turnaround" time. For instance, Omais et al. [8] discussed the possibilities of noise prediction using RANS results to serve as inputs, and more recently, Souza et al. [9] employed RANS simulations coupled with statistical noise prediction method to provide relatively rapid and accurate assessment of broadband noise associated with a jet in cross-flow at transonic speed.

However, as noted by Garrison et al. [10], the accuracy of such noise prediction techniques relies heavily on the accuracy of the RANS simulations. Due to constraints imposed by commercial solvers, it is often difficult to tailor the numerical schemes and solution strategies toward specific flow conditions for improved accuracy and efficiency. On the other hand, the open-source computational fluid dynamics (CFD) tool, OpenFOAM, has become increasingly popular in the past decade, due to its economic advantage and its well-established code structures and solver flexibility. Hence, it is timely for the present research work to explore the use of this tool in the numerical simulation of supersonic flows. It will not only allow the assessment of the solver performance and shock-capturing schemes in OpenFOAM but also the examination and better understanding of the flow structures and shock-associated dynamics of beveled nozzle with relatively larger inclination angle of 60° at different exit conditions (i.e., over- and under-expanded, respectively).

2 Numerical Methodology and Procedures

In the present study, a beveled convergent-divergent (CD) nozzle with 60° inclination angle was numerically investigated using unsteady RANS approach in OpenFOAM. The nozzle undergoes perfect expansion at nozzle pressure ratio (NPR) of 3.4 at a designed Mach number of 1.45, within the range of operating conditions typical for supersonic jet engines [4]. More design and test details of present CD nozzles can be found in Wu and New [11]. Figure 1 shows the Cartesian coordinates used as well as the definition of inclination angle θ. Jet

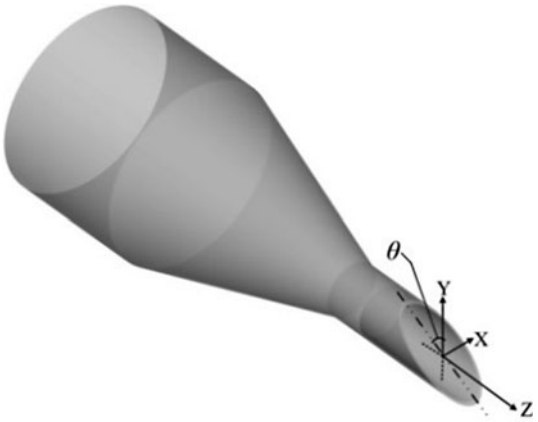

Fig. 1 Definition of the nozzle coordinate systems and angle of inclination ($\theta = 60°$)

flows at two different NPRs of 2.8 and 4, corresponding to over- and under-expanded conditions, respectively, were freely exhausted from the beveled nozzle into a quiescent ambience, and *rhoCentralFoam* solver was employed to capture the development of the flow fields.

The compressible solver, *rhoCentralFoam*, is based on a central upwind flux schemes proposed by Kurganov and Tadmor [12]. Essentially, flux of any conservative flow field quantities (such as density and pressure) can be evaluated by splitting the flux in two directions, namely, the incoming and outgoing fluxes to the face of an owner cell, which yield:

$$\begin{aligned}\int_V \nabla \cdot [U\psi]\, dV &= \sum_f \phi_f \psi_f \\ &= \sum_f \left[a\phi_{f+}\psi_{f+} + (1-a)\,\phi_{f-}\psi_{f-} + w_f\left(\psi_{f-} - \psi_{f+}\right)\right] \quad (1)\end{aligned}$$

where φ_f is the volumetric flux, being splitted into "+" and "−" sides, and ψ_f represents any field of quantities to be evaluated with a, the weighting coefficient. Readers are advised to refer to Kurganov and Tadmor [12] for details on the evaluation of the fluxes. Subsequently, the positive (i.e., "+") and negative (i.e., "−") fluxes at each cell can be reconstructed by a limiter function that satisfies total variation diminishing (TVD) criteria. In particular, Gutiérrez Marcantonia et al. [13] have benchmarked *rhoCentralFoam* against several well-defined problems, such as supersonic flow over a wedge and past a slender diamond-shaped airfoil and concluded that *van Leer* flux limiter was able to provide most balanced performance with reasonable accuracy. Thus, the field variables were reconstructed using *van Leer* scheme in the present simulations, which results in a second-order accuracy in spatial discretization for smooth regions.

Figure 2a shows the simulation domain of the jet flows, which extends up to 40D (i.e., D is the jet diameter) downstream of the jet exit in the streamwise direction

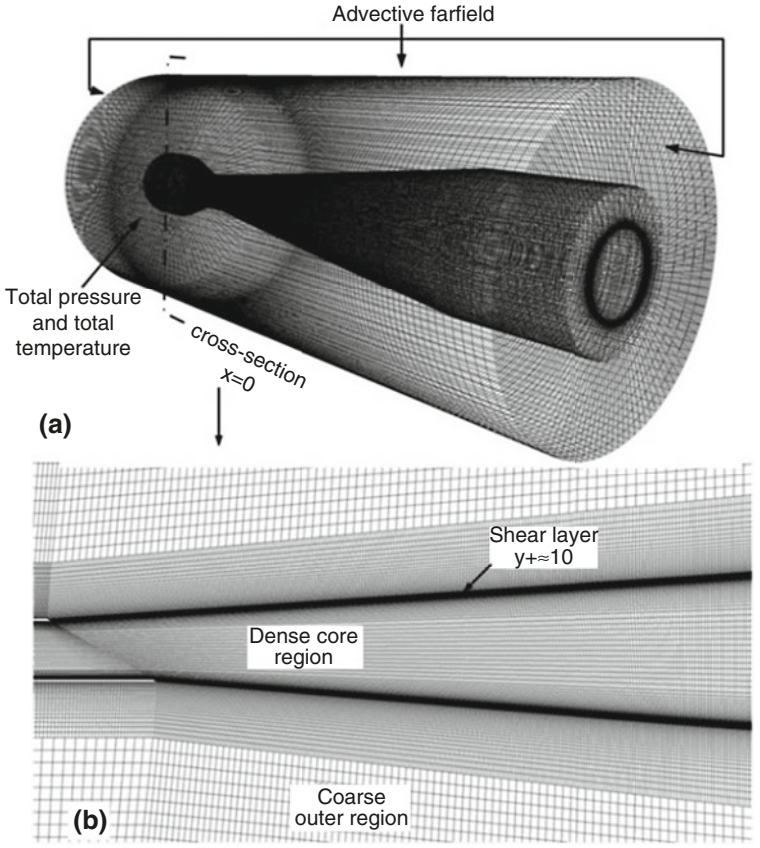

Fig. 2 (**a**) Mesh topology and boundary conditions for the present three-dimensional flow field and (**b**) two-layered structured mesh construction with increased density along shear layers

and 10D in the cross-stream direction, respectively. In order to improve upon computational efficiency while not compromising on accuracy, the fully structured grid was partitioned into two regions, a dense core region and a coarse outer region, as shown in Fig. 2b. The grid density in the core region closely follows that employed by Shen and Tam [14] in their numerical studies of jet screech tones and hence was deemed sufficiently fine to resolve the present flow fields. Moreover, a factor of three was subsequently applied to the outer region with reference to the core, which gave rise to a total number of approximately 24 million cells. Lastly, additional refinement was imposed upon the grids adjacent to the nozzle wall and shear layers to achieve $y + \approx 10$, such that the flow turbulence could be captured satisfactorily by k-ω shear stress transport model. Time-averaged results were then obtained through approximately 100,000 time steps after the jet flows became stabilized and fully developed.

3 Results and Discussion

3.1 Near-Field Shock Structures

It is useful to begin the discussion by first examining the dominant shock structures of the 60° beveled nozzle at two differently expanded conditions. Figure 3 shows the isometric view of the Mach number contour maps cut along both asymmetric (i.e., beveled x = 0) and symmetric (i.e., y = 0) planes. Significant differences can be observed between the over- and under-expanded jet flows. When the jet is over-expanded at NPR = 2.8, the resulting shocks cell structures are well-organized and exhibit some form of periodicity, which is characteristic of imperfectly expanded axisymmetric jets [15]. Such periodicity is even clearer when the Mach number developments along the centerline are extracted and shown in Fig. 4, where the spatial intervals between the peak and trough remain relatively constant for the over-expanded jet (i.e., solid lines) along both planes. On the other hand, the dominant shock structures of the under-expanded jet at NPR = 4 are essentially irregular in their formation as seen from Figs. 3b and 4. Such shock cell formations suggest that pressure correction and relief of the beveled jet against the ambience is likely to be more gradual for the over-expanded jet. In fact, a closer examination of the flow development in Fig. 4b reveals that the Mach number decays much faster for the under-expanded jet along the symmetric centerline, indicating a faster and possibly more drastic process in achieving pressure equilibrium with the ambience.

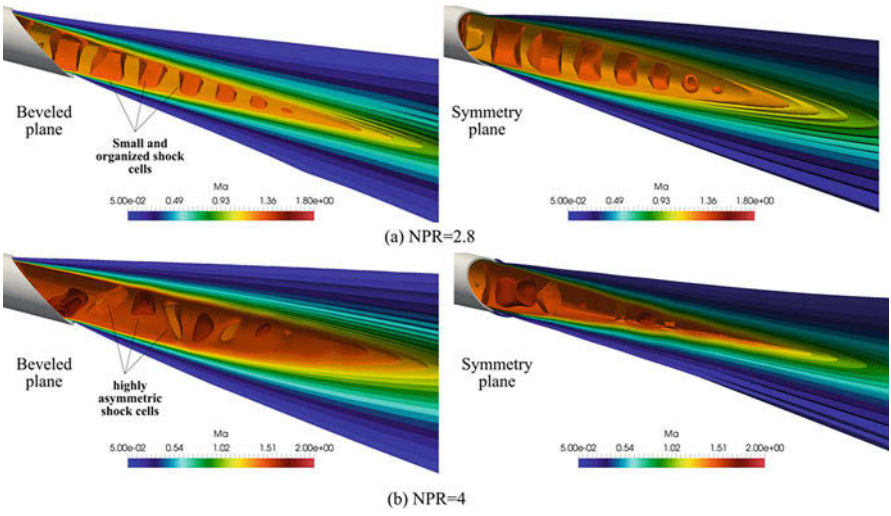

Fig. 3 Near-field shock cell structures of (**a**) over-expanded NPR2.8 and (**b**) under-expanded NPR 4 beveled jet flows

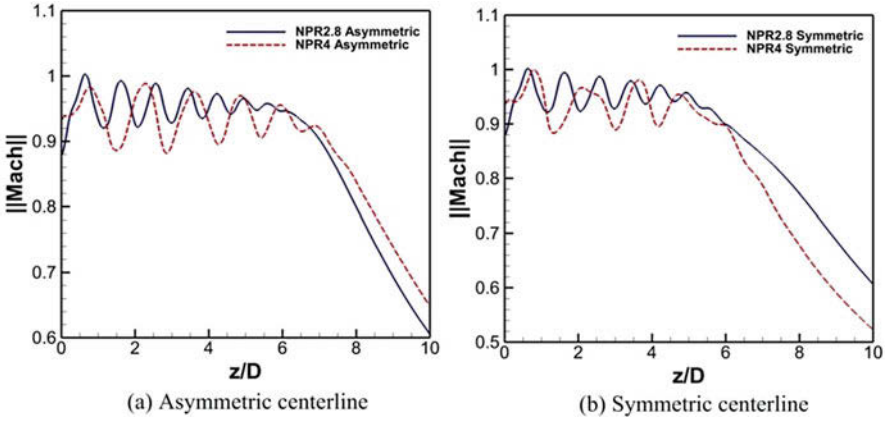

Fig. 4 Comparisons of the jet centerline flow development between over- and under-expanded jet flows along both (**a**) asymmetric and (**b**) symmetric planes

3.2 Jet Vectoring

Vectoring of the beveled jet flows occurs naturally as direct result of the nonuniform pressure distribution and existence of strong pressure gradient between the short and long nozzle tips. The phenomena have been reported by a number of studies [1, 3, 4]; nevertheless relationships between nozzle pressure ratio as well as inclination angle and the extent of the jet deflections remain unclear. The present simulations aim to provide some quantification on the jet deflection angles at both over- and under-expanded conditions. First of all, Fig. 5 compares the RANS pressure field results with the experimental schlieren images along the asymmetric (i.e., beveled) plane. Initially, two distinct shocks can be seen to reflect off close to the exit of the longer nozzle length, which later appear to interact and merge as a single shock propagating downstream, regardless of the exit flow condition. This good qualitative agreement between the simulation and experimental results reassures the validity and accuracy of the present RANS simulations. Subsequently, the streamwise evolution of the jet Mach number was extracted along several downstream locations, as shown in Fig. 6, and a reasonable estimate of the angle of jet deflection can be determined from the collection of Mach number peaks, thus jet velocity profiles. The results are tabulated and compared with experimental measurement in Table 1. Interestingly, the jet core deflects in opposite directions between over- and under-expanded jets. Note that positive angle corresponds to upward deflection along y-axis. Though some uncertainties are expected in the method, there are satisfactory agreements between the simulation and experimental results. It is noteworthy that much more significant deflection of the under-expanded jet could possibly arise from the high asymmetry in the shock structures, as observed from Fig. 3b along the beveled plane.

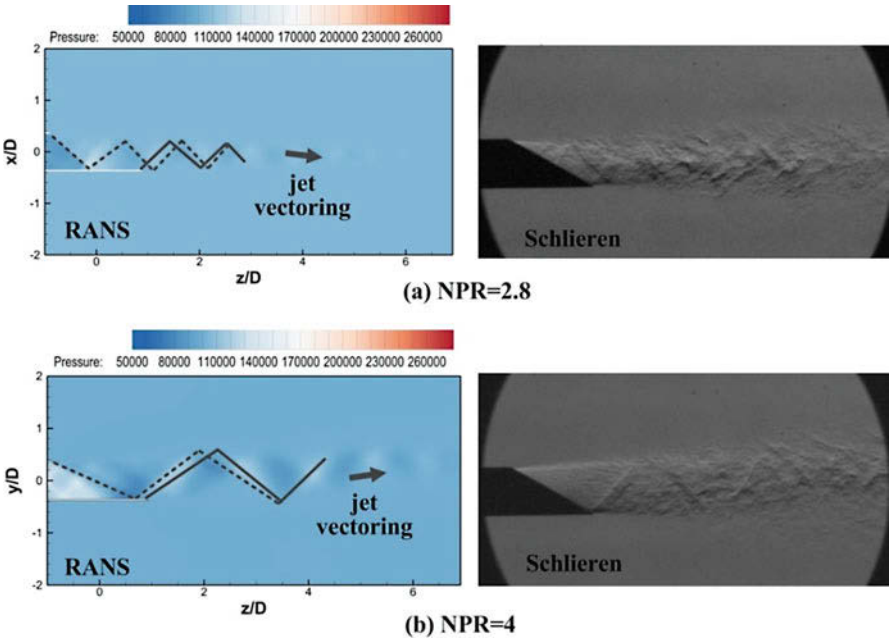

Fig. 5 Comparison of the shock structures between RANS and experimental results taken at (**a**) NPR = 2.8 and (**b**) NPR = 4. (Schlieren images courtesy of Lim H.D. and Wei X)

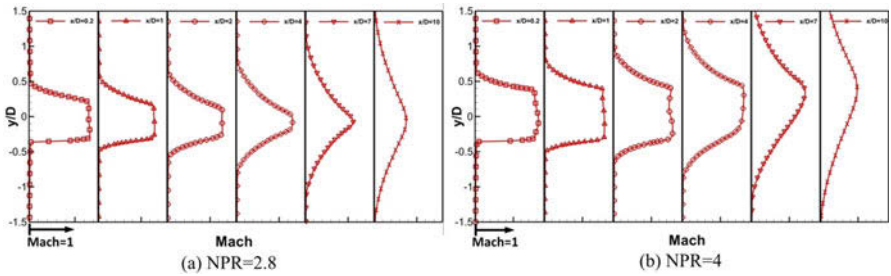

Fig. 6 Streamwise evolution of the jet Mach number extracted along several downstream locations for (**a**) over- and (**b**) under-expanded beveled jet flows

Table 1 Comparison of the jet deflection angles between RANS simulation and experiments

NPR	RANS simulations	Experiments
2.8	−0.7 degree	−0.7 degree
4.0	2.9 degree	2.8 degree

4 Conclusions

Unsteady RANS simulations were performed on beveled supersonic jet flows with relatively large nozzle inclination angle of 60°, using *rhoCentralFoam* solver in OpenFOAM. The near-field shock structures are in good qualitative agreement with the experimental schlieren images and are found to be relatively smaller and well-organized for over-expanded jet than those for under-expanded one. Moreover, jet vectoring can be observed for both cases, while the exact direction and extent of the deflection are highly dependent on the exit conditions. The deflection angles determined from the simulations compare relatively well with the experiments, which provide confidence in this open-source CFD solver and encourage further investigation into the beveled supersonic jet flows, such as the computation of the aeroacoustics field.

Acknowledgment The authors would like to acknowledge Lim H.D. and Wei X. for the schlieren flow images, as well as the support for this study by a Singapore Ministry of Education AcRF Tier-2 grant (grant number: MOE2014-T2-1-002) and Singapore National Supercomputing Center (NSCC).

References

1. E.J. Rice, G. Raman, in *NASA Tech Report* N94-19484 (1993)
2. H. Xie, P.G. Tucker, S. Eastwood, Int. J. Heat Fluid Fl. **30**, 1067–1079 (2009)
3. K. Viswanathan, M. Shur, P.R. Spalart, M. Strelets, AIAA J. **46**(3), 601–626 (2008)
4. K.M. Aikens, G.A. Blaisdell, A.S. Lyrintzis, in *53rd AIAA Aerospace Sciences Meeting*, AIAA 2015-0509 (2015)
5. G. Lehnasch, P. Bruel, Int. J. Numer. Meth. Fluids **56**, 2179–2205 (2008)
6. S. Arunajatesan, in *50th AIAA Aerospace Sciences Meeting*, AIAA 2012-1199 (2012)
7. R. Chaplin, in *31st AIAA Applied Aerodynamics Conference*, AIAA 2013-2911 (2013)
8. M. Omais, S. Redonnet, B. Caruelle, E. Manoha, J. Acoust. Soc. Am. **123**(5):3818 (2008)
9. P.R. Souza, O. de Almeida, C. R. Ilário da Silva, in *55th AIAA Aerospace Sciences Meeting*, AIAA 2017-0233 (2017)
10. L. Garrison, A.S. Lyrintzis, G. Blaisdell, in *12th AIAA/CEAS Aeroacoustics Conference*, AIAA 2006-2599 (2006)
11. J. Wu, T.H. New, Aero. Sci. Tech. **63**, 278–293 (2017)
12. A. Kurganov, E. Tadmor, J. Comput. Phys. **160**(1), 241–282 (2000)
13. L.F. Gutiérrez Marcantonia, J.P. Tamagno, S.A. Elaskar, in *Mecánica Computacional*, vol. XXXI, ed. Cardona et al. (2012), pp. 2939–2959
14. H. Shen, C.K.W. Tam, AIAA J. **36**(10), 1801–1807 (1998)
15. C.K.W. Tam, J.A. Jackson, J. Fluid Mech. **153**, 123–149 (1985)

Exploration of Under-Expanded Free and Impinging Supersonic Jet Flows

D. Donjat, F. Nicolas, O. Leon, F. Micheli, G. Le Besnerais, and F. Champagnat

Abstract The impact of jets on a wall remains one of the most effective means allowing a significant increase in local exchanges of heat. These configurations are therefore particularly used in aerothermal systems. The literature reports several studies on the impact of moderately to strongly under-relaxed jets, both from an aeroacoustics and thermal point of view. Nevertheless, the aerothermal behavior and consequently the effects of exchange with the wall remain little known. Moreover, these flows appear to be difficult to simulate from a numerical point of view. We propose here to describe the first part of an experimental study focused on the description of the topology and dynamics of both free and impinged under-expanded jets with the aim to define an accurate database dedicated to the improvement of numerical flow models.

1 Introduction

The physics of supersonic circular jets has been under investigation since a long time due to the many aerospace and industrial applications. When gas exits a circular nozzle with a pressure higher than the surrounding one, an under-expanded jet forms. In this case, the pressure of the jet reaches the ambient pressure through a series of shock and expansion waves. This configuration becomes more complicated when the enthalpy of the jet is important or when it interacts with an impingement surface. This jet is widely described in the literature (see the synthesis established by Franquet [1]). Particularly, numerous studies focused on the comprehension of under-expanded jet flow structures [2] and on the specific mechanism being the source of instabilities such as the production of screech noise [3].

D. Donjat (✉) · F. Nicolas · O. Leon · F. Micheli
ONERA, Toulouse, France
e-mail: david.donjat@onera.fr

G. Le Besnerais · F. Champagnat
ONERA, Palaiseau, France

A. Sasoh et al. (eds.), *31st International Symposium on Shock Waves 2*,
https://doi.org/10.1007/978-3-319-91017-8_145

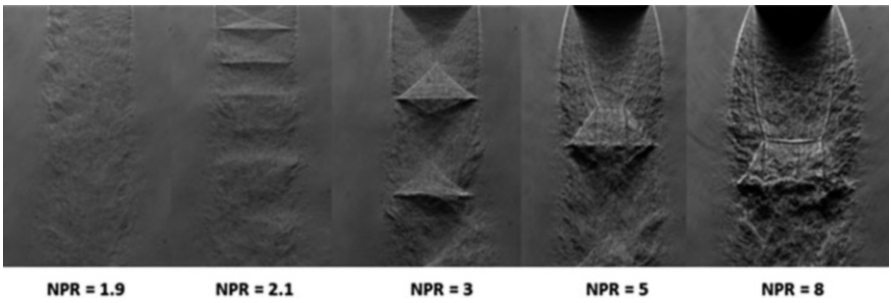

Fig. 1 Evolution of shock wave structures for different NPRs (instantaneous schlieren images)

Under-expanded jets are characterized by the nozzle pressure ratio (NPR), which is equal to the ratio between the total pressure of the jet (P_i) and the ambient pressure (P_a). Figure 1 gives a qualitative evolution of the NPR jet topology from schlieren visualizations realized in the present study. A detailed description of the flow can be found in Cumber [4]. The classical main geometric criteria that allow the characterization of the evolution of the shock structure in the near-field zone for NPRs greater than 2 are the position and diameter of the first Mach disk. A set of data as well as a set of correlations exist (e.g., Antsupov [5], Ashkenas [6], Alvi [7], gathered in Franquet [1]); nevertheless, their comparison shows a non-negligible deviation of results, probably due to the difficulty of the measurement and the generation of the jets. Indeed, performing measurements in supersonic jets is quite a challenge. Recent studies demonstrate the ability of achieving measurement with nonintrusive laser techniques such as LDV or tomo-PIV. Schlieren optical techniques are also a classical way to observe the complex structure of this kind of flow. Among them, the background-oriented schlieren (called BOS) allows the assessment of the density field and its fluctuations. Combined with additional measurements, BOS technique will improve the understanding of such a complex flow as proposed by [9].

In impingement condition, the structure of the flow is conventionally divided into three distinct zones called, respectively, “free jet zone,” “impinged zone,” and “parietal flow zone.” In the supersonic case, this structure depends strongly on the distance h between the nozzle section and the wall which conditions the development or not of a recirculation zone at impact. For a very small distance h, the deflection of the current lines at supersonic velocity near the wall induces the formation of a so-called “plateau” shock that extends over the width of the supersonic jet core. In the case where this distance h remains low, the first Mach disk can interact directly with the plateau shock to form a double central shock structure. As the gap increases, the annular shock is positioned downstream of the Mach disk and the first shock structure remains insensitive to the impingement. Depending on the NPR and the distance h, this sliding line can interact with the boundary layer developing at the wall, and a recirculation bubble can appear in front of the impinging zone. This evolution of the flow structure is well characterized by Henderson [8].

In the present article, we describe an experimental campaign on the case of an under-expanded jet (NPR = 5) in free conditions and perpendicularly impinging a flat wall considering a small spacing (h/D = 3). The main aims of this work are first to acquire a complete and robust experimental database by performing advanced measurement methods as 3DBOS. Second, we want to improve the knowledge of the flow behavior during impingement for such a configuration with the final objective of defining a validation case for a high-fidelity numerical simulation approach.

2 The Experiment: Test Section and Measurements

The BAT facility of ONERA consists of a 22 mm diameter convergent nozzle, supplied by 80 bar pressurized air tank (as shown on Fig. 2). A 570 kW electric heater allows output temperature regulation up to 400 °C at a maximum pressure of 10 bar. For a flow rate of less than 0.45 kg.s^{-1}, the bench can operate continuously. The pipe is insulated downstream of the heater to minimize thermal losses. The nozzle is covered by a flat flange in order to be under confined conditions. The shape of the nozzle ensures a straight sonic condition on the jet exit. Experiments with nozzle pressure ratios ranging between 2 and 8 are performed with two total temperature T_i conditions (i.e., 293 K and 423 K). For impingement conditions, the jet produced by the nozzle impinged a titanium plate placed perpendicularly to its axis at a distance h such that h/D = 3.

In order to characterize the flow of both free and impinging cases, a visualization campaign is carried out with a Z-shape schlieren bench. Two approaches are

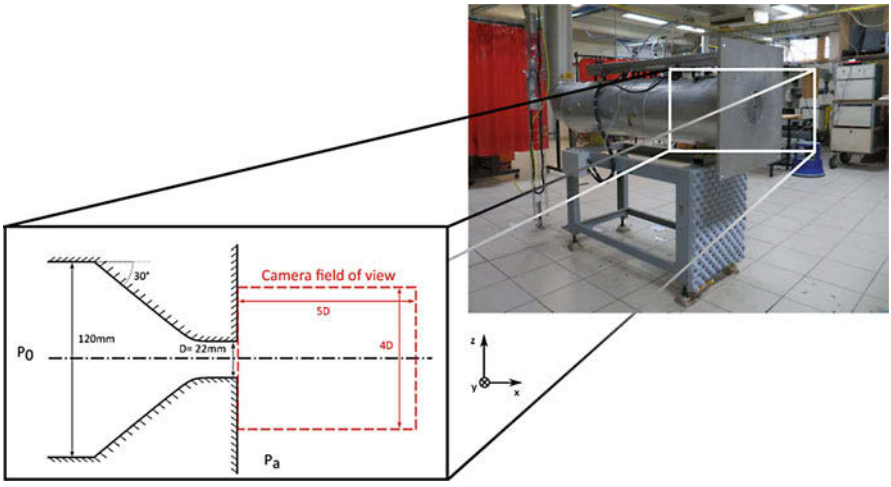

Fig. 2 The aerothermal jet facility BAT used for under-expanded jet studies. General view (top right) and sketch of the nozzle and camera field of view for BOS application (bottom left)

considered. First, averaged schlieren images are produced for exposure times of several milliseconds captured on CCD camera. The images obtained give an approximation of the structure of the flow and allow an estimation of the averaged position of compressible structures. In a second step, images of the instantaneous flow are produced by using a "Nanolite" type light source coupled to a condenser allowing exposure times of the order of 200 ns as illustrated in Fig. 1. In order to have some information on aeroacoustics behavior of the jet with impingement, a microphone is positioned in the vicinity of the flow to record the noise spectra of the jet. The database is completed with both velocity and density measurements.

The density measurements are performed with the 3DBOS technique proposed in Nicolas [9] which provides physically consistent 3D reconstructions of instantaneous and mean density fields. The technique is used in a first step to characterize free jet configuration.

The characterization of flow dynamics for a NPR = 5 in cold condition (T_i = 293 K) is performed with LDV technique. Indeed, velocity measurements for this type of flow remain difficult due to the wide range of velocities and the important gradients encountered (shock passage, mixing layer, and impinging zone). In this study, LDV technique has been preferred and the configuration of the system optimized according to the choice of the frequency ranges (imposed by the limits of the apparatus). The two-component measurements are carried out following a forward scattering configuration with a seeding of silica particles whose mean diameter is around 0.4 μm. According to a numerical pre-study performed in order to estimate the drag of the particles during the shock crossing, source of bias, this kind of particles does not affect the measurement of velocity upstream of the shock structures.

The acquisition system used for this study is a TSI FSA 4000 signal analyzer allowing a rapid scan over a very wide band of frequencies. The 3D mesh is composed of 3000 points. Depending on the explored area, between 10,000 and 20,000 particles are acquired per point.

3 Free Under-Expanded Jet: Results and Discussions

Based on schlieren visualization, the evolution of the experimental mean diameter and position of the Mach disk for each free jet configuration is gathered in Fig. 3. By comparing with classical correlations identified by [1], the results obtained for the diameter are comparable to Antsupov's correlation for the low NPR cases (i.e., less than 6). For higher NPRs, Mach disk diameters deviate from all the selected correlations except for Addy and Alvy's database [7, 9].

Figure 4 gives a reconstruction of the mean density field of the jet for NPR = 5. The 3D reconstruction is performed from displacement fields averaged over 900 images with 12 points of view (i.e., cameras) distributed around the flow (see [9]). The flow topology is well recovered, with two shock cells visible. Behind the normal shock of the first Mach disk, the subsonic zone is present. The 3DBOS

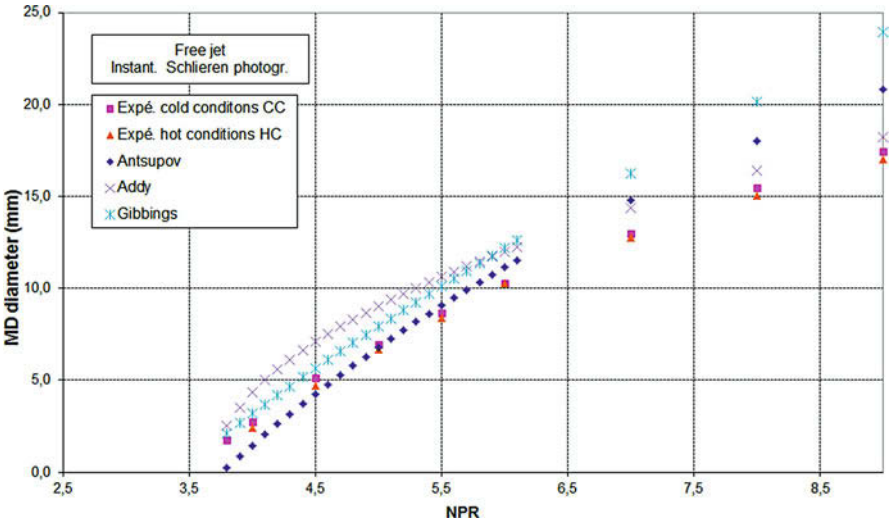

Fig. 3 Diameter of Mach disk compared with correlations gathered in [9]

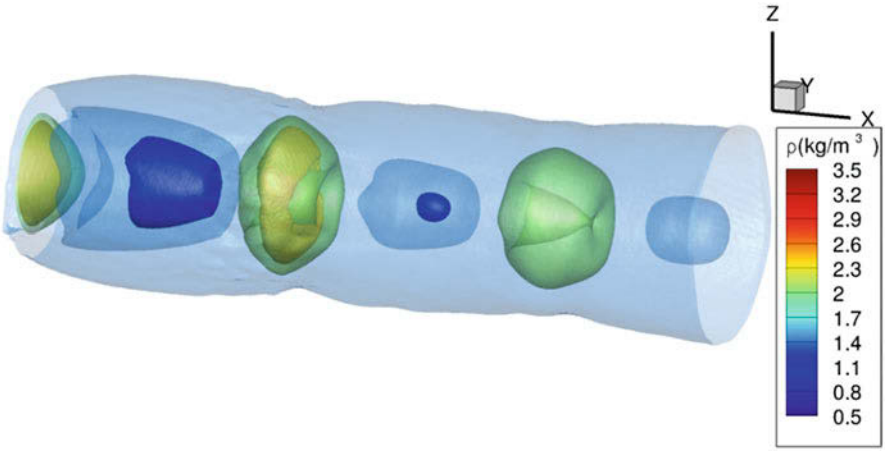

Fig. 4 3D mean density field reconstruction (iso-surfaces) NPR = 5

reconstruction shows very good result, and density levels as well as flow topology are well recovered, with a consistent location of the shock cells compared to schlieren data.

4 Impinged Under-Expanded Jet: Results and Discussions

A set of images obtained with averaged schlieren approach was performed and helped to determine the evolution of the flow topology (structure of the compressible flow, shocks, and impinging flow behavior) and to confirm the highly unsteady nature of the flow. They tend to show that, for the spacing considered here, the impinged wall slightly affects the structure of the jet upstream of the impact. This is confirmed by the measurements of the position (on the axis) and the diameter of the Mach disk which indicate that in both cases the free jet zone is comparable with free conditions' case.

The structure of the flow is given in Fig. 5. The impingement zone is well marked by the presence of an annular shock. One can note also the presence of acoustic waves propagating from this zone of impact through the confined space. The instantaneous schlieren images show that these waves are able to interact strongly with the upstream jet flow (oscillations or deformation of the shock structure around the triple point).

As we consider aeroacoustics of the jets, the spectra acquired reveal the presence of high-amplitude frequency peaks (up to 130 dB) accompanied by their harmonics, and the presence of the plate imposes a second peak which can be associated with the oscillations of the impact zone as pointed out by Henderson [5]. For the dynamic field, the velocity profiles obtained in the axial plane of the jet by LDV as shown in Fig. 6 reveal a recirculation zone localized in front of the stagnation

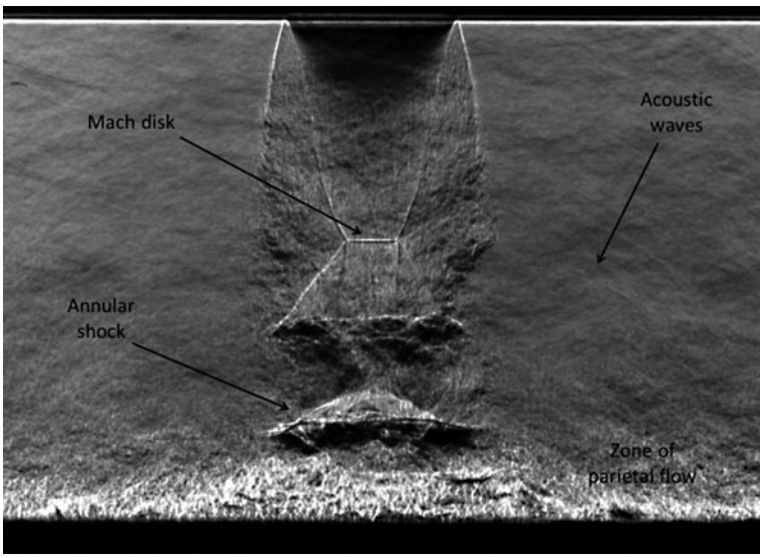

Fig. 5 Impinged under-expanded jet observed by schlieren technique (NPR = 5, T_i = 293 K, h/D = 3)

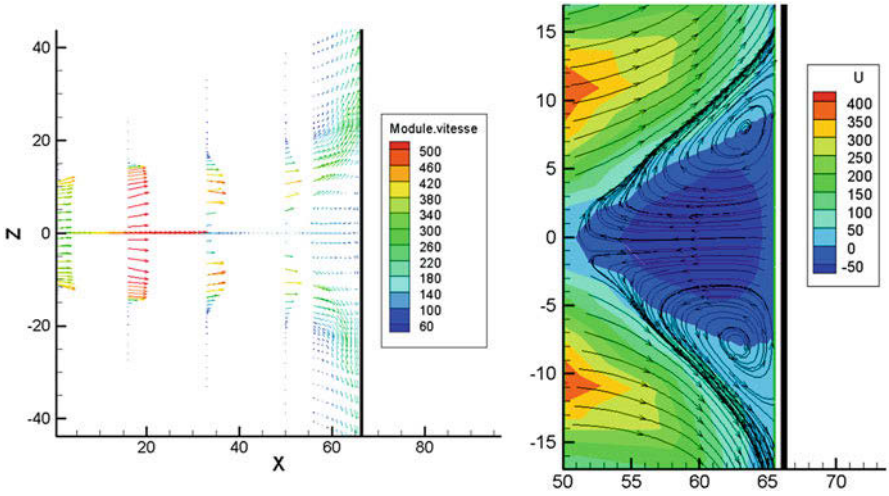

Fig. 6 Averaged velocity obtained by LDV for impinged jet (NPR = 5, T_i = 293 K); left, vector field colored by the norm of velocity (in m.s^{-1}); right, axial velocity field of the impinged region with streamlines (in m.s^{-1})

point. A comparison between schlieren images and mean dynamic field shows the implication of the annular shock which contains this recirculation. Due to the complexity of the flow, the post-processing of the LDV data requires a fine analysis of the velocity histograms obtained for meshing points localized close to shock wave position and strong gradients characterizing mixing layer regions. By this way, we are able to track the presence of shock waves by analyzing the evolution of velocity histogram peaks.

5 Conclusions

A first exploration of an under-expanded jet is performed in order to characterize the topology and a part of the dynamics of both free and impinged flow (with h/D = 3) for ambient conditions (T_i = 293 K) for a nozzle pressure ratio of 5. For impingement case, the data highlight the highly unsteady nature of the flow due to the presence of a large recirculation in the area of impact and the circulation of intense acoustic waves which are reflected in the confined space. In a next step, these results will be completed by additional characterization of the dynamics of the flow. Thermal transfer measurement on wall will be also performed. Moreover, the 3D BOS technique could allow an analysis of the jet density structure dynamics in combination with far-field noise measurements in order to characterize the jet shear layer and shock wave interaction, which will be extended to impingement case. At the end, the completed database will be used as a validation for high-fidelity numerical simulations of the aerothermal configuration.

References

1. E. Franquet et al., Free underexpanded jets in a quiescent medium: A review. Prog. Aerosp. Sci. **77**, 27–53 (2015)
2. J. Soria, O. Amili, Under-expanded impinging supersonic jet flow, in *10th Pacific Symposium on Flow Visualization and Image Processing*, Naples, 15–18 June 2015
3. J. Panda et al., Experimental investigation of density fluctuations in high-speed jets and correlation with generated noise. J. Fluid Mech. **450**, 97–130 (2002)
4. P.S. Cumber et al., Prediction of the structure of turbulent, highly underexpanded jets. AIAA J. **117**, 599–604 (1995)
5. A.V. Antsupov, Properties of underexpanded and overexpanded supersonic gas jets. Sov. Phys. Tech. Phys. **19**(2), 234–238 (1974)
6. H. Ashkenas et al., The structure and utilization of supersonic free jets in low density wind tunnel, in *Advances in Applied Mechanics – Rarefied Gas Dynamics*, (Academic Press, New York, 1966), pp. 84–105
7. F.S. Alvi et al., Experimental and computational investigation of supersonic impinging jets. AIAA J. **40**(4), 599–609 (2002)
8. B. Henderson et al., An experimental study of the oscillatory flow structure of tone-producing supersonic impinging jets. J. Fluid Mech. **542**, 115–137 (2005)
9. F. Nicolas et al., 3D reconstruction of a compressible flow by synchronized multi-camera BOS. Exp. Fluids **58**, 46 (2017)

PIV Studies on the Effect of the Number of Lobes in a Supersonic ESTS Lobed Nozzle

S. K. Karthick, V. Albin, Srisha M. V. Rao, and Gopalan Jagadeesh

Abstract ESTS lobed nozzle is found to be efficient in supersonic jet mixing applications. In this study, the influence of a number of lobes on the aspects of mixing is probed using the 2D-PIV measurements. From the analysis of the obtained 2D velocity field, the kinematics of the lobed nozzle is reported for the first time experimentally. Centerline velocity decay, turbulence intensity, and mass efflux are calculated to compare the influence of a different number of lobes in the lobed nozzle. The conical nozzle is used as the base nozzle for comparison. It is observed that the three-lobed nozzle is efficient in terms of mixing and jet spread. Especially an increment of 70% in the jet spread is observed for three-lobed nozzle. The primary reason for the observed enhancement is due to the higher penetration of the lobe tip into the core flow (by 30% compared with the six-lobed nozzle) which produces larger-scale streamwise vortices than the other cases under consideration.

1 Introduction

Exotic nozzle geometries are found to be an effective passive technique to enhance mixing and entrainment in supersonic jets [1, 2]. They are found to be useful in the design and development of high-performance supersonic ejectors and combustors. Recently, supersonic Elliptic Sharp Tipped Shallow (ESTS) lobed nozzles are found to be efficient in mixing enhancement [3, 4]. These nozzles are easy to produce, and the shallow tips are found to be effective in enhancing the mixing process by producing streamwise vortices with lower total pressure loss. Typical time-averaged flow field observed in the conical nozzle and the four-lobed ESTS nozzle using planar laser Mie scattering (PLMS) imaging is shown in Fig. 1. Key features like free shear layer, weak shocks, and higher jet spread can be easily observed in four-lobed ESTS nozzle (Fig. 1b). However, the sufficient number of lobes required for the optimized geometry of a supersonic ESTS lobed nozzle is still unclear

S. K. Karthick (✉) · V. Albin · S. M. V. Rao · G. Jagadeesh
Department of Aerospace Engineering, Indian Institute of Science, Bangalore, India

A. Sasoh et al. (eds.), *31st International Symposium on Shock Waves 2*,
https://doi.org/10.1007/978-3-319-91017-8_146

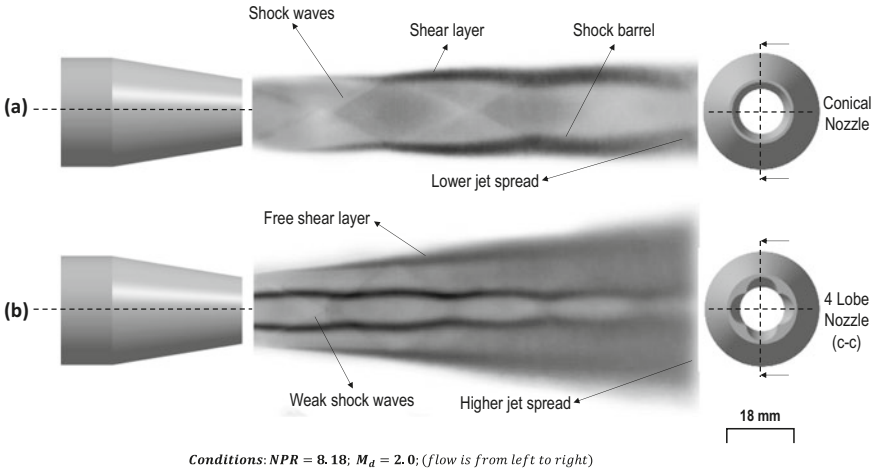

Fig. 1 Time-averaged planar laser Mie scattering (PLMS) image taken along the flow direction for (**a**) Conical nozzle and (**b**) Four-lobed ESTS nozzle (crest-crest, c-c) shows the distinct flow features, especially jet spread, in the case of petal nozzle compared with conical nozzle (conditions: NPR = 8.18; M_d = 2.0; flow is from left to right)

which motivates the authors to study further. Fluid mixing and entrainment can be better understood through the momentum exchange happening between the nearby fluids. The variations going on in the momentum flux of the jet could be easily studied by monitoring the kinematic properties of the moving fluid both spatially and temporally. Two-dimensional planar image velocimetry (2D-PIV) technique is chosen to understand the supersonic free jet flow field from the ESTS and conical nozzle, as it is a nonintrusive optical flow diagnosis to measure the flow velocity at a better spatial resolution.

2 Experiments

Experiments are carried out in the supersonic blowdown facility in LHSR, IISc – Bangalore. Nozzles are mounted at the end of the stagnation chamber. In the case of lobed nozzles, the positions are varied by rotating the nozzle and clamping it using the grub screw. More details regarding the rigging and sizing of the facility can be found in the work of Rao [3].

2.1 2D-PIV Technique

Currently employed 2D-PIV system comprises a Nd:YLF dual-cavity Litron laser (527 nm), operating at 0.8–1.0 kHz repetition (each cavity), with a pulse separation (dt) of 0.7 μs and with a maximum energy of 24 mJ/pulse. Consistent pulse segregation in the double-pulse operation mode of the laser is ensured by using the Laser Time Stabilizer Unit from LaVision. The primary supersonic flow field is seeded using the refined sunflower oil particles in the beginning portion of the stagnation chamber itself. The oil particles are generated using the in-house particle seeder [5] that works on the principle of modified Laskin nozzle. The ambient is seeded with smoke particles so that the entrained flow into the shear layer of the supersonic jet can be captured clearly. The particle size varies between 0.6 and 1.2 μm and provides a response time of 0.8–3.0 μs in the shock-laden flow field. A Phantom Miro 110 camera is used in the frame-straddling mode at full-frame resolution of 1280 × 800 pixels (20 μm pixel width). From the nozzle exit, 12D along the flow direction and 3D along the transverse flow direction are selected as the field of view. The nozzle exit is kept in the middle-left edge of the frame which gives an effective spatial resolution of 0.17 mm/pixel. A 527 nm band-pass filter is used to avoid parasite reflections and stray light from the background. A Nikon AF-S DX Micro 40 mm prime lens is used at f/2.8 to capture the scattering light better in the camera. The laser beam is transported to the required location using the guide arm, and a thin sheet of the laser (<1 mm thick) is formed using the appropriate sheet optics. The laser system and the camera are synced and controlled by the high-speed control (HSC) unit. DaVis 8.4 module is used as the software interface during the operation. Planar velocity fields are computed using the adaptive cross-correlation algorithm with a multi-pass (three times) decreasing window size from 64 × 64 pixels to 32 × 32 pixels. Nearly 800 images are used to represent the time-averaged velocity field, and the uncertainty involved in the velocity field computations is found to be not more than ±15 m/s. A typical schematic of the experimental facility for 2D-PIV studies can be seen in Fig. 2a.

2.2 Flow Conditions

For the cases discussed in this paper, three different numbers of lobes (3, 4, and 6) are considered, and they are compared with the base nozzle that is conical. The key dimensions of the nozzles can be seen in Fig. 2b, c. The nozzle is operated at three different conditions as shown in Table 1. The nozzles are operated for almost 3 s during which the PIV images are acquired. The instantaneous velocity field is represented as $V = \overline{V} + V'$, and the components of the given velocity vector can be represented as $V = u + v$ throughout this paper.

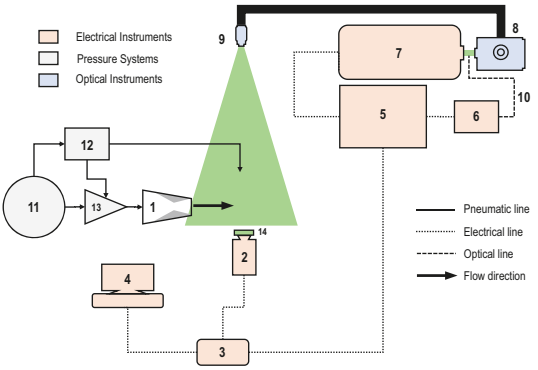

1. Primary supersonic flow nozzle (conical & Petal); 2. Phantom Miro 110 PIV camera; 3. High speed controller; 4. High performance computer; 5. Laser controller/Chiller; 6. Laser time stabilizer; 7. Dual Cavity, Litron: Nd-YLF laser (537 nm); 8. Laser guiding arm; 9. Sheet making optics; 10. Optic fiber; 11. High pressure air storage tanks; 12. Particle seeding unit; 13. Primary flow stagnation chamber; 14. 527 nm band pass filter ; 20. Ball valve

(a)

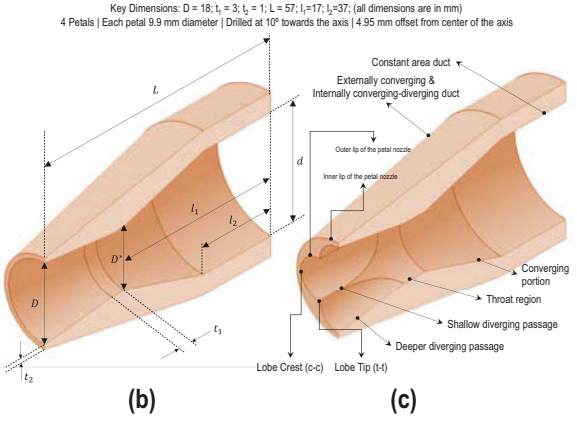

(b) (c)

Table 1 Experimental conditions observed in the nozzle flow studies

M_d	P_o (bar)	NPR	M_j	Nozzle operating condition
2.0	3.54	4.01	1.56	Overexpanded (OE)
	6.52	7.61	1.99	Nearly expanded (NE)
	7.20	8.18	2.03	Slightly under-expanded (UE)

M_d nozzle design Mach number, M_j fully expanded jet Mach number, P_o total pressure of the primary flow, P_a ambient pressure, 0.88 bar, NPR nozzle pressure ratio, P_0/P_a, T_0 total temperature, 300 K

3 Results and Discussions

Most of the discussions will be on the nozzle flows at NPR = 4.01 for brevity. Typical 2D velocity field obtained for different nozzles and at different operating conditions is shown in Fig. 3. From Fig. 3a, it can be seen that the spreading rate is

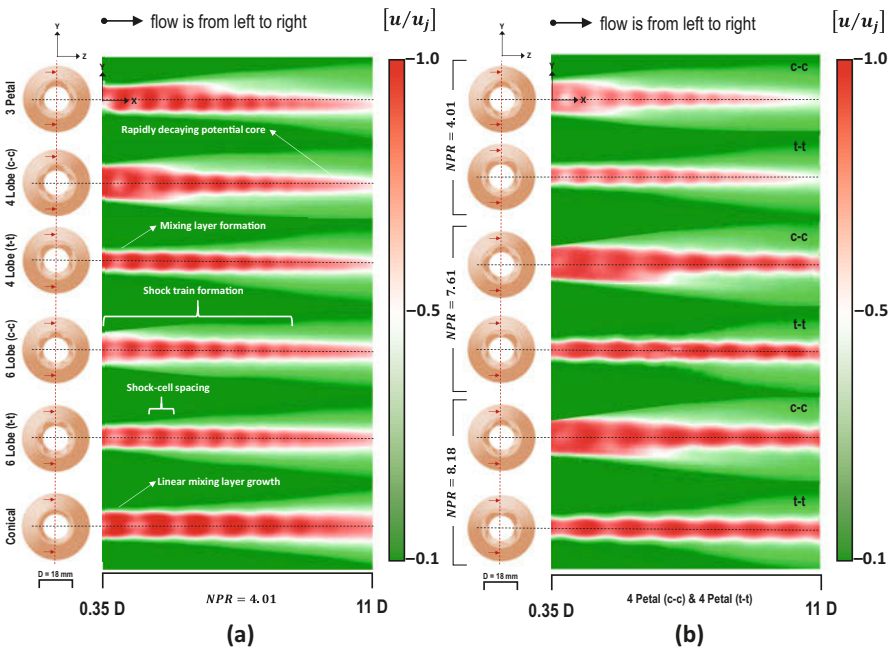

Fig. 3 Time-averaged, normalized 2D velocity field observed for $M_d = 2.0$ nozzle flows; (**a**) Different numbers of lobes in the lobed nozzles and conical nozzle at NPR = 4.01; (**b**) Different NPR in the case of four-lobed nozzle at two cross-sectional planes (crest-crest, c-c, and tip-tip, t-t)

maximum for three-lobed nozzle. Also, from Fig. 3b, it can be seen that the influence of NPR on the jet spread is not significant for the four-lobed nozzle; however, the length of the potential core is affected. The penetration of the lobe tip might be one reason for this behavior.

3.1 Centerline Velocity Decay

In Fig. 4, normalized centerline velocity decay is shown for all the nozzles at NPR = 4.01. From the figure, it is evident that velocity is decaying at a faster rate for the three-lobed nozzle compared with the other cases. On the contrary, the shock strength in the potential core shows a different trend. The peaks and valleys in the near field of the jet (<5D) shed information regarding the shock strength. Analyzing the magnitude between peaks and valleys for all the cases, six-lobed nozzle is found to have a potential core with lower shock strength compared with other cases. However, the shock cell spacing is comparative in the lobed nozzle than in the conical nozzle. As told earlier, for a similar exit area, the penetration of lobe tip in the case of three-lobed nozzle is larger than the six-lobed nozzle (by 30%).

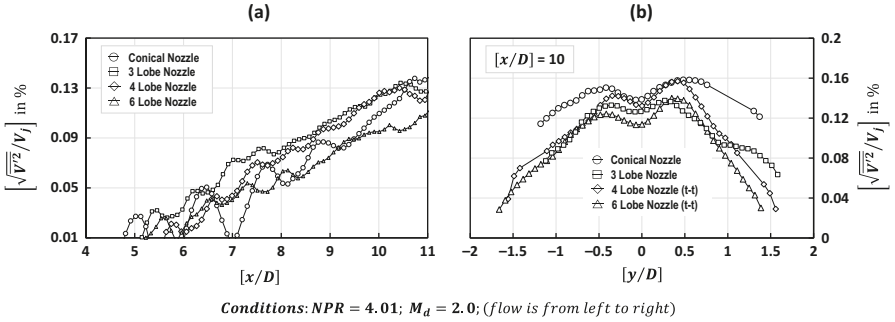

Fig. 4 (**a**) Turbulent intensity variation along the centerline for different lobed nozzles and conical nozzle; (**b**) Turbulent intensity variation along the transverse section (x/D = 10) for different lobed nozzles and conical nozzle (conditions: NPR = 4.01; M_d = 2.0; flow is from left to right)

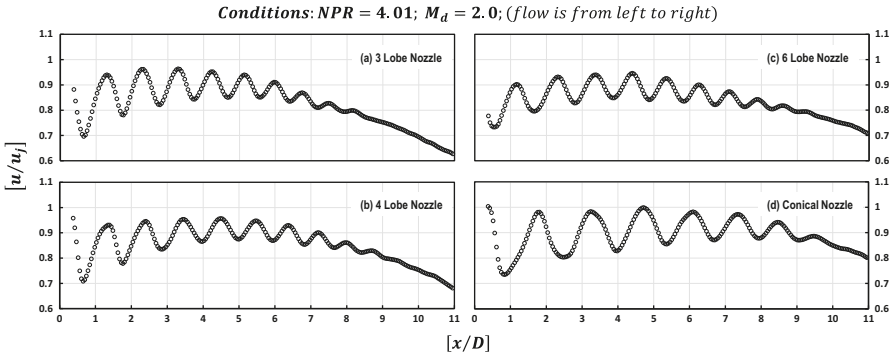

Fig. 5 Normalized centerline velocity decay observed in different nozzles; (**a**) Three-lobed nozzle; (**b**) Four-lobed nozzle; (**c**) Six-lobed nozzle; (**d**) conical nozzle (conditions: NPR = 4.01; M_d = 2.0; flow is from left to right)

3.2 Turbulent Intensity (TI)

Turbulent intensity (TI) variations along the centerline and the transverse sections provide information regarding the mixing aspects and jet spreading. In Fig. 5a, the centerline TI variations for different nozzles are plotted. Along the jet direction, due to the interaction of the inner shear layer with the potential core and the turbulence production due to the shocks, TI increases. Due to higher shock strength in the conical nozzle, the TI fluctuates between 1% and 5% till 8D and gradually increases to 11% at 11D. However, in the case of three-lobed nozzle, the increment in TI is observed from 6D onward and reaches to a maximum of 14% at 11D. This again justifies the argument made in Sect. 3.1. Figure 5b yields information regarding the jet spread at [x/D] = 10. There is a prominent asymmetry in the jet spread (almost by 70%) from the axis line for three-lobed nozzle owing to its asymmetry on the lobe placement in the considered cross section. Except for conical nozzle, lobed nozzles have a comparable jet spread.

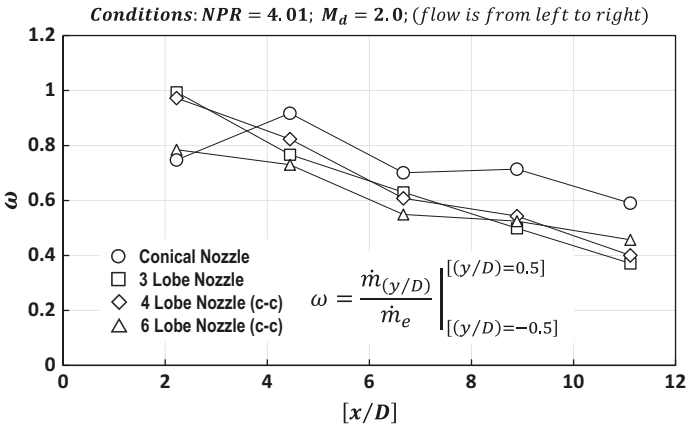

Fig. 6 Variation of mass flux inside the imaginary tube of 1D diameter for different lobed nozzles and conical nozzles. The representation is aimed to qualitatively figure out the effect of the number of lobes through the mass transfer on the jet spread and fluid mixing (conditions: NPR = 4.01; $M_d = 2.0$; flow is from left to right)

3.3 Mass Efflux

To comment on the momentum transferred from the primary flow to the entrained ambient flow for different lobed nozzles, an imaginary tube of diameter 1D is considered, and the ratio of the mass flow rate (ω) is calculated at five different sections. Irrespective of the radial velocity profile obtained for different nozzles, the analysis is carried out to emphasize the influence of lobe numbers qualitatively. From Fig. 6, in the near field, due to higher shock strength, there will be a mass deficient in conical nozzle flows and hence the fluctuations in the trend. But considering the values downstream, it can be seen that the lobed nozzles are effective in transferring the momentum to the entrained secondary fluid. In the considered experiments, the three-lobed nozzle loses ω rapidly by 40% than the conical nozzle. Also, the six-lobed nozzle is observed to lose ω by only 25%. It once again confirms the influence of the lobe tip penetration on the jet spread and mixing. The penetration of the lobe tip plays a prominent role as it dictates the strength of the generated streamwise vortices.

4 Conclusions

Experiments are carried out for a different number of lobes in the ESTS lobed nozzle, and they are compared with the conical nozzle. 2D-PIV measurements are carried out, and the velocity field is used to compare the kinematics of the considered nozzles. Three-lobed nozzle shows better mixing and spreading characteristics

owing to the higher penetration length of the lobe tip than the other nozzle. Further studies in terms of the streamwise vorticity generation and different operating conditions are underway.

Acknowledgment Ministry of Human Resource Development (MHRD), India; Defence Research and Development Organisation (DRDO), India; and Council for Scientific and Industrial Research (CSIR), India.

References

1. T.G. Tillman et al., J. Propuls. Power **8**, 2 (1992)
2. K.B.M.Q. Zaman, J. Fluid Mech. **383**, 197–228 (1999)
3. S.M.V. Rao, G. Jagadeesh, Appl. Therm. Eng. **71**, 1 (2014)
4. S.M.V. Rao et al., Appl. Therm. Eng. **99**, 599 (2016)
5. S.K. Karthick et al., J. Indian Inst. Sci. **96**, 1 (2016)

Numerical Study of Heat Transfer on Confined Under-Expanded Impinging Jet from Slot into a Plenum

Tinglong Huang, Lianjie Yue, and Xinyu Chang

Abstract The aerodynamic thermal loads on under-expanded jet from bleed slot into a plenum are obtained at different conditions. It grossly differs from the unconfined impinging jet due to the appearance of left-confined wall. The numerical results show that at low slot angle, heat flux along impinging wall peaks twice due to the stagnation of high enthalpy flow and the shock wave/boundary layer interactions, whereas only one peak occurs at higher slot angle due to the former mechanism. When impingement angle is larger than 50°, the highest thermal loads change a little. As the impingement height increases, the overall aerodynamic thermal loads decrease at the same freestream conditions. Generally, it is the confined wall that makes the flow behind the plate shock supersonic, which allows the SWBLIs to occur.

1 Introduction

The internal flow path features some complex flow phenomena. Different types of irreversible processes are involved, such as shocks and shock-induced boundary layer separations [1]. As one of the most powerful methods to suppress boundary layer separations, the bleed systems were introduced into scramjet design. However, the bleed slots would suffer from aerothermal load at hypersonic conditions although the bleed can even reduce vortex-induced highly localized thermal loads by eliminating the boundary layer separation [2]. Yue et al. [3] found, besides the maximum thermal load at the stagnation point of the bleed corner, a localized high heat flux occurred within the slot passage, attributed to a boundary layer separation triggered by the bleed barrier shock. But aerodynamic thermal load on solid surfaces, caused by under-expanded jet from bleed slot impinging into a plenum, is still unclear. Under-expanded impingement jet can induce high heat

T. Huang · L. Yue (✉) · X. Chang
Institute of Mechanics, Chinese Academy of Sciences, Beijing, China
e-mail: yuelj@imech.ac.cn

A. Sasoh et al. (eds.), *31st International Symposium on Shock Waves 2*,
https://doi.org/10.1007/978-3-319-91017-8_147

transfer rate on the impinged surface, which would be severe in fully confined hypersonic bleed slot systems.

Under-expanded supersonic impinging jet has attracted many investigators' attention due to high heat transfer rates in the impingement zone. The mean flow visualization and properties, including pressure distributions and heat transfer rates, and the instantaneous flow field of axisymmetric or two-dimensional impingement jet have been studied extensively [4–7]. It was revealed that the jet impingement essentially depends on the following parameters, the ratio of total pressure and ambient pressure *Pt/Pa*, the jet-to-plate distance *h/d*, and impingement angle θ. Donaldson and Snedeker [4] noted that the impinging flow field can be generally divided into three regions, including the primary jet flow region upstream the strong interaction effects of impingement, the impingement region, and the wall jet region. The impingement region sometimes appears a stagnation bubble [8, 9]. For highly under-expanded impinging jet, a Mach disk occurs and interacts with jet shock. For oblique jet impingement, Yusuke et al. [10] classified the flow pattern into three types by the observation of shock wave configurations and the pressure maps, which can be estimated based on θ and *h/d*, and the shock cell length of corresponding free jet. Song et al. [11] observed that the low recovery factor region moves downstream and the cooling/heating effect declines overall as θ decreases.

Although in-depth understanding has been achieved regarding the impingement jet flow, aforementioned works mainly focus on the unconfined jet impingement. In the bleed system, the impingement jet flow characteristics would be much different due to the geometric confinement. It is necessary to investigate the flow patterns and the associated aerodynamic thermal loads for the fully confined under-expanded supersonic impinging jet.

2 Numerical Method and Computational Details

2.1 Numerical Methods

The steady-state Reynolds-averaged Navier-Stokes equations are solved for two-dimensional turbulence flow by using commercial code CFD++. The turbulence model of k-ω SST is employed to enclose the governing equations. Our previous studies have verified that the adopted numerical algorithm is very credible and can efficiently resolve high Mach number flows and aerodynamic heating, including type IV shock interference and shock wave/boundary layer interactions [3, 12, 13].

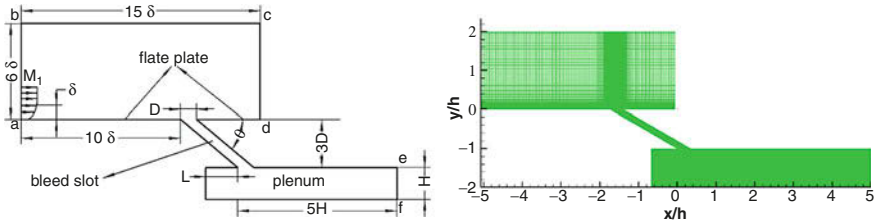

Fig. 1 Computational domain, grid mesh distribution

2.2 Computational Details

Figure 1 shows the solution domain used in our two-dimensional simulations. It includes three regions, a region above the plate, a bleed slot, and a plenum. The conjunction of two walls is simply a sharp corner. At the inflow boundary a-b, a freestream high enthalpy airflow with $T_t = 1824.5$ K, $Ma_1 = 4$, $p_1 = 22{,}755$ Pa, and $Re = 1.071 \times 106\ \mathrm{m}^{-1}$ is imposed, which approximately corresponds to the flow conditions in the internal contraction section of hypersonic inlets operating at flight Mach number of 6 and altitude of 26 km [3]. Bleed systems are usually installed around this section [2, 14, 15]. The inflow boundary a-b has a turbulent boundary layer with stream-wise velocity profile described by the Van Direst profile with one-seventh power law, where the boundary layer thickness δ is 2.5 mm. At the outflow boundary c–d, all flow parameters are extrapolated from interior region. At the plenum outflow boundary e–f, a back pressure boundary which allows reversed flow is applied. At all solid surfaces, no-slip isothermal temperature conditions are imposed, where $T_w = 300$ K.

Quadrilateral structured cells are used in the simulation as shown in Fig. 1. The first mesh size normal to the wall is 1 μm, corresponding to $y + < 1$ on the solid surface. The grid number in turbulent boundary layer is greater than 50 so as to resolve the temperature gradient well. The total number of mesh grids is about 0.18–0.25 million.

3 Numerical Results and Discussion

The flow patterns and aerodynamic thermal loads on the wall are discussed in the present section. Slot angle is changed from 30° to 90°. Detailed flow patterns and aerodynamic thermal loads within the bleed slot region were studied by Yue et al. [3]. Present works will pay more attention to the plenum region. In the following discussions, the local heat flux rates are nondimensionalized with respect to freestream conditions:

$$St = \frac{q_w}{\rho_1 U_1 C_p (T_t - T_w)} \tag{1}$$

where q_w, ρ_1, U_1, C_p, T_t, and T_w denoted the local heat flux on the solid surface, freestream density, freestream velocity, local specific heat, total temperature, and wall temperature, respectively.

3.1 Effects of Slot Angle on Aerodynamic Thermal Loads

Figure 2 shows the Mach contour in the plenum region with different slot angles where $h/d = 3$ and the back pressure on the exit of plenum doesn't exert influence on the upstream flow. Figure 3 shows the schematic picture of flow structures in the plenum region. At $\theta = 30$–$40°$, on the left of plenum are two large recirculation regions R1 and R2 with opposite rotation direction. On the middle, a shock (plate shock wave) over the impinged wall occurs. The plate shock induces the recirculation region SB1. An incident shock wave occurs in the core flow region and intersects with plate shock. The transmitted incident shock interacts with boundary layer on the impinged wall and induces a separation bubble SB. Between the separation bubble SB and SB1 is an aerodynamic throat. For $\theta > 40°$, the separation bubble SB disappears. At $\theta = 90°$, the left two recirculation regions combine and lead to secondary impingement to the left-confined wall.

The corresponding Stanton number distributions along the impinged surface at $\theta = 30°$ are shown in Fig. 3. There are two peaks of heat flux on the impinged wall. The left heat peak is relatively small and is considered to be generated by the stagnation of the supersonic flow. The right heat peak locates at the reattachment point of separation bubble induced by incident shock and is the highest heat flux

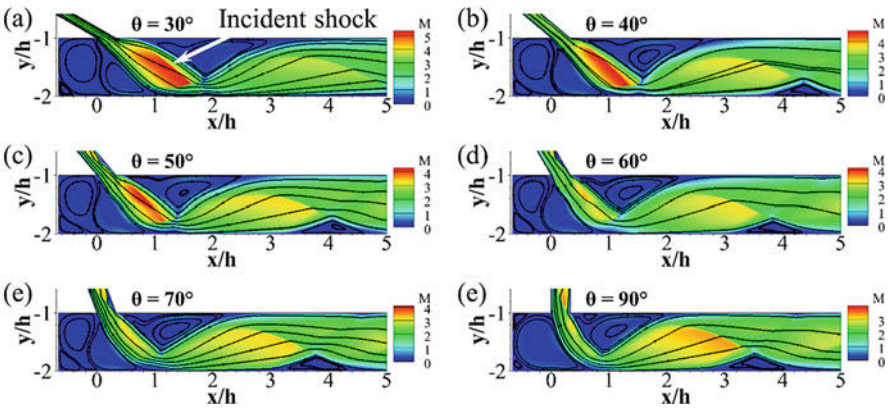

Fig. 2 Mach contour map on the plenum at various slot angles

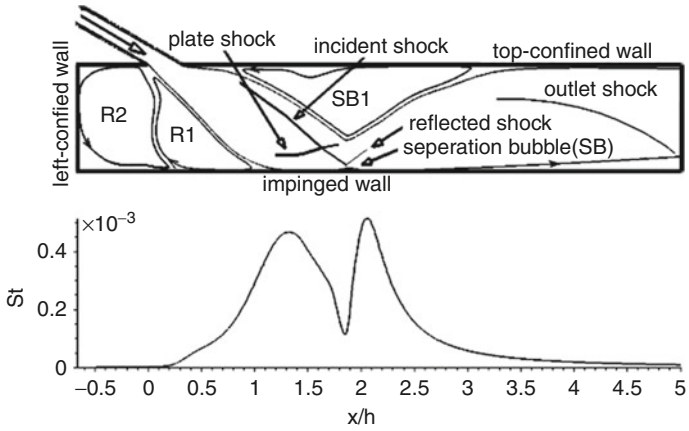

Fig. 3 Schematic of flow structures, St distributions on the impinged wall at $\theta = 30°$

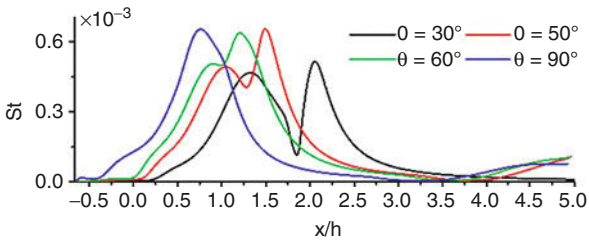

Fig. 4 Stanton number distributions on the impinging wall at various slot angles

peak due to the SWBLIs. Near the recirculation region R2, the heat flux is low which indicates the difficulty of the high enthalpy flow to reach this region.

The St number distributions along the impinged wall are presented in Fig. 4. For $\theta = 30$–$60°$, the oblique impinging jet generates two peaks. And the first peak is 0.00047, 0.00051, 0.00049, and 0.00051, respectively. It changes a little as the slot angle increases as indicated. The second peak due to SWBLIs is 0.00052, 0.00073, 0.00066, and 0.00064, respectively. For $\theta = 70°$ and $90°$, only one peak appears on the impinged wall. Their maximum values of St number are 0.00061 and 0.00065, respectively. Comparing all the highest peaks at various slot angles, the highest heat flux peak changes a little when $\theta > 50°$.

The St number distributions along the top-confined wall and left-confined wall are shown in Fig. 5. The local maximum heat flux appears on the reattachment position of the recirculation region SB1. These peaks are 0.000227, 0.000252, 0.000263, 0.000224, 0.000249, and 0.000223, for $\theta = 30$–$90°$, respectively. The highest of these peaks is about 44% of the corresponding highest St on impinged wall. At the corner of the slot exit, it is always a high thermal load area due to the high transport speed of jet flow and small blunted radius. For the left-confined wall, the maximum heat flux rate is no more than 3% of heat peak on impinged wall for $\theta < 90°$ due to the low-speed separated flow in this region. At $\theta = 90°$, the thermal

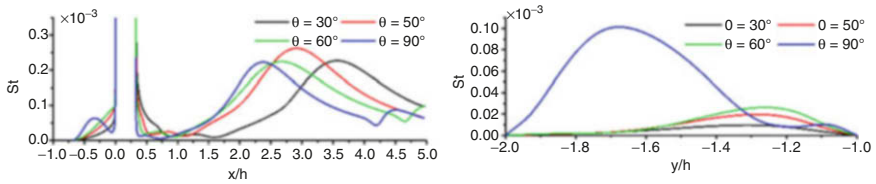

Fig. 5 St number distributions at various θ on top-confined wall, left-confined wall

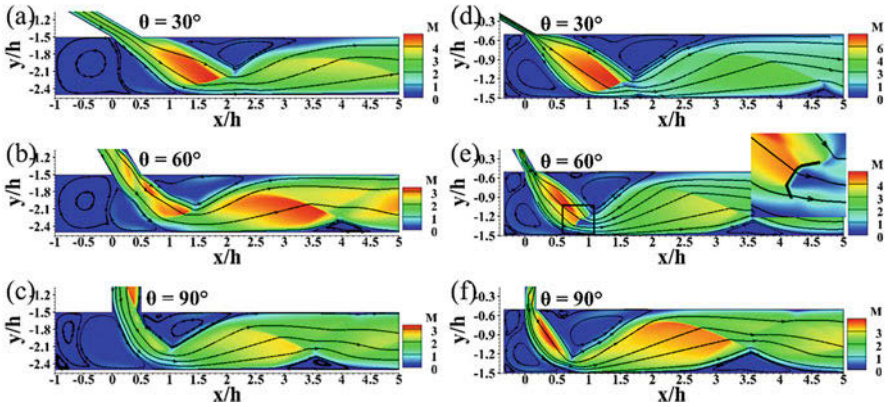

Fig. 6 Mach number contour map at various θ and at $h/d = 2$ (a, b, c), 6 (d, e, f)

loads increase dramatically due to the subsonic jet impingement. But the peak heat flux is still no more than 16% of the one on impinged wall.

3.2 *Effects of Plenum Height*

To investigate the effects of plenum height on aerodynamic thermal loads, three typical slot angles, $\theta = 30°$, 60°, and 90°, and ratio of $h/d = 2$, 3, 6 are selected to extensively discuss. Figure 6 shows that the flow patterns change a little as h/d increases. When the plenum height increases, the remarkable change is the appearance of Mach stem structure at $h/d = 6$ and $\theta = 60°$.

Figure 7 shows that for a same θ, almost all distributions maintain the same profile for different h/d, but the maximum St number decreases as h/d increases due to the drop of the capacity for energy transport.

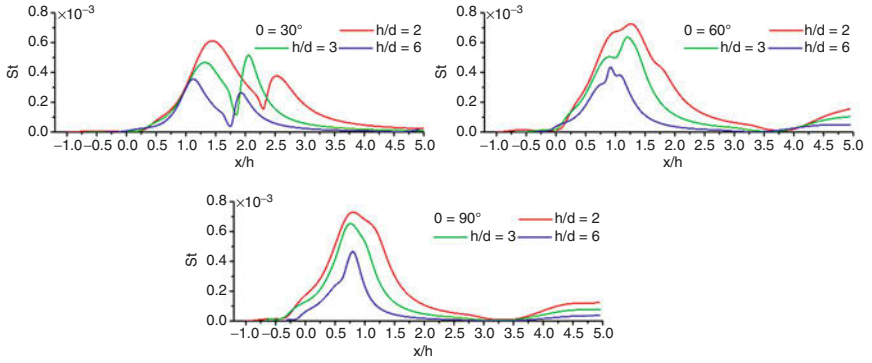

Fig. 7 Stanton number distributions on the impinging wall at various θ and h/d

4 Conclusions

A two-dimensional numerical investigation is conducted to study the aerodynamic thermal loads on the surfaces of plenum of bleed systems in high enthalpy flows. Bleed slot angle and plenum height are chosen to examine the influences of the appearance of confined wall. Numerical results show that due to the confinement of confined wall, several recirculation regions occur. In addition, the shock wave boundary layer interactions (SWBLIs) play an important role on heating the plenum and bleed slot surfaces. In this fully confined supersonic impinging jet flow, the mechanism of aerodynamic heating is mainly the same as the reattachment position of separation bubble induced by SWBLI effects.

At fixed freestream conditions, for lower bleed slot angle, a key separation bubble is induced by SWBLIs over the impinging wall, resulting in a maximum heat flux at the reattachment position. As the slot angle increases, the maximum and averaged heat flux increases.

When the plenum height increases, the flow patterns change a little except the case with $\theta = 60°$ and $h/d = 6$. In this special case, Mach stem occurs due to the overlarge deflection angle. However, the overall thermal loads reduce as h/d increases due to the decrease of mass flow.

References

1. J. Häberle, A. Gülhan, Experimental investigation of a two-dimensional and a three-dimensional scramjet inlet at Mach 7. J. Propuls. Power **24**(2008–09), 1023–1034 (2008)
2. T. Kouchi, T. Mitani, G. Masuya, Numerical simulations in scramjet combustion with boundary-layer bleeding. J. Propuls. Power **21**(4), 642–649 (2012)
3. L. Yue et al., Aerothermal characteristics of bleed slot in hypersonic flows. Sci. China Phys. Mech. Astron. **58**(10), 1–14 (2015)

4. C.D. Donaldson, R.S. Snedeker, A study of free jet impingement. Part 1. Mean properties of free and impinging jets. J. Fluid Mech **45**(2), 281–319 (1971)
5. D. Schulte, A. Henckels, U. Wepler, Reduction of shock induced boundary layer separation in hypersonic inlets using bleed. Aerosp. Sci. Technol. **2**(4), 231–239 (1998)
6. B. Henderson, J. Bridges, M. Wernet, An experimental study of the oscillatory flow structure of tone-producing supersonic impinging jets. J. Fluid Mech. **542**, 115–137 (2005)
7. F. Alvi, J. Ladd, W. Bower, Experimental and computational investigation of supersonic impinging jets. AIAA J. **40**(4), 599–609 (2002)
8. F. Alvi, K. Iyer, Mean and unsteady flowfield properties of supersonic impinging jets with lift plates. AIAA paper **1829**, 1999 (1999)
9. G. Kalghatgi, B. Hunt, Occurrence of stagnation bubbles in supersonic jet impingement flows. Aeronaut. Q. **27**, 169–185 (1976)
10. Y. Nakai, N. Fujimatsu, K. Fujii, Experimental study of underexpanded supersonic jet impingement on an inclined flat plate. AIAA J. **44**(11), 2691–2699 (2006)
11. J. Song et al., Thermal characteristics of inclined plate impinged by underexpanded sonic jet. Int. J. Heat Mass Transf. **62**, 223–229 (2013)
12. H. Lu, L. Yue, X. Chang, Flow characteristics of hypersonic inlets with different cowl-lip blunting methods. Sci. China Phys. Mech. Astron. **57**(4), 741–752 (2014)
13. H. Lu et al., Interaction of isentropic compression waves with a bow shock. AIAA J. **51**(10), 2474–2484 (2013)
14. J. Häberle, A. Gülhan, Internal flowfield investigation of a hypersonic inlet at Mach 6 with bleed. J. Propuls. Power **23**(2007–10), 1007–1017 (2007)
15. T. Mitani et al., Boundary-layer control in Mach 4 and Mach 6 scramjet engines. J. Propuls. Power **21**(4), 636–641 (2005)

Correction to: Three-Dimensional Instability of Shock-Wave/ Boundary-Layer Interaction for Rocket Engine Nozzle Applications

A. Sansica, J.-Ch. Robinet, Eric Goncalves, and J. Herpe

Correction to:
Chapter 67 in: A. Sasoh et al. (eds.), *31st International Symposium on Shock Waves 2*,
https://doi.org/10.1007/978-3-319-91017-8_67

The original version of the book was inadvertently published with incorrect sequence of authors. The correct sequence of authors has now been corrected as

"A. Sansica, J.-Ch. Robinet, Eric Goncalves, and J. Herpe".

The updated online version of this chapter can be found at
https://doi.org/10.1007/978-3-319-91017-8_67

A. Sasoh et al. (eds.), *31st International Symposium on Shock Waves 2*,
https://doi.org/10.1007/978-3-319-91017-8_148

Correction to: 31st International Symposium on Shock Waves 2

Akihiro Sasoh, Toshiyuki Aoki, and Masahide Katayama

Correction to:
A. Sasoh et al. (eds.), *31st International Symposium on Shock Waves 2*,
https://doi.org/10.1007/978-3-319-91017-8

Chapter 2
The original version of the chapter was inadvertently published as non-open access. This chapter is now available open access under a Creative Commons Attribution 4.0 International License via link.springer.com.

Chapter 58
The original version of the book was inadvertently published with the second author's name incorrectly spelt as "B. Dia Zeidan". The author's name has now been updated as "Dia Zeidan".

The updated online version of these chapters can be found at
https://doi.org/10.1007/978-3-319-91017-8_2
https://doi.org/10.1007/978-3-319-91017-8_58

A. Sasoh et al. (eds.), *31st International Symposium on Shock Waves 2*,
https://doi.org/10.1007/978-3-319-91017-8_149